IAEA-TECDOC-799

Atomic and molecular data for radiotherapy and radiation research

Final report of a co-ordinated research programme

INTERNATIONAL ATOMIC ENERGY AGENCY

May 1995

The IAEA does not normally maintain stocks of reports in this series. However, microfiche copies of these reports can be obtained from

INIS Clearinghouse
International Atomic Energy Agency
Wagramerstrasse 5
P O Box 100
A 1400 Vienna, Austria

Orders should be accompanied by prepayment of Austrian Schillings 100,– in the form of a cheque or in the form of IAEA microfiche service coupons which may be ordered separately from the INIS Clearinghouse.

The originating Section of this publication in the IAEA was:

Nuclear Data Section
International Atomic Energy Agency
Wagramerstrasse 5
P.O. Box 100
A-1400 Vienna, Austria

ATOMIC AND MOLECULAR DATA FOR RADIOTHERAPY
AND RADIATION RESEARCH
IAEA VIENNA, 1995
IAEA-TECDOC-799
ISSN 1011-4289

Printed by the IAEA in Austria
May 1995

FOREWORD

The advent of cancer therapy with the use of varous particle beams requires full understanding of radiation interactions with tumours and other materials for its optimal perfomance. Relevant knowledge in this respect comes from physics, chemistry, biology, medicine, and related technologies. A basic item of required knowledge are the physical data that characterize the earliest phase of radiation interactions on the molecular level, which sets a stage for subsequent chemical and biological effects including the control of cancer. In view of the necessity of an interdisciplinary approach to full understanding, it is desirable to compile the physical data, to evaluate them for reliability, and to present them in a comprehensive form for use by radiation scientists in general.

Recognizing this need, the Nuclear Data Section of the International Atomic Energy Agency launched the Co-ordinated Research Programme (CRP) on Atomic and Molecular Data for Radiotherapy and Radiation Research. The present volume is a comprehensive report of the programme.

The germ of ideas for the CRP was born at a meeting at Rijswijk, Netherlands, in 1985. The ideas were fully discussed and the scope of the CRP was established at a follow-up meeting held in Vienna in 1988. The CRP, which held three meetings altogether, was commissioned to survey the current status of atomic and molecular data needed for radiotherapy and related research, to identify outstanding problems suitable for study in the near future, and to present findings in the form of a comprehensive report for the benefit of data users and producers. Although the relevance of certain atomic and molecular data to radiation interactions with matter is generally understood, it is appropriate to discuss briefly the needs and availability of specific kinds of atomic and molecular data that are required for special purposes.

In radiotherapy, the clinician must design methods and instruments to assure that a desired dose will be delivered to a specified region of treatment, with a minimal dose delivered elsewhere in the human body. A central problem here is accurate dosimetry, which often rests on the knowledge of certain data. Examples of such data are stopping powers (discussed in Chapter 7) and ionization yields of human tissue substances and of materials used in dosimetry, for various charged particles (discussed in Chapter 8). Needs for data of improved quality and quantity in this context are especially notable for high-energy ions and for low-energy recoil ions resulting from the interactional neutrons with tissue substances, as fully described in Chapter 1.

More generally, in radiation research one addresses a fundamental question: What are the physical and chemical mechanisms that lead to eventual changes in matter caused by ionizing radiation? This question is important in many contexts including dosimetry, probing and diagnosis in medicine or materials science, as well as industrial processing of materials. It is also crucial to the estimation of the risk of health effects of all radiations present in our environment. Some of these radiations come from natural sources such as cosmic rays and terrestrial radioactivity, and others from human activities such as nuclear energy technology and the use of radiation in medicine and industry. In most applications radiation doses relevant to the assessment of risk estimate are low. Biological effects of such low doses are minute and therefore difficult to determine through direct measurements. For this reason, the study of the underlying mechanisms of radiation action is important. When it is fully developed, the knowledge of these mechanisms should permit us to predict the low-dose effects reliably.

EDITORIAL NOTE

In preparing this publication for press, staff of the IAEA have made up the pages from the original manuscripts as submitted by the authors. The views expressed do not necessarily reflect those of the governments of the nominating Member States or of the nominating organizations.

Throughout the text names of Member States are retained as they were when the text was compiled.

The use of particular designations of countries or territories does not imply any judgement by the publisher, the IAEA, as to the legal status of such countries or territories, of their authorities and institutions or of the delimitation of their boundaries.

The mention of names of specific companies or products (whether or not indicated as registered) does not imply any intention to infringe proprietary rights, nor should it be construed as an endorsement or recommendation on the part of the IAEA.

The authors are responsible for having obtained the necessary permission for the IAEA to reproduce, translate or use material from sources already protected by copyrights.

CONTENTS

PLEASE BE AWARE THAT
ALL OF THE MISSING PAGES IN THIS DOCUMENT
WERE ORIGINALLY BLANK

Chapter 1

DEVELOPMENT OF PARTICLE THERAPY IN CANCER MANAGEMENT. EXPECTATIONS AND JUSTIFICATION OF THE HEAVY-ION THERAPY PROGRAMMES

A. Wambersie
Service de Radiothérapie, Neutron- et Curiethérapie,
Cliniques Universitaires St-Luc, Université Catholique de Louvain,
Brussels, Belgium

1.1. INTRODUCTION. PRESENT STATUS OF CANCER MANAGEMENT

Today about 45 % of all cancer patients can be cured (an average for all cancer types)[**1**] [**2**].

At the moment of the first admittance, around 65 % of the patients are presenting with localized tumours. About 2/3 of them are cured either by surgery (22 % of the total number of patients), radiotherapy (12 %) or a combination of both treatment modalities (6 %) (Table 1.1). In this group of patients, with localized tumours, with probable but unproved subclinical metastatic disease, chemotherapy or immunotherapy, used as an adjuvant treatment, may prolong life and maybe cure some additional patients.

Among the 35 % other patients presenting , at the first consultation, with either inoperable or metastatic disease, only 5 % will be cured by combined treatment including radiotherapy, chemotherapy and/or immunotherapy.

The most prominent progress in this field has been made by the medical treatment of solid pediatric tumours, leukemias and lymphomas, and testicular tumours. These tumours represent about 5 % of all cancers seen in a general population.

TABLE 1.1

Summary of the present situation concerning cancer cure rate		
		Cure rate
Patients presenting with localized tumour:	65 %	
cured by surgery		22 %
cured by radiotherapy		12 %
cured by combination of surgery and radiotherapy		6 %
Patients presenting with inoperable or metastatic disease :	35 %	
cured by combined treatment including e.g. chemo-and immunotherapy	5 %	
Total :	100 %	45 %

After Devita [1]

In any case, a strong effort is needed to improve local control of the tumours if we want to see a reduction in the present cancer mortality rate, which is not declining as fast as one may have hoped [**2**] [**3**] [**4**]. Following Devita, it is "axiomatic that you must control local disease if you are ultimately to cure any cancer patient". In fact, it has been shown that 1/3 of the patients dying with cancer had uncontrolled local disease. If local failure could be reduced by 50 %, one could expect a 10 to 15 % improvement in cure rate [**5**].

The techniques of surgery have already reached a very high level of efficiency. Further improvement will be seen in a reduction of the mutilating procedures (limb sparing operation, breast conserving treatment, reduction of colostomies and urinary diversions). On the other hand wider excisions are still foreseeable in relation with safer anesthesiology, intensive care support and improvement in reconstructive surgery. The association of surgery with irradiation on a wider scale will help to increase the local control rate.

Radiotherapy is still open to new developments. In the field of radiobiology (differential effect) , future improvement can be expected from the use of better fractionation schedules or new radiosensitizers. But it is through the development of the irradiation techniques that the most promising progress can be expected. The increase in dose to the tumour, without exceeding the tolerance dose of the surrounding normal tissues, has always been the key to better clinical results. Many new techniques like stereotactic radiosurgery, intra-operative radiotherapy, high dose-rate brachytherapy, conformation therapy offer already encouraging results.

However, in this paper, will shall concentrate on the application of new types of radiation qualities : proton beams, fast neutrons and heavy ions.

When discussing the potential value of non-conventional types of radiations, one has to distinguish :

- particle beams which only improve the physical selectivity of the irradiation, i.e. the dose distribution (e.g. proton beams or helium ion beams);

- high-LET radiations which produce different types of biological effects, and which aim at improving the differential effect between tumour and normal tissues (e.g. : fast neutrons);

- the two approaches can be combined and one could seek after a high physical selectivity with high-LET radiation. This can be achieved with heavy ions.

A large number of patients could benefit from progress in cancer management. Indeed, the two following evaluations have to be kept in mind. In the year 1980, there were 730 000

deaths attributed to cancer in the European Community countries, and there were 1 186 000 new (incident) cases in that year alone [6]. If the current prevention programmes are not effective, these numbers will further increase. These estimates exclude non-melanoma skin cancers which, although a rare cause of death, nevertheless demand adequate medical care.

1.2. IMPROVEMENT OF THE PHYSICAL SELECTIVITY WITH PROTON BEAMS (OR HELIUM ION BEAMS)

1.2.1 RATIONALE

Historically, the major improvement in the efficiency of radiation therapy was the replacement of conventional X-rays (200 kV X-rays) by high-energy photons or electrons [7]. The clinical benefit was rapidly evident for all, or for the majority, of the patients (Table 1.2). This illustrates the importance of the physical selectivity in radiation therapy.

TABLE 1.2

Improved survival of several types of cancer when treated with megavoltage radiotherapy

Localization / Type of cancer	Survival rate (%) with kilovoltage X-rays (1955)	Survival rate (%) with megavoltage X-rays (1970)
Hodgkin's disease	30-35	70-75
Cancer of the cervix	35-45	55-65
Cancer of the ovary	15-20	50-60
Cancer of the bladder	0-5	25-35
Cancer of the prostate	5-15	55-60
Seminoma of the testis	65-70	90-95
Embryonal cancer of the testis	20-25	55-70
Cancer of the nasopharynx	20-25	45-50
Cancer of the tonsil	25-30	40-50
Retinoblastoma	30-40	80-85

From Conquest of Cancer, Report of the National Panel of Consultants, prepared for the Committee on Labour and Public Welfare of the United States Senate, November 1970, p. 51. [7].

We are now close to making a further step : the introduction of proton beams. The characteristics of the proton beams make them superior to high-energy photons from the point of view of the physical selectivity. No advantage can be expected from the radiobiological point of view : for the high-energies required to the protons in external beam therapy we stay in the field of low-LET radiations. On the other hand, at known doses, no unexpected radiobiological effects could be feared [8]. For the present discussion, we can assume that helium-ion beams are similar to proton beams from the radiobiological point of view.

It is logical to expect that, as in the past with the replacement of 200 kV X-rays by high-energy X-rays, a further improvement of the physical selectivity will result in a further improvement in the clinical results. Indeed, the available clinical data indicate a clinical benefit for the selected tumour types for which proton beams have been already applied.

In principle, the best indications for proton beams are radioresistant tumours, relatively small in size, located close (or adjacent to) radiosensitive critical normal structures.

1.2.2 PROTON BEAMS FOR UVEAL MELANOMA

Among the tumours for which the excellent physical selectivity of the proton beams could be mostly exploited, uveal melanoma is probably one of the best examples. Between 1961 and

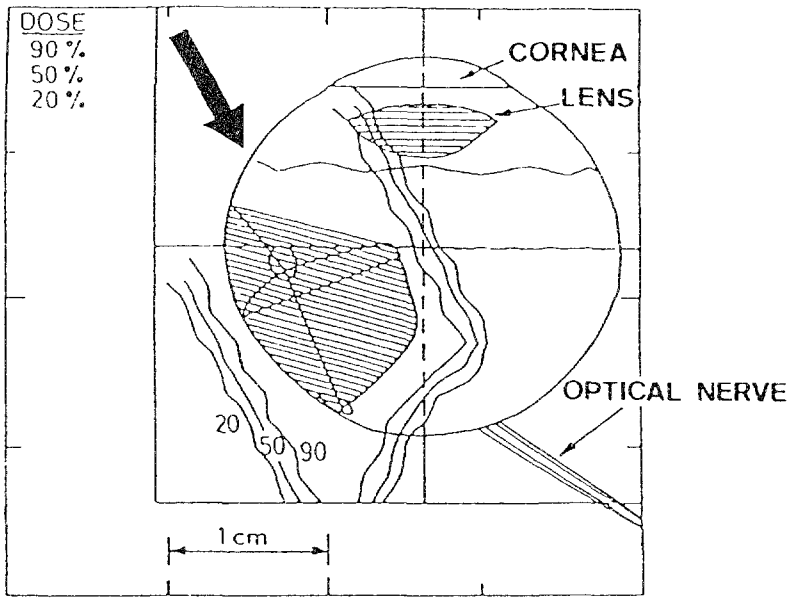

Figure 1.1

Protontherapy of uveal melanoma. Dose distribution for a 60 MeV proton beam; the Bragg peak has been spread out by modulating the energy from 0 to 46 MeV. The tumour (hatched area), as well as some normal structures (cornea, lens, optic nerve) are indicated. The thick arrow corresponds to the beam axis and the 90 %, 50 % and 20 % isodoses are drawn. Proton beams allow achieving a homogeneous irradiation of the target volume with an efficient sparing of the normal tissues. However, an accurate patient positioning is required.
[Courtesy Ch. Perret, PSI-Villigen, 1986]

TABLE 1.3

THE PROTON THERAPY FACILITIES WORLDWIDE
(1 January 1994)

Location - Country			Date of first treatment	Date of * last treatment	Total number of patients	Date of evaluation
USA	California	Berkeley-184	1954	1957	30	
	Massachusetts	Harvard	1961	→	6 010	Dec. 1993
	California	Loma Linda	1990	→	682	Dec 1993
	Indiana University		1993	→	1	Dec. 1993
JAPAN		Chiba	1979	→	86	June 1993
		Tsukuba	1983	→	354	Sept. 1993
SOUTH AFRICA		NAC-Faure	1993	→	6	Nov 1993
EUROPE	Sweden	Uppsala	1957	1976	73	(1)
		Uppsala	1989	→	41	Dec 1993 (2)
	Russia	Dubna	1967	1974	84	(3)
		Moscow	1969	→	2 550	Oct 1992
		St Petersburg	1975	→	719	June 1991
		Dubna	1987	→	24	Aug. 1992 (4)
	U K.	Clatterbridge	1989	→	463	Jan 1994
	Switzerland	PSI-Villigen	1984	→	1.600	March 1994
	France	Nice	1991	→	337	Dec 1993
		Orsay	1991	→	334	Dec 1993
	Belgium	Louvain-la-Neuve	1991	→	24	Dec. 1993

* If the facility was closed.
(1) first proton therapy programme in Uppsala
(2) new proton therapy programme in Uppsala
(3) first proton therapy programme in Dubna
(4) new proton therapy programme in Dubna.

March 1994, 2004 patients suffering from uveal melanoma were treated at the Harvard University Cyclotron in the USA. A local control rate of 96 % and a survival rate of 80 % were reported [9]. Similar results were obtained with helium ion beams at Berkeley, where the local control rate was 96 % [10].

As a result of these promising observations, several other centres initiated a proton therapy program. Among them the OPTIS program was started at PSI-Villigen in Switzerland in 1984 and more that 1,600 patients with uveal melanoma were treated with protons from 1984 to March 1994 (Fig. 1.1) [11] [12].

In addition, 3 other centres in Europe are treating uveal melanoma with proton beams : Clatterbridge in UK, Nice and Orsay in France. The numbers of patients treated up to December 1993 in these 3 centres reached 463, 337 and 334 respectively [13].

1.2.3 PROTON BEAMS FOR TUMOURS OF THE CNS AND SKULL

Besides uveal melanoma, there are other localizations where the high physical selectivity of the proton beams can be fully exploited, e.g. chordomas or chondrosarcomas of the base of the skull, and paraspinal tumours. At the Harvard cyclotron, local control rates of 82 % and 63 % were reported at 5 and 10 years respectively [**14**]). A local control rate (actuarial at 3 years) of 70 % for chordomas, chondrosarcomas and meningiomas was reported from Berkeley after helium ion treatment [**15**] [**16**].

The potential benefit of proton beams compared to X-ray beams for the treatment of brain lesions especially in children has been evaluated (Figures 1.2, 1.3, 1.4) [**17**]. A significant reduction in late sequellae (mental retardation) can be expected.

1.2.4 OTHER CLINICAL INDICATIONS

There is an increasing number of programmes and new projects which aim at treating with protons many other tumour types, and larger proportions of patients. As a matter of fact, since an improved physical selectivity is, in itself, always a benefit, all photon patients could be, in principle, potential candidates for proton treatment.

Prostatic adenocarcinomas, soft tissue sarcomas, some head and neck and rectal tumours are treated with protons at the Harvard cyclotron [**14**]. In Japan, 250 MeV protons are used at the University of Tsukuba for different localizations, including deep seated tumours [**18**]. The Russian proton therapy programmes have been reviewed [**19**] [**20**].

A new proton therapy programme has been initiated at the Svedberg Laboratory in Uppsala-Sweden. From April 1989 to December 1993, 20 patients have been treated with a 72 MeV proton beam for uveal melanoma (54.5 Gy in 4 fractions using a single field). From April 1991, 21 patients with inoperable AVM's have been treated with modified 100 and 180 MeV proton beams (20-25 Gy in 2-4 fractions, using 2-3 fields). Treatments of pituitary tumours, brain metastases, malignant gliomas, as well as meningiomas of the base of the skull are planned for 1994. In addition, a 200 MeV scanned beam with rotational gantry is in preparation [**21**].

At the National Accelerator Centre (NAC) in Faure - South Africa, the first patients were treated with 250 MeV protons in 1993. An ambitious therapy programme using 250 MeV protons is in preparation at the PSI in Villigen. At the Orsay-synchrocyclotron, besides the therapy programme for eye tumours, a 250 MeV proton beam is in preparation [**13**] . In Jülich - Germany, there is also a high-energy proton therapy project for deep seated tumours. The Gröningen project , in the Netherlands, is making further progress (200 MeV protons).

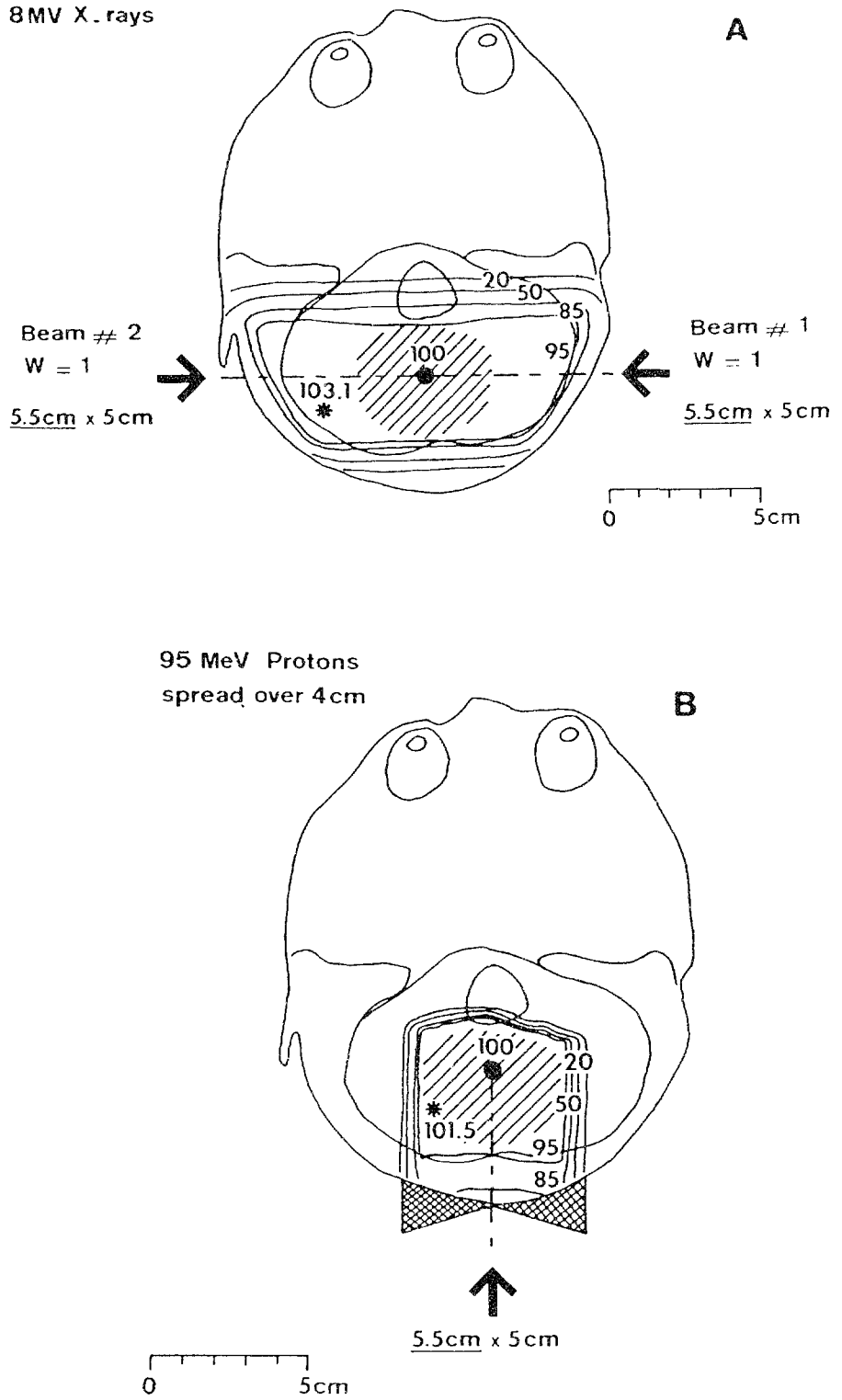

Figure 1.2

Tumour boost for a cerebellar medulloblastoma in a 2 year old child. Comparison of typical planning sections for photon (a) and proton (b) irradiations. For 8 MV photons, the target volume (hatched area) was boosted with 2 opposed lateral fields. For protons, the target volume was treated with a direct posterior field. The Bragg peak of the 95 MeV proton beam was spread over 4 cm. A bolus was needed to shape the treatment volume to the boost target volume. In figures 1.2, 1.3 and 1.4, the indicated proton energies correspond to the incident energies [17].

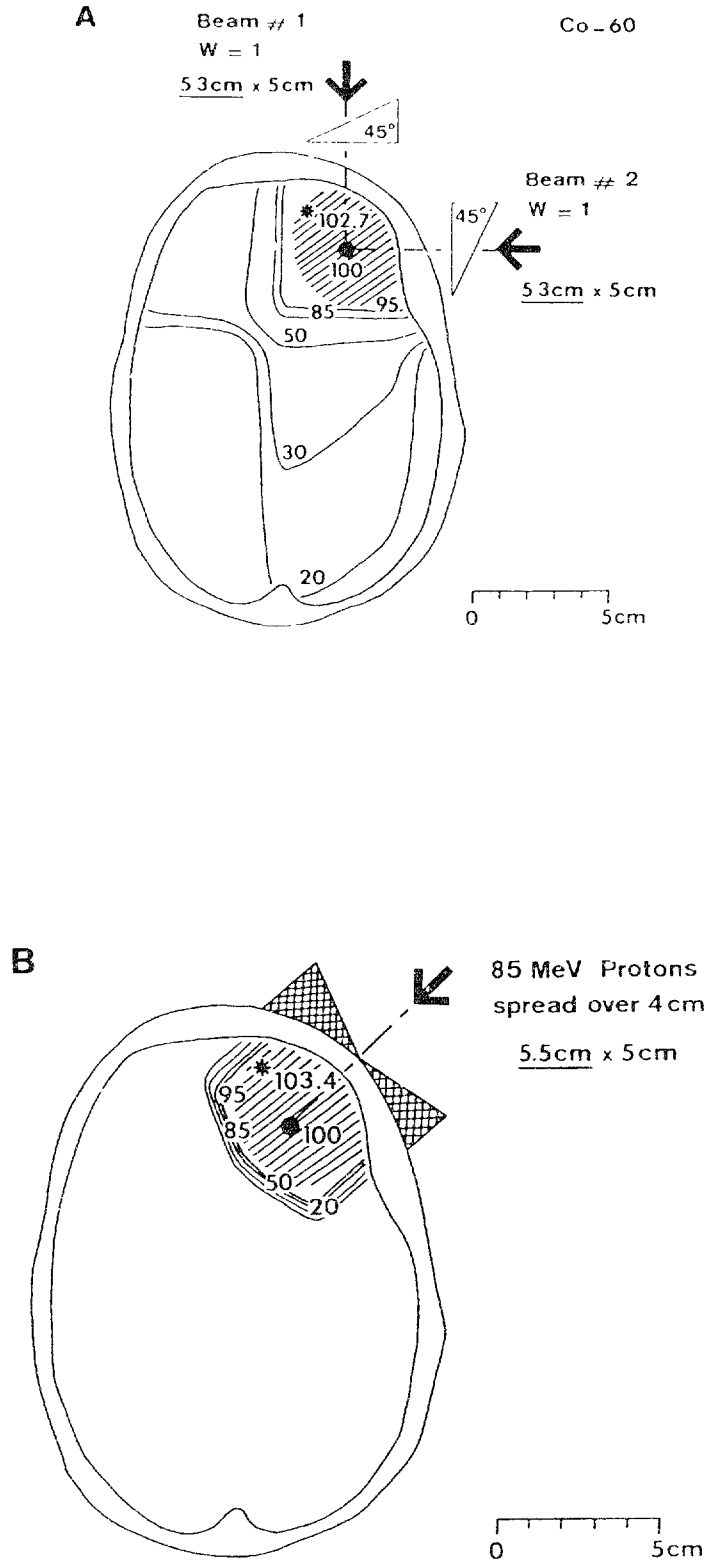

Figure 1.3

Typical planning sections (boost) for an astrocytoma of the right cerebral hemisphere treated by cobalt-60 γ–rays (a) or 85 MeV protons spread over 4 cm (b). For cobalt-60, 2 perpendicular equally weighted, wedged beams were used; the normalization point was chosen at the intersection of the beam axes. For protons, the target volume (hatched area) was treated with a direct beam; a bolus was added to better shape the treatment volume [17].

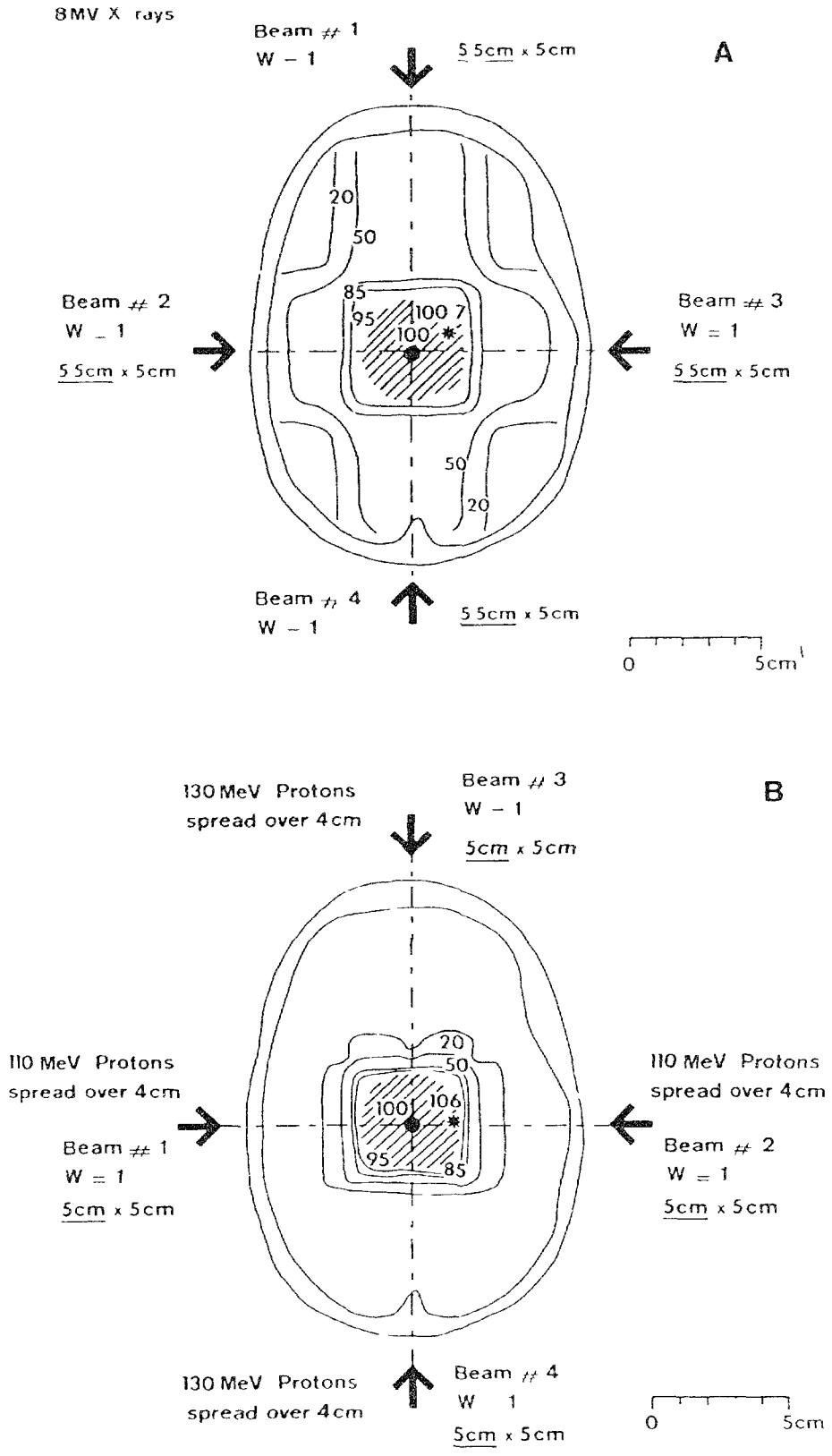

Figure 1 4

Typical planning sections for a large suprasellar craniopharyngioma in a 3 year old child treated with photons (a) or protons (b) The target volume is indicated by the hatched area For photons and protons, four equally weighted beams were used and the normalization point was chose at the intersection of the beams axes For the 4 proton beams, the Bragg peak was spread over 4 cm [17]

1.2.5 TWO DEDICATED HOSPITAL-BASED PROTON THERAPY FACILITIES

One of the most impressive proton therapy programme has been developed at the Loma Linda University Medical Centre in California. A variable energy synchrotron (70-250 MeV), and 3 treatment rooms with isocentric rotating gantry, are the "core" of a large oncology department. Two additional rooms with horizontal fixed beams are reserved for eye and brain irradiation and research respectively. Once all treatment rooms will be fully operational, the centre is expected to have a capacity of treating 1 000 patients per year with protons.

The first patients were treated in 1990, and 682 patients had been treated by December 1993. The Loma Linda group is acting as a pioneer in the field to the extent that, based on a superior physical selectivity, the proton facility is really aiming at systematically substituting proton beams to conventional photon beams. However, the complexity and mainly the cost of the existing equipment will probably limit the spreading of this type of approach.

The approach followed at the Massachusetts General Hospital (MGH) in Boston is rather different. Taking into account the results obtained with the Harvard University Cyclotron, the US National Cancer Institute has decided to support the installation within the walls of the MGH of a new dedicated proton therapy facility (about $ 17 Millions).

A 235 MeV cyclotron, two treatment rooms with isocentric gantry and a third room with a fixed horizontal beam are planned. The beam penetration should be 32 cm in tissues. The facility will be designed and constructed by the Ion Beam Applications Company (IBA) from Louvain-la-Neuve in Belgium. Conventional cyclotron technology has been selected, as well as passive scattering to achieve beam homogeneity. However, further addition of a wobbler system and of a scanning beam should be possible. The aim of the engineers is to provide a rather simple, compact, safe, reliable, low-cost facility, easy to use and cheap to maintain. In the long term, it is only in these conditions that proton beam therapy can really expand clinically, and gain its place among the other radiotherapy techniques.

1.3 IMPROVEMENT OF THE DIFFERENTIAL EFFECT WITH FAST NEUTRONS

After the first studies of Stone [22], neutron therapy programmes were initiated at the Hammermith Hospital in London in 1970, and a few years later in several other centres. They were based on radiobiological arguments. It is thus logical to discuss first these radiobiological arguments before reviewing the clinical data as well as the technical developments.

1.3.1 RADIOBIOLOGICAL DATA

1.3.1.1. The hypoxic cells

Historically, the rationale for introducing fast neutrons was the existence of hypoxic cells in all (or in most of) the malignant tumours and a specific resistance of these hypoxic cells to X-rays. The Oxygen Enhancement Ratio (OER) is approximately 3. With fast neutrons, the OER is reduced from 3 to 1.6 and, to the extent that the tumour radioresistance is due to the hypoxic cells, a therapeutic gain of about 1.9 (3 : 1.6) should be achieved.

Two points should be stressed: according to this rationale, the potential gain factor of 1.9 is high and it applies to all (or most of the) tumours since all (or most of them) are assumed to contain hypoxic cells. In the seventies, when neutron therapy was started, it was expected that the *radiobiological* therapeutic gain would be high enough to overcome the technical difficulties which nevertheless were recognized.

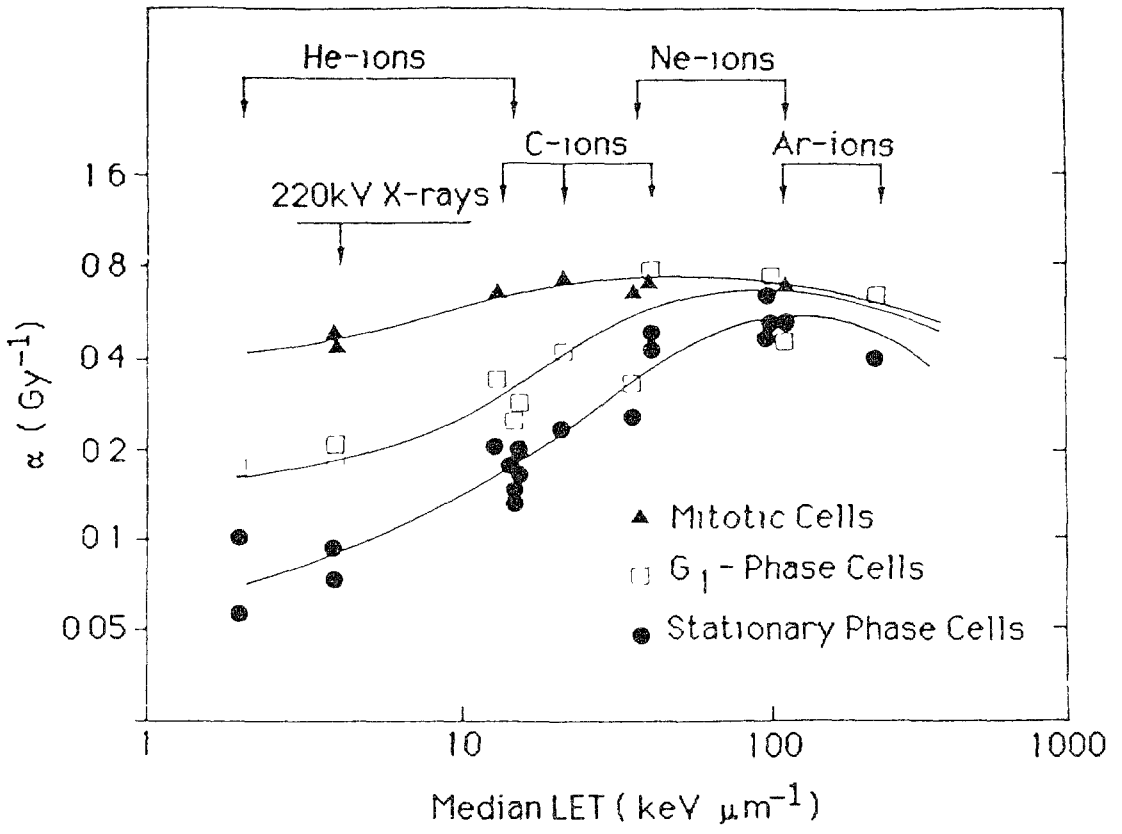

Figure 1.5

The differences in cell radiosensitivity related to the position in the mitotic cycle decrease with increasing LET. On the ordinate, the cell radiosensitivity is expressed by the parameter α (single-hit inactivation coefficient). Synchronized populations of Chinesse hamster cells were irradiated in mitosis (closed triangles), G_1 phase (open squares) and stationary phase (closed circles), with 220 kV X-rays and various beams of charged particles. The α coefficients are plotted as a function of the median LET (in keV.μm^{-1}).

After Chapman [23].

Today it can still be assumed that hypoxic cells do play a major role in the radioresistance of some tumours, but certainly not in all of them because of the reoxygenation phenomenon, which can be more or less efficient This raises the problem of the identification of the tumours in which the hypoxic cells are relevant The importance of patient selection will be stressed again in the next sections

1.3.1.2 A reduction of the differences in radiosensitivity

When comparing the effects produced by neutrons and X-rays, other differences than simply a reduction in OER are observed

With neutrons there is in general a reduction *in the differences* of radiosensitivity between cell populations For example, Figure 1 5 illustrates the reduction in the radiosensitivity

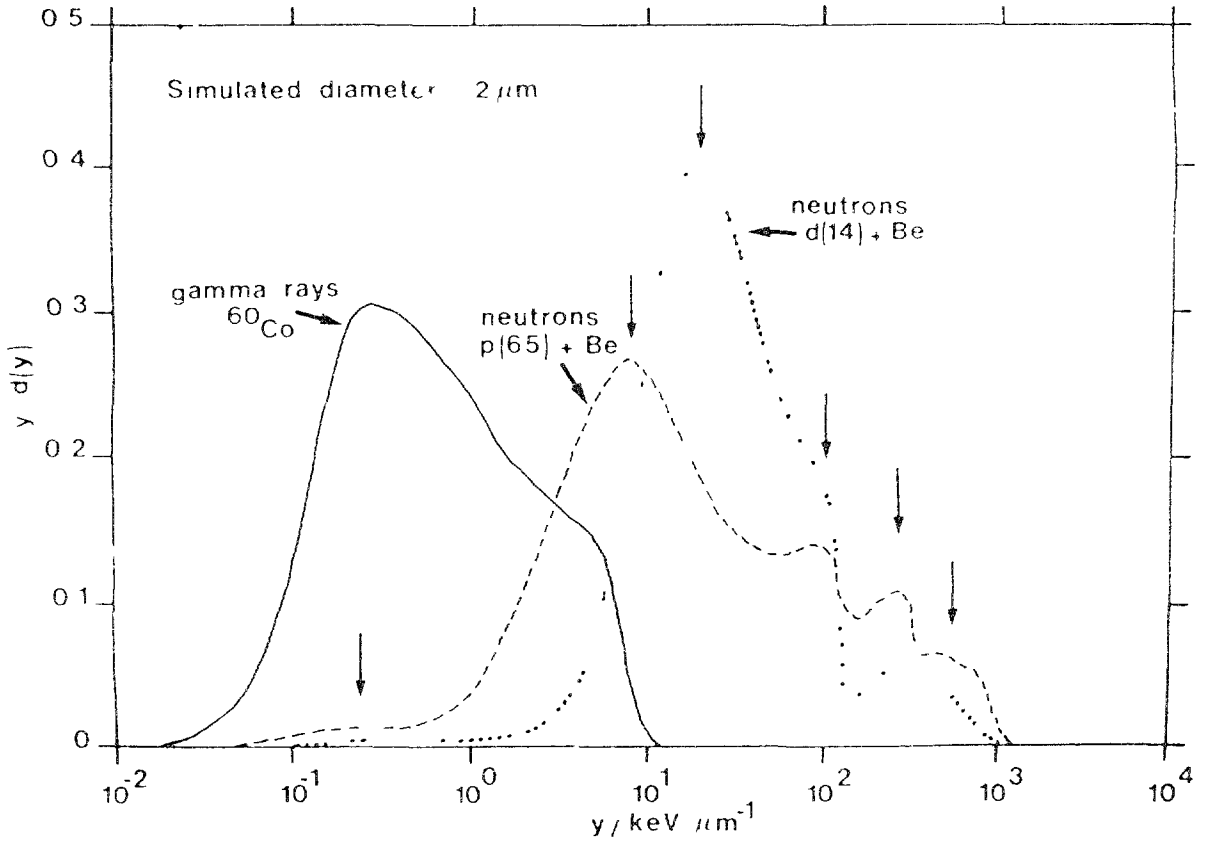

Figure 1 6

Comparison of energy depositions after irradiation with fast neutrons and γ-rays The curves indicate the distributions of individual energy-deposition events in a simulated volume of tissue 2 μm in diameter The parameter y (lineal energy) represents the energy deposited by a single charged particle traversing the sphere, divided by the mean cord length The peak with γ rays is at 0·3 keV μm $^{-1}$ and with d(14)+Be neutrons at 20 keV μm $^{-1}$ The spectrum for p(65)+Be neutrons shows 4 peaks the first is at 8 keV μm $^{-1}$ and corresponds to high energy protons, the second at 100 keV μm $^{-1}$ corresponds to low energy protons, the third at 300 keV μm $^{-1}$ is due to α particles and the last at 700 keV μm $^{-1}$ is due to recoil nuclei

After Menzel et al [25]

differences of the cells related to their position in the mitotic cycle [23]. Cell populations, synchronized in vitro, are irradiated in different phases of the mitotic cycle. The large differences, which are observed with X-rays (low-LET radiation), are progressively but markedly reduced with increasing LET.

A reduction in the difference of intrinsic radiosensitivity between cell lines has also been observed, although other data suggest that the ranking of radiosensitivity of some cell lines could be altered when X-rays are replaced by fast neutrons [24].

Finally, with increasing LET there is a reduction in the importance of the sublethal lesions. Differences in the capacity of accumulating and repairing sublethal lesions are then of less importance. In practice, this implies that the dose per fraction also becomes less critical.

It could thus be concluded that all cell populations in all conditions tend to respond in a more similar way to neutrons than to X-rays. This can be logically related to the increase, by a factor of about 100, in the sizes of the individual energy deposits as can be derived from microdosimetric measurements (Fig. 1.6) [25].

1.3.1.3. Practical conclusions for radiation therapy

Two practical conclusions can be derived from the available radiobiological data.

Need for proper patient selection

A reduction in the differences of radiosensitivity related to the position of the cells in the mitotic cycle, cell line or repair capacity can be an *advantage* or a *disadvantage* depending on the characteristics of the tumours and of the normal tissues at risk [26].

This stresses the importance of patient selection : an incorrect choice of the radiation quality can worsen the clinical results. More generally, if a subgroup suitable for high-LET radiation cannot be identified, and if the whole group is treated with neutrons, the advantage gained in the subgroup will be diluted or counterbalanced by the worse results obtained in the other subgroups which would have been better treated with photons. In practice this could lead to erroneous clinical conclusions.

The importance of physical selectivity.

As a result of the reduction in the (radiobiological) differential effect with increasing LET, the therapeutic efficiency of the treatment will depend to a larger extent on the physical selectivity (dose distribution). Thus, physical selectivity is at least as important with high-LET as with low-LET radiations This is the second important practical conclusion which can be derived from the radiobiological data [27].

1.3.2 REVIEW AND DISCUSSION OF THE CLINICAL DATA

1.3.2.1 Introduction

The clinical data should be reviewed and interpreted bearing in mind the two main conclusions of the radiobiological analysis : the need for patient selection and the importance of physical selectivity for high-LET radiations. The initial groups of patients were treated in far from optimal technical conditions. This has resulted in complications which in turn have influenced patient recruitment and have impaired the development of neutron therapy.

The clinical indications for fast neutrons are summarized in Table 1.4. They represent more than 15 % of the patients currently referred to the radiation therapy departments. In addition, the tumour types for which neutrons were shown to bring a benefit correspond to a large extent to those predicted by the radiobiological data. Indeed, the most striking results

TABLE 1.4

Clinical Indications for Neutron Therapy (Summary)
1. SALIVARY GLAND TUMOURS locally extended, inoperable or recurrent / well differentiated
2. PARANASAL SINUSES adenocarcinomas, adenoid cystic carcinomas, other histology (?)
3. SOME TUMOURS OF THE HEAD AND NECK AREA locally extended, metastatic adenopathies
4. SOFT TISSUE SARCOMAS, OSTEOSARCOMAS, CHONDROSARCOMAS slowly growing/well differentiated
5. PROSTATIC ADENOCARCINOMAS locally extended/ well differentiated
6 RECTUM CARCINOMAS Inoperable or recurrent
7 SOME NON-SMALL-CELL BRONCHUS CARCINOMAS
8 MELANOMAS inoperable/recurrent (palliative treatment).

were obtained for well differentiated, slowly growing tumours, often resistant to X-rays as well as to chemotherapy. The clinical results are reviewed in more detail elsewhere [28]. Only three important localizations are discussed here.

1.3.2.2. Salivary gland tumours

The conclusions of the National Cancer Institute (NCI) can be summarized as follows :
The results of the non-random clinical studies and of the prospective randomized trial overwhelmingly support the contention that *fast neutrons offer a significant advance in the treatment of inoperable and unresectable primary or recurrent malignant salivary gland tumours*. Fast neutron therapy alone should be the treatment of choice for advanced stage salivary gland tumours, and surgery should be limited to cases where there is a high likelihood of achieving a negative surgical margin and where the risk of facial nerve damage is small [29].

1.3.2.3. Soft tissue sarcomas

Slowly growing, well differentiated soft tissue sarcomas have been treated in most of the neutron therapy centres, mainly because they are often resistant to X-rays and also because of the excellent results reported from Hammersmith [30]. When evaluating the results of neutron therapy, comparison with historical series should be made very carefully, since the series may differ by histology, degree of differentiation, localization, local extent, etc.... Furthermore, patient recruitment, in a given centre, is influenced by the general treatment policy (i.e.the relative place of surgery and/or chemotherapy). Therefore, ideally randomized trials are required, but so far have been difficult to achieve for practical reasons.

A review of the results reported from the different centres (Table 1.5) indicates an overall local control rate after neutron therapy of 53 % for inoperable soft tissue sarcomas. This value is higher than the value of 38 % currently observed after low-LET radiation for similar patients series [31]. High complication rates were reported in some series. They have to be related mainly to the poor technical conditions of the irradiation (e.g. skin necrosis) or to the patient recruitment (e.g. late fibrosis when large fields had to be used to cover extended target volumes) [15] [28].

The proposed indications of neutron therapy (and/or photon therapy), for low grade soft tissue sarcomas, are presented in Table 1.6, after Pötter et al. [32].

1.3.2.4. Prostatic adenocarcinomas

Prostatic adenocarcinomas, having in general a long doubling time, should be a good indication for neutron therapy taking into account the available radiobiological data [33]. In

TABLE 1.5

REVIEW OF THE LOCAL CONTROL RATES FOR SOFT-TISSUE SARCOMAS TREATED DEFINITIVELY WITH RADIATION THERAPY				
NEUTRONS				
Institutions	Number of patients *	Local control (%)		
Essen + Heidelberg,1983	60	31	(52 %)	
Hammersmith, 1987	50	26	(52 %)	
Hamburg, 1987	45	27	(60 %)	
TAMVEC, 1980	29	18	(62 %)	
Fermilaboratory, 1984	26	13	(50 %)	
Seattle, 1989	21	15	(71 %)	**
Louvain-la-Neuve, 1982	19	4	(21 %)	
Amsterdam, 1981	13	8	(61 %)	
NIRS, 1979	12	7	(58 %)	
Edinburgh, 1986	12	5	(42 %)	
MANTA, 1980	10	4	(40 %)	
Overall	297	158	(53 %)	
PHOTONS/ELECTRONS				
Institutions	Number of patients *	Local control (%)		
Tepper & Suit, 1985	51	17	(33 %)	
Duncan & Dewar, 1985	25	5	(20 %)	
McNeer et al., 1968	25	14	(56 %)	
Windeyer et al., 1966	22	13	(59 %)	
Leibel et al., 1983	5	0		
Overall	128	49	(38 %)	

* Patients treated de novo or for gross disease after surgery are included but not patients treated postoperatively for microscopic residual disease or for limited macroscopic residual disease.

** Two-year actuarial data

Modified from Laramore et al., [31]

TABLE 1.6

Indications of neutron (and/or photon) radiotherapy for low grade soft tissue sarcomas.					
Type of surgery	Plane of dissection	Microscopic appearance	Local control after surgery	Indication for radiotherapy	Local control after combined modality
Intracapsular	Within lesion	Tumour at margin	0 %	Neutrons (+photons ?)	30 - 50 %
Marginal	Within reactive zone - extracapsular	Reactive tissue microsatellite tumour	10 - 20 %	Neutrons (+photons ?)	> 50 %
Wide	Beyond reactive zone through normal tissue within compartment	Normal tissue	50 - 60 %	Photons	90 %
Radical	Normal tissue extracompartmental	Normal tissue	80 - 90 %	Photons (rare)	> 90 %

(Modified after Pötter et al. [32]).

fact, the benefit of neutron therapy was rapidly recognized in several centres, e.g. in Hamburg by Franke [34], in Chiba by Tsunemoto et al. [35], and in Louvain-la-Neuve by Richard et al. [36].

However, the most convincing data are the results of two randomized trials, initiated by the Radiation Therapy Oncology Group (RTOG), on locally advanced adenocarcinoma of the prostatic gland (Stages C and D1).

In the first trial, between June 1977 and April 1983, the patients were randomized between photon and mixed beam (neutron+photon) therapy. Neutrons were delivered using physics-laboratory-based machines. A total of 91 analyzable patients were entered into the study, and the two patient groups were balanced with respect to the major prognostic variables. Ten-year results for clinically assessed local control are 70 % for the mixed beam group vs. 58 % for the photon group (p=0.03). The ten-year survival rates were 46 % for mixed beams vs. 29 % for photons (p=0.04); and ten-year disease-specific survival rates were 58 % for mixed beams vs. 43 % for photons (p=0.05) [37].

This study suggested that a regional method of treatment can influence both local tumour control and survival in patient with locally advanced adenocarcinoma of the prostatic gland.

While these results were impressive, a confirmatory study was designed comparing neutrons only and photons, and using state-of-the art, hospital-based cyclotrons.

From April 1986 to October 1990, 178 patients were randomized on this follow-up study comparing 20.4 Gy of neutrons delivered in 12 fractions over 4 weeks with 70 Gy of photons delivered in 35 fractions over 7 weeks. Four institutions participated in the study : the University of Washington in Seattle, the University of California in Los Angeles (UCLA), the M.D. Anderson Hospital in Houston and the Great Lakes Neutron Treatment Association (GLANTA). The depth-dose properties and isocentric delivery capabilities of the high energy neutron beams allowed treatment with neutrons alone to this deep-seated tumour [38].

Patients eligible for the study were those with stages T3-4, N0-1, M0 tumours with any histological grade, as well as patients with high-grade T2 tumours. After stratification for stage, Gleason grade, and the presence or absence of surgical nodal staging, 89 patients were randomized to each treatment arm. The two treatment arms were balanced for all known prognostic factors.

With a follow-up time ranging from 40 to 86 months (68 months median follow-up) the 5-year actuarial clinical local-regional failure rate for patients treated with neutrons was 11 %, vs. 32 % for photons ($p < 0.01$). Incorporating the results of routine post-treatment prostate biopsies, the resulting "histological" local-regional tumour failure rates were 13 % for neutrons vs. 32 % for photons ($p = 0.01$) (Table 1.7).

TABLE 1.7

Neutrons vs. photons for locally advanced prostatic adenocarcinoma Site of first failure			
	Assigned treatment		
First failure	Neutrons No (%)	Photons No (%)	Total No (%)
Local only	7 (8%)	20 (24%)	27 (16%)
Local-regional	0 (0%)	1 (1%)	1 (1%)
Local-distant	1 (1%)	0 (0%)	1 (1%)
Regional-distant	1 (1%)	0 (0%)	1 (1%)
Distant only	24 (28%)	22 (26%)	46 (27%)

After Russell et al. [38].

TABLE 1.8

Neutrontherapy of prostatic adenocarcinoma: bowel morbidity by institution	
Institution	Colostomies
University of Washington - Seattle - p(50)+Be neutrons - multileaf collimator	0/49 (0 %)
UCLA - Los Angeles - p(45)+Be neutrons - movable jaw collimator	2/25 (8 %)
M.D. Anderson - Houston - p(42)+Be neutrons - fixed cone collimator	4/10(40 %)

After NCI, Report 1991 [29].

To date, actuarial survival and cause-specific survival rates are statistically indistinguishable for the two patient cohorts, with 32 % of the neutron-treated patient deaths and 41 % of the photon-treated patient deaths caused by prostate cancer (p = n.s.). Prostate specific antigen (PSA) values were elevated in 17 % of neutron-treated patients and 45 % of photon-treated patients at 5 years ($p < 0.001$) .

Severe late complications of treatment were higher for the neutron-treated patients (11 % vs. 3%), and were inversely correlated with the degree of neutron beam shaping available at the participating institutions.

The differences in major complication rates are primarily due to differences in large bowel toxicities resulting in surgical intervention and colostomies. The colostomy rates for neutron-treated patients are facility dependent (Table 1.8) and the differences in rates observed between the Cyclotron Corporation machines at M.D. Anderson and UCLA, and the Scanditronix machine at the University of Washington are statistically significant (p=0.01). Differences in these major complication rates are probably due to differences in beam collimation capabilities among the neutron facilities, but may also be due to differences in beam energy spectra [27] [39]. The multileaf collimator allows the radiotherapist to better match the size and shape of the neutron beam with the size and shape of the target volume and thus to reduce the volumes of normal tissues unnecessarily exposed.

It can be concluded from this study that high-energy fast neutron radiotherapy is safe and effective when adequate beam delivery systems and collimations are available, and it is significantly superior to external beam photon radiotherapy in the local-regional treatment of large prostatic tumours.

Of course, account must be taken of the slow natural history of prostatic adenocarcinoma and caution is necessary before deriving definitive conclusions. However, the clinical data at present available indicate a *significant benefit for fast neutrons (used alone or in mixed schedule ?) compared to the current photon irradiation modalities for locally advanced cases*. They confirm the selective efficiency of neutrons against slowly growing, well differentiated tumours, as well as the importance of the physical selectivity when high-LET radiations are used, as could be expected from the radiobiological data. The role of the collimation system on the complication rate is especially illustrative.

1.3.3. TECHNICAL DEVELOPMENTS

The technical conditions, in which fast neutron therapy is applied, have progressively been improved during the two last decades.

As far as neutron energy is concerned, many of the first patient series were treated with low-energy cyclotrons (16 MeV deuterons). Today, neutron beams produced by protons of 45 MeV

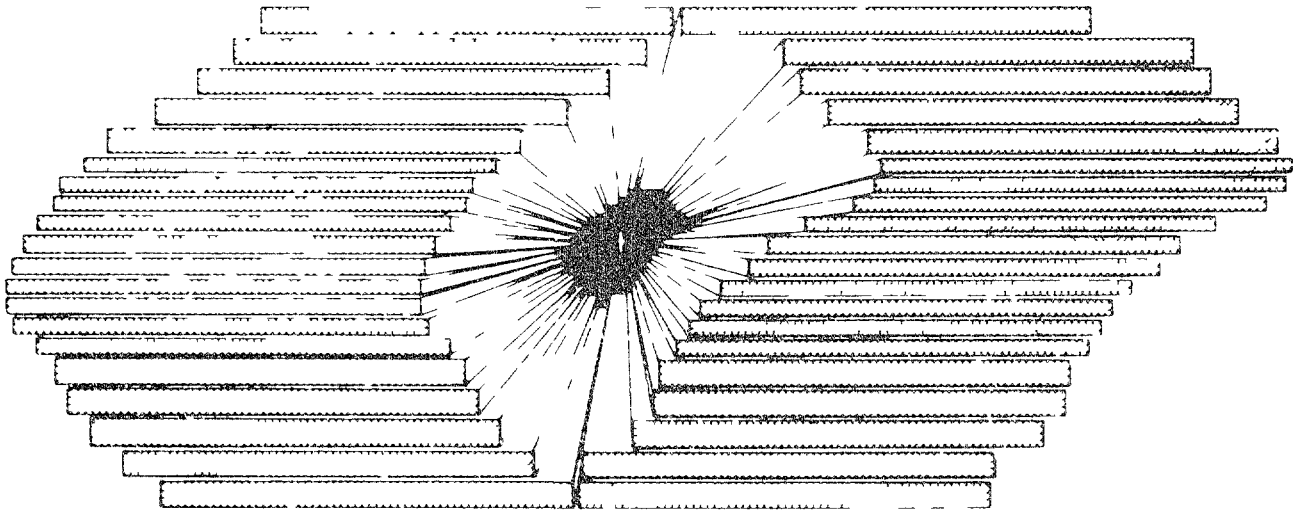

Figure 1.7 (a)

Variable multi leaf collimator in neutron therapy

Diagram of a variable multi leaf collimator showing the lower end of the leaves and the collimation surfaces which are all aligned with the proton target (symbolized by the +) Each leaf has its own motor drive and position readout (after Brahme cited in ref [27])

(or more) are available at several facilities and in 4 centres neutrons are produced by 60 MeV protons, i e Clatterbridge, Faure, Fermilab and Louvain-la-Neuve The depth doses and skin sparing are similar to that of a 8-10 MV photon linear accelerator

A fixed horizontal beam was often a practical limitation for patient set up when physics laboratory-based cyclotrons were used Today, a rotational gantry is available in several centres such as Clatterbridge, Detroit, Houston, Faure, Seoul, Seattle UCLA, etc

Variable collimators (movable jaws) are used in Clatterbridge, Faure, UCLA, and multileaf collimators are used in Chiba, Detroit, Louvain-la-Neuve, Nice and Seattle (Fig 1.7)

The neutron therapy facilities operational today are listed in Table 1.9 with their main characteristics Of course, the technical problems raised by the beam collimation and the isocentric gantry are far more complex and thus more expensive for neutrons than for photons

Dosimetric data about neutron beams and protocols for neutron therapy, accepted at the international level, have been published [40] In addition, several intercomparisons were performed between the different neutron therapy centres These comparisons implied dosimetric, microdosimetric and radiobiological determinations [41] [42]

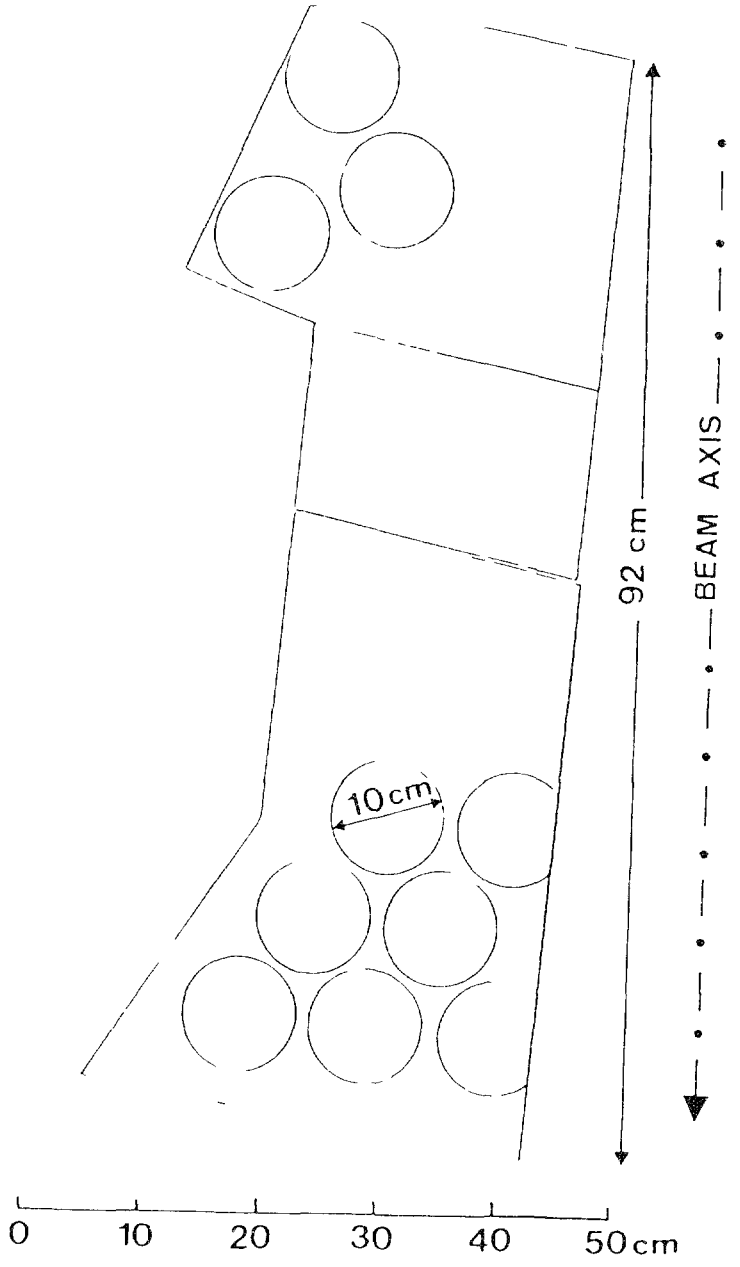

Figure 1.7 (b)

Variable multi-leaf collimator in neutron therapy.

Diagram of one of the leaves of the variable multi-leaf collimator recently installed at the cyclotron of Louvain-la-Neuve. The collimator, which has been installed on a vertical neutron beam line, consists of 2 sets of 22 leaves made of steel and borated polyethylene discs (10 cm in ∅). The leaves, calculated for p(65)+Be neutrons, are 92 cm thick. Their width is about 1 cm [28].

TABLE 1.9.

THE NEUTRON THERAPY FACILITIES WORLDWIDE
1st January 1994

Centre		Neutron Producing Reaction	Comments
		EUROPE	
U K	MRC-Clatterbridge	p(62)+Be	Rotational gantry Variable collimator
France	Orléans	p(34)+Be	Vertical beam (horizontal beam planned)
	Nice	p(60)+Be	vertical beam multileaf collimator
Belgium	UCL- Louvain-la-Neuve	p(65)+Be	Vertical beam Multileaf collimator (horizontal beam in preparation)
Germany	Hamburg	(d + T)	Rotational gantry
	Heidelberg	(d + T)	"
	Munster	(d + T)	"
	Essen	d(14)+Be	Rotational gantry
	Garching - T.U. Munich	reactor neutrons (av.energy 2 MeV)	Mixed beam
		UNITED STATES	
Texas	M. D. Anderson- Houston	p(42)+Be	Rotational gantry
California	UCLA - Los Angeles	p(46)+Be	Rotational gantry Variable collimator
Washington	Seattle	p(50)+Be	Rotational gantry Multileaf collimator
Illinois	Fermilab	p(66)+Be	Horizontal beam
Michigan	Detroit	d(48)+Be	Isocentric mounting Multi-rod collimator
		ASIA	
Japan	National Institute of Radiological Sciences (NIRS) - Chiba	d(30)+Be	Vertical beam Multileaf collimator
	Institute for Medical Sciences (IMS) - Tokyo	d(14)+Be	Horizontal beam
Korea	Korea Cancer Center Hospital (KCCH) - Seoul	p(50 5)+Be	Rotational gantry
China	Institute of High Energy Physics - Beijing	p(35)+Be	Proton Linac
Saudi Arabia	King Faisal Hospital-Riyadh	p(26)+Be	Rotational gantry
		AFRICA	
South Africa	National Accelerator Centre (NAC),Faure	p(66)+Be	Rotational gantry Variable collimator

1.4. THERAPEUTIC APPLICATIONS OF HEAVY IONS BEAMS

1.4.1 RATIONALE FOR HEAVY-ION THERAPY

Heavy ions combine the advantage of a high physical selectivity with high-LET characteristics (Fig. 1.8). Their physical selectivity is similar to that of proton or helium ion beams. They even have a smaller penumbra, but it is questionable whether this factor could be of clinical relevance.

More important is the fact that, with heavy ions, the higher RBE at the level of the spread-out Bragg peak compared to the initial plateau enhances the advantage of the dose distribution. A further advantage can be obtained through fractionation due to differences in repair possibility between, on the one hand, tissues located at the level of the initial plateau (repair possible for these normal tissues) and, on the other hand, tissues located at the level of the spread out Bragg peak (the target volume) where high-LET does not allow for repair.

The LET depends on the type and energy of the particles as well as on the width of the spread out Bragg peak. This implies that the parameters which depend on LET, such as RBE, OER and repair capacity, have to be determined for each type of treatment.

Heavy ion therapy programmes are justified by three sets of arguments :

1) the importance of a high physical selectivity which has been clearly demonstrated with low-LET radiations. The benefit of replacing 200 kV X-rays by high-energy photons was obvious, and the benefit of further improving the physical selectivity by the introduction of proton beams has been proven for some selected tumour sites.

As stressed above (see section 1.3.1.3), the available radiobiological data indicate that a high physical selectivity is even more important with high- than with low-LET radiations due to a general reduction in the differences in radiosensitivity between cell populations.

2) the radiobiological and clinical data indicating that, for the treatment of some tumour types and/or sites, high-LET radiations do bring a benefit compared to low-LET radiations.

Radiobiology indicates some mechanims through which high-LET radiations could bring a benefit in the treatment of some tumour types.

Review of the clinical results of fast neutron therapy indicates that indeed neutrons are superior to photons for some tumour types as summarized in Table IV.

3) the encouraging clinical results available with heavy ions, although it is recognized that they were obtained only from one centre, i.e. Berkeley, and on limited and selected groups of patients.

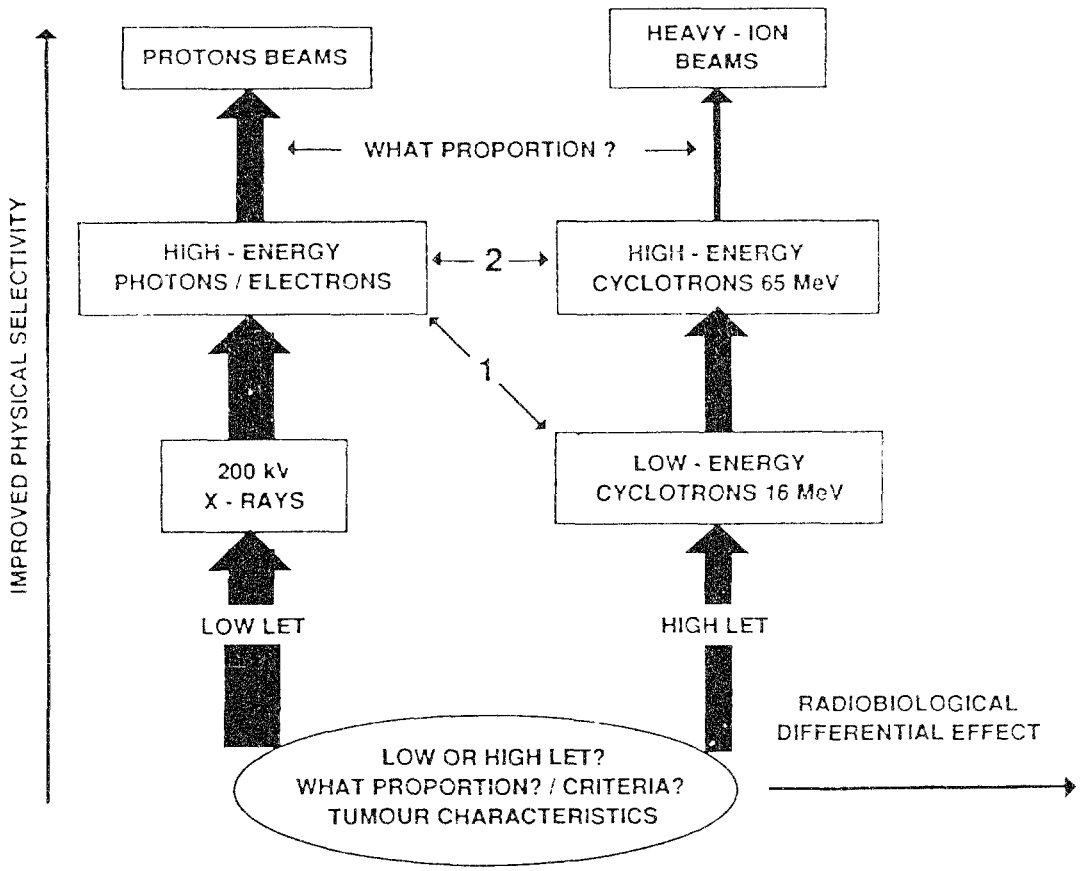

Figure 1.8

Technical development has improved the physical selectivity of the treatments for high-, as well as for low-LET radiations. In both groups of radiations, 3 steps are schematically identified. For low-LET radiations, the 200 kV X-rays have now been completely replaced by high-energy photons (or electrons), which tend, in turn, to be replaced for well selected tumour types/sites by proton beams. The proportion of patients deserving proton beam therapy needs to be assessed. Three steps in technological development are also schematically identified for high-LET radiations : low-energy cyclotrons, high-energy cyclotrons, and heavy ions. The proportion of high-LET patients which deserves heavy ions also needs to be assessed (similar question as for the low-LET proton beams). The main question which remains is the proportion of patients which could be better treated with high-LET than with low-LET radiations. It is a radiobiological problem related only to the characteristics of the tumour and not to the machines. The clinical value of high-LET radiations has been assessed mainly in the past by comparing high-energy linear accelerators and low-energy cyclotrons (arrow 1). The right comparison (arrow 2) started later on, and all the final reports are not yet available. Some limited patient series were also treated at the Berkeley heavy-ion facility.
From [15]

1.4.2 THE CLINICAL DATA FROM BERKELEY

The results obtained at Berkeley are summarized on Table 1.10 Some data obtained with helium ions (low-LET) are compared with the neon ion data (high-LET) [43].

Comparison is difficult since the patient series are too small and probably not similar. In particular, the soft tissue sarcomas treated with neon ions were more advanced, and the clinical impression clearly suggests a greater efficiency of neon ions (which is not reflected in the results presented in Table 1.10) [J. Castro, personal communication].

Comparison of the neon and of the neutron clinical data is of interest (Table 1.11). The best neon data were obtained for those tumours for which neutrons were proven to bring a benefit. It is thus reasonable to assume that these results are related to the high-LET characteristics of the beams [44].

TABLE 1.10

SUMMARY OF THE CLINICAL RESULTS OBTAINED WITH HELIUM IONS AND NEON IONS AT BERKELEY

Tumour site	Local control rate with :		
	Helium ions	Neon ions	Conventional Treatment
Salivary gland		80 % (10 patients)	28 % (188 patients) (Literature review)
Nasopharynx Paranasal sinus	53 % (13 patients)	63 % (21 patients)	21 % (97 patients) (UCSF)
Sarcoma	65 % (17 patients)	45 % (24 patients)	28 % (Literature review)
Prostate		100 % (9 patients)	60-70 % (Literature review)
Lung		39 % (18 patients)	22-40 % (UCSF)
Glioblastoma Brain		Median survival: 17 months (13 patients)	Median survival: 9-12 months (UCSF, RTOG, NCOG)

Modified from J.R. Castro, [43].

TABLE 1.11

SUMMARY OF THE CLINICAL RESULTS OBTAINED WITH HIGH-LET RADIATIONS (FAST NEUTRONS AND NEON IONS)

Tumour site (or type)	Local control rates after :	
	Fast neutrons	Neon ions
- salivary gland tumours	67 % (24 %)	80 % (28 %)
- paranasal sinuses	67 %	63 % (21 %)
- fixed lymph nodes	69 % (55 %)	
- sarcomas	53 % (38 %)	45 % (28 %)
- prostatic adenocarcinomas	77 % (31 %)	100% (60-70%)

( ) for comparison, the local control rates currently obtained with conventional low-LET radiations for patient series as similar as possible.

From A. Wambersie [**44**]

1.4.3 PATIENT SELECTION FOR HEAVY ION BEAM THERAPY

The general principles of patient selection for heavy-ion beam therapy are presented on Table 1.12. Two main groups of indications can be identified depending whether the biological effects of high-LET radiations or the high physical selectivity of the beams is thought to be the most important factor. In addition, more specific indications can be proposed (G.R.H. Sealy, in [**15**]).

Concerning the first group of indications (for which the high-LET is considered to be most important), it is possible to make a tentative prediction of the clinical benefit which could be expected from heavy ion beams by considering both the conclusions of the neutron studies and the heavy ion results from Berkeley (Tables 1.10 and 1.11).

It should be stressed again that neutron data were, in many centres, not obtained in optimal technical conditions. A similar remark also applies, but for other reasons, to the neon results for which in addition there was a severe (often negative) patient selection.

Concerning the second group of indications for heavy ions (for which the physical selectivity is considered to be the most important factor), one can normally expect the same results as

TABLE 1.12

GENERAL PRINCIPLES OF PATIENT SELECTION FOR HEAVY-ION BEAM THERAPY To take advantage of the biological **AND** physical characteristics of the beams
A - The **radiobiological advantage** (high-LET) is thought to be the most important factor, followed by the physical selectivity of the beams
a. where high-LET radiation already demonstrated to be useful - salivary gland tumours - paranasal sinuses - fixed lymph nodes - prostatic adenocarcinomas - sarcomas, etc. b. where additional information is needed - pelvic tumours : bladder, rectum, cervix, etc. - other tumours : stomach, biliary duct, etc.
B . - The **physical selectivity (dose distribution)** of the beams is thought to be the most important factor followed by the radiobiological advantage of high-LET
Tumours in technically difficult situations, but where high-LET radiation may be better than low-LET radiation (e.g. slowly growing tumours) - adjacent to CNS : meningioma, pharyngioma, chordoma, optic nerve, glioma, AVM, paraspinal cord tumour, paraaortic lymph node, etc. - root of neck disease : upper oesophagus, post cricoïd carcinoma, etc - thoracic disease : tumour of the lung with mediastinal disease after resection of primary, mesothelioma, etc.
C.- Additional indications - where possible later surgery should not be prejudiced : tongue, avoiding mandible, etc. - very poor prognosis disease : unresectable hepatoma, pancreas, retroperitoneal sarcoma, recurrent after previous radiotherapy, etc. .

Modified after G.R.H. Sealy in [15].

with protons, but with the additional advantage of high-LET radiations for slowly growing tumours. Heavy ions could extend the field of the indications of radiation therapy by allowing the oncologists to envisage irradiation of groups of tumours "traditionally" considered to be radioresistant (e.g. adenocarcinomas).

1.4.4 THE HEAVY ION THERAPY FACILITIES WORLDWIDE

Since the Berkeley facility was closed in 1993, there is unfortunately no further heavy-ion therapy facility anywhere in the world. However, the follow-up studies on the patients treated at Berkeley are still going on.

Another heavy ion therapy program will start, in 1994, in Chiba-Japan, at the National Institute for Radiological Sciences (NIRS). Clinical protocols are now being designed and the facility is prepared to accept patients from all parts of the world to be treated according to these protocols.

The Chiba HIMAC (Heavy Ion Medical Accelerator) facility consists of an injector linac, two synchrotron rings and the beam delivery systems. Three treatment rooms are constructed : one with a vertical beam, the second one with a horizontal beam, the third one with a vertical and horizontal beams. In the last one, the patient can be irradiated simultaneously with the vertical and the horizontal beams (at different energies if needed). This is possible because of the two synchroton rings. The dose rate (> 5 Gy/min) is sufficient to permit completion of the treatments in much less than one minute.

Ion types from He to Ar can be accelerated at a maximum energy of 800 MeV/amu and at a minimum energy of 100 MeV/amu. A these energies, any tumour even deep seated (30 cm) can be reached [45] [46].

In Europe, the Commission of the European Communities initiated a feasibility study for the project EULIMA (European Light Ion Medical Accelerators), but, at the end, was not able to support such a complex and expensive project [15].

At the GSI-Darmstadt, in Germany, a heavy ion therapy program is in preparation in collaboration with the University of Heidelberg Cancer Centre. In France, the possibility of treating patients at the Accelerator Saturne in Saclay is now under examination.

1.5 SUMMARY AND CONCLUSIONS

More than any other medical discipline, radiation therapy is dependent on technological developments. Historically, this has been clearly illustrated when 200 kV X-rays were replaced by modern high-energy linear accelerators. In addition, it is recognized that radiation therapy has taken advantage of the progress made in other technical disciplines such as medical imaging, dosimetry, computerized treatment planning.

Today, one of the most promizing approaches to improve the efficiency of radiotherapy (and thus the local control rate of malignant tumours) is the replacement of X-rays by other radiation qualities (i.e. particle beam therapy). The importance of technological developments in the field of particle therapy is particularly evident as shown below.

Proton beams aim at improving the physical selectivity of the irradiation while fast neutrons aim at improving the (radiobiological) differential effect. Proton beams can be expected to be especially useful for patients when physical selectivity is important, i.e. when a radioresistant tumour is located close a radiosensitive critical normal structure. The potential benefit of protons can be, to some extent, evaluated from the critical comparison of the "dose distributions", since at equal dose, the biological effects produced by protons and X-rays are similar.

Identification of the patients (or of the groups of patients) who could benefit from neutron therapy is a more difficult problem since it involves radiobiological arguments. In principle, the indications for neutron therapy could be derived from several already available data :

- when hypoxic cells are shown to be the cause of tumour resistance to X-rays (cf. the clinical studies with hyperbaric oxygen, with hypoxic cell radiosensitizers, etc) [26] [28];
- slowly growing, well differentiated tumours [23];
- cell strains intrinsically resistant to X-rays;
- rapidly proliferating tumours for which a short overall time could be of interest. Since the dose per fraction is less critical with neutrons, shorter overall times can be applied more easily than whith X-rays.

This last argument may seem in contradiction with some of the previous ones and the clinical data only will allow deriving the right conclusion. Clinical data are accumulating continuously and more than 20 000 patients have been treated so far with neutrons worldwide.

However, today, for a given patient, the choice of the appropriate radiation quality (low- or high-LET) remains so far a difficult problem, and much hope is placed in the development of predictive tests.

When evaluating the clinical results of proton and neutron therapy, the technical conditions in which they were applied should be kept in mind. Most of the first patient series were treated in "sub-optimal" technical conditions, with laboratory machines designed initially for physics experiments and later on adapted for clinical applications. These machines were often cumbersome, complex to run and expensive to maintain, not fully available for therapy, located outside the hospital, and the fixed radiation beams raised difficult problems for patient positioning.

In neutron therapy, there was, with some machines, an additional difficulty due to the poor beam penetration, as well as a lack of appropriate collimation system. These poor technical conditions resulted in complications (mainly late complications) which in turn impaired the development of neutron therapy for several years.

The situation has today considerably improved, and progress has been made in 2 quite independent directions due to technicalogical developments. Firstly, hospital-based

accelerators were installed, fully available for therapy and with technical characteristics suitable for routine clinical applications : for example, for neutron therapy, in Seattle (USA), Clatterbridge (UK), Seoul (Korea) and, for proton beam therapy, a pioneer centre is Loma-Linda in the USA.

Secondly, some physics machines were adapted to meet the clinical requirements. For example, for neutron therapy, the beams used in Louvain-la-Neuve, Faure and Fermilab fully meet the therapy requirements. The same is true for the proton beams used for uveal melanoma in different centres such as Harvard, PSI-Villigen, Orsay, etc.

As a result of these different developments and improvements, patients can be treated today in safe conditions with neutrons or protons at different facilities worldwide. However, there is only a limited number of such facilities, and thus only a small proportion of the patients who need them can benefit today from these new therapeutic modalities. This is partly related to the fact that the existing facilities are expensive, cumbersome, complex and expensive to run and to maintain, although it is recognized that the available clinical data justify a further development of neutron and proton therapy.

Finally, one has to stress that recent technological developments have significantly changed the situation. Using super-conducting magnets or even conventional technology, the engineers are now able to offer compact, reliable machines, easy to use and to maintain, at reasonable price, which allow the therapist to irradiate with neutrons and protons as safely and as accurately as with the modern electron linacs. The first example for neutron therapy is a super-conducting cyclotron installed in Detroit which is as compact as a modern electron linac and can also rotate around the patient (Table 1.9). For proton therapy, the first example of the new generation of compact, simple, reliable, proton therapy machine is the 235 MeV cyclotron planned for the Massachusetts General Hospital (MGH) for which conventional cyclotron technology has been chosen.

These two examples will probably be the first ones of a larger series, and it is only with this type of machine that neutron therapy and proton therapy could clinically expand and gain a real place, in cancer treatment, among the other radiotherapy techniques.

The problems raised by heavy ion beam therapy are quite different due to the high cost and technical complexity of the equipment [15] [47]. At present, only a few facilities could be planned worldwide.

An international cooperation is necessary in order to ensure a rapid exchange or information and an appropriate patient recruitment. Sufficient patient recruitment is needed for se-selecting tumour types or sites for which there is evidence that better results could be expected with heavy ions than with conventional treatments. From a more scientific point

of view, appropriate recruitment is needed for initiating randomized trials designed to answer specific questions of great relevance in radiobiology and/or radiation therapy.

In photon therapy, an accuracy on dose delivery as high as 3.5 % (i.e., one standard deviation on the absorbed dose at the specification point) is required. This requirement is due to the steepness of the dose-effect relations for local tumour control and normal tissue complications. For high-LET radiations, the available clinical and radiobiological data indicate that the dose-effect relations are as steep as those observed for photons, and consequently the same degree of accuracy must to be achieved. Furthermore, as discussed above, at least the same physical selectivity (dose distribution) is required due to a reduced differential effect with high-LET radiations [48].

Therefore, in order to obtain the maximum benefit of the application of these new beams (neutrons, protons, heavy ions), and to use them in optimal conditions, research in dosimetry is necessary as well as development of quality assurance programmes. In addition, further research on atomic and molecular data is justified for the different components of human (and biological) tissues and detectors, as well as for materials used for the beam collimation and shielding. Acquisition of data should be extended to the types of particles and energy ranges considered in this report.

REFERENCES

1 DEVITA V. T.
Progress in Cancer Management
Cancer , **51** : 2401-2409, 1983

2 DEVITA V. T., KORN D.
Progress against cancer
New Engl. J. Med., **315** : 964, 1986

3 DAVIS D.L. , HOEL D. , FOX J. , LOPEZ A.
International trends in cancer mortality in France, West Germany, Italy, Japan, England and Wales, and the USA
The Lancet, **336**, 474- 481, 1990,

4 DOLL R.
Are we winning the fight against cancer ? An epidemiological assessment
EACR - Mühlbock Memorial Lecture
Eur. J.Cancer, **26** , 500-508, 1990.

5 SUIT H. D.
Potential for improving survival rates for the cancer patient by increasing the efficacy of treatment of the primary lesion
Cancer, 50, 1227-1234, 1982.

6 MUIR C.S., BOYLE P.
The Burden of Cancer in Europe
Eur. J.Cancer, 26 , 1111-1113, 1990

7 (Report of the) NATIONAL PANEL OF CONSULTANTS ON THE CONQUEST OF CANCER, prepared for the Committee on Labor and Public Welfare United States Senate, Novembrer 1970, U.S. Government Printing Office Washington, 1970, Part 2, p. 51.

8 WAMBERSIE A.
Les faisceaux de protons dans le traitement des cancers. Espoirs et Réalités. Louvain Méd. 110: 13-33, 1991.

9 SUIT H.D., GOITEN M., MUZENRIDER J., VERHEY L., URIE M., GRAGOUDAS E., KOEHLER A., GOTTSCHALK B., SISTERSON, J., TATSUZAKI H, MIRALBELL R.,
Increased efficacy of radiation therapy by use of proton beam
Strahlenther. Onkol. 1990; 166: 40-44.

10 J.R. CASTRO, G. GADEMANN, J.M. COLLIER, D. LINSTAD, S.PITLUCK, K. WOODRUFF, G.GAUGER, D. CHAR, Ph. GUTIN, Th L. PHILLIPS, W. CHU, Sh. HENDERSON
Strahlentherapie mit schweren Teilchen am Lawrence Berkeley Laboratory der Universität von Kalifornien; Strahlentherapie und Onkologie 163, 1987, 9-16.

11 ZOGRAFOS L., UFFER S., GAILLOUD C., BERCHER L.
Les mélanomes de la conjonctive et leur traitement.
Klin Monatsbl. Augernheilkd. 1990; 196:285-289.

12 BERCHER L., ZOGRAFOS L., EGGER E., CHAMOT L., UFFER S., GAILLOUD C., DUCREY N.
Le traitement des mélanomes extériorisés de la choroïde par faisceau de protons accélérés.
Klin Monatsbl. Augernheilkd. 1992; 200 : 440-443.

13 MAZAL AL A.
Centre de Protonthérapie d'Orsay, Rapport Technique, Décembre 1993, Centre Universitaire, Bât. 101, F-91400 - Orsay-France.

14 M. AUSTIN-SEYMOUR, M.URIE, J. MUZENRIDER, C. WILLETT, M. GOITEIN, L. VERHEY, R. GENTRY, P.McNULTY, A. KOEHLER, H.SUIT Considerations in Fractionated Proton Radiation Therapy Clinical Potential and Results.
Radiotherapy and Oncology, 1990, **17**, 29-35.

15 CHAUVEL P., WAMBERSIE A. (Editors),
EULIMA Workshop on the Potential Value of Light Ion Beam Therapy.
Publication EUR 12165 EN of the Commission of the European Communities,
c ECSC-EEC-EAEC, Brussels-Luxembourg and CAL Edition, 1989 .

16 J.R. CASTRO, NOWAKOWSKI V., LINSTADT D., COLLIER J.M., PETTI P.L., LYMAN J., PHILLIPS T.L., CHAR D., GAUGER G.E., WOODRUFF K., CHU W., LUDEWIGT B;, RENNER T., SINGH R.P., PITLUCK, S; WHITCOMB T.
Heavy charged particle therapy at the Lawrence Berkely Laboratory, pp. 219-232, In: Ref. **15**.

17 A. WAMBERSIE, V. GREGOIRE, J.M. BRUCHER
Potential Clinical Gain of Proton (and Heavy Ion) Beams for Brain Tumors in Children, Int. J. Radiation Oncology Biol. Phys., 1991, **22**, 275-286.

18 KITAGAWA T.
Proton beam therapy at the Tsukuba University, pp. 191-196. In: Ref. **15**.

19 LARSSON B.
Use of Medium Energy Particles in Radiobiology and Radiotherapy. Journal Européen de Radiothérapie, 3, 223-234, 1984.

20 LARSSON B.
Proton therapy : review of the clinical results, pp. 139-164. In: Ref. **15**.

21 BLOOMQUIST E. et al.
Medical projects at the Svedberg Laboratory, pp. 68-69. In: The Svedberg Laboratory progress report, 1992-1993, Uppsala, Sweden.

22 STONE R.S.
Neutron therapy and specific ionization. *Am. J. Roentgenol.*, **59** : 771-785, 1948.

23 CHAPMAN J.D.
Biophysical models of mammalian cell inactivation by radiation, in : *Radiation biology in cancer research* (R.E. Meyn, H.R. Withers, eds), pp 21-32. Raven Press, New York, 1988.

24 FERTIL B., DESCHAVANNE P.J., GUEULETTE J., POSSOZ A., WAMBERSIE A., MALAISE E.P.. *In vitro* radiosensitivity of six human cell lines. Relation to the RBE of 50-MeV neutrons. *Radiat. Res.*, **90**: 526-537,1982.

25 MENZEL H.G., PIHET P, WAMBERSIE A.
Microdosimetric specification of radiation quality in neutron radiation therapy. *International Journal of Radiation Biology*, **57**, 865-883,1990.

26 TUBIANA M., DUTREIX J., WAMBERSIE A.
Introduction to Radiobiology, *Taylor & Francis*, London, (371 pages), 1990.

27 A. WAMBERSIE
Neutron therapy : from radiobiological expectation to clinical reality. Radiation Protection Dosimetry (Nuclear Technology Publishing), **44**, 379-395, 1992.

28 WAMBERSIE A., RICHARD F., BRETEAU N.
Development of Fast-Neutron Therapy Worldwide. Radiobiological, Clinical and Technical Aspects, Acta Oncologica, 1994 (in press).

29 NATIONAL CANCER INSTITUTE (NCI)
Fast Neutron Radiation Therapy in the United States : A Twenty-Year NCI Sponsored Research Program (NTCWG Annual Report, 1991), National Cancer Institute, Bethesda, MD 20892, USA, 1991.

30 CATTERALL M., BEWLEY D.K.
Fast neutrons in the treatment of cancer. London, *Academic Press.*, 1979.

31 LARAMORE G.E., GRIFFITH J.T., BOESPFLUG M., PELTON J.G., GRIFFIN T., GRIFFIN B.R., RUSSELL K.J., KOH W., PARKER R.G., DAVIS L.W.
Fast neutron radiotherapy for sarcomas of soft tissue, bone, and cartilage. Am. J. Clin. Oncol. (CCT) **12**: 320-326,1989.

32 PÖTTER R., KNOCKE T.H., HAVERKAMP U., AL-DANDASHI CHR.
Treatment planning and delivery in neutron radiotherapy of soft tissue sarcomas, *Strahlentherapie und Onkologie*, **166**, 102-106, 1990.

33 BATTERMANN J.J.
Clinical application of fast neutrons, the Amsterdam experience. Thesis, University of Amsterdam (The Netherlands), 1981.

34 FRANKE H.D., LANGENDORFF G., HESS A.
Die Strahlenbehandlung des Prostata-Carcinoms in Stadium C mit schnellen Neutronen. Verhandlungsbericht der Deutschen Gesellschaft für Urologie, 32 Tagung 1980, Berlin, Heidelberg, New-York Springer-Verlag, 1981, 175-180.

35 TSUNEMOTO, H., MORITA, S., SATHO, S., IINO, Y., YUL YOO, S.
Present status of fast neutron therapy in Asian countries. Strahlentherapie und Onkologie, 165, 330-336, 1989.

36 F. RICHARD, P. J. VAN CANGH, A. WAMBERSIE
Intérêt de la neutronthérapie des adénocarcinomes localement étendus de la prostate (stade C). Résultats obtenus au cyclotron de Louvain-la-Neuve. *Acta Urologica Belgica*, **59**, 35-52, 1991.

37 LARAMORE G.E., KRALL J.M., THOMAS F.J., RUSSELL K.J., MAOR M.H., HENDRICKSON F.R., MARTZ, K.L. GRIFFIN T.W. DAVIS L.W.: Fast neutron radiotherapy for locally advanced prostate cancer : Final report of a Radiation Therapy Oncology Group randomized clinical trial. *Am J Clin Oncol (CCT)* **16**: 164-167, 1993

38 RUSSELL, K.J., CAPLAN R.J., LARAMORE G.E., BURNISON C.M., MAOR M.H., TAYLOR M.E., ZINK S., DAVIS L.W., GRIFFIN T.W.
Photon versus fast neutron external beam radiotherapy in the treatment of locally advanced prostate cancer: results of a randomized prospective trial. *Int. J. Radiat. Oncol. Biol. Phys.* , **28**, 47-54, 1993

39 V. GREGOIRE, M. BEAUDUIN, J. GUEULETTE, B.M. DE COSTER, M. OCTAVE-PRIGNOT, S.VYNCKIER, A. WAMBERSIE
Radiobiological intercomparison of p(45)+Be and p(65)+Be neutron beams for lung tolerance in mice after single and fractionated irradiation
Radiation Research, **133**, 27-32,1993

40 INTERNATIONAL COMMISSION ON RADIATION UNITS AND MEASUREMENTS.
Clinical Neutron Dosimetry. Part I: Determination of Absorbed Dose in a Patient Treated by External Beams of Fast Neutrons. *ICRU Report 45*, 85 pages (1989)
ICRU Publications 7910 Woodmont avenue, Suite 1016, BETHESDA, Maryland 20814, USA.

41 PIHET P., MENZEL H. G., SCHMIDT R., BEAUDUIN M.AND WAMBERSIE A.
Evaluation of a microdosimetric intercomparison of european neutron therapy centres, in *Radiation Protection Dosimetry, Microdosimetry* , 31, 437-442 ,1990.

42 WAMBERSIE A.
Fast neutron therapy at the end of 1988 - a survey of the clinical data. *Strahlentherapie und Onkologie*, 166, 52-60, 1990.

43 J.R. CASTRO
Heavy ion radiotherapy In G. Kraft and U. Grundinger (Ed.). Third workshop on heavy charged particles in biology and medicine, GSI - Darmstadt, Report 87-11, ISSN 0171-4546, 1987, KO I-5.

44 WAMBERSIE A.
The future of high-LET radiation in cancer therapy. Justification of the Heavy-Ion Therapy Programs. pp. XIX- LIII, in : Ref. [15].

45 SATO K.
HIMAC Project Status I - Accelerator Complex, pp.23-35. In: Akifuni ITANO and Tatsuaki KANAI (Eds). Proceedings of the NIRS International Workshop on Heavy Charged Particle Therapy and Related Subjects , July-4-5, 1991, NIRS-M-81. National Institute of Radiological Sciences, 9-1, Anagawa 4-Chome, Chiba 260, Japan.

46 SOGA F.
HIMACProject Status II - Irradiation Facility, pp.36-42. In: Akifuni ITANO and Tatsuaki KANAI (Eds). Proceedings of the NIRS International Workshop on Heavy Charged Particle Therapy and Related Subjects , July-4-5, 1991, NIRS-M81, National Institute of Radiological Sciences, 9-1, Anagawa 4-Chome, Chiba 260, Japan.

47 WAMBERSIE A.
Radiobiological and clinical bases of particle therapy (review), pp. S1-S3. In P. Chauvel, A. Wambersie, P. Mandrillon (Eds). **EPAC 90**, Medical Satellite Meeting, Acropolis, Nice-France, June 14-16, 1990. Editions Frontières, B.P. 33, F-91192 Gif -sur-Yvette, France

48 MIJNHEER B.J., BATTERMANN J.J., WAMBERSIE A.
What degree of accuracy is required and can be delivered in photon and neutron therapy ? *Radiotherapy and Oncology*, 8, 237-252, 1987.

Chapter 2

IONIZATION BY FAST CHARGED PARTICLES*

L.H. Toburen**
Pacific Northwest Laboratory,
Richland, Washington,
United States of America

The author acknowledges valuable contributions to this chapter by R.D. Dubois, Pacific Northwest Laboratory, Richland, WA 99352, USA, H. Paul, Institut für Experimentalphysik der Universität Linz, Austria, M.E. Rudd, University of Nebraska, Lincoln, NB 68588, USA and W.E. Wilson, Pacific Northwest Laboratory, Richland WA 99352, USA.

* This research was supported in part by the US Department of Energy, Office of Health and Environmental Research, Contract no. DE-AC06-76RLO-1830.

** Present address: National Academy of Sciences, 2101 Constitution Ave. N.W., Washington, D.C. 20418, USA.

Glossary of commonly used terms and symbols in chapter II
(Because this review encompasses several subfields of physics symbols may, in some cases, be redefined in the text)

a_o	Bohr radius (5.29×10^{-11} m)
B_i	binding energy of the i^{th} electronic shell of an atom or molecule
CCT	charge transfer to the ionization continuum of the projectile
CDW-EIS	continuum distorted wave-eikonal initial state; atomic wave function model
CTMC	classical trajectory Monte Carlo computational model
DDCS	doubly differential ionization cross section, differential in elected electron energy and solid angle of emission
$\frac{d\sigma}{dQ}$	singly differential ionization cross section, differential in energy loss Q
$\frac{d^2\sigma}{dQd\Omega}$	doubly differential ionization cross section, differential in energy loss Q and solid angle Ω of electron emission
ϵ	ejected electron energy
E	energy of the incident particle (projectile)
eV	electron volts
f	dipole oscillator strength
I	ionization potential on the outermost bound electron in the target atom or molecule
keV	thousand electron volts
LET	linear energy transfer
m	electron mass (also designated as m_e)
m_o	rest mass of the electron
MeV	million electron volts
N_i	number of electrons in the i^{th} subshell of the target
PWBA	plane wave Born approximation
π	pi = 3.1416
q	net charge of the incident particle (for bare ions q=z)
Q	energy loss, i.e., normally $Q = \epsilon + I$, however, for consideration of atomic or molecular electronic subshells, $Q_i = \epsilon + B_i$
RBE	relative biological effectiveness
SDCS	singly differential ionization cross section; in this chapter, refers to electron emission cross sections differential with respect to ejected electron energy
σ or σ_T	total cross section; in this chapter, commonly refers to the total ionization cross section
$\sigma(\epsilon)$	singly differential ionization cross section, differential with respect to ejected electron energy ϵ; experimentally determined, and, therefore, averaged over the energy resolution of the detection system.
$\sigma(\theta)$	singly differential ionization cross section, differential with respect to the solid angle of detection for ejected electrons at an emission angle θ; experimentally determined, and, therefore, averaged over the angular resolution of the detection system.
$\sigma(\epsilon,\theta)$	doubly differential ionization cross section, differential with respect to the ejected electron energy ϵ and the solid angle for detection of an electron at an emission angle θ; experimentally determined, and, therefore, averaged over the energy and angular acceptance of the detection system.
R	Rydberg unit of energy (R = 13.6 eV)
T	energy of the incident particle in units of the energy of an electron of equal velocity, $T=\frac{1}{2}m_e v_p^2$, where m_e is the rest mass of the electron and v_p is the projectile velocity.

TOF	time-of-flight; refers to an electron energy analysis technique
θ	ejected electron emission angle measured with respect to the forward direction the incident projectile.
Y(Q,T)	ratio of the measured SDCS, for energy loss Q and projectile scaled energy T, to the corresponding values derived from the Rutherford formula
v	incident particle velocity
w	ϵ/I; or, for atomic or molecular subshells $w_i = \epsilon/B_i$
Z or Z_2	target nuclear charge
z or Z_1	projectile nuclear charge
$Z(Q,T,\theta)$	ratio of the measured DDCS, for energy loss Q from an incident particle of scaled energy T to an electron ejected at an angle θ, to the corresponding SDCS obtained from the Rutherford formula

2.1. INTRODUCTION

Understanding the biological consequences of the interaction of radiation with matter, whether for developing protocol for radiation therapy or for the practice of radiation protection, relies on an accurate knowledge of a broad range of atomic and molecular data. A common feature of energy deposition by all ionizing radiation is the production and degradation of secondary electrons in the absorbing medium. The relative biological effectiveness (RBE) of different radiations must, therefore, be related to the detailed characteristics of these events and how they influence the subsequent chemical and biological processes. For radiation of high-linear-energy-transfer (high-LET) the interactions contributing to energy loss may lead to the release of fast secondary electrons and energetic recoil ions that, in turn, may produce further ionization, as well as lead to excited states of the atomic and molecular constituents of the medium. These interactions result in locally dense regions of energy deposition that spawn highly inhomogeneous chemical reactions, the products of which must subsequently be confronted by the biological system.

Considerable progress has been made in understanding the effects of radiation quality on biological effectiveness through the study of microdosimetry, charged particle track structure, and biochemically based biophysical models of the damage initiated by ionizing radiation. Common to all these studies is the application of a detailed data base of excitation and ionization cross sections for the interaction of charged particles with atomic, molecular and condensed phase targets. Inokuti [1] has emphasized that to be useful for radiological applications this data base must be "right, absolute, and comprehensive". In this chapter we review the present status of data base contributing to our understanding of ionization for interactions of charged particles with biologically important material and explore techniques to assess the accuracy of the available data. This review will be limited primarily to those ionization cross sections that have been presented as absolute values or that can be placed on an absolute scale in an unambiguous manner. Some departure from this condition is allowed where the systematics of cross sections, such as their energy dependence, is explored.

This chapter focuses on review of differential and total ionization cross sections for charged particle impact, with a more limited discussion of charge transfer, inner-shell ionization, and the use of effective charge in radiobiology. Total ionization cross sections are useful in radiobiology for determination of ion mean-free-paths and they provide useful information for assessing the accuracy of differential ionization cross sections. Cross sections differential in ejected electron energy (SDCS) provide detailed information on the energy loss process and doubly differential cross sections (DDCS), differential in ejected electron energy and emission angle, provide data necessary for determining the spatial patterns of energy deposition. We do not treat triply differential cross sections, differential in the angle of the scattered primary as well as in ejected electron energy and emission angle, in this report; the availability of such data is limited in extent and has limited application to radiation biology. Singly and doubly differential cross sections are discussed for electron impact, proton impact, and heavy ion impact; in this context heavy ions are considered to be those ions heavier than protons, including neutral hydrogen.

A serious attempt was made in preparing this chapter to be consistent with notation commonly used in the field of radiation physics. Being a review, however, we have selected data from many sources and in numerous occasions the notation used in those sources is different from the "standard" adopted for this chapter. In cases where the work of referenced authors differs from our style, either their notation is changed to conform to ours, or their notation is retained with proper definition of the symbols used. The

notation we have used in reference to measured doubly differential cross sections is that the quantity $\sigma(\epsilon,\theta)$ represents the differential cross section in units of area, per unit energy (eV) and per unit solid angle (averaged over the energy and angular acceptance of the detector), for ejection of an electron of energy ϵ at an emission angle of θ with respect to the outgoing ionizing particle; the energy of the incident ion is not explicitly shown. For singly differential cross sections, $\sigma(\epsilon)$ represents the cross section, per unit energy, for emission of an electron of energy ϵ, and $\sigma(\theta)$ is the cross section per unit solid angle for emission of an electron at an angle θ. The total cross section for electron production is given simply by σ, or in some cases the more explicit notation σ_T is used. The use of σ, $\sigma(\epsilon)$, and $\sigma(\epsilon,\theta)$ are limited for reference to measured quantities; differential cross sections obtained from theoretical calculations are designated by $d\sigma/dQ$ (differential with respect to energy loss) and $d^2\sigma/dQd\Omega$ (differential with respect to both energy loss of the projectile and solid angle of the ejected electron) to explicitly indicate the true differential character of these quantities. Charge transfer cross section commonly use the notation σ_{if} to refer to collisions in which the incident particle has charge i and the final charge state of the ion is given by f.

The review of total ionization cross sections in this chapter is limited to ion impact; total ionization cross sections for electron impact will be discussed in chapter 3. All ionization cross section measurements that are reviewed in this chapter were obtained in experiments under single collision conditions using gas phase targets with the exception of some of the measeruments of innershell ionization cross section, and stopping power, where, in some instances, solid targets were used. Portions of this chapter were also included in a recent review of Atomic and Molecular Physics in the Gas Phase presented by Toburen [2] at a Symposium sponsored by the U. S. Department of Energy.

2.2. DOUBLY DIFFERENTIAL IONIZATION CROSS SECTIONS

2.2.1. Electron Impact

Ionizing radiation, by definition, results in the deposition of energy through the release of free electrons and, thereby, the generation of ions in matter. The chemical and biological response of the medium to the absorption of energy from the radiation field is largely determined by the fate of these electrons as they undergo subsequent interactions with the constitutents of the stopping medium and ultimately thermalize. Energy transport by the slowing down of electrons leads to the spatial pattern of energy deposition that, on a microscopic scale, is uniquely, albeit stochastically, defined by the parameters of the radiation field. This initial pattern of energy deposition sets the stage for subsequent chemical reactions that ultimately lead to the response of the biological system. It is, therefore, important that one have a detailed knowledge of the cross sections for interactions of electrons with the stopping medium of interest if an assessment of the effects of radiation quality on biological effectiveness is to be possible. Of particular importance to radiation biology is the energy and angular distribution of secondary electrons ejected in collisions between moving electrons and the bound electrons of the absorbing media. These cross sections determine the transport of energy via secondary electrons and define the spatial characteristics of the absorbed energy. Singly differential and total ionization cross sections play a role, not only in determining the pattern of energy deposition, but also in assessing the reliability of the doubly differential cross sections.

An excellent review of the doubly differential cross sections for electron impact ionization has been published by McDaniel et al. [3] and a

TABLE 2.1

PUBLISHED DOUBLY DIFFERENTIAL CROSS SECTIONS

ELECTRON IMPACT

Target	Incident Electron Energy (eV)	Ejected Electron Energy (eV)	Ejected Electron Angle (Degrees)	Investigators
He	50 - 300	1-1/2(E-I)	6 - 156	Shyn and Sharp [5]
He	100, 200	3-(E-I)	10 - 150	Rudd and DuBois [6]
He	50 - 2000	4 - 2000	30 - 150	Opal, Beaty, and Peterson [7,8]
He	200 - 2000	2 - E	30 - 150	Goruganthu and Bonham [9]
He	100 - 600	2 - 40	18 - 150	Muller-Fiedler, Jung, and Ehrhardt [10]
He	100	1 - (E-I)	2.5 - 164	Goodrich [11]
He	50 - 500	4 - (E-I)	10 -150	Sethuraman, Rees, and Gibson [12]
He	500, 1000	25 - 45	10 - 130	Oda, Nishimura, and Tahira [13]
Ne	100 - 500	4-(E-I)	10 - 150	DuBois and Rudd [14]
Ne	500	4 - 200	30 - 150	Opal, Beaty, and Peterson [7,8]
Ar	100 - 500	4-(E-I)	10 - 150	DuBois and Rudd [14]
Ar	500	4 - 200	30 - 150	Opal, Beaty, and Peterson [7,8]
Ar	1000	4 - 500	90	Mathis and Vroom [15]
Kr	500	4 - 200	30 - 150	Opal, Beaty, and Peterson [7,8]
Kr	1000	21 - 52	10 - 130	Oda, Nishimura, and Tahira [13]
Xe	500	4 - 200	30 - 150	Opal, Beaty, and Peterson [7,8]
H_2	100 - 500	4-(E-I)	10 - 150	DuBois and Rudd [14]
H_2	500	4 - 200	30 - 150	Opal, Beaty, and Peterson [7,8]
H_2	25 - 250	1-1/2(E-I)	12 - 156	Shyn, Sharp, and Kim [16]
N_2	100 - 500	4-(E-I)	10 - 150	DuBois and Rudd [14]
N_2	50 - 2000	4 - 200	30 - 150	Opal, Beaty, and Peterson [7,8]
N_2	200 - 2000	2-E	30 - 150	Goruganthu, Wilson, and Bonham [17]
N_2	500 - 1000	5 - 500	40 - 115	Tisone [18]

TABLE 2.1 (cont'd)

PUBLISHED DOUBLY DIFFERENTIAL CROSS SECTIONS

ELECTRON IMPACT

Target	Incident Electron Energy (eV)	Ejected Electron Energy (eV)	Ejected Electron Angle (Degrees)	Investigators
N_2	1000	4 - 500	90	Mathis and Vroom [15]
N_2	50 - 400	1-1/2(E-I)	12 - 156	Shyn [19]
O_2	50 - 2000	4 - 200	30 - 150	Opal, Beaty, and Peterson [7,8]
O_2	25 - 250	1-1/2(E-I)	12 - 156	Shyn and Sharp [20]
CH_4	200	4 - 200	30 - 150	Opal, Beaty, and Peterson [7,8]
CH_4	500, 1000	5 - 1000	15 - 148	Oda [21]
NH_3	200	4 - 200	30 - 150	Opal, Beaty, and Peterson [7,8]
H_2O	50 - 2000	2-(E-I)	15 - 150	Bolorizadeh and Rudd [22]
H_2O	1500	2 - 1500	15 - 150	Hollman, Kerby, Rudd, Miller, and Manson [23]
H_2O	500	4 - 200	30 - 150	Opal, Beaty, and Peterson [7,8]
H_2O	1000	4 - 500	90	Mathis and Vroom [15]
H_2O	1000	4 - 500	90	Mathis and Vroom [15] (clusters)
H_2O	500, 1000	5 - 1000	15 - 148	Oda [21]
C_2H_2	500	4 - 200	30 - 150	Opal, Beaty, and Peterson [7,8]
CO	800	.9 - 393	30 - 150	Ma and Bonham [24]
CO	500	4 - 200	30 - 150	Opal, Beaty, and Peterson [7,8]
NO	500	4 - 200	30 - 150	Opal, Beaty, and Peterson [7,8]
CO_2	500	4 - 200	30 - 150	Opal, Beaty, and Peterson [7,8]
CO_2	50 - 400	1-1/2(E-I)	12 - 156	Shyn and Sharp [25]
CO_2	500, 1000	5 - 1000	15 - 148	Oda [21]

more recent review by Paretzke [4] provides an excellent guide to the literature of electron interactions of interest to radiobiology and to radiation chemistry. Table 2.1 of this chapter provides a listing of the measured doubly-differential electron emission cross sections, differential with respect to "ejected" electron energy and emission angle, that has been obtained from a search of the literature through 1990. Since electrons are indistinguishable, the slower of the two electrons leaving a collision is defined as the secondary "ejected" electron. To completely define the

collision for electron impact one would need to measure triply-differential cross section, i.e., also detect the scattering angle of the primary electron. A limited number of triply-differential cross sections have been measured for simple gas targets such as helium and argon; see, for example, Ehrhardt et al. [26,27], Beaty et al.[28], and Hong and Beaty [29]. As indicated above, these data are considered out of the scope of the present review as they have been of little practical use in microdosimetry and track structure calculations. However, they have been excellent tools for the detailed testing of collision theory.

Although Table 2.1 illustrates that there is a relatively large amount of data available regarding the DDCS's for ionization of atomic and molecular targets by incident electrons, only a limited subset of this data is appropriate to targets of direct interest to radiation therapy or radiation biology. In addition, where data have been obtained by different groups, such as the cross sections for ionization of water vapor shown in FIG. 2.1, there is, in certain regions of the spectra, considerable scatter among the data sets. For the data shown in FIG. 2.1, general agreement is observed among the data of Opal et al. [7], Oda [21], and Bolorizadeh and Rudd [22] for electrons

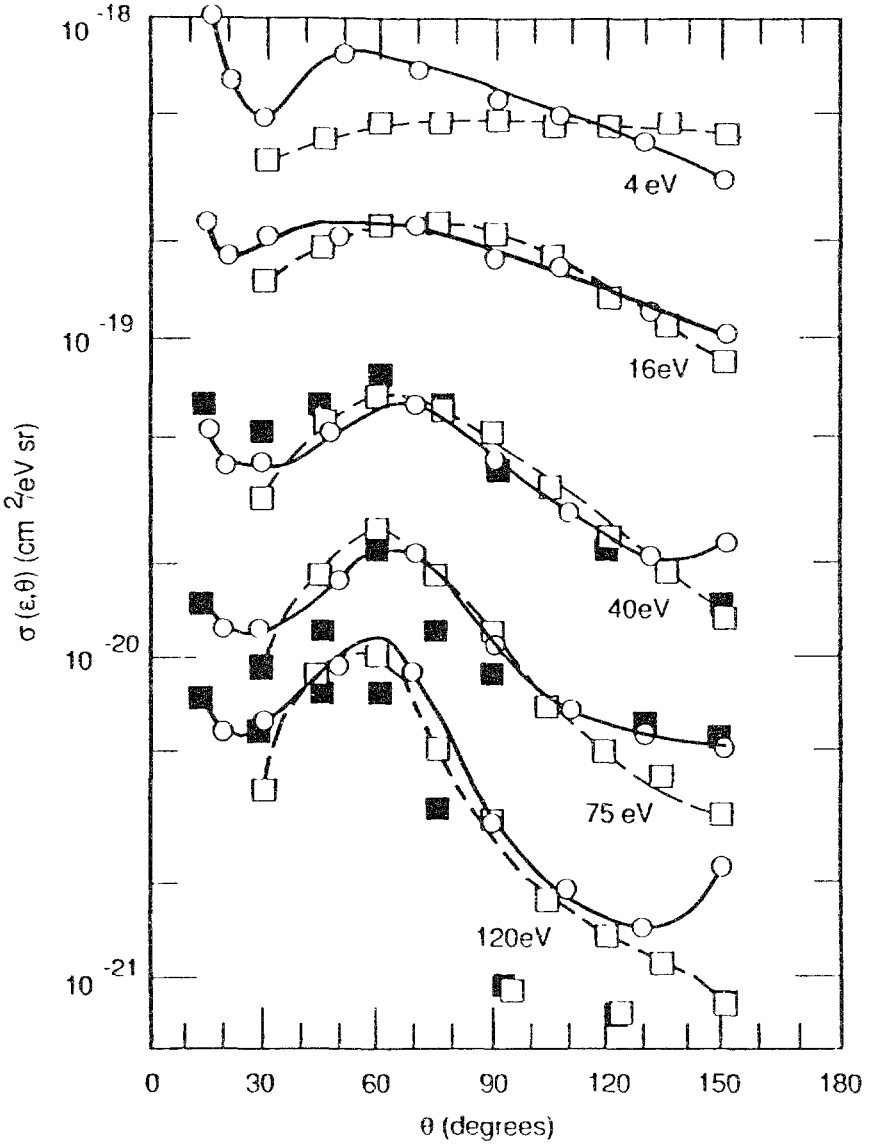

FIG. 2.1. Angular distributions of electrons ejected from water vapor by 500eV electron impact. The data are from (□) Opal et al. [7], (■) Oda [21], and (o) Bolorizadeh and Rudd [22].

emitted at intermediate angles , however, at both large and small emission angles the cross sections of Opal et al. tend to be smaller than the other two measurements. These differences are attributed to instrumental effects and the manner by which the authors use different methods to account for the finite size of the target as it is viewed from different angles. The true cross sections are probably somewhere between the extremes represented by the data of Opal et al. [7] and of Bolorizadeh and Rudd [22] .

The increase in the cross section for small emission angles has been a consistent feature in the data of the University of Nebraska [6, 14, 22] and has also been observed by Oda [21] and Ehrhardt et al. [30]. However, a peak at small emission angles was not observed in more recent measurements of Gorunganthu et al. [17] that focussed on the ionization of molecular nitrogen by electrons of comparable impact energy. This latter data is particularly significant in that Gorunganthu et al. used an entirely different experimental technique in their study. They used a time-of-flight system to measure the energy spectrum of ejected electrons and determined the absolute scale by matching the experimental elastic differential cross sections to the absolute measurements at each primary energy. Gorunganthu et al. found no evidence of a peak at small angles at any of the electron energies they investigated. In addition, in his analysis of doubly differential cross sections for ionization of helium by electrons (discussed below) Kim [31] concluded there was no theoretical justification for such a peak at small emission angles. In addition, more recent work at the University of Nebraska, with improved methods of spurious electron suppression [23] has resulted in only a slight indication of a forward peak. These latter results cast doubt on the validity of the data for small emission angles presented by Rudd and DuBois [6], Oda [21], Bolorizadeh and Rudd [22], and Ehrhardt et al. [30].

Because of the lack of a comprehensive set of electron impact data and the scatter among experimental data from different research groups, a good deal of effort has gone into theoretical techniques to evaluate the accuracy of measured cross sections and to provide a means to extrapolate data to regions where data are nonexistent. Following the lead of Platzman, Kim has explored the consistency of experimental data for electron and proton collisions using well established theory [31-36]. In the study of DDCS for ionization of helium by electron impact Kim [31] described six major requirements that the data must exhibit if they are to be considered correct. These requirements are 1) proper threshold behavior, 2) appropriate asymptotic (high-energy) behavior, 3) angular symmetry in the slope of the Fano plot, 4) correct integrated cross sections, 5) correct energy-loss cross sections, and 6) proper kinetics of the binary peak. As Kim points out, the first requirement is trivial; this requires that the cross sections must vanish at the appropriate thresholds. The second requirement implies that, when the DDCS for a specific ejected electron energy ϵ and emission angle θ are plotted as a function of ln(T/R) the limiting slopes must be proportional to the oscillator strengths for photoionization; here T is the kinetic energy of the incident electron and R is the Rydberg unit of energy. The third requirement indicates that the slopes observed in plots of the form described in requirement 2 should be similar for comparison of doubly differential cross sections at complementary angles, i.e., for $\theta_1+\theta_2=180$; this results from the nature of the angular distributions of photoelectrons. Requirement 4 is that the integrated cross sections must yield the proper single differential and total ionization cross sections and that they must exhibit the proper slopes when plotted as a Fano plot, i.e., the slope as determined from the corresponding oscillator strengths for photoionization. Requirement 5 provides no direct information on the DDCS, but insures consistency with energy loss measurements following integration of the DDCS. The last requirement, number 6 above, is that the scattering kinematics for collisions

resulting in large energy loss must reflect a classical description of the scattering process; i.e., electron-electron or ion-electron scattering should obey classical scattering relationships when the energy transfer is large compared to the electron binding energy.

Because of the effects of electron binding ,the kinematic requirement, the last of Kim's requirements listed above, becomes more a qualitative guideline than a definitive test. For electron collisions, assuming a free target electron, classical kinematics give the relationship $T = T_{max}\cos^2\theta$, where T is the energy transferred to the free electron, T_{max} is the initial kinetic energy of the incident electron, and θ is the angle between the direction of the extended path of the incident electron and that of the ejected electron. Except for the lowest ejected electron energy data of Bolorizadeh and Rudd the angular distributions shown in FIG. 2.1 peak near the kinematic prediction. The widths of the angular distributions reflect the effect of the initial momentum distributions of the bound electrons.

Another direct test of the DDCS described by the consistency requirements of Kim is provided by a Fano plot as stated in condition 3. The Fano plot of the DDCS plotted for supplementary angles (but for the same ejected electron energy) should have the same slope. This condition results from relationship between the differential oscillator strengths, photoionization cross sections, and the angular distribution of electrons ejected by unpolarized photons. To illustrate these relationships it is convenient to follow the convention introduced by Kim and first scale the DDCS in units of the corresponding Rutherford cross section. By scaling the DDCS in this way it is possible to reduce the wide dynamic range of the DDCS and exhibit them on linear, rather than logarithmic, scales. This enables one to see features in the experimental cross sections that may otherwise go unnoticed in a logarithmic display. The Rutherford cross section for an energy loss Q in a collision between a bare charged particle of charge z and a bound electron is given by

$$\frac{d\sigma_R}{dQ} = \frac{4\pi a_o^2 z^2}{T}\frac{R^2}{Q^2} \quad , \tag{2.1}$$

where a_o is the Bohr radius, R is the Rydberg energy (13.6 eV), $T=\frac{1}{2}mv^2$ (m is the electron mass and v is the incident particle velocity), and $Q=\epsilon+I$ (ϵ is the ejected electron energy and I is the ionization potential of the target atom or molecule). Equation 2.1 gives the cross section per target electron; the total cross section would be a sum over all bound electrons, and the ionization potential I required to evaluate Eq. 2.1 refers to each respective electron in that sum. Unfortunately the experiments can not normally distinguish in which electronic shell the electron was initially bound. Therefore for scaling purposes the Rutherford cross section per electron is used and, for an atom with more than one electronic shell, the ionization potential is taken as that for the outermost, most loosely bound, electron.

The Rutherford cross section can be used to scale either the DDCS or the singly differential cross sections (SDCS) that are obtained by integration of the DDCS with respect to the solid angle of emission. Conventionally the scaled SDCS's for electron impact (z = 1) are defined as

$$Y(Q,T) = \frac{\sigma(\epsilon)}{d\sigma_R/dQ} = \sigma(\epsilon)\frac{T}{4\pi a_o^2}\frac{Q^2}{R^2} \tag{2.2}$$

and the scaled DDCS's are defined as

$$Z(Q,T,\theta) = \frac{\sigma(\epsilon,\theta)}{d\sigma_R/dQ} = \sigma(\epsilon,\theta)\frac{T}{4\pi a_o^2}\frac{Q^2}{R^2} \quad . \tag{2.3}$$

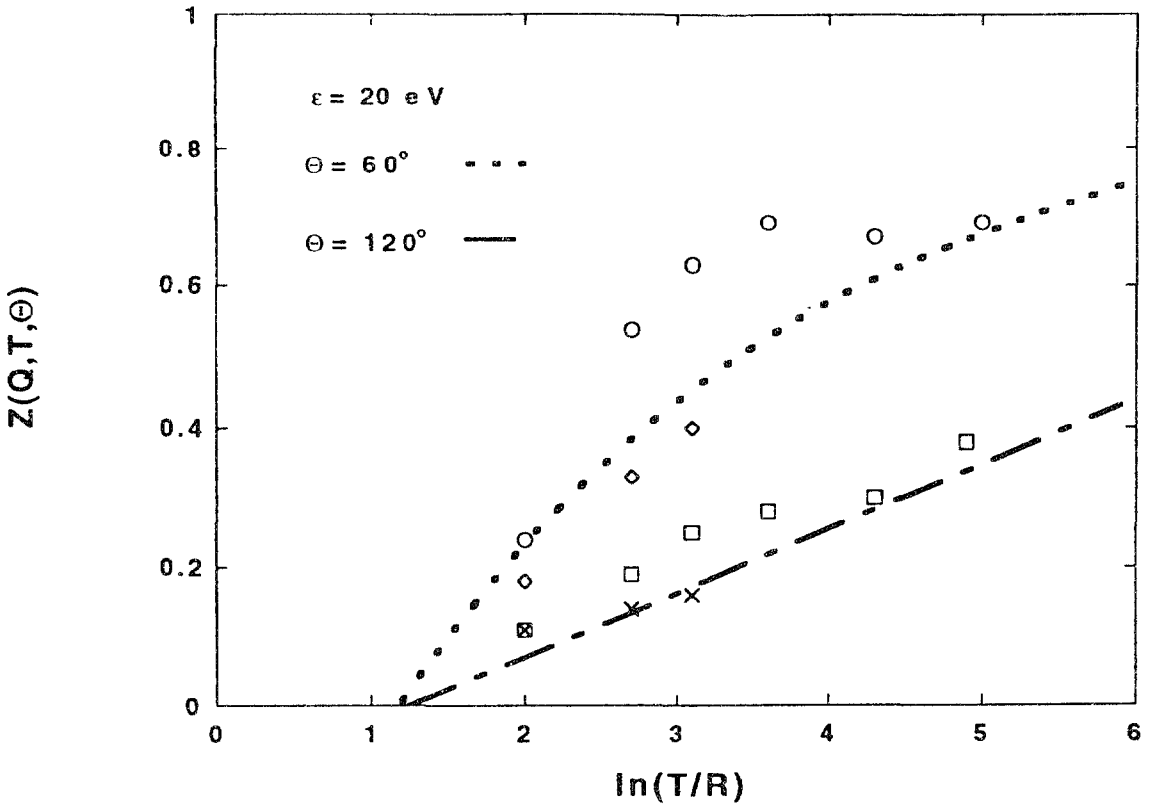

FIG. 2.2. Fano plot of the DDCS for secondary electron emission by electron impact ionization of helium. Cross sections are plotted for a secondary electron energy of 20 eV at the supplementary angles of 60 and 120 degrees. Experimental data are from (o,□) Opal et al. [8] and (◊,x) Shyn and Sharp [5]. The dashed and solid lines are the asymptotic slopes derived from photoionization data by Kim [31].

One of the tests of the reliability and consistency of experimental cross sections (the Fano plot) takes advantage of the asymptotic (high-T) behavior of the Born approximation [37,38]. One can express the Born cross section for ionization by electrons as

$$\sigma_B = \frac{4\pi a_o^2}{T/R}[A \ln(T/R) + B] \quad , \tag{2.4}$$

where A and B, known as the Bethe parameters, are constants that depend on the properties of the target atom, but not on the projectile properties or its energy. In addition, the parameter A is directly related to the dipole oscillator strength f through the relationship

$$A = \frac{f}{Q/R} \quad . \tag{2.5}$$

By using Eqs. 2.4 and 2.5 in either Eq. 2.2 or 2.3 one can show that both Y(Q,T) and Z(T,Q,θ) are proportional to f ℓn(T/R) at sufficiently high projectile energy T. Therefore, if one is to plot Y(Q,T) or Z(Q,T,θ) versus ln(T/R) at a fixed electron emission angle θ, and/or ejected electron energy ϵ, at sufficiently large T the slope of the curve should be proportional to the dipole oscillator strength. This plot, known as the Fano plot, provides an estimate of the reliability of the cross sections in that data sets that do

not approach a straight line dependence for large T, with slope proportional to the dipole oscillator strengths, would be suspect. For DDCS's one can perform an additional consistency test based on the proportionality between the dipole oscillator strengths and the photoionization process. Remembering that the angular distribution of photoelectrons has the general form

$$\sigma_{ph,E}(\theta) = \frac{\sigma_E}{4\pi}[1 - \tfrac{1}{2}\beta(E)P_2(\cos\theta)] \quad , \tag{2.6}$$

where E is the photon energy, σ_E is the integrated photoionization cross section at photon energy E, β is the asymmetry parameter, and P_2 is the second order Legendre polynomial, one can see that the slope of the high T portion of the curve will be the same for emission angles where $P_2(\cos\theta_1)$ is equal to $P_2(\cos\theta_2)$; this will occur under the condition that $\theta_1 + \theta_2 = 180°$. A Fano plot of the experimental data for electron impact ionization of helium is shown in FIG. 2.2 for 20 eV electrons ejected at 60 and 120 degrees. Note that, although there is considerable scatter in the data, the curves drawn through the data points do tend to have the same slope as the line that Kim [31] derived from photoionization data.

A semi-empirical model for the DDCS for electron impact which meets all six of the requirements specified by Kim, above, was presented by Rudd [39]. The model for the angular distributions is part of a more comprehensive model which includes the SDCS and the total ionization cross sections that will be discussed in later sections. So far, the model has only been applied to single-shell targets (H_2 and He), but it may be possible to extend it to more complex targets by adding contributions from individual subshells.

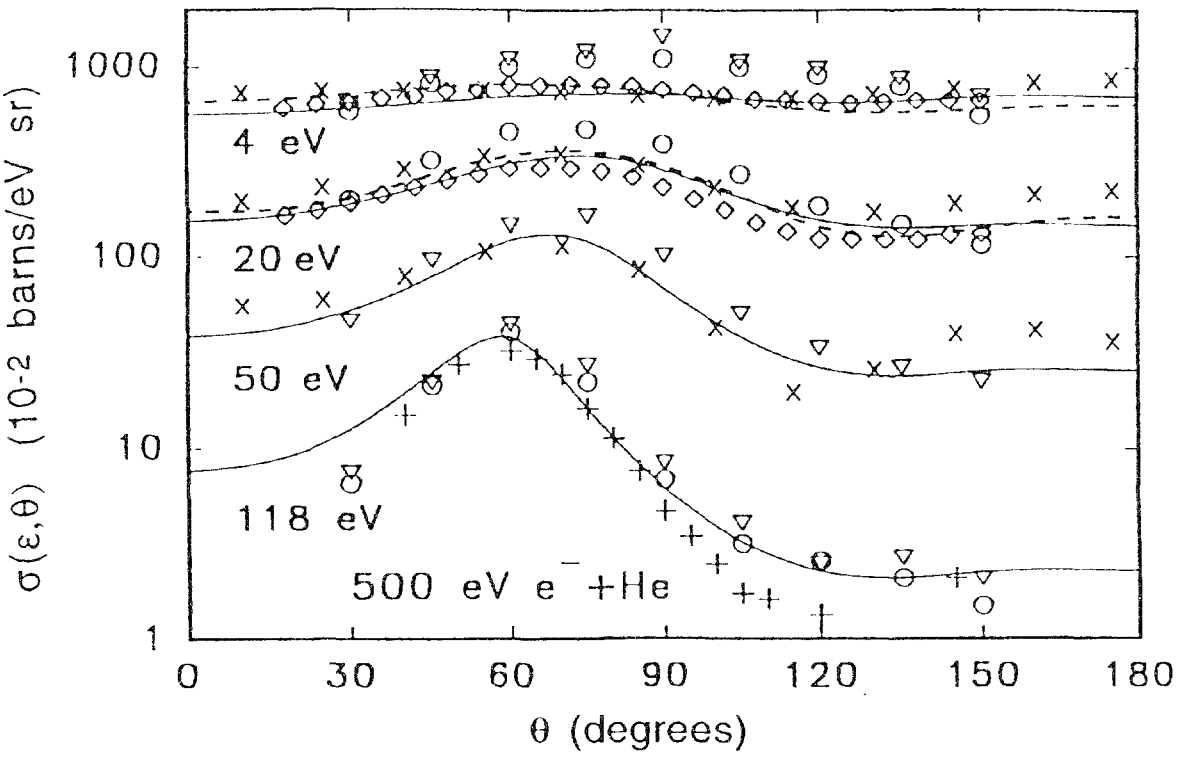

FIG. 2.3. Double differential cross sections for 500 eV e^- + He collisions plotted versus angle for various ejected electron energies. The full line was calculated using Eq. 2.7.

TABLE 2.2

PUBLISHED DOUBLY DIFFERENTIAL CROSS SECTIONS

PROTON IMPACT

Target	Ion Energy Range (keV)	Ejected Electron Energy Range(eV)	Ejected Electron Angle (Degrees)	Investigators
H_2	50 - 100	4 - 300	23 - 152	Kuyatt and Jorgensen [46]
H_2	50 - 100	1 - 500	10 - 160	Rudd and Jorgensen [47]
H_2	100 - 300	2 - 1000	10 - 160	Rudd, Sautter and Bailey [48]
H_2	300	2 - 800	20 - 130	Toburen [49]
H_2	300 - 1500	2 - 3500	20 - 130	Toburen and Wilson [50]
H_2	1000	100 - 1000	20 - 130	Toburen [51]
H_2	5 - 100	1.5 - 300	10 - 160	Rudd [52]
He	75 - 150	1 - 550	10 - 160	Cheng, Rudd, and Hsu [53]
He	50 - 150	1 - 500	10 - 160	Rudd and Jorgensen [47]
He	100 - 300	2 - 1000	10 - 160	Rudd, Sautter, and Bailey [48]
He	2 - 100	5 - 100	0 - 100	Gibson and Reid [54]
He	2000	30 - 1500	20 - 130	Toburen [51]
He	300	1 - 1030	20 - 150	Stolterfoht [55]
He	300 - 5000	1 - 8577	15 - 160	Manson, Toburen, Madison and Stolterfoht [56]
He	5 - 5000	1 - 8577	10 - 160	Rudd, Toburen and Stolterfoht [57]
He	5 - 100	10 - 200	10 - 160	Rudd, Webster, Blocker, and Madison [58]
He	300 - 1500	1 - 3500	15 - 125	Toburen, Manson, and Kim [59]
He	5 - 100	10 - 200	10 - 160	Rudd and Madison [60]
He	100 - 300	40 - 180	0	Crooks and Rudd [61]
He	50, 100	5 - 300	0 - 90	Bernardi, Suarez, Fainstein, Garibotti, Meckbach, Focke [62]
He	1000	2.5 - 2500	20 - 160	Pedersen, Hvelplund, Petersen and Fainstein [63]
Ne	7.5 - 150	1 - 550	10 - 160	Cheng, Rudd, and Hsu [53]
Ne	50 - 300	1.5 - 1057	10 - 160	Crooks and Rudd [64]
Ne	1000	1 - 2000	15 - 125	Toburen and Manson [65]
Ne	300 - 1500	1 - 3500	15 - 125	Toburen, Manson, and Kim [59]
Ar	50 - 300	1.5 - 1057	10 - 160	Crooks and Rudd [64]

TABLE 2.2 (cont'd)

PUBLISHED DOUBLY DIFFERENTIAL CROSS SECTIONS

PROTON IMPACT

Target	Ion Energy Range (keV)	Ejected Electron Energy Range(eV)	Ejected Electron Angle (Degrees)	Investigators
Ar	5 - 1500	1 - 3500	15 - 160	Criswell, Toburen, and Rudd [66]
Ar	300 - 5000	1.1 - 10000	25 - 150	Gabler [67]
Ar	5 - 2000	1 - 3500	15 - 125	Criswell, Wilson, and Toburen [68]
Ar	1000	1 - 360	15 - 125	Manson and Toburen [69]
Ar	300 - 1500	1 - 3500	15 - 125	Toburen, Manson, and Kim [59]
Ar	100	3 - 250	160	Rudd, Jorgensen, and Volz [70]
Ar	5 - 20	1 - 26	30 - 140	Sataka, Okuno, Urakawa and Oda [71]
Ar	5 - 5000	1 - 10000	10 - 160	Rudd, Toburen, and Stolterfoht [72]
Kr	7.5 - 150	1 - 550	10 - 1601	Cheng, Rudd, and Hsu [53]
Kr	1000	1 - 3000	15 & 90	Manson and Toburen [73]
Kr	1000 - 4200	30, 136	15 - 90	Toburen and Manson [74]
Xe	300 - 2000	2 - 4620	20 - 130	Toburen [75]
N_2	300 - 1700	2 - 4000	20 - 130	Toburen [49]
N_2	50 - 300	1.5 - 1057	10 - 160	Crooks and Rudd [64]
N_2	5 - 70	1.5 - 300	10 - 160	Rudd [52]
N_2	200 - 500	1 - 1300	20 - 150	Stolterfoht [55]
O_2	50 - 300	1.5 - 1057	10 - 160	Crooks and Rudd [64]
O_2	300 - 1500	1 - 3500	15 - 125	Toburen and Wilson [76]
H_2O	15 - 150	1 - 3000	10 - 160	Bolorizadeh and Rudd [77]
H_2O	300 - 1500	1 - 3500	15 - 125	Toburen and Wilson [76]
CH_4	200 - 400	1 - 1270	20 - 150	Stolterfoht [78]
CH_4	300 - 1000	4 - 5000	20 - 130	Wilson and Toburen [79]
CH_4	250 - 2000	1 - 5000	20 - 130	Lynch, Toburen, and Wilson [80]
C_2H_2	300 - 1000	4 - 5000	20 - 130	Wilson and Toburen [79]
C_2H_4	300 - 1000	4 - 5000	20 - 130	Wilson and Toburen [79]
C_2H_6	300 - 1000	4 - 5000	20 - 130	Wilson and Toburen [79]

TABLE 2.2 (cont'd)

PUBLISHED DOUBLY DIFFERENTIAL CROSS SECTIONS

PROTON IMPACT

Target	Ion Energy Range (keV)	Ejected Electron Energy Range (eV)	Ejected Electron Angle (Degrees)	Investigators
C_6H_6	300 - 2000	4 - 5000	20 - 130	Wilson and Toburen [79]
NH_3	250 - 2000	1 - 5000	20 - 130	Lynch, Toburen, and Wilson [80]
CH_3NH_2	250 - 2000	1 - 5000	20 - 130	Lynch, Toburen, and Wilson [80]
$(CH_3)_2NH$	250 - 2000	1 - 5000	20 - 130	Lynch, Toburen, and Wilson [80]
TeF_6	300 - 1800	1 - 5000	20 - 130	Toburen, Wilson, and Porter [81]
SF_6	300 - 1800	1 - 5000	20 - 130	Toburen, Wilson, and Porter [81]

In the model of Rudd the angular distribution of ejected electrons, whether true secondary electrons from the target or scattered primaries, can be represented by two Lorentzian peaks; the binary peak centered at an angle which depends on the primary and secondary electron energies, and a backward peak centered at 180°. The doubly differential cross section, in terms of the dimensionless variables $w=\epsilon/I$ and $t=T/I$, $\sigma_t(w,\theta)$, where ϵ is the detected electron energy, T the primary energy, and I the target electron binding energy, is given by

$$\sigma_t(w,\theta) = G_1 \left[\frac{1}{1 + \left(\frac{\cos\theta - G_2}{G_3} \right)^2} + \frac{G_4}{1 + \left(\frac{\cos\theta + 1}{G_5} \right)^2} \right] . \qquad (2.7)$$

The quantities $G_1 \ldots G_5$ are the fitting parameters which, in general are functions of w and t. The center of the binary peak, G_2, is obtainable from momentum and energy considerations and is given by $G_2=[(w+1)/t]^{1/2}$. G_3 is the width of the binary peak which is given by $G_3=0.60[(1-G_2^2)/w]^{1/2}$. The relative size of the backward peak is given by $G_4=10(1-w/t)^3/[t(w+1)]$. The value of G_5, the width of the backward peak, can be taken to be a constant equal to 0.33. G_1 is determined by equating the integral over angle of Eq. 2.7 to the singly differential cross sections $\sigma_t(w)$ (to be discussed later). This yields

$$G_1 = \frac{\sigma_t(w)/2\pi}{G_3 \left[\tan^{-1}\left(\frac{1-G_2}{G_3} \right) + \tan^{-1}\left(\frac{1+G_2}{G_3} \right) \right] + G_4 G_5 \tan^{-1}\left(\frac{2}{G_5} \right)} . \qquad (2.8)$$

The DDCS calculated from the model are compared to experimental values for 500 eV e^-+He in FIG. 2.3.

TABLE 2.3

PUBLISHED DOUBLY DIFFERENTIAL CROSS SECTIONS

STRUCTURED-ION IMPACT

Reaction	Ion Energy Range (keV)	Ejected Electron Energy Range (eV)	Ejected Electron Angle (Degrees)	Investigators
$H_2^+ + H_2$	600 - 1500	2 - 2000	20 - 125	Wilson and Toburen [82]
$Ne^+ + Ne$	50 - 300	1.5 - 1000	10 - 160	Cacak and Jorgensen [83]
$Ne^{n+} + Ne$ (n=1-4)	25 - 800	1.6 - 1100	45 - 135	Woerlee, Gordeev, de Waard, and Saris [84]; and Woerlee [85]
$Ar^+ + Ar$	50 - 300	1.5 - 1000	10 - 160	Cacak and Jorgensen [83]
$Ar^+ + Ar$	100	3 - 250	160	Rudd, Jorgensen, and Volz [70]
$O^{n+} = O_2$ (n=4-8)	30000	10 - 4000	25 - 90	Stolterfoht, et al. [86]
H_2^+ + He^+ He	1000, 2000	20 - 1000	30 - 140	Oda and Nishimura [87]
H_2^+ + He° Ar	5 - 20	1 - 26	30 - 140	Sataka, Okuno, Urakawa, and Oda [71]
H° + He H_2° + He $^3He^\circ$ + He $^4He^\circ$ + He	15 - 150	1.5 - 300	10 - 160	Fryar, Rudd, and Risley [88]
H° + He	15 - 150	1.5 - 300	15 - 150	Rudd, Risley, Friar, and Rolfes [89]
$He^{2+} + He$	50, 100	5 - 300	0 - 90	Bernardi, Suarez, Fainstein, Garibotti, Meckbach, Focke [62]
He^+ + Ne He^{2+} Ar	1200	1 - 3500	15 - 125	Toburen and Wilson [90]
He^+ + Ar He^{2+}	300 - 2000	1 - 4000	15 - 125	Toburen and Wilson [91]
He^+ + H_2O He^{2+}	300 - 2000	1 - 4000	15 - 125	Toburen, Wilson, and Popowich [92]

TABLE 2.3 (cont'd)

PUBLISHED DOUBLY DIFFERENTIAL CROSS SECTIONS

STRUCTURED-ION IMPACT

Reaction	Ion Energy Range (keV)	Ejected Electron Energy Range (eV)	Ejected Electron Angle (Degrees)	Investigators
H^o + H_2O	20 - 150	1 - 300	10 - 160	Bolorizadeh and Rudd [93]
H_2^+ + He H_3^+	5 - 20	2 - 50	30 - 120	Urakawa, Tokoro, and Oda [94]
H^+ H_2^+ + Ar He^+	5 - 20	2 - 26	30, 90	Sataka, Urakawa, and Oda [95]
He^{2+} C^{6+} + He O^{8+}	1000/u	2 - 2500	20 - 160	Pedersen, Hvelplund, Petersen, and Fainstein [63]
C^+ + He, Ne, Ar, CH_4	1200	1 - 800	30, 90	Toburen [96]
C^+ + He	800 - 4200	10 - 1500	15 - 130	Reinhold, Schultz, Olson, Toburen, and DuBois [97]; and Toburen, DuBois, Reinhold, Schultz, and Olson [98]
C^{n+} + Ar (n=1-3)	1300 - 3000	1 - 4000	15 - 130	Toburen [99]
O^+ N^+ + Ar	50 - 500	5 - 500	16 - 160	Stolterfoht and Schneider [100]
Kr^{n+} + Kr (n=2-5)	50 - 1000	80 - 1000	45 - 135	Gordeev, Woerlee, deWaard and Saris [101]; and Woerlee [85]
Kr^{n+} + Kr (n=2-5)	25 - 800	16 - 1100	45 - 135	Gordeev, Woerlee, DeWaard, and Saris [102]; and Woerlee [85]

TABLE 2.3 (cont'd)

PUBLISHED DOUBLY DIFFERENTIAL CROSS SECTIONS

STRUCTURED-ION IMPACT

Reaction	Ion Energy Range (keV)	Ejected Electron Energy Range (eV)	Ejected Electron Angle (Degrees)	Investigators
Fe^{17+} + He, Ar Fe^{22+}	3500/u	5 - 8000	27 - 155	Schneider, DeWitt, Bauer, Mowat, Graham, Schlachter, Skogvall, Fainstein, and Rivarola [103]
Mo^{40+} + He	2500/u	2 - 5000	20 - 160	Stolterfoht et al. [104]
U^{33+} + Ar	1400/u	1 - 4000	20 - 90	Kelbch, Olson, Schmidt, Schmidt-Böcking, and Hagmann [105]
U^{33+} + Ne	1400/u	1 - 4000	20 - 90	Kelbch, Olson, Schmidt, Schmidt-Böcking, and Hagmann [105]
U^{33+} + Ar	1400/u	1 - 4000	20 - 90	Schmidt-Böcking, Ramm, Kraft, Ullrich,Berg, Kelbch, Olson, DuBois, Hagmann, and Jiazhen [106]
U^{38+} + He Th^{38+} + Ar	6000/u	5 - 5000	20 - 150	Schneider et al. [107]

2.2.2. Proton Impact

There has been a wide range of experimental and theoretical studies of doubly-differential cross sections for proton impact ionization of atomic and molecular targets and, to a much lesser extent, data are available for much heavier bare, or nearly bare, ions. Several reviews of doubly-differential cross sections for ion impact have been published including those by Toburen [1, 40-42], Rudd and Macek [43], Rudd [44] and Stolterfoht [45]. An updated listing, first published by Toburen [41], of the publications that report measured doubly differential cross sections for proton impact is presented in Table 2.2 of this chapter and a listing of publications concerned with data for heavier ions and neutral particles is given in Table 2.3. These listings focus on studies that report absolute cross sections and that cover a broad spectrum of ejected electron energies and angles. We have not included in this review studies of special features of the emission spectra such as "convoy electrons" (see, for example, Breinig, et al., [108] or studies that focus on a narrow angular range, eg. publications that focus on electrons ejected at zero degrees; such studies are not considered highly relevant to Radiation Therapy, or to Radiological Physics in general.

2.2.2.1 Available experimental data:

From a survey of the proton impact data presented in Table 2.2, doubly differential cross sections are observed to be available that span the regions of low (5-50 keV), intermediate (50-300 keV), and high (greater than about 300 keV) proton energies; these energy ranges reflect regions requiring different theoretical approaches to describe the collision process. Only a few molecular targets, eg., hydrogen, nitrogen, oxygen, and water vapor, have been studied throughout these energy ranges. Those molecules, however, provide a good representation of the constituents of tissue. The majority of the data base that has been used to investigate effects of molecular bonding on electron emission cross sections has been developed in the region of high-energy proton collisions.

An indication of the precision of the various measurements that have been reported can be addressed by an evaluation of the uncertainties contributing to the individual measurements and by comparison of measurements of different investigators. A comparison of DDCS for ejection of electrons from nitrogen

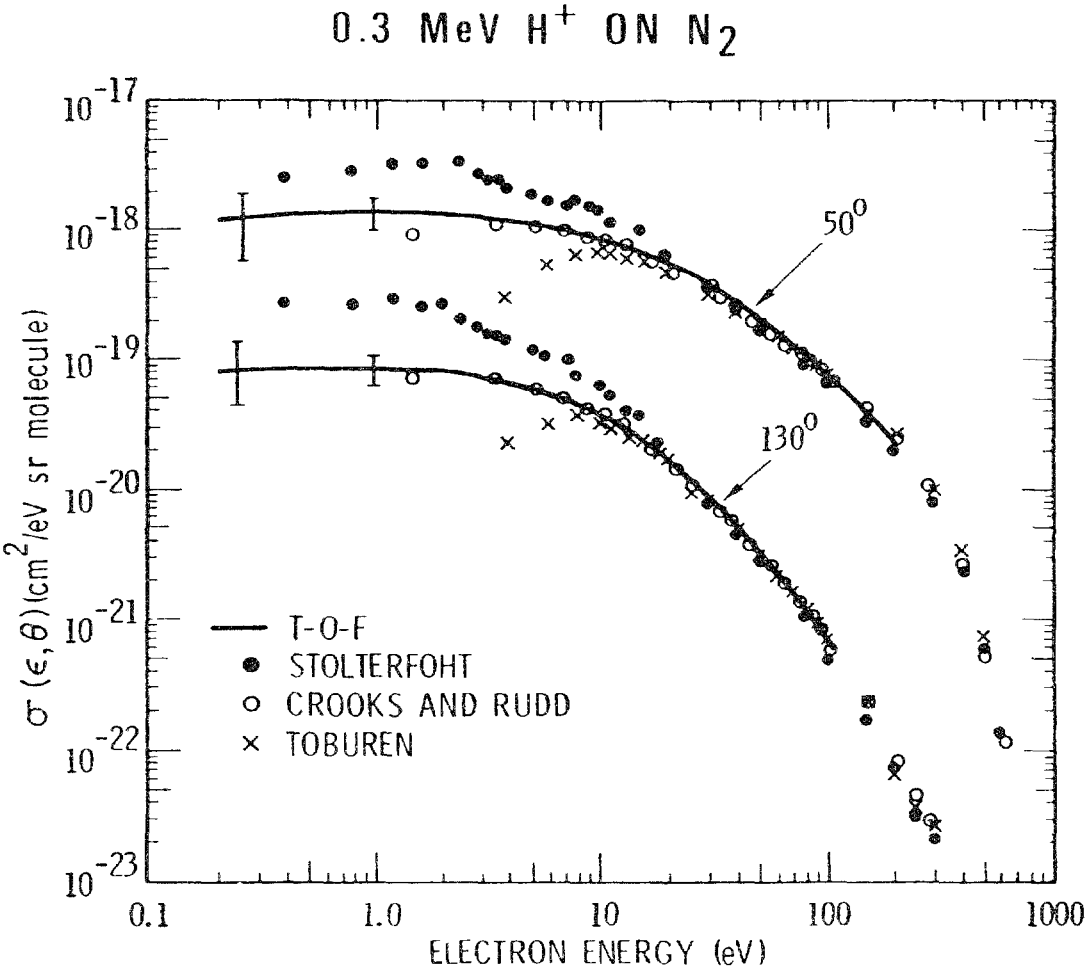

FIG. 2.4. Comparison of absolute doubly differential cross sections $\sigma(\epsilon,\theta)$ plotted as a function of ejected electron energy ϵ for ionization of N_2 by 0.3 MeV protons measured by (•) Stolterfoht [55], (O) Crooks and Rudd [64], and (x) Toburen [49]. The solid lines represent cross sections obtained for low-energy ejected electrons measured by time-of-flight techniques by Toburen and Wilson [109].

by 0.3 Mev protons measured by three different research groups is shown in FIG. 2.4. For ejected electron energies greater than about 15 eV the agreement is well within the estimated uncertainties in the individual measurements of approximately 20%. For low-energy ejected electrons the data of Toburen [49], Stolterfoht [55], and Crooks and Rudd [64], obtained using electrostatic energy analysis of the ejected electrons, diverge. These disagreements are attributed to several possible experimental difficulties, including scattering of the low-energy electrons in the target and residual gas, uncertainties in detection efficiencies for low-energy electrons, and/or effects of stray electrostatic and magnetic fields on the transmission of electrons through the electrostatic energy analyzers. In an effort to resolve some of these uncertainties in the cross sections for low energy electron emission a time-of-flight (TOF) technique was developed by Toburen and Wilson [109] that was optimized to measure relative cross sections for ejected electron energies in the range from 1 to 200 eV. This system used a short TOF path (about 7.5 cm) from the collision region to the detector to minimize effects of stray electric and magnetic fields on the transmission of low-energy electrons, had no analyzing fields that might be distorted by surface affects or fringing, and employed a gas jet as the target to minimize the scattering of low-energy electrons during their transit from the target to the detector. The solid lines shown in FIG. 2.4 were derived from TOF measurements of the relative electron yields converted to absolute cross sections by normalization to the electrostatic results of Toburen [49] at 100 eV. The combination of electrostatic and TOF measurements provides reliable cross sections for the ejected energy range from approximately 1 to 5000 eV, thus providing a wide range of data for analysis of cross section systematics and for development of theoretical models. Cross sections measured using this combination of experimental techniques have been published for proton impact ionization of a number of carbon containing molecules [79], and nitrogen containing molecules [80], as well as noble gas atoms [66,110].

2.2.2.2. Theoretical studies:

Coincident with the proliferation of experimental results for the energy and angular distributions of electrons ejected in proton collisions with atomic and molecular targets was a similar activity in the theoretical description of these collisions. Although confined to "fast" collisions, where fast refers to collisions in which the projectile velocity is much greater than the bound electron velocity, both quantum mechanical and classical methods were exploited (See the reviews by Rudd and Macek [43], Stolterfoht [45], and Rudd and Gregoire [111]). The simplest of these theories to apply in practice is the classical binary encounter theory first advanced for differential ionization cross sections by Vriens [112] and exploited by Rudd and Gregoire [111], Bonsen and Vriens [113], and numerous others. This method is essentially a classical description of the collision between an incoming bare charged particle and a free electron. The major contribution of these authors beyond earlier classical methods was the inclusion of techniques to account for the effects of electronic binding of target electrons to an atom or molecule. This was accomplished by considering the target electron to have an initial non-zero velocity distribution owing to the fact that it is bound. Various means of estimating this initial velocity distribution for bound electrons were devised; these ranged from the simple procedure of setting the kinetic energy of the bound electron equal to its binding energy, to the more elaborate scheme of calculating the velocity distribution from a Hartree-Fock description of the electrons in the atom.

The most common method is to assume the velocity distribution to be isotropic with a quantum-mechanical speed distribution deduced from a Fock distribution (see, for example, Rudd and Macek [43], Rudd and Gregoire [111], and Toburen et al. [114,115]. The primary effect of different assumptions of the initial velocity distribution of the target electron is observed in the energy distributions of ejected electrons and will be discussed in a later section of this chapter that deals with the singly differential electron emission cross sections.

In general, the angular distributions of ejected electrons obtained by binary encounter calculations are somewhat more sharply peaked at the classically predicted angles than are measured values. This is illustrated in FIG. 2.5 where calculated angular distributions of electrons ejected at selected energies are compared with measurements for ionization of helium by 2-MeV protons. Although there is excellent agreement between the measured and calculated cross sections near the peak in each distribution there are discrepancies as large as an order of magnitude at both the largest and smallest emission angles.

Considerable effort has also been given to quantum mechanical calculations of the energy and angular distributions of electrons ejected in proton-atom collisions. The Born approximation has been applied to the study of proton ionization of helium in a number of studies (see, for example, Manson et al., [56], Madison [116], and Oldham [117]). The use of the Born approximation with hydrogenic wave functions to describe initial discrete and final continuum states leads to angular distributions similar to those obtained with binary encounter theory. However, with the use of more realistic wave functions to describe both the bound and continuum states of the target the Born approximation provides a notable improvement over the semi-classical treatments. The calculations of Madison [116], shown in FIG. 2.5, are based on a Born approximation with Hartree-Fock initial discrete and final continuum wave functions. This calculation is observed to provide much improved agreement with experimental cross sections compared to the cross sections obtained from binary encounter theory. There are, however, still sizeable discrepancies between the Born calculations and measurements for electrons ejected into small emission angles with velocity comparable to the outgoing proton. These discrepancies are attributed to an enhancement of the measured cross sections by the process of continuum-charge-transfer [44]. As first suggested by Oldham [117], this process is due to an interaction between the ejected electron and the scattered proton in which the projectile is considered to "pull" a bound target electron from its orbit as though to capture it, but rather than be captured into a bound projectile state the electron is "captured" into a continuum projectile state. This ionization mechanism exhibits its primary influence for electron emission into small angles for ejected electron velocities near that of the projectile velocity. Continuum-charge-transfer (CCT), also referred to as electron capture to the continuum (ECC) or charge transfer to the continuum (CTC), can lead to sizeable differences between calculated and measured cross sections, as are observed in FIG. 2.5, because the final state interaction between the projectile and the ejected electron is not usually included as a part of the theoretical calculation; i.e., it is not included in the the plane wave Born calculation of FIG. 2.5. The theory for the CCT process was first explored by Salin [118] using the Born distorted wave approximation and by Macek [119] using the Neuman expansion of Faddeev's equation for the final state of the electron-proton-residual ion system. The Faddeev results of Macek [119,120] are compared in FIG. 2.6 to a hydrogenic Born calculation that includes no contribution from CCT and to measurements for electrons ejected with

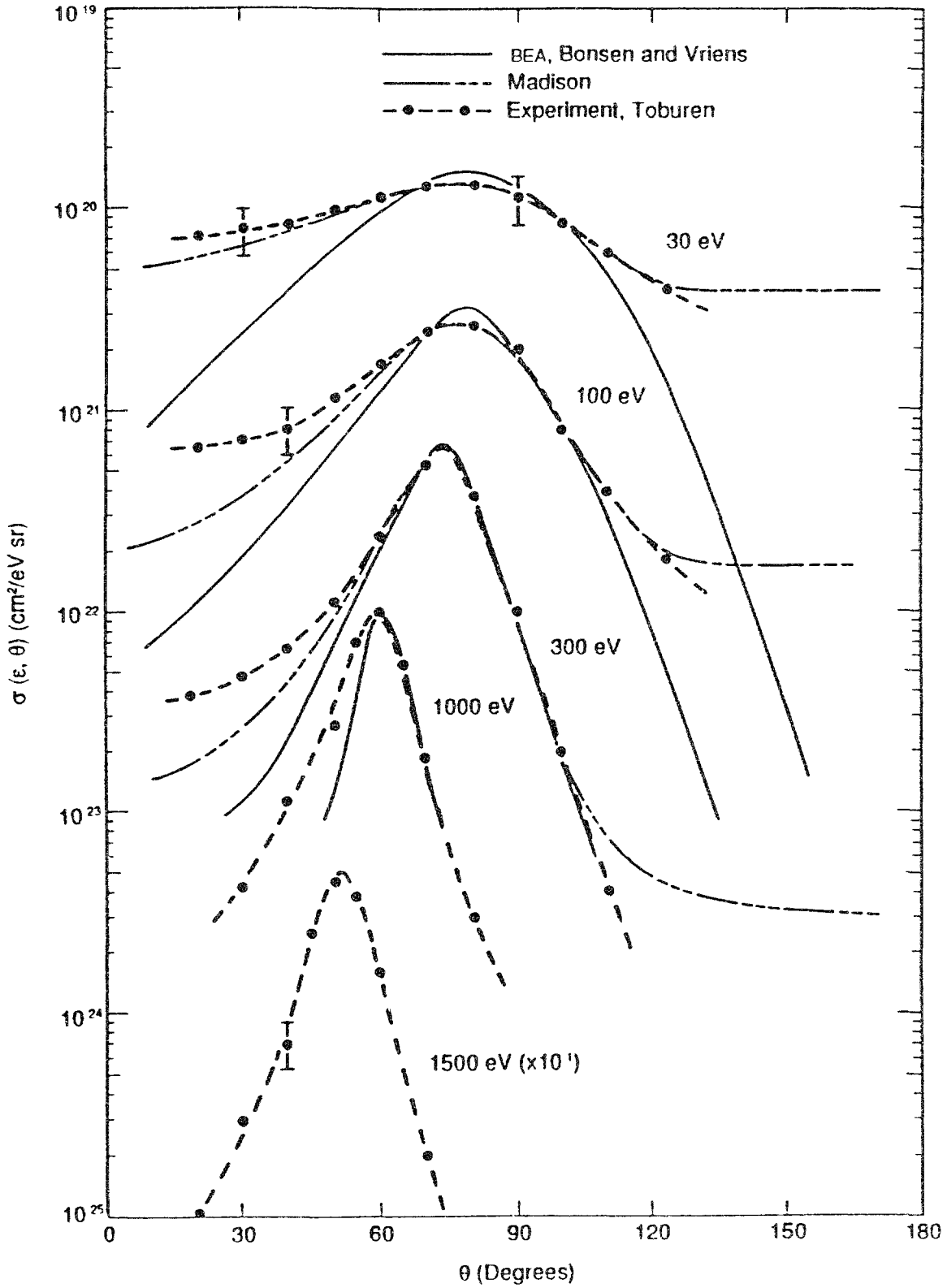

FIG. 2.5. Doubly differential cross sections for ionization of helium by 2 MeV protons. The binary encounter theory calculation (BEA) is from Bonson and Vriens [113] and the plane wave Born calculation is from the work of Madison [116].

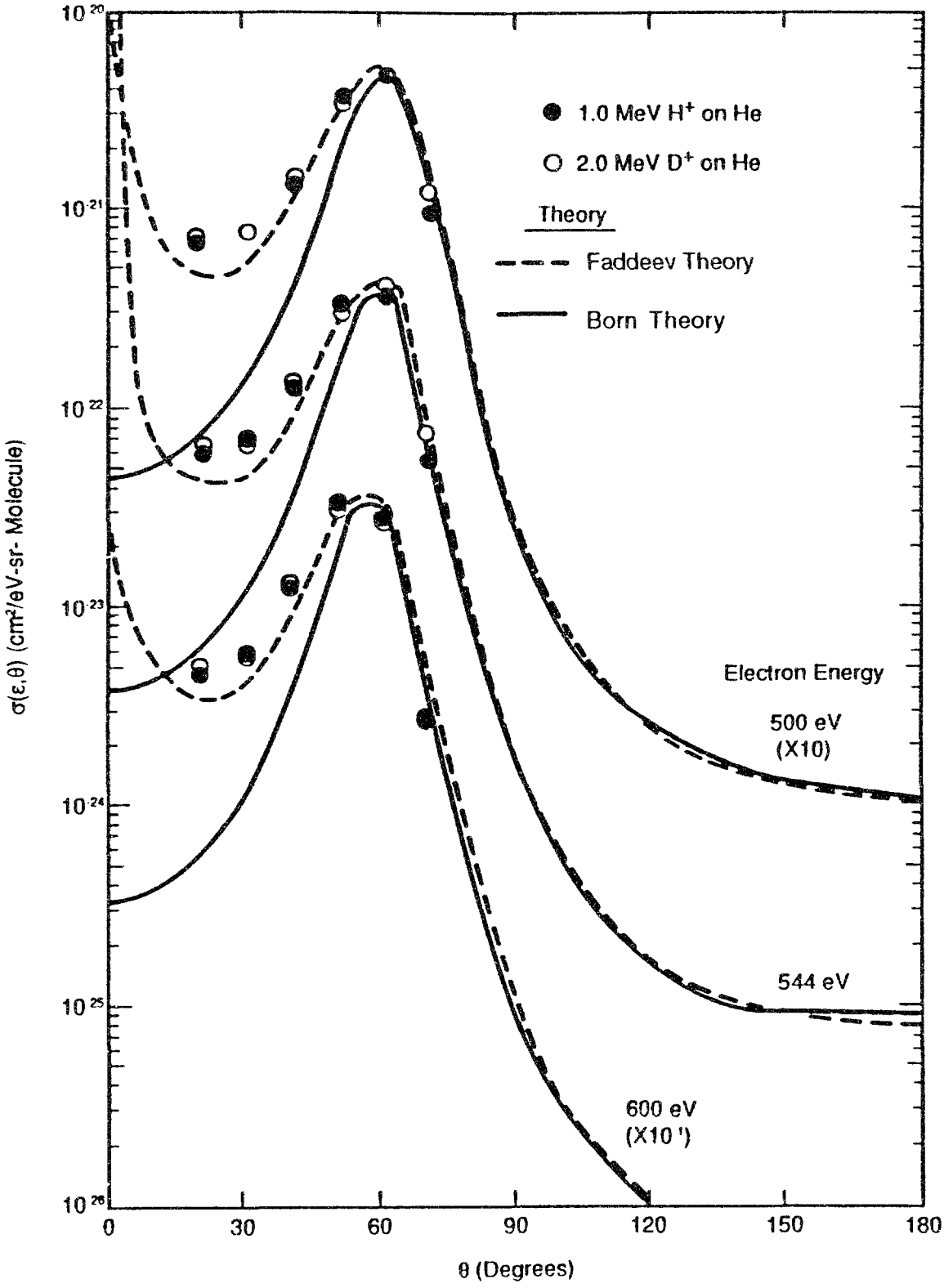

FIG. 2.6. Doubly differential cross sections for emission of electrons of velocity comparable to the projectile [51] compared to the Faddeev and Plane Wave Born calculations of Macek [120].

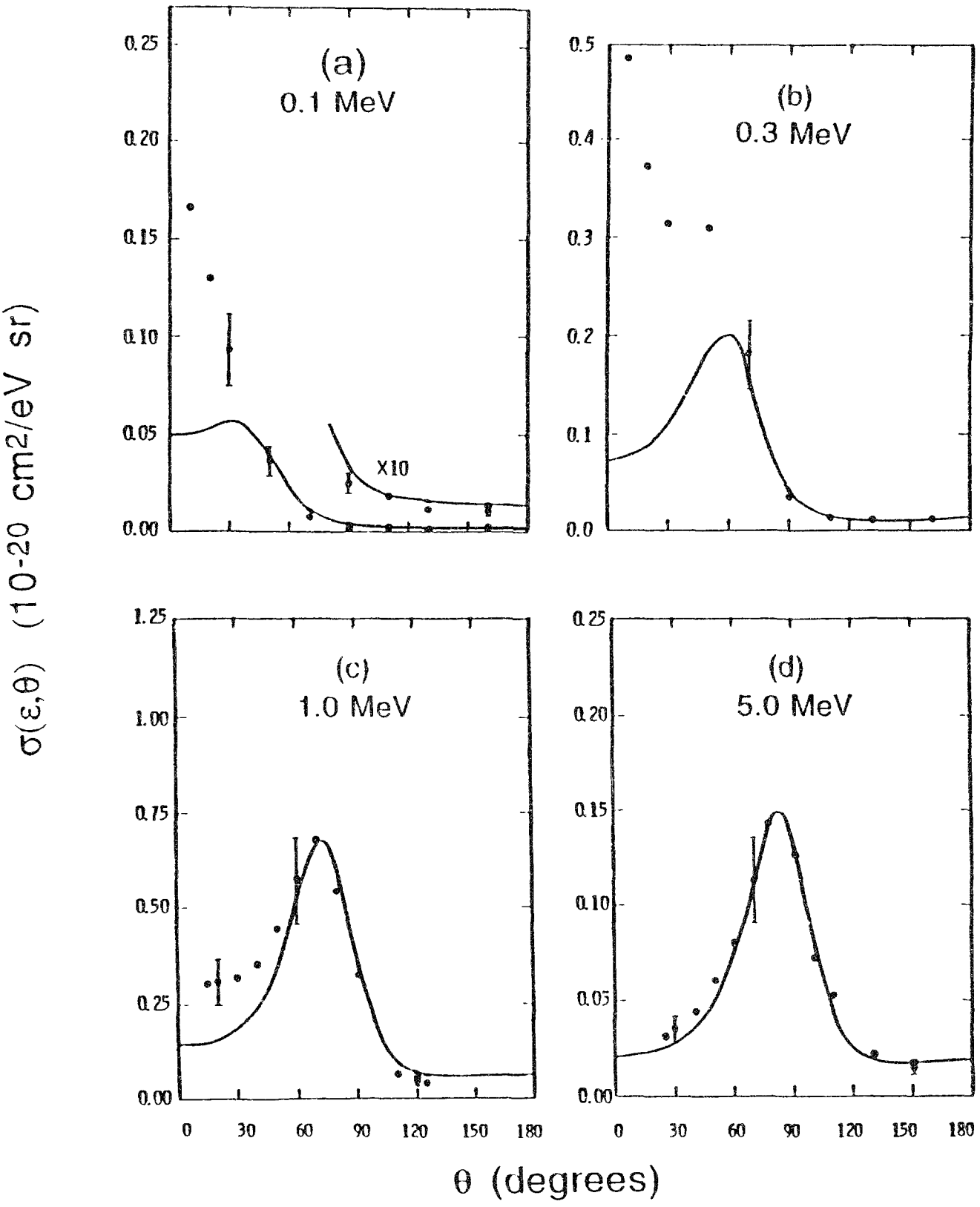

FIG. 2.7. Angular distributions of 81.6 eV electrons ejected from helium by protons of a) 100 keV, b) 300 keV, c) 1000 keV, and d) 5000 keV. The solid line is a plane wave Born calculation; the calculation and experimental points are from Manson et al. [56].

velocities near that of the incident proton (the equivalent electron velocity for a 1 MeV proton is 544 eV) where the maximum contribution from CCT is expected. The Faddeev calculation of Macek is shown to be in excellent agreement with the measurements. These comparisons between theory and experiment illustrate the important role DDCS's can play in investigating the basic interaction mechanism and testing our theoretical understanding.

Although there have been Born calculations of doubly differential cross sections for proton impact ionization of a number of atomic targets including neon [65], argon [69], and krypton [73,74], the only comprehensive experimental and theoretical studies have been for helium targets [56,60,116]. In general the agreement between theory and experiment has been quite good for high energy proton impact, i.e., for proton energies greater than about 500 keV. There are, of course, discrepancies in the region of the spectra where continuum-charge transfer is important since it is not included in the plane wave Born approximation. As the proton energy increases the agreement between Born calculations and experiment improves because the CCT process falls off much more rapidly with proton velocity than does direct ionization. This is illustrated in FIG. 2.7, where the angular distribution of 81.6 eV electrons ejected by protons with energies of 100-, 300-, 1000-, and 5000-keV are compared with Born calculations. The Born calculations by Manson et al. [56] are based on the use of Hartree-Slater wave functions for the initial discrete and final continuum states; these wave functions are only slightly different from the Hartree-Fock wavefunctions used by Madison [116]. At the highest proton energy excellent agreement is obtained between the measured and calculated cross sections. It should also be noted that cross sections calculated for electron impact at comparable velocities to the highest energy protons shown in FIG. 2.7 are in equally good agreement with experiment [56]. This comparison leads one to the conclusion that the plane wave Born approximation is very good at describing the direct ionization of helium by fast protons and electrons and that the differences observed between theory and experiment at the lower energies, but still within the expected range of validity of the Born approximation, are a measure of the importance of the CCT mechanism of target ionization. Using this reasoning, Manson et al. [56] looked at the relative contribution of CCT to the doubly differential cross sections for electron energies where this mechanism was expected to be maximum. The results of their analysis are shown in FIG. 2.8 as a function of ejected electron emission angle and incident proton energy. The CCT contribution is observed to peak for proton energies somewhere between 300 and 500 keV which is approximately where the velocity of the bound electron and the incident proton coincide. It should be noted that, although the maximum contribution of the CCT process to the doubly differential cross sections may be quite large, its influence is over a relatively small region of ejected electron energy and emission angle and therefore does not contribute significantly to the total yield of ejected electrons. This will be apparent in the discussion of singly differential and total electron production cross sections that is presented later in this chapter.

The phenomenon of post-collision electron-projectile interactions has received a good deal of attention in the last few years. Interest was rekindled by the studies of Meckbach et al. [121] who noted that CCT is only a special case of the full three-body final state in which all three particles interact equally. In their work the similarities of this interaction to that of the escape of two electrons from a positive core as treated within the Wannier theory was exploited. They were able to show that the ridge in the doubly differential cross section surface along the 0 degree axis was produced by electrons that were ejected in the combined field of the projectile and the

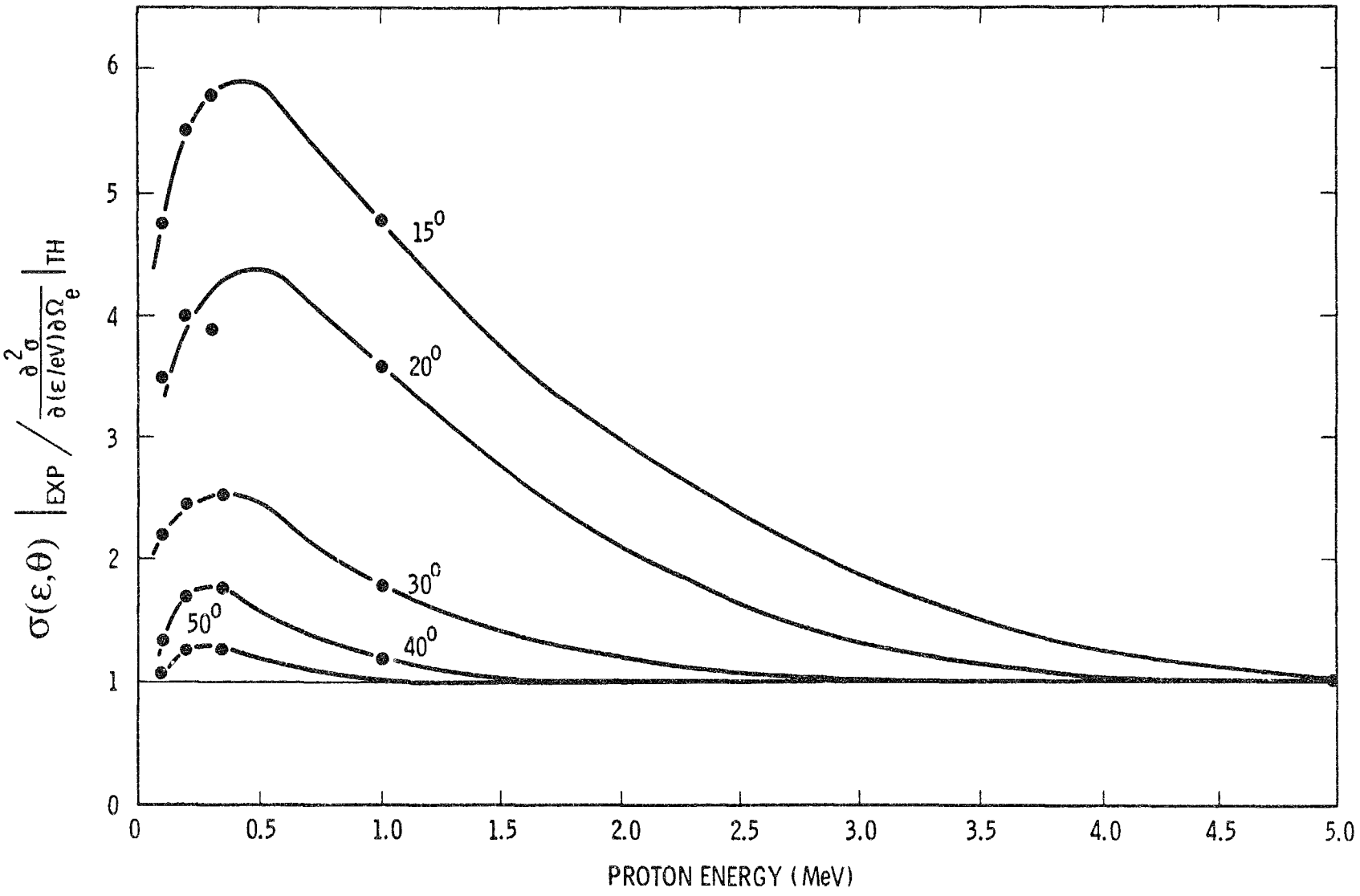

FIG. 2.8. Ratio of experimental to theoretical doubly differential cross sections for proton impact ionization of helium for equal velocity ejected electrons and incident protons shown as a function of proton energy and ejected electron angle. The solid lines are only a guide to the eye through the data points that are then extrapolated to higher energy proton energies based on the shape of the curves measured at the larger angles where there are sufficient data points to define the curve shape.

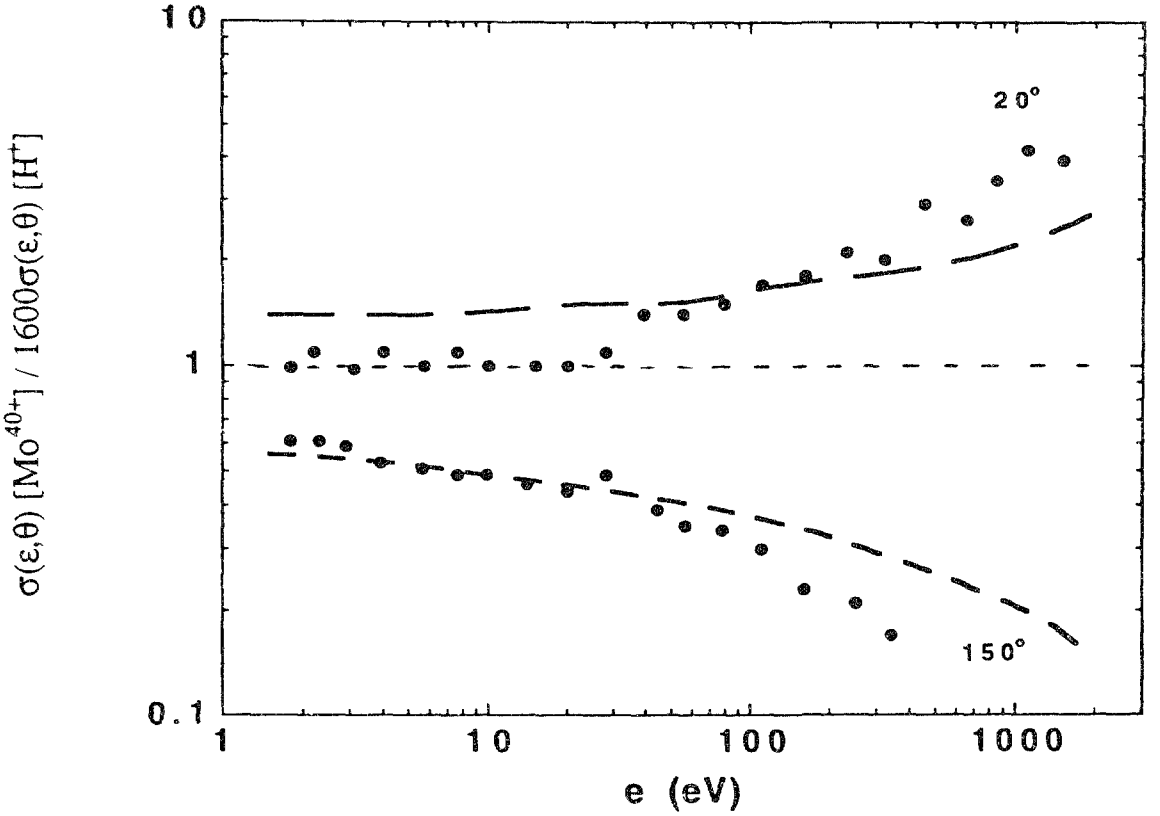

FIG. 2.9. Ratio of doubly differential cross sections for electron emission from Helium by 25 MeV/u Mo^{40+} and H^+ impact. The Mo^{40+} data were divided by H^+ results from a Born approximation (PWBA). The long dashed lines are from a CDW-EIS calculation for both H^+ and Mo^{40+} impact. Both experimental and theoretical data are from Stolterfoht et al. [104].

residual target ion. These "saddle-point" electrons were also successfully treated using the Classical Trajectory Monte Carlo Theory (CTMC) of Olson et al. [122]. The CTMC theory treats the classical motion of the electron in the combined coulomb field of the collision partners. In their CTMC calculation the saddle-point electrons were shown to be produced by a classically understandable mechanism and observed at non-zero scattering angles.

Both the CTMC and the Wannier calculations mentioned above had focussed on understanding that portion of the electron spectra between the CCT peak and the low energy peak resulting from electrons escaping with low energies from the target. In measurements of the secondary electrons emitted in collisions of projectiles with higher charge states [63,104,107] the effect of the two charge centers could be seen over a broad range of the ejected electron spectra. In these studies the emission cross sections are enhanced in the forward direction and reduced for angles greater than 90°; results from the work of Stolterfoht are shown in FIG. 2.9. Variations from the expected charge scaling are observed to occur for ejected electron energies well beyond the equal velocity considerations of CCT. In these collisions first order Born calculations are found to give an incomplete representation of the process and appear to be inadequate to describe the doubly differential cross sections even for what might be considered "high enough" collision velocities. These two-center effects have been quite successfully described by Fainstein et al. [123] using the continuum-distorted-wave eikonal-initial-state (CDW-EIS) model (see also, Pedersen et al., [63] and Stolterfoht et al. [104]).

The Coulombic behavior due to the active electron-projectile interaction is included in the entry channel by choosing a distorted initial wavefunction where the initial bound state is multiplied by an eikonal phase associated with that interaction. In the exit channel, the active electron is assumed to feel simultaneously the fields of the projectile and of the residual target.

2.2.2.3. Consistency tests:

In principle, the DDCS for electron emission in collisions of protons, or other ions, with atomic or molecular targets are subject to the same consistency tests described above for electron impact. Ions are in some ways simpler to deal with than electrons, since, owing to their large mass, they have nominally straight line trajectories and one does not have to consider exchange processes as is necessary for ionization by electrons. On the other hand, positive ions present additional ionization channels not found for incident electrons. For example, positive ions can produce ionization by capturing electrons from the target atom or molecule into either bound or continuum states of the ion. Once an ion has captured an electron into a bound state it can release that electron in a subsequent collision. In this section of this chapter we are considering only bare projectiles, therefore only capture into continuum states is of concern here. With that condition, the consistency test developed above for electron impact become valuable tools for examining the reliability of proton impact data so long as we take care to apply them to only the regions of the emission spectra that are relatively unaffected by CCT. For comparing ion and electron cross sections it is also convenient to express the ion energy in units of the equivalent electron energy. For example the proton energy is expressed as $T = \frac{1}{2}mv_p^2$, where m is the electron mass and v_p is the proton velocity (or $T = E_p m/M$, where E_p is the proton energy and M is the proton mass). This notation can also be generalized to any ion impact by simply using the ion velocity (or ion energy and mass) in place of the proton value in the relationship given for T.

One of the consistency requirements discussed by Kim [31] was that the observed kinematics of the cross sections must be consistent with well established classical scattering relationships for ion-electron collisions. For collisions of a proton of energy T (as defined above) with a free electron the kinematic collision conditions are only slightly different from the relationship discussed in the previous section for electron impact. For an incident proton of energy T the ejected electron energy ϵ and emission angle θ must satisfy the condition $\epsilon = 4T\cos^2\theta$. This relationship is valid for all ions of sufficiently high velocity that the incident ion is not significantly deflected during the collision. Figure 2.10 shows the angular distributions of ejected electrons of a number of energies resulting from ionization of xenon by 2 MeV protons. The dashed line indicates the position of the peak of the angular distribution determined from the kinematics of a proton collision with a free electron. This peak is often referred to as the binary encounter peak because it reflects the kinematics of a two-body (or binary) collision between the incident proton (or ion) and the target electron. For the lowest energy electrons the measured angular distribution shows only a vague indication of a peak at the position predicted for free electrons. This absence of a peak results because the ejected electron has an initial velocity distribution, owing to its being bound, that dominates the observed angular distribution at low energies. At higher ejected electron energies the peak in the observed angular distribution is more pronounced and the width of that peak reflects the initial velocity distribution of the bound electrons. In general the maximum in the peak in the angular distribution occurs at the

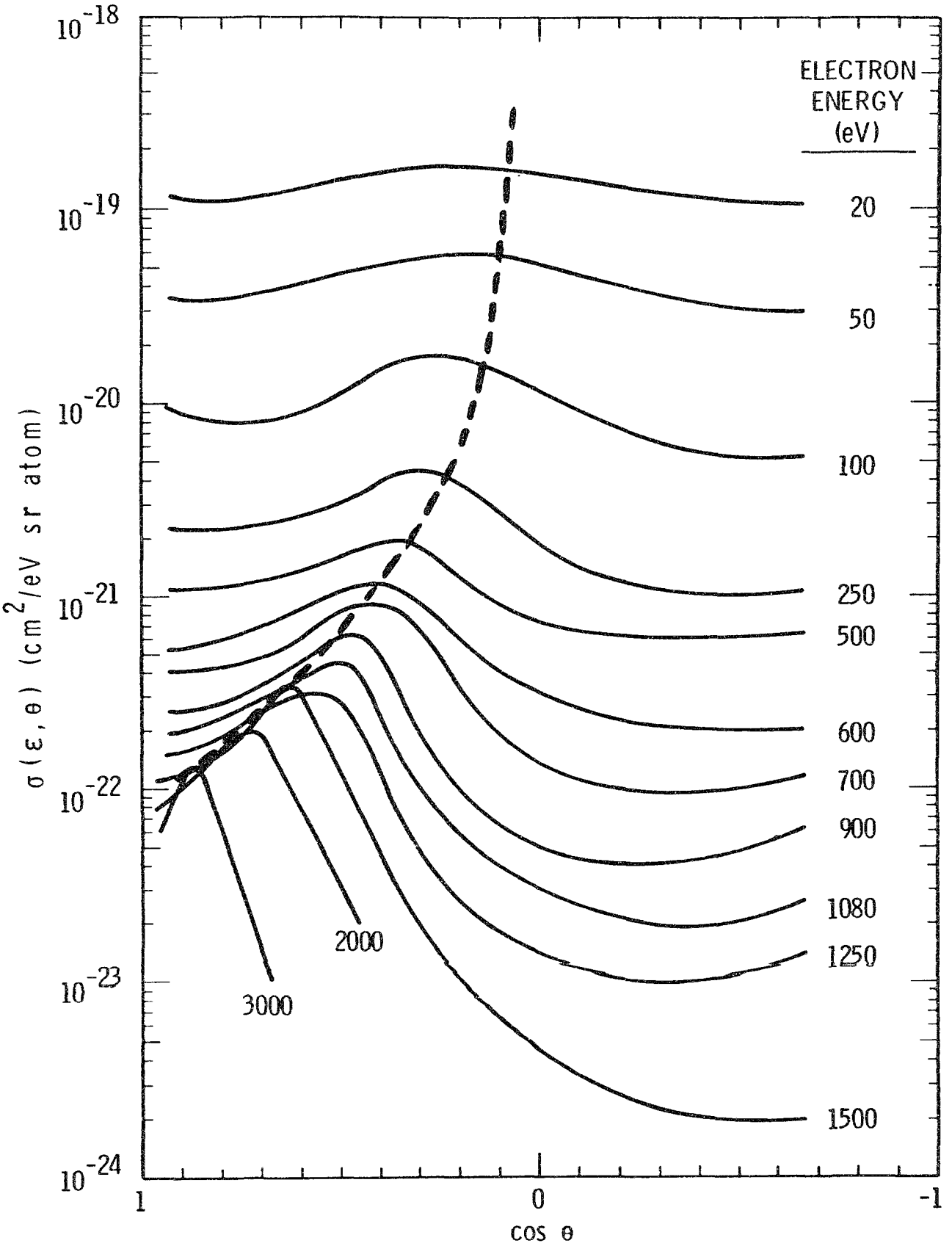

FIG. 2.10. Angular distribution of electrons of several energies ejected from xenon by 2-MeV protons as measured by Toburen [75]. The dashed line indicates the expected peak in the angular distribution as given by classical kinematics for a free electron.

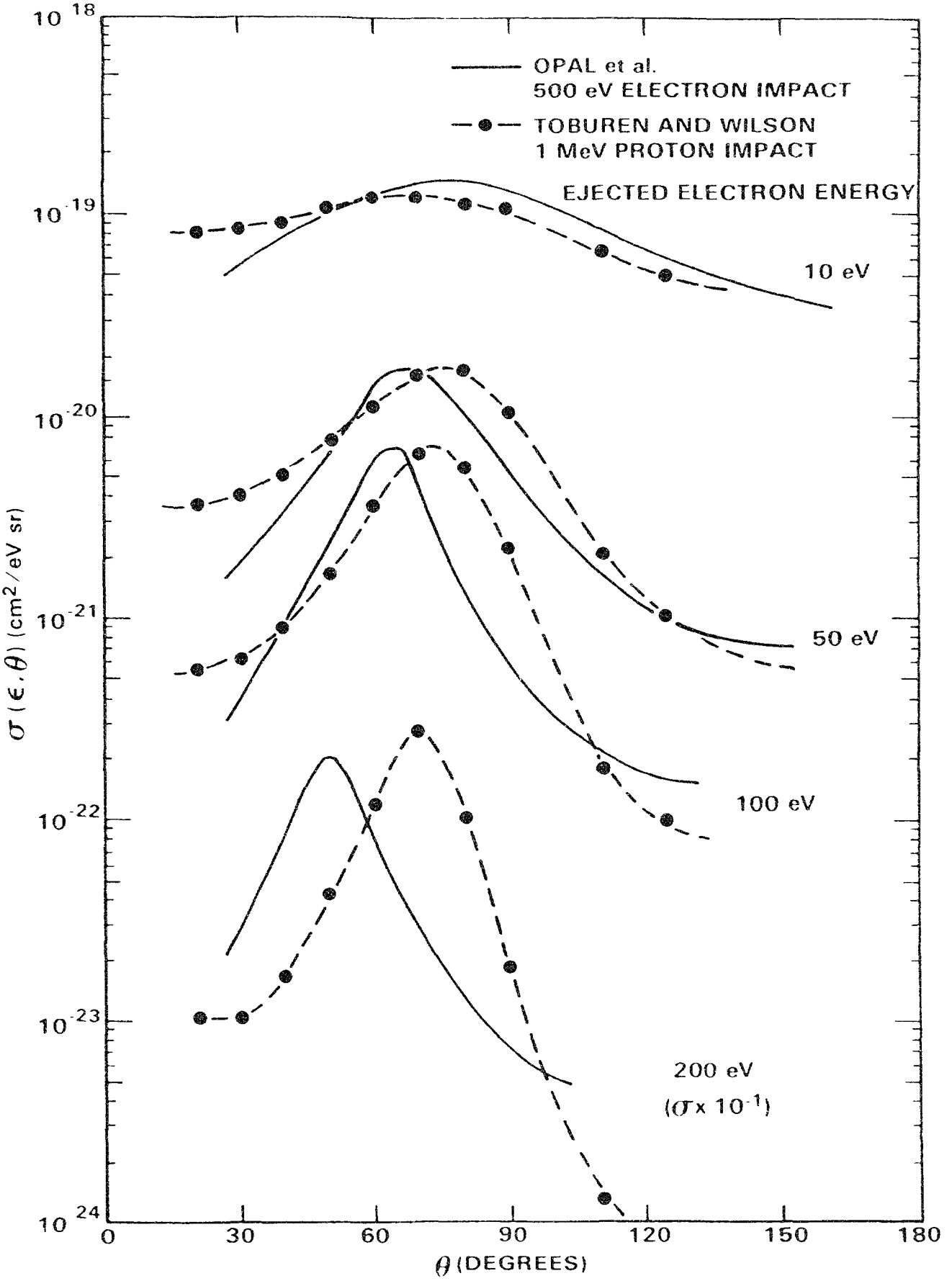

FIG. 2.11. Doubly differential cross sections for ionization of molecular hydrogen by electrons and protons of equal velocity illustrating the effect of projectile mass on the scattering kinematics. Electron impact data are from Opal et al. [7] and the proton data are from Toburen and Wilson [50].

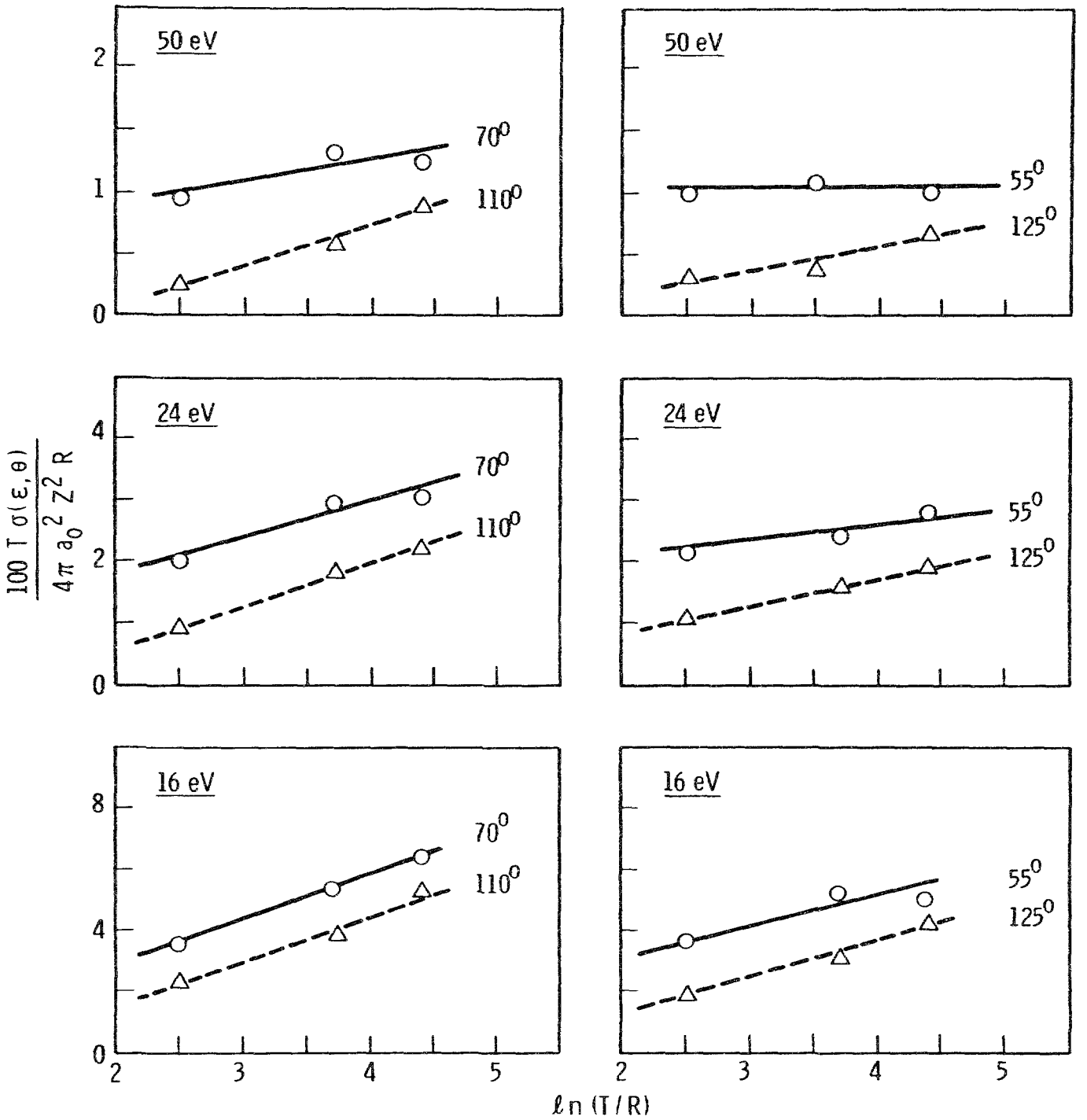

FIG. 2.12. Comparison of the ratio of measured doubly differential electron emission cross sections to the Rutherford scattering cross section as a function of ln(T/R) for low-energy electrons ejected in fast proton-SF_6 collisions. The existence of parallel slopes for data plotted at supplementary angles is evidence of data consistency. The data are from Toburen et al.[81].

angle that is expected from the classical prediction. The angular distributions for the three highest energies exhibited in FIG. 2.10 seem to peak at somewhat smaller angles than is expected based on the classical prediction. The shift of the peak to smaller angles may be an indication of experimental difficulties in these measurements or it may reflect a breakdown in the classical description of the collision process. In a study of the binary encounter peak for electrons ejected from helium by 1 Mev protons conducted by Pedersen et al. [63] it was found that the peak energies were shifted by about 4% to lower energies than predicted by classical theory. In that work this shift was attributed to the interaction of the outgoing electron with the combined charge of the residual target and the projectile. Such an interaction would also be expected to affect the position of the peak in the angular distribution and may contribute to the shift observed in FIG. 2.10.

It is interesting to consider the difference in the position of the binary encounter electron peak with respect to the angular distributions of electrons ejected by electron and proton impact. The observed difference reflects the influence of the mass of the incident particle on the kinematics of the collision; recall that for electrons θ is given by $\cos^{-1}(\epsilon/T)^{\frac{1}{2}}$, whereas for ions θ is given by $\cos^{-1}(\epsilon/4T)^{\frac{1}{2}}$. Data for electron ejection by equal velocity proton and electron impact are shown in FIG. 2.11. These data show explicitly the difficulty of directly scaling doubly differential cross sections from proton to electron impact.

The second consistency test advocated by Kim [31] to test the reliability of doubly differential cross sections was the use of the Fano plot. As discussed above for electron impact, a plot of $Z(T,\epsilon,\theta)$ versus $\ln(T/R)$ for electrons ejected at supplementary angles should produce straight lines with similar slopes. Data from ionization of SF_6 by protons [81] are plotted in this manner in FIG. 2.12. The slopes of the curves for supplementary angles are found to be parallel indicating that the proton energy dependence of the doubly differential cross sections is consistent with theoretical expectations. As indicated above, however, one must be careful not to choose data that are dominated by CCT if this test is to be considered valid. Since CCT is more important in the spectra of electrons ejected into small angles and has an ion energy dependence different from direct ionization it may contribute to supplementary angles having different slopes within the Fano plot. This must be taken into consideration when using the Fano plot to evaluate the consistency of doubly differential cross sections for positive ions.

2.2.2.4. Cross section systematics:

To this point the discussion of doubly differential cross sections for proton impact has been limited predominantly to atomic targets; with the majority of the work, experimental and theoretical, being for the target helium. Helium is the simplest target amenable to experiments and provides a good test case for theoretical developments. For applications to radiological physics, or radiation therapy, cross sections are needed for molecular targets and, more specifically, there is a need to know the emission cross sections for heterogenous condensed phase targets. Such targets are not amenable to measurements of secondary electron cross sections, however, because the electrons are absorbed in the targets before they can be detected, i.e., the ranges of electrons for the energies of interest are shorter than the thinnest practical targets. The challenge for the physicist is then to develop an understanding of the systematics of the emission cross sections that will

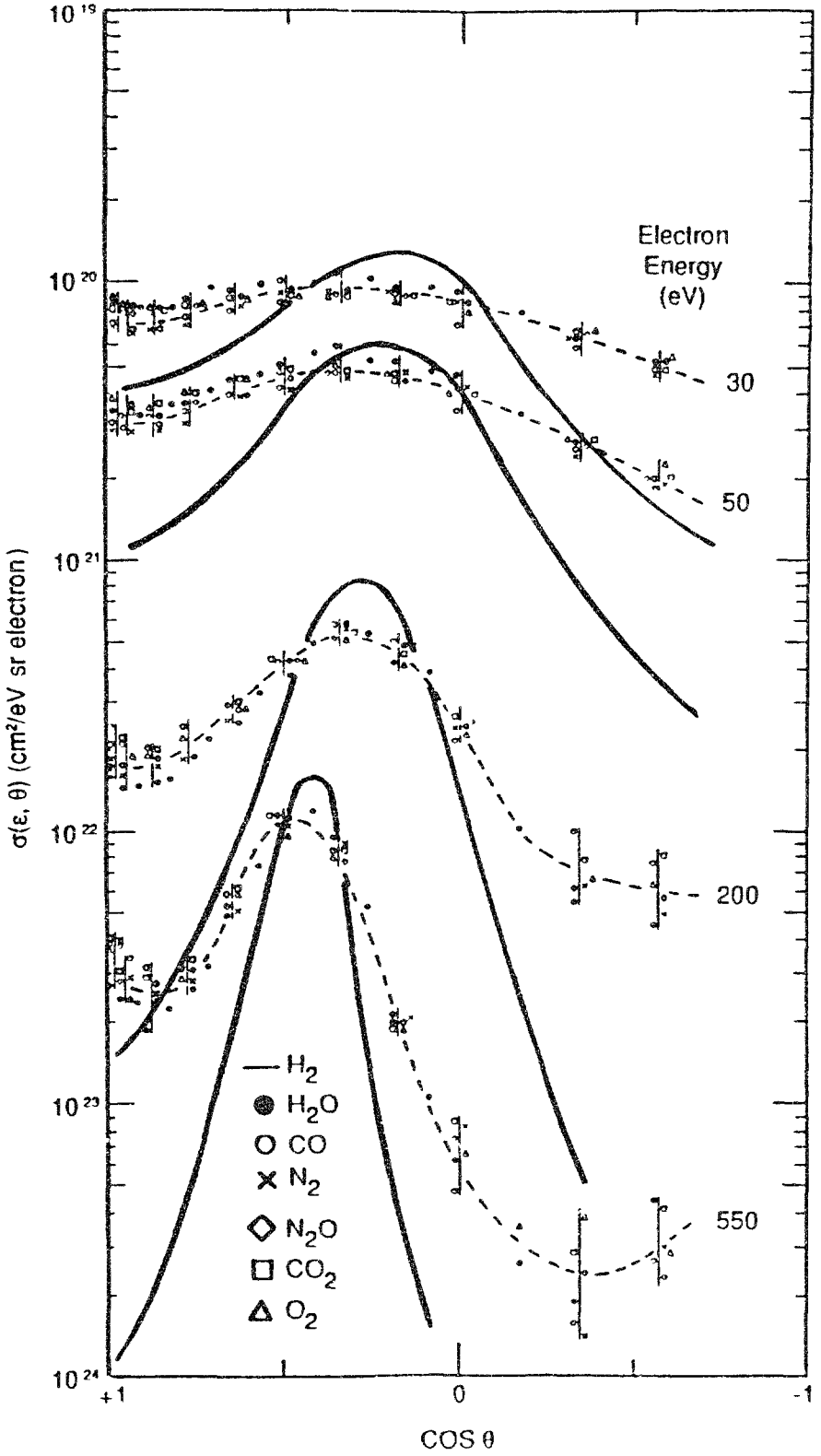

FIG. 2.13. Doubly-differential cross sections measured for ionization of a number of molecules by 1.5 MeV protons [H_2 - Toburen and Wilson [50] N_2 - Toburen [49]; H_2O, O_2 - Toburen and Wilson [76]; and CO, CO_2, N_2O - Toburen, unpublished]. The data have all been scaled by dividing the measured cross sections by the number of loosely bound electrons in the respective molecule. In this work the number of weakly bound electrons is defined as all electrons except the K-shell electrons of carbon, nitrogen, and oxygen.

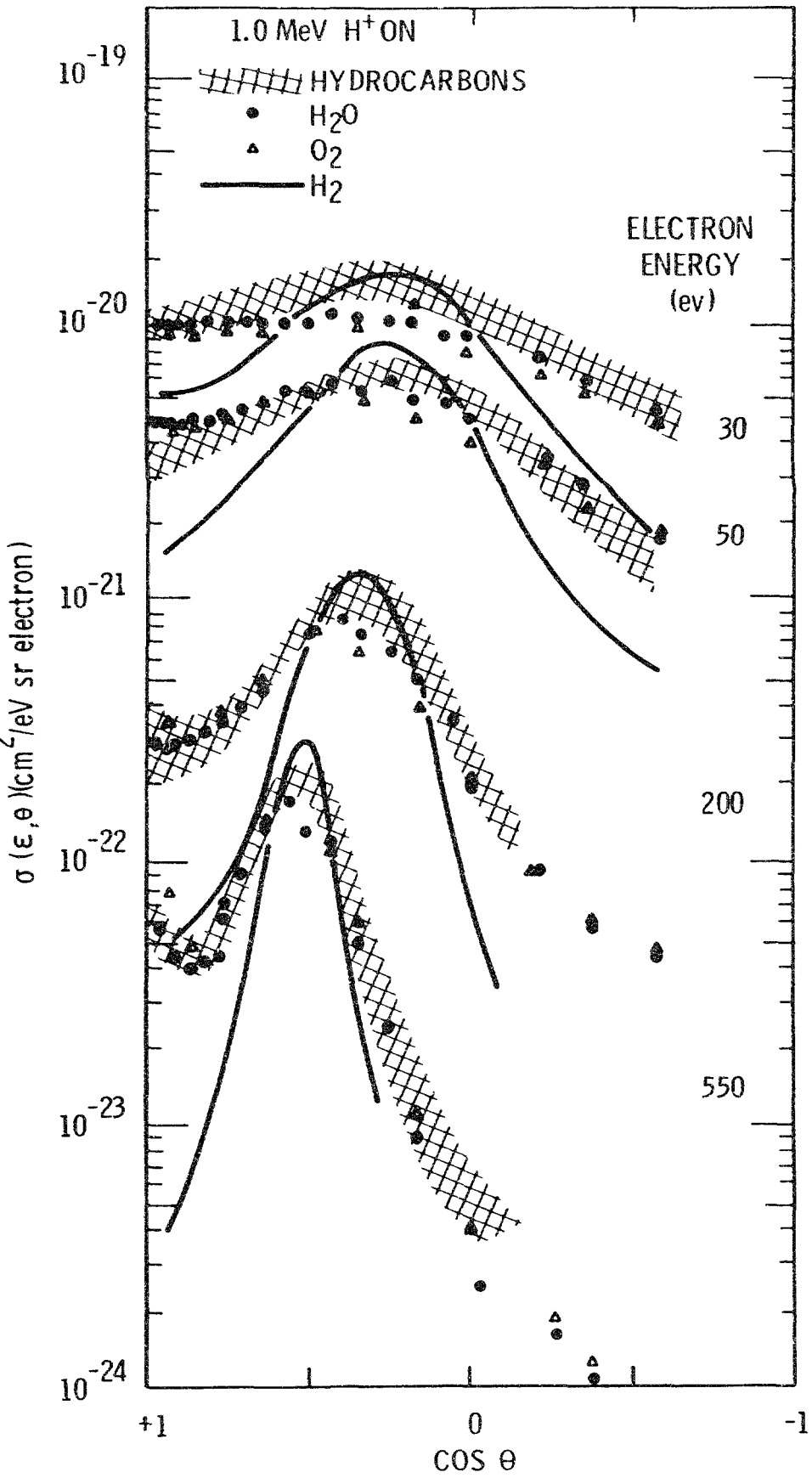

FIG. 2.14. Doubly-differential cross sections for ionization of a number of molecules by 1 MeV protons scaled by the number of weakly bound target electrons. The hydrocarbon data are from the work of Wilson and Toburen [79], H_2O and O_2 data are from Toburen and Wilson [76] and the N_2 data are from Toburen [49].

enable him to scale the gas phase cross sections for application in condensed phase material.

A great deal of effort has gone into studies of the effects of electronic binding and molecular structure on interaction cross sections. For molecular targets, there is considerable similarity in the angular distributions of electrons ejected by protons for all of the molecules that have been studied, with the exception of molecular hydrogen. Data for a number of simple molecular targets are shown in FIG. 2.13 for 1.5 MeV proton impact. For comparing cross sections for different molecules we have scaled the cross sections by dividing each by the number of weakly bound electrons in the respective molecule. For this purpose we define weakly bound electrons to be all electrons except the K-shell electrons of carbon, oxygen, and nitrogen. The K-shell electrons of these atoms are excluded because, at the proton energy shown, they contribute little to the total yield of electrons. Scaled in this way, data for all molecules, except hydrogen, agree within experimental uncertainties. Similar results were obtained for cross sections measured for hydrocarbon molecules; this is illustrated in FIG. 2.14. In this comparison, the cross-hatched area of the curves represent data from a number of simple hydrocarbon molecules [79] including CH_4, C_2H_2, C_2H_4, C_2H_6, and C_6H_6. The data for hydrocarbon molecules show slightly higher values at the peaks in the angular distributions, i.e., they exhibit a somewhat more hydrogen-like character in the binary-encounter peaks, than the non-hydrogen containing molecular targets. When scaled in this manner all of these molecular targets provide cross sections that agree well at both, large and small emission angles. If cross sections for higher ejected electron energies were plotted the peaks in the angular distributions would move to smaller angles in agreement with classical kinematics; i.e., proportional to $\cos^2\theta$. Evidence of ionization via the CCT mechanism is also seen in figs. 2.13 and 2.14; this ionization mechanism contributes to the increase in the cross sections for the smallest angles of ejection with the largest contribution at the highest energy electrons shown. We would expect enhancement due to CCT to be most evident in distributions for ejected electron energies near 817 eV in FIG. 2.13 and 544 eV in FIG. 2.14; these electrons are of equivalent velocity to the incident 1.5- and 1.0-MeV protons, respectively, shown in these figures.

The most dramatic differences observed among the data for the different molecules shown in Figs. 2.13 and 2.14 are between the scaled molecular hydrogen cross sections and those of all the other molecules. Differences of more than an order of magnitude occur at both, small and large emission angle. These differences carry an even more important meaning when we recall that semi-classical and hydrogenic Born calculations yield results that mimic the hydrogen measurements. It is only when realistic wave functions are used for both bound and continuum states that the Born approximation gives adequate agreement with measured doubly differential cross sections [56]. Unfortunately techniques have not been developed for application of Born theory to molecular targets owing primarily to the unavailability of adequate target wave functions.

The general trends of the angular distributions shown in Figs. 2.13 and 2.14 are representative of what we may call "fast" collisions; collisions in which the incident proton is fast relative to the speed of the bound electrons. These conditions lead to the appearance of the binary encounter peak in the angular distribution of ejected electrons; this is particularly evident for ejected electrons with energies significantly greater than the initial binding energy of the ejected electron. An examination of the angular distributions of electrons ejected by much lower energy proton impact, shown in FIG. 2.15, illustrates that these have a quite different distribution. For

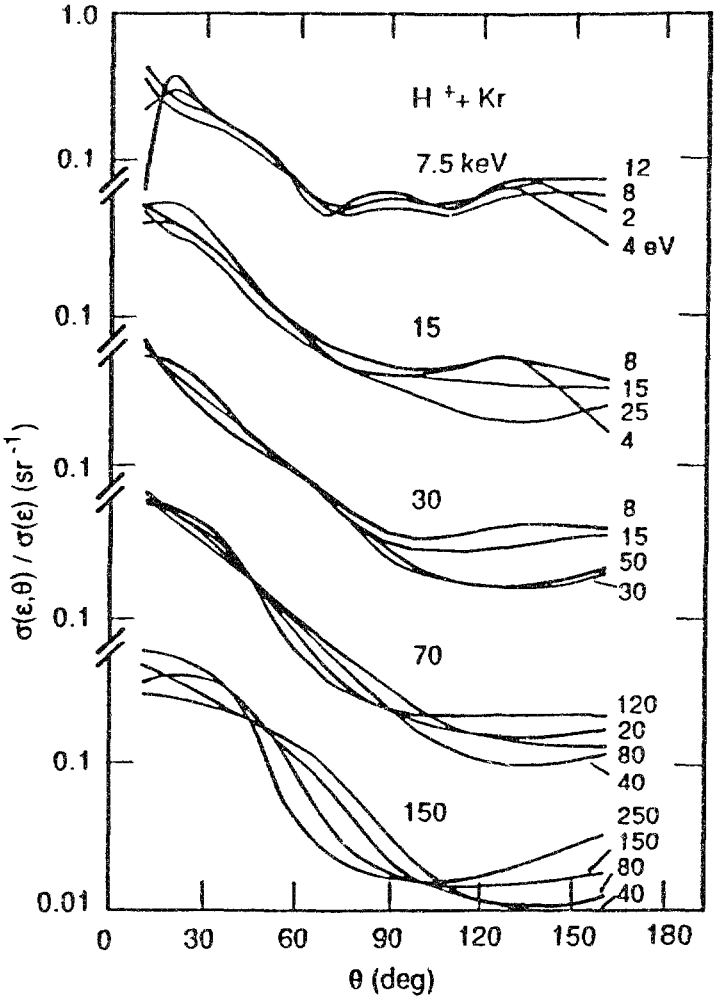

FIG. 2.15. Angular distributions of electrons of several energies ejected from krypton by low energy protons; this figure was reproduced from Cheng et al. [53].

such low-energy protons the ejected electron distributions peak at zero degrees for all ejected electron energies [53].

As can be seen, there have been a wide range of measurements of doubly differential cross sections for proton impact and these results provide a clear indication of the cross section systematics. However, no theoretical models have been developed for the DDCS's for molecular targets and there has been little work published with regard to phenomenological models of these cross sections that can be used in radiobiological modeling. One model of the doubly differential cross sections for electron emission from molecular targets presently in use for Monte Carlo track structure calculations is that of Wilson [124, 125]. Wilson bases his semi-theoretical model on Bethe-Born theory (Eq. 2.4) where the doubly differential cross section for electron emission is given by Kim [32] as

$$\frac{d^2\sigma}{d\epsilon d\theta} = \frac{4\pi a_o^2 z^2}{T/R}\left[A(\epsilon,\theta)\ln\left(\frac{T}{R}\right) + B(\epsilon,\theta) + O(T^{-1})\right], \qquad (2.9)$$

where z is the charge of the incident particle and A and B are defined below. The first term in the brackets of Eq. 2.9 describes the distant interactions involving small momentum transfers, glancing collisions. The second term is the "hard" collision component, representing close interactions that transfer significant momentum to the target particle. In Wilson's current model the higher order terms, O(1/T), are considered negligible and ignored.

The angular dependent part of the glancing collisions term, $A(\epsilon,\theta)$, is represented in the optical approximation by

$$A(\epsilon,\theta) = \frac{1}{4\pi}\sum_j \left(\frac{R}{\epsilon + I_j} \frac{df_j}{d\epsilon} [1 + \frac{\beta_j}{2} P_2(\cos\theta)] \right) , \qquad (2.10)$$

where $R/(\epsilon+I_j)\ df_j/d\epsilon$ is the dipole optical oscillator strength for shell j. In Eq. 2.10, β_j is the photoelectron asymmetry parameter, P_2 is the Legendre polynomial of second order and I_j is the ionization threshold for shell j. For the oscillator strengths, Wilson uses a piece-wise polynomial representation of the Berkowitz tabulation [126] of the total oscillator strength and branching ratios of Tan et al. [127] and of Blake and Carter [128]. The asymmetry parameter β_j is theoretically equal to 2 for S states, (the $2a_1$ orbital of water); for other states β_j is energy dependent and a phenomenological fit to experimental DDCS data [76] is used.

The fast collisions component, $B(\epsilon,\theta)$, of the experimental angular distributions is well represented by a (Gaussian) normal distribution [124, 125]. Therefore, this component in Eq. 2.9 is approximated by a product of three functions; $g_\epsilon(\theta)$, $S_{bea}(\epsilon)$, and $f_b(\epsilon)$. The angular dependence, $g_\epsilon(\theta)$, is described by a normalized Gaussian function

$$g_\epsilon(\theta) = \frac{1}{\sqrt{2\pi}\ \Gamma} \exp\left[- \left(\frac{\cos\theta - \cos\bar{\theta}}{\Gamma} \right)^2 \right] , \qquad (2.11)$$

where θ_{bar} is the mean value of the angle at which the binary encounter peak occurs in the angular distribution and Γ is the width of the Gaussian fit to that peak. The coefficients, Γ and $\cos\bar{\theta}$, contained in Eq. 2.11 are parameterized as a function of proton energy and energy loss by least squares fitting to the experimental angular distributions. The amplitude of the hard collisions term is determined primarily by the second function, $S_{bea}(\epsilon)$. For it, Wilson uses a simple singly differential binary-encounter treatment [43]. Finally, the function f_b is introduced to force the hard collisions component to tend to zero as $\epsilon \rightarrow 0$, in order to achieve better agreement with experiment (ϵ in eV),

$$f_b(\epsilon) = \max \begin{cases} 1 - \exp\left(\frac{9 - \epsilon}{16.5} \right) \\ 0 \end{cases} . \qquad (2.12)$$

This scheme has been used by Wilson for representing water vapor cross sections and the results of his calculations plotted as differential partial stopping cross sections $[\epsilon\sigma(\epsilon,\theta)]$, i.e., that part of the stopping cross section arising from energy loss to kinetic energy of electrons ejected at specific angles, are reproduced for 1 MeV proton impact in FIG. 2.16. The partial stopping cross section for ionization can be obtained from the measured doubly differential cross sections by carrying out the integration in the expression $\int d\epsilon \int d\Omega (I+\epsilon)\sigma(\epsilon,\theta)$, where I is the initial binding energy of the ejected electron.

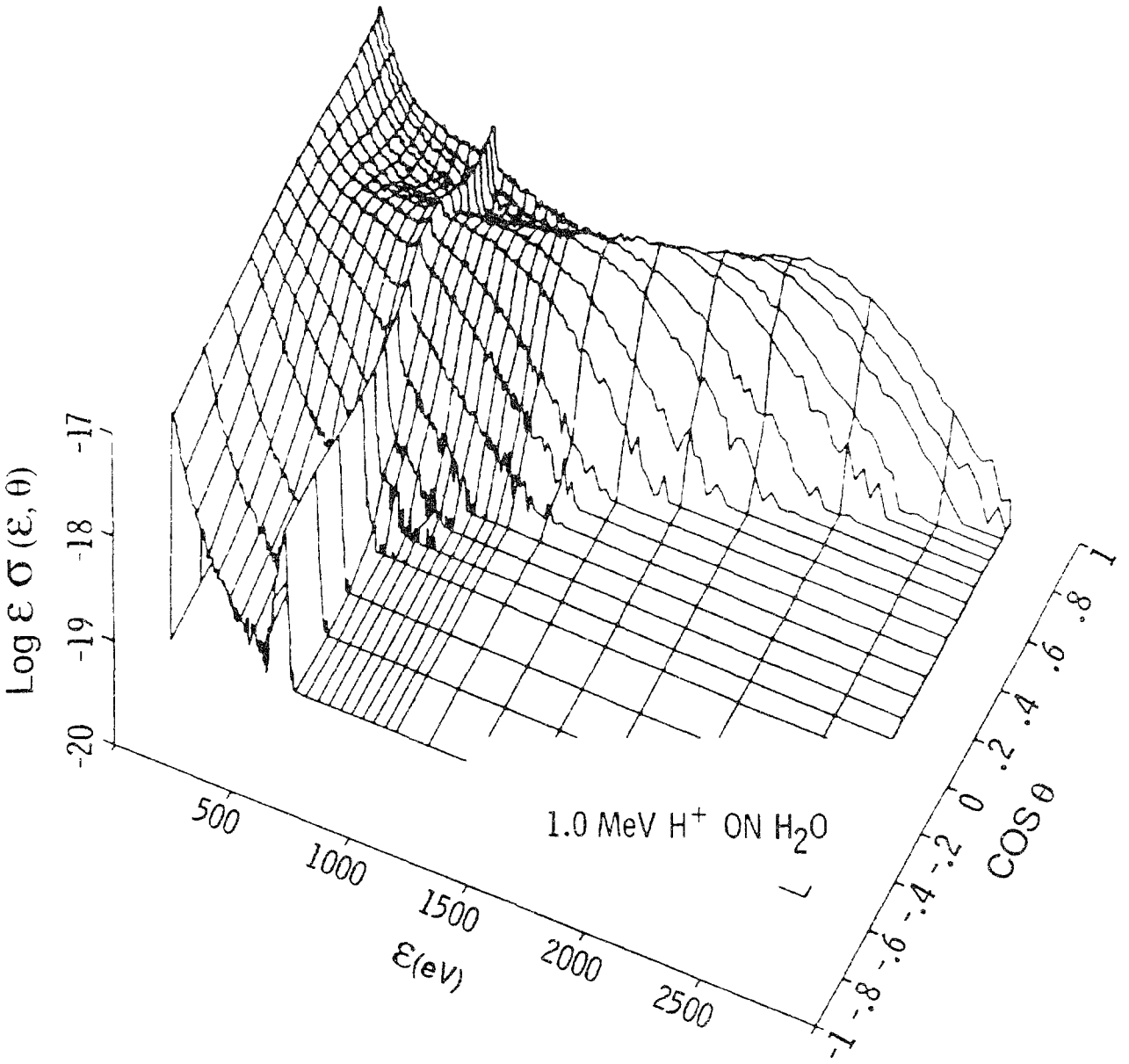

FIG. 2.16. Doubly differential energy loss cross sections for energy deposited as kinetic energy of ejected electrons [$\epsilon\sigma(\epsilon,\theta)$, in units of cm^2/sr molecule] calculated using the model of Wilson [124,125] with parameters obtained from fitting the data of Toburen and Wilson [76] for proton impact ionization of water vapor.

From a review of the doubly differential cross sections for electron emission by protons it would appear that the mechanisms responsible for ionization are well understood; this is particularly true for fast ions where the Born approximation in expected to be valid. Theoretical techniques to predict doubly differential cross sections in the high energy region (energies greater than a few hundred keV) have been successful based on the Born approximation. Binary encounter theory and hydrogenic Born calculations both underestimate the cross sections for emission of electrons into large and small angles. The similarity of angular distributions for a wide range of molecular targets, however, is conducive to the development of molecular models for use in track structure calculations. Charge-transfer-to-continuum states contribute to an enhancement of the cross sections for small emission angles, but do not contribute significantly to the total yield of electrons.

Before moving on to the discussion of doubly differential electron emission cross sections for heavier ions it is appropriate to comment on the general features of the angular distributions of electrons ejected in proton collisions and the relationship of what is observed to that assumed in common radiological calculations for high LET radiation. The angular distributions of ejected electrons have been shown to have a broad angular distribution that, in the intermediate- and high-energy range, varies from nearly isotropic for the lowest energy ejected electrons to narrow distributions peaked at the classical emission angles for high-energy ejected electrons. This is summarized here to emphasize that not all electrons are ejected at 90 degrees to the ion path as has been assumed in traditional track structure calculations (see, for example, Butts and Katz [129] and Chatterjee and Shaeffer, [130]).

2.2.3. **Heavy Ion Impact**

2.2.3.1. Bare Ions:

Protons represent, by far, the most comprehensive data base of doubly differential cross sections for bare ions. The second largest data set for a bare ion is that available for alpha particles, He^{2+}. There have also been some measurements of doubly differential cross sections for heavier ions, such as C^{6+}, and O^{8+} [63], O^{8+} [86], and the nearly bare Mo^{40+} ion [104]. These data, for somewhat isolated collision systems, serve to examine methods for ion charge-state scaling of cross sections and provide tests of evolving theory, eg., these data were mentioned briefly above in the context of theoretical techniques that include the effects of the two charge centers, projectile and target, on the ejected electron spectra. It suffices to repeat here that, for projectiles of sufficiently high charge states, z^2 scaling may be modified somewhat compared to that expected on the basis of first order classical and quantum calculations.

The doubly differential cross sections for ejection of electrons into a "large" emission angle (125 degrees) from argon by 1.2 and 2.0 MeV alpha particles are shown in FIG. 2.17 where they are compared to cross sections for electron emission by equal velocity protons. Here the cross sections for proton impact were multiplied by a factor of 4 to scale them according to z^2 scaling, as predicted by classical (Eq. 2.1) and quantum mechanical (Eq. 2.8) theory, for comparison to the alpha particle results. Note that there is excellent agreement between the scaled proton data and the equal velocity alpha particle cross sections. The only difference observed among the data for the two projectiles is the somewhat broader Auger electron spectra superimposed on the continuum spectra at approximately 200 eV for the alpha particle impact. The extra width of the alpha particle induced Auger spectra results from increased multiple ionization of the target by alpha particles, thus resulting in Auger transitions with a broader energy range [131]. A similar comparison of doubly differential cross sections is shown in FIG. 2.18 for electron emission into a forward angle. Here we see that the z^2 scaling provides excellent agreement among the data for the two projectiles at the largest and smallest ejected electron energies. Discrepancies are observed, however, at the intermediate electron energies. These discrepancies are attributed to the influence of the CCT ionization mechanism. CCT is expected to scale as z^3 [132] compared to the z^2 scaling of direct ionization; this would lead to larger cross sections for the alpha particles in the region of the spectra where CCT contributes. This mechanism should have a maximum effect at ejected electron energies such that the outgoing projectile and electron have comparable velocity; equal velocities occur at ejected electron

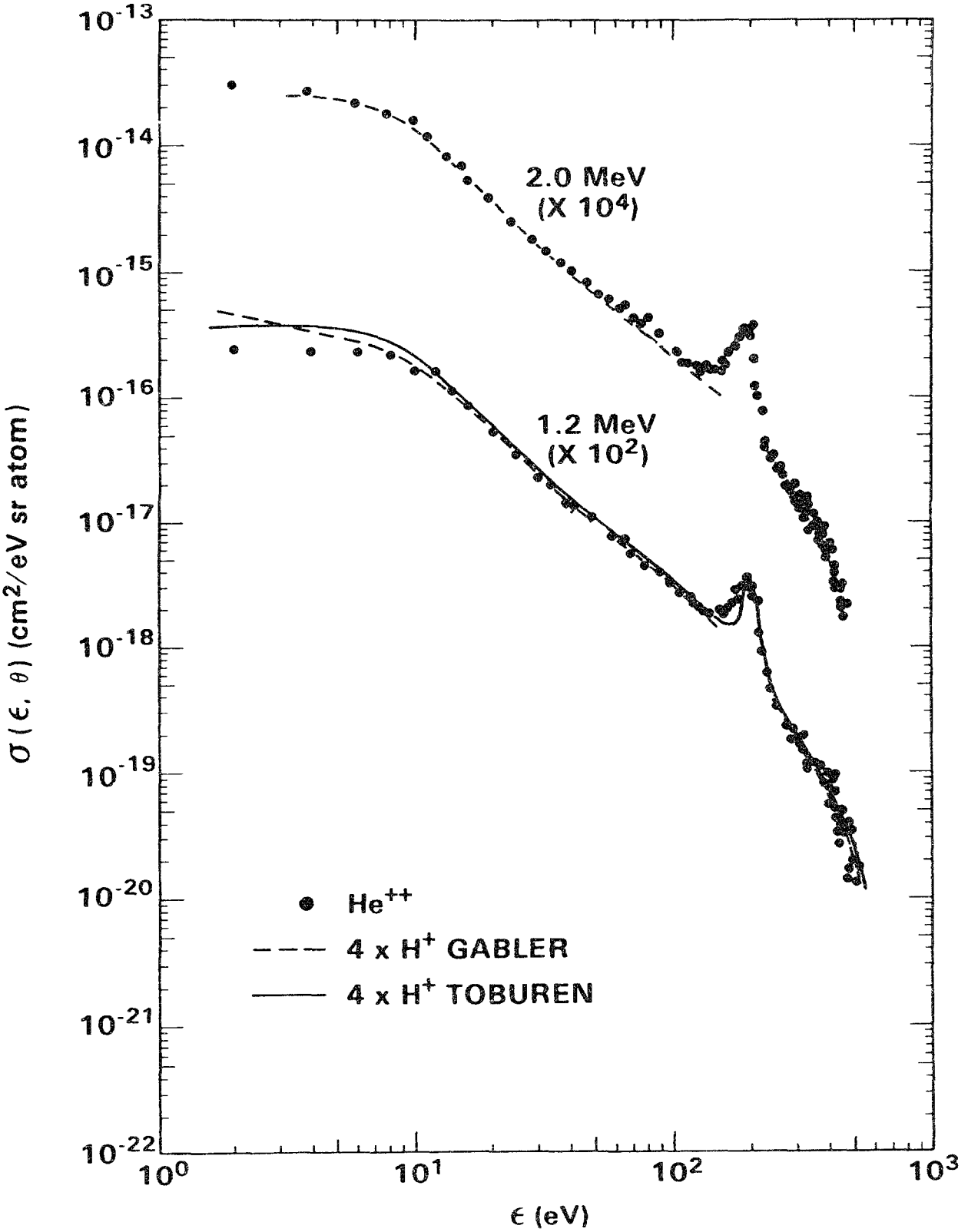

FIG. 2.17. Doubly differential cross sections for ejection of electron into 125° from argon by protons and alpha particles. The proton data were multiplied by 4, scaled by z^2, for comparison to the alpha particle results. The data are from (for •, —) Toburen and Wilson [91] and (---) Gabler [67].

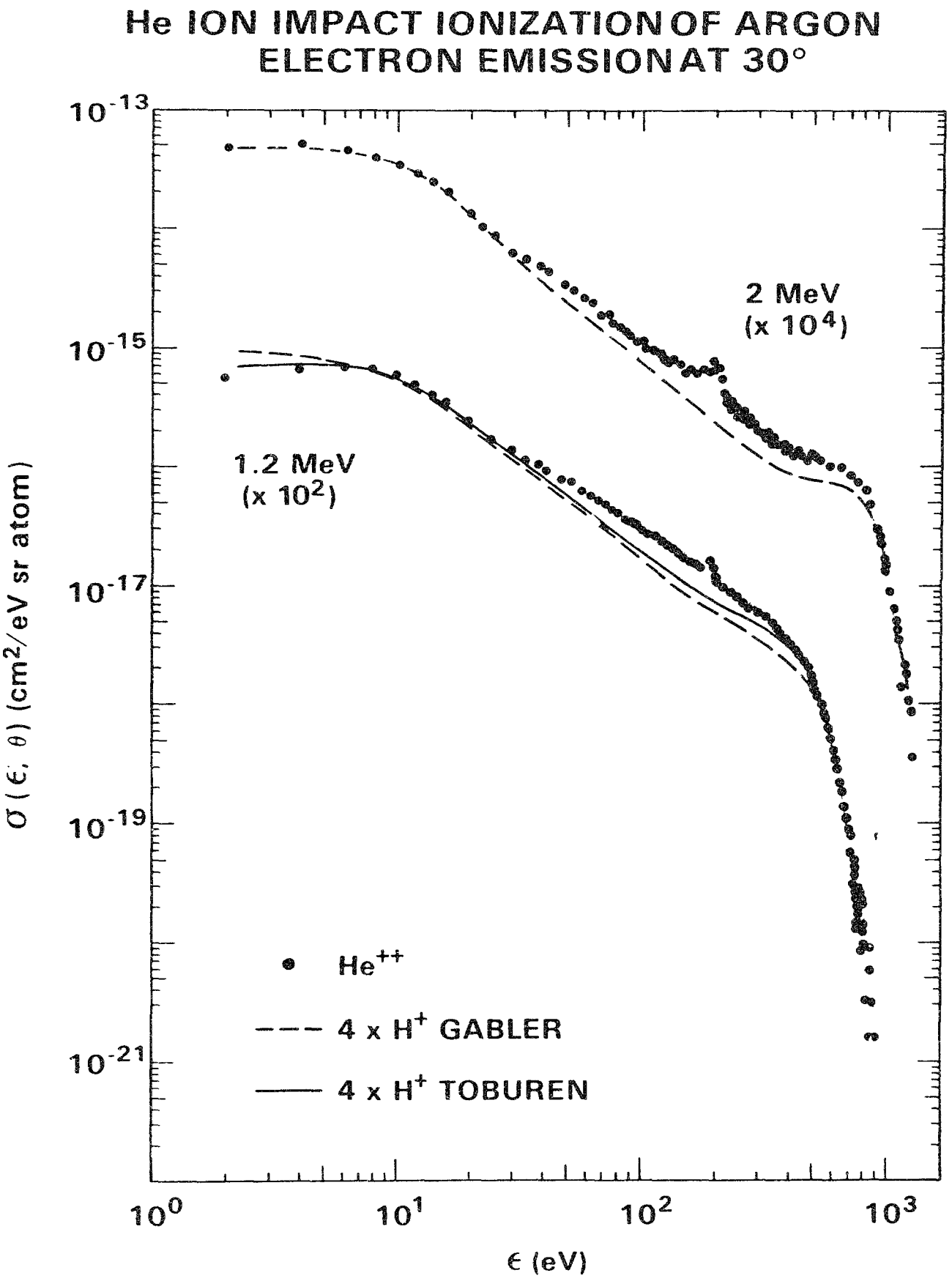

FIG. 2.18. Doubly differential cross sections for ejection of electron into 30° from argon by protons and alpha particles. The data were scaled as discussed in FIG. 2.17. The data are from (•, —) Toburen and Wilson [91] and (---) Gabler [67].

energies of 272 eV and 163 eV for alpha particle (proton) energies of 2 MeV (0.5 MeV) and 1.2 MeV (0.3 MeV), respectively. These data would suggest that the CCT ionization mechanism is an important contribution to the ionized electron spectra over a broad range of electron energies and emission angles.

2.2.3.2. Structured Ions:

Studies of ionization of atomic and molecular targets by structured ions, i.e., ions that carry bound electrons and are sometimes referred to as clothed or dressed ions, have been underway for more than 20 years (see for example, Rudd et al. [70], Cacak and Jorgensen, [83], Wilson and Toburen, [82], and have been discussed in reviews by Toburen [1, 41, 42], Rudd and Macek [43], Rudd [44], and Stolterfoht [45]. Publications addressing doubly-differential cross sections for a broad range of collision partners are reviewed in table 2.3; in preparing this table the publications were limited to those that present measurements of <u>absolute</u> cross sections and that cover a reasonably wide range of ejected electron energies and angles.

The primary differences in the spectra of electrons ejected by fast ions that carry bound electrons from those ejected by bare ions can be seen in FIG. 2.19, where spectra are shown for ejection of electrons from water vapor by 0.3 MeV/u H^+, He^{++}, and He^+ ions [92]; the proton data are shown both, as unscaled cross sections for low-energy electron emission, and as full spectra multiplied by a factor of 4 to account for z^2 scaling for comparison to the helium ion data. Note that the scaled proton data are in excellent agreement with the He^{++} results over most of the energy and angular range. The greatest differences between the scaled proton and bare helium ion cross sections occur at the smallest angles and for electron energies near 160 eV; the latter is the electron energy at which the electron and ion have comparable velocity. These differences are attributed, as discussed above, to the CCT mechanism of ionization which scales as a higher power of z than direct ionization.

In contrast to the excellent agreement observed between scaled H^+ and He^{++} cross sections the emission cross sections for He^+ impact exhibit marked differences from the bare ion results. Most evident is the reduction in cross section for ejection of low-energy electrons; at the smallest ejected electron energies the cross sections more nearly reflect the unscaled proton results. Low-energy electrons are ejected in distant "soft" collisions in which the bound projectile electron provides an effective electrostatic shield of the helium ion nucleus [114] such that the strength of the electrostatic interaction is greatly reduced. Higher energy electrons, on the other hand, are ejected with increasingly close collisions that penetrate the shielding radius of the He^+ bound electron and are subject to the Coulomb potential of the full nuclear charge of the projectile. Thus, cross sections for high-energy electrons ejected in He^+ collisions are similar to those for He^{++} impact, whereas the low-energy data are more nearly equal to those of unscaled proton cross sections. More explicitly, one finds a gradual change in the nature of the cross sections, from low-energy electrons that are ejected in large-impact parameter collisions by what would appear to be a proton ("heavy" particle) of charge +1, to fast electrons ejected in close collisions by an effectively bare alpha particle of charge +2. Unfortunately the functional relationship that allows one to scale the charge as a function of energy loss, or impact parameter, has not been determined for different ion species and different molecular targets. The most obvious implication of the energy dependence of the "effective" nuclear charge is that the effective charge of stopping power theory, i.e., an effective charge that is only a function of the nuclear charge and particle velocity, is totally inadequate for use in any theory of <u>differential</u> energy loss by dressed ions. On the other hand, the dependence of effective charge on energy loss determined from measured

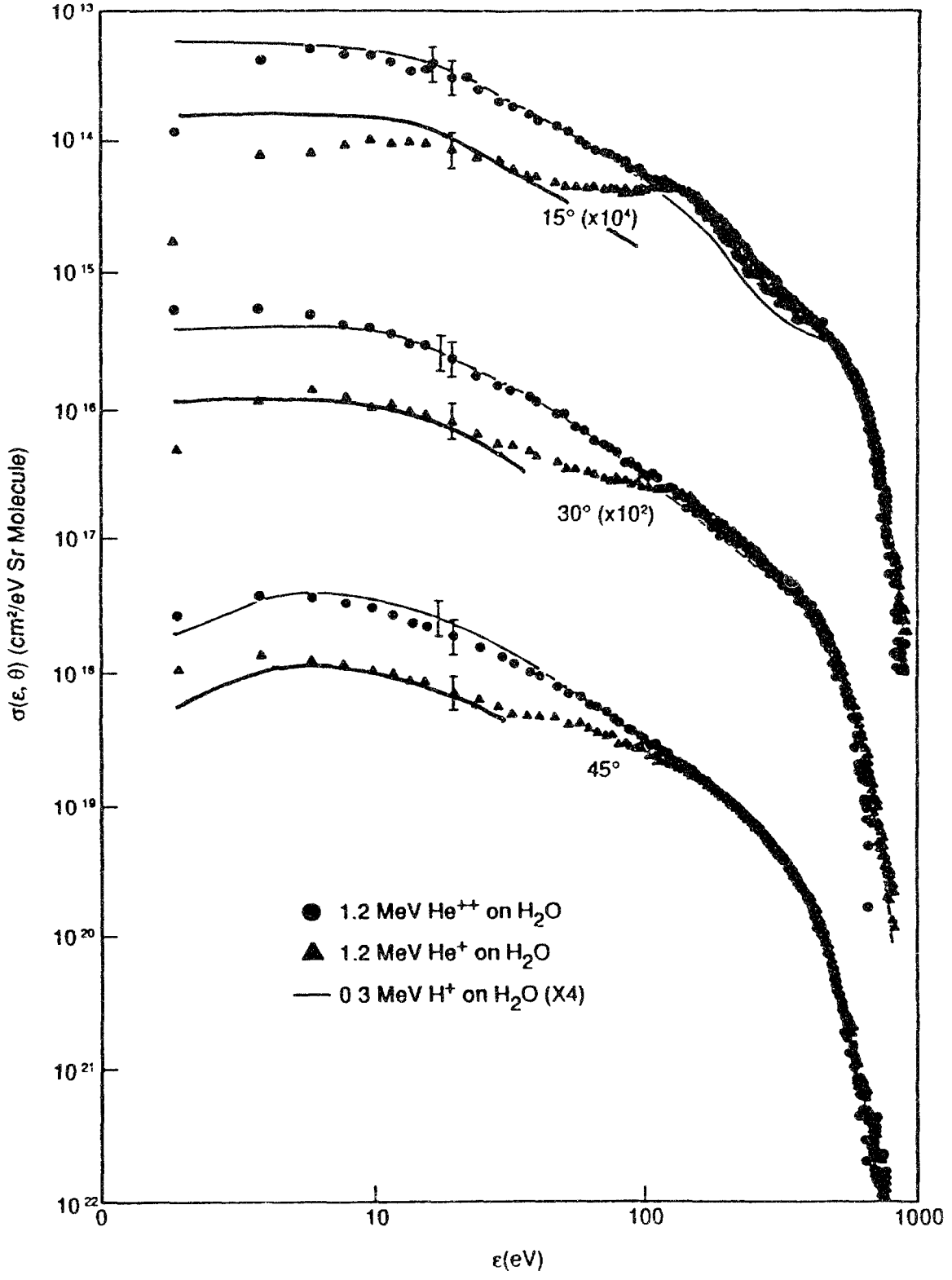

FIG. 2.19. Doubly differential cross sections for electron emission from water vapor by 0.3 MeV/u protons and helium ions. Proton data are shown multiplied by 4 (as implied by z^2 scaling) and unscaled for the low energy portion of the spectra for comparison to the helium ion results; the data are from Toburen et al. [92].

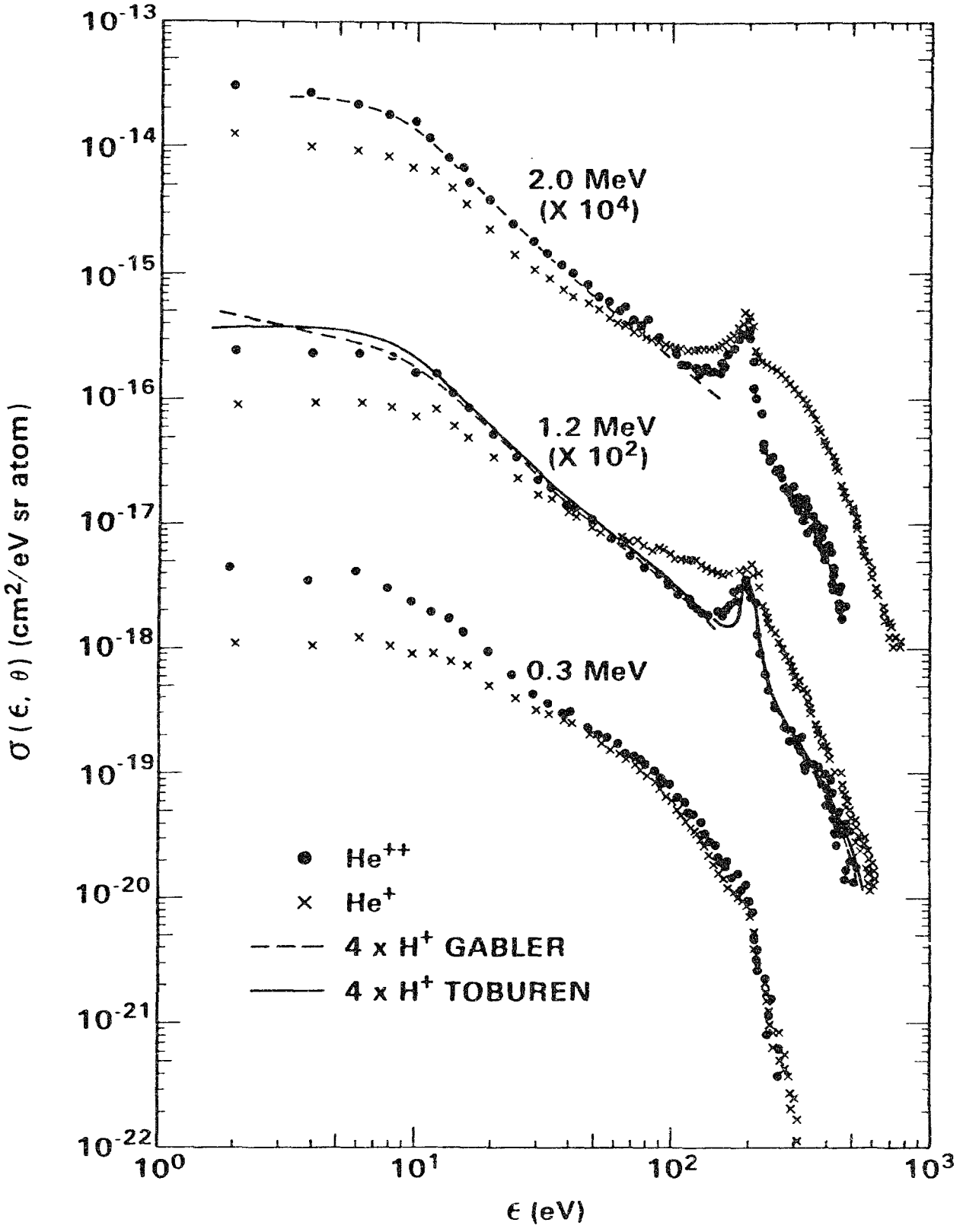

FIG. 2.20. Representative electron spectra for electron emission from argon at 125 degrees by equal velocity H^+, He^+, and He^{2+} ion impact. The scaled proton data are from Gabler [67], Criswell et al. [66], and Toburen et al. [110].

differential ionization cross sections can provide insights into the origins of the effective charge of stopping power theory; if the contribution to stopping power from target excitation is small the effective charge of stopping power theory can be obtained from an integral over the energy-loss dependent effective charge derived from ionization data such as those shown in FIG. 2.19 when averaged over the population of charge states in a charge equilibrated beam. The concept of effective charge will be treated in greater detail in a later section of this chapter and again in Chapter 7.5.

The second feature observed in the electron spectra measured for structured ion impact that is different from bare ions is the presence of a broad peak in the spectra originating from electrons that are stripped from the incident ion. These electrons are found predominantly in the forward directions, small emission angles in the laboratory reference frame, and at electron energies that correspond to electrons of the same velocity as the ion. Such a peak is visible in FIG. 2.19 in the 15- and 30-degree spectra at approximately 160 eV. In the 15-degree spectrum the contribution from projectile electron loss actually enhances the cross sections in the He^{+} spectrum to the point that it is larger than that of the He^{++} spectrum. At the larger emission angles the contribution to the spectra from projectile electron loss is less obvious and the primary difference between the spectra for the different ions is the strong influence of the bound He^{+} electron in screening the projectile nucleus. The contribution to the electron emission spectra from projectile-electron loss is also strongly dependent upon the projectile energy in this intermediate energy range. The cross sections for electron emission into an angle of 125 degrees from ionization of argon by He^{+} ions is shown in FIG. 2.20 for ion energies from 0.3 MeV to 2 MeV, i.e., 75 to 500 keV/u. Here the contribution from electron loss is seen to disappear as the ion energy is decreased. This reflects the well known tendency of the electron stripping cross sections to decrease as the ion energy decreases.

Theoretical studies of doubly differential cross sections for He^{+} impact have been limited primarily to the Born approximation (see, for example, Manson and Toburen, [133], and McGuire, et al., [134]), although efforts have also been made to apply the binary encounter approximation [114]. A comparison of the doubly-differential cross sections calculated with the Born approximation for the He^{+}-He collision system to spectra measured at 15 and 60 degrees with respect to the outgoing He^{+} ion is shown in FIG. 2.21, this is reprinted from the work of Manson and Toburen [133]. Excellent agreement between theory and experiment is observed for electrons ejected at 60 degrees, but differences of approximately a factor of 2 are found for the 15 degree spectra. Since electrons are indistinguishable in these measurement it could not be determined whether the discrepancy were with the calculation of target or projectile ionization. More recently measurements were made in which electrons were detected in coincidence with either the transmitted He^{+} or stripped He^{++} ion [135]. Those measurements demonstrated the inadequacy of the theoretical treatment to address simultaneous ionization processes, eg., ionization of both the projectile and target in a single collision. It was not clear from this work, however, whether discrepancies were the result of the use of inadequate wave functions or if they were a result of a breakdown in the Born approximation itself. More recently measurements have been undertaken for the H^{o}-He collision system [136] that now indicate that the Born approximation is sufficient to describe these few electron systems if adequate wave functions are used for both, discrete and continuum states.

An example of the spectrum of electrons ejected in He^{+} collisions with water vapor in which electrons are detected in coincidence with the stripped He^{2+} ion is shown in FIG. 2.22. These measurements were conducted at the Pacific Northwest Laboratory by R. D. DuBois using experimental techniques

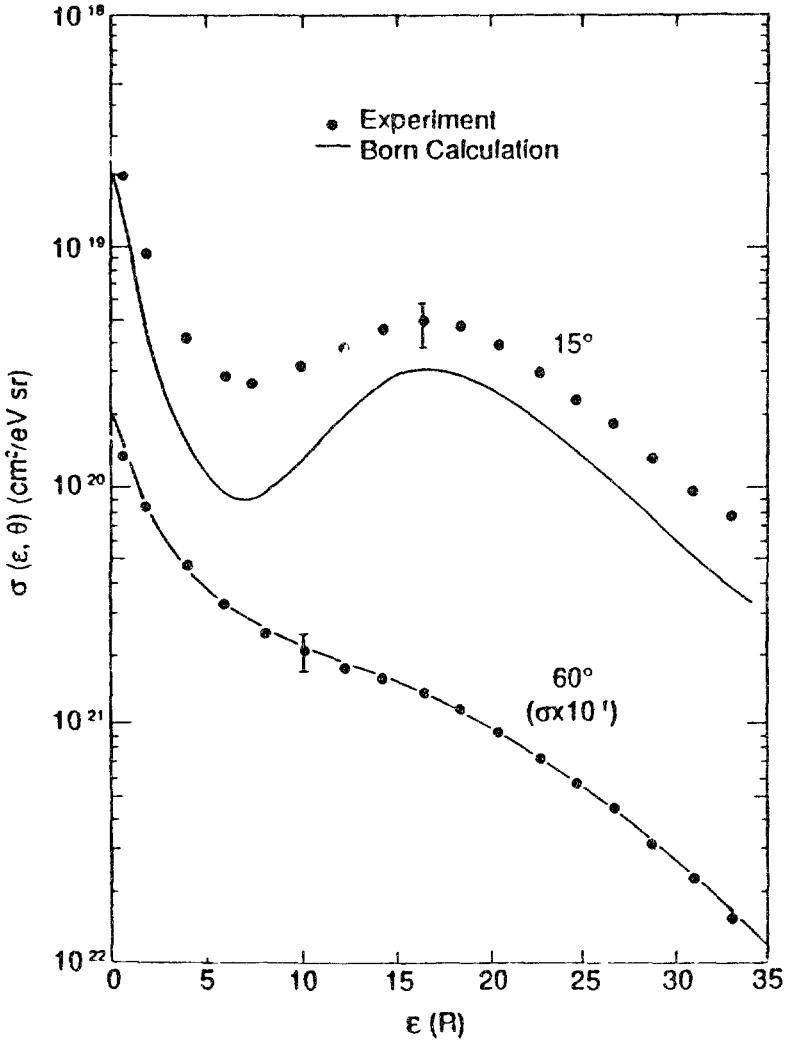

FIG. 2.21. Comparison of the measured doubly-differential cross sections for ionization of helium by 2 MeV He^+ to calculations based on the Born approximation [133].

described by DuBois and Manson [135]. One would expect the coincidence spectrum to be dominated by electrons lost by the projectile; a spectrum that peaks at approximately 400 eV for the ion energy considered here. The expected spectrum of electrons stripped from the projectiles, based on the transformation of an ejected electron spectrum from the projectile frame of reference to the laboratory frame is shown as the dashed line in FIG. 2.22. The large contribution of electrons ejected with energies less than 400 eV in the coincidence spectrum is attributed to simultaneous projectile and target ionization. This simultaneous ionization implies there will be a significant amount of correlation between the two ejected electrons as they slow down in a biological medium. Such correlation may influence the subsequent chemical reactions and lead to biologically active chemical species that are different from those following non-correlated energy deposition events.

Only a limited amount of data are available for structured ions heavier than helium (see Table 2.3 for details). At the low-energy end of the projectile energy spectrum these studies range from the pioneering work of Jorgensen and his colleagues at the University of Nebraska for symmetric Ar^+ - Ar and Ne^+ - Ne collisions [70,83] to the more recent work of Woerlee et al. [84,85] for Ne^{n+} - Ne, n=1-3, Stolterfoht and Schneider [100] for O^+ and N^+

collisions with Ar, and Toburen et al. [98] for ionization of He by C^+. High-energy projectile studies range from the early studies of Stolterfoht et al. [86] for fast oxygen ions to the very fast, very heavy ion work of Schneider et al. [103] for Fe^{17+} and Fe^{22+} ions, Stolterfoht et al. [104] for Mo^{40+} ions, Kelbch et al. [105] for U^{33+} ions, Schmidt-Böcking et al. [106]) for U^{33+} ions, and Schneider et al. [107] for Th^{38+} and U^{38+} ions. For the most part, these data for heavy ions are limited in scope; by this we mean they do not cover a broad enough range in projectile energy or charge state to gain a detailed understanding of the collision systematics. They do, however, provide excellent tests of collision theory. Such tests were discussed above for bare ions and will be examined further later in this section.

In our studies at the Pacific Northwest Laboratory we have investigated the cross section systematics for intermediate-energy "light" heavy ions, eg., carbon and oxygen ions. The general features of the ejected electron spectra for these intermediate-energy clothed ions are illustrated in FIG. 2.23 for ionization of water vapor by oxygen ions. For an ion of the relatively small velocity shown in FIG. 2.23, we see only a small contribution to the ejected

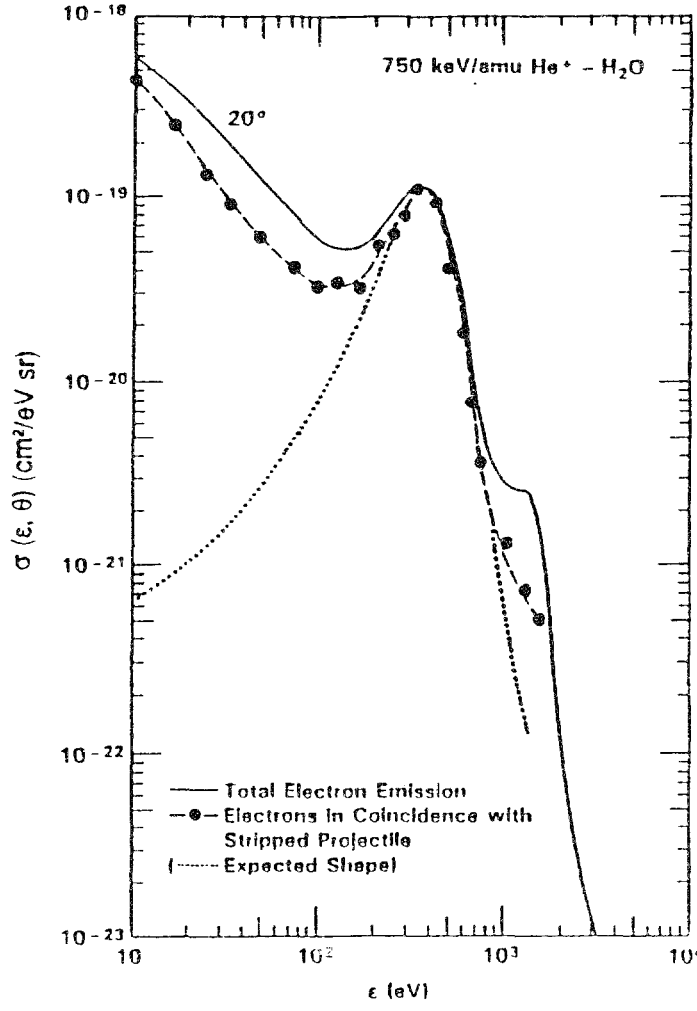

FIG. 2.22. Comparison of the spectrum of electrons detected in coincidence with ionization of the He^+ projectile to that of all electrons ejected at 20 degrees with respect to the exiting ion. These unpublished data were measured by R. D. DuBois at the Pacific Northwest Laboratory using the technique described by DuBois and Manson [135].

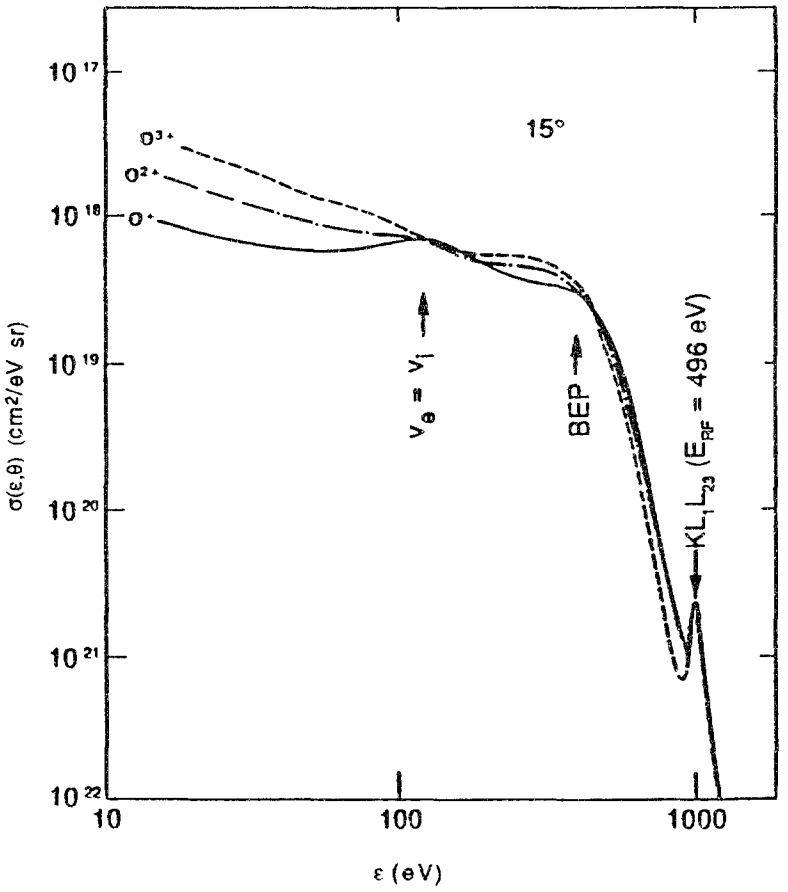

FIG. 2.23. Cross sections for emission of electrons at 15 degrees for ionization of water vapor by oxygen ions. The position in the spectrum at which the ejected electron velovity is equal to the ion velocity is noted by $v_e = v_i$; the binary encounter peak is designated as BEP and the high energy peak is attributed to the KL_1L_{23} Auger electron emitted from the oxygen ion excited and decaying in flight. These are unpublished data from the author's studies at the Pacific Northwest Laboratory.

electron spectra resulting from electron loss from the projectile (exhibited as a small peak where the ejected electron velocity V_e is nearly equal to the ion velocity v_i). The contribution is largest for the singly charged ion and then decreases as the projectile charge state increases. The binary encounter peak (BEP) for "fast" electrons ejected in these collisions is observed as a shoulder on the high energy portion of the spectra and this contribution is observed to increase slightly with increased projectile charge state. Above the BEP the cross sections decrease rapidly; the "width" of the binary peak reflects the initial velocity distribution of the bound target electrons. It is interesting to note the somewhat faster fall-off of the cross sections for the higher projectile charge states. This may be the effect of the electrons feeling the potential of the two charge centers which tends to decrease the cross sections for electrons that exit the collision with velocities greater than the projectile [63,104,123]. The peak observed in the spectra at approximately 1000 eV results from Auger electrons emitted from the oxygen projectile following collision induced K-shell vacancy production. The Auger spectra are observed in the laboratory frame-of-reference at the Doppler shifted energy (For a review of the kinematics of projectile emitted Auger processes, see Stolterfoht [45]). The effect of projectile electron screening

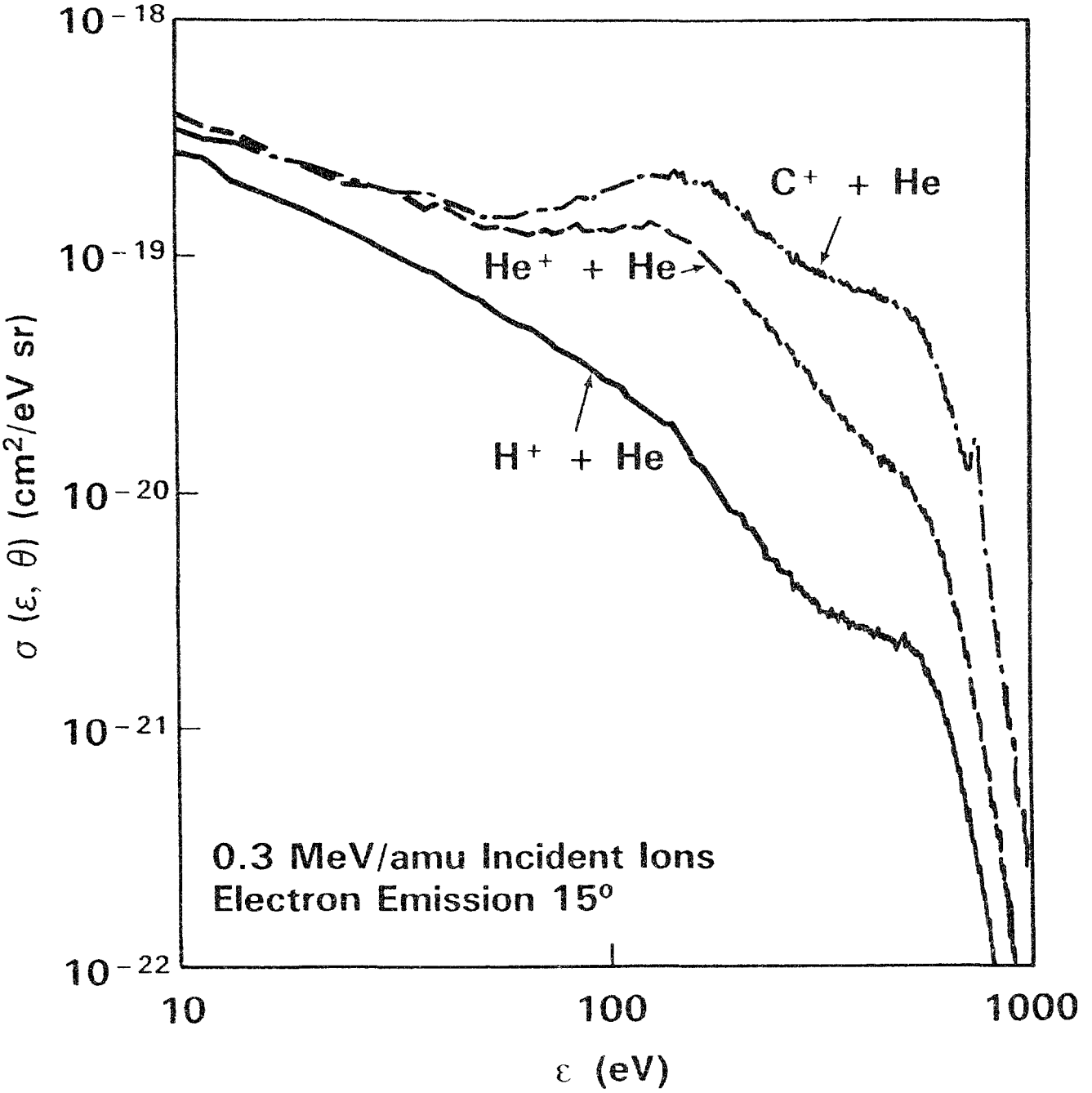

FIG. 2.24. Secondary electron emission are shown for electron emission at 15 degrees with respect to the out going projectile by equal velocity H^+, He^+, and C^+ ions colliding with a helium target. The proton data are from the compilation of Rudd et al. [72], the He^+ data are from Toburen and Wilson [90], and the C^+ data are from Toburen et al. [98].

on the collision cross sections is seen in the decreasing cross section for low-energy electron emission as the charge state of the ion decreases. For the lowest energy electrons ejected, those resulting from the most distant collisions, one would expect the cross sections to be representative of a projectile point charge equal to the net ion charge. Thus the results for O^+ may be expected to approach the cross sections obtained for equal velocity protons. Likewise cross sections for O^{2+} and O^{3+} may be expected to be factors of 4 and 9 larger than O^+ results, reflecting "z^2" scaling, at sufficiently

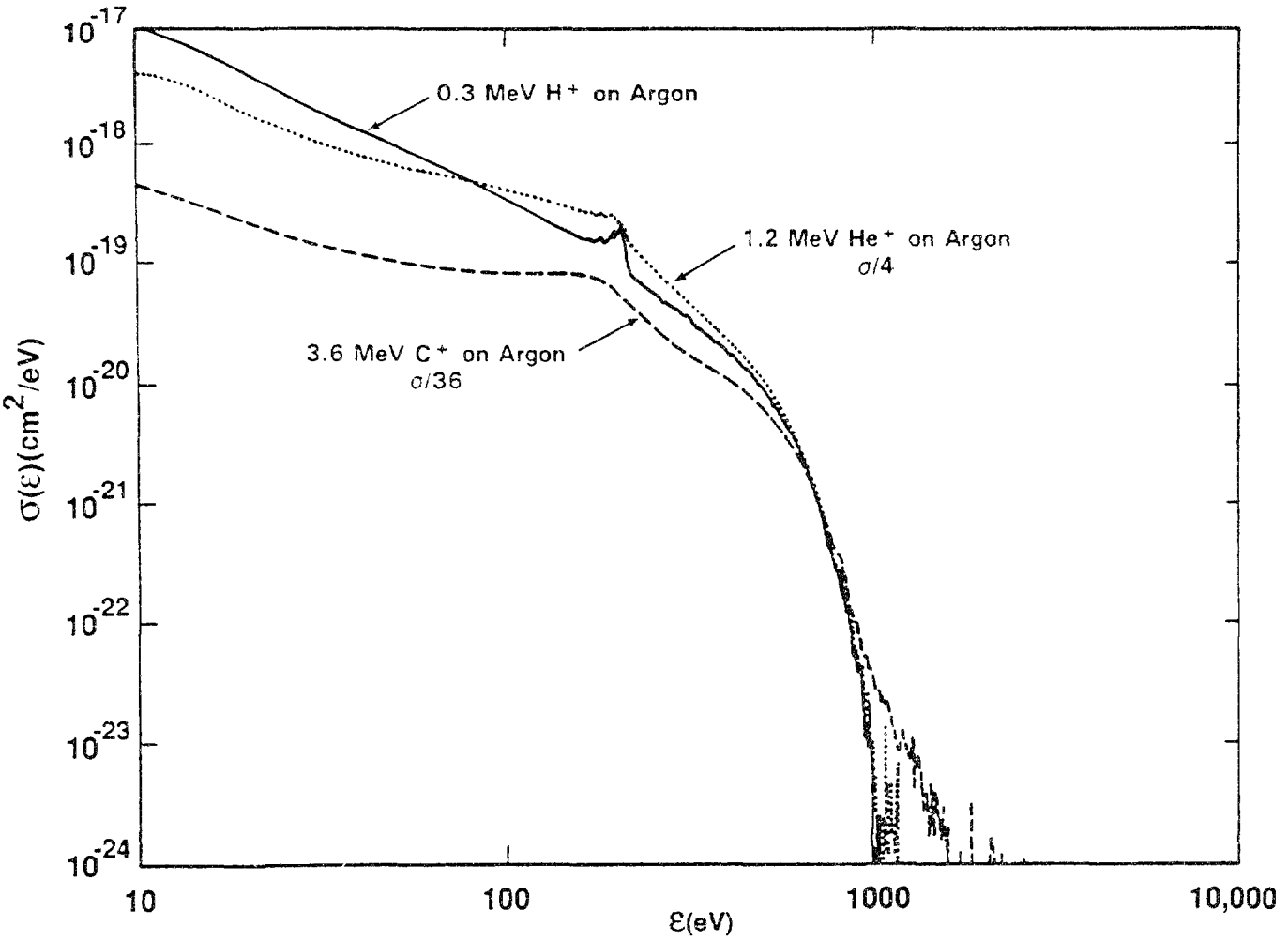

FIG. 2.25. Single differential cross sections for ionization of argon by equal velocity H^+, He^+, and C^+ ions. The data for He^+ and C^+ ion impact have been divided by 4 and 36, respectively, in accord with z^2 scaling for comparison to the proton results.

low ejected electron energies. The fact that the cross sections at the lowest energies shown do not exhibit these ratios is either because we have not yet measured low enough ejected electron energies, or that the basic scaling assumption is invalid.

Cross sections for emission of electrons into an angle of 15 degrees for ionization of He by equal velocity 300 keV/u H^+, He^+, and C^+ ions are shown in FIG. 2.24. The cross sections for low-energy electron emission by C^+ ions approach the same values as those for the other two singly charged ions illustrating the screening efficiency of projectile electrons. For higher electron energies, those ejected in small impact parameter collisions, the carbon cross sections are approximately 36 times greater than the proton results; this reflect interactions between the incident ion and bound electron that occur with an essentially unscreened carbon nucleus. This dramatic effect of nuclear screening by the projectile electrons is perhaps more clearly seen in the data for singly differential cross sections, obtained from measured doubly differential cross sections by integration with respect to emission angle, shown in FIG. 2.25. Here it is reasonably clear that the high-energy electrons scale as the square of the projectile nuclear charge,

whereas the low-energy electrons ejected in soft, or distant, collisions are representative of interactions with a highly screened projectile nuclear charge. Although the comparison of secondary electron spectra to proton data clearly shows that the effective charge of heavier, clothed ions is a function of the energy loss, there is no theory available, nor is there adequate experimental data at this time, to accurately define the functional relationships of this "effective charge" with ion energy, ion species, and energy loss.

The interpretation of the cross sections in terms of theory for electron emission in collisions involving structured ions depends strongly on the energy range of the incident ions. At the highest energies of the incident ions one can expect calculations based on the Born approximation to be reasonably successful. At high projectile energies the ions have an equilibrium charge that is representative of nearly bare nuclei and theoretical calculations for collisions with such ions are in good agreement with measurements [63,104,123].

For low-energy dressed ions the ejected electron energy spectra have a nearly exponential shape. This is illustrated in FIG. 2.26 where the data of Woerlee [84,85] are compared with the somewhat higher energy results from the author's work at the Pacific Northwest Laboratory. The observation by Woerlee [85] that the differential cross sections exhibit an exponential dependence on ejected electron energy and, for given ion energy, decrease with increasing projectile charge has lead to the use of quasi-molecular theory to describe these collisions [43,84,85]. In that theory the electron emission is considered as a result of direct coupling of the discrete and continuum electronic states via a rotational or radial coupling. This leads to the functional form of the cross section given by

$$\sigma(\epsilon,\theta) = R_o^2 \exp\left(\frac{-(\epsilon - \delta)a}{v}\right) \qquad (2.13)$$

where the electrons are assumed to be emitted isotropically and, in their notation, R_o, a, and δ are parameters that can be determined from the experimental data [84]. The physical interpretation of these parameters is that a is the width of the region where the coupling to the continuum takes place, δ is the energy of the discrete state, and R_o is the internuclear distance where the coupling is strongest. In the fitting of their experimental Ne^+ - Ne data, Woerlee et al. found valves of R_o = 1.32 au, a = 0.42 au, and δ = 10 eV which are reasonable values within the assumed mechanism. It should be noted, however, that the angular distributions are not found experimentally to be isotropic as assumed in arriving at Eq. 2.13. Woerlee et al. [84] find the angular distributions of ejected electrons to be approximately $\cos\theta$ in shape in the center-of-mass reference frame with the 90 degree minimum to be about 30% of the values at 50 and 140 degrees.

Although the direct coupling theory is expected to be valid only at the extreme low-energy end of the range of ion-atoms collision energies we have taken the liberty to add our unpublished carbon ion data obtained at somewhat higher ion energy to the Woerlee et al. data for comparison in FIG. 2.26. The good agreement in shape and magnitude between the C^+ and Ne^{2+} ion data is quite interesting. It would seem to imply that the details of the projectile-target electronic structure is not very important in this ion energy range. This conclusion could also be drawn from the similarity of cross sections found for different neon ion charge states by Woerlee et al. [84]. If this conclusion is valid and not simply a coincidence of the particular data sets being compared, then the direct coupling theory may provide a good method for parameterizing data for use in radiological modeling. For example, Eq. 2.13 would suggest that if the logarithm of the doubly differential cross sections

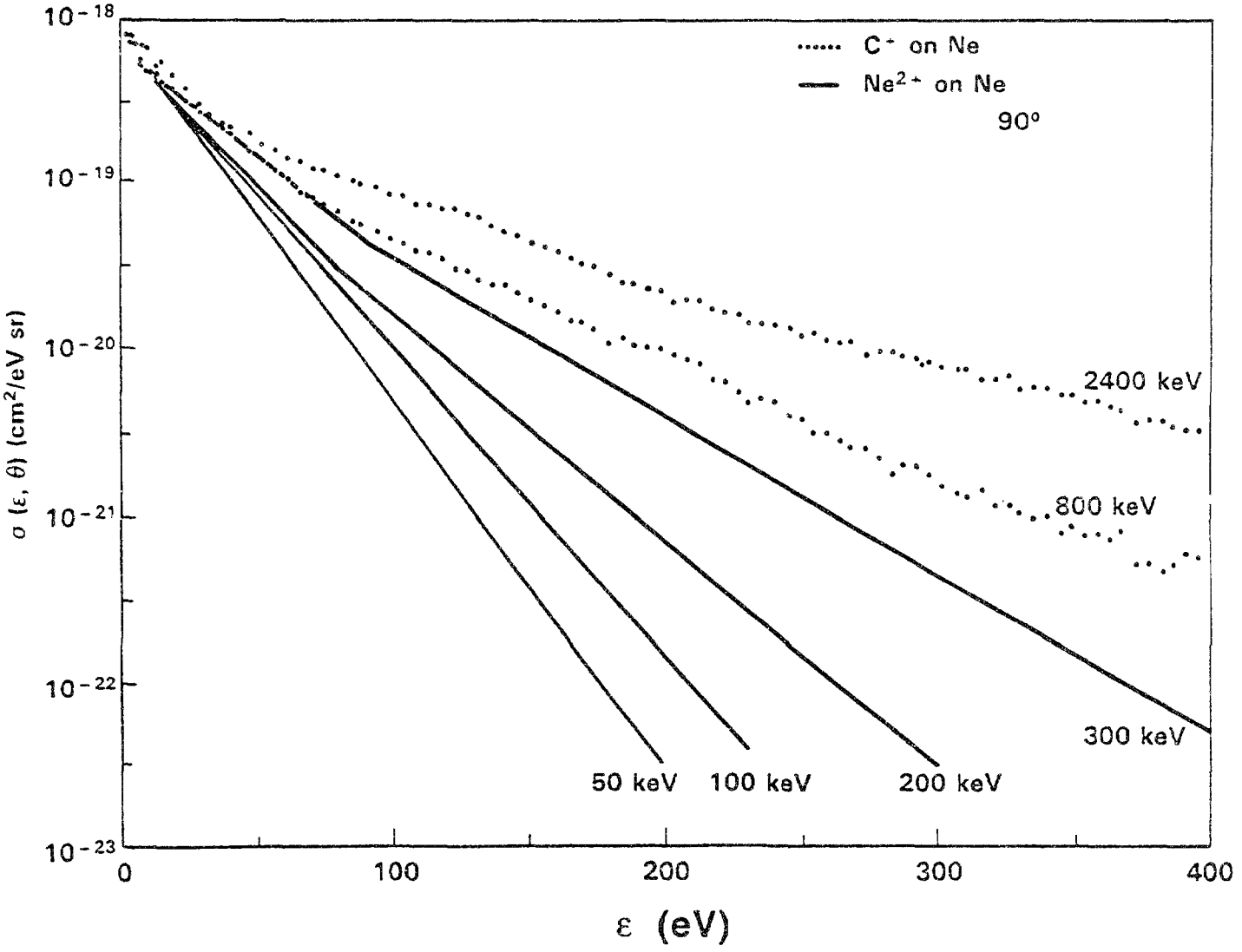

FIG. 2.26. Doubly differential cross sections for production of electrons in collisions of Ne^{2+} and C^+ ions with neon; the emission angle is 90 degrees. The data for Ne^{2+} are from Woerlee [85] and the C^+ results are unpublished results of Toburen at PNL.

were plotted versus the reciprocal of the ion velocity for a specified electron emission angle the curves for constant ejected electron energy should form straight lines. Data for ionization of neon by C^+ and Ne^+ ions are shown plotted in this manner in FIG. 2.27. Except for the lowest energy ejected electrons it would appear the curves of constant electron energy are straight lines in agreement with Eq. 2.13, and, remarkably, these straight lines extend through the data obtained with the higher energy carbon ion impact. The curvature in the lowest energy electron cross sections may be evidence of a breakdown in the direct coupling model and a transition to the direct Coulomb ionization model where the ion is moving relatively fast compared to the ejected electron velocity. As a matter of caution we should note that this interpretation of the interaction mechanisms may be fortuitous since data for ionization of CH_4 by C^+ ions, shown in FIG. 2.27 for one ejected electron energy at 30 degrees tend to exhibit a more sharply decreasing slope with decreasing ion velocity; these data are connected with a dashed line to guide the eye. What appeared to be scatter of the data points around the straight

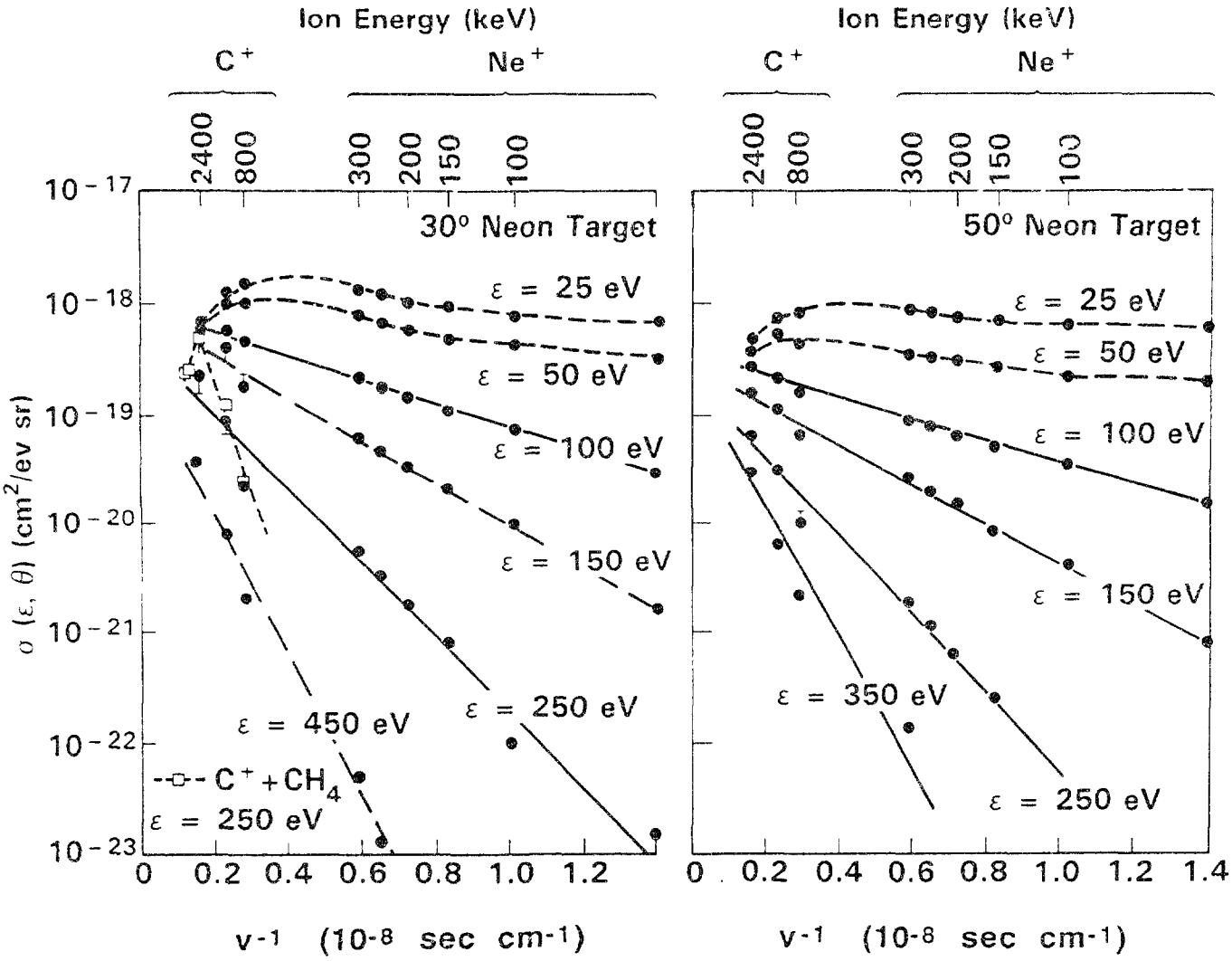

FIG. 2.27. Cross sections for ionization of neon by C^+ and Ne^+ ions plotted as recommended by the theory of direct coupling between discrete and continuum states. The Ne ion data are from the work of Cacak and Jorgensen [83] and the carbon ion data are unpublished data from the Pacific Northwest Laboratory using the techniques discussed by Toburen [96B, 99B].

line in the neon target data is accurately reproduced in the CH_4 data. One must ask whether the high energy C^+ data do indeed exhibit a different slope than the solid lines suggests, or are we justified in connecting the high energy C^+ data with the lower energy Ne^+ ion data? Resolving this question will require more study.

Although the direct coupling theory seems to describe the general features of the ejected electron spectra for low and intermediate energy collisions of structured ions with atomic targets this theory is of limited application as it does not provide ab initio absolute cross sections. Only with the recent developments of the Classical Trajectory Monte Carlo (CTMC) theory [97,98,105] does it appear that one may be able to address the problem of calculating absolute cross sections for collisions involving intermediate-energy structured ions. Doubly differential cross sections for ionization of helium by 200 keV/u C^+ ions are compared at an emission angle of 50 degrees with CTMC results in FIG. 2.28. In this illustration the experimental results

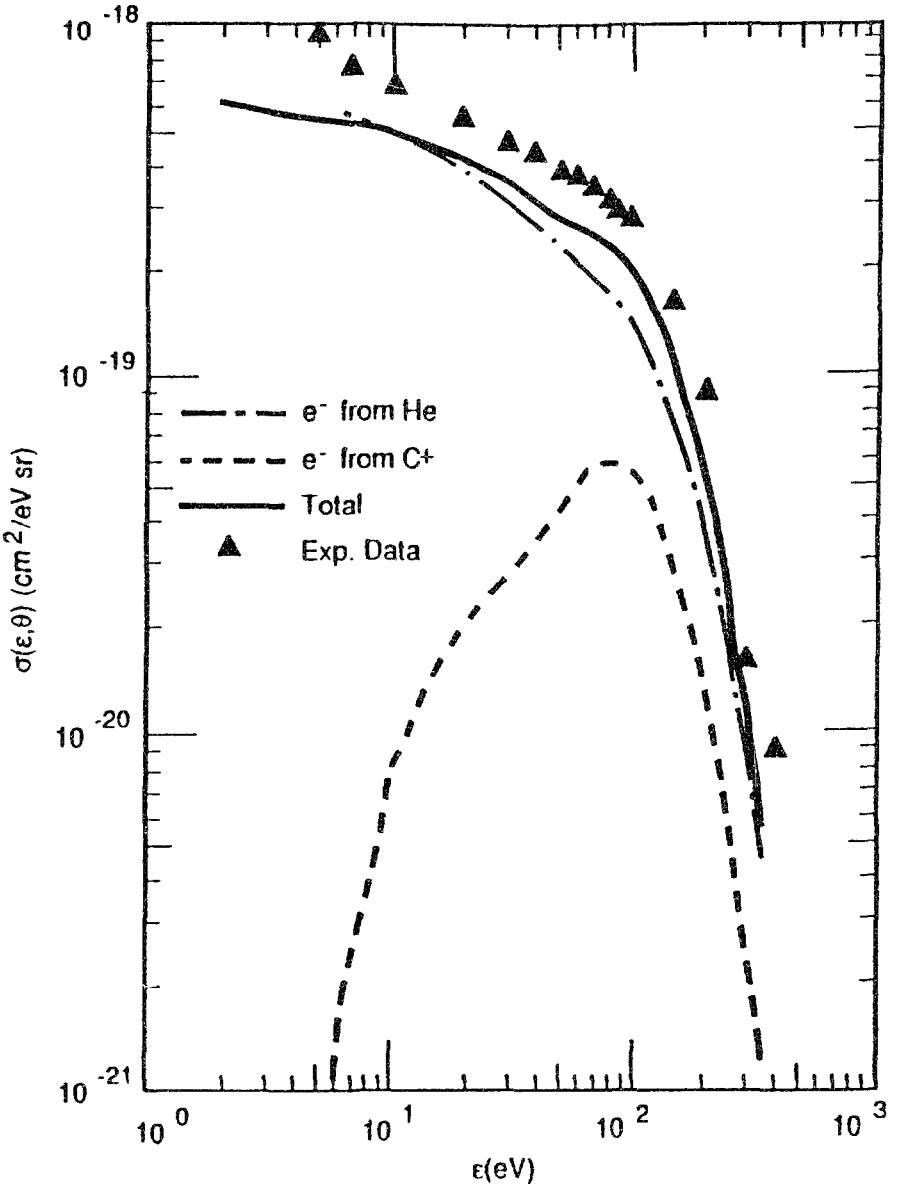

FIG. 2.28. Comparison of measured doubly differential cross sections for emission of electrons at 50 degrees by C^+ ions to classical trajectory Monte Carlo (CTMC) calculations, see Reinhold et al. [97].

are about 40% larger than the CTMC results, however the agreement tends to improve as one compares at both larger and smaller angles and excellent agreement is obtained for this ion energy and electrons emitted at 20 degrees (see, for example, Toburen et al. [98]). A powerful aspect of the CTMC theory is that it can follow the fate of electrons from both target and projectile during the collision and thereby provide information on the relative contribution of these electrons to the various regions of the observed spectra. The dashed line in FIG. 2.28 is the contribution of electrons that are emitted from the projectile. Without this calculation it would not be possible to know whether the broad "peak" at an electron energy of about 200 eV superimposed on an otherwise smooth continuum was the result of a binary encounter peak of electrons from the target or the effect of electrons lost from the projectile. A difficulty with application of the CTMC theory is the computer intensive nature of the calculations. It is not practical to calculate cross sections for wide ranges of the parameters of the collision

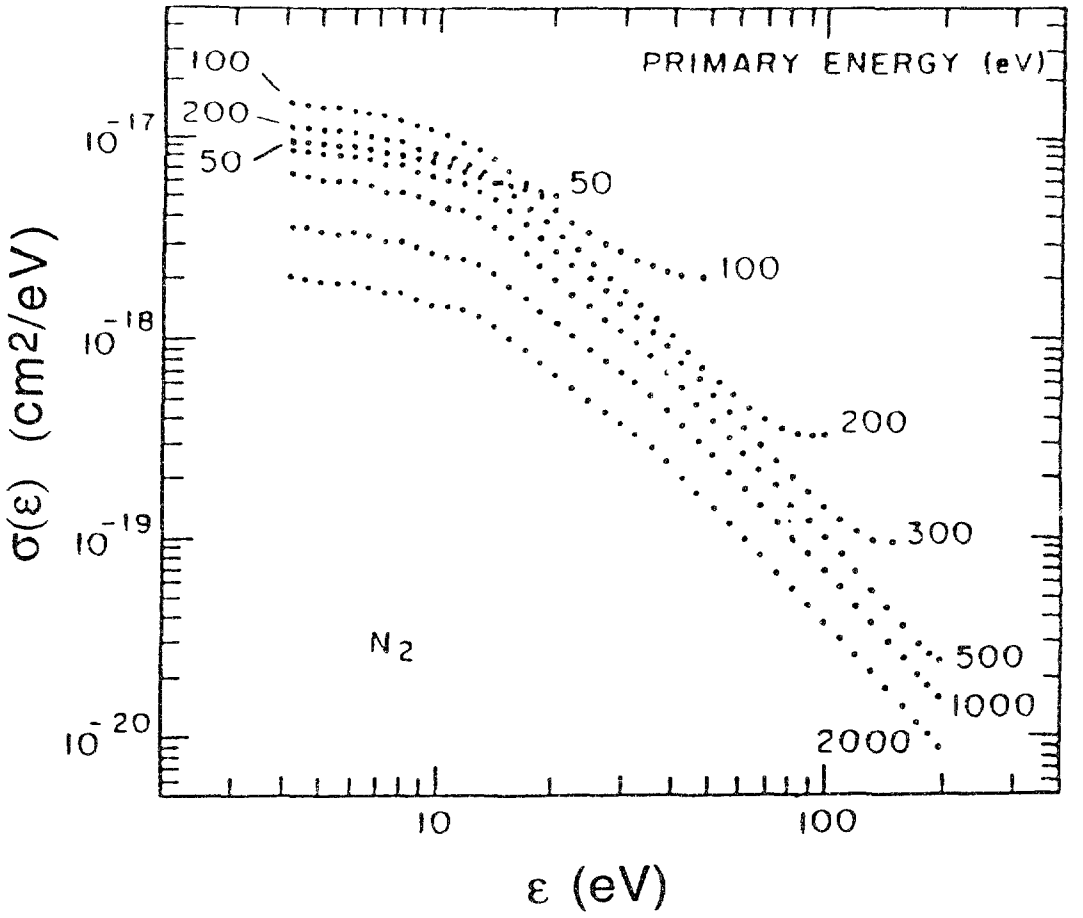

FIG. 2.29. Single differential cross sections for ionization of molecular nitrogen by 500 eV electron impact. The data are from the work of Opal. et al. [7].

systems of interest to radiobiology and radiation therapy. However it may be possible to use this technique to gain a better understanding of the collision process that will enable the development of phenomenological models that can still reproduce the features of the ejected electron spectra with more simple computational forms.

2.3. SINGLY DIFFERENTIAL IONIZATION CROSS SECTIONS

2.3.1 **Electron Impact**

Although singly differential cross sections (SDCS) for electron emission in ion atom/molecule collisions are in concept simpler than doubly differential cross sections there have been essentially[1] no experiments designed that measure them directly. Singly differential cross sections are normally obtained by integration of the doubly differential cross sections with respect to either ejected electron energy or emission angle. The SDCS

[1]The electron spectrometer developed by Mathis and Vroom [15] could, in principle measure singly differential cross sections directly by electrically connecting the angular electron detectors together. In practice, however, the spectrometer was not used in that fashion.

are somewhat less sensitive to the details of the collision physics because the act of integration over one collision variable tends to average subtle features of the ejected electron spectra. However, for many applications in radiological physics the SDCS provide an adequate description of the collisions, eg., the SDCS, $\sigma(\epsilon)$, obtained from integration of DDCS over emission angle is an accurate indicator of the probability of energy loss by a projectile in an encounter with the target electron. The SDCS obtained by integration of DDCS's also provide additional tests of the accuracy and reliability of experimental data.

Singly differential cross sections, $\sigma(\epsilon)$, for the ionization of molecular nitrogen are shown in FIG. 2.29. These data from the work of Opal et al. [7] illustrate the general shape of the secondary electron spectra; for electron impact, secondary electrons are defined as electrons detected with less then one half of the incident electron energy. From collision kinematics it is known that for each secondary electron detected with energy ϵ, the primary electron will be observed in the spectrum with an energy given by $E_e - \epsilon - I_e$, where E_e is the incident electron energy, and I_e is the initial binding energy of the ejected electron. The contribution to the spectra from degraded primaries is observed as the tendency of the cross sections to increase at the high energy end of the spectra for the four lowest energy incident electrons shown in FIG. 2.29. If each of the spectra had been continued out to the primary energy the high-energy half of the spectra would mirror that of the low-energy half, however shifted slightly to lower energies to account for the loss of energy in overcoming electron binding, and at $\epsilon = E_e$ the elastic scattering peak would be seen. A full electron spectrum for ionization of methane by 500 eV electrons is shown in FIG. 2.30. This comparison from the work of Oda [21] also demonstrates the good agreement between his results and the measurements of Opal et al. [7]. The Mott cross sections given in the work of Oda agree well with the experimental data through the center of the spectrum, but fall below the experimental values for low-energy ejected electrons and overestimate the cross sections at the upper end of the spectrum. The steps, or discontinuities, seen in the Mott cross sections are due to the effects of inner-shell contributions to the electron spectrum.

The data for ionization of atomic and molecular targets by electron impact are available for only a limited range of incident energies and target species; see the publications cited in Table 2.1. Because of this limited range of the availability of experimental data, and the scatter in the data from different sources, a good deal of effort has gone into the development of theoretical techniques to test and extend the existing data. As indicated above in the discussion of doubly differential cross section, Kim and his colleagues [32-36] have developed methods based on established theory to test the reliability and to extend the range of electron emission cross sections. For the analysis of singly differential electron emission cross sections it is convenient to present the SDCS's as their ratio to the Rutherford or, in the case of electron impact, the Mott cross sections; this reduces the wide dynamic range of the energy loss spectra enabling their display on a linear scale and helps to illustrate established theoretical constraints on the cross sections. To determine this ratio, presented explicitly for the Rutherford cross sections in Eq. 2.2, above, to targets with more than one electronic shell it is necessary to sum over all contributing electronic levels. In that case Eq. 2.2 should be rewritten as

$$Y(T,Q) = \sum_i Y_i(T,Q) = \frac{T}{4\pi a_o^2 R^2 z^2} \sum_i (\epsilon + I_i)^2 \, \sigma(\epsilon)_i \quad , \qquad (2.14)$$

where i refers to the electronic level from which the ejected electron originated, I_i is the electron binding energy of the i^{th} level, and $\sigma(\epsilon)_i$ is

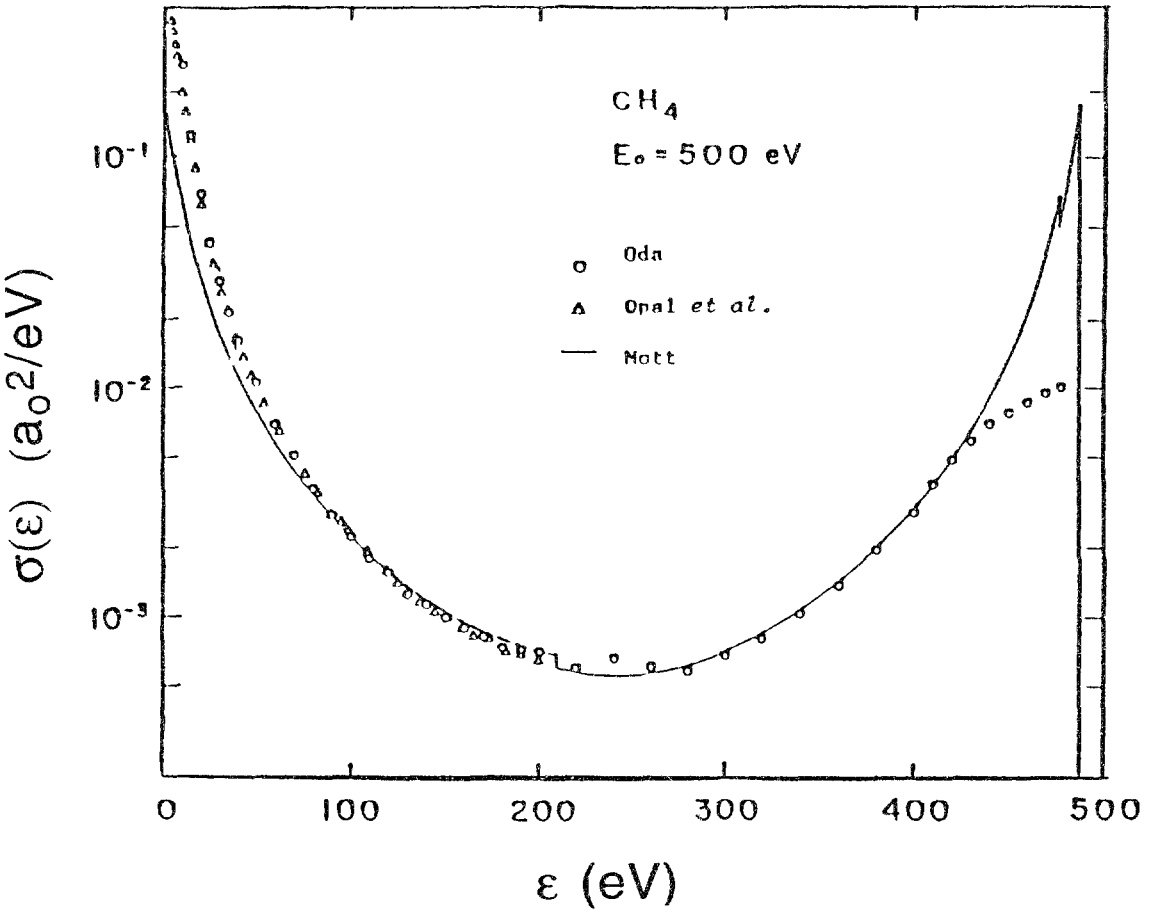

FIG. 2.30. Single differential cross sections for ionization of methane gas by 500 eV electron impact. The data are from Opal et al. [8] and Oda [21]. The Mott calculation was presented by Oda [21].

the differential cross section for ejection of an electron from the i^{th} level. Unfortunately the experiments do not normally determine the shell or subshell from which the detected electron was ejected. Therefore the valence shell binding energy I_1 is used for all ejected electrons reducing Eq. 2.14 to

$$Y(T,Q) = \frac{T}{4\pi a_o^2 R^2 z^2} (\epsilon + I_1)^2 \sigma(\epsilon) \quad . \tag{2.15}$$

This approximation is considered appropriate based on the fact that, at the electron energies we are considering, the valence electrons provide the majority of the contribution to the energy loss cross section. The simplification afforded by Eq. 2.15 is equivalent to dividing the experimental cross sections by the Rutherford cross section per target valence electron. For electron impact it is instructive to plot the experimental data in the form of Y(Q,T) defined in Eq. 2.15 against the reciprocal of the energy loss. As was pointed out by Kim and Noguchi [36], the area under the curve in a plot of Y(Q,t) versus R/Q can be shown to be proportional to the total ionization cross section

$$\sigma_{ion} = \int_I^{E_o} \sigma(Q)\, dQ = \int_{1/E_o}^{1/I} \sigma(Q) Q^2 d\left(\frac{1}{Q}\right) \quad , \tag{2.16}$$

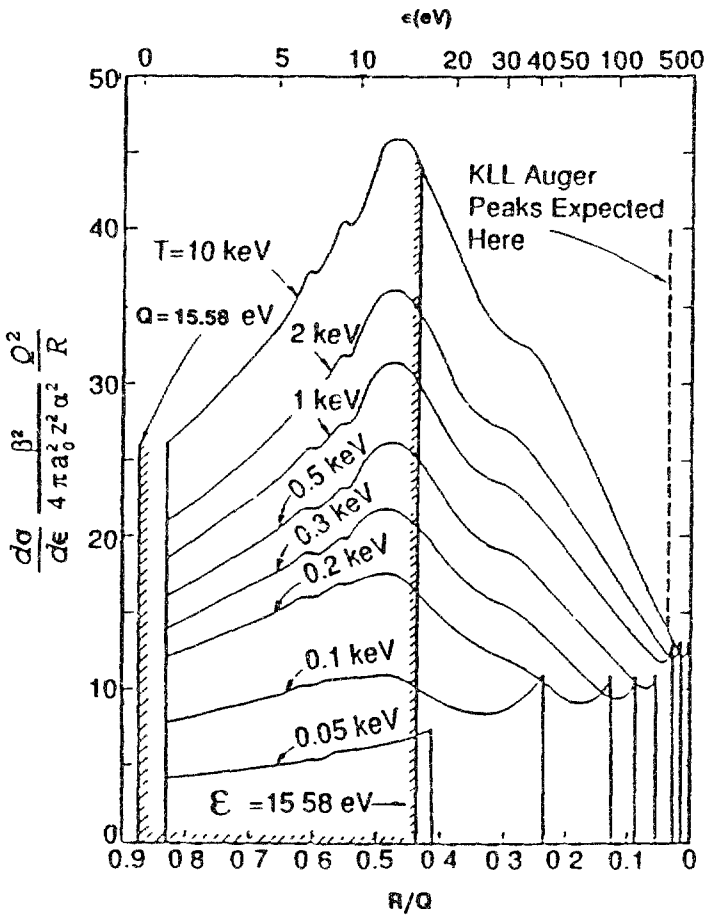

FIG. 2.31. Secondary electron spectra for electron impact ionization of N_2. The areas under the curves have been normalized to the respective total ionization cross sections. The area between the shaded lines corresponds to the fraction of the electrons ejected with insufficient energies to produce further ionization in the target medium. These data are from Kim [33].

where I is the electron binding energy and E_o is the incident electron energy. Such a plot is useful for testing absolute normalization of the differential cross sections and for determining the importance of specific features of the spectra as contributors to the overall yield of ionization. Total ionization cross sections are available with accuracies of 5% to 10% for a wide range of atoms and molecules (Total ionization cross sections for electron impact ionization are reviewed in Chapter 3 of this report.). The functional form of the differential cross sections can be determined for specified energy regions by the use of appropriate theory. For example, the Mott cross section should be accurate for providing the magnitude of the SDCS for fast electrons ejected in collisions involving sufficiently high-energy incident electrons. For electrons ejected with low energies the Bethe-Born theory provides a convenient framework to investigate the features of the singly differential cross sections and their dependence upon projectile parameters. The Bethe-Born formula can be written [137] as

$$\frac{d\sigma}{dQ} = \frac{4\pi a_o^2 z^2}{T}\left[\frac{R^2}{Q}\frac{df}{dQ}\ln\left(\frac{4T}{R}\right) + B(Q) + O\left(\frac{Q}{T}\right)\right] , \qquad (2.17)$$

where df/dQ is the differential optical oscillator strength distribution. The first term in the brackets includes a dependence on the logarithm of the incident electron energy, thus leading to its dominance as the incident particle energy increases. That combined with the 1/Q dependence leads to the low-energy ejected electron spectral shape that is determined by the dipole oscillator strength at sufficiently high energies of the incident electrons (or any charged particle); the spectra should become increasingly optical in nature as the ion energy increases. The second term in the brackets of Eq. 2.17 is independent of the incident particle energy except for the kinematic restrictions in the maximum energy loss that can occur in a collision. Although B(Q) contributes at all Q it is expected to dominate at high Q where the first term has become negligible. An estimate of B(Q) can be obtained from use of the Mott formalism at sufficiently high values of the energy loss. The last term in the expression includes all contributions from terms of higher order in 1/T; these are normally negligible in the energy range of validity of the Bethe-Born approximation. An example of the utility of this method of data analysis taken from Kim [32] is shown in FIG. 2.31, where the ratios of the experimental cross sections to the corresponding Rutherford cross sections are plotted as a function of the reciprocal of the energy loss. Plotted in this way the area under the curve is proportional to the total ionization cross section and the shape of the low-energy portion of the curve is representative of the dipole oscillator strength. The fraction of the electrons ejected with energies between the shaded vertical lines, that correspond to ϵ=o and ϵ=15.6 eV with Q=15.6 eV, represents those electrons that are unable to produce further ionization as they slow down in the target medium. In the example shown in FIG. 2.31, the only experimental differential cross sections used to establish the family of curves were those for electron emission by 500 eV incident electrons. Those data were used, along with the dipole oscillator strengths, to define the overall shape of the curve for 500 eV primaries. The magnitude of the cross sections was then established by normalization of the area under the curve to the total ionization cross section. Curves for other primary energies were then drawn by extrapolation based on maintaining 1) a curve shape consistent with the optical oscillator strengths, 2) the proper integrated area consistent with total ionization cross sections, and 3) the proper kinematic limit to the secondary electron energy consistent with the maximum energy transfer. Models of this type provide means to evaluate experimental consistency, to extrapolate data to regions where data are unavailable, and provide convenient methods of introducing data into computer codes for track structure calculations. This technique of data analysis and extrapolation takes advantage of the availability of a wide range of experimental data on total ionization cross sections (see, for example, reviews by Schram et al.,[138] and Shimamura, [139]) and oscillator strengths [126,140]. In addition, the use of spectra based on oscillator strength distributions has the potential for application

Table 2.4

Values of fitting parameters

Parameter	Hydrogen	Helium
A_1	0.74	0.85
A_2	0.87	0.36
A_3	-0.60	-0.10
n	2.4	2.4

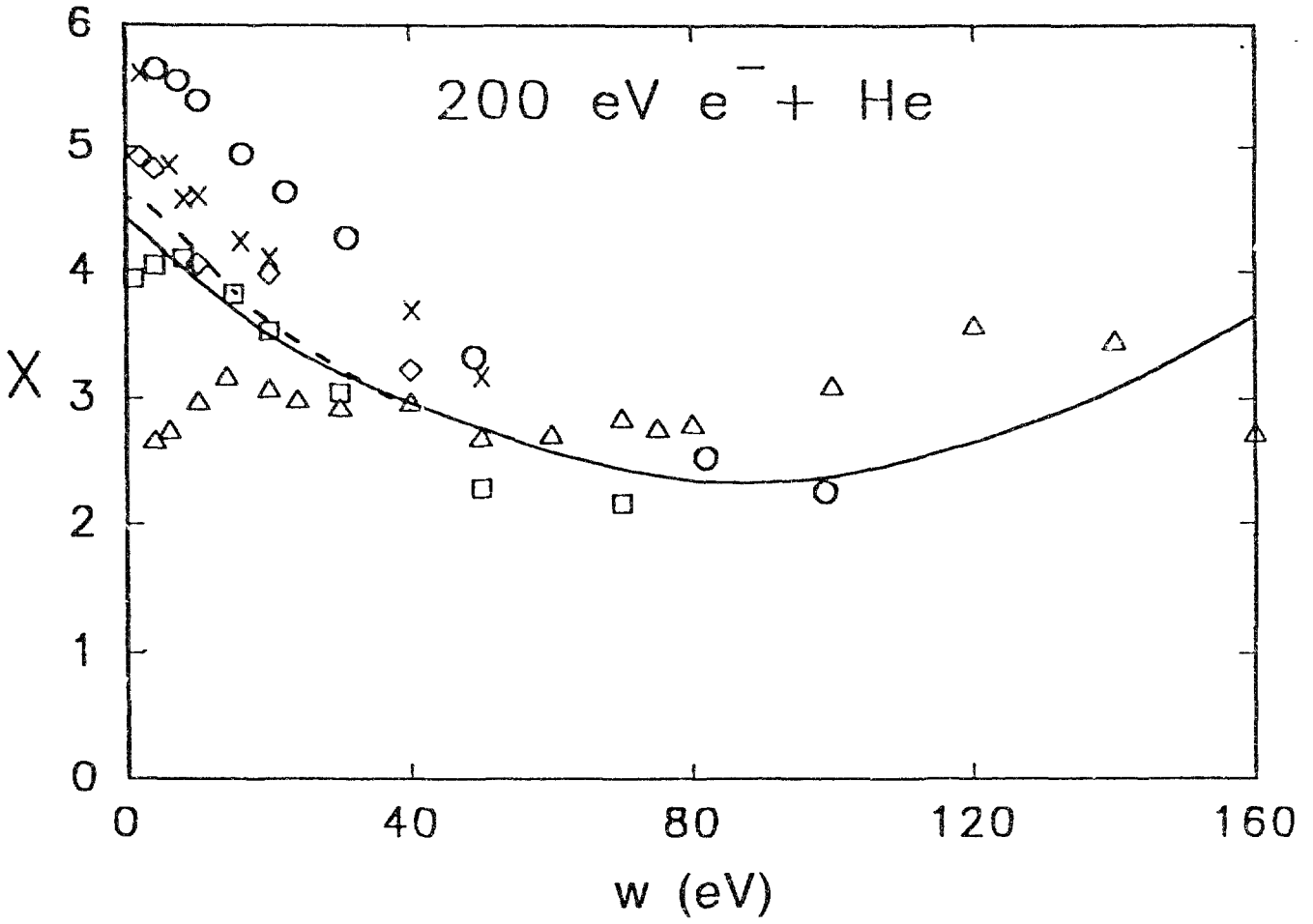

FIG. 2.32. Single differential cross sections for 200-eV e^- + He collisions plotted as X versus w, where X is the ratio of the experimental cross section to the Mott cross section and w is the ejected electron energy. The data plotted are; solid lines - calculated from Eq. 2.18, dashed line is from the recommended values of Kim [31], squares - Shyn and Sharp [5], circles are from the data of Opal et al. [8], x's are the data of Goruganthu and Bonham [9], triangles are data of Rudd and DuBois [6], and diamonds are the data of Mueller-Fiedler [10].

to both gas and condensed phase targets by simply using the proper oscillator strengths. These techniques will be described in more detail in the following sections with regard to their application to proton-induced ionization. For greater detail in the application of this method to electron-impact ionization the interested reader is directed to the work of Kim referenced above, as well as to his review [33], and to studies by Miller et al. [137] and Miller and Manson [141].

The semi-empirical model of Rudd [39], described earlier for DDCS, Eqs. 2.7 and 2.8, is part of a comprehensive model that includes the following expression for the SDCS, $\sigma_t(w)$, for ejection of an electron of scaled energy w ($w=\epsilon/I$) by impact on an incident electron of scaled energy t ($t=T/I$):

$$\sigma_t(w) = \frac{SF(t)}{I}\left[\frac{1}{(w+1)^n} + \frac{1}{(t-w)^n} - \frac{1}{[(w+1)(t-w)]^{n/2}}\right], \qquad (2.18)$$

where $S=4\pi a_0^2 N(R/I)^2$, N is the number of electrons of binding energy I, R is the Rydberg unit of energy (13.6 eV), a_0 is the Bohr radius, and n is an

adjustable parameter evaluated by fitting to experimental electron spectra, and

$$F(t) = (A_1 \ln(t) + A_2 + A_3/t)/t \quad . \tag{2.19}$$

The values of A_1, A_2, and A_3 are obtained either by fitting to experimental SDCSs or, more accurately, by fitting the integral of the SDCS expression to the experimental total cross sections. The expression for the total cross section given by this model will be given in a later section. The values of these fitting parameters and of n for hydrogen and helium targets are given in Table 2.4. A sample plot of the ratio of the results of Eq. 2.18 to the corresponding Mott cross section is shown in FIG. 2.32 as the quantity X plotted versus the reduced electron energy w.

One of the major gaps in our knowledge of differential cross sections for interactions of electrons with biologically relevant targets is the lack of direct measurements of these processes for the condensed phase. Presently the basis of condensed phase electron transport used in track structure simulation is deduced from the theory of charged particle interactions in condensed phase, and from oscillator strengths for photoabsorption [126,140]. During the past few years, however, there have been significant advances in our understanding of electron interactions in the condensed phase brought about by the pioneering work of Leon Sanche and his coworkers [142-145]. Measurements that they have conducted, and continue to conduct, on the scattering of low-energy electrons in thin films are providing detailed information on the energy-loss mechanisms associated with the slowing down of low-energy electrons. A particularly interesting feature in the preliminary studies has been the similarity of elastic and inelastic electron scattering processes in the solid to those observed in the gas phase, eg., resonant processes, such as transient negative-ion formation [143], are strong features in the energy-loss spectra for very low-energy electrons. A detailed discussion of electron transport in the condensed phase is presented in chapter 4 of this report.

2.3.2. Proton Impact

Singly differential cross sections for proton impact ionization of atomic and molecular targets are normally obtained, as discussed above for electron impact, by integration of measured doubly differential cross sections with respect to either the electron ejection energy or the emission angle. In general the integration is performed with respect to emission angle and the SDCS, $\sigma(\epsilon)$, differential in ejected electron energy is presented. This spectrum gives the probability of a given energy loss occurring in an ionizing collision and is therefore of relatively high interest in Radiological Physics. An excellent review of the energy distributions of electrons emitted in collisions of protons with atomic and molecular targets has recently been published by Rudd et al. [146].

As with electron impact, discussed above, it is convenient to display the SDCS for proton impact as the ratio of the measured cross sections to the respective Rutherford cross sections. For fast proton impact ionization the high energy extremes of the ejected electron spectra are expected to be reliably given by the Rutherford cross section. Therefore, if we plot Y(Q,T), as defined by Eq. 2.15, against the energy loss Q, the ratio Y(Q,T) should approach a constant value for large ejected electron energies. Owing to the fact that the Rutherford formula incorporated in Eq. 2.15 gives the cross section per target electron, the magnitude of that constant should be equal to the number of electrons in the atomic or molecular target. In FIG. 2.33, this ratio, Y(Q,T), is plotted versus Q for an atomic helium target. In this illustration the ratios approach a value of approximately 2.2 which is

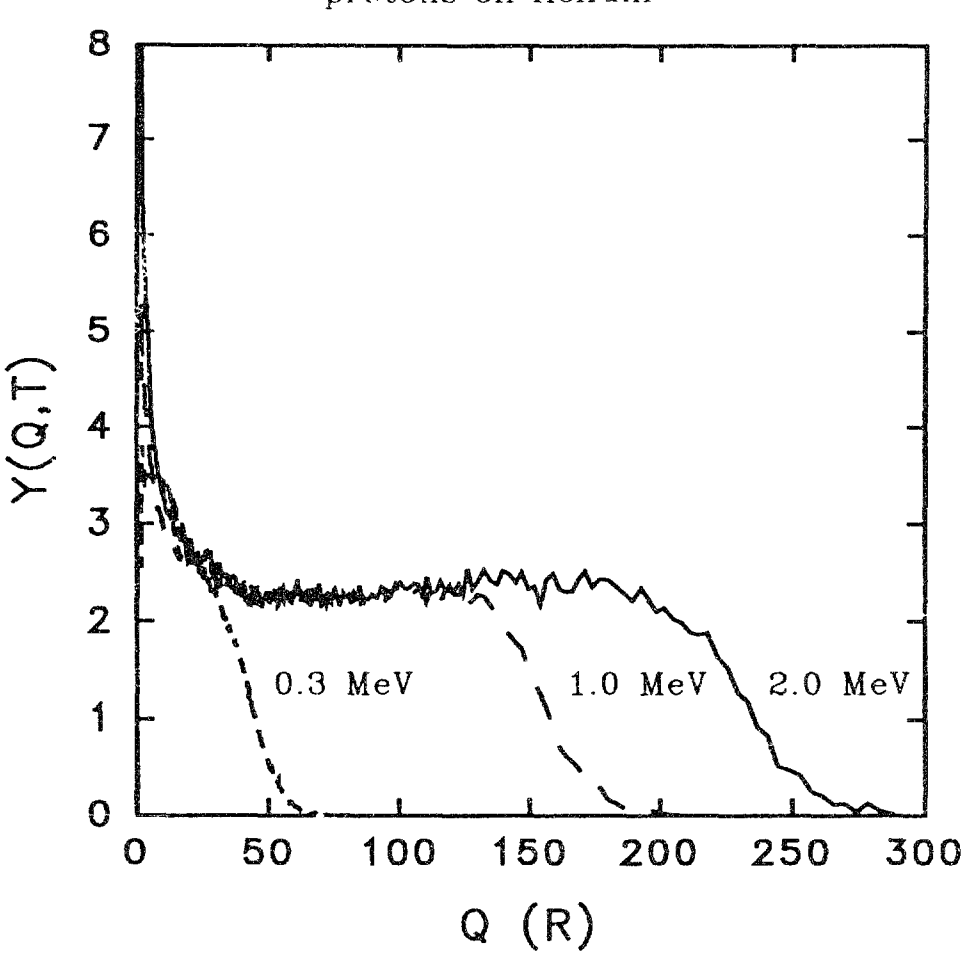

FIG. 2.33. The ratio of the measured singly-differential cross section for proton ionization of helium [110] to the Rutherford cross section plotted versus collisional energy loss.

indicative that the measured cross sections may be systematically 10% too large; that is, if the Rutherford cross section can be expected to be valid. Similar ratios are plotted in FIG. 2.34 for a wider range of proton energies and an atomic neon target; note that, at the two largest proton energies, the high-energy cutoff of these spectra is due to spectrometer limitations, not a lack of high-energy electrons. In principle, for an atom such as neon, where the electron can be ejected from inner shells or sub-shells, the ionization potential used in the Rutherford formula should reflect the origin of the electron. However, the experiments are not able to determine the origin of the detected electron, therefore, the ratio is calculated assuming that all electrons originate from the valence shell [110]. For neon the ratio Y(Q,T) approaches a value of approximately 10, indicative of the number of bound electrons in the atom; the peak observed at approximately 800 eV results from Auger electron emission following K-shell vacancy production that occurs in a small fraction of the collisions. For the highest energy protons Y(Q,T) approaches a value somewhat greater than 10, the total number of electrons in neon; this is, as for the helium data shown in FIG. 2.33, again indicative that the experimental values may be systematically about 10% higher than would be expected. It should be noted, however, that the ratio Y(Q,T) observed for 1.5 MeV protons reaches a plateau at approximately 8 which is in good agreement with the Rutherford prediction if only the outer, n = 2, shell

electrons participate; the inner-shell electrons are tightly bound and contribute little to the Rutherford cross section at this proton energy.

An increased scatter in the Y(Q,T) data is observed for the higher energy ejected electrons shown in FIG. 2.34. This scatter occurs because the cross sections are becoming significantly smaller and statistical uncertainties are greater; the $1/Q^2$ factor in the Rutherford cross section masks the absolute value, and therefore the rapid decrease of these cross sections. The Rutherford analysis generally confirms that the differential cross sections obtained in the work at the Pacific Northwest Laboratory (PNL) are accurate to within the stated absolute uncertainties, approximately 20%, derived from the experimental parameters; data for proton impact from other laboratories are generally at lower proton energies and not amenable to this theoretical test, but where data from different laboratories overlap there is good agreement.

Data have been obtained for proton impact ionization of a wide range of molecular targets for investigating the effects of molecular structure on electron emission cross sections. In FIG. 2.35 are displayed the single differential electron emission cross sections, $\sigma(\epsilon)$, for a number of carbon containing molecules plotted as the ratio to the respective Rutherford cross sections against the energy loss. The horizontal lines with the number to the right give the Rutherford estimate of the asymptotic value those cross

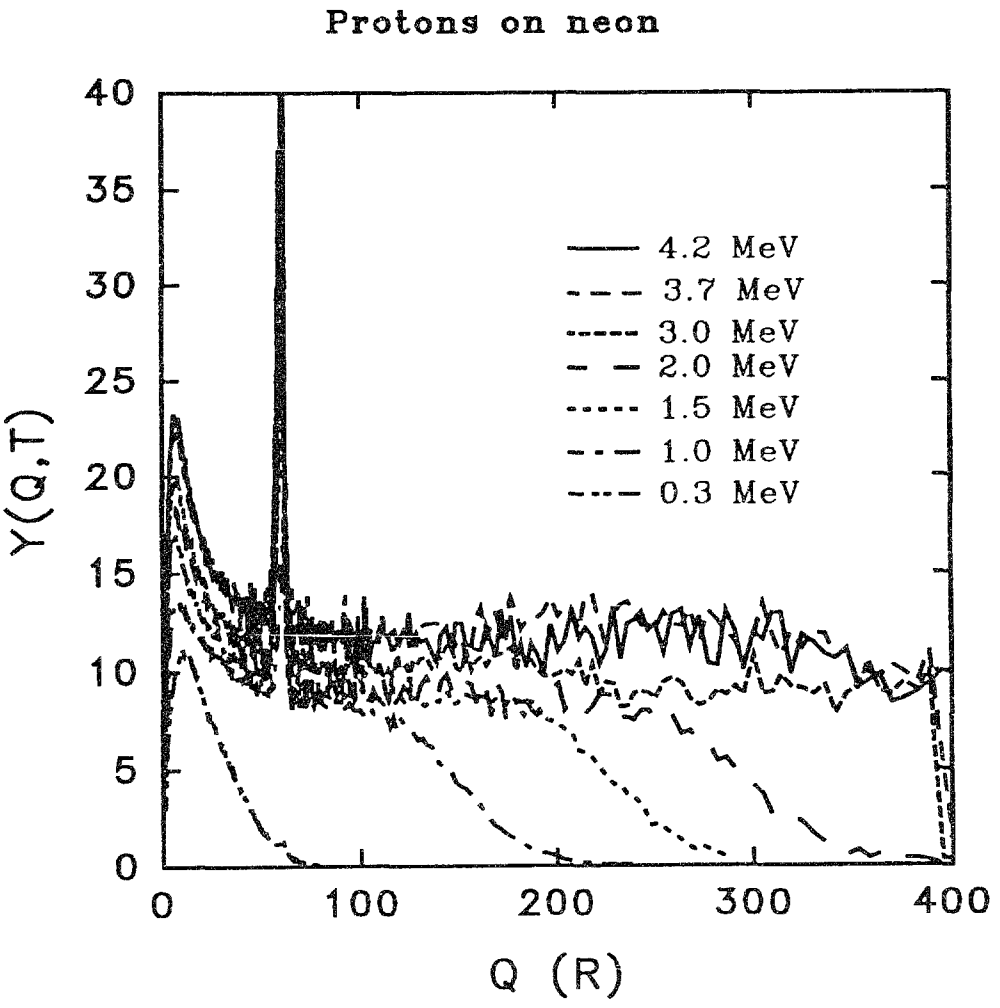

FIG. 2.34. The ratio of the measured singly-differential cross section to the Rutherford cross sections for ionization of neon by protons (data of Toburen et al., [110]).

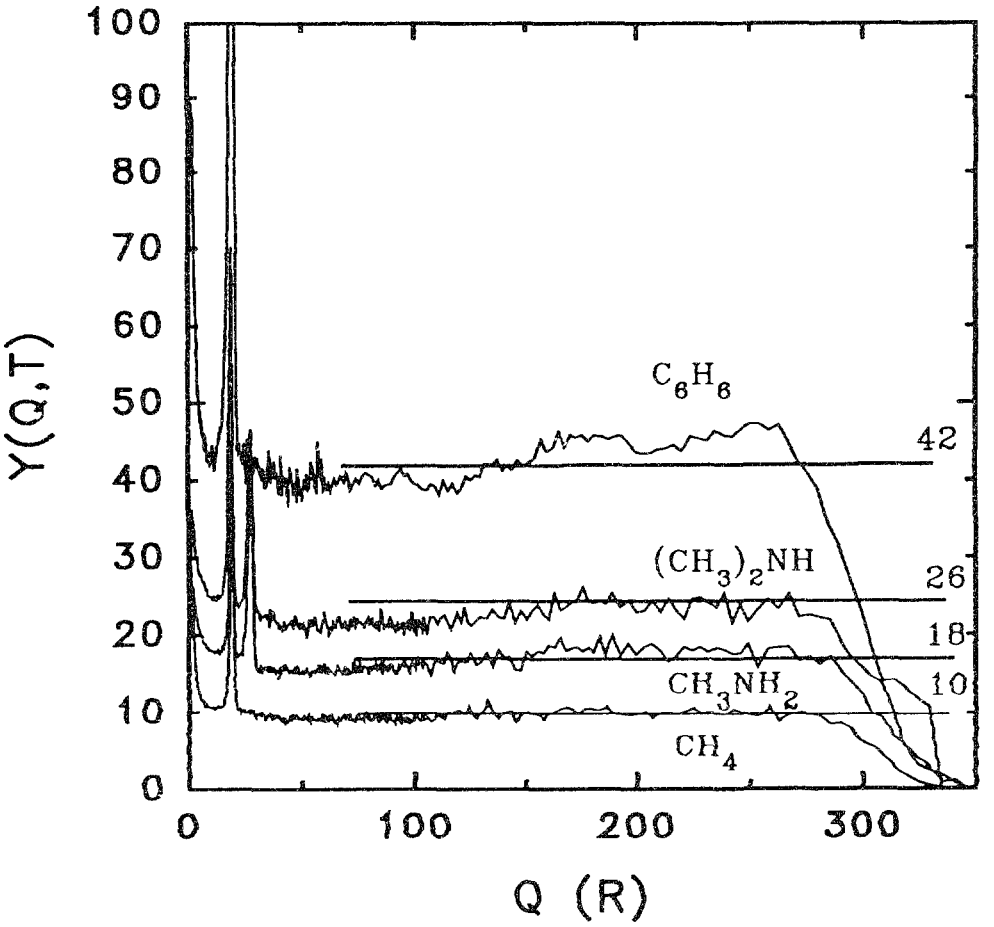

FIG. 2.35. The ratio of the measured to Rutherford singly-differential cross sections for ionization of a number of molecules by protons; data are from Lynch et al., [80].

sections should attain; i.e., the number of electrons actively contributing to the cross section. This agreement between experimental data and the predictions is simply a confirmation of the Bragg rule for scaling cross sections for emission of fast electrons or, alternatively, a statement of the independent particle model for ionization. One must be careful at this point to stress that this independent electron model is a scaling feature of collisions involving large energy loss and it does not apply to soft collisions; this will be discussed in detail later. It does, however, provide justification for application of simplified theory and scaling techniques that are very useful in track structure calculations.

The limits of applicability and reliability of various theoretical calculations can be assessed by comparison of their predictions to experimental data. In FIG. 2.36 the results of binary encounter theory, the Born approximation, and Rutherford theory are plotted as the ratio to the corresponding Rutherford cross section for ionization of the outermost electron of neon and compared with measured cross sections. The primary reason for comparing results by dividing by the Rutherford cross section is that the principal dependence on energy loss, $1/Q^2$, is removed and one can compare data on a linear, rather than a logarithmic scale, thus accentuating spectral features. The gradual increase with energy loss of the Rutherford cross sections, in this case calculated for each bound electron, summed and

then divided by the Rutherford cross section for an outer shell electron, that is plotted as the solid occurs because of the contribution of electrons ejected from inner shells [33]; at larger values of the energy loss the more tightly bound electrons contribute more to the total.

Rutherford theory for ionization of a free electron by a 1 MeV proton would predict an abrupt decrease in the SDCS at approximately 160 R as that is the kinematic maximum energy that can be transferred in classical proton-electron collision. The measured cross sections, on the other hand, show a gradual decrease in magnitude between approximately 100 R and 160 R reflecting the initial momentum distribution of the bound electrons. The increasing Rutherford cross section, owing to inner shell contributions, combined with the decrease in the experimental values near the maximum energy transfer, owing to binding effects, renders Rutherford theory inappropriate as a definitive test of the accuracy of measured cross sections in this proton energy range for target atoms or molecules with tightly bound inner-shell electrons. At higher proton energies, as shown in FIG. 2.34, a plateau value of 10 can be expected over a broader ejected electron energy range.

Binary encounter theory (reviewed by Rudd and Macek [43] and Rudd [44]) extends the classical Rutherford-like approach to collisions of charged particles with electrons that have an initial velocity distribution owing to the fact that they are bound to the atom. By integrating the classical collision spectrum over a quantum mechanical distribution of bound electron velocities the high energy portion of the ejected electron spectra is well represented. The only parameter that is not well defined in this computational technique is the mean value of the initial distribution of

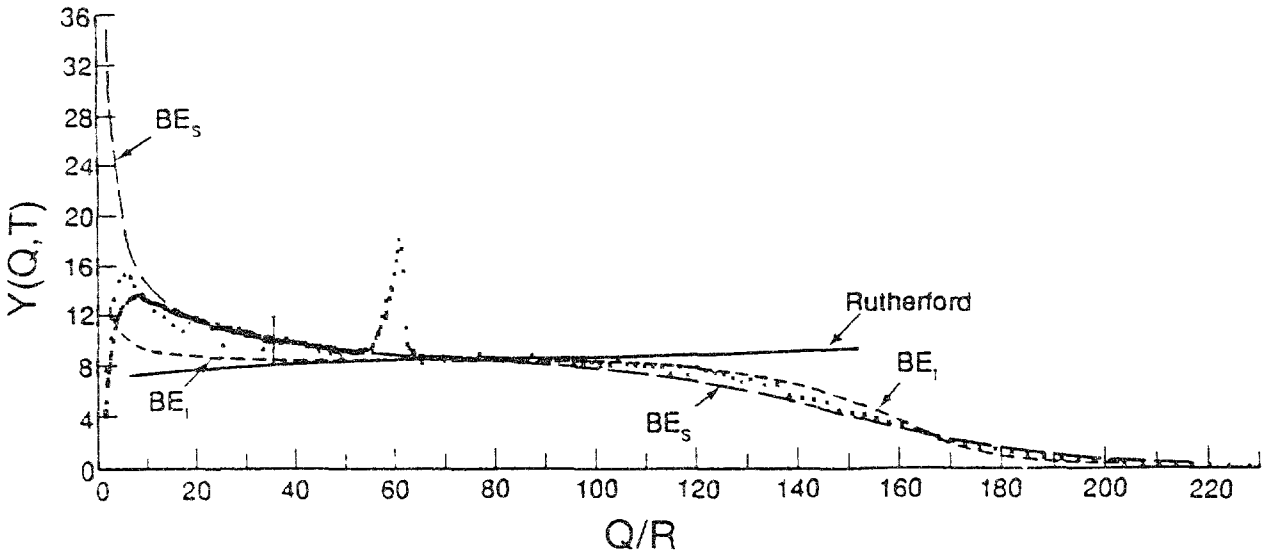

FIG. 2.36. Comparison of measured and calculated singly-differential cross sections for ionization of neon by 1.0 MeV protons; cross sections are presented as the ratio to the Rutherford cross section for outer-shell ionization of neon. The measured single differential cross sections (x) are from Toburen et al. [110]. The cross section for zero energy ejected electrons (□) is from Grissom [147]. The binary encounter calculations are from a program of Rudd [44] and includes results assuming the average kinetic energy of the bound electron is equal to the binding energy (BE_I) or given by Slater's rules (BE_S). The Rutherford cross section is calculated including inner-shell contributions [34] and the Plane wave Born Calculation (Δ) is described by Toburen et al., [110].

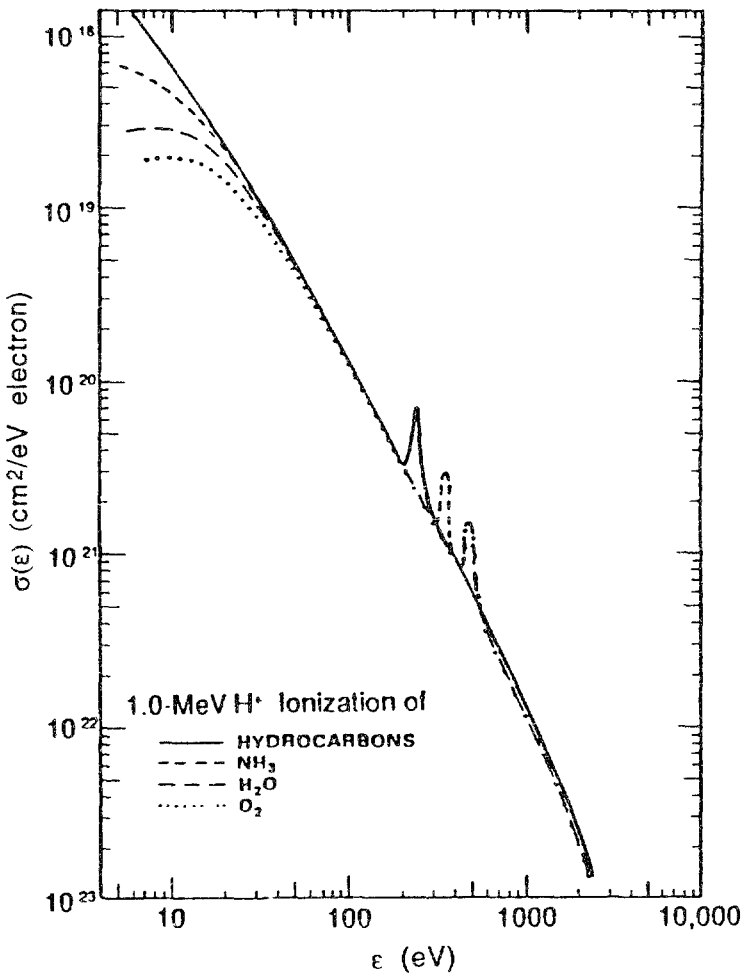

FIG. 2.37. Singly-differential cross sections for ionization of several molecules by 1 MeV protons.

kinetic energies exhibited by the orbital electrons. Calculations that assume the initial kinetic energy is equal to the binding energy, BE_I, and that use the kinetic energy derived from Slater's rules (see Robinson, [148]), BE_S, are shown in FIG. 2.36; the use of Slater's rules seems to provide a slightly better agreement at high energies than the binding energy approach. For low-energy electron emission neither approach is very good, although the use of Slater's rules extends the agreement with experimental data to somewhat lower energies.

The results of calculations based on the plane wave Born approximation [110] are also shown in FIG. 2.36. This calculation is in good agreement with the measured differential cross sections for ejection of low-energy electrons and with the independent measurement of Grissom et al. [147] for electrons ejected with near zero kinetic energy; the Born calculation was not carried out to ejected electron energies greater than 64 R because it is based on a partial wave analysis and the number of partial waves necessary to describe the higher energy processes makes the calculation unwieldy. Similar Born calculations are in good agreement for helium targets [56]. The use of this technique for molecules has not been attempted, however, due to a lack of adequate wave functions to describe the molecular systems.

The data shown in FIG. 2.36 clearly illustrate the limitations of classical and semi-classical theory for predicting the cross sections for ejection of low-energy electrons. The relative importance of this region of the spectra and the variations one observes for different target species is illustrated in FIG. 2.37, where ejected electron distributions are displayed for ionization of several different molecules by 1 MeV protons. The hydrocarbons referenced in FIG. 2.37, are the same as those of FIG. 2.35, now scaled on a per "effective" electron basis. For this purpose the effective number of electrons in a molecule is taken as the total number of electrons bound to the molecule minus the K-shell electrons [79,80]; from the data for neon shown in FIG. 2.34 one would not expect the K-shell electrons to contribute significantly to the emission cross sections for ionization of low-Z, first row, elements by 1 MeV protons. Note the large differences in the electron yields associated with different molecules as the ejected electron energies decrease below approximately 20 eV. This is also the portion of the emission spectrum that is the major contributor to the total yield of electrons and therefore directly influences the total ionization cross section.

As was discussed above for electron impact, one can make use of the analysis developed by Kim to focus on the accuracy and consistency of the low-energy portion of the ejected electron spectra. This is seen in FIG. 2.38,

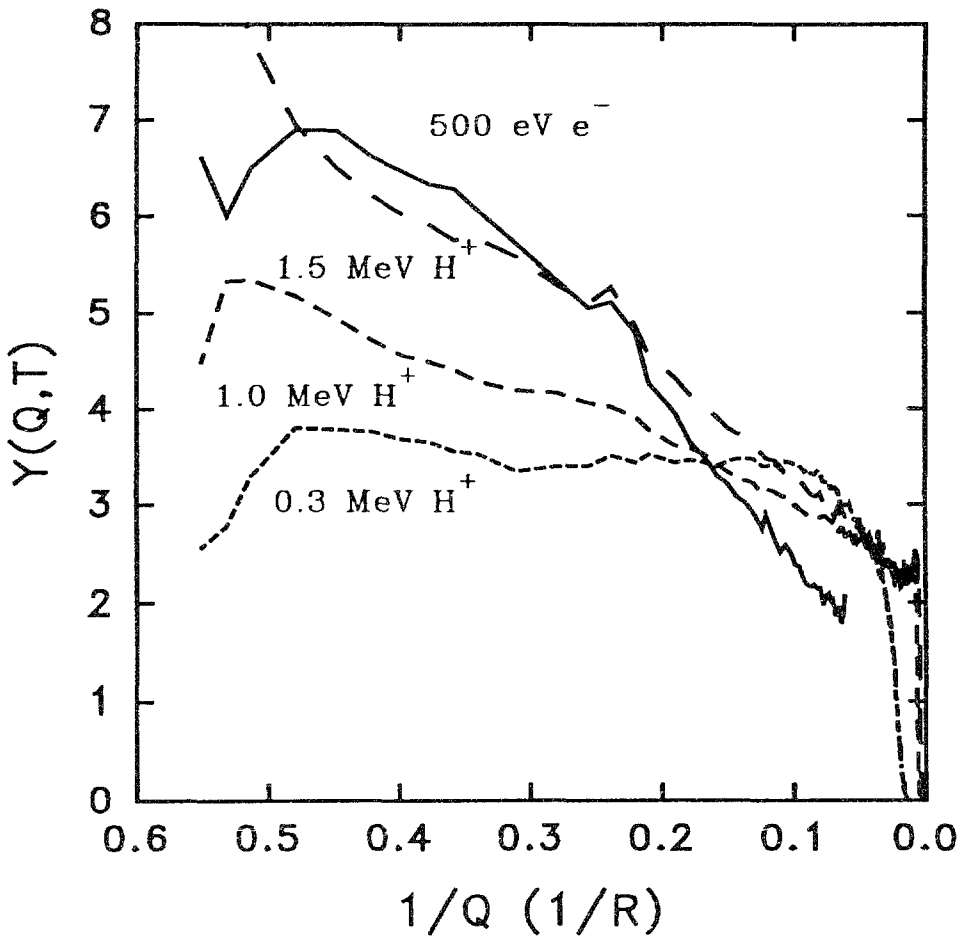

FIG. 2.38. Ratio of the measured singly-differential cross sections to the corresponding Rutherford values plotted as a function of 1/energy-loss for ionization of neon by protons and electrons. The electron results are from Opal et al. [7] and the proton data are from Toburen et al., [110].

where data for ionization of helium by protons of different energies are shown plotted as Y(Q,T) versus 1/Q; also shown for comparison are data of Opal et al [7] for 500 eV electrons; 500 eV electrons are of comparable velocity to 1 MeV protons. The shape of the spectra for low-energy electron ejection are similar in shape for electron and proton impact reflecting the dependence on the optical oscillator strengths. Recall from the discussion for electron impact that equal areas under the cross section curves contribute equally to the total ionization cross section; the total area is proportional to the total ionization cross section. The data displayed in FIG. 2.38 illustrate the importance of knowing the shape of the low-energy portion of the spectra if one is to be able to gain an accurate knowledge of the total yield of electrons; a major fraction of the electrons have energies less than 25 eV (R/Q=0.27). The need for accurate low-energy electron ejection cross sections presents no difficulties where cross section have been measured using both, electrostatic and TOF techniques, such as was done for the proton impact data in FIG. 2.38. However, where TOF is not available there may be large uncertainties in the low-energy portion of the spectra; see, for example the data in fig. 2.4 at the beginning of this chapter.

An accurate knowledge of the total yield of electrons produced in collisions of charged particles with biological material can be important in the analysis of such radiologically important quantities as W-values, mean free paths, stopping power, etc. The importance of the low-energy portion of the spectra to determination of the total yield of electrons, total ionization cross sections, was demonstrated in Figs. 2.37 and 2.38. To overcome the potential experimental uncertainties in low-energy electron emission data Miller et al. [149] applied the Bethe-Born approximation, as originally advocated by Kim and Inokuti [35], to develop a method to combine experimental data on SDCS's and dipole oscillator strengths to obtain reliable low-energy electron yields. Inspection of Eq. 2.17 indicates that if we have experimental data at any proton energy for which the Born approximation is valid those data can be used with optical oscillator strengths to evaluate what has been called the hard collision component of the interaction B(Q); some authors have expressed this quantity in ejected electron energy $B(\epsilon)$ rather than in energy loss Q, $Q=\epsilon+I$, because the experimental data are for measured electron energy, not energy loss (see Wilson et al. [150]). Evaluation of B(Q), or $B(\epsilon)$, using experimental data assumes that terms of higher order in Q/T are negligible. Since B(Q) is independent of the incident proton energy, once determined that spectrum can be used to obtain cross sections at other energies. In principle B(Q) could be calculated, however this is impractical for most atomic and molecular targets because of the lack of adequate wave functions to accurately describe the system.

In practice experimental data for oscillator strengths and SDCS's are used to obtain B(Q) for low-energy ejected electrons and the results are then merged with binary encounter theory to obtain an estimate of B(Q)+O(Q/T) for high energy ejected electrons in order to obtain the full spectrum; binary encounter has been shown to describe fast ejected electrons reasonably well. The hard collisions contribution, $B(\epsilon)$, for ionization of water vapor by protons, as determined by Wilson et al. [150] using this technique, is shown in FIG. 2.39. Although $B(\epsilon)$ is theoretically independent of ion energy there was considerable scatter among the data for $B(\epsilon)$ derived from different proton energies. To determine the spectrum of $B(\epsilon)$ for use in calculating emission cross sections these authors used a simple average of the experimental values at different ion energies (the solid line in FIG. 2.39). Cross sections derived from this determination of $B(\epsilon)$ are shown in FIG. 2.40. This model of the differential cross sections provides values in good agreement with the 0.5- and 1.5-MeV data, as it must be because these data were used in the determination of $B(\epsilon)$, and there is good agreement for electron energies

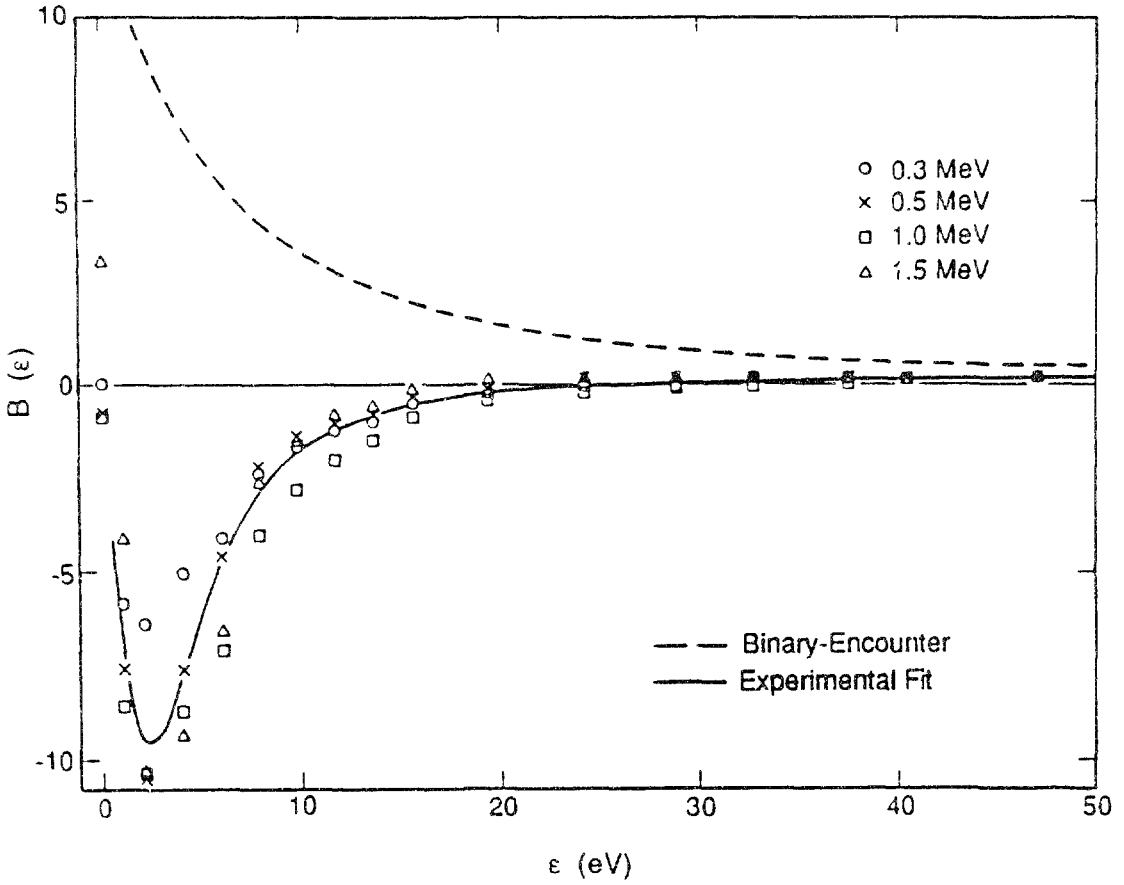

FIG. 2.39. The hard collision component of the Bethe-Born cross section, B(Q), for ionization of water vapor by protons as determined by Wilson et al. [150].

greater than about 20 eV with the measurements for 3.0- and 4.2-MeV protons; these high energy data were obtained with a different experimental system and were not included in the fitting process. The measured low-energy cross sections ϵ < 25-eV have large uncertainties owing to the effects of residual electric and magnetic fields in the analyzing field of the electron spectrometer; no TOF measurements are available for this target system. An important attribute of the modeling technique is that a high degree of accuracy can be obtained for the determination of the low-energy portion of the ejected electron spectra owing to the use of optical oscillator strengths that dominate in this region.

Models of the ejected electron spectra based on Eq. 2.17 rely on two primary sources of experimental data; differential electron emission cross sections, for at least one ion energy, and a source of optical oscillator strengths. We have discussed the electron spectra at length, but have said little regarding the availability of oscillator strengths. For the water vapor data discussed above, oscillator strengths were derived from the photoabsorption cross sections compiled by Berkowitz [126] using the expression

$$R\frac{df}{dQ} = \frac{\sigma_{ph}/Mb}{8.06} \quad , \tag{2.20}$$

where σ_{ph}/Mb is the photo absorption cross section in units of megabarns (Mb) and R=13.6. A good review of photoabsorption cross sections is also given by Gallagher et al. [140]. Oscillator strengths are also available for a number of molecules of biological interest, such as DNA [151,152] and DNA bases [153,154]. We can also expect considerable progress to be made in the measurement of photoabsorption cross sections in the near future as synchrotron light sources become more widely used. A more thorough review of optical oscillator strength can be found in Chapter 5 of this report.

One of the shortcomings of models of secondary electron emission cross sections based on Bethe-Born theory, as expressed in Eq. 2.17, is that the application is limited to ion energies that are sufficiently large for the Born approximation to be valid. A model developed by Rudd [155] overcomes this difficulty by incorporating aspects of molecular promotion theory to enable extensions of the model to low-energy ions. Rudd's model is not as versatile as the Bethe-Born, however, with respect to changing target

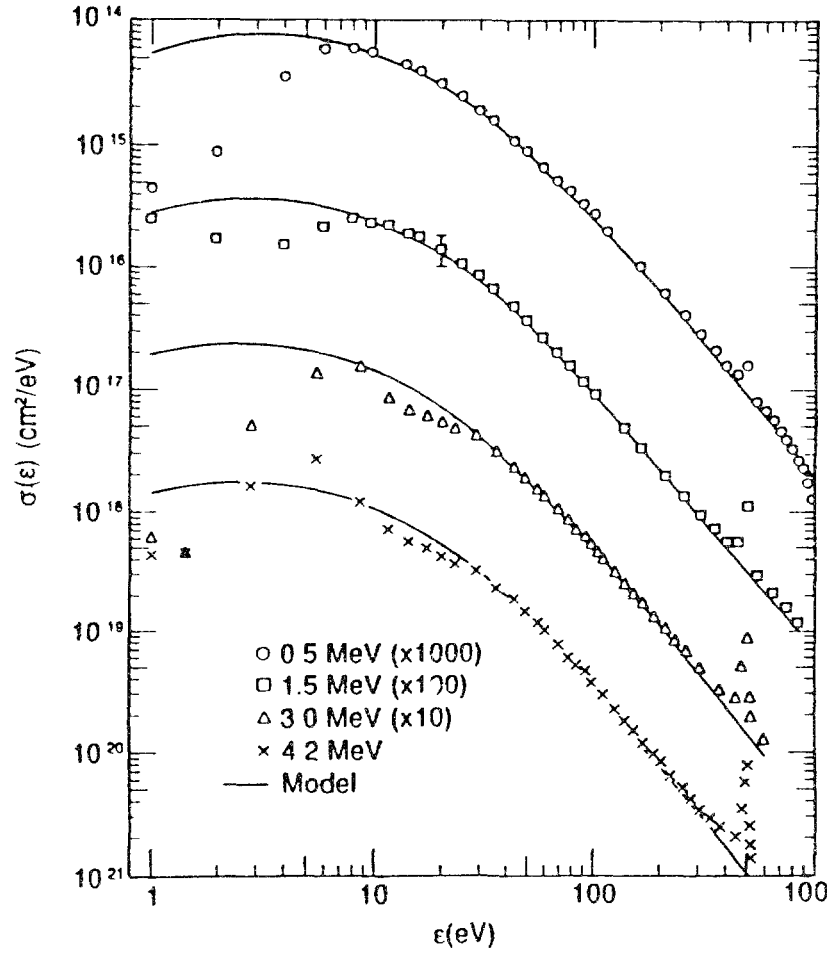

FIG. 2.40. Singly-differential cross sections for ionization of water vapor by protons as presented by Wilson et al [150]. The solid lines are derived from the model of Miller et al. [149] with the hard collisions component evaluated by fitting the low-energy proton data of Toburen and Wilson [76]. This comparison illustrates the value of the model in providing reliable cross sections for low-energy ejected electrons where the experimental cross sections scattered owing to experimental difficulties. The 0.5- and 1.5-MeV cross sections are from the work of Toburen and Wilson [76] and the higher energy proton data are unpublished data of Toburen.

parameters and it requires a much more extensive set of data to determine the full range of model parameters. Rudd's model is based on the molecular promotion model at low proton energies and on the classical binary encounter approximation, modified to agree with Bethe-Born theory, at higher energies.

The expression for the singly differential cross sections given by Rudd's model is as follows:

$$\sigma(w) = \frac{(S/I)(F_1+F_2w)}{(w+1)^3\{1+\exp[\alpha(w-w_c)/v]\}} \quad , \tag{2.21}$$

where $w=\epsilon/I$, $v=(T/I)^{\frac{1}{2}}$, $T=\lambda E_p$, λ is the ratio of the electron to proton mass, E_p is the incident proton energy, $S=4\pi a_0^2 N(R/I)^2$, $w_c=4v^2-2v-R/4I$, N is the number of electrons in the target atom or molecule, and where

$$F_1(v) = L_1 + H_1 \tag{2.22}$$

and

$$F_2(v) = L_2H_2/[L_2 + H_2] \quad , \tag{2.23}$$

with

$$H_1 = A_1 \ln[1 + v^2]/[v^2 + B_1/v^2] \quad , \tag{2.24}$$

$$L_1 = C_1v^{D_1}/[1 + E_1v^{(D_1+4)}] \quad , \tag{2.25}$$

$$H_2 = A_2/v^2 + B_2/v^4 \quad , \tag{2.26}$$

and

$$L_2 = C_2v^{D_2} \quad . \tag{2.27}$$

The ten basic parameters, $A_1 \ldots E_1$, $A_2 \ldots D_2$ and α are given for various targets in Table 2.5.

Table 2.5

Parameters for fitting singly differential cross sections to the model of Rudd

	He	Ne	Ar	Kr	H_2	N_2	O_2	H_2O	CO_2	CH_4	inner shells
A_1	1.02	0.58	1.20	1.46	0.96	1.05	1.02	0.97	1.09	1.15	1.25
B_1	2.4	65	8.0	5.7	2.6	12.0	50	82	25	14	0.50
C_1	0.70	0.23	0.86	0.65	0.38	0.74	0.40	0.40	0.75	0.35	1.00
D_1	1.15	0.55	0.00	-.55	0.23	-.39	0.12	-.30	0.75	0.50	1.00
E_1	0.70	0.16	0.80	1.00	2.2	0.80	0.30	0.38	0.65	3.0	3.0
A_2	0.84	1.40	0.90	1.30	1.04	0.95	1.00	1.04	0.78	0.60	1.10
B_2	6.0	0.0	2.7	22	5.9	1.20	5.0	17.3	3.0	3.8	1.3
C_2	0.70	0.72	0.75	0.95	1.15	1.00	0.55	0.76	0.70	1.20	1.00
D_2	0.50	1.35	0.80	-1.0	0.20	1.30	0.0	0.04	0.85	0.45	0.0
α	0.86	0.57	0.71	0.78	0.87	0.70	0.59	0.64	0.53	0.61	0.66

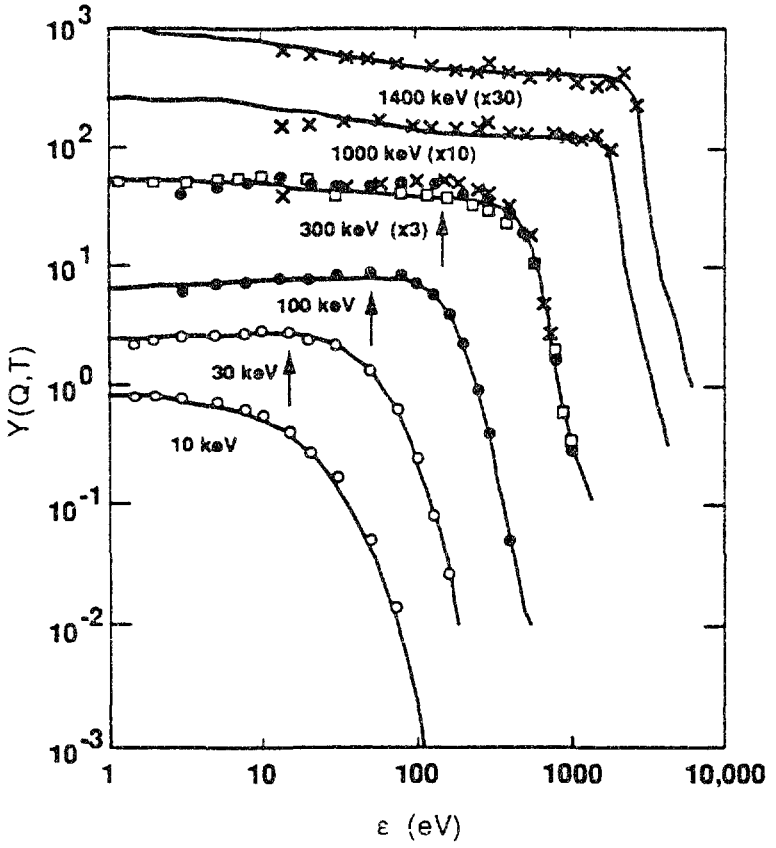

FIG. 2.41. The calculated singly-differential cross sections for ionization of N_2 by protons from the model of Rudd [155] (solid lines) compared to the experimental data of (o) Rudd [52], (●) Crooks and Rudd [64], (x) Toburen [49], and (□) Stolterfoht [55]. The arrows indicate the position in the spectra where one may expect an enhancement on the cross sections from the continuum charge transfer (CCT) ionization mechanism; this mechanism is not explicitly included in the model calculations.

In total, Rudd's model requires 10 basic fitting parameters for each electronic shell of each target. These parameters have been published for proton impact ionization of H_2, He, and Ar by Rudd [155] and He, Ne, Ar, and Kr by Cheng et al. [53]. Model parameters for N_2, CO_2, H_2O, and O_2 are available from Rudd by private communication. An example of the results of Rudd's model fit to molecular nitrogen data and divided by the corresponding Rutherford cross sections for an outer shell electron is shown in FIG. 2.41 for proton ionization of molecular nitrogen. This example illustrates the wide range in proton energy attainable by this model. The experimental data shown in FIG. 2.41 also illustrates the excellent agreement among the different experimental groups; Toburen [49], Rudd [52], Stolterfoht [55], and Crooks and Rudd [64]. The arrows in the figure point to the electron energy where one would expect to see enhancement of the cross sections by the process of continuum-charge-transfer (CCT). This mechanism can be described as an electron being "dragged" out of the collision by the proton owing to the coulomb attraction, but failing to be captured into a bound state of the projectile [44]. This mechanism should enhance the cross section for electron energies where the velocity of the out-going electron and proton are comparable; the arrows in FIG. 2.41 are placed at those electron energies.

The lack of observable enhancement in the singly differential cross sections at the appropriate energy is evidence that this mechanism does not contribute markedly to the total electron yield; the model of Rudd does not include any theoretical mechanism for this process.

2.3.3. **Heavy Ion Impact**

The singly differential cross sections for electron emission in collisions of structured ions with atomic and molecular targets provide a convenient means to access the effects of electrons bound to the projectile on the energy loss process. Using Eq. 2.15 and plotting Y(Q,T) versus R/Q the effect of the bound projectile electron on the yield of electrons ejected by different ions can be easily seen. Data for ionization of helium by H^+, He^+, and He^{2+} are shown plotted in this manner in FIG. 2.42. Excellent agreement is observed between the H^+ and He^{++} induced cross sections illustrating the accuracy of z-squared scaling of bare ions in this energy range; the only differences observed are at electron energies less than about 18 eV (R/Q=0.3). At ejected electron energies less than 10 to 20 eV one can expect larger uncertainties in the helium ion cross sections because only electrostatic analysis was used in these measurements, no TOF data are available. For small

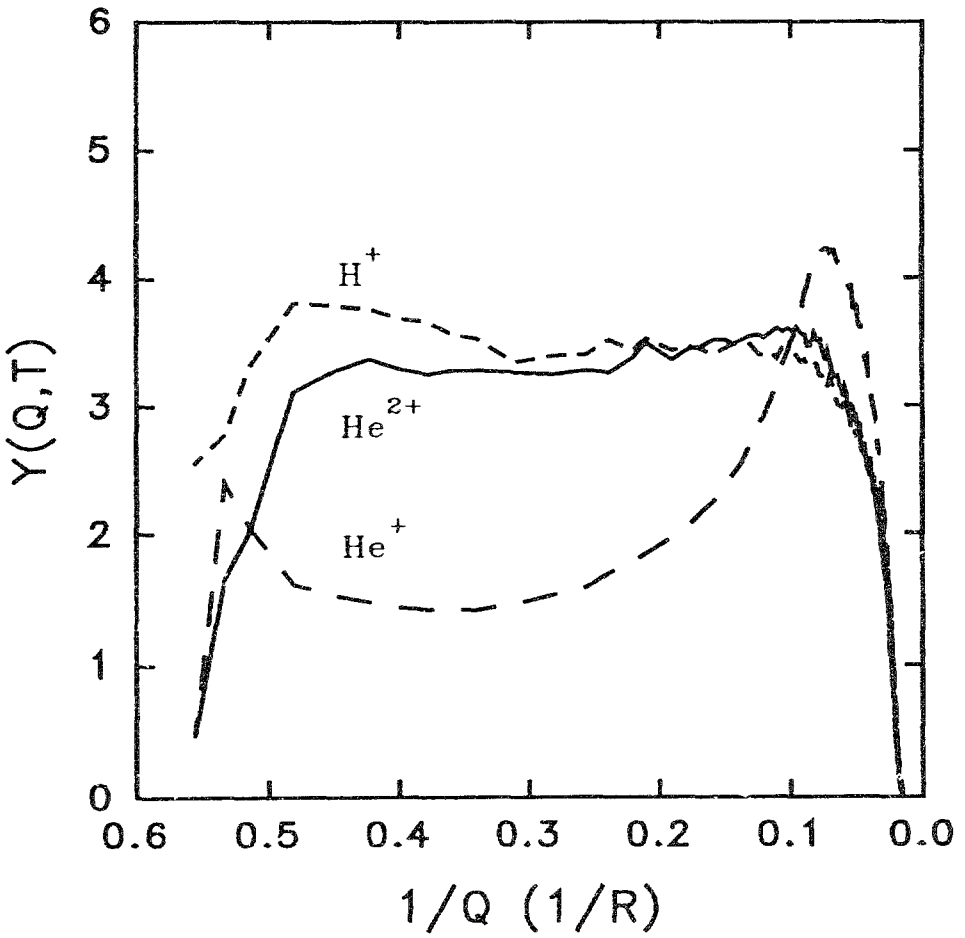

FIG. 2.42. Ratio of the measured singly-differential cross sections for ionization of helium by 0.3 MeV/u protons and helium ions to the corresponding Rutherford cross sections plotted against the reciprocal of the collisional energy loss; data are from Toburen and Wilson [90]. The area under the curve in this plot is proportional to the total ionization cross section.

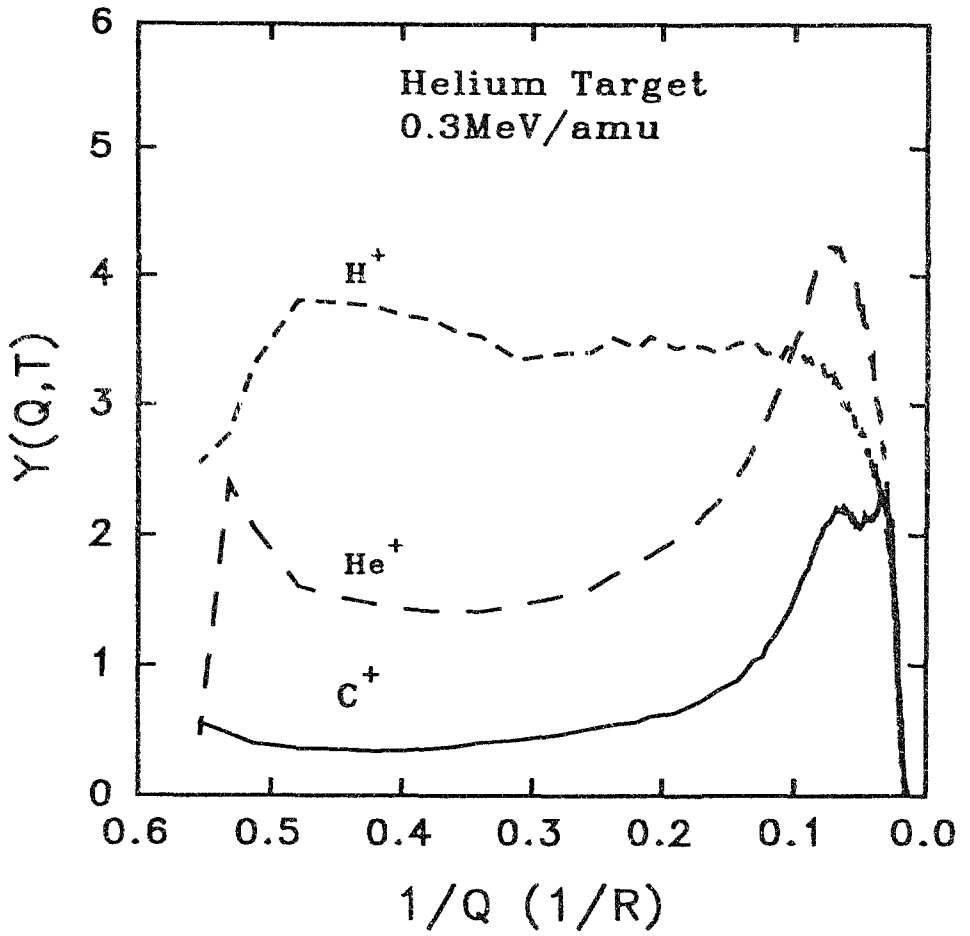

FIG. 2.43. Comparison of the singly differential cross sections for ionization of helium by 0.3 MeV/u H^+, He^+, and C^+ ions plotted as the ratio to the corresponding Rutherford cross sections versus the reciprocal of the energy loss. The H^+ and He^+ data are the same as plotted in FIG. 2.42.

values of energy loss the spectrum for He^+ impact is considerably smaller than for the bare ions. This reflects the screening of the He nuclear charge by the He^+ bound electron, thus reducing the strength of the interactions involving the large impact parameter collisions contributing to small energy losses. In FIG. 2.42 the effect of electron loss from the projectile is clearly seen in the He^+ data; it enhances the cross sections for He^+ impact well over those for bare ions in the region near electron energies of 160 eV (R/Q=.07); this corresponds to emission of electrons with velocity comparable to the ion velocity. The actual contribution of electron loss to the total electron production cross section is, however, hard to determine accurately because the effects of projectile screening make identification of the portion of the curve due to target ionization alone difficult. One can see from this illustration, recalling that equal areas under the curve contribute equally to the total ionization cross section, that the mean energy of the ejected electrons will certainly be greater for He^+ ions than for bare ions, i.e., the electron spectrum is biased toward higher electron energies in the case of the He^+ ion impact.

The relative importance of interactions leading to energy loss by clothed ions is further explored in FIG. 2.43 where the ratio Y(Q,T) for ionization of helium is plotted versus R/Q for singly charged carbon, helium, and hydrogen

ions. The effect of screening by projectile electrons is clearly seen in this illustration in that the z-squared scaling implicit in the definition of Y(Q,T) has reduced the cross sections for carbon ion impact by approximately an order of magnitude below the proton values for the collisions involving small energy loss. Recall that data for electron energies less than about 15 eV (R/Q > .35) are subject to large uncertainties and should not be taken seriously. They are plotted here, where the area under the curves are proportional to the total ionization cross sections, to show that these uncertainties have very little influence on the total yield of electrons that would be obtained from integration of the SDCS's for carbon ion impact. That is an important fact to keep in mind when using integrated cross sections to test absolute calibration of the cross section scale by comparison to measured total ionization cross sections. In particular, this uncertainty contributed by low-energy electron cross sections becomes increasingly small as the atomic number of the ion increases for ions that possess a large fraction of their bound electrons. As the degree of ionization of the projectile increases, the importance of low-energy electrons as contributors to the total energy loss process increases until, for a bare projectile, it should approach the shape of the proton curve given in Figs. 2.42 and 2.43.

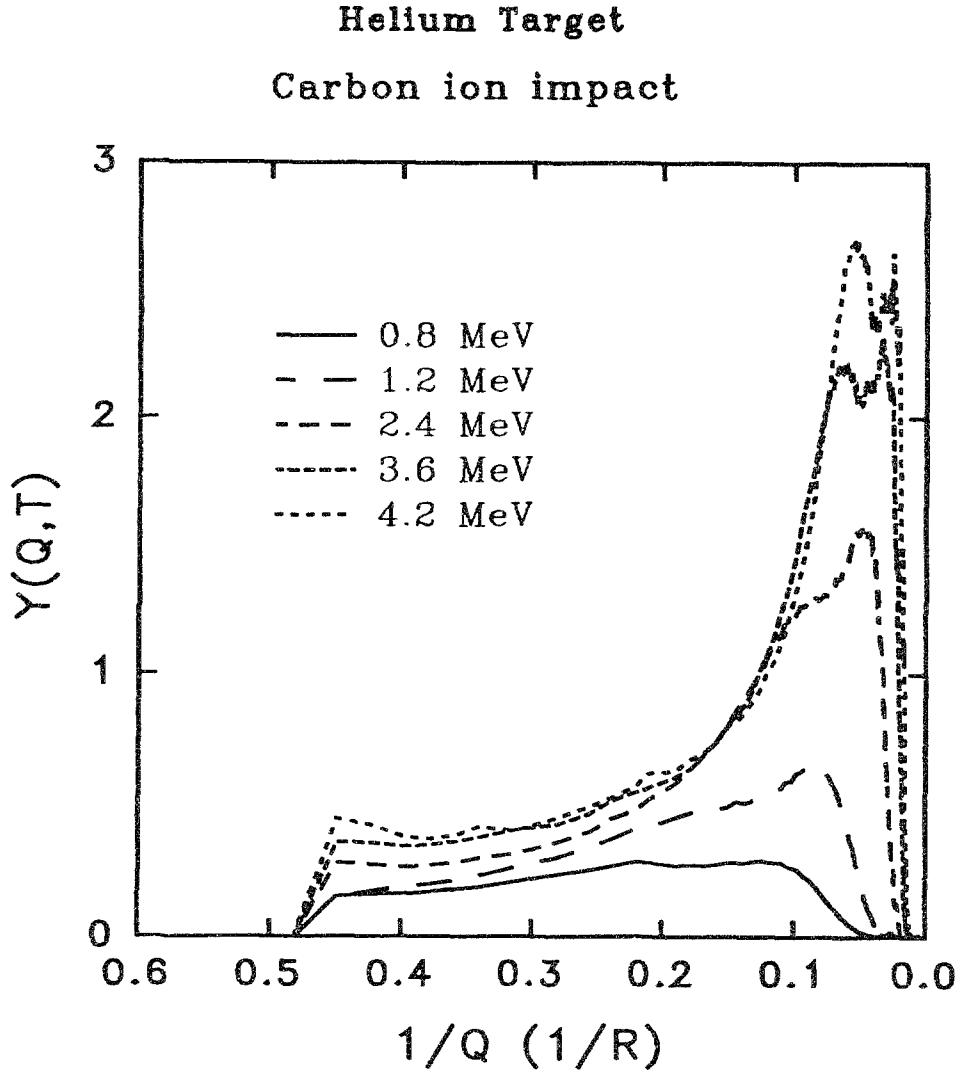

FIG. 2.44. The ratio of measured and Rutherford cross sections for ionization of helium by singly-charged carbon ions of several energies plotted as a function of the inverse of the energy loss.

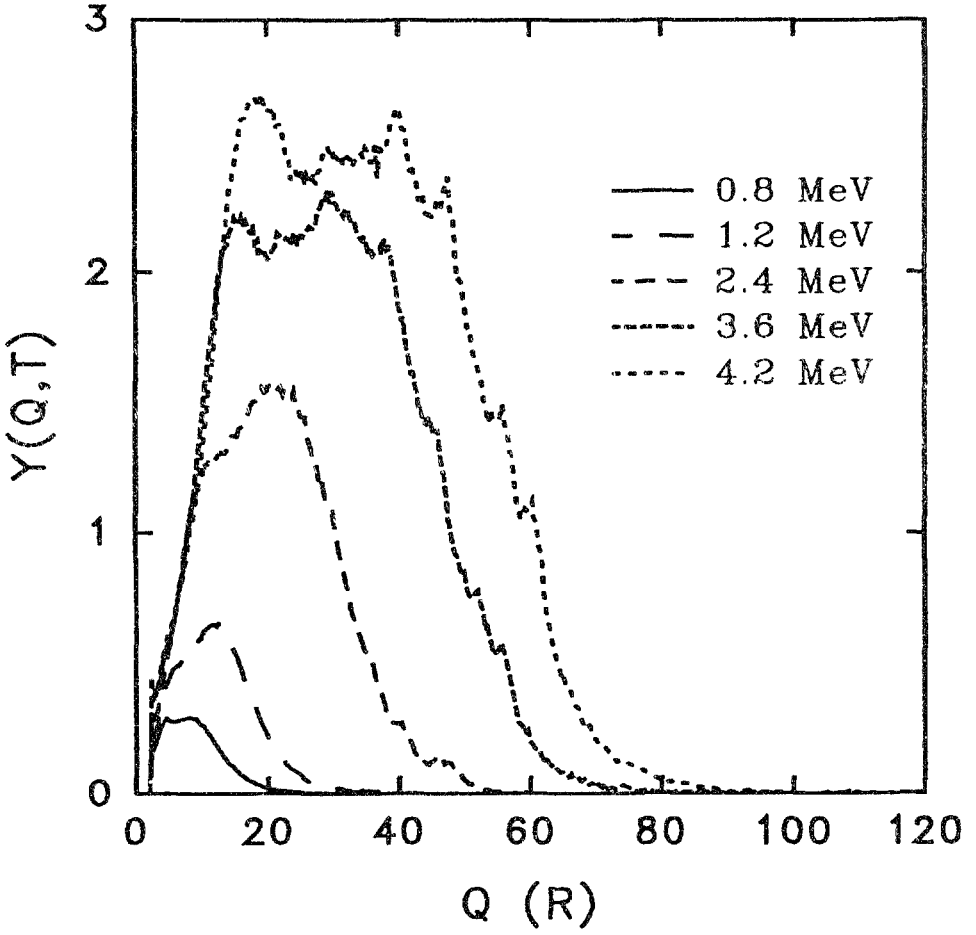

FIG. 2.45. The ratio of measured and Rutherford cross sections for ionization of helium by singly charged carbon ions plotted as a function of the energy loss.

The spectra for the clothed ions in Figs. 2.42 and 2.43 are all scaled according to Rutherford theory by simply the square of the bare projectile charge, therefore only the highest energy cross sections, produced by very close collisions, may be expected to scale to the same values; low-energy ejected electron cross sections reflect the extent of screening by the bound electrons.

There is evidence of a peak in the ejected electron spectra of Figs. 2.42 and 2.43 at the equal velocity condition, $v_e=v_i$ (this occurs for R/Q=0.07), for both the He^+ and C^+ ions; this indicates contributions to the spectra arising predominantly from electron loss from the projectile; charge transfer to the continuum is expected to be a relatively small contribution. It is interesting to note that, although the carbon ion has a greater number of bound electrons and they are more loosely bound than in the helium ion, the relative strength of the electron loss contribution from the carbon ion is much smaller. The mechanistic implications of this observation on the ionization process are not clear at this point in time.

A comparison of spectra for different C^+ ion energies is shown in FIG. 2.44. This illustration shows that the electron loss contribution grows as the ion velocity increases reflecting the increasing cross section for electron loss. The most obvious characteristic of energy loss in collisions of C^+ ions with atomic targets seen in Figs. 2.43 and 2.44 is the much lower fraction of low-energy electrons resulting from dressed ion collisions

compared to bare ions. This leads to a much higher mean energy of the ejected electron in such collisions. Also note that it is not possible to scale proton cross sections to structured ion impact in any simple manner.

In the relatively low energy range where we have studied differential cross sections for carbon and oxygen ion impact, the analysis advocated by Kim, where the electron spectra are tested against the plateau value determined from Rutherford theory, does not enable a test of the absolute cross sections; there is no high energy plateau in the plot of Y(Q,T) versus Q for carbon ions in this energy range. This lack of high energy plateau, in contrast to the plateau observed in Figs. 2.33-2.36 for higher velocity proton impact, is illustrated in FIG. 2.45. Absolute cross sections must, therefore be evaluated from parameters of the experiment and/or from measured total ionization cross sections [97,98].

Because of the combination of effects of screening by projectile electrons, and electron loss from the projectile, the origin of the spectral features observed in FIG. 2.45 are more difficult to identify than for bare ions. The peak, or what appears as a shoulder on the spectra for lower energy ions, at the low-energy end of the spectra ($10 < Q/R < 20$, for ion energies from 0.3 to 4.2 MeV, respectively) is a result of electron loss from the projectile; the maximum contribution from this process for 4.2 MeV ions should occur at about 190 eV (Q/R=16). The electron loss peaks appear at a somewhat higher energy than predicted by kinematics because these peaks are on a rapidly increasing background of electrons from target ionization. The binary encounter peak should occur with about 4 times higher energy, or at approximately 58 Rydbergs for the 4.2 MeV spectrum. For even the largest particle velocity shown here one cannot expect a well defined binary encounter peak, see for example the proton impact data of FIG. 2.31.

The small peaks observed superimposed on the spectra for the two highest energy ions in FIG. 2.45, result from Auger transitions following inner-shell vacancy production in the carbon projectile. These transitions are observed at Doppler shifted energies in the laboratory reference frame as determined by the kinematics of the collision (for a discussion of the kinematics of projectile electron emission, see Stolterfoht [45]). Since the spectra shown in FIG. 2.45 were obtained from integration of doubly-differential electron energy distributions measured at discrete angles, these peaks carry forward as discrete peaks in the integral spectrum. The intensity of these transitions in the double differential cross sections also provides a means to determine the consistency of the magnitude of the measured absolute cross sections and the energy scales by comparison to other measurements on inner-shell ionization. That was exploited in a recent study of the doubly differential cross sections for ionization of helium by carbon ions [98].

As discussed above with regard to doubly differential cross sections, there has been very little collision theory developed for application to the study of ionization by structured ions. The most promising theory is presently the classical trajectory monte carlo (CTMC) technique [97,156]. This technique is attractive in that it provides ab initio absolute cross sections and includes continuum charge transfer and multiple ionization processes, as well as being appropriate to the intermediate ion energy range. The primary disadvantage of this technique is the extraordinarily long computer times required for the computation. In FIG. 2.46 are shown recent calculations by Reinhold et al. [97] (also presented in a more detailed comparison to experiment by Toburen et al. [98]) of the singly differential cross sections for ejection of electrons in C^+ + He collisions at 200 keV/u. There is good agreement between theory and experiment for the high energy portion of the spectra with the experimental data being about 50% larger than theory at the low energies. A strength of theory, as contrast to experiments, is that one is able to estimate the contribution, and the spectral shape, of

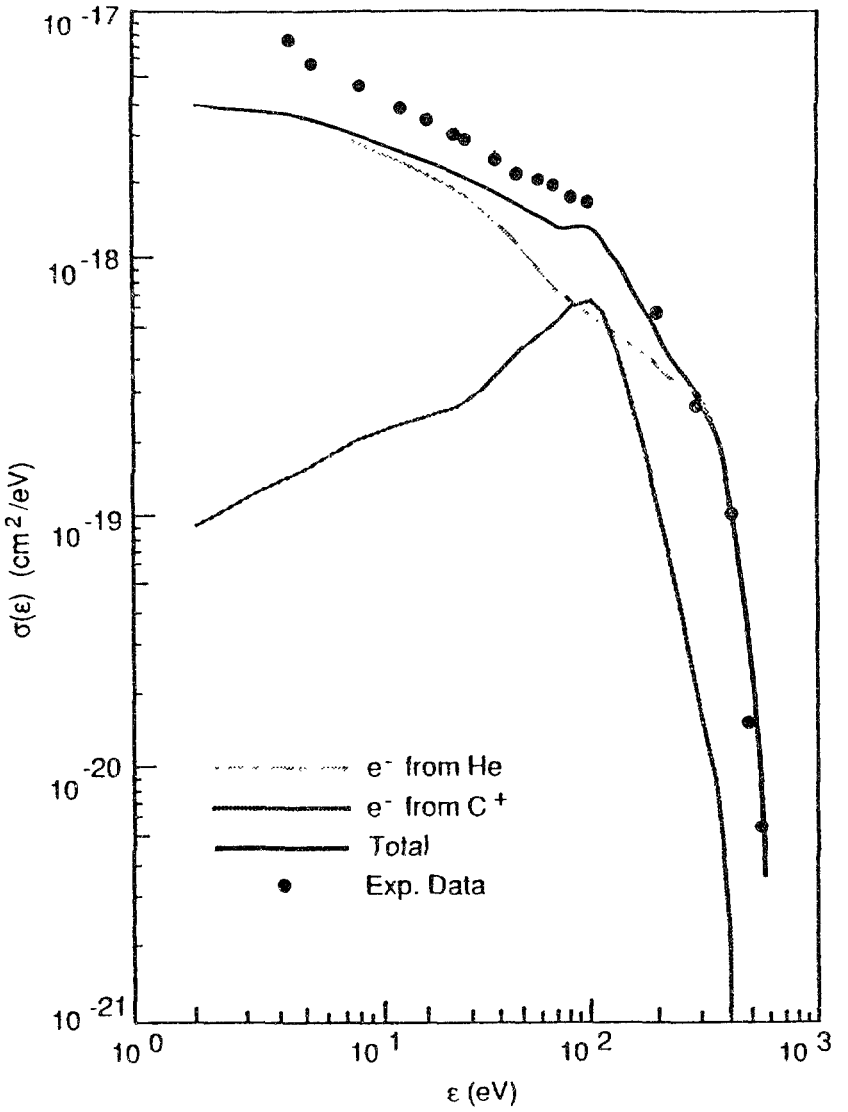

FIG. 2.46. Comparison of measured singly differential cross sections (SDCS) to those calculated using classical trajectory Monte Carlo (CTMC) theory. The solid line is the CTMC calculation of the sum of electrons ejected from the target and projectile; CTMC calculations of electrons originating for the target are given by the light stippled line and those originating from the projectile are given by the heavy stippled line. The result were taken from the work of Toburen et al. [98].

electrons coming from either the target or the projectile. The dashed line in FIG. 2.46 is the calculated contribution of electrons ejected from the projectile. Although there are discrepancies between the CTMC calculations and experiment, the agreement is comparable to, or better than, that seen earlier for Born calculations for simple collision systems. This, plus the fact that the CTMC calculations can be applied to essentially any system, as it does not rely on special system wave functions, make this theory highly attractive for complex collision systems.

One could summarize our knowledge of differential ionization cross sections for structured ions as fragmentary. We have a reasonable understanding of collisions for light projectiles such as H° and He^{+}, although there is no theoretical means of calculating doubly-differential cross sections for molecular targets at the present time; neither have models been

developed for fitting or extrapolating such cross sections. Data presently in existence, however, show dramatically that scaling from bare ions to dressed ions is not possible with a single parameter, such as the effective charge of stopping power theory, and that the mean energy of electrons emitted in collisions involving structured ions is much higher than that for bare ions. There is a long way to go before cross sections for structured ions will be understood with the same detail as bare ions, but recent advances in the development of theory and in experimental techniques give optimism to a vastly improved understanding in the near future.

2.4. TOTAL IONIZATION CROSS SECTIONS

2.4.1. **Proton Impact**

Total ionization cross sections for collisions of protons with atomic and molecular targets have been the subject of a large number of experimental and theoretical investigation. Perhaps the most comprehensive experimental study has been that of Rudd et al. [157], where targets of He, Ne, Ar, Kr, H_2, N_2, CO, O_2, CH_4, and CO_2 were investigated over the proton energy range from 5 to 4000 keV. A comprehensive review of all proton impact total ionization cross sections has been prepared by Rudd et al. [158]. In that report over 130 references are reviewed, data are compiled, fitted, and recommended cross sections presented. For the most part, data from different experiments for proton energies of greater than a few hundred keV are in good agreement, however a considerable amount of scatter exists among data at low proton energies and there is often disagreement between experimental data sets that overlap only at the extremes of the proton energy ranges covered by each experiment.

Before discussing the recommended cross sections of Rudd et al. [158] it is necessary to define precisely what is meant by an ionization cross section. When a positively charged particle collides with a neutral atom or molecule, free electrons may be produced and/or electrons may be captured from the target by the projectile. The total cross sections for production of electrons and positive [target] ions are commonly defined as σ_- and σ_+, respectively. If σ_{ie} is defined as the cross section for the production of i electrons and σ_{jc} is the cross section for the capture of j electrons by the incident ion, then in the notation of Rudd et al. [158]

$$\sigma_+ \equiv \sum_i i\sigma_{ie} + \sum_j j\sigma_{jc} \tag{2.28}$$

and

$$\sigma_- \equiv \sum_i i\sigma_{ie} \quad . \tag{2.29}$$

Using this definition, σ_{ie} includes all processes that produce i electrons including those in which excitation or charge transfer occur simultaneously; similarly for σ_{jc}. From these definitions it is clear that

$$\sigma_+ - \sigma_- = \sum_j j\sigma_{jc} \quad . \tag{2.30}$$

For protons where only single and double capture processes are observed. Then

$$\sigma_+ - \sigma_- = \sigma_{1c} + 2\sigma_{2c} \quad . \tag{2.31}$$

For application of total ionization cross sections to testing the accuracy of differential electron emission cross sections, the quantity of interest is the

electron production cross section; that is the quantity to which the integrated doubly differential electron emission cross sections should be compared. This comparison then provides a stringent test of the doubly differential cross sections in that the total cross sections can be measured with a much higher degree of accuracy. The recommended cross sections of Rudd et al. [158] are considered to be accurate to better than 10%, with those for a wide range of incident energy and target species considered accurate to a few percent.

In providing recommended ionization cross sections, Rudd et al. [158] fit each set of data for a given target to an empirical equation. This provided cross sections as a continuous function of energy whereas a simple average of the available data would have resulted in discontinuities in energy regions where different data sets meet. The criteria he used for deriving the fitting equation were as follows.

(1) The equation should have the correct high-energy dependence; that behavior was assumed to be predicted by the Bethe-Born approximation.
(2) It should have a power-law dependence on proton energy at the low energies.
(3) The equation should be relatively simple.
(4) There should be a small number of adjustable parameters.
(5) The same form of the equation should be appropriate to all targets.
(6) It should fit the energy dependence of the data within experimental uncertainty.

The empirical equation chosen is a simple combination of the cross sections appropriate to the low- and high-energy regions;

$$\sigma_{-} = (\sigma_l^{-1} + \sigma_h^{-1})^{-1} \quad , \tag{2.32}$$

where

$$\sigma_l = 4\pi a_o^2 C x^D \tag{2.33}$$

and

$$\sigma_h = 4\pi a_o^2 [A \ln(1 + x) + B]/x \quad . \tag{2.34}$$

In Eqs. 2.33 and 2.34, $x=T/R= E_p/1836R$, a_o = 0.529 Å, and R = 13.6 eV and A, B, C, and D are the adjustable fitting parameters. Values of the fitting parameters obtained by Rudd et al. [158] are presented in Table 2.6. These fitting parameters lead to recommended cross sections that are in agreement with the measured values to within 10% to 25%; agreement is best, commonly better than 10%, for higher energy protons with the largest discrepancies, 25% or more, occurring for low-energy protons.

By careful analysis of the published data, and fitting the model to that data, Rudd has been able to provide recommended total cross sections for ionization of a number of atomic and molecular targets by protons [158]. An example of their fit to the data is shown in FIG. 2.47 for ionization of molecular oxygen. Here the recommended values from the model are in excellent agreement with published results of Crooks and Rudd [64], Hooper et al. [159], De Heer et al. [160], McNeal and Birely [161], and with the high energy portion of Rudd et al. [157]. The data of Dufay et al. [162] appear to be much too large and the results of Park et al. [163] much too small. Data used to fit the model to molecular oxygen data, as well as a number of other gas targets, are given in Table 2.6. For molecular targets where data are not available one may provide estimates of the total cross sections from simple

Table 2.6

Values of the fitting parameters for Eqs. 2.22 and 2.23.

Target	A	B	C	D
H	0.28	1.15	0.44	.907
He	0.49	0.62	0.13	1.52
Ne	1.63	0.73	0.31	1.14
Ar	3.85	1.98	1.89	0.89
Kr	5.67	5.5	2.42	0.65
Xe	7.33	11.1	4.12	0.41
H_2	0.71	1.63	0.51	1.24
N_2	3.83	2.78	1.80	0.70
O_2	4.77	0.00	1.76	0.93
CO	3.67	2.79	2.08	1.05
CO_2	6.55	0.00	3.74	1.16
NH_3	4.01	0.00	1.73	1.02
CH_4	4.55	2.07	2.54	1.08

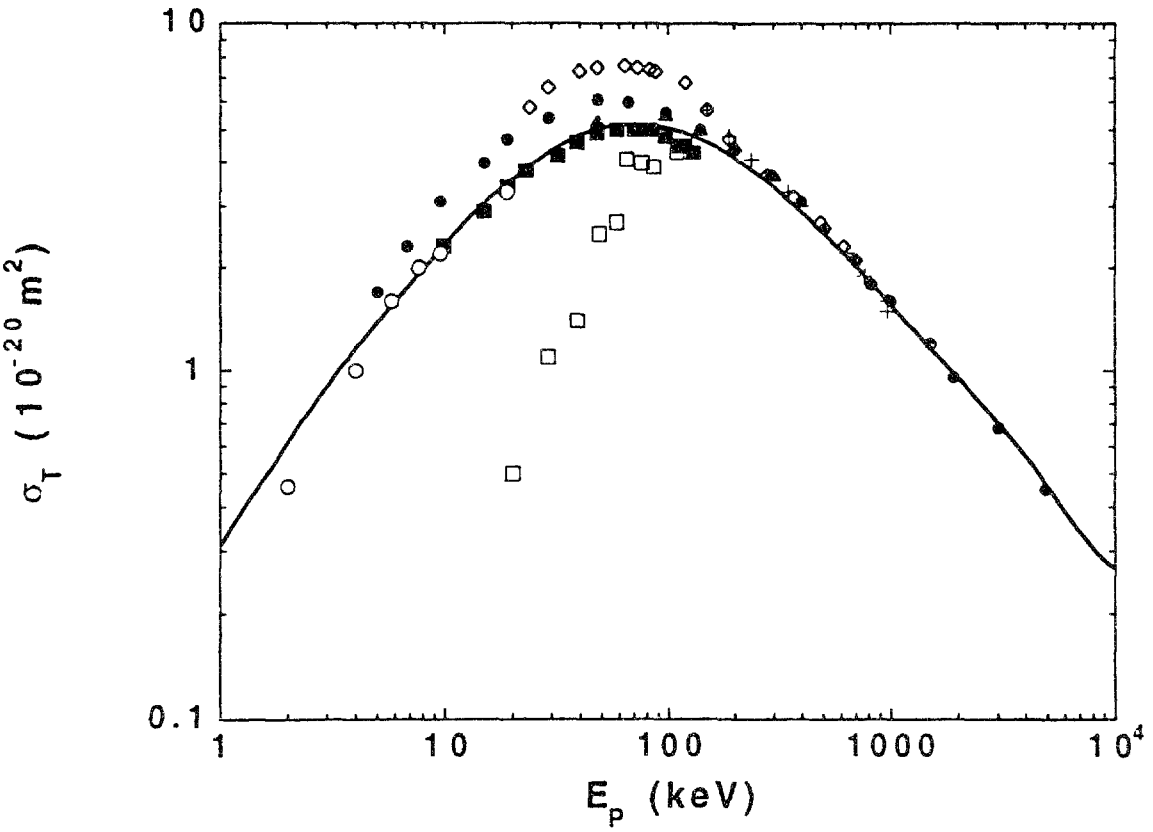

FIG. 2.47. Cross sections for production of electrons in the ionization of molecular oxygen by protons. The solid line is the recommended fit of Rudd et al. [158]. Experimental data are: (▲), Crooks and Rudd [64]; (♦) Rudd et al. [157]; (+) Hooper et al. [159]; (■) De Heer et al. [160]; (○) McNeal and Birely [161]; (◇) Dufay et al. [162]; and (□) Park et al. [163].

scaling techniques. Scaling by the number of outer shell electrons was found to be reasonably successful in studies of ionization of hydrocarbons and amines for relatively high-energy protons [79,80].

2.4.2. Heavy Ion Impact

The largest amount of information on total ionization cross sections for heavy, or dressed, ions and neutral particles has been obtained for the simplest collision systems. There has been a considerable number of studies involving collisions of helium ions with different targets. Total cross section measurements for collisions of H, H_2, He and Li atoms and ions with atoms and molecules have been reviewed by Barnett, et al. [164] in the ORNL "Redbooks", Vol. I of the 6086 series. Since this review focusses only on data for the light targets of helium, hydrogen, and lithium of interest to fusion studies it is of limited value for radiological applications, but provides a data base to help estimate cross sections for some applications. A number of total cross sections for helium ion impact have been obtained for rare gas and alkali targets (see for example, DuBois and Toburen, [165], and DuBois, [166-170] and other ions on simple targets such as molecular hydrogen [171,172], rare gases [173,174], and helium [98]. A review of cross sections for collisions of C^{q+} and O^{q+} with H, H_2, and He has been published by Gilbody et al. [175]. Total ionization cross sections can also be obtained from doubly differential cross sections for the collision systems listed in Table 2.3 where sufficiently broad ranges of ejected electron energies and angles were measured for reliable integration to be performed.

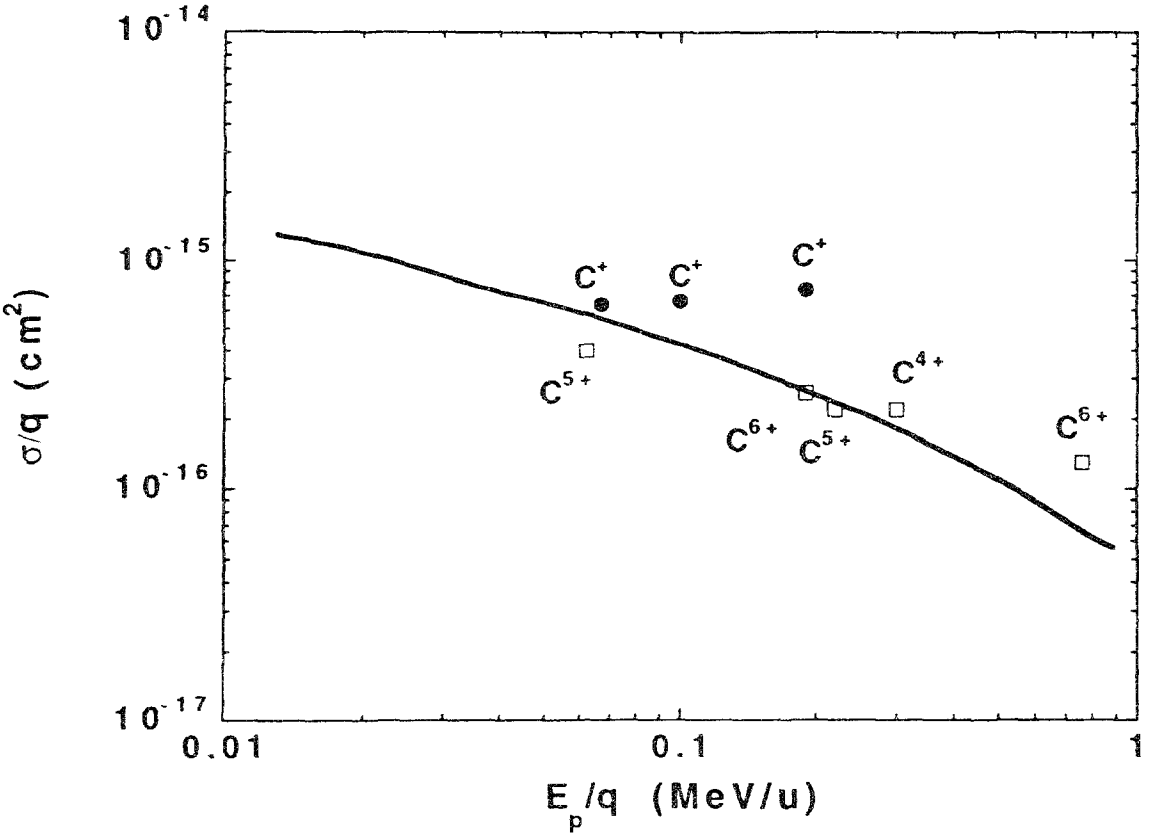

FIG. 2.48. Total cross sections for ionization of neon by carbon ions. The data for highly charged states of carbon are from the work of Schlachter et al. [173] and the singly charged carbon ion data are unpublished data of Toburen from the Pacific Northwest Laboratory.

By far the largest quantity of data concerning ionization by heavy ions (mass greater than helium) has come from the Berkeley group of Schlachter and his co-workers. In their studies with fast multiply charged ions they were able to define a scaling relationship for the ionization cross sections. When the ionization cross section divided by the projectile charge was plotted as a function of the energy per nucleon of the incident ion the data for highly charged ions tend to form a common line. This scaling breaks down at lower charge states as is shown in FIG. 2.48 where the highly charged ion data of Schlachter et al. [173] for ionization of neon by carbon ions are compared to unpublished results for singly charged carbon ions from our laboratory. The scaled data for singly charged ions are somewhat larger than the multiply charged ion cross sections and exhibit a considerably different energy dependence. Unfortunately there is not sufficient experimental or theoretical work available for ionization by heavy ions to provide any significant guide to cross section systematics covering other than a narrow range of experimental parameters.

2.5. CHARGE TRANSFER CROSS SECTIONS

The process of charge transfer between a moving ion, or neutral particle, and the atomic constituents of the stopping material becomes increasingly important as the velocity of the moving particle decreases, i.e., for ion energies less than approximately 1 MeV/u. Processes of electron capture and loss contribute to the energy loss process in several different ways. The actual process of electron transfer may lead to either an energy loss or an energy gain by the projectile depending on the initial and final electronic binding energies. This direct contribution of charge transfer processes to the total energy transfer that occurs between the projectile and the medium may be quite small, if not negligible. However, the transfer of electrons may have important consequences on the subsequent interaction probabilities and thereby have profound effects on energy transfer, eg. see the discussion earlier in this chapter regarding the effects of electronic screening by bound projectile electrons on the ejected electron energy distributions observed in ionization of atomic and molecular targets by dressed ions. A knowledge of the charge state of an ion is also necessary when evaluating experimental studies of interactions involving charged particles since such experiments usually depend on measurements of beam current as a measure of beam fluence. In the study of charged particle track structure and its influence on the relative biological effectiveness of high-LET radiation the processes of charge transfer are particularly important near the ends of the tracks. It is here (ion energies less than about 0.5 to 1 MeV/u) that charge transfer plays an important role in mean free paths between ionizing events and in the relative amount or energy loss that occurs in each interaction.

By far the largest body of data describing charge transfer collisions has been generated by experiments directed towards reactions of interest to fusion energy. These studies have focussed on reactions of plasma components such as H^+, H°, He^+, etc. with plasma impurity atoms and molecules such as H_2, N_2, O_2, H_2O, etc. Some studies with heavier ions have been conducted for the molecules H, H_2, and He for application as plasma diagnostics. These data are very important as data sources for radiological physics as well, but many of the important interactions, such as interactions with biological constituents (water, hydrocarbons, etc.) or interactions involving ions representative of recoiling tissue constituents (carbon, nitrogen, oxygen, etc.) have not been measured and there is no reliable theory that can predict charge transfer cross sections for intermediate energy ions of most interest to radiological issues.

As noted above, there has been an extensive data base established for charged particle interactions of interest to controlled fusion research. The fusion community has also had a dedicated effort to the review of that data and to the presentation of recommended cross sections. In 1977, a two volume compilation of atomic data relevant to fusion research was published as ORNL reports ORNL-5206 and ORNL-5207. Since that time a good deal of new data was published and that is included in the most recent update of that compilation. The most recent reviews have been issued as ORNL report 6086 which consists of a six volume set of data compilations: Vol. 1, "Collisions of H, H_2, He, and Li Atoms and Ions with Atoms and Molecules" [164]; Vol. 2, "Collisions of Electrons with Atoms and Molecules" [176]; Vol. 3, "Particle Interactions with Surfaces" [177]; Vol. 4, "Spectroscopic Data for Iron" [178]; Vol. 5, "Collisions of Carbon and Oxygen Ions with Electrons, H, H_2, and He" [179]; and Vol. 6, "Spectroscopic Data for Titanium, Chromium, and Nickel" [180]. Of particular interest to work in Radiological Physics and Radiation Therapy are Volumes 1 and 2.

In addition to the ORNL compilations an excellent source of data on charge transfer and ionization is found in a data compilation published by McDaniel et al. [3]. These authors review data for a wide range of collision processes and collision partners. Volume 1 of this compilation [3] includes cross sections for electron capture and loss in collisions of noble gas ions with noble gas atoms with collision energies less than about 100 keV. They also include cross sections for excitation occurring in charge transfer collisions. Data for heavy ion collisions involving electron capture and loss by the projectile, as well as target excitation and dissociation are reviewed in Vol. IV of the review of McDaniel et al. They include such reactions as He° collisions with CH_4 leading to products H^+, CH_4^+, CH_3^+, CH_2^+, CH^+, C^+, H_2^+, etc.

Perhaps the most thorough review of charge changing cross sections for fast heavy ions is that of Betz [181]. This review focuses on ions with atomic numbers in the range $16<z<92$ and includes ion energies up to 400 MeV. Charge transfer in both gaseous and solid targets is discussed.

There are only limited data available involving ions heavier than helium in collision with molecular targets of interest to radiobiology, i.e., targets such as H_2O, CH_4 etc. Fleischmann et al. [182] have reviewed a broad base of data on electron stripping collisions involving such targets as helium, neon, argon, krypton, xenon, molecular hydrogen, molecular nitrogen, and molecular nitrogen. Their review included ions and neutral particles of hydrogen, noble gases, lithium, barium, boron, and nitrogen with energies in the range of a few keV to several MeV/u. They also compared the data to Firsov theory. Cross sections for charge exchange between high charge states of C, N, and O and hydrogen gas have been reported by Crandall et al. [183] and in helium by Crandall [184] for ion energies of from 25 to about 75 keV. Somewhat higher energies were covered for these same ions in collisions with atomic and molecular hydrogen by Phaneuf et al. [185]. Olsen and Hvelplund [186] have measured electron capture and loss for oxygen ions of 100 to 500 keV in molecular hydrogen. Lockwood [187] studied charge transfer in F^+ collisions with H_2, N_2, He, Ne, and Ar in the energy range 14 to 100 keV. Collisions of multiply charged ions of nitrogen and neon have been studied by Dmitriev et al. [188] as they interact with helium, nitrogen, neon, and argon with ion velocities of 2.7, 4.0, and 8 X 10^8cm/sec. Electron capture by 60 to 200 keV Ne^{2+} on He. Ne, Ar, Kr, and Xe has been measured by Suk et al. [189] and electron loss has been measured by Hird and Suk [190] for 35 to 140 keV N^+ ions in Ne, Ar, and Kr. These references illustrate that, although there has been a good deal of work performed in the study of charge transfer, there is still a lack of data relevant to radiobiology and radiation therapy.

2.6. MULTIPLE IONIZATION

Cross sections for electron emission from energy loss collisions of charged particles with atomic and molecular targets are of primary importance for the development of track structure descriptions of the spatial pattern of energy deposition by high-LET radiation. However, the traditional studies of electron production do not provide any information regarding the fate of the projectile or target following electron emission nor do they include information on ionization (positive ion production) produced by charge transfer. In addition, such measurements do not provide information on the number of electrons that may be emitted in a single collision when multiple electron capture and loss events occur. The latter may be biologically significant because the multiply emitted electrons would slow down in a spatially and temporally correlated way. To fully describe the interactions appropriate to charged particles one must have information on the charge transfer cross sections, the spectrum of electrons emitted (if any) during charge transfer events, the number of electrons emitted per interaction and

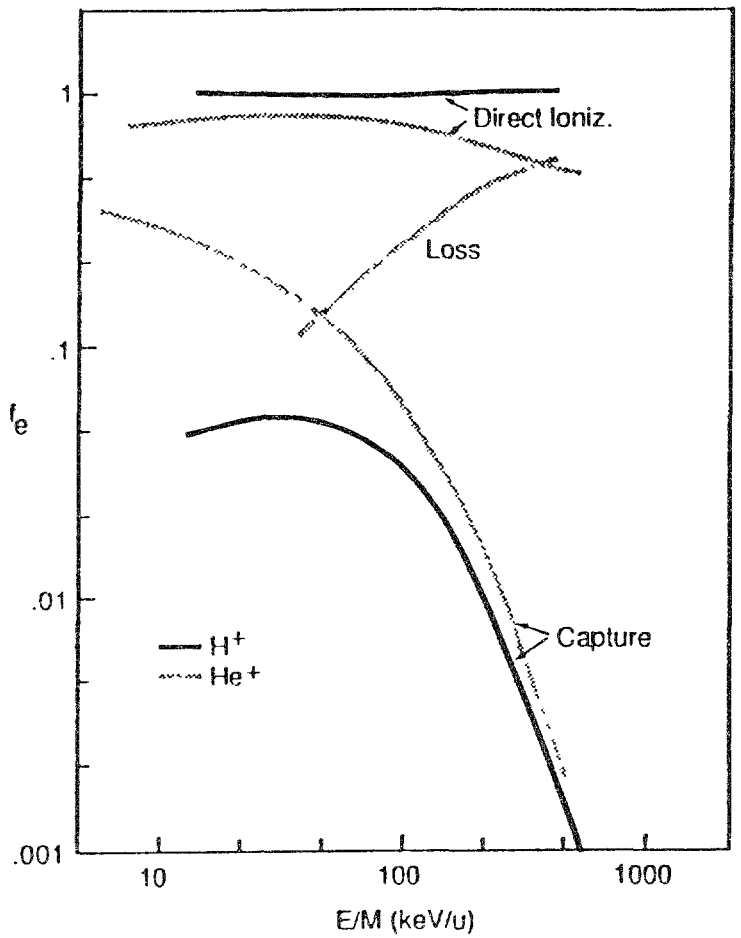

FIG. 2.49. Comparison of the relative importance of the principal mechanisms for production of free electrons in collisions of protons and helium ions with neon. f_e is the fraction of the total number of electrons that are emitted as a consequence of the indicated ionization mechanism; direct ionization of the target, electron loss from the projectile, and electron capture by the projectile. For electron capture to result in electron production requires simultaneous electron ejection from the target; double ionization of the target.

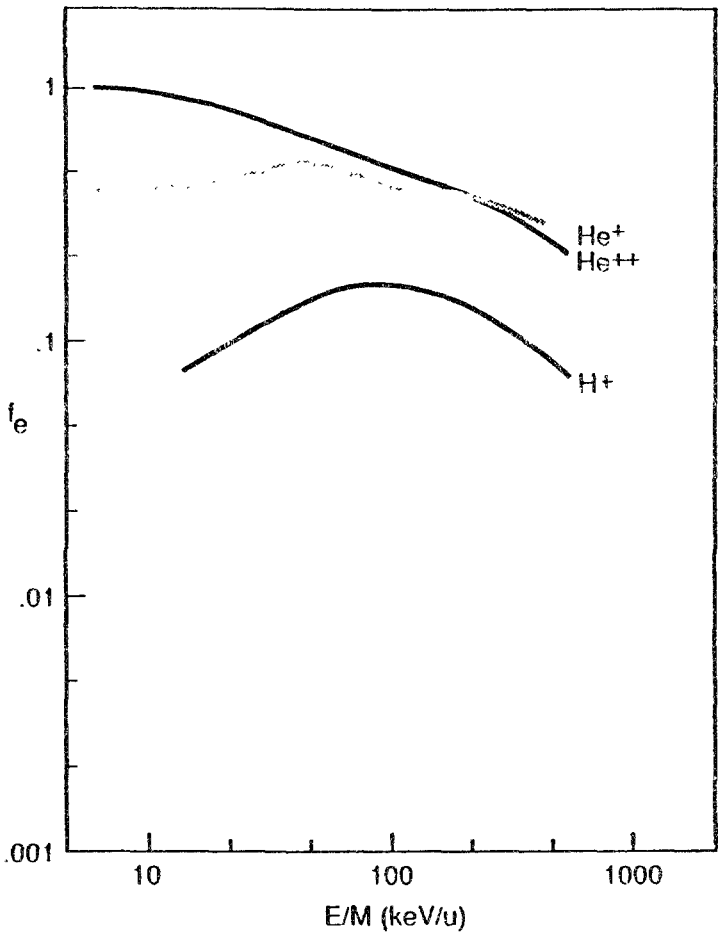

FIG. 2.50. Comparison of the fractions of free electrons produced from multiple ionization events for protons and helium ions colliding with neon atoms. f_e is the fraction of the total electron ejected that result from collisions that leave the target multiply ionized.

their individual energy and angular distributions, and the excitation and dissociation states of the target molecules. To have detailed information on all of these processes, and the effect of target structure on them, is a tall order. As a first step, an assessment of the relative importance of the different processes can be very useful. For the past few years studies have been ongoing in our laboratory at PNL, as elsewhere, to measure the spectrum of charge states of atomic and molecular products following ionizing collisions with light ions. Such studies enable one to gain insight into the relative importance of different ionization channels appropriate to energy loss by ions and neutrals (see for example, DuBois and Toburen [165], DuBois [166-169,191], DuBois and Kover, [192], and DuBois et al., [193].

The principal interaction mechanisms leading to the release of free electrons following collisions of H^+ and He^+ ions with a neon target are illustrated in FIG. 2.49 for ion energies from a few keV/u to a few hundred keV/u. As expected, direct ionization of the target is the primary source of electrons for proton collisions throughout the proton energy range shown. Electron capture, which requires simultaneous target ionization to release a free electron, is at most a 5% contribution to free electron production. For helium ion impact, however, electron capture and loss can make a sizeable contribution to the free electron production. In the case of electron capture this implies a high probability of simultaneous capture-plus-target ionization

leaving the target multiply ionized. It is also found that target ionization is produced with a high probability in collisions resulting in projectile ionization, although it is not obvious from this illustration. The message to be derived from this analysis is that, as energy loss by projectiles heavier than protons are considered, processes other than direct ionization of the target must by considered if electron production along the charged particle track is to be fully described.

In addition to the process of electron capture-plus-target ionization that leaves the target atom doubly ionized it is also possible to produce a doubly ionized target simply by direct ionization. The fraction of free electrons that result from multiple ionization of neon by protons and helium ions is shown in FIG. 2.50. This fraction never goes above 10% for proton impact, however, for alpha particles the fraction approaches 100% at very low energies and is nearly 40% for He^+ ions over a rather broad energy range. These data should serve as a reminder that one cannot simply scale data from protons to heavier ions. It should also encourage the investigation of the biological consequences of multiple ionization, ie., what are the affects of a transient build-up of localized Coulomb charge on biological damage. It is no doubt true that multiple ionization is less frequent in molecular and condensed phase targets than the examples displayed for atomic targets, however, the difference in multiple ionization cross sections for different ions may be manifest as different molecular fragmentation patterns and yields that may be important in leading to biologically important damage. With the present emphasis on fundamental studies in molecular science we should see, in the near future, an enhanced understanding of the relationship between the initial products of radiation and the subsequent chemistry and biology that is initiated. With advances that are taking place in molecular biology a molecular description of radiation damage that follows events from energy deposition to the expression of biological damage is within our grasp.

2.7. EFFECTIVE CHARGE

The concept of average effective ionic charge was first introduced by Bohr [194,195] to describe effects of the capture and loss of electrons on the slowing down of fission fragments in cloud chambers. With decreasing ion velocity he noted that the fragment-charge that was effective in electronic interactions would rapidly decrease owing to the capture of target electrons into bound states of the projectile. He observed that the direct transfer of momentum from the fragment to the gas atoms of the media through nuclear collisions would gradually become of increasing importance as the projectile slowed. In that work he assumed that the fragment, to a first approximation, would possess an average effective charge equal to the ratio of its velocity v to the orbital velocity of the least tightly bound electron in the atom. Thus all electrons carried by the ion would have velocities greater than, or equal to, the ion velocity v and the rest of the electrons would have been stripped from the moving ion. Bohr [195] introduced his concept of an average effective charge into the formulation of energy loss in order to provide a quantitative description of the velocity-range relationships observed for fission fragments. Since that time, the concept of average effective charge has been firmly established in studies of stopping power (see, for example, Kreussler et al., [196], Anthony and Lanford, [197], and Bichsel, [198]). The effective charge is usually determined experimentally from the ratio of the stopping power for the ion of interest to that for a bare charged ion, such as a proton.

The spectra of energy loss measured for collisions of projectiles with well characterized charge states provide a new perspective from which to assess the influence of bound projectile electrons on energy loss and on which

to base concepts of effective charge. Whereas stopping power provides only average quantities, averages over all charge states of the ion and all processes leading to energy loss, the ejected electron spectra measured in single collisions of ions with atomic and molecular targets provides detail on the effective charge responsible for a specified quantity of energy loss as a function of projectile charge. Examples of the influence of projectile electrons on the yield of secondary electrons, or energy loss, were shown above in Figs. 2.19-2.25 and 2.42-2.46 in the discussion of cross sections for electron emission for structured ions. Those data clearly illustrated that, within the concepts of high energy theories such as the plane wave Born approximation or binary encounter theory, the effective charge of the ion is a strong function of the energy loss; for small values of energy loss that occur predominately in large impact parameter collisions the bound electrons serve as an effective screen of the projectile nucleus, whereas collisions involving large energy loss occur at small impact parameters where the bound projectile electrons provide essentially no screening of the projectile nucleus, at least at the energies of ions considered in this chapter.

The relationship between the ejected electron spectra and stopping power can be easily shown. In the study of ionization of water vapor by helium ions Toburen et al. [92] examined the mean electrons energies, total ionization cross sections and partial stopping cross sections for He^+, He^{2+}, and equal velocity H^+ ions. In that work the total ionization cross sections were derived from measured doubly differential electron emission cross sections using the expression

$$\sigma_T = 2\pi\int_0^{\epsilon_{max}} d\epsilon \int_0^{180} \sigma(\epsilon,\theta)\sin\theta d\theta \quad , \tag{2.35}$$

where $\sigma(\epsilon,\theta)$ are the measured doubly differential cross sections for ionization by a particle of reduced energy T. The major fraction of the total stopping power can also be derived from doubly differential cross sections and the density of the medium. Projectile energy loss that is transferred to kinetic energy of ejected electrons plus the energy lost in overcoming the binding energy to eject electrons account for as much as 90% of the total stopping power for 0.5 MeV/u ions [199]; additional energy may be lost through charge transfer processes and excitation of the target. The partial stopping cross section owing to energy loss to ionization can be calculated from the expression

$$S_I = 2\pi I\int_0^{\epsilon_{max}} d\epsilon \int_0^{180} \sigma(\epsilon,\theta)\sin\theta d\theta + 2\pi\int_o^{\epsilon_{max}} \epsilon d\epsilon \int_0^{180} \sigma(\epsilon,\theta)\sin\theta d\theta \quad , \tag{2.36}$$

where $\sigma(\epsilon,\theta)$ are the measured doubly differential cross sections (DDCS) for electron emission. Similarly, one can obtain the mean energy of ejected electron from the measured DDCS using the following expression

$$\bar{\epsilon} = \frac{2\pi \int_0^{\epsilon_{max}} \epsilon d\epsilon \int_o^{180} \sigma(\epsilon,\theta)\sin\theta d\theta}{2\pi \int_0^{\epsilon_{max}} d\epsilon \int_0^{180} \sigma(\theta,\epsilon)\sin\theta d\theta} \quad . \tag{2.37}$$

These derived quantities σ_T, $\bar{\epsilon}$, and $\bar{\epsilon}\sigma_T$ (the partial stopping cross section for energy deposited as kinetic energy of ionized electrons) for collisions of protons and helium ions with water vapor are reproduced from Toburen et al. [92] in Table 2.7. In this energy range the total ionization cross section is decreasing with increasing ion energy. The mean energy of the electrons ejected by the bare ions is, however, nearly constant over this energy range. The most dramatic change in these quantities in this energy range is the

TABLE 2.7

Energy loss as kinetic energy of free electrons in water vapor

Ion Energy (MeV/u)	He^{2+}			He^{+}			H^{+}		
	σ_T	$\bar{\epsilon}$	$\bar{\epsilon}\sigma_T$	σ_T	$\bar{\epsilon}$	$\bar{\epsilon}\sigma_T$	σ_T	$\bar{\epsilon}$	$\bar{\epsilon}\sigma_T$
0.075				0.838	39	33.0			
0.20	1.23	45	55.6	0.661	63	41.6			
0.30	0.90	52	47.1	0.557	78	43.3	0.257	45	11.6
0.40	0.95	49	46.7	0.476	92	44.1			
0.50	0.77	51	39.5	0.362	112	40.5	0.170	56	9.6

σ_T in units of 10^{-15} cm^2 (total ionization cross section)

$\bar{\epsilon}$ in units of eV (mean energy of ejected electrons)

$\bar{\epsilon}\sigma_T$ in units of 10^{-15}eVcm^2 (partial energy loss cross section for energy loss as kinetic energy of free electrons)

TABLE 2.8

Partial and Total Stopping Cross Sections for water

Ion Energy (MeV/u)	Partial Stopping Cross Sections[a]			Stopping Cross Sections[b]		
	He^{+}	He^{2+}	charge state average	Matteson et al.[c]	Palmer and Akhavan-Rezayat[d]	
	vapor	vapor	vapor	liquid	liquid	vapor
0.075	43.5			63.2		
0.200	50	71	60.5	72.9	68	77
0.300	50	58	56	66.6	64	62
0.400	50	59	58	58.7	56	56
0.500	45	49	49	52.1	51	51

a) Partial stopping cross sections including contributions from binding energy and kinetic energy of electrons released in ionizing collisions; cross sections in units of 10^{-15} eV cm^2/molecule.

b) Stopping cross sections in units of 10^{-15} eV cm^2/molecule.

c) Data from Matteson et al., [200].

d) Data from Palmer and Akhavan-Rezayat, [201]

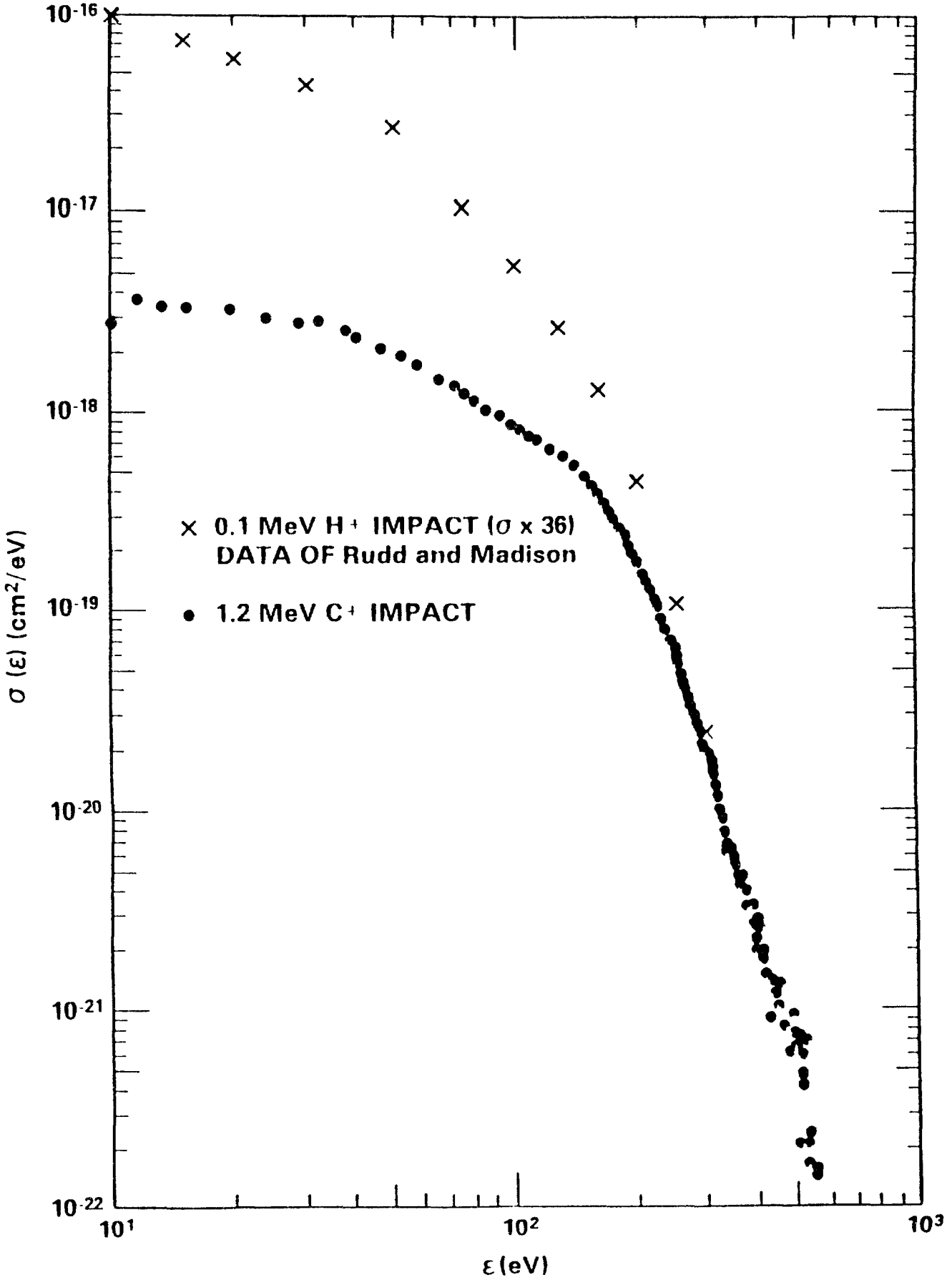

FIG. 2.51. Single differential cross sections for electron emission from helium in collisions of equal velocity protons and singly charged carbon ions. The proton data are from Rudd and Madison [60] and the carbon ion data are from Toburen et al. [98]

increase in the mean energy of electrons ejected by the He^+ ions as their energy increases. The partial stopping cross sections for the transfer of energy to ejected electron kinetic energy for He^+ and He^{2+} ions are very similar and, within experimental uncertainties, equal to four times the comparable partial stopping cross sections for protons as would be expected from z^2 scaling. It is interesting that the total ionization cross section for He^+ tends to decrease at about the same rate as the mean energy of the ejected electron energy increases such that the partial stopping cross section remains nearly constant for He^+ and equal to that of He^{2+}.

In order to compare the stopping cross sections obtained from differential cross sections for electron emission to measured stopping cross sections it is necessary to include the contributions from electron binding to that contributing to electron kinetic energy given in Table 2.7 as prescribed in Eq. 2.36, and one must sum over the fractions of the beam in different charge states; stopping cross section and stopping power measurements are made for particles in charge state equilibrium. For the energy range of the measurements shown in Table 2.7 only the singly and doubly charged ions are significant components of the equilibrated beam. Also, one should note that Eq. 2.36 does not include contributions from production of excited states of energy transfer in charge transfer collisions. The charge state average stopping cross sections obtained by using Eq. 2.36 are shown in Table 2.8 along with measured values. The partial cross sections obtained from the differential cross sections are smaller than the measurements [200,201] by about 20% at the lowest ion energy and 5-10% at the higher energies. These differences are consistent with the expected contributions for excitation [199] that need to be added to the partial cross sections based solely on ionization. Note also the partial cross sections are for water vapor. Stopping cross sections for the vapor are found to be somewhat smaller than for liquid or solid as indicated from the work of Palmer and Akhavan-Rezayat [201].

When we examine the partial stopping cross sections of ions of a specified charge state in single collisions with atomic or molecular targets the normal concepts of effective charge become difficult to visualize. For example, in stopping power theory, as indicated above, it is common to relate the effective charge to the number of electrons that are effectively stripped off the swift ion by the medium [194-197]. This seems inappropriate when we compare the spectra of energy that is lost to ionization electrons by equal velocity H^+ and C^+ ions shown in FIG. 2.51. If the effective charge for C^+ is determined from the differential ionization cross sections, namely that z_{eff} is given by

$$z_{eff} = \left\{ \frac{[(I + \bar{\epsilon})\sigma_T]_{C^+}}{[(I + \bar{\epsilon})\sigma_T]_{H^+}} \right\}^{\frac{1}{2}} , \qquad (2.38)$$

then the effective charge for the singly charged 1.2 MeV carbon ion, as determined from the data shown in FIG. 2.51, is approximately 2.7 and it is found to increase with increasing ion energy. This would imply that the effective charge for energy loss must be somewhat larger than the actual charge on a moving ion because screening by the bound projectile is not 100% efficient. This has also been noted in the work of Brandt and Kitagawa [202] in their analysis of stopping power data. Some of the ionization that contributes to the energy loss of the ion occurs with impact parameters within the screening radius of the bound projectile electrons. If one were to take the assumption literally, that the effective charge on a moving ion is equal

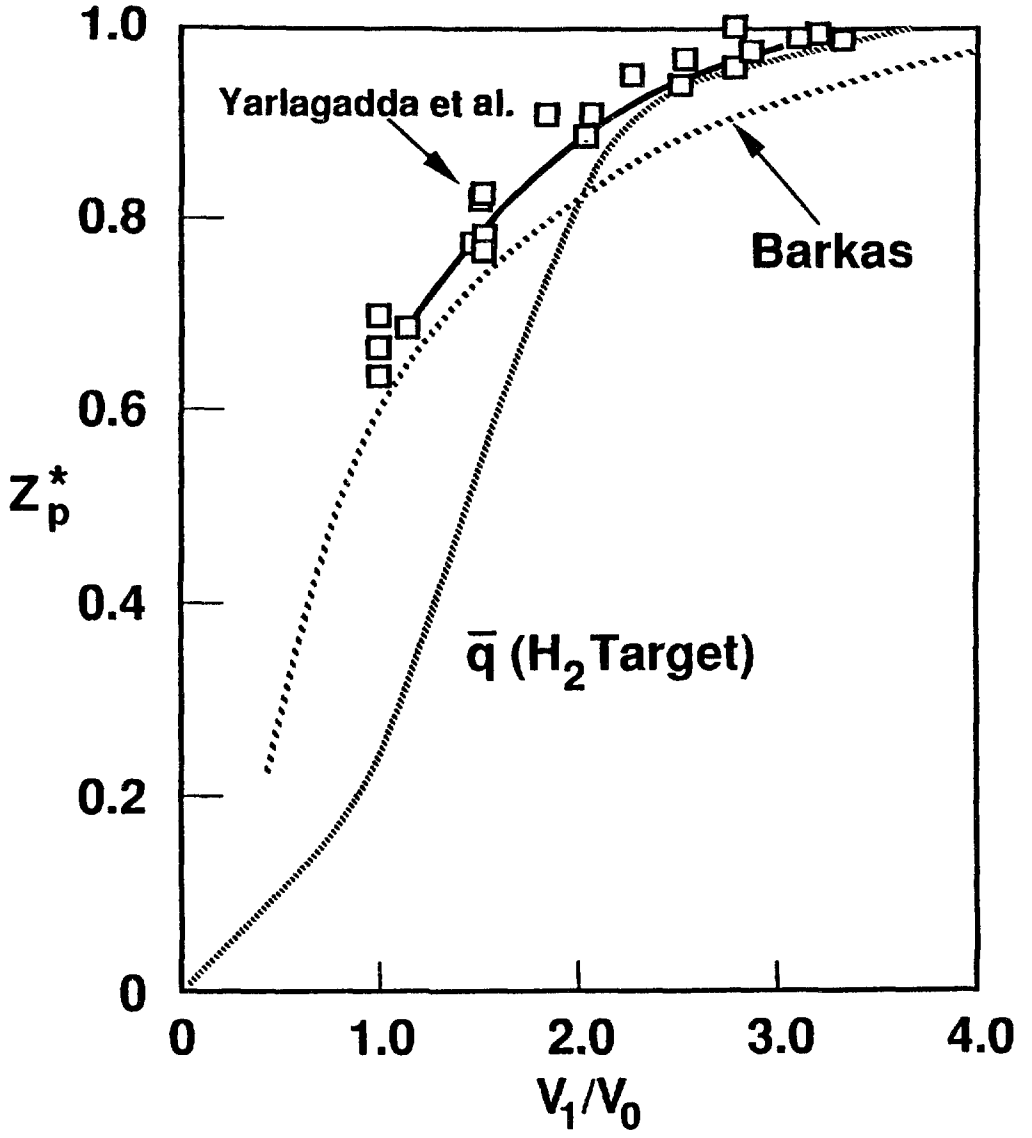

FIG. 2.52. Comparison of the empirical effective proton charge obtained in the work of Yarlagadda et al. [203] using stopping power and theory to the average ion charge obtained from charge transfer cross sections for proton-hydrogen collisions tabulated by McDaniel et al. [3]. The solid line is drawn through the data points to guide the eye. Also shown is the effective charge given by the empirical formula of Barkas [204].

to the mean charge on the ion, (as some authors still maintain) then a slow ion that has become neutralized by electron capture would not be expected to interact in any way with the electrons of the media it was traversing. This is certainly <u>not</u> true and is clearly demonstrated in studies of ionization of atoms and molecules by the passage of neutral hydrogen particles (see for example, Rudd et al. [89]; ionization remains a dominant mechanism for energy loss even at H^0 velocities slower that that of the bound projectile electron in contradiction to the assumptions of Bohr [194].

A comparison of the average effective charge obtained from stopping power measurements and the mean ion charge obtained from charge transfer measurements is shown in FIG. 2.52 as a function of ion velocity for proton impact. For relative velocities greater than about v_1/v_o=2.5 the two methods of arriving at an effective charge are equivalent; at those high velocities

the moving ion is effectively bare. At lower proton energies, however, there is a considerable difference between these two methods of arriving at an effective charge. As discussed above, the effective charge for energy loss is larger than that obtained based on equilibrium charge transfer cross sections. Also shown in FIG. 2.52 is the effective charge derived from the empirical formula of Barkas [204]. The Barkas formula is in relatively good agreement with the effective charge from stopping power data; to be expected as it was originally derived from stopping power data. The data of FIG. 2.52 would suggest that the equilibrium charge measurements may not be a good indication of the effective charge for energy loss at low velocities of the incident particle where the equilibrium charge is relatively small due to capture of electrons.

Anthony and Lanford measured stopping power for a wide range of heavy ions with energies near the peak in the stopping power and for several

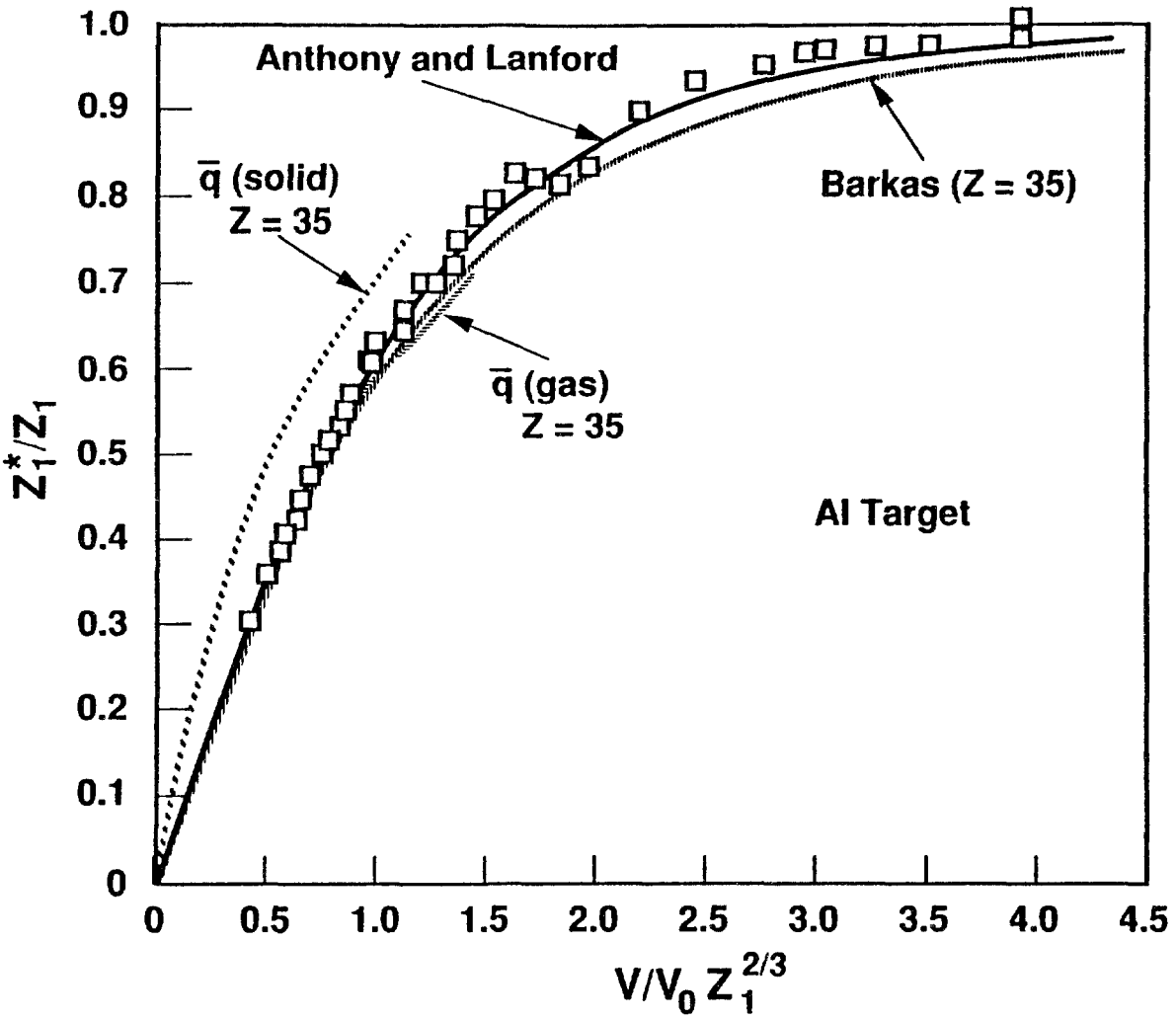

FIG. 2.53. Values of the effective charge, divided by the ion atomic number, obtained from stopping power and from equilibrium charge measurements. The solid line is from a fit to the effective charge determined by Anthony and Lansford [197] from experimental stopping power for a number of ions including higher order z corrections. The dotted lines are the average charge of bromine ions measured as they exit gases and solids by Betz [181]. Also shown is the effective charge of bromine ions obtained from the empirical formula of Barkas [204].

targets. From these data they derived the projectile effective charge from a ratio to proton stopping power and compared the results to equilibrium charge measurements compiled by Betz [181]. A comparison of their results to Betz and to the Barkas formula is shown in FIG. 2.53. In general stopping power measurements lead to an effective projectile charge that is independent of the target material (see, for example, J. F. Ziegler, [205] and Ziegler et al., [206]), whereas the equilibrium charge measured in different material is observed to be larger for targets of higher atomic number. Anthony and Lanford took this difference in target dependence for the different methods of measurements to be an artifact of the means by which the stopping power data were analyzed, ie, that a z^2 dependence on stopping power was used implicitly in the analysis. By invoking higher order z contributions in the theory of stopping power they were able to demonstrate a target dependence that was in agreement with equilibrium charge measurements. Still, their results, shown in FIG. 2.53, mimicked the gas phase equilibrium charge measurements, ie., they were considerably smaller than the solid state measurements. This occurred in spite of the fact that their stopping power measurements were made in solid targets. The use of higher order terms in projectile charge in the analysis of stopping power data does tend to result in effective charges that agree with the average equilibrium charge of the beam. However, one may question whether this agreement is forced by the assumptions inherent in the constraint applied by Anthony and Lansford in their analysis, i.e. that the effective charge must have the same target dependence as that of the equilibrium charge. Recognize that the lack of target dependence observed when stopping power data are analyzed in terms of a z^2 dependence on projectile charge is more in agreement with the studies of differential ionization cross sections.

To explore the effect of target structure on stopping power one can examine the relative contributions of the energy loss spectra to stopping power and compare that with the effect of target structure on energy loss. From the spectra of energy loss in charged particle collisions with different atomic and molecular targets (see, for example, the data of FIG. 2.37) one observes that the effects of target electronic structure is evident only for the very low-energy portion of the ejected electron spectrum, i.e., ejected electron energies less than about 20 eV. This has an important effect on the yield of electrons ejected in ionizing collisions because cross sections for low-energy electrons are very large. The cross section for energy loss, however, entails the product of ejected electron energy, plus the binding energy, times the respective cross section for electron ejection, ie., probability of energy loss is given by $(\epsilon+I)\sigma(\epsilon)$. This shifts the influence of the spectral shape on stopping power to higher electron energies. The result is that one would expect a greatly reduced effect of target structure on stopping power relative to its effect on ionization. Thus, one would expect the stopping power to be a function of target electron density, but not on the detailed electronic structure of the target. On the other hand, equilibrium charge states depend on the probability of electron capture and loss processes that are more characteristic of low-energy ionization processes. This echoes the sentiment expressed by Yarlagadda et al. [203] that "a model useful and adequate for stopping power need not apply to other phenomena".

2.8. INNER SHELL IONIZATION

Most of the results discussed to this point in this chapter refer to the ionization of the outer electronic shells of atomic or molecular targets. But when the energy of the projectile is large enough, inner atomic shells may also be ionized, although with smaller probability. The total ionization

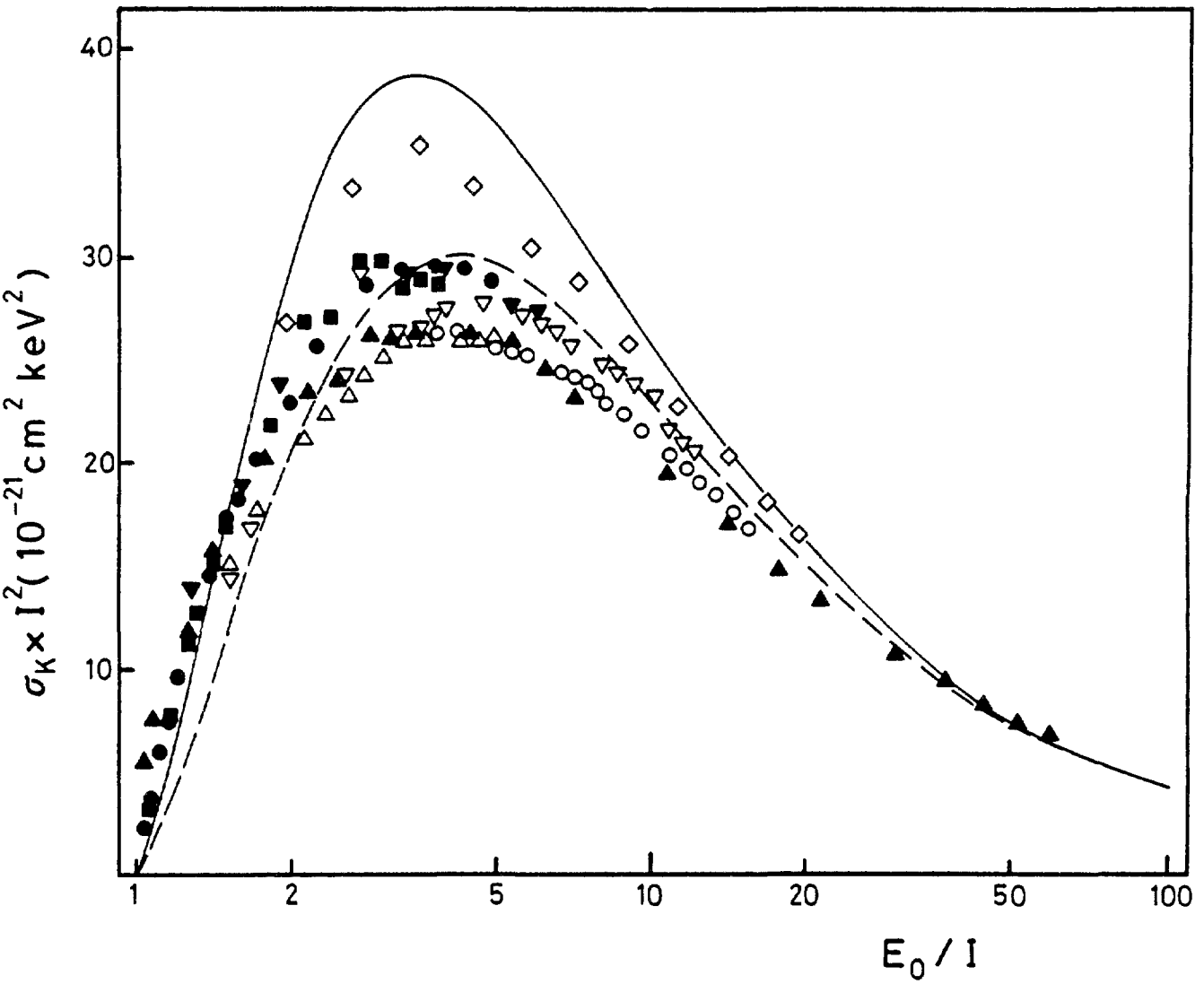

FIG. 2.54. Comparison between experimental and theoretical cross sections for K-shell ionization of light atoms (Z_2 = 6 to 18) by electron impact. $\sigma_K x I^2$ is plotted versus T/I. Curves and symbols are defined as follows: ___ PWBA calculation for θ = 0.70 [209], --- Born-Ochkur calculation for θ = 0.70 [209]; Experimental data for O-carbon [210], ▽-nitrogen [210], △-neon [210], ●-neon [211], ◇-aluminum [212], ■-argon [213]. The x-ray data of Tawara et al. [214], for ▲-carbon, are normalized to Glupe and Mehlhorn's data [210]. The data for ▼-argon, have been converted to ionization cross sections using a fluorescence yield w = 0.118 [207].

cross section for an inner shell, for example the K shell, σ_K, can be obtained either from the x-ray production cross section $\sigma_{K\text{-x ray}}$ or from the Auger-electron production cross section $\sigma_{K\text{-Auger}}$ if the fluorescence yield ω is known (see, for example, Krause, [207]. The total K-shell ionization cross section is obtained from the x-ray cross sections by $\sigma_K = \sigma_{K\text{-x ray}}/\omega$, or from the K-Auger cross sections using $\sigma = \sigma_{K\text{-Auger}}/(1-\omega)$. For targets involving light atoms, ω is small and we have $\sigma_K \simeq \sigma_{K\text{-Auger}}$. The data in FIG. 2.54, taken from the very useful review by R. Hippler [208], illustrate experimental and theoretical cross sections for K-shell ionization of light atoms by electron

impact; here the total cross section σ_K is multiplied by I^2, where I is the K-shell ionization energy, and plotted versus T/I. All the data shown in FIG. 2.54 are well represented by the Born-Ochkur calculation [209] for θ = 0.7. In this calculation, $\theta = I/(Z_2-0.3)^2R$ measures the effect of screening by outer electrons, the constant 0.3 corrects for the screening by the second K-shell electron, and R is the Rydberg energy. The cross section rises from threshold (at T = I) to a maximum at about 4I and then decreases again.

The experimental total K-shell ionization cross sections for excitation by light ions have been reviewed by Paul and Muhr [215] and specifically for H and He ions by G. Lapicki [216]. The data are fairly well described by the ECPSSR theory [217] which is based on the PWBA and contains several corrections for higher order effects. At a certain normalized projectile energy T/I, the cross section is approximately proportional to Z^2_1/Z^4_2, to first order.

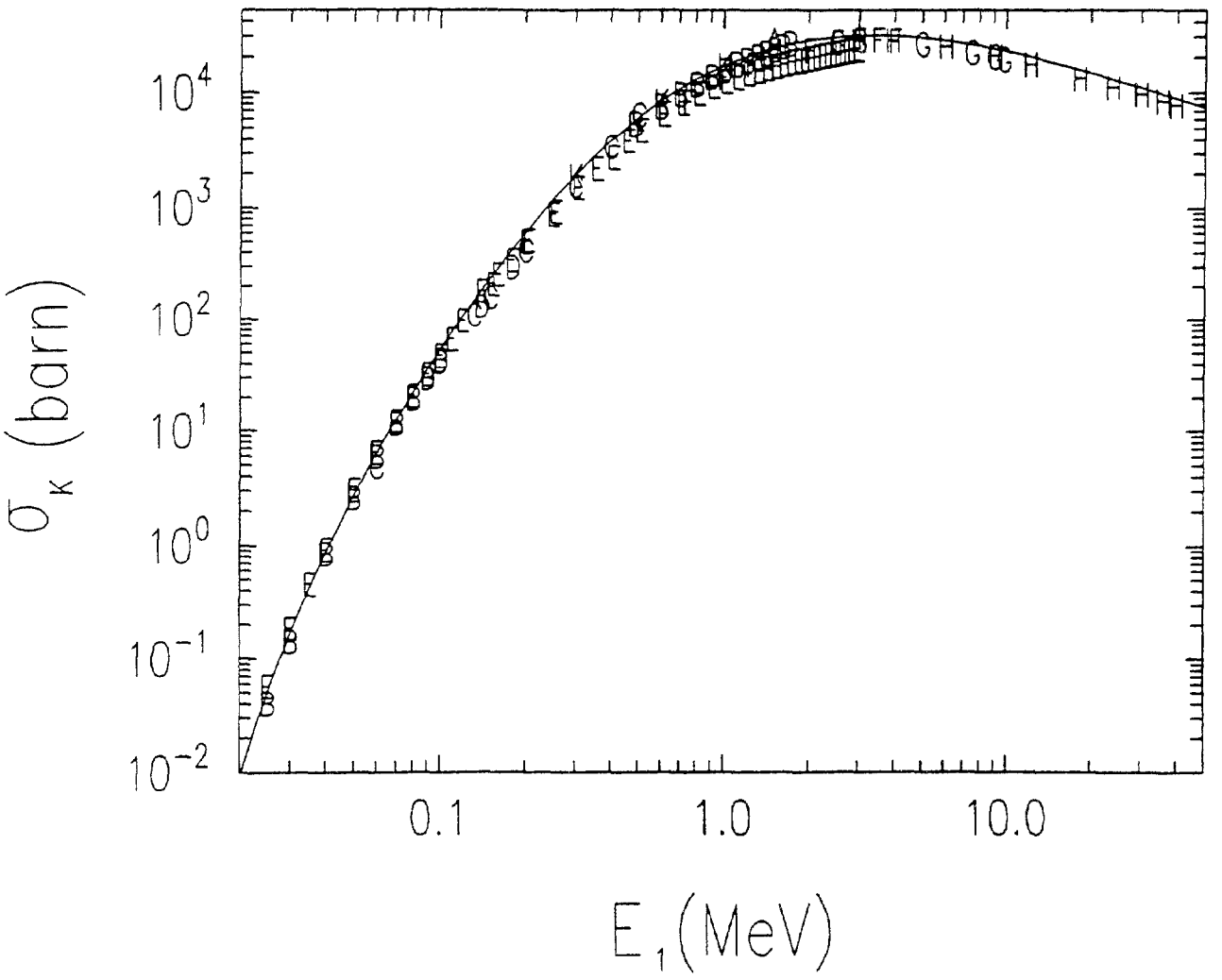

FIG. 2.55. K-shell ionization cross section for protons on aluminum in units of $10^{-28}m^2$, versus proton energy. The curve is the ECPSSR theory [217]; the letters signify measured points compiled from various publications by Paul and Sacher [218] including: A, Ogier et al. [219]; B, Khan et al. [220]; C, Khan et al. [221]; D, Shima et al. [222]; E, Basbas et al. [223]; F, Tawara et al. [224]; G, Basbas et al. [225]; H, Sera et al. [226]; I, Bonani et al. [227]; and K, Geretschläger, M., Benka, O., [228].

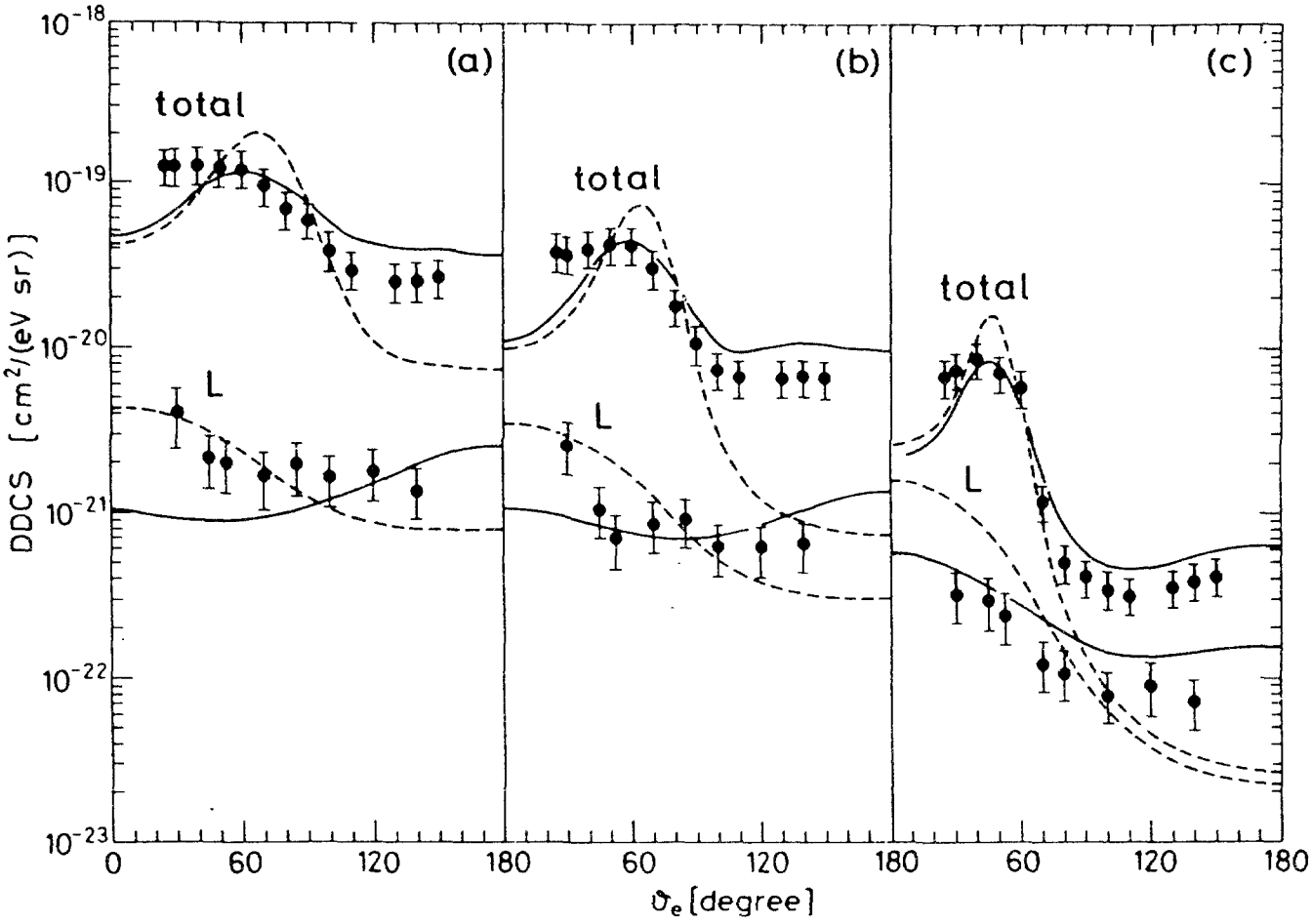

FIG. 2.56. Double differential cross section (DDCS) vs. electron ejection angle for 350 keV proton-argon collisions and δ-electron energies of (a) 47 eV, (b) 100 eV, and (c) 308 eV. DDCS for total (M-, L-, and K-shell) and for L-shell δ-electron ejection are shown. Experimental data of Gabler et al. (as presented in Rudd et al. [72]) and Sarkadi et al. [231] are compared with PWBA calculations using (---) hydrogenic or (___) Hartree-Fock/Hartree-Slater wave functions. (from Sarkadi et al., [231])

By normalizing the experimental data (i.e., dividing them by the ECPSSR theory) and by averaging and interpolating these normalized data, Paul and Sacher [218] produced a table of empirical reference cross sections for K-shell ionization by protons, for any element between Be and U. For example, for protons on O_2 they obtain a maximum cross section of 2.9×10^{-23} m^2. This cross section for K-shell ionization is much lower than that shown for the total ionization cross section in FIG. 2.47 and the maximum in the cross section occurs at 1.4 MeV, an energy much higher than that for the corresponding total cross sections shown in FIG. 2.47. Experimental data for ionization of Al by protons [215] are compared to ECPSSR theory in FIG. 2.55. The shape of the curve (quite different from that for electrons shown in FIG. 2.54) looks similar for all other targets; the maximum cross section occurs at a projectile speed that roughly equals the speed of the K-shell electron. Although the proton cross section must have a threshold also at T = I, it is hardly possible to measure down to energies below about 10 I. For He projectiles, a table of empirical K-shell reference cross sections is in preparation by Paul and Bolik [229].

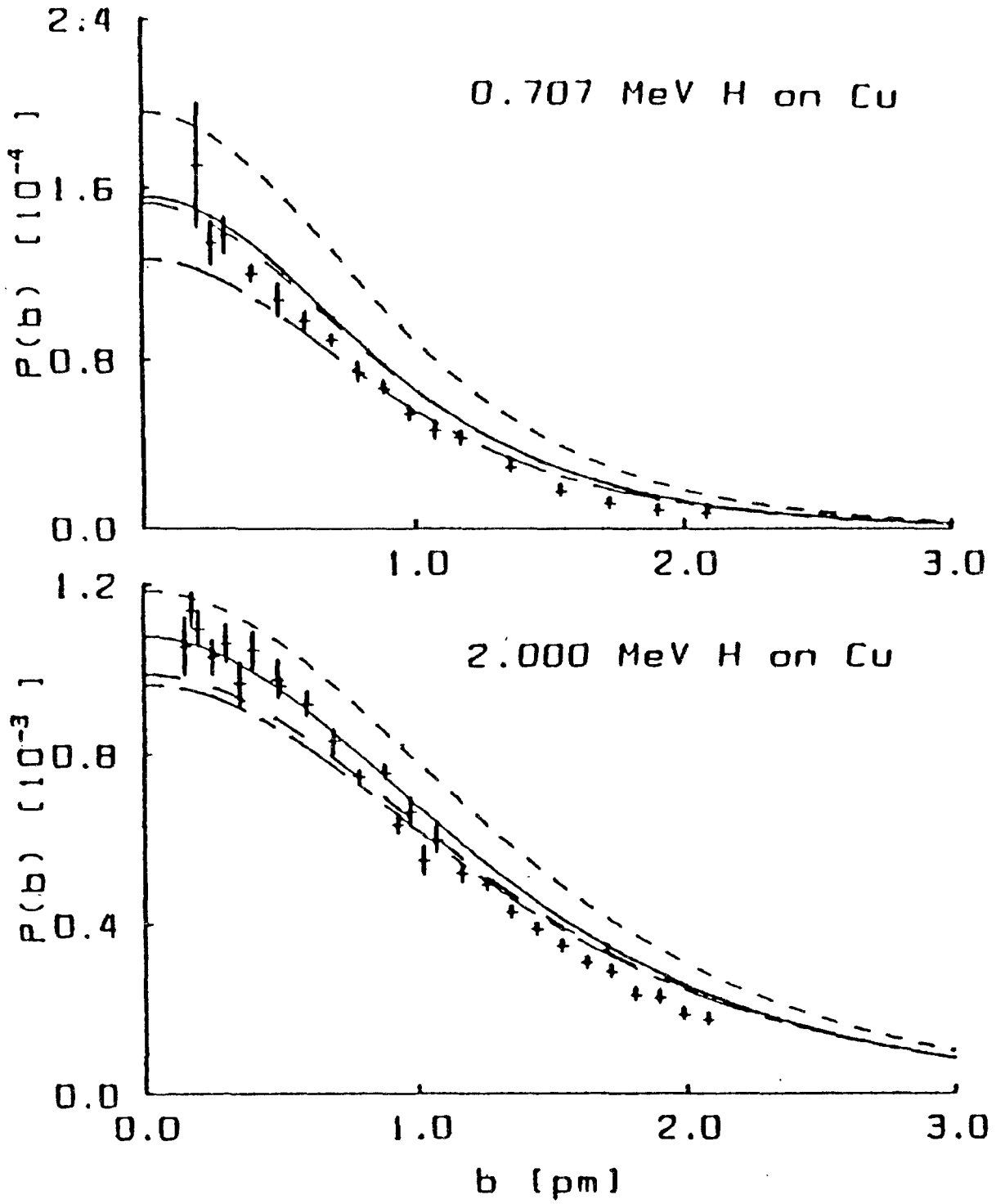

FIG. 2.57. Impact parameter dependence of K-shell ionization probability in proton-copper collisions. Experimental data (+) due to Andersen et al [232] are compared to the semi-classical approximation (SCA) including various corrections. The solid curve includes corrections for Coulomb repulsion, energy loss, increased binding, and relativistic electron motion [232].

Concerning L-shell ionization, a compilation of experimental x-ray production and ionization cross sections has been produced by Sokhi and Crumpton [230]. For the L-shell, the curve of the cross section versus energy looks similar to that for the K-shell, but the maximum occurs at lower ion impact energies (since the L-shell electrons are slower, i.e., smaller binding energy) and the cross section at the maximum is larger. The cross sections corresponding to the three L-subshells differ; the one for the L_3 subshell being largest.

At low projectile energies, there is, in addition to direct ionization, the possibility of ionizing the inner shell by charge transfer (or electron capture by the projectile, as it is often called). This process contributes about 6% to the total K-shell ionization cross sections of N_2 by protons, and less for heavier targets [216]. Since the reference cross sections [218] are based on empirical ionization data, they include this contribution.

Doubly differential cross sections (differential in ejected electron energy and angle) can also be measured for electrons ejected from inner shells by requiring a coincidence between Auger electrons or characteristic x-rays that signal the decay of an inner shell hole and the ejected electron. Measurements of electron spectra from argon are shown in FIG. 2.56 [231]. The curves marked "L" refer to the L-shell; the "total" is essentially M-shell. Another type of differential cross section can be measured by requiring a coincidence between the projectile scattered at a certain angle and the characteristic x-ray (or Auger electron). Since the scattering angle depends on the impact parameter b of the projectile with respect to the target nucleus, this effectively measures the probability P(b) of inner-shell ionization for a particle incident at an impact parameter b. A typical impact parameter dependent measurement is shown in FIG. 2.57 for ionization of copper by 0.7- and 2-MeV protons [232].

ACKNOWLEDGEMENTS

The authors of this chapter would like to thank Professor M. E. Rudd, University of Nebraska, and W. E. Wilson, Pacific Northwest Laboratory, for their contributions on cross section modeling that were presented in this chapter and R. D. DuBois for many fruitful discussion on the various interaction cross section that lead to energy loss by fast charged particles. The author also wishes to thank members of this report committee and the IAEA for their comments, support, and encouragement. This work was supported in part by the Office of Health and Environmental Research (OHER), U. S. Department of Energy under Contract DE-AC06-76RLO 1830.

REFERENCES

[1] INOKUTI, M. "Introductory Remarks", (TECDOC-506, 1989) IAEA, Vienna (1989) 7.

[2] L. H. TOBUREN, 1991, "Atomic and Molecular Physics in the Gas Phase", Physical and Chemical Mechanisms in Molecular Radiation Biology, (Glass, W.A., Varma, N.M., Eds) Plenum Press, New York (1991) 51.

[3] McDANIEL, E.W. FLANNERY, M.R., THOMAS, E.W., ELLIS, H.W., McCANN, K.J., MANSON, S.T., GALLAGHER, J.W., RUMBLE, J.R., BEATY, E.C., ROBERTS, T.G., Compilation of Data Relevant to Nuclear Pumped Lasers,(Technical Report H-78-1) Vol. V, US Army Missile Research and Development Command, Redstone Arsenal, Alabama (1979) 1917.

[4] PARETZKE, H.G., "Radiation Track Structure Theory", Kinetics of Nonhomogeneous Processes (G. R. Freeman, G.R., Ed), John Wiley & Sons, New York, (1987) 89.

[5] SHYN T.W., SHARP, W.E., Doubly differential cross sections of secondary electrons ejected from gases by electron impact: 50-300 eV on helium, Phys. Rev. A **19** (1979) 557.

[6] RUDD, M.E., DUBOIS, R.D., Absolute doubly differential cross sections for ejection of secondary electrons from gases by electron impact. I. 100 and 200 eV electrons on helium, Phys. Rev. A **16** (1977) 26.

[7] OPAL, C.B., BEATY, E.C., PETERSON, W.K., Tables of energy and angular distributions of electrons ejected from simple gases by electron impact, joint institute for laboratory astrophysics (JILA) Report No. 108 (1971).

[8] OPAL, C.B., BEATY, E.C., PETERSON, W.K., Tables of secondary electron production cross sections, Atomic Data **4** (1972) 209.

[9] GORUGANTHU, R.R., BONHAM, R.A., Secondary-electron-production cross sections for electron impact ionization of helium, Phys. Rev. A **34** (1986) 103.

[10] MULLER-FIEDLER, R., JUNG, K., EHRHARDT, H., Double differential cross sections for electron impact ionization of helium, J. Phys. B **19** (1986) 1211.

[11] GOODRICH, M., Electron scattering in helium, Phys. Rev. **52** (1937) 259.

[12] SETHURAMAN, S.K., REES, J.A., GIBSON, J.R., Report of the University of Liverpool, Dept. of Electrical Engineering and Electronics (1972).

[13] ODA, N., NISHIMURA, F., TAHIRA, S., Energy and angular distributions of secondary electrons resulting from ionizing collisions of electrons with helium and krypton, J. Phys. Soc. Japan **33** (1972) 462.

[14] DuBOIS, R.D., M. E. RUDD, M.E., Absolute doubly differential cross sections for ejection of secondary electrons from gases by electron impact. II. 100-500 eV electrons on neon, argon, molecular hydrogen and molecular nitrogen, Phys. Rev. A **17** (1978) 843.

[15] MATHIS, R.E., VROOM, D.A., The Energy distributions of secondary electrons from Ar, N_2, H_2O and H_2O with clusters present, J. Chem. Phys. **64** (1976) 1146.

[16] SHYN, T.W., SHARP, W.E., KIM, Y.-K., Doubly Differential cross sections of secondary electrons ejected from gases by electron impact: 25-250 eV on H2, Phys. Rev. A **24** (1981) 79.

[17] GORUGANTHU, R.R., WILSON, W.G., BONHAM, R.A., Secondary electron production cross sections for electron impact ionization of molecular nitrogen, Phys. Rev. A **35** (1987) 540.

[18] TISONE, G.C., Energy and angular distributions of electrons ejected from N_2 by electron impact, Sandia Laboratory Report SC-RR-710051, Sandia Laboratories, Albuquerque, New Mexico (1971) 1.

[19] SHYN, T.W., Doubly differential cross sections of secondary electrons ejected from gases by electron impact: 50-400 eV on N_2, Phys. Rev. A **27** (1983) 2388.

[20] SHYN, T.W., SHARP, W.E., Doubly differential cross sections of secondary electrons ejected from molecular oxygen by electron impact, Phys. Rev. A **43** (1991) 2300.

[21] ODA, N., Energy and angular distributions of electrons from atoms and molecules by electron impact, Radiat. Res. **64** (1975) 80.

[22] BOLORIZADEH, M.A., RUDD, M.E., Angular and energy dependence of cross sections for ejection of electrons from water vapor. I. 50-2000 eV electron impact, Phys. Rev A **33** (1986) 882.

[23] HOLLMAN, K.W., KERBY III, G.W., RUDD,M.E., MILLER, J.H., MANSON, S.T., Differential cross sections for secondary electron production by 1.5-keV electrons in water vapor, Phys. Rev. A **38** (1988) 3299.

[24] MA, C., BONHAM, R.A., Secondary electron production cross sections for 800 ev electron-impact ionization of carbon monoxide, Phys. Rev. A **38** (1988) 2160.

[25] SHYN, T.W., SHARP, W.E., Doubly differential cross sections of secondary electrons ejected from gases by electron impact: 50-400 eV on CO_2, Phys. Rev. A **20** (1979) 2332.

[26] EHRHARDT, H., HASSELBACHER, J.H., JUNG, K., SCHULZ, M., WILLMANN, K., Collisional ionization of helium by 250 eV electrons: experiments with completely determined kinematics. J. Phys. **B** 5 (1972) 2107.

[27] EHRHARDT, H., HASSELBACHER, K.H., JUNG, K., SCHUBERT, E., WILLMANN, K., Electron impact ionization of argon: measurements of triple differential cross sections, J. Phys. B **7** (1974) 69.

[28] BEATY, E.C., HESSELBACHER, K.H., HONG, S.P., MOORE, J.H., Measurements of the triple-differential cross sections for low-energy electron-impact Ionization of Helium, Phys. Rev. A **17** (1978)1592.

[29] HONG, S.P., BEATY, E.C., Measurements of the triple-differential cross section for low-energy electron-impact ionization of argon, Phys. Rev. A **17** (1978) 1829.

[30] EHRHARDT, H., HASSELBACHER, K.H., JUNG, K., SCHULZ, M., TAKAAT, T., WILLMANN, K., Z. Phys. **244** (1971) 254.

[31] KIM, Y.-K., Angular and energy distributions of secondary electrons from helium: Slow electrons ejected by electron impact. Phys. Rev. A **28** (1983)656.

[32] KIM, Y.-K., Angular distribution of secondary electrons in the dipole approximation, Phys. Rev. A **6** (1972) 666.

[33] KIM, Y.-K., "Secondary electron spectra", Radiation Research, Biomedical, Chemical, and Physical Prospectives, Academic Press, Inc., New York (1975) 219.

[34] KIM, Y.-K., Energy distributions of secondary electrons I. Consistency of experimental data, Radiat. Res. **61** (1975) 21.

[35] KIM, Y.-K., INOKUTI, M., Slow electrons ejected by fast charged particles, Phys. Rev. A **7** (1973) 1257.

[36] KIM Y.-K., NOGUCHI, T., Secondary electrons ejected from he by protons and electrons, Int. J. Radiat. Phys. Chem. **7** (1975) 77.

[37] INOKUTI, M., Inelastic collisions of fast charged particles with atoms and molecules - the Bethe theory revisited, Rev. Mod. Phys. **43** (1971) 297.

[38] INOKUTI, M., ITIKAWA, Y., TURNER, T.E., Addenda: Inelastic collisions of fast charged particles with atoms and molecules - the Bethe theory revisited, Rev. Mod. Phys. **50** (1978) 23.

[39] RUDD, M.E., Differential and total cross sections for ionization of helium and hydrogen by electrons, Phys. Rev. A **44** (1991) 1644.

[40] TOBUREN, L.H., Angular distributions of electrons emitted from gases and thin foils during light ion bombardment, Scanning Microscopy Supplement **4** (1990) 239.

[41] TOBUREN, L.H., 1982, "Continuum electron emission in heavy-ion collisions", Nuclear Methods 2; High-Energy Ion-Atom Collisions (BRENYI, D., HOCK, G., Eds), Elsever, New York, (1982) 53.

[42] TOBUREN, L.H., "Atomic and Molecular Processes of Energy Loss by Energetic Charged Particles", (TECDOC-506, 1989) IAEA, Vienna (1989)160.

[43] RUDD, M.E., MACEK, J., Mechanisms of electron production in ion-atom collisions, Case Studies At. Phys. **3** (1972) 47.

[44] RUDD, M.E., Mechanisms of electron production in ion-atom collisions, Radiat. Res. **64** (1975) 153.

[45] STOLTERFOHT, N., "Excitation in energetic ion-atom collisions accompanied by electron emission", Topics in Current Physics V.: Structure and Collisions of Ions and Atoms, (SELLIN, I.A., Ed.) Springer-Verlag, Berlin (1978) 155.

[46] KUYATT, C.E., JORGENSEN, Jr., T., Energy and angular dependence of the differential cross section for production of electrons by 50-100 keV protons in hydrogen gas, Phys. Rev. **130** (1963) 1444.

[47] RUDD, M.E., JORGENSEN, Jr., T., Energy and angular distributions of electrons ejected from hydrogen and helium gas by protons, Phys. Rev. **131** (1963) 666.

[48] RUDD, M.E., SAUTTER, C.A., BAILEY, C.L., Energy and angular distributions of electrons ejected from hydrogen and helium by 100 to 300 keV protons, Phys. Rev. **151** (1966) 20.

[49] TOBUREN, L.H., Distributions in energy and angle of electrons ejected from molecular nitrogen by 0.3-1.7 Mev protons, Phys. Rev. A **3** (1971)216.

[50] TOBUREN, L.H., WILSON, W.E., Distributions in energy and angle by electrons ejected from molecular hydrogen by 0.3-1.5 MeV protons, Phys. Rev. A **5** (1972) 247.

[51] TOBUREN, L.H., "Angular distributions of electrons ejected by fast protons", VII International Conference on the Physics of Electronic and Atomic Collisions, Abstracts of Papers, North Holland, Amsterdam (1971) 1120.

[52] RUDD, M.E., Energy and angular distributions of secondary electrons from 5-100 keV proton collisions with hydrogen and nitrogen molecules, Phys. Rev. A **20** (1979) 787.

[53] CHENG, W.-Q., RUDD, M.E., HSU, Y.-Y., Differential cross sections for ejection of electrons from rare gases by 7.5-150 keV protons, Phys. Rev. A **39** (1989) 2359.

[54] GIBSON, D.K., REID, I.D., Double differential cross sections for electron ejection from helium by fast protons, J. Phys. B **19** (1986) 3265.

[55] STOLTERFOHT, N., Angular and energy distributions of electrons produced by 200-500 keV protons in gases II. Results for nitrogen, Z. Physik **248** (1971) 92; and STOLTERFOHT, N., "Energy and angular distribution of electrons ejected from atoms ionized by protons", VII International Conference on the Physics of Electronic and Atomic Collisions, Abstracts of Papers, North Holland, Amsterdam, (1971) 1123.

[56] MANSON, S.T., TOBUREN, L.H., MADISON, D.H., STOLTERFOHT, N., Energy and angular distribution of electrons ejected by fast protons and electrons: Theory and experiment, Phys. Rev. A **12** (1975) 60.

[57] RUDD, M.E., TOBUREN, L.H., STOLTERFOHT, N., Differential cross sections for ejection of electrons from helium by protons, Atomic Data and Nuclear Data Tables **18** (1976) 413.

[58] RUDD, M.E., WEBSTER, G.L., BLOCKER, C.A., MADISON, D.A., "Ejection of electrons from helium by protons from 5-100 keV", IX International Conference on the Physics of Electronic and Atomic Collisions, Abstracts of Papers, University of Washington Press, Seattle (1975) 745.

[59] TOBUREN, L.H., MANSON, S.T., KIM Y.-K., Energy distributions of secondary electrons III. Projectile energy dependence for ionization of He, Ne, and Ar by protons, Phys. Rev.A **17** (1978) 148.

[60] RUDD, M.E., MADISON, D.H., Comparison of experimental and theoretical electron ejection cross sections in helium by proton impact from 5 to 100 keV, Phys. Rev. A **14** (1976) 128.

[61] CROOKS, G.B., RUDD, M.E., Experimental evidence for the mechanism of charge transfer to continuum states, Phys. Rev. Lett. **25** (1970) 1599.

[62] BERNARDI, G.C., SUAREZ, S., FAINSTEIN, P.D., GARBOTTI, C.R., MECKBACH, W., KOCKE, P., Two-center effects in electron emission in $^{3}He^{2+}$ - He and H^{+} - He collisions at intermediate energies, Phys. Rev. A **40** (1989) 6863.

[63] PEDERSEN, J.O., HVELPLUND, P., PETERSEN, A.G., FAINSTEIN, P.D., Two-center effects in electron emission from the impact of fast multiply charged projectiles on helium, J. Phys. B **23** (1990) L597.

[64] CROOKS, J.B., RUDD, M.E., Angular and energy distributions of cross sections for electron production by 50-300 keV proton impact on N_2, O_2, Ne, and Ar, Phys. Rev. A 3 (1971) 1628.

[65] TOBUREN, L,H. MANSON, S.T., "On the unreliability of the hydrogenic approximation for inelastic collision of fast charged particles with atoms: Ionization of neon by protons", VIII International Conference on the Physics of Electronic and Atomic Collisions, Abstracts of Papers, Institute of Physics, Belgrad (1973) 695.

[66] CRISWELL, T.L., TOBUREN, L.H., RUDD, M.E., Energy and angular distributions of electrons ejected from argon by 5 keV to 1.5 MeV protons, Phys. Rev. A **16** (1977) 508.

[67] GABLER, H., "Emission von elektronen beim stoss hochenergetischer protonen mit argon", Ph.D. Thesis, Free University, Berlin (1974).

[68] CRISWELL, T.L., WILSON, W.E., TOBUREN, L.H., "Energy and angular distribution of electrons ejected from argon by 5-2000 keV H_2^+ impact", IX International Conference on the Physics of Electronic and Atomic Collisions, Abstracts of Papers, University of Washington Press, Seattle (1975) 749.

[69] MANSON, S.T., TOBUREN, L.H., "Energy and angular distribution of electrons ejected from ar by 1-MeV proton impact ionization: Theory and experiment", IX International Conference on the Physics of Electronic and Atomic Collisions, Abstracts of Papers, University of Washington Press, Seattle (1975) 751.

[70] RUDD, M.E., JORGENSEN, JR., T., VOLZ, D.J., Electron energy spectrum from Ar^+ - Ar and H^+ - Ar collisions, Phys. Rev. **151** (1966) 28.

[71] SATAKA, M., OKUNO, K., URAKAWA, J., ODA, N., "Doubly differential cross sections of electron ejection from argon by 5-20 keV H^+, H_2^+, and $He^{+"}$, International Conference on the Physics of Electronic and Atomic Collisions, Abstracts of Papers, The Society of Atomic Collision Research, Kyoto, (1979) 620.

[72] RUDD, M.E., TOBUREN, L.H., STOLTERFOHT, N., Differential cross sections for ejection of electrons from argon by protons, Atomic Data and Nuclear Data Tables **23** (1979) 405.

[73] MANSON, S.T., TOBUREN, L.H., "Energy and angular distribution of electrons ejected from Kr by 1 MeV proton impact ionization: Theory and experiment", X International Conference on the Physics of Electronic and Atomic Collisions, Abstracts of Papers, Commissariat A L'Energie Atomique, Paris (1977) 990.

[74] TOBUREN, L.H., MANSON, S.T., "Differential cross sections for ionization of krypton by fast protons: Theory and experiment", XI International Conference on the Physics of Electronic and Atomic Collisions, Abstracts of Papers, The Society for Atomic Collision Research, Kyoto, (1979) 628.

[75] TOBUREN, L.H., Distributions in energy and angle of electrons ejected from xenon by 0.3 to 2.0 Mev protons, Phys. Rev. A **9** (1974) 2505.

[76] TOBUREN, L.H., WILSON, W.E., Energy and angular distributions of electrons ejected from water vapor by 0.3 - 1.5 MeV protons, J. Chem. Phys. **66** (1977) 5202.

[77] BOLORIZADEH, M.A., RUDD, M.E., Angular and energy dependence of cross sections for ejection of electrons from water vapor. II. 15-150 keV proton impact, Phys. Rev. A **33** (1986) 888.

[78] STOLTERFOHT, N., Angular and energy distribution of electrons produced by 200-500 keV protons in gases: I. Experimental Arrangement, Z. Physik **248** (1971) 81.

[79] WILSON, W.E, TOBUREN, L.H., Electron emission from proton-hydrocarbons-molecule collisions at 0.3 to 2 MeV, Phys. Rev. A **11** (1975) 1303.

[80] LYNCH, D,J., TOBUREN, L.H., WILSON, W.E., Electron emission from methane, ammonia, monomethylamine and dimethylamine by 0.25 to 2.0 MeV protons, J. Chem. Phys. **64** (1976) 2616.

[81] TOBUREN, L.H., WILSON, W.E., PORTER, L.E., Energy and angular distributions of electrons ejected in ionization of SF_6 and TeF_6 by fast protons, J. Chem. Phys. **67** (1977) 4212.

[82] WILSON, W.E., TOBUREN, L.H., Electron emission in H_2^+ - H_2 collisions from 0.6 to 1.5 MeV, Phys. Rev. A **7** (1973) 1535.

[83] CACAK, R.K., JORGENSEN, Jr., T., Absolute doubly differential cross sections for production of electrons in He^+-Ne and Ar^+-Ar collisions, Phys. Rev. A **2** (1970) 1322.

[84] WOERLEE, P.H., GORDEEV, Yu. S., DE WAARD, H., SARIS, F.W.,1981, The production of continuous electron spectra in collisions of heavy ions and atoms. B: direct coupling with the continuum, J. Phys. B **14** (1981) 527.

[85] WOERLEE, P.H., Electron and x-ray emission in collisions of multiply charged ions and atoms, Thesis, University of Amsterdam, (1979) Unpublished.

[86] STOLTERFOHT, N., SCHNEIDER, D., BURCH, D., WIEMAN, H., RISLEY, J.S., Mechanisms for electron production in 30-MeV O^{n+} + O_2 collisions, Phys. Rev. Lett. **33** (1974) 59.

[87] N. ODA, N., NISHIMURA, F., "Energy and angular distributions of electrons ejected from He and H_2 bombarded by equal velocity H_2^+ and He^+ ions", XI International Conference on the Physics of Electronics and Atomic Collisions, Abstracts of Papers, The Society for Atomic Collision Research, Kyoto, (1979) 622.

[88] FRYAR, J., RUDD, M.E., and J. S. Risley, Doubly differential cross sections for electron production by impact of H^o, H_2^o, $^3He^o$, and $^4He^o$ on helium, XI International Conference on the Physics of Electronic and Atomic Collisions, Abstracts of Papers, Commissariat A L'Energie Atomique, Paris (1977) 984.

[89] RUDD, M.E., RISLEY, J.S., FRYAR, J., ROLFES, R.G., Angular and energy distribution of electrons form 15-to 150-keV H° + He Collisions, Phys. Rev. A **21** (1980) 506; and RUDD, M.E., RISLEY, J.S., FRYAR, J., "Double differential cross sections for electron production by neutral hydrogen on helium", XI International Conference on the Physics of Electronic and Atomic Collisions, Abstracts of Papers, Commissariat A L'Energie Atomique, Paris(1977) 986.

[90] TOBUREN, L.H., WILSON, W.E., Ionization of noble gases by equal velocity He^{+}, He^{++}, and H^{+} ions, X International Conference on the Physics of Electronic and Atomic Collisions, Abstracts of Papers (Commissariat A L'Energie Atomique, Paris (1977) 1006.

[91] TOBUREN, L.H., WILSON, W.E., Differential cross sections for ionization of argon by .3-2 MeV He^{2+} and He^{+} ions, Phys. Rev. A **19** (1979) 2214.

[92] TOBUREN, L.H., WILSON, W.E., POPOWICH, R.J., Secondary electron emission from ionization of water vapor by 0.3- to 2.0-MeV He^{+} and He^{2+} ions, Radiat. Res. **82** (1980) 27.

[93] BOLORIZADEH, M.A., RUDD, M.E., Angular and energy dependence of cross sections for ejection of electrons from water vapor. III. 20-150 keV Neutral Hydrogen Impact, Phys. Rev A **33** (1986) 893.

[94] URAKAWA, J., TOKORO, N., ODA, N., Differential cross sections for ejection of electrons and dissociative ionization cross sections for 5-20 keV H_2+ and H_3^{+} impacts on helium, J. Phys. B **14** (1981) L431.

[95] SATAKA, M., URAKAWA, J., ODA, N., Measurements of double differential cross sections for electrons ejected from 5-20 keV H^{+}, H_2^{+}, and He^{+} impacts on argon, J. Phys. B **12** (1979) L729-L734.

[96] TOBUREN, L.H., "Secondary electron emission in collisions of 1.2 MeV C^{+} ions with He, Ne, Ar, and CH_4", XI International Conference on the Physics of Electronic and Atomic Collisions, Abstracts of Papers, The Society for Atomic Collisions Research, Kyoto (1979) 630.

[97] REINHOLD, C.O., SCHULTZ, D.R., OLSON, R.E., TOBUREN, L.H., DUBOIS, R.D.,1990, Electron emission from both target and projectile in C+ + He collisions, J. Phys. B **23** (1990) L297.

[98] TOBUREN, L.H., DUBOIS, R.D., REINHOLD, C.O., SCHULTZ, D.R., OLSON, R.E., Experimental and theoretical study of the electron spectra in 66.7-350-keV/u C^{+} + He collisions, Phys. Rev. A **42** (1990) 5338.

[99] TOBUREN, L.H., "Differential cross sections for electron emission in heavy ion-atom collisions", Proceedings of the Fifth Conference on the use of Small Accelerators, IEEE Transactions on Nuclear Science **NS-26** (1979) 1056.

[100] STOLTERFOHT, N., SCHNEIDER, D., "Double differential cross sections for electron emission from argon by 50-500-keV N^{+} and O^{+} impact", Proceedings of the Fifth Conference on the Use of Small Accelerators, IEEE Transactions on Nuclear Science **NS-26** (1979) 135.

[101] GORDEEV, Yu.S., WOERLEE, P.H., DE WAARD, H., SARIS, F.W., "Continuous electron spectra produced in Kr^{n+} - Kr collisions", XI International Conference on the Physics of Electronic and Atomic Collisions, Abstracts of Papers, The Society for Atomic Collision Research, Japan, (1979) 746.

[102] GORDEEV, Yu.S., WOERLEE, P.H., DE WAARD, H., SARIS, F.W., The production of continuous electron spectra in collisions of heavy ions and atoms. A. Molecular autoionization, J. Phys. B **14** (1981) 513.

[103] SCHNEIDER, D.H., DEWITT, D.R., BAUER, R.W., MOWAT, J.R., GRAHAM, W.G., SCHLACHTER, A.S., SKOGVALL, B., FAINSTEIN, P., RIVAROLA, R.D., Absolute doubly differential cross sections for electron emission in collisions of 3.5-MeV/u Fe^{17+} and Fe^{22+} ions with he and ar gas targets, Phys. Rev. A **46** (1992) 1296.

[104] STOLTERFOHT, N., SCHNEIDER, D., TANIS, J., ALTEVOGT, H., SALIN, A., FAINSTEIN, P.D., RIVAROLA, R., GRANDIN, J.P., SCHEURER, J.N., ANDRIAMONJE, S., BERTAULT, D., CHEMIN, J.F., Evidence for two-center effects in the electron emission from 25 MeV/u Mo^{40+} + He collisions: Theory and experiment, Europhysics Lett. **4** (1987) 899.

[105] KELBCH, C., OLSON, R.E., SCHMIDT, S., SCHMIDT-BÖCKING, H., HAGMANN, S., Unexpected angular distribution of the δ-electron emission in 1.4 MeV/u U^{33+} - rare gas collisions, J. Phys. B **22** (1989) 2171.

[106] SCHMIDT-BÖCKING, H., RAMM, U., KRAFT, G., ULLRICH, J., BERG, H., KELBCH, C., OLSON, R.E., HAGMANN, S., JAIZHEN, F., δ-electron emission in fast heavy ion atom collisions, Adv. Space Res. **12** (1992) 7.

[107] SCHNEIDER, D.H., DEWITT, D.R., SCHLACHTER, A.S., OLSON, R.E., GRAHAM, W.G., MOWAT, J.R., DUBOIS, R.D., LLOYD, D.H., NONTEMAYOR, V., SCHIWIETZ, G., Strong continuum-continuum couplings in the direct ionization of Ar and He atoms by 6-MeV/u U^{38+} and Th^{38+} Projectiles, Phys. Rev. A **40** (1989) 2971.

[108] BREINIG, M., ELSTON, S.B.,HULDT, S., LILJEBY, L., VANE, C.R., BERRY, S.D., GLASS, G.A., SCHAUER, M., SELLIN, I.A., ALTON, G.D., DATZ, S., OVERBURY,S., LAUBERT, R., SUTER,M., Experiments concerning electron capture and loss to the continuum and convey electron electron production by highly ionized projectiles in the 0.7-8.5 MeV/u range traversing the rare gases, polycrystalline solids, and axial channels in gold, Phys.Rev A **25** (1982) 3015.

[109] TOBUREN, L.H., WILSON, W.E.,1975, Time-of-flight measurements of low-energy electron energy distributions from ion-atom collisions, Rev. Sci. Instrum. **46** (1975) 851.

[110] TOBUREN, L.H., MANSON, S. T., KIM, Y.-K., Energy distributions of secondary electrons. III: Projectile energy dependence for ionization of He, Ne, and Ar by protons, Phys. Rev. A **17** (1978) 148.

[111] RUDD, M.E., GREGOIRE, D.,1969, "Energy distribution of electrons from ionization of helium and hydrogen by proton collisions: Comparison of classical theories and experiment", Physics of the One- and Two-Electron Atoms, (BOPP, F., KLEINPOPPEN, H., Eds) North Holland, Amsterdam, (1969) 795.

[112] VRIENS, L., Binary-encounter proton-atom collision theory, Proc. Phys. Soc. **90** (1967) 935.

[113] BONSEN, T.F.M, VRIENS, L., Angular distribution of electrons ejected by charged particles I. Ionization of He and H_2 by protons, Physica **47** (1970) 307.

[114] TOBUREN, L.H., STOLTERFOHT, N.,ZIEM, P., SCHNEIDER, D., Electronic Screeening in heavy-ion-atom collisions, Phys. Rev. **24** (1981) 1741.

[115] TOBUREN, L.H., ZIEM, P., STOLTERFOHT, N., SCHNEIDER,D., PROST, M., Dynamic screening by projectile electrons in heavy ion collisions, IEEE Transactions on Nuclear Science, **NS-28** (1981) 1131.

[116] MADISON, D.H., Angular distribution of electrons ejected from helium by proton impact, Phys. Rev. A **8** (1973) 2449.

[117] OLDHAM, Jr., W.J,B., Calculations of the energy and angular distributions of electrons ejected from helium by protons, Phys. Rev. **161** (1967) 1.

[118] SALIN, A., Ionization of atomic hydrogen by proton impact, J. Phys. B **2** (1969) 631.

[119] MACEK, J., Theory of the forward peak in the angular distribution of electrons ejected by fast protons, Phys. Rev. A **1** (1970) 235.

[120] MACEK, J., private communication, (1971).

[121] MECKBACH, W., KOCKE, P.J., GONI, A.R., SUAREZ, S., Effects of the Wannier ridge on secondary-electron spectra in proton-helium collisions, Phys. Rev. Lett. **57** (1986) 1587.

[122] OLSON, R.E., GAY, T.J., BERRY, H.G., HALE, E.B., IRBY, V.D., Saddle-point electrons in ionizing ion-atom collisions, Phys. Rev. Lett. **59** (1987) 36.

[123] FAINSTEIN, P.D., PONCE, V.H., RIVAROLA, D., Electron emission from multielectron atoms by ion impact at intermediate and high energies, J. Phys. B **22** (1989) 1207.

[124] WILSON, W.E., "Analytical expression for cross section data", Pacific Northwest Laboratory Annual Report for 1976, Part 4, BNWL-2100 PT4/UC-48, (1977), 40.

[125] WILSON, W.E., "Analytical expression for cross section data", Pacific Northwest Laboratory Annual Report for 1977, Part 4, PNL-2500 PT4/UC-48, (1978) 2.7.

[126] BERKOWITZ, J., Photoabsorption, Photoionization and Photoelectron Spectroscopy, Academic Press, New York, (1979).

[127] TAN, K.H., BRION, C.E., VAN DER LEEUW, PH.E., VAN DER WIEL, M.J., 1978, Absolute oscillator strengths (10 - 60 eV) for the photoabsorption, photoionization, and photofragmentation of H_2O, Chem. Phys. **29** (1978) 299.

[128] BLAKE, A.J., CARVER, J.H.,1967, Determination of partial photoionization cross sections by photoelectron spectroscopy, J. Chem. Phys. **47** (1967) 1038.

[129] BUTTS, J.J., KATZ, R., Theory of RBE for heavy ion bombardment of dry enzymes and viruses, Radiat. Res. **30** (1967) 855.

[130] CHATTERJEE, A., SHAEFER, H.J., Microdosimetric structure of heavy ion tracks in tissue, Rad. and Environm. Biophys. **13** (1976) 215.

[131] WATSON, R.L., TOBUREN, L.H., Auger spectra of carbon and argon following ionization by equal-velocity α particles and deuterons, Phys. Rev. A **7** (1973) 1853.

[132] DETTMAN, K., HARRISON, K.G., LUCAS, M.W., Charge exchange to the continuum for light ions in solids, J. Phys. B **7** (1974) 269.

[133] MANSON, S.T., TOBUREN, L.H., Energy and angular distributions of electrons from fast He^+ + He collisions, Phys. Rev. Lett. **46** (1981) 529.

[134] McGUIRE, J.H., STOLTERFOHT, N., SIMONY, P.R., Screening and anti-screening by projectile electrons in high-velocity atomic collisions, Phys. Rev. A **24** (1981) 97.

[135] DUBOIS, R.D., MANSON, S. T., Coincidence study of doubly differential cross sections: projectile ionization in He^+-He collisions, Phys. Rev. Lett. **57** (1986) 1130.

[136] HEIL, O., MAIER, R., HUZEL, M., GROENEVELD, K.-O., DUBOIS, R.D., A systematic investigation of ionization occurring in few electron systems, Phys. Rev. Lett., in press.

[137] MILLER, J.H., WILSON, W.E., MANSON, S.T., RUDD, M.E., Differential cross sections for ionization of water vapor by high-velocity bare ions and electrons, J. Chem. Phys. **86** (1987) 157.

[138] SCHRAM, B.L., DE HEER, F.J., VAN DER WIEL, M/J., KISTEMAKER, J., Ionization cross sections for electrons (0.6 - 20 keV) in noble and diatomic gases, Physica **31** (1965) 94.

[139] SHIMAMURA, I., Cross sections for collisions of electrons with atoms and molecules, Scientific Papers of the Institute of Physical and Chemical Research (Japan) **82** (1989) 1.

[140] GALLAGHER, J.W., BRION, C.E., SAMSON, J.A.R., LANGHOFF, P.W., Absolute cross sections for molecular photoabsorption, partial photoionization, and ionic photofragmentation processes, J. Phys. Chem. Ref. Data **17** (1988) 9.

[141] MILLER J.H., MANSON, S.T. Differential cross sections for ionization of helium, neon, and argon by fast electrons, Phys. Rev. A **29** (1984) 2435.

[142] MICHAUD, M., SANCHE, L., Total cross sections for slow-electron (1-20 eV) scattering in solid H_2O, Phys. Rev. A **36** (1987) 4672.

[143] SANCHE, L., Investigation of ultra-fast events in radiation chemistry with low-energy electrons, Radiat. Phys. Chem. **34** (1989) 15.

[144] CLOUTIER, P., SANCHE, L., A trochoidal spectrometer for the analysis of low-energy inelastically backscattered electrons, Rev. Sci. Instrum. **60** (1989) 1054.

[145] MARSOLAIS, R.M., SANCHE, L., Mechanisms producing inelastic structures in low-energy electron transmission spectra, Phys. Rev. B **38** (1988) 11 118.

[146] RUDD, M.E., KIM, Y.-K., MADISON, D.H.,GAY, T.J., Electron production in proton collisions with atoms and molecules: energy distributions, Rev. Mod. Phys. **64** (1992) 441.

[147] GRISSOM, J.T., COMPTON, R.N., GARRETT, W.R., Slow electrons from electron impact ionization of He, Ne, and Ar, Phys Rev. A **6** (1972) 977.

[148] ROBINSON, B.B., Modifications of the impulse approximation for ionization and detachment cross sections, Phys. Rev. **140** (1965) A764.

[149] MILLER, J.H., TOBUREN, L.H., MANSON, S.T., Differential cross sections for ionization of helium, neon, and argon by high-velocity ions, Phys. Rev. A **27** (1983) 1337.

[150] WILSON, W.E., MILLER, J.H., TOBUREN, L.H., MANSON, S.T., Differential cross sections for ionization of methane, ammonia, and water vapor by high velocity ions, J. Chem Phys. **80** (1984) 5631.

[151] INAGAKI, T., HAMM, R.N., ARAKAWA, E.T., Optical and dielectric properties of DNA in the extreme ultraviolet, J. Chem. Phys. **61** (1974) 4246.

[152] SONTAG, W., WEIBEZAHN, F., Absorption of DNA in the region of vacuum-UV, Rad. and Environm. Biophys. **12** (1975) 169.

[153] FUJII, M., TAMURA, T., MIKAMI, N., ITO, M., Electronic spectra of uracil in a supersonic jet, Chem. Phys. Lett. **126** (1986) 583.

[154] DILLON, M., Private communication (1990).

[155] RUDD, M.E., Differential cross sections for secondary electron production by proton impact, Phys. Rev. A **38** (1988) 6129.

[156] SCHMIDT, S., EULER, J., KELBCH, C., KELBCH, S., KOCH, R., KRAFT, G., OLSON, R.E., RAMM, U., ULLRICH, J., SCHMIDT-BÖCKING, H., Doubly differential stopping powers of 1.4 Mev/u U^{33+} in Ne and Ar derived from electron production and multiple ionization cross sections, GSI-89-19, Gesellschaft fur Schwerionenforschung mbH, D-6100 Darmstadt, W. Germany (1989).

[157] RUDD, M.E., DUBOIS, R.D., TOBUREN, L.H., RATCLIFFE, C.A., GOFFE, T.V., Cross sections for ionization of gases by 5-4000 keV protons and for electron capture by 5-150 keV protons, Phys. Rev. A **28** (1983) 3244.

[158] RUDD, M.E., KIM, Y.-K., MADISON, D.H., GALLAHER, J.W., Electron production in proton collisions: total cross sections, Rev. Mod. Phys. **57** (1985) 965.

[159] HOOPER, J.W., McDANIEL, E.W., MARTIN, D.W., HARMER, D.S., Ionization cross sections for protons and hydrogen ions in the energy range 0.15 to 1.10 MeV, Phys. Rev. **121** (1961) 1123.

[160] De HEER, F. J., SCHUTTEN, J., MOUSTAFA, H., Ionization and electron capture cross sections for protons incident on noble and diatomic gases between 10 and 140 keV, Physica **32** (1966) 1766.

[161] McNEAL, R.J., BIRELY, J.H., Laboratory studies of collisions of energetic H^+ and hydrogen with atmospheric constituents, Rev. Geophys. Space Phys. **11** (1973) 633.

[162] DUFAY, M., DESESQUELLES, J., DRUETTA, M., EIDELSBERG, M., Study of nitrogen and oxygen excitation by proton shocks, Ann. Geophys. **22** (1966) 614.

[163] PARK, J.T., SCHOWENGERDT, F.D., SCHOONOVWE, D.R., Collision cross sections for the excitation of the shumann-runge dissociation continuum in molecular oxygen by 20-110 keV protons, Phys. Rev. A **3** (1971) 679.

[164] BARNETT, C.F., HUNTER, H.T., KIRKPATRICK, M.I., ALVAREZ, I., CISNEROS, C., PHANEUF, R.A., "Collisions of H, H_2, He, and Li Atoms and Ions with Atoms and Molecules" ORNL-6086, Vol. 1, Oak Ridge National Laboratory, Oak Ridge, TN, (1990); see also the earlier review of BARNETT, C.F., RAY, J.A., RICCI, E., WILKER, M.I., McDANIEL, W.W., THOMAS, E.W., GILBODY, H.B.,1977, "Atomic data for controlled fusion research" ORNL-5206, Vols. I and II, Oak Ridge National Laboratory, Oak Ridge, TN, (1977).

[165] DUBOIS, R.D., TOBUREN, L.H., Single and double ionization of helium by neutral-particle to fully stripped ion impact, Phys. Rev. A **38** (1988) 3960.

[166] DUBOIS, R.D., Ionization and charge transfer in He^{2+}-rare gas collisions, Phys. Rev. A **33** (1986) 1595.

[167] DUBOIS, R.D., Charge transfer leading to multiple ionization of neon, sodium, and magnesium, Phys. Rev. A **34** (1986) 2738.

[168] DUBOIS, R.D., Ionization and charge transfer in He^{2+}-rare-gas collisions. II, Phys. Rev. A **36** (1987) 2585.

[169] DUBOIS, R.D., Recent studies of simultaneous ionization and charge transfer in helium ion-atom collisions, Nucl. Instrum. Meth. **B24/25** (1987) 209.

[170] DUBOIS, R.D., Multiple ionization of He^+-rare-gas collisions, Phys. Rev. A **39** (1989) 4440.

[171] BERKNER, K.H., GRAHAM, W.G., PYLE, R.V., SCHLACHTER, A.S., STERNS, J.W., Electron-capture, electron-loss, and impact-ionization cross sections for 103- to 3400-keV/u multicharged iron ions colliding with molecular hydrogen, Phys. Rev. A **23** (1981) 2891.

[172] SCHLACHTER, A.S., BERKNER, K.H., GRAHAM, W.G., PYLE, P.V., STERNS, J.W., TANIS, J.A., Collisions of fast, highly stripped carbon, niobium, and lead ions with molecular hydrogen, Phys. Rev. A **24** (1981) 1110.

[173] SCHLACHTER, A.S., Collisions of highly stripped ions at MeV energies in gas targets: charge transfer and ionization, IEEE Transactions on Nuclear Science **NS-28** (1981) 1039.

[174] SCHLACHTER, A.S., BERKNER, K.H., GRAHAM, W.G., PYLE, R.V., SCHNEIDER, P.J., STADER, K.R., STERNS, J.W., TANIS, J.A., Ionization of rare-gas targets by fast highly charged projectiles, Phys. Rev. A **23** (1981) 2331.

[175] GILBODY, H.B., SALIN, A., AUMAYR, R., BARANY, A., BELKIC, D.S., DE HEER, F.J., HOEKSTRA, R., JANEV, R.K., NAKAI, Y., RIVAROLA, R.D., TAWARA, H., WATANABE, T., Reviews of the data base for collisions of C^{q+} and O^{q+} ions with H, H_2, and He, Physica Scripta **T28** (1989) 8.

[176] GALLAGHER, J.W., "Collisions of Electrons with Atoms and Molecules", ORNL, Oak Ridge National Laboratory, Oak Ridge, TN, In preparation.

[177] THOMAS, E.W., "Particle interactions with surfaces", ORNL-6088, Vol. 3 of ORNL-6086, Oak Ridge National Laboratory, Oak Ridge, TN, (1985).

[178] WEISE, W.L., Spectroscopic Data for Iron, ORNL-6089, Vol. 4 of ORNL-6086, Oak Ridge National Laboratory, Oak Ridge, TN, (1985).

[179] PHANEUF, R.A., JANEV, P.K., PINDZOLA, M.S. Collisions of carbon and oxygen ions with electrons, H, H_2, and He, ORNL-6090, vol. 5 of ORNL-6086, Oak Ridge National Laboratory, Oak Ridge, TN, (1987).

[180] WEISE, W.L., MUSGROVE, A., Spectroscopic Data for Titanium, Chromium, and Nickel, ORNL-6551, Vol. 6 of ORNL-6086, Oak Ridge National Laboratory, Oak Ridge, TN, (1989).

[181] BETZ, H., Charge states and charge-changing cross sections of fast heavy ions penetrating through gaseous and solid media, Rev. Mod. Phys. **44** (1972) 465.

[182] FLEISCHMANN, H.H., DEHMAL, R.C., LEE, S.K., Direct-transition features in stripping collisions of heavy neutral atoms and ions, Phys. Rev. A **5** (1973) 1784.

[183] CRANDALL, D.H., MALLORY, M.L., KOCHER, D.C., Charge exchange between multicharged ions of C, N, and O and molecular hydrogen, Phys. Rev. A **15** (1977) 61.

[184] CRANDALL, D.H., Electron transfer between He-like ions and He, Phys. Rev. A **16** (1977) 958.

[185] PHANEAF, R.A., MEYER, F.W., MCKNIGHT, R.H., Single electron capture by multiply charged ions of carbon, nitrogen, and oxygen in atomic and molecular hydrogen, Phys. Rev. A **17** (1978) 534.

[186] OLSEN J.O., HVELPLUND, P., Electron capture and loss in collisions of 100- to 500-keV oxygen in molecular hydrogen, J. Phys. B **7** (1974) 1331.

[187] LOCKWOOD, G.J., Total cross sections for charge transfer for F^+ in H_2, N_2, He, Ne, and Ar, Phys. Rev. A **9** (1974) 1916.

[188] DMITRIEV, I.S., TASHAEV, Yu.A., NIKOIAEV, V.S., TEPLOVA, Ya.A., POPOV, B.M., Experimental study of the loss and capture of electrons by fast multiply charged nitrogen and neon ions in various gases, Sov. Phys. JETP **46** (1977) 884.

[189] SUK, H.C., GUILBAUD, A., HIRD, B., Cross sections for electron capture by Ne^{2+} in He, Ne, Ar, Kr, and Xe between 60 and 200 keV, J. Phys. B **11** (1978) 1463.

[190] HIRD B., SUK, H.C., Single-electron stripping cross sections of N^+ in Ne, Ar, and Kr between 35 and 140 keV, Phys Rev A **14** (1976) 928.

[191] DUBOIS, R.D., Electron production in collisions between light ions and rare gases: The Importance of the Charge-Transfer and Direct-Ionization Channels, Phys. Rev. Lett. **52** (1984) 2348.

[192] DUBOIS, R.D., KOVER, A., Single and double ionization of helium by hydrogen-atom impact, Phys. Rev. A **40** (1989) 3605.

[193] DUBOIS, R.D., TOBUREN, L.H., RUDD, M.E., Multiple ionization of rare gases by H^+ and He^+ impact, Phys. Rev. A **29** (1984) 70.

[194] BOHR, N., Scattering and stopping of fission fragments, Phys. Rev. **58** (1940) 654.

[195] BOHR, N., Velocity-range relation for fission fragments, Phys. Rev. **59** (1941) 270.

[196] KREUSSLER, S., VARELAS, C., BRANDT, W., Target dependence of effective charge in stopping power, Phys. Rev. B **23** (1981) 82.

[197] ANTHONY J.M., LANFORD, W.A., Stopping power and effective charge of heavy ions in solids, Phys. Rev. A **25** (1982) 1868.

[198] BICHSEL, H., Barkas effect and effective charge in the theory of stopping power, Phys. Rev. A **41** (1990) 3642.

[199] MILLER, J.H., GREEN, A.E.S., Proton energy degradation in water vapor, Radiat. Res. **54** (1973) 343.

[200] MATTESON, S., POWER, D., CHAU, E.K.L., Physical state effect in the stopping cross section of H2O ice and vapor for 0.3-2.0 MeV alpha particles, Phys. Rev. A **15**(1977) 856.

[201] PALMER, R.B.J., AKHAVAN-REZAYAT, A., Range-energy relation in stopping power of water, water vapor, and tissue equivalent liquids for alpha particles over the energy range 0.5 - 8 MeV, Proceedings of the Sixth Symposium on Microdosimetry (BOOZ J., EBERT, H.G., Eds) Harwood Publishers, Amsterdam, (1978) 739.

[202] BRANDT, W., KITAGAWA, M., Effective stopping-power charges of swift ions in condensed matter, Phys. Rev. B **25** (1982) 5631.

[203] YARLAGADDA, B.S., ROBINSON, J.E., BRANDT, W., Effective-charge theory and the electronic stopping power of solids, Phys. Rev. B **17** (1978) 3173.

[204] BARKAS, W.H., Nuclear Research Emulsions-I. Techniques and Theory, Academic Press, New York, (1963).

[205] ZIEGLER, J.F., Handbook of stopping cross sections of energetic ions in all elements, Vol. 5, Pergamon Press, New York, (1980).

[206] ZIEGLER, J.F., BIERSACK, J.T., LITTMARK, U., The Stopping and range of ions in solids, Vol. 1, Pergamon Press, New York, (1985).

[207] KRAUSE, M.O., Atomic radiative and radiationless yields for K and L shells, J. Phys. Chem. Ref. Data **8** (1979) 307.

[208] HIPPLER, R., "Impact ionization by fast projectiles", Progress in Atomic Spectroscopy, Part C, (BEYER, H.J., KLEINPOPPEN, H., Eds) Plenum Press, New York, (1984) 511.

[209] HIPPLER, R., JITSCHIN, W., Plane wave born cross sections including exchange for K-shell ionization of light atoms, Z. Physik A **307** (1982) 287.

[210] GLUPE, G., MEHLHORN, W., A new method for measuring electron impact ionization cross sections for inner shells, Phys. Lett. **25A** (1967) 274.

[211] HINK, W., LEES, L., SCHMITT, H.-P., WOLF, A., "Near K-ionization threshold Auger electron measurements for neon under electron impact", Inner-Shell and X-ray Physics of Atoms and Solids (FABIAN, D., KLEINPOPPEN, H., WATSON, L.M., Eds) Plenum Press, New York, (1981) 327.

[212] W. HINK, W., ZIEGLER, A., Der Werkungsquerschnitt fur die Ionisierung der K-Schale von Aluminium Durch Electronenstoss (3-30keV), Z. Physik **226** (1969) 222.

[213] HIPPLER, R., SAEED, K., MCGREGOR, I., KLEINPOPPEN, H., Energy Dependence of characteristic and bremsstrahlung cross sections of argon induced by electron bombardment at low energies, Z. Physik A **307** (1982) 83.

[214] TAWARA, H., HARRISON, K.G., DE HEER, F.J., X-ray emission cross sections and flourescence yields for light atoms and molecules by electron impact, Physica **63** (1973) 351.

[215] PAUL H., MUHR, J., Review of experimental cross sections for K-shell ionization by light ions, Phys. Reports **135** (1986) 47.

[216] LAPICKI, G., Cross sections for K-shell X-ray production by hydrogen and helium ions in elements from beryllium to uranium, J. Phys. Chem. Ref. Data **18** (1989) 111.

[217] BRANDT, W., LAPICKI, G., Energy-loss effect in inner-shell coulomb ionization by heavy charged particles, Phys. Rev. A **23** (1981) 1717.

[218] PAUL, H., SACHER, J., Fitted empirical reference cross sections for k-shell ionization by protons, Atomic Data and Nuclear Data Tables **42** (1989) 105.

[219] OGIER, W.T., LUCUS, G.J., MURRY, J.S., HOLZER, T..E., Soft X-ray production by 1.5-MeV protons, Phys. Rev. **134A** (1964) 1070.

[220] KHAN, J.M., POTTER, D.L., WORLEY, R.D., Studies in X-ray production ny proton bombardment of Cr, Mg, Al, Nd, Sm, Gd, Tb, Dy, and Ho, Phys.Rev. **139A** (1965) 1735.

[221] KHAN, J.M., POTTER, D.L., WORLEY, R.D., Characteristic K-shell X-ray production in magnesium, aluminum, and copper by 60- to 500-keV protons, Phys. Rev. **133A** (1964) 890.

[222] SHIMA, K., MAKINO, I., SAKISAKA, M., Isotope dependence in K-, L-, and M-shell ionization cross sections by protons and deuterons, J. Phys. Soc. Japan **30** (1971) 611.

[223] BASBAS, G., BRANDT, W., LAUBERT, R., Universal cross sections for K-shell ionization by heavy charged particles. I. Low particle velocities, Phys. Rev. A **7** (1973) 983.

[224] TAWARA, H., HASHIYA, Y., ISHII, K., MORITA, S., K-shell ionization of light elements by protons and helium-3 ion impact, Phys. Rev. A **13** (1976) 572.

[225] BASBAS, G., BRANDT, W., LAUBERT, R., Universal cross sections for K-shell ionization by heavy charged particles. II. Intermediate particle velocities, Phys. Rev. A **17** (1978) 1655.

[226] SERA, K., ISHII, K., KEMIYA, M., KUWAKO, A., MORITA, S., K-shell ionization of Al and Cu for 0.5- to 40-MeV proton impact, Phys. Rev. A **21** (1980) 1412.

[227] BONANI, G., STROLLER, Ch., STOECKLI, M., SUTER, M., WOELFLI, W., Quantitative spurenanalyse mit ioneninduzierter Röntgenstrahlung, Helv Phys. Acta **51** (1978) 272.

[228] GERETSCHLÄGER, M., BENKA, O., K-shell ionization cross sections for Al, Ti, V, Cr, Fe, Ni, Cu, and Mg by protons and oxygen ions in the energy range 0.3-6.4 MeV, Phys. Rev. A **34** (1986) 866.

[229] PAUL, H., BOLIK, O., Fitted empirical reference cross sections for K-shell ionization by alpha particles. in preparation

[230] SOKHI, R.S., CRUMPTON, D., Experimental L-shell X-ray production and ionization cross sections for proton impact, Atomic Data and Nuclear Data Tables **30** (1984) 49.

[231] SARKADI, L., BOSSLER, J., HIPPLER, R., LUTZ, H.O., Angular distribution of electrons ejected from the argon L-Shell by 350 keV proton impact, J. Phys. B **16** (1982) 71.

[232] ANDERSEN, J.U., LAEGSGAARD, E., LUND, M., Impact parameter dependence of K-shell ionization, Nuclear Instruments and Methods **192** (1982) 79.

Chapter 3

ELECTRON COLLISION CROSS SECTIONS

T.D. Märk
Institut für Ionenphysik, Leopold Franzens Universität,
Innsbruck, Austria

Y. Hatano
Department of Chemistry, Tokyo Institute of Technology,
Tokyo, Japan

F. Linder
Fachbereich Physik, Universität Kaiserslautern,
Kaiserslautern, Germany

3.1. Introduction

The major mechanism for energy loss of fast charged particles (electrons, protons, heavier ions) and photons is the ionization of atomic and molecular constituents (i.e. production of electron-ion pairs) of the irradiated materials (in their gaseous, liquid and solid state). Therefore a large fraction of the primary energy is converted to kinetic energy of secondary electrons, including electrons with energies ranging from thermal up to very high energies. The interaction of these secondary electrons as well as that of the primary electrons with matter is of utmost importance in assessing radiation damage occurring in radiation therapy.

In order to carry out these calculations, cross section functions (cross sections versus electron energy) must be known for inelastic and elastic electron collisions for targets and materials used in dosimetry and radiotherapy (i.e., in particular key substances such as Ne, Ar, H_2, N_2, O_2, H_2O, CO_2, CH_4 and C_3H_8 gases; see also chapter 1), i.e. including total and differential elastic scattering cross sections; total, partial, and differential ionization cross sections for parent and fragment ions; partial electronic, vibrational and rotational excitation cross sections; total and partial attachment cross sections, and cross sections for the dissociation of molecules into neutral fragments.

Differential cross sections have been discussed in chapter 1. Here, experimental data and theoretical formulae for partial and total cross sections will be presented and discussed critically. The chapter will start with a short introduction and definition of the concept of ionization cross sections.

3.2. Electron impact ionization mechanism and definitions

Electrons accelerated through a potential of several tens of volts have a de Broglie wavelength of ~ 0.1 nm. This wavelength and the molecular dimensions are similar and mutual quantum effects (distortions) occur; that is, an electron may be promoted from a lower to a higher orbital (excitation) or-if the electron energy is greater than a critical value (the ionization energy or appearance energy) - an electron may be ejected from the target, thus producing a positive ion (cation).

Conversely, direct attachment of the incident electron to an atomic target to give a stable anion is less likely. The reason for this is that the translational energy of the attaching electron and the binding energy (electron affinity) must be taken up (accommodated) in the emerging product (anion). Usually, the excess energy leads to either fragmentation (in the case of a molecular target) of the anion or shake-off (detachement) of the electron.

As the electron energy is increased, the variety and abundance of the cations produced from a specific molecular target will increase, because the electron ionization process may proceed via different reaction channels, each of which gives rise to characteristic ionized and neutral products. These include the following types of ions [1,2]: parent ion, fragment ion, multiply charged ion, excited ion, metastable ion, rearrangement ion, and ion pair. For the simple case of a diatomic molecule AB these reaction channels are (including excitation and dissociation):

$\mathbf{AB + e \rightarrow}$

$AB^+ + e_s + e_e$	(single ionization)	(3.1)
$AB^{2+} + e_s + 2e_e$	(double ionization)	(3.2)
$AB^{z+} + e_s + ze_e$	(multiple ionization)	(3.3)
$AB^{K+} + e_s + e_e$	(K-shell ionization)	(3.4)
$AB^{**} + e_s \rightarrow AB^+ + e_s + e_e$	(autoionization)	(3.5)
$AB^{+*} + e_s + e_e \rightarrow A^+ + B + e_s + e_e$	(fragmentation)	(3.6)
$AB^{2+} + e_s + 2e_e$	(autoionization)	(3.7)
$AB^+ + e_s + e_e + hv$	(radiative ionization)	(3.8)
$A^+ + B + e_s + e_e$	(dissociative ionization)	(3.9)
$A^+ + B^- + e_s$	(ion pair formation)	(3.10)
$AB^* + e_s$	(excitation)	(3.11)
AB^{-*}	(attachment)	(3.12)
$A^- + B$	(dissociative attachment)	(3.13)
$A + B + e$	(dissociation into neutrals)	(3.14)
$A^* + B + e$	(dissociation into excited neutrals)	(3.15)

where e_s is a "scattered" electron and e_e an "ejected" electron. Other products may be obtained, especially when one is using complex atomic targets (i.e., polyatomic molecules [1] or clusters [3,4,5]).

Most of the ionization reactions summarized above (e.g., process (3.1) through (3.4), (3.9), and (3.10)) can be classified as direct ionization events, in which the ejected and the scattered electron leave the ion within 10^{-16} sec. Conversely, there exist alternative ionization channels (competing with direct ionization) in which the electrons are ejected one after the other (see Fig. 3.1 for a schematic representation of possible ionization mechanism [6]). For instance, autoionization (e.g., process (3.5) and (3.7)) can be described as a two-step reaction: First, a neutral molecule (or atom) is raised to a superexcited state, which can exist for some finite time. Then, radiationless transition into the continuum occurs. For molecules, the upper autoionization rate (and hence the ionization cross section) is limited

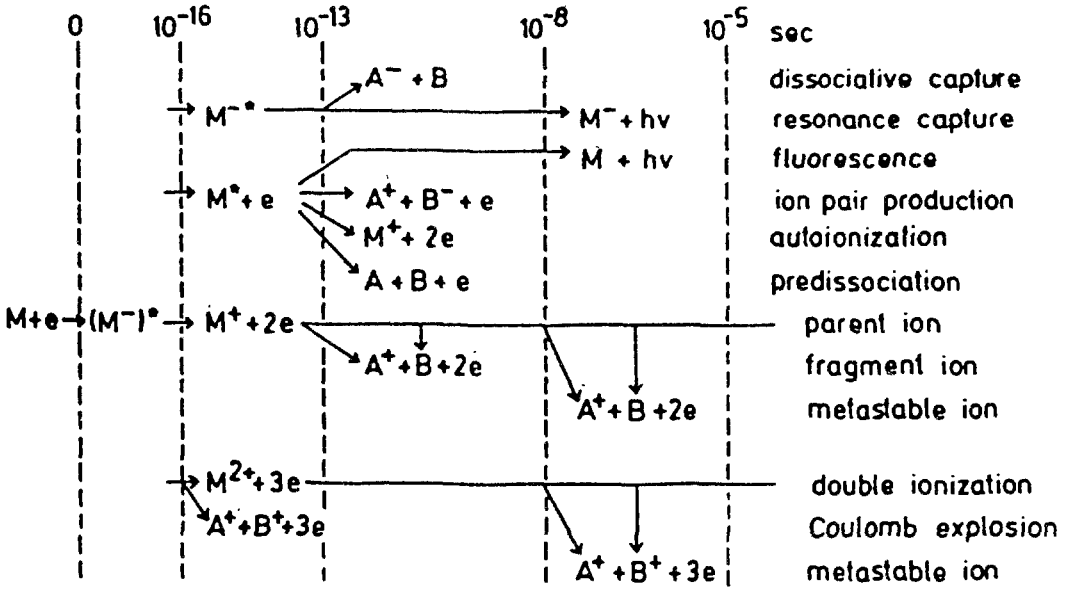

Fig. 3.1 Schematic time chart of possible electron impact ionization processes after Märk [6].

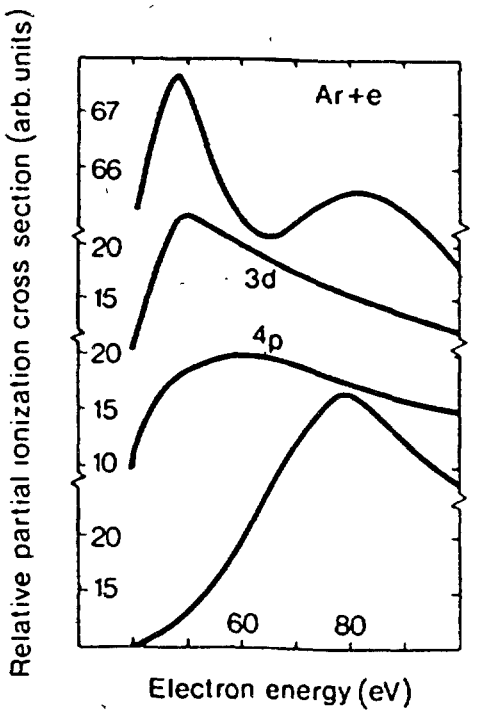

Fig. 3.2 Partial ionization cross section function for Ar + e → Ar^+ + 2e after Crowe et al. [7]. Middle curves illustrate the variation of the strengths of the 3d and 4p autoionization features (see text). Bottom curve shows the efficiency of production of Ar^+ via direct ionization processes. Top curve is the sum of the two middle curves and the bottom curve.

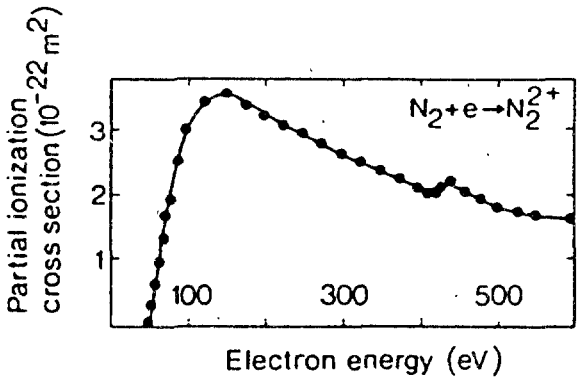

Fig. 3.3 Partial electron impact ionization cross section function for the reaction $N_2 + e \rightarrow N_2^{2+} + 3e$ after Halas and Adamczyk [8].

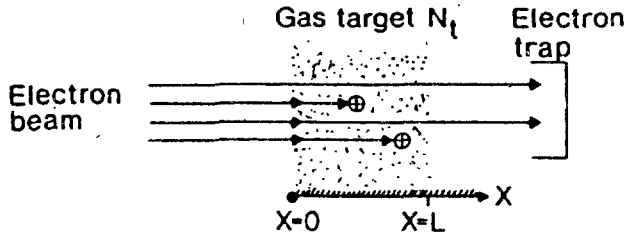

Fig. 3.4 Schematic view of an electron impact ionization experiment after Märk [6].

by the characteristic energy-storage mode frequency. In addition, if predissociation (into two neutrals) is faster than autoionization, the latter will not occur at an appreciable rate.

Moreover, autoionization is a resonance process and this will complicate the respective ionization cross-section dependence (i) at low electron energy (e.g., deviation from the threshold law; e.g., see Ref.[1]), but also (ii) at higher energies (e.g., see the partial ionization cross-section function for the production of Ar^+ shown in Fig. 3.2 [7]). The top curve in Fig. 3.2 shows the variation of the cross-section function obtained by summing over all possible ionization mechanisms. The two curves in the middle illustrate the variation of the strengths of the 3d and 4p autoionization processes (e.g., $Ar + e \rightarrow Ar^*(3s3p^63d) + e \rightarrow Ar^+ (3s^23p^5) + 2e$). The bottom curve shows the behavior of the direct ionization mechanism (see reaction (3.1)).

Quite similarly, multiply charged ions can be formed in a two-step autoionization process. First, a singly charged ion is produced by the ejection of an electron from an inner shell (inner-shell ionization process (3.4)). This internally ionized atom (or molecule) may then be transformed (see reaction (3.7)) into a multiply charged ion by a series of

radiationless transitions (Auger effect). Figure 3.3 shows as an example the ionization cross section curve for the production of N_2^{2+}, which demonstrates the occurrence and effect of this Auger autoionization process at ~ 430 eV [8].

Because of ambiguities in the nomenclature in the literature some definitions will be given here concerning various ionization cross section terms used:
Consider, as shown in Fig. 3.4, a parallel, homogeneous, and monoenergetic beam of electrons crossing a semiinfinite medium containing N_t target particles per cubic centimeter at rest. If $n(0)_e$ represents the incident electron current, i.e., the number of electrons per unit time, the unscattered electron current at depth x (taking into account only the ionizing collisions) is given by the exponential absorption law

$$n(x)_e = n(0)_e \exp(-N_t \sigma x) \tag{3.16}$$

If $N_t \sigma x << 1$ (single-collision condition*), the number of ions, $n(L)_i$, generated per second along the collision interaction path x = L (over which the ions collected and analyzed) is

$$n(L)_i = n(0)_e N_t \sigma_c L, \tag{3.17}$$

where σ_c is the counting ionization cross section in square centimeters. The total positive-ion current, i_t, produced in this interaction volume is given by

$$i_t = n(0)_e \, eN_t \sigma_t L, \tag{3.18}$$

where σ_t is the total ionization cross section and e the elemental charge. In the measurement of σ_t no information is obtained in general about individual partial cross sections. If the produced ions are analyzed with a mass spectrometer according to their mass, m, to charge z ratio, however, the respective individual ion currents, i_{ms}, are given by

$$i_{ms} = n(0)_e eN_t \, \sigma_{zi} \, zL, \tag{3.19}$$

where σ_{zi} is the partial ionization cross section for the production of a specific ion i with charge ze.

---

* This condition my be achieved by using low enough number densities N_t and this condition is necessary in order to avoid multiple electron collisions and secondary ion molecule reactions, both of which would lead to erroneous cross section results. If this condition is fullfilled, equ. (3.16) may be linearized allowing to derive the relationship given in equ. (3.17).

Total and counting ionization cross sections of a specific target system are the weighted and the simple sum of the various single and multiple partial cross sections, respectively, i.e.

$$\sigma_t = \Sigma\sigma_{zi} \cdot z \quad \text{and} \quad \sigma_c = \Sigma\sigma_{zi} \tag{3.20}$$

Under certain circumstances single ionization is dominant (e.g., for atoms at electron energies below the double ionization threshold and for many molecules in the entire energy regime) and then

$$\sigma_t = \sigma_c \tag{3.21}$$

Sometimes the macroscopic cross section $s = \sigma_t N_t$ which represents the total effective cross-sectional area for ionization of all target molecules in 1 cm^3 of the target medium, is used. This quantity is numerically equal to the ionization efficiency, usually defined as the number of charges (or ion pairs) produced per centimeter of path at 1 Torr and 0°C.

For more information and details on the ionization mechanisms and processes see Ref. [1,2,6, 9-12].

3.3. Total electron impact ionization cross sections of atoms and molecules

3.3.1. Experimental

According to equ. (3.18) the determination of the total ionization cross section σ_t requires the measurement of four quantities, i.e., i_t, $n(0)_e$, N_t and L. Kieffer and Dunn [13] have extensively discussed the problems encountered when trying to measure accurate experimental σ_t values (see also a more recent review [14]).

One of the earliest and widest used experimental methods to determine total ionization cross sections is the condenser plate method of Tate and Smith [15]. This method was later used very successfully by Rapp et al. [16] to produce their benchmark total ionization cross section functions for the rare gases and several small molecules. In short (see Fig. 3.5), in this method a magnetically collimated electron beam is directed through a target gas of known density N_t. All ions which are produced in a well defined region are completely removed and collected. The main limitation of this method is the absolute measurement of the gas density, a difficult matter for many gases. Djuric et al. [17,18] have recently overcome some of the difficulties by using a capacitance manometer to determine the gas pressure in their parallel plate ionization chamber. De Heer and Inokuti [14], in their definitive 1985 review on total electron impact ionization cross sections, discussed and

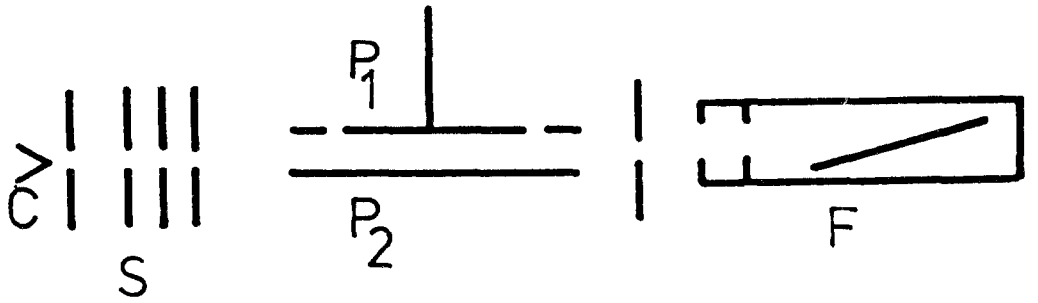

Fig 3 5 Schematic view of the parallel plate condensor apparatus after Tate and Smith [15] C cathode, S collimator slits, P_1 and P_2 condensor plates and F Faraday cage

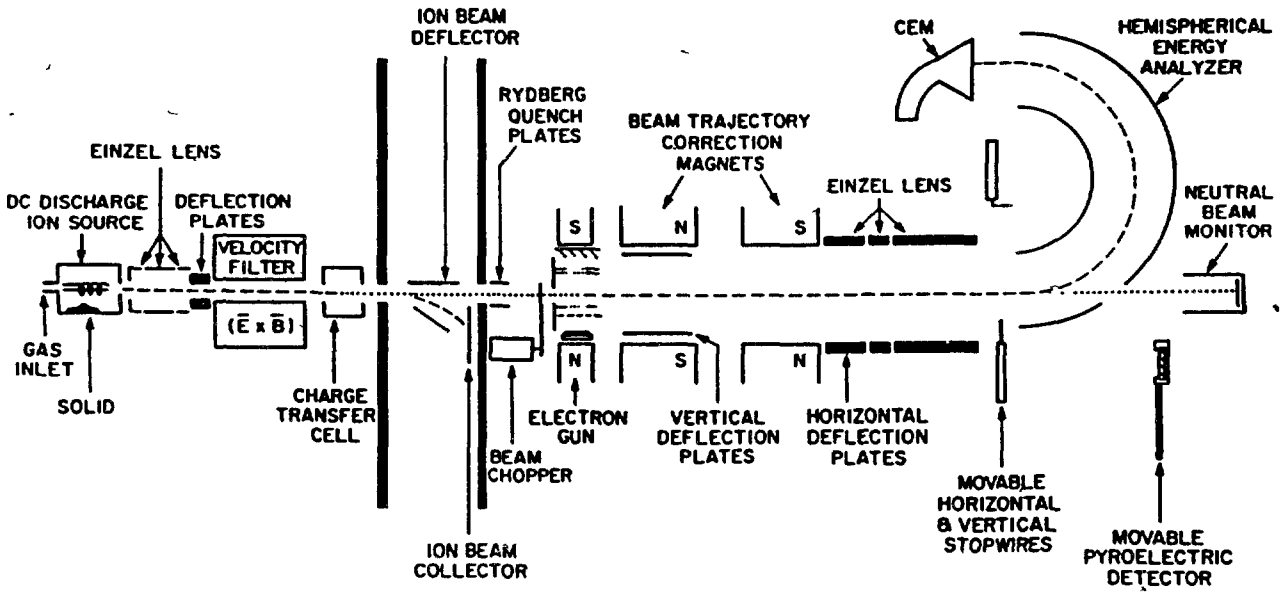

Fig 3 6 Schematic view of the fast neutral beam apparatus after Freund et al [39]

summarized experiments and results up to this year, including also the Lozier tube [19], the summation method [20], gas-filled counters [21] and crossed beam methods [22]

Excellent data on total (and partial, see below) ionization cross sections have been obtained recently by Freund and coworkers [23] using a modified crossed-beam method where an electron beam is crossed with a fast neutral beam, prepared by charge transfer neutralization of a mass selected ion beam. This approach was first used for atomic ionization cross-section measurements by Peterson et al [24]; it has since been used by Ziegler et al [25] and has been refined by Harrison and coworkers [26-29]. Extensions by Freund and coworkers [30-39] have made it a powerful method (see also Becker and coworkers [40]).

In the fast neutral beam apparatus of Freund et al. (Fig. 3.6), atomic or molecular ions are (i) extracted from a dc discharge, (ii) accelerated to 3 kV, and (iii) mass-separated by a Wien filter. The ion beam is then neutralized by charge transfer with a gas selected to have an ionization energy resonant with that of the ions. The pressure is adjusted to neutralize several percent of the ions, with the remainder being deflected to a collector. According to Freund [23] the resulting neutral beam in general has a flux of $10^{10}s^{-1}$. Its relative intensity is measured by kinetic electron ejection from a metal surface. For accurate flux measurements, a pyroelectric crystal is used to calibrate the electron ejection coefficient. Ionization is produced by crossing the fast neutral beam with a well-characterized electron beam. The resulting ions are steered and focussed with magnetic and electrostratic fields to a hemispherical energy analyzer. This analyzer separates ions of different charge or mass, since all ions retain essentially the same velocity of the 3 keV parent neutral beam. For molecular species, 100% collection of fragments is possible. Ions are finally detected by a channel electron multiplier. The biggest advantage of this method is that it permits preparation of a pure beam even of unstable species, and that the high beam velocity permits accurate flux measurements.

3.3.2. Theoretical

The theoretical treatment of the basic electron impact ionization process (i.e., in the exit channel a full three body problem) has received a great deal of attention. Quantum mechanical (approximation) calculations are difficult, few and some of them not as accurate as necessary [41]. Therefore, other methods have been developed, with the goal to obtain reasonably accurate cross sections. Three different approaches have been used, i.e., (i) empirical and semiempirical formulae, (ii) classical theories, and (iii) semiclassical collision theories. Theoretical methods have been reviewed several times in great detail [1,2,6,9,11,41-50], in particular the accuracy and reliability of the most widely used formulae [1,47,50]. Most of these treatments apply only to single ionization. Nevertheless these formulae (for a compilation of these fomulae see Ref. [47,50]) are used in general also for the estimation of total ionization cross sections (e.g., see equ. (3.21)). In the following, very recent theoretical developments will be presented which allow the easy calculation of electron impact (single) ionization cross sections as a function of electron energy for (ground state and excited) atoms, radicals, molecules and clusters [51-57].

Using classical mechanics, Thomson [58] was the first to derive a formula for the electron impact ionization cross section (for single ionization), i.e.,

$$\sigma = \sum_n 4\pi a_o^2 \, \xi_n \left(\frac{E_i^H}{E_{in}} \right) \frac{u-1}{u^2} \qquad (3.22)$$

with a_o the Bohr radius, ξ_n the number of electrons in the n-th subshell, E_{in} the ionization energy in the n-th subshell, E_i^H, ionization energy of H, $u = E/E_{in}$, and E energy of incident electron. This classical treatment has been modified by several authors (e.g. see Ref. [47,50]) using different initial conditions. None of these formulae, however, represents according to Rudge [41] a substantial improvement over the Thomson formula, because all of them suffer from the same large deviations at high and low energies as does the Thomson treatment. A definitive improvement introduced by Gryzinski [59] is the assumption of a continuous velocity distribution for atomic electrons, leading to an expression for the cross section

$$\sigma = \sum_n 4\pi a_o^2 \xi_n \left(\frac{E_i^H}{E_{in}}\right)^2 \frac{1}{u}\left(\frac{u-1}{u+1}\right)^{3/2} \left\{1+\frac{2}{3}\left(1-\frac{1}{2u}\right)\ln(2.7+(u-1)^{1/2}\right\} \tag{3.23}$$

Burgess [60] and Vriens [61] also suggested further means to improve the classical theory by incorporating certain quantal features, e.g. exchange effects. Although all these formulae constitute a significant improvement, they still fail in case of rather simple atoms such as for instance neon, nitrogen and fluorine in predicting the correct magnitude of ionization cross section functions (e.g. see Ref. [51,52]). Moreover, while in certain cases empirical formulas (such as the Lotz formula [62]) are helpful, many of them are of limited usefulness [41] (they are providing good fits to certain classes of known data (see also the approximate analytic formula given by Bell et al. [63]), but will not allow reliable predictions for other unknown systems) and have been superseeded by later formulas which we discuss in the following.

Based on a comparison between these classical formulae and the Born-Bethe formula [64] (which is only accurate at higher energies due to the use of the Born approximation),

$$\sigma = \sum_n 4\pi a_o^2 \xi_n \frac{M_{nl}^2}{u} \ln\left(4c_{nl}u\right) \tag{3.24}$$

with M_{nl} dipole matrix element and c_{nl} collisional parameter (to be determined by Fano plot analyses, see Ref. [14,43]), Deutsch and Märk [52] recently suggested to replace the Bohr radius in the classical formulae (3.23) by the radius of the corresponding electron subshell. This step is in line (i) with a result of Bethe's calculation that the ionization cross section of an atomic electron with quantum numbers (n,l) is approximately proportional to the mean square radius $\langle r^2 \rangle_{nl}$ of the electron shell (n,l) [65] and (ii) with the experimental observation of a correlation between the maximum of the atomic cross section and the sum

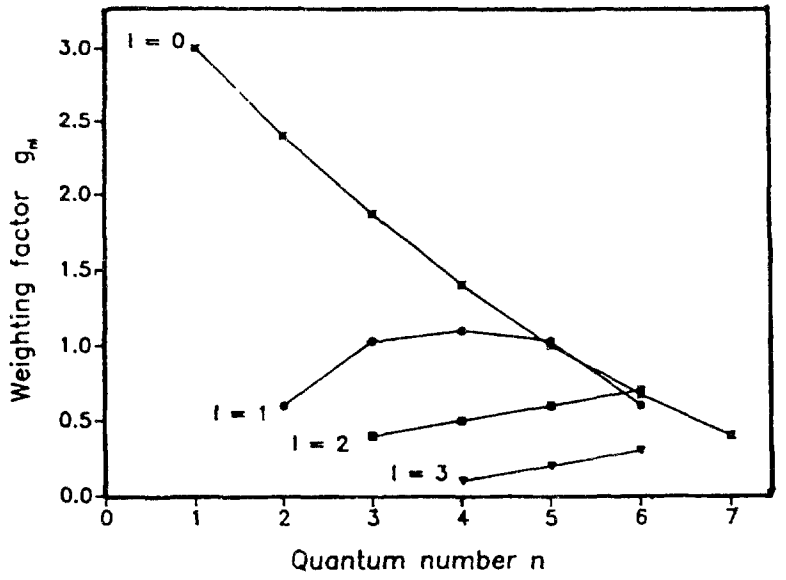

Fig. 3.7 Weighting factors g_{nl} as a function of quantum numbers n and l after Margreiter et al. [53,54].

of the mean square radii of all outer electrons [65-67]. Following up this suggestion, Margreiter et al. [53,68] successfully applied this DM approach to a large number of ground state and excited state atoms using

$$\sigma = \sum_{n,l} g_{nl}\, \pi r_{nl}^2\, \xi_{nl}\, \frac{1}{u}\left(\frac{u-1}{u+1}\right)^{3/2}\left\{1+\frac{2}{3}\left(1-\frac{1}{2u}\right)\ln\left(2.7+(u-1)^{1/2}\right)\right\} \tag{3.25}$$

with r_{nl}^2 the mean square radius of the nl shell, and g_{nl} weighting factors (following the original approach of Bethe [64], who calculated these "Ionisierungsfaktoren" as a function of the quantum numbers n and l using hydrogenic wave functions; see also considerations by Mann [66]). Margreiter et al. [53,54] determined via a fitting procedure these generalized weighting factors g_{nl} (see Fig. 3.7) using accurate experimental data of the rare gases and uranium as test cases. It was demonstrated that formula (3.25) leads in general to an improved agreement with the experimental results not only in case of ground state atoms, but also in case of excited state atoms [53]. Recently, these authors derived relationships for the product $g_{nl} \cdot E_{in}$ yielding with its use even better agreement with the experimental data [68,69], allowing also the calculation of inner-shell ionization cross sections [55] (e.g. see corresponding data for Ne and Ar in Figs 3.8 and 3.9) and outer-shell ionization cross sections [80]. For more information on inner-shell ionization cross sections and their possible applications see Ref. [55,81].

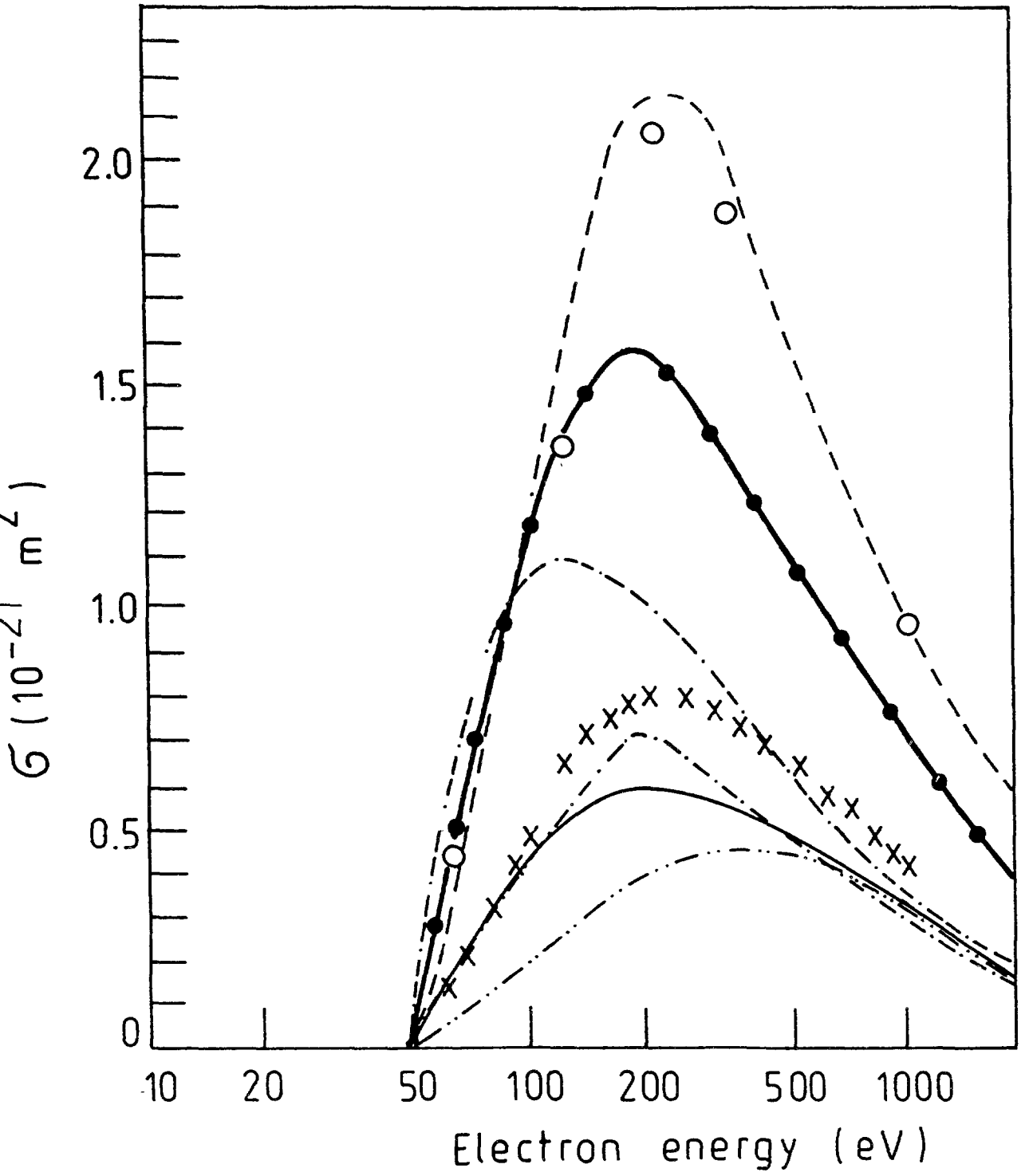

Fig. 3.8 L_I-shell ionization cross section versus electron energy for neon: x experimental results of Luyken et al. [70], ---- Born approximation by Peach [71], o Born approximation by Omidvar and Kyle [72], -.-.- binary encounter calculation by Vriens [73], — ·· — semi-empirical calculation by Lotz [62], --.-- Born approximation by Mc Guire [74], - - - semiclassical calculation (after Gryzinski [50]) using equ. (3.23), and —— DM approach [52] using modified equ. (3.25), see Ref. [55]. It is interesting to note the failure of the semiclassical concept (equ (3.23)) and, moreover, it is important to note that recently de Heer and coworkers [75] revised their experimental data [70] downwards by a factor of 3.7.

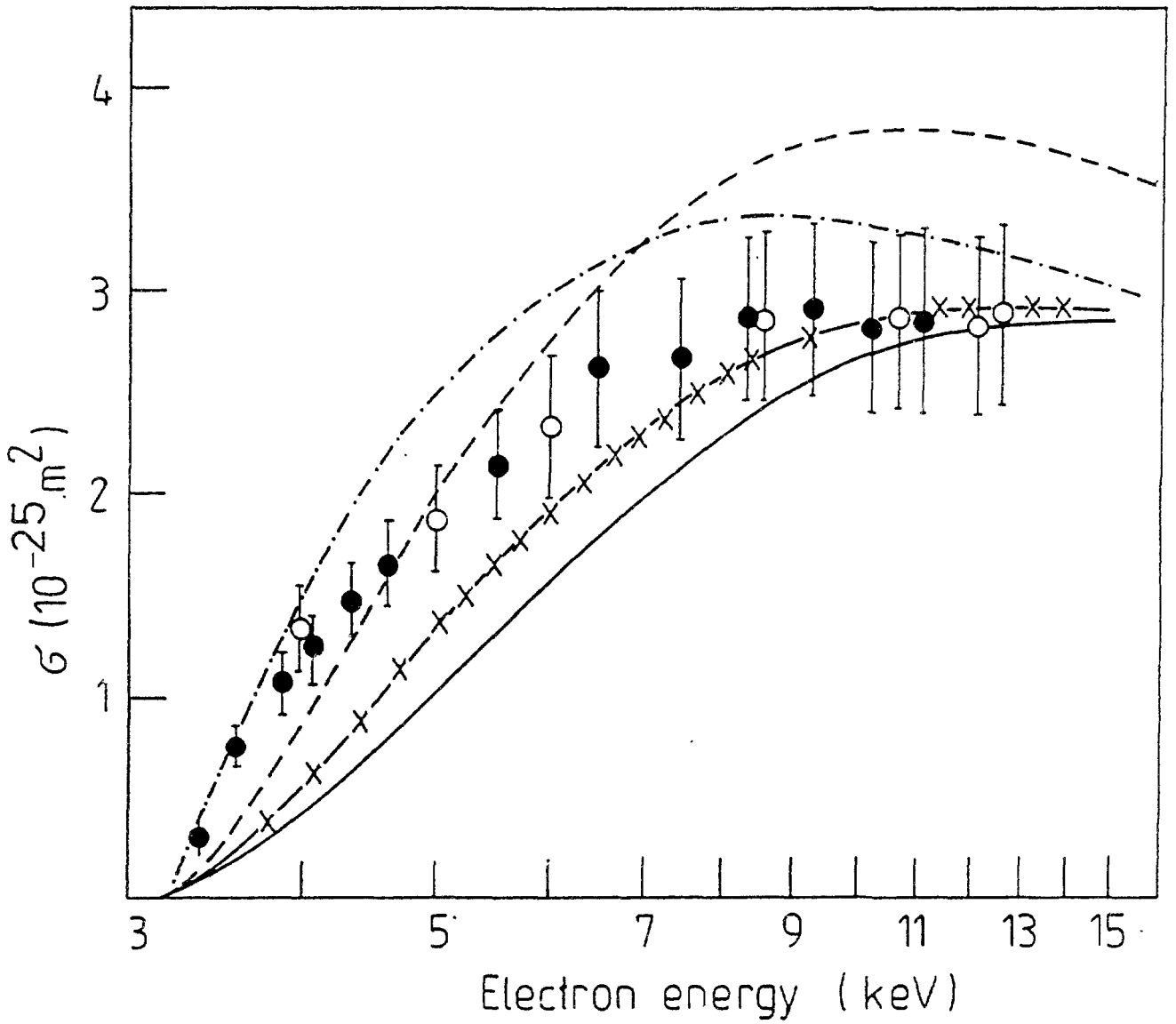

Fig. 3.9 K-shell ionization cross section versus electron energy for argon: • experimental results of Hippler et al. [76], o experimental results of Tawara et al. [77], ---PWBA calculation of Hippler et al. [78], -x-x PWBA Ochkur calculation of Hippler et al. [78], - - - -Coulomb Born exchange calculation of Moores et al. [79] and —— DM approach [52] using a modified equ. (3.25), see Ref. 55.

Whereas in the case of atoms several approaches at various theoretical levels (quantum mechanical, semi-classical, classical, empirical) are existing (see above), in the case of molecules the available theoretical tools are not yet sufficiently accurate and/or versatile. Some of the classical and semiclassical formulae developed for atoms have been applied with limited success (see also below) to certain selected cases or classes of molecules (e.g. H_2, hydrocarbons, chlorine compounds [50,82]); these formulae fail however in predicting data for other cases or classes of molecules (e.g. molecules containing fluorine [51,83,84]). Based on the successful concept of the additivity rule [65-67, 83,84],

Deutsch et al. [51] introduced recently an empirical correction factor which allows the use of these previous classical and semiclassical theories to calculate ionization cross section functions of molecules containing fluorine and related atoms.

Conversely, Khare and associates [85,86] were among the first to suggest a formula specifically designed to allow the calculation of total (and recently also partial [87,88]) ionization cross sections of molecules. This Jain-Khare formula is based on a semi-empirical

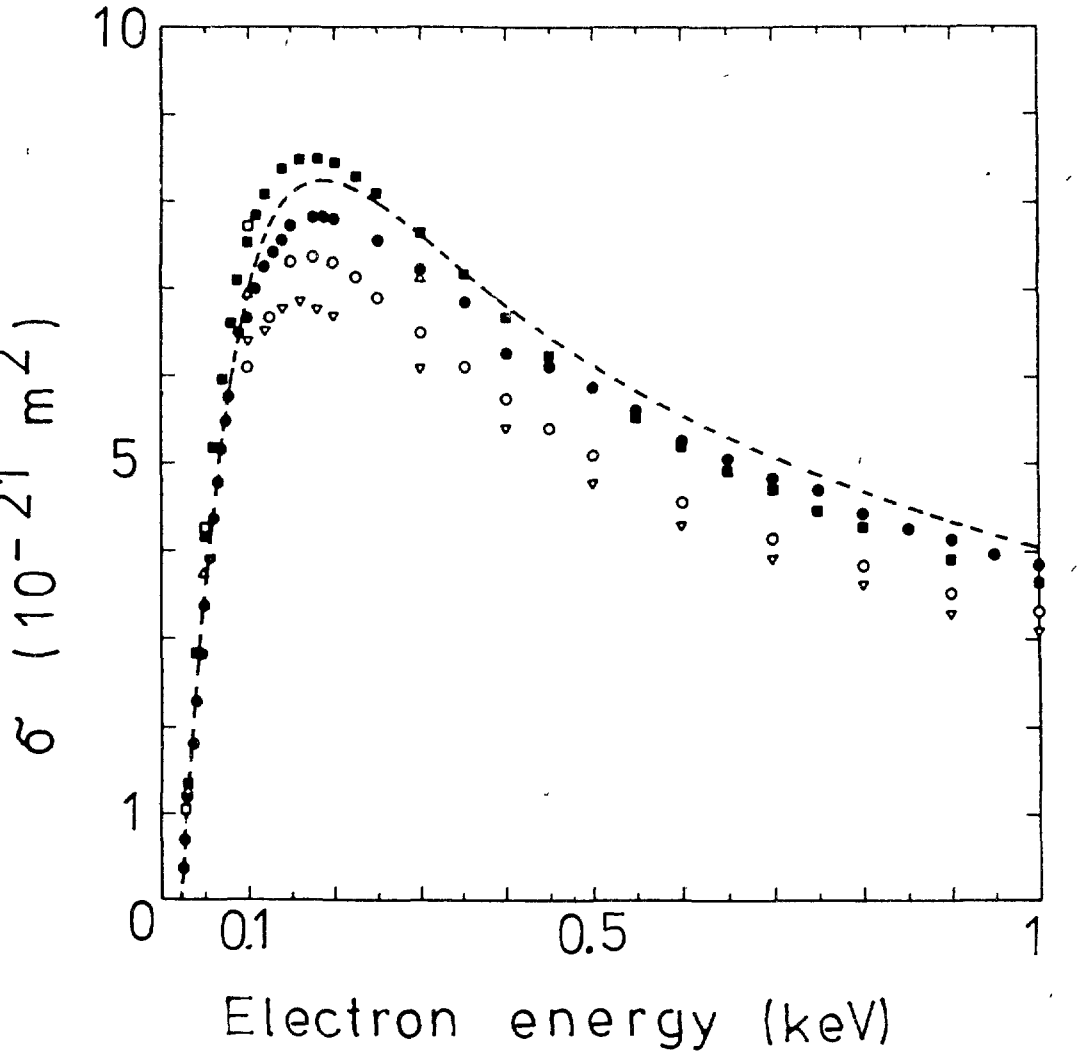

Fig. 3.10 Total electron impact ionization cross section function for neon. ■ Smith [101], □ Asundi and Kurepa [102], ● Rapp and Englander-Golden [16], ∇ Schram et al. [103, 104], o Gaudin and Hagemann [105], Δ Fletcher and Cowling [106], --- Krishnakumar and Srivastava [107]. The recent results of Wetzel et. al. [33] (not shown for the sake of clarity) are in good agreement with those of Rapp and Englander-Golden [16]. The data of Schram et al. [104] extend up to an electron energy of 20 keV. Mc Clure [108] summarizes data in the MeV region. For more details on the accuracy and reliability see discussion in Ref. [11,13,14,23,107].

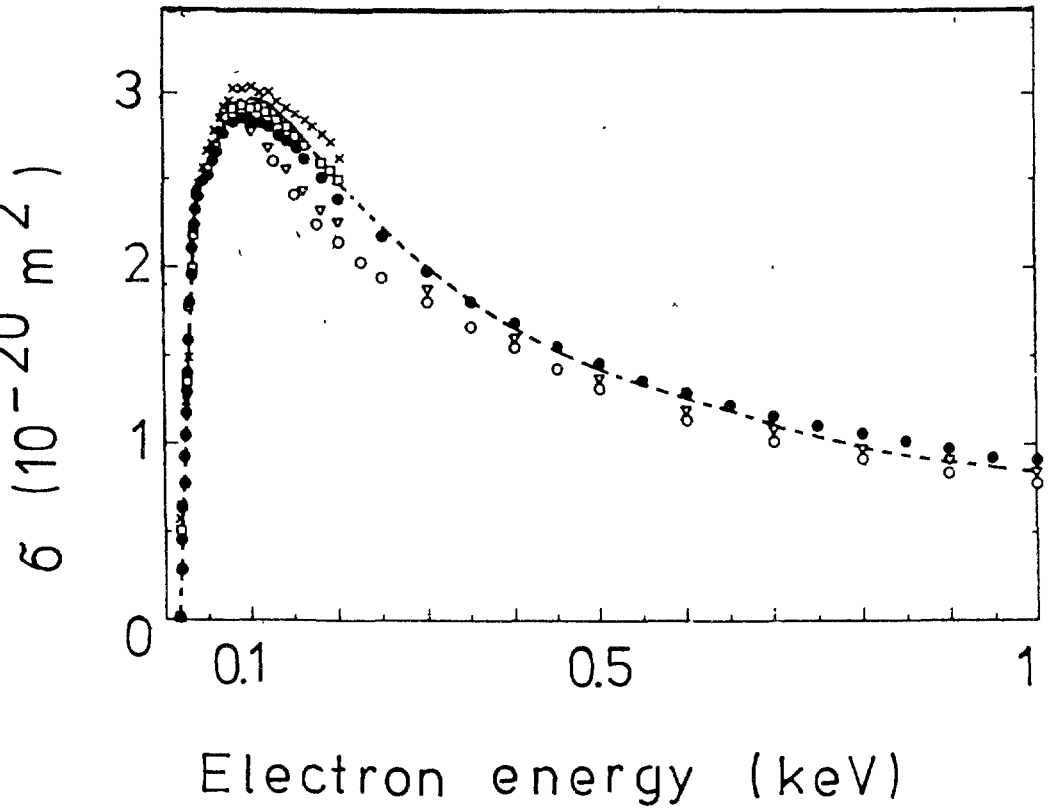

Fig. 3.11 Total electron impact ionization cross section function for argon. ● Rapp and Englander-Golden [16], ∇ Schram et al. [103,104], o Gaudin and Hagemann [105], Kurepa et al. [109], x Wetzel et al. [33], - - - Krishnakumar and Srivastava [107]. The data of Schram et al. [104] extend up to an electron energy of 20 keV (see also a recent study by Mc Callion et al. [110] extending up to 5.3 keV). Mc Clure [108] summarizes data in the MeV region (see also Rieke and Prepejchal [111]). For more details on the accuracy and reliability see disscusions in Ref. [11,13,14,23,107].

combination of the Born-Bethe (equ. (3.24)) and the Mott differential cross sections. Besides other atomic properties it is necessary to know the differential optical oscillator strengths and the collisional parameter of the molecule under study. This, unfortunately, limits the approach of Khare and coworkers to those molecules which have been studied already by photon or electron collisions.

Recently, Margreiter et al. [54] have extended the above mentioned DM approach to molecules using the additivity rule according to which the ionization cross section of a molecule is the sum of the cross sections of the constituent atoms [65-67]. In order to calculate molecular ionization cross sections with the DM equ. (3.25) it is essential to identify the corresponding atomic orbitals of the molecular electrons (using available Mulliken population analyses of the respective molecules). The main advantage of this DM treatment is that ionization cross sections can be described by a simple analytical formula

(depending only on basic atomic properties), which yields results in better agreement with experimental data than classical, semiclassical or empirical formulae [54]. Very recently formula (3.25) has also been shown to be applicable to radicals [56] and clusters [57,69] (see 3.5.).

3.3.3. Recommended total cross sections

As mentioned above, there exists a number of comprehensive reviews on experimental and theoretical cross section determinations [1,2,6,11,13,14,23,39-50,89,90] including also compilations of recommended data [91-100]. It is outside the scope of this

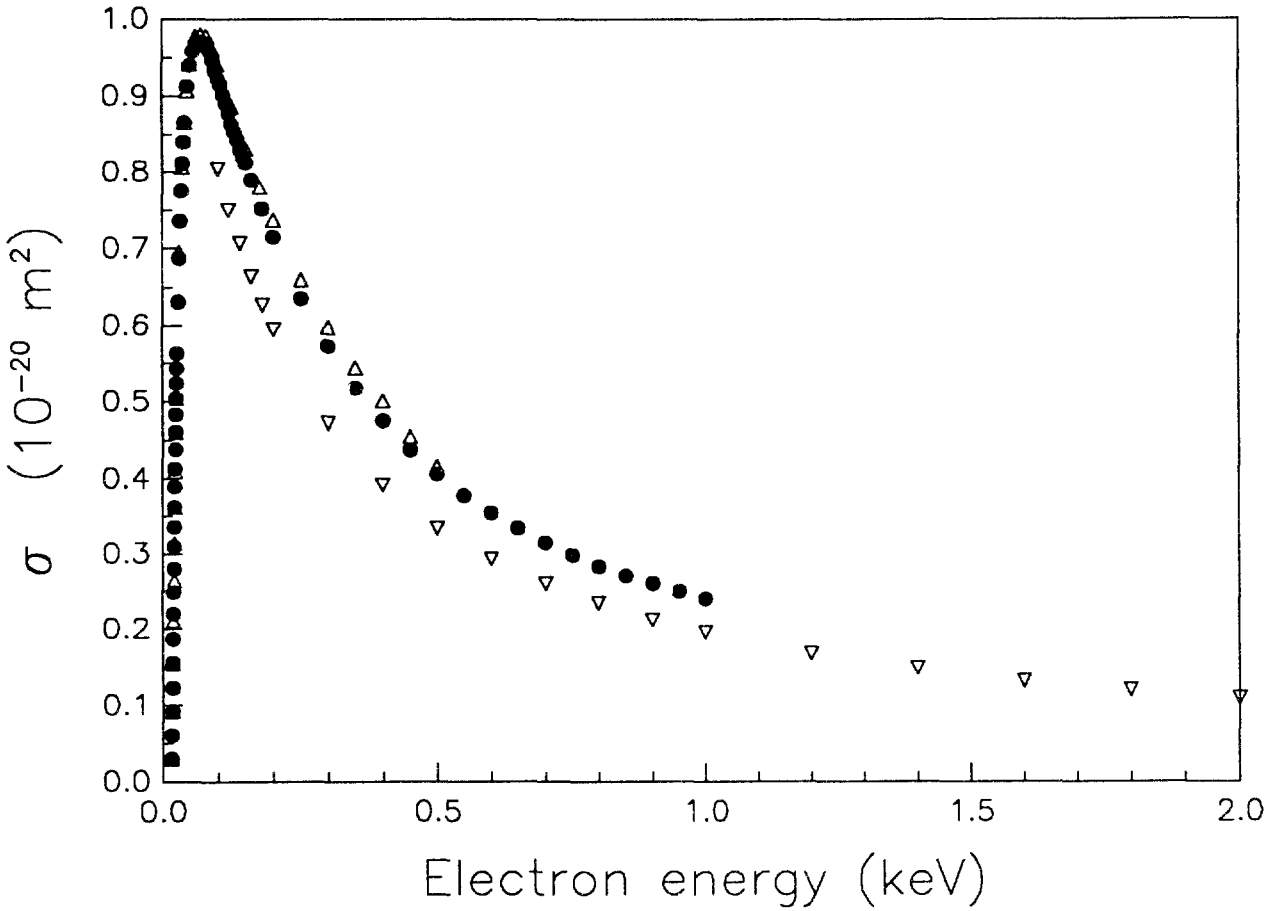

Fig. 3.12 Total electron impact ionization cross section function for H_2. ● Rapp and Englander-Golden [16], ∇ Schram et al. [103,104] (these data extend up to an electron energy of 20 keV), Δ Cowling and Fletcher [112]. Data reported in the MeV range are summarized by Mc Clure [108] and de Heer [92] (see also Rieke and Prepejchal [111]). For more details on the accuracy and reliability see discussions in Ref. [11,13,14,92].

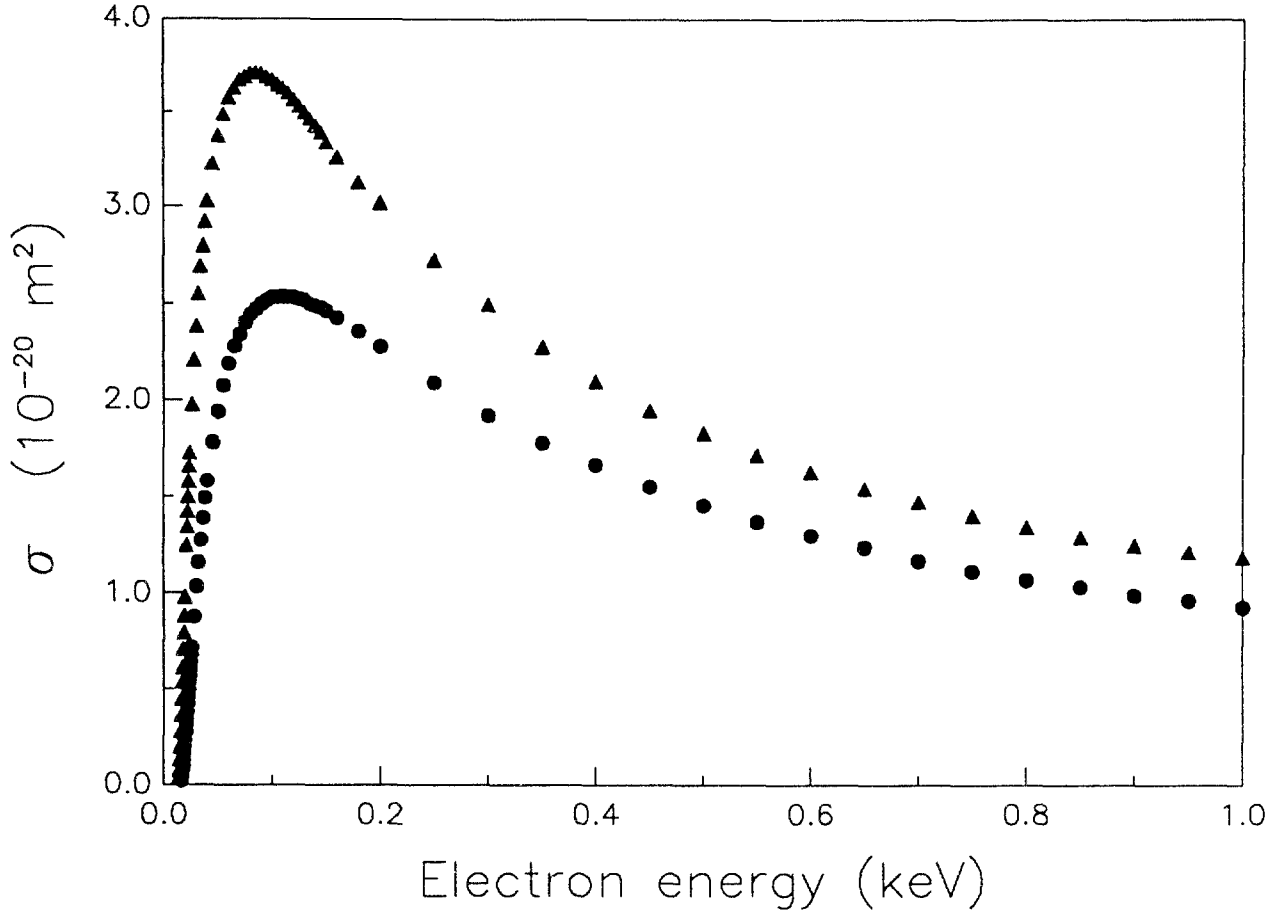

Fig. 3.13 Total electron impact ionization cross section function for N_2 (designated ●), and CH_4 (designated Δ) after Rapp and Englander-Golden [16], whose total ionization cross sections are regarded to be the most reliable data sets available. The results (not shown) of Schram et al. [103,104] for N_2 and of Schram et al. [113] for CH_4 extend up to an electron energy of 20 keV and 12 keV, respectively (MeV data see Ref. [111]). The recent results on CH_4 of Chatham et al. [114] (not shown) are in good agreement with those of Rapp and Englander-Golden [16].

review to give a detailed account of all available results. Nevertheless, total ionization cross section functions for the most important targets related to radiotherapy (i.e., Ne, Ar, H_2, N_2, O_2, H_2O, CO_2, CH_4, C_3H_8) have been assessed and reviewed here and the best data sets available at the time (see discussion in figure headings) are presented in graphical form in Figs. 3.10-3.17.

3.4. Partial electron impact ionization cross sections

3.4.1. Experimental

According to relation (3.19) the determination of partial electron impact ionization cross sections σ_{zi} not only requires the measurement of $n(0)_e$, N_t, L and i_t (as in the case of

total cross section measurements), but in addition an accurate analysis of i_t in terms of individual ion currents, i_{ms}, produced. In order to measure individual ion currents, i_{ms}, mass spectrometers must be used in the respective experimental set up. Because of the great difficulty in achieving a known and reliable transmission and collection efficiency (independent from the m/z value of the ion to be analyzed) in those instruments, their primary value has been for a long time the identification of different ions produced and the measurement of approximate partial cross section ratios.

The first mass spectrometric determination of partial electron impact ionization cross section functions have been made in the 30's. Some of these studies were repeated later on, however, up to recently large differences (as an example see a comparison of the cross section ratio between singly and doubly charged Ar ions shown in Fig. 3.18) existed in both, magnitude and shape, of partial electron impact ionization cross section functions

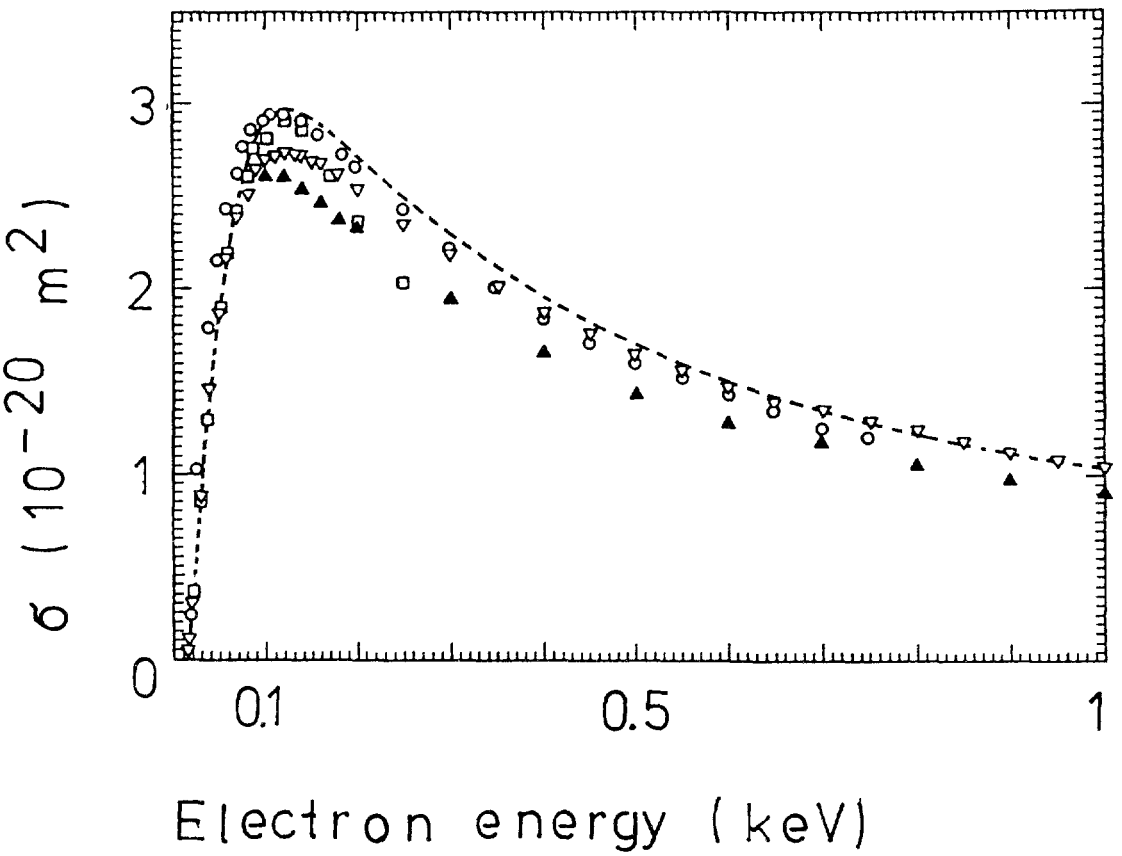

Fig. 3.14 Total electron impact ionization cross section function for O_2. o Tate and Smith [15], ∇ Rapp and Englander-Golden [16], Δ Schram et al. [103,104], Peresse and Tuffin [115], - - - Krishnakumar and Srivastava [116]. The data of Schram et al. [104] extend up to an electron energy of 20 keV (MeV data see Ref. [111]) For more details on the accuracy and reliability see discussions in Ref. [11,13,14,112].

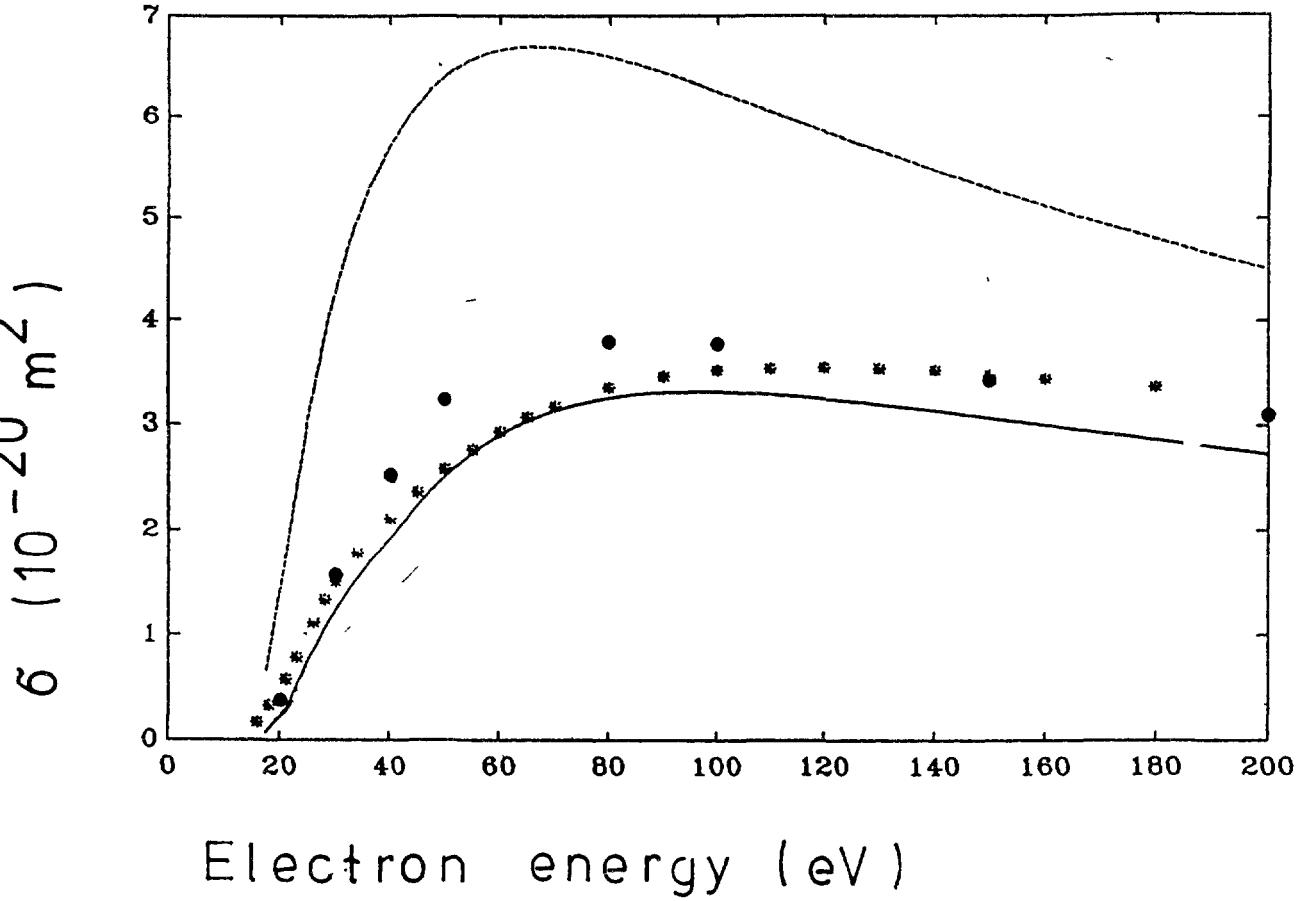

Fig. 3.15 Total electron impact ionization cross section function for CO_2 after Rapp and Englander-Golden [16] (designated *). Also shown for comparison calculated cross sections using the Jain Khare method [85,86] (designated ●), the DM formulation [54], equ. (3.25), (designated ——) and the Gryzinski formula [59] , equ (3.23), (designated - - - -) As described in the text the Gryzinski formula gives erroneous results for molecular targets.

[1,2,6,11,13,23,47,89,90,126,127]. As pointed out by many workers [1,2,13,126] this is due to large discrimination effects occurring at the ion source exit and at the mass spectrometer slits (discussed in more detail below). Moreover, a common problem (never solved satisfactorily) is the absolute calibration. Closely related to this is the fact that discrimination may also occur at the ion detector (see [124,128] and references therein).

There exist, however, some recent experimental studies using new and sophisticated approaches in order to overcome these difficulties. Some of these new studies come very close to meet the main prerequisites for measuring accurate partial ionization cross section functions, i.e. a constant (known) or complete ion source-mass spectrometer collection

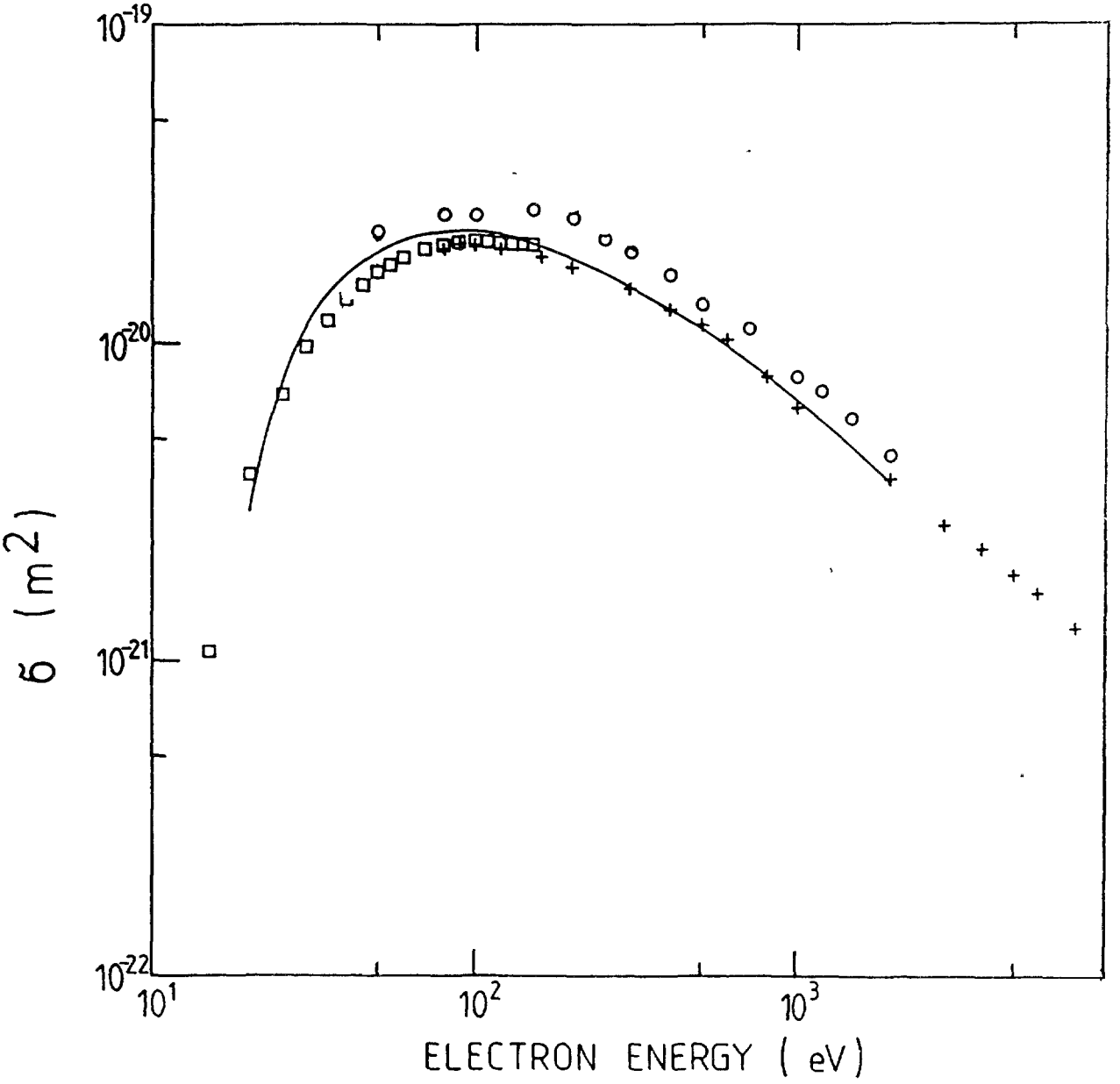

Fig. 3.16 Total electron impact ionization cross section function for H_2O. + Schutten et al. [117], o Bolorizadeh and Rudd [118], and □ Djuric et al. [17]. Also shown for comparison calculated cross sections using the Jain Khare method [85,86] designated as full line. For more details on the accuracy and reliability see Ref. 17 (MeV data see Ref. [111]).

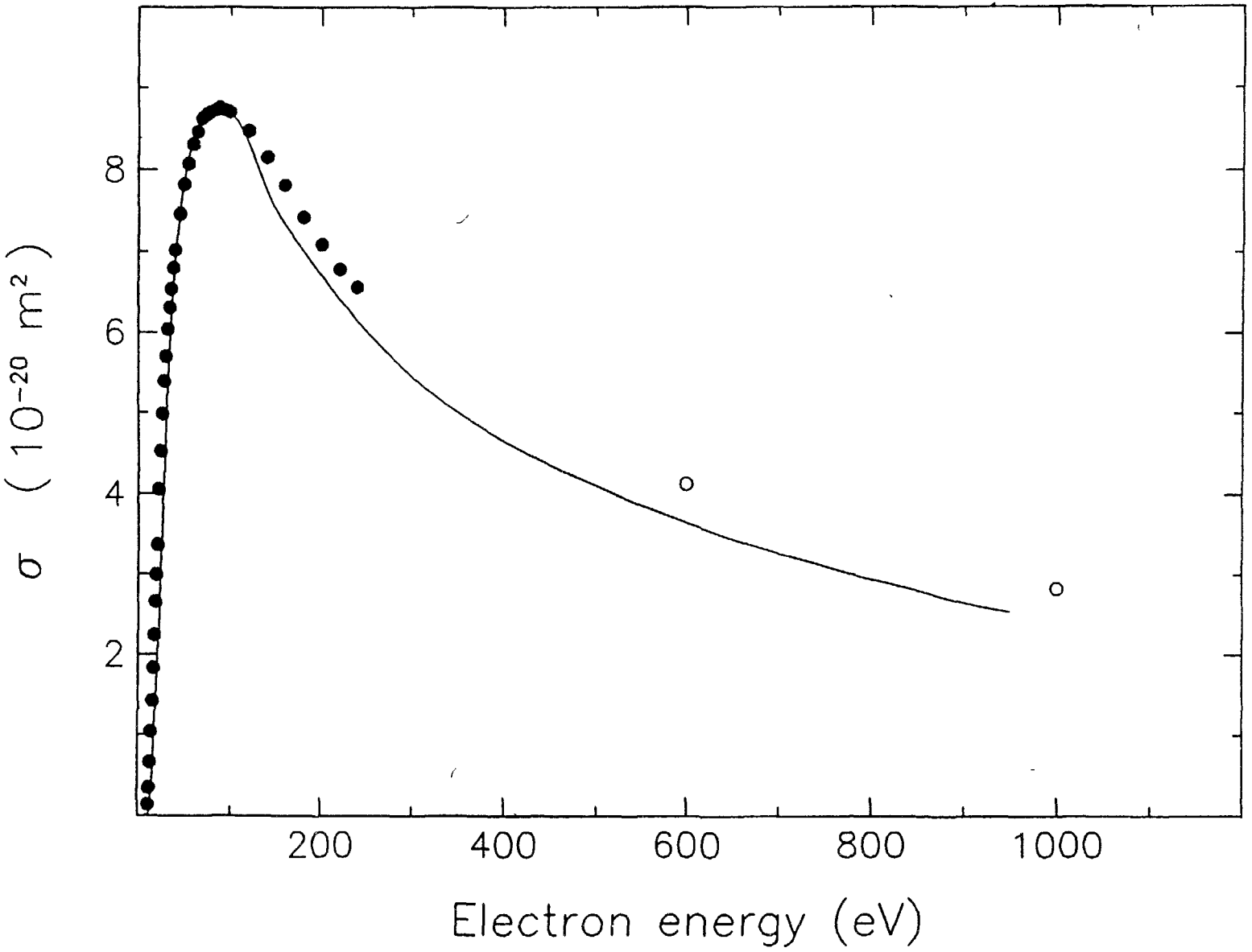

Fig. 3.17 Total electron impact ionization cross section for C_3H_8. o Schram et al. [113] (extending up to an electron energy of 12keV, MeV data see Ref. [111]), ● Djuric et al. [18] and —— Grill et al. [119]. For more details on the accuracy and reliability see Ref. [119].

efficiency independent (i) of the mass to charge ratio of the ion under study, independent (ii) of the incident electron energy, and in some cases independent (iii) of the initial kinetic ion energy. These studies include:

1. Improved crossed thermal beam methods [124, 129-133]
2. Crossed fast atom beam techniques [23-40,90,134,135]
3. Improved metastable ion detection [136-139,134]
4. Trapped ion mass spectrometry [140]
5. Improved ion extraction and transmission techniques (also in combination with molecular beam techniques), i.e.
   - 5.1. Cycloidal mass spectrometry [8,117,141-147]
   - 5.2. Fourier transform mass spectrometry [148]
   - 5.3. Large acceptance sector field mass spectrometry [149]
   - 5.4. Fieldfree diffusive extraction [7,150]
   - 5.5. Pulsed electron beam and ion extraction technique [107,110,116,124,125,151-165] or coincidences technique [165,166]
   - 5.6. Penetrating-field-extraction and ion beam deflection method [47,89,119,120,123,167-180]

The last of these methods (developed and constantly improved over the past 10 years in the Innsbruck laboratory) employing a Nier type ion source in combination with a sector field mass spectrometer system (e.g. see Fig. 3.19), will be discussed as an example in detail in the following paragraph, because (i) of the widespread use of this instrumentation in mass spectrometer laboratories and (ii) its recent success in the determination of accurate partial ionization cross section functions for atoms and molecules. For a detailed and critical discussion of the other rather successful very recent approaches (applied to a series of target systems), including the groups of Freund and Becker and coworkers, Srivastava and coworkers, Gilbody and coworkers, Syage, and Bonham and coworkers, see Ref. 90.

The extraction of ions from the ionization region in a Nier type ion source depends under usual experimental conditions on various parameters, i.e. the initial energy of the ions, the mass to charge ratio, m/z, the guiding magnetic field, the electron beam space charge and the applied extraction field. Usually, ions are extracted from the ionization region (in which there is a crossed electric and magnetic field) by a weak electric field applied between the collision chamber exit slit and an electrode opposite to the exit slit,.i.e., the pusher. This extraction, however, is not complete and results in discrimination for ions with different m/z (e.g., see detailed discussions in Ref. [1,2,13,47,126]). In an alternative approach a penetrating field from external electrodes may be used, i.e. all electrodes confining the collision chamber are kept at the same potential (e.g. ion acceleration voltage of 3 kV), and ions are drawn out of the collision chamber through the ion source exit slit under the action of an electric field applied to the external electrodes (Fig. 3.19). It has been shown that this penetrating field extraction assures saturation of the parent ion current [123,167]. Ions

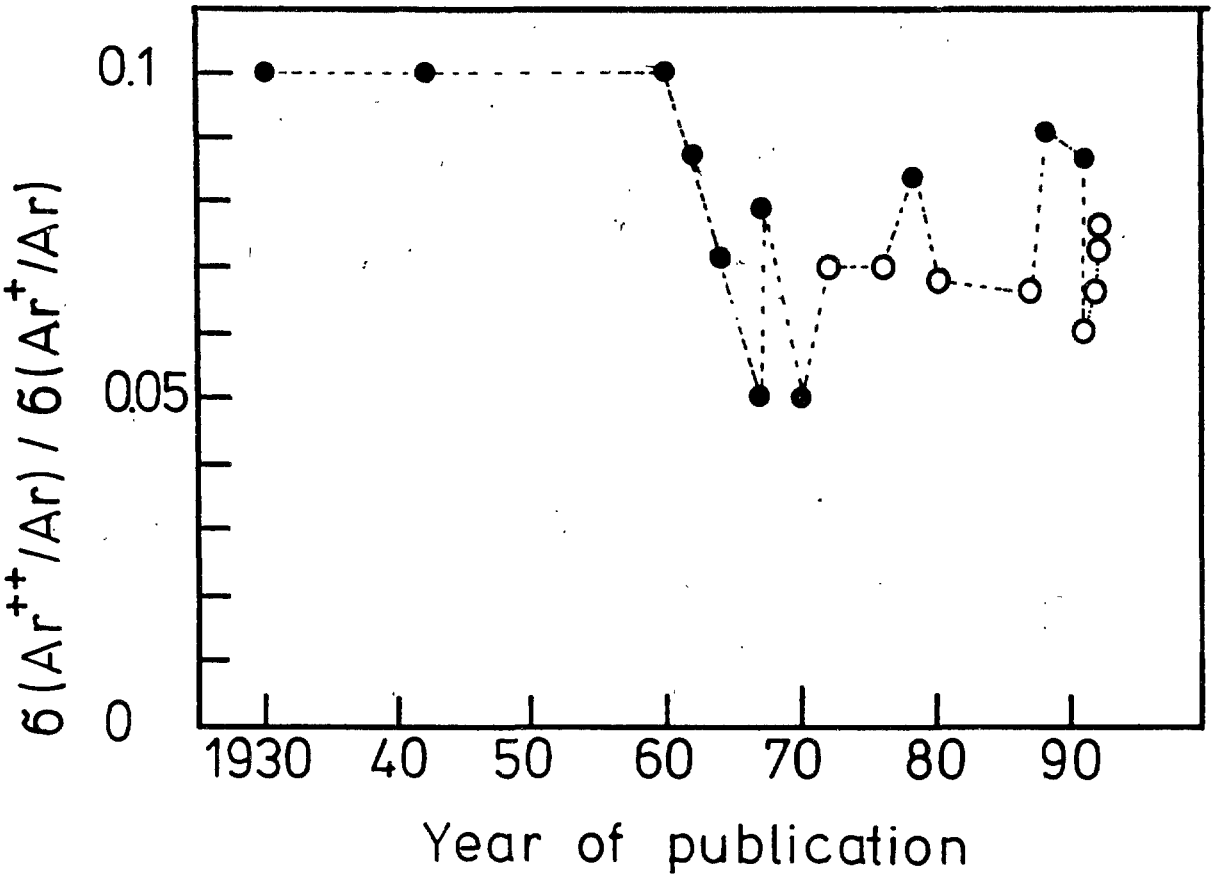

Fig. 3.18 Measured partial ionization cross section ratio $\sigma(Ar^{2+}/Ar)/ \sigma (Ar^{+}/Ar)$ at 100 eV electron energy versus year of publication of these results (original data references given in Ref. [89] and [120]). Cross section ratios designated with open circles are measured with improved and controlled experimental conditions (see text) and agree quite well with each other within the experimental error bars, i.e. including the results of Crowe et al. 1972 [7], Drewitz 1976 [121,122], Stephan et al. 1980 [123], Wetzel et al. 1987 [33], Syage 1991 [124], Bruce and Bonham 1992 [128], Tarnovsky and Becker 1992 [40] and Mc Callion et al. 1992 [110].

extracted in this manner are then centered and focussed by various elements and reach the end of the acceleration region at the so called earth slit. Stephan et al. [123] additionally introduced in front of the mass spectrometer entrance slit S_1 pairs of deflection plates (see L_6-L_9 in Fig. 3.19), which serve to sweep the ion beam across the mass spectrometer entrance slit S_1 in the y direction (perpendicular to S_1) and z direction (parallel to S_1). This allows the recording and integration of the ion beam profile, and hence discrimination at S_1 can be avoided.

It is of special interest to note that this technique has been recently extended to the quantitative detection of fragment ions. Stephan et al. [175] have shown for CF_4 that the

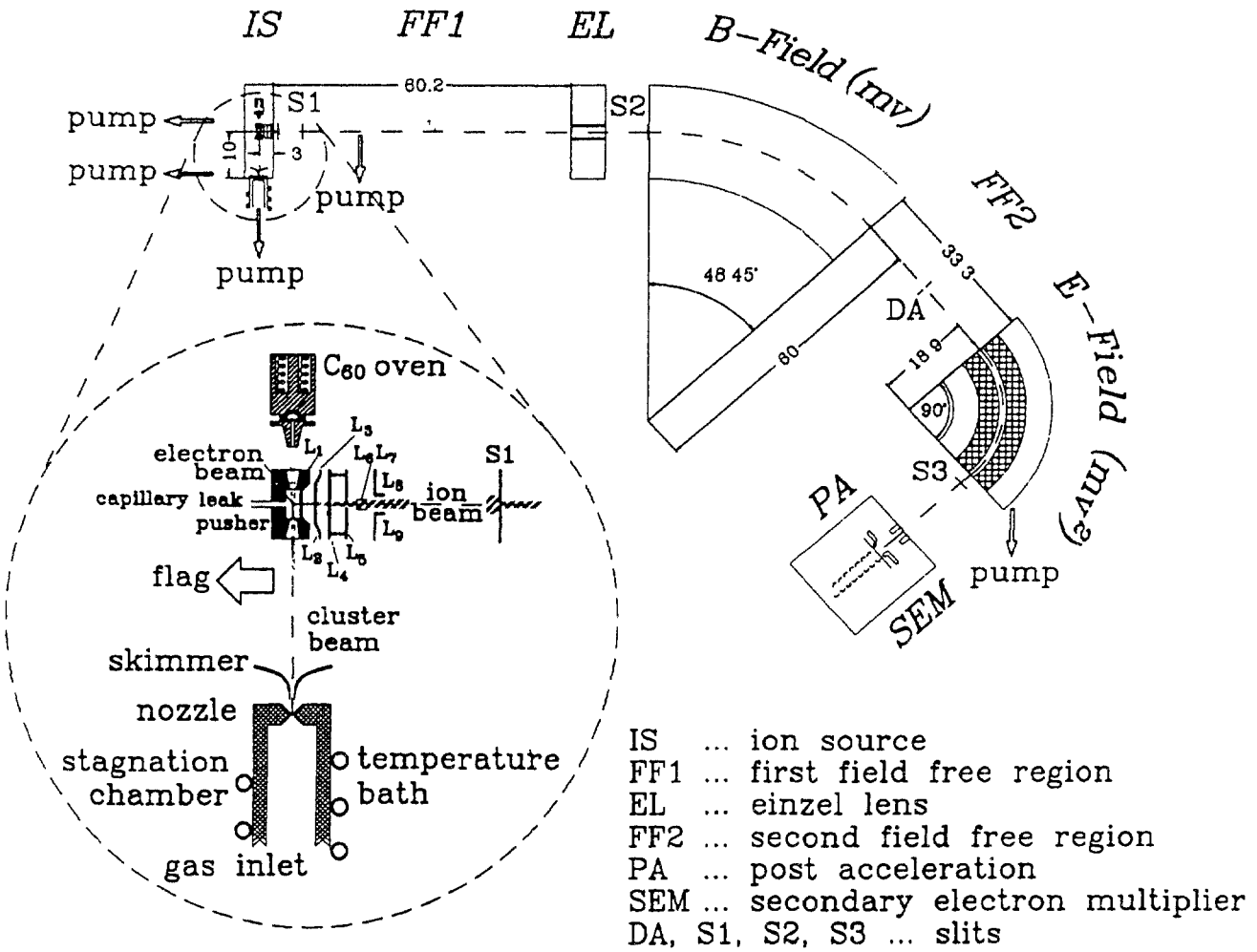

Fig. 3.19 View (to scale, numbers given in cm) of the electron impact ion source and of the double focussing mass spectrometer system after Ref. [119]. L_1, collision chamber exit slit electrodes; L_2 penetrating field electrodes, L_3 and L_4, focussing electrodes, L_5, ground slit; L_6, L_7, L_8 and L_9, ion beam deflection electrodes; S_1 mass spectrometer entrance slit; z-direction: perpendicular to the x-y plane (right-hand axes).

overall ion beam shapes are essentially a product of the profiles in either direction. Thus, in order to account for the overall discrimination at S_1 Stephan et al. have demonstrated that it is sufficient to determine separately the profile in the z direction at one particular y value (e.g., $U_y = 0$ V) and the profile in the y direction at one particular z value (e.g., $U_z = 0$ V) and then integrate with help of these two data sets over the whole beam shape. This integration method was improved [178] by operating a 1 kHz sweep generator on the y-deflection plates during the z scan. It is then sufficient to integrate over this y-integrated z-ion-beam profile in order to obtain a representative measure of the total ion current of the ion under study.

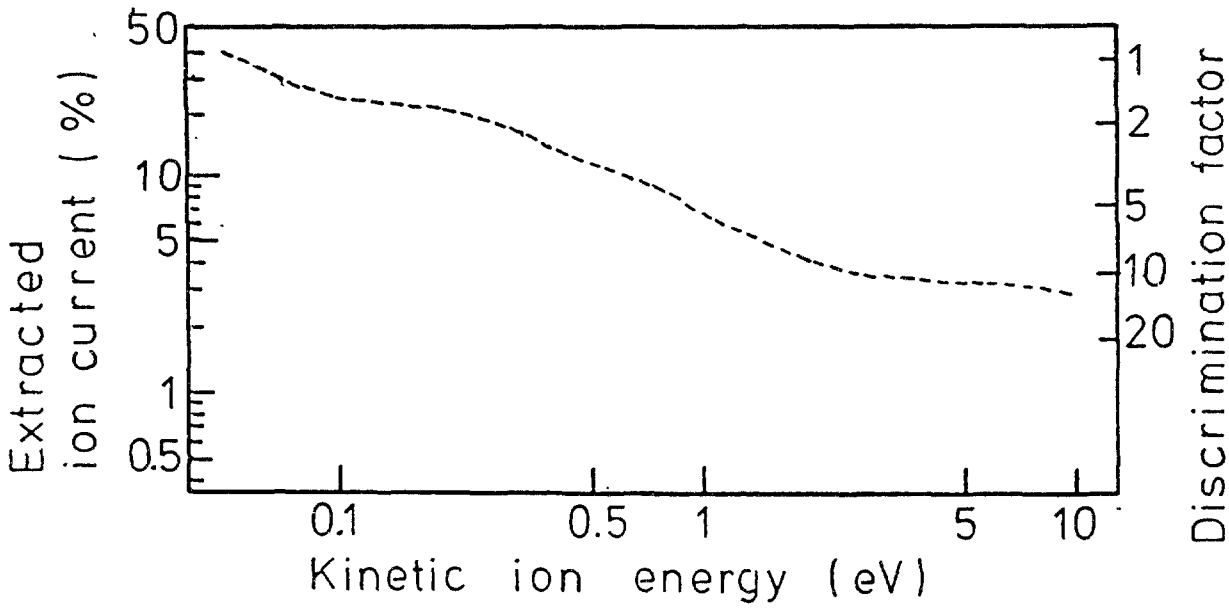

Fig. 3.20 Calculated extracted ion fraction and discrimination factor (see text) as a function of initial kinetic ion energy for the Nier type ion source used in combination with a double focussing mass spectrometer (see Fig. 3.19) after Poll et al. [179].

Moreover, Margreiter et al. [120] recently introduced an additional correction procedure to account for an non-permissible discrimination of energetic fragment ions at the ion source exit slits. It was demonstrated in the case of SF_6 that the smaller fragment ions (which have larger excess kinetic energies than the larger fragment ions) are not extracted out of the ion source with the same efficiency as the large fragment ions despite the experimental improvements employed previously [175,178]. This new correction procedure is based on a study of the discrimination in the ion source and mass spectrometer by means of computer simulations [179]. Ion trajectories were calculated in this study as a function of initial kinetic energy, starting position and starting angle in the ion source. Fig.3.20 shows the calculated extracted ion fraction as a function of initial kinetic energy. This relationship may be used to correct measured (total) fragment ion currents or in the case of earlier measurements uncorrected partial ionization cross sections. The discrimination factor is defined, according to Fig. 3.20 and Ref. [179], as the ratio between the calculated extracted ion fraction of an ion with initial thermal kinetic energy and of the ion under study (having a higher kinetic energy), respectively. A representative measure for the kinetic energies has been obtained in these studies [119,120,179,180] by measuring the z-deflection curves of all fragment ions in comparison to Ar^+ and Ar^{2+} (using a relationship between the kinetic energy and the deflection voltage derived by Franklin and coworkers [181]).

In order to complete this survey on recent experimental studies a number of other studies -mostly using quadrupole mass filters or time of flight mass spectrometers - should be mentioned, e.g., see reference [114, 182-188].

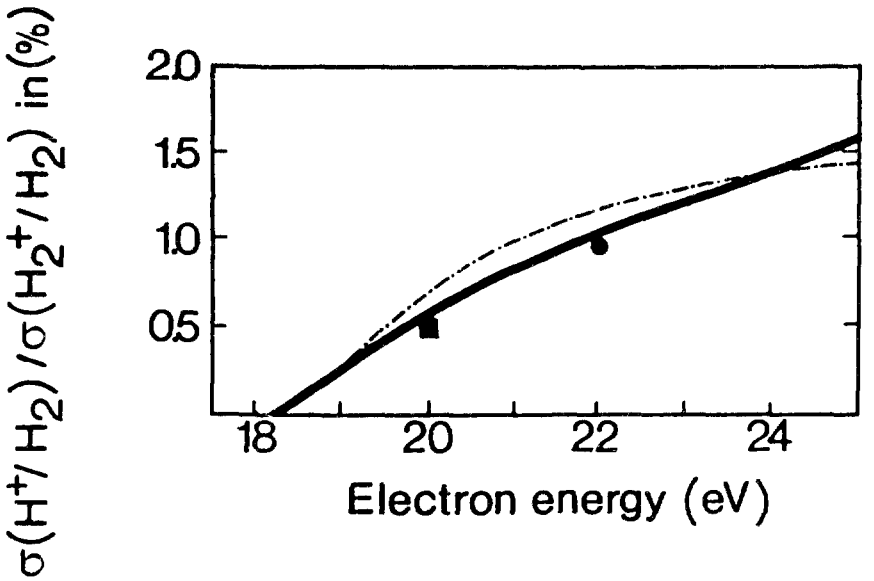

Fig. 3.21 Partial ionization cross section ratio $\sigma(H^+/H_2)$ / $\sigma(H_2^+/H_2)$ for the electron impact ionization of H_2 as a function of electron energy given by Hipple (see Ref. [190]) designated ●, by Adamczyk et al. [141] designated ■ and by Crowe and Mc Conkey [191] designated ——. Also shown (designated -.-.-.) for comparison are predictions by Browning and Fryar [192] using Franck Condon factors (see text).

3.4.2. Theoretical

In contrast to the situation for total ionization cross sections almost no theoretical treatments are available for the determination of absolute partial ionization cross sections (except for those cases with atomic targets where the total cross section is about equal to the single ionization cross section, see above). Besides a few quantum and classical approximations for the production of doubly charged rare gase atoms (see Figs. 16 to 19 in Ref. [47]) which are disagreeing strongly with the accepted experimental results, the only approach to calculate absolute partial ionization cross section functions is the semiempirical formulation by Khare and coworkers [87,88]. In this approach Khare et al. utilized a modified Jain-Khare formula (see 3.3.2.) in order to predict the dissociative ionization of small molecules such as NH_3, H_2O and H_2S. Whereas the cross sections for the dominant ions are in good agreement with the experimental results, for the minor ions the theory underestimates the cross sections.

Another possibility to predict in the case of diatomic or pseudo-diatomic molecules at least cross section ratios is the use of the Franck-Condon principle. If the corresponding potential energy curves of the neutral and ionized diatomic molecule are known, the resulting fragmentation ratios between atomic and diatomic ion may be derived from the

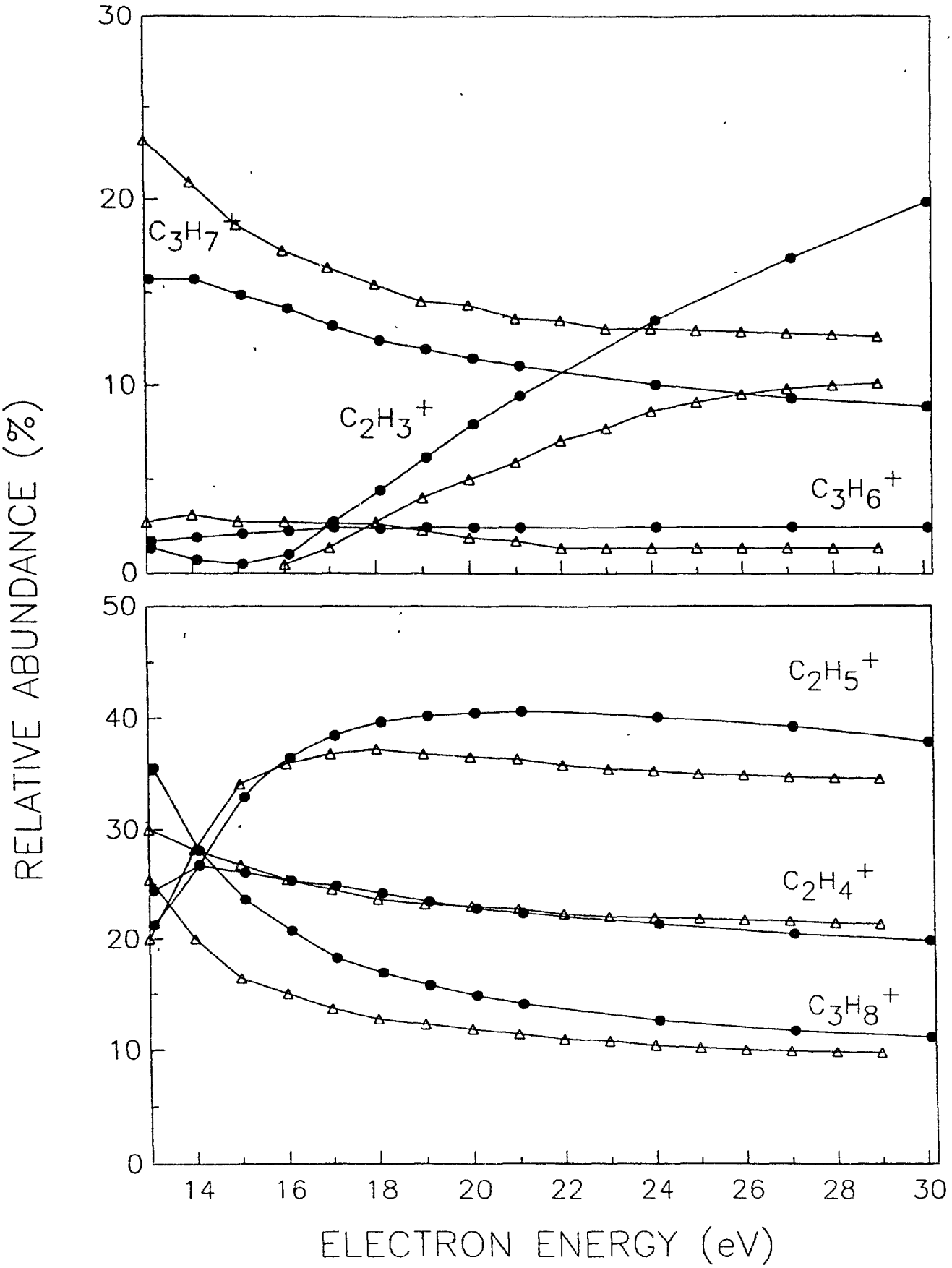

Fig. 3.22 Relative partial electron impact ionization cross sections for C_3H_8 after Grill et al. [119], designated by open triangles. Also shown for comparison are QET calculations by Vestal [195] designated by full dots .

calculated normalized vibrational overlap integrals called Franck-Condon factors (see Ref. [126] and [189] and references therein). Fig. 3.21 shows as an example calculated and measured results for the H^+/H_2^+ ratio for H_2 as a function of electron energy from threshold up to 25 eV, i.e. including therefore only contributions from the $^2\Sigma_g^+$ state of H_2^+ (see Fig. 5-1 in Ref. [126]).

The electron impact ionization of large polyatomic compounds also proceeds without nuclear displacement, however, the few two-dimensional potential energy curves have to be replaced by a multitude of n-dimensional potential energy hypersurfaces. Moreover, subsequent dissociation is not occurring directly, but only via unimolecular decomposition reactions after the excess energy has been transferred and distributed to the many degrees of freedom. In order to describe this ionization and fragmentation process it is possible to use statistical methods, i.e. the Quasi-Equilibrium Theory (QET) developed in 1952 by Rosenstock et al. [193] or its equivalent, the RRKM theory (see Ref. [194]). In the framework of QET ionization cross section ratios may be derived [126,189] by (i) determining the rate of dissociation, k(E), for each fragmentation channel as a function of the internal energy E, (ii) constructing the breakdown graph from these individual dissociation rates and (iii) convoluting this breakdown graph with the total internal energy distribution (which can be obtained from photoelectron spectroscopy, photoionization studies or from the second derivative of the total electron impact ionization cross section function). The whole procedure hinges on the assumption of a linear electron ionization threshold law and needs detailed knowledge of the polyatomic compound in terms of vibrational frequencies, activation energies and structure of the transition state. Despite these drawbacks the mass spectra (cross section ratios) of a variety of smaller and also more complex molecules have been calculated (see references in [126,189]). Fig. 3.22 shows as an example experimental and calculated normalized partial cross sections as a function of electron energy for the C_3H_8 molecule.

3.4.3. State selected partial cross sections

Most of the partial electron impact ionization cross section functions reported in the literature so far concern ionization of stagnant (in thermal equilibrium) target gas systems in their electronic ground state into specific ions only distinguished by charge and mass and not due to their electronic state. For a limited number of cases, however, there exist partial cross sections for electron impact ionization reactions taking into account the electronic states of either the neutral target or the ion produced (for a detailed discussion see Ref. [126]). In order to illustrate this point Fig. 3.23 shows the corresponding cross section function for the single ionization of metastable neon atoms. It is interesting to note that this cross section is about one order of magnitude larger than that for the ground state atom. Moreover, in certain instances it is of interest also to determine the (state-selected) partial cross section

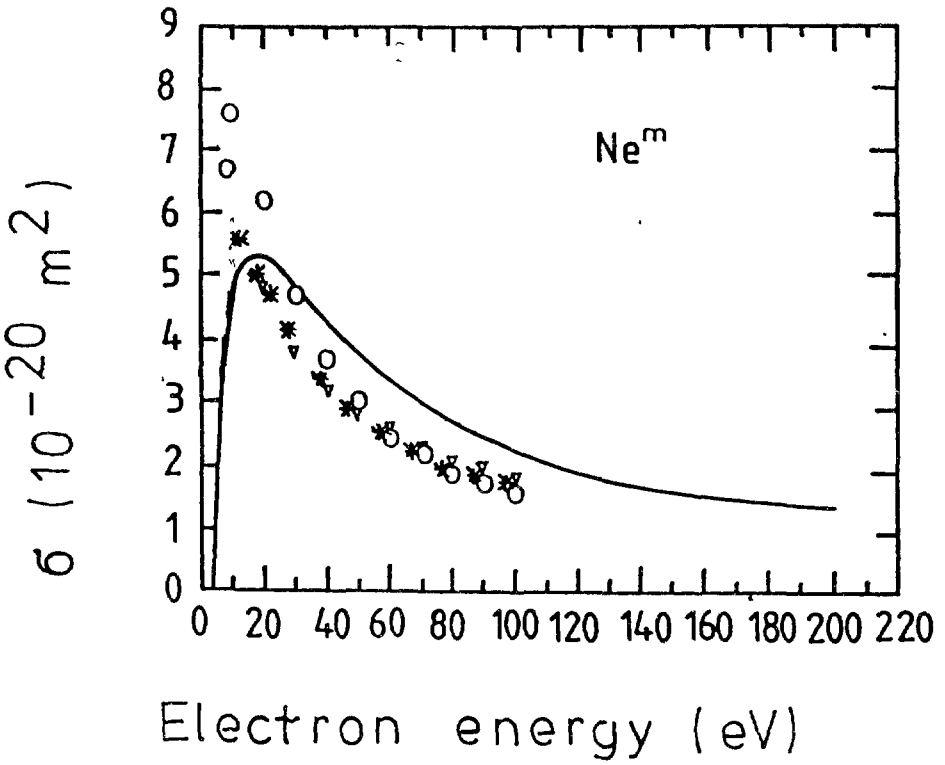

Fig. 3.23 Partial electron impact ionization cross section function for the reaction $Ne^m + e \rightarrow Ne^+ + 2e$ after Dixon et al. [196] designated * Also shown for comparison theoretical data using the Born approximation (Ton That and Flannery [197]) designated o, using the scaled Born approximation (Mc Guire [198]) designated ∇, and using the semiclassical DM approach, equ. (3 25) (Margreiter et al [53]) designated ——

for the removal of specific electrons from the target shell in the course of an electron impact ionization process. Typical examples for this case are inner-shell ionization reactions [55] (see Fig 3.9) or outer-shell ionization reactions [80] (see Fig 3 8).

3.4.4. Recommended partial cross sections

As mentioned above, there exists a number of comprehensive reviews on partial electron impact ionization cross section determinations [1,2,6,11,13,23,47,63,89-100,126,127] including also compilations of recommended data. Moreover, as discussed above, the data for partial cross sections are less reliable than those for total cross sections due to errors introduced by discrimination effects in the mass spectrometers, ion sources and at the detector and due to problems arising in the absolute calibration [126] These effects have only been taken into account properly in the past few years. Nevertheless, most of the

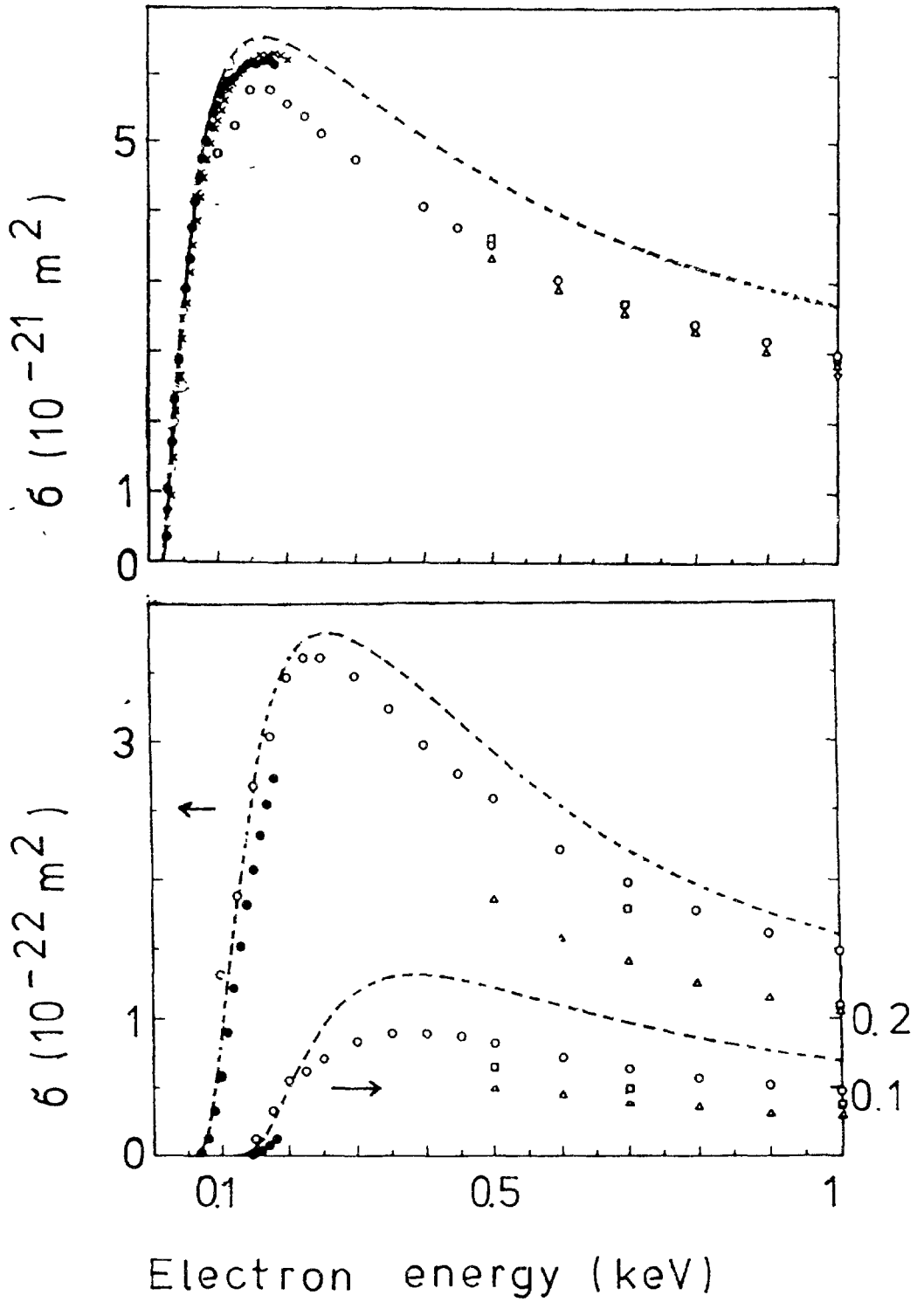

Fig. 3.24 Partial electron impact ionization cross section function for the reactions Ne + e → Ne^+ + 2e (upper part), Ne + e → Ne^{2+} + 3e (lower part, left scale) and Ne + e → Ne^{3+} + 4e (lower part, right scale). Δ Schram et al. [199], o Gaudin and Hagemann [105], □ Nagy et al. [149], ● Stephan et al. [123], x Wetzel et al. [33] and - - - Krishnakumar and Srivastava [107]. The data of Nagy et al. extend up to 5 keV and of Schram et al. up to 18 keV (including up to fivefold charged ions). For more details on the accuracy and reliability see discussions in Ref. [11,23,47,107 and 126].

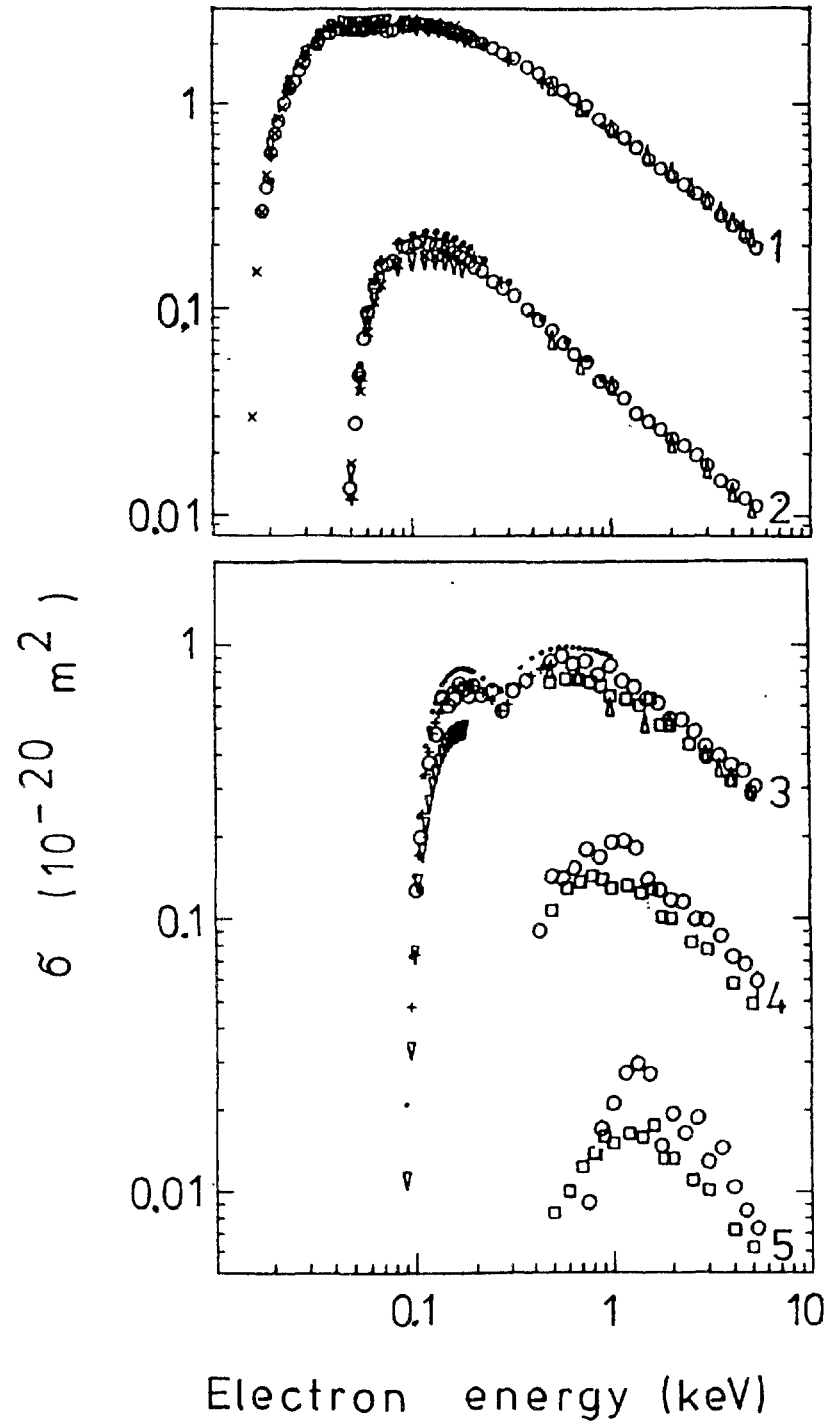

Fig. 3.25 Partial electron impact ionization cross section function for the reactions Ar + e → Ar^+ + 2e (designated 1), Ar + e → Ar^{2+} + 3e (designated 2), Ar + e → Ar^{3+} + 4e (designated 3), Ar + e → Ar^{4+} + 5e (designated 4) and Ar + e → Ar^{5+} + 6e (designated 5). □ Schram [200], Δ Nagy et al. [149], ∇ Stephan et al. [123], x Wetzel et al. [33], • Krishnakumar and Srivastava [107], + Ma et al. [161] and o Mc Callion et al. [110]. The data of Schram extend up to 18 keV including up to sevenfold charged ions. For more details on the accuracy and reliability see discussions in Ref. [11, 23, 47, 107, 110 and 126] (see also Fig. 3.18 and the corresponding discussion in the text).

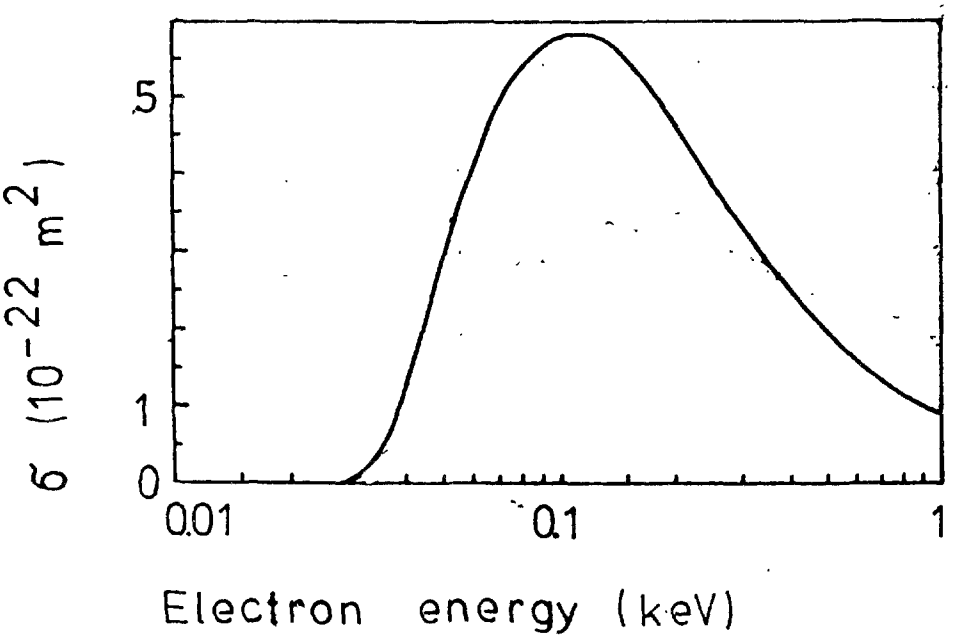

Fig. 3.26 Partial electron impact ionization cross section function for the reaction $H_2 + e \rightarrow H^+$ (with kinetic energies > 0.25 eV) + H + 2e after Rapp et al. [201]. For further partial cross sections and ratios see Fig. 3.21 and Table 3.1. For more details see Ref. [92 and 99]. Double ionization of H_2 has been recently studied by Edwards et al. [154].

Table 1. Partial electron impact ionization cross sections (in 10^{-22} m^2) for the reaction $H_2 + e \rightarrow H^+ + H + 2e$ and $H_2 + e \rightarrow H_2^+ + 2e$, respectively, as a function of electron energy E after Adamczyk et al. [141].

E(eV)	H^+	H_2^+
20	0.118	24
30	0.71	58
50	1.68	81
70	2.1	86
100	2.0	80
150	1.76	71
200	1.56	62
300	1.08	48
400	0.91	41
500	0.75	33
600	0.67	29
700	0.62	26
800	0.55	24
900	0.52	23
1000	0.49	21

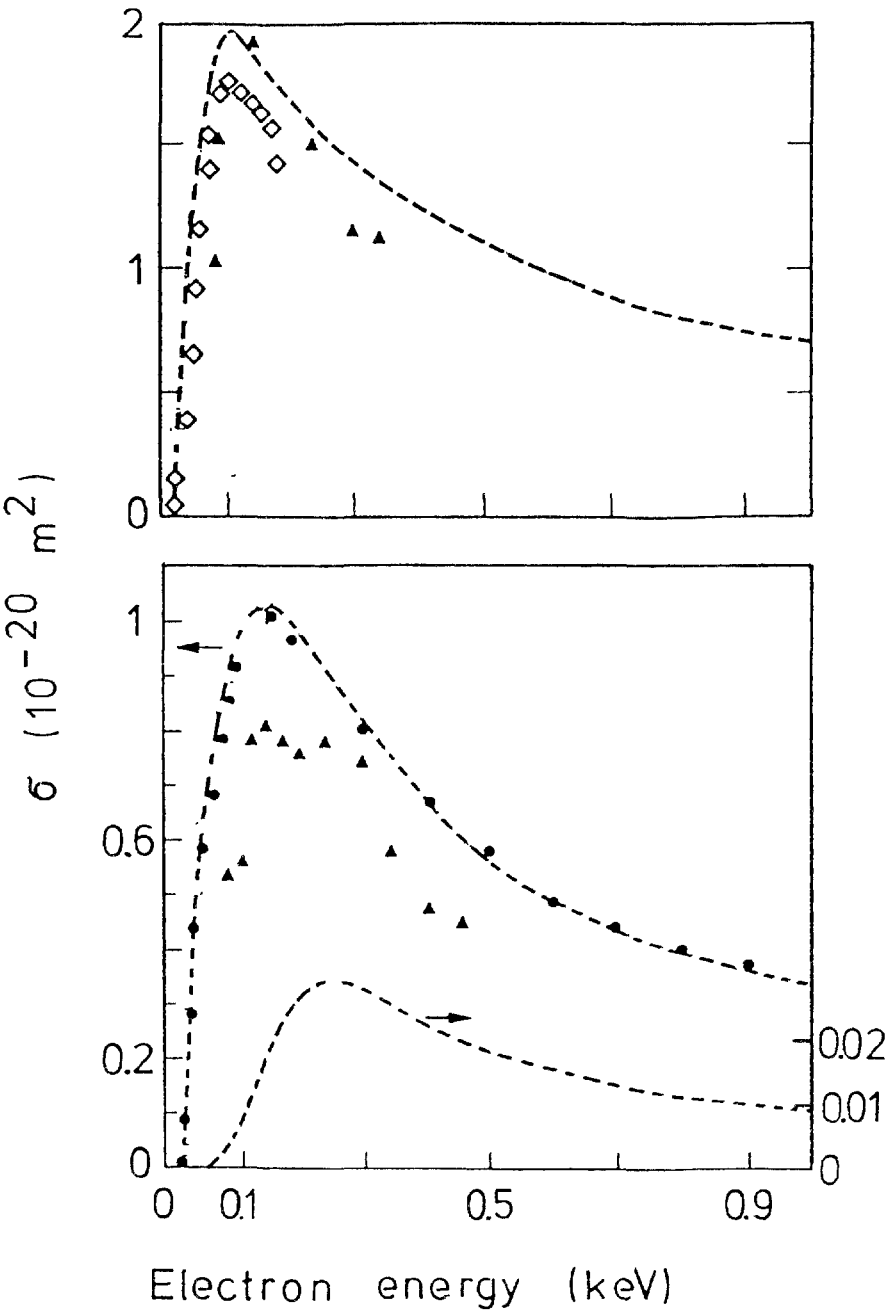

Fig. 3.27 Partial electron impact ionization cross section function for the reactions $O_2 + e \rightarrow O_2^+ + 2e$ (upper part) and $O_2 + e \rightarrow O^{2+}$ (lower part, right hand scale) and the production of O_2^{2+} plus O^+ (lower part, left hand scale). ● Rapp et al. [201], ◊ Märk [202], Δ Evans et al. [203] and - - - Krishnakumar and Srivastava [116]. The data of Rapp et al. relate to cross sections for the production of ions with kinetic energies larger than 0.25 eV and can be best compared with the results of other authors for O^+ production. Double ionization of O_2 has been studied and discussed by Märk [202] (see Table 3.2). Triple ionization has been estimated to amount at 1 keV to appr. 7.1 x 10^{-4} of the total ionization cross section [166]. For more details on the accuracy and reliability see discussions in Ref. [11, 116, 126 and 202].

Table 2 Partial electron impact ionization cross sections for the reactions $O_2 + e \rightarrow O_2^{2+} + 3e$ and $N_2 + e \rightarrow N_2^{2+} + 3e$, respectively, as a function of electron energy E after Märk [202].

E(eV)	$O_2^{2+}(10^{-22}m^2)$	E(eV)	$N_2^{2+}(10^{-22}m^2)$
42	0.011	44.5	0.006
44	0.023	46.5	0.028
48	0.045	50	0.11
51.5	0.080	53.5	0.28
53	0.10	57	0.49
62	0.24	60.5	0.76
73	0.41	68.5	1.30
94.5	0.87	78.5	2.17
109	1.02	98.5	2.95
126	1.04	118.5	3.32
139	1.07	124.5	3.35
156	1.04	145.5	3.22
167	1.00	165.5	2.59

cross sections for the most important targets related to radiotherapy (i.e. Ne, Ar, H_2, N_2, O_2, H_2O, CO_2, CH_4, C_3H_8) have been measured recently. The data on these targets have been assessed and reviewed here and the best data sets available (partial cross section functions and/or ratios) at the present time are presented in graphical form in Figs. 3.24-3.32.

3.5. Electron impact ionization of clusters

In recent years, there has been a growing interest in a new category of molecules, i.e. the clusters (see also the discussion in other chapters of this report). Neutral atomic or molecular clusters (bound by weak forces such as dispersion forces) are produced in free jet nozzle expansion, and most of these experiments on so called van der Waals clusters (see Ref. [4]) use electron impact ionization in combination with mass spectrometry for the detection of these species. However, very little quantitative information is known yet in terms of ionization cross sections. This is mainly due to the fact that it is not possible to produce beams of neutral clusters of known density and defined size [3-5].

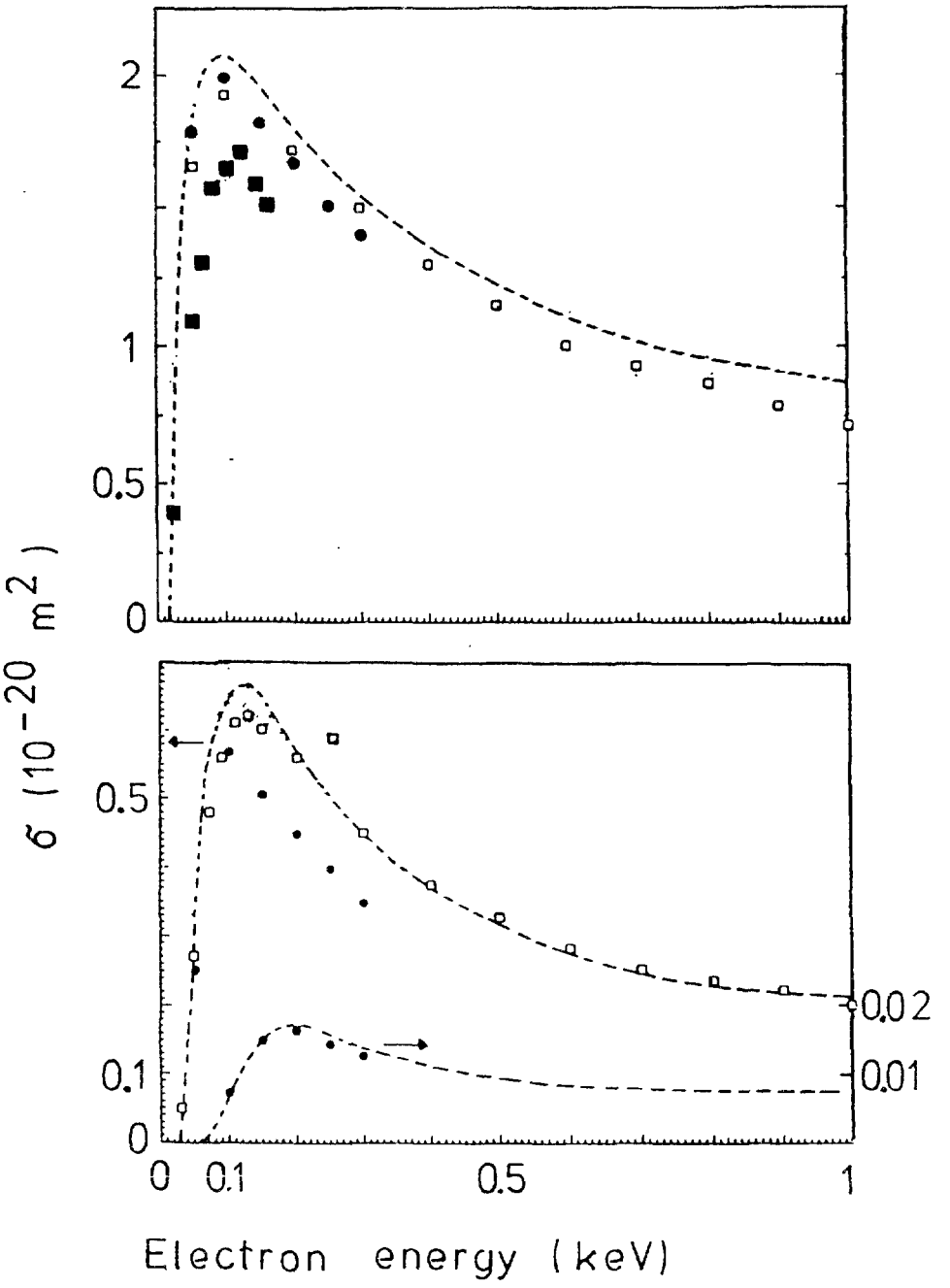

Fig. 3.28 Partial electron impact ionization cross section function for the reactions $N_2 + e \rightarrow N_2^+ + 2e$ (upper part) and $N_2 + e \rightarrow N^{2+}$ (lower part, right hand scale) and the production of N_2^{2+} plus N^+ (lower part, left hand scale). ● Crowe and Mc Conkey [191], □ Rapp and Englander-Golden [16] and Rapp et al. [201], ■ Märk [202], and - - - Krishnakumar and Srivastava [159]. The data of Rapp et al. [201] (lower part) relate to cross sections for the production of ions with kinetic energies larger than 0.25 eV and can be best compared with the results of other authors for N^+ production. Double ionization of N_2 has been studied and discussed by Märk [202] (see Table 3.2). Triple ionization has been estimated to amount at 1 keV to appr. 7.4×10^{-4} of the total ionization cross section [166]. For more details on the accuracy and reliability see discussions in Ref. [11, 126, 159 and 202].

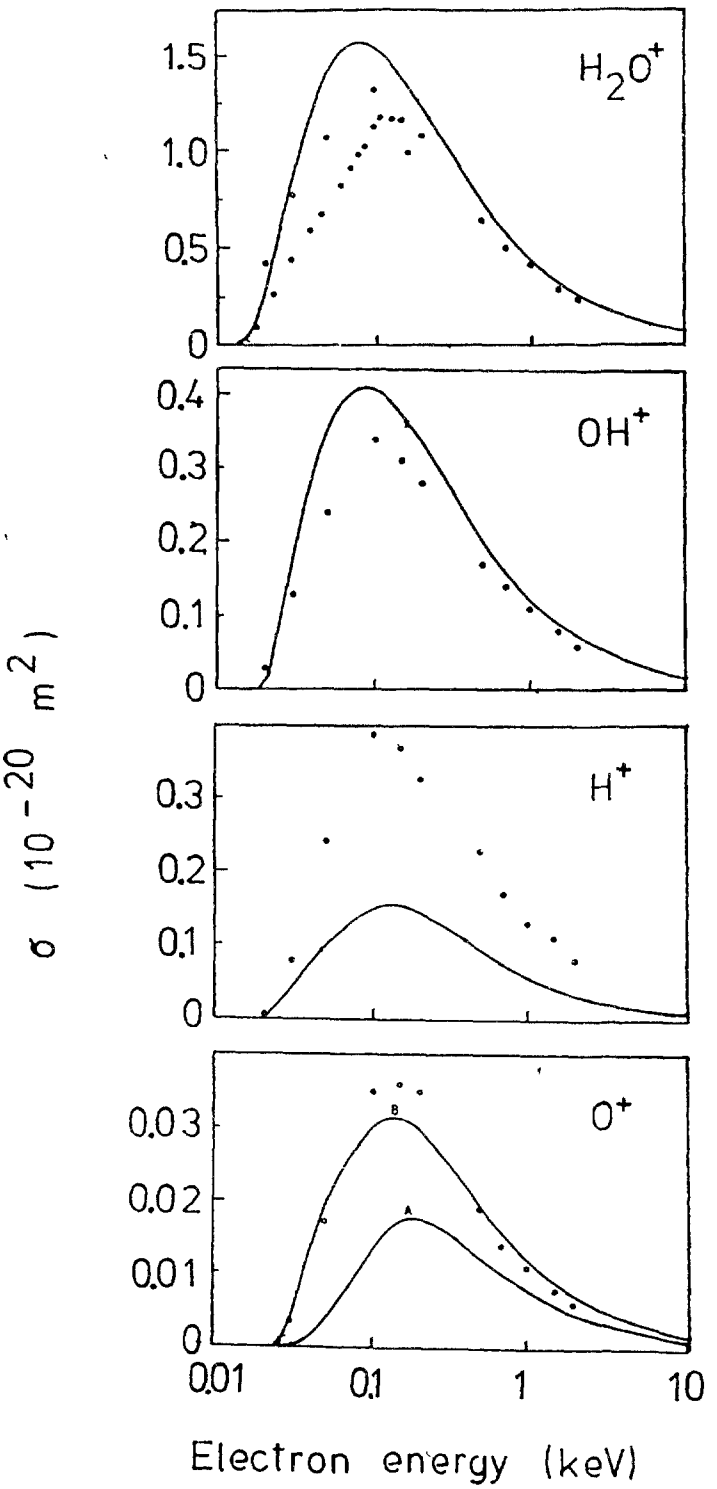

Fig. 3.29 Partial electron impact ionization cross section functions for the reactions $H_2O + e \rightarrow H_2O^+ + 2e$, $H_2O + e \rightarrow OH^+ + H + 2e$, $H_2O + e \rightarrow H^+ +$ products, and $H_2O + e \rightarrow O^+ +$ products after Schutten et al. [117], designated o, (for the much smaller production channels concerning the O^{2+} and H_2^+ fragments see [117]). Also shown for comparison the experimental data of Märk and Egger [205] for the case of H_2O^+, designated ●, and theoretical estimates of Khare and Meath [87], designated — (curve A without and curve B with transfer of a certain percentage of the oscillator strengths corresponding to H_2O^+ and OH^+ to those of O^+).

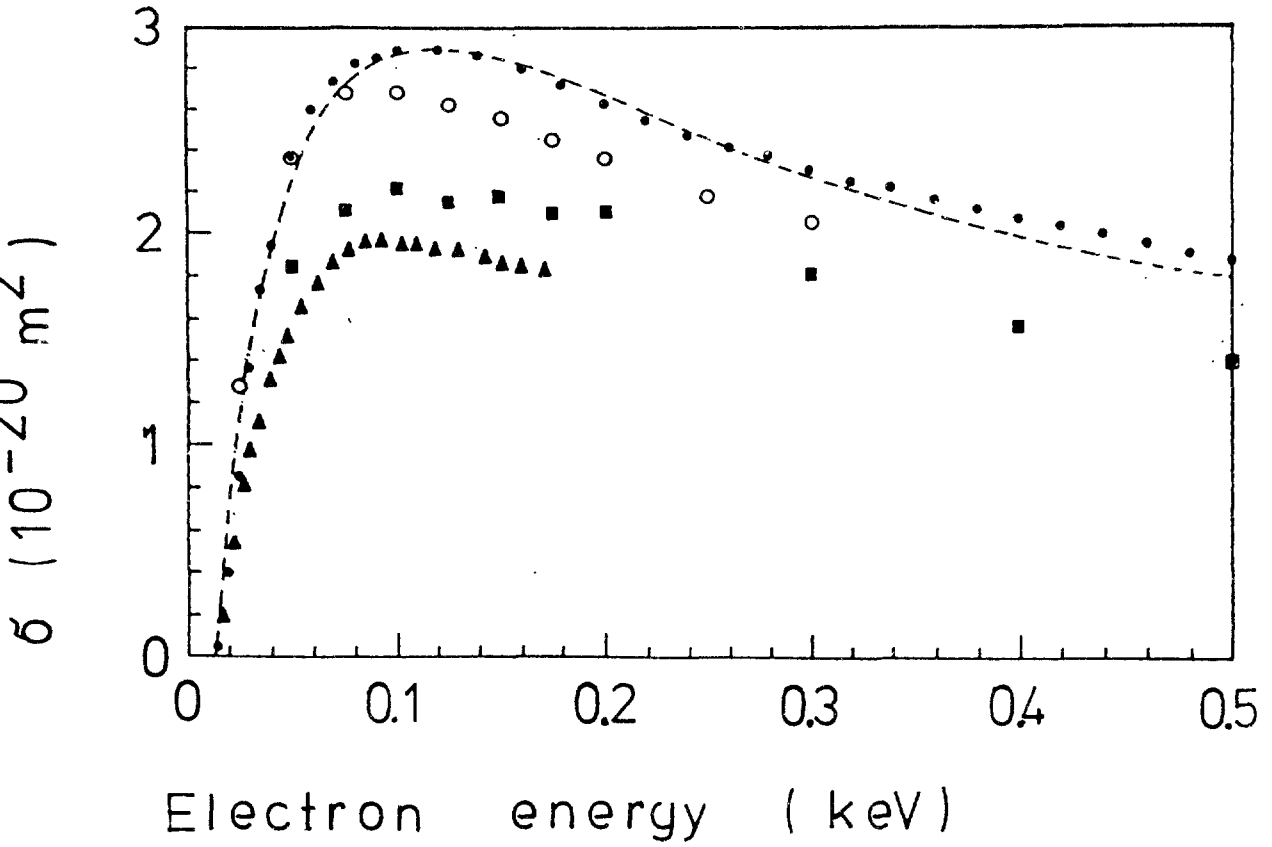

Fig. 3.30 Partial electron impact ionization cross section function for the reaction CO_2 + e $\rightarrow$ CO_2^+ + 2e: ■ Adamcyzk et al. [143], o Crowe and Mc Conkey [205], Δ Märk and Hille [206], ● Orient and Srivastava [185] and - - - Krishnakumar [158]. Double ionization of CO_2 has been studied by Märk and Hille [206] and other partial cross sections have been reported by Adamczyk et al. [143]. Moreover, Jackson et al. [207] have reported on the influence of the temperature on the dissociative ionization of CO_2.

No absolute total, counting or partial ionization cross sections for a specific cluster size (except for dimers, see Fig. 3.33 and Table 3.3 [4,126]) have been reported up to date. Conversely, total, counting and partial ionization cross sections have been measured for cluster distributions of H_2 and CO_2 (for more detail see references given in Ref.[4]). Fig. 3.34 and 3.35 show the total ionization cross section functions divided by the averaged number of cluster constituents ("effective" cross section) for various H_2 and CO_2 cluster distributions, respectively. The position of the maximum of the cross section shifts to higher electron energies with larger averaged cluster size m and the magnitude of the effective cross section decreases for larger m. Also shown in Figs. 3.34 and 35 are theoretical estimates from Deutsch et al. [69] using a modified DM approach.

According to theoretical considerations [210,211] supported by a limited number of experiments, the total ionization cross section $\sigma_{t,m}$ for a cluster of size m may be envisioned to be the product of three terms times the total cross section of the monomer, $\sigma_{t,1}$, i.e ,

$$\sigma_{t,m} = \sigma_{t,1} (T_1 \cdot T_2 \cdot T_3) . \qquad (3.26)$$

The first term T_1 involves the probability that an electron strikes the cluster. This depends on the geometric cross-sectional area of the cluster and is proportional to $m^{2/3}$ for a spherical (or cubic) cluster of m constituents if the density of the cluster is assumed to be independent of cluster size. One must also assume that the cross-section of a molecule within the cluster is the same as that of the free molecule. The next term, T_2, corresponds to the probability that a colliding electron can cause an ionizing event within the cluster This

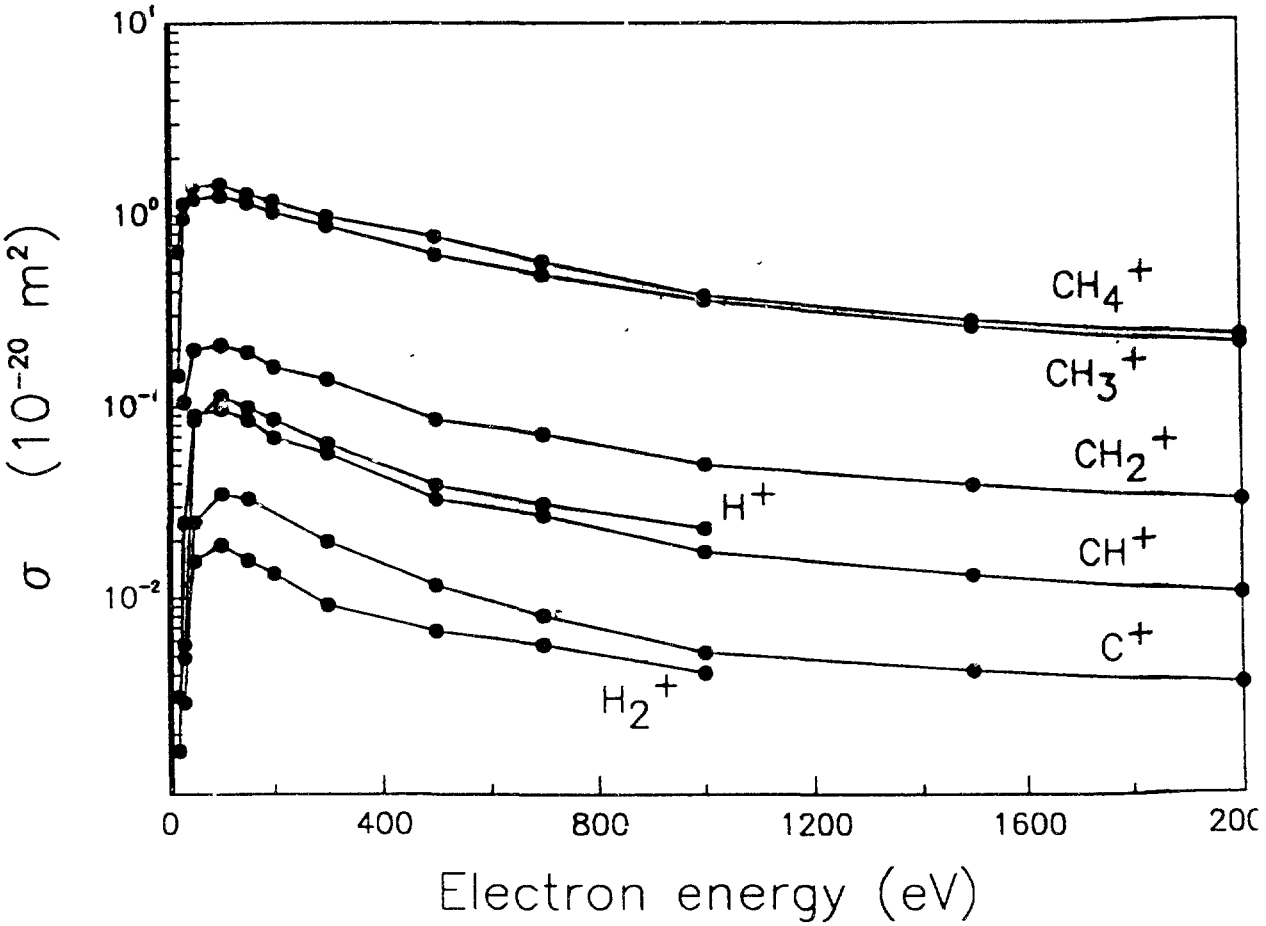

Fig. 3.31 Partial electron impact ionization cross section functions for the reactions $CH_4 + e \rightarrow CH_4^+$, $CH_4 + e \rightarrow CH_3^+$, $CH_4 + e \rightarrow CH_2^+$, $CH_4 + e \rightarrow CH^+$, $CH_4 + e \rightarrow C^+$, $CH_4 + e \rightarrow H_2^+$,and $CH_4 + e \rightarrow H^+$ after Adamczyk et al [141] (Neutral products also produced in these reactions are not considered in this context). Similar results have been obtained recently by Chatham et al. [114].

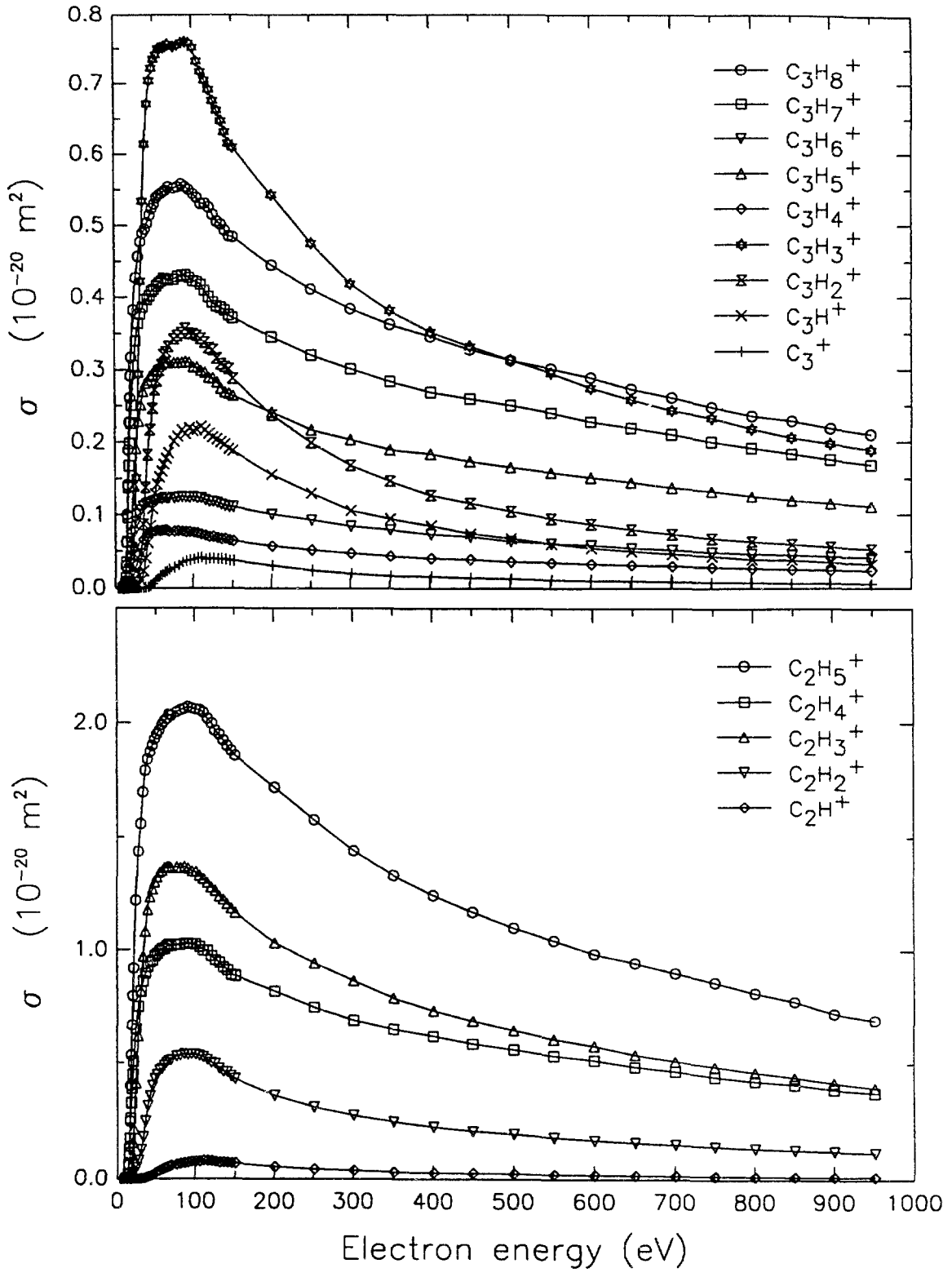

Fig. 3.32 Partial electron impact ionization cross section functions for the production of $C_3H_8^+$, $C_3H_7^+$, $C_3H_6^+$, $C_3H_5^+$, $C_3H_4^+$, $C_3H_3^+$, $C_3H_2^+$, C_3H^+, C_3^+; $C_2H_5^+$, $C_2H_4^+$,$C_2H_3^+$, $C_2H_2^+$, C_2H^+, C_2^+; CH_3^+, CH_2^+, CH^+, C^+; $C_3H_5^{2+}$, $C_3H_4^{2+}$, $C_3H_3^{2+}$ and $C_3H_2^{2+}$ ions via electron impact ionization of C_3H_8 after Grill et al. [119]. See also relative partial cross sections given in Fig. 3.22 and corresponding discussion in the text.

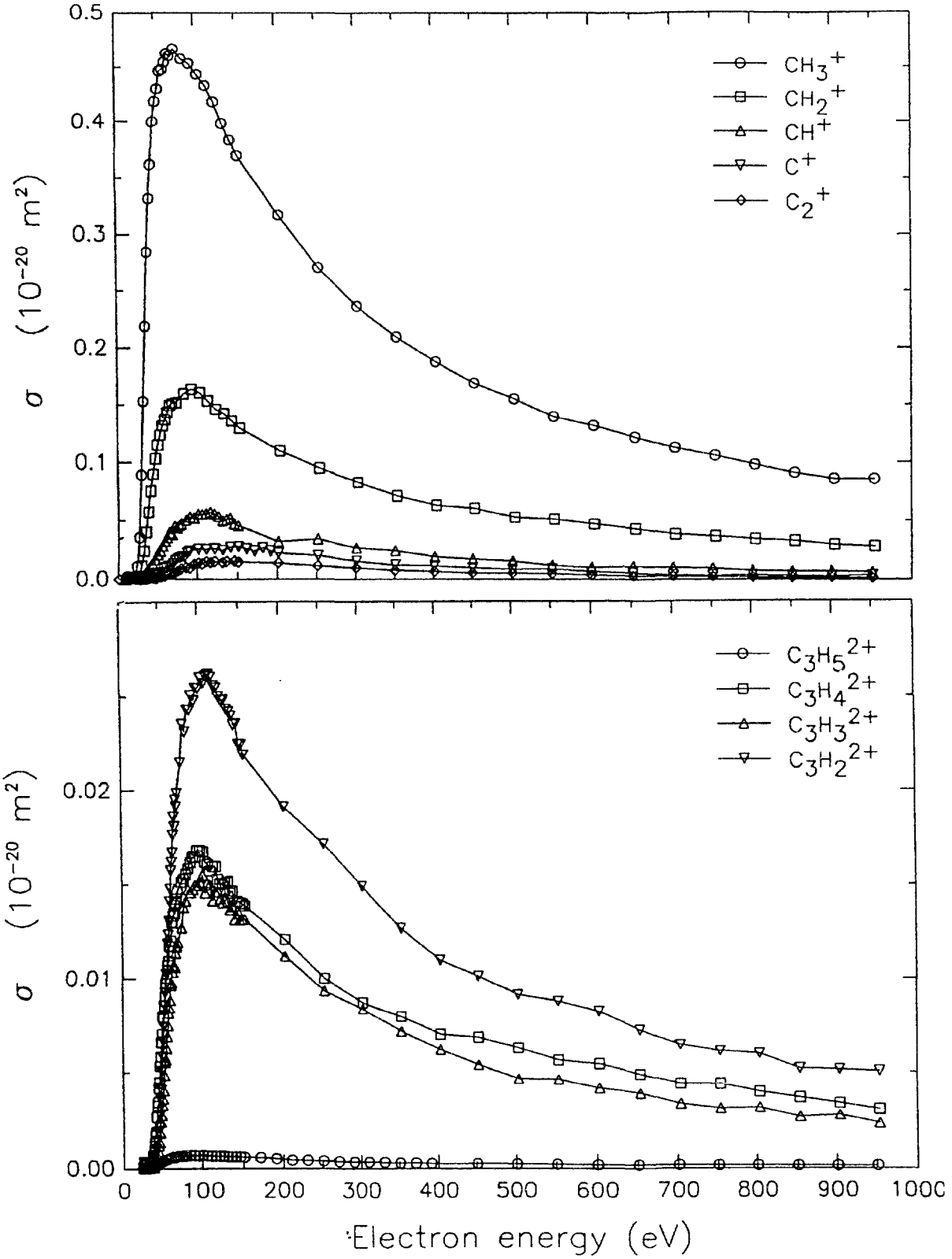
0.5
0.4
0.3
0.2
0.1
0.0
σ (10⁻²⁰ m²)
CH3+
CH2+
CH+
C+
C2+
0.02
0.01
0.00
C3H5 2+
C3H4 2+
C3H3 2+
C3H2 2+
0
100
200
300
400
500
600
700
800
900
1000
Electron energy (eV)

Fig 3.32 (cont.)

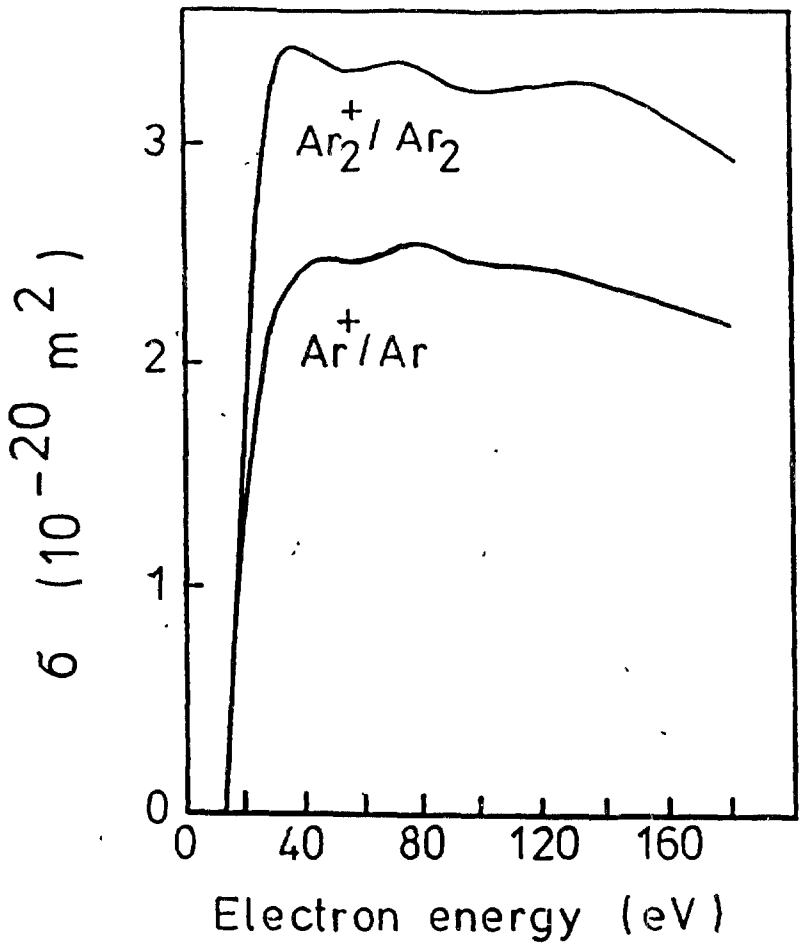

Fig 3.33 Partial electron impact ionization cross sections for the reaction Ar + e → Ar^+ + 2e and Ar_2 + e → Ar_2^+ + 2e, respectively, as a function of electron energy after Mark [4]

term can be expressed as $1 - e^{-d/\lambda}$ where d is the mean distance traveled inside the cluster by the incident electron and λ is the mean free path for ionization within the cluster The mean free path λ depends only on the energy of the incident electron, whereas d depends on the radial dimension of the cluster which is proportional to $m^{1/3}$. Thus, for a small cluster ($d << \lambda$), $1 - e^{-d/\lambda}$ is proportional to $m^{1/3}$ and for a large cluster ($d >> \lambda$), the term is unity The last term, T_3, considers the probability that the ensuing secondary electron escapes the cluster This probability is given by $1 - e^{-D/\lambda}$ where D is the mean distance that a secondary electron can travel in the cluster and still have sufficient energy to escape the cluster. In this case, for a small cluster ($d << D$), the probability is unity, whereas for a large cluster the probability is proportional to $m^{-1/3}$. Therefore, the total ionization probability for a small cluster ($d << \lambda$ or D) is directly proportional to the cluster size m. For a larger cluster ($d >> \lambda$ or D) the probability becomes proportional to $m^{2/3}$. The dimension D is expected to be smaller than λ, so the expected criterion for this proportionality is $d >> D$. If

Table 3. Estimated absolute partial ionization cross sections for the production of parent ions in Ar_2, ArKr, Kr_2, KrXe and Xe_2 after Märk [126]. Electron energy in eV and cross sections in $10^{-20}m^2$.

Electron energy	$\sigma(Ar_2^+/Ar_2)$	$\sigma(ArKr^+/ArKr)$	$\sigma(Kr_2^+/Kr_2)$	$\sigma(KrXe^+/KrXe)$	$\sigma(Xe_2^+/Xe_2)$
12.5	-	-	-	0.21	0.25
15	-	0.24	0.51	1.53	2.91
20	1.49	1.43	2.21	4.03	6.14
25	2.66	2.54	3.59	5.74	7.49
30	3.17	3.44	4.73	6.17	7.69
35	3.40	3.82	4.96	6.36	7.40
40	3.46	3.98	5.11	6.15	7.27
45	3.43	4.10	5.32	6.09	7.43
50	3.38	4.03	5.29	5.92	7.18
60	3.41	4.08	5.58	6.05	7.43
70	3.43	4.15	5.57	6.13	7.58
80	3.38	4.08	5.23	6.24	7.27
90	3.33	3.99	4.93	5.71	6.84
100	3.28	3.97	4.67	5.61	6.54
110	3.30	3.89	4.96	5.64	6.56
120	3.32	4.07	4.90	5.71	6.63
130	3.32	4.09	4.69	5.52	6.51
140	3.29	4.05	4.49	5.28	6.09
150	3.25	3.99	4.31	5.01	6.06
160	3.17	3.98	4.10	4.77	5.48
170	3.10	3.90	3.71	4.41	5.11
180	3.02	3.71	3.62	4.06	4.68

the cluster is very large ($d >> \lambda$ and D), the proportionality should fall to $m^{1/3}$. Bottiglioni et al. [210] point out that electrons of about 80 eV incident energy can be captured only by clusters exceeding 10^8 molecules.

From the dependence of the total charge production cross section on cluster size (see Fig. 3.34,3.35), Henkes and coworkers determined the ionization shell thickness D to be about three molecular layers for CO_2 clusters [209] and five and one-half for the H_2 clusters

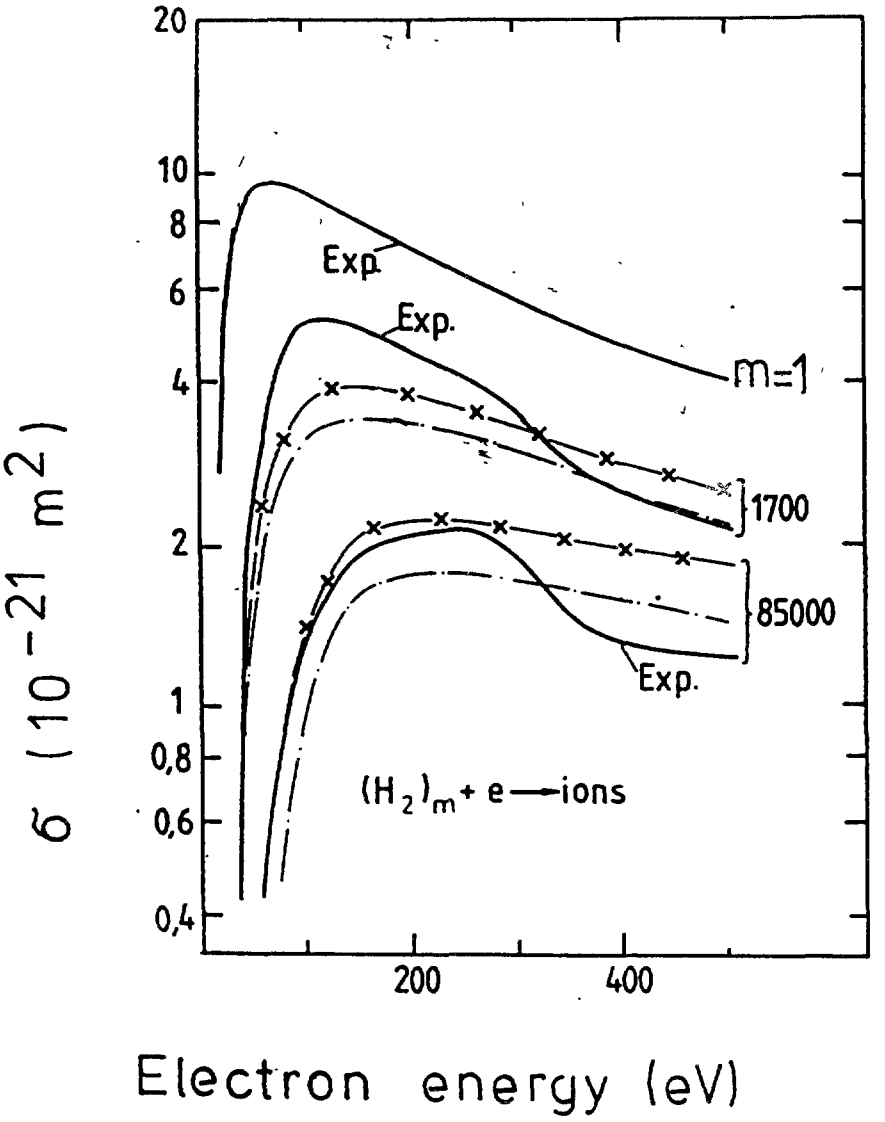

Fig. 3.34 Effective total electron impact ionization cross section functions for various $(H_2)_m$ cluster distributions with an averaged cluster size m after Henkes and Mikosch [208] designated Exp. Also shown for comparison are calculated values using a modified DM approach after Deutsch et al. [69], designated -.-.- (a = 0.47) and -*-*- (a = 0.48). In this case r_{nl}, ξ_{nl} and g_{nl} in equ. (3.25) have been replaced by $m^a r_{nl}$, $m\xi_{nl}$ and g_{nl}/m , respectively [69].

[208]. In the case of the H_2 clusters, however, the cross-sections to be used in the relationship (3.26) were found to be about half of the cross-section for the free molecule.

A few relative partial ionization cross section functions have been reported (the most extensive study concerns Ar clusters [212]; others are summarized in Ref. [4,126]). For the reasons given above no absolute values are available. Owing to this deficiency of data, the additivity rule [63-65,83,84] (despite being only valid for total cross sections) has been used

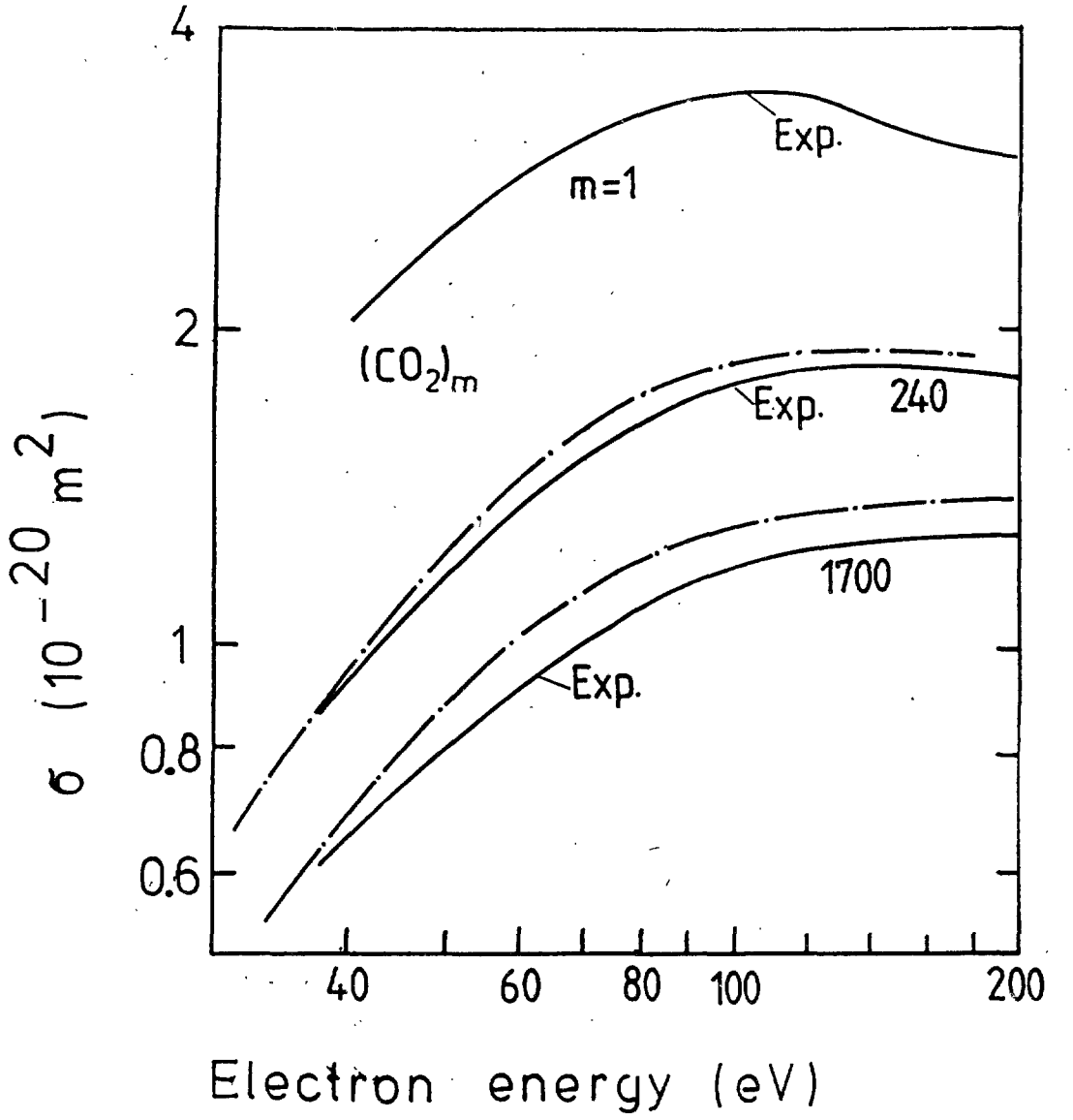

Fig. 3.35 Effective total electron impact ionization cross section functions for various $(CO_2)_m$ cluster distributions with an averaged cluster size m after Hagena and Henkes [209] designated Exp. Also shown for comparison are calculated values using a modified DM approach after Deutsch et al. [69], designated -.-.- (a = 0.41; see Fig. 3.34).

Table 4 Fragmentation ratio f_{nm} for electron ionization of Ar_2 and Ar_3. This ratio is defined as $f_{nm} = X_m^+/\Sigma X_m^+$ for reaction $X_n + e \rightarrow X_m^+ + 2e + (n-m)X$.

	f_{n1}	f_{n2}	f_{n3}
Ar_2	0.33 [216]	0.67 [216]	--
	0.40 [217]	0.60 [217]	--
Ar_3	0.30 [217]	0.70 [217]	$< 10^{-4}$ [217]

occasionally to calibrate cluster ion signals detected by mass spectrometry, i.e. assuming for instance that the dimer ion signal is twice the monomer ion signal and so forth. This procedure, however, is at variance with the results presented above (Fig.3.33). It neglects possible fragmentation of the neutral under study and possible cascading from larger neutral clusters present in the distributions. Using a modified additivity rule taking into account dissociative channels, it is possible to deduce at least for rare gas dimers absolute partial ionization cross sections [4,47] (e.g., see Fig. 3.33 and Table 3.3). Moreover, in a few cases accurate partial ionization cross section ratios have been determined for small clusters using either spectroscopic methods [213] or the method of producing size selected neutral clusters by momentum transfer via scattering [214]. As expected from the mass spectrometry of ordinary molecules [1,2] appreciable fragmentation is occurring for some of the clusters studied [4,215]. Fragmentation ratios deduced for Ar_2 and Ar_3 are given in Table 3.4 i.e., 40% of the ions produced (including prompt and metastable dissociation) from Ar_2 are Ar^+ fragment ions, and in the case of Ar_3 almost 100% of the ions are ending up as Ar_2^+ or Ar^+ fragment ions.

For more details and information on the electron impact ionization of clusters see Ref. [3-5, 126,211 and 215].

3.6. Electron Attachment

Electron attachment is a process in which electrons are captured by atoms or molecules to form negative ions and classified into two types; dissociative and non-dissociative processes as shown in the following reaction scheme,

$$e^- + AX \underset{1/\tau}{\overset{\sigma \text{ or } k}{\Leftrightarrow}} AX^{-*} \Rightarrow \begin{cases} A + X^- & (3.27) \\ AX^- + \text{energy} . & (3.28) \end{cases}$$

Interaction of low-energy electrons with molecules, AX, produces unstable negative ions, AX^{-*}, with a cross section σ or a rate constant k. The autodetachment of electrons from AX^{-*} with a lifetime τ may compete with the dissociation of AX^{-*} or with the formation of stable molecular negative ions, AX^-, which requires the release of the excess energy from AX^{-*}. The lifetime τ is related to the electron-energy width of the attachment resonance. The value of $1/\tau$ is a rate constant for the autodetachment process. In the presence of third-body molecules, AX^{-*} is collisionally stabilized to form stable AX^-. The branching ratios among the unimolecular processes of decaying AX^{-*} depend on the interrelationship of the potential energy curves between AX and AX^-, and also on electron energies. The relative

importance of the collisional stabilization process in the overall decaying processes of electrons depends largely on these unimolecular processes particularly the lifetime τ and on the number density and character of third-body molecules, in which one may expect some environmental effects on the over-all scheme of electron attachment processes. In addition to the determination of cross sections or rate constants for electron attachment or negative-ion formation and their electron energy dependences, it has been of prime importance in electron attachment studies to clarify the attachment mechanism, not only the two-body mechanism but also the overall mechanism and how environmental conditions affect the mechanism.

Electron attachment processes have been extensively studied theoretically and experimentally, and these are comprehensively summarized in recent review papers [218-229]. A brief survey is given here of only the experimental studies.
Low-energy electron attachment to molecules has been studied using,

1) Beam methods
   - 1.1. Electron scattering spectroscopy
   - 1.2. Electron impact mass spectroscopy of negative ions
   - 1.3. Photo-electron spectroscopy of negative ions
   - 1.4. Collision of Rydberg atoms with molecules
   - 1.5. Collision of alkali metal atoms with molecules
2) Swarm methods
   - 2.1. Electron-swarm (or drift-tube) techniques
   - 2.2. Microwave techniques combined with flowing or static afterglow methods (or with electrical discharges)
   - 2.3. Microwave technique combined with pulse radiolysis methods
   - 2.4. Electron cyclotron resonance spectroscopy
   - 2.5. Pulse sampling technique
   - 2.6. Electron density sampling method (the Cavalleri method)

Various types of electron scattering experiments at low energies less than several eV have given cross sections of electron attachment and information on the initial interaction potential between electron and molecule, and thus provided an efficient knowledge of the structure of formed negative ions or the interrelationship of the potential curves between AX and AX^-. Since it has been difficult, in general, to make electron attachment experiments using beam methods at extremely low energies particularly near thermal energies [230,231], heavy particle collisions such as those using Rydberg atoms [232,233] or alkali metal atoms [234,235] as low energy electron sources have been a good substitute giving an important information on electron attachment processes. Electron scattering experiments using beam

methods at such low energies including even thermal energies are certainly one of the important subjects not only in collision physics itself but also as a bridge between beam experiments and swarm experiments.

Instead of beam methods, electron-swarm or drift tube techniques have played a major role in those investigations and accumulated data on attachment rate constants, their electron energy dependences, formed negative ions, etc. Most electron swarm studies monitor the rate of removal of electrons in the swarm drifting in a tube, usually under DC electric field in the presence of a buffer gas. In addition to usual swarm techniques an interesting approach of measuring cyclotron resonance signals due to free electrons in gases has been carried out for the study of electron attachment to various molecules as a function of electron energy in the range of 1 to 10 kT. Another interesting approach to electron attachment studies is highly sensitive monitoring of electron density in the swarm by the Cavalleri method. The pulse sampling technique is simple but capable of yielding precise data particularly on energetics of negative-ion formation. A microwave technique for monitoring the rate of removal of electrons in the swarm has been combined with static or flowing afterglows produced by electrical discharges. This technique has been combined also with the pulse radiolysis method in order to eliminate essential limitations inherent to the above-mentioned microwave technique. The response time of the detection system for electrons has been highly improved and the effect of the presence of various species in afterglows on electron attachment processes has been eliminated. This combination has shown, therefore, a distinct advantage in studying thermal electron attachment to molecules, making possible to perform time-resolved observation of decaying electrons with very fast response in a wide range of the pressure of an environmental gas which is chosen with virtually no limitation (see 4.2). Thus, the mechanism of low-energy electron attachment to molecules has been discussed primarily in terms of the interaction of electrons with molecules even in a multiple collision system. Recent studies of thermal electron attachment to O_2, N_2O and other molecules using this technique have revealed interesting features of the electron attachment to van der Waals molecules, i.e., the effect of the van der Waals potential on the electron attachment resonance (see 4.2.). This experiment has triggered a recent development in beam experiments of electron-van der Waals molecule collisions [4,5,236,237].

Experimental data on electron attachment processes have been recently surveyed by Shimamori [218] and classified into two-body and three-body attachment processes. The two-body processes consist mainly of dissociative attachment and additionally of nondissociative attachment. In the latter attachment the overall mechanism is essentially a three-body process, but looks like a two-body process because of a long lifetime of AX^{-*} in comparison with the collision frequency between AX^{-*} and M. The three-body processes

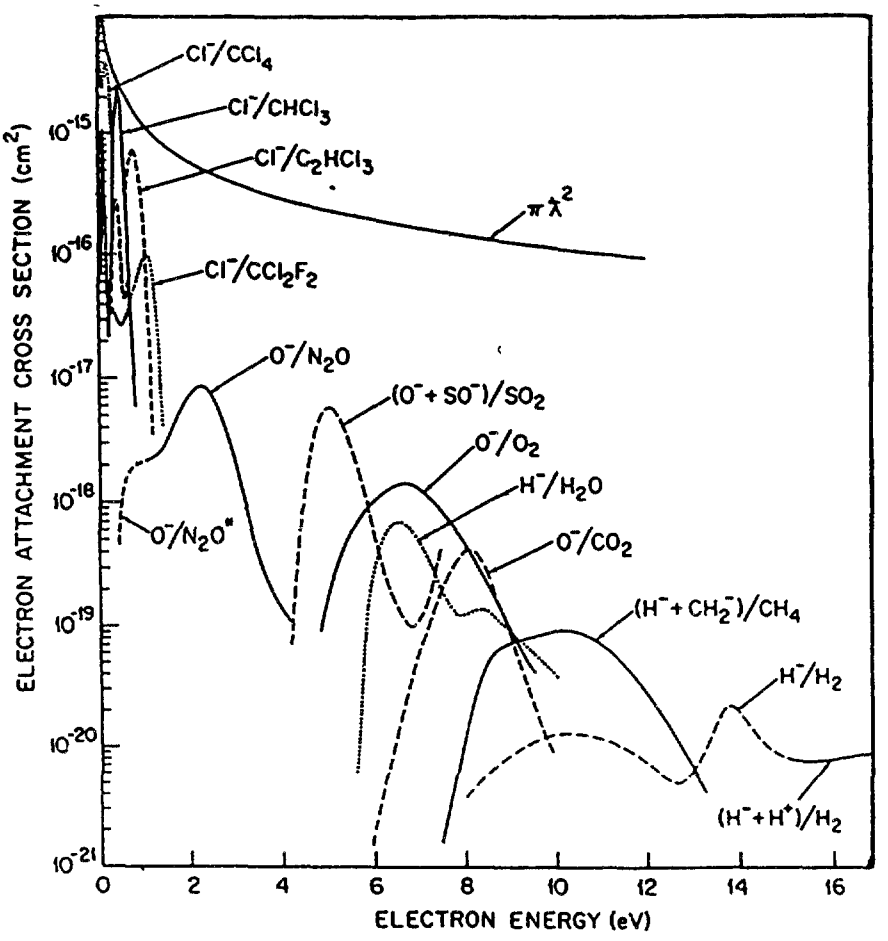

Fig. 3.36 Dissociative attachment cross sections as a function of electron energy in comparison with the theoretical maximum cross section $\pi\lambda^2$ after [221].

consist totally of the non-dissociative attachment which needs the stabilization of AX^{-*} in collision with M to form stable AX^-.

Christophorou et al. [221] summarized, as shown in Fig 3.36, dissociative attachment processes in terms of their cross section values as a function of electron energy and demonstrated an interesting comparison between $\pi\lambda^2$, i.e., the theoretical maximum attachment cross section, where λ is the electron de Broglie wave length, and the observed maximum ones. The difference in the cross section value between the two, which increases with increasing the electron energy, is ascribed to the decrease in the survival probability with increasing the electron energy. The magnitude of extremely large cross sections at relatively lower electron energies is of great interest when such attachment occurs in the condensed phase, because the electron de Broglie wavelength in this case is much larger than an average distance between molecules in the medium.

The hydrogen isotope effect of the cross section for dissociative electron attachment, in which a heavier molecule has a smaller cross section in comparison with that for a lighter molecule, is well known and explained in terms of the effect of the difference in the reduced mass of the dissociation fragments, A and X^-, also on the survival probability. Another interesting isotope effect has been recently observed also in a nondissociative attachment process. Three-body attachment rate constants have been measured for $^{16}O_2$ and $^{18}O_2$, in which the difference in the attachment resonance energy between the two is expected [238,239]. In some attachment processes, the effect of the temperature of gases on the cross section or rate constant has been observed. The effect has been ascribed, in most cases, to the vibrational excitation of a molecule AX. As described in section 4.2., another type of the temperature effect has been recently observed. This is the effect of the temperature of gases on the density of a van der Waals molecule, which has an attachment rate constant to be much larger than an isolated molecule.

Oxygen is cited here as a good example of AX in both dissociative and nondissociative electron attachment processes because this molecule is probably the most extensively studied molecule in the investigation of low-energy electron attachment [219,222,240], mainly because this is one of the simplest molecules and is also the main constituent of atmospheric gases. The dissociative attachment has been investigated by many people and general agreement on the cross section has been reached. The cross section has a broad peak with its maximum at about 6.7 eV. This peak is interpreted as a resonance process

$$e^- + O_2(X^3\Sigma_g^-) \rightarrow O_2^-(^2\Pi_u) \rightarrow O^-(^2P) + O(^3P) . \qquad (3.29)$$

The nondissociative process has been also extensively studied with an electron beam or swarm technique. From those experimental studies, together with theoretical ones, the attachment process for thermal electrons is understood to proceed in the following way. First the electron of ~ 80 meV is resonantly captured by O_2:

$$e^- + O_2(X^3\Sigma_g^-, v = 0) \rightarrow O_2^{-*}(^2\Pi_g, v' = 4) \qquad (3.30)$$

The lifetime of the resonant state O_2^{-*} in terms of the autodetachment of electrons:

$$O_2^{-*}(^2\Pi_g, v' = 4) \rightarrow O_2(X^3\Sigma_g^-, v=0) + e^- \qquad (3.31)$$

is known to be ~ 100 ps, which gives a resonance width of ~ 10 μeV. In the presence of a third-body molecule M, O_2^{-*} is collisionally stabilized in competing with the process (3.31) to form stable O_2^-:

$$O_2^{-*}(^2\Pi_g, v' = 4) + M \rightarrow O_2^-(^2\Pi_g, v' \leq 3) + M \qquad (3.32)$$

The processes (3.30)-(3.32) are reduced to the overall three-body attachment,

$$e^- + O_2 + M \rightarrow O_2^- + M \qquad (3.33)$$

The rate constants of the process (3.33) have been measured for a variety of third bodies M ranging from rare gas atoms and diatomic molecules to complex molecules such as hydrocarbons and alcohols. The difference in the obtained rate constant values are interpreted in terms of the vibrational energy transfer from O_2^{-*} to M. By changing widely the pressure of M, the electron attachment to van der Waals molecules (O_2.M) or $(O_2)_2$ has been observed (see 4.2.).

3.7. Electron Impact Dissociation of Molecules

Electron impact dissociation of molecules has been extensively studied by measuring either the excitation spectra of dissociation, i.e., dissociation cross sections vs. electron-impact energy [241,242], or the translational energy of dissociation fragments [243] (This section is concerned with the dissociation into neutral fragments because the dissociation into ionic fragments is described in Section 3.4.). The former measurements have been limited mostly to the dissociation into optically emissive fragments and in some cases into optically non-emitting but excited fragments, e.g., H(2s) and high Rydberg atoms, because of experimental difficulties in the measurement of non-emissive fragments at the ground state, although the cross sections to form ground state fragments are generally much larger than those to form excited ones. The latter measurements have been also carried out exclusively with excited fragments and divided further to the following two types depending on measurement techniques [243]:

1. Time of flight measurements

2. Doppler profile measurements.

Electron impact dissociation of molecules has been investigated most extensively by focussing on optically emitting dissociation fragments. In this section, therefore, a brief survey is given by referring some typical results of the excitation spectrum measurements and translational spectroscopy, and brief comments are added on the measurements of non-emissive fragments in the ground state formed in the electron impact dissociation of molecules.

Excitation spectrum measurements:

Optical emission from excited atoms or free radicals has been observed in electron impact dissociative excitation of a variety of molecules [241,242]. Good examples are chosen and briefly described in the following.

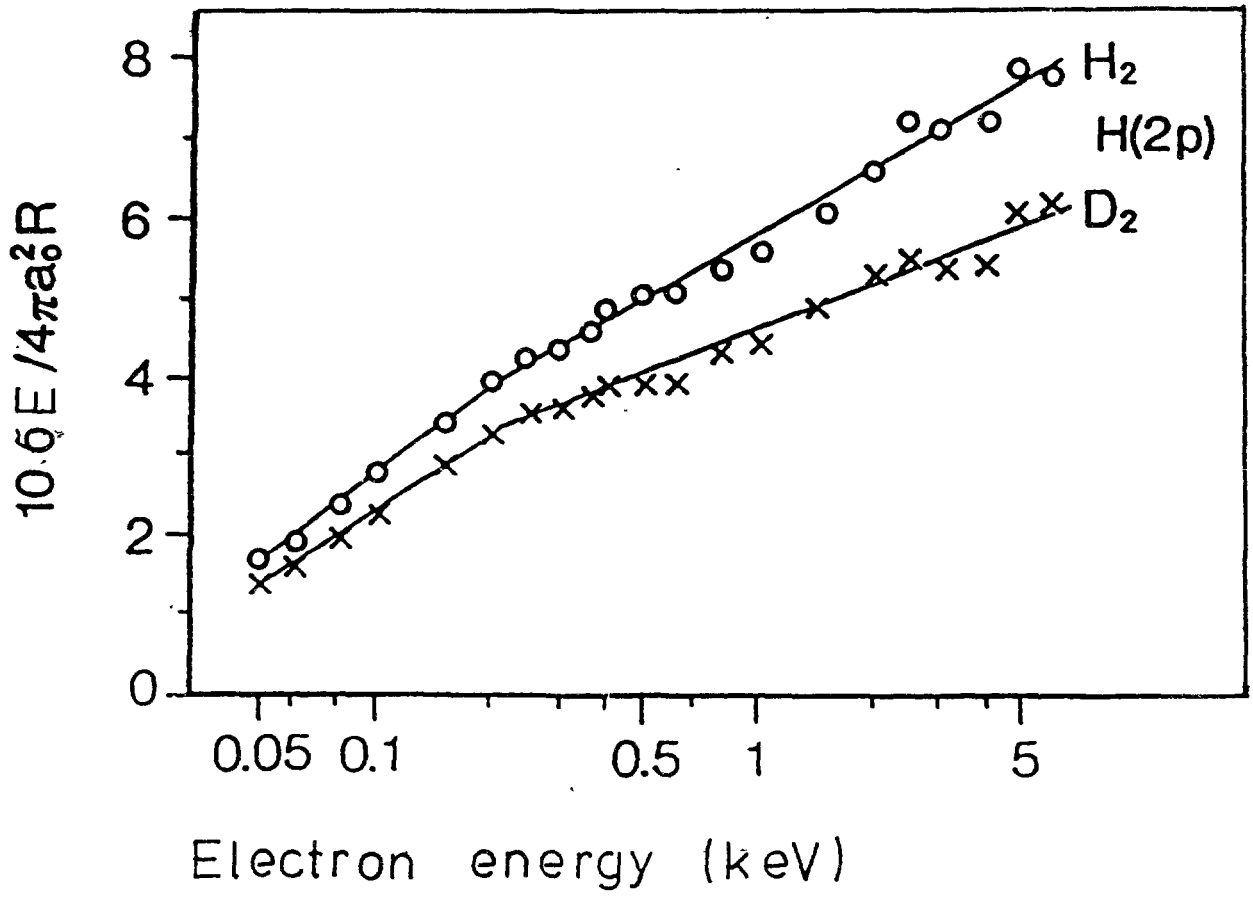

Fig. 3.37 Emission cross sections for Lyman-α radiation presented in the form of a Fano plot (see Ref. [14,43]) for electron impact on H_2 and D_2 after [244].

Absolute emission cross sections for production of hydrogen atoms in the n=2-6 excited states, where n is the principal quantum number, have been determined for dissociative excitation of molecular hydrogen and deuterium by electron impact in the energy range from 0.05 to 6 keV [244]. The excited atoms have been observed by optical detection of their fluorescence, Lyman-α radiation in the case of n = 2 and Balmer-α, β,γ, and δ radiation in the case of the higher states. The Fano plot (see Ref. [14,43]) of H(2p) formation is shown in Fig. 3.37, from which the dipole matrix element for its formation is obtained (see Chapter 5). Figure 3.37 clearly shows that H(2p) is produced from optically allowed excitation of H_2. A strong isotope effect is observed for the production of excited atoms from molecular hydrogen and deuterium and ascribed to a competition in the decay of superexcited states between dissociation and autoionization.

De Heer and his coworkers extended this experiment to other molecules, HF, HCl, H_2O and hydrocarbons [245-248]. The results of hydrocarbons showed a marked contrast in the Fano plot for the production of excited hydrogen atoms as compared with the result of H_2, HF, HCl and H_2O. Figure 3.38 shows the Fano plot for the Balmer β radiation

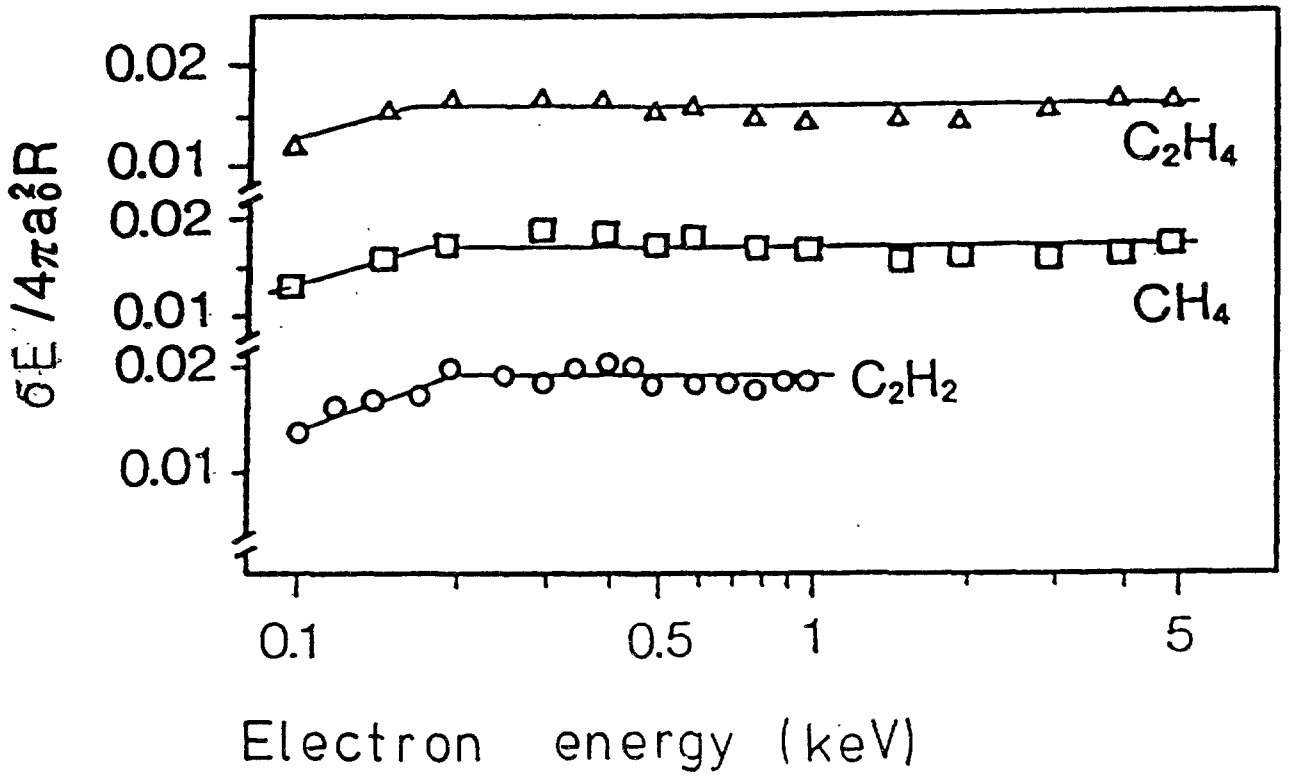

Fig. 3.38 Emission cross sections for Balmer β radiation presented in the form of a Fano plot (see Ref. [14,43]) for electron impact on acetylene, methane and ethylene after [247].

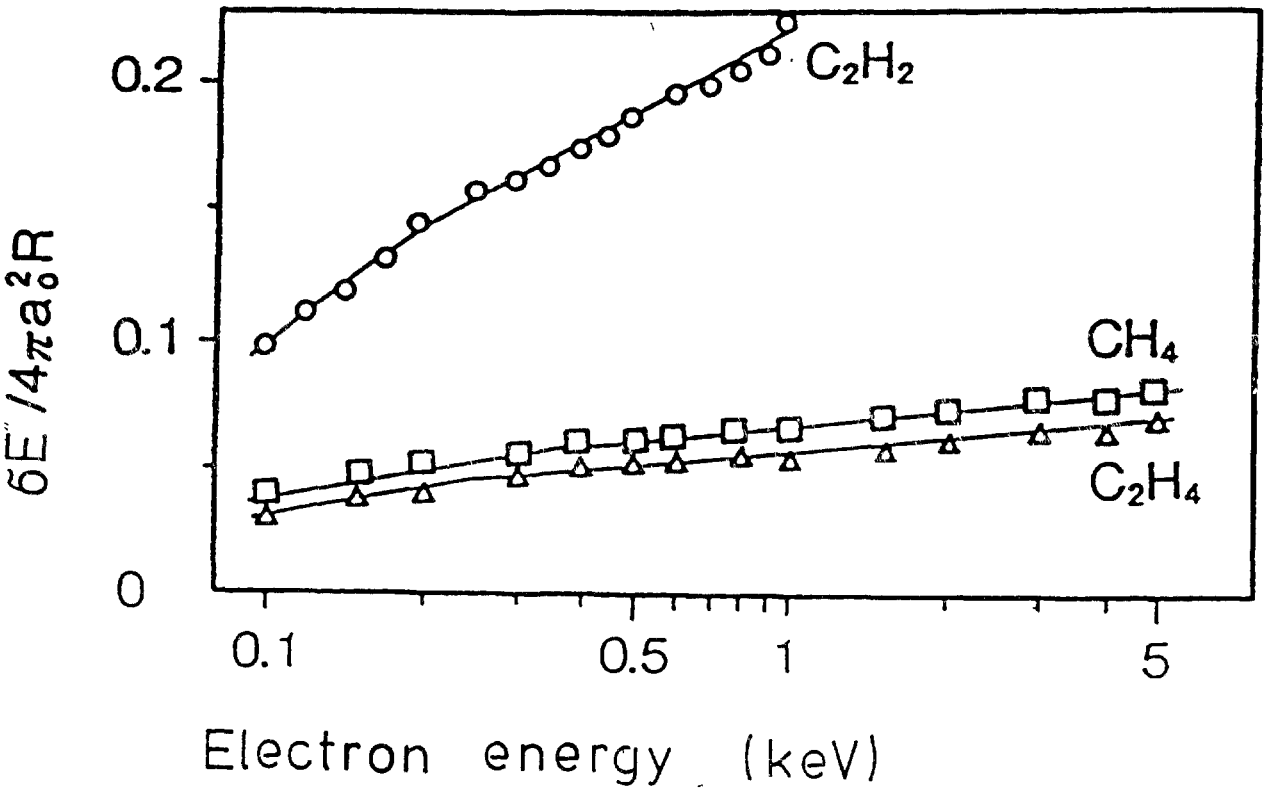

Fig. 3.39 Emission cross sections for CH($A^2\Delta \rightarrow X^2\Pi$) radiation in the form of a Fano plot (see Ref. [14,43]) for electron impact on acetylene, methane and ethylene after [247].

produced from the electron impact on simple hydrocarbons. The slopes of the straight lines at higher electron energies are almost horizontal, which shows that the production of excited hydrogen atoms is due to optically forbidden excitation of a hydrocarbon molecule.

In Fig. 3.39, however, the Fano plot for the CH($A^2\Delta \rightarrow X^2\Pi$) emission shows clearly the positive slope of the straight line for each hydrocarbon molecule, indicating that CH($A^2\Delta$) is produced by optically allowed transitions in the excitation which may involve superexcited states of the parent hydrocarbon molecules. De Heer and his coworkers attempted to compare results on excited fragments produced by optically allowed or forbidden transitions with the results of photoexcitation experiments. However, it was very difficult for them at that time to make such comparison because of relatively very few results of photoexcitation experiments in the energy range above the first ionization potential. Since, however, photodissociation experiments of molecules excited into that energy range are recently available, as described in Chapter 5, using synchrotron radiation, it is necessary to make systematic comparison of the experimental results of molecular dissociation between electron impact and photon impact.

Translational spectroscopy of dissociation fragments:

The broadening of an atomic line spectrum is generally ascribed to several well known factors: natural, Doppler, pressure, Stark and Zeeman broadenings [249]. Recently, Doppler profiles which are ascribed to molecular dissocation have been observed in electron-molecule collision experiments, from which direct information has been obtained on the energy and electronic-structure of molecular-dissociation potential-curves [243].

In the electron impact dissociation of H_2 the translational energy of H(n), i.e., excited hydrogen atoms with principal quantum number n, formed from doubly excited states $(2p\sigma_u)(nl\lambda)$ as well as from vibrationally excited states $(1s\sigma_g)(nl\lambda)$, has been obtained from Doppler profiles of Balmer emission lines. The hydrogen isotope effect has been also examined by measuring D(n) formed from D_2. These are typical evidence for the Platzman's prediction of the dissociation of superexcited states of molecules. In the case of molecular hydrogen, therefore, excess energies beyond the ionization threshold of a molecule result from vibrational or double excitation. For other molecules one can estimate another type of excess energy resulting from inner-valence excitation. This experimental technique has been further applied to H_2O, HF, NH_3, CH_4 and other more complex molecules, giving direct evidence for the dissociation potential of inner-valence excited states as well as doubly excited states [243,250].

In a series of these investigations the internal energies of these highly excited states have been found to be in good agreement with the energies of corresponding molecular ions obtained from photoelectron or ESCA (electron spectroscopy for chemical analysis) spectra and from (e,2e) experiments. This agreement shows that superexcited states are molecular high-Rydberg states converging to corresponding ionic states, and supports the core-ion model proposed for high-Rydberg atomic dissociation fragments [243].

Optically non-emitting fragments at the ground state formed in the electron impact dissociation of molecules:

To measure non-emitting fragments at the ground state formed in the electron impact dissociation of molecules, there have been the following three types of experiments:

1. Measurements of the decay rate of a target-gas pressure due to electron impact
2. Measurements of laser induced fluorescence from non-emitting fragments
3. Threshold-ionization mass-spectrometry of non-emitting fragments

These experiments are still in a preliminary stage of investigations to substantiate the dissociation dynamics into non-emitting fragments. In the experiment (1), the absolute value for the total dissociation cross section is obtained from the decay rate of a target-gas pressure due to electron impact [251]. This experiment is conceptually simple, but it is practically difficult to obtain real cross section values. The experiment (2) is also conceptually easy, but it is practically difficult to get enough fluorescence intensity under a single-collision condition and limited in terms of detected fragments. In the experiment (3), the increase in the yield of fragment ions due to electron impact ionization of neutral dissociation fragments is observed and ascribed to the field of neutral dissociation fragments initially formed [252]. This experiment is useful to understand quantitatively the dissociation into non-emitting fragments.

It is greatly needed to investigate systematically the dissociation into non-emitting fragments in electron impact experiments as well as in photon impact experiments (see Chapter 5).

3.8. Elastic and inelastic scattering of electrons

3.8.1. Scope of presentation

When an electron collides with an atom or molecule, the processes can be divided into two general categories: (1) elastic collisions in which no energy is transferred into the internal degrees of freedom of the target system and (2) inelastic collisions in which such energy transfer takes place. The following processes are considered here: (i) elastic scattering; (ii) rotational excitation; (iii) vibrational excitation; (iv) electronic excitation. The other inelastic processes, i.e., electron impact ionization and dissociation as well as electron attachment, are discussed in previous paragraphs of this chapter.

In both elastic and inelastic scattering, the electron loses some energy due to momentum transfer. While this energy loss is small in a single collision, it has to be taken into account because of the multitude of collisions experienced by the electron along its path. The cross section for momentum transfer is therefore included here.

The discussion will be confined to selected target species (i.e. Ne, Ar, H_2, N_2, O_2, H_2O, CO_2, CH_4, C_3H_8) which play a key role in radiation dosimetry and therapy and related instrumentation. The energy range covered is from 10^{-2} eV to 10^3 eV. Only collisions in the gas phase, i.e. with free atoms and molecules, are considered here.

In an ideal scattering experiment, one would like to measure the cross section for a transition between two completely defined quantum states. Although this may be desirable from a basic point of view, it is not always necessary. In practice, it is often also not

possible; in most cases, one measures cross sections which are averaged over a number of experimentally unresolved quantum states. For example, processes involving individual hyperfine levels or magnetic sublevels of electronic states are not of primary concern here. Such processes are measured in specially designed scattering experiments (e.g.,using laser excitation or electron-photon coincidence techniques). These measurements are outside the scope of the present survey. Similarly, electron spin polarization effects are not considered here, i.e., reported cross sections represent an average over electron spin orientations before and after the collision.

In electron-molecule collisions, the rotational and vibrational degrees of freedom often play an important role. With the presently available energy resolution in electron scattering experiments (typically 10-30 meV), individual rotational transitions can only be resolved for H_2. For other molecules, rotationally inelastic scattering is usually not separated from pure elastic scattering, so that in these cases the reported cross sections for 'elastic' scattering should be interpreted as 'vibrationally elastic' cross sections. It should be noted that there are some experiments in which information on rotational excitation is extracted by deconvolution methods [253-259].

As regards vibrational excitation, individual state-to-state transitions (starting from v = 0) are usually resolved in the case of diatomic molecules, whereas for polyatomic molecules the different excitation processes can only be partially separated. In many cases, even the fundamental modes are not clearly separable in the energy loss spectra of the scattered electrons. Additional complications arise for the excitation of higher harmonics and combination modes. A way of treating this problem usually consists in presenting electron impact excitation cross sections for certain composites of vibrational modes.

Some remarks may be added concerning the initial target states involved in the processes for which cross section data are reported here. First, we note that only collisions with atoms and molecules in their electronic ground state have been taken into account. Studies of electron collisions with atoms and molecules in electronically excited states, either metastable or short-lived, are still rather sparse. For the species considered here, only very few examples are found in the literature [260-264]. The subject of electron collisions with molecules in excited states has recently been reviewed by Christophorou [265].

At room temperature (kT = 25 meV), molecular targets are predominantly in their vibrational ground state. Only low-frequency modes of polyatomic molecules are excited to an appreciable degree (e.g., the bending mode vibration of CO_2 is populated with about 7 % at room temperature). As in the case of electronic states, we consider only collisions with molecules in their vibrational ground state. It is worth mentioning, however, that certain

processes, e.g. dissociative electron attachment, can show a strong dependence on the initial vibrational state of the target molecule. For the present species, there exist studies on electron collisions with vibrationally excited molecules for H_2, N_2 and CO_2 [265-290].

Under the same conditions as above (room temperature, kT = 25 meV), free molecules are populated in many rotational states, the population distribution depending on the rotational constant of the molecule. In the adiabatic approximation (i.e., molecular rotation slow compared to electron collision time), the cross section for any rotational transition $j_i \rightarrow j_f$ can be related to those for transitions from the rotational ground state ($j_i = 0$). This relation is given by

$$\sigma_{rot}\left(j_i \rightarrow j_f\right) = \sum_j \left[C\left(j_i j j_f; 000\right)\right]^2 \cdot \sigma_{rot}(0 \rightarrow j) \qquad (3.34)$$

where $C\left(j_i j j_f; 000\right)$ is the Clebsch-Gordan coefficient. The range of validity of this formula is discussed in more detail in [291,292].

If rotational excitation is not resolved, an average cross section is given by

$$\bar{\sigma}_{vib,el}\ (E,T) = \sum_{j_i} f_{j_i}(T) \sum_{j_f} \sigma_{rot}\left(j_i \rightarrow j_f\right) \qquad (3.35)$$

is measured, which may be called 'vibrationally elastic' in the case of $\Delta v = 0$ transitions. Here T is the gas temperature and $f_{j_i}(T)$ is the fractional population of the rotational state j_i at this temperature. Within the framework of the adiabatic approximation mentioned above, it can be shown that

$$\bar{\sigma}_{vib,el}(E) = \sum_j \sigma_{rot}\ (0 \rightarrow j)\,, \qquad (3.36)$$

which means that the resulting cross section for 'vibrationally elastic' scattering is independent of the gas temperature T.

Each of the processes discussed above is characterized by a differential cross section $d\sigma/d\Omega\ (E,\theta)$ which determines the intensity of scattered electrons going into a solid angle element $d\Omega$ as a function of collision energy E and scattering angle θ (for more details see 3.8.2.). The angular distribution of scattered electrons can be very different, both for a given process at different collision energies as well as for different processes at a given

energy. In many cases, such detailed data are available. However, for reasons of space the full set of differential cross section data cannot be presented here. This survey will be confined to the presentation of angle-integrated cross sections as a function of collision energy E. Fine details such as narrow resonances are usually omitted, except in a few cases (e.g., N_2, O_2) where the resonance structure plays a dominant role.

3.8.2. Definition of cross sections

When an electron beam of current density j (in units of electrons per cm^2 and per second) impinges on a gas target consisting of N atoms or molecules, then the current I_s of scattered electrons (in units of electrons per second) going into a solid angle element $d\Omega$ under polar angle θ and azimuthal angle ϕ is given by

$$I_s = \frac{d\sigma}{d\Omega}(E,\theta,\phi) \,.\, j \,.\, N \,.\, d\Omega. \qquad (3.37)$$

Here, E denotes the kinetic energy of the incident electrons and $d\Omega = \sin\theta d\theta d\phi$. The quantity $d\sigma/d\Omega$ is called the differential cross section (DCS) and has the dimension of area per unit solid angle, i.e. cm^2/sr. For atoms and for randomly oriented molecules, the DCS is independent of the azimuthal angle ϕ. Thus, the DCS may be written as $(d\sigma/d\Omega)_n\,(E,\theta)$ where we have now specified by the index n an individual elastic or inelastic scattering process. It is assumed that only transitions between discrete states are considered. Otherwise, a double differential cross section (DDCS) of the form $(d^2\sigma/d\Omega dE_f)_n\,(E_i,E_f,\theta)$ has to be introduced, where E_i and E_f denote the initial and final electron energy, respectively, and dE_f is an energy element of the continuous energy distribution of the scattered electrons. This occurs, for example, in the case of excitation of molecules to dissociative states. In practice, it may also be relevant in the case of close-lying, experimentally unresolved discrete states such as vibrational excitation of polyatomic molecules or excitation to high-lying electronic states. In order to arrive again at the ordinary DCS as defined by equation 3.37, the DDCS must be integrated over an appropriate energy interval ΔE_f of the final energy distribution.

In general, the measured DCS represents an average over unresolved initial states and a sum over unresolved final states, i.e.,

$$\left(\frac{d\sigma}{d\Omega}\right)_n (E,\theta) = \sum_i N_i \sum_f \left(\frac{d\sigma}{d\Omega}\right)_n^{i\to f} (E,\theta)., \qquad (3.38)$$

where N_i is the fractional population of the initial state $|i>$. An example has been given in equation 3.35 above. In comparing theoretical and experimental results, care must be exercised concerning the question to which extent such averaging has been performed or not. Furthermore, it must be recognized that any measured cross section (state-resolved or not) represents an average over the finite energy and angular resolution of the apparatus. In present beam experiments, the energy resolution is typically in the range of 10-30 meV, whereas the angular resolution may vary between a few tenths of a degree in experiments at higher collision energies and about 5^o in experiments at very low energies.

The integral cross section $\sigma_n(E)$ for each process is obtained by integrating the DCS over all scattering angles:

$$\sigma_n(E) = 2\pi \int_o^\pi \left(\frac{d\sigma}{d\Omega}\right)_n (E,\theta) \sin\theta \, d\theta \tag{3.39}$$

In the following, angle-integrated cross sections as a function of electron energy E are presented which are denoted as follows: σ_0 for elastic scattering, σ_{rot} for rotational excitation, σ_{vib} or σ_v for vibrational excitation, and σ_e for electronic excitation. Other processes are treated in previous paragraphs of this chapter.

The grand total cross section $\sigma_T(E)$ is given by

$$\sigma_T(E) = \sum_n \sigma_n(E) , \tag{3.40}$$

where the summation includes the elastic and all inelastic processes, i.e., the processes mentioned above as well as dissociation, ionization and attachment.

The momentum transfer cross section, which is important in relation to electron transport in gases, is defined by

$$\sigma_M^{(n)}(E) = 2\pi \int_o^\pi \left(\frac{d\sigma}{d\Omega}\right)_n (E,\theta) \left(1 - \frac{k_n}{k_o}\cos\theta\right) \sin\theta d\theta . \tag{3.41}$$

Here, $\hbar k_o$ and $\hbar k_n$ are the magnitudes of the initial and final momentum of the electron, respectively. The total momentum transfer cross section $\sigma_M(E)$ is again the sum over all contributing processes. In many cases, $\sigma_M(E)$ is dominated by the contribution from elastic scattering. Under these conditions, a good approximation may be obtained from the relation

$$\sigma_M(E) = 2\pi\int_0^{\pi} \left(\frac{d\sigma}{d\Omega}\right)_0 (E,\theta)\ (1-\cos\theta)\ \sin\theta d\theta\,, \qquad (3.42)$$

which is often used in practice. Here, $(d\sigma/d\Omega)_0(E,\theta)$ denotes the DCS for elastic scattering.

3.8.3. Experimental methods

Here we give only a brief survey of the main experimental methods. More details can be found in the general literature given below as well as in the original literature cited together with the presentation of the data.

Total scattering cross sections σ_T are measured in transmission experiments in which the attenuation of an electron beam is measured as a function of the target gas density in a scattering cell. Three different types of experiments may be distinguished: Ramsauer-type experiments, linear transmission experiments, and transmission experiments using time-of-flight (TOF) techniques. In the latter type of experiment, the TOF distribution of an electron pulse traversing the gas cell is measured and then converted to an energy distribution. The energy dependence of the cross section can be determined over a wide energy range by splicing many data sets, each obtained in a smaller energy interval. The realm of the TOF method lies at low energies where the resolution is the highest and where the other methods become increasingly difficult.

These transmission/attenuation experiments are simple by principle and therefore allow measurements of high accuracy. The main error sources are due to the pressure measurement, the effective path length determination, and contributions from forward scattering which cannot be completely suppressed because of the finite angular resolution of the set-up. An overall accuracy of 2-5 % is typically obtained in modern experiments and the cross section data reported by various investigators generally agree with each other within these error limits.

More detailed information on the collision processes is obtained from differential scattering experiments. Firstly, these experiments allow one to separate the total cross section into the contributions from the individual elastic and inelastic processes. Secondly, DCS data are obtained which give information on the angular dependence of the scattering process. This type of data is needed for the modelling of electron transport in gases. Furthermore, the DCS can be integrated over angles to yield integral cross sections $\sigma_n(E)$ for the individual processes as well as momentum transfer cross sections $\sigma_M^{(n)}(E)$.

In the past, two types of target configurations have been used in these experiments. One is a static gas target which may either be represented by the gas-filled vacuum chamber itself or which may consist of a small gas cell separately mounted in the vacuum. The other configuration, which is most widely employed in current experiments, uses an atomic or molecular beam as the target. In this type of experiment, a monochromatized electron beam (say of 10-20 meV energy width) is crossed at right angles with the gas beam. The latter is usually an effusive beam simply formed by a needle of 0.5 - 1 mm diameter or by a multicapillary array. Supersonic nozzle beams are seldom used in electron scattering experiments. The scattered electrons are detected as a function of energy and angle by a detector system whose main components are an energy analyzer and an electron multiplier. Usually, the electron gun is fixed in position and the detector is rotated around the scattering centre. The data are taken in different modes of operation: (i) energy loss spectra in which the detector energy is varied, while the primary energy E_0 and the scattering angle θ are fixed; (ii) excitation functions for a certain energy loss process in which the primary energy and the detector energy are varied simultaneously at fixed energy loss ΔE and scattering angle θ, (iii) angular distributions in which for a certain process (with E_0 and ΔE fixed) the angular dependence of the DCS is measured.

It is evident that this type of experiment gives both very detailed and nearly complete information on the scattering process. However, we also point out some problems which arise in these measurements. The first problem to be mentioned is the finite energy resolution (typically 10-30 meV in present-day experiments). Particularly for molecules, the energy loss spectra of the scattered electrons are very complex, since many rotational and vibrational levels are involved. It is generally a difficult task to decompose the complex overlapping structures of molecular energy loss spectra into the contributions from the individual processes. As already mentioned, rotational excitation is usually not resolved (except for H_2). The process termed 'elastic' scattering must therefore be interpreted as 'vibrationally elastic' scattering. The problems arising in vibrational excitation of polyatomic molecules have also been mentioned before. Regarding electronic excitation, the lower states of atoms and simple (diatomic) molecules are usually well resolved in the energy loss spectra of the scattered electrons. For higher excitations and in the presence of dissociative excitations, it becomes much more difficult to separate the individual contributions. In the case of polyatomic molecules, the energy loss spectra for electronic excitation usually appear as broad and unresolved structures. This is due to the manifold of excited states, the complex rovibrational structure and the strong participation of dissociative states. In spite of these difficulties it should be kept in mind, however, that the data obtained in differential scattering experiments give the most detailed information on the scattering processes. These data are extremely useful in situations where results obtained by other experimental methods, which are more global and more indirect in character (e.g., optical emission, metastable production, swarm type experiments), have to be evaluated and interpreted.

Another problem is the determination of the DCS in absolute units, i.e. the conversion of the measured scattering intensities into absolute values of the cross section. This problem has been treated in detail in a series of articles by Trajmar and coworkers [293-296]. Direct determination of absolute DCS based on the defining relation 3.37 is generally difficult, since it is not easy to obtain an accurate measure for the effective scattering volume as viewed by the detector. In order to make absolute measurements, one needs to know absolute beam densities including their spatial distribution, the overlap integral of the two beams, the effective acceptance angle of the detector and other factors. This is hardly possible without large errors. Therefore, one has to rely on other methods. There are several methods which are used in practice. At high energies and small angles, the experimental DCS can be normalized to theory by utilizing a Born or Born-type approximation. Another method, which is most favourably used at low energies where not too many channels are open, is based on normalization to measured total cross sections. First, all DCS are measured in relative units, then the data are integrated over angles, summed over all contributing channels and finally normalized to an absolute total cross section which is known from transmission experiments. In this way, the whole set of DCS values can be put on an absolute scale. A third method, which is probably the most practical one, is the relative flow technique. This method was originally developed in Trajmar's group [293] and is now widely used in many laboratories around the world. Absolute DCS values are determined by comparing the scattering intensities for the gas under study with those obtained under the same conditions for another gas whose elastic DCS values are well known. More precisely, the measurements are performed under such conditions that both gases satisfy the same molecular flow condition (see also Ref. [202]). The reference gas is usually helium for which the elastic DCS values are known with an accuracy in the order of 1 %.

In DCS measurements, it is generally impossible to cover the full angular range from 0° to 180° because of instrumental limitations. At small scattering angles, the primary electron beam begins to interfere with the elastic scattering signal, the critical angle depending on the energy of the primary beam. In low energy experiments, the limit is already reached at about 10° typically. At large angles, the accessible angular range is limited by the fact that the rotatable detector and the electron gun collide with each other. A typical value for the maximum angle reached in DCS measurements is 130-140°. In order to obtain integral cross sections $\sigma_n(E)$ and $\sigma_M^{(n)}(E)$ from the measured DCS data, it is necessary to extrapolate into the experimentally inaccessible regions. This introduces additional errors into the determination of integral cross sections by this method. It should be noted, however, that these errors can be minimized if the extrapolation is based on a phase-shift analysis of the experimental data. Nevertheless, the problem of extrapolation is especially important for σ_M, because backward scattering is heavily weighted in this cross section.

A useful cross-check of the data thus obtained can be made by using the relation

$$\sigma_T = \sigma_0 + \sigma_{exc} + \sigma_{att} + \sigma_t \,, \tag{3.43}$$

where σ_0 is the elastic cross section, σ_{exc} is the cross section sum for all inelastic processes including dissociation, σ_{att} is the cross section for electron attachment, and σ_t is the total ionization cross section (see equ. 3.18 and 3.20). The quantities, which are usually well known with an accuracy of 5% or better, are σ_T and σ_t. The attachment cross section σ_{att} often plays only a minor role (except for strongly electronegative gases such as halogens). The cross sections, which usually have the largest uncertainty, are σ_0 and σ_{exc}. Whereas the errors of σ_0 are typically in the range of 10-30 % depending on the system and the collision energy, no general statement can be made concerning the errors involved in the determination of the inelastic collision cross sections. These errors strongly depend on the process and the energy range considered. They may be in the order of 10% in favourable cases and may go up to a factor of two in situations where special difficulties exist in the measurements (e.g. threshold region). In some cases, the presently available inelastic cross sections represent only order-of-magnitude estimates. More specific comments will be given together with the presentation of the data.

Integral electron-impact excitation cross sections can also be obtained by measuring optical excitation functions, i.e. light emission at a particular wavelength induced by electron impact is measured as a function of impact energy. An optical excitation function (or optical emission cross section) measured in this way can only be regarded as an "apparent" excitation cross section for the state from which photoemission is observed. Various corrections are necessary to obtain the "true" excitation cross section, the most important of which being the correction for cascading from higher states. A further difficulty consists in making absolute measurements of the photon yield. Altogether, the experimental determination of electron-impact excitation cross sections by this method is difficult and not very accurate. On the other hand, the optical emission cross section may be compared with directly (i.e., cascade-free) measured excitation cross sections, if the latter are properly summed over all contributing states. In many cases, the agreement is satisfactory.

Similar considerations apply to the measurement of the total metastable production by electron impact. This cross section also contains contributions from cascades. Besides the usual difficulties inherent in all of these measurements (beam densities, effective scattering volume, collection efficiency, etc.), a special problem in the present case lies in the accurate determination of the detection efficiency of the metastables. In most experiments, the metastables are detected by secondary electron emission from a metal surface. The conversion efficiency for this process is generally not accurately known and often a matter of

debate. As in the case of the optical emission cross section, the total metastable production cross section may be compared with directly measured excitation cross sections summed over all contributing states. Again, reasonable agreement has been found in those cases where this comparison could be carried out.

An important contribution to the determination of electron collision cross sections comes from electron swarm experiments. We briefly comment on the principle of the method. Extensive reviews can be found in the literature [297,298]. In the first step, transport and reaction coefficients of an electron swarm drifting in a gas under the influence of an electric field are measured. Various experimental techniques are used for this purpose. Among the swarm parameters commonly measured are the drift velocity w, the transverse and longitudinal diffusion coefficient D_T and D_L, respectively, the characteristic energy $\varepsilon_K = eD_T/\mu$ (with μ = electron mobility) which is closely related to the mean energy $\langle\varepsilon\rangle$ of the electron swarm, the ionization coefficient α, the excitation coefficient β, and the attachment coefficient η. The quantities, which can be measured with the highest accuracy (about 1-2%), are the drift velocity w and the ionization coefficient α. The other quantities have typical errors of 5-10%, except the excitation coefficient β for which the experimental uncertainty is usually largest (about 20-30%).

The second step consists in deriving cross sections from the measured swarm data. The theoretical analysis is based on numerical solutions of the Boltzmann equation or on Monte Carlo simulation of the electron swarm. This provides the connection between the microscopic cross sections of the electron-atom and electron-molecule collision processes and the macroscopic transport and reaction coefficients. The actual determination of cross sections from the swarm data is usually accomplished by assuming a set of energy-dependent input cross sections based on any available information, solving the Boltzmann equation and the transport integrals with this set, comparing the calculated transport and reaction coefficients with experiment, and adjusting the input cross sections to improve the fit. This procedure is repeated iteratively until an optimum fit is obtained. The result is a set of elastic and inelastic cross sections which reproduces the measured swarm parameters within their respective error bars.

An important and well recognized regime of the electron swarm technique lies at low electron energies (say below 1 eV), where beam experiments have always been difficult to perform. If the energy is low enough, all electron-atom and virtually all electron-molecule collisions are elastic, and it is possible to obtain very accurate values for the momentum transfer cross section σ_M from measurements of the transport properties of the electron swarm Such cross sections have been determined for a large variety of gases. At higher energies, rotational and vibrational excitation begins to play a role in the case of molecular

gases. If the energy is still further increased, also electronic excitation and ionization become important processes for both atomic and molecular species. In these situations, it becomes difficult to derive a unique set of cross sections from swarm data alone. In general, complementary information from beam experiments or from theory has to be used to solve this problem. On the other hand, it must be noted that also under these conditions, where several inelastic channels are open, swarm experiments can give important contributions to the determination of the cross sections. As a particular example, we mention the threshold regions of rotational and vibrational excitation, where results from beam experiments either are not available or have large uncertainties. Another example is the determination of cross sections for electronic excitation, for which in many cases the data are incomplete or non-existent. In swarm experiments, lumped cross sections for electronic excitation (σ_e) can be derived from measurements of the Townsend ionization coefficient α, if sufficiently accurate data for the ionization cross section σ_t are known. The values of α are particularly sensitive to the values of σ_e in the low energy regime.

As a final remark, we mention that there is now a good overlap of the energy ranges of beam and swarm experiments, since beam experiments can now be performed down to collision energies in the order of 0.1 eV. The two kinds of experiments thus give complementary information which can be used to cross-check the accuracy of the data. In many cases, the data are consistent with each other, but there are also some cases where the data are still controversial. Recent developments in both beam and swarm experiments, with special emphasis on the relationship of the two techniques, are discussed in some conference books [299,300]. We especially mention the work of Hayashi [301, 302] who has determined comprehensive cross section sets for a large number of atoms and molecules by combining the information from both types of experiments.

3.8.4. General literature

More general accounts of the present subject can be found in a number of books dealing with atomic collision physics in general or with electron-molecule collisions in particular. These books are well known to the experts in the field; they are mentioned here as reference for those who are not immediately involved in this field. Needless to say that this list is by no means exhaustive.

A comprehensive review of the earlier developments of the field (up to late sixties) has been given by Massey et al. [303] in the classic volumes on 'Electronic and Ionic Impact Phenomena'. The applied aspects of atomic collision physics have been emphasized in a series of volumes entitled 'Applied Atomic Collision Physics' edited by Massey, McDaniel

and Bederson [304]. Two excellent books on electron-molecule collisions, both of them comprising experimental as well as theoretical aspects, have been published by Christophorou [305] and by Shimamura and Takayanagi [306]. Very recently, some very fine books covering the whole field of atomic collision physics have been published by McDaniel et al. [307,308].

In addition to these books, there is a large number of review articles, each dealing with a specific aspect of the field. We mention a few of them here [309-334], partly because they contain information which is of immediate interest for the present purpose and partly because they may be of general interest to the readers of this chapter.

Like in every field, the current developments are documented by conference proceedings. Two such books originating from a conference have already been mentioned in the preceding paragraph [299,300]. The main international conference in this field is the 'International Conference on the Physics of Electronic and Atomic Collisions' (ICPEAC), which is held every two years. The invited papers of the conference and the abstracts of contributed papers are published in separate volumes. In order to give access to this work, we quote here the conference proceedings (book of invited papers) of the last six conferences covering a period of about 12 years [335-340].

3.8.5. Cross section data

In figures 3.40-3.46, we present elastic, inelastic and total cross sections for the individual gases. For the sake of clarity, the momentum transfer cross sections are presented in separate figures (Figs. 3.47-3.50).

The level of accuracy of the different data can be summarized as follows (see discussion in section 3.8.3). The data for σ_T should generally be accurate to 5% or better. The errors of σ_0 are in the order of 10-30%. No general statement can be made concerning the accuracy of the inelastic cross section data. The quality of the data varies from 10% accuracy in favourable cases to only order-of-magnitude estimates in other cases. Specific comments will be made where appropriate. Equation 3.43 has been used to check the consistency of the data. Agreement is generally found within the given error limits. The data for σ_M have an accuracy of 5% or better at low energies, whereas at intermediate and higher energies the errors are about 10-20%.

Cross section data for Ne and Ar are shown in Figs. 3.40 and 3.41, respectively. Besides the total cross section σ_T and the integral elastic cross section σ_0, a selection of

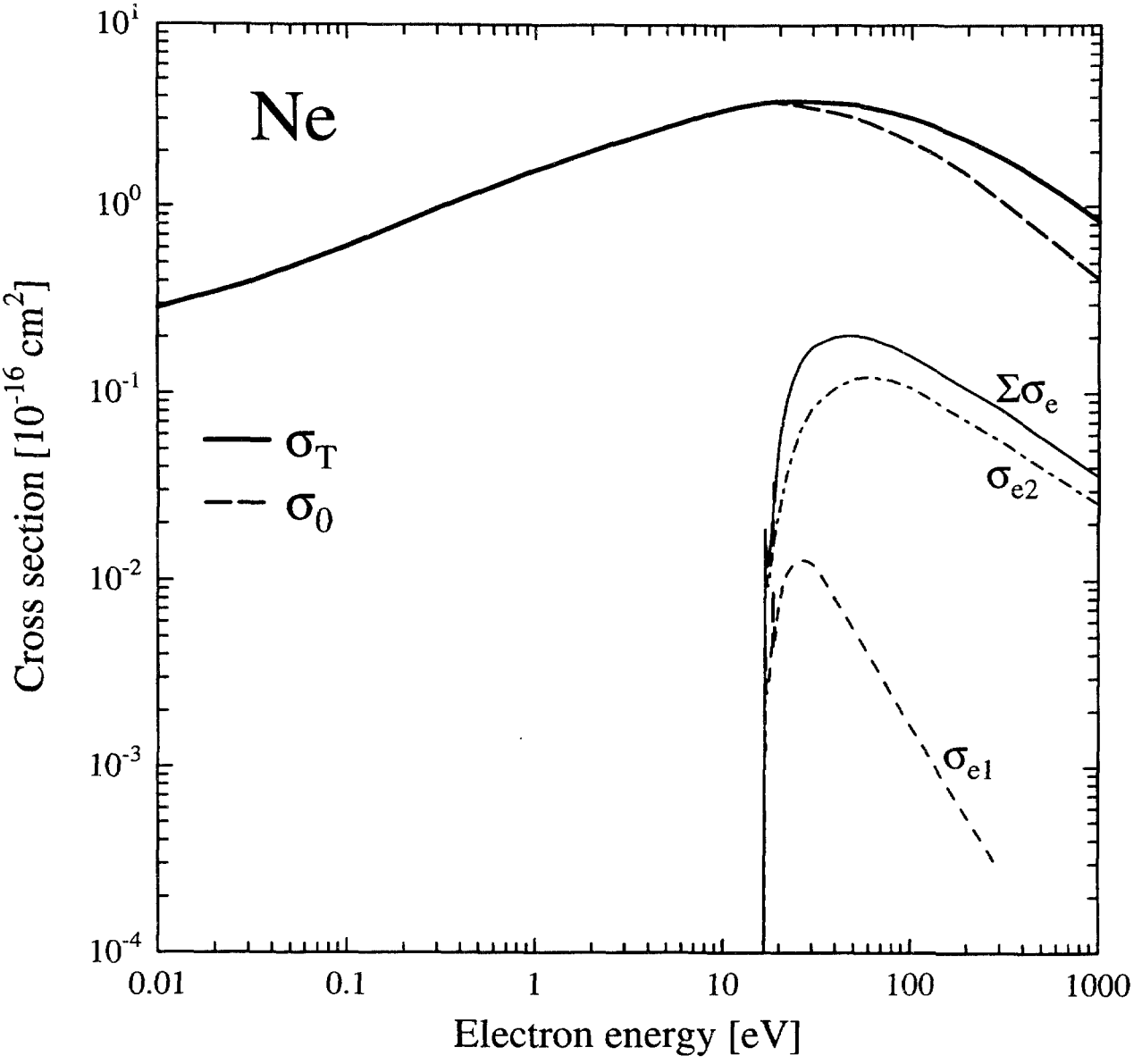

Fig. 3.40 Elastic and inelastic collision cross sections for Ne . σ_T: grand total cross section; σ_o: integral elastic cross section. The other cross sections are explained in the text.

inelastic cross sections is shown. In the case of Ne, σ_{e1} represents the cross section sum for excitation of the two lowest metastable states $2p^53s(^3P_2)$ and $2p^53s(^3P_o)$, whereas σ_{e2} gives the cross section sum for excitation of the two lowest optically allowed states $2p^53s(^3P_1)$ and $2p^53s(^1P_1)$. The data for Ar are presented in the same way: σ_{e1} is the cross section sum for excitation of the two lowest metastable states $3p^54s(^3P_2)$ and $3p^54s(^3P_o)$; σ_{e2} is the cross section sum for excitation of the two lowest optically allowed states $3p^54s(^3P_1)$ and $3p^54s(^1P_1)$. In both cases, $\Sigma\sigma_e$ represents the cross section sum for electronic excitation including higher states (see discussion further below).

Data on σ_T are found in many papers [341-355]. Apart from some minor discrepancies which existed in some of the measurements and which have been resolved in the meantime, the data are consistent with each other. References to earlier work can be found in these papers. Reliable measurements reach down to about 0.1 eV. The extension to lower energies is accomplished by means of MERT analysis [356]. For energies above 1 eV, the present data are in good agreement with the data given by Shimamura [318]. Below 1 eV, the present data slightly deviate from the data given in [318].

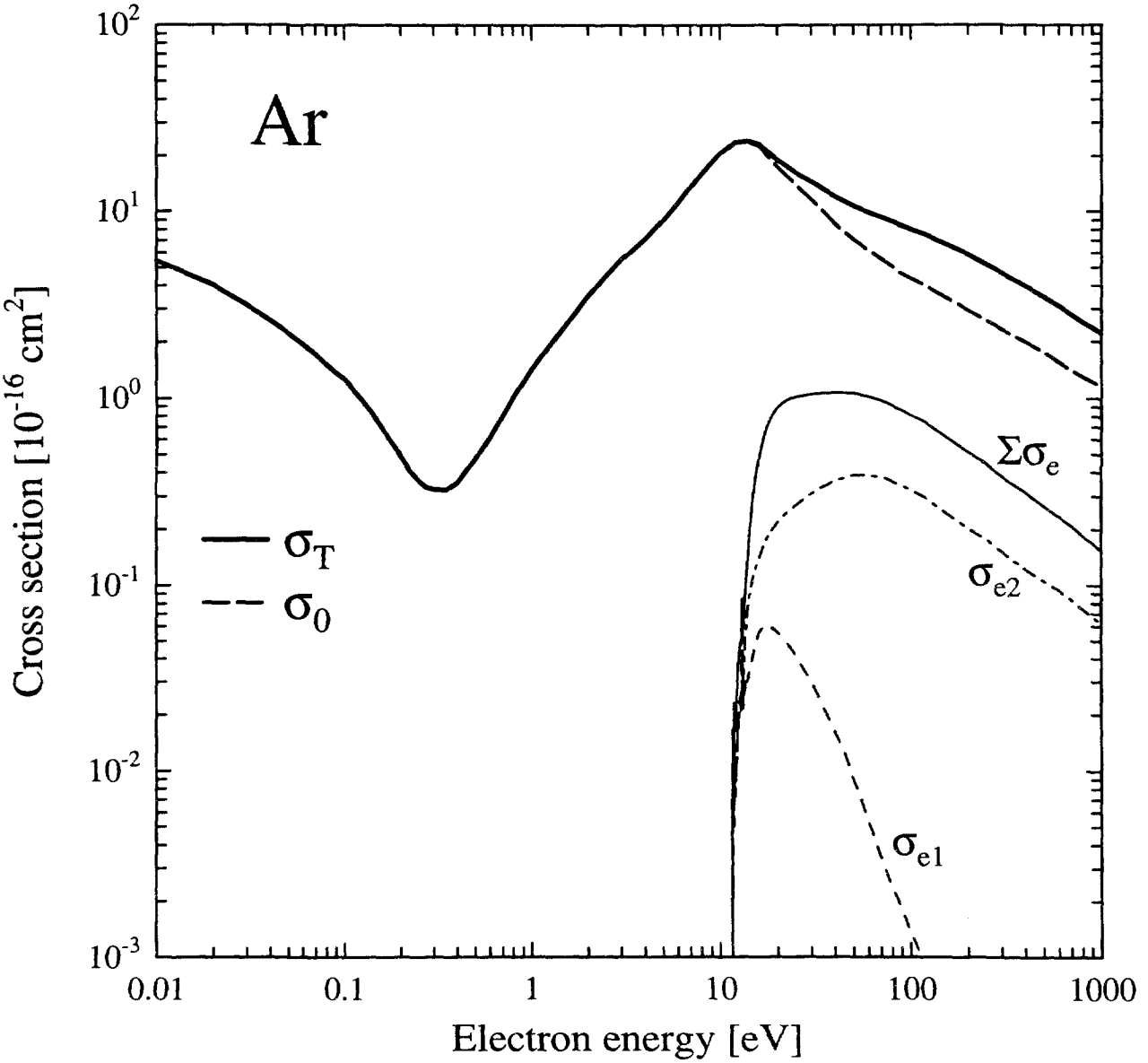

Fig. 3.41 Elastic and inelastic collision cross sections for Ar. σ_T: grand total cross section; σ_0: integral elastic cross section. The other cross sections are explained in the text.

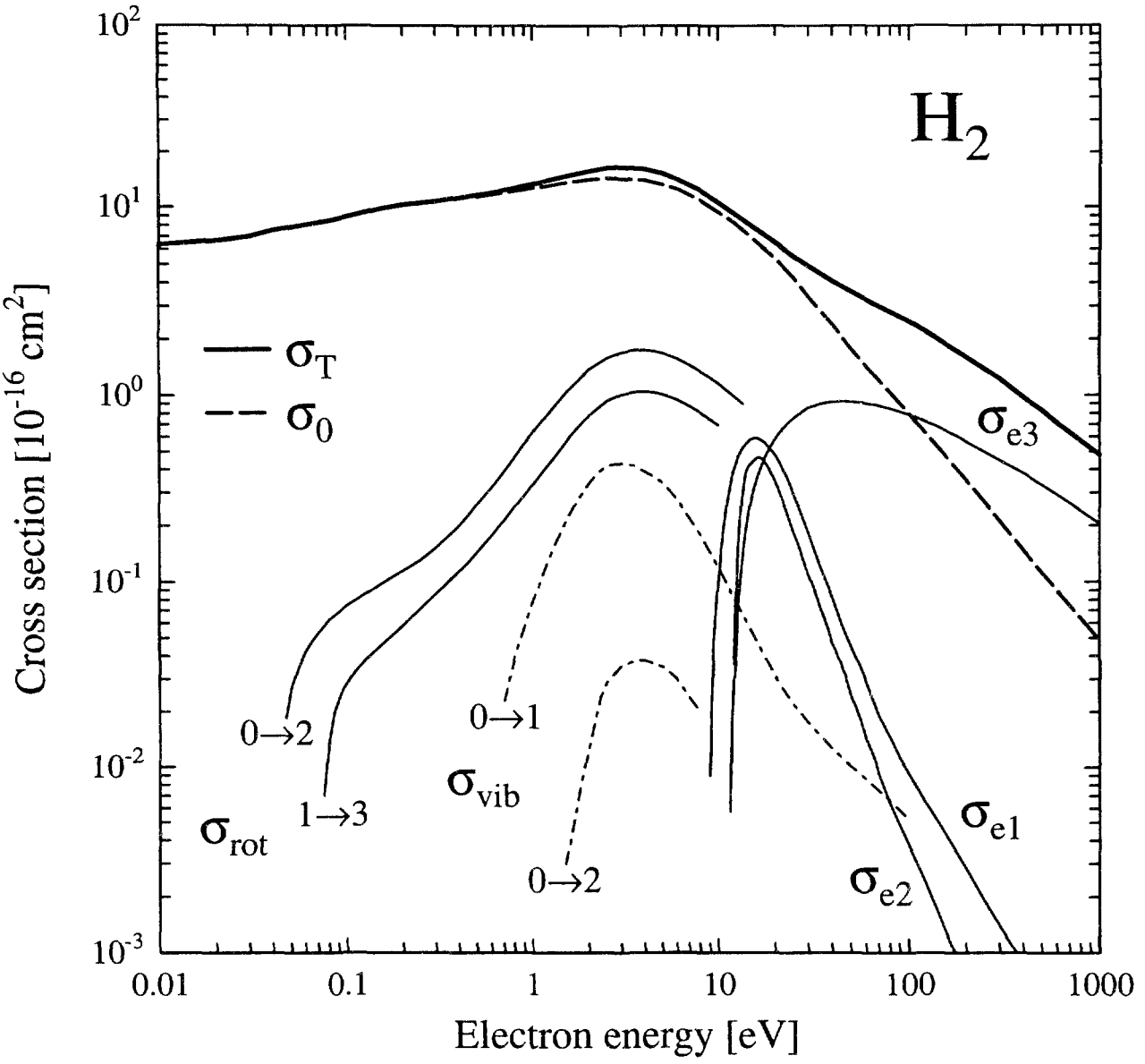

Fig. 3.42 Elastic and inelastic collision cross sections for H_2. σ_T: grand total cross section; σ_0: integral elastic cross section. The other cross sections are explained in the text.

The determination of σ_0 uses information from two sides: (i) DCS measurements [357-376]; (ii) theoretical calculations [377-403]. In the case of Ne and Ar, the whole energy range relevant to the present purpose is well covered both by experiment and theory. We further mention the papers by de Heer et al. [346] and Stauffer et al. [404], which give comprehensive data on Ne and Ar. The final data derived from these sources are shown in Figs. 3.40 and 3.41; they are in good agreement with the data given in Shimamura's article [318]. Note that σ_0 and σ_T are identical for energies below the threshold of electronic excitation. The consistency check based on equation 3.43 is very satisfactory for Ne and Ar.

The inelastic collision cross section data shown for Ne (see Fig. 3.40) are primarily based on the work of Register et al. [405]. Additional information is obtained from the work of deHeer et al. [346], who used a semi-empirical approach to determine the total cross section for electron-impact excitation of Ne and the other rare gases. Comparison with other work (e.g., optical emission studies, metastable production, theoretical calculations including respective references) can be found in these papers. More recent studies of total metastable production in Ne have been reported by Zavilopulo et al. [406], Teubner et al. [407] and Mason and Newell [408].

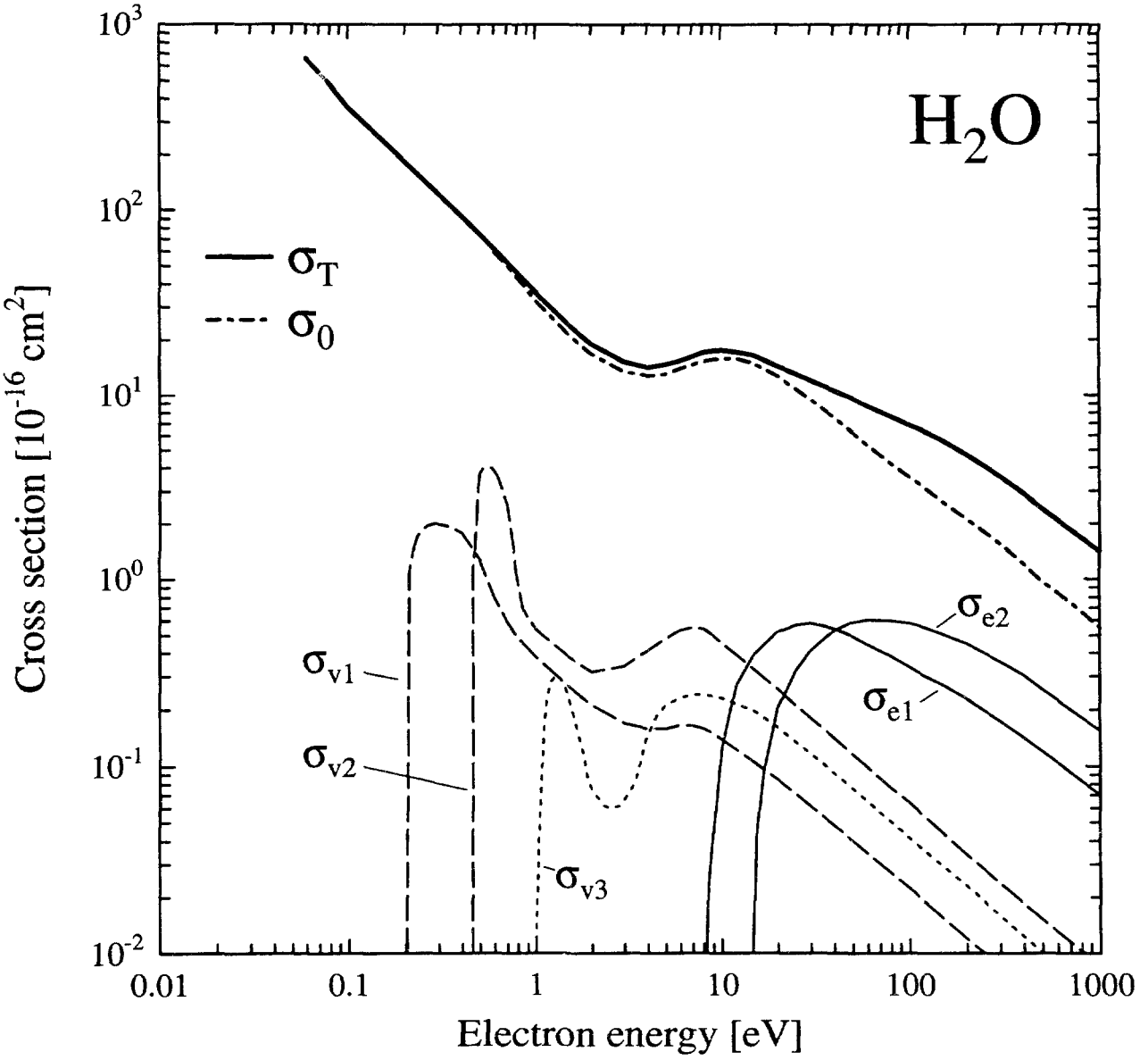

Fig. 3.43 Elastic and inelastic collision cross sections for H_2O. σ_T: grand total cross section; σ_0: integral elastic cross section. The other cross sections are explained in the text.

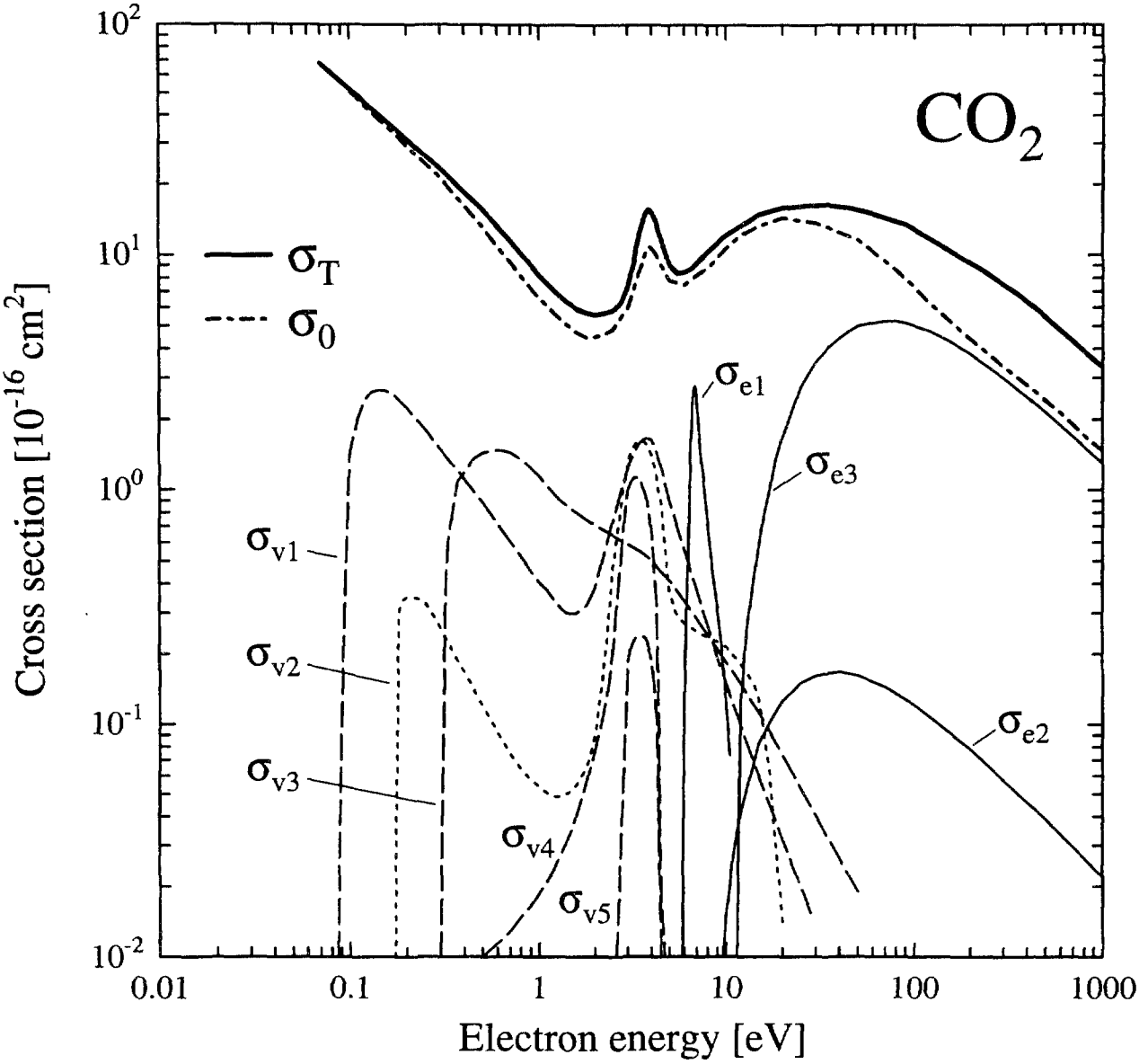

Fig. 3.44 Elastic and inelastic collision cross sections for CO_2. σ_T: grand total cross section; σ_0: integral elastic cross section. The other cross sections are explained in the text.

The first-mentioned authors [405] performed absolute DCS measurements for electron-impact excitation of the lowest forty electronic levels in Ne. The inelastic collision cross sections which are derived from the energy-loss spectra of the scattered electrons, could be grouped into fifteen features, six of which correspond to excitation of individually resolved electronic levels and the remaining nine are composed of unresolved contributions from two or more electronic levels each. The DCS data are extrapolated to 0° and 180° and then integrated over angles to yield absolute integral cross sections as a function of impact energy. The estimated errors are typically in the range 20-40 %. The four lowest excited states, for which cross section data are shown in Fig. 3.40, are fully resolved in the original measurements. Here, we give cross sections suitably combined for clarity of presentation. The curve $\Sigma\sigma_e$ includes all excited states observed in the measurements.

These cross sections are confirmed by swarm-type experiments. Tachibana and Phelps [409] measured excitation coefficients in Ne by using a drift-tube technique combined with laser absorption and laser-induced fluorescence techniques. A Boltzmann analysis is performed to derive a set of elastic and inelastic collision cross sections which reproduces the measured excitation coefficients as well as published transport and ionization coefficients within their respective uncertainties. These cross sections are in good agreement with the data of Register et al. [405], but in less satisfactory agreement with other data [410].

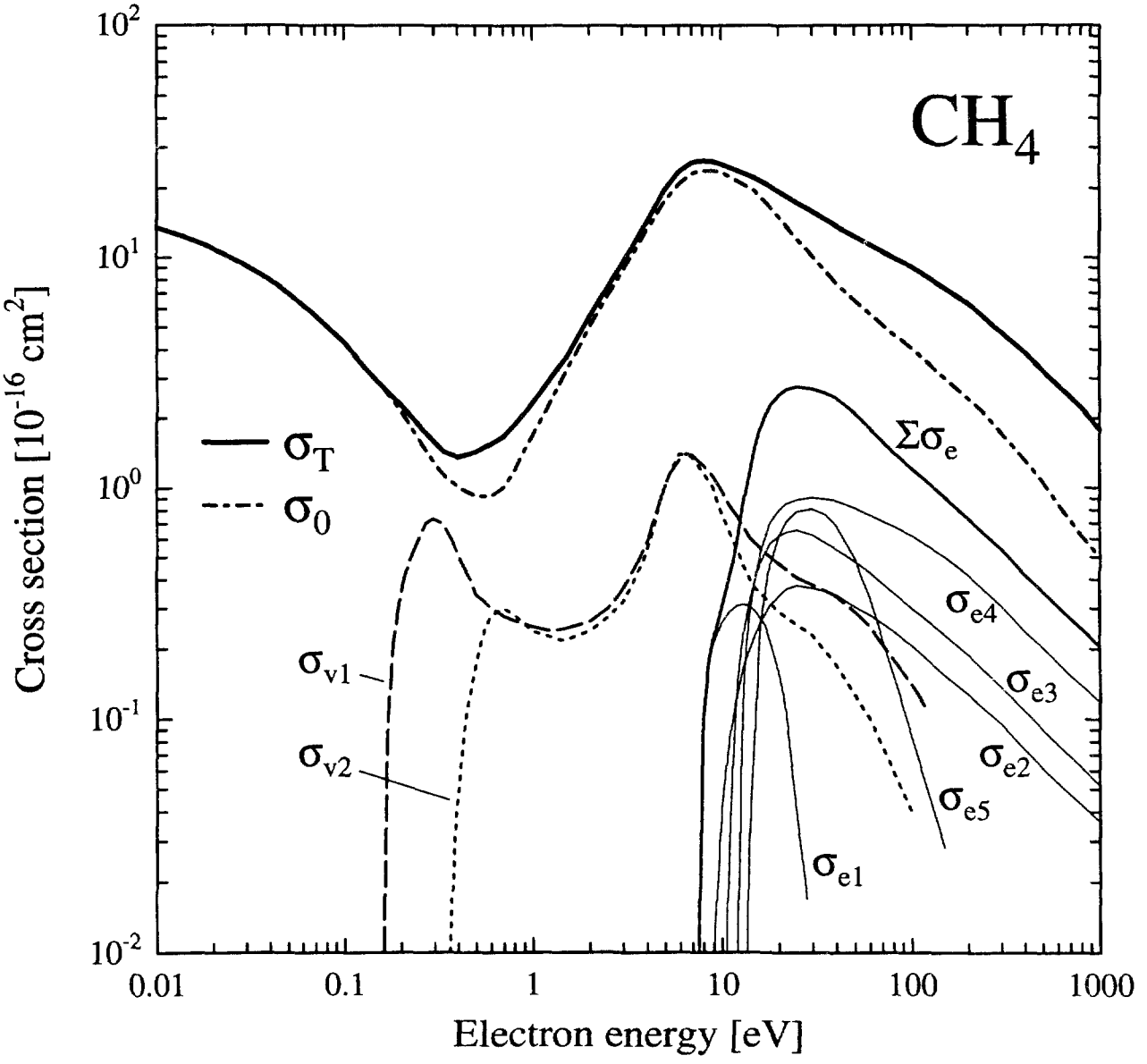

Fig. 3.45 Elastic and inelastic collision cross sections for CH_4. σ_T: grand total cross section; σ_0: integral elastic cross section. The other cross sections are explained in the text.

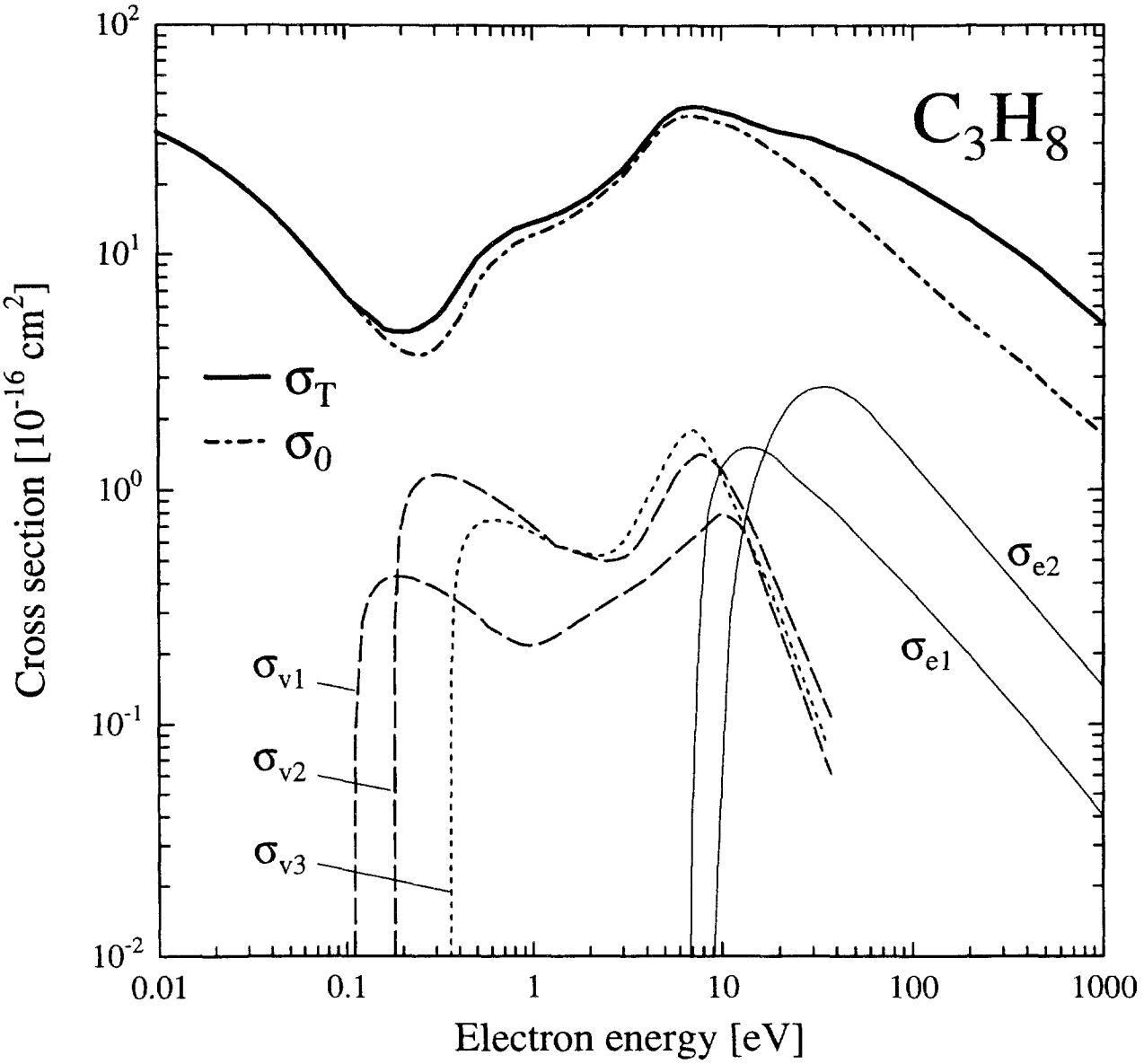

Fig. 3.46 Elastic and inelastic collision cross sections for C_3H_8. σ_T: grand total cross section; σ_0: integral elastic cross section. The other cross sections are explained in the text.

The inelastic collision cross section data for Ar (see Fig. 3.41) are obtained in a similar way as for Ne. They are primarily based on the work of Chutjian and Cartwright [411], Eggarter [412] and deHeer et al. [346]. Comparison with other work can be found in these papers. There are a few recent studies which give supplementary information [406,408,413-421].

The experimental technique used by Chutjian and Cartwright [411] is the same as that of Register et al. [405]. Absolute differential and integral cross have been measured for 23 individual or composite electronic states lying within 14.3 eV from the ground state. The estimated errors of the integral cross sections are in the range 30-50%. As in the case of Ne, the lowest excited states are fully resolved in the original measurements, but are shown here

in combined form for the sake of clarity. The curve $\Sigma\sigma_e$ includes (i) all excited states observed in the measurements of [411] and (ii) additional contributions from higher electronic states for which semi-empirical cross sections are given by Eggarter [412].

Again, these cross sections can be checked by swarm-type experiments as described in the case of Ne. Such work has been performed by Tachibana [422], for example. The measured reaction and transport coefficients of the drift-tube experiments are well repoduced by this set of cross sections. Work of similar kind is described in many papers [e.g., 423-426]. In general, the beam data are slightly adjusted (keeping within the stated error limits, if possible) in order to fit the swarm results.

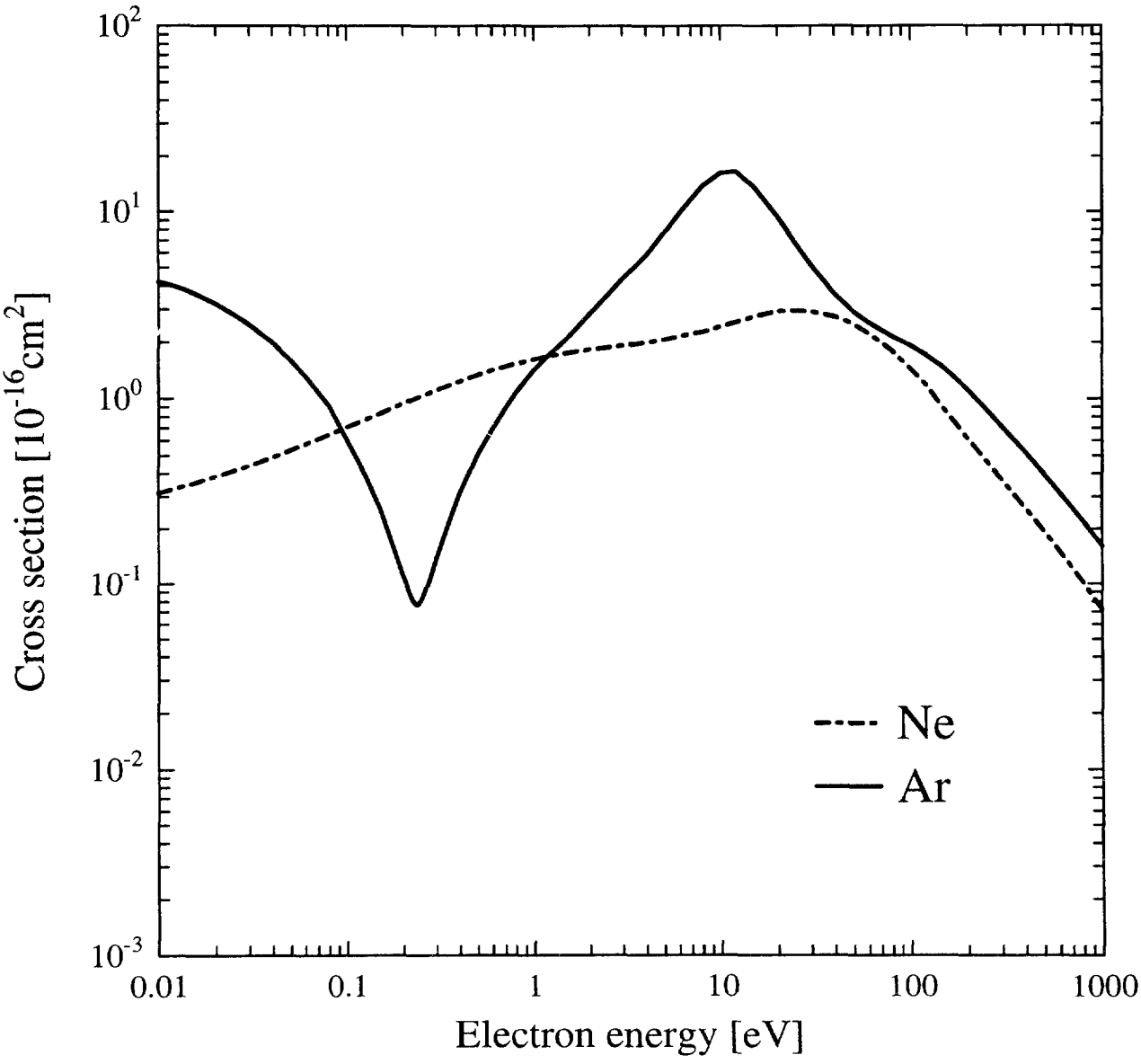

Fig. 3.47 Momentum transfer cross section for Ne and Ar.

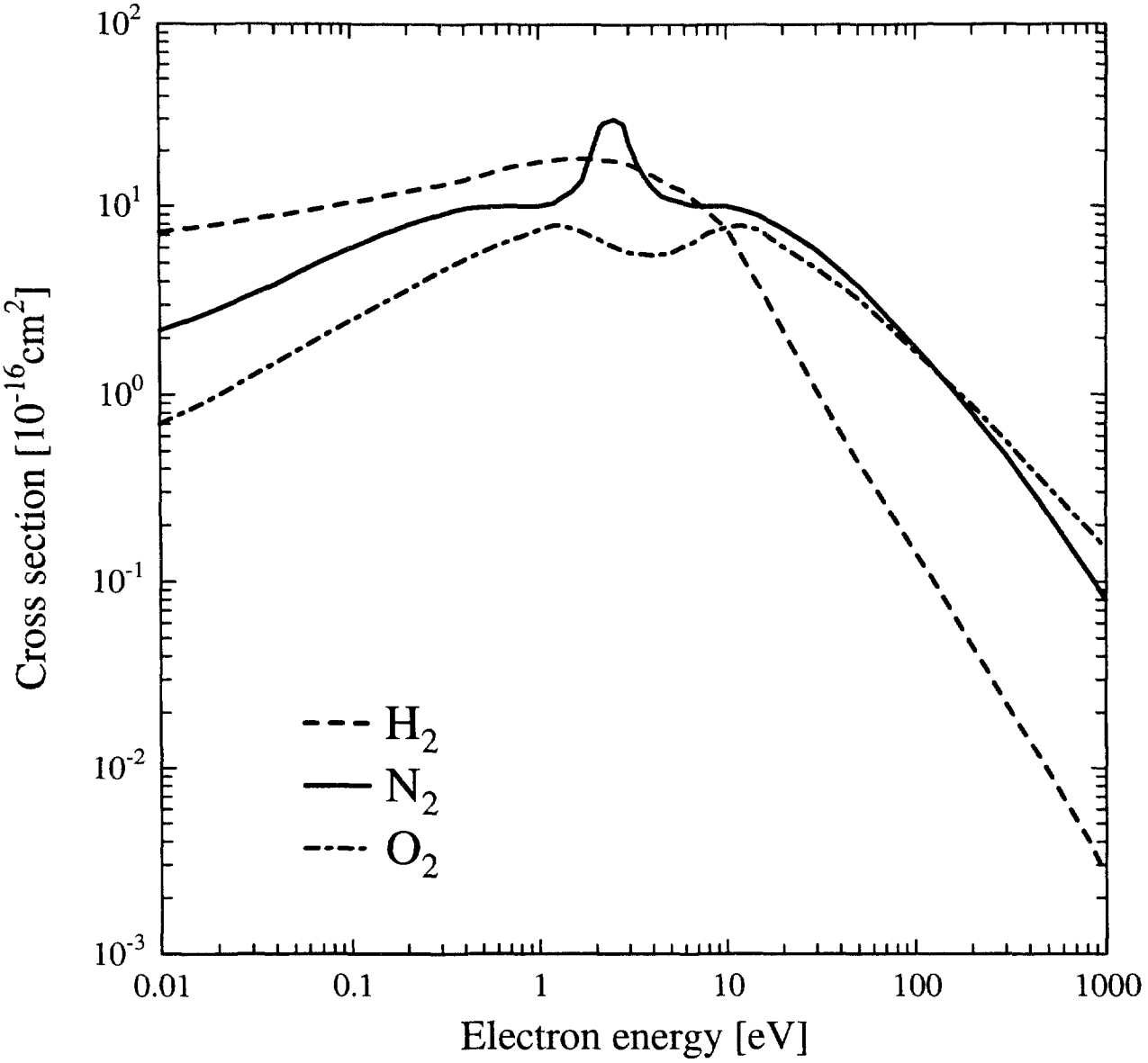

Fig. 3.48 Momentum transfer cross section for H_2, N_2 and O_2.

As already mentioned before, studies of electron collisions with atoms and molecules in electronically excited states are extremely scarce. We quote here a few of such studies for the rare gases [427-435].

In Fig. 3.42, we present cross section data for the H_2 molecule. Besides σ_T and σ_O, representative cross sections for the main inelastic processes are shown: for rotational excitation $j = 0 \rightarrow 2$ and $j = 1 \rightarrow 3$, for vibrational excitation $v = 0 \rightarrow 1$ and $v = 0 \rightarrow 2$, and three cross sections for electronic excitation. The latter are grouped in the following way: σ_{e1} gives the cross section for excitation of the $b^3\Sigma_u^+$ state, σ_{e2} is the cross section sum for excitation of other triplet states ($c^3\Pi_u$, $a^3\Sigma_g^+$, $e^3\Sigma_u^+$, $d^3\Pi_u$), and σ_{e3} is the cross section sum for excitation of several singlet states ($B^1\Sigma_u^+$, $E^1\Sigma_g^+$, $C^1\Pi_u$,$B'^1\Sigma_u^+$, $D^1\Pi_u$).

Cross sections for the individual states can be found in the literature (see below). The data are given in combined form here for clarity of presentation.

An excellent summary report on cross sections and related data for electron collisions with hydrogen molecules and molecular ions has been given by Tawara et al. [436]. The main sources, on which the present data compilation is based, are found in this article. We further refer to articles by Gerhart [437], Douthat [438], deHeer [439], Buckman and Phelps [440,441] and McConkey et al. [442], which give comprehensive accounts of electron collisions with H_2. Extensive references to original work and other review articles can be found in these papers.

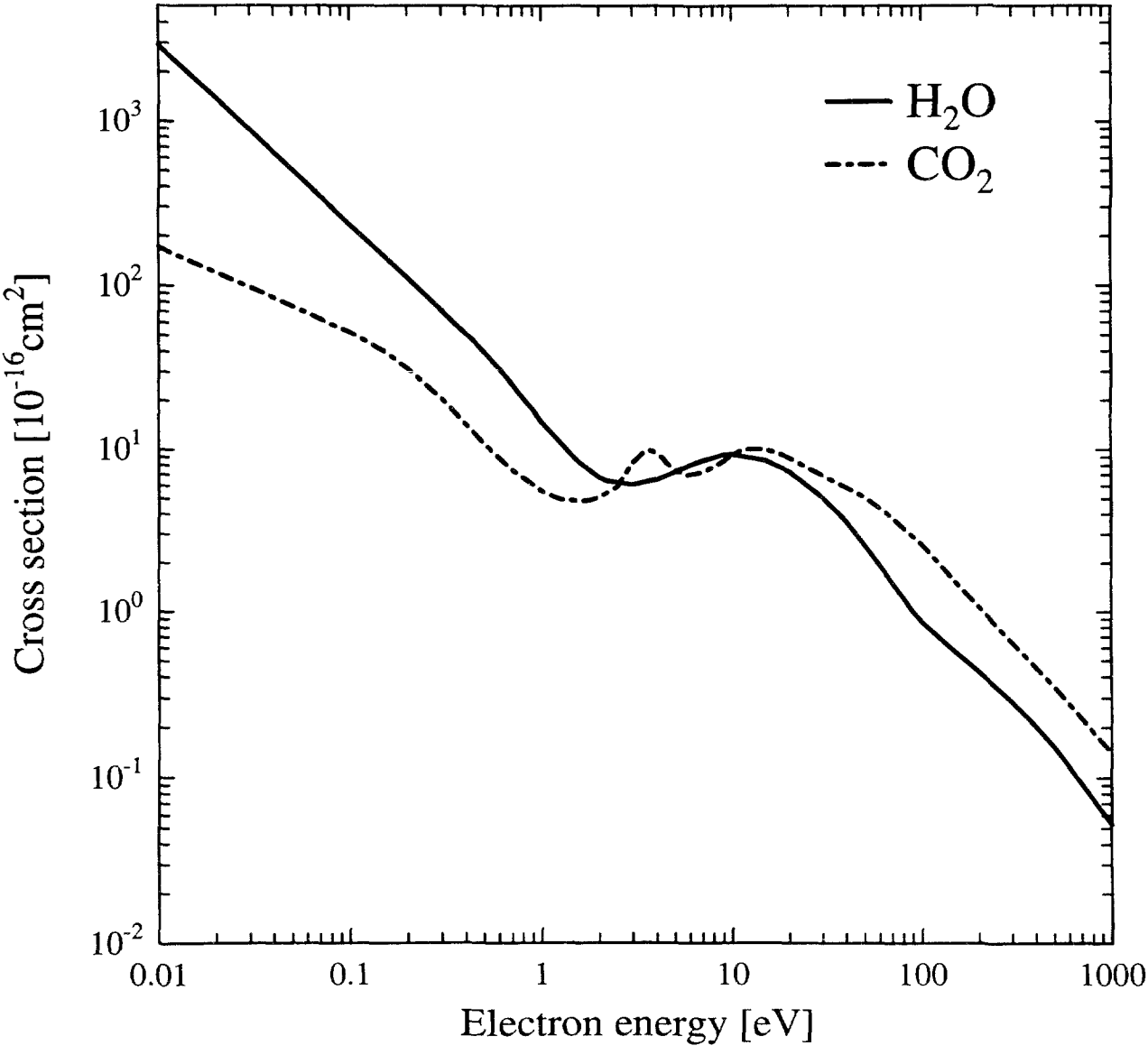

Fig. 3.49 Momentum transfer cross section for H_2O and CO_2.

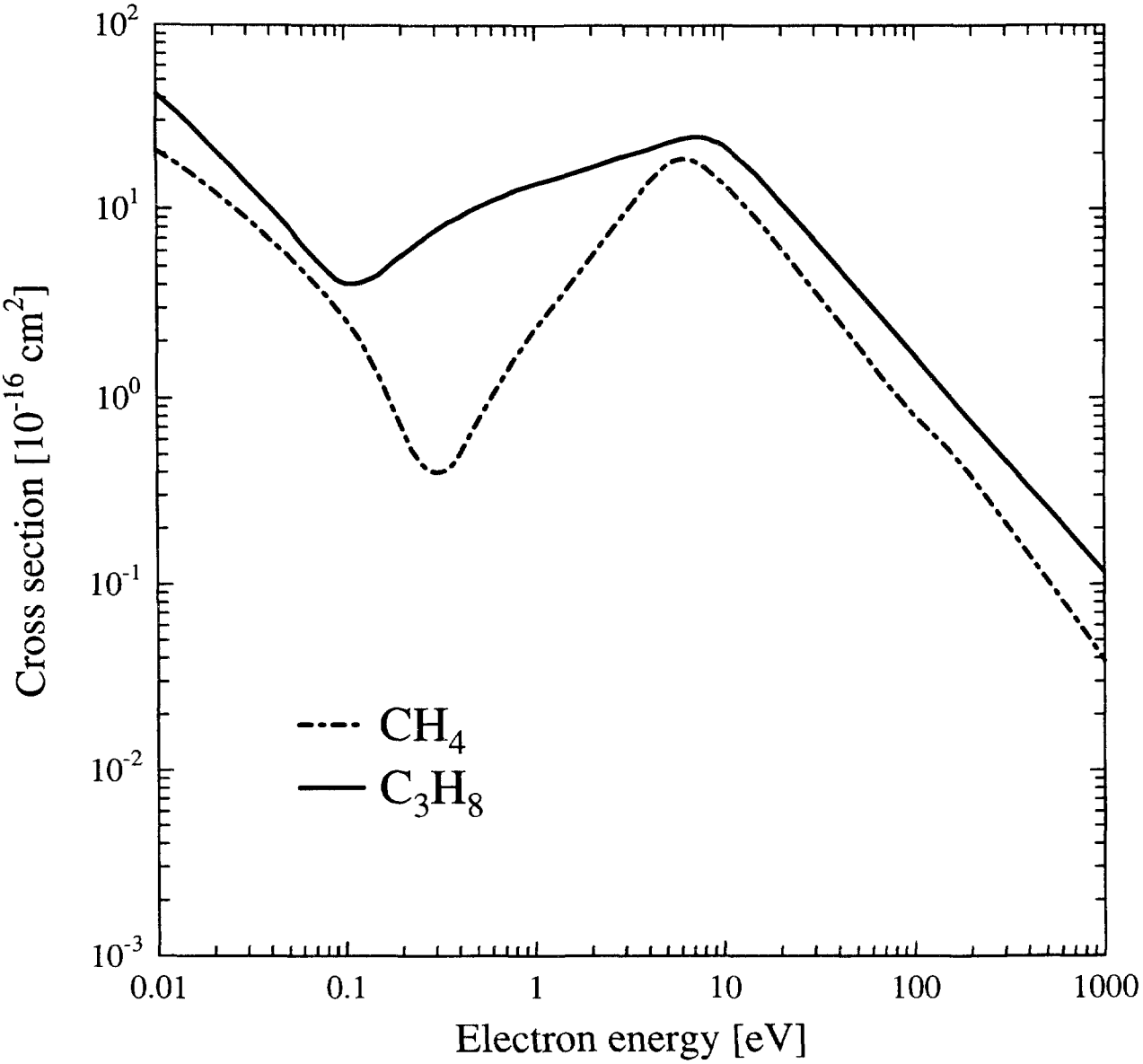

Fig. 3.50 Momentum transfer cross section for CH_4 and C_3H_8.

Recent measurements of the total cross section for H_2 are reported in [443-450]. For the individual elastic and inelastic processes, we mainly refer to the above-mentioned articles and references therein. Some further studies on H_2, both experimental and theoretical, have been reported more recently [275-280, 451-456].

An important contribution to the determination of electron collision cross sections comes again from electron swarm experiments, in particular for the range of low collision energies [457-465]. For H_2, there is a remarkable and long-standing controversy between beam and swarm results for near-threshold vibrational excitation [466-468]. Highly elaborate calculations have been performed to resolve this discrepancy ([469] and theoretical contributions in [466-468]). At present, the discrepancy remains unresolved - a fact which is

particularly troublesome because for a prototype system like e-H_2 one would expect swarm analysis, beam experiments and theory to arrive at the same result. The reader is referred to the quoted papers for further study of this interesting problem.

For N_2 and O_2, there are comprehensive data reports available [470-473] in which all information relevant to the present purpose can be found. These data are not reproduced here, and the reader is referred to the quoted reports. Very recently, an updating of the state of knowledge has been given by Itikawa [474]. Some further references to recent work on N_2 and O_2 may be added here [475-482].

Fig. 3.43 gives our cross section data for H_2O. As usual, the total cross section σ_T and the integral elastic cross section σ_0 are presented. Vibrational excitation has been separated into three parts: σ_{v1} is the cross section for excitation of the bending mode 010 (threshold energy 0.198 eV); σ_{v2} is the summed cross section for excitation of the two stretching modes, the symmetric stretch 100 with threshold energy 0.453 eV and the asymmetric stretch 001 with threshold energy 0.466 eV. The latter two modes are not resolved in current scattering experiments and their excitation behaviour can only be described in summed form. The third cross section σ_{v3} represents a lump-sum cross section for other kinds of vibrational excitation (higher harmonics, combination modes); a threshold energy of 1.0 eV has been assigned to this cross section. Finally, σ_{e1} and σ_{e2} are tentative cross sections for electronic excitation, the origin of which will be discussed later. The assigned threshold energies are 7.5 eV and 13.3. eV, respectively.

Recent summary reports on electron collision cross section data for H_2O and the behaviour of low energy electrons in water vapour have been given by Hayashi [483], Ness and Robson [484] and Elford [485]. A survey of experimental data can also be found in [313].

Measurements of the total cross section σ_T for H_2O are reported in [486-494] covering the energy range from 0.01 eV up to 3000 eV. For energies above 10 eV, the measurements are in good agreement, except the data of [489], which are generally too low. In the energy range 1-10 eV, there are discrepancies of up to 30% between the various measurements. Here, we have adopted the data of [487]. For very low energies, we have scaled down the data of [488] by a factor of 0.6 (which is still within the stated error bars of these measurements) in order to match the data of [487] in the 0.5-1 eV energy range. We consider it important to mention the work of Okamoto et al. [495] at this point. These authors have recently performed a thorough theoretical study of electron scattering from H_2O molecules. They point out that the measured values of σ_T for H_2O (and any other polar molecules) may generally be too small because of insufficient correction for small-

angle scattering. For these molecules, the DCS increases very steeply in the forward direction. This makes it very difficult to estimate the small-angle contribution by which the measured data have to be corrected in order to obtain the true cross section. It is likely that all experiments on σ_T reported so far suffer from this difficulty.

The integral elastic cross section σ_0 is obtained in the same way as described for Ne and Ar. The principal data sources are DCS measurements [487,496-500] and theoretical calculations [501-508]. On the whole, the present data are in good agreement with those reported in [483], except for the energy range 20-300 eV, where the present data are slightly lower. The consistency of the data is checked by means of equation 3.43; the result is satisfactory. It should be noted, however, that for σ_0 the same difficulty exists as for σ_T regarding the strong forward-scattering component.

Rotational excitation of H_2O has been studied by Jung et al. [257] experimentally and by Itikawa [509] and Jain and Thompson [510] theoretically. Under normal conditions, a multitude of rotational excitation and deexcitation processes takes place. Representative cross sections for the most important processes have been summarized by Ness and Robson [484].

Vibrational excitation of H_2O has been studied by several workers [511-518]. However, only a few of these studies represent absolute measurements [514,517,518]. The data presented here (Fig. 3.43) are based mainly on the measurements of Seng and Linder [514] and Shyn et al. [517]. The data beyond 20 eV are simple extrapolations and should not be regarded as very certain. From the swarm side, a need is sometimes claimed for an up-scaling of these cross sections by a factor of 2 or so in order to obtain a better fit to measured swarm parameters [483]. We have not made use of such a re-scaling of the original data, because the results of independent beam measurements [514,517] are in good agreement with each other. The cross sections σ_{v1} and σ_{v2} have estimated errors of about 20-30% in the energy range 1-20 eV. In the threshold region, the errors are definitely larger. A higher uncertainty must also be assigned to the cross section σ_{v3}.

Experimental information on electronic excitation of H_2O by electron impact is very scarce. Some energy-loss spectra of scattered electrons, which were taken under different conditions of impact energy and scattering angle, can be found in [519,520], for example. These measurements were intended to determine generalized oscillator strengths of optically allowed transitions on the one hand and energetic positions and configurational assignments of triplet states on the other hand. Cross section data for electronic excitation are only available from indirect methods. Such data can be derived from measurements of the Townsend ionization coefficient α, provided that the ionization cross section σ_t and other

cross section data are sufficiently well known In particular, the threshold region of σ_e is quite sensitive to the values of α at low electric field strengths In the present case, we have taken the values from Hayashi [483], which are obtained by this method The cross section σ_e has been divided into two parts, σ_{e1} and σ_{e2}, with threshold energies of 7 5 eV and 13 3 eV, respectively. Another set of cross sections, which has been divided into four parts, is reported by Ness and Robson [484]

In Fig 3.44, we present cross section data for CO_2 The cross sections σ_T and σ_0 have their usual meaning Vibrational excitation is described by five separate cross sections σ_{v1}, σ_{v2} and σ_{v3} are the cross sections for excitation of the fundamental modes of CO_2, the bending mode 010 (threshold energy 0 083 eV), the symmetric stretch mode 100 (threshold energy 0 172 eV) and the asymmetric stretch mode 001 (threshold energy 0 291 eV), respectively σ_{v2} contains some contribution from 020 excitation (threshold energy 0 159 eV) which cannot be separated experimentally The cross sections σ_{v4} and σ_{v5} are summed cross sections which represent excitation of higher modes (higher harmonics and combination modes) These cross sections have assigned threshold energies of 0 36 eV and 2 50 eV, respectively Similar to the case of H_2O, only tentative cross sections can be given for electronic excitation The three cross sections σ_{e1}, σ_{e2} and σ_{e3} shown in Fig 3 44 have assigned threshold energies of 5 7 eV, 9 0 eV and 11 0 eV, respectively The origin of the various cross sections is discussed further below

Electron scattering by CO_2 is markedly influenced by a strong resonance in the 3-5 eV energy range This resonance is responsible for the enhanced vibrational excitation observed in that energy range Furthermore, all cross sections show a pronounced fine structure in the resonance region which strongly depends on the process observed, the type of cross section measured and the scattering angle under which the electrons are detected in DCS measurements No attempt is made here to reproduce the details of this structure, the cross sections shown in Fig 3 44 rather represent an average over the fine structure of the resonance

Recent measurements of the total cross section σ_T for CO_2 are reported in [521-525, 286,287] These measurements cover the energy range from 0 07 eV up to 3000 eV With a few exceptions, the data are in good agreement with each other We have adopted the data of [521,286,287] for energies up to 9 0 eV (see discussion below) and the data of [525] for higher energies

Recently, it has been observed [286,287] that the total cross section for e-CO_2 scattering shows a significant dependence on the gas temperature The cross section increases when the temperature is increased from 250 K to 520 K [287] This is attributed to

the presence of molecules thermally excited to vibrational states, principally the first bending mode 010, which increases with the gas temperature. By making some simplifying, but plausible assumptions, the authors derived from the measured data a cross section $\sigma_T(000)$ for scattering from ground state molecules and a cross section $\sigma_T(010)$ for scattering from molecules excited to the first bending mode (with some possible admixture of 020 population). The following features are observed. The cross section $\sigma_T(010)$ is generally larger than $\sigma_T(000)$. For the non-resonant part, the excess of $\sigma_T(010)$ decreases with energy from about 60% at 1 eV to 10% at 8 eV. In the resonance region, the peak cross section for $\sigma_T(010)$ is higher by 35%, the width of the peak is wider by 8% and - most noteworthy - the peak position is shifted towards lower energies by 0.3 eV. The reader is referred to the original papers for more details. It is evident that these observations are of general importance for the study of electron interactions with polyatomic molecules where low-frequency vibrations are easily excited at elevated temperatures.

The integral elastic cross section σ_0 is again determined from DCS measurements [526-532] and theoretical calculations [533-538, 476]. We briefly comment on some points which are worth noting in this case. For energies below 2 eV, experimental data on σ_0 are rather scarce and uncertain (see also discussion in [302]). The present data have therefore been derived through the relation $\sigma_0 = \sigma_T - \Sigma\sigma_v$ in this energy range, since both σ_T and $\Sigma\sigma_v$ are relatively well known here. In the resonance region, in particular on the rising slope of the resonance peak near 2-4 eV, the cross section is expected to be rather sensitive to temperature effects (see discussion above). The data presented in Fig. 3.44 should be valid for room temperature. For energies above 30 eV, the sum of the individual cross sections adopted here (right side of equation 3.43) exceeds the experimental values of σ_T by about 30%. This apparent inconsisteny of the data must be attributed to uncertainties in either σ_0 or σ_e (or both), because σ_T should be accurate to about 5% in this energy range [525].

Vibrational excitation of CO_2 has been discussed in many papers. The earlier work, which was mainly concerned with the role of resonances in e-CO_2 scattering, is well summarized in several review and book articles [305,306,310,313]. We especially mention the work of Danner [525] and Register et al. [529], who measured absolute cross sections for the different processes. In most of the other work, the measured scattering intensity is given only in arbitrary units. More recently, special attention has been devoted to vibrational excitation in the near-threshold region [539-542, 531]. For all three fundamental modes, enhanced threshold excitation has been found. For the bending and the asymmetric stretch modes, this is explained by a direct mechanism and can be described by the Born-dipole approximation [543]. For the symmetric stretch mode, the enhanced threshold excitation is attributed to a virtual state mechanism. The cross sections σ_{v1}, σ_{v2} and σ_{v3} have estimated errors of about 20-30% in the energy range 2-20 eV. The errors are larger in

the threshold region and at higher energies. This is also the case for the cross sections σ_{v4} and σ_{v5} which are generally less certain. We finally mention that important information on vibrational excitation and other inelastic processes in e-CO_2 collisions is also obtained from electron swarm experiments [544-546].

Some special experiments on e-CO_2 scattering may be mentioned here. Antoni et al. [547] carried out a rotational branch analysis of vibrational excitation for all three fundamental modes of CO_2. Johnstone et al. [289, 290] performed differential scattering experiments from vibrationally excited CO_2 molecules. Data for elastic, inelastic and superelastic scattering are presented. Theoretical studies of rotational excitation in e-CO_2 collisions are reported by Morrison and Lane [548] and by Onda and Truhlar [534].

Concerning electronic excitation, the situation is the same as for H_2O. There are no direct measurements for σ_e. The data shown in Fig. 3.44 have been determined from measurements of the Townsend ionization coefficient α just as described for H_2O. For CO_2 the cross section σ_e for electronic excitation has been divided into three parts with threshold energies of 5.7 eV, 9.0 eV and 11.0 eV, respectively. We have adopted the data derived by Hayashi [302,549]. Another set of cross sections, which is divided into two parts, has been reported by Lowke et al. [545].

Fig. 3.45 shows our cross section data for CH_4. As usual, σ_T and σ_0 are the grand total cross section and the integral elastic cross section, respectively. Vibrational excitation is divided into two parts: one cross section σ_{v1} for excitation of the modes υ_2 and υ_4 (threshold energies 0.190 eV and 0.162 eV, respectively) and a second cross section σ_{v2} for excitation of the modes υ_1 and υ_3 (threshold energies 0.362 eV and 0.374 eV, respectively). In either case, the two vibrational modes are too close in energy to be separated in current scattering experiments (see however [258]). Their cross sections are therefore given in summed form. Excitation of higher modes is of minor importance in CH_4 and is not represented here. Electronic excitation is described by five cross sections with assigned threshold values of 7.5 eV, 9.0 eV, 10.5 eV, 12.0 eV, and 13.5 eV, respectively. These cross sections are discussed further below.

CH_4 is often regarded as a prototype system for the study of polyatomic molecules. This also applies to electron-molecule scattering. Hence, there is an extensive literature dealing with e-CH_4 collision processes. Compilations and critical assessments of e-CH_4 cross section data can be found in several summary reports and other articles [301,302,313,550-553].

Recent measurements of σ_T for CH_4 are reported in [554-562]. The measurements cover the energy range from 0.085 eV to 4000 eV. The data are in good agreement with

each other, which makes it relatively straightforward to construct a recommeded data set for σ_T. The data reported in [563], which are often discussed in the literature, should be discarded because they are obviously in error. In Fig. 3.45, we have extended the data to lower energies by using a MERT fit based on the parameters given by Ferch et al. [554].

The sources for determining the integral elastic cross section σ_0 are again DCS measurements [564-573, 601] and theoretical calculations [574-587, 331,476]. There has been much activity on this subject in recent years which must be ascribed to the above-mentioned prototype role of CH_4. Recommended data sets for σ_0 have been derived from these studies [549-551]. The present data set has been constructed with both the original results for σ_0 and the consistency of the data according to equation 3.43 in mind. The consistency check based on equation 3.43 is satisfactory within the error limits for the energy range 1-300 eV. Some previous problems, which existed in the energy range 4-20 eV (i.e., measured values for σ_0 were too low), have been resolved by new measurements [571]. There are two regions where the consistency check fails. One region is above 300 eV, where the results for σ_0 obtained from DCS measurements [569] seem to be rather high. It is also possible, of course, that the other inelastic cross sections, in particular σ_e, are in error. The second region is near the Raumsauer-Townsend minimum, where the measured data for σ_0 [568] and the difference cross section $\sigma_0 = \sigma_T - \Sigma\sigma_V$ obtained from equation 3.43 are not consistent with each other. The present data for σ_0 in the range 0.1-1 eV (as given in Fig. 3.45) represent a compromise between the two conflicting data sets. Further measurements in this energy range, including more definite results for vibrational excitation in the near-threshold region, are clearly needed.

Cross sections for vibrational excitation are available from various sources: (i) beam measurements [564, 566,567,573,588-590,258], (ii) swarm experiments [591-597,552], and (iii) summary reports [301, 550-553]. Extensive measurements by beam experiments have been performed for the energy range 3-20 eV [567,589,590]. However, the results from different experiments agree only within a factor of 2. From the analysis of swarm experiments, it was found necessary to increase the peak cross section around 7 eV by a significant amount (nearly a factor of 2 compared to the results reported in [589]) in order to obtain agreement with the measured swarm parameters [552]. For the near-threshold region (below 2 eV), the results of beam experiments are only fragmentary and also significantly different from each other [564,566,573]. A variety of different data sets for σ_V has been derived from swarm experiments for this energy range [591-597,552]. We have to conclude that the data for σ_V in the energy range below 2 eV are rather uncertain. The same is certainly true for the data beyond 20 eV. In Fig. 3.45, we have adopted the data set reported by Nakamura [552]. These data are identical with those given by Tawara et al. [550,551]. From the discussion above, it is clear that these data are accurate within a factor of 2 at best.

Some information is also available on rotational excitation in e-CH_4 scattering. To our knowledge, there are two experiments [256,258] and several theoretical studies [574,579,585,598-600] on this energy-loss process.

For electronic excitation, direct experimental information is again very scarce. The data presented in Fig. 3.45 are mainly based on the work of Vuskovic and Trajmar [601]. These authors measured energy-loss spectra of scattered electrons at impact energies in the range 20-200 eV and for scattering angles of 8-130°. The energy-loss range 7.5-15.0 eV was covered in the measurements. Since only broad and unresolved structures are observable in the otherwise continuous energy-loss spectra (probably because nearly all electronic excitation leads to dissociative processes in CH_4), the inelastic region of the spectrum between 7.5 eV and 15.0 eV was divided into five equidistant segments, each corresponding to a number of unassigned electronic transitions. Differential scattering intensities were measured for these segments and then converted to absolute DCS values by normalization to the elastic scattering cross section. After integration over angles, the cross sections σ_{e1} to σ_{e5} are obtained, each representing one of the five sections of the energy-loss spectrum. The errors of the integral cross sections are estimated to about 40%.

Concerning the data presented in Fig. 3.45, it must be noted that the original data of Vuskovic and Trajmar [601] have been modified in order to fit the swarm results for the Townsend ionization coefficient α [549]. For σ_{e1}, a new cross section has been constructed, whereas the values for σ_{e2} to σ_{e5} have been increased by 40% (which is still within the error bars of the original data). The resulting data set ([549]; see also [301]) is shown in Fig. 3.45. The cross section $\Sigma\sigma_e$ represents the sum of σ_{e1} to σ_{e5}. Other sets of cross sections, which are used to describe electronic excitation in CH_4, can be found in [594,595,552,553]. Some recent studies are reported by Nakano et al. [602] and Winstead et al. [603,604].

Fig. 3.46 gives our cross section data for C_3H_8 (n-propane). Besides the total cross section σ_T and the integral elastic cross section σ_0, we present three cross sections for vibrational excitation and two cross sections for electronic excitation. More details of these cross sections are discussed further below.

Measurements of σ_T for C_3H_8 are reported in [555,605,606]. The measurements cover the energy range from 1 eV to 500 eV. The data are in fair agreement in the regions of overlap. We have used these data to construct the present σ_T cross section in the energy range 2-500 eV. The extension to 1000 eV is based on a semi-empirical extrapolation. The data for energies below 2 eV have been derived from measurements of differential elastic and inelastic e-C_3H_8 scattering which have recently been performed at the University of Kaiserslautern [607]. The details of the method are discussed in connection with σ_0 and σ_v

below. In this context, it should be noted that we have discarded the data of [605] for energies below 2 eV, because they are obviously too low. This seems to be a general conclusion for Brüche's data at the low energy end of his range of measurement. The same observation has also been made for other gases [607].

Summary reports on cross section data for electron collisions with hydrocarbon molecules have been given by Tawara et al. [550,551]. Besides the species discussed here, these reports include other hydrocarbon molecules as well. We also mention that several authors [555,606,608] have designed semi-empirical formulae based on a few molecular parameters, by which total positron and electron cross sections at intermediate energies (about 100-500 eV) are reasonably well described for a large number of molecules. Such formulae are extremely useful to obtain an estimate of the total cross section in cases where experimental information is not available.

Until very recently, experimental data on differential scattering of electrons from C_3H_8 were extremely scarce. The only reported DCS measurements were those of Matsunaga et al. [609,610] for the energy range 3-20 eV. Hayashi [549] used these data to construct a data set for σ_0 over the energy range 1-1000 eV. The extension to higher energies was accomplished by semi-empirical relations in which use is made of the observed systematics in electron-hydrocarbon molecule scattering [555,605,606,608]. Data available for CH_4 and C_2H_6 provided the basis to obtain an estimate for e-C_3H_8 cross sections.

Recently, the situation has changed significantly. As mentioned above, Merz et al. [607] performed measurements of differential elastic and inelastic e-C_3H_8 scattering in the energy range 0.5-10 eV. A description of the experimental method can be found in [374,611]. These new experimental data have been used to reconstruct the data set for σ_0 up to 10 eV. Towards higher energies, the data have been smoothly connected to the data of Hayashi [549]. The consistency check for σ_0 based on equation 3.43 is quite satisfactory for this energy range. On the low energy side, the data for σ_0 have been extended to 0.01 eV by means of MERT analysis [356,374,611]. Together with estimates of the inelastic cross sections for vibrational excitation (see discussion below), the total cross section σ_T for the energy range 0.01-2 eV is obtained by using the relation $\sigma_T = \sigma_0 + \Sigma\sigma_V$.

A theoretical study of elastic electron scattering from C_3H_8 (and from other polyatomic molecules) in the energy range 5-30 eV has recently been reported by Winstead et al. [612]. Since the calculations were carried out on the static-exchange level, they were not expected to give highly quantitative results. Nevertheless, the comparison with experimental data shows generally good agreement. Further progress is expected from calculations at higher levels of approximation (e.g., with inclusion of target polarization). It

is also planned to extend these calculations to vibrationally and electronically inelastic scattering [612]. These theoretical developments are very encouraging, because they promise the possibility of stimulating feed-back between theory and experiment in the study of electron-polyatomic molecule scattering for the coming years.

During the writing of this article, we became aware of a paper by Boesten et al. [613] who measured elastic and vibrationally inelastic scattering of electrons from C_3H_8 molecules in the energy range 2-100 eV. Their data for σ_0 are in excellent agreement with the data shown in Fig. 3.46.

The propane molecule has 27 vibrational modes with excitation energies ranging from 0.041 eV to 0.368 eV [614]. In an electron scattering experiment with 20-30 meV energy resolution, one cannot expect that the excitation of all individual modes is resolved in the energy-loss spectra of the scattered electrons. Like in other polyatomic molecules, one can hope that excitation cross sections for certain composites of vibrational modes can be derived from the measurements. In the above-mentioned experiments [607], three structures are discernible in the energy-loss spectra which can be attributed to excitation of C-C stretching modes, CH_x bending modes and CH_x stretching modes. Other types of modes (e.g. C-C bending and CH_x rocking modes) are not clearly observed in the measurements. Cross sections are therefore evaluated for the three composites of vibrational modes quoted above. These cross sections are designated σ_{v1}, σ_{v2}, and σ_{v3}, respectively, in Fig. 3.46. The assigned threshold values are 0.110 eV, 0.180 eV, and 0.360 eV, respectively.

The cross sections σ_{v1} to σ_{v3} have been determined experimentally only for the energy range 1-10 eV. The experimental errors are estimated to about 30% for this energy range. Beyond 10 eV, the data shown in Fig. 3.46 are simple extrapolations and should not be regarded as very certain. For energies below 1 eV, a Born-type cross section [543] has been fitted to the experimental data in each case in order to provide a rough estimate for the continuation of the cross sections towards low energies. Note that only the shape of the cross section is given by the Born-dipole approximation [543]; the absolute magnitude is determined by the normalization to the experimental data at 1 eV. It is clear that these cross sections can only be regarded as tentative. Some justification may be derived from analogy with CH_4. The corresponding cross sections in CH_4 are fairly well reproduced by this procedure, in a formal sense at least. The physical interpretation of the near-threshold behaviour of the cross sections certainly requires a more thorough discussion [566]. In any case, it must be stressed that measurements are needed to clarify the situation. We finally note that excitation of higher harmonics, like in the case of CH_4 , is of minor importance in C_3H_8 and is not considered here.

In their recent paper on e-C_3H_8, Boesten et al. [613] give cross sections for excitation of the bending composite (here σ_{v2}) and the stretching composite (here σ_{v3}) of vibrational modes in the energy range 2-15 eV. Within the error bars, the results are in agreement with the data given in Fig. 3.46.

Only little information is available on electronic excitation of C_3H_8 by electron impact. Some energy-loss spectra taken at impact energies of 50 eV and 70 eV, respectively, can be found in [615,616]. The spectra exhibit a continuum of energy losses with only a few relatively broad structures. Optical absorption spectra in the VUV show a quite similar appearance [617]. Some cross section measurements for electron-impact dissociation of C_3H_8 (and other molecules) leading to the production of high-Rydberg atomic fragments are reported in [618]. Otherwise, there are no direct measurements for σ_e. In this respect, the situation is similar to the cases of H_2O and CO_2. The data shown in Fig. 3.46 have been derived from measurements of the Townsend ionization coefficient α [549]. The cross section σ_e has been divided into two parts, σ_{e1} and σ_{e2}, with threshold energies of 6.80 eV and 9.10 eV, respectively. It is clear that these data must be regarded as very tentative. Direct beam measurements (such as those reported for CH_4 above) would be helpful to determine more definite cross sections for electronic excitation of C_3H_8.

In Fig. 3.47-3.50 we present momentum transfer cross sections $\sigma_M(E)$ for all nine species discussed in this article. These cross sections play an important role for the transport properties of electrons in gases [297]. The definition of σ_M has been given in section 3.8.2. Momentum transfer cross sections are determined from swarm experiments at low energies and from DCS measurements at higher energies. In the energy range of overlap (about 0.1-1 eV), MERT analysis (e.g. [356,374]) represents a useful tool to make the connection between results obtained by different methods. As mentioned before, the data for σ_M are expected to be accurate to 5 % or better at low energies and to about 10-20 % at intermediate and higher energies.

Results for momentum transfer cross sections are reported in many papers. The data presented here are generally not collected from the original literature, but are taken from data compilations. A recent compilation of σ_M data for various atoms and molecules has been given by Shimamura [318]. These data are regularly updated with the advent of new information [549]. Here, we have used the most recent data as they were available to us. In the following, we briefly mention the sources which have been used in the individual cases.

The data for Ne and Ar (Fig. 3.47) are mainly based on the data compilation given by Shimamura ([318] and references therein). In the case of Ar the data have slightly changed due to a recent updating by Hayashi [549]. In Fig. 3.47 we present the revised data for Ar. It

may be interesting to compare the data in Fig. 3.47 with the recent MERT analysis by Buckman and Mitroy [356] for energies below 1 or 2 eV. In the case of Ne the σ_M data obtained from the MERT parameters of [356] are in excellent agreement with the present data up to 2 eV. For Ar the agreement holds up to 0.2 eV, but then the data based on the MERT fit tend to be slightly higher.

For H_2 (Fig. 3.48) we have used the data of England et al. [463] for energies up to 10 eV. For energies above 30 eV we have taken the data reported by Shimamura [318] which are based on an analysis of Hayashi [312] and which have recently been updated by Hayashi [549]. In the energy range 10-30 eV the two data sets have been smoothly connected. The data reported by Buckman and Phelps [441] essentially agree with the data of England et al. [463] for energies up to 5 eV.

For N_2 we have used the data reported by Phelps and Pitchford [472] for energies up to 8 eV and then smoothly connected to the data given by Shimamura [318] for energies above 10 eV. For energies below the resonance (i.e., below 1.7 eV) the data reported by Shimamura are in almost perfect agreement with the data of Phelps and Pitchford, whereas in the resonance region (i.e., 1.9-3.5 eV) the two data sets are different. For more detailed accounts of the collision processes in the resonance region the reader is referred to the articles by Itikawa et al. [470] and Itikawa [474].

For O_2 Shimamura [318] presents two data sets, one set based on an analysis by Hayashi [312] and another set proposed by Phelps [473]. For energies below 0.5 eV only data from [473] are available. In the energy range 0.6-10 eV the two data sets are in fair agreement, though not identical. For energies above 10 eV the data sets are in severe disagreement with each other. Here we have adopted the data of Phelps [473] for energies up to 8 eV and the data of Hayashi [312] for energies above 20 eV. In the intervening energy range the data have been smoothly connected, following the maximum indicated by the data of Hayashi. As in the case of N_2 we refer for further details of e-O_2 collisions to the articles by Itikawa et al. [471] and Itikawa [474].

For H_2O (Fig. 3.49) the data sets reported by Shimamura [318] and by Hayashi [483] are identical. A recent updating using new DCS values has led to a slight correction of the σ_M data, mainly in the energy range 20-300 eV [549]. We have used this latest revised version of σ_M data here. The data reported by Ness and Robson [484] are in fair agreement with the data presented here.

For CO_2 the data presented in Fig. 3.49 are essentially those reported by Shimamura [318] except for the energy range 3-8 eV, where the present data are slightly higher, again due to a recent revision of the data [549].

The momentum transfer cross sections for CH_4 and C_3H_8 are presented in Fig. 3.50. We have chosen the data evaluated by Hayashi [301,302,549]. In the case of CH_4 a slightly different cross section has been reported by Tawara et al. [550,551]. For C_3H_8 a large portion of the cross section had to be estimated from semi-empirical relations (see discussion of σ_0 above). The new experimental results which are becoming available for C_3H_8 [607,613] will lead to a redetermination of the momentum transfer cross section for this system. However, this will not change the basic structure of the cross section, i.e., the minimum near 0.1 eV and the maximum near 8 eV will remain the dominant features.

As a general conclusion we can state that there is continuous progress in the determination of electron collision cross sections. We have tried to review the present state of cross section data relevant to this field. As far as completeness and quantitative aspects are concerned the cross section data are subject to continuous development and are never really final.

Acknowledgements

One of the authors (F.L.) is greatly indebted to Professor M. Hayashi for providing a wealth of information on cross section data concerning the gases discussed in this report. His invaluable help in preparing this article is gratefully acknowledged. T.D.M. likes to acknowledge support by the Österreichischer Fonds zur Förderung der Wissenschaftlichen Forschung,Wien,Austria.

References

[1] MÄRK, T.D., in Electron Molecule Interactions and their Applications, Vol. 1 (L.G. Christophorou, Ed.), Academic Press, New York (1984) 251-334

[2] MÄRK, T.D., Int. J. Mass Spectrom. Ion Proc., **45** (1982) 125

[3] MÄRK T.D.and A.W. CASTLEMAN, Jr., Adv. Atom. Molec. Phys., **20** (1985) 65

[4] MÄRK, T.D., Int. J. Mass Spectrom. Ion Proc., **79** (1987) 1

[5] MÄRK, T.D., Int. J. Mass Spectrom. Ion Proc., **107** (1991) 143

[6] MÄRK,T.D., in Gaseous Ion Chemistry and Mass Spectrometry (J.H. Futrell, Ed.), Wiley, New York (1986) 61-93

[7] CROWE, A., PRESTON, J.A., Mc CONKEY, J.W., J. Chem. Phys., **57** (1972) 1620

[8] HALAS, S., ADAMCZYK, B., Int. J. Mass Spectrom. Ion Proc., **10** (1972/73) 157

[9] MASSEY, H.S.W., BURHOP, E.H.S., GILBODY, H.B., Electronic and Ionic Impact Phenomena, Clarendon Press, Oxford (1969)

[10] FIELD, F.H., FRANKLIN, J.L., Electron Impact Phenomena, Academic Press, New York (1970)
[11] MÄRK, T.D., DUNN, G.H., Electron Impact Ionization, Springer, Wien (1985)
[12] ILLENBERGER, E., MOMIGNY, J., Gaseous Molecular Ions, Steinkopff, Darmstadt (1992)
[13] KIEFFER, L.J., DUNN, G.H., Rev. Mod. Phys., **38** (1966) 1
[14] De HEER, F.J., INOKUTI, M., Chapter 7 in Ref. 11
[15] TATE, J.T., SMITH, P.T., Phys. Rev., **39** (1932) 270
[16] RAPP, D., ENGLANDER-GOLDEN, P., J. Chem. Phys., **43** (1965) 1964
[17] DJURIC, N.L., CADEZ, I.M., KUREPA, M.V., Int. J. Mass Spectrom. Ion Proc., **83** (1988) R7; FIZIKA, **21** (1989) 339
[18] DJURIC, N.L., CADEZ, I.M., KUREPA, M.V., Int. J. Mass Spectrom. Ion Proc. **108** (1991) R1
[19] LOZIER, W.W., Phys. Rev., **46** (1934) 268
[20] MÄRK, T.D., EGGER, F., J. Chem. Phys., **67** (1977) 2629
[21] GRAF,T., J. Phys. Radium, **10** (1939) 513
[22] FUNK, H., Ann. Physik, **4** (1930) 149
[23] FREUND,R.S., in Swarm Studies and Inelastic Electron Molecule Collisions (L.C. Pitchford, B.V. Mc Koy, A. Chutjian, S. Trajmar, Eds.) Springer, New York (1987) 329-346
[24] COOK, C.J., PETERSON, J.R., Phys. Rev. Lett., **9** (1976) 164
[25] ZIEGLER, D.L., NEWMAN, J.H., SMITH, K.A., STEBBINGS, R.F., Planet. Space Sci., **30** (1982) 451
[26] DIXON, A.J., Von ENGEL, A., HARRISON, M.F.A., Proc. Roy. Soc. Lond., **A 343** (1975) 333
[27] DIXON, A.J., HARRISON, M.F.A., SMITH, A.C.H., J. Phys., **B9** (1976) 2617
[28] BROOK, E., HARRISON, M.F.A., SMITH, A.C.H., J. Phys., **B11** (1978) 3155
[29] MONTAGUE, R.G., HARRISON, M.F.A., SMITH, A.C.H., J. Phys., **B17** (1984) 3295
[30] ARMENTROUT, P.B., TORR, S.M., DOSI, A., FREUND, R.S., J. Chem. Phys., **75** (1981) 2786
[31] BAIOCCHI, F.A., WETZEL, R.C., FREUND, R.S., Phys. Rev. Lett., **55** (1984) 771
[32] HAYES, T.R., WETZEL, R.C., FREUND, R.S., Phys. Rev., **A35** (1987) 578
[33] WETZEL, R.C., BAIOCCHI, F.A., HAYES, T.R., FREUND, R.S., Phys. Rev., **A35** (1987) 559
[34] HAYES,T.R., WETZEL, R.C., BAIOCCHI, F.A., FREUND, R.S., J. Chem. Phys., **88** (1988) 823
[35] HAYES, T.R., SHUL, R.J., BAIOCCHI, F.A., WETZEL, R.C., FREUND, R.S, J. Chem. Phys., **89** (1988) 4035

[36] SHUL, R.J., HAYES, T.R., WETZEL, R.C., BAIOCCHI, F.A., FREUND, R.S., J. Chem. Phys., **89** (1989) 4042
[37] SHUL, R.J., WETZEL, R.C., FREUND, R.S., Phys. Rev., **39** (1989) 5586
[38] SHUL, R.J., FREUND, R.S., WETZEL, R.C., Phys. Rev., **41** (1990) 5856
[39] FREUND, R.S., WETZEL, R.C., SHUL, R.J., HAYES, T.R.,Phys. Rev., **A41** (1990) 3575
[40] TARNOVSKY, V., BECKER, K., Z.Phys., **D22** (1992) 603
[41] RUDGE, M.R.H., Revs. Mod.Phys. **40** (1968) 564
[42] VRIENS, L., Case Studies in Atomic Collisions Physics (E.W. Mc Daniel, M.R.C. Mc Dowell, Eds.) North Holland, Amsterdam, **1** (1969) 337
[43] INOKUTI, M., Revs. Mod.Phys., **43** (1971) 297
[44] VAINSTEIN, L.A., SOBELMAN, I.I., YUKOV, E.A., Electron excitation cross sections of atoms and ions, NAUKA, Moscow (1973)
[45] BELL, K.L., KINGSTON, A.E., Adv. Atom. Molec.Phys., **10** (1974) 53
[46] PETERKOP, R.K., Theory of ionization of atoms by electron impact (D.G. Hummel, Transl.) Colorado Ass. Univ. Press, Boulder (1977)
[47] MÄRK, T.D., Beitr. Plasmaphysik, **22** (1982) 257
[48] KIM, Y.K., in Physics of Ion-Ion and Electron-Ion Collisions (F. Brouillard, J.W. Mc Gowan Eds.) Plenum, New York (1983) 101-165
[49] YOUNGER, S.M., Chapter 1 in Ref. 11
[50] YOUNGER, S.M., MÄRK, T.D., Chapter 2 in Ref. 11
[51] DEUTSCH, H., SCHEIER, P., MÄRK, T.D., Int. J. Mass Spectrom. Ion Proc., **74** (1986) 81
[52] DEUTSCH, H., MÄRK, T.D., Int. J. Mass Spectrom. Ion Proc., **79** (1987) R1
[53] MARGREITER, D., DEUTSCH, H., MÄRK, T.D., Contr. Plasma Phys., **30** (1990) 487
[54] MARGREITER, D., DEUTSCH, H., SCHMIDT, M., MÄRK, T.D., Int. J. Mass Spectrom. Ion Proc., **100** (1990) 157
[55] DEUTSCH, H., MARGREITER, D., MÄRK, T.D., Z.Phys., D **29** (1994) 31
[56] DEUTSCH, H., CORNELISSEN, C., CESPIVA, L., BONACIC-KOUTECKY, V., MARGREITER, D., MÄRK, T.D., Int. J. Mass Spectrom. Ion Proc., **129** (1993) 43
[57] DEUTSCH, H., CESPIVA, L., BONACIC-KOUTECKY, V., Bonacic-Koutecky, MÄRK, T.D., submitted for publication (1994)
[58] THOMSON, J.J., Philos. Mag., 23 (1912) 449
[59] GRYZINSKI, M.,Phys. Rev., **A138** (1965) 305
[60] BURGESS, A., In: Atomic Collision Processes (M.R.C. Mc Dowell, Ed.) North Holland, Amsterdam (1963) p. 237
[61] VRIENS, L.,Phys. Rev., **141** (1966) 88
[62] LOTZ, W., AstroPhys., Suppl. **14** (1967) 207; Z.Phys., **206** (1967) 205, **216** (1968) 241, **232** (1970) 101

[63] BELL,K.L., GILBODY, H.B., HUGHES, J.G., KINGSTON, A.E., SMITH, F.J., J.Phys. Chem. Ref. Data, **12** (1983) 891
[64] BETHE, H. Bethe, Ann. Physik, **5** (1930) 325
[65] OTVOS, J.W., STEVENSON, D.P., J.Am.Chem. Soc., **78** (1956) 546
[66] MANN, J.B., J. Chem.Phys., **46** (1967) 1646
[67] TIWARI, P., RAI, D.K., RUSTGI, M.L., J. Chem.Phys., **50** (1969) 3040
[68] MARGREITER, D., DEUTSCH, H., MÄRK, Proc. Symp. Atomic Surface Physics (SASP 94), Maria Alm, in print (1994). See also D. Margreiter, Thesis, Universität Innsbruck, 1988, 1993
[69] DEUTSCH, H., MARGREITER, D., MÄRK, T.D., Proc. 1st EPCLP (1991) p. 28-40
[70] LUYKEN, B.F.J., de HEER, F.J., BAAS, R.C., Physica, **61** (1972) 200
[71] PEACH, G., J.Phys., **B3** (1970) 328 and ibid. **B4** (1971) 1670
[72] OMIDVAR, K., KYLE, H.L., VIIth ICPEAC, Amsterdam, North Holland (Amsterdam, 1971) p. 890
873] VRIENS, L., Proc.Phys. Soc., **89** (1966) 13
[74] McGUIRE, E.J.,Phys. Rev., **A3** (1971) 267
[75] DIJKAMP, D., de HEER, J.Phys., **B14** (1981) 1327
[76] HIPPLER, R, SAEED, K., McGREGOR, I., KLEINPOPPEN, J.Phys., **A307** (1982) 83
[77] TAWARA, H., HARRISON, K.G., De HEER, F.J., Physica, **63** (1973) 351
[78] HIPPLER, R.H., JITSCHIN, W., Z.Phys., **A307** (1982) 287
[79] MOORES, D.L., GOLDEN, L.B., SAMSON, D.H., J.Phys., **B13** (1980) 385
[80] DEUTSCH, H., MÄRK, T.D., Contr. Plasma Phys., **34** (1994) 19
[81] POWELL, C.J., Chapter 6 in Ref. 11
[82] DEUTSCH, H., SCHMIDT, M., Beitr. Plasma Phys., **24** (1984) 475
[83] DEUTSCH, H., SCHMIDT, M., Contr. Plasma Phys., **25** (1985) 475
[84] DEUTSCH, H., MARGREITER, D., MÄRK, T.D., Int. J. Mass Spectrom. Ion Proc., **93** (1989) 259 and references therein
[85] JAIN, D.K., KHARE, S.P., J.Phys. **B9** (1976) 1429; Ind. J. Pure Appl.Phys., **14** (1976) 201
[86] KHARE, S.P., KUMAR, A., J.Phys., **B10** (1977) 2239 and **11** (1978) 2403
[87] KHARE, S.P., MEATH, W.J., J.Phys., **B20** (1987) 2101
[88] KHARE, S.P., PRAKASH, S., MEATH, W.J., Int. J. Mass Spectrom. Ion Proc., **88** (1989) 299
[89] MÄRK, T.D., PlasmaPhys. Controlled Fusion, **34** (1992) 2083
[90] BECKER, K., Proc. XVIIIth ICPEAC, Aarhus (1993)
[91] LABORIE, P., ROCARD, J.M., REES, J.A., DELCROIX, J.L., CRAGGS, J.D. Craggs, Electronic Cross Sections and Macroscopic Coefficients, Dunod, Paris (1968)

[92] De HEER, F.J.,Phys. Scripta, **23** (1981) 170
[93] TAWARA, H., KATO, T., OHNISHI, M., Institute of Plasma Physics, IPPJ-AM-37, Nagoya (1985)
[94] TAWARA, H., KATO, T., Atomic Data Nucl. Data Tables, **36** (1987) 167
[95] HAYASHI, M., In Swarm Studies and Inelastic Electron Molecule Collisions (L.C. Pitchford, B.V. Mc Koy, A. Chutjian and S. Trajmar, Eds.) Springer, New York (1987) 167-187
[96] LENNON, M.A., BELL, K.L., GILBODY, H.B., HUGHES, J.G., KINGSTON, A.E., MURRAY, M.J., SMITH, F.J., J.Phys. Chem. Ref. Data, **17** (1988) 1285
[97] SHIMAMURA, I., Scient. Papers Inst.Phys. Chem. Research, **82** (1989) 1
[98] TAWARA, H., ITIKAWA, Y., NISHIMURA, H., YOSHINO, M., J.Phys. Chem. Ref. Data, **19** (1990) 617
[99] TAWARA, H., ITIKAWA, Y., NISHIMURA, H., TANAKA, H., NAKAMURA, Y., Atomic and Plasma-Material Interaction Data for Fusion, Vol. 2 (Suppl. J. Nucl. Fusion), 1992, p.41
[100] TAWARA, H., NIFS-DATA, in print 1992/93
[101] SMITH, P.T.,Phys. Rev., **36** (1930) 1293
[102] ASUNDI, P.K., KUREPA, J. Electron. Contr., **15** (1963) 41
[103] SCHRAM, B.L., MOUSTAFA, H.R., SCHUTTEN, J., de HEER, F.J., Physica, **32** (1966) 734
[104] SCHRAM, B.L., de HEER, F.J., Van der WIEL, M.J., KISTEMAKER, J., Physica, **31** (1965) 94
[105] GAUDIN, A., HAGEMANN, R., J. Chim.Phys., **64** (1967) 1209
[106] FLETCHER, J., COWLING, I.R., J.Phys., **B6** (1973) L 258
[107] KRISHNAKUMAR, E., SRIVASTAVA, S.K., J.Phys., **B21** (1988) 1055
[108] Mc CLURE, G.W.,Phys. Rev., **90** (1953) 796
[109] KUREPA, M.V., CADEZ, I.M., PEJCEV, V.M., Fizika, **6** (1974) 185
[110] Mc CALLION, P., SHAH, M.B., GILBODY, H.B., J.Phys., **B25** (1992) 1061
[111] RIECKE, F.F., PREPEJCHAL, W.,Phys. Rev., **A6** (1972) 1507
[112] COWLING, I.R., FLETCHER, J., J.Phys., **B6** (1973) 665
[113] SCHRAM, B.L., Van der WIEL, M.J., De HEER, F.J., MOUSTAFA, H.R., J. Chem.Phys., **44** (1966) 49
[114] CHATHAM, H., HILS, D., ROBERTSON, R., GALLAGHER, A., J. Chem.Phys., **81** (1984) 1770
[115] PERESSE, J., TUFFIN, F., Meth.Phys. Anal., **3** (1967)
[116] KRISHNAKUMAR, E., SRIVASTAVA, S.K., Int. J. Mass Spectrom. Ion Proc., **113** (1992) 1
[117] SCHUTTEN, J., De HEER, F.J., MOUSTAFA, H.R., BOERBOOM, A.J.H., KISTEMAKER, J., J. Chem.Phys., **44** (1966) 3924

[118] BOLORIZADEH, M.A., RUDD, M.E.,Phys. Rev., **A33** (1986) 822
[119] GRILL, V., WALDER, G., MARGREITER, D., RAUTH, T., POLL, H.U., SCHEIER, P., MÄRK, T.D., Z.Phys., **D25** (1993) 217
[120] MARGREITER, D., WALDER, G., DEUTSCH, H., POLL, H.U., WINKLER, C., STEPHAN, K., MÄRK, T.D., Int. J. Mass Spectrom. Ion Proc., **100** (1990) 143
[121] DREWITZ, H.J., Int. J. Mass Spectrom. Ion Phys., **19** (1976) 313
[122] DREWITZ, H.J., Int. J. Mass Spectrom. Ion Phys., **21** (1976) 212
[123] STEPHAN, K., HELM, H., MÄRK, T.D., J. Chem.Phys., **73** (1980) 3763
[124] SYAGE, J.A., J.Phys., **B24** (1991) L 527
[125] BRUCE, M.R., BONHAM, R.A., Z.Phys., **D24** (1992) 149
[126] MÄRK, T.D., Chapter 5 in Ref. 11
[127] MÄRK, T.D., In: The Physics of Ionized Gases (J. Puric, D. Belic, Eds.) World Scientific, Singapure (1987) 145-160; IAEA-TECDOC - **506** (1989) 179-192
[128] AUMAYR, F., MÄRK, T.D., WINTER, H., Int. J. Mass Spectrom. Ion Proc., **129** (1993) 17
[129] KARSTENSEN, F., KÖSTER, H., Astron. AstroPhys., **13** (1971) 116
[130] SCHNEIDER, M., J.Phys., **D7** (1974) L 83
[131] KARSTENSEN, F., SCHNEIDER, M., Z. Phys., **A273** (1975) 321; J.Phys. **B11** (1978) 167
[132] DEFRANCE, P., CLAEYS, W., CORNET, A., POULAERT, G., J.Phys., **B14** (1981) 111
[133] DETTMANN, J.M., KARSTENSEN, F., J.Phys., **B15** (1982) 287; WENDT, H.H., KARSTENSEN, F.,Phys. Rev., **A29** (1984) 562
[134] FREUND, R.S., WETZEL, R.C.,Phys. Rev., **A41** (1990) 5861
[135] TARNOVSKY, V., BECKER, K., DEUTSCH, H., MÄRK, T.D., Bull. Am.Phys., (1992) in print
[136] ADAMS, N.G., SMITH, D., GRIEF, D., J.Phys., **B12** (1979) 791
[137] VARGA, P., HOFER, W., WINTER, H., J.Phys., **B14** (1981) 1341
[138] WIESEMANN, K., PUERTA, J., HUBER, B.A., J.Phys., **B20** (1987) 58
[139] KOSLOWSKI, H.R., BINDER, J., HUBER, B.A., WIESEMANN, K., J.Phys., **B20** (1987) 5903
[140] GEFEN, S., LIFSHITZ, C., Int. J. Mass Spectrom. Ion Proc., **58** (1984) 251 and references therein
[141] ADAMCZYK, B., BOERBOOM, A.J.H., SCHRAM, B.L., KISTEMAKER, J. Chem.Phys., **44** (1966) 4640
[142] SCHRAM, B.L., ADAMCZYK, B., BOERBOOM, A.J.H., Rev. Sci. Instrum., **43** (1966) 638
[143] ADAMCZYK, B., BOERBOOM, A.J.H., LUKASIEWICZ, M., Int. J. Mass Spectrom. Ion Phys., **9** (1972) 407

[144] BEDERSKI, K., WOJCIK, L., ADAMCZYK, B., Int. J. Mass Spectrom. Ion Phys., **35** (1980) 171
[145] STANSKI, T., ADAMCZYK, B., Int. J. Mass Spectrom. Ion Phys., **46** (1983) 31
[146] ADAMCZYK, B., BEDERSKI, K., WOJCIK, L., Biomed. Environm. Mass Spectrom., **16** (1988) 415
[147] MICHALAK, L., ADAMCZYK, B., MARCINKOWSKA, E., Int. Mass Spectrom. Ion Proc., **107** (1991) 9
[148] HAALAND, P., Chem.Phys. Lett., **170** (1990) 146
[149] NAGY, N., SKUTLARTZ, P., SCHMIDT, V., J.Phys., **B13** (1980) 1241
[150] CROWE, A., Mc CONKEY, J.W., Int. J. Mass Spectrom. Ion Phys., **24** (1977) 181 and references therein
[151] SHAH, M.B., ELLIOTT, D.S., GILBODY, H.B., J.Phys., **B20** (1987) 3501
[152] SHAH, M.A., EILLIOTT, D.S., Mc CALLION, P., GILBODY, H.B., J.Phys., **B21** (1988) 2751
[153] Mc CALLION, P., SHAH, M.B., GILBODY, H.B., J.Phys., **B25** (1992) 1051
[154] EDWARDS, A.K., WOOD, R.M., BEARD, A.S., EZELL, R.L.,Phys. Rev., **A37** (1988) 3687
[155] SYAGE, J.A., Chem.Phys. Lett., **143** (1988) 19
[156] SYAGE, J.A.,Phys. Rev., **A46** (1992) 5666
[157] WANG, D.P., LEE, L.C., SRIVASTAVA, S.K., Chem.Phys. Lett., **152** (1988) 513
[158] KRISHNAKUMAR, E., Int. J. Mass Spectrom. Ion Proc., **97** (1990) 283
[159] KRISHNAKUMAR, E., SRIVASTAVA, S.K., J.Phys., **B23** (1990) 1893
[160] HAYDEN, C.C., PENN, S.M., CARLSON MUYSKENS, K.J., CRIM, F.F., Rev. Sci. Instr., **61** (1990) 775
[161] MA, C., SPORLEDER, C.R., BONHAM, R.A., Rev. Sci. Instr., **62** (1991) 909
[162] MA, C., BRUCE, M.R., BONHAM, R.A.,Phys. Rev., **A44** (1991) 2921
[163] BONHAM, R.A., BRUCE, M.R., Astr. J.Phys., **45** (1992)
[164] MA, C., BRUCE, M.R., BONHAM, R.A.,Phys. Rev., **A45** (1992) 6932
[165] BRUCE, M. R., MA, C., BONHAM, R.A., Chem.Phys. Lett., **190** (1992) 285
[166] SPEKOWIUS, G., BREHM, B., Chem.Phys. Lett., **187** (1991) 442
[167] STEPHAN, K., HELM, H., MÄRK, T.D., Adv. Mass Spectrom., **8A** (1980) 122
[168] MÄRK, T.D., CASTLEMAN, A.W., J.Phys., **E13** (1980) 1121
[169] STEPHAN, K., HELM, H., KIM, Y.B., SEJKORA, G., RAMLER, J., GRÖSSL, M., MÄRK, E., MÄRK, T.D., J. Chem.Phys., **73** (1980) 303
[170] MÄRK, T.D., MÄRK, E., STEPHAN, K., J. Chem.Phys., **74** (1981) 3633
[171] KIM, Y.B., STEPHAN, K., MÄRK, E., MÄRK, T.D., J. Chem.Phys., **74** (1981) 6771
[172] MÄRK, E., MÄRK, T.D., KIM, Y.B., STEPHAN, K., J. Chem.Phys., **75** (1981) 4446

[173] STEPHAN, K., MÄRK, T.D., J. Chem.Phys., **81** (1984) 3116
[174] LEITER, K., STEPHAN, K., MÄRK, E., MÄRK, T.D., Plasma Chem. Plasma Proc., **4** (1984) 235
[175] STEPHAN, K., DEUTSCH, H., MÄRK, T.D., J. Chem.Phys., **83** (1985) 5712
[176] SEEFELDT, R., MÖLLER, W., SCHMIDT, M., Z.Phys. Chemie Leipzig, **226** (1985) 4
[177] GOROKHOV, L.N., KHANDAMIROVA, N.E., Proc. 10th Int. Mass Spectrom. Conf., Swansea (1985)
[178] LEITER, K., SCHEIER, P., WALDER, G., MÄRK, T.D., Int. J. Mass Spectrom. Ion Proc., **87** (1989) 209
[179] POLL, H.U., WINKLER, C., MARGREITER, D., GRILL, V., MÄRK, T.D., Int. J. Mass Spectrom. Ion Proc., **112** (1992) 1
[180] GRILL, V., WALDER, G., SCHEIER, P., KURDEL, M., MÄRK, T.D., Int. J. Mass Spectrom. Ion Proc., **129** (1993) 31
[181] SEN SHARMA, D.K., FRANKLIN, J.L., Int. J. Mass Spectrom. Ion Phys., **13** (1974) 139
[182] SMITH, O.I., STEVENSON, J.S., J. Chem.Phys., **74** (1981) 6777; SMITH, O.I., Int. J. Mass Spectrom. Ion Proc., **54** (1983) 55
[183] SIEGEL, M.W., Int. J. Mass Spectrom. Ion Phys., **44** (1982) 19
[184] WIEGANG, M.J., BOEDECKER, L.R., Appl.Phys. Lett., **40** (1982) 225
[185] ORIENT, O.J., SRIVASTAVA, S.K., J. Chem.Phys., **78** (1983) 2949; J. Chem.Phys., **80** (1984) 140; J.Phys., **B20** (1987) 3923
[186] MONNOM, G., GAUCHEREL, P., PAPARODITIS, C., J. Physique, **45** (1984) 77
[187] MATHUR, D., BADRINATHAN, D., Int. J. Mass Spectrom. Ion Proc., **57** (1984) 167 and **68** (1986) 9; Phys. Rev., **A35** (1987) 1033
[188] ARMENANTE, M., CESARO, R., SANTORO, V., SPINELLI, N., VANOLI, F., DelRE, G., PELUSO, A. FILIPPI, S.,Int. J. Mass Spectrom. Ion Proc., **87** (1989) 41 and references therein
[189] LEVSEN, K., Fundamental Aspects of Organic Mass Spectrometry, Verlag Chemie, Weinheim (1978)
[190] BLEAKNEY, W., CONDON, E.U., SMITH, L.G., J.Phys., Chem., **41** (1937) 197
[191] CROWE, A., Mc CONKEY, J.W., J.Phys., **B6** (1973) 2108
[192] BROWNING, R., FRYAR, J., J.Phys., **B6** (1973) 364
[193] ROSENSTOCK, H.M., WALLENSTEIN, M.B., WAHRHAFTIG, A.L., EYRING, H., Proc. Natl.Acad. Sci., **38** (1952) 667
[194] FORST, W., Theory of Unimolecular Reactions, Academic Press, New York (1973)
[195] VESTAL, M.L., J. Chem.Phys., **43** (1965) 1356
[196] DIXON, A.J., HARRISON, M.F.A., SMITH, A.C.H., Proc. 8th ICPEAC, Beograd (1973) p. 405

[197] TON-THAT, D., FLANNERY, M.R.,Phys. Rev., **A15** (1977) 517
[198] Mc GUIRE, E.J.,Phys. Rev., **A20** (1979) 445
[199] SCHRAM, B.L., BOERBOOM, A.J.H., KISTEMAKER, J., Physica, **32** (1966) 185
[200] SCHRAM, B.L., Physica, **32** (1966) 197
[201] RAPP, P., ENGLANDER-GOLDEN, P., BRIGLIA, P.B., J. Chem.Phys., **42** (1965) 4081
[202] MÄRK, T.D., J. Chem.Phys., **63** (1975) 3731
[203] EVANS, B., CHANG, J.S., YAN, A.W., NICHOLLS, R.W., HOBSON, R.M.,Phys. Rev., **A38** (1988) 2782
[204] MÄRK, T.D., EGGER, F., Int. J. Mass Spectrom. Ion Phys., **20** (1976) 89
[205] CROWE, A., Mc CONKEY, W.J., J.Phys., **B7** (1974) 349
[206] MÄRK, T.D., HILLE, E., J. Chem.Phys., **69** (1978) 2492
[207] JACKSON, W.M., BRACKMANN, R.T., FITE, W.L., Int. J. Mass Spectrom. Ion Phys., **13** (1974) 237
[208] HENKES, W., MIKOSCH, F., Int. J. Mass Spectrom. Ion Phys., **13** (1974) 151
[209] HAGENA, O.F., HENKES, W., Z. Naturforschg., **20a** (1965) 1344
[210] BOTTIGLIONI, F., COUTANT, J., FOIS, M. , Phys. Rev., **A6** (1972) 1830
[211] KEESEE, R.G., CASTLEMAN, A.W., Jr., MÄRK, T.D., In: Swarm Studies and Inelastic Electron Molecule Collisions (L.C. Pitchford, B.V. Mc Koy, A. Chutjian and S. Trajmar, Eds.) Springer, New York (1987) 351-366
[212] LEZIUS, M., MÄRK, T.D., Chem.Phys. Lett., **155** (1989) 496
[213] GOUGH, T.E., MILLER, R.E., Chem.Phys. Lett., **87** (1982) 280; GERAEDTS, J., STOLTE, S., REUSS, J., Z.Phys., **A304** (1982) 167
[214] BUCK, U., J.Phys. Chem., **92** (1988) 1023
[215] MÄRK, T.D., ECHT, O., In: Clusters of Atoms and Molecules, Vol. 2 (H. Haberland, Ed.), Springer, Heidelberg (1994) in print
[216] HELM, H., STEPHAN, K., MÄRK, T.D.,Phys. Rev., **A19** (1980) 2154
[217] BUCK, U., MEYER, H., J. Chem.Phys., **84** (1986) 4854
[218] SHIMAMORI, H., Electron attachment, in: CRC Handbook of Radiation Chemistry, eds. Y. Tabata, Y. Ito and S. Tagawa (CRC, Boca Raton, 1991)
[219] HATANO, Y., Electron attachment to van der Waals molecules, in: Electronic and Atomic Collisions, eds. D.C. Lorentz, W. E. Meyerhof, and J.R. Peterson (Elsevier, 1986), p. 153
[220] COMPTON, R.N., Negative-ion states, in: Photophysics and Photochemistry in the Vacuum Ultraviolet, eds. S.P. McGlynn, G.L. Findley and R.H., Huebner (D. Reidel Publ. Co., 1985) p. 261]
[221] CHRISTOPHOROU, L.G., Mc CORKLE, D.L., CHRISTODOULIDES, A.A., Electron attachment processes, in: Electron-Molecule Interactions and Their Applications, Vol. 1, ed. L.G. Christophorou (Academic Press, 1984) p. 477

[222] HATANO, Y., SHIMAMORI, H., Electron attachment in dense gases, in: Electron and Ion Swarms, ed. L.G. Christophorou (Pergamon Press, 1981) p. 103
[223] COMPTON, R.N., Electron attachment to molecules, in: Electronic and Atomic Collisions, eds. N. Oda and K. Takayanagi (North-Holland, 1980) p. 251
[224] MASSEY, H.S.W., Negative Ions (Cambridge Univ. Press, 1976).
[225] CALEDONIA, G.E., Chem. Rev., **75** (1975) 333
[226] SCHULZ, G.J., Revs. Mod.Phys., **45** (1973) 423
[227] CHRISTOPHOROU, L.G., Atomic and Molecular Radiation Physics (Wiley Interscience, 1971)
[228] COMPTON, R.N., HUEBNER, R.H., Adv. Radiat. Chem., **2** (1970) 281
[229] BARDSLEY, J.N., HANDL, F., Rept. Prog.Phys., **31** (1968) 471
[230] CHUTJIAN, A., ALAJAJIAN, S.H., Phys. Rev., **A31** (1985) 2885
[231] FIELD, D., ZIESEL, J.P., GUYON, P.M., GOVERS, T.R., J.Phys., **B17** (1984) 4565
[232] MATSUZAWA, M., Theory of thermal collisions between high-Rydberg atoms and neutral species, in: Electronic and Atomic Collisions, eds. N. Oda and K. Takayanagi (North-Holland, 1980), p. 493
[233] KONDOW, T., Negative ion formation by collision of Rydberg atoms with clusters, in: Electron and Atomic Collisions, eds. D.C. Lorentz, W.E. Meyerhof, and J.R. Peterson (Elsevier, 1986), p. 153
[234] LACMANN, K. , Adv. Chem.Phys., **42** (1980) 513
[235] QUITEVIS, E.L., BOWEN, K.H., LIESEGANG, G.W., HERSCHBACH, D.R., J.Phys. Chem., **87** (1983) 2076
[236] MÄRK, T.D., LEITER, K., RITTER, W., STAMATOVIC, A., Phys. Rev. Lett., **55** (1985) 2559
[237] STAMATOVIC, A., Electron attachment to van der Waals clusters: The zero energy resonance, in: Electronic and Atomic Collisions, eds., H.B. Gilbody, W.R. Newell, F.H. Read and A.C.H. Smnith (North-Holland, 1988) p. 729
[238] SHIMAMORI, H., HOTTA, H., J. Chem.Phys., **78** (1983) 1381
[239] SHIMAMORI, H., HOTTA, H., J. Chem.Phys., **81** (19884) 1271
[240] ITIKAWA, Y., ICHIMURA, A., ONDA, K., SAKIMOTO, K., TAKAYANAGI, K., HATANO, Y., HAYASHI, M., NISHIMURA, H., TSURUBUCHI, S., J.Phys., Chem. Ref. Data, **18** (1989) 23
[241] De HEER, F.J., Int. J. Radiat.Phys. Chem., **7** (1975) 137
[242] De HEER, F.J., Van SPANG, H.A., J. chim.Phys., **77** (1980) 773
[243] HATANO, Y., Comments At. Mol.Phys., **13** (1983) 259
[244] VROOM, D.A., De HEER, F.J., J. Chem.Phys., **50** (1969) 580
[245] VROOM, D.A., De HEER, F.J., J. Chem.Phys., **50** (1969) 573
[246] VROOM, D.A., De HEER, F.J., J. Chem.Phys., **50** (1969) 1883

[247] De HEER, MOUSTAFA MOUSSA, H.R., INOKUTI, M., Chem.Phys. Lett., **1** (1967) 484
[248] BEENAKER, C.I.M., De HEER, F.J., Chem.Phys., **7** (1975) 130
[249] MITCHELL, A.C.G., ZEMANSKY, M.W., "Resonance Radiation and Excited Atoms", Cambridge Univ. Press, London (1961)
[250] KOUCHI, N., OHNO, M., ITO, K., ODA, N., HATANO, Y., Chem.Phys., **67** (1982) 287
[251] WINTERS, H., J. Chem.Phys., **63** (1975) 3462
[252] NAKANO, T., TOYODA, H., SUGAI, H., Jpn. J. Appl.Phys., **30** (1991), in press
[253] COMER, J., HARRISON, M., J.Phys., **B6** (1973) L70
[254] WONG, S.F., DUB'E, L., Phys. Rev., **A 17** (1978) 570
[255] TANAKA, H., BOESTEN, L., SHIMAMURA, I., Proc. 7th ICAP, Cambrigde/ Massachusetts (1980) p.43
[256] TANAKA, H., ONODERA, N., BOESTEN, L., Proc. 13th ICPEAC, Berlin (1983) p.245
[257] JUNG, K., ANTONI, T., MÜLLER, R., KOCHEM, K.H., EHRHARDT, H., J.Phys., **B 15** (1982) 3535
[258] MÜLLER, R., JUNG, K., KOCHEM, K.H., SOHN, W., EHRHARDT, H., J.Phys., **B 18** (1985) 3971
[259] ANTONI, T., JUNG, K., EHRHARDT, H., CHANG, E.S., J.Phys., **B 19** (1986) 1377
[260] BURROW, P.D., J. Chem.Phys., **59** (1973) 4922
[261] HALL, R.I., TRAJMAR, S., J.Phys., **B 8** (1975) L 293
[262] BELIC, D.S., HALL, R.I., J.Phys., **B 14** (1981) 365
[263] KHAKOO, M.A., NEWELL, W.R., SMITH, A.C.H., J.Phys., **B 16** (1983) L 317
[264] BOTTCHER, C., BUCKLEY, B.D., J.Phys., **B 12** (1979) L 497
[265] CHRISTOPHOROU, L.G., Invited papers 20th ICPIG, Pisa/Italy (1991) p.3
[266] ALLAN, M., WONG, S.F., Phys. Rev. Lett., **41** (1978) 1791
[267] WADEHRA, J.M., BARDSLEY, J.N., Phys. Rev. Lett., **41** (1978) 1795
[268] BARDSLEY, J.N., WADEHRA, J.M., Phys. Rev., **A 20** (1979) 1398
[269] WADEHRA, J.M., Phys. Rev., **A 29** (1984) 106
[270] GAUYACQ, J.P., J.Phys., **B 18** (1985) 1859
[271] MÜNDEL, C., BERMAN, M., DOMCKE, W., Phys. Rev., **A 32** (1985) 181
[272] HALL, R.I., CADEZ, I., LANDAU, M., PICHOU, F., SCHERMANN C., Phys. Rev. Lett., **60** (1988) 337
[273] CADEZ, I., HALL, R.I., LANDAU, M., PICHOU, F., SCHERMANN, C., J.Phys., **B 21** (1988) 3271
[274] HICKMAN, A.P., Phys. Rev., **A 43** (1991) 3495
[275] CELIBERTO, R., CACCIATORE, M., CAPITELLI, M., GORSE, C., Chem.Phys., **133** (1989) 355

[276] CELIBERTO, M., CACCIATORE, M., CAPITELLI, M., Chem.Phys., **133** (1989) 369

[277] CELIBERTO, R., CAPITELLI, M., CACCIATORE, M., Chem.Phys., **140** (1990) 209

[278] HISKES, J.R., J. Appl.Phys., **70** (1991) 3409

[279] CELIBERTO, R., RESCIGNO, T.N., Phys. Rev., **A47** (1993) 1939

[280] CELIBERTO, R., Proc. 18th ICPEAC, Aarhus/Denmark (1993) p. 341

[281] BURROW, P.D., DAVIDOVITS, Phys. Rev. Lett., **21** (1968) 1789

[282] WHITE, M.D., ROSS, K.J., LEWIS, E.W., JONATHAN, N.B.H., J.Phys., **B9** (1976) 1035

[283] WHITE M.D., ROSS, K.J., J.Phys., **B9** (1976) 2147

[284] HUETZ, A., GRESTEAU, F., HALL, R.I., MAZEAU, J., J. Chem.Phys., **72** (1980) 5297

[285] HADDAD, G.N., ELFORD, M.T., J.Phys., **B12** (1979) L 743

[286] BUCKMAN, S.J., ELFORD, M.T., NEWMAN, D.S., J.Phys., **B20** (1987) 5175

[287] FERCH, J., MASCHE, C., RAITH, W., WIEMANN, L., Phys. Rev., **A40** (1989) 5407

[288] SRIVASTAVA, S.K., ORIENT. O.J., Phys. Rev., **A27** (1983) 1209

[289] JOHNSTONE, W.M., MASON, N.J., NEWELL, W.R., J.Phys., **B26** (1993) L 147

[290] JOHNSTONE, W.M., AKTHER, P., MASON, N.J., NEWELL, W.R., Proc. 18th ICPEAC, Aarhus/Denmark (1993) p. 302

[291] SHIMAMURA, I., Chem.Phys. Lett., **73** (1980) 328

[292] SHIMAMURA, I., in "Electron-Molecule Collisions" (eds. I. Shimamura and K. Takayanagi), Plenum, New York (1984) 89-190

[293] SRIVASTAVA, S.K., CHUTJIAN, A., TRAJMAR, S., J. Chem.Phys., **63** (1975) 2659

[294] BRINKMANN, R.T., TRAJMAR, S., J.Phys., **E14** (1981) 245

[295] TRAJMAR, S., REGISTER, D.F. in "Electron-Molecule Collisions" (eds. I. Shimamura and K. Takayanagi), Plenum, New York (1984) 427-494

[296] NICKEL, J.C., ZETNER, P.W., SHEN, G., TRAJMAR, S., J.Phys., **E22** (1989) 730

[297] HUXLEY, L.G.H., CROMPTON, R.W., "The Diffusion and Drift of Electrons in Gases", Wiley, New York (1974)

[298] HUNTER, S.R., CHRISTOPHOROU, L.G. in "Electron-Molecule Interactions and their Applications", Vol. 2 (ed. L.G. Christophorou), Academic Press, New York (1984) 89-220

[299] PITCHFORD, L.C., McKOY, B.V., CHUTJIAN, A., TRAJMAR, S. (eds), "Swarm Studies and Inelastic Electron-Molecule Collisions", Springer, New York (1987)

[300] CROMPTON, R.W. , HAYASHI, M., BOYD, D.E., MAKABE, T. (eds), "Gaseous Electronics and its Applications", KTK Scientific Publishers, Tokyo (1991)

[301] HAYASHI, M., "Electron Collision Cross Sections for Molecules Determined from Beam and Swarm Data", in reference [299], p. 167-187

[302] HAYASHI, M., "Electron Collision Cross Sections of Atoms and Molecules", in reference [300], p. 9-33

[303] MASSEY, H.S.W., BURHOP, E.H.S., GILBODY, H.B. (eds), "Electronic and Ionic Impact Phenomena", Vol. I-V, Clarendon Press, Oxford (1969-1974)

[304] MASSEY, H.S.W., McDANIEL, E.W., BEDERSON, B. (eds.), "Applied Atomic Collision Physics", Vol. 1-5, Academic Press, New York (1982-1984)

[305] CHRISTOPHOROU, L.G. (ed.), "Electron-Molecule Interactions and their Applications", Vol. 1-2, Academic Press, New York (1984)

[306] SHIMAMURA, I., TAKAYANAGI, K. (eds), "Electron-Molecule Collisions", Plenum Press, New York (1984)

[307] McDANIEL, E.W., "Atomic Collisions: Electron and Photon Projectiles", Wiley, New York (1989)

[308] McDANIEL, E.W., MITCHELL, J.B.A., RUDD, M.E., "Atomic Collisions: Heavy Particle Projectiles", Wiley, New York (1993)

[309] SCHULZ, G.J., Revs. Mod.Phys., **45** (1973) 378

[310] SCHULZ, G.J., in "Electron-Molecule Scattering" (ed. S.C. Brown), Wiley, New York (1979) 1

[311] BRANSDEN, B.H., McDOWELL, M.R.C., Phys. Rep., **46** (1978) 249

[312] HAYASHI, M., "Recommended Values of Transport Cross Sections for Elastic Collisions and Total Collision Cross Sections for Electrons in Atomic and Molecular Gases", Rep. IPPJ-AM-19, Institute of Plasma Physics, Nagoya University, Nagoya (1981)

[313] TRAJMAR, S., REGISTER, D.F., CHUTJIAN, A., Phys. Rep., **97** (1983) 219

[314] GALLAGHER, J.W., BEATY, E.C., DUTTON, J., PITCHFORD, L.C., J.Phys. Chem. Ref. Data, **12** (1983) 109

[315] FABRIKANT, I.I., SHPENIK, O.B., SNEGURSKY, A.V., ZAVILOPULO, A.N., Phys. Rep., **159** (1988) 1

[316] HEDDLE, D.W.O., GALLAGHER, J.W., Revs. Mod.Phys., **61** (1989) 221

[317] VAN DER BURGT, P.J.M., WESTERVELD, W.B., RISLEY, J.S., J.Phys. Chem. Ref. Data, **18** (1989) 1757

[318] SHIMAMURA, I., Scientific Papers of the Institute of Physical and Chemical Research, Vol. **82**, p. 1-51, Saitama/Japan (1989)

[319] ALLAN, M., J. Electron Spectrosc. Relat. Phenom., **48** (1989) 219

[320] KAUPPILA, W.E., STEIN, T.S., Adv. At. Mol. Opt.Phys., **26** (1990) 1

[321] TAKAYANAGI, K., ITIKAWA, Y., Adv. At. Mol.Phys., **6** (1970) 105

[322] GOLDEN, D.E., LANE, N.F., TEMKIN, A., GERJUOY, E., Revs. Mod.Phys., **43** (1971) 642

[323] GARRETT, W.R., Mol.Phys., **24** (1972) 465
[324] ITIKAWA, Y., Phys. Rep., **46** (1978) 117
[325] BURKE, P.G., Adv. At. Mol.Phys., **15** (1979) 471
[326] LANE, N.F., Revs. Mod.Phys., **52** (1980) 29
[327] NORCROSS, D.W., COLLINS, L.A., Adv. At. Mol.Phys., **18** (1982) 341
[328] MORRISON, M.A., Austr. J.Phys., **36** (1983) 239
[329] THOMPSON, D.G., Adv. At. Mol.Phys., **19** (1983) 309
[330] KAZANSKII, A.K., FABRIKANT, I.I., Sov.Phys. Usp., **27** (1984) 607
[331] GIANTURCO, F.A., JAIN, A., Phys. Rep., **143** (1986) 347
[332] MORRISON, M.A., Adv. At. Mol.Phys., **24** (1988) 51
[333] KIMURA, M., SATO, H., Comments At. Mol.Phys., **26** (1991) 333
[334] DOMCKE, W., Phys. Rep., **208** (1991) 97
[335] EICHLER, J., HERTEL, I.V., STOLTERFOHT, N. (eds), "Electronic and Atomic Collisions" (Proc. 13th ICPEAC, Berlin 1983), North Holland, Amsterdam (1984)
[336] LORENTS, D.C., MEYERHOF, W.E., PETERSON, J.R. (eds.), "Electronic and Atomic Collisions" (Proc. 14th ICPEAC, Palo Alto/USA 1985), North Holland, Amsterdam (1986)
[337] GILBODY, H.B., NEWELL, W.R., READ, F.H., SMITH, A.C.H., (eds.), "Electronic and Atomic Collisions" (Proc. 15th ICPEAC, Brighton/UK 1987), North Holland, Amsterdam (1988)
[338] DALGARNO, A., FREUND, R.S., KOCH, P.M., LUBELL, M.S., LUCCATORTO, T.B., (eds.). "The Physics of Electronic and Atomic Collisions" (Proc. 16th ICPEAC, New York 1989), American Institute of Physics, New York (1990)
[339] MacGILLIVRAY, W.R., McCARTHY, I.E., STANDAGE, M.C. (eds.), "Electronic and Atomic Collisions" (Proc. 17th ICPEAC, Brisbane /Australia 1991), Adam Hilger, Bristol/UK (1992)
[340] ANDERSEN, T., FASTRUP, B., FOLKMANN, F., KNUDSEN, H. (eds.), "The Physics of Electronic and Atomic Collisions" (Proc. 18th ICPEAC, Aarhus/Denmark 1993), American Institute of Physics, New York (1993)
[341] KAUPPILA, W.E., STEIN, T.S., JESION, G., DABABNEH , M.S., POL, V., Rev.Sci. Instrum., **48** (1977) 822
[342] STEIN, T.S., KAUPPILA, W.E., POL, V., SMART J.H., JESION, G., Phys. Rev., **A17** (1978) 1600
[343] KAUPPILA, W.E., STEIN, T.S., SMART, J.H., DABABNEH, M.S., HO, Y.K., DOWNING, J.P., POL, V., Phys. Rev., **A24** (1981) 725
[344] CHARLTON, M., GRIFFITH, T.C., HEYLAND, G.R., TWOMEY, T.R., J.Phys., **B13** (1980) L 239
[345] CHARLTON, M., LARICCHIA, G., GRIFFITH, T.C., WRIGTH, G.L., HEYLAND, G.R., J.Phys., **B17** (1984) 4945

[346] DeHEER, F.J., JANSEN, R.H.J., van der KAAY, W., J.Phys., **B12** (1979) 979
[347] WAGENAAR, R.W., de HEER, F.J., J.Phys., **B13** (1980) 3855
[348] WAGENAAR, R.W., de HEER, F.J., J.Phys., **B18** (1985) 2021
[349] NICKEL, J.C., IMRE, K., REGISTER, D.F., TRAJMAR, S., J.Phys., **B18** (1985) 125
[350] FERCH, J., GRANITZA, B., MASCHE, C., RAITH, W., J.Phys., **B18** (1985) 967
[351] BUCKMAN S.J., LOHMANN, B., J.Phys., **B19** (1986) 2547
[352] BUCKMAN, S.J., (1989), cited in reference [356]
[353] ZECCA, A., OSS, S., KARWASZ, G., GRISENTI, R., BRUSA, R.S., J.Phys., **B20** (1987) 5157
[354] SUBRAMANIAN, K.P., KUMAR, V., J.Phys., **B20** (1987) 5505
[355] NISHIMURA, H., YANO, K., J.Phys. Soc. Japan, **57** (1988) 1951
[356] BUCKMAN, S.J., MITROY, J., J.Phys., **B22** (1989) 1365
[357] BROMBERG, J.P., J. Chem.Phys.,**61** (1974) 963
[358] LEWIS, B.R., FURNESS, J.B., TEUBNER, P.J.O., WEIGOLD, E., J.Phys., **B7** (1974) 1083
[359] LEWIS, B.R., McCARTHY, I.E., TEUBNER, P.J.O., WEIGOLD, E., J.Phys., **B7** (1974) 2549
[360] GUPTA, S.C., REES, J.A., J.Phys., **B8** (1975) 417
[361] GUPTA, S.C., REES, J.A., J.Phys., **B8** (1975) 1267
[362] WILLIAMS, J.F., WILLIS, B.A., J.Phys., **B8** (1975) 1670
[363] WILLIAMS, J.F., CROWE, A., J.Phys., **B8** (1975) 2233
[364] DuBOIS, R.D., RUDD, M.E., J.Phys., **B8** (1975) 1474
[365] JANSEN, R.H.J., de HEER, F.J., LUYKEN, H.J., van WINGERDEN, B., BLAAUW, H.J., J.Phys., **B9** (1976) 185
[366] VUSKOVIC, L., KUREPA, M.V., J.Phys., **B9** (1976) 837
[367] DuBOIS, R.D., RUDD, M.E., J.Phys., **B9** (1976) 2657
[368] WILLIAMS, J.F., J.Phys., **B12** (1979) 265
[369] SRIVASTAVA, S.K., TANAKA, H., CHUTJIAN, A., TRAJMAR, S., Phys. Rev., **A23** (1981)2156
[370] BREWER, D.F.C., NEWELL, W.R., HARPER, S.F.W., SMITH, A.C.H., J.Phys., **B14** (1981) L 749
[371] QING, Z., BEERLAGE, M.J.M., van der WIEL, M.J., Physica, **113C** (1982) 225
[372] REGISTER, D.F., TRAJMAR, S., Phys. Rev., **A29** (1984) 1785
[373] WAGENAAR, R.W., de BOER, A., van TUBERGEN, T., LOS, J., de HEER, F.J., J.Phys., **B19** (1986) 3121
[374] WEYHRETER, M., BARZICK, B., MANN, A., LINDER, F., Z.Phys., **D7** (1988) 333
[375] FURST, J.E., GOLDEN, D.E., MAHGEREFTEH, M., ZHOU, J., MUELLER, D., Phys. Rev., **A40** (1989) 5592

[376] SHI, X , BURROW, P D , J Phys , **B25**, (1992) 4273
[377] BYRON, F W , JOACHAIN, C J , Phys Rev , **A15** (1977) 128
[378] McCARTHY, I E , NOBLE, C J , PHILLIPS, B A , TURNBULL, A D , Phys Rev , **A15** (1977) 2173
[379] JHANWAR, B L , KHARE, S P , KUMAR, A , J Phys , **B11** (1978) 887
[380] FON, W C , BERRINGTON, K A , J Phys , **B14** (1981) 323
[381] THIRUMALAI, D , TRUHLAR, D G , Phys Rev , **A25** (1982) 3058, Phys Rev , **A26** (1982) 793
[382] FON, W C , BERRINGTON, K A , BURKE, P G , HIBBERT, A , J Phys , **B16** (1983) 307
[383] McEACHRAN, R P , STAUFFER, A D , J Phys , **B16** (1983) 4023
[384] McEACHRAN, R P , STAUFFER, A D , Phys Lett , **107A** (1985) 397
[385] DASGUPTA, A , BHATIA, A K , Phys Rev , **A30** (1984) 1241
[386] BELL, K L , SCOTT, N S ,LENNON, M A , J Phys , **B17** (1984) 4757
[387] KEMPER, F , ROSICKY, F , FEDER, R , J Phys , **B17** (1984) 3763, J Phys , **B18** (1985) 1223
[388] HABERLAND, R , FRITSCHE, L , NOFFKE, J ,Phys Rev , **A33** (1986) 2305
[389] NAKANISHI,H , SCHRADER, D M , Phys Rev , **A34** (1986) 1823
[390] SIENKIEWICZ, J E , BAYLIS, W E , J Phys , **B20** (1987) 5145
[391] BARTSCHAT, K , McEACHRAN, R P , STAUFFER, A.D , J Phys , **B21** (1988) 2789
[392] YUAN, J , J Phys , **B21** (1988) 3753
[393] PLENKIEWICZ, B , PLENKIEWICZ, P , JAY-GERIN, J P , Phys Rev , **A38** (1988) 4460
[394] KARIM, K R , JAIN, A , Physica Scripta, **39** (1989) 238
[395] SAHA, H P , Phys Rev , **A39** (1989) 5048
[396] BARTSCHAT, K , McEACHRAN, R P , STAUFFER, A D , J Phys , **B23** (1990) 2349
[397] SAHA, H P , Phys Rev Lett , **65** (1990) 2003
[398] NAHAR, S N , WADEHRA, J M , Phys Rev , **A 43** (1991) 1275
[399] SAHA, H P , Phys Rev , **A43** (1991) 4712
[400] IHRA, W , FRIEDRICH, H , Phys Rev , **A45** (1992) 5278
[401] FRONGILLO, Y , PLENKIEWICZ, B , PLENKIEWICZ, P , JAY-GERIN, J P , Can J Phys , **70** (1992) 305
[402] SAHA, H P , Phys Rev , **A 47** (1993) 273
[403] GIANTURCO, F A , RODRIGUEZ-RUIZ, J A , Phys Rev , **A47** (1993) 1075
[404] STAUFFER, A D , DIAS, T H V T , CONDE, C A N , Nucl Instr and Meth , **A242** (1986) 327
[405] REGISTER, D F , TRAJMAR, S , STEFFENSEN, G , CARTWRIGHT, D C , Phys Rev , **A 29** (1984) 1793

[406] ZAVILOPULO, A.N., SNEGURSKII, A.V., SHPENIK, O.B., J. Appl. Spectrosc., **42** (1985) 125
[407] TEUBNER, P.J.O., RILEY, J.L., TONKIN, M.C., FURST, J.E., BUCKMAN, S.J., J.Phys., **B18** (1985) 3641
[408] MASON, N.J., NEWELL, W.R., J.Phys., **B20** (1987) 1357
[409] TACHIBANA, K., PHELPS, A.V., Phys. Rev., **A36** (1987) 999
[410] PHILLIPS, M.H., ANDERSON, L.W., LIN, C.C., Phys. Rev., **A32** (1985) 2117
[411] CHUTJIAN, A., CARTWRIGHT, D.C., Phys. Rev., **A23** (1981) 2178
[412] EGGARTER, E., J. Chem.Phys., **62** (1975) 833
[413] BUCKMAN. S.J., HAMMOND, P., KING, G.C., READ, F.H., J.Phys., **B16** (1983) 4219
[414] BRETAGNE, J., CALLEDE, G., LEGENTIL, M., PUECH, V., J.Phys., **D19** (1986) 761
[415] MITYUREVA, A.A., SMIRNOV, V.V., Opt. Spectrosc., **61** (1986) 413
[416] MITYUREVA, A.A., PENKIN, N.P., SMIRNOV, V.V., Proc. 15th ICPEAC, Brighton/UK (1987) p. 189
[417] FORAND, J.L., WANG, S., WOOLSEY, J.M., McCONKEY, J.W., Can J.Phys., **66** (1988) 349
[418] LI, G.P., TAKAYANAGI, T., WAKIYA, K., SUZUKI, H., AJIRO, T., YAGI, S., KANO, S.S., TAKUMA, H., Phys. Rev., **A38** (1988) 1240
[419] AJELLO, J.M., JAMES, G.K., FRANKLIN, B., HOWELL, S., J.Phys., **B23** (1990) 4355
[420] ZUO, T., McEACHRAN, R.P., STAUFFER, A.D., J.Phys., **B25** (1992) 3393
[421] BLANCO, F., SANCHEZ, J.A., CAMPOS, J., J.Phys., **B25** (1992) 3531
[422] TACHIBANA, K., Phys. Rev., **A34** (1986) 1007
[423] FERREIRA, C.M., LOUREIRO, J., J.Phys., **D16** (1983) 1611
[424] PUECH, V., TORCHIN, L., J.Phys., **D19** (1986) 2309
[425] VLCEK, J., J.Phys., **D22** (1989) 623
[426] VLCEK, J., PELIKÁN, V., J.Phys., **D22** (1989) 632
[427] CELOTTA, R., BROWN, H., MOLOF, R., BEDERSON, B., Phys. Rev., **A3** (1971) 1622
[428] MITYUREVA, A.A., PENKIN, N.P., Opt. Spectrosc., **38** (1975) 229
[429] WILSON, W.G., WILLIAMS, W.L., J.Phys., **B9** (1976) 423
[430] KHAKHAEV, A.D., GOSTEV, V.A., ZAITSEV, Y.V., Proc. 7th ICPEAC, Paris (1977) p. 1308
[431] GOSTEV, V.A., ELAKHOVSKII, D.V., ZAITSEV, Y.V., LUIZOVA, L.A., KHAKHAEV, A.D., Opt. Spectrosc., **48** (1980) 251
[432] MÜLLER-FIEDLER, R., SCHLEMMER, P., JUNG, K., HOTOP, H., EHRHARDT, H., J.Phys., **B17** (1984) 259

[433] TAYLOR, K T , CLARK, C W , FON, W C , J Phys , **B18** (1985) 2967
[434] MITYUREVA, A A , PENKIN, N P , SMIRNOV, V V , Opt Spectrosc , **66** (1989) 140
[435] RALL, D L A , SHARPTON, F A , SCHULMAN, M B , ANDERSON, L W , LAWLER, J E , LIN, C C , Phys Rev Lett , **62** (1989) 2253
[436] TAWARA, H , ITIKAWA, Y , NISHIMURA, H , YOSHINO, M , J Phys , Chem Ref Data, **19** (1990) 617
[437] GERHART, D E , J Chem Phys , **62** (1975) 821
[438] DOUTHAT, D A , J Phys , **B12** (1979) 663
[439] DeHEER, F J , Physica Scripta, **23** (1981) 170
[440] BUCKMAN, S J , PHELPS, A V , J Chem Phys , **82** (1985) 4999
[441] BUCKMAN, S J , PHELPS, A V , "Tabulations of Collision Cross Sections and Calculated Transport and Reaction Coefficients for Electrons in H_2 and D_2", JILA Information Center Report No 27, University of Colorado, Boulder/Colorado (1985)
[442] McCONKEY, J W , TRAJMAR, S , KING, G C M , Comments At Mol Phys , **22** (1988) 17
[443] FERCH, J , RAITH, W , SCHRODER, K , J Phys , **B13** (1980) 1481
[444] DALBA, G , FORNASINI, P , LAZZIZZERA, I , RANIERI, G , ZECCA, A , J Phys , **B13**(1980) 2839
[445] Van WINGERDEN, B , WAGENAAR, R W , de HEER, F J , J Phys , **B13** (1980) 3481
[446] HOFFMAN, K R , DABABNEH, M S , HSIEH, Y F , KAUPPILA, W E , POL, V , SMART, J H , STEIN, T S , Phys Rev , **A25** (1982) 1393
[447] DEURING,A , FLOEDER, K , FROMME, D , RAITH, W , SCHWAB, A , SINAPIUS, G , ZITZEWITZ, P W , KRUG, J , J Phys , **B16** (1983) 1633
[448] JONES, R K , Phys Rev , **A31** (1985) 2898
[449] SUBRAMANIAN, K P , KUMAR, V , J Phys , **B22** (1989) 2387
[450] NICKEL, J C , KANIK, I , TRAJMAR, S , IMRE, K , J Phys , **B25** (1992) 2427
[451] BRUNGER, M J , BUCKMAN, S J , NEWMAN, D S , Aust J Phys , **43** (1990) 665
[452] BRUNGER, M J , BUCKMAN, S J , NEWMAN, D S , ALLE, D T , J Phys , **B24** (1991) 1435
[453] OTTINGER C , ROX, T , Phys Lett , **A161** (1991) 135
[454] MU-TAO, L , MACHADO, L E , BRESCANSIN, L M , MENESES, G D , J Phys , **B24** (1991) 509
[455] BRANCHETT, S E , TENNYSON, J , MORGAN, L A , J Phys , **B24** (1991) 3479
[456] GAO, H , Phys Rev , **A45** (1992) 6895
[457] ENGELHARDT, A G , PHELPS, A V , Phys Rev , **131** (1963) 2115
[458] PHELPS, A V , Revs Mod Phys , **40** (1968) 399
[459] CROMPTON R W , GIBSON, D K , McINTOSH, A I , Aust J Phys , **22** (1969) 715

[460] CROMPTON, R.W., GIBSON, D.K., ROBERTSON, A.G., Phys. Rev., **A2** (1970) 1386
[461] HADDAD, G.N., CROMPTON, R.W., Aust. J.Phys., **33** (1980) 975
[462] PETROVIC, Z.L., CROMPTON, R.W., Aust. J.Phys., **40** (1987) 347
[463] ENGLAND, J.P., ELFORD, M.T., CROMPTON, R.W., Aust. J.Phys., **41** (1988) 573
[464] RAMANAN, G., FREEMAN, G.R., J. Chem.Phys., **95** (1991) 4195
[465] SCHMIDT, B., BERKHAN, K., GÖTZ, B., MÜLLER, M., Physica Scripta, (1994), in press
[466] MORRISON, M.A., CROMPTON, R.W., SAHA, B.C., PETROVIC, Z.L., Aust. J.Phys., **40** (1987) 239
[467] BUCKMAN, S.J., BRUNGER, M.J., NEWMAN, D.S., SNITCHLER, G., ALSTON, S., NORCROSS, D.W., MORRISON, M.A., SAHA, B.C., DANBY, G., TRAIL, W.K., Phys. Rev. Lett. **65** (1990) 3253
[468] CROMPTON, R.W., MORRISON, M.A., Aust. J.Phys., **46** (1993) 203
[469] MORRISON, M.A., TRAIL, W.K., Phys. Rev., **A48** (1993) 2874
[470] ITIKAWA, Y., HAYASHI, M., ICHIMURA, A., ONDA, K., SAKIMOTO, K., TAKAYANAGI, K., NAKAMURA, M., NISHIMURA, H., TAKAYANAGI, T., J.Phys. Chem. Ref. Data, **15** (1986) 985
[471] ITIKAWA, Y., ICHIMURA, A., ONDA, K., SAKIMOTO, K., TAKAYANAGI, K., HATANO, Y., HAYASHI, M., NISHIMURA, H., TSURUBUCHI, S., J.Phys. Chem. Ref. Data, **18** (1989) 23
[472] PHELPS, A.V., PITCHFORD, L.C., "Anisotropic Scattering of Electrons by N_2 and Its Effects on Electron Transport: Tabulations of Cross Sections and Results", JILA Information Center Report No. 26, University of Colorado, Boulder/Colorado (1985)
[473] PHELPS, A.V., "Tabulations of Collision Cross Sections and Calculated Transport and Reaction Coefficients for Electron Collisions with O_2", JILA Information Center Report No. 28, University of Colorado, Boulder/Colorado (1985)
[474] ITIKAWA, Y., Adv. At. Mol. Opt.Phys., **33** (1994) 253
[475] KHARE, S.P., RAJ, D., J.Phys., **B24** (1991) 3045
[476] JAIN, A., BALUJA, K.L., Phys. Rev., **A45** (1992) 202
[477] DaPAIXAO, F.J., LIMA, M.A.P., McKOY, V., Phys. Rev. Lett., **68** (1992) 1698
[478] MIDDLETON, A.G., BRUNGER, M.J., TEUBNER, P.J.O, J.Phys., **B25** (1992) 3541
[479] SHYN, T.W., SWEENEY, C.J., Phys. Rev., **A47** (1993) 1006
[480] SHYN, T.W., SWEENEY, C.J., Phys. Rev., **A48** (1993) 1214
[481] ZIESEL, J.P., RANDELL, J., FIELD, D., LUNT, S.L., MROTZEK, G., MARTIN, P., J.Phys., **B26** (1993) 527
[482] RANDELL, J., LUNT, S.L., MROTZEK, G., ZIESEL, J.P., FIELD, D., J.Phys., **B27** (1994) in press
[483] HAYASHI, M., IAEA-TECDOC, **506** (1988) 193

[484] NESS, K.F., ROBSON, R.E., Phys. Rev., **A38** (1988) 1446
[485] ELFORD, M.T., "The Behaviour of Low Energy Electrons in Water Vapour", in reference [300], p. 34-50
[486] BRÜCHE, E., Ann.Phys., **1** (1929) 93
[487] SENG, G., PhD Thesis (unpublished), University of Kaiserslautern, Kaiserslautern/Germany (1975)
[488] SOKOLOV, V.F., SOKOLOVA, Y.A., Sov. Tech.Phys.Lett., 7 (1981) 268
[489] SUEOKA, O., MORI, S., KATAYAMA, Y., J.Phys., **B19** (1986) L 373
[490] SZMYTKOWSKI, Chem.Phys. Lett., **136** (1987) 363
[491] ZECCA, A., KARWASZ, G., OSS, S., GRISENTI, R., BRUSA, R.S., J.Phys., **B20** (1987) L133
[492] NISHIMURA, H., YANO, K., J.Phys. Soc. Japan, **57** (1988) 1951
[493] SAGLAM, Z., AKTEKIN, N., J.Phys., **B23** (1990) 1529
[494] SAGLAM, Z., AKTEKIN, N., J.Phys., **B24** (1991) 3491
[495] OKAMOTO, Y., ONDA, K., ITIKAWA, Y., J.Phys., **B26** (1993) 745
[496] DANJO, A., NISHIMURA, H., J.Phys. Soc. Japan, **54** (1985) 1224
[497] KATASE, A., ISHIBASHI, K., MATSUMOTO, Y., SAKAE, T., MAEZONO, S., MURAKAMI, E., WATANABE, K., MAKI, H., J.Phys., **B19** (1986) 2715
[498] SHYN, T.W., CHO, S.Y., Phys. Rev., **A36** (1987) 5138
[499] JOHNSTONE, W.M., NEWELL, W.R., J.Phys., **B24** (1991) 3633
[500] SHYN, T.W., GRAFE, A., Phys. Rev., **A46** (1992) 4406; Phys. Rev., **A47** (1993) 3456 (Erratum)
[501] BRESCANSIN, L.M., LIMA, M.A.P., GIBSON, T.L., McKOY, V., HUO, W.M., J. Chem.Phys., **85** (1986) 1854
[502] GIANTURCO, F.A., SCIALLA, S., J. Chem.Phys., **87** (1987) 6468
[503] JAIN, A.K., TRIPATHI, A.N., JAIN, A., Phys. Rev., **A37** (1988) 2893
[504] JAIN, A., J.Phys., **B21** (1988) 905
[505] SATO, H., KIMURA, M., FUJIMA, K., Chem.Phys. Lett., **145** (1988) 21
[506] GIANTURCO, F.A., J.Phys., **B24** (1991) 3837
[507] YUAN, J., ZHANG, Z., Phys. Rev., **A45** (1992) 4565
[508] RESCIGNO, T.N., LENGFIELD, B.H., Z.Phys., **D24** (1992) 117
[509] ITIKAWA, Y., J.Phys. Soc. Japan, **32** (1972) 217
[510] JAIN, A., THOMPSON, D.G., J.Phys., **B16** (1983) 3077
[511] TRAJMAR, S., WILLIAMS, W., KUPPERMANN, A., J. Chem.Phys., **58** (1973) 2521
[512] ITIKAWA, Y., J.Phys. Soc. Japan, **36** (1974) 1127
[513] SENG, G., LINDER, F., J.Phys., **B7** (1974) L 509
[514] SENG, G., LINDER, F., J.Phys., **B9** (1976) 2539
[515] ROHR, K., J.Phys., **B10** (1977) L735
[516] JAIN, A., THOMPSON, D.G., J.Phys., **B16** (1983) L 347

[517] SHYN, T.W., CHO, S.Y., CRAVENS, T.E., Phys. Rev., **A38** (1988) 678
[518] FURLAN, M., HUBIN-FRANSKIN, M.J., DELWICHE, J., COLLIN, J.E., J. Chem.Phys., **95** (1991) 1671
[519] LASSETTRE, E.N., SKERBELE, A., J. Chem.Phys., **60** (1974) 2464
[520] CHUTJIAN, A., HALL, R.I., TRAJMAR, S., J. Chem.Phys., **63** (1975) 892
[521] FERCH, J., MASCHE, C., RAITH, W., J.Phys., **B14** (1981) L 97
[522] HOFFMAN, K.R., DABABNEH, M.S., HSIEH, Y.F., KAUPPILA, W.E., POL, V., SMART, J.H., STEIN, T.S., Phys. Rev., **A25** (1982) 1393
[523] KWAN, C.K., HSIEH, Y.F., KAUPPILA, W.E., SMITH, S.J., STEIN, T.S., UDDIN, M.N., DABABNEH, M.S., Phys. Rev., **A27** (1983) 1328
[524] SUEOKA, O., MORI, S., J.Phys. Soc. Japan, **53** (1984) 2491
[525] SZMYTKOWSKI, C., ZECCA, A., KARWASZ, G., OSS, S., MACIAG, K., MARINKOVIC, B., BRUSA, R.S., GRISENTI, R., J.Phys., **B20** (1987) 5817
[526] DANNER, D., Diploma thesis (unpublished), University of Freiburg, Freiburg/Germany (1970)
[527] BROMBERG, J.P., J. Chem.Phys., **60** (1974) 1717
[528] SHYN, T.W., SHARP, W.E., CARIGNAN, G.R., Phys. Rev., **A17** (1978) 1855
[529] REGISTER, D.F., NISHIMURA, H., TRAJMAR, S., J.Phys., **B13** (1980) 1651
[530] IGA, I., NOGUEIRA, J.C., MU-TAO, L., J.Phys., **B17** (1984) L 185
[531] KOCHEM, K.H., SOHN, W., HEBEL, N., JUNG, K., EHRHARDT, H., J.Phys., **B18** (1985) 4455
[532] KANIK, I., McCOLLUM, D.C., NICKEL, J.C., J.Phys., **B22** (1989) 1225
[533] MORRISON, M.A., LANE, N.F., COLLINS, L.A., Phys. Rev., **A15** (1977) 2186
[534] ONDA, K., TRUHLAR, D.G., J.Phys., **B12** (1979) 283
[535] LYNCH, M.G., DILL, D., SIEGEL, J., DEHMER, J.L., J. Chem.Phys., **71** (1979) 4249
[536] COLLINS, L.A., MORRISON, M.A., Phys. Rev., **A25** (1982) 1764
[537] JAIN, A., TAYAL, S.S., J.Phys., **B15** (1982) L 867
[538] BOTELHO, L.F., FREITAS, L.C.G., MU-TAO, L., JAIN, A., TAYAL, S.S., J.Phys., **B17** (1984) L 641
[539] MORRISON, M.A., LANE, N.F., Chem.Phys. Lett., **66** (1979) 527
[540] MORRISON, M.A., Phys. Rev., **A25** (1982) 1445
[541] WHITTEN, B.L., LANE, N.F., Phys. Rev., **A26** (1982) 3170
[542] ESTRADA, H., DOMCKE, W., J.Phys., **B18** (1985) 4469
[543] ITIKAWA, Y., J.Phys. Soc. Japan, **36** (1974) 1121
[544] HAKE, R.D., PHELPS, A.V., Phys. Rev., **158** (1967) 70
[545] LOWKE, J.J., PHELPS, A.V., IRWIN, B.W., J. Appl.Phys., **44** (1973) 4664
[546] BULOS, B.R., PHELPS, A.V., Phys. Rev., **A14** (1976) 615
[547] ANTONI, T., JUNG, K., EHRHARDT, H., CHANG, E.S., J.Phys., **B19** (1986) 1377

[548] MORRISON, M.A., LANE, N.F., Phys. Rev., **A16** (1977) 975

[549] HAYASHI, M., private communication (1993)

[550] TAWARA, H., ITIKAWA, Y., NISHIMURA, H., TANAKA, H., NAKAMURA, Y., "Collision Data Involving Hydrocarbon Molecules", Research Report NIFS-DATA-6, National Institute for Fusion Science, Nagoya/Japan (1990)

[551] TAWARA, H., ITIKAWA, Y., NISHIMURA, H., TANAKA, H., NAKAMURA, Y., "Cross Section Data for Collisions of Electrons with Hydrocarbon Molecules", in Atomic and Plasma-Material Interaction Data for Fusion (ed. R.K. Janev), IAEA Vienna (1992)

[552] NAKAMURA, Y., "Recent Electron Swarm Studies Using Rare Gas/Molecular Gas Mixtures", in reference [300], p. 178-200

[553] MORGAN, W.L., "A Critical Evaluation of Low Energy Electron Impact Cross Sections for Plasma Processing Modelling: I. Cl_2, F_2, and HCl; II. CF_4, SiH_4, and CH_4", JILA Data Center Report No. 34, University of Colorado, Boulder/Colorado (1991)

[554] FERCH, J., GRANITZA, B., RAITH, W., J.Phys., **B18** (1985) L 445

[555] FLOEDER, K., FROMME, D., RAITH, W., SCHWAB, A., SINAPIUS, G., J.Phys., **B18** (1985) 3347

[556] JONES, R.K., J. Chem.Phys., **82** (1985) 5424

[557] LOHMANN, B., BUCKMAN, S.J., J.Phys., **B19** (1986) 2565

[558] SUEOKA, O., MORI, S., J.Phys., **B19** (1986) 4035

[559] DABABNEH, M.S., HSIEH, Y.F., KAUPPILA, W.E., KWAN, C.K., SMITH, S.J., STEIN, T.S., UDDIN, M.N., Phys. Rev., **A 38** (1988) 1207

[560] NISHIMURA, H., SAKAE, T., Jap. J. Appl.Phys., **29** (1990) 1372

[561] ZECCA, A., KARWASZ, G., BRUSA, R.S., SZMYTKOWSKI, C., J.Phys., **B24** (1991) 2747

[562] KANIK, I., TRAJMAR, S., NICKEL, J.C., Chem.Phys. Lett., **193** (1992) 281

[563] BARBARITO, E., BASTA, M., CALICCHIO, M., TRESSARI, G., J. Chem.Phys., **71** (1979) 54

[564] ROHR, K., J.Phys., **B13** (1980) 4897

[565] TANAKA, H., OKADA, T., BOESTEN, L., SUZUKI, T., YAMAMOTO, T., KUBO, M., J.Phys., **B15** (1982) 3305

[566] SOHN, W., JUNG, K., EHRHARDT, H., J.Phys., **B16** (1983) 891

[567] CURRY, P.J., NEWELL, W.R., SMITH, A.C.H., J.Phys., **B18** (1985) 2303

[568] SOHN, W., KOCHEM, K.H., SCHEUERLEIN, K.M., JUNG, K., EHRHARDT, H., J.Phys., **B19** (1986) 3625

[569] SAKAE, T., SUMIYOSHI, S., MURAKAMI, E., MATSUMOTO, Y., ISHIBASHI, K., KATASE, A., J.Phys., **B22** (1989) 1385

[570] SHYN, T.W., CRAVENS, T.E., J.Phys., **B23** (1990) 293

[571] BOESTEN, L., TANAKA, H., J.Phys., **B24** (1991) 821

[572] MAPSTONE, B., NEWELL, W.R., J.Phys., **B25** (1992) 491
[573] LUNT, S.L., RANDELL, J., ZIESEL, J.P., MROTZEK, G., FIELD, D., J.Phys., **27** (1994) 1407
[574] ABUSALBI, N., EADES, R.A., NAM, T., THIRUMALAI, D., DIXON, D.A., TRUHLAR, D.G., DUPUIS, M., J. Chem.Phys., **78** (1983) 1213
[575] JAIN, A., J. Chem.Phys., **78** (1983) 6579
[576] JAIN, A., J. Chem.Phys., **81** (1984) 724
[577] JAIN, A., Phys. Rev., **A 34** (1986) 3707
[578] BLOOR, J.E., SHERROD, R.E., J.Phys. Chem., **90** (1986) 5508
[579] GIANTURCO, F.A., JAIN, A., PANTANO, L.C., J.Phys., **B20** (1987) 571
[580] GIANTURCO, F.A., SCIALLA, S., J.Phys., **B20** (1987) 3171
[581] LIMA, M.A.P., GIBSON, T.L., HUO, W.M., McKOY, V., Phys. Rev., **A32** (1985) 2696
[582] LIMA, M.A.P., WATARI, K., McKOY V., Phys. Rev., **A39** (1989) 4312
[583] YUAN, J., J.Phys., **B21** (1988) 3113
[584] JAIN, A., WEATHERFORD, C.A., THOMPSON, D.G., McNAUGHTEN, P., Phys. Rev., **A40** (1989) 6730
[585] McNAUGHTEN, P., THOMPSON, D.G., JAIN, A., J.Phys., **B23** (1990) 2405 S
[586] McCURDY, C.W., RESCIGNO, T.N., Phys. Rev., **A39** (1989) 4487
[587] Mc CURDY, C.W., Aust. J.Phys., **45** (1992) 337
[588] KUBO, M., MATSUNAGA, D., TANAKA, H., Proc. 12th ICPEAC, Gatlinburg/Tennessee (1981) p. 344
[589] TANAKA, H., KUBO, M., ONODERA, N., SUZUKI, A., J.Phys., **B16** (1983) 2861
[590] SHYN, T.W., J.Phys., **B24** (1991) 5169
[591] POLLOCK, W.J., Trans. Faraday Soc., **64** (1968) 2919
[592] DUNCAN, C.W., WALKER, I.C., J. Chem. Soc. Faraday Trans.II, **68** (1972) 1514
[593] HADDAD, G.N., Aust. J.Phys., **38** (1985) 677
[594] OHMORI, Y., KITAMORI, K., SHIMOZUMA, M., TAGASHIRA, H., J.Phys., **D19** (1986) 437
[595] DAVIES, D.K., KLINE, L.E., BIES, W.E., J. Appl.Phys., **65** (1989) 3311
[596] SCHMIDT, B., J.Phys., **B24** (1991) 4809
[597] SCHMIDT, B., Comments At. Mol.Phys., **28** (1993) 379
[598] JAIN, A., THOMPSON, D.G., J.Phys., **B16** (1983) 3077
[599] ABUSALBI, N., SCHWENKE, D.W., MEAD, C.A., TRUHLAR, D.G., Theor. Chim. Acta, **71** (1987) 359
[600] BRESCANSIN, L.M., LIMA, M.A.P., McKOY, V., Phys. Rev., **A40** (1989) 5577
[601] VUSKOVIC, L., TRAJMAR, S., J. Chem.Phys., **78** (1983) 4947
[602] NAKANO, T., TOYODA, H., SUGAI, H., Jap. J. Appl.Phys., **30** (1991) 2908; ibid., **30** (1991) 2912

[603] WINSTEAD, C , SUN, Q , McKOY, V , da SILVA LINO, J L , LIMA, M A P , Z Phys , **D24** (1992) 141

[604] WINSTEAD, C , SUN Q , McKOY, V , da SILVA LINO, J L , LIMA, M A P , J Chem Phys , **98** (1993) 2132

[605] BRUCHE, E , Ann Phys , **4** (1930) 387

[606] NISHIMURA, H , TAWARA, H , J Phys , **B24** (1991) L 363

[607] MERZ, R , PIRRUNG, K , LINDER, F , to be published (1994)

[608] SZMYTKOWSKI, C , Z Phys , **D13** (1989) 69

[609] MATSUNAGA, D , KUBO, M , TANAKA, H , Proc 12th ICPEAC , Gatlinburg/Tennessee (1981) p 358

[610] MATSUNAGA, D , KUBO, M , ONODERA, N , TANAKA, H , in "Atomic Collision Research in Japan", Progress Report No 7 (eds Y Hatano et al), Tokyo (1981) p 6

[611] MANN, A , LINDER, F , J Phys , **B25** (1992) 533, ibid , **25** (1992) 545

[612] WINSTEAD, C HIPES, P G , LIMA, M A P , McKOY, V , J Chem Phys , **94** (1991) 5455

[613] BOESTEN, L , DILLON, M A , TANAKA, H , KIMURA, M , SATO, H , J Phys , **B27** (1994) 1845

[614] HERZBERG, G , "Molecular Spectra and Molecular Structure II Infrared and Raman Spectra of Polyatomic Molecules", Van Nostrand, Princeton/New Jersey (1945)

[615] EHRHARDT, H , LINDER, F , MEISTER, G , Z Naturf , **20a** (1965) 989

[616] LASSETTRE, E N , SKERBELE, A , DILLON, M A , J Chem Phys , **49** (1968) 2382

[617] KOCH, E E , SKIBOWSKI, M , Chem Phys Lett , **9** (1971) 429

[618] SCHIAVONE, J A , TARR, S M , FREUND, R S , J Chem Phys , **70** (1979) 4468

Chapter 4

LOW ENERGY ELECTRON INTERACTION WITH CONDENSED MATTER

L. Sanche
MRC Group in the Radiation Sciences, Faculty of Medicine,
Université de Sherbrooke, Sherbrooke, Canada

T.D. Märk
Institut für Ionenphysik der Universität Innsbruck,
Innsbruck, Austria

Y. Hatano
Department of Chemistry, Tokyo Institute of Technology,
Tokyo, Japan

4.1 INTRODUCTION

The effects of high-energy radiation can be perceived as the result of a sequence of events or processes which follow the interaction of the initial particle. Many chapters in this book deal with the interaction of high-energy photons, electrons, protons and ions incident on biological media and with the subsequent interactions of the fast electrons generated in the initial energy deposit. Fast electrons ionize the medium, producing a distribution of excited atoms and molecules, ions and secondary electrons. These latter are created in large quantities (10^5/MeV) and carry most of the energy of the fast primaries. Secondary electrons have low energies with a distribution lying essentially below 70 eV and a most probable energy around 10 eV [1]. At those energies electrons have their highest cross section for scattering by atoms and molecules [2]. Hence, they interact rapidly and within a very short range (~10-100 Å) in the irradiated medium, where they generate highly reactive species which in turn initiate chemical reactions. Any analysis of the sequence of events leading to chemical modification of an irradiated substance must therefore include a description of the action of secondary low-energy electrons.

In radiotherapy, the medium of interest is the living cell or more specially components of the cell which play a vital role in its proliferative capabilities. Thus, the information generated in the fields of radiation physics and chemistry must be transferable to the actual processes which take place within the cell if we are to understand, at the microscopic level, doses in radiotherapy including the combined effects of radiation and drugs. For the problem of interest in this book, we need to consider if the data obtained from the interaction of an isolated molecular or atomic target with a single projectile are still valid in the condensed phase where the target is surrounded by neighbouring atoms and/or molecules. This is usually the case for high energy particles including the fast primary electrons whose wavelength is short in comparison with the "diameter" of the elementary constituents of condensed matter. The short wavelength of these electrons make it possible to consider that each projectile interact individually with the atoms and/or molecules of the condensed system. This concept is no longer valid at low energies and more specifically below ~30 eV where the electron's wavelength is of the order of the interatomic or intermolecular distances. In this case, the electron is scattered collectively from many targets and the scattered

intensity must be derived from the sum of the interaction potentials between the electron and each of the atoms and/or molecules present in the liquid or solid. The geometrical arrangement of condensed matter must therefore be taken into account in order to describe the interference of the electron waves arising from multiple scattering. However, for many processes (e.g., those by which energy localization occurs at specific sites), it may still be possible to describe low-energy electron scattering in the condensed phase in terms of gas-phase phenomena provided that the modification to the isolated electron-molecule system are properly taken into account. A number of experiments have been devised to explore these modifications and investigate the gradual changes which occur as the density of the scattering medium increases. These may be divided into three major categories:

(1) high-pressure gas-phase (and liquid-phase) electron scattering experiments, including drift mobility and pulse radiolysis measurements, where electron motion is investigated as function of number density, mean energy and gas-pressure up to the liquid state;

(2) cluster experiments, in which a low-energy electron beam crosses a high-density molecular beam containing clusters of atoms and/or molecules;

(3) solid-film experiments, in which a low-energy electron beam strikes a multilayer film of condensed atoms and/or molecules. These experiments are briefly described in this chapter.

We first provide a short description in the following section (i.e., 4.2) of the scattering of a low-energy electron with an isolated target. In the subsequent sections, we explain how the fundamental properties of the isolated scattering phenomena are modified when the density of the targets is increased up to that of the condensed phase. It is shown that our present knowledge of electron scattering in high-pressure gases and liquids (sec. 4.3), clusters (sec. 4.4) and condensed molecular films (sec. 4.5) provides valuable models for excess electrons interactions in liquids and solids thereby linking gas phase properties to those of the other phases. This transfer of information is of fundamental importance for our understanding of the action of secondary electrons in biological structures. A list of the acronyms used in this chapter is given in Table 4.1.

Table 4.1. List of acronyms

2-D	Two-dimensional
DA	Dissociative attachment
DD	Dipolar dissociation
DOS	Density of states
EA	Electron affinity
ESD	Electron stimulated desorption
HREEL	High resolution electron energy lost
KE	Kinetic energy
LEET	Low energy electron transmission
PDI	Post dissociation interaction
QSE	Quantum size effects
TOF	Time-of-flight
vdW	van der Waals

4.2. INTERACTION OF LOW-ENERGY ELECTRONS WITH ATOMS AND MOLECULES

The interaction of a low-energy electron with an isolated target may be described, outside the target itself, by a potential [3] which takes into account the force between the two particles due to the dipole, quadrupole and higher moments of the target as well as induced polarization effects. By analysing as function of incident electron energy and scattering angle the various scattering cross sections, it may be possible in particular cases to sort out which part of the potential is dominant. For example, certain energy losses may be characterized as due to "dipolar scattering" meaning that interaction with the permanent dipole of the molecule is dominant. However, if the electron penetrates significantly into the target "region" the interaction becomes more complex due to the possibility of spin-exchange and constructive interference of the electron wave within the target. This latter phenomenon gives rise to electron resonances. Thus, resonances occur when the scattered electron resides for a time much longer than the usual scattering

time in the neighborhood of the target atom or molecule. From an atomic or molecular orbital point of view, a resonant state may be considered as a negative ion formed by an electron which occupies temporarily an orbital of the target [4].

Fig. 4.1 illustrates the possible decay channels of a diatomic transient anion AB^-. The departing electron may leave the molecule in a rotationally, vibrationally [reaction (1) in Fig. 4.1] or electronically (2 in Fig. 4.1) excited state. In the condensed state librational and translational excitation is also possible. If the resulting electronically excited neutral state is dissociative, fragments in the ground or excited states can be produced (2). If the lifetime of the resonance is, at least, of the order of a vibrational period, the AB^- state is dissociative in the Franck-Condon region and one of the possible fragments has a positive electron affinity, then the anion may dissociate into a stable anion and a neutral fragment in the ground (3 in Fig. 4.1) or an excited (4) state. This process is called dissociative attachment (DA). If during its lifetime, the transient anion transfers energy to another system (e.g., to another molecule by collisional interaction) it can become stable when the parent molecule has a positive electron affinity (5 in Fig. 4.1). Finally, when the transient anion is formed at energies above the ionization potential, two-electron

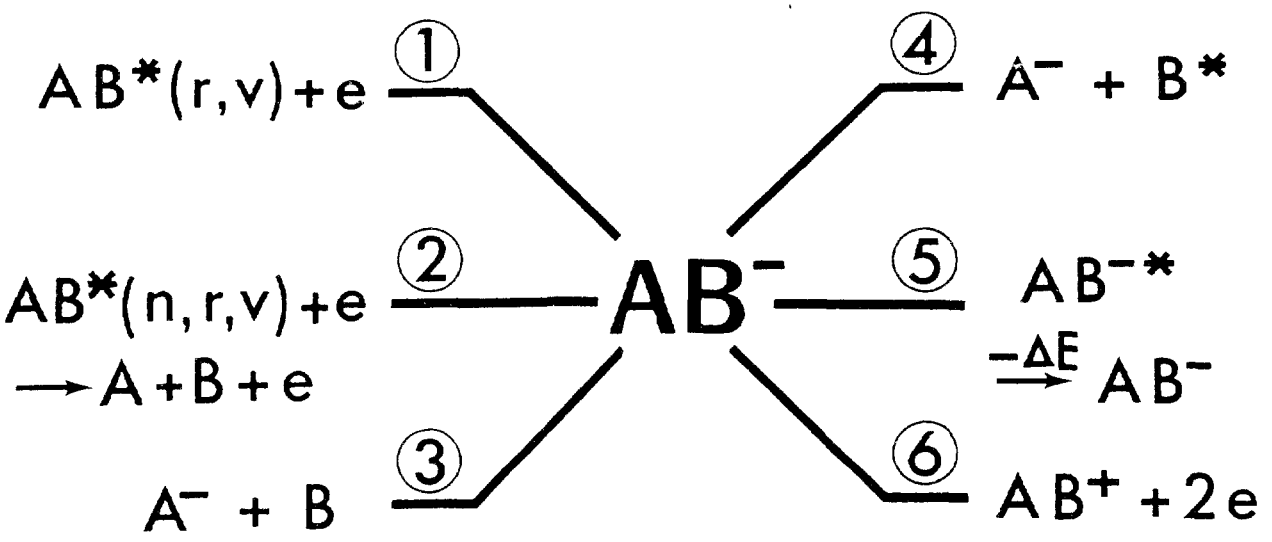

Fig. 4.1 Possible decay channels for a transitory anion AB^-. r, v and n represent, respectively, rotational, vibrational and electronic excitation. AB^* and B^* represent excited electronic states of molecule AB and fragment B, respectively.

emission is possible (6 in Fig. 4.1). Not shown among the reactions of Fig. 4.1, is the spontaneous emission of a photon by the transitory anion followed by stabilization of the electron on the molecule (i.e., $AB^{-*} \rightarrow AB^{-} + h\nu$), since emission of electromagnetic radiation is rarely faster than electron emission. In the condensed phase and in high pressure gases, this latter process can be enhanced with the help of an additional stabilizing interaction with other targets. Autodetachment lifetimes of transient anions vary from $\simeq 10^{-15}$ s up to the millisecond time scale for large polyatomic molecules, where the excess energy of the anion may be accommodated among its many degrees of freedom, thereby delaying autodetachment.

The amplitudes of the vibrational excitation cross sections are also affected by the lifetime Δt of transitory anions. Long-lived resonances ($\Delta t > 10^{-14}$ s) cause a significant displacement of the nuclei of a molecule when the additional electron occupies a strongly bonding or antibonding orbital. When the electron leaves the molecule, nuclear motion is initiated toward the initial internuclear distance, causing strong vibrational excitation including many overtones of the molecule. On the other hand, when the lifetime is much smaller than a typical vibrational period ($\Delta t << 10^{-14}$ s), the nuclei are not displaced significantly and only the lower vibrational levels become excited with considerable amplitude.

In the condensed state, we expect not only the single-electron-target potential to be modified by the proximity of neighbouring atoms or molecules, but also the amplitude, lifetime, symmetry and energy of the isolated transient anions. Among the "environmental effects" or factors which may contribute to these modifications we note: (i) the change in the symmetry of the scattering problem introduced by the presence of other nearby targets; (ii) the polarisation of these targets by the electron and transient anion; (iii) the fixed orientation of the molecule with respect to a given frame of reference and (iv) the possible distortion and modification of the target molecule by the adjacent matter. The change in symmetry may be viewed to arise from multiple scattering of the electron waves between the molecules of a solid. This condition changes the partial wave content of a resonant electron which in turn influences the lifetime of the state [5]. By acting on the isolated electron-molecule potential, the polarization force can also modify the resonance lifetime, by promoting electron transfer to the neighbouring targets and lowering the

resonance energy with the introduction of an attractive potential. This perturbation may reduce the number of decay channels; thus, affecting in a drastic manner certain cross sections and increasing the lifetime or decreasing total decay width of the resonance. Lowering of the resonance energy may be viewed as a change in the electron affinity (EA) of the target molecule (even from negative to positive) which in clusters can be monitored as a function of size. In the case of well ordered solids, the orientation of the molecule is fixed so that the differential cross sections and angular distributions are greatly modified [6] from those of the gas phase, where they are measured from randomly oriented molecules.

4.3 ELECTRONS IN DENSE GASES AND LIQUIDS

The behavior of excess electrons as in electron transport and reactions in dense molecular media both polar and nonpolar has recently attracted great interest [7-19]. Excess electron mobilities μ_e have been measured extensively in a variety of molecular compounds ranging from rare gas atoms and diatomic molecules to complex molecules such as hydrocarbons and alcohols in the liquid phase or in the dense-gas phase (see Fig. 4.2), and several theoretical models have been proposed for the transport mechanism of excess electrons in these media. Excess-electron reactivities with solute molecules or positive ions in these media, which are closely related to the transport phenomena, have been also extensively investigated.

In this section, a survey is given of recent understanding of the behavior of excess electrons in particular electron attachment, recombination, solvation, and localization in dense gases and liquids.

4.3.1 ELECTRON ATTACHMENT [13,19]

As described in section 3.6 of chapter 3, one may expect some environmental effects on the overall scheme of electron attachment processes in the presence of third-body molecules or in bulk media (i.e., channel no 5. in Fig. 4.1). In addition to the determination of cross sections or rate constants for electron attachment or negative-ion formation and their electron energy dependences, it has been of prime importance to clarify the attachment mechanism, not only the overall mechanism itself but also the influence of environmental conditions on the mechanism.

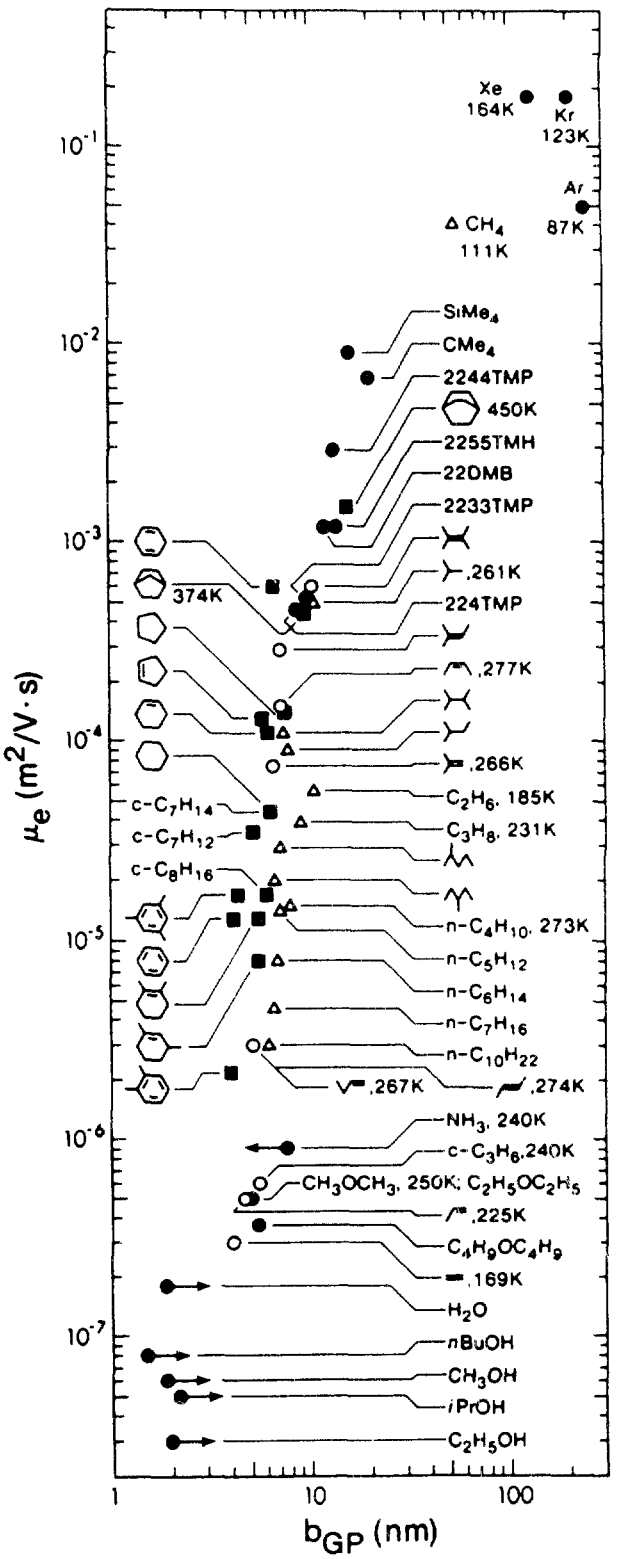

Fig. 4.2 Drift mobilities μ_e of thermal electrons and thermalization distances b_{GP} of secondary electrons in dielectric liquids at 296K unless otherwise states [11].

In the investigation of low energy electron attachment in bulk gases, electron-swarm or drift-tube techniques have played a major role, accumulating data on attachment rate constants, their electron energy dependence, formation of negative ions, etc. Christophorou and his co-workers [20,21] have extensively studied electron attachment in dense gases as quasi-liquids by using a high-pressure swarm technique. In addition to usual swarm techniques an interesting approach of measuring cyclotron resonance signals due to free electrons in gases has been carried out for the study of electron attachment to various molecules as a function of electron energy in the range of 1 to 10kT [22]. Another interesting approach to electron attachment studies which is highly sensitive consists of monitoring of electron density in swarms by the Cavalleri method [23]. The pulse sampling technique [24] is simple but capable of yielding precise data particularly on energetics of negative-ion formation. A microwave technique for monitoring the rate of removal of electrons in a swarm has been combined with static or flowing afterglows produced by electrical discharges [25]. This technique has been combined also with the pulse radiolysis method in order to eliminate essential limitations including those in the above-mentioned microwave techniques [13,19,26]. The response time of the detection system for electrons has been greatly improved and the effect of the presence of various species in afterglows on electron attachment processes has been eliminated. This combination, therefore, has given a reasonably good selectivity for measuring electron attachment processes, even in multiple collision systems.

For the study of electron attachment mechanism ordinary swarm techniques may have some essential limitations, as they are limited to the use of only a few buffer gases for which the swarm parameters, electron energy distributions, etc., are well known. Therefore, in cases where the attachment mechanism is strongly dependent on the particular nature of environmental gases, the technique may not give enough information to evaluate adequately the mechanism in detail. Usual beam techniques are evidently not suitable for the study of environmental effects on the attachment mechanism. On the other hand, the microwave technique has been used as an alternative means for such studies with the main advantage of the technique allowing the observation of the behavior of thermal electrons, thus excluding any factor dependent on the electron-energy distribution. For usual swarm and beam techniques, it has been difficult to study electron collision processes at very low energies such as thermal, whereas the microwave technique combined with

Table 4.2

Rate constant, resonance energy, and resonance width for electron attachment to O_2 or $(O_2 \cdot M)$ [13]

$(O_2 \cdot M)$	Rate Constant (10^{-11} cm^3/sec)	Resonance Energy (meV)	Resonance Width (μeV)
$(O_2 \cdot N_2)$	3000	20	800
$(O_2 \cdot C_2H_6)$	1100	30	450
$(O_2 \cdot C_2H_4)$	380	45	270
O_2	3	88	10

the pulse radiolysis method has shown recently a distinct advantage in studying thermal electron attachment to molecules [13,19,26]. In the pulse radiolysis method it is possible to time-resolve the disappearance of decaying electrons over a very wide range of the pressure of a buffer gas which may be chosen with virtually no limitation. Thus, the mechanism of low-energy electron attachment to molecules has been discussed primarily in terms of the interaction of electrons with molecules.

Recent studies of thermal electron attachment to O_2, N_2O and other molecules have revealed that the electron attachment to pre-existing van der Waals (vdW) molecules or neutral clusters plays a significant role in the stabilization mechanism [13,19,26]. The rate constants for the electron attachment to these vdW molecules (e.g., $(O_2.M)$ and $(N_2O.M)$ where M is O_2, N_2O or any other molecule) are much larger than those for the electron attachment to isolated O_2 or N_2O. This clearly shows that the electron attachment to an ordinary isolated single molecule is greatly enhanced by the presence of a surrounding guest molecule M as summarized by the values given in Table 4.2. The modification of the single-electron-molecule potential by the formation of vdW molecules reflects the departure from the gas-phase characteristics toward those of the condensed phase. Similar to the electron attachment process in clusters and solid films (Sec. 4.4 and 4.5) the following changes are observed [13]; i.e.,

(1) The lowering of the resonance energy due to a deeper ion-neutral potential in comparison with neutral-neutral potential of the vdW molecule,

(2) The additional vibrational structures of the vdW molecule,

(3) The symmetry breaking due to the vdW interaction which allows the molecule to attach the electron with additional partial waves,

(4) The deformation of the molecular structure or the change of the vibrational modes due to the surrounding molecules,

(5) The effective vibrational relaxation of the formed negative ion with excess energies due to the presence of a built-in third body molecule in vdW molecule.

The distinct features of the electron attachment to vdW molecules as summarized above may become a substantial clue to understand the fundamental nature of electron attachment not only in dense gases but also in the condensed phase. It is also apparent that most of the electron attachment in bulk systems is no longer a simple process consisting of the interaction of electrons with isolated molecules. From this point of view, interesting phenomena in ionized gases such as the attachment cooling effect and the response-time of the air-filled fast response ionization chamber should be analyzed by taking into account the important role of vdW molecules in the electron attachment mechanism. It should be noted here also that such attachment studies in dense gases have been complemented by recent beam experiments between electron and van der Waals clusters [27,28] (See section 4.4).

4.3.3 ELECTRON SOLVATION AND LOCALIZATION IN THE CONDENSED PHASE

This problem has been one of the central subjects in radiation chemistry and it is now relevant to a variety of chemical areas, and even biological or physical areas. Experimental evidence for the solvated electron has been obtained using the radiolysis-product analysis, photoconductivity and optical or electron spin resonance spectroscopy techniques [43-45]. Solvated electrons have been observed in a variety of polar solvents including water, alcohols, ammonia, amines, and ethers, and even in nonpolar solvents such as hydrocarbons [46]. Optical absorption spectra of the solvated electron in various solvents are characterized by a broad, structureless, and asymmetric band, and are positioned at wavelength regions from visible to near-infrared depending on the solvent. Formation processes of solvated electrons, i.e., solvation processes of pre-solvated electrons, have been recently observed using femtosecond laser spectroscopy

[47,48]. It is also of great interest that negatively charged clusters formed in sonic nozzle beams be compared with the theoretical model of solvated electrons (See section 4.4).

Theoretical investigation of the solvated electron has been also extensively carried out to explain the above-mentioned experimental results and therefore to obtain information on electron solvent-molecule interaction or the structure of the solvated electron [45]. The stability of negatively charged water clusters has been theoretically investigated in terms of the modelling of the hydrated electron [49,50].

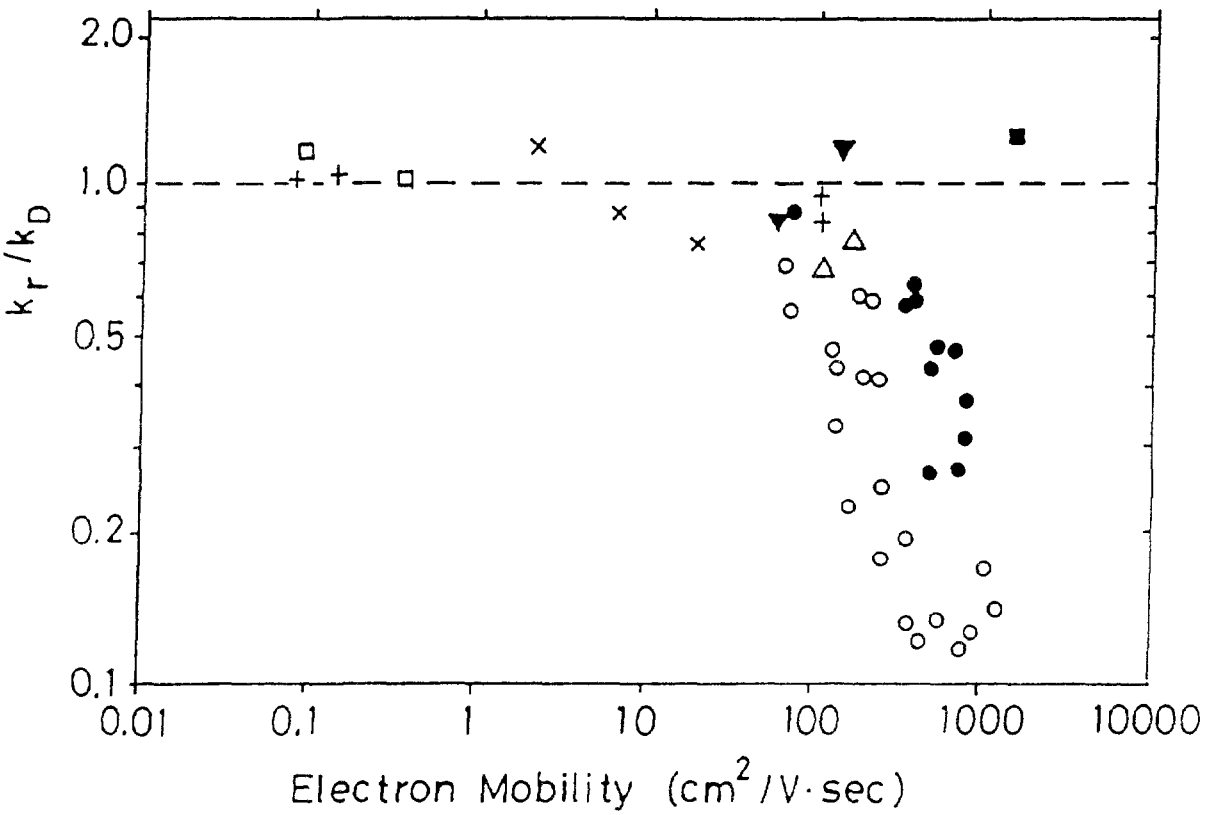

Fig. 4.3 Plots of k_r/k_D vs μ_e in several fluids; ■, solid methane; ●, liquid methane; O, gaseous methane; x, liquid mixtures of neopentane and n-hexane; ▼, liquid and solid neopentane; Δ, liquid and solid tetramethylsilane; +, liquid n-pentane, n-hexane, and tetramethylsilane; ❑, liquid n-hexane and cyclohexane [7].

Electrons are also localized or trapped in low temperature glassy or amorphous matrices of these solvent-molecules and are observable by optical or electron spin resonance spectroscopy techniques [51,52]. Electron localization and reactivities in various condensed media, particularly in nonpolar media, have been investigated also by measuring excess-electrons electrical conductivities [12-15,17,18]. As seen in Fig. 4.2, the measured electron mobilities are strongly dependent on the molecular structure. These values, and their temperature and density dependences have been measured in a variety of liquids.

(1) A semi empirical treatment by Warman [34] taking both the diffusion-controlled and the electron-energy-exchange controlled recombination processes into account,

(2) A Monte Carlo simulation by Tachiya [35-37] with the parameter $\ell/\underline{a}$ where ℓ is the mean free path of electrons and $\underline{a}$ the reaction radius of recombination,

(3) A molecular dynamics simulation by Morgan [38],

(4) A fractal treatment by Lopez-Quintela et al. [39],

(5) A gas kinetic approach by Kitahara et al [40],

(6) An approach based on the Fokker-Planck equation by Sceats [41], and

(7) A fractal treatment by Mozumder [42].

Warman first proposed a theoretical formula of the recombination rate constant to explain the result of $k_r << k_d$. In spite of many assumptions to derive the formula, the calculated value for liquid argon is in rather good agreement with the experimental one. For dense gaseous argon, however, the calculated value is far from the experimental one. Recently, Tachiya pointed out using a Monte Carlo method that if $\ell/\underline{a}$ is not negligible, the rate constant for bulk recombination deviates from k_d. Experimental k_r values for liquid methane lie around the theoretical curve of his simulation which uses $\ell/\underline{a}$ only as a parameter. He also explains the effect of the electron field strength on k_r. The values of k_r, in both dense methane and argon, increase roughly in proportion to the field strength in the lower field strength region and form a peak at around the critical field strength (e.g., 10^{-19} V.cm^2 in Fig. 4.4); the height of the peak is almost of the same magnitude as that for μ_e. These results are explained in terms of the effect of the field strength on the trajectory of electrons to be recombined. In the lower field region, disentangling of random electron

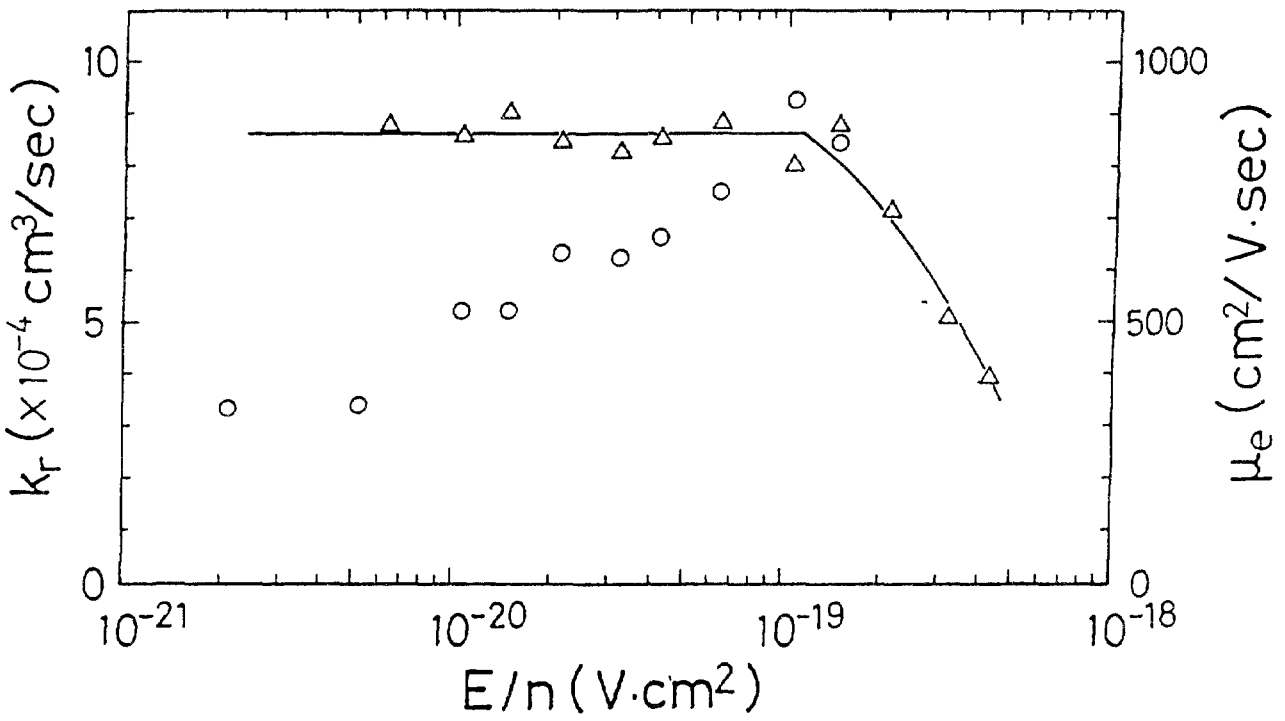

Fig. 4.4 Electric field dependence of μ_e and k_r in liquid methane at 170K (n = 1.2 x 10^{22}cm^{-3}); Δ, μ_e; o, k_r [33].

trajectories caused by the presence of the external electric field should increase the k_r value. In the field region higher than the critical field strength, the internal energy of an electron-ion pair (i.e., the energy in excess of the electron's kinetic energy) decreases the k_r value.

4.3.3 ELECTRON SOLVATION AND LOCALIZATION IN THE CONDENSED PHASE

This problem has been one of the central subjects in radiation chemistry and it is now relevant to a variety of chemical areas, and even biological or physical areas. Experimental evidence for the solvated electron has been obtained using the radiolysis-product analysis, photoconductivity and optical or electron spin resonance spectroscopy techniques [43-45]. Solvated electrons have been observed in a variety of polar solvents including water, alcohols, ammonia, amines, and ethers, and even in nonpolar solvents such as hydrocarbons [46]. Optical absorption spectra of the solvated electron in various solvents are characterized by a broad, structureless, and asymmetric band, and are positioned at wavelength regions from visible to near-infrared depending on the solvent. Formation processes of solvated electrons, i.e., solvation processes of

pre-solvated electrons, have been recently observed using femtosecond laser spectroscopy [47,48]. It is also of great interest that negatively charged clusters formed in sonic nozzle beams be compared with the theoretical model of solvated electrons (See section 4.4).

Theoretical investigation of the solvated electron has been also extensively carried out to explain the above-mentioned experimental results and therefore to obtain information on electron solvent-molecule interaction or the structure of the solvated electron [45]. The stability of negatively charged water clusters has been theoretically investigated in terms of the modelling of the hydrated electron [49,50].

Electrons are also localized or trapped in low temperature glassy or amorphous matrices of these solvent-molecules and are observable by optical or electron spin resonance spectroscopy techniques [51,52]. Electron localization and reactivities in various condensed media, particularly in nonpolar media, have been investigated also by measuring excess-electrons electrical conductivities [12-15,17,18]. As seen in Fig. 4.2, the measured electron mobilities are strongly dependent on the molecular structure. These values, and their temperature and density dependences have been measured in a variety of liquids.

4.4 ELECTRON ATTACHMENT TO VAN DER WAALS CLUSTERS

It is the purpose of this section to focus on electrons scattering in clusters and in particular to summarize differences between a negatively charged isolated molecule and its aggregated counterpart. We will develop this theme by first describing the physical properties of negative cluster ions (electron affinity, electronic states) and then by discussing the kinetics of electron attachment (attachment cross sections).

4.4.1 LOCALIZED EXCESS ELECTRON STATES IN CLUSTERS

Electrons residing in clusters are corresponding to the following three types of ions and electron localization:

1. Cluster anions consisting of monomers with positive electron affinity (EA)

In this case the electron is bound by a single cluster constituent with a positive EA. The stable monomer anion is solvated by the surrounding cluster constituents. The excess energy released during the primary electron attachment process

$$(M)_n + e \rightarrow (M^{-*} \cdot M_{n-1}) \tag{4.3}$$

can either be accommodated within the molecule (in case of large molecules such as SF_6) giving $M^{*-} \cdot M_{n-1}$, or within the whole cluster, giving $(M^- \cdot M_{n-1})^*$. In general, however, the excess energy will be subsequently removed by monomer evaporation

$$(M^- \cdot M_{n-1})^* \rightarrow (M^- \cdot M_{n-2}) + M \tag{4.4}$$

In this way, it is possible to produce completely stable anions (even of the monomer) without need of other stabilizing processes. In a similar reaction sequence a primary DA process may end up in a stable non-stoichiometric cluster anion, i.e.

$$(M)_n + e \rightarrow (A^- \cdot M_{n-1})^* + B \qquad \text{(with } M = AB\text{)}$$

$$(A^- \cdot M_{n-1})^* \rightarrow A^- \cdot M_{n-2} + M \tag{4.5}$$

In both cases subsequent solvation and isomerization reactions (of M^- in Eq. 4.4 and A^- in Eq. 4.5 may lead to further stabilizing evaporations. Systems falling in this category, whose properties have been studied by free electron attachment, include O_2 [27,53,54], N_2O [54-57], SO_2 [58], SF_6 [56,59], and halogenated hydrocarbons [60,61].

2. Cluster ions consisting of monomers with negative EA

Because the EA of the CO_2 monomer (EA = -0.6 eV [62]) is negative (the most stable configuration of CO_2 being a bent structure [63]), attempts to attach free electrons to CO_2 monomers have only resulted in transient formation of CO_2^- which can decay by DA, mainly forming O^-. Conversely, the EA of the CO_2 dimer (consisting of a bent CO_2^-, solvated by a linear CO_2) is positive in accordance with theoretical predictions [63] and confirmed by the experimen-

tal observation of $(CO_2)_2^-$ and larger homologues [54,64]. Moreover, also CO_2^- is observable [55] if electrons are attached to clusters. Its yield exhibits a resonance well below the vertical EA of the monomer, because the precursor of CO_2^- is a cluster. As in case of the first class of cluster anions, the excess energy released by electron attachment is removed by monomer evaporation. Moreover, DA to clusters of this type followed by isomerization and evaporation again leads to non-stoichiometric cluster anion series, i.e. in case of CO_2 to $CO_3^- \cdot (CO_2)_n$ ions. The prototypical case of CO_2 has been investigated by free electron attachment in detail by several authors [54-57,64], CF_4 has been studied by Illenberger and coworkers [60].

3. Cluster ions consisting of monomers with near-zero EA: The solvated electron

Atoms and molecules with closed shell electronic structure (e.g. the rare gases, H_2O, NH_3, hydrogen halides) cannot bind an additional electron, because the EA is exceedingly small if not zero. Conversely, solids or liquids consisting of these constituents are known to strongly bind excess electrons (e.g., up to 1.5 eV below the vacuum level for bulk H_2O), indicating a positive EA in the condensed state. These so called solvated (or hydrated) electrons (see Sec. 4.3.3) constitute self-trapped localized electrons in a potential created by the polarization of the surrounding polar molecules leading to large intermolecular configurational changes [65]. In case of clusters consisting of these constituents a transition has therefore been observed as a function of cluster size from an unbound to a bound level for the additional electron. A series of successful experiments to elucidate this transition has been performed by Haberland [66] and by Echt [56,57] and their coworkers. Fig. 4.5 shows as an example a mass spectrum of D_2O cluster anions obtained with electrons of approximately zero energy. It can be seen that the appearance size of stoichiometric water cluster anions is 12 (n = 11 for ordinary H_2O), whereas non-stoichiometric anions produced via DA (with electrons of higher energy) appear at all cluster sizes. In case of ammonia the observed appearance size of $(NH_3)_n^-$ is n = 36. The existence of these solvated electron states in clusters has been theoretically attributed to either interior or surface states depending on the system and size considered [68-70].

In the next paragraph the kinetics of the production by free electron attachment processes of cluster anions belonging to these categories will be described. It should be mentioned how-

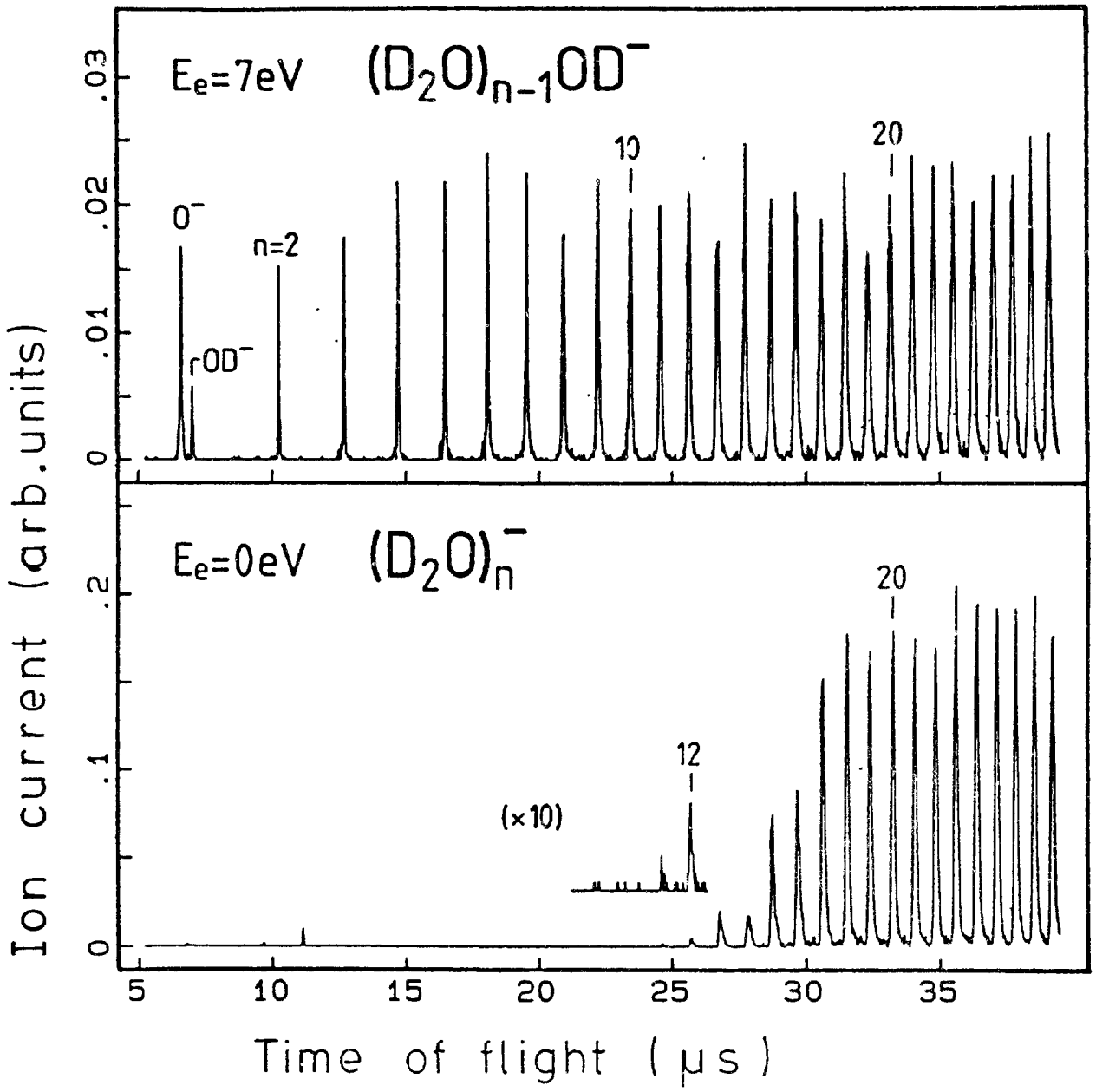

Fig. 4.5 Mass spectra of water cluster anions obtained with 7 eV (upper part) and appr. 0 eV (lower part) incident electrons after Knapp et al. [67].

ever, that there exist in addition several studies involving bound electron capture by clusters, including charge transfer from fast alkali beams to hydrogen halides, $(Cl_2)_n$, $(SO_2)_n$, $(NO_2)_n$, $(CO_2)_2$ and $(H_2S)_n$ clusters [71], and capture of bound electrons from high Rydberg atoms by NO, CO_2, N_2O, SF_6, OCS, CS_2, CH_3CN, C_5H_5N clusters [72] including those studies using Rydberg atoms in well defined nl states [73]. Moreover, during the past ten years

photoelectron spectroscopy, photodissociation and reactions of negative ions have proven to be powerful means of establishing some of the properties of cluster anions including, not only van der Waals [74,76], but also valence [75,77] and metal [78,79] cluster anions.

4.4.2 ELECTRON ATTACHMENT CROSS SECTIONS

Up to now, five groups (Oak Ridge [54], Innsbruck [53,58,59,64], Konstanz [55,56,61,67], Novosibirsk [57] and Berlin [60]) have studied the attachment of free electrons to clusters as a function of electron energy, including O_2, CO_2, H_2O, N_2O, SO_2, SF_6, CF_4, C_2F_4, C_2F_6, CF_6Cl, C_2F_3Cl and $C_2F_4Cl_2$ clusters. In all of these experiments, electrons from an electron gun are attached to a beam of neutral clusters produced by supersonic expansion through a nozzle. Due to the statistical nature of the condensing process in such a nozzle expansion a broad distribution of neutral cluster sizes is generated. Therefore it has not been possible - at least for anions [80] - to determine absolute attachment cross sections for specific cluster sizes. Moreover, relative attachment cross sections reported for a specific cluster anion are always the result of the interaction of electrons with a distribution of neutral cluster sizes. Nevertheless, mass spectrometric studies concerning the dependence of measured ion abundances on size and electron energy yield valuable information on (i) ion stability (magic numbers), on (ii) overall ion production efficiency (mean effective total cross section), and (iii) size dependent structure in attachment cross section functions (resonances).

1. Ion stability (size distribution, magic numbers, autodetachment)

If vdW clusters are formed by a mild supersonic expansion the measured size distribution of cations (produced by electron impact ionization) is found to be in general quasi-exponential [81]. Superimposed on this general trend are local abundance anomalies called magic numbers, which are attributed to the intrinsic stability of specific cluster ion sizes [80]. Size distributions of cluster anions are completely different from cation spectra in most cases investigated so far. Fig. 4.6 shows a comparison of mass spectra of (a) $(O_2)_n^+$, produced by electron impact ionization with 100 eV electrons and (b) $(O_2)_n^-$, produced by attachment of electrons with approximately 0 eV. It can be seen that the same neutral distribution leads for instance via electron impact ionization to a strong signal for $(O_2)_{24}^+$ and $(O_2)_{25}^+$ and via electron attachment to strong minima for

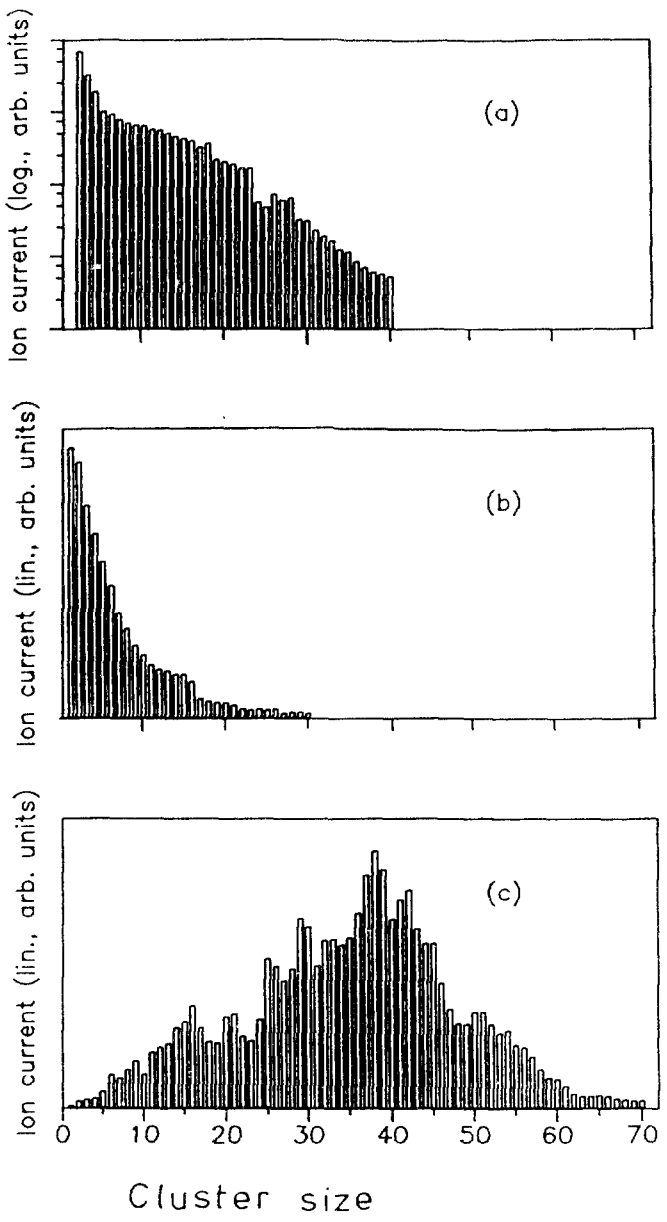

Fig. 4.6 (a) Positive mass spectrum of an $(O_2)_n$ beam (100 eV electrons. (b) Negative mass spectrum of an $(O_2)_n$ beam at early times after ion production (appr. 0 eV electrons). (c) Negative mass spectrum of an $(O_2)_n$ beam at late times after ion production (appr. 0 eV electrons) after Walder et al [53].

$(O_2)_{22}^-$ and $(O_2)_{23}^-$. Moreover, the two negative-ion spectra recorded at different times after ion production ((b) and (c) in Fig. 4.6), exhibit completely different overall shapes of distribution. Whereas the spectrum at early times (b) shows a general decreasing abundance with cluster size, the spectrum at later times (c) is strongly depleted at small cluster sizes. This depletion is believed to be due to autodetachment [53]. The strong dependence of the depletion on cluster size (i.e. increasing depletion with decreasing cluster size) implies shorter lifetimes for smaller cluster ions. This is in accordance with observations in case of polyatomic molecules [20], where the reported autodetachment lifetimes increase with complexity (i.e., with the number of vibrational degrees of freedom).

2. Mean effective total attachment cross sections

Vostrikov et al. [57] reported the determination of an absolute effective total attachment cross sections for H_2O clusters of average size 900, N_2O clusters of average size 350, and CO_2 clusters of average size 1100. These effective total cross sections (total cross section divided by cluster size) are shown in Fig. 4.7. From these data (whose accuracy is not known) follows that the effective attachment cross sections for clusters (in the size of several 100) are much larger (reaching for very low electron energies values larger than the geometrical cross section) than that of the monomer, which is in contrast to observations in the case of positive cluster ion production [82]. These large cross sections reported by Vostrikov et al. [57] are in accordance with quantitative observations by Echt and coworkers [83], who reported that attachment of low energy electrons to large O_2 clusters is at least as efficient as positive electron impact ionization with 30 eV electrons. Moreover, the direct comparison of the total ion yield for anions and cations for large H_2 and N_2 clusters at one electron energy (44 eV) shows a strong almost linear dependence of the cross section ratio on averaged cluster [84].

3. Size dependence and structure of relative partial attachment cross section functions

Low energy electron attachment to the O_2 monomer yields O^- as the only observable product ion via DA

$$\text{i.e., } O_2\left(X^3\Sigma_g^-\right) + e \rightarrow O_2^{-*}\left(^2\Pi_u\right) \rightarrow O^-\left(^2P\right) + O\left(^3P\right) \qquad (4.6)$$

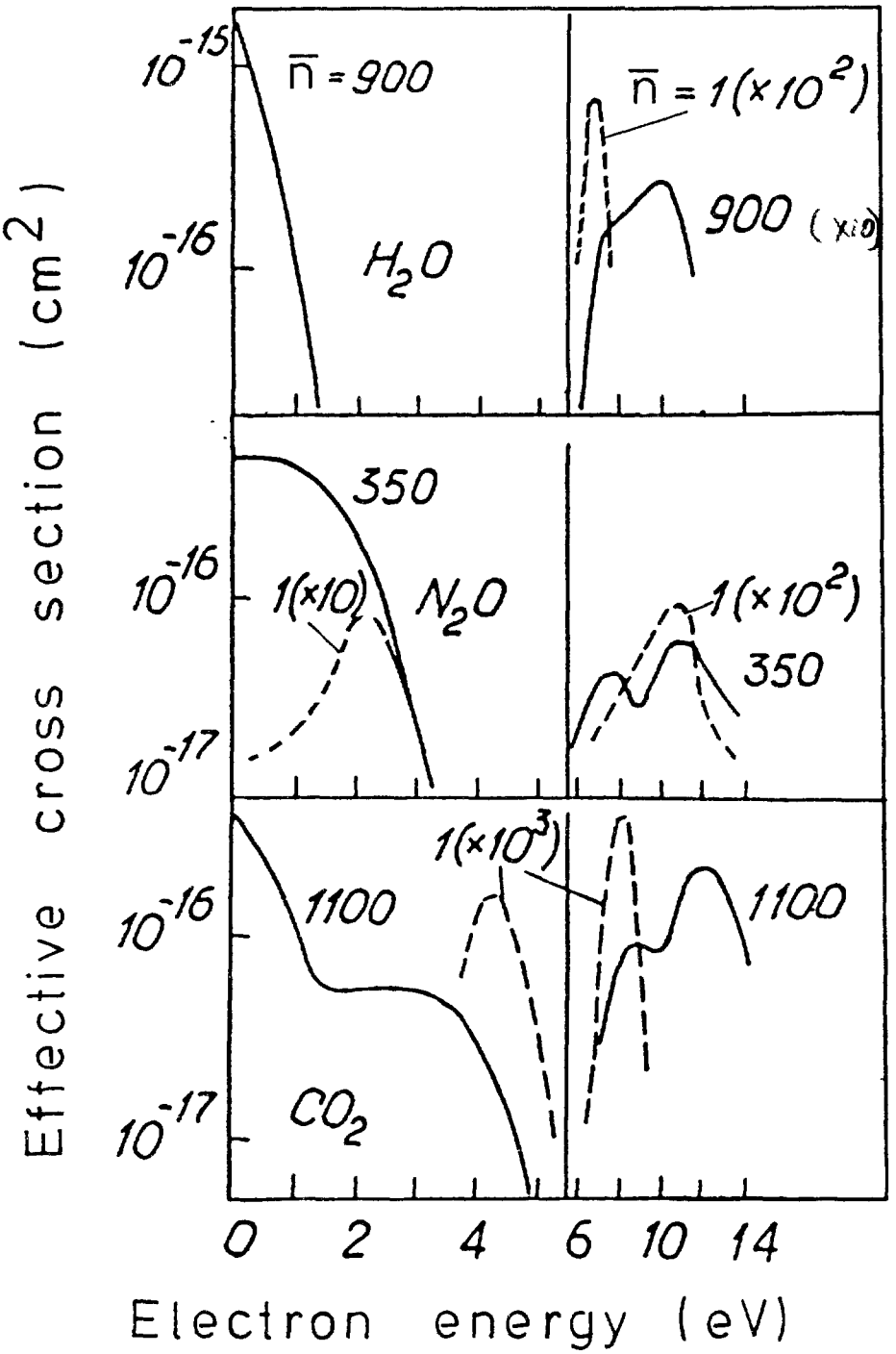

Fig. 4.7 Effective total attachment cross section (total cross section divided by the average cluster size $\bar{n}$) versus electron energy after Vostrikov et al. [57] for H_2O, N_2O and CO_2. Also shown (dashed line) is the total attachment cross section for the respective monomers (multiplied by a factor given in brackets).

The cross section for this process shows a single structureless peak at $\simeq$ 7 eV with an onset at about 4 eV. The same reaction contributes to dissociative electron attachment to clusters yielding $(O_2)_n O^-$ ions, but in this case the cross section arises from contributions (see Fig. 4.8) of both the $^2\Pi_u$ and the $^2\Sigma_u^+$ state of O_2^- producing essentially a broad single peak at near 7 eV and showing a slight solvation shift at the onset. The $^2\Sigma_u^+$ is formed in clusters due to a breakdown of the $\Sigma^- \leftrightarrow \Sigma^+$ selection rule [85,86] which is operative in the single-electron-target frame of reference. Additional structure above the 7 eV peak, not present in the case of the monomer, is attributed essentially to the production of the $^2\Sigma_u^+$ state of O_2^- which is also forbidden by the symmetry rule.

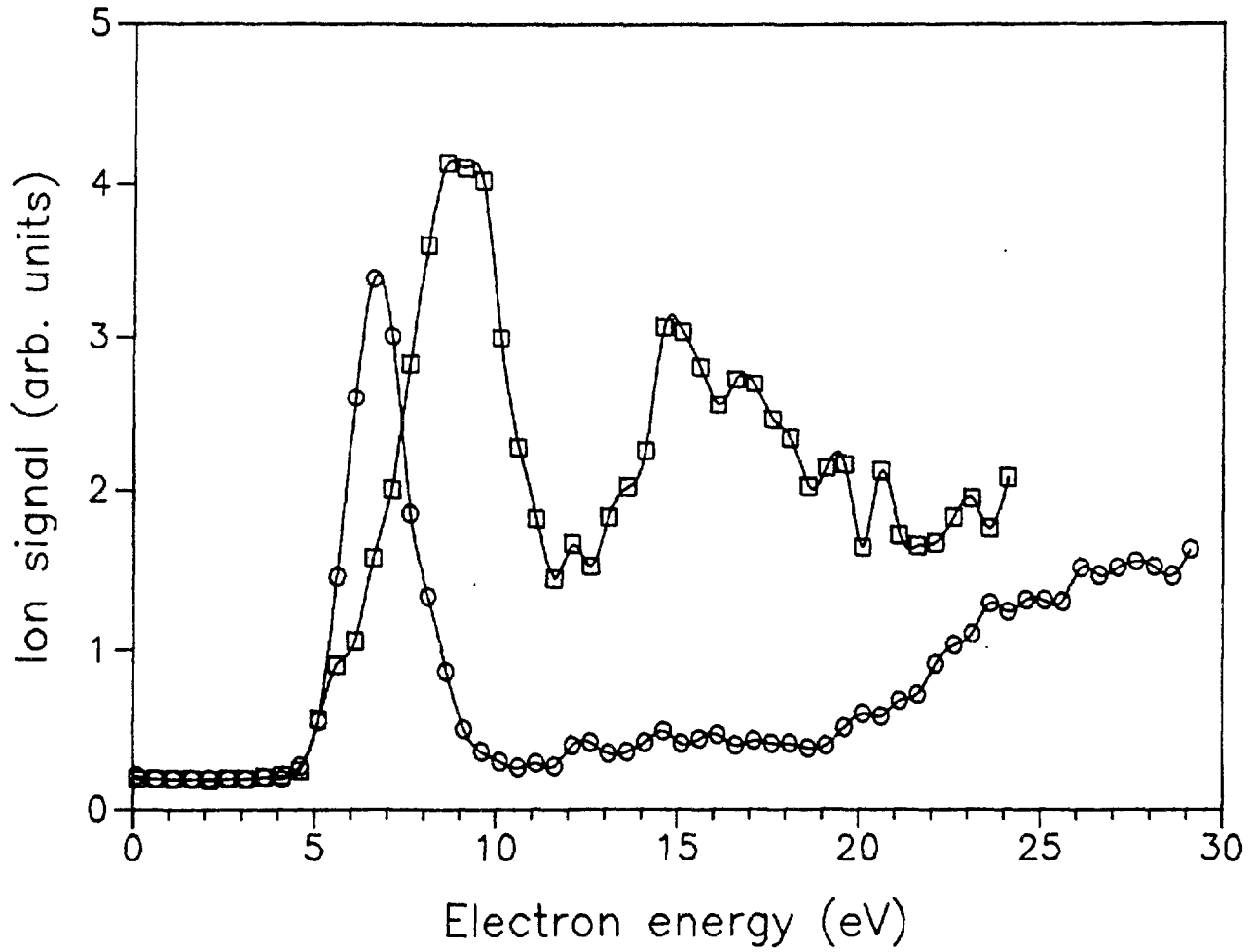

Fig. 4.8 $(O_2)_4O^-$ anion signal (designated by open squares) produced by electron attachment to O_2 clusters as a function of electron energy after Märk et al. [53]. Also shown is the energy dependence of the O^- (designated by open circles) produced via dissociative attachment to O_2 (i.e., reaction (5)).

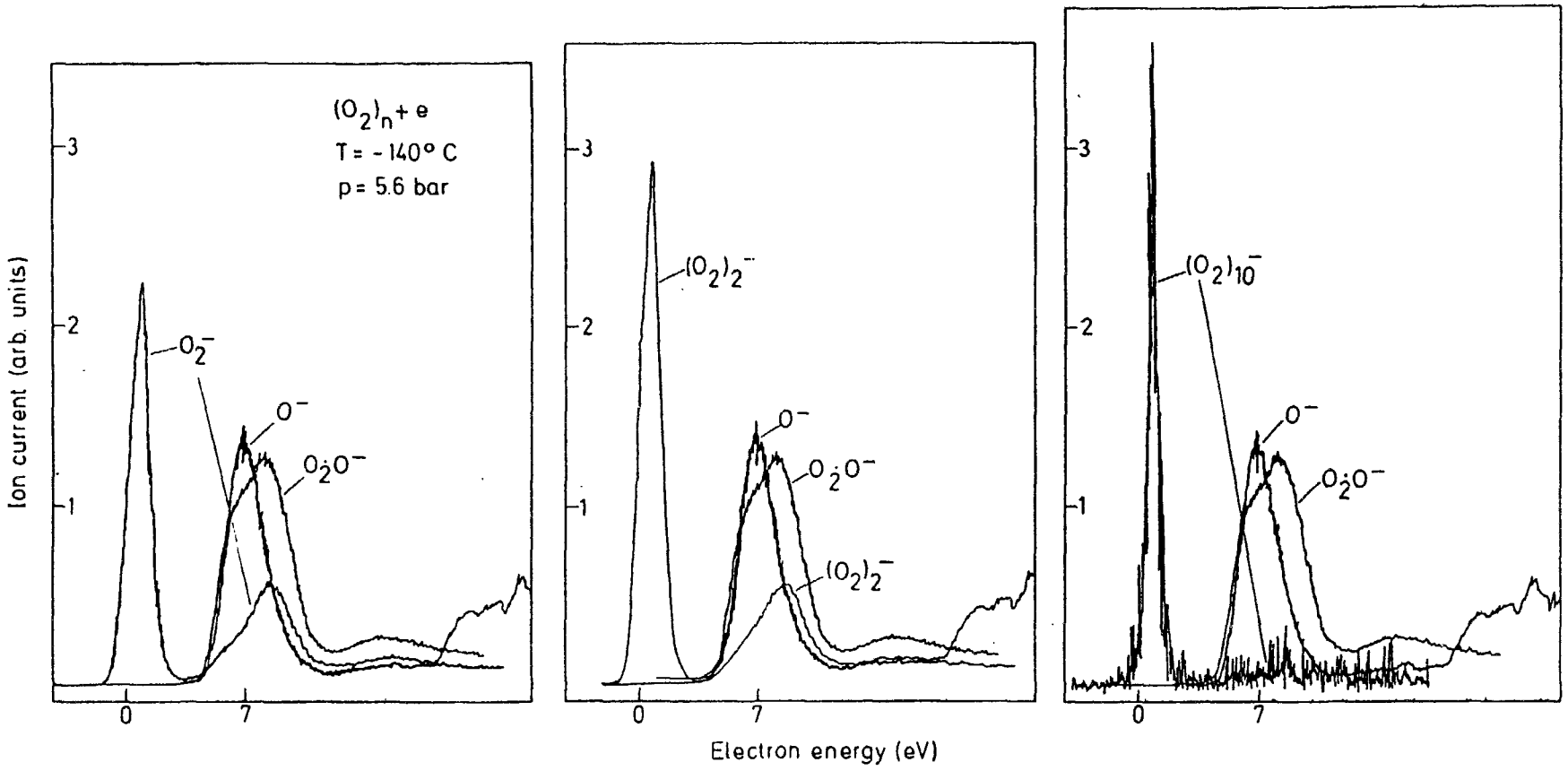

Fig. 4.9 Anion signal produced by electron attachment to O_2 clusters as a function of electron energy after Märk et al. [53] for three different ion sizes. Also shown for comparison the O^- and O_3^- ion yield (see Fig. 8).

In contrast to the monomer, electron attachment to O_2 clusters also yields stoichiometric oxygen cluster anions $(O_2)_n^-$. The respective attachment cross section function (see Fig. 4.9) not only shows a peak at approximately 7 eV (involving the anion states $^2\Pi_u$ and $^2\Sigma_u^+$), but in addition a strong resonance peak close to zero energy. This zero energy resonance peak (which becomes more dominant with increasing cluster size) has been attributed [53] to production via the $X^2\Pi_g$ state with subsequent stabilization by monomer evaporation, in accordance with observations on electron attachment in dense gases [13].

Some of the other systems studied (e.g. CO_2, H_2O, SO_2, SF_6, $C_2F_3Cl_2$) show a similar dependence of the cross section on electron energy and the size of the target. For instance, the production of $(CO_2)_nO^-$ ions is dominated by the same reactions, albeit with significant red shifts due to solvation effects, as the DA in CO_2, i.e. the peak at approximately 4.4 eV due to the first shape resonance ($^2\Pi_u$ state) and at about 8.2 eV due to an electron excited Feshbach resonance ($^2\Sigma_u^+$ state) [54-56,64]. The most remarkable feature for the stoichiometric CO_2 cluster anions is again the appearance of an additional resonance at about zero energy, first discovered by Stamatovic et al. [64]. Very recently, production of $(CO_2)_nO_2^-$ ions and of the other CO_2 cluster anion via the $^2\Phi_g$ anion state has also been observed [87].

As discussed above, free electrons of almost zero energy can be attached to water clusters with high efficiency (see Fig. 4.10). The maximum cross section for the formation of $(D_2O)_n^-$ at approximately zero energy is at least one order of magnitude larger than that for the formation of $(D_2O)_{n-1}DO^-$ at approximately 7 eV (e.g. for n = 20) [67]. The attachment cross section of the hydroxygenated cluster anions is very similar in shape to that obtained by DA to the monomer (Fig. 4.10).

Anion yield functions have been recorded for a number of other type of molecular clusters including those formed with SO_2, SF_6, C_2F_3Cl, $C_2F_4Cl_2$, CF_4, C_2F_4, C_2F_6, CF_6Cl and N_2O [55,56,58-61,88]. The main characteristics of electron attachment in these aggregates has been found to be similar to those described in this section, although in some instances significant differences have been observed. For example, in SO_2 clusters the first resonance is very effi-

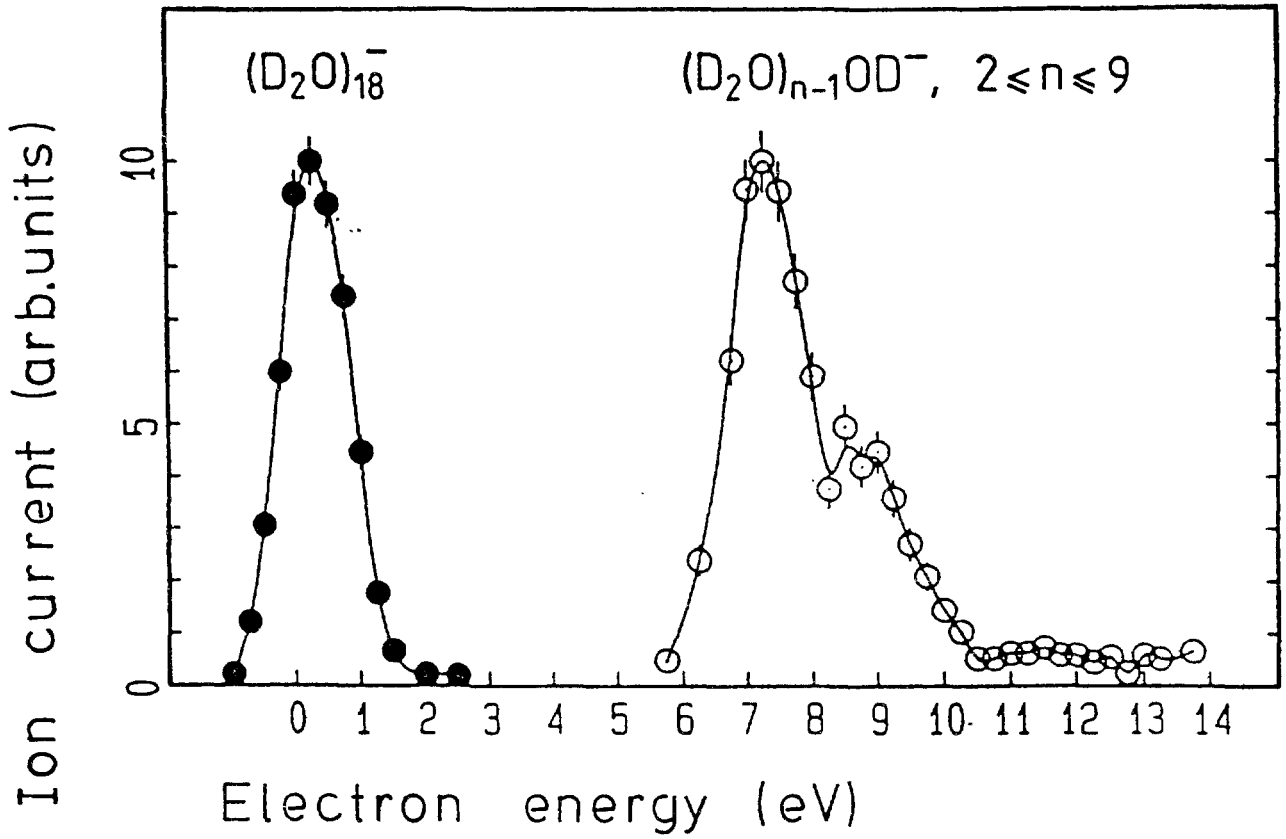

Fig. 4.10 Yield of $(D_2O)_8^-$ and $(D_2O)_{n-1}DO^-$ as a function of electron energy after Knapp et al. [67]. The yield being displaced for the solvated hydroxyl anions is the weighted sum over several cluster sizes between 2 and 9.

ciently quenched in favor of SO_2^- production [58]. This is in contrast to the findings in O_2, CO_2 and H_2O. Further information on the incident electron energy dependence of anion and cluster-anion formation from the above-mentioned molecular systems can be found in the recent review articles by Märk et al and Stamatovic [28] and Oster et al [89].

4.5 ELECTRONS IN SOLIDS

In this section, we describe electron scattering experiments performed with molecular solid films in the energy range 0-20 eV. Some of the results of these experiments are presented in order to illustrate the most important processes related to the action of electrons in condensed media.

Molecular solids are of particular interest in the present context because (1) they often retain many of the properties of their individual component atoms or molecules, making possible comparisons with gas-phase data and (2) many organic molecules, which are the building blocks of the more complex biological molecules, form molecular solids in the condensed state.

Furthermore, the description of slow electron scattering processes in terms of intramolecular resonance mechanisms and potential scattering is an approach which has proven successful to describe the interaction of low energy electrons with molecular solids [90]. With this approach, it has often been possible to explain structures in the energy dependence of an inelastic cross section (or a signal proportional to that cross section) by invoking the formation, at specific energies, of transient anions within the solid or near its surface. Comparison with gas-phase data has been most useful in identifying the resonant states and in investigating the modifications to the characteristics of the isolated transient anion induced by the presence of neighboring targets. Other non-resonant features in the energy dependence of the cross sections could usually be explained by specifying which part of the interaction potential is dominant.

4.5.1 EXPERIMENTS

The interaction of low-energy electrons with rare-gas and molecular solids can be investigated by allowing monoenergetic electrons to impinge on a thin multilayer film grown in an ultra-high-vacuum system by the condensation of gases or organic vapors on a clean metal substrate held at cryogenic temperatures (15-100 K) [90]. The substrate can be either a single crystal or polycrystalline. Depending on the type of apparatus, it is possible to measure the dependence on primary electron energy of the current transmitted through [91], trapped [92] in, or reflected from the film [93,94] or that of the positive ion, [95] negative ion, [96] and neutral species fluxes [97,98] emanating from its surface. As a general rule, the film thickness must be larger than the total electron mean free path in order to minimize effects of the metal substrate. Evidence that a given process occurs within the bulk of the material arises from the presence of multiple scattering effects in the data [99,100]. It can also be provided by specific experiments such as matrix isolation [93,101].

Low-energy electron transmission (LEET) spectra are obtained by measuring, as a function of incident electron energy, the current $I_t(E)$ which after traversing a multilayer film arrives at a metal substrate [91]. In these experiments, I_t and the beam resolution are of the order of a few nA and 0.04 eV, respectively. The absolute electron energy scale is calibrated within ± 0.15 eV with respect to the vacuum level by measuring the onset of electron transmission through the films. When the film is charged by the electron beam, this onset is shifted by ΔV to a higher accelerating potential since the incoming electrons must then possess additional kinetic energy (KE) to overcome the negative potential barrier caused by accumulated charges. Such measurements are usually performed in conjunction with LEET and other multilayer-film experiments to make sure that no significant charge accumulation occurs during the time of the experiment. However, if the film is purposely allowed to charge by an easily measurable potential ΔV, this latter can be related to the trapping cross section by treating the dielectric film as a charged capacitor [92].

Energy losses by electrons scattered within the condensed film can be measured by high resolution electron energy loss (HREEL) spectroscopy [93]. In these experiments, electrons leaving a monochromator are focused on the film and those re-emitted from its surface within narrow cone at another angle are energy analysed by another electron deflector (i.e., the analyser). Depending on the apparatus, it may be possible to vary the angle of incidence θ_i or the analysing angle θ_r (defined from the surface normal) or both. The absolute electron energy scale is calibrated from LEET spectra. HREEL spectra are recorded by sweeping the energy of either the monochromator or the analyser. The energy dependence of the magnitude of a given energy loss event (i.e. the excitation function) is obtained by sweeping the energy of both the monochromator and the analyser with a potential difference between them corresonding to the probed energy loss. HREEL spectra are usually recorded at overall resolutions ranging from 6 to 20 meV with corresponding incident currents lying in the 10^{-10} - 10^{-9}A range [93,102].

A portion of the positive and negative ions produced by electron impact on condensed molecules can be measured by placing a mass spectrometer near the film surface [95,103]. In these electron stimulated desorption (ESD) measurements, ions emerging from the surface are focused by lenses located in front of the entrance of the mass spectrometer. Grids can be inserted

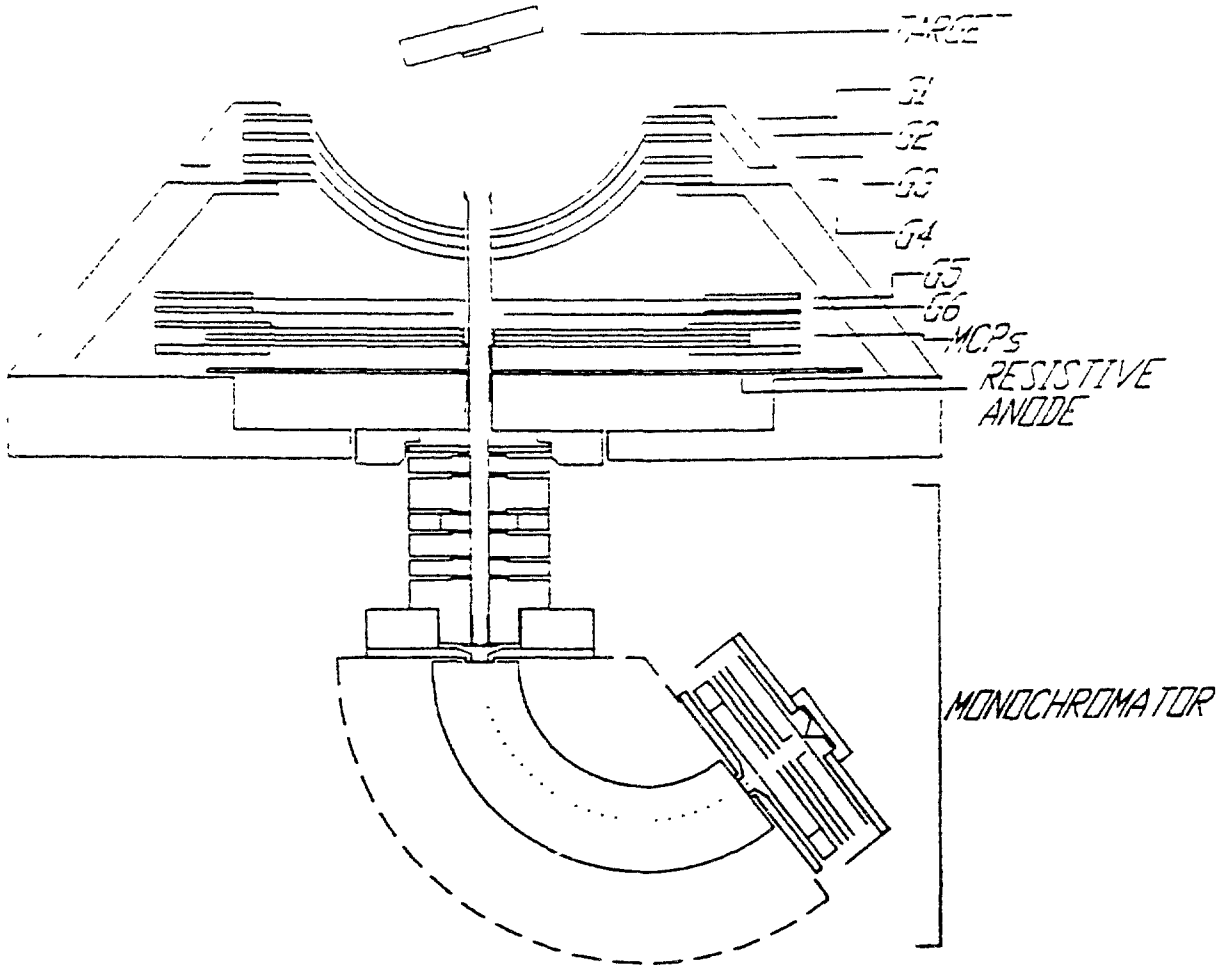

Fig. 4.11 Schematics of the angle-resolved electron stimulated desorption apparatus. The target is tilted by 15° with respect to the incident electron beam. Grids G1 to G6 are used for charge and energy discrimination. The electron energy can be varied from 1 to 30 eV.

between the lenses and the mass spectrometer in order to analyse the ion energies by the retarding potential method. It is also possible to measure the angular distribution of ESD yields of ions and metastable neutrals by combining position sensitive detection with monochromatic electrons as shown in Fig. 4.11. In this apparatus, [97] an electron beam, emanating from an electrostatic monochromator, is incident on a target film. Backscattered electrons and desorbed ions are energy-analyzed by a set of 4 grids (G1-G4) before they enter a field-free region between G4 and G5. They are then accelerated onto an imaging device consisting of a stack of two gold-coated microchannel plates (75 mm diameter detecting area) mounted above a resistive anode. The latter

is coupled to a pulse counting position computer. The image coordinates are digitized, buffered distortion-corrected in real-time and stored in a microcomputer. This storage can be time-discriminated following an incident-electron pulse so as to perform two-dimensional (2-D) time-of-flight (TOF) analysis. This analysis for metastable species and photons is obtained with large positive and negative potentials on grids G2 and G3 respectively, in order to repel all charged particles. With these potentials the space integrated TOF spectra consist of a sharp photon peak followed by other peaks corresponding to metastable species of different energies and/or masses. Allowing positive charges to pass through the grids superimposes the contribution of the positive ions, whereas allowing negatively charged particle to reach the detector superimposes the contribution from electrons and anions. In the negative-charge counting mode, the 2-D image at short time corresponds to electrons and those at longer times to anions. On single crystals the electrons produce sharp diffraction patterns which determine the substrate and film crystalline structure. In this manner, electrons are also space differentiated from photons, metastables and anions. From mass spectrometric ESD data, the electron energy can usually be chosen to produce a unique anion or cation in order to avoid mass ambiguities and determine the ion energies by TOF.

4.5.2 Elastic scattering

The structure in the energy dependence of elastically transmitted or reflected currents of molecular films can be explained by invoking multiple scattering of the electron waves between the potentials of the individual atoms or molecules. Structures in the elastic cross section due to intermolecular interferences of the electron waves are most prominent in elastic reflectivity experiments, since in these both the incident and outgoing electron momenta are measured with a HREEL spectrometer. In well ordered films, the diffraction structure is dominated by long-range order [104] whereas, in amorphous substances, it is due to short-range order. This effect of this latter can be detected in the energy dependence of the elastic reflectivity or elastic scattering cross section [100]. The energy dependence of such a cross section is given by the curve at the top of figure 4.12 (a), obtained from the analysis of elastic reflectivity data of a 30 monolayer (ML) amorphous H_2O film. It exhibits a rise at low energy and two broad structures whose maxima are located at 6 and 14.5 eV. The relative position of these features can be calculated from the experimental values [105] for the structure factor of amorphous ice at 10 K assuming other parameters to be constant.

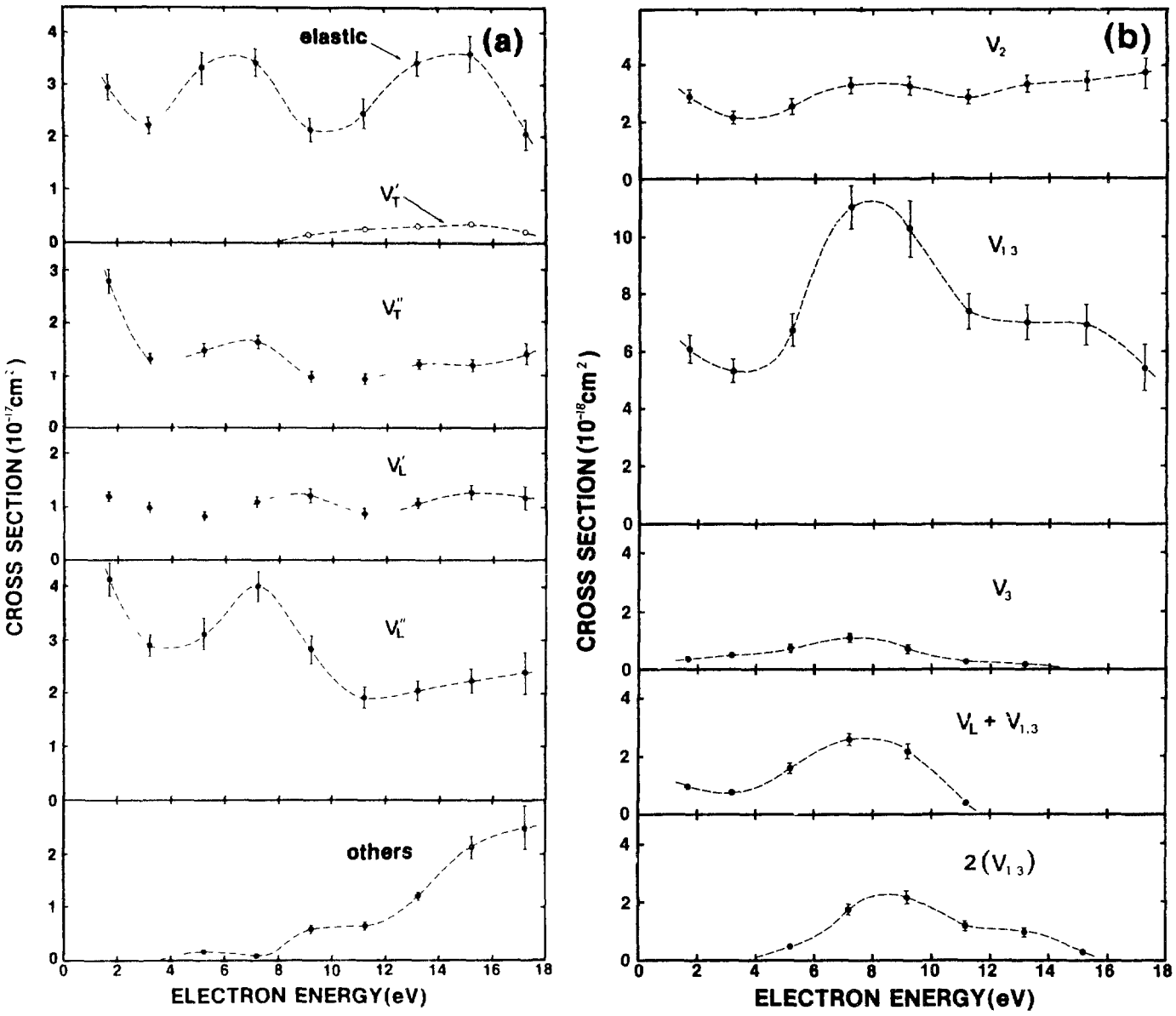

Fig. 4.12 Energy dependence of the elastic and vibrational electron scattering cross sections per scatterer in amorphous ice derived from multiple scattering analysis of energy-loss spectra. The bottom curve in (a) represents the cross section ascribed mainly to the sum of electronic excitations, dissociative attachment and ionization.

LEET spectroscopy is also sensitive to elastic scattering below the energy threshold for electronic excitation, in a region where the transmitted current is purely or vibrationally elastic. However, in transmission only the incident beam has a well defined momentum since electrons which have been scattered into any angle can be measured at the metal substrate. Furthermore, when the film is highly disordered, electrons can be scattered in all possible directions near the surface, so that the

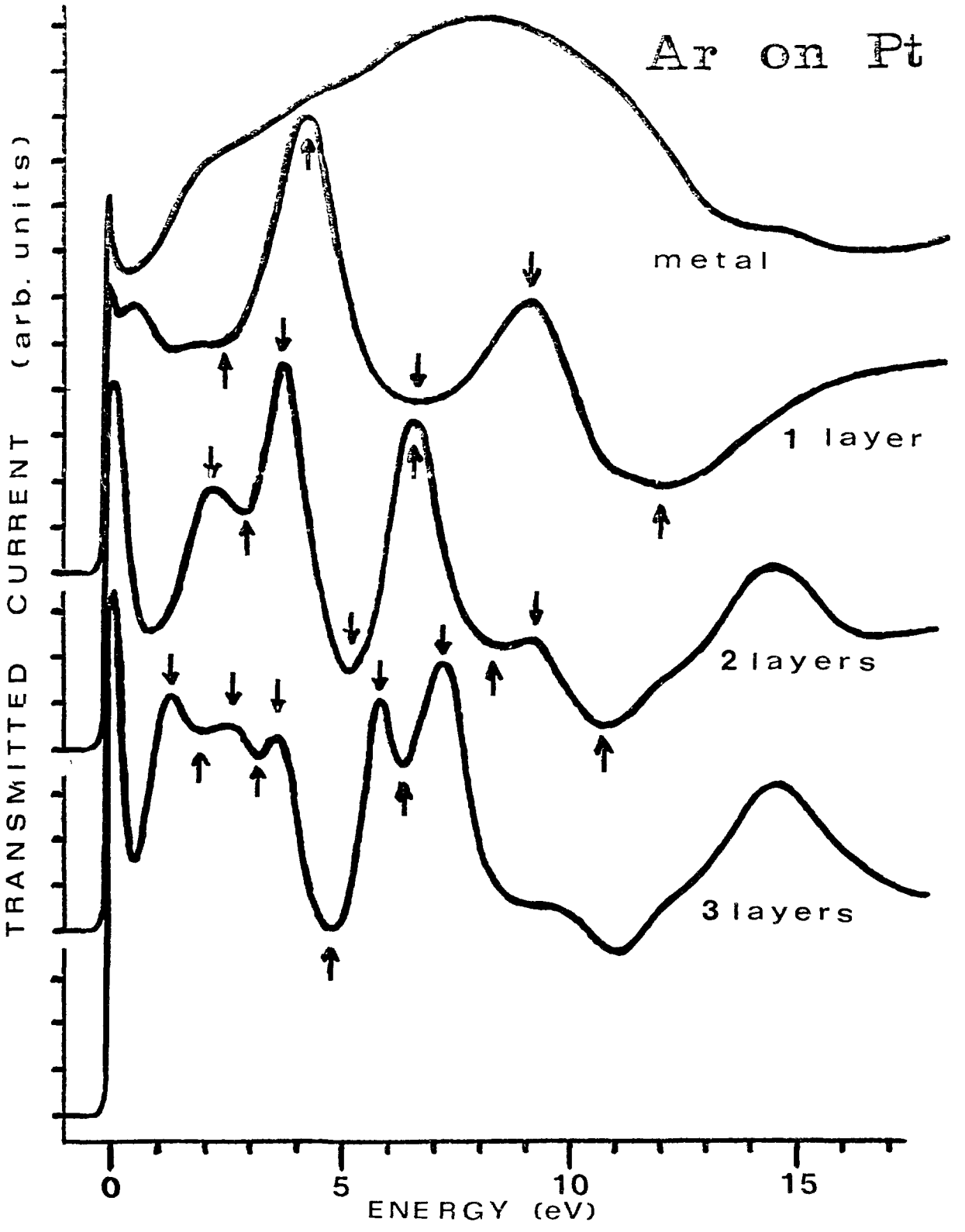

Fig. 4.13 Electron current transmitted through Ar films as a function of electron energy. The film thickness is indicated on the right-hand side of each curve. The arrows indicate the position of structures characteristic of the number of monolayers. The current measured on the clean Pt substrate is shown at the top.

penetrating momentum is also unspecified. So under these conditions, LEET spectra are expected to represent a directionally averaged band structure [106]. This implies that the elastic portion of the transmitted current should be related to the electronic conduction band density of states (DOS) of the condensed material [107,110]. Analysis of the LEET spectra of Ar, Xe, CH_4 films according to the Fermi golden rule has been compared with respective DOS calculations. These comparisons clearly indicate a relationship between elastic LEET currents and the DOS [107,111-118].

For thin well ordered films where scattering by defects is not sufficiently intense to redistribute most electrons in random directions and where energy losses to phonons and intra-molecular vibrations are small, a portion of the penetrating electrons are capable of conserving a specific momentum during their residence in the film. Then, constructive and destructive interference of the electron wave can evolve between the film-vacuum and film-substrate boundaries. This phenomenon, called quantum size effect (QSE), modulates the usual transmission features arising from the bulk DOS [119,120]. This is shown in Fig. 4.13 by the LEET spectra of 1-3 Ar layers deposited on a polycrystalline platinum surface having microfacets with the (lll) orientation. The drastic differences between these curves is due to the dominance of QSE features (shown by the arrows in Fig. 4.13) at low coverages. Similar effects are expected for layered structures located within cells. Coherent scattering of the electron wave within solids and near their surfaces considerably reduces the gas-phase elastic scattering cross sections (e.g. by at least an order of magnitude) [100,112] and renders elastic scattering "thickness dependent" within ordered layers.

4.5.3 Inelastic scattering

By scattering within molecular solids and at their surfaces low-energy electrons can excite with considerable cross sections phonon modes of the lattice [93,100,121,122] and individual vibrational levels of the molecular constituents [93,100,121-131] of the solid. Electronic excitation also occurs but with a much smaller cross section. All types of energy levels can be populated either by potential (i.e., direct) or by resonant scattering depending on the mechanism prevailing at specific energies, but as a general rule resonances have a tendency to dominate the electron-impact vibrational excitation cross sections in molecular solids. However, for solids composed of molecules having a strong dipole moment, direct scattering may be sufficiently strong to excite at all energies, with considerable amplitude, the lowest- energy lattice and molecular vibrational modes [100,131]. Results obtained

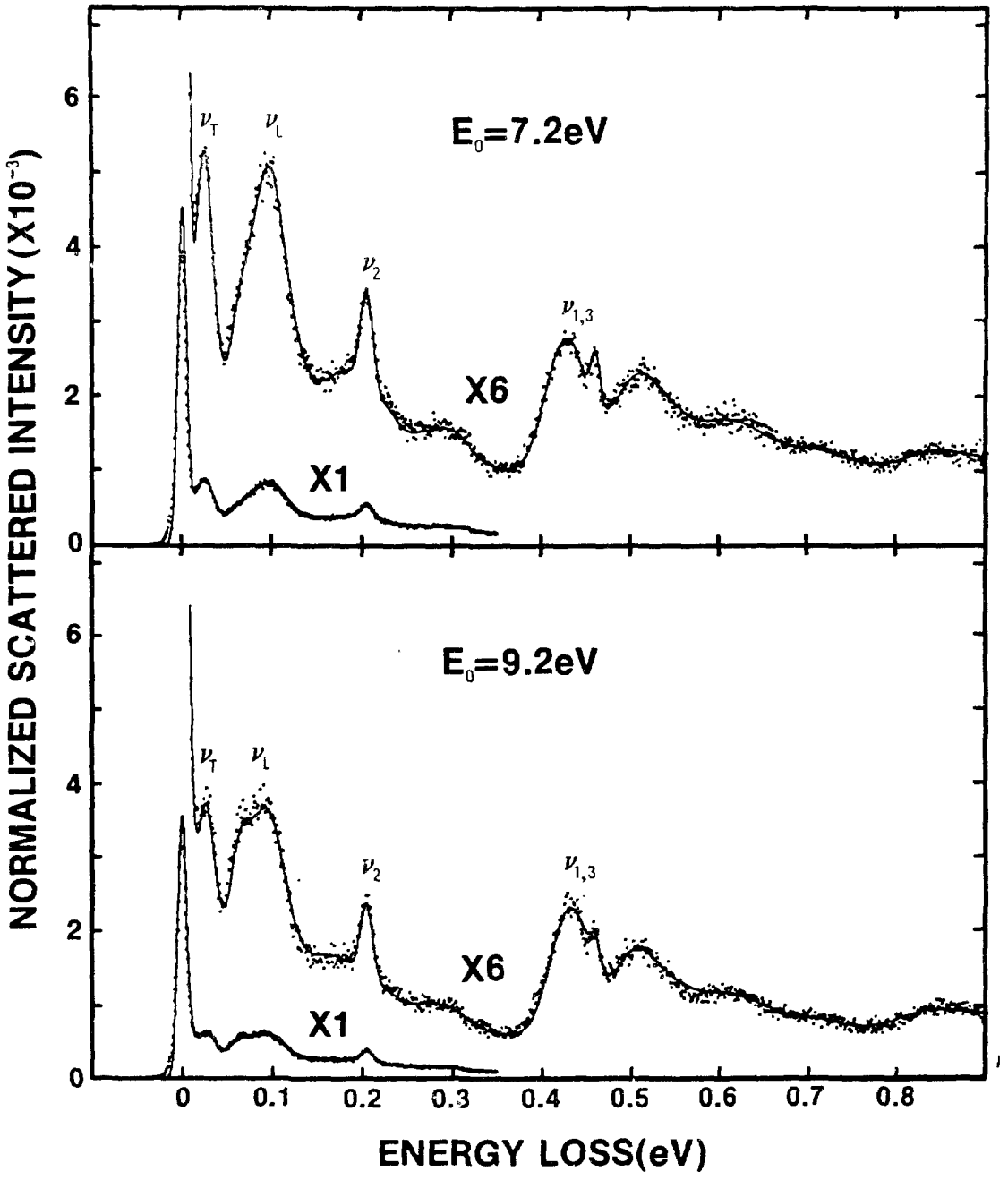

Fig. 4.14 HREEL spectra of a 30-monolayers (ML) ice film recorded at θ_i = 14° and θ_r = 45° (dotted curves). The superimposed continuous curves result from multiple-scattering calculations of the electron backscattered intensities. E_o represents the incident electron energy.

with amorphous H20 films provide a good example of the competition between resonance and dipolar scattering in producing inter- and intra-molecular vibrational excitation [99,100,121,122,131].

HREEL spectra [121] for a 30-ML film of amorphous ice recorded at $\theta_i = 14°$ and $\theta_r = 45°$ and for incident energies of 7.2 and 9.2 eV are shown in Fig. 4.14. These spectra can be compared with infrared and Raman spectra of ice [132]. The major energy-loss peaks are identified as a translational mode (ν_T) at 24 meV, librational modes (ν_L) at 62 and 95 meV, the bending mode (ν_2) at 205 meV and the unresolved stretching modes ($\nu_{1,3}$) at 425 meV. The remaining features along with the background signal are mainly attributed to overlapping and multiple-scattering [132]. In order to extract scattering cross sections per scatterer from such spectra, HREEL spectra recorded at different incident electron energies must be fitted to multiple scattering calculations [99,100,133] based on a

Table 4.3

Total effective $\sigma_{T,eff}$ and total inelastic, $\sigma_{T,i}$ cross section per scatterer (10^{-16} cm^2) with the corresponding $1/\alpha_{eff}$ and $1/\alpha_i$ MFP values (Å) for electron scattering in the low-density amorphous form of ice.

Electron energy (eV)	$\sigma_{T,eff}$	$1/\alpha_{eff}$	$\sigma_{T,i}$	$1/\alpha_i$	Gas[a]
1.2	1.40	22.7	1.06	30.0	0.74
2.2	1.03	30.8	0.77	41.2	0.46
3.2	0.83	38.2	0.61	52.0	0.46
4.2	0.96	33.1	0.65	48.8	0.55
5.2	1.02	31.1	0.68	46.7	0.61
6.2	1.02	31.1	0.70	45.3	0.66
7.2	1.23	25.8	0.88	36.1	0.68
8.2	1.18	26.9	0.89	35.7	0.65
9.2	0.98	32.4	0.75	42.3	0.57
10.2	0.82	38.7	0.60	52.9	
11.2	0.83	38.2	0.56	56.7	
12.2	0.90	35.3	0.59	53.8	
13.2	1.03	30.8	0.66	48.1	
14.2	1.18	26.9	0.76	41.8	
15.2	1.19	26.7	0.80	39.7	
16.2	1.05	30.2	0.77	41.2	
17.2	1.17	27.1	0.94	33.8	
18.2	0.97	32.7	0.82	38.7	
19.2	0.90	35.3	0.81	39.2	

model which takes into account the magnitudes of the relevant cross sections. Such fits [132] are shown by the continuous curves which pass through the experimental points in Fig. 4.14. From these and total reflectivity measurements, the absolute cross sections per scatterer given in Table 4.3 were generated. The cross sections so extracted include intrinsically quantum effects pertaining to a single site as well as those due to the presence of neighboring similar sites. The fit includes an effective (α_{eff}) and inelastic (α_{in}) coefficient of angular anisotropy which allows to evaluate the contribution of forward scattering. The energy dependence of the cross sections for the major energy losses is shown in Fig. 4.12.

The absolute electron scattering cross sections for exciting the translational (ν and ν_T'') and librational (ν_T' and ν_T'') modes of amorphous ice in the 2-18 eV range are shown in Fig. 4.12 (a). The bottom curve labeled "others" represents contributions to the inelastic cross section arising from DA, electronic excitation and ionization. Cross sections for exciting the bending (ν_2) and stretching (ν_1 and ν_3) modes are shown in Fig. 4.12 (b). The latter two are found at two slightly different frequencies giving rise to the curve labeled $\nu_{1,3}$ which represents the cross section for an unresolved peak containing energy-loss contributions from both the symmetric and asymmetric stretching modes. The 2-18 eV behavior of the absolute cross section for exciting the strongest combination mode ($\nu_L + \nu_{1,3}$) and the most intense of the overtones [$2(\nu_{1,3})$] are shown at the bottom of Fig. 4.12 (b). The ν and ν_T'' lattice modes are clearly characterized by a peak around 7 eV having $\simeq$ 2 eV FWHM and a rise at low energy. The $\nu_{1,3}$ modes exhibit a broader ($\simeq$ 4 eV FWHM) feature around 8 eV with a smaller rise at low energy.

In the curves of Fig. 4.12, any increase toward lower energies has been ascribed to direct scattering (i.e., electron-dipole and electron-polarization interaction) which is present throughout the spectra and possibly accounts for the constant portion in the magnitude of the cross sections [100]. Note that no constant portion exists in the cross section shown in the bottom curve of Fig. 4.12 (b). In the absence of a large quadrupole moment, the magnitude of the cross section for overtones can only arises via resonance scattering since the dipolar interaction, which is dominant, can only impart to the molecule one quantum of vibrational energy.

From comparison of the energies and widths of the features of Fig. 4.12 with those found in the gas-phase cross sections the strong enhancement of the amplitude of the $\nu_{1,3}$ mode near 8 eV can be ascribed to the formation of a $^2B_2$ H_2O^- transient anion state whereas the broad peak near 7 eV in the ν_T'' excitation function correlates to a $^2B_1$ anion state [121]. While the excitation of an intramolecular vibrational mode by a resonance process can be inferred from gas-phase mechanisms, the excitation of lattice vibrational modes by the longer-lived $^2B_1$ state requires a new mechanism. Because of the overlapping of electron-molecule interaction potentials in the condensed phase, a transient anion state is also coupled with the nuclear and electronic polarization modes of the surrounding medium. When an electron is localized in the vicinity of an H_2O molecule a force is exerted between the H_2O^- state and the permanent dipoles of the surrounding molecules which pull these latter toward the anion initiating translational and rotational motion. Calculations with a classical harmonic oscillator model [121] indicate that, a resonance whose lifetime is greater than 10^{-14} sec can transfer a significant amount of energy to librational motion by this mechanism, which is also effective in producing translation motion for resonance times of the order or larger than 10^{-13} sec.

Electronic excitation by low energy electrons in multilayer atomic and molecular films condensed on metallic substrates has been investigated by LEET [10,91,106,108,109,118,134-139], HREEL [101,125,130,140] and metastable emission [97] spectroscopy. The inelastic features in LEET spectroscopy usually appear as broad maxima resulting from a convolution of inelastically scattered current distributions created by the much reduced energy of electrons having produced excitons and band-to-band transitions within the film [91,138].

With HREEL spectroscopy sharp energy loss peaks can be observed, when the band-structure dispersion is small as shown in Fig. 14.5 for 16-eV electrons incident on a 15-ML N_2 film [93]. Each peak can be ascribed to a vibrational progression belonging to the electronic states indicated in the figure. These results are representative of electronic excitation in molecular solids induced by slow electrons which has been found to be similar to the gas-phase below the band gap. Above this energy, Rydberg transitions disappear as well as electron resonances associated with such states. Electronic transitions have larger widths and slightly different energies than in the gas-phase. As expected from the strength of the exchange interaction at low energies, spin- forbidden states are prominent below 20

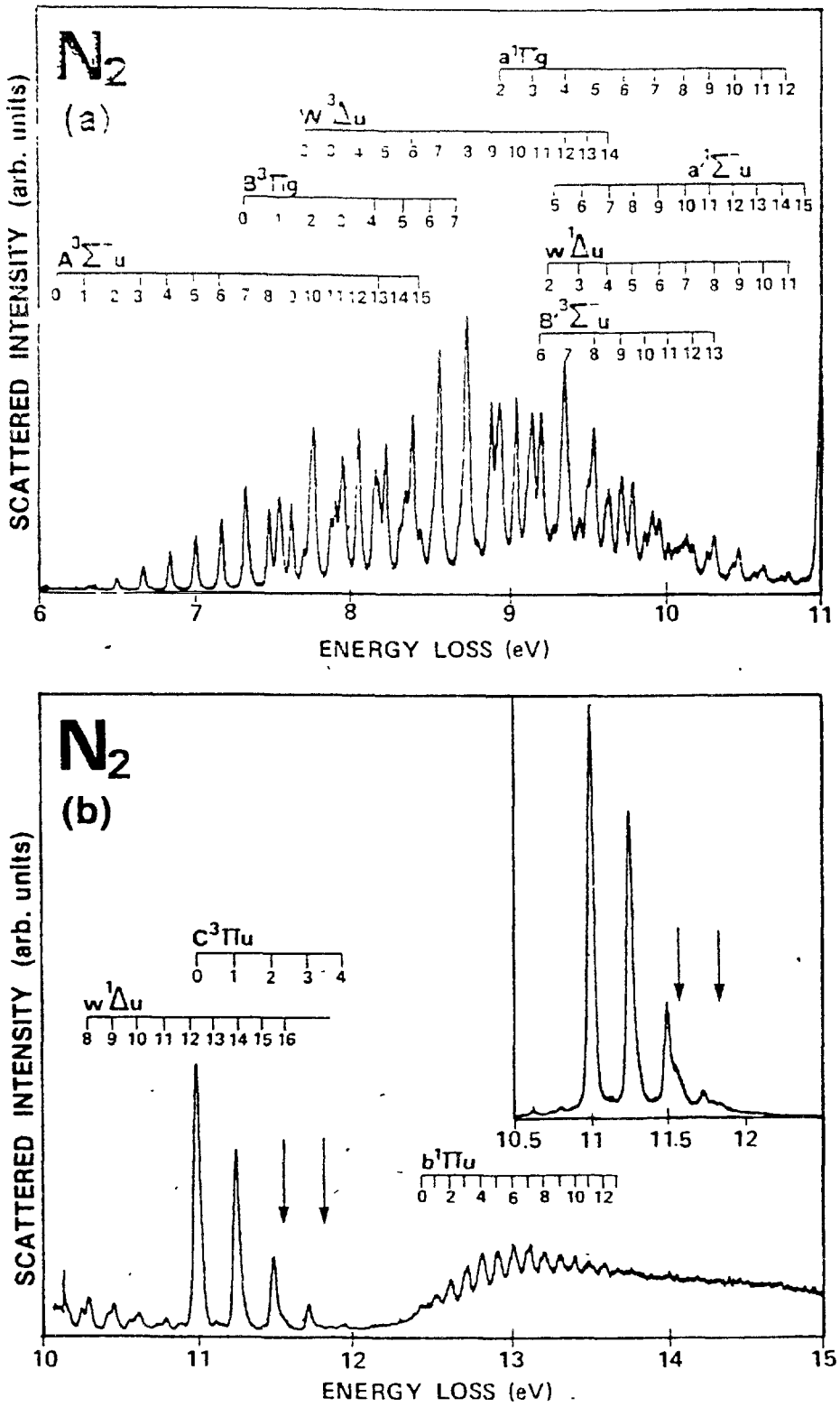

Fig. 4.15 (a) HREEL spectrum of a 50 Å N_2 film condensed on Nb in the range 6-11 eV. The incident energy was 16 eV. (b) HREEL spectrum of N_2 on Nb in the range 10-15 eV. The incident energy was 16 eV. The arrows indicate the position of two weak peaks whose enhanced visibility at 13.5 eV incident energy (inset) is attributed to a resonance.

eV. In fact, below 10.5 eV in Fig. 4.15, the data are qualitatively similar in amplitude and energy to those recorded in gas-phase N_2 at the same primary beam energy. Above 11 eV, in a region where an abundance of Rydberg states appears in the gas phase, we only observe the $B^1\Pi_u$ valence state in solid N_2.

The curves in Fig. 4.16 give an example of the results obtained from the application of the three techniques (LEET, HREEL and metastable) to a thick (>100 ML) multilayer Ar film. The top curve represents the HREEL excitation function for producing the n' = 1 (j = 1/2) exciton of solid Ar. Some of these excited states and of the n = 1 (j = 3/2) states, can convert to $3p^54s$ $^1P_1$ and $^3P_1$ vacuum states of Ar as seen from the ESD results of the middle curve. This latter exhibits the incident electron energy dependence of the yield of metastable argon emitted in vacuum with an average energy of 50 meV. Since higher electronically excited states of the solid are much shorter-lived than the TOF in

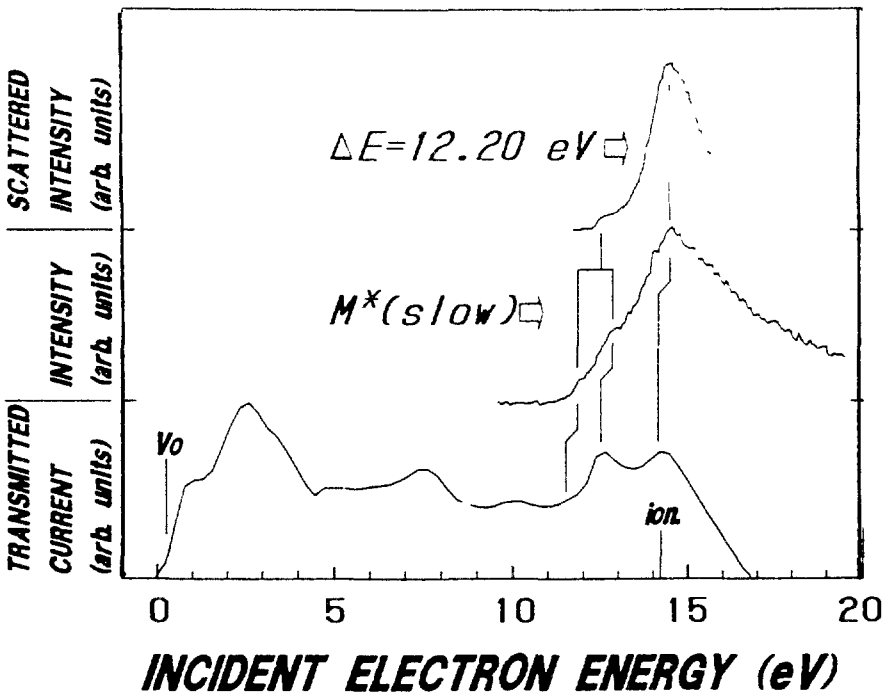

Fig. 4.16 (Top) Excitation function of an energy loss of 12.20 eV. (Middle) Function for metastable Ar production. (Bottom) Electron transmission spectrum. Structures are correlated *via* electron density of states for solid Ar. All three curves were recorded with a multilayer Ar film condensed on Pt.

these measurements, the middle tracing is believed to represent the yield function for the production of the $3p^5 4s$ states of Ar. The structure above 11 eV in the LEET curve at the bottom of Fig. 4.16 represents the excitation function for exciton creation at incident energies close to that of their excitation threshold. The similarity in the line shape of the three different spectra reflects the dependence of exciton production on the joint densities of initial and final states available to the electron before and after the energy loss event, respectively; these densities intervene in the three different measurements. The LEET spectrum and metastable yield were recorded with the apparatus shown in Fig. 4.11; the other curve with a HREEL spectrometer.

4.5.4 MOLECULAR DISSOCIATION

Above a certain energy threshold, electrons impinging on isolated or condensed molecules can cause disruption of internuclear bonds which leads to fragmentation. Depending on the intermediate state involved and charge exchange processes, these fragments can be either neutral, positively, or negatively charged. In molecular film experiments, dissociation products can be measured by the ESD techniques of the types described in 4.5.1. Charged particles observed by ESD are those which possess sufficient KE to overcome the polarization forces they induce in the solid. The other charged particles which are unable to leave the solid can be monitored by measuring the trapping cross section as described in the experimental section.

Anion emergence into vacuum from electron bombarded molecular solids [96,103, 141-149] can proceed via DA and/or dipolar dissociation (DD) (i.e., for a molecule AB, $e + AB \rightarrow AB^* + e \rightarrow A^+ + B^- + e$). This latter process produces a smooth continuous signal which, beyond threshold, increases monotonically with electron energy. The threshold energy for dissociation within the solid corresponds to the dissociation energy of the isolated positive and negative species screened by the polarization induced by the products in the solid. Below the energy threshold for DD, ESD of negative ions can only proceed via DA [96]. This process constitutes a particular channel for the decay of molecular transient anions (Fig. 4.1) formed within molecular solids and near their surfaces and within clusters as explained in section 4.4. Since a given molecular configuration of a transient anion appears at a well-defined energy each peak in the electron-energy dependence of the anion ESD yield identifies the energy of a particular resonant state.

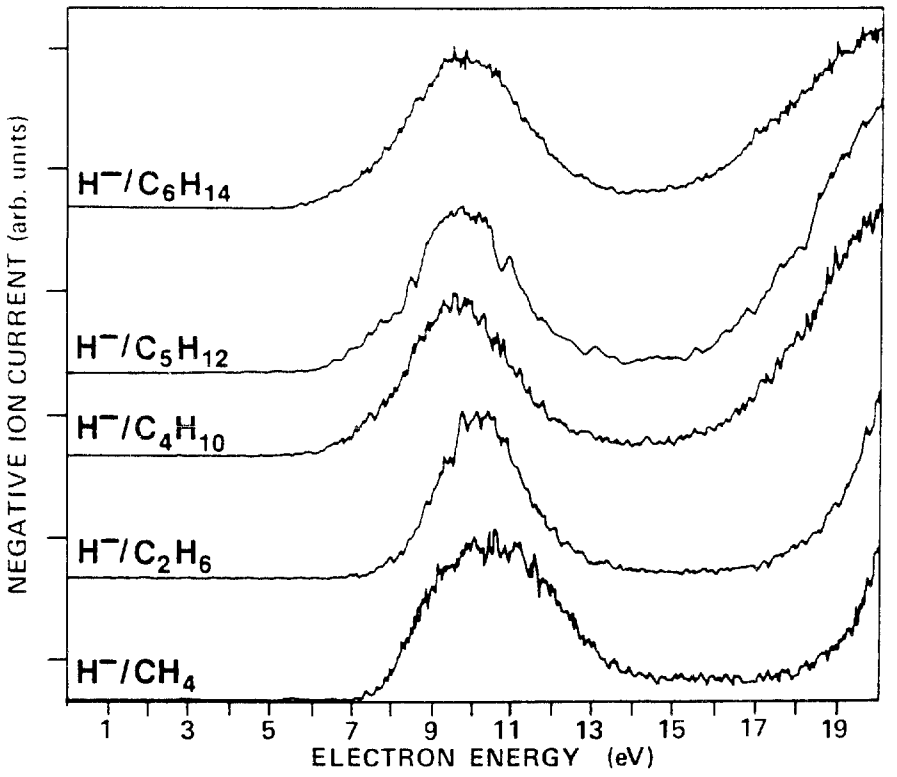

Fig. 4.17 Energy dependence of H^- signal desorbed by electrons impinging on a 6-ML film of C_nH_{2n+2} molecules deposited on a Pt substrate.

Anion ESD by both DA and DD processes is exemplified in Fig. 4.7 by the energy dependence of H^- yields recorded with multilayer films of condensed C_nH_{2n+2} (n = 1,2,4,5,6) molecules [146]. All curves exhibit a single peak, whose maximum is located around 10 eV, and a rise which onsets at higher energy (16-18 eV). This latter is due to DD. The 10-eV peak is caused by the DA reaction

$$e^- + C_nH_{2n+2} \rightarrow (C_nH_{2n+2})^- \rightarrow H^- + C_nH_{2n+1}$$

Similar yield functions are observed for CH_3^-, CH_2^-, and CH^- ions, in order of decreasing intensity [146]. These anions also arise from the decay of transitory $(C_nH_{2n+2})^-$ states. DA features have also been observed in the O^-, C^-, Cl^- and H^- ESD yield functions measured from molecular solids formed by condensing O_2, NO, CO, Cl_2, N_2O, H_2O and hydrocarbon molecules on a metal substrate [103,141-147]. More recently, the anion-complexes $Ar.O^-$, $Ar.Cl^-$ were produced by ESD from Ar matrices containing N_2O and Cl_2, respectively [86]. O^-, $Ar.O^-$, $Kr.O^-$, O_3^- (or $O_2.O^-$) and O_2^- were also produced by ESD from solid rare-gas matrices containing O_2 [86,148]. The ESD yield functions

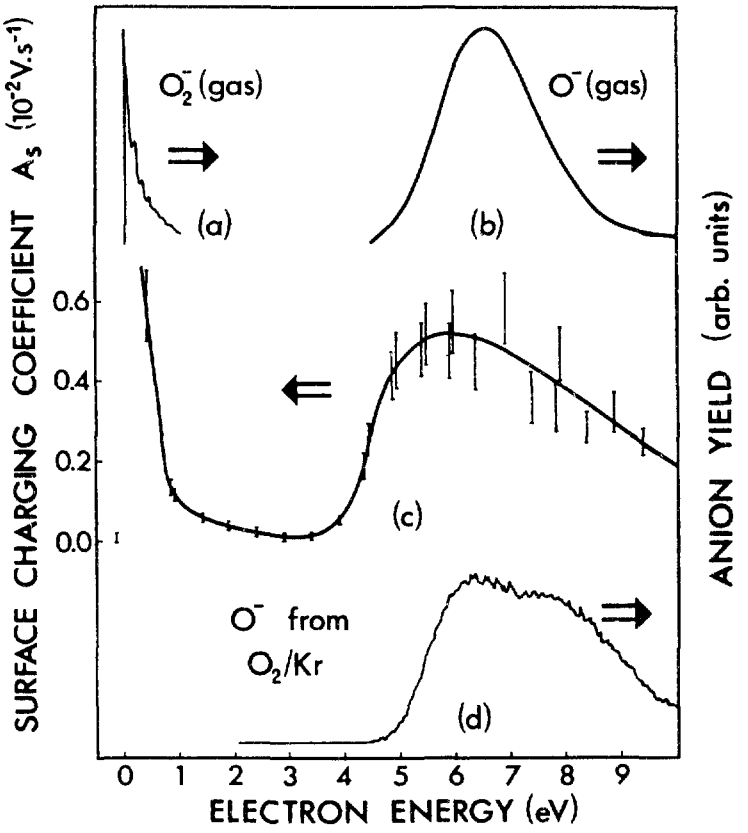

Fig. 4.18 Anion yields produced by 0-10 eV electron impact on (a and b) gaseous O_2 and on (d) a 20-ML Kr film covered with 0.1 ML of O_2. The electron energy dependence of the surface charging coefficient A_s for 0.1 ML O_2 on a 20 ML Kr film is shown in (c).

from O_2 isolated on solid rare-gas surfaces have also been reported [142,145]. The O^- yield function for submonolayer O_2 on a 20 ML Kr film is shown in Fig. 4.18 (d). It results from dissociation of the $^2\Pi_u$ transitory O_2^- state. Many of the DA reactions in the condensed state and particularly those observed in ESD from multilayer films, were found to be similar to the processes found in the cluster experiments described in section 4.4. For example, the ESD results from condensed multilayer O_2 films resembles that shown in Fig. 4.9 for the $O_2.O^-$ and $(O_2)_2^-$ yields above 6 eV and results from the same three O_2^- ionic states.

Analysis of the electron energy dependence of these anion yields revealed that the gas-phase DA mechanism was perturbed in the condensed phase by: multiple electron scattering prior to electron attachment to a molecule; post-dissociation interaction (PDI) of the resulting anion with the solid; and

changes in the symmetry of the single-electron-molecule potential introduced by the presence of neighboring targets. This latter change in symmetry led to the observation of $\Sigma^- \leftrightarrow \Sigma^+$ transitions which are forbidden by electron impact in the gas-phase [85]. In addition, coherent scattering within solids was found to enhance ESD yields [145]. By analyzing the energy distributions of the desorbing anions as a function of incident electron energy, [103,143,144] it has been possible to distinguish between the contribution to the total yield arising directly from DA at a molecular site and the other two portions of the signal which involve multiple scattering and PDI. It was concluded that the lattice was not involved in the dissociation dynamics and that, therefore, the energy and momentum conservation laws of the free molecule could be applied to solid state DA reactions [103,144].

Compared to other types of slow electron beam experiments the energy dependence of cation ESD signals receding from surfaces covered with molecules, does not exhibit appreciable structure [95,149-155]. In general, the signal rises monotonically from threshold to reach a maximum around 70 eV. The dissociating states are usually not dipole allowed and often involve two electron excitations. Near threshold, the parent electronic states correspond to excited states of the neutral rather than those of the ionized configuration. So, dipolar dissociation (DD) is the effective mechanism in this limit. Predissociation and shake-up contribute to the cation yield at higher energies [151].

ESD of neutrals arising from dissociative states has been recorded primarily from species chemisorbed on metal surfaces [98,156] and it is only recently that such measurements have been extended to multilayer molecular films; [97,157] namely, amorphous ice. The 1-30 eV yield function has been recorded for both molecular and atomic hydrogen. The H_2 signal onsets at 6.3 ± 0.3 eV and exhibits two broad peaks at 15 and 28 eV. The effective cross section for H_2 ESD from a 4-ML H_2O film was found to lie within 10^{-18}-10^{-17} cm^2 in the incident energy range 10-30 eV.

4.5.5 Charge trapping

As mentioned in section 4.3.1, LEET measurements near the threshold for electron injection into multilayer films made it possible to obtain absolute values for electron trapping by molecules condensed at the surface of such films. Measuring the dependence on incident electron energy of the trapping cross section disclosed fundamental mechanisms for electron stabilization at the surface of

dielectrics. In many ways, these mechanisms can be related to those responsible for solvation in liquids [158,159] discussed in section 4.3.3 and also to those responsible for charge localization within and at the surface of clusters (sec. 4.4).

The charge trapping measurements are exemplified with the result of Fig. 4.18 (c) for trapping by 0.1 ML of O_2 molecules condensed onto a 20 ML Kr film [160]. This figure shows the electron energy dependence of A_s, a charging coefficient directly proportional to the absolute charge trapping cross section [161]. The results are comparable to the energy dependence of the anion yields derived from O_2 in the gas phase (i.e., a and b). No signal has been reported between 1.2 and 4.5 eV in the gas-phase. The similarity with the gas phase data indicates that the surface charging in the 0-2 eV range is due to vibrational stabilization via the $^2\Pi_g$ O_2^- resonance, i.e.,

$$e^- + O_2\left(X^3\Sigma_g^-\right)/Kr \rightarrow O_2^-\left(^2\Pi_g\right)/Kr;$$

as it also occurs in high pressure gases and clusters. The trapping cross section in the region 4-10 eV is due to DA via the intermediate $^2\Pi_u$ state of O_2^- [160], i.e., Eq. (4.6) sec. 4.4.2.

Since the ESD of O^- from the surface is also known to proceed through this process, the O^- ESD and charging proceed via the same mechanism in this energy region. The small shift in energy between the peaks for the gas-phase, ESD and charge trapping yields is due to the polarization force of the Kr film. The maximum in A_s around 6 eV gives a value of $(2.2 \pm 0.7) \times 10^{-17}$ cm^2 for the trapping cross section. This can be compared with the cross section in the gas phase at 6.7 eV of $(1.3 \pm 0.2) \times 10^{-18}$ [162]. An enhancement of the DA cross section by at least a factor of 17 occurs on the surface. The origin of this enhancement has been explained [161] by invoking the reduction of autoionization of the $^2\Pi_u$ O_2^- state into the A $^3\Sigma_u^+$, $C^3\Delta_u$ and $C^1\Sigma_u^-$ states of O_2 and into the ground state configurations due to the lower energy of the resonance at the Kr surface. According to calculations [161] the change in the internuclear crossing points between the $^2\Pi_u$ and neutral states increases the dissociation probability into the limit $O(^3P) + O^-(^2P)$ by a factor of 21, thus accounting for observations.

The electron trapping cross section per H2O molecule has recently been measured for water cluster deposited on a 20 ML Kr film [163]. The incident electron energy dependence of the cross section follows the trend observed for $(D_2O)_n^-$ and $(D_2O)_{n-1}$ OD^- production from

Table 4.4

Charge trapping cross sections per H_2O molecule μ (10^{-17} cm^2) in H_2O clusters condensed onto a Kr surface as a function of initial incident energy E_O (eV) [163]. Also shown are the total inelastic cross-section per scatterer (μ_{in}) and the cross section per scatterer for inelastic processes other than inter- and intra-molecular excitation in amorphous ice films (μ_{other}) obtained from Michaud and Sanche [100]. Error on the absolute value of cross section μ ± 47% at 0.5 eV incident energy and ±40% elsewhere.

Electron energy (eV)	μ	μ_{in}	μ_{other}
0.4	52.8		
1.0	11.8		
1.8	1.03	8.8	
2.8	0.44	6.5	
3.3	0.44	6.0	
3.9	0.30	6.3	
4.3	0.74	6.6	
4.6	0.21	6.7	
4.9	0.38	6.8	
5.3	0.23	6.8	0.17
5.9	0.30	6.8	0.12
6.5	1.19	7.4	0.07
6.9	0.94	8.3	0.05
7.4	1.30	9.0	0.09
7.5	1.78	9.1	0.12
7.9	0.80	9.1	0.21
8.4	1.43	8.7	0.36
8.9	1.40	7.9	0.53
9.4	3.09	7.1	0.63
9.6	4.74	6.8	0.65
9.9	7.78	6.3	0.68
10.1	9.63	6.1	0.68
10.4	4.72	5.8	0.68
10.6	2.90	5.7	0.67
10.9	3.77	5.6	0.66

Tabulated values for μ_{in} and μ_{other} were interpolated using cubic spline from the values given at other energies [100].

cluster containing $1<n<10$ molecules shown in Fig. 4.10. A sharp rise is observed near 0 eV indicating strong energy losses to vibrational excitation followed by electron trapping. Similar to the data in Fig. 4.10, a maximum is observed near 7 eV due to DA. The cross section for this process is found to be of the order of 10-17 cm^2 which is about the same as the gas-phase value. These electron trapping cross sections per H_2O molecule (m) in clusters are listed in Table 4.4 for incident energies lying between 0.5 and 10.9 eV. Other inelastic cross section in amorphous ice are also shown in the third and fourth column. The values for μ can be compared with those obtained by Vostrikov et al [57] shown in Fig. 4.7. The high cross sections found by these authors at the lowest energies are also reproduced in the 0.5-1.0 eV data shown in Table 4.4.

4.6 CONCLUSION

We have shown that recent advances in electron collision experiments make it possible to obtain reliable information on low-energy electron scattering phenomena in high pressures gases, clusters and solids. Probing these different forms of the condensation states of matter allows abundant information on isolated electron-target interactions to be transferred to the liquid and solid phases. The interaction of a low-energy electron with a molecule is found to be sensitive to the "environment" in the condensed phase (i.e., the production of excited molecules, radicals, anions and cations by low energy electron impact is dependent on the nature of the neighbors surrounding the target molecule). This may render the transfer of information to particular condensed systems more difficult; but on the other hand, this dependence makes it possible to modify the energy deposited at the molecular level by changing the "environment" of a specific target (e.g. at a specific bond along the DNA chain). This control of a relatively large amount of energy within the sequence of energy depositing events offers extremely promising possibilities in radiotherapy; in particular, in the fabrication of site specific drugs that could channel part of the energy flow to vital targets within a cell.

ACKNOWLEDGMENTS

L.S. is indebted to Mrs Francine Lussier for her valuable assistance in the preparation of this chapter. The work was supported by the Medical Research Council of Canada and the IAEA. T.D.M. acknowledges support by the Österreichischer Fonds zur Förderung der wissenschaftlichen Forschung, Wien.

REFERENCES

[1] PIMBLOTT, S M , LAVERNE, J A , MOZUMDER, A , GREEN, N J B , J Phys Chem **94** (1990) 488

[2] MOTT, N F , MASSEY, H S W , The Theory of Atomic Collisions, Clarendon, Oxford (1965)

[3] TAKAYANAGI, K , Prog Theor Phys Suppl Japan **40** (1967) 216-48

[4] For a review on electron resonances in gases see ALLAN, M , J Electron Spectrosc Relat Phenom **48** (1989) 219-351

[5] GERBER, A , HERZENBERG, A , Phys Rev **B31** (1985) 6219-27

[6] DAVENPORT, J W , HO, W , SCHRIEFFER, J R , Phys Rev B **17** (1978) 3115-27

[7] SHINSAKA, K , HATANO, Y , "Non-Equilibrium Effects in Ion and Electron Transport", ed E E Kunhardt, R Van Brunt, J Gallagher, and D Hudson, Plenum (1990) 275, SHINSAKA, K , HATANO, Y , Nucl Instr Methods, **A327** (1993) 7

[8] HOLROYD, R A , SCHMIDT, W F , Annu Rev Phys Chem **40** (1989) 439

[9] SCHMIDT, W F , IEEE Trans Electr Insul **19** (1988) 389

[10] MARSOLAIS, R M , SANCHE L , Phys. Rev **B38** (1988) 1118

[11] FREEMAN, G R , "Kinetics on Nonhomogeneous Processes", ed G R Freeman,Wiley (1987) 19

[12] HOLROYD, R A , "Radiation Chemistry", ed Farhataziz and M A J Rodgers, VCH Publ (1987) 201

[13] HATANO, Y "Electronic and Atomic Collisions", ed D C Lorents, W E Meyerhof, and J R Peterson, Elsevier (1986) 153

[14] JOHNSEN, R , LEE, H S , "Swsarm Studies and Inelastic Electron-Molecule Collisions", ed L C Pitchford, B V McKoy, A Chutjian, and S Trajmar, Springer-Verlag (1985) 23

[15] MORGAN, W L , ibid 43

[16] CHRISTOPOROU, L G and SIOMOS, K , "Electron-Molecule Interactions and Their Applications", ed L G Christophorou, Academic Press (1984), Vol 2, 221

[17] WARMAN, J M , "The Study of Fast Processes and Transient Species by Electron Pulse Radiolysis", ed J H Baxendale and F Busi, D Reidel Pub Co (1982) 433

[18] FREEMAN, G R , "Electron and Ion Swarms", ed L G Christophorou, Pergamon Press (1981) 93

[19] HATANO, Y , SHIMAMORI, H , ibid 103

[20] CHRISTOPHOROU, L G , McCORKLE, D L , CHRISTODOULIDES, A A , "Electron-Molecule Interactions and Their Applications", ed L G Christophorou, Academic Press (1984), Vol 1, 477

[21] CHRISTOPHOROU, L G , HUNTER, S R , "Swarms of Ions and Electrons in Gases", ed W Lindinger, T D Mark and F Howorka, Springer-Verlag (1984) 241

[22] MOTHES, K G , SCHULTES, E , SCHINDLER, R N , J Phys Chem **76** (1972) 3758

[23] HEGERBERG, R , CROMPTON, R W , Aust J Phys **36** (1983) 831

[24] WENTWORTH, W E , STEELHAMMER, J C , Adv Chem Ser **82** (1968) 75

[25] BIONDI, M A , Adv Elect Electron Phys **16** (1963) 67

[26] HATANO, Y , Radiat Phys Chem **34** (1989) 675, HATANO, Y , "Pulse Radiolysis", ed Y Tabata, CRC Press, Boca Raton (1991) 199

[27] MARK, T D , LEITER, K , RITTER, W , STAMATOVIC, A , Phys Rev Lett **55** (1985) 2559

[28] MARK, T D , CASTLEMAN, A W Jr , Adv Atom Mol Phys **20** (1983) 65, MARK, T D , Int J Mass Spectrom Ion Proc **79** (1987) 1, STAMATOVIC, A , "Electronic and Atomic Collisions" ed , H B Gilbody, W R Newell, F H Read and A C H North-Holland (1988) 729

[29] SENNHAUSER, E S , ARMSTRONG, D A , WARMAN, J M , Radiat Phys Chem **15** (1980) 479

[30] TEZUKA, T , NAMBA, H , NAKAMURA, Y , CHIBA, M , SHINSAKA, D , HATANO, Y , Radiat Phys Chem **21** (1983) 197
[31] NAKAMURA, Y , SHINSAKA, K , HATANO, Y , J Chem Phys **78** (1983) 5820
[32] SHINSAKA, K , CODAMA, M , SRITHANRATANA, T , YAMAMOTO, M , HATANO, Y , ibid **88** (1988) 7529
[33] SHINSAKA, K , CODAMA, M , NAKAMURA, Y , SERIZAWA, K , HATANO, Y , Radiat Phys Chem **34** (1989) 519
[34] WARMAN, J M , J Phys Chem **87** (1983) 4353
[35] TACHIYA, M , J Chem Phys **84** (1986) 6178
[36] TACHIYA, M , ibid **87** (1987) 4108
[37] TACHIYA, M , ibid **87** (1987) 4622
[38] MORGAN, W L , ibid **84** (1986) 2298
[39] LOPEZ-QUINTELA, M A , BUJAN-NUNES, M C , PEREZ-MOURE, J C , ibid **88** (1988) 7478
[40] KANEKO, K , USAMI, Y , KITAHARA, K , ibid **89** (1988) 6420
[41] SCEATS, M G , ibid **90** (1989) 2666
[42] MOZUMDER, A , ibid **92** (1990) 1015
[43] Colloque Weyl VI, J Phys Chem **88** (1984) 3699
[44] HART, E J , ANBER, M "The Hydrated Electron", Wiley-Interscience (1970)
[45] FENG, D , KEVAN, L , Chem Rev **80** (1980) 1
[46] DORFMAN, L M , JOU, F Y , "Electrons in Fluids", ed J Jortner and N R Kestner, Springer Verlag (1973) 447
[47] MIGUS, A , GAUDUEL, Y , MARTIN, J L , ANTONETTI, A , Phys Rev Lett **58** (1987) 1559
[48] LONG, F H , LU, H , SHI, X , EISENTHAL, K B , Chem Phys Lett **169** (1990) 165
[49] KESTNER, N R , JORTNER, J , J Phys Chem **88** (1984) 3818
[50] RAO, B K , KESTNER, N R , J Chem Phys **80** (1984) 1587
[51] FUNABASHI, K , Adv Radiat Chem **4** (1974) 103
[52] KEVAN, L , Adv Radiat Chem **4** (1974) 181
[53] MARK, T D , LEITER, K , RITTER, W , STAMATOVIC, A , Int J Mass Spectrom Ion Phys **74** (1986) 265, LEITER, K , RITTER, W , STAMATOVIC, A , MARK, T D , Int J Mass Spectrom Ion Proc **68** (1986) 341, WALDER, G , MARGREITER, D , WINKLER, C , STAMATOVIC, A , HERMAN, Z , MARK, T D , J Chem Soc Faraday Trans **86** (1990) 2395, WALDER, G , MARGREITER, D , WINKLER, C , STAMATOVIC, A , HERMAN, Z , FOLTIN, M , MARK, T D , Z Phys D (1990) in print
[54] KLOTS, C E , COMPTON, R N , J Chem Phys **69** (1978) 1636, 1644, Chem Phys Lett **73** (1980) 589, KLOTS, C E , Radiat Chem **20** (1982) 51
[55] KNAPP, M , KREISLE, D , ECHT, O , SATTLER, K , RECKNAGEL, E , Surf Science **156** (1985) 313, KNAPP, M , ECHT, O , KREISLE, D , MARK, T D , RECKNAGEL, E , Chem Phys Lett **126** (1986) 225
[56] KNAPP, M , ECHT, O , KREISLE, D , MARK, T D , RECKNAGEL, E , Phys Chem Small Clusters, ed M Jena, S K Rao, and S N Khanna, Plenum, New York (1987) 693
[57] VOSTRIKOV, A A , DUBOV, D Y , PREDTECHENSKIY, M R , Proc 15th ICPEAC, Brighton (1987) 893, REBROV, A K , VOSTRIKOV, A A , DUBOV, D Y , PRED-TECHENSKIY, M R , Proc XIth Int Symp Mol Beams, Edinburgh (1987) and references therein
[58] MARK, T D , SCHEIER, P , STAMATOVIC, A , Chem Phys Lett **136** (1987) 177, STAMATOVIC, A , SCHEIER, P , MARK, T D , Z Phys D **6** (1987) 351
[59] MARK, T D , STAMATOVIC, A , SCHEIER, P , Z Phys D **12** (1989) 303, STAMATOVIC, A , SCHEIER, P , MARK, T D , J Chem Phys **88** (1988) 6884

[60] HASHEMI, R, KOHN, A, ILLENBERGER, E, Int J Mass Spectrom Ion Proc **100** (1990) in print, KOHN, A, ILLENBERGER, E, J Chem Phys **93** (1990) 357
[61] SCHWARZ, C, Laborbericht, Universitat Konstanz, Fakultat Physik (1987) See Also ECHT, O, KNAPP, M, SCHWARZ, C, RECKNAGEL, E, Proc 20th Jerusalem Symp Large Finite Systems (1987)
[62] COMPTON, R N, REINHARDT, P W, COOPER, C D, J Chem Phys **63** (1975) 381
[63] ROSSI, A R, JORDAN, K D, J Chem Phys **70** (1979) 4422
[64] STAMATOVIC, A, STEPHAN, K, MARK, T D, Int J Mass Spectrom Ion Proc **63** (1985) 37, STAMATOVIC, A, LEITER, K, RITTER, W, STEPHAN, K, MARK, T D, J Chem Phys **83** (1985) 2942
[65] JORTNER, J, Ber Bunsenges, Phys Chem **88** (1984) 188
[66] ARMBRUSTER, M, HABERLAND, H, SCHINDLER, H G, Phys Rev Lett **47** (1981) 323, HABERLAND, H, SCHINDLER, H G, WORSNOP, D R, Ber Bunsenges Phys Chem **88** (1984) 270, HABERLAND, H, RICHTER, T, Z Phys D **10** (1988) 99, HABERLAND, H, KOLAR, T, REINERS, T, Phys Rev Lett **63** (1989) 1219
[67] KNAPP, M, ECHT, O, KREISLE, D, RECKNAGEL, E, J Chem Phys **85** (1986) 636, J Phys Chem **91** (1987) 2601
[68] WALLQVIST, A, THIRUMALAI, D, BERNE, B J, J Chem Phys **86** (1987) 6404
[69] BARNETT, R N, LANDMAN, U, CLEVELAND, C L, KESTNER, N R, JORTNER, J, J Chem Phys **88** (1988) 6670, Chem Phys Lett **148** (1988) 249, BARNETT, R N, LANDMAN, U, CLEVELAND, C L, JORTNER, J, Chem Phys Lett **145** (1988) 382, J Chem Phys **88** (1988) 4421, 4429
[70] STAMPFLI, P, BENNEMANN, K H, Phys Rev Lett **58** (1987) 2635, Phys Rev A **38** (1988) 4431
[71] BOWEN, K H, LIESEGANG, G W, SANDERS, R A, HERSCHBACH, D R, J Phys Chem **87** (1983) 557, QUITEVIS, E L, BOWEN, K H, LIESEGANG, G W, HERSCHBACH, D R, J Phys Chem **87** (1983) 2076, ROSS, U, SCHULZE, T, J Chem Phys **85** (1986) 2664
[72] KONDOW, T, "Electronic and Atomic Collisions", ed D Lorents, W E Meyerhof, and J R Peterson, Elsevier (1986) 517 and references therein
[73] DESFRANCOIS, C, KHELIFA, N, SCHERMANN, J P, J Chem Phys **91** (1989) 5853, KRAFT, T, RUF, M W, HOTOP, H, Z Phys D **14** (1989) 179, D**17** (1990) 37
[74] COE, J V, SNODGRASS, J T, TREIDHOFF, C B, McHUGH, K M, BOWEN, K H, J Chem Phys **83** (1985) 3169, Chem Phys Lett **124** (1986) 274, COE, J V, LEE, G H, EATON, J G, ARNOLD, S T, SARKAS, H W, BOWEN, K H, LUDEWIGT, C, HABERLAND, H, WORSNOP, D R, J Chem Phys **92** (1990) 3980
[75] ALEXANDER, M L, JOHNSON, M A, LEVINGER, N E, LINEBERGER, W C, Phys Rev Lett **57** (1986) 976, POSEY, L A, DE LUCA, M J, JOHNSON, M A, Chem Phys Lett **131** (1986) 170, POSEY, L A, JOHNSON, M A, J Chem Phys **88** (1988) 5383, Chem Phys Lett **152** (1988) 67, DE LUCA, M J, NIU, B, JOHNSON, M A, J Chem Phys **88** (1988) 5857, POSEY, L A, DELUCA, M J, CAMPAGNOLA, P J, JOHNSON, M A, J Phys Chem **93** (1989) 1178, DE LUCA, M J, HAN, C C, JOHNSON, M A, J Chem Phys **93** (1990) 268
[76] SNODGRASS, J T, ROEHE, C M, KOPPEN, P A M, PALKE, W E, BOWERS, M T, J Chem Phys **92** (1990) 5935
[77] BLOOMFIELD, L A, GEUSIC, M G, FREEMAN, R R, BROWN, W L, Chem Phys Lett **121** (1985) 39
[78] FAYET, P, WOSTE, L
[79] ZHENG, L S, BRUCAT, P J, PETTIETTE, C L, YANG, S, SMALLEY, R E, J Chem Phys **83** (1985) 4273, ZHENG, L S, KARNER, C M, BRUCET, P J, YANG, S H, PETTIETTE, C L, CRAYCRAFT, M J, SMALLEY, R E, J Chem Phys **85** (1986) 1681

[80] MARK, T D , ECHT, O , In
[81] ECHT, O , KNAPP, M , RECKNAGEL, E , Z Phys B **53** (1983) 71
[82] HENKES, W , MIKOSCH, F , Int J Mass Spectrom Ion Phys **13** (1974) 151
[83] ECHT, O , In Elemental and Molecular Clusters, ed G Benedek, T P Martin, and G Pacchioni, Springer, Berlin (1988) 279
[84] GSPANN, J , KORTING, K , J Chem Phys **59** (1973) 4726
[85] SAMBE, H , RAMAKER, D E , Chem Phys Lett **139** (1987) 386, Phys Rev A **40** (1989) 3651
[86] SANCHE, L , PARENTEAU, L , CLOUTIER, P , J Chem Phys **91** (1989) 2664
[87] LEZIUS, M , MARK, T D , unpublished results (1990)
[88] ILLENBERGER, E , BAUMGARTEL, H , J Electron Spectr Rel Phenom **33** (1984) 123
[89] OSTER, T , KUHN, A , ILLENBERGER, E , Int J Mass Spectrom Ion Proc **89** (1989) 1
[90] For a review of electron scattering from condensed molecules, see SANCHE, L , J Phys B **23** (1990) 1597
[91] SANCHE, L , J Chem Phys **71** (1979) 4860, SANCHE, L , BADER, G , CARON, L , J Chem Phys **76** (1982) 4016
[92] MARSOLAIS, R M , DESCHENES, M , SANCHE, L , Rev Sci Instr **60** (1989) 2724
[93] SANCHE, L , MICHAUD, M , Phys Rev B **30** (1984) 6078
[94] CLOUTIER, P , SANCHE, L , Rev Sci Instr **60** (1989) 1054
[95] For a review of the data on ESD of cations and the techniques used for measuring positive ion formation by electron impact on molecules or atoms adsorbed or chemisorbed on surface, see TOLK, N H , TRAUM, M M , TULLY, J C , MADEY, T E , In "Desorption Induced by Electronic Transitions", Springer Ser in Chem Phys , Vol 24, Springer-Verlag, New York (1983)
[96] For a review of anions formation by electron impact on condensed molecular solids, see SANCHE, L , In "Desorption Induced by Electronic Transitions Diet III", Springer Ser in Surface Sci , Vol 13, ed R H Stulen, and M L Knotek, Springer-Verlag, Berlin (1988) 78
[97] LECLERC, G , BASS, A D , SANCHE, L , J Electron Phys Rel Phenom , **52** (1990) 725
[98] ALVEY, M D , DRESSER, M J , YATES, J T , Phys Rev Lett **56** (1986) 367
[99] MICHAUD, M , SANCHE, L , Phys Rev A **36** (1987) 4672
[100] MICHAUD, M, SANCHE, L , Phys Rev A **36** (1987) 4684
[101] SANCHE, L , MICHAUD, M , Chem Phys Lett **80** (1981) 184
[102] For a review of surface analysis by high resolution electron energy loss spectroscopy see IBACH, H , and MILLS, D L , "Electron Energy Loss Spectroscopy and Surface Vibrations", Academic, New York (1982)
[103] AZRIA, R , PARENTEAU, L , SANCHE, L , J Chem Phys **87** (1987) 2292
[104] MICHAUD, M , SANCHE, L , GAUBERT, C , BAUDOING, R , Surf Sci **205** (1988) 447
[105] NARTEN, A H , VENKATESH, C G , RICE, S A , J Chem Phys **64** (1976) 1106
[106] BADER, G , PERLUZZO, G , CARON, L G , SANCHE, L , Phys Rev B **30** (1984) 78, CARON, L G , PERLUZZO, G , BADER, G , SANCHE, L , Phys Rev B **33** (1986) 3027
[107] PLENKIEWICZ, B , PLENKIEWICZ, P , PERLUZZO, G , JAY-GERIN, J -P , Phys Rev B **32** (1985) 1253, PLENKIEWICZ, B , PLENKIEWICZ, P , JAY-GERIN, J -P , Phys Rev B **33** (1986) 5744
[108] HARRIGAN, M E , LEE, H J , J Chem Phys **60** (1974) 4909
[109] HUANG, J T J , MAGEE, J L , J Chem Phys **61** (1974) 2736
[110] CHENG, I Y , FUNABASHI, K , J Chem Phys **59** (1973) 2977
[111] UENO, N , SUGITA, K , SEKI, K , INOKUCHI, H , Phys Rev B **34** (1986) 6386
[112] BADER, G , PERLUZZO, G , CARON, L G , SANCHE, L , Phys Rev B **26** (1982) 6019

[113] JAY-GERIN, J -P , PLENKIEWICZ, B , PLENKIEWICZ, P , PERLUZZO, G , SANCHE, L , Sol State Comm **55** (1985) 1115, KESZEI, E , JAY-GERIN, J -P , PERLUZZO, G , SANCHE, L , J Chem Phys **85** (1986) 7396
[114] PLENKIEWICZ, P , JAY-GERIN, J -P , PLENKIEWICZ, B , PERLUZZO, G , Sol State Comm **57** (1986) 203
[115] PLENKIEWICZ, P , PLENKIEWICZ, B , JAY-GERIN, J -P , Sol State Comm **65** (1988) 1227
[116] HIRAOKA, K , NARA, M , Bull Chem Soc Jpn **57** (1984) 2243, HIRAOKA, K , NARA, M , Chem Phys Lett **94** (1983) 589
[117] PERLUZZO, G , BADER, G , CARON, L G , SANCHE, L , Phys Rev B **26** (1982) 3976
[118] SANCHE, L , PERLUZZO, G , BADER, G , CARON, L G , J Chem Phys **77** (1982) 3285
[119] PERLUZZO, G , SANCHE, L , GAUBERT, C , BAUDOING, R , Phys Rev B **30** (1984) 4292
[120] PERLUZZO, G , BADER, G , CARON, L G , SANCHE, L , Phys Rev Lett **55** (1985) 545
[121] MICHAUD, M , SANCHE, L , Phys Rev Lett **59** (1987) 645
[122] THIEL, P A , HOFFMANN, F M , WEINBERG, W H , J Chem Phys **75** (1981) 5556
[123] SANCHE, L , MICHAUD, M , J Chem Phys **81** (1984) 257
[124] SANCHE, L , MICHAUD, M , Chem Phys Lett **84** (1981) 497
[125] SANCHE, L , MICHAUD, M , Phys Rev Lett **47** (1981) 1008
[126] SANCHE, L , MICHAUD, M , In "Resonances in Electron-Molecules Scattering van der Waals Complexes and Reactive Chemical Dynamics", ed D G Truhlar, ACS Symp Series no 263 (1984) 211
[127] SANCHE, L , MICHAUD, M , Phys Rev B **27** (1983) 3856, MICHAUD, M , SANCHE, L , J Electron Spectr Rel Phenom **51** (1990) 237
[128] SAKURAI, M , OKANO, T , TUZI, Y , J Vac Sci Technol A **5** (1987) 431
[129] HOFFMAN, F M , FELTER, T E , THIEL, P A , WEINBERG, W H , Surf Sci **130** (1983) 173
[130] DEMUTH, J E , SCHMEISSER, D , AVOURIS, P , Phys Rev Lett **47** (1981) 1166, SCHMEISSER, D , DEMUTH, J E , AVOURIS, P , Phys Rev **B26** (1982) 4857
[131] BADER, G , CHIASSON, J , CARON, L G , MICHAUD, M , PERLUZZO, G , SANCHE, L , Rad Res **114** (1988) 467
[132] HAGEN, W , TIELENS, A G G M , GREENBERG, J M , Chem Phys **56** (1981) 367, WONG, P T T , WHALLEY, E , J Chem Phys **64** (1976) 2359
[133] MICHAUD, M , SANCHE, L , Phys Rev B **30** (1984) 6067
[134] HIRAOKA, K , HAMILL, W H , J Chem Phys **57** (1972) 3870, HIRAOKA, K , HAMILL, W H , J Chem Phys **59** (1973) 5749
[135] HIRAOKA, K , J Phys Chem **85** (1981) 4008, HIRAOKA, K , NARA, M , Bull Chem Soc Jpn **54** (1981) 1589
[136] LECLERC, G , GOULET, T , CLOUTIER, P , JAY-GERIN, J -P , SANCHE, L , J Phys Chem **91** (1987) 4999
[137] ASHBY, C I H , Appl Phys Lett **43** (1983) 609
[138] MARSOLAIS, R M , MICHAUD, M , SANCHE, L , Phys Rev A **35** (1987) 607
[139] SANCHE, L , Chem Phys Lett **65** (1979) 61, J Phys C **13** (1980) L677
[140] MERKEL, P B , HAMILL, W H , J Chem Phys **55** (1971) 1409
[141] SANCHE, L , Phys Rev Lett **53** (1984) 1638
[142] SAMBE, H , RAMAKER, D E , PARENTEAU, L , SANCHE, L , Phys Rev Lett **59** (1987) 236
[143] AZRIA, R , PARENTEAU, L , SANCHE, L , Phys Rev Lett **59** (1987) 638
[144] AZRIA, R , PARENTEAU, L , SANCHE, L , J Chem Phys **88** (1988) 5166, AZRIA, R , SANCHE, L , PARENTEAU, L , Chem Phys Lett **156** (1989) 606

[145] SAMBE, H., RAMAKER, D.E., PAREANTEAU, L., SANCHE, L., Phys. Rev. Lett. **59** (1987) 505.
[146] SANCHE, L., PARENTEAU, L., Phys. Rev. Lett. **59** (1987) 136.
[147] SANCHE, L., PARENTEAU, L., J. Vac. Sci. Technol. A **4** (1986) 1240.
[148] SANCHE, L., PARENTEAU, L., J. Chem. Phys. **90** (1989) 3402.
[149] STULEN, R.H., KNOTEK, M.L., In "Desorption Induced by Electronic Transitions DIET III", Springer Ser. in Surface Sci., Vol. 13, Springer-Verlag, Berlin (1988).
[150] STULEN, R.H., THIEL, P.A., Surf. Sci. **157** (1985) 99.
[151] NOELL, J.O., MELIUS, C.F., STULEN, R.H., Surf. Sci. **157** (1985) 119.
[152] STOCKBAUER, R., BERTEL, E., MADEY, T.E., J. Chem. Phys. **76** (1982) 5639.
[153] KELBER, J.A., KNOTEK, M.L., Phys. Rev. B **30** (1984) 400.
[154] KELBER, J.A., KNOTEK, M.L., Surf. Sci. **121** (1982) L499.
[155] ROSENBERG, R.A., REHN, V., KNOTEK, M.L., STULEN, R.H., J. Vac. Sci. Technol. A **5** (1987) 1085.
[156] BURNS, A.R., STECHEL, E.B., JENNISON, D.R.; STECHEL, E.B., JENNISON, D.R., BURNS, A.R., In "Desorption Induced by Electronic Transitions DIET III", Springer Ser. in Surface Sci., Vol. 13, ed. R.H. Stulen, and M.L. Knotek, Springer-Verlag, Berlin (1988) 67 and 136.
[157] VÉZINA, C., SANCHE, L., Proceedings of the "Journées d'Études en Chimie sous Rayonnement", JECR, Sherbrooke, QC (1990).
[158] GOULET, T., JAY-GERIN, J.-P., Rad. Res. **118** (1989) 46.
[159] GOULET, T., JAY-GERIN, J.-P., J. Phys. Chem. **92** (1988) 6871.
[160] SANCHE, L., DESCHÊNES, M., Phys. Rev. Lett. **61** (1988) 2096.
[161] SAMBE, H., RAMAKER, D.E., DESCHÊNES, M., BASS, A.D., SANCHE, L., Phys. Rev. Lett. **64** (1990) 523.
[162] SCHULZ, G.J., Phys. Rev. **128** (1962) 178.
[163] BASS, A.D., SANCHE, L., J. Chem. Phys. **95** (1991) 2910.
[164] SENG, G., LINDER, F., J. Phys. B **9** (1976) 2539.

Chapter 5

PHOTOABSORPTION, PHOTOIONIZATION AND PHOTODISSOCIATION CROSS SECTIONS

Y. Hatano
Department of Chemistry, Tokyo Institute of Technology,
Tokyo, Japan

M. Inokuti
Argonne National Laboratory,
Argonne, Illinois,
United States of America

5.1 INTRODUCTION

Cross section data on the interaction of photons with molecules are of great importance in radiotherapy [1]. They must be correct, absolute, and comprehensive [2]. Photoabsorption cross sections are related to the cross sections for impact of fast charged particles as discussed in Chapters 2 and 3. The cross sections for high energy photons, viz., for hard x-rays, are directly pertinent to radiotherapy [3-7].

The interactions of photons with molecules are classified into absorption, scattering, and pair production. In this chapter, photons of moderate energies are discussed, and therefore only the absorption process is considered. The absorption of a single photon by a molecule changes its electronic state from the ground state to a final excited or ionized state. Its transition probability is expressed in terms of the optical oscillator strength, which is proportional to the photoabsorption cross section.

Oscillator-strength values have long been measured for various molecules in the wavelength regions at least longer than the near-ultraviolet (UV) region, whereas until recently measurements in the wavelength region shorter than the LiF cutoff at 105 nm (at which the photon energy is 11.8 eV) were relatively few because of experimental difficulties in obtaining appropriate photon sources and because no suitable window materials were available [8]. The cutoff energy of 11.8 eV corresponds, roughly speaking, to the ionization potentials of commonly occurring molecules. The sum of the oscillator strengths below 11.8 eV amounts to only a few percent [8] of the total sum, which is equal to the total number of electrons in a molecule, according to the Thomas-Kuhn-Reiche sum rule. The absorption in the vacuum ultraviolet and soft x-ray (VUV-SX) region is much stronger than in all other wavelength regions. (See Table I .) Since there have been remarkable advances in synchrotron radiation (SR) research and related experimental techniques in the VUV-SX region, many measurements in this region are now available [8].

TABLE 5.1 **SUM OF DIPOLE OSCILLATOR STRENGTH DISTRIBUTIONS OF C_3H_6 [20]**

Photon Energy (eV)	Cyclopropane	Propylene
Below Ip	0.746	0.507
Ip-11.8	0.715	0.666
11.8-35.4	11.744	12.176
35.4<	10.251	
Total	23.46	23.60
Z	24	

Ip:the first ionization potential.
Ip(Cyclopropane)=10.60eV
Ip(Propylene)=10.03eV
Z: the number of electrons in a molecule.

This chapter gives a survey of recent results of measurement of photoabsorption, photoionization, and photodissociation cross sections of molecules in the VUV-SX region, and also a summary of our understanding in spectroscopy and dynamics of molecules in highly excited or ionized states. Molecules treated here are chosen from the point of view of basic radiation research. They are hydrocarbons, alcohols, ethers, and other organic molecules. Some remarks are presented on molecules in the condensed phase. Problems to be solved are also indicated.

It is well known that the interaction of high energy electrons with a medium produces photons, viz., the Čerenkov light, in the spectrum range between infrared and ultraviolet. A possibility of photo-excitation processes due to the absorption of the Cerenkov light by solute molecules was discussed in the γ-radiolysis of aqueous solutions of biological molecules [9-12]. Recently, however, it has been concluded in pico-second pulse-radiolysis studies that the contribution of such a photoexcitation process to the observed total excitation processes of solute

molecules is negligibly small in some hydrocarbon systems [13, 14]. Since the magnitude of this contribution seems to depend largely on the solute molecule, investigations by changing systematically the molecule will be necessary to substantiate this contribution.

A list of the acronyms used in this chapter is given in Table II .

TABLE 5.2 **LIST OF ACRONYMS**

UV	Ultraviolet
VUV	Vacuum ultraviolet
EUV	Extreme ultraviolet
SX	Soft X-ray
HX	Hard X-ray
SR	Synchrotron radiation
TKR	Thomas-Kuhn-Reiche

5.2 VUV—OPTICAL OSCILLATOR STRENGTH DISTRIBUTIONS OF POLYATOMIC MOLECULES

Figure 1 shows the wavelengths of electromagnetic radiation from the infrared to the γ-ray regions and corresponding photon energies [8]. Characteristic x-rays, ^{60}Co-γ rays, and VUV light from discharge lamps are indicated by the arrows. The shaded areas (1-12 eV and above 5 keV) indicate regions for which photon sources, apart from SR, are available. Figure 1 clearly demonstrates that SR bridges the wide gap in the photon energy between radiation chemistry and photochemistry, i.e., "electron-collision chemistry" and "photon-collision chemistry", respectively.

It is important to recognize that a major part of both photoabsorption and photoionization intensities lies in the wide gap between the two for almost all molecules [8]. The experimental data for cross section values in this wavelength region have

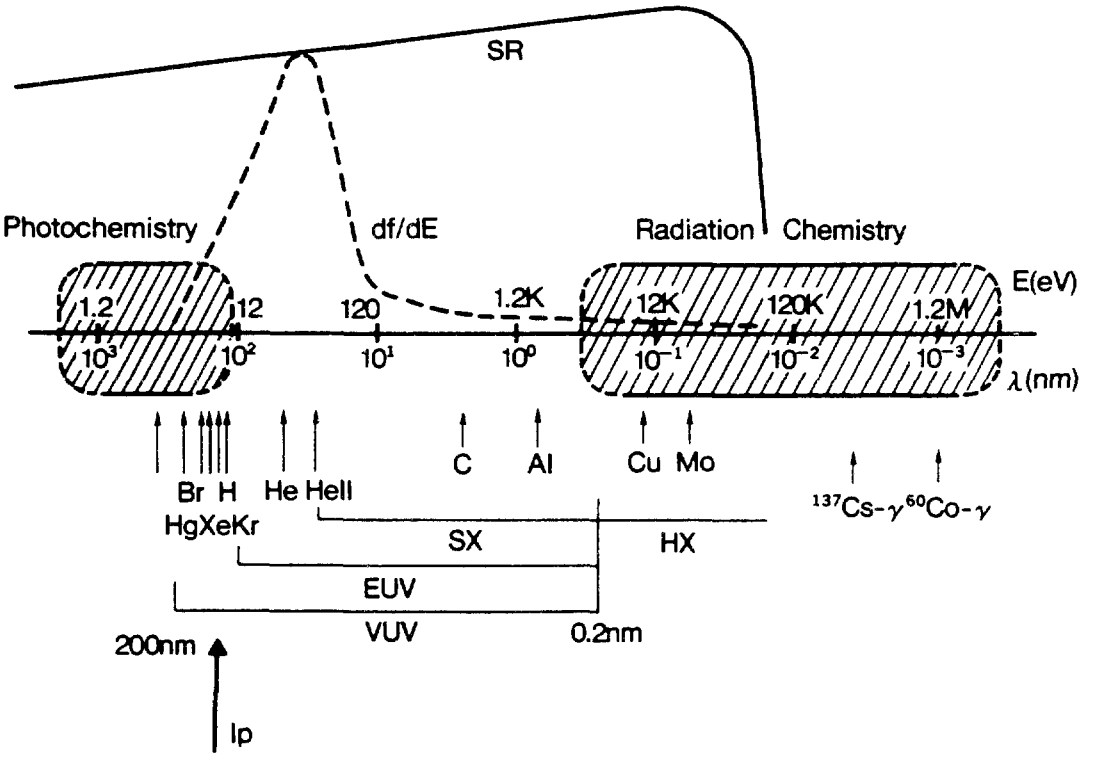

FIG. 5.1 *Synchrotron radiation (SR) chemistry as a bridge between radiation chemistry and photochemistry [8]. The dipole oscillator strength df/dE is shown as a function of wavelength λ and photon energy E. Note the relation* $E \cdot \lambda = 1.24 \times 10^3$ *(eV·nm). The intensity of SR is also shown, as are the energies of photons from several line sources. VUV, EUV, SX, and HX stand for vacuum ultraviolet, extreme ultraviolet, soft X-ray, and hard X-ray, respectively.*

been incomplete in general because of experimental difficulties related to suitable photon sources and window materials. As an alternative, electron energy-loss spectroscopy has been used. Even then, cross section data are limited, particularly for chemically important complex molecules such as hydrocarbons and other organic molecules [8].

The absorption of a single photon results in an electronic transition of a molecule from the ground state O to a final state j [15]. The transition probability is expressed in terms of the optical oscillator strength f_j. It is in turn expressed in terms

of E_j/R, the transition energy measured in units of $R=me^4/(2\hbar^2)=13.6$ eV and of M_j^2, the dipole matrix element squared as measured in a_o^2, where $a_o=\hbar^2/me^2=0.0529$ nm, as

$$f_j(E_j) = (E_j/R)\, M_j^2. \tag{1}$$

A set of E_j and f_j characterizes a discrete spectrum. To discuss a continuous spectrum, one expresses the oscillator strength in a small region of the excitation energy between E and E+dE as (df/dE)dE, and calls df/dE the oscillator-strength distribution, or, more precisely, the spectral density of the oscillator strength. The total sum of the oscillator strength including discrete and continuous spectra is equal to the total number Z of electrons in the molecule, viz.,

$$\sum_j f_j(E_j) + \int_I^\infty (df/dE)dE = Z, \tag{2}$$

where I represents the (first) ionization potential. Equation (2) is called the Thomas-Kuhn-Reiche (TKR) sum rule.

The oscillator-strength distribution is proportional to the cross section σ for the absorption of a photon of energy E. Explicitly one may write

$$\sigma = 4\pi^2 \alpha a_o^2 R \frac{df}{dE}$$

$$= 8.067 \cdot 10^{-4} \frac{df}{d(E/R)} \ (\mathrm{nm}^2)$$

$$= 0.01098 \frac{df}{dE} \ (\mathrm{eV}^{-1}\cdot \mathrm{nm}^2), \tag{3}$$

where $\alpha=e^2/\hbar c=1/137.04$.

A decisive step in the physical and physicochemical stages of the action of any ionizing radiation on matter is collisions of secondary electrons in a wide energy range with molecules. At energies T higher than about 10^2 eV, the total cross section $Q_j(T)$ to excite a molecule to the state j is at least approximately given by the Bethe cross section [16,17]. Using the Bethe

cross section and further assumptions, Platzman [18,19] showed that the number of product species j (e.g., an excited state or a dissociation product) formed per 100 eV absorbed is approximately proportional to the dipole matrix element squared

$$M_j^2 = \int_J^\infty \Phi_j(E) \frac{R}{E} \frac{df}{dE} dE, \tag{4}$$

where $\Phi_j(E)$ is the quantum yield and J is the threshold energy, both for the formation of j. With the use of the W value, viz., the mean energy, measured in eV, for the production of an ion pair (extensively discussed in Chapter 8), one may write

$$G_j = \frac{100}{W} \frac{M_j^2}{M_i^2} \tag{5}$$

where M_i^2 is the dipole matrix element squared for ionization, i.e.,

$$M_i^2 = \int_I^\infty \eta(E) \frac{R}{E} \frac{df}{dE} dE, \tag{6}$$

where $\eta(E)$ is the quantum yield for ionization. Since

$$\eta(E) = \sigma_i(E)/\sigma_t(E), \tag{7}$$

where $\sigma_i(E)$ and $\sigma_t(E)$ are, respectively, the photoionization cross section and the photoabsorption cross section, Eq. (5) means that the radiation chemical yield G_j is obtained from optical cross section data. Equation (5) is therefore called the optical approximation. Optical cross section data are, thus, of fundamental importance in understanding not only the interactions of photons with molecules, but also the actions of any ionizing radiation with matter.

It is important to obtain photoabsorption and related cross sections for polyatomic molecules such as hydrocarbons and other organic molecules and relate them with molecular structure. With this idea, photoabsorption and photoionization cross sections for molecules in several stereo-isomer series have been systematically measured and compared with each other [20-23]. The main

purpose of these investigations is to reveal how df/dE changes with changing molecular structures; for this purpose isomers have been chosen as examples. Since isomer molecules consist of the same kind and same number of atoms, the df/dE of isomers are expected to have the following properties:

1) The sum of df/dE of an isomer over the entire energy region should be equal to that of another isomer, and also to the number of electrons in the molecule, according to the TKR sum rule.
2) The features of the df/dE of isomers are expected to be almost identical with each other in the energy region where inner-core electrons are excited, because the molecular structure of isomers would have a little influence on inner-core electrons. Moreover, the value of df/dE in such a region would be almost equal to the sum of df/dE values of the constituent atoms.

With these expectations, the photoabsorption cross sections have been measured for five series of isomers: C_3H_6 (cyclopropane and propylene), C_4H_8 (1-butene, iso-butene, cis-2-butene, and trans-2-butene), C_6H_{12} (cyclohexane, 1-hexene, and tetramethyl-ethylene), C_2H_6O (ethyl alcohol and dimethyl ether), and C_3H_8O (n-propyl alcohol, i-propyl alcohol, and ethylmethyl ether) in the wavelength region from about 30 nm (41 eV) to 140 nm (9 eV), and compared with each other [20-23].

Figure 2 shows, as an example, the absorption cross sections of C_3H_6 isomer molecules, cyclopropane and propylene [20]. Similar cross section data have been obtained also for the other isomer series, giving the common new features of absorption cross sections or oscillator strength distributions summarized as follows:

1) The values of σ_t show a maximum at 70-80 nm (16-18 eV) for each molecule.
2) In the high energy side of the maximum the values of σ_t are almost the same among the isomer molecules, e.g., cyclopropane and propylene, and equal to the sum of the cross sections for the constituent atoms.

3) In the low energy side, the cross sections have different peaks and shoulders depending on an isomer, i.e., on its molecular structure. The sum of the cross sections in this energy region is, however, almost equal among the isomer molecules.

These results represent an important contribution to fundamental physical chemistry particularly as an inducement to a new development in quantum chemistry, and also a useful contribution to radiation research in enabling estimates of the energy deposition spectra of molecules. These results, e.g., those in Fig. 2, are fully consistent with the TKR sum rule. The results for C_3H_6 isomers are shown in Table I . The agreement is good between the sum of the obtained oscillator strength values (partly including semiempirical ones in the higher energy region)

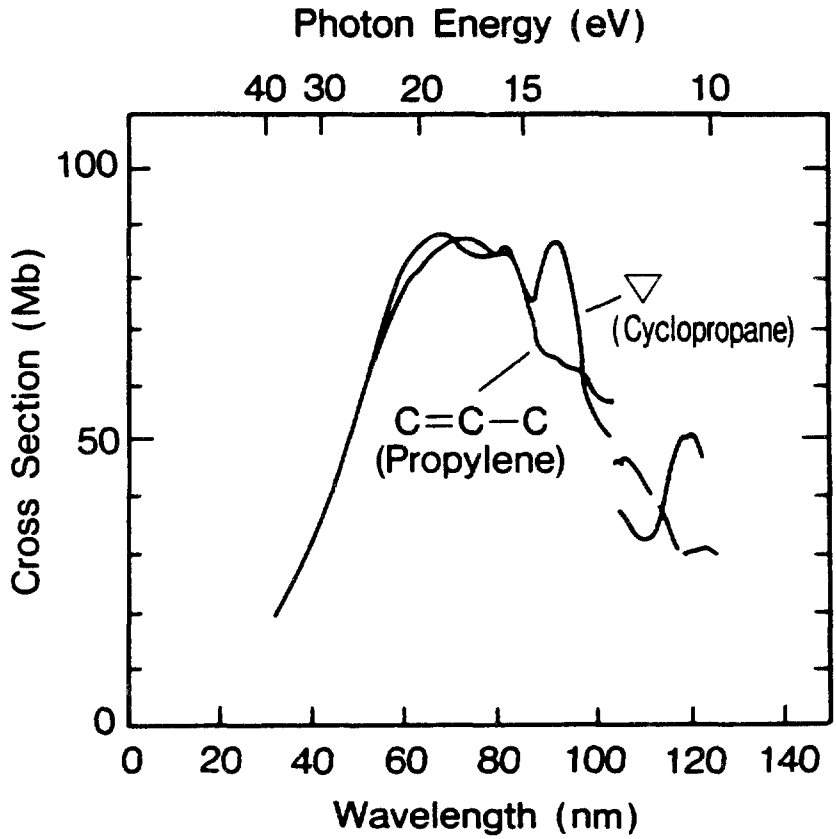

FIG. 5.2 *Photoabsorption cross sections for cyclopropane and propylene [20]. The wavelength resolution is approximately 0.8 nm.*

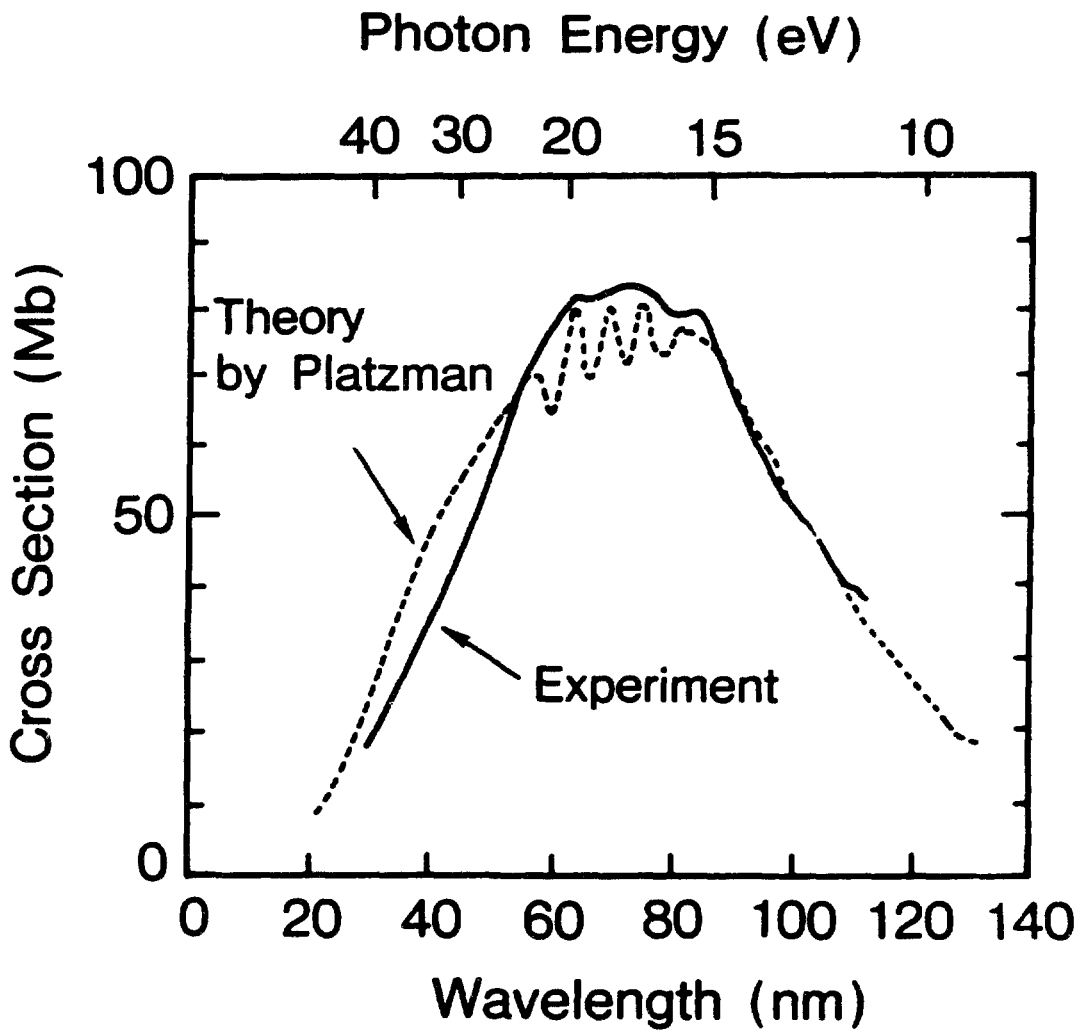

FIG. 5.3 *Photoabsorption cross sections for ethyl alcohol vapor [21]. Experimental wavelength-resolution is approximately 0.8 nm.*

and the number of electrons, Z. Table I also clearly shows that the sum of the oscillator strength in the energy region below the first ionization potential amounts to only a few percent of the total, and the spectra in the VUV-SX region are of great importance in understanding the ionization and excitation of molecules. Figure 3 presents comparison of the recently measured oscillator strength distribution of ethanol vapor and Platzman's estimate in 1965. The gross features agree well with each other, although the prediction shows several large peaks, which are spurious as discussed in Ref.[21].

5.3 PHOTOIONIZATION QUANTUM YIELDS

A molecule that has received energy exceeding its ionization threshold (I_p) does not necessarily ionize because there are in general other decay channels such as dissociation into neutral fragments, and the ionization process competes with the neutral fragmentation. Various pathways are schematically represented in the following for a molecule AB [19,24-29].

$$AB + \text{energy} (>I_p) \rightarrow AB^+ + e^- \quad ; \text{Direct ionization} \quad (8)$$

$$\rightarrow AB' \quad ; \text{Superexcitation} \quad (9)$$

$$AB' \rightarrow AB^+ + e^- \quad ; \text{Autoionization} \quad (10)$$

$$AB' \rightarrow A + B \quad ; \text{Dissociation} \quad (11)$$

$$AB' \rightarrow \text{Others} \quad (12)$$

In this mechanism AB' is a superexcited molecule which decays through autoionization or dissociation. The cross section σ_i corresponds to the sum of the cross sections for both direct- and auto-ionization processes, while σ_t to the sum of the cross sections for direct ionization and superexcitation. The value of η in the energy region below I_p is zero , while above I_p it increases with increasing energy, as described in the preceding section, and eventually approaches unity in the energy region well above I_p; however, in the energy region close to I_p the dissociation process plays a very important role in the decay of a superexcited molecule. Note that "Others" in Eq.(12) include decay with photon emission and internal conversion.

It has been pointed out both theoretically [24-26] and experimentally [19] that superexcited states, and hence neutral fragments formed from their dissociation play an important role in radiolysis. The neutral fragments are translationally, vibrationally, or sometimes electronically excited, because of a large internal energy of superexcited states. Such fragments are called

hot atoms or free radicals, and have anomalous chemical reactivities [27].

In order to understand the electronic structure and dissociation dynamics of superexcited states, electron impact spectroscopy and more recently spectroscopy combined with SR have been extensively applied [28,29].

In the past two decades electron impact studies, such as measurement of the excitation spectrum and the translational spectroscopy of neutral fragments, photoelectron spectroscopy using line sources, and (e, 2e) experiments, have uncovered an outline of the electronic structure and dissociation dynamics of superexcited molecules [28]. A major part of the superexcited states of molecules are molecular high Rydberg states converging to various ionic states and are classified into the following three types: 1)vibrationally excited states, 2)doubly excited states, and 3)inner-core excited states [28].

Recently SR has been used to obtain more detailed information about the properties of superexcited molecules [8,29].

In summary, photoionization cross sections and photoionization quantum yields are of great importance as key features of superexcited states, which characterize the primary processes, (8)-(12), of both photolysis and radiolysis of molecules.

The photoionization quantum yield η is a quantity of considerable importance, and serves as an index for the degree of competition between direct ionization and excitation to the superexcited states opening to autoionization and dissociation. Several experimental efforts have been devoted to the measurement of η. Serious conflicts exist even for simple molecules, not only between photon impact experiments and "simulated" ones by electron impact but also between photon impact experiments themselves [30]. The problems have originated mainly from lack of an intense light source and a suitable window material in the VUV region particularly in the wavelength region shorter than the LiF cutoff at 105 nm. Experiments with differential pumping and without a window for the entrance of a photon beam into an ionization

chamber also present several significant problems, such as an effusion of sample gases into the beam transportation region or a contribution from a diffracted photon beam in the higher order, making it difficult to determine correct, absolute, and comprehensive values of η. In most cases, the η-values have been assumed to be unity in the energy region far above the first ionization potential.

Recently systematic measurements have been reported of the photoionization quantum yields, as well as the photoabsorption cross sections, of C_3H_6, C_4H_8, C_6H_{12}, C_2H_6O, and C_3H_8O isomers using a multiple-staged photoionization chamber and a synchrotron radiation light source in the wavelength region from 105 nm (11.8 eV) up to their respective ionization potentials at about 120-140 nm (9-10 eV) [22]. This work has been further extended to the first attempt of measuring photoionization quantum yields in the wavelength region of 54-92 nm (13-23 eV) using synchrotron radiation combined with metal thin foil windows [31]. In what follows, a survey is given of recent progress in the measurement of η values.

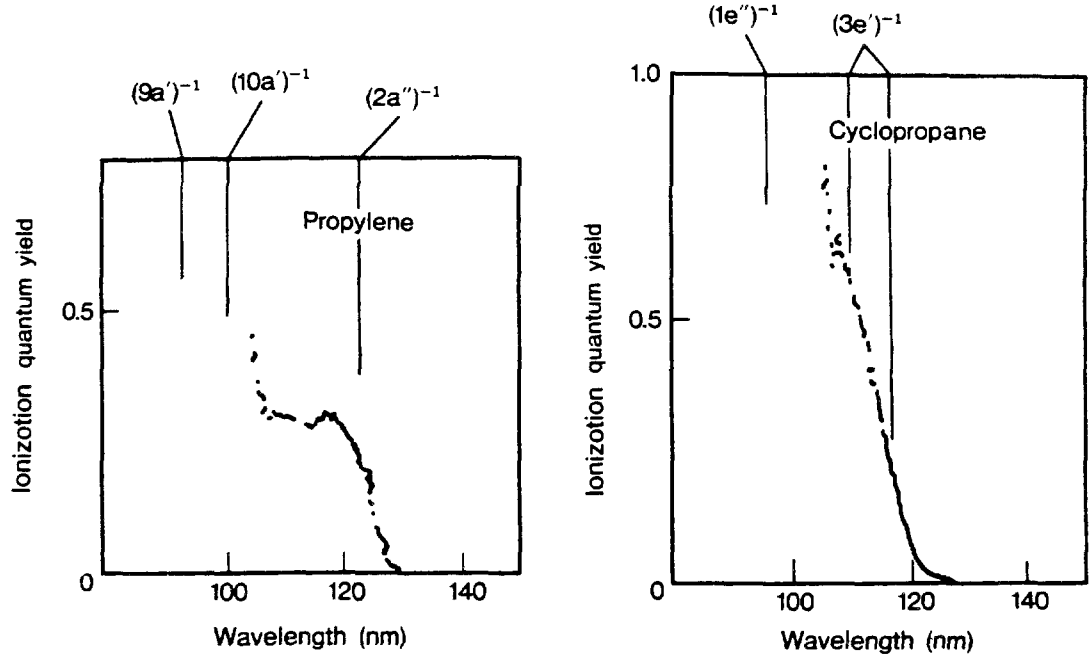

FIG. 5.4 *Photoionization quantum yields for C_3H_6 isomers [23]. The energies of ionic states corresponding to molecular orbitals are indicated.*

The values of η have been systematically measured in the wavelength region below the LiF cutoff at 105 nm (11.8 eV) for the molecules in several isomer series of which, as described in Section 5.2, the photoabsorption cross sections have also been measured. Some of the results are shown in Fig.4 for cyclopropane and propylene [22]. The η-curves for the same C_3H_6 isomer molecules are very different from each other. The η-curve for cyclopropane rises almost monotonically , and indeed much more rapidly than that for propylene, which has a step or a shoulder at 110-120 nm. The η-curves for other molecules whose figures are not given here have shown interesting common features of η-curves as a function of photon energy that the energy difference between the first and the second ionization potentials correlates well with the shape of the η-curves. A bigger energy difference corresponds to a longer step-length as seen for propylene in Fig.4. This result means that the η-value increases rapidly in the wavelength or energy region close to the ionization potential, and agrees well with the conclusion that the most important part of the superexcited states is high-Rydberg states converging to each ion state. It is, therefore, concluded that the shape of the η curves as a function of the energy at least for these chemically important molecules is determined by the density of converging Rydberg states, i.e., superexcited states, which increases rapidly with increasing energy in the energy region close to the ionization potential.

In the wavelength region shorter than the LiF cutoff at 105 nm (11.8 eV), metal foil filters are employed as window materials for the incoming SR beam from a VUV monochromator. The filters prevent sample gas effusion and eliminate higher order radiation. In the wavelength regions of 54-80 nm (16-23 eV) and 74-92 nm (13-17 eV), Sn and In foils respectively, are used. Their thickness is about 100 nm, with transmittance of about 1%.

Figure 5 shows the ionization quantum yields measured in the wavelength region of 54-92 nm (13-23 eV) together with those in the wavelength region longer than 105 nm (11.8 eV). No data are shown in the wavelength region between the two because there is no thin metal window convenient for the measurement of ionization

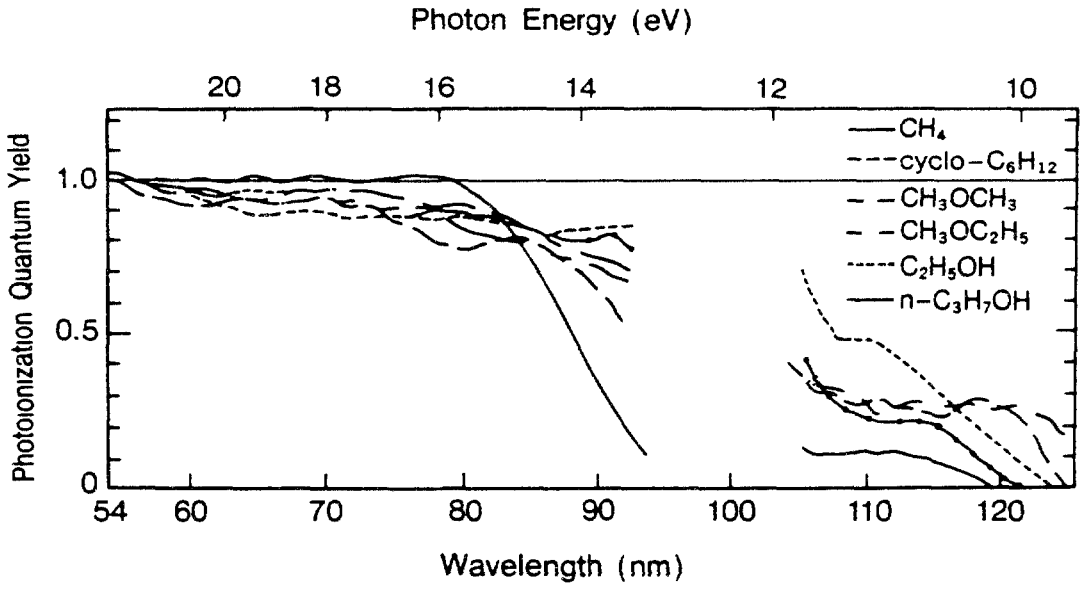

FIG. 5.5 *Photoionization quantum yields for several molecules [31].*

quantum yields and because there are large effects of higher order light.

The present result clearly shows that

1) η-values in the region close to the first ionization potential are much less than unity, which means that the molecules shown at least in Fig.5 are not easily ionized even when they have received enough energy to ionize.
2) η-values do not reach unity even in the energy range more than about 10eV above the first ionization potential.
3) η-values increase with increasing photon energy and reach unity at around 23 eV (or 54 nm).
4) η-curves show considerable structures.

In summary, non-ionizing processes, such as the neutral fragmentation of superexcited molecules, are important among their decay channels. Neutral fragments thus formed often have excess energies electronically, vibrationally, rotationally, or translationally, because the photon energies corresponding to the wavelengths in Fig.5 are much larger than the bond dissociation energies to form the fragments in their ground states. It is, therefore, of great interest to observe optical emissions from

excited fragments as a function of wavelength, i.e., to obtain excitation spectra of optical emission, as compared with the structures in η-curves.

5.4 COMPARATIVE STUDIES OF IONIZATION QUANTUM YIELDS WITH EXCITATION SPECTRA OF OPTICAL EMISSION FROM DISSOCIATION FRAGMENTS

5.4.1 DIMETHYLETHER [32]

In studies of the oscillator strength distributions and ionization quantum yields for isomer molecules, interesting structures have been observed in the η-curve of dimethylether in the wavelength region of 54-92 nm (13-23 eV). The optical emission at the wavelength of 115-200 nm, at which one expects to see Lyman-α emission from fragment $H^*(n=2)$, is shown in Fig.6, together with the ionization quantum yield for comparison.

A clear deviation of the η-value from unity with the three characteristic minima shows that a considerable portion of the superexcited states in the region decays into dissociation and other nonionizing channels. The minima correspond well to the energies of ionic states with the vacancies of π_{CH3} and σ_{CO} or another molecular orbital correlating to the C(2s) orbital, which are identified from the HeII photoelectron spectra for dimethylether [33]. This correspondence indicates that the superexcited states corresponding to the minima are high-Rydberg states converging to the ionic states. The large difference from unity of the η-value, which diminishes with the increase in the photon energy, is explained by the rate of autoionization in competition with dissociation and by the state density of the continuum correlating to the superexcited states. The rate of autoionization decreases with the excess energy above the ionization potential. If the photon energy further exceeds other ionization limits, new channels correlating to higher ionization continua increase the rate.

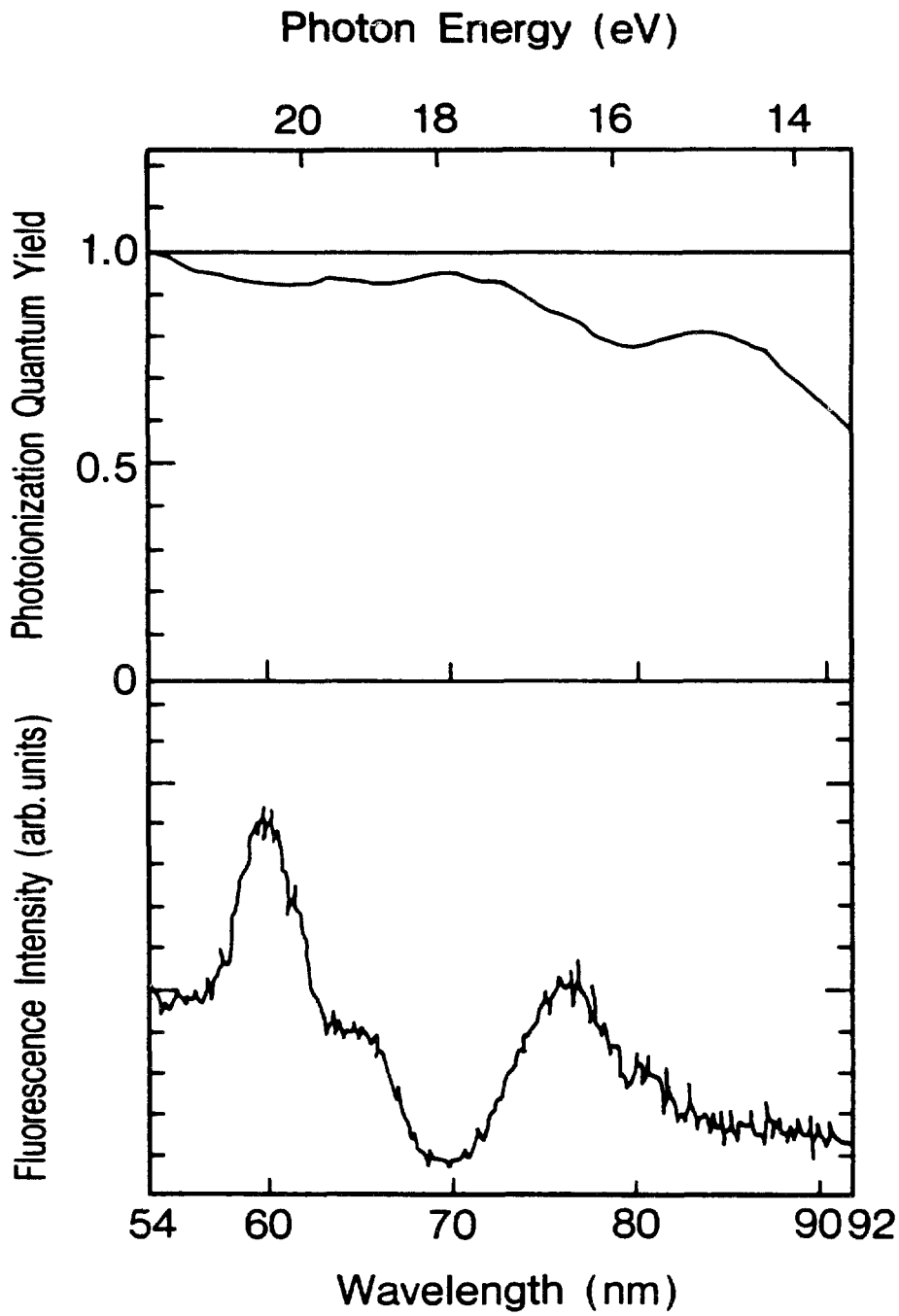

FIG. 5.6 *Photoionization quantum yields and the excitation spectrum of Lyman-α emission for dimethylether CH_3OCH_3 [32].*

The excitation spectrum shows also characteristic structures at around 60, 65, and 77 nm which agree well with the minima in the η-curve. These results clearly show that the dissociation of the superexcited states is followed by fluorescence emission. The Lyman-α emission from dissociated hydrogen atoms is observed in the excitation spectrum.

5.4.2 ACETYLENE [34]

The photoionization quantum yield of acetylene measured using synchrotron radiation combined with metal thin foil windows is shown in Fig.7, together with those measured previously using discharge lamps or electron beams as virtual photon sources. In the energy range between 18-24 eV the yields obtained using virtual photon sources are larger than those obtained using SR,

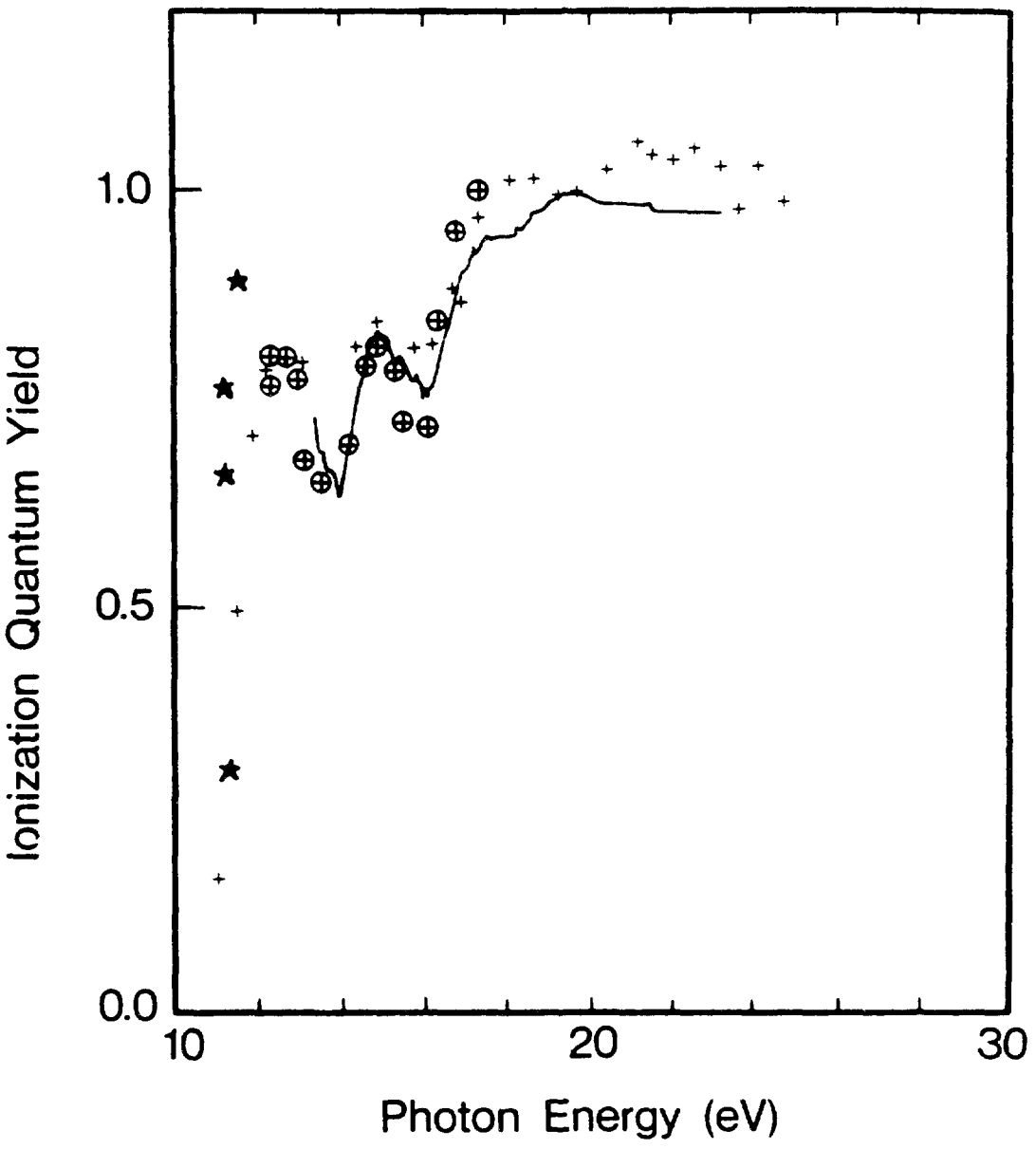

FIG. 5.7 *Photoionization quantum yields for acetylene C_2H_2 [34]; ⊕ : Metzger and Cook (Discharge lamp); ★ : Person and Nicole (Discharge lamp); +: Cooper et. al. (Electron scattering); and —— : Ukai et al. (Synchrotron radiation).*

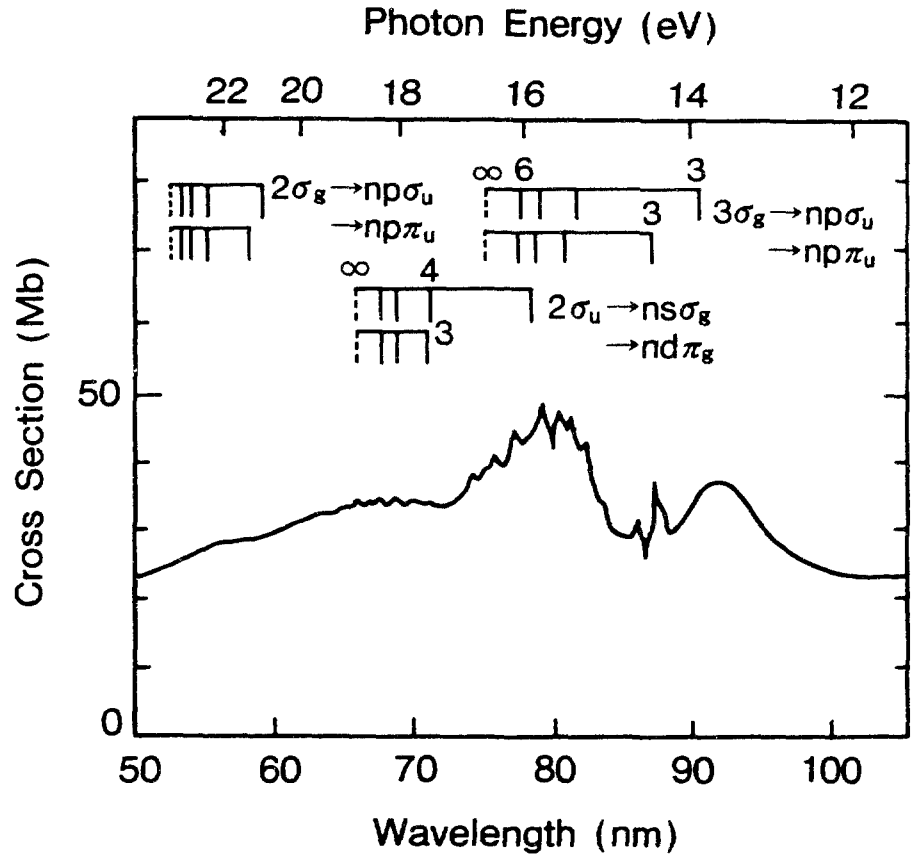

FIG. 5.8 *Photoabsorption cross sections for acetylene [34].*

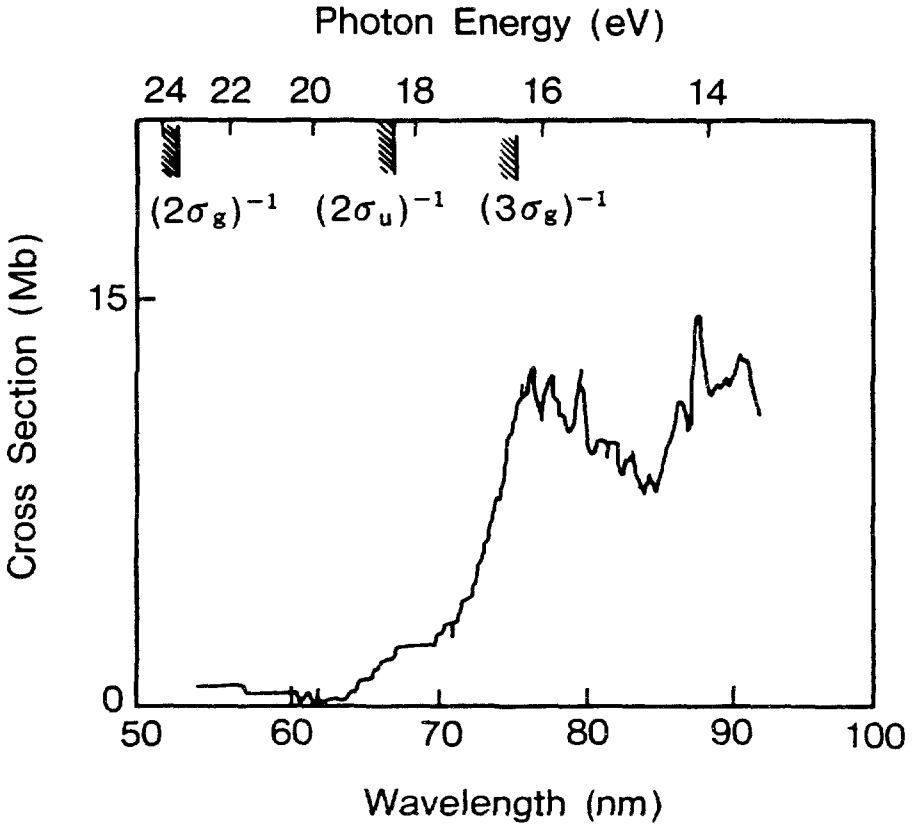

FIG. 5.9 *Non-ionization cross sections for acetylene [34].*

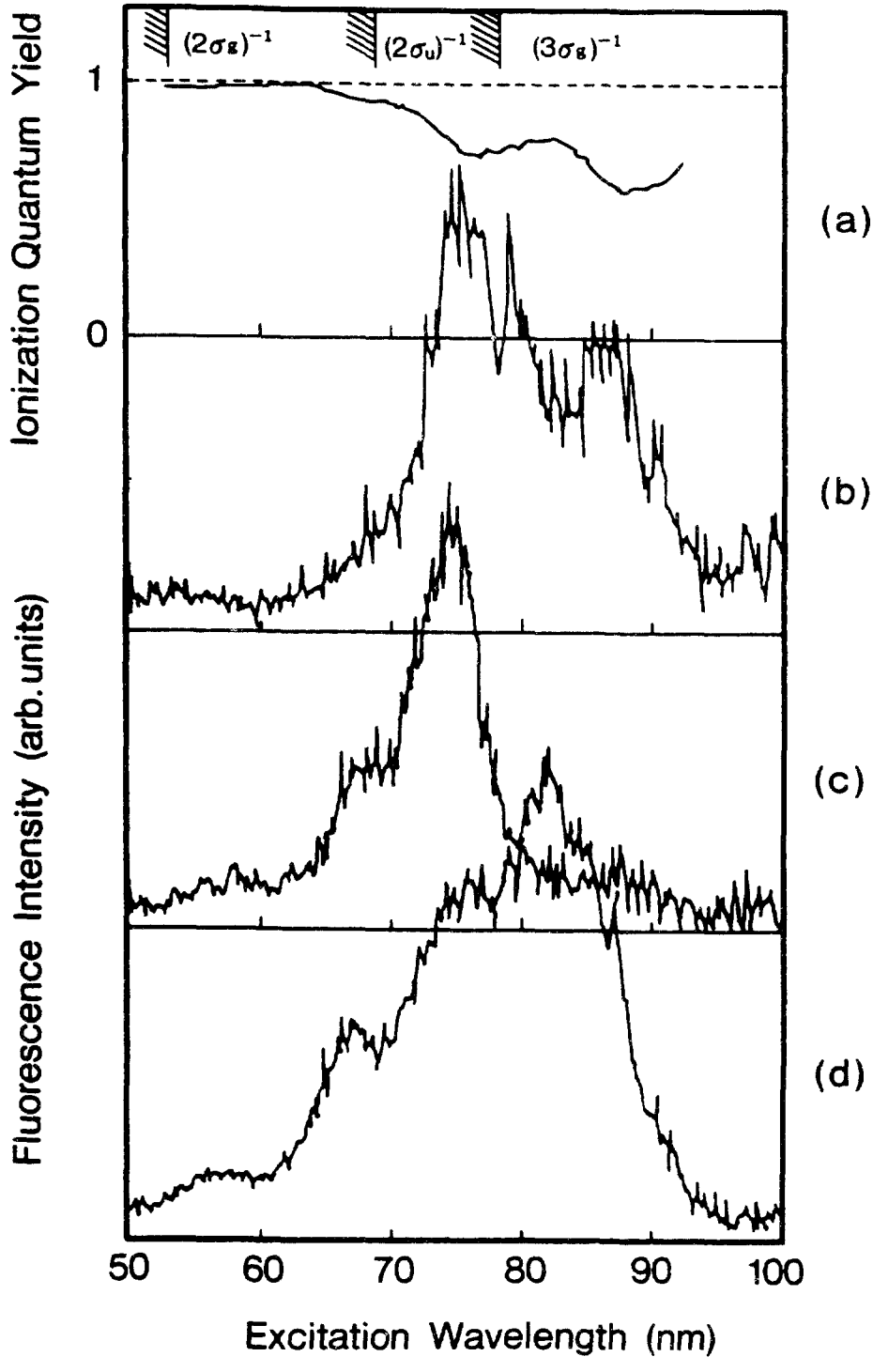

FIG. 5.10 *Photoionization quantum yield (a) and the excitation spectra (b-d) of optical emissions for acetylene; (b): C_2 ($d^3\Pi_g \rightarrow a^3\Pi_u$); (c): $C_2(C^1\Pi_g \rightarrow A^1\Pi_u)$; and (d): $CH(A^2\Delta \rightarrow X^2\Pi)$ [34].*

while in the lower energy range agreement is better between the yields obtained using the different methods. The yield function obtained using SR (solid curve) shows the three minima, whereas those obtained using either virtual photon sources or discharge lamps do not show them clearly. Obvious deviations from unity in the ionization quantum yield indicate the neutral dissociation of a superexcited acetylene molecule strongly competing with auto-ionization. Figure 8 shows the photoabsorption cross sections of acetylene, the structures of which are assigned to Rydberg series converging to each of the ionic states, $(3\sigma_g)^{-1}$, $(2\sigma_u)^{-1}$, and $(2\sigma_g)^{-1}$. Combining the photoionization quantum yields and the photoabsorption cross sections, one obtains the cross sections for non-ionizing decay processes. Results are shown in Fig.9.

Excitation spectra of fluorescence from excited fragments produced in the dissociation of a superexcited acetylene molecule have been observed using band-pass filters to disperse the fluorescence. The excitation spectra of the dispersed fluorescence corresponding to the emission spectra of specific fragments are summarized in Fig.10 for comparison with the ionization quantum yields. Comparing the threshold wavelengths of the excitation spectra with the calculated thresholds of related dissociation processes, one arrives at the assignment as follows.

1) The measurement of C_2 (d → a) is ascribed to
   $C_2H_2 \rightarrow C_2$ (d) + H_2 (and partly C_2 (d) + 2H),
2) The measurement of C_2 (C → A) is ascribed to
   $C_2H_2 \rightarrow C_2$ (C) + 2H, and
3) The measurement of CH (A → X) is ascribed to
   $C_2H_2 \rightarrow$ CH (A) + CH (and partly CH (A) + C + H).

The three minima in the ionization quantum yields correlate well with the structures observed in the excitation spectra.

5.4.3 SILANE [35]

Absolute values have been obtained of the photoabsorption cross section, photoionization cross section and ionization quantum yield of SiH_4 in the energy range of 13-40 eV (Figs.11 and 12) [35].

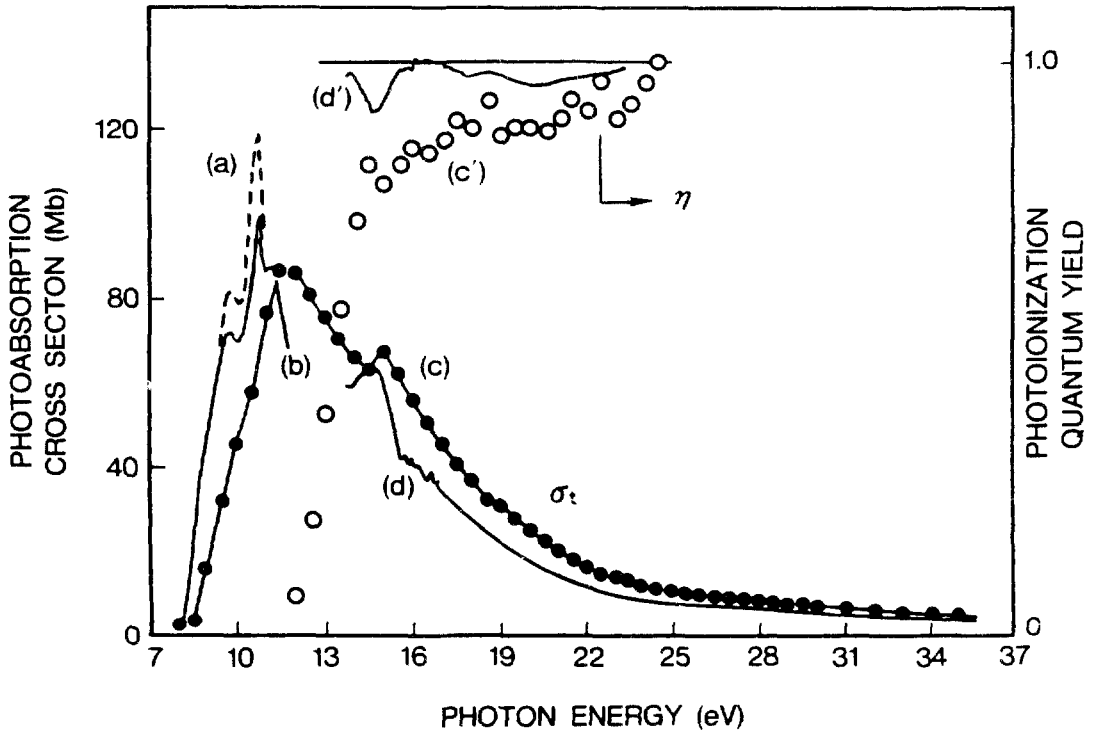

FIG. 5.11 *Photoabsorption cross sections (σ_t) and photoionization quantum yields (η) for Si_2H_4 [35]. Synchrotron radiation experiments by Itoh et al. (a), Suto and Lee (b), and Kameta et al. (d)(d'), and electron scattering experiments by Cooper et al. (c)(c').*

Figure 11 shows experimental results for the photoabsorption cross section of SiH_4. There is some discrepancy between the results obtained from experiments by SR and those by electron scattering [36], in particular, in the energy region of 8-12 eV. One also sees a systematic shift toward a higher energy range of the cross section curve obtained in the dipole (e, e) experiment from that obtained in the SR experiment in the energy region of 13-37 eV. However, the sum of the cross sections in each experiment agrees well with the TKR rule.

A broad peak at 14.6 eV is seen in Fig.12. This is also observed in electron energy loss spectra and assigned to the optically allowed transition of a $3a_1$ electron to an antibonding $\sigma^*(t_2)$ orbital. In the energy region in this broad peak, the ionization quantum yield, as clearly shown in Fig.12, deviates from unity, i.e., the cross section for the neutral fragmentation has a maximum.

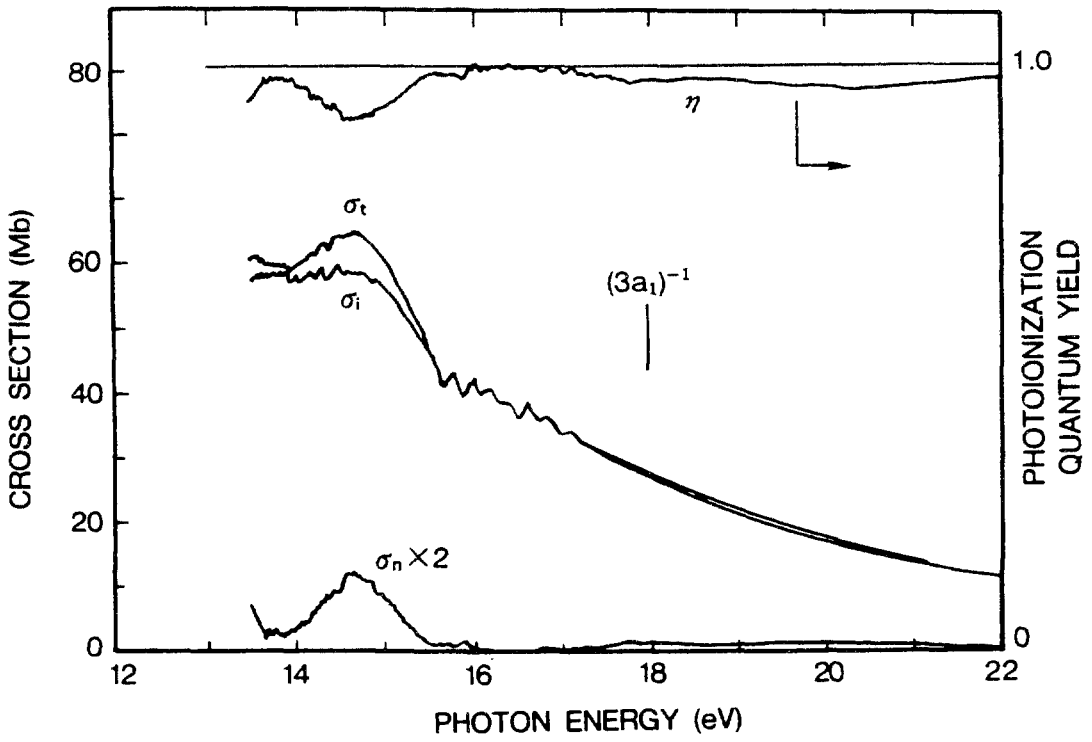

FIG. 5.12 *Photoabsorption cross sections (σ_t), photoionization cross sections (σ_i), photoionization quantum yields (η), and total cross sections for neutral fragmention (σ_n) for Si_2H_4 [35].*

In the energy range just above this range, an interesting structure is observed in both absorption and ionization cross sections. The cross sections are almost equal with each other, and the ionization quantum yield is unity. This structure is assigned to the $(3a_1)^{-1}(npt_2)$ Rydberg state, which decays predominantly through autoionization as seen in Fig.12. The superexcited states of SiH_4 in the energy range shown in Fig.12 are characterized as these two types, i.e., the valence excited states and the Rydberg states. The former decays predominantly through neutral fragmentation while the latter through autoionization. As concluded in Section 5.2 from electron impact experiments, an important part of the molecular superexcited states is high Rydberg states either vibrationally, doubly, or inner-core excited and converging to each ion state. The present SR experiment of SiH_4 has therefore clarified further details of the electronic states of superexcited molecules.

5.4.4 OTHER EXAMPLES [29]

Photoabsorption cross sections have been measured also of Cl_2, H_2S, BF_3, BCl_3, CF_4, CF_3X (X=H, Cl, Br), SiF_4, GeH_4 and C_2H_5OH in the wavelength region similar to that described in the preceding sections.

5.5 BASIC IDEAS FOR TREATING CONDENSED MATTER

5.5.1. A SKETCH OF THEORY

The notion of the dielectric-response function, or the frequency-dependent permeability, is useful for describing the dipole interactions of photons or fast charged particles with any neutral material including condensed matter. It is the purpose of this section to supplement the foregoing discussion on photoabsorption and related processes in gases and to present a resume of basic ideas for treating condensed matter. Elementary treatments of the topic are found in textbooks, e.g., Landau and Lifshitz [37]. Earlier and more technical treatments are seen in Nozières and Pines [38], who focused on an electron gas, and in Fano [39,40] who dealt with matter in general.

Consider an electromagnetic wave whose intensity is uniform in space and varies harmonically with time, viz., a plane wave of photons with a fixed energy $\hbar\omega$. The amplitude of the electric field is expressed as $E(\omega)\exp(-i\omega t)$ (to be precise, the real part of the amplitude is the strength of the electric field). When the electric field is present in matter, there will be an electric flux density of the form $D(\omega)\exp(-i\omega t)$. The spatial uniformity of the electric field and the electric flux density is a condition for the dipole approximation. The ratio $D(\omega)/E(\omega)=\varepsilon(\omega)$ is the dielectric permeability, which is a property of matter independent of $E(\omega)$ so long as it is weak enough. The permeability is a complex-valued function of the frequency ω, i.e.,

$$\varepsilon(\omega) = \varepsilon_1(\omega)+i\varepsilon_2(\omega). \qquad (13)$$

The real part $\varepsilon_1(\omega)$ describes dispersion, and the imaginary part $\varepsilon_2(\omega)$ describes absorption of the electromagnetic wave. For an isotropic and homogeneous material, which we shall consider throughout, $\varepsilon(\omega)$ is a scalar; otherwise, it is a tensor.

The two functions, ε_1 and ε_2, are not independent. Indeed, they are related to each other through a set of formulas called the Kramers-Kronig relations. Thus, it is useful to express $\varepsilon(\omega)$ in terms of a single real-valued function $df(\omega)/d\omega$, called the oscillator-strength spectrum, as

$$\varepsilon(\omega) = 1 + \frac{4\pi e^2}{m} \int_0^\infty d\omega' \, \frac{df(\omega')/d\omega'}{\omega'^2 - \omega^2 - ig\omega'} , \tag{14}$$

where g is a small positive number related to the relaxation of excited states of the material. The physical meaning of $df(\omega)/d\omega$ is as follows. Imagine that there are harmonic oscillators with natural frequencies ω that respond to the electric field $E(\omega)\exp(-i\omega t)$, and suppose that there are $df(\omega)$ oscillators within the frequency range between ω and $\omega+d\omega$. Historically, this idea came from J.J.Thomson before the advent of quantum theory. However, the same idea remains valid in quantum theory, which moreover gives a procedure for calculating $df(\omega)/d\omega$ from first principles. The total number of the imaginary harmonic oscillators is the same as the total number of electrons in matter, i.e., a generalization of the TKR sum rule: That is to say,

$$\int_0^\infty d\omega [df(\omega)/d\omega] = N, \tag{15}$$

where N is the total number of electrons per unit volume. For treating macroscopic matter, for which N is very large, it is often convenient to use $N^{-1}df(\omega)/d\omega$, viz., the oscillator-strength spectrum per electron, as Fano [39] does. For a fuller discussion of the oscillator-strength spectra, see Fano and Cooper [41] and Inokuti [42].

In the limit of weak relaxation, i.e., $g \to 0$, Eq.(14) leads to separate expressions for $\varepsilon_1(\omega)$ and $\varepsilon_2(\omega)$:

$$\varepsilon_1(\omega) = 1 + \frac{4\pi e^2}{m} P\int_0^\infty d\omega' \, \frac{df(\omega')/d\omega'}{\omega'^2 - \omega^2} , \tag{16}$$

where P means the Cauchy principal value, and

$$\varepsilon_2(\omega) = \frac{2\pi^2 e^2}{m} \frac{1}{\omega} \frac{df(\omega)}{d\omega} . \tag{17}$$

Consider a frequency ω so high that $h\omega$ exceeds the binding energies of all the electrons in the material. Then, virtually all the oscillator strength lies below ω, and we may set $\omega^2 >> \omega'^2$ in the denominator of Eq.(16). Using the sum rule, Eq.(15), we obtain an asymptotic expression

$$\varepsilon_1(\omega) = 1 - 4\pi e^2 N/(m\omega^2). \tag{18}$$

Let us introduce the nominal plasma frequency ω_p corresponding to the total electron density N through

$$\omega_p^2 = 4\pi e^2 N/m. \tag{19}$$

Then we may write simply

$$\varepsilon_1(\omega) = 1 - (\omega_p/\omega)^2. \tag{20}$$

For a material with density $\rho(g/cm^3)$, atomic weight A, and atomic number Z, the nominal plasma energy may be expressed as

$$\hbar\omega_p = 28.816(\rho Z/A)^{1/2}(eV). \tag{21}$$

The ratio Z/A for all ordinary substances is about 1/2. Thus, we see that $\hbar\omega_p$ ranges from 20 eV to 60 eV for condensed matter with ρ ranging from unity to 10. Equation (20) holds for $\hbar\omega$ exceeding the K shell, and shows that $\varepsilon_1(\omega)$ approaches unity from below.

From Eq. (17) we see that $\omega\varepsilon_2(\omega)$ is the same as $df(\omega)/d\omega$ apart from a universal constant. Therefore, we may rewrite the sum rule as

$$\int_0^\infty d\omega \; \omega\varepsilon_2(\omega) = 2\pi^2 e^2 N/m, \tag{22}$$

or as

$$\int_0^\infty d(\omega/\omega_p)^2 \varepsilon_2(\omega) = \pi. \tag{23}$$

Let us now consider the propagation of an electromagnetic plane wave of frequency ω in a material with dielectric permeability $\varepsilon(\omega)$ and magnetic permeability $\mu(\omega)$. It is elementary to show from the Maxwell equations that the electric field E as a function of the distance x in the line of propagation obeys [37]

$$d^2E/dx^2+(\omega/c)^2\varepsilon(\omega)\mu(\omega)E = 0. \tag{24}$$

This equation has a solution of the form exp(ikx), where the wave number

$$k = (\omega/c)[\varepsilon(\omega)\mu(\omega)]^{1/2} \tag{25}$$

is a complex number. It is customary to express

$$[\varepsilon(\omega)\mu(\varepsilon)]^{1/2} = n(\omega)+i\kappa(\omega), \tag{26}$$

and call $n(\omega)$ the refractive index and $\kappa(\omega)$ the extinction coefficient, following the tradition of optics. For nonmagnetic materials, $\mu(\omega)=1$, we obtain from Eq.(26) relations

$$\varepsilon_1(\omega) = n^2(\omega)-\kappa^2(\omega), \tag{27}$$

$$\varepsilon_2(\omega) = 2n(\omega)\kappa(\omega). \tag{28}$$

The physical meanings of $n(\omega)$ and $\kappa(\omega)$ are seen from the behavior of the electric field given by $\exp[i(\omega/c)n(\omega)x]\ \exp[-(\omega/c)\kappa(\omega)x]$. Recalling the presumed time-dependence $\exp(-i\omega t)$, we see that the wave propagates at velocity c/n in an ideal case where the refractive index n is independent of ω. Otherwise, dispersion occurs, and a wave packet propagates at the group velocity $c/[d\omega n(\omega)/d\omega]$. The energy density carried by the wave is proportional to the square of the electric field, and it decreases with distance x as $\exp[-2(\omega/c)\kappa(\omega)x]$. Therefore, we call

$$A(\omega) = 2(\omega/c)\kappa(\omega) \tag{29}$$

the attenuation coefficient or the absorption coefficient, which has the dimension of an inverse length.

Let us now consider a material of low density, e.g., a gas at low pressure. Then $\varepsilon_1(\omega)$ and $n(\omega)$ are close to unity. Therefore, $\kappa(\omega)=\varepsilon_2(\omega)/2$ according to Eq.(28), and we may rewrite Eq.(29) as

$$A(\omega) = (\omega/c)\varepsilon_2(\omega) = (2\pi^2e^2/mc)df(\omega)/d\omega, \tag{30}$$

with the use of Eq.(17). Suppose that the material contains N_m molecules per unit volume, we call $\rho(\omega)=A(\omega)/N_m$ the photoabsorption cross section of the molecule, and $df_m(\omega)/d\omega=[df(\omega)/d\omega]/N_m$ the oscillator-strength spectrum of the molecule. Then, we rewrite Eq.(30) as

$$\sigma(\omega) = (2\pi^2e^2/mc)df_m(\omega)/d\omega. \tag{31}$$

Thus we see the relation of the present discussion with the earlier discussion on gaseous molecules.

Finally, we point out the relevance of $\varepsilon(\omega)$ to the relative probability of different amounts of energy transfer from a fast charged particle to materials in glancing collisions, which occur most often. This topic originates from the famous paper by Bethe [43], and has been followed up extensively by many workers [39,40,44]. Here we give only a single point of importance to the theme of the present Chapter. The probability for the transfer of energy $h\omega$ in a glancing collision of a fast charged particle is proportional to

$$\Pi(\omega) \equiv \mathrm{Im}[-1/\varepsilon(\omega)] = \varepsilon_2(\omega)/[\varepsilon_1^2(\omega)+\varepsilon_2^2(\omega)]. \tag{32}$$

This result seems to have been first recognized by Fermi [45], and has been derived by many authors at varying levels of rigor and generality, e.g., by Fano [39,40]. An excellent treatment is seen in the textbook of Landau and Lifshitz [37]. Remarks by Fano [46] on Eq.(32) and related topics such as collective excitation are also useful.

A few points about Eq.(32) are noteworthy. Recall that the largest impact parameter effective for the energy transfer $\hbar\omega$ from a particle of speed v is about v/ω, which corresponds to some tens of intermolecular distance in ordinary condensed matter for a relativistic speed v close to c. Then, there are many molecules within the impact parameter and they screen in part the electric field of the charged particle. The denominator $\varepsilon_1^2(\omega)+\varepsilon_2^2(\omega)$ represents the degree of screening of the interactions between the charged particle and electrons that receive energy. The denominator makes $\Pi(\omega)$ different from the strength of photoabsorption which is given by $\varepsilon_2(\omega)$ according to Eq.(30).

Consider again a low-density material, e.g., a low-pressure gas. Then $\varepsilon_1(\omega)$ is close to unity, and $\varepsilon_2(\omega)$ is much smaller than unity; therefore, the denominator is close to unity, and $\Pi(\omega)$ is nearly the same as $\varepsilon_2(\omega)$.

In condensed matter, $\Pi(\omega)$ may differ from $\varepsilon_2(\omega)$ in some frequency domains. The most drastic difference between $\Pi(\omega)$ and $\varepsilon_2(\omega)$ is seen near ω at which $\varepsilon_1(\omega)=0$, if this occurs at all. In this event $\Pi(\omega)=1/\varepsilon_2(\omega)$ at that ω, and has high values in the neighborhood. The vanishing of $\varepsilon_1(\omega)$ indeed occurs for metals, as is readily expected for the following reason. At low frequencies $\varepsilon_1(\omega)$ must be negative for a conductor [37], at very high frequencies $\varepsilon_1(\omega)$ must be positive for any material according to Eq.(18). Therefore, at some frequency ω_{pc}, we must have $\varepsilon_1(\omega_{pc})=0$, so long as $\varepsilon_1(\omega)$ is a continuous function of ω. We call ω_{pc} the plasma frequency for conduction electrons. If we calculate the effective density n_c of conduction electrons according to $\omega_{pc}=(4\pi e^2 n_c/m)^{1/2}$ the result usually comes out to be sensible. In metallic aluminum [47,48], for example, $\hbar\omega_{pc}=15$eV, and hence $n_c=2.7$ per atom. This agrees roughly with the number of valence electrons (three) of an aluminum atom.

5.5.2 SELECTED DATA

A comprehensive survey of data on $\varepsilon(\omega)$ for various materials is beyond the scope of the present report. Extensive data on metals, semiconductors, and inorganic insulators are given in a handbook edited by Palik [48]. A monograph by Egerton [49] is

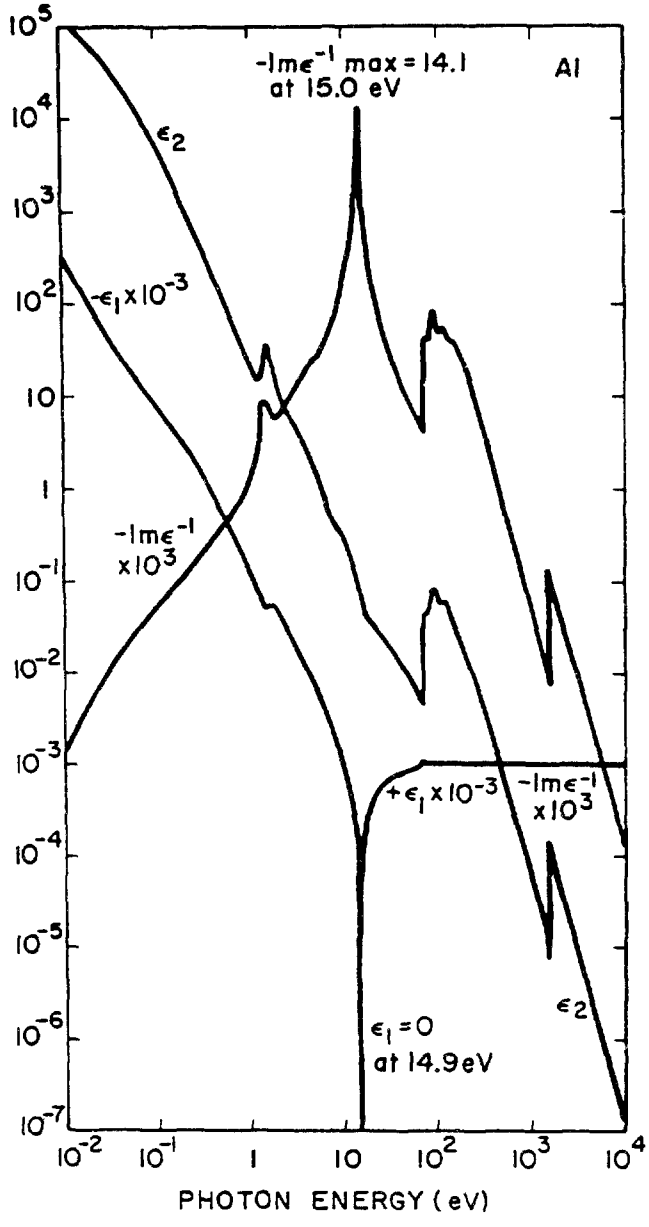

FIG. 5.13 *Dielectric response function for metallic alminum [50]. The real part $\varepsilon_1(\omega)$ is negative and has a large absolute value below 14.9 eV; therefore, $-\varepsilon_1(\omega)x10^3$ is plotted. The imaginary part $\varepsilon_2(\omega)$ shows a generally decreasing trend with increasing photon energy $\hbar\omega$. The small peak at about 2 eV arises from intra-band transitions of conduction electrons, the large peak around 110 eV from the L-shell excitation, and the peak around 1200 eV from the K-shell excitation.*

also valuable as a source of data. In what follows, we present a discussion on materials selected for the illustration of a few notable points.

As an example of metals, we take aluminum, for which a comprehensive analysis has been given [47,50]. A similar analysis for silicon has been also given [51]. Figure 13 is a summary of the result on aluminum [50]. At low energies $\hbar\omega$ up to several eV, $\varepsilon(\omega)$ is represented well with a fit according to the Drude model, i.e.,

$$\varepsilon(\omega) = 1-(\omega^*)^2/(\omega^2-i\gamma\omega), \tag{33}$$

where $\hbar\omega^*$=12.5 eV and $\hbar\gamma$=0.0614 eV. This value of $\hbar\omega^*$ is close to the plasma energy of the conduction electrons, $\hbar\omega_{pc}$=14.9 eV, but not equal to it. This means that a simple model often describes the behavior of $\varepsilon(\omega)$ over a limited range, but cannot be correct over the entire range. At low energies, both $-\varepsilon_1(\omega)$ and $\varepsilon_2(\omega)$ are large, and $\Pi(\omega)$ is small. Near the plasma energy of conduction electrons $\Pi(\omega)$ shows a prominent peak. At energies far above

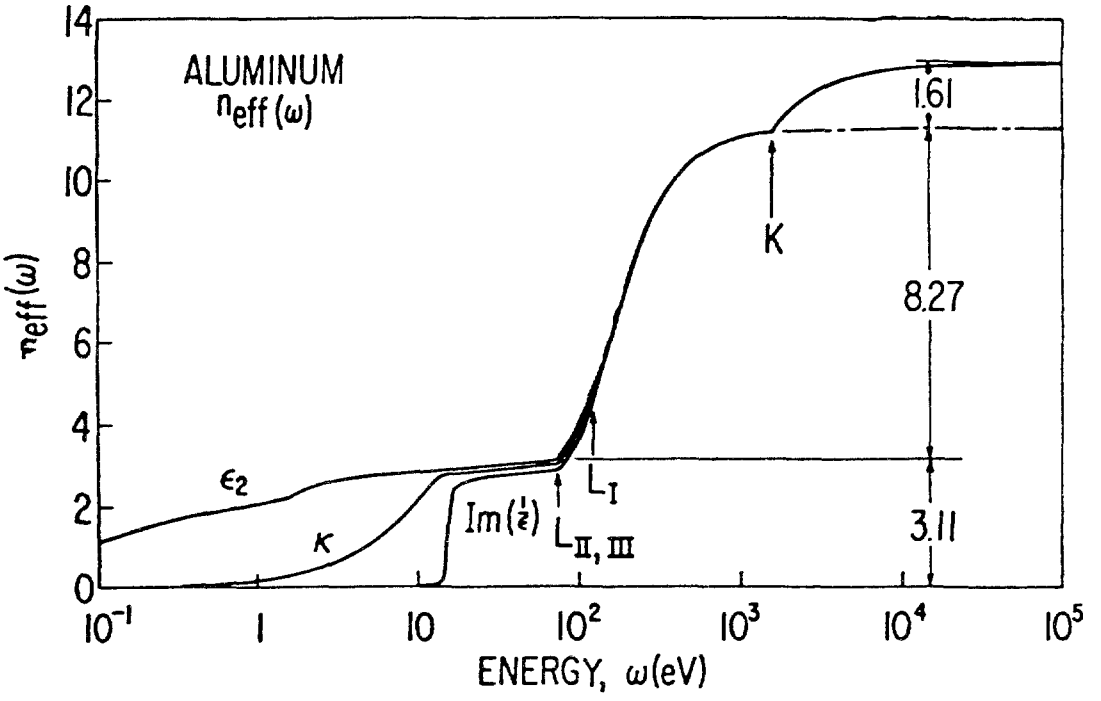

FIG. 5.14 *Illustration of the sum rules for metallic aluminum [47].*

$h\omega_{pc}$, $\varepsilon_1(\omega)$ is practically unity and $\varepsilon_2(\varepsilon)$ is much smaller than unity. As a result, $\Pi(\omega)$ is almost the same as $\varepsilon_2(\omega)$. However, exceptions arise near the L-shell and K-shell thresholds, where $\varepsilon_2(\omega)$ and $\Pi(\omega)$ differ in fine structures (which are undiscernible in Fig.13). Figure 14 illustrates the sum rules [47]. The curve labeled "$\varepsilon_2(\omega)$" represents an effective electron number, i.e.,

$$n_{eff}(\omega) = \frac{m}{2\pi^2 e^2}\int_0^{\omega} d\omega' \omega' \varepsilon_2(\omega'). \qquad (34)$$

According to Eq.(22), $n_{eff}(\omega)$ should approach 13 as $\omega \to \infty$. The figure also includes two other quantities defined by replacing $\varepsilon_2(\omega)$ with $\mathrm{Im}[-1/\varepsilon(\omega)]$ or $\kappa(\omega)$ in Eq.(34). The total effective number of electrons is 3.11 for the M-shell, 8.27 for the L-shell, and 1.61 for the K-shell. These values roughly correspond to the electron configuration $1s^2 2s^2 2p^6 3s^2 3p$ of a free atom of aluminum.

The occurrence of the plasma excitation in metals is most often explained by the theory of a free-electron gas with a background of uniform positive charge, as developed by Bohm and Pines [52-54]. More generally, the occurrence is understandable from a criterion for collective excitation given by Fano [55]. Suppose that a condensed material is formed from structural units, e.g., atoms or molecules, which we may call monomers. Let the oscillator-strength spectrum of the isolated monomer by $df_m(\omega)/d\omega$. Fano showed that

$$u(\omega) = \omega_{pv}^2 df(\omega)/d\omega^2 \qquad (35)$$

is a crucial index, where ω_{pv} represents the plasma frequency of the valence electrons in the condensed matter. Note that the differential in Eq.(35) is with respect to ω^2 and not ω. The quantity $u(\omega)$ signifies the density of oscillator strength in space and energy squared. (A more general interpretation of $u(\omega)$ has been given recently [56]. If the density is sufficiently high, the condensed-matter spectrum will differ appreciably from the monomer spectrum. When this occurs, excited electrons in the condensed matter will be spatially limited by the presence of neighbouring monomers, and an associated oscillator strength will be shifted to higher energies upon going from a monomer to the

condensed matter. When $u(\omega)$ is much greater than unity in a region of ω, the condensed-matter spectrum differs considerably from the monomer spectrum in that region. When $u(\omega)$ is much smaller than unity, the two spectra are the same. If we examine data for an element that form a metal, we find that the lowest valence excitation in an atom indicates $u(\omega)>>1$ and thus leads to the plasma excitation. Inokuti [42] showed this in an example of lithium.

Materials of interest to radiation chemistry and biology include water and organic substances. The spectra of many molecules of such substances are known, as described earlier in the present chapter. With the use of data on those molecules, we find that $u(\omega)$ often reaches a maximum of 0.1-0.3 somewhere at excitation energies of $h\omega$ ranging from 10 to 25 eV, as first pointed out by Platzman [18]. The values 0.1-0.3 are tantalizing. The influence of collective effects is not as clear-cut as in metals, but is not negligible. However, in certain cases we have a clear conclusion. In benzene and other aromatic molecules, we find that $u(\omega)>1$ in a narrow region around several eV. This indicates the occurrence of excitons as we know in crystals of those molecules.

Finally, we turn to data on $\varepsilon(\omega)$ for materials of this kind. Birkhoff, Painter, and coworkers [57-63] measured reflection of photons by liquid water, liquid organics and solid organics, and thereby determine $\varepsilon(\omega)$ up to $\hbar\omega \simeq 20$eV. Another method of study is the measurements of the electron energy loss spectra, which are closely related to $\Pi(\omega)$. For example, studies by Killat [64,65] on hydrocarbons and by Isaacson [66] on nucleic acid bases are of particular interest to radiation chemists and biologists. More recently, Dillon et al [67]. measured electron energy-loss spectra of adenine in gas and found them similar to spectra in solid films [66]. More data are seen in many references quoted by Egerton [49] and in a review article by Koch and Otto [68].

Typical data are seen in Fig.15 for polyethylene [63]. The function $\Pi(\omega)$ shows a prominent peak around 20 eV. However, this peak is similar to a peak in the corresponding monomer spectrum and is located only a few eV higher. The real part $\varepsilon_1(\omega)$ does not

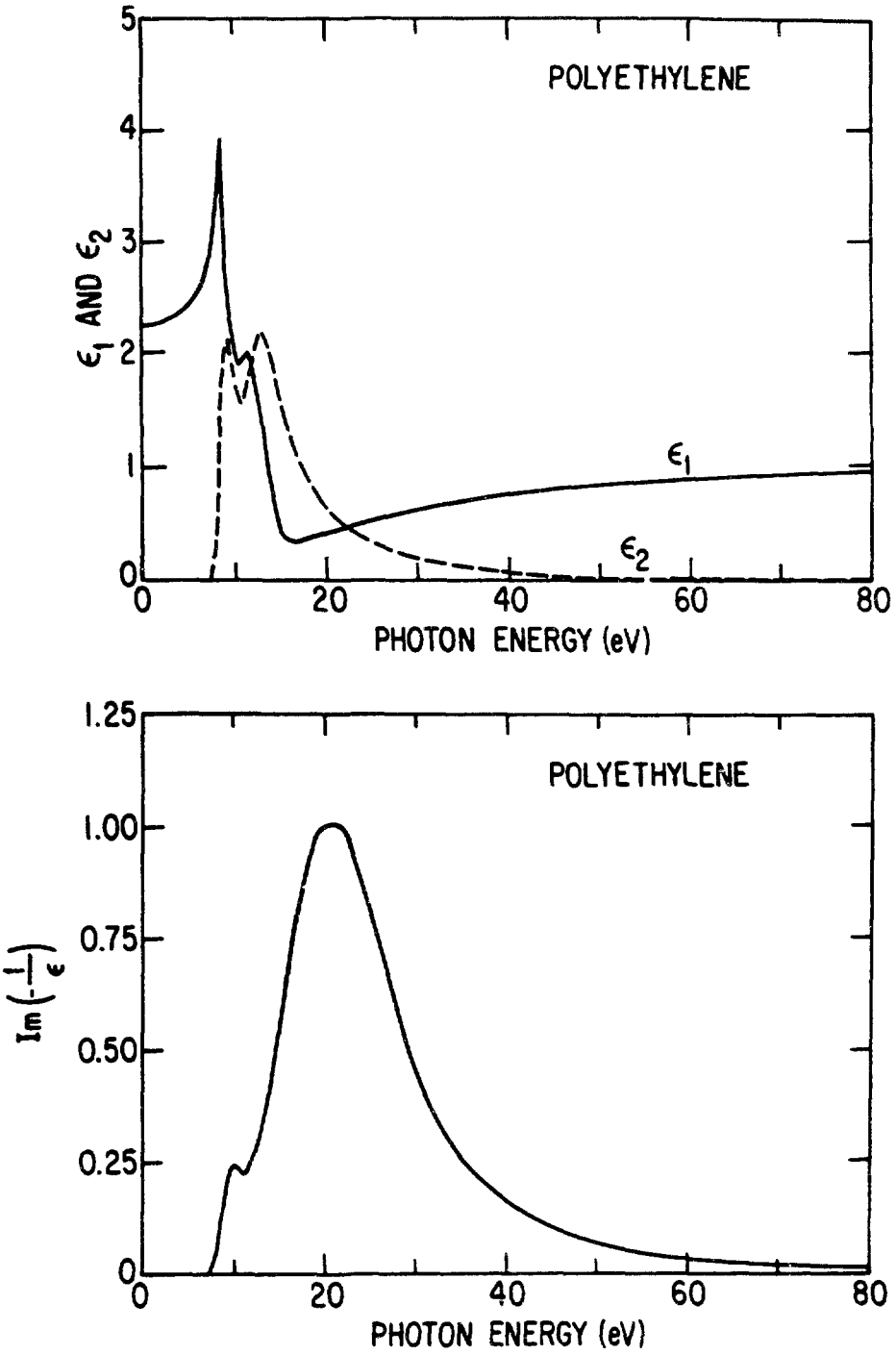

FIG. 5.15 *Dielectric-response function for polyethylene [63].*

vanish and merely shows a minimum around 15 eV. In general $\varepsilon_1(\omega)$ is positive throughout, although at low ω, $\varepsilon_1(\omega)$ shows some structures. The imaginary part $\varepsilon_2(\omega)$ certainly differs from $\Pi(\omega)$, but the difference is not as dramatic as in metals. This observation is consistent with the result that $u(\omega)$ is not negligible compared with unity but is substantially smaller than unity. Consequently, we may conclude that there are modest effects of collective excitation in the materials of this kind.

5.6 CONCLUDING REMARKS

The measurements of photoabsorption, photoionization, and photodissociation cross sections have advanced rapidly for a variety of polyatomic molecules at least in the gas phase in a wide range of energy including the VUV-SX region, and have just started to bridge a wide gap existing between radiation chemistry and photochemistry.

Some future problems to need more work are,

1) Cross sections should be measured for more of the chemically and biologically important molecules.
2) Cross sections should be measured for condensed phase systems which are of importance in radiation research.
3) The cross sections should be measured also for high pressure gases or cluster systems to provide a basis for understanding the effect of inter-molecular interactions on the cross sections.
4) For better substantiation of ionization phenomena in the condensed phase as compared with those in the gas phase, the measurement has been already made of the ionization threshold energy in nonpolar liquids. A key experiment, however, for this purpose should be the measurement of the absolute ionization quantum yield values in liquids.

ACKNOWLEDGEMENTS

Y.H. is indebted to Drs. N.Kouchi, M.Ukai, K.Kameta, and graduate students in his group for their excellent collaboration in the synchrotron radiation research described in this chapter. This research has been supported scientifically by the staffs of the PF-KEK and financially by the Ministry of Education, Science and Culture, Japan. The M.I.'s work described herein was supported by the US Department of Energy, Office of Health and Environmental Research.

REFERENCES

[1] Proceedings of the IAEA Advisory Group Meeting on Atomic and Molecular Data for Radiotherapy, Vienna, June 13-16, 1988, IAEA-TECDOC-506 (1989).
[2] INOKUTI, M., ed., Proceedings of the Workshop on Electronic and Ionic Collision Cross Sections Needed in the Modeling of Radiation Interactions with Matter, ANL-84-28 (1984).
[3] GERWARD, L., Radiat.Phys.Chem. 41(1993)783.
[4] BERGER, M. and HUBBELL, J.H., National Bureau of Standards Internal Report (1987) 87-3597.
[5] CREAGH, D.C. and HUBBELL, J.H., International Tables for Crystallography, Vol.C, ed. A.J.C. Wilson, Kluwer Academic, Dordrecht (1992) p.189.
[6] HENKE, B.L., LEE, P., TANAKA, T.J., SHIMABUKURO, R.L., and FUJIKAWA, B.K., Atom. Data Nucl. Data Tables, 27(1982)1.
[7] SALOMAN, E.B., HUBBELL, J.H., and SCOTFIELD, J.H., ibid., 38 (1988)1.
[8] HATANO, Y., "The Chemistry of Synchrotron Radiation" in "Radiation Research", ed. E.M. Fielden, J.F. Fowler, J.H. Hendry, and D. Scott, Taylor & Francis (1987) p.35.
[9] KAPLAN, I.G., personal communication.
[10] MOROSOV, I.I. and MYASNIK, M.N., Radiat.Res. 82(1980)336.
[11] REDPATH, J.L., ZABILANSKY, E., MORGAN, T., and WARD, J.F., Int.J.Radiat.Biol. 39(1981)569.
[12] MICHAEL, B.D., HARROP, H.A., and HELD, K.D., J.Radiat.Biol. 82(1981)580.
[13] KATSUMURA, Y., Handbook of Radiation Chemistry, ed. Y. Tabata, Y. Ito, and S. Tagawa, CRC Press, Boca Raton (1991) p.300.
[14] KATSUMURA, Y., TABATA, Y., and TAGAWA, S., Radiat.Phys. Chem. 24(1985)489.
[15] INOKUTI, M., Photochem.Photobiol. 44(1986)279.
[16] INOKUTI, M., Rev.Mod.Phys. 43(1971)297.
[17] INOKUTI, M., "Radiation physics as a basis of radiation chemistry and biology", in: Applied Atomic Collision Physics, Vol.4, ed. S. Datz, Academic Press, New York (1983) p.179.
[18] PLATZMAN, R.L., in "Radiation Research", Proceedings of the Third Congress of Radiation Research, Cortina d'Ampezzo. Italy, 1966, ed. G. Silini, North-Holland, Amsterdam (1967) p.20.

[19] SHIDA, S. and HATANO, Y., Int.J.Radat.Phys.Chem. 8(1976)171.
[20] KOIZUMI, H., YOSHIMI, T., SHINSAKA, K., UKAI, M., MORITA, M., HATANO, Y., YAGISHITA, A., and ITO, K., J.Chem.Phys. 82 (1985)4856.
[21] KOIZUMI, H., HIRONAKA, K., SHINSAKA, K., ARAI, S., NAKAZAWA, H., KIMURA, A., HATANO, Y., ITO, Y., ZHANG, Y.W., YAGISHITA, A., ITO, K., and TANAKA, K., ibid., 85(1986)4276.
[22] KOIZUMI, H., SHINSAKA, K., YOSHIMI, T., HIRONAKA, K., ARAI, S., UKAI, M., MORITA, M., NAKAZAWA, H., KIMURA, A., HATANO, Y., ITO, Y., ZHANG, Y.W., YAGISHITA, A., ITO, K., and TANAKA, K., Radiat.Phys.Chem. 32(1988)111.
[23] KOIZUMI, H., SHINSAKA, K., and HATANO, Y., ibid., 34(1989) 87.
[24] PLATZMAN, R.L., Vortex, 23(1962)372.
[25] PLATZMAN, R.L., Radiat.Res. 17(1962)419.
[26] KAPLAN, I.G. and MITEREV, A.M., Adv.Chem.Phys. 68(1987)255.
[27] HATANO, Y., Radiochim.Acta. 43(1989)119.
[28] HATANO, Y., Comm.At.Mol.Phys. 13(1983)259.
[29] HATANO, Y., "Dynamics of Superexcited Molecules", in "Dynamics of Excited Molecules", ed. K. Kuchitsu, Elsevier, Amsterdam, in press.
[30] GALLAGHER, J.W., BRION, C.E., SAMSON, J.A.R., and LANGHOFF, P.W., J.Phys.Chem.Ref.Data, 17(1988)9.
[31] UKAI, M. et al., to be published.
[32] KAMETA, K., UKAI, M., KAMOSAKI, T., SHINSAKA, K., KOUCHI, N., HATANO, Y., and TANAKA, K., J.Chem.Phys. 96(1992)4911.
[33] POTTS, A.W., WILLIAMS, T.A., and PRICE, W.C., Faraday Discuss.Chem.Soc. 54(1972)104.
[34] UKAI, M., KAMETA, K., CHIBA, R., NAGANO, K., KOUCHI, N., SHINSAKA, K., HATANO, Y., UMEMOTO, H., ITO, Y., and TANAKA, K., J.Chem.Phys. 95(1991)4142.
[35] KAMETA, K., UKAI, M., CHIBA, R., NAGANO, K., KOUCHI, N., HATANO, Y. and TANAKA, K., ibid., 95(1991)1456.
[36] COOPER, G., IBUKI, T., and BRION, C.E., Chem.Phys. 140(1990) 133.
[37] LANDAU, L.D. and LIFSHITZ, E.M., Electrodynamics of Continuous Media, translated by J.B. Sykes and J.S. Bell, Pergamon Press, Oxford (1960), Chapters 9 and 12.
[38] NOZIERES, P. and PINES, D., Nuovo Cimento 2(1958)470.
[39] FANO, U., Phys.Rev. 103(1956)1202.
[40] FANO, U., Ann.Rev.Nucl.Sci. 13(1962)1.
[41] FANO, U. and COOPER, J.W., Rev.Mod.Phys. 40(1968)441.
[42] INOKUTI, M., Radiat. Effects Defects Solids 117(1991)143.
[43] BETHE, H., Ann.Phys. (Leipzig) 5(1930)325.
[44] INOKUTI, M., Rev.Mod.Phys. 43(1971)297.
[45] FERMI, E., Phys.Rev. 57(1940)485.
[46] FANO, U., in Penetration of Charged Particles in Matter, Proceedings of an Informal Conference, Gatlinburg, Tennessee. 15-18 September 1958, ed. A. Edwin Vehling, Publication 752, National Academy of Sciences National Research Council, Washington, D.C. (1960) p.158.
[47] SHILES, E., SASAKI, T., INOKUTI, M., and SMITH, Y.D., Phys. Rev. B22(1980)1612. See also p.369 of Ref.[48].
[48] PALIK, E.D., ed., Handbook of Optical Constants of Solids, Academic Press, Inc., Orlando, Florida (1985).
[49] EGERTON, R.F., Electron Energy-Loss Spectroscopy in the Electron Microscope, Plenum Press, New York (1986).
[50] INOKUTI, M. and SMITH, D.Y., Phys.Rev. B25(1982)61.
[51] BICHSEL, H., Rev.Mod.Phys. 60(1988)663.

[52] PINES, D. and BOHM, D., Phys.Rev. 85(1952)338.
[53] BOHM, D. and PINES, D., ibid., 92(1953)609.
[54] PINES, D., ibid., 92(1953)626.
[55] FANO, U., ibid., 118(1960)451.
[56] FANO, U., Rev.Mod.Phys. 64(1992)314.
[57] KERR, G.D., HAMM, R.N., WILLIAMS, M.W., BIRKHOFF, R.D., and PAINTER, L.A., Phys.Rev. A5(1972)2523.
[58] HELLER, J.M.Jr., BIRKHOFF, R.D., WILLIAMS, M.W. and PAINTER, L.R., Radiat.Res. 52(1972)25.
[59] HELLER, J.M. Jr., HAMM, R.N., BIRKHOFF, R.D. and PAINTER, L.R., J.Chem.Phys. 60(1974)3483.
[60] INAGAKI, T., HAMM, R.N., ARAKAWA, E.T. and PAINTER, L.R., ibid., 61(1974)4246.
[61] WILLIAMS, M.W., HAMM, R.N., ARAKAWA, E.T. and PAINTER, L.R., Int.J.Radiat.Phys.Chem. 7(1975)95.
[62] BIRKHOFF, R.D., PAINTER, L.R. and HELLER, J.M., J.Chem.Phys. 69(1978)4185.
[63] PAINTER, L.R., ARAKAWA, E.T., WILLIAMS, M.W. and ASHLEY, J.C., Radiat.Res. 83(1980)1.
[64] KILLAT, U., Z.Phys. 263(1973)83.
[65] KILLAT, U., J.Phys. C7(1974)2396.
[66] ISAACSON, M., J.Chem.Phys. 56(1972)1803.
[67] DILLON, M.A., TANAKA, H. and SPENCE, D., Radiat.Res. 117 (1989)1.
[68] KOCH, E. and OTTO, A., Int.J.Radiat.Phys.Chem. 8(1976)113.

Chapter 6

COLLISION PROCESSES BETWEEN IONS AND EXCITED NEUTRALS AND SURROUNDING MOLECULES

Z. Herman
J. Heyrovský Institute of Physical Chemistry and Electrochemistry,
Prague, Czech Republic

T.D. Märk
Universität Innsbruck,
Innsbruck, Austria

L. Sanche
Université de Sherbrooke,
Sherbrooke, Canada

The authors acknowledge the valuable contribution to this chapter by Y. Hatano, Tokyo Institute of Technology, Tokyo, Japan.

6.1. INTRODUCTION

In this chapter we deal with elementary processes in the physico-chemical stage of radiolysis in which ions and excited neutrals (formed in primary events or secondary electron processes) change their chemical or energetic nature in collisions with other molecules. These processes represent an important step in the development of the system which links the physics of the initial processes with the chemistry of subsequent events (mainly chemical reactions of radicals formed by neutralization of relatively stable charged species and/or dissociation of energy rich neutral species).

Better understanding of radiation effects related to radiation therapy includes understanding of basic features of fundamental processes in this stage of interaction of radiation with matter. Quantitative information, namely, cross section or rate data on various elementary processes are provided by atomic and molecular physics research. We summarize here information on main elementary processes relevant to the problem.

The elementary processes concern, first of all, a large variety of encounters between ions and molecules, namely:

- chemical reactions of positive and negative ions
- charge transfer processes
- recombination processes between ions and electrons or between ions of opposite charge

Secondly, there are elementary processes involving collisions of electronically excited neutrals with molecules, in particular

- ionization processes
- excitation energy transfer leading to neutral species

In the following, first of all the basic characteristics of the above mentioned processes will be given, as obtained from studies in the gaseous phase. Then the fundamental processes involving clusters will be discussed, and - finally - fundamental processes in the condensed phase will be shortly treated. Thereafter, relevant data on the elementary processes will be summarized in tables. The tables concern data on cross sections or rate constants of the elementary processes in question. It is important to complement the rate data with thermochemical data of the species on question. Therefore, the tables contain also data on ionzation potentials, proton and electron affinities of molecules, and heats of formation of ions and neutral species.

There have been several reviews on the above mentioned elementary processes over the last twenty years as well as data tabulations. Here we

point out some of the useful sources of information. Thermochemical data on the species in question have been summarized in excellent reviews [1,2], proton affinities in recent tables [3], and general data on properties of atoms, molecules nad ions are given in the Radzig-Smirnov book [4]. Data on rate constants of ion-molecule reactions and charge transfer processes have been summarized in two large reviews [5,6], Penning ionization and related processes have been treated in [7]. Quite recently, fundamental processes in radiation chemistry have been extensively reviewed [8].

6.2. ELEMENTARY PROCESSES

6.2.1. **Chemical Reactions of Positive and Negative Ions**

Chemical reactions of ions are elementary collisions processes occurring between a (positively or negatively) charged particle and a neutral molecule in which a chemical bond rearrangement takes place (usually an old bond is broken and a new bond formed). As a result, products chemically different from reactants are formed, one of the products is charged. Schematically one can write

$$A^+ + BC \rightarrow AB^+ + C \qquad (1)$$

or, for example,

$$A^- + BC \rightarrow AB + C^- \qquad (2)$$

where A, B, C are atoms or groups of atoms.

Ion-molecule reactions have been systematically investigated by mass spectrometric methods as single-collision processes since the early fifties and large amount of data was accumulated on reactive cross sections and their dependence on energy. Dynamics of the reactions has been ivestigated. From the point of view of reaction data, perhaps the most valuable source of information are results of swarm studies. Flow-tube (FT) and selected-ion-flow-tube (SIFT) investigation of ion-molecule chemical reactions has provided a wealth of reaction rate constants on a variety of processes in the thermal energy region. An equally important source of information on reaction rate constants are results of ion cyclotron resonance studies.

In this chapter we deal with the collision behaviour of ions and excited neutrals formed in primary and secondary energy-deposition events.

Therefore, we are concerned primarily with collision processes of energy-rich particles of thermal translational energies, and we will omit from discussion their hyperthermal behaviour.

Rates of chemical reactions of ions are given usually as the reaction cross section, $\sigma(v)$, for a specific relative velocity v of the reactants, and measured usually in cm^2 or $Å^2$. For thermal particles the rate is more often expressed as reaction rate constant k(T), at a given temperature T, in units of cm^3/s. The relation between these two important quantities one obtains, if one realizes that the rate constant is a quantity averaged over the Boltzmann distribution of the reactant relative velocities at a given temperature. It holds, therefore,

$$k(T) = \int_0^\infty f(v,T)\, \sigma(v)\, v\, dv \qquad (3)$$

where f(v,T) is the velocity distribution temperature T. One can write compactly as

$$k(T) = \langle v\, \sigma(v) \rangle \qquad (4)$$

an average of cross section over the Boltzmann distribution of velocities. A full calculation leads to the expression

$$k(T) = (\pi\mu)^{-1/2}\, (2/kT)^{3/2} \int_0^\infty dE_{tr}\, E_{tr}\, \sigma(E_{tr})\, \exp(-E_{tr}/kT) \qquad (5)$$

where $\sigma(v)$ is replaced by $\sigma(E_{tr})$, cross section in dependence on (relative) translational energy of the reactants (μ is reduced mass, k - Boltzmann constant).

A basic feature of chemical reactions of ions is their very high rate in comparison with chemical reactions of neutrals (cross sections of the order of $10^{-14} cm^2$ at thermal energies or rate constats of about $10^{-9} cm^3/s$). The reason for it is the attractive ion - induced dipole interaction between the colliding particles which results in potential energy surfaces of basically attractive type without an activation barrier. (Activation barriers, if any in ion-molecule processes, result rather from crossing of potential energy surfaces in cases of reactions occurring non-adiabatically than from a movement of the system on a single potential energy surface). Reaction thus tend to occur at every collision and thermal reaction rates approach often the "Langevin collisional limit", k_L

$$k_L = 2\pi e (\alpha/\mu)^{1/2} \qquad (6)$$

(e - electron charge, α - neutral partner polarizability) which essentially determines, when a colliding pair ion - induced dipole can still be brought together within the orbiting capture radius. A rate constant appreciably

smaller than k_L means usually that there is a competing (or consecutive) process to the formation of a product in question. Endoergic processes of ground-state species have mostly negligible rates being limited by the exponential factor in the translational energy distribution. Moreover, translational energy is usually not very efficient in overcoming the endoergicity barrier. On the other hand, internal energy (i.e. vibrational or electronic excitation) of reactants has been shown to be very often quite efficient in overcoming the endoergicity barrier.

Chemical reactions of ions may be grouped into various classes according to which particle is being transferred during the process. A very important class of reactions represent processes in which a proton or a H-atom is transferred and a protonated molecule formed as the ion product:

$$AH^+ + B \rightarrow A + BH^+ \quad (7)$$

$$A^+ + BH \rightarrow AH^+ + B \quad (8)$$

The proton and H-atom transfer processes occur usually in a direct manner, i.e. the chemical change is accomplished during about one vibrational period; in many cases, however, an intermediate, thermodynamically stable species may be formed. Thus, e.g., the important reaction between water and water cation - a basic reaction in water containing systems -

$$H_2O^+ + H_2O \rightarrow H_3O^+ + OH \quad (9)$$

occurs by both direct proton and H-atom transfer, and by the intermediate species formation. The formation of the intermediate complex is important especially in condensed phases, where it may be stabilized in collisions with the surrounding molecules to form $(H_3O..OH)^+$.

Another important reaction type is H^- (hydride ion) transfer

$$A^+ + BH \rightarrow AH + B^+ \quad (10)$$

Other reactions concern transfer of functional groups, formation of new C-C bonds, transfer of other atoms etc. as can be seen in processes listed in the tables.

6.2.2. Charge Transfer Processes

Charge transfer (charge exchange, electron transfer, electron capture) processes represent another important elementary process in collisions of ions and molecules. They can be symbolized as

$$A^+ + BC \rightarrow A + BC^+ \quad (11)$$

$$A^+ + BC \rightarrow A + B^+ + C \quad (12)$$

Process (11) is usually referred to as non-dissociative, (12) as dissociative charge transfer. Thus, an electron is exchanged between the colliding particles, no new bond is formed, a bond may be broken in the dissociative process. Analogous processes occur with negative ions, too.

Positive ions, as electron-deficient species, have very often low-lying electonic states. Therefore, several electronic states may be involved in their collision processes. Charge transfer represents a typically non-adiabatic process during which the system passes from one potential energy surface, correlating with the reactant pair, to another surface, characterizing the product pair. Charge transfer processes often occur as competing processes to chemical reactions of ions.

Cross sections of charge transfer processes are usually comparable in size with cross sections of chemical reactions of ions. For rate processes of charge transfer at thermal energies analogous relations hold as for chemical reactions (see paragraph 2.1.). Rate constats are often used instead of velocity dependent reaction cross sections; some of the data are summarized in the tables of this chapter.

6.2.3. Recombination Processes

A positive ion can recombine either with an electron or with a negative ion.

In a recombination process of a positive ion and an electron, the surplus energy may be either radiated (radiative recombination (13)), released in a dissociative process (dissociative recombination (14)), or taken away by a third body (three-body recombination (15)). In all cases part of the energy may be stored as internal excitation of the molecular species formed in the process (e.g., M').

$$AB^+ + e \rightarrow AB + h\nu \qquad (13)$$

$$AB^+ + e \rightarrow A + B \qquad (14)$$

$$AB^+ + e + M \rightarrow AB + M' \qquad (15)$$

Quantitative data on rates of recombination processes are presented as recombination coefficients α_R (in cm /s) and for two-body recombination they are of the order of 10^{-7} cm^3/s; this corresponds, for thermal velocities, to average cross sections of the order of 10^{-12} to 10^{-11} cm^2.

Recombination processes occurring in collisions of positive and negative ions may be described in an analogous way as radiative

recombination (16), mutual neutralization by electron exchange (17), and three-body recombination (18)

$$A^+ + B^- \rightarrow AB + h\nu \quad (16)$$

$$A^+ + B^- \rightarrow A' + B' \quad (17)$$

$$A^+ + B^- + M \rightarrow AB + M' \quad (18)$$

Recombination rate coefficients areeven larger than for the ion-electron recombination being of the order of $10^{-6}cm^3/s$ for most simple gases; this corresponds to the average cross sections at thermal energies of 10^{-10} to 10^{-9} cm^2.

6.2.4. Ionization Processes in Collisions of Electronically Excited Neutrals

Elementrary ionization processes in collision of electronically excited neutral particles with molecules are Penning ionization(19), associative ionization (20), and chemical rearrangement ionization (21).

$$A^* + BC \rightarrow A + BC^+ + e \quad (19)$$

$$A^* + BC \rightarrow ABC^+ + e \quad (20)$$

$$A^* + BC \rightarrow AB^+ + C + e \quad (21)$$

The necessary conditions for these processes is that the excitation energy of A^*, $E_e(A^*)$, is higher than the ionization potenial of BC, IP(BC). The energy of the released electron, E_{el}, is given by

$$E_{el} = E_e(A^*) - IP(BC) - \Delta E \quad (22)$$

where $\Delta E = E_r - E_p$ is an energy term which takes into account interactions between the reactant (E_r) and product (E_p) particles at the internuclear distance where the ionization process occurs.

A collision of an electronically excited neutral particle with a molecule does not necessarily result in an ionization process [19,20,21], even if the excitation energy is higher than ionization energy of the molecule BC. An exitation energy transfer leading to a superexcited neutral molecule may occur, with the excitation energy of the neutral molecule being higher than its ionization potential. This is the basis of the Jesse effect, discussed in detail elsewhere in this book (Chapter 5) because of its importance in highly energized systems.

A schematic of potential energy curves for the Penning and associative ionization process X^*+ Y suggest the mechanism [9] (Fig.1a): Penning

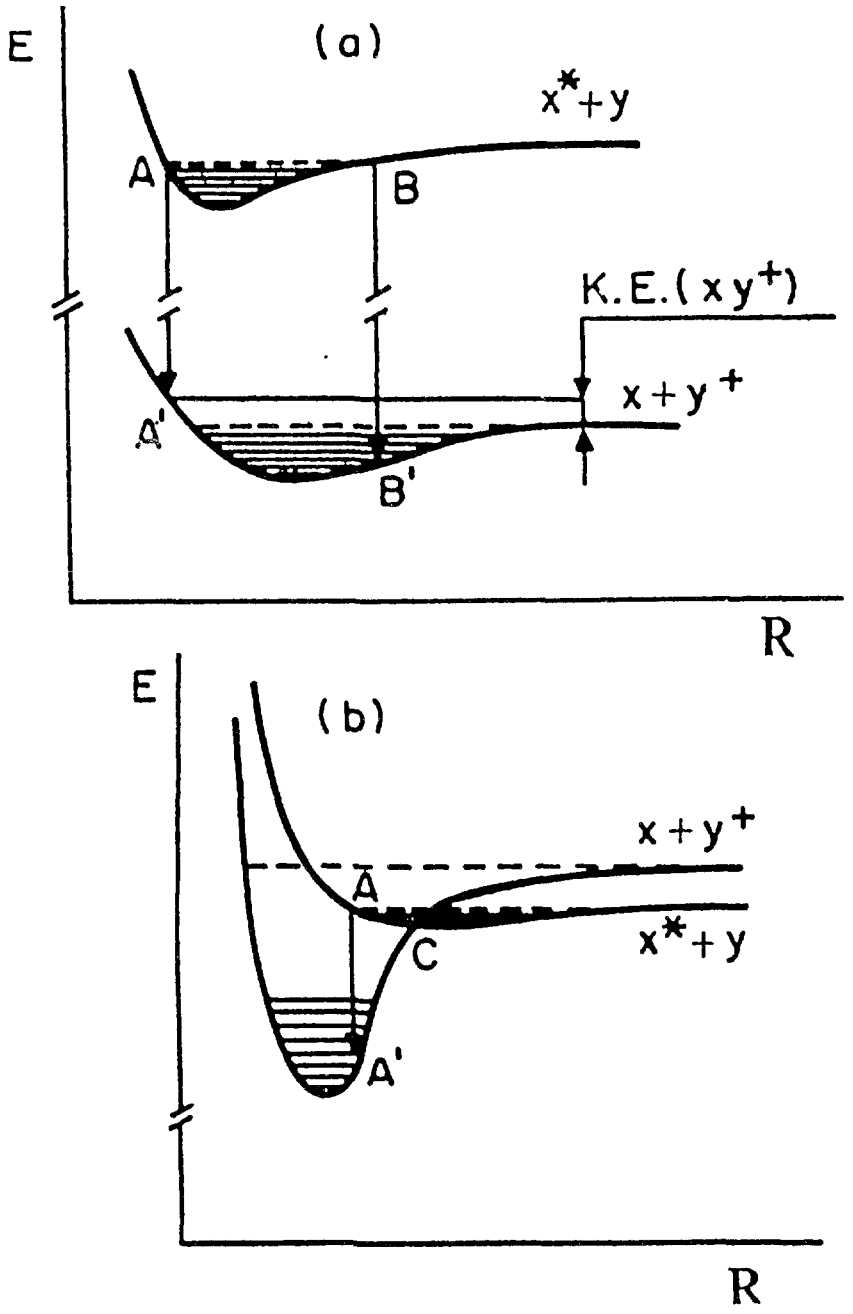

FIG. 6.1. Schematics of the mechanism of the Penning and associative ionization (a) and of the chemiionization (b) process (after [9]).

ionization occurs in the A-A' transition, associative ionization in B-B'. The latter takes place, if the sum of ΔE and the relative collision energy of reactants is negative. The Penning, associative, and chemical rearrangement ionization may occur in competition.

A special case of associative ionization is the chemiionization process in which the excitation energy of A^* is lower than the ionization potential of the target particle CD and ionization occurs on the expenses of forming a chemical bond, process (23); potential energy curves for the chemiionization $X^* + Y$ are shown in Fig. 1b.

$$A^* + CD \rightarrow ACD^+ + e \qquad (23)$$

and $E_e(A) < IP(CD)$

A chemical rearrangement process (24) may occur in some cases as a competing process to chemiionization

$$A^* + CD \rightarrow AC^* + D + e \qquad (24)$$

under the same condition, i.e. $E_e(A) < IP(CD)$.

Penning and associative ionization processes have been investigated mostly in collisions of metastable rare gas atoms and atoms or molecules. A large amount of data on these processes show that thermal rate constants are of the order of 10^{-11} to 10^{-10} cm^3/s which corresponds to average cross sections of 10^{-16} to 10^{-14} cm^2. General conclusions relating the cross sections to the spatial electron distributions of the outermost orbital of the target have been recently formulated [10a]. However, studies have been by no means limited only to excited noble gas projectiles. Among others, higher lying electonic excited states of other atoms or molecules as well as Rydberg states of atoms and molecules have been used as projectiles in studies of Penning, associative, chemical rearrangement and chemiionization processes. Quantitative data are, however, often missing due to inherent difficulty of determining the excited state concentration, and only relative data on the competition of various processes may be available. Examples of some of the investigated processes are (25) and (26).

$$He_m^* + H_2 \rightarrow H_2^+ + He + e \qquad (25a)$$

$$\rightarrow HeH^* + H + e \qquad (25b)$$

$$\rightarrow HeH_2^+ + e \qquad (25c)$$

$$H_2^* + C_2H_4 \rightarrow C_2H_2^+ + H_2 + e \qquad (26a)$$

$$\rightarrow C_2H_3^+ + H + e \qquad (26b)$$

The extent of fragmentation of polyatomic molecules ionized by metastable noble gas atoms was investigated with the conclusion that the extent of fragmentation was practically the same as that one obtained by impact of electrons of the same energy as the excitation energy of the excited projectile [10b].

6.2.5. Electronic Excitation Energy Transfer between Neutral Particles

Transfer of electronic excitation energy in gas phase collisions which results in excited neutral species belongs to one of the oldest areas of research in atomic and molecular studies. Many specific cases have been studied and it is very difficult to review all the possible outcomes of these studies. In general, the main elementary processes are electronic-to-electronic (27) and electronic-to-vibrational energy transfer (28), if we limit our attention to higly-energized particles common to irradiated systems.

$$A^* + BC \rightarrow A + BC^* \qquad (27)$$

$$A^* + BC \rightarrow A + BC' \qquad (28)$$

The product excited particle may loose its energy by further energy transfer in subsequent collisions, by a radiative process or by dissociation.

Two basic rules apply in description of processes (27) and (28):

- the Wigner spin conservation rule (total spin of the systems is conserved through the inelastic collision);
- the energy resonance rule (energy transfer is most efficient when the internal energy given up by A^* is precisely equal to the energy absorbed in the process $BC - BC^*$ or BC' (i.e. the relative translational energy of the colliding pair tends to be conserved).

A very important energy transfer process in irradiated systems is the excitation transfer (27) under the conditions that the electronic excitation energy of A is higher than the ionization potential of BC. This process is then effectively competing with ionization processes and leads to the formation of neutral superexcited molecules which dissociate to formexcited neutral fragments as discussed more in detail in Chapter 5.

As already mentioned in chapters 3 and 4, clusters of atoms or molecules may have rather different properties and show a rather different reaction behaviour than single monomers consisting of the same atom or molecule. It has been mentioned in those chapters that clusters present systems which bridge the gap between the gaseous and the bulk state. Therefore, knowledge ofcluster properties may help to understand reactions in the bulk state by extrapolating the evolution from the atomic or molecular to the bulk properties with increasing cluster size.

In contrast to atomic and molecular ions discussed in chapter 2, cluster ions may not only react with other neutral targets (e.g., see the case of ion-neutral reactions), but there exists also the possibility of reactions within the cluster ion, i.e. reactions between cluster constituents termed internal ion molecule reactions). In this brief review we will discuss first these internal reactions, and then the reactivity of entire cluster ions. For more information see the specialized literature on cluster ion reactivity given in [11].

6.3.1. Internal Reactions

After initial formation of an excited or ionized cluster (by either electron or photon impact) we can distinguish between four classes of reactions: associative ionization, Penning ionization, ion molecule reactions, and unimolecular dissociation.

6.3.1.1. Associative Ionization (Chemiionization)

In these processes bond formation is involved. Investigations of Dehmer and Poliakoff [12] of Ar_2in the VUV using mass spectrometric detection showed that besides autoionization of Ar_2^* , Ar_2^+ is also formed via the associative ionization reaction $Ar^* + Ar \rightarrow Ar_2^+ + e$ within the excited $(Ar^* .Ar)$. Ng and coworkers [5] were able to edentify and study the relative reaction probabilities for the formation of various product channels of the chemiionization process $CS_2(v,n).CS_2 \rightarrow$ yielding $(CS_2)_2^+$. and various fragment ions as a function of Rydberg level n.

6.3.1.2. Penning Ionization

In Penning ionization an electron is transferred: In this case initial energy deposition from the bombarding electron (or photon) into an excited state of one cluster constituent (usually a rare gas atom) is followed by

Penning energy transfer to a seed cluster constituent leading to its ionization. For instance, Birkhofer et al. [14] have described Penning ionization or Ar clusters by metastable He (a process which has been also studied outside of the cluster [15]). Kamke et al. [16] have demonstrated the energy transfer from excited Ar atoms in clusters leading to the ionization of organic seed molecules, and Dao et al. [17] reported the possibility of Penning transfer of energy from an organic molecule in a cluster involving delay times of up to 0.2 μs. Considering that this intermolecular Penning ionization may in principle occur as soon as the adiabatic ionization energy of the cluster as a whole is below the excitation energy of any of its (solvated) constituents Hertel and coworkers [18] recently suggested that this process is a rather common ionzation channel, since the ionization energy of molecular clusters is usually much lower than for any of its constituents.

6.3.1.3. Ion Molecule Reactions

A very common phenomenon, especially in mixed and molecular clusters, are reactions within the energized ion-neutral complex after the primary ionization event; also referred to as ion-neutral half collision processes. These reactions usually lead to prompt fragmentation of the cluster ion. There exists now a large body of molecular beam photoionization and electron impact ionization studies of these reactions [9-11]. Information about these reactions are usually deduced from cluster fragmentation mass spectra measured as a function of electron (photon) energy and stagnation conditions taking also into account known properties of the respective reactions in the gas phase. In these studies the fragmentation pattern is normally interrogated at times where not only prompt but also metastable dissociations have already influenced the original pattern.

Recently, the photoion-photoelectron coincidence (PIPECO) techniques [19], which utilize flight time correlation of an ion-electron pair, have been used extensively as an ideal approach to incorporate state and energy selection into these studies. For instance, the dissociation of $Ar^+(^2P_j)$. CO into CO^+ + Ar (produced by photoionization of Ar.CO and studied with PIPECO) is rationalized by Ng and coworkers [20] by a stepwise mechanism involving the formation of a vibrationally excited $CO^+(X,v)$.Ar complex by near- resonance intermolecular charge transfer and the subsequent unimolecular dissociation of the complex by vibrational predissociation. This is in line with the interpretation of the unimolecular (prompt) dissociation of single ethylene ions in association with large argon

clusters (up to Ar_{130}), where charge transfer on or close to the surface is made responsible for the observed fragment abundances [21].

The most common reactions are, however, proton transfer reactions and association reactions [22,23]. The production of the protonated ammonia cluster series $NH_4^+ . (NH_3)_n$ is an example for the occurrence of an exoergic proton exchange reaction, whereas $H_3O^+(H_2O)_n$ for an endoergic reaction. The ammonia reaction has been studied extensively [24], and Castleman and coworkers [25], using multiphoton ionization, found that the protonated pentamer is an unusually prominent species due to a presumed closed solvation shell. A similar prominent feature is the protonated 21mer in H_2O clusterspectra, its structure has been ascribed to clathrate formation via an ion-induced mechanism [26]. It is interesting to note that in both cases ionization also leads to the production of stoichiometric cluster ion series, albeit with much smaller probability than in the protonated cases. Recently, evidence of multiple McLafferty rearrangements in protonated n-butanoic acid clusters was reported [27]. The fragmentation pattern inducedby such ion molecule reactions has been studied for several molecular clusters by Buck and coworkers [28] using size-selected neutral clusters as collision partners in the primary ionization process. In the case of ethylene clusters, it is assumed that one ethylene unit is ionized, which leads via an association reaction to a higly excited $C_4H_8^+$.This complex either decays to $C_3H_5^+$ or $C_4H_7^+$,or, in the case of clusters larger than the dimer, the $C_4H_8^+$ complex may be stabilized by a third body collision. The occurrence of $C_2H_5^+$ ions is rationalized by the endothermic H-atom transfer reaction within the cluster $C_2H_4^+ . C_2H_4 \rightarrow C_2H_5^+ + C_2H_3$.
Another method to follow the ion chemistry has been presented by Brutschy et al. [29], where the neutral precursor of product ions is assigned using the optical fingerprint in two-color-two-photon ionization spectroscopy. Finally, it is quite noteworthy that similar ion molecule reactions are to be expected in negative molecular cluster ions [30].

6.3.1.4. Metastable Dissociations

An interesting variation on the theme of unimolecular cluster ion reactivity is the decomposition in the metastable time regime. Whereas prompt dissociation reactions in the cluster ion (as described above) cannot be observed directly and identified unambigously from the measured fragmentation patterns, metastable dissociation reactions may be detected directly in the field-free regions of certain mass spectrometer systems. This offers an opportunity to study in detail energetics, kinetics, and dynamics of selected ion dissociation processes of uniquely selected cluster

ion species. The existence of metastable cluster ions after electron (or photon) ionization of van-der-Waals clusters has been established only in the last decade [9,10] despite the fact that (i) delayed unimolecular decay was to be expected and that (ii) a series of cluster ions, differing only in size constitute an ideal testing ground for statistical unimolecular decay theories. Today, a large number of studies exists [9,10] on the properties of metastable decay reactions of cluster ions (with lifetimes from 10^{-7}s [31,32] up to several 100 μs [33-35]) produced by either electron or photon ionization of vdW clusters.

Fragmentation of an excited molecular ion usually occurs immediately after the ionization event (prompt dissociative ionization via repulsive hypersurfaces). However, in certain cases such a dissociation cannot take place immediately due to obstacles along the possible reaction pathways. Ordinary polyatomic metastable ions can be categorized into three groups corresponding to three different mechanisms (storage and disposal of excess energy).

1. Electronic (forbidden) predissociation: In this case the radiative decay or the radiationless transition from an excited (bound) state to a repulsive state (leading to instantaneous dissociation) is strongly forbidden by some selection rules. A typical example is the metastable decay of $Ar_2^+ (^2\Pi_{1/2})_u$ via $Ar_2^+ (^2\Pi_{1/2})_g$ into $Ar^4 (^2P_{3/2})$ + Ar with a lifetime of ~ 90 μs [36,37].

2. Barrier penetration: A second possible mechanism giving rise to metastable decay of ions is the excitation to bound levels which are above the dissociation limit of this ion but below the top of a weak dissociation barrier. The quantum mechanical tunnel effect is responsible for the observed metastable decay and the corresponding lifetimes. A particular variant of this mechanism is tunneling through a centrifugal barrier (rotational predissociation). On the basis of experimental findings [36] and of a model calculation [38], it was suggested that tunneling through a rotational barrier is responsible for the slow decay of small Ar cluster ions.

3. Vibrational predissociation: If a polyatomic ion is complex enough, the Lissajous motion of an activated ion on its potential hypesurface will be complicated enough to increase the lifetime into the metastable time regime. This process has to be described in the framework of a statistical theory where the unimolecular rate constant k (and other properties such as the release of translational kinetic energy ξ) are assumed to depend only on the internal energy of the activated ion. The excitation process is

assumed to have no influence on the values of k or T. Vibrational predissociation is thought to be the dominant metastable dissociation mechanism for large cluster ions and several variants of statistical theory have been applied to this rather new field [39,40]. Moreover, Scharf et al. [41] have recently explored by classical molecular dynamics vibrational predissociation induced by exciton trapping in neutral rare gas clusters.

It is now well established that under certain conditions following the ionization of a cluster, metastable decay not only proceeds according to one of the above mentioned (intramolecular) meachanisms, but also via mechanisms only possible in the complex environment of a cluster. To date two intermolecular mechanisms are known to occur:

1. Delayed internal ion molecule reaction: One of the first examples discussed in this context was the formation of protonated water clusters by Klots and Compton [30], where they attributed observed metastable fragments to an ion molecule reaction taking place within a water cluster following its ionization. They also reported observing metastable components in the formation of $C_3H_5^+$ following the ionization of the ethylene dimer. Other authors have made similar observations [42]; for instance Futrell et al. [43] reported that in case of ammonia clusters a rearrangement channel is a relevant factor for metastable dissociation. Morgan et. al. [44] have recently obtained first evidence for a delayed internal cluster reaction, namely, the metastable loss of H_2O following the ionization. This is in contrast to earlier work, where the product ions detected were also present as peaks in the direct ionization spectrum.

2. Intermolecular energy transfer: In this case vibrational or electronic energy stored in one moiety of a cluster ion is released with a delay into intermolecular motion leading to the evaporation of specific (magic) mumbers of monomers. In particular, up to four vibrational quanta may be stored in a nitrogen cluster ion [45] leading to a rather peculiar metastable evaporation pattern. A similar process involving the transfer of electronic energy in the metastable time regime has been observed for argon cluster ions resulting in the preferential evaporation of specific magic numbers of Ar atoms [32]. Furthermore, metastable dissociations have been also reported in case of negative cluster ions [46,47].

A particular variant of a delayed decay in these systems is the occurrence of electron autodetachment in the metastable time regime [46,48]. For more details on the properties of these metastable decay reactions see Ref. [10].

6.3.2. Reactivity of Cluster Ions

The field of cluster ion reactions with neutrals comprises a very large subset of the general subject of ion molecule reactions treated in section 2. Association reactions are the most common variant of cluster ion reactions. The vast majority of association reactions (which are sometimes called clustering reactions, because they may be seen as production sequence for cluster ions) have been investigated using either flowing afterglow or high pressure pulsed mass spectrometry techniques. This subject has been reviewed several times; in particular, the reader is referred to the collected data by Albritton anda recent review by Smith and coworkers [49].

The basic mechanisms of ion/molecule association reactions are well understood. The reactions are visualized to proceed via an intermediate complex $(AL)^*$ which has a lifetime τ_r, against unimolecular decomposition back to the reactants A and L. 'A' may be taken to represent the reactant ion, perhaps already containing some cluster subunits, and L the next associating molecule. Collision with a third body, M, can either remove excess energy from the complex and result in the formation of a stable entity, or it can provide collisional energy necessary for dissociation back to the original reactants as follows [9]:

$$\begin{aligned} A + L &\underset{k_r}{\overset{k_c}{\rightleftharpoons}} (AL)^* \\ (AL)^* + M &\xrightarrow{k_s} AL + M \qquad (29) \\ A + L &\xrightarrow{k_{fo}} AL \\ AL + M &\underset{k_s}{\overset{k_a}{\rightleftharpoons}} (AL)^* + M \end{aligned}$$

$$(AL)^* \xrightarrow{k_\tau} A + L \qquad (30)$$

$$AL \xrightarrow{k_{ro}} A + L$$

Taking k_c to represent the rate of clustering, k_r (proportional to $1/\tau$), the rate of dissociation of the complex, and k_s, the rate of stabilization of the complex by a third body (M), a steady-state treatment for the complex $(AL)^*$ leads to the following equation for the overall forward rate, k_{fo}, Likewise, the overall reverse rate is given by k_{ro} as follows:

$$k_{fo} = \frac{k_c k_s [M]}{k_r + k_s [M]} \tag{31}$$

$$k_{ro} = \frac{k_r k_a [M]}{k_r + k_s [M]} \tag{32}$$

As seen from the above equations, the reactions can be written in terms of low- and high-pressure limit, respectively,

$$k_{fo} = \frac{k_c k_s [M]}{k_r} \qquad k_{ro} = k_a [M] \qquad \text{(low)} \tag{33}$$

$$k_{fo} = k_c \qquad k_{ro} = \frac{k_r k_a}{k_s} \qquad \text{(high)} \tag{34}$$

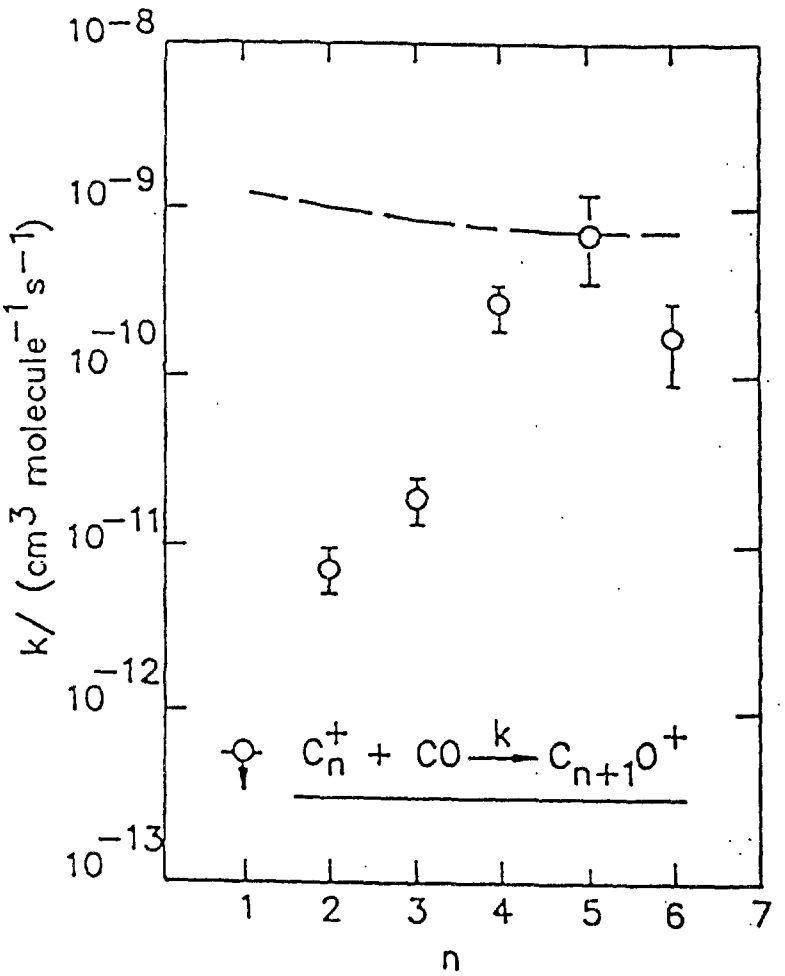

FIG. 6.2. Variation in the effective biomolecular rate constant (at 296 K) for the addition of one molecule of CO to C_n^+ as a function of cluster size (after Bohme et al. [62]; the dashed curve represents the variation in the collision rate constant.

Although the basic mechanisms and kinetics of cluster formation are well understood (e.g. see Fig. 1), the details are still subject to intense investigations [1].

Fig. 2 shows the observed [50] trend in the biomolecular specific rate of the association reaction

$$C_n^+ + CO \rightarrow C_{n+1}O^+ \qquad (35)$$

as a function of n. The specific rate is seen to increase with n. Similar trends are reen also in other reactions. Theories for association reactions indicate that the specific rate of association is increasing with the increasing lifetime of the intermediate association complex (AL) $\neq \tau_r$. This lifetime is determined by the energy of association and the number of atoms in the complex. The observed increase in the specific rate of association (Fig.2) is attributed primarily to an increase in τ which is expected from the increase of the number of constituents.

The area which has received by far the greatest attention in this field is experimental studies of the thermochemical properties [9,51]. Comparing relative bond strengths for a variety of ligands about a given positive ion as a function of clustersize n is very instructive in elucidating the role of the ligand. Data for molecules having a wide range of properties (dipole moment, polarizability, etc.) clustering around Na^+ are shown in Fig. 3 [9]. It is interesting to note that individual $\Delta H_{n,n+1}$ values seem to approach the corresponding bulk value ΔH_v° at rather small cluster sizes.

Experimental information in the backward analog of association reactions, i.e., declustering reaction or collision-induced dissociation, is scarce and limited to a few cluster ions [9]. Kebarle and coworkers [52] demonstrated that cross sections for collision-induced dissociation increase rapidly with the number of ligands, and with the internal energy of the cluster ion, but decreases with the increasing dissociation energy. Ligand switching reactions in general proceed rapidly ($k \geq 10^{-10}$ cm^3/s) when exothermic [53]. Depending on the energetics of solvation, the successive exchange may come to a halt at some intermediate stage of mixed solvation [54]. In the following we will only consider reactive (cluster) ion-molecule reactions, including charge transfer, proton transfer, and ion-atom interchange processes [55].

The effect of clustering on the reactivity of ions is important for an understanding of ion chemistry in dense gases, as well as solvation chemistry in general. Smith at al. [56] found that, for example, association of N_2 to N_2^+ does not seriously modify the reactivity of the N_2^+ except that it reduces somewhat the energy available for reaction. The most common

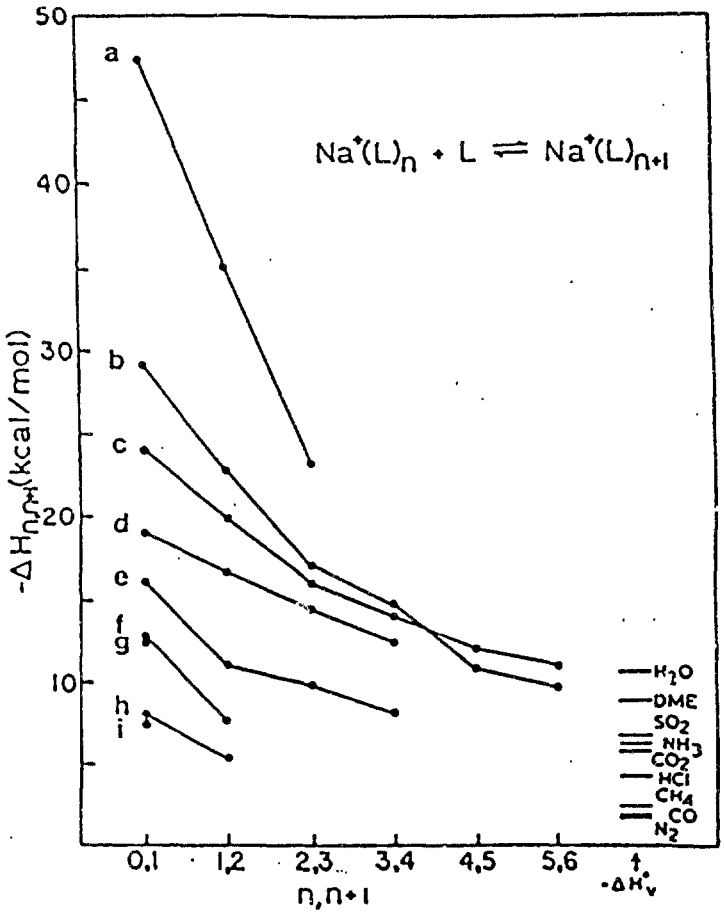

FIG. 6.3. Values of $-\Delta H_{n,n+1}$ vs. cluster reaction n, n+1, for (a) DME, (b) NH_3, (c) H_2O, (d) SO_2, (e) CO_2, (f) CO, (g) HCl, (h) N_2, and (i) CH_4 clustered to Na (after [9]).

mechanism apparently is direct charge transfer, usually followed by fragmentation with the nitrogen - nitrogen bonds in the reacting ions remainig intact (see also reactios of $(CO_2)_n^+$ [57]). Similarly, for ligand exchange (see above), some (non-resonant) charge tranfer processes of $O^-.(H_2O)_n$, and reactions of hydrated hydronium ions, increased hydration of the reactant ion does not significantly decrease the reaction constant [53,58]. In contrast, for some (resonant) charge transfer processes [58] and in several ion-atom interchange and/or nucleophilic displacement reactions [59], increased solvation of the reactant ion resulted in a significant decrease in reactivity (see also results obtained by Howard et. al. [60] for associative detachment of negative ions, in which the reactivities arealso reduced by clustering with H_2O). Similary, Bohme et. al. [61] found that stepwise hydration leads to a decrease of the reaction rate constant for proton transfer from H_3O^+, e.g., to H_2S with a concomitant change in ΔG°

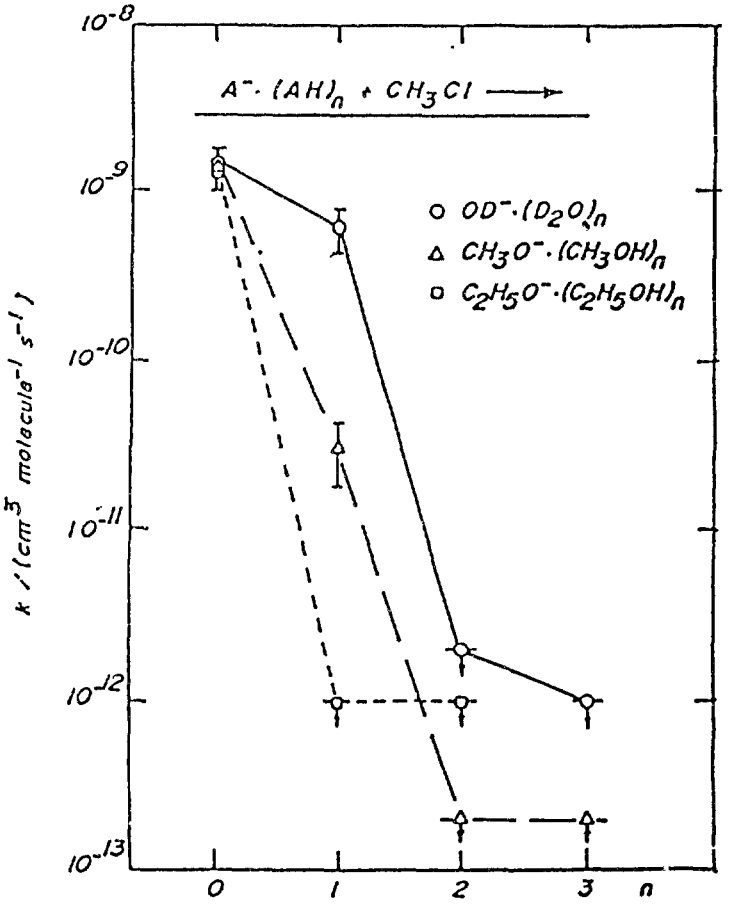

FIG. 6.4. Reaction rate constants for gas phase nucleophilic displacement reactions of solvated anions with metyl chloride as a function of the extent of solvation (after [9]).

(see also [62] for solvated proton transfer reactions). In case of nucleophilic displacement reactions (e.g. see Fig. 4) these striking results may be interpreted, according to Henchman et al. [59] in terms of the qualitative model developed by Pellerite and Brauman [63].

On the other hand, an enormous reactivity enhancement has been found by Rowe et. al. [64] for a new class of ion-catalyzed reactions between neutrals occurring in cluster ions in which the central ion does not form chemical bonds, e.g , the rate constant for the homologous gas phase reaction of N_2O_5 with NO is smaller than 10^{-20} cm^2/s, whereas the rate for this reaction on an alkali ion cluster increases at least seven orders of magnitude in the case of Na^+ as central ion, and in excess of nine orders of magnitude in the case of Li^+(this subject has been recently extended to several more reactions yielding rate enhancements up to 30 orders of magnitude [65]).

6.4. PROCESSES IN CONDENSED PHASE

The recent results obtained on processes of ions and excited neutrals in the condensed phase are of particular interest to radiotherapy since in this field the medium of interest is the living cell. Information obtained in the gas-phase must in some way be transferable to the radiation processes which take place in the cell; and, in that respect, the condensed phase data provide a link between the abundant information found in the gas-phase and the extremely limited knowledge of initial ultra-rapid ion molecule, radical-molecule and molecule-molecule reactions which may occur in the condensed phase environment of the cell. We present in the next section the results of solid-phase ion-molecule reactions in which the positive or negative ion reacts with energy of several eV with a condensed molecule. Thus, these processes correspond to those oftheinitial ion-molecule reactions in radiolysis.

6.4.1. Chemical Reactions of Ions

The data presently available on initial ion-molecule reactions in the condensed phase have been obtained from electron stimulated desorption (ESD) experiments. In these studies [66], monoenergetic electrons impinge on a thin film grown in an ultra-high-vacuum system by the condensation of gases or organic vapors on a clean metal substrate held at cryogenic temperatures (15-100K). The positive and negative ion currents emanating from the film surface are measured as a function of primary electron energy. The ion desorption into vacuum is recorded by a quadrupole mass spectrometer having an input lens located near the film surface. An energy filter can be placed in front of the mass spectometer to discriminate the energies of the ions. The ion yields can be recorded with films whose thickness (10- 2000 Å) is limited by charge accumulation. The data are usually obtained at temperatures near 20 K, with incident currents varying between 10^{-10} and 10^{-8} A depending on the desired resolution (5-200 meV).

It has been shown by these experiments [67-69] that anions created by dissociative attachment could react with surrounding molecules with energies (eV's) defined by the dissociative process. The unique features of the reaction and its pathways could be deduced by monitoring the magnitude of a reaction-product signal as a function of incident electron energy and concetration of one of the reactants [67,68]. For example, the observation of reactions

$$O^- + C_nH_{2n+2} \rightarrow OH^- + C_nH_{2n+1} \quad (36)$$

(n = 1,2,4,5 and 6) is reported for C_nH_{2n2} molecules condensed on the surface of a multilayer O_2film deposited on a platinum substrate [67]. The energetic O^-ions are generated by the dissociative association reaction

$$e^- + O_2(^3\Sigma_g^-) \rightarrow O_2^-(^2\Pi_u, {}^2\Sigma^+) \quad (37a)$$

$$\rightarrow O^-(^2P) + O(^3P) \quad (37b)$$

This reaction is evidenced by first measuring the O^- ESD yield from a pure multilayer O_2 and other molecules as shown in Fig. 5 (a) and (b). Here, the 8 eV peak arises from the decay of the $^2\Pi_u$ and $^2\Sigma_g^+$ transitory states of O_2^-whereas the 13 eV peak contains contributions from these and a higher-energy symmetry-forbidden ($^2\Sigma_u^+$) O_2^- states [70]. The features in the curve representing the electron energy dependence of the O^-yield are reflected into the electron energy dependence od the OH^-yield and thus serve as a "signature" to detect and identify reaction(36).

Curves (c) to (g) in Fig. 5 represent the energy dependence of the OH^- yields produced by electron impact on three-layer oxygen film covered by a monolayer of C_nH_{2n+2} molecules. At submonolayer coverages, these OH^- yield functions exhibit the same characteristics but the signal is lower. In fact, in the submonolayer regime the magnitude of the OH^- signal is found to be directly proportional to the number of condensed hydrocarbon molecules. Results similar to those in Fig. 1 were also obtained for submonolayer coverages of O_2on three-layer hydrocarbon films [68]. Since no compound at the film surface contains both hydrogen and oxygen, OH^- ions cannot be produced by direct electron impact. However, they can result from reactions between ground state molecules (i.e.,O_2 and C_nH_{2n+2}) and anions produced directly by the electron beam (i.e., O^-, H^- and CH_n^- , n = 1 to 3). The ion OH^- can be formed via reaction (36) or the reactions

$$H^- + O_2 \rightarrow OH^- + O \quad (38)$$

$$CH_n^- + O_2 \rightarrow OH^- + CH_{n-1}O \quad (39)$$

Any OH^- formed by these latter would bear the "signature" of the yield function for H^- or CH_n^- which exhibits only a single peak at 10 eV [68]. Thus, the line shapes in Fig. 1 can only be produced via reaction (1).

Reaction of positive ions with molecules in solid films can also be detected by monitoring reaction products [69]. In this case, cations are monitored as a function of electron energy. Fig. 6 shows the result of an experiment where a 50 Å film composed of 20% volume O_2 and 80% volume N_2 is bombarded with 15 to 31 eV electrons. The curve labelled O^+ was obtained by

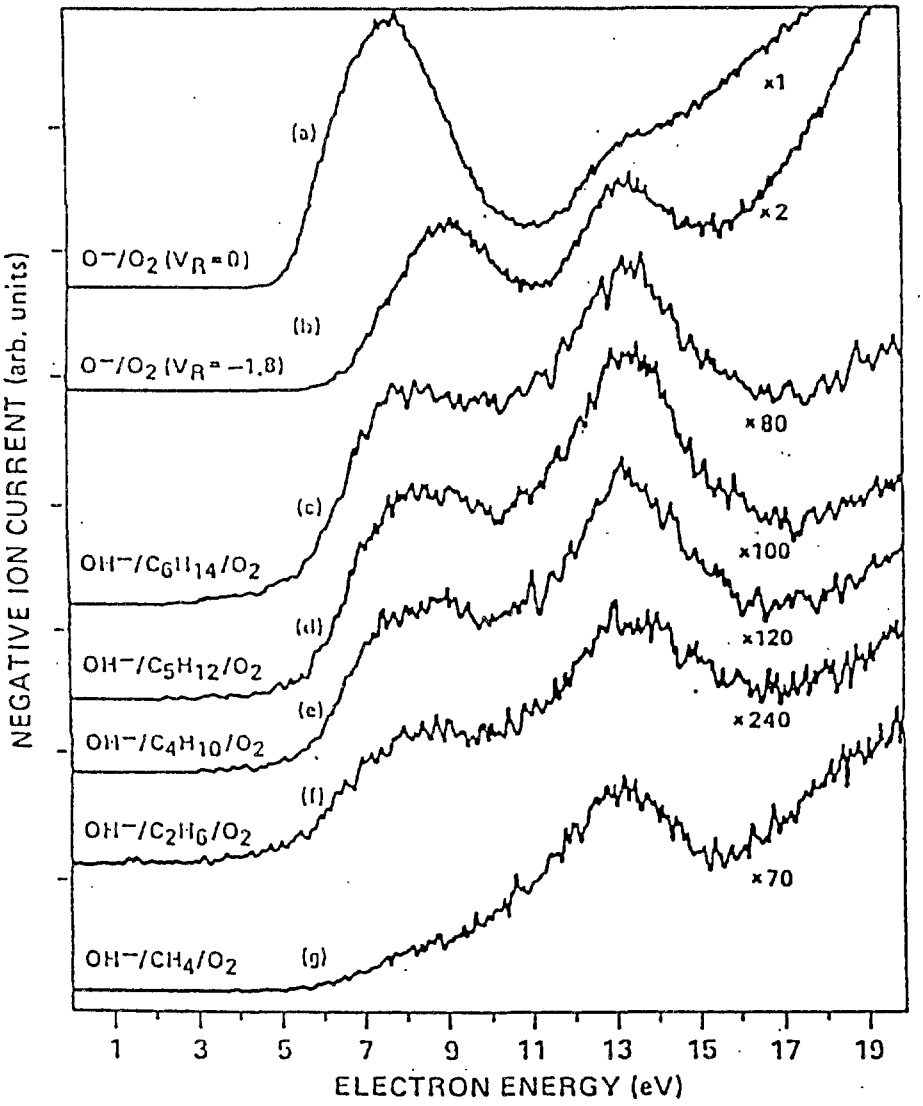

FIG.6.5. Energy dependence of electron-stimulated desorption (ESD) of negative ions in the range 1 - 10 eV. Curves a nad b: O^- desorption from a three-layer O_2 film; V_R is a potential retarding the negative ions at the entrance of the mass spectrometer. Curves c-g: OH^- desorption from a three-layer O_2 film covered with a single layer of C_nH_{2n+2} (n=1,2,3,4,5 and 6) molecules; curves c-g recorded with V_R=0.

measuring the energy dependence of the O^+ signal. Similarly, the curves labelled N^+ and NO^+ represent the ESD yields of these cations, respectively. The O^+ signal can arise from either reactions

$$e^- + O^2 \rightarrow (O_2^+)^* + 2e^- \rightarrow O^+ + O + 2e^- \qquad (40)$$

$$e^- + O_2 \rightarrow O_2^* + e^- \rightarrow O^+ + O^- + e^- \qquad (41)$$

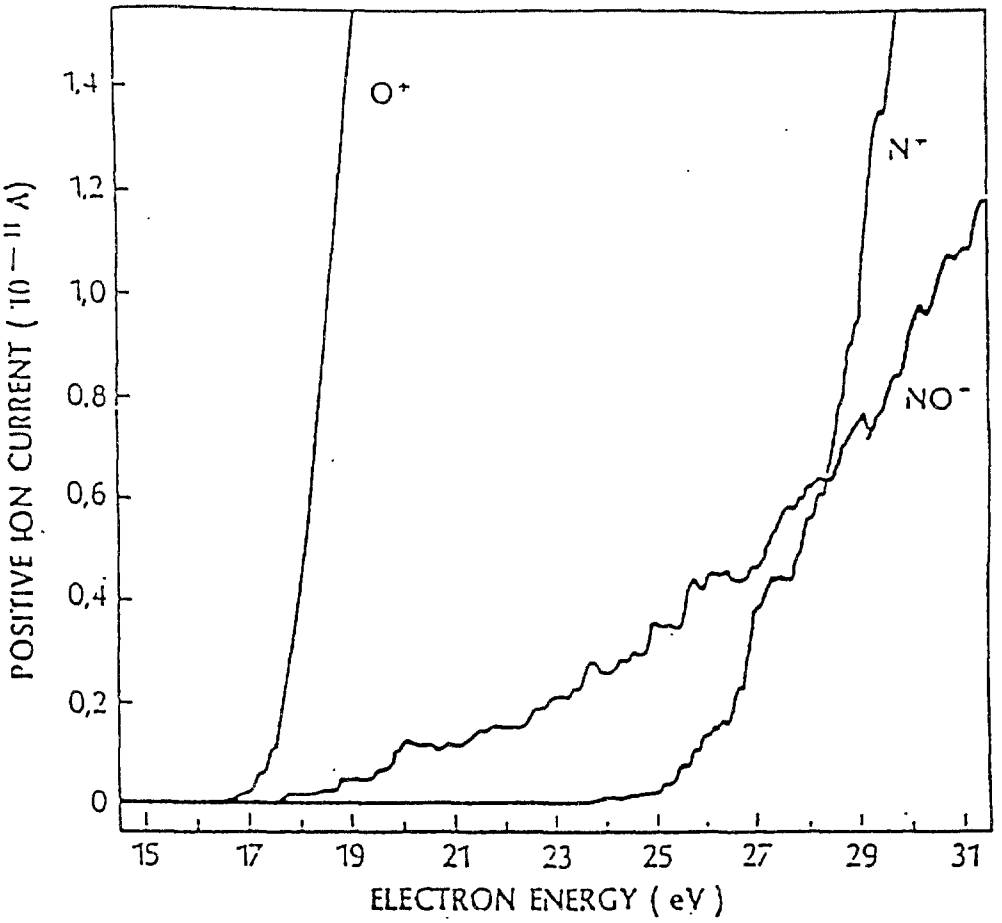

FIG. 6.6. ESD yields of O^+, N^+ and NO^+ ions produced by electron impact on a multilayer film composed of 20% volume O_2 and 80% volume N_2.

Near threshold, the O^+ signal should arise exclusively from the latter reaction which requires the least energy. The onset of the reaction

$$e^- + N_2 \rightarrow (N_2^+)^* + 2e^- \rightarrow N^+ + N + 2e^- \qquad (42)$$

lies around 25 eV. The magnitude of the O^+ signal is about four times higher than the N^+ signal and more than an order of magnitude larger than the NO^+ signal. Below 25 eV, since no N^+ ions can be formed, the NO^+ signal aries from the reaction of energetic O^+ with N_2. The possible reaction of N_2^+ with O_2 or O_2^+ with N_2 yielding NO_2 + NO must be eliminated because any intermediate NO^+ state in the 17-25 eV range could not lead to NO^+ ions having sufficient kinetic energy to overcome the polarization barrier of the film. Furthemore, the coincidence of the energy threshold of the $O^+$and NO^+signals dictates interpreration involving the reaction

$$N_2 + O^+ \rightarrow N_2O^+ \rightarrow N + NO^+ \qquad (43)$$

Here, the O^+ is created with a few eV of kinetic energy by the dissociation of a repulsive state. The intermediate N_2O^+ state is also repulsive yielding a NO^+ product with enough kinetic energy to overcome the polarization attraction ($\simeq$ 0.5 eV) [71] of the positive charge toward the film. The reaction occurs during times characteristic of a vibrational period of the N_2O^+ cation ($\simeq 10^{-14}$ s).

TABLE 6.1. IONIZATION POTENTIALS OF ELEMENTS

Element	IP(eV)	Element	IP(eV)
H	13.598	Mg	7.464
He	24.587	Al	5.986
Li	5.391	Si	8.152
Be	9.323	P	10.487
B	8.298	S	10.360
C	11.260	Cl	12.968
N	14.534	Ar	15.760
O	13.618	K	4.341
F	17.423	Ca	6.113
Ne	21.565	Br	11.814
Na	5.139	Kr	13.999
I	10.451	Xe	12.130

TABLE 6.2. IONIZATION POTENTIALS OF MOLECULES AND RADICALS AND HEATS OF FORMATION OF THE RESPECTIVE IONS

Molecule	IP(eV)	$\Delta H_{f\ o}^{o}(g)$[kJ mol^{-1}]
CH	10.64	1619
C_2	12.15	1992
CO	14.014	1238
Cl_2	11.50	1109
F_2	15.686	1514
H_2	15.426	1488.4
I_2	9.3995	971
CN	14.03	1794
N_2	15.581	1503
NO	9.264	983.6
O_2	12.059	1165
OH	13.18	1287
CH_2	10.50	1398
CO_2	13.79	935
CS_2	10.07	1089
HCN	13.50	1447
H_2O	12.614	978
NH_2	11.40	1263
N_2O	12.89	1330
O_3	12.52	1368
SO_2	12.35	895
BF_3	15.55	367
CH_3	9.842	1095
C_2H_2	11.406	1328
H_2O_2	10.92	( )
NH_3	10.15	941
CCl_4	11.47	1006
CH_4	12.615	1150

Molecule	IP(eV)	$\Delta H_f^{\circ}{}_o(g)$[kJ mol^{-1}]
C_2H_4	10.51	1175
C_2H_5	8.37	917
C_2H_6	11.521	1041
C_3H_5	8.05	946
C_3H_6	9.74	960
c-C_3H_6	10.06	999
i-C_3H_7	7.55	800
C_3H_8	10.95	953
i-C_4H_8	9.11	871
i-C_4H_9	8.01	830
n-C_4H_{10}	10.55	887
i-C_4H_{10}	10.57	879
C_6H_6	9.247	975
c-C_6H_{10}	8.945	858
c-C_6H_{12}	9,45	871
CH_3CN	12.19	1270
C_5H_5N[a)]	9.266	1034
HCOH[b)]	10.88	936
CH_2OH	8.14	720
CH_3OH	10.85	856
C_2H_5OH	10.48	793

[a)] pyridin; [b)] formaldehyde

TABLE 6.3. HEATS OF FORMATION OF SOME NEUTRAL RADICALS

Radical	$\Delta H_{f\ o}^{o}$ [kJ mol^{-1}]	Radical	$\Delta H_{f\ o}^{o}$ [kJ mol^{-1}]
H	216.003	O	246.785
B	557.64	O_3	145.35
BH	446.4	OH	38.70
C	711.2	CH_2OH	-113.4
CH	592.5		
CH_2	392.9	F	76.9
CH_3	145.6	CF	251.5
C_2H_5	107.5	CF_3	-467.4
C_3H_5	169.9		
$i\text{-}C_3H_7$	73.6	S	276.6
$n\text{-}C_3H_7$	86.6	SH	142
		CS	269.4
N	470.842	SO	6.3
NH	331		
NH_2	172	Cl	120.00
CN	431.8	Br	117.94
		I	107.24

TABLE 6.4. PROTON AFFINITIES OF ATOMS AND MOLECULES

Atom/Molecule	PA[eV]	Atom/Molecule	PA[eV]
Ar	3.84	CH_2	8.55
Br	5.72	CO_2	5.68
Cl	5.36	HCN	7.43
F	3.51	HCO	6.6
H	2.650	H_2O	7.22
He	1.845	HO_2	6.9
I	6.3	H_2S	7.4
Kr	4.40	NH_2	8.10
N	3.4	NO_2	6.6
Ne	2.08	N_2O	5.92
O	5.05	SO_2	7.0
S	6.9		
Xe	5.14	CH_3	5.4
		C_2H_2	6.7
CO	6.15	H_2CO	7.44
CN	5.1	HCOH	9.92
H_2	4.38	H_2O_2	7.22
HCl	5.86	NH_3	8.85
HF	4.09	CF_4	5.46
HS	7.2	CH_4	5.72
N_2	5.125	C_2H_4	7.05
NH	6.1	CH_3OH	7.89
NO	5.50	C_2H_6	6.22
O_2	4.38	C_3H_8	6.50
OH	6.18	C_6H_6	7.87

TABLE 6.5. ELECTRON AFFINITIES OF ATOMS AND MOLECULES

Atom/Molecule	EA[eV]	Atom/Molecule	EA[eV]
H	0.7542	C_2H	3.73
B	0.28	CH_2	0.21
C	1.263	CNS	2.0
O	1.46	COS	0.5
F	3.40	CS_2	0.8
Na	0.5479	HNO	0.34
S	2.077	HO_2	1.19
Cl	3.62	NH_2	0.76
K	0.5015	NF_2	1.7
Br	3.37	NO_2	2.28
I	3.059	N_2O	0.24
		O_3	2.103
Br_2	2.6	SCN	2.2
C_2	3.39	SH_2	1.1
CF	3.3	SO_2	1.06
CN	3.82		
CS	0.21	CCl_3	1.2
Cl_2	2.44	CF_3	1.92
F_2	2.96	CH_3	1.07
I_2	2.51	NO_3	3.7
NH	0.38	SO_3	1.7
NO	0.03		
O_2	0.44	$CClF_3$	1.1
OH	1.828	CH_3O	1.57
S_2	1.66	$OH.H_2O$	1.95
SH	2.31	C_3H_3	2.3
SO	1.09	C_2H_5	0.89
		SF_6	0.6
C_3	2.1	C_2H_5O	0.6
CF_2	2.1	C_3H_7	0.6

TABLE 6.6. RATE CONSTANTS OF SELECTED ION-MOLECULE REACTIONS AND CHARGE TRANSFER PROCESSES

Reactants	Product(s)	Rate Constant ($molecule^{-1}cm^3s^{-1}$)	Method[a])
$HO^+ + CH_4$	$CH_5^+ + O(13\%)$	1.5 (-9)	SIFT
	$H_3O^+ + CH_2(87\%)$		
$HO^+ + CO$	$CHO^+ + H$	6.2 (-10)	SIFT
$HO^+ + CO_2$	$CHO_2^+ + O$	1.44(-9)	SIFT
$OH^+ + H_2$	$H_2O^+ + H$	1.01(-9)	SIFT
$OH^+ + H_2O$	$H_3O^+ + H$	3.4 (-9)	ICR
$OH^+ + H_2S$	$H_3S^+ + O(40\%)$	2.05(-9)	SIFT
	$H_2S^+ + OH(60\%)$		
$OH^+ + NO$	$HNO^+ + O(63\%)$	9.7(-10)	SIFT
	$NO^+ + OH(37\%)$		
$OH^+ + N_2$	$HN_2^+ + O$	2.2(-9)	SIFT
$OH^+ + N_2O$	$HN_2O^+ + O(72\%)$	1.56(-9)	SIFT
	$N_2O^+ + OH(16\%)$		
	$NO^+ + NOH(11\%)$		
$OH^+ + O_2$	$O_2^+ + OH(90\%)$	1.9(-10)	SIFT
	$HO_2^+ + O(10\%)$		
$HO_2^+ + Ar$	$ArH^+ + O_2$	1.9(-11)	FDT
$HO_2^+ + CH_4$	products	1.0(-9)	ICR
$HO_2^+ + CO_2$	$CHO_2^+ + O_2$	1.1(-9)	FDT
$HO_2^+ + C_2H_4$	products	1.1(-9)	ICR
$HO_2^+ + C_2H_6$	products	1.4(-9)	ICR
$HO_2^+ + H_2$	$H_3^+ + O_2$	3.3(-10)	SIFT

[a])EXPERIMENTAL METHODS:

DT - drift tube; FA - flowing afterglow; FDT - flow-drift tube; ICR - ion cyclotron resonance; MS - mass spectrometer ion source; SIFT - selected-ion flow tube; SIFDT - selected-ion flow drift tube.

Reactants	Product(s)	Rate Constant ($molecule^{-1}cm^3s^{-1}$)	Method
$HO_2^+ + NH_3$	$H_4N^+ + O_2$	2.0(-9)	FDT
$HO_2^+ + NO$	$HNO^+ + O_2$	7.3(-10)	FDT
$HO_2^+ + N_2$	$HN_2^+ + O_2$	8.0(-10)	FDT
$H_2N^+ + H_2CO$	CH_3O^+(80%) H_3N^+(20%)	2.8(-10)	SIFT
$H_2N^+ + HCOOH$	$H_4N^+, (CH_3O_2^+)$	2.7(-9)	FA
$H_2N^+ + CH_4$	$H_3N^+ + CH_3$	9.2(-10)	SIFT
$H_2N^+ + CH_3OH$	$H_3N^+ + CH_2OH$(13%) $CH_5O^+ + NH$(87%)	3.0(-9)	DT
$H_2N^+ + CO$	$H_2N.CO^+$	2.4(-11)	SIFT
$H_2N^+ C_2H_4$	$C_2H_4^+, CH_4N^+$(30%); $C_2H_5^+, C_2H_5N^+$(20%);	1.5(-9)	SIFT
$H_2N^+ + H_2$	$H_3N^+ + H$	2.7(-10)	SIFT
$H_2N^+ + H_2O$	H_3O^+(95%), H_3N^+(5%)	2.9(-9)	SIFT
$H_2N^+ + NH_3$	$H_4N^+ + H$	2.2(-9)	ICR
$H_2N^+ + NO$	NO^+	7.0(-10)	SIFT
$H_2O^+ + HCN$	$CH_2N^+ + OH$ $H_3O^+ + CN$	2.1(-9)	MS
$H_2O^+ + CH_4$	$H_3O^+ + CH_3$	2.52(-9)	MS
$H_2O^+ + CO$	$CHO^+ + OH$	5.3(-9)	SIFT
$H_2O^+ + C_2H_2$	$C_2H_2^+$	1.9(-9)	DT
$H_2O^+ + C_2H_4$	$C_2H_4^+$	1.5(-9)	DT
$H_2O^+ + C_2H_6$	H_3O^+(83%), $C_2H_4^+$(12%) $C_2H_6^+$(4%), $C_2H_5^+$(1%)	1.6(-9)	SIFT
$H_2O^+ + H_2$	$H_3O^+ + H$	8.3(-10)	SIFT
$H_2O^+ + H_2O$	$H_3O^+ + OH$	1.6(-9)	MS
$D_2O^+ + D_2O$	$D_3O^+ + OD$	1.19(-9)	MS

Reactants	Product(s)	Rate Constant ($molecule^{-1}cm^3s^{-1}$)	Method
$H_2O^+ + H_2S$	H_3S^+(43%), H_2S^+(54%) H_3O^+(3%)	1.8(-9)	SIFT
$H_2O^+ + NO$	$NO^+ + H_2O$	5.9(-10)	SIFT
$H_2O^+ + O$	$O_2^+ + H_2$	1.5(-10)	SIFT
$H_2O^+ + O_2$	$O_2^+ + H_2O$	4.3(-10)	SIFT
$H_2O_2^+ + CO$	$CHO^+ + HO_2$	5.5(-11)	FDT
$H_2O_2^+ + H_2O$	$H_3O^+ + HO_2$	1.7(-9)	FDT
$H_2O_2^+ + H_2O_2$	$H_3O_2^+ + HO_2$	6 (-10)	FDT
$H_2O_2^+ + NH_3$	$H_4N^+ + HO_2$	1.8(-9)	FDT
$H_2O_2^+ + NO$	$NO^+ + H_2O_2$	5.0(-10)	FDT
$H_3^+ + HCN$	$CH_2N^+ + H_2$	7.0(-9)	FA
$H_3^+ + CH_2O$	$CH_3O^+ + H_2$	6.3(-9)	FA
$H_3^+ + HCOOH$	$CHO^+ + H_2O + H_2$(70%) $H_3O^+ + CO + H_2$(30%)	8.03(-9)	FA
$H_3^+ + CH_4$	$CH_5^+ + H_2$	2.3(-9)	SIFT
$H_3^+ + CO$	$CHO^+ + H_2$	2.0(-9)	SIFT
$H_3^+ + CO_2$	$CHO_2^+ + H_2$	2.0(-9)	SIFT
$H_3^+ + C_2H_2$	$C_2H_3^+ + H_2$	2.9(-9)	SIFT
$H_3^+ + C_2H_4$	$C_2H_3^+ + 2H_2$(6%) $C_2H_5^+ + H_2$ (94%)	2.02(-9)	FA
$H_3^+ + CH_3COOH$	$C_2H_3O^+ + H_2O + H_2$	6.8(-9)	FA
$H_3^+ + H_2O$	$H_3O^+ + H_2$	4.3(-9)	FA
$H_3^+ + H_2S$	$H_3S^+ + H_2$	3.4(-9)	FA
$H_3^+ + NH_3$	$H_4N^+ + H_2$	4.2(-9)	FDT
$H_3^+ + NO$	$HNO^+ + H_2$	1.1(-9)	SIFT
$H_3^+ + O$	products	8.0(-10)	FA
$H_3^+ + O_2$	$HO_2^+ + H_2$	6.7(-10)	FDT

Reactants	Product(s)	Rate Constant ($molecule^{-1}cm^3s^{-1}$)	Method
H_3N^+ + HCN	H_4N^+ + CH	6 (-10)	ICR
H_3N^+ + H_2CO	H_4N^++HCO	1.1(-9)	SIFT
H_3N^+ + HCOOH	H_4N^+ + ..	9 (-10)	FA
H_3N^+ + CH_4	H_4N^+ + CH_3	4.8(-10)	SIFT
H_3N^+ + CH_3OH	H_4N^+ +CH_3O	2.2(-9)	SIFT
H_3N^+ + CO	products	< 5 (-13)	SIFT
H_3N^+ + CO_2	products	< 1 (-13)	SIFT
H_3N^+ + C_2H_4	H_4N^+ + ...	1.4(-9)	SIFT
H_3N^+ + H_2	H_4N^+ + H	5 (-13)	SIFT
H_3N^+ + H_2O	H_4N^+ + ..	< 3 (-11)	SIFT
H_3N^+ + NH_3	H_4N^+ + NH_2	2.2(-9)	SIFT
H_3N^+ + NO	NO^+ + NH_3	7.2(-10)	SIFT
H_3O^+ + HCH	CH_2N^+ + H_2O	4.5(-9)	FA
H_3O^+ + CH_2O	CH_3O^+ + H_2O	3 (-9)	SIFT
H_3O^+ + HCOOH	$CH_3O_2^+$ + H_2O	2.7 (-9)	FA
H_3O^+ + CH_3OH	CH_5O^+ + H_2O	2.2(-9)	FDT
H_3O^+ + CH_2CO	$C_2H_3O^+$ + H_2O	2.0(-9)	FA
H_3O^+ + C_2H_4	$C_2H_5^+$ + H_2O	6.3(-11)	SIFT
H_3O^+ + CH_3CHO	$C_2H_5O^+$ + H_2O	3.6(-9)	FA
H_3O^+ + CH_3COOH	$C_2H_5O_2^+$ + H_2O(95%) $C_2H_3O^+$ + $2H_2O$(5%)	3.0(-9)	FA
H_3O^+ + $(CH_3)_2O$	$C_2H_7O^+$ + H_2O	2.7(-9)	FA
H_3O^+ + C_2H_5OH	$C_2H_7O^+$ + H_2O	2.8(-9)	FA
H_3O^+ + H_2	products	< 5 (-15)	SIFT
H_3O^+ + H_2S	H_3S^+ + H_2O	1.4(-9)	FA
H_3O^+ + NH_3	H_4N^+ + H_2O	2.5(-9)	SIFT
H_3O^+ + NO	NO^+ + H_2O	1.5(-12)	SIFT

Reactants	Product(s)	Rate Constant ($molecule^{-1}cm^3s^{-1}$)	Method
$C^+ + HCN$	$C_2N^+ + H$	3.1(-9)	SIFT
$C^+ + CH_2O$	CHO^+(20%), CH_2^+(60%) CH_2O^+(20%)	3.9(-9)	SIFT
$C^+ + HCOOH$	CHO^+	3.3(-9)	SIFT
$C^+ + CH_3OH$	CH_4O^+(33%), CH_3O^+(30%) CHO^+(8%), CH_3^+(29%)	4.1(-9)	SIFT
$C^+ + CO_2$	$CO^+ + CO$	1.1(-9)	SIFT
$C^+ + C_2H_2$	$C_3H^+ + H$	2.7(-9)	SIFT
$C^+ + C_2H_4$	$C_3H_4^+$(85%), $C_2H_4^+$(15%)	1.82(-9)	SIFT
$C^+ + H_2$	products	< 5 (-13)	SIFT
$C^+ + H_2O$	$CHO^+ + H$	2.7(-9)	SIFT
$C^+ + NH_3$	H_3N^+(22%), CH_2N^+(75%)	2.3(-9)	SIFT
$C^+ + N_2$	products	< 5 (-13)	SIFT
$C^+ + O_2$	$CO^+ + O$ $O^+ + CO$	9.9(-10)	SIFT
$CH^+ + CH_2O$	$CH_3^+ + CO$	3.2(-10)1ICR	
$CH^+ + CH_4$	$C_2H_2^+ + H_2 + H$(11%) $C_2H_3^+ + H_2$(84%) $C_2H_4^+ + H$(5%)	1.3(-9)	SIFT
$CH^+ + CH_3OH$	$CH_3^+ + CH_2O$(50%) $CH_3O^+ + CH_2$(10%) $CH_5O^+ + H$(5%)	2.9(-9)	SIFT
$CH^+ + CO$	$CHO^+ + C$	7 (-12)	SIFT
$CH^+ + H_2$	$CH_2^+ + H$	1.2(-9)	SIFT
$CH^+ + H_2O$	$CHO^+ + H_2$(main)	2.9(-9)	SIFT
$CH^+ + NO$	$NO^+ + CH$	7.6(-10)	SIFT
$CH^+ + O_2$	$CHO^+ + O$(main)	2.9(-9)	SIFT

Reactants	Product(s)	Rate Constant ($molecule^{-1}cm^3s^{-1}$)	Method
$CHO^+ + HCN$	$CH_2N^+ + CO$	3.1(-9)	SIFT
$CHO^+ + CH_2O$	$CH_3O^+ + CO$	6.1(-10)	ICR
$CHO^+ + CH_4$	$CH_5^+ + CO$	< 1 (-13)	SIFT
$CHO^+ + CH_3OH$	$CH_5O^+ + CO$	2.4(-9)	SIFT
$CHO^+ + CO_2$	products	< 2 (-13)	SIFT
$CHO^+ + C_2H_2$	$C_2H_3^+ + CO$	1.36(-9)	SIFT
$CHO^+ + H_2O$	$H_3O^+ + CO$	2.5(-9)	SIFT
$CHO^+ + NH_3$	$H_4N^+ + CO$	2.3(-9)	SIFT
$CH_2^+ + HCN$	$C_2H_2N^+ + H$	1.8(-9)	ICR
$CH_2^+ + CH_4$	$C_2H_4^+ + H_2$(70%)	1.2(-9)	SIFT
	$C_2H_5^+ + H$(30%)		
$CH_2^+ + CO$	$CHO^+ + CH$	< % (-12)	SIFT
$CH_2^+ + H_2$	$CH_3^+ + H$	1.6(-9)	SIFT
$CH_2^+ + H_2O$	$CH_3O^+ + H$	2.9(-9)	SIFT
	$H_3O^+ + CH$		
$CH_2^+ + NH_3$	$CH_4N^+ + H$(55%)	2.8(-9)	SIFT
	$H_4N^+ + CH$(45%)		
$CH_2N^+ + H_2O$	$H_3O^+ + HCN$	8.8(-13)	FA
$CH_2N^+ + NH_3$	$H_4N^+ + HCN$	1.2(-9)	FA
$CH_2O^+ + CH_2O$	$CH_3O^+ + CHO$	3.2(-9)	SIFT
$CH_2O^+ + CH_3OH$	$CH_3O^+ + CH_3O$((10%)	2.4(-9)	SIFT
	$CH_5O^+ + CHO$(90%)		
$CH_2O^+ + H_2O$	$H_3O^+ + CHO$	2.6(-9)	SIFT
$CH_2O^+ + O_2$	$CHO^+ + HO_2$(70%)	1.7(-9)	SIFT
	$H_2O_2^+ + CO$(30%)		
$CH_3^+ + HCOOH$	$CH_5^+ + ..$	2.1(-9)	FA
$CH_3^+ + CH_4$	$C_2H_5^+ + H_2$	1.2(-9)	SIFT

Reactants	Product(s)	Rate Constant ($molecule^{-1}cm^3s^{-1}$)	Method
$CH_3^+ + C_2H_2$	$C_3H_3^+ + H_2$	1.2(-9)	SIFT
$CH_3^+ + H_2$	$CH_4^+ + H$	5 (-13)	ICR
$CH_3^+ + H_2O$	$CH_2OH^+ + ..$	< 1 (-11)	ICR
$CH_3^+ + NH_3$	$CH_3NH_3^+$(20%) $CH_4N^+ + H_2$(70%) $H_4N^+ + CH_2$(10%0	2.2(-9)	SIFT
$CH_3O^+ + CH_3OH$	$CH_5O^+ + CH_2O$	1.9(-9)	SIFT
$CH_3O^+ + H_2$	products	< 4 (-14)	SIFT
$CH_3O^+ + H_2O$	$H_3O^+ + CH_2O$	3 (-11)	SIFT
$CH_4^+ + HCN$	$CH_2N^+ + CH_2$	2.1(-9)	ICR
$CH_4^+ + CH_4$	$CH_5^+ + CH_3$	1.5(-9)	SIFT
$CH_4^+ + CO$	$CHO^+ + CH_3$	1.4(-9)	SIFT
$CH_4^+ + H_2$	$CH_5^+ + H$	3.3(-11)	SIFT
$CH_4^+ + H_2O$	$H_3O^+ + CH_3$	2.6(-9)	SIFT
$CH_4^+ + O_2$	$O_2^+ + CH_4$	4.4(-10)	SIFT
$CN^+ + CH_4$	CH_2N^+(60%), CHN^+(35%)	1.2(-9)	ICR
$CN^+ + CO$	$CO^+ + CN$	2.5(-10)	SIFT
$CN^+ + H_2$	$CHN^+ + H$	1.0(-9)	SIFT
$CN^+ + H_2O$	CHN^+(50%), $CHNO^+$(20%), CH_2N^+(15%), H_2O^+(10%)	3.2(-9)	ICR
$CO^+ + CH_4$	CHO^+(35%), CH_4^+(60%), $C_2H_3O^+$(5%)	1.36(-9)	SIFT
$CO^+ + H_2$	$CHO^+ + H$	1.8(-9)	SIFT
$CO^+ + H_2O$	H_2O^+(66%), CHO^+(34%)	2.6(-9)	ICR
$CO^+ + O_2$	$O_2^+ + CO$	1.2(-10)	SIFT
$O^+ + CH_2O$	CHO^+(40%), CH_2O^+(60%)	3.5(-9)	SIFT

Reactants	Product(s)	Rate Constant ($molecule^{-1}cm^3s^{-1}$)	Method
$O^+ + HCOOH$	$CHO^+(70\%), HO_2^+(30\%)$	5.0(-9)	FA
$O^+ + CH_4$	$CH_3^+(11\%), CH_4^+(89\%)$	1.0(-9)	SIFT
$O^+ + CO$	products	< 5 (-13)	SIFT
$O^+ + CO_2$	$O_2^+ + CO$	1 (-9)	DT
$O^+ + H_2$	$HO^+ + H$	1.7((-9)	SIFT
$O^+ + H_2O$	$H_2O^+ + O$	3.2(-9)	SIFT
$O^+ + N_2$	$NO^+ + O$	1.2(-12)	SIFT
$O^+ + O_2$	$O_2^+ + O$	2.3(-11)	SIFT
$O_2^+ + CH_2O$	$CHO^+(10\%), CH_2O^+(90\%)$	2.3(-9)	SIFT
$O_2^+ + HCOOH$	$CH_2O_2^+(65\%), CHO_2^+(35\%)$	1.8(-9)	SIFT
$O_2^+ + CH_4$	$CH_2O^+(15\%), CH_3O_2^+(70\%), H_2O^+(15\%)$	6.3(-12)	SIFT
$O_2^+ + CH_3OH$	$CH_3O^+(50\%), CH_4O^+(50\%)$	1.0(-9)	SIFT
$O_2^+ + C_2H_4$	$C_2H_4^+ + O_2$	6.8(-10)	SIDT
$O_2^+ + H_2O$	$H_2O^+ + O_2$	< 1 (-12)	FDT

TABLE 6.7. RATE CONSTANTS OF REACTIONS OF WATER CLUSTER IONS WITH MOLECULES

Reactants	Product Ions	Rate Constant [molecule^{-1}cm^{3}s^{-1}]
$H_3O^+.H_2O + HCN$	$CH_2N^+.H_2O$	1.0(-10)
$H_3O^+.H_2O + CH_2O$	$CH_3O^+, CH_3O^+.H_2O$	3.0(-9)
$H_3O^+.H_2O + HCOOH$	$CH_3O_2^+, CH_3O_2^+.H_2O$	2.4(-9)
$H_3O^+.H_2O + CH_4$	H_3O^+	5.4(-9)
$H_3O^+.H_2O + CH_3OH$	$CH_5O^+, CH_5O^+.H_2O$	2.4(-9)
$H_3O^+.H_2O + CH_3CHO$	$C_2H_5O^+, C_2H_5O^+.H_2O$	3.1(-9)
$H_3O^+.H_2O + CH_3COOH$	$C_2H_5O_2^+, C_2H_5O_2^+.H_2O$	2.7(-9)
$H_3O^+.H_2O + C_2H_5OH$	$C_2H_7O^+, C_2H_7O^+.H_2O$	2.5(-9)
$H_3O^+.H_2O + (CH_3)_2O$	$C_2H_7O^+, C_2H_7O^+.H_2O$	2.2(-9)
$H_3O^+.H_2O + (CH_3)_2CO$	$C_3H_7O^+, C_3H_7O^+.H_2O$	3.5(-9)
$H_3O^+.H_2O + NH_3$	$N_4H^+, N_4H^+.H_2O$	2.2(-9)
$H_3O^+.2H_2O + CH_2O$	$CH_3O^+.(2-m)H_2O$[a]	1.0(-10)
$H_3O^+.2H_2O + HCOOH$	$CH_3O_2^+.H_2O, C_3H_2O^+.2H_2O$	1.5(-9)
$H_3O^+.2H_2O + CH_3OH$	$CH_5O^+.(2-m)H_2O$	2.0(-9)
$H_3O^+.2H_2O + CH_3CHO$	$C_2H_5O^+.(2-m)H_2O$	2.6(-9)
$H_3O^+.2H_2O + CH_3COOH$	$C_2H_5O_2^+.(2-m)H_2O$	2.4(-9)
$H_3O^+.2H_2O + C_2H_5OH$	$C_2H_7O^+.(2-m)H_2O$	2.0(-9)
$H_3O^+.2H_2O + (CH_3)_2O$	$C_2H_7O^+.(2-m)H_2O$	2.0(-9)
$H_3O^+.2H_2O + (CH_3)_2CO$	$C_3H_7O^+.(2-m)H_2O$	3.0(-9)
$H_3O^+.2H_2O + NH_3$	$N_4H^+.(2-m)H_2O$	1.2(-9)
$H_3O^+.3H_2O + CH_2O$	$CH_3O^+.(3-n)H_2O$[a]	> 1.0(-10)
$H_3O^+.3H_2O + HCOOH$	$C_3H_2O^+.(3-n)H_2O$	> 1.0(-9)
$H_3O^+.3H_2O + CH_3OH$	$CH_5O^+.(3-n)H_2O$	1.5(-9)
$H_3O^+.3H_2O + CH_3CHO$	$C_2H_5O^+.(3-n)H_2O$	2.3(-9)
$H_3O^+.3H_2O + CH_3COOH$	$C_2H_5O_2^+.(3-n)H_2O$	2.2(-9)
$H_3O^+.3H_2O + C_2H_5OH$	$C_2H_7O^+.(3-n)H_2O$	1.7(-9)
$H_3O^+.3H_2O + (CH_3)_2O$	$C_2H_7O^+.(3-n)H_2O$	1.8(-9)
$H_3O^+.3H_2O + (CH_3)_2CO$	$C_3H_7O^+.(3-n)H_2O$	2.9(-9)
$H_3O^+.3H_2O + NH_3$	$H_4N^+.(3-n)H_2O$	1.8(-9)

[a] m,n - number of freed water molecules; $0<m<2$, $0<n<3$.

5. REFERENCES

1. FRANKLIN, J.L., DILLARD, J.G., ROSENSTOCK, H.M., HERRON, J.T., DRAXL, K.: Ionization Potentials, Appearance Potentials and Heats of Formation of Gaseous Positive Ions. Natl. Stand. Ref. Data Syst., NBS **26** (1969).
2. ROSENSTOCK, H.M., DRAXL, K., STEINER, B.W.,HERRON, J.T.: Energetics of Gaseous Ions. J. Phys. Chem. Ref. Data, Vol. **6**, Suppl. 1 (1977).
3. LIAS, S.G., LIEBMAN, J.F., LEVIN, R.D.: Proton Affinities and Heats of Formation of Molecules and Corresponding Protonated Species. J. Phys. Chem. Ref. Data, Vol. **13**, Suppl. 3 (1984).
4. RADZIG, A.A., SMIRNOV, B.M.: Refenrence Data on Atoms. Molecules and Ions. Springer Ser. Chem. Phys. **31**, Springer Verlag (1985).
5. ALBRITTON, D.L.: Ion-Neutral Reaction Rate Constants Measured in flow Reactors Through 1977. Atomic Data and Nuclear Tables, Vol. **22**,No 1, Academic Press (1978).
6. IKEZOE, Y., MATSUOKA, S., TAKEBE, M., VIGGIANO, A.: Gas Phase Ion-Molecule Reaction Rate Constants Through 1986. Ion Reaction Res. Group, Japan (1987) (Distributed through Maruzen Comp., Tokyo).
7. YENCHA, A.J.: Penning Ionization and Related Processes. in Electron Spectroscopy (BRUNDLE C.R., BAKER A.D., Eds.) Vol. **5**, p. 197. Academic Press, London (1984).
   UKAI, M.,HATANO, Y.: Gaseous Electronics and its Applications (by CROMPTON, R.W., HAYASHI, M., BOYD, D.E., MAKABE, T.). KTK Scientific, Tokyo (1991), p.51.
   SISKA, P.E.: Molecular Beam Studies of Penning Ionization. Rev.Mod.Phys. **25** (1993) 337.
8. HATANO, Y. in Handbook of Radiation Chemistry (TABATA Y.,ITO Y., TAGAWA S., Eds.) CRS Press (1990).
9. HERMAN, Z., ČERMÁK, V., Collection Czech. Chem. Commun. **31** (1966) 649.
10a. YOSHIDA, H., KITAJIMA, M., KAWAMURA, H., HIDAKA, K., UKAI, M., KOUCHI, N., HATANO, Y.: J.Chem.Phys. **98** (1993) 6190.
10b. ČERMÁK, V., HERMAN, Z.: Collection Czech. Chem. Commun. **30** (1965) 169.
11. MÄRK, T.D., CASTLEMAN, A.W.,Jr., Adv. Atom. Mol. Phys. **20** (1985) 65. MÄRK, T.D., ECHT, O. , Chapter 5.7. in: Clusters of Atoms and Molecules (H. Haberland, Ed.), Springer (1991); MÄRK, T.D., Z. Phys. **D12** (1989) 263; Int. J. Mass Spectrom. Ion Proc. 79 (1987) 11; NG,C.Y., Adv. Chem. Phys., **52** (1983) 263; KEESEE, R.G.,CASTLEMMAN, A.W.,: In Swarm Studies and Inelastic Electron Molecule Collision (PITCHFORD, L.C. et al)

Springer, New York (1987) 351; MEOTNER, M., SPELLER, C.V., J. Phys. Chem., **90** (1986) 6616; COMBIE, J. Mc, SCOLES, G. in: The Physics of Electronic and Atomic Collisions (DALGARNO, A. et al., Eds.) AIP, New York (1990) 430.

12. DEHMER,P.M., POLIAKOFF, E.D., Chem. Phys. Lett., **77** (1981) 326.
13. ONO, Y., LINN, S.H., PREST,H.F., GRESS, M.E., NG, C.Y., J. Chem. Phys. **74** (1981) 1125.
14. BIRKHOFER, H.P., HABERLAND,H., WINTERER, M., WORSNOP, D., Bunsenges. Physik, Chem. **88** (1984) 207.
15. SIDDIQUI, H.R., BERNFELD D., SISKA, P.E., J. Chem. Phys., **80** (1984) 567.
16. KAMKE, W., KAMKE, B., KIEFL, H.U., HERTEL, I.V., Chem. Phys. Lett., **122** (1985) 356.
17. DAO, P.D., CASTLEMAN, A.W., Jr., J. Chem. Phys., **84** (1986) 1435.
18. KAMKE, B., KAMKE, W., HERMANN, R., HERTEL, I.V., Z. Phys. **D11** (1989) 153.
19. POLIAKOFF, E.D., DEHMER, P.M., DEHMER J.L., STOCKBAUER, R., J. Chem. Phys., **76** (1982) 5214.
20. NORWOOD, K., GUO, J.H., LUO, G., NG, C.Y.,Chem.phys., in print (1990).
21. STACE, A.J., BERNHARD, D.M., Chem. Phys. Lett., **146** (1988) 531 and earlier references therein.
22. KLOTS, C.E., RADIAT, C.E., Phys. Chem., **20** (1982) 51.
23. STACE, A.J., SHUKLA, A.K., J. Phys. Chem., **86** (1982) 157; STEPHAN, K., RUTREL, J.H., PETERSON, K.I,, CASTLEMAN, A.W., Jr., WAGNER, H.E., DJURIC, N., MÄRK, T.D., Int. J. Mass Spectrom, Ion Phys., **44** (1982) 167; NG, C.Y., TREVOR, D.J., TIEDEMANN, P.W., CEYER, S.T., KRONEBUSCH, P.L., B.H. MAHAN, B.H., LEE, Y.T., J. Chem. Phys., **67** (1977) 4235.
24. COOLBAUGH, M.T., PFEIFFER, W.R., GARVEY, J.F., Chem. Phys. Lett., **156** (1986) 19 and references herein.
25. ECHT, O., S. MORGAN, S., DAO, P.D., STANLEY, R.J., CASTLEMAN, A.W.,Jr., Ber. Bunsenges. Physik. Chem., **88** (1984) 217.
26. HERMANN, V., KAY, B.D., CASTLEMAN, A.W., Jr., Chem. Phys. **72** (1982) 185.
27. BERNARD, D.M., STACE, A.J., Int. J. Mass Spectrom. Ion Proc., **84** (1988) 215.
28. BUCK, U., LAUENSTEIN, C., MEYER, H., SROKA, R., J. Phys. Chem., **92** (1988) 1916.
29. BRUTSCHY, B., EGGERT, J., RIEHN, C.R., BAUMAGÄRTEL, H., Contr. Symp. Atomic Surface Physics (MÄRK, T.D., HOWORKA,I., Eds.) Obertraun (1990) pp. 293-298.

30. KLOTS, C.E., COMPTON, R.N., J. Chem. Phys., **69** (1978) 1636 and 1644; STAMATOVIC, A., SCHEIER, P.,T.D. MÄRK, T.D., Z. Phys. **D6** (1987) 351; HASHEMI, R., KÜHN, A., ILLENBERGER, E., Int. J. Mass Spectrom. Ion Proc. **100** (1990) 753.
31. ECHT, O., COOK, M.C., CASTLEMAN, A.W., Jr., Chem. Phys. Lett., **135** (1987) 229.
32. FOLTIN, M., WALDER, G., MOHR, S.,SCHEIER, P., CASTLEMAN,A.W., Jr., MÄRK, T.D., Z. Phys.D, **20** (1991) 157.
33. KREISLE,D., ECHT, O.,KNAPP, M., RECKNAGEL,E., Phys. Rev. **A33** (1986) 768.
34. LETHBRIDGE, P.G., STACE, A.J., J. Chem. Phys., **91** (1989) 7685.
35. WALDER, G., FOLTIN, M., LEZIUS, M., MOHR, S., SONDEREGGER, M., CLEMOT, N., SCHEIER, P., MÄRK, T.D., Contr. Symp. Atomic Surface Physics (MÄRK, T.D., HOWORKA, F., Eds.) Obertraun (1990) pp. 449-454.
36. STEPHAN, K., STAMATOVIC, A., MÄRK, T.D., Phys. Rev. **A28** (1983) 3105; STEPHAN, K., MÄRK, T.D., Chem. Phys. Lett., **90** (1982) 51.
37. NORWOOD, K., GUO, J.H., NG, C.Y., J. Chem. Phys., **90** (1989) 2995.
38. FERGUSON, E.E., ALBERTONI, C.R., KÜHN, R., CHEN, Z.Y., KEESEE, R.G., CASTLEMAN,A.W., Jr., J. Chem. Phys., **88** (1988) 6335.
39. KLOTS, C.E., J. Phys. Chem., **92** (1988) 5864; J.Chem.Phys. **83** (1985) 5854.
40. ENGELKING, P.C., J. Chem. Phys., **87** (1987) 936.
41. SCHARF, D., JORTNER, J., LANDMANN, U., Chem. Phys. Lett., **126** (1986) 495.
42. STACE, A.J., SHUKLA, A.K., J. Am. Chem. Soc. **104** (1982) 5314.
43. FUTRELL, J.H., STEPHAN,K., MÄRK, T.D., J. Chem. Phys., **76** (1982) 5893.
44. MORGAN, S., CASTLEMAN, A.W., Jr., J. Am. Chem. Soc., **109** (1987) 2667.
45. MAGNERA, T.F., DAVID, D.E., MICHL, J., Chem. Phys. Lett., **123** (1986) 327; ENGELKING, P.C., Chem. Phys. Lett., **139** (1987) 6; LEISNER, T., ECHT, O., KANDLER,O., YAN, X.J., RECKNAGEL, E., Chem. Phys. Lett. **18** (1988) 393; WALDER, G., WINKLER, C., MÄRK, T.D., Chem. Phys. Lett., **157** (1989) 224.
46. WALDER, G., MARGREITER, D., WINKLER, C., STAMATOVIC, A., HERMAN, Z., MÄRK, T.D., J. Chem. Soc. Faraday Trans. **86** (1990) 2395.
47. WALDER, G., MARGREITER, D., WINKLER, C., STAMATOVIC, A., HERMAN, Z., FOLTIN, M., MÄRK, T.D., Z. Phys. D. **20** (1991) 201.
48. KNAPP, M., ECHT, O., KREISLE, D., RECKNATEL, E., J. Phys. Chem., **91** (1987) 2601.
49. ALBRITTON, D.L., Atom. Data Nucl. Tables, 22* (1978) 1; ADAMS, N.G., SMITH, S., in: Reactionof Small Transient Species, Kinetics and Energetics (A. FONTIJN, Ed.) Academic Press, New York (1983); SMITH, D., ADAMS,N.G., Top. Curr. Chem., **89** (1980) 1.

50.BOHME, D.K., WLODEK, S., WILLIAMS, L, FORTE, L., FOX, A., J. Chem. Phys., **87** (1987) 6934.

51.CASTLEMAN, A.W., KEESEE, R.G., J. Phys. Chem. Ref. Data, **15** (1986) 1011.

52.SUNNER, J., KEBARLE, P., J. Phys. Chem., 85 (1981) 327; Y.K. LAU, Y.K., KEBARLE, P., Can. J. Chem. **59** (1981) 151.

53.BOHME, D.K., NATO Adv. Study Inst. (Vimeiro) 1982.

54.SMITH, D., ADAMS, N.G., ALGE, E., Planet Spase Sci., **29** (1981) 449.

55.FERGUSON, E.E., Ann. Conf. Mass Spectrom. Allied Topics, 30th, Honolulu (1982) 200.

56.SMITH, D., ADAMS, N.G., MILLER, T.M., J. Chem. Phys., **69** (1978) 308.

57.RAKSHIT, A.B., WARNECK, P., Int. J. Mass Spectrom. Ion Phys., **40** (1981) 135.

58.FAHEY, D.W., BÖHRINGER, H., FEHSENFELD, F.C., FERGUSON, E.E., J. Chem. Phys., **76** (1982) 1799.

59.HENCHMAN, M., PAULSON, J.F, HIERL, P.M., J. Am. Chem. Soc. **105** (1983) 5509.

60.HOWARD, C.J., FEHSENFELD, F. C., M. McFARLAND, M. ,J. Chem. Phys., **60** (1974) 5086.

61.BOHME, D.K., MACKAY, G.I., TANNER, S.D.,J. Am. Chem. Soc., **101** (1978) 3724.

62.BOHME, D.,K., RAKSHIT, A.B., MACKAY, G.I., J. Am. Chem. Soc., **104** (1982) 110; A.A. Viggiano, F. Dale and J.F. Paulson, J. Chem. Phys., 88 (1988) 2469.

63.PELLERITE, M.J., BRAUMANN, J.I., J. Am. Chem. Soc., **102** (1980) 5993.

64.ROWE, B.R., VIGGIANO, A.A., FEHSENFELD, F.C., FAHEY, D,W., FERGUSON, E.E. J. Chem. Phys., **76** (1982) 742.

65.VIGGIANO, A.A., DEAKYNE, C.A., DALE, F., PAULSON, J.F., J. Chem.Phys., **87** (1987) 6544.

66.AZRIA, R., PARENTEAU, L., SANCHE, L., J.Chem.Phys. **87** (1987) 2292.

67.SANCHE, L., PARENTEAU, L., Phys. Rev. Lett., **59** (1987) 136.

68.SANCHE, L., PARENTEAU, L., J. Chem. Phys., (1990)

69.SANCHE, L., Radiat. Phys. Chem., **34** (1989) 15.

70.SANCHE, L., PARANTEAU,L., Chem. Phys., **91** (1989) 2664.

71.SANCHE, L., PERLUZZO, G., MICHAUD, M., J. Chem. Phys., **83** (1985) 3837.

Chapter 7

STOPPING POWERS, RANGES AND STRAGGLING

H. Paul
Johannes-Kepler-Universität,
Linz, Austria

M.J. Berger
National Institute of Standards and Technology,
Gaithersburg, Maryland,
United States of America

The authors acknowledge the valuable contribution to this chapter by H. Bichsel, 1211, 22nd Ave. East, Seattle, WA 98112, USA.

LIST OF SYMBOLS FOR CHAPTER 7

A_1	mass number of projectile (7.3.1.1)
A_2	relative atomic mass of natural target element (7.2.1.1, 7.3.1.1)
A_1-A_8	expansion coefficients for stopping power fits (Table 7.10)
α	angle of emergence with respect to entrance angle (7.5.4)
$\alpha_{1/2}$	half-maximum angle (7.5.4)
$\tilde{\alpha}$	reduced scattering angle (7.5.4)
β	$= v_1/c$
C/Z_2	shell correction (7.3.1.1)
c	speed of light
δ	density effect correction (7.2.1.1, 7.3.1.1)
Δ	energy loss for path length s (7.2.4)
$\langle\Delta\rangle$	average energy loss (7.1, 7.2.4)
E	total relativistic energy (7.1)
$\varepsilon = S/n$	stopping cross section (7.1)
ϕ_c	fraction of energy imparted to medium (7.3.1.5)
I	mean excitation energy (7.2.1.1, 7.3.1.1)
L(T)	Stopping number (7.2.1)
L_0, L_1, L_2	see 7.3.1.1
LFCTR	correction factor for screening length (7.5.1.1)
λ	scaled energy loss parameter (7.2.4)
Λ	screening length for the projectile (7.5.1.1)
m_e	rest mass of electron
M_1	relative atomic mass of projectile (7.3.1.1)
M_2	relative atomic mass of target atom (7.3.3)
M_p	relative atomic mass of proton
μ_i	i^{th} moment of a distribution (7.1)
n	number of atoms or molecules per unit volume (7.1)
N	number of electrons carried by ion (7.5.1)
N_A	Avogadro constant
Ω	energy straggling (root-mean-square deviation of energy) (7.3.3)
Ω_B	Bohr energy straggling (7.3.3)
Ω_{FH}	energy straggling according to Firsov-Hvelplund (7.5.3)
Ω_s	energy straggling due to surface roughness (7.5.3)
Ω_T	energy straggling for smooth foil (7.5.3)
p(T)	mean free path between inelastic collisions (7.2.5)
q	$= (Z_1 - N)/Z_1$ fractional projectile charge (7.5.1.1)
r_e	$= e^2/(4\pi\varepsilon_0 m_e c^2)$ classical electron radius (in SI units) (7.2.1.1, 7.3.1.1)

R csda range (7.1)

$\overline{R_V}$ vector range (average straight-line distance from point of emission to end of path, 7.1, 7.3.6)

$\overline{R_x}$ mean projected range (7.1)

ρ density of target (7.1)

s path length variable (7.1) (in units of length, except for 7.2.4)

s_{av} average path length (7.2.5)

$S = -\frac{dT}{ds}$ linear stopping power (7.1)

σ_R range straggling (root-mean-square deviation of $\overline{R_x}$) (7.1)

$d\sigma$ differential cross section for an energy transfer W (7.1)

t target thickness (7.5.4)

τ reduced target thickness (7.5.4)

T kinetic energy of projectile

T_0 initial kinetic energy

T_{eq} equivalent proton energy (7.3.1.1)

T_n kinetic energy of neutron (7.3.1.5)

$T_r = T/M_1$ energy per mass unit (7.3.1.1)

u atomic mass constant, $m(^{12}C)/12$ (7.2.1.1, 7.3.1.1)

v_0 Bohr velocity (= c/137; v_0^2= 24.8 keV/u)

v_1 projectile speed

v_F Fermi velocity for solid target (7.5.1.1)

w_j fraction by weight (7.2.1.5)

W energy transfer in a single collision (7.1)

W_c cut-off for energy transfer (7.1)

W_m maximum energy transfer to an electron (7.3.3)

x coordinate axis corresponding to initial beam direction (7.1)

ξ energy loss variable (7.2.4)

Z_1 atomic number of projectile

$Z_{1,eff}$ effective charge of projectile (in units of electron charge) (7.4.1.2, 7.5.1)

Z_2 atomic number of target atom

ζ relative effective charge (7.4.1.2, 7.5.1)

ζ_s relative effective charge in the solid (7.5.1.3)

When charged particles traverse a medium, they are scattered and they lose energy; the energy lost is then imparted to the medium (or carried away by electromagnetic radiation). In dosimetry and radiology, one needs to understand not only the energy lost by the primary particle, but also the energy transfer to the medium through all generations of secondary particles [1]. The stopping power only describes the energy lost. This is only a first step toward a full treatment, but an indispensable step.

The stopping power is defined as the rate at which particles lose energy along their tracks, averaged over many particles. The linear stopping power, with dimension of energy/length, is therefore expressed as $S = -(dT/ds)_{av}$, where T is the kinetic energy of the projectile, and s is its path length[1)]. Here, dT is, of course, identical to dE (where E is the total relativistic energy). If the particle path is essentially straight and in the x-direction, one can also write $S = -(dE/dx)_{av}$. If, in a transmission measurement of stopping power, the absorber thickness Δt is so small that the energy loss ΔT is a small fraction of the initial kinetic energy, and if the path length increase due to multiple scattering can be neglected (cf. Sec. 7.5.4), then one has approximately $S = -\Delta T_{av}/\Delta t$ (One has to be careful, however, if the charge of the projectile is not constant, see below).

It is often useful to consider the mass stopping power S/ρ (dimension energy/areal density) since, to first order, this quantity is independent of the density of the medium. From a theoretical standpoint, one defines the stopping cross section $\varepsilon = \int W d\sigma$ (dimension energy/number of atoms (or molecules) per unit area), where $d\sigma$ is the differential cross section for an energy transfer W. Under certain circumstances [2,3,4], ε is equal to S/n, where $n = \rho N_A/A_2$ is the number of atoms (or molecules) per unit volume. If S/n is expressed in units of eV/(10^{15} atoms/cm^2), it gives approximately the energy loss per monolayer.

---

1) This notation seems to imply that T is a unique, continuous function of s, but that is only approximately true.

One can separate the stopping power into three components which must be calculated by different methods:

* the *electronic stopping power* (sometimes also called *collision stopping power* [5]) which is due to the transfer of energy to bound electrons in inelastic Coulomb collisions;

* the *radiative stopping power* which is due to the emission of bremsstrahlung quanta in Coulomb collisions with atomic nuclei or bound electrons;

* the *nuclear stopping power* which is due to the transfer of energy to target atoms in elastic Coulomb collisions.[2)]

For electrons and positrons, the nuclear stopping power is negligible compared to the electronic stopping power except at energies below the threshold for electronic excitations (a few eV). For heavy charged particles (mesons, protons and heavier), the radiative stopping power is negligible compared to the electronic stopping power except at enormously high energies, and the nuclear stopping power is important only at low energies. Electronic stopping leaves the direction of the heavy projectile almost unchanged, whereas nuclear stopping is accompanied by a change of direction.

The restricted collision stopping power [5] often used in radiobiology is defined as the mean energy loss per unit path length involving energy transfers W smaller than some chosen cut-off energy W_c. It is also called "linear energy transfer" (LET) [6], and describes, approximately, the energy imparted to the medium in the vicinity of the particle track. For unrestricted W, it equals the collision stopping power defined above. Results for electrons are given in [5], for several values of W_c. See also Table 7.19 below.

---

2) The term "nuclear" is customarily used, even though no nuclear forces are involved. Janni [7], however, included truly nonelastic *nuclear* interactions in his calculations of stopping.

The dependence of nuclear stopping on the solid angle of detection ("angle-restricted nuclear stopping") is discussed in Sec. 7.4.2.

If a particle has a fixed charge and if the differential cross section $d\sigma$ for an energy transfer W leading to ionization (Ch.2) or excitation is known, then the stopping cross section can be determined by integrating $Wd\sigma$ (see Sec. 7.2.1.7). If only the "partial stopping cross section" (without excitation) is integrated, one obtains a slightly smaller result (see table 2.8). Bichsel [4] finds that the integrated energy loss spectrum for various projectiles in silicon agrees well with stopping power as given by the Bethe theory.

A slow heavy particle, when passing through matter, will capture and lose electrons until its charge reaches a dynamic equilibrium state. In this case, if one wants to determine the stopping cross section by integrating $Wd\sigma$, one has to include the contribution of charge changing collisions [8]. In practice, the effect of the charge state upon stopping power is normally described by the "effective charge" (see 7.4.1.2 and 7.5.1.1, and also chapters 2 and 9). Tabulated stopping power values normally correspond to this equilibrium state. If the thickness of a target is too small to produce charge equilibrium, then division of energy loss by target thickness will not yield the stopping power unless a correction is applied [9]. To describe the situation of a projectile that changes its charge state toward equilibrium while entering the surface of some material, one speaks of "pre-equilibrium stopping".

The history of particles passing through matter is described by stochastic, i.e., statistically distributed quantities. For many purposes, the description by a simple average is sufficient, but higher moments μ_i of the energy (or range) distribution may also be needed. For example, the energy distribution of a particle beam of initial energy T_0 after traversing a certain amount of material is completely described by the straggling function $F(\Delta)$, i.e., the distribution of energy losses $\Delta = T_0 - T$. Less completely, the distribution can be described by its average energy $\langle T \rangle$ or the average energy loss $\langle \Delta \rangle = T_0 - \langle T \rangle$ and by its energy straggling $\Omega = \sqrt{\langle (T-\langle T \rangle)^2 \rangle} = \sqrt{\langle (\Delta-\langle \Delta \rangle)^2 \rangle}$, the root of the second moment, μ_2. For a Gaussian function, the full width at half maximum is $2.355 \times \Omega$. Deviations from Gaussian shape are described by the skewness $\mu_3 = \langle (T-\langle T \rangle)^3 \rangle$ (or the dimensionless skewness coefficient μ_3/Ω^3) and the kurtosis $\mu_4 = \langle (T-\langle T \rangle)^4 \rangle$.

Following in part the suggestions of the Subcommittee on Penetration of Charged Particles [10, p. iv], we define the following terms:

* The "range" of a group of particles of a given initial energy T_0 is their mean (rectified) path length from the point of departure to the point where they come to rest. This definition is not further used here.

* The "csda range" is defined by the integral $R = \int_0^{T_0} \frac{dT}{s}$ that corresponds to the continuous-slowing-down-approximation. This quantity is an extremely good approximation [11] to the range defined above and will be used instead in this chapter (see, however, Sec. 7.2.5 for an exception).

* We assume that the particles enter the medium along the x-axis. Then the "projected range" $\langle R_x \rangle$ is the mean of the path lengths projected onto the x-axis. The distribution of individual projected ranges is described [12] by this mean and by the root of the second moment of the distribution $\sigma_R = \sqrt{\langle (R_x - \langle R_x \rangle)^2 \rangle}$, also called range straggling. Clearly, we always have $R \geq \langle R_x \rangle$.

* In cases where the particles are emitted from a point source, it may be useful to introduce the additional definition "vector range" $\langle R_v \rangle$, i.e., the average straight-line distance from the point of emission to the point where the particles come to rest (cf. H.H.Andersen [134]).

In the following, the available data will be discussed mainly in regard to the "key substances" that are of interest to radiation therapy (cf. the INTRODUCTION to this book). Also, we assume the solids to be amorphous (or polycrystalline), i.e., we neglect channeling effects.

7.2. ELECTRONS

7.2.1. Electronic stopping power

7.2.1.1. Stopping Power Formula.

Because of the scarcity of experimental data, all tables [10, 13-15, 5] of electronic stopping powers for electrons (also called collision

stopping powers, cf. Sec. 7.1) have been based on the use of Bethe's theory [16, 17]. The formula for the mass collision stopping power, $\frac{1}{\rho} S_{col}(T)$, is:

$$\frac{1}{\rho} S_{col}(T) = \frac{4\pi r_e^2 m_e c^2}{u} \frac{1}{\beta^2} \frac{Z_2}{A_2} L(T). \qquad (7.1)$$

L(T) is the stopping number, T is the kinetic energy of the electron, r_e is the classical electron radius, $m_e c^2$ is the electron rest energy, u is the atomic mass unit, β is the electron velocity in units of velocity of light, and Z_2 and A_2 are the atomic number and relative atomic mass of the target atom. With r_e in cm, $m_e c^2$ in MeV, and u in g, the constant in eq. (7.1) becomes $4\pi r_e^2 m_e c^2/u = 0.307075$ MeV cm^2/g, and S_{col}/ρ is given in the same units. The stopping number is given by

$$L(T) = \frac{1}{2}\left[\log \frac{m_e c^2 \beta^2 T}{2I^2(1-\beta^2)} - (2\sqrt{1-\beta^2} - 1 + \beta^2) \log 2 + \right.$$

$$\left. + 1 - \beta^2 + \frac{1}{8}(1 - \sqrt{1-\beta^2})^2 - \delta \right], \qquad (7.2)$$

where I is the mean excitation energy, δ is the density-effect correction, and log means the natural logarithm. The mean excitation energy is approximately equal to $I_0 \times Z_2$, with I_0 = 10 eV, and must be determined more accurately from experimental data.

7.2.1.2. Absence of Barkas, Bloch and Shell Correction.

Eqs.(7.1,7.2) were derived in the first Born approximation. Whereas for heavy charged particles higher-order approximations are available in the form of Barkas and Bloch corrections (proportional to the third, respectively fourth power of the charge of the projectile), similar correction terms applicable to electrons have not yet been worked out.

The derivation of the stopping-power formula is based on the assumption that the velocity of the incident electron is large compared to the velocities of the atomic electrons. For collisions with inner-shell electrons, especially in high-Z materials, this condition is no longer satisfied for incident electrons with energies below about 100 keV.

Corrections are required analogous to the shell corrections which have been introduced into stopping power theory for heavy charged particles. However, a theory of such corrections for electrons is not yet available.[3,4] In stopping-power tabulations for electrons it is therefore customary to limit the use of Eqs.(7.1,7.2) to energies above 10 keV, and to construct stopping powers at lower energies from atomic or molecular cross sections (see Sec. 7.2.1.7).

7.2.1.3. Absence of Binding Corrections for Large Energy Transfers.

In Bethe's derivation of the stopping power formula for electrons, large energy transfers are treated with use of Møller's [19] cross section for the collision of an electron with a stationary free electron. No estimates are available for the error incurred by the neglect of the binding and of the velocity distribution of the atomic electrons.

7.2.1.4. Mean Excitation Energies for Elements.

The mean excitation energy in Eq.(7.2), also denoted as *I*-value, is the most important non-trivial parameter that characterizes the stopping properties of a material, and must be determined with use of experimental data. This involves (a) the analysis of stopping-power and range data for protons, deuterons or alpha particles, or (b) the use of oscillator-strength distributions for gases, or dielectric response functions for materials in the condensed phase. Method (a) is the one more widely used.

---

[3] Bethe and Ashkin [18] point out that the use of the first Born approximation down to very low energies in the evaluation of shell corrections is justified by the fact that an incident heavy particle can be treated as equivalent to a perturbing potential that moves with constant velocity. This consideration does not apply to electrons.

[4] Inelastic collision cross sections for silicon developed by Bichsel [4] implicitly contain shell corrections. The use of these cross sections results in collision stopping powers for electrons that are 4.6 % lower at 10 keV, and 8.3% lower at 1 keV, than those from Eq.(7.1). However, the reliability of these results is uncertain because they were obtained in the first Born approximation.

However, method (b) has acquired increasing importance in recent years, and made possible very accurate determinations of I-values for many molecular gases [20], for liquid water [21,22] and for aluminum [23].

The accuracy requirement for I-values is not very stringent. Because I enters logarithmically into Eq.(7.2), the uncertainties of the collision stopping powers are several times smaller than the uncertainties of the I-value. This is shown in Table 7.1, which gives the percent decrease of the stopping power that would result from a 10-percent increase of the mean excitation energy.

Numerous evaluations of I-values have been published in the course of the years [5, 10, 11, 24-27, 7]. The estimates keep changing as the database of relevant stopping-power data increases. Choices of I-values are also influenced by unavoidable subjective judgments. In one of the most recent compilations [5], experimental data to determine I-values were available for 44 elements, and interpolation with respect to atomic number was used for the other elements. For the 44 elements, the uncertainties of the adopted I-values were estimated to be smaller than 5% for 36 elements, between 5 and 10% for 5 elements, and between 10 and 15% for 3 elements.

The extraction of I-values from measured stopping-powers and ranges of protons, deuterons or alpha particles depends on the use of the Bethe stopping power formula with appropriate shell, Barkas and Bloch corrections. The difficulty arises that in general the first two of these

TABLE 7.1. PERCENT DECREASE OF THE COLLISION STOPPING POWER FOR ELECTRONS ASSOCIATED WITH A 10 PERCENT INCREASE OF THE MEAN EXCITATION ENERGY.

Energy	Percent Decrease of the Collision Stopping Power						
(MeV)	Air	Water	Graphite	Aluminum	Copper	Silver	Gold
0.01	2.0	2.0	2.0	2.4	2.8	3.1	3.7
0.1	1.4	1.4	1.4	1.6	1.7	1.8	2.0
1.0	1.0	0.6	0.7	1.1	0.9	1.1	1.1
10.0	0.8	0.2	0.3	0.3	0.4	0.4	0.5
100.0	0.2	0.01	0.01	0.04	0.08	0.08	0.12

TABLE 7.2. COMPARISON OF MEAN EXCITATION ENERGIES FOR SELECTED ELEMENTS, ADOPTED IN VARIOUS COMPILATIONS, AND OBTAINED IN RECENT EXPERIMENTS.

Compilations:
- AZ: Andersen and Ziegler, 1977 [26]
- Janni: Janni, 1982 [7]
- ICRU: ICRU Report 37, 1984 [5]
- B: Bichsel, 1991 [30]

Experiments:
- Sak88: Sakamoto et al, 1988 [28]; 6.5-MeV protons
- Sak91: Sakamoto et al, 1991 [29]; 73-MeV protons
- BH: Bichsel and Hiraoka, 1991 [31]; 70-MeV protons

		Mean Excitation Energy, eV							
		AZ	Janni (a)	ICRU (a)	Sak88 (b)	B (a)	Sak91 (b)	Sak91 (a)	BH (a,c)
4	Be	62.7	65.2	63.7	63.9				
13	Al	162	160.1	166	167.7		169.7	169.4	[166]
22	Ti	230	228	233	232		247	246	242
26	Fe	280	278	286	282				293
29	Cu	322	323	322	323		343	341	339
42	Mo	406	423	424	413		466	463	440
47	Ag	466	469	470	463		507	504	489
50	Sn	487	500	488	471		491	488	508
73	Ta	684	738	718	674	734	753	763	736
74	W	693	753	727		775			765
78	Pt	759	826	790	728	786	773	786	
79	Au	755	807	790	745	790	799	813	
82	Pb	759	819	823	743	786	836	853	816
92	U	847	880	890		836			

(a) Based on use of shell corrections calculated according to the prescription of Bichsel [5,30].

(b) Based on use of shell corrections from Bonderup [37].

(c) Based on I = 166 eV from ICRU [5]

corrections are not known independently with sufficient accuracy, so that they must be determined jointly with the mean excitation energy. Therefore the *I*-values adopted by various authors depend to a certain extent on the assumptions made in regard to the shell or Barkas corrections. These difficulties are minimized at high energies where the influence of the Barkas and shell corrections is small.

The current situation in regard to *I*-values for elements is indicated in Table 7.2, which compares values adopted in several compilations with values from recent experiments by Sakamoto et al [28,29], Bichsel [30], and Bichsel and Hiraoka [31]. For low-Z elements the agreement is satisfactorily close, but there are discrepancies for high-Z elements which deserve further attention.

7.2.1.5. Mean Excitation Energies for Compounds.

It is preferable to use direct experimental *I*-values for compounds. Such information is often unavailable. However, approximate *I*-values can be obtained by using Bragg's additivity rule, according to which the mass collision stopping power for compounds is a linear combination of the stopping powers of the constituent elements. From Eqs.(7.1,7.2) it follows that the corresponding additivity relation for the mean excitation energy is

$$\log I = \frac{\sum_j w_j \, (Z_2/A_2)_j \, \log I_j}{\sum_j w_j (Z_2/A_2)_j} , \qquad (7.3)$$

where w_j is the fraction by weight, I_j is the mean excitation energy, and $(Z_2/A_2)_j$ is the ratio of atomic number to atomic weight for the j'th atomic constituent of the compound. For improved accuracy, the I_j values used in Eq.(7.3) should take into account atomic binding effects, and should be different for compounds in the gaseous or condensed phase. Table 7.3 shows the *I*-values for atomic constituents in gaseous and condensed compounds used in ICRU Report 37 [5]. This assignment scheme was justified by showing that it provides *I*-values for 13 gaseous, 27 liquid and 14 solids compounds that are close to the *I*-values obtained directly from experimental data. Nevertheless, the scheme is simplistic, and should be replaced by a sounder scheme that takes into account the physics of binding and phase effects, for example, along lines suggested by Thompson [32] and Brandt [33].

TABLE 7.3. MEAN EXCITATION ENERGIES ADOPTED IN ICRU REPORT 37 [5] FOR ATOMIC CONSTITUENTS OF COMPOUNDS, TO BE USED IN THE ADDITIVITY EQ.(7.3).

Constituent	Mean Excitation Energy, eV	
	Gases	Liquids or or Solids
H	19.2	19.2
C	70	81
N	82	82
O	97	106
F		112
Cl		180
Others		1.13 x value for elements

There are also considerable discrepancies between the experimental *I*-values for graphite, usually obtained by the measurement of the ranges of high-energy protons beams in graphite relative to the ranges in other materials. The experimental *I*-values listed in [5] extend from 91.7 ± 8.6 eV to 78.0 ± 4.0 eV. Bichsel and Tschalär (priv. comm. to M. Berger) obtained 78 eV at 19 MeV, and Bichsel and Hiraoka [31] obtained 86.9 eV at 70 MeV.

Of particular interest for medical and radiobiological applications is the mean excitation energy of liquid water. In [5], a value of 75±3 eV was adopted, based on four experimental results: 75.4±1.9 eV from the analysis of Thompson's [32] measurements of partial ranges of 340-MeV protons; 74.6±2.7 eV from the stopping-power measurements of Nordin and Henkelman [34] with 61-MeV pions; 75 eV from Ritchie et al [21], and 75.4 eV from Ashley [22], both obtained from measured optical data. Recently, in an experiment with 70-MeV protons, Bichsel and Hiraoka [31] determined the stopping powers of water relative to that of aluminum. Assuming for aluminum the accurately known *I*-value of 166 eV, they determined the *I*-value of liquid water to be 79.7±0.5 eV, which differs significantly from earlier values.

For tissue-equivalent A-150 plastic, Ishiwari and coworkers [36] made stopping-power measurements with 2.5 to 7.5 MeV protons, and estimated an *I*-value of 64.7 eV, using shell corrections from Bonderup's theory [37]. Re-analysis of their data with shell corrections from [5] leads to *I*-values of 64.4 eV at 2.5 MeV and 62.3 eV at 7.5 MeV. These results are significantly lower than the values of 70.2±0.7 eV to 72.8±0.7 eV obtained by Hiraoka and collaborators at 70 MeV with various A-150 targets of slightly different composition.

Table 7.5 indicates the percent changes of the collision stopping powers for water and various organic solids that are caused by the replacement of *I*-values from [5] by those from [31,35]. The changes are in most instances smaller than the uncertainties due to the approximations in the derivation of the stopping power formula.

TABLE 7.5. PERCENT CHANGE OF COLLISION STOPPING POWERS FOR ELECTRONS THAT RESULT WHEN THE *I*-VALUES ADOPTED IN ICRU REPORT 37 [5] ARE REPLACED BY THOSE OF BICHSEL AND HIRAOKA [31] FOR WATER, AND BY THOSE OF HIRAOKA AND COLLABORATORS [35] FOR THE OTHER MATERIALS.

	Electron Energy, MeV			
	0.01	0.1	1	10
Water(liquid)	-1.21	-0.84	-0.37	-0.11
Graphite	-2.16	-1.47	-0.83	-0.36
A-150 TE plastic	-1.46	-1.02	-0.38	-0.13[a]
	-2.00	-1.40	-0.52	-0.18[a]
	-2.16	-1.51	-0.57	-0.19[a]
White Lucite	-0.16	-0.11	-0.04	-0.02
Clear Lucite	0.08	0.06	0.02	0.01
Polyethylene	-1.15	-0.81	-0.29	-0.10
Polypropylene	-1.60	-1.12	-0.41	-0.14
Nylon 6	-2.19	-1.53	-0.57	-0.19
Polystyrene	0.30	0.21	0.08	0.03
Polyvinyl chloride	0.52	0.35	0.16	0.06
Polycarbonate	-0.95	-0.66	-0.26	-0.09
Mylar	0.88	0.61	0.23	0.08
Teflon	-3.40	-2.32	-1.00	-0.32

a. Three different targets with slightly different composition

7.2.1.6. Density-Effect Correction.

This correction takes into account the reduction of the collision stopping power due to the polarization of the medium by the passage of the incident charged particle. The correction depends on the density and the dielectric response function of the medium. Sternheimer [38,39] developed a simple dielectric model which uses binding energies and occupation numbers for various atomic shells as input. The key to the success of his model is the adjustment of the binding energies, which are multiplied by a factor chosen so that the mean excitation energy agrees with the empirical mean excitation energy adopted used in the stopping power formula.

More accurate calculations of the density effect, based on the use of experimental optical data were made by Inokuti and Smith [40] for aluminum, by Ashley [41] for water, and by Bichsel [4] for silicon. The use of density-effect corrections from these authors in place of those from the Sternheimer theory changes the collision stopping power by less than 0.4% for electrons with energies between 1 and 10 MeV, and even less at higher energies.

Difficulties arise in the evaluation of the density effect for inhomogeneous media. An important case is that of graphite, a material that is widely used for radiation detectors such as ionization chambers and calorimeters. Graphite is a porous, anisotropic material, consisting of loosely packed crystallites. The crystallite density is 2.265 g/cm^3, whereas the bulk density of graphite can vary from 1.5 to 1.9 g/cm^3. In [5], a homogeneous medium with a bulk density of 1.7 g/cm^3 was assumed, and the errors of stopping power incurred thereby might be as large as 1 percent.

7.2.1.7. Data below 10 keV.

At energies below 10 keV, where the Bethe theory ceases to be applicable, stopping cross sections can be constructed as energy-weighted integrals over the cross sections for electron-impact excitation and ionization (see Sec. 7.1). But one must realize that at low enough energies, one can no longer use the concept of stopping power to describe the gradual energy loss along the electron track (see Sec. 7.2.5, and [5]).

Experimental and theoretical information about electron-impact cross sections is quite limited. Therefore, explicitely or implicitely, the Weizsäcker-Williams method [41a] is usually employed , which permits the use of the more abundant cross section data for photon interactions with matter.

Electron-impact cross sections for soft collisions (that result in small energy and momentum transfers) are obtained from oscillator-strength distributions for gases or dielectric response functions for liquids or solids. Sum rules for these distributions provide useful constraints that aid the analysis of experimental data. Hard collisions (that result in large energy and momentum transfers), are described by the Mott cross section, modified by an approximate binding correction. The Mott cross section also takes into account exchange effects resulting from the fact that the incident electron and atomic electrons are indistinguishable. Collisions of intermediate magnitude, which can be considered neither soft nor hard, are treated by heuristic models which interpolate between the two limiting cases of soft and hard collisions. The model parameters are adjusted to get the best possible agreement with the available experimental data on electron-impact ionization. The Weizsäcker-Williams method implicitly assumes the validity of the first Born approximation. When the calculation of stopping powers is extended down to energies of 100 eV or even 10 eV, as is often the case, the failure of the first Born approximation can be expected to result in sizeable errors.

Inelastic scattering cross sections for gases were obtained in this manner by Gerhart [42] for molecular hydrogen, by Eggarter [43,44] for argon, by Paretzke [45-47], Olivero et al [48], Dayashankar and Green [49], and by Laverne and Mozumder [50] for water vapor, by Jackman et al [51] for various atmospheric gases, and by Waibel and Grosswendt [52,53] for nitrogen, carbon dioxide and tissue-equivalent gas. The main purpose of these data compilations was to provide input for the calculation of electron energy-degradation spectra and yields of excitations and ionizations. Stopping powers were obtained as a by-product of this work.

The calculation of stopping powers of solids is usually based on methods introduced by Lindhard [54] and Ritchie [55] involving the use of dielectric response functions. The differential inelastic scattering cross section is proportional to Im $[-1/\varepsilon(\omega,k)]$, where Im indicates the imaginary part and $\varepsilon(\omega,k)$ is the dielectric response function, a complex-valued function of the energy transfer $\hbar\omega$ and momentum transfer $\hbar k$ to the medium.

The stopping power is obtained by integrating the energy-weighted differential cross section with respect to ω and k.

A variety of procedures has been used to evaluate the required dielectric response function, involving the combination of experimental input (optical data) with the local-plasma approximation (free electron model) of Lindhard [54,56]. Ritchie, Ashley, Tung and collaborators at the Oak Ridge National Laboratory applied the method to calculate stopping powers, and mean free paths for inelastic scattering, for various materials [57-67]. They used different dielectric models appropriate for conductors,

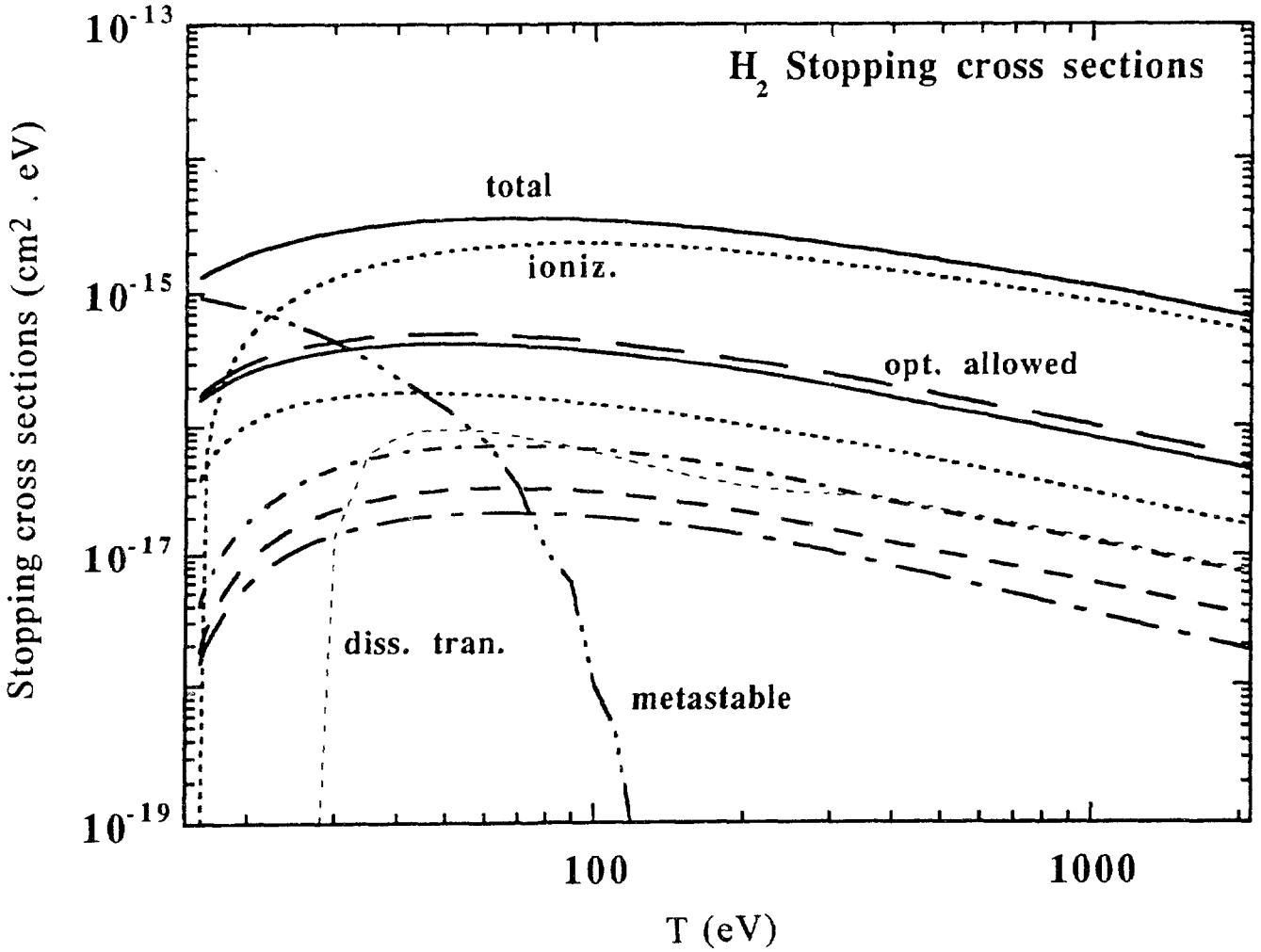

Fig.7.1. Stopping cross section of molecular hydrogen gas for electrons. Calculated by M. Kimura (private communication) from cross sections compiled by Gerhart [42] and used by Kimura et al [71] for the calculation of energy degradation spectra. The figure shows, in addition to the total stopping cross section, the contributions from ionizations, from excitations resulting in optically allowed transitions and in transitions leading to metastable states, and contributions from dissociative transitions.

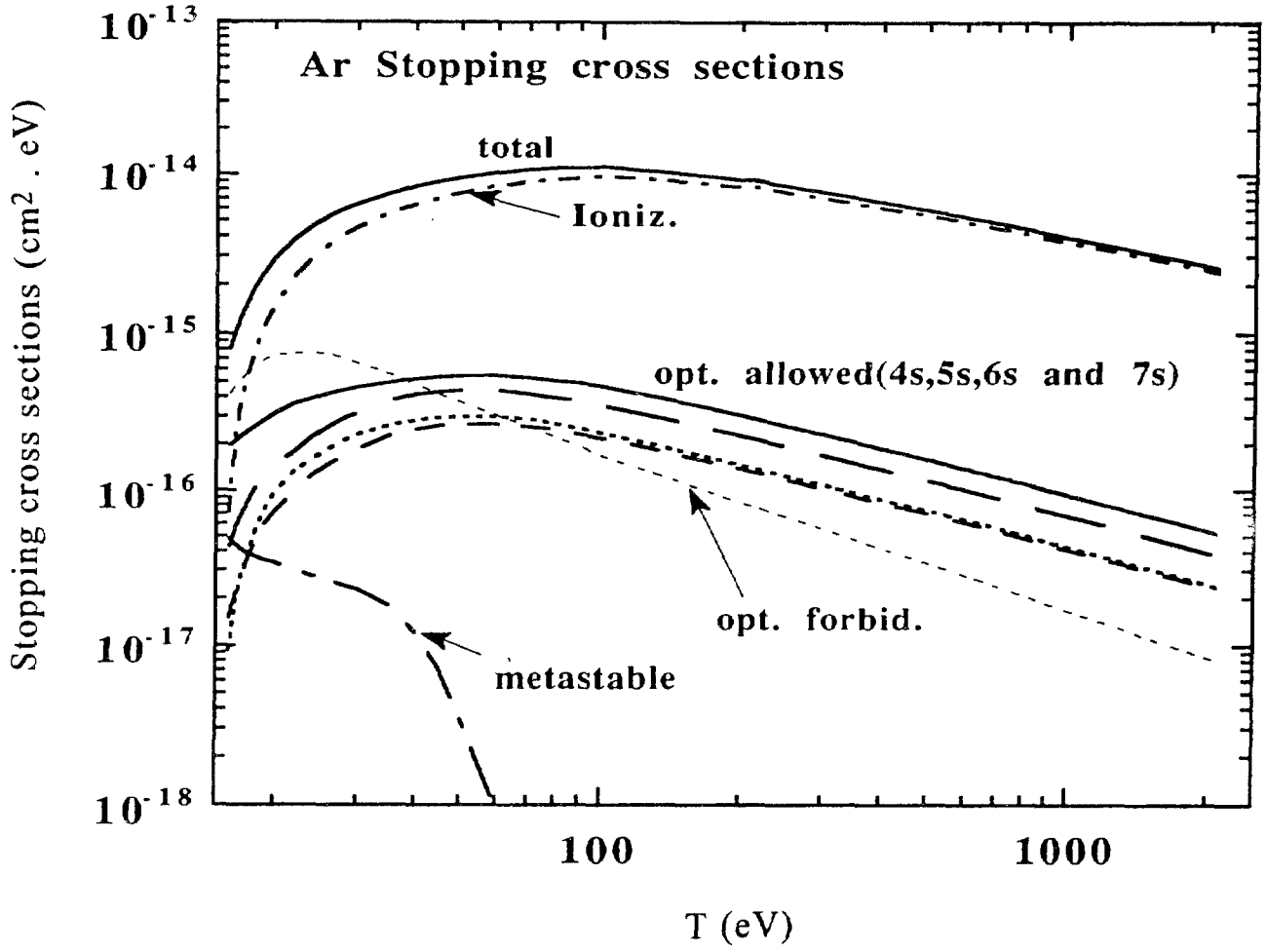

Fig.7.2. Stopping cross section of argon gas for electrons. Calculated by M.Kimura (private communication) from cross sections compiled by Eggarter [43,44], and used by Kimura et al [71] for the calculation of energy degradation spectra. The figure shows, in addition to the total stopping cross section, the contributions from ionizations and from excitations involving optically allowed and forbidden transitions and transitions to metastable states.

semiconductors and insulators, which take into account single-electron excitations and collective excitations (plasmons). Measured optical data were used to determine the dielectric response function in the limit of zero momentum transfer. The response function was extrapolated into the region of non-vanishing momentum transfer in such a manner that the resulting cross section for large energy transfers approaches the Mott cross section. The contribution to the stopping power from inner-shell electrons was evaluated from generalized atomic oscillator strength distributions, because the wave functions of inner-shell electrons are insensitive to the state of aggregation of the medium. Similar calculations were made by LaVerne and Mozumder [33], Akkerman and Chernov [68], Khlupin and Akkerman [69], and Liljequist [70].

Data for Gases. Fig. 7.1 shows the stopping cross section for molecular hydrogen, and Fig.7.2 the stopping cross section for argon. Also indicated in these figures are the contributions of ionization and of various excitations to the total cross section. The stopping powers were calculated by M.Kimura (private communication) with cross section sets compiled by Gerhart [42] for hydrogen and by Eggarter [43,44] for argon. These cross sections were used in recent calculations of energy-degradation spectra [71].

Figs.7.3 and 7.4 show the stopping powers of carbon dioxide and of methane-based tissue-equivalent gas (64.5 CH_4, 32.2% CO_2 and 3.2% N_2 by

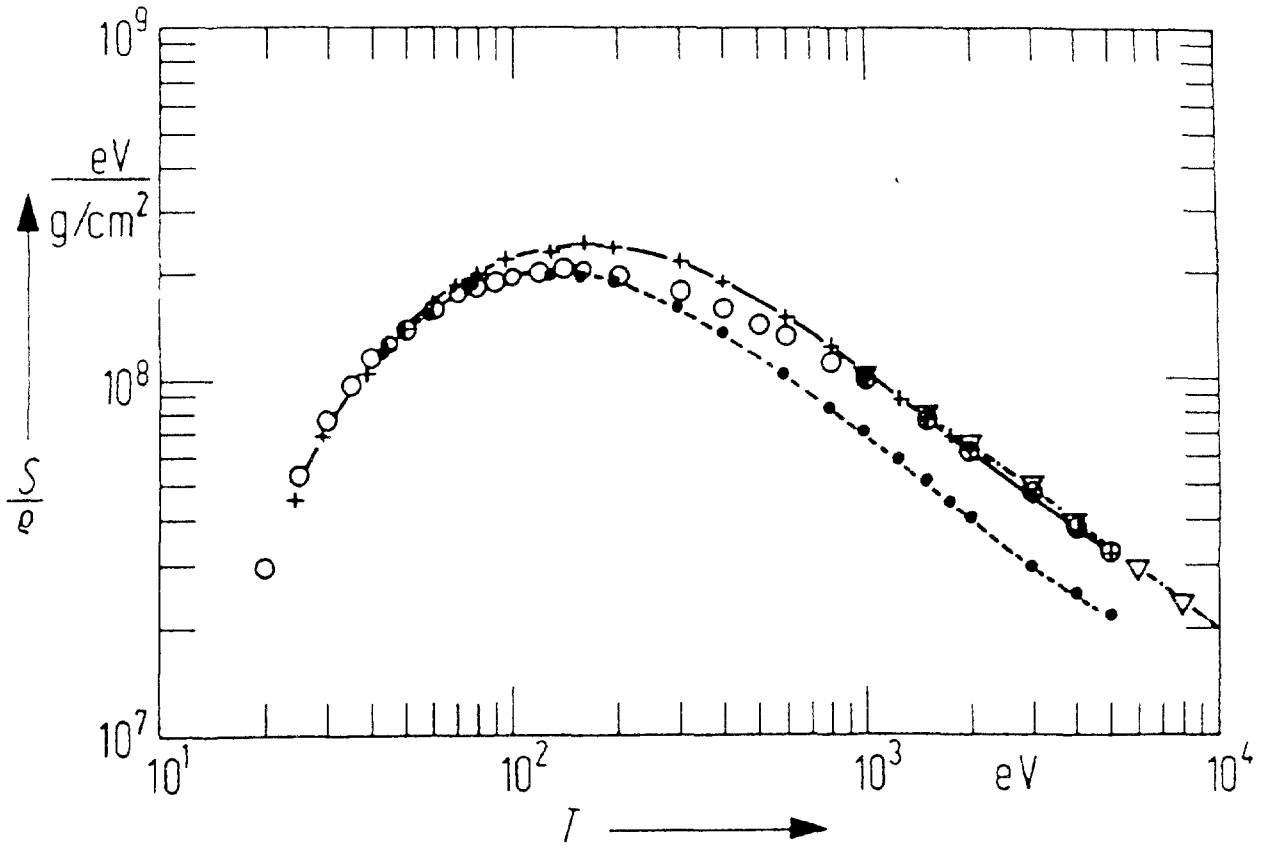

Fig.7.3. Mass stopping power of carbon dioxide gas for electrons, determined by Waibel and Grosswendt [52].

\+ : *from ionization measurements, with correction for energy carried away by secondary electrons*

● : *from ionization measurements, without correction for secondary electron escape*

○ : *calculated from inelastic scattering cross sections*

▽ : *Bethe theory, from [5]*

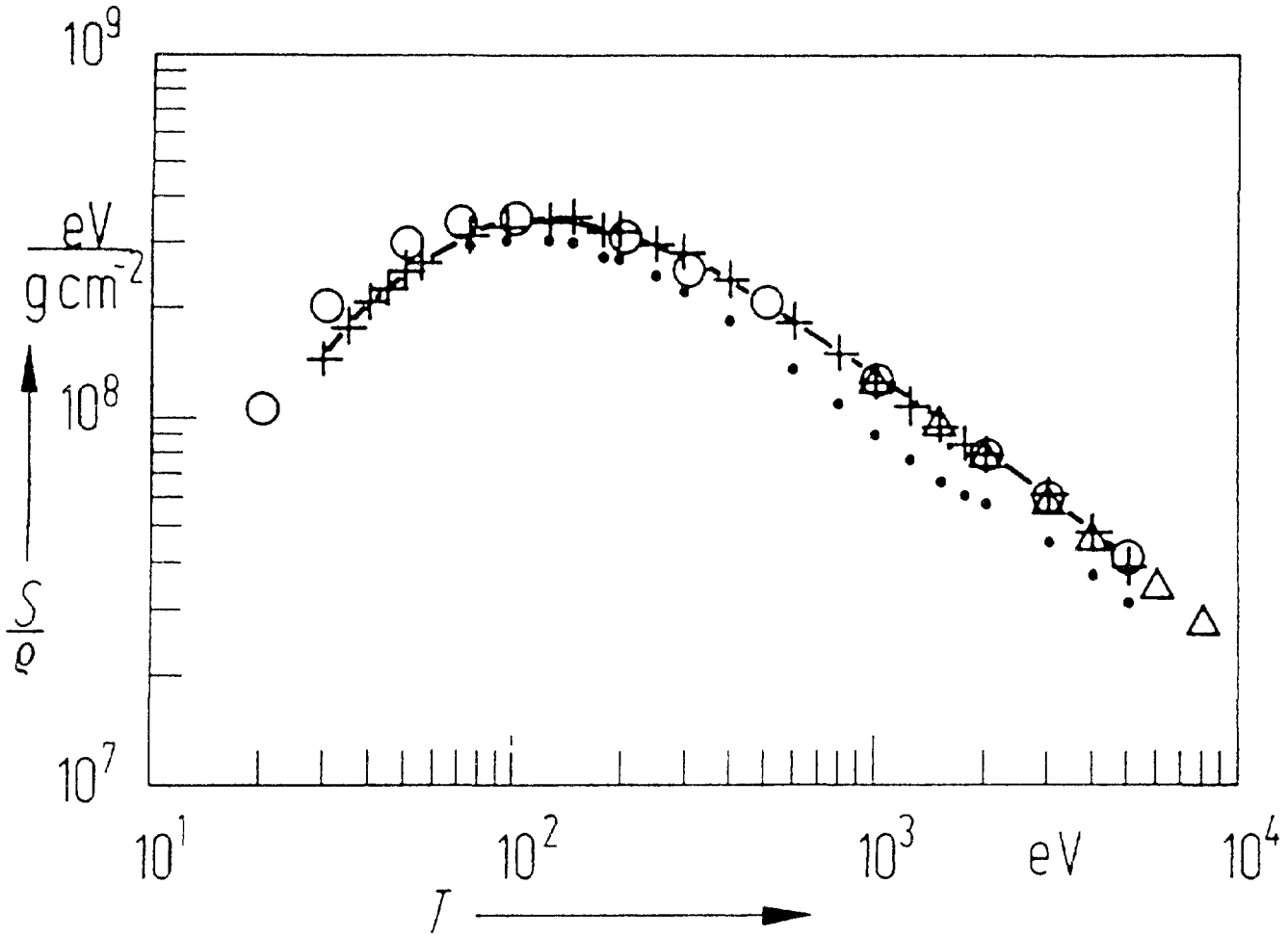

Fig.7.4. *Mass stopping power of methane-based tissue-equivalent gas for electrons, determined by Waibel and Grosswendt [53].*

+ : *from ionization measurements, with correction for energy carried away by secondary electrons*

● : *from ionization data, without correction for secondary-electron escape*

o : *calculated from inelastic scattering cross sections*

▽ : *Bethe theory, from [5]*

partial pressure) determined by Waibel and Grosswendt [52,53]. This is one of the rare instances where stopping powers were calculated as well as measured. In the experiments of Waibel and Grosswendt, electron beams were injected into a parallel-plate ionization chamber, and the ionization current of positive charge carriers was measured as a function of gas pressure. The stopping power was obtained as the derivative of the current with respect to pressure, extrapolated to zero pressure. A fairly substantial correction had to be applied to account for the escape of

energy carried by secondary electrons. Figs. 7.3 and 7.4 show stopping powers calculated with, and without, this correction. Waibel and Grosswendt estimated the uncertainties of the measured stopping powers to be 10%. Also shown in the figures are stopping powers calculated by Waibel and Grosswendt from estimated electron-impact cross sections, which they estimated to have uncertainties of 15%. Within the limits of error, the agreement between the experimental and theoretical stopping powers is satisfactory.

The left panel of Fig.7.5 shows stopping powers of water vapor calculated by Paretzke [45-47] and by Laverne and Mozumder [50]. Paretzke

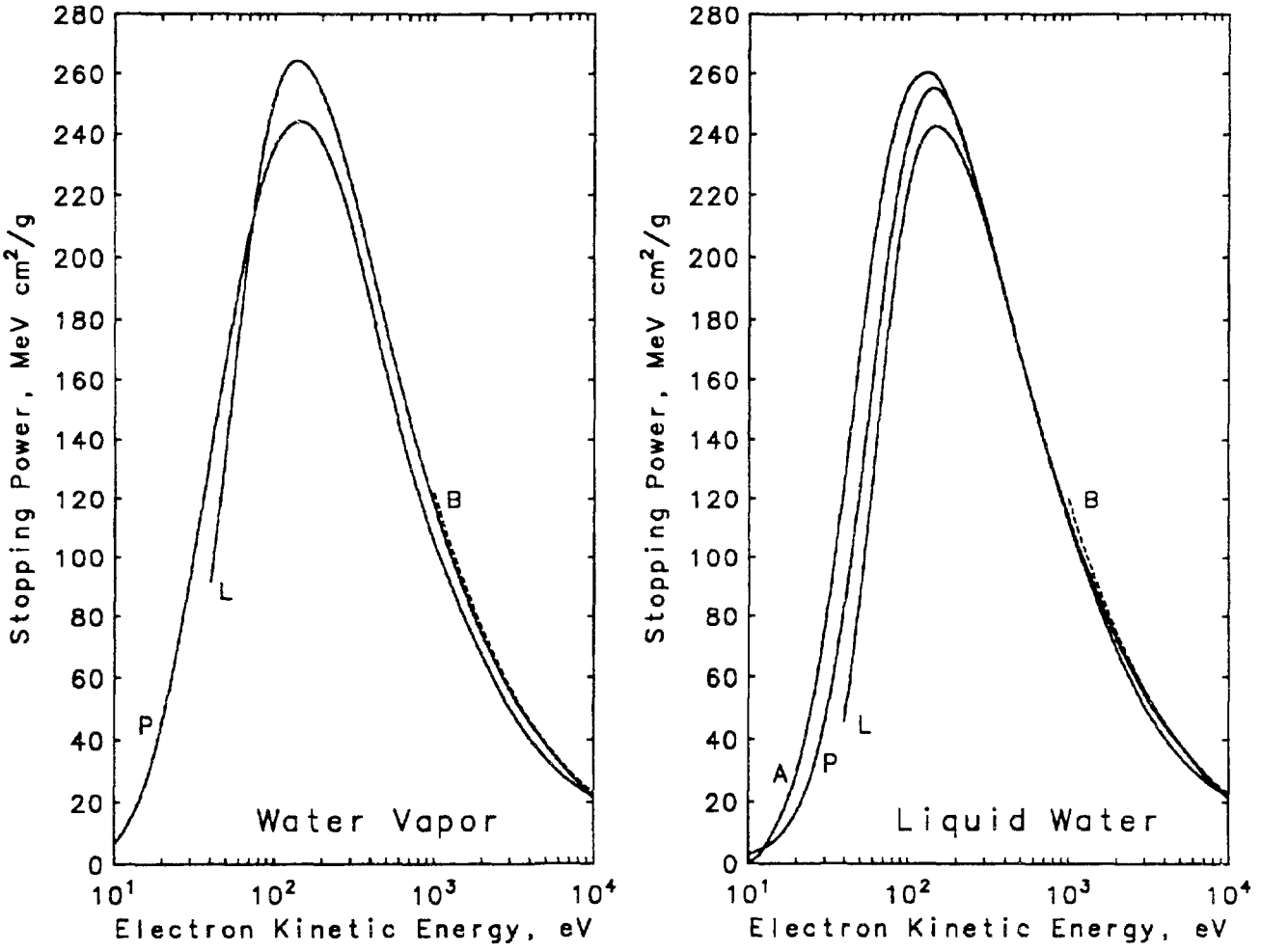

Fig.7.5. Stopping power of water vapor and of liquid water for electrons.

A: Ashley [66]
P: Paretzke et al [45-47]
L: LaVerne and Mozumder [50].
B: Bethe theory, from [5], calculated with mean excitation energy 71.6 eV for water vapor and 75 eV for liquid water.

carried out a critical data analysis for water vapor with the same approach used earlier by Gerhart and Eggarter. Laverne and Mozumder relied on the oscillator-strength distribution for water vapor compiled by Zeiss et al [72] but provided few details of the procedure used. Also shown in Fig. 7.5 is the prediction from Bethe's theory (with a mean excitation energy of 71.6 eV).

Data for the Condensed Phase. The right panel of Fig.7.5 shows stopping powers for liquid water calculated by Ashley [66], Paretzke et al [45-47], by Laverne and Mozumder [50], and again - for comparison - the stopping power from Bethe's theory (calculated with a mean excitation energy of 75 eV). In Ashley's work, the dielectric response function was calculated with an insulator model whose parameters were adjusted to take into account the measured optical data up to 26 eV of Heller et al [73]. Ionization from the K shell was treated with generalized atomic oscillator strength distributions.

The calculation of Laverne and Mozumder was similar to that of Ashley. However, a somewhat different method was used to extrapolate the optical data to higher energies, and exchange effects were not explicitly included in the dielectric model but treated in a more approximate manner by an energy-loss cut-off.

The cross sections for liquid water used by Paretzke et al were obtained by modifying their cross sections for water vapor in the following respects: The optical data of Heller et al were taken into account; the binding energies of the outer ionization levels were reduced by 4 eV; the energy-loss spectrum $\mathrm{Im}[-1/\varepsilon(\omega,k)]$ was shifted to higher energies; oscillator-strength distributions for discrete transitions were decreased and broadened.

It can be seen in Fig.7.5, that the three calculations agree closely with the Bethe theory down to 1 keV, and with each other down to about 300 eV. The differences below 300 eV are an indication of the uncertainties inherent in the calculation. A comparison of the results in the left and right panels of Fig.7.5 suggests that the phase effect on the stopping power of water is small. The stopping powers of LaVerne and Mozumder are slightly larger for vapor than for liquid at the energy where the stopping power peaks, which is plausible, and consistent with corresponding results

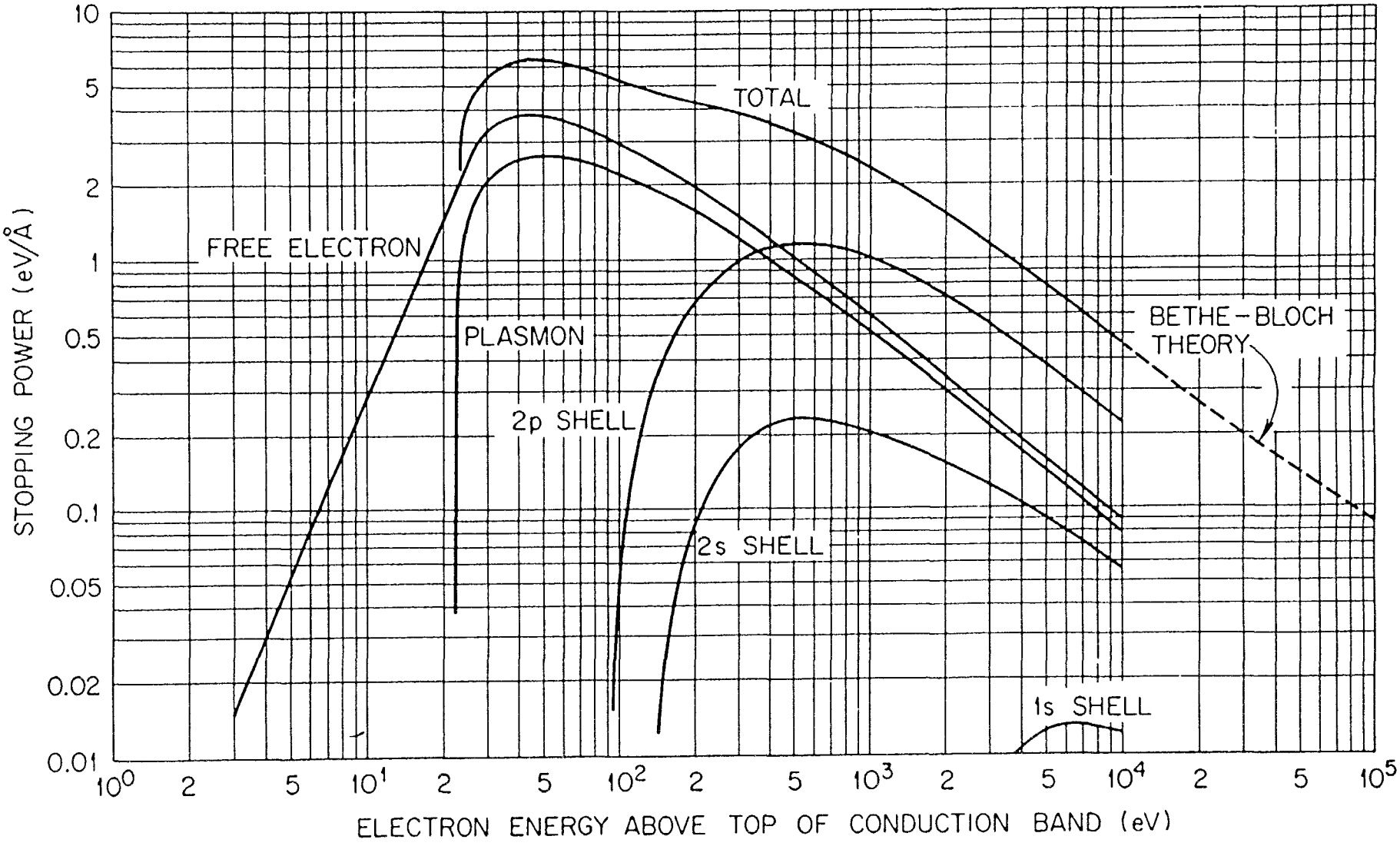

Fig.7.6. Contribution of various processes to the stopping power of aluminum for electrons. From Tung et al [57].

for protons and alpha particles. A small opposite phase effect indicated by the results of Paretzke et al is probably a spurious result due to the uncertainties of the calculations.

Fig.7.6, from Tung et al [57] shows the stopping power of aluminum and the contributions of various modes of energy loss. This calculation, also described by Ashley et al [60], takes into account separately the interactions with electrons in the conduction band and with the tightly bound electrons in the ion core.

Table 7.6 shows electron stopping powers calculated by Ashley [65,67a,b] for a few compounds of low atomic number. In these calculations the dielectric response function was constructed with the use of

TABLE 7.6. LOW-ENERGY ELECTRON STOPPING POWERS OF COMPOUNDS. THE RESULTS FOR POLYETHYLENE, POLYMETHYL METHACRYLATE (PMMA), WATER AND ALUMINUM WERE CALCULATED BY ASHLEY [67a,b], AND THOSE FOR SILICON DIOXIDE BY ASHLEY AND ANDERSON [65]. THE VALUES IN PARENTHESES ARE FROM BETHE'S STOPPING-POWER FORMULA EVALUATED WITH MEAN EXCITATION ENERGIES FROM [5].

	Stopping Power, MeV cm^2/g				
Energy (eV)	Poly-ethylene	PMMA	Water	Aluminum	Silicon dioxide
40	77.0	54.1	56.6	157	55.1
60	219	161	159	168	105
80	290	224	215	162	128
100	319	253	242	153	137
150	319	266	258	132	141
200	296	254	248	121	137
300	250	220	220	111	127
400	215	193	194	104	117
500	189	172	173	97.8	108
600	170	156	157	92.2	99.6
800	142	132	133	82.2	87.5
1000	125 (135)	115 (117)	116 (120)	74.4 (73.8)	78.1 (83.4)
1500	95.9 (102)	89.1 (89.6)	89.2 (91.8)	60.0 (59.5)	62.6 (66.3)
2000	78.7 (83.3)	73.3 (73.4)	73.4 (75.2)	50.4 (50.2)	52.8 (55.5)
3000	57.0 (61.8)	55.0 (54.8)	55.1 (56.2)	38.5 (38.7)	40.8 (42.4)
4000	47.5 (49.7)	44.3 (44.3)	44.6 (45.4)	31.8 (31.8)	33.5 (34.7)
6000	34.9 (36.4)	32.3 (32.6)	32.8 (33.4)	24.0 (23.9)	25.1 (25.0)
8000	27.8 (29.1)	25.7 (26.1)	26.2 (26.8)	19.5 (19.4)	20.4 (21.0)
10000	23.3 (24.4)	21.4 (22.0)	22.0 (22.6)	16.5 (16.5)	17.4 (17.8)

TABLE 7.7.EXCHANGE CORRECTION FACTORS, FROM ASHLEY [67b], CALCULATED BY TAKING THE RATIO OF THE ELECTRON STOPPING POWER (WITH THE EXCHANGE CORRECTION) TO THE POSITRON STOPPING POWER (WITHOUT THE EXCHANGE CORRECTION).

	EXCHANGE CORRECTION FACTOR				
Energy (keV)	C	Al	Cu	Ag	Au
0.04	0.625	0.648	0.641	0.661	0.656
0.06	0.624	0.703	0.657	0.640	0.626
0.08	0.645	0.726	0.670	0.638	0.625
0.10	0.670	0.737	0.680	0.643	0.634
0.15	0.720	0.750	0.699	0.665	0.663
0.20	0.751	0.758	0.712	0.688	0.688
0.30	0.786	0.770	0.731	0.728	0.726
0.40	0.805	0.779	0.745	0.756	0.752
0.50	0.817	0.786	0.756	0.775	0.769
0.60	0.824	0.793	0.765	0.788	0.781
0.80	0.833	0.804	0.781	0.803	0.795
1.00	0.839	0.812	0.794	0.811	0.802
1.50	0.847	0.829	0.815	0.818	0.811
2.00	0.853	0.840	0.828	0.823	0.816
3.00	0.864	0.855	0.839	0.834	0.826
4.00	0.875	0.864	0.843	0.845	0.835
6.00	0.888	0.874	0.849	0.859	0.847
8.00	0.894	0.881	0.856	0.865	0.852
10.00	0.896	0.888	0.865	0.864	0.851

experimental optical data, and exchange effects were taken into account in the dielectric model. Table 7.6 also shows the corresponding stopping powers from Bethe's theory.

Ashley [67b] calculated stopping powers not only for electrons (with the exchange correction) but also for positrons (without the exchange correction, leaving all other aspects of the calculation unchanged). We have made a least-squares fit of Ashley's electron/positron stopping-power ratios as functions of the particle energy. These ratios (exchange correction factors) are given in Table 7.7 for C, Al, Cu, Ag and Au, and can be seen to be rather insensitive to the atomic number of the target material.

TABLE 7.8. ELECTRON STOPPING POWERS (in MeV cm^2/g) OF ELEMENTAL SOLIDS CALCULATED BY KHLUPIN AND AKKERMAN [69]. 3.94E2 means 3.94×10^2, etc.

Energy (eV)	Li	Be	C	Na	Mg	Al	Si	K
100	3.94E2	3.72E2	4.30E2	2.32E2	2.05E2	2.04E2	2.53E2	2.13E2
150	3.35E2	3.05E2	3.66E2	2.26E2	1.94E2	1.82E2	2.11E2	1.90E2
200	2.96E2	2.65E2	3.13E2	2.12E2	1.83E2	1.69E2	1.88E2	1.69E2
300	2.43E2	2.17E2	2.43E2	1.83E2	1.63E2	1.49E2	1.61E2	1.38E2
400	2.08E2	1.87E2	2.03E2	1.60E2	1.45E2	1.34E2	1.43E2	1.18E2
600	1.63E2	1.48E2	1.56E2	1.28E2	1.19E2	1.11E2	1.18E2	9.53E1
800	1.35E2	1.24E2	1.29E2	1.07E2	1.01E2	9.52E1	1.01E2	8.15E1
1000	1.16E2	1.08E2	1.11E2	9.24E1	8.84E1	8.35E1	8.86E1	7.19E1
1400	9.08E1	8.59E1	8.85E1	7.34E1	7.09E1	6.75E1	7.18E1	5.89E1
2000	6.96E1	6.67E1	6.88E1	5.71E1	5.56E1	5.31E1	5.65E1	4.71E1
3000	5.09E1	4.94E1	5.10E1	4.25E1	4.17E1	4.00E1	4.25E1	3.59E1
4000	4.05E1	3.96E1	4.10E1	3.44E1	3.39E1	3.25E1	3.46E1	2.96E1
6000	2.93E1	2.88E1	2.99E1	2.53E1	2.51E1	2.41E1	2.56E1	2.19E1
8000	2.32E1	2.29E1	2.38E1	2.03E1	2.02E1	1.94E1	2.06E1	1.78E1
10000	1.93E1	1.91E1	1.99E1	1.71E1	1.70E1	1.64E1	1.74E1	1.50E1

Energy (eV)	Ca	Ti	Fe	Ni	Cu	Zn	Ge	Mo
100	2.09E2	2.02E2	1.51E2	1.32E2	1.23E2	1.62E2	1.49E2	1.09E2
150	1.89E2	1.86E2	1.52E2	1.50E2	1.42E2	1.65E2	1.39E2	1.02E2
200	1.70E2	1.69E2	1.42E2	1.43E2	1.34E2	1.51E2	1.29E2	9.30E1
300	1.41E2	1.42E2	1.21E2	1.23E2	1.16E2	1.28E2	1.14E2	7.91E1
400	1.21E2	1.22E2	1.06E2	1.08E2	1.01E2	1.11E2	1.02E2	7.03E1
600	9.70E1	9.70E1	8.47E1	8.65E1	8.12E1	8.83E1	8.39E1	5.95E1
800	8.29E1	8.22E1	7.11E1	7.26E1	6.81E1	7.40E1	7.17E1	5.25E1
1000	7.31E1	7.22E1	6.20E1	6.30E1	5.91E1	6.41E1	6.28E1	4.74E1
1400	6.00E1	5.89E1	5.03E1	5.09E1	4.75E1	5.13E1	5.08E1	3.99E1
2000	4.81E1	4.71E1	4.01E1	4.04E1	3.76E1	4.04E1	4.03E1	3.27E1
3000	3.68E1	3.60E1	3.07E1	3.09E1	2.87E1	3.07E1	3.07E1	2.55E1
4000	3.01E1	2.95E1	2.53E1	2.54E1	2.35E1	2.51E1	2.52E1	2.12E1
6000	2.25E1	2.20E1	1.90E1	1.90E1	1.77E1	1.88E1	1.90E1	1.62E1
8000	1.82E1	1.78E1	1.54E1	1.54E1	1.43E1	1.52E1	1.54E1	1.33E1
10000	1.54E1	1.51E1	1.30E1	1.31E1	1.21E1	1.29E1	1.31E1	1.14E1

Energy (eV)	Ag	Sn	Sb	Ba	W	Au	Pb	Bi
100	1.11E2	9.59E1	9.95E1	7.32E1	7.74E1	6.13E1	6.43E1	6.81E1
150	1.07E2	8.97E1	9.15E1	6.76E1	7.93E1	6.33E1	5.85E1	6.13E1
200	9.82E1	8.37E1	8.50E1	6.33E1	7.59E1	6.14E1	5.49E1	5.65E1
300	8.24E1	7.32E1	7.43E1	5.71E1	6.72E1	5.59E1	5.00E1	5.08E1
400	7.11E1	6.49E1	6.60E1	5.23E1	6.02E1	5.09E1	4.59E1	4.64E1
600	5.75E1	5.32E1	5.42E1	4.48E1	5.03E1	4.35E1	3.97E1	3.99E1
800	4.96E1	4.59E1	4.67E1	3.92E1	4.37E1	3.84E1	3.54E1	3.54E1
1000	4.42E1	4.09E1	4.16E1	3.51E1	3.89E1	3.46E1	3.21E1	3.21E1
1400	3.69E1	3.43E1	3.48E1	2.96E1	3.22E1	2.91E1	2.73E1	2.73E1
2000	3.02E1	2.82E1	2.85E1	2.45E1	2.60E1	2.38E1	2.25E1	2.25E1
3000	2.36E1	2.21E1	2.24E1	1.95E1	2.01E1	1.86E1	1.78E1	1.78E1
4000	1.96E1	1.85E1	1.87E1	1.65E1	1.67E1	1.55E1	1.49E1	1.49E1
6000	1.50E1	1.42E1	1.43E1	1.27E1	1.28E1	1.20E1	1.15E1	1.15E1
8000	1.23E1	1.17E1	1.18E1	1.06E1	1.06E1	9.92E0	9.58E0	9.57E0
10000	1.05E1	1.00E1	1.01E1	9.11E0	9.07E0	8.53E0	8.26E0	8.26E0

Khlupin and Akkerman [69], extending earlier work by Akkerman and Chernov [68], calculated electron stopping powers in 24 solids at energies between 0.1 keV and 100 keV. They treated the response of the electrons in the valence bands with a dielectric response function calculated according to Lindhard and Winther [56], and calculated the interactions with inner-shell electrons using the binary-encounter theory of Garcia [74]. Exchange effects were not taken into account. Table 7.8 gives stopping powers excerpted from the more extensive tables of Khlupin and Akkerman. It would be a simple matter to apply Ashley's exchange effect to the Khlupin-Akkerman results, using correction factors obtained by interpolation from Table 7.7.

Fig.7.7a compares the Khlupin-Akkerman stopping powers of Al, Cu, Ag and Au with the corresponding results of Ashley [67b] calculated without

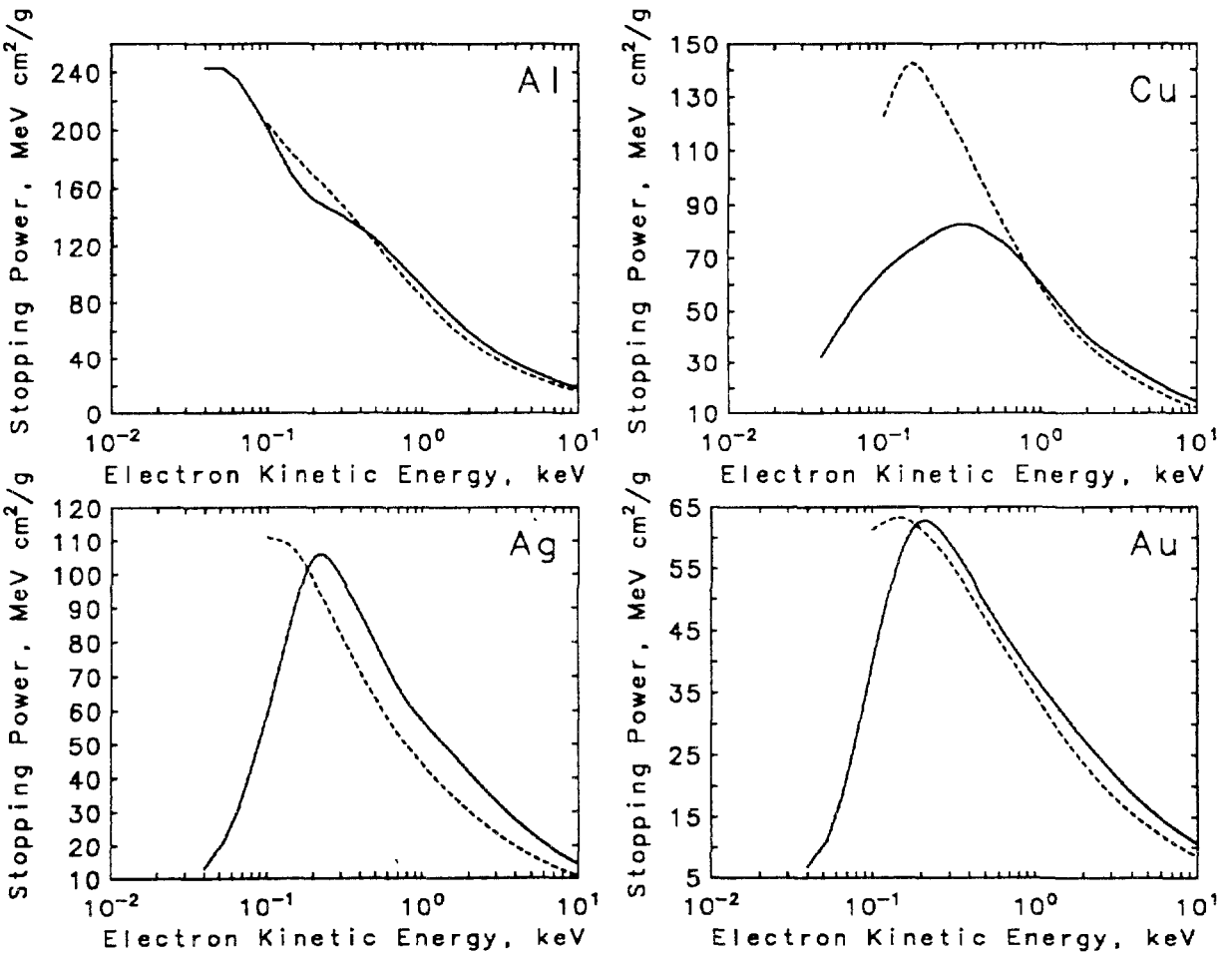

Fig.7.7a. Comparison of stopping powers of Al, Cu, Ag and Au for electrons, calculated without exchange corrections. Solid curves: Ashley [67a,b]; Dashed curves: Akkerman and Khlupin [69].

the exchange correction. The agreement between the two sets of calculations is good for Al and Au, and fair for Ag. For Cu, however, Ashley's stopping powers are much smaller than those of Khlupin and Akkerman. A somewhat similar discrepancy was found by Ashley [67a], who noted that the stopping powers obtained with his optical-data model are slightly higher for Ag and Au, but considerably lower for Cu, than the stopping powers obtained earlier by him with a statistical model [58,61].

Al-Ahmad and Watt measured the stopping powers of Al, Ni, Cu, Ag and Au [69a] and of polyethylene [69b] for electrons with energies from 10 keV to 1 keV. Ref.[69a] also presents comparisons with earlier stopping-power measurements by other authors. A calorimetric method was used by Al-Ahmad and Watt to determine the amount of energy lost by electrons in very thin foils. To interpret these measurements, they had to determine the average path lengths of the electrons in the foils, which was done with a simple multiple-scattering correction. Furthermore the effective energy, i.e. the

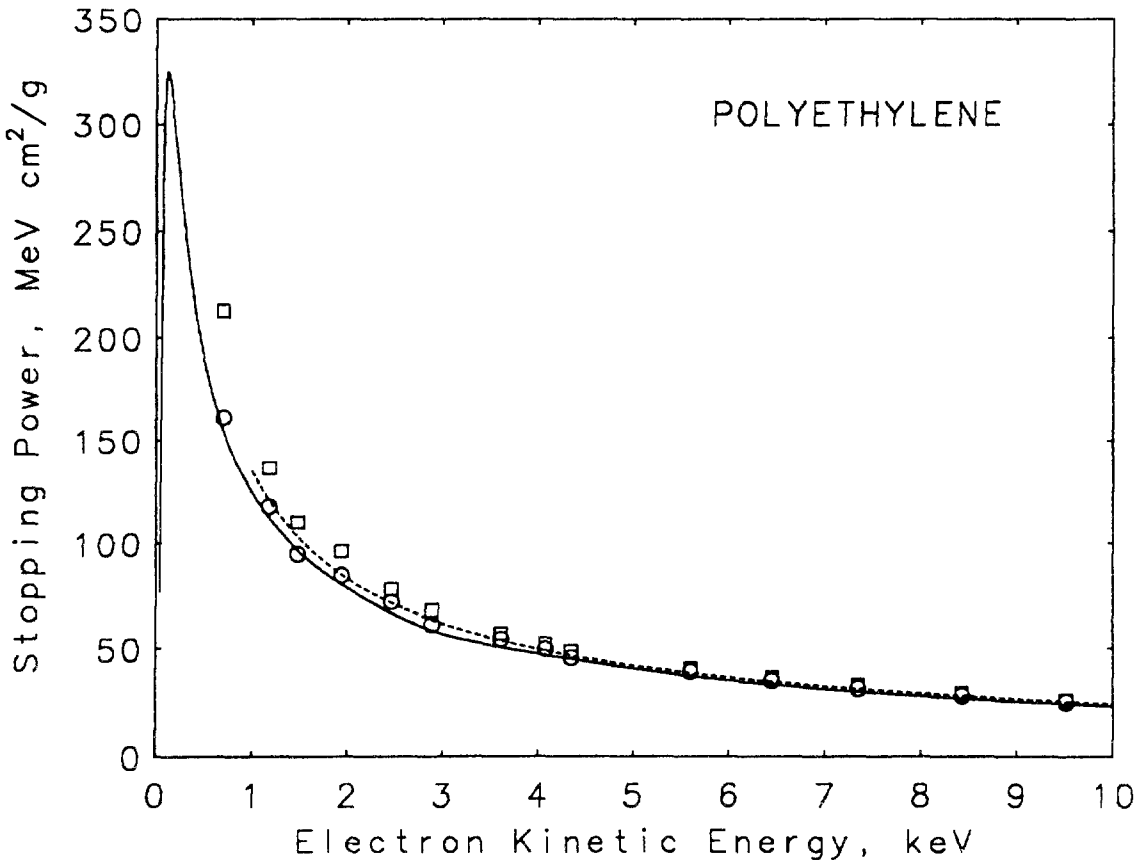

Fig.7.7b. Comparison of stopping powers of polyethylene for electrons. Solid curve: Ashley [67a,b]; short-dashed curve: Bethe's theory; Squares and circles: experimental results of Al-Ahmad and Watt [69b], obtained with two different type of multiple-scattering corrections.

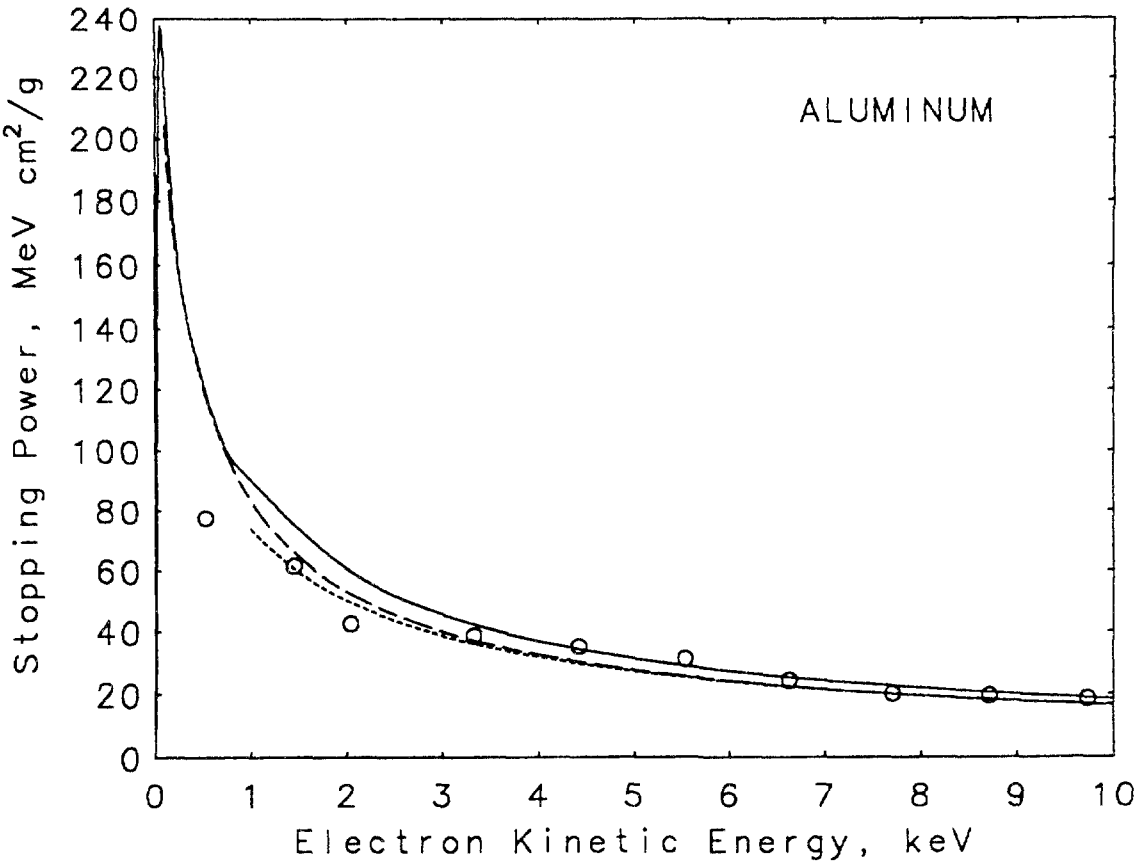

Fig.7.7c. Comparison of stopping powers of aluminum for electrons. Solid curve: Ashley [67a,b]; long-dashed curve: Khlupin and Akkerman [69]; short-dashed curve: Bethe's theory; circles: experimental results of Al-Ahmad and Watt [69a].

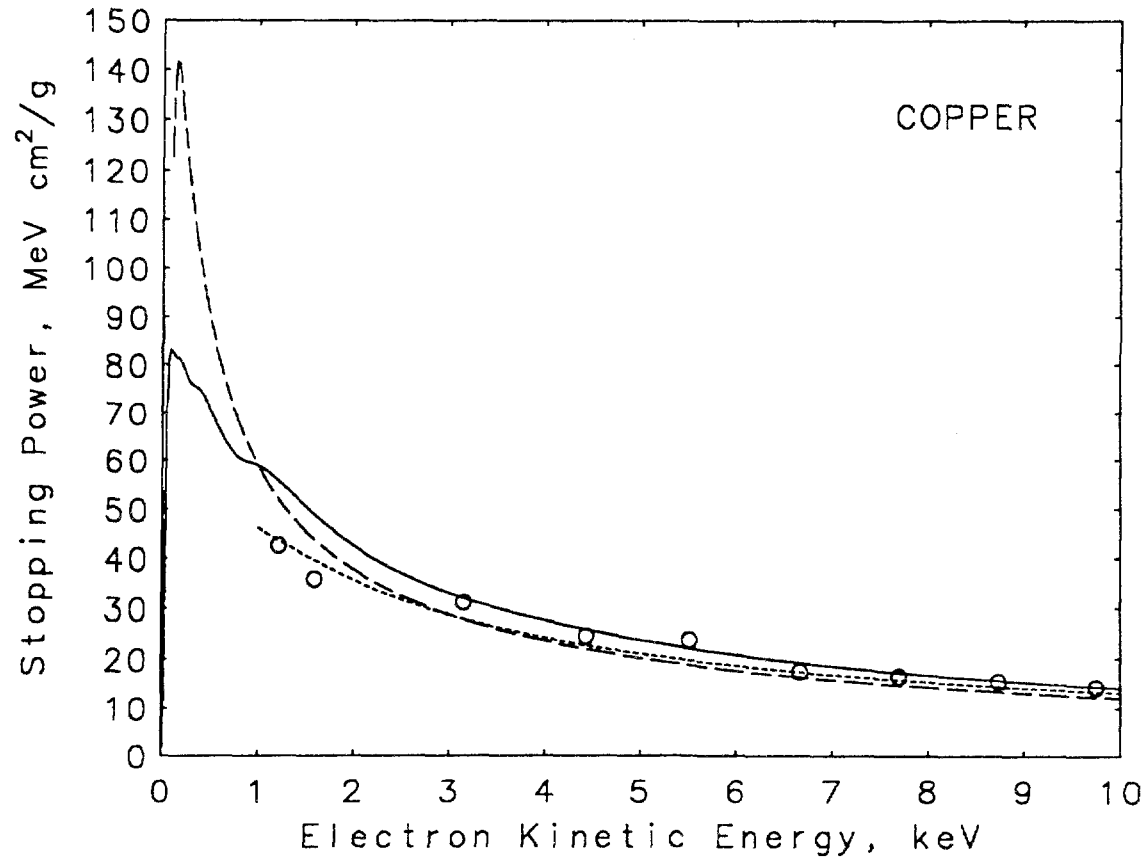

Fig.7.7d. Comparison of stopping powers of copper for electrons. (similar to Fig.7.7c).

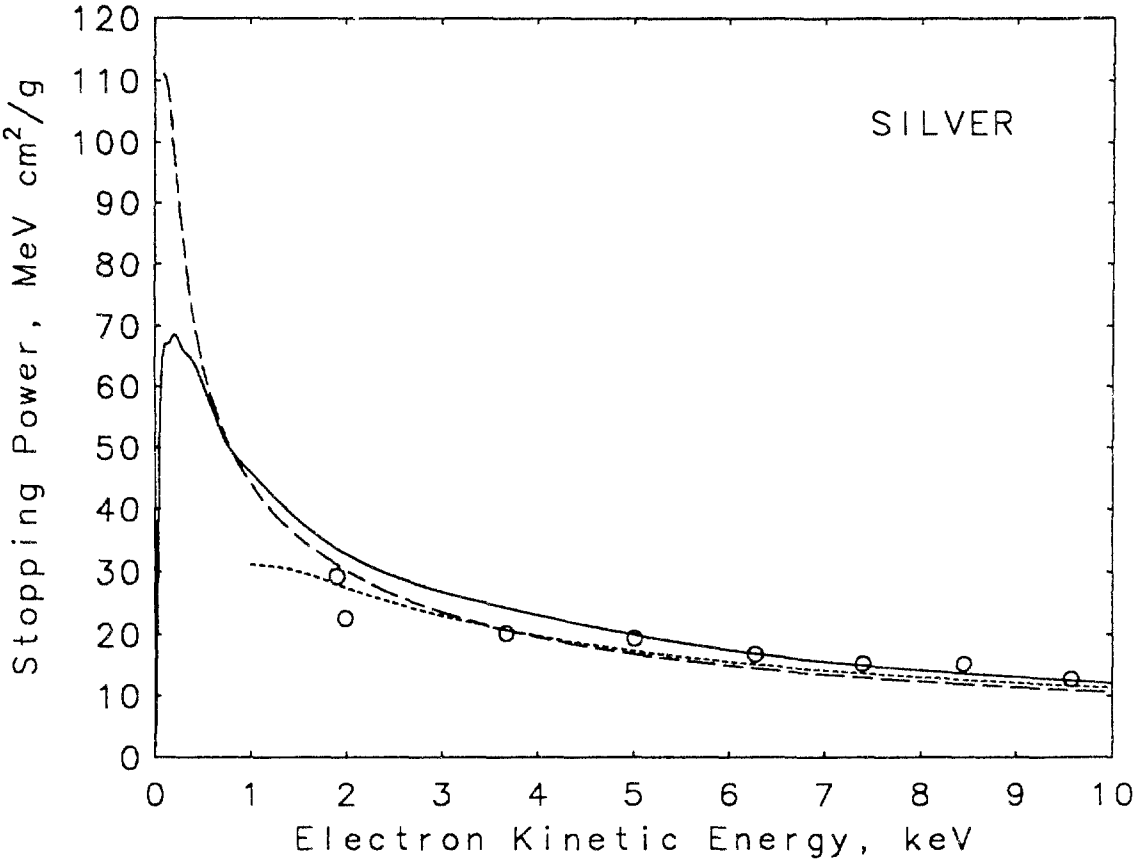

Fig.7.7e. Comparison of stopping powers of silver for electrons. (similar to Fig.7.7c).

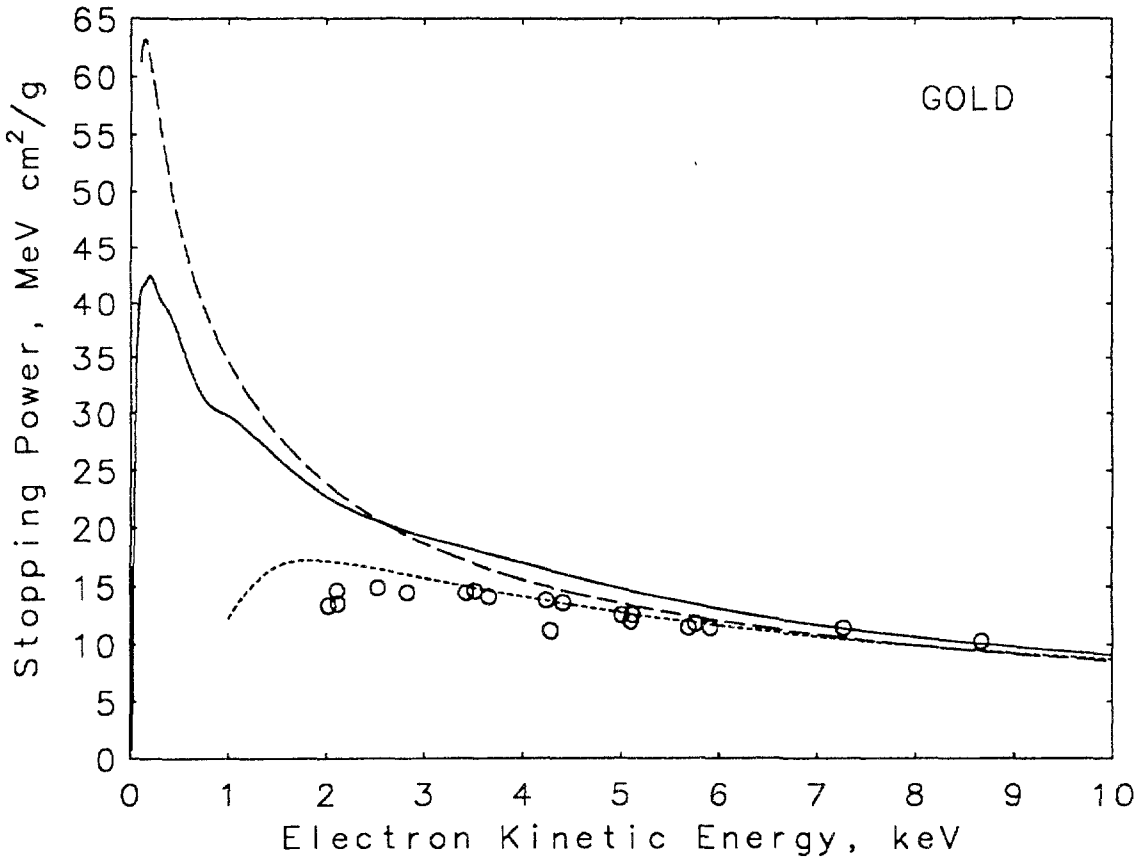

Fig.7.7f. Comparison of stopping powers of gold for electrons. (similar to Fig.7.7c).

average energy of the electron in the foil, had to be estimated iteratively. For example, for 4-keV electrons incident on the foil the pertinent parameters had the following values:

Material	Foil thickness ($\mu g/cm^2$)	Energy loss (keV)	Effective energy (keV)	Ratio of average path length to foil thickness
Polyethylene	13.24	0.0766	3.61	1.06
Al	27.94	0.1334	3.33	1.24
Au	55.88	0.3743	2.12	4.97

Except for low-Z materials, the multiple-scattering correction is large, and somewhat uncertain. Nevertheless the stopping powers extracted by Al-Ahmad and Watt from their data are in fair agreement with calculated stopping powers. This can be seen in Figs. 7.7b to 7.7f which contain comparisons with the results of Ashley [67a,b] and of Khlupin and Akkerman [69], and with predictions from Bethe's theory. It would be interesting to analyze the energy-loss data not only with a simple multiple-scattering correction, but by a complete transport calculation.

7.2.1.8. Uncertainties.

The number of measurements of stopping powers for electrons is very small, and the available body of data is not adequate to determine the accuracy of the stopping power formula. Error estimates must rely on the uncertainties of the parameters in this formula (see Sections 7.2.1.4 to 7.2.1.6), and must take into account the absence of various needed corrections (see Sections 7.2.1.2 and 7.2.1.3). In ICRU Report 37 [5] it is concluded that the differences between measured and calculated stopping powers in the region 2 keV to 100 keV do not form a consistent pattern and provide little guidance how the Bethe theory should be modified at lower energies. In [5] it is estimated that the uncertainties of the collision stopping powers tabulated with the use of the stopping power formula are 1-2% above 100 keV, and 2-3% in low-Z_2 and 5-10% in high-Z_2 materials between 100 keV and 10 keV.

The error estimate for the region 100 keV to 10 keV is consistent with the differences between the results from the Bethe theory and from other low-energy calculations in Table 7.9.

TABLE 7.9. PERCENTAGE AMOUNT Δ BY WHICH THE ELECTRON STOPPING POWERS AT 10 keV CALCULATED BY KHLUPIN AND AKKERMAN [69] AND BY ASHLEY AND COLLABORATORS [59,65,66,67] DIFFER FROM THE RESULTS OF THE BETHE THEORY FROM [5].

	Δ,%		Δ,%		Δ,%		Δ,%
Li	-2.4	Si	3.0	Cu	-7.6	Sb	-5.2
Be	2.3	K	-6.5	Zn	-2.2	Ba	12.2
C	-1.5	Ca	-6.5	Ge	5.9	W	1.1
Na	1.9	Ti	4.0	Mo	-2.3	Au	-1.6
Mg	-0.9	Fe	-6.3	Ag	-6.4	Pb	-2.0
Al	-0.7	Ni	-6.3	Sn	-7.8	Bi	-2.4

	Δ,%
Polyethylene	0.6
Polystyrene	-1.0
Water	0.0
Silicon Dioxide	3.3

7.2.2. Radiative Stopping Power

The radiative stopping power, $\frac{1}{\rho} S_{rad}$, represents the mean energy loss per unit path length due to the emission of bremsstrahlung quanta. An accurate evaluation can be accomplished through the combination of several theories applicable in different energy regions. Such a combination was used in ICRU Report 37 [5]. At energies above 50 MeV, the emission of bremsstrahlung in the screened Coulomb field of the atomic nucleus was calculated from the analytical theory of Davies, Bethe and Maximon [76]; below 2 MeV, the numerical values of the cross sections of Pratt, Tseng and collaborators [77] were used, obtained by numerical phase-shift calculations for a static, screened Coulomb potential. The radiative stopping powers calculated with these cross sections above 50 MeV and below 2 MeV were used as input for a cubic-spline, least-squares fitting formula, which was then used for interpolation in the intermediate energy region from 2 to 50 MeV.

A similar interpolation scheme was used subsequently [78,79] for the bremsstrahlung cross sections themselves, and the validity of the interpolation scheme was confirmed by comparisons with a few direct calculations according the method of Tseng and Pratt at 5 and 10 MeV. The

radiative stopping powers in the energy region 2 - 50 MeV determined in this manner differ slightly from the values obtained when interpolation is applied directly to radiative stopping powers, but the differences are generally smaller than 1%.

The contribution to the radiative stopping power from bremsstrahlung in the field of the atomic electrons was calculated in [5] according to the theory of Haug [80], combined with screening corrections derived from Hartree-Fock incoherent-scattering form factors.

In ICRU Report 37 [5] the uncertainties of the tabulated radiative stopping powers are estimated to be 2% above 50 MeV, 2-5% between 50 MeV and 2 MeV, and 5% below 2 MeV. These estimates are based on comparisons between measured and calculated bremsstrahlung cross sections in [78], and on the inherent uncertainties arising in the combination of various bremsstrahlung theories.

7.2.3. Computer Program.

A computer program, called ESTAR, has been developed [81] which calculates electron stopping powers, ranges and related quantities for any element, compound or mixture (see appendix).

ESTAR calculates collision stopping powers for electrons according to Eqs.(7.1,7.2), and radiative stopping powers according to the procedure outlined in Sec. 7.2.2. The output from ESTAR also includes electron ranges calculated in the continuous-slowing-down approximation (CSDA), i.e., neglecting energy-loss straggling. The CSDA range is a close approximation to the average path length traveled by an electron in the course of slowing down to rest, and is calculated by integrating the reciprocal of the total stopping power (collision plus radiative) with respect to energy:

$$R = \int_0^{T_0} \frac{dT}{S_{col}(T) + S_{rad}(T)} , \qquad (7.4)$$

where T_0 is the initial electron energy.

The ESTAR program is accompanied by a database of composition data (I-values and fractions by weight of the atomic constituents) for 278 materials. The default values of mean excitation energies are those used in

[5]. However, the user of ESTAR has the option of choosing different I-values.

7.2.4. Energy Loss Straggling

The energy loss Δ which an electron suffers in traversing a given path length is the sum of the numerous energy losses in individual inelastic collisions. For a short path length s such that the average energy loss is only a small fraction of the initial electron energy, the distribution of energy losses, $F(\Delta,s)$, can be calculated according to the theory of Landau [82]:

$$F(\Delta,s)d\Delta = F_L(\lambda)\, d\lambda \tag{7.5}$$

where

$$F_L(\lambda) = \int_{c-i\infty}^{c+i\infty} \exp\,(u \log u + \lambda u)\, du \tag{7.6}$$

is a universal function of a scaled energy loss parameter λ. The Landau function $F_L(\lambda)$ was accurately tabulated by Börsch-Supan [83]. The relation between the scaled and actual energy loss is

$$\Delta = \xi \left[\lambda + \log \frac{2\,\xi\, m_e c^2\, \beta^2}{I^2\,(1-\beta^2)} - \beta^2 + 0.4228 - \delta\right] \tag{7.7}$$

where I is the mean excitation energy, δ the density-effect correction, and

$$\xi = \frac{2\pi\, r_e^2 m_e c^2}{u} \frac{1}{\beta^2} \frac{Z_2}{A_2}\, s, \tag{7.8}$$

with $2\pi r_e^2 m_e c^2/u = 0.153537$ MeVcm^2/g, and s is expressed in terms of areal density. The quantity ξ has the significance that in a path length s there will occur - on the average - only a single collision which results in an energy loss greater than ξ.

Landau's theory takes into account accurately only the mean value but not the higher moments of the cross section for small energy losses. Blunck and Leisegang [84] introduced a correction which treats the second moment more carefully. It involves the convolution of the Landau distribution with

a Gaussian distribution. Various prescriptions for the standard deviation of this Gaussian can be found in the literature. Blunck and Westphal [85] recommended the approximation

$$\Omega_{BW} = \left[(10\ \text{eV})\ Z_2^{4/3} <\Delta> \right]^{1/2}, \qquad (7.9)$$

where $<\Delta> = s \frac{1}{\rho} S_{col}$ is the average energy loss in path length s. Seltzer [86] analyzed many experimental energy-loss distributions in terms of the most probable energy loss and the full width at half maximum. He found that use of Eq.(7.9) leads to predictions in fairly good agreement with experiment.

Due to approximations in its derivation, the Landau distribution (even with the Blunck-Leisegang correction) is accurate only if $\xi >> I$, where I is the mean excitation energy [82,87]. Fair accuracy is obtained when $\xi > 10\ I$, and very good accuracy when $\xi > 100\ I$. Under these conditions the Landau theory with the Blunck-Leisegang correction has the great advantage that it requires knowledge only about the mean and mean-squared energy loss, but not about the energy-loss cross section itself, which is often hard to obtain.

Landau's theory is approximate in that it admits arbitrarily large energy losses in individual inelastic collisions. This has the consequence that the function $F_L(\lambda)$ extends to arbitrarily large values of λ, and does not have a finite mean value. When the Landau distribution is used in transport calculations, it must be truncated at a suitable value λ_c, so that the mean value of the truncated distribution, via eq.(7.7), corresponds to the correct mean energy loss $\frac{1}{\rho} S_{col}$. The appropriate cut-off values as functions of energy were determined by Seltzer [86].

Finally we note that Landau's theory takes into account only energy losses due to collisions resulting in the ionization of atoms. Blunck and Westphal [85] developed an approximate theory to include energy-losses due to the emission of bremsstrahlung. In a more detailed treatment by the Monte Carlo method [86,88], the use of Landau's theory was combined with random sampling of all individual bremsstrahlung emission events.

When the Landau theory is not applicable, it is necessary to fall back on more laborious methods involving (a) the evaluation of the energy-loss

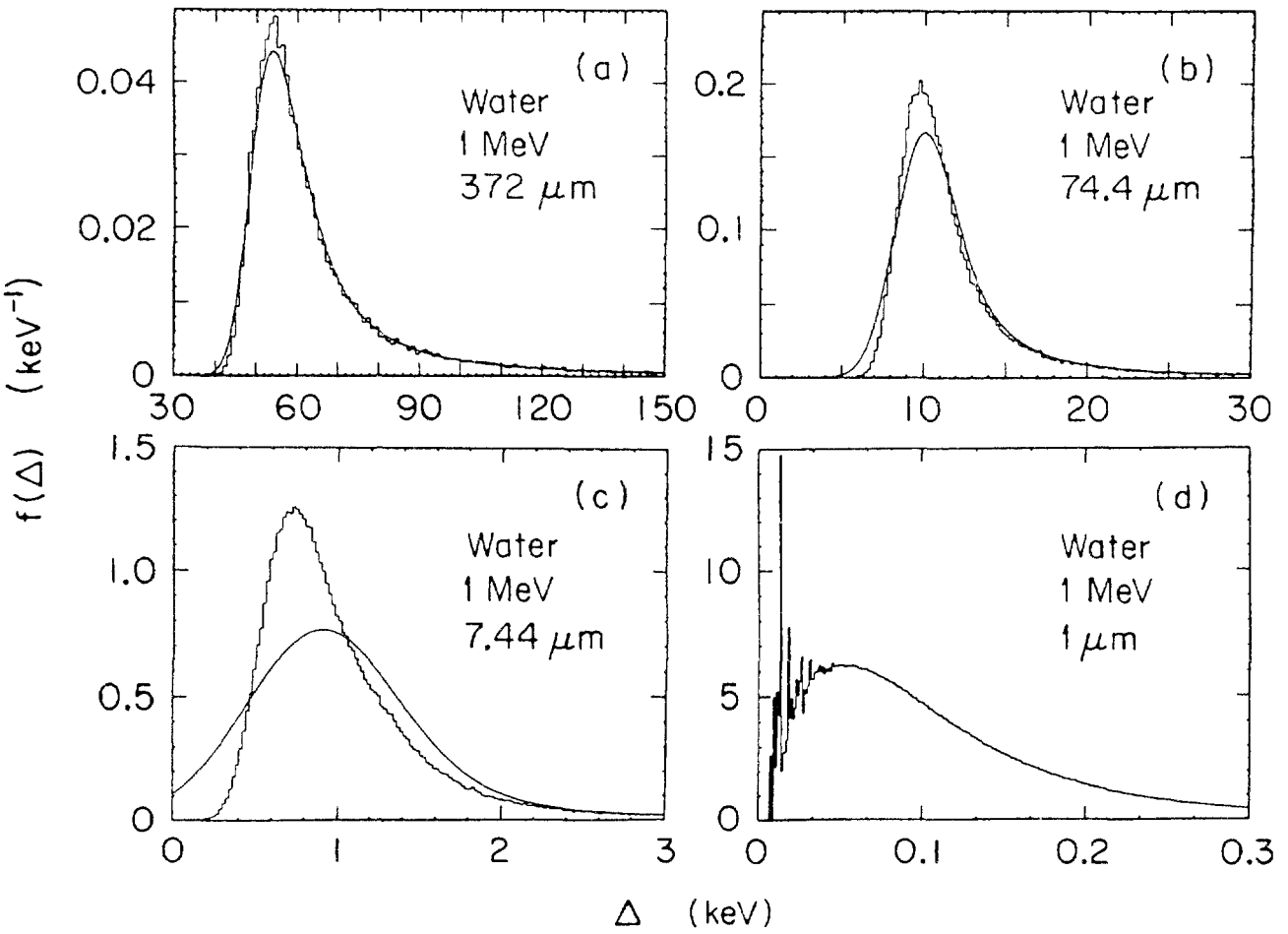

Fig.7.8. Energy-loss Distributions for 1-MeV electrons in water (from [90]). The histograms are Monte Carlo results calculated by simulating all individual excitations and ionizations, using cross sections for water vapor. The smooth curves are from the Landau theory with the Blunck-Leisegang binding correction.

	(a)	(b)	(c)	(d)
Path length, μm	*372*	*74.4*	*7.44*	*1.0*
Avg.number of inelastic collisions	*1230*	*246*	*24.6*	*3.3*
Average energy loss, keV	*71.6*	*14.3*	*1.43*	*0.19*
ξ/I	*50*	*10*	*1*	*0.134*

cross section, and (b) the development of a suitable mathematical method for calculating multiple inelastic scattering. The preparation of the necessary database of inelastic scattering cross sections has been carried out only for a small number of materials. Especially thorough evaluations were done by Bichsel and Saxon [89] for aluminum, and by Bichsel [4] for silicon. These authors used an efficient numerical convolution method devised by Kellerer to calculate the energy-loss distribution from the inelastic cross sections.

Energy-loss cross sections for water vapor have been compiled and applied to the calculation of energy-loss distributions by the Monte Carlo method [90]. These results, for 1-MeV electrons, are illustrated in Fig.7.8 for four path lengths, and are compared with the predictions of the Landau theory (with the Blunck-Leisegang correction). The agreement is excellent for a path length such that $\xi = 50\ I$, still rather good when $\xi = 10\ I$, and poor when $\xi = I$. For a path length of 1 μm (of interest in microdosimetry), ξ/I is 0.134, and the Landau distribution is inapplicable and is not shown.

7.2.5. Limitations of the usefulness of Stopping Powers.

Stopping powers are essential ingredients for calculating penetration, diffusion and slowing down of electrons in extended media, but by themselves they are sufficient only for rough estimates. Transport of electrons and energy deposition are strongly influenced by angular deflections due to multiple elastic scattering, by energy-loss straggling, and by the transport of energy by secondary electrons and photons. Scattering effects are much larger for electrons than for protons, because the elastic-scattering cross section depends inversely on the square of the projectile mass. Energy-loss straggling is more important for electrons than for protons, because in a single inelastic collision an electron can lose up to half its energy, whereas the energy loss of a proton is limited to the much smaller value $2m_e c^2\beta^2/(1 - \beta^2)$, where $m_e c^2$ is the electron rest mass and β the proton velocity divided by the speed of light.

The limited utility of stopping powers for calculations of electron transport is illustrated in Fig. 7.9, which pertains to the energy-loss per unit depth, dT/dx, in a water medium irradiated by a monoenergetic electron beam incident along the x-direction. dT/dx is plotted as function of the depth in units of the CSDA range. Results are given for beam energies of 1 MeV (Fig.a) and 20 MeV (Fig.b). The short-dashed curves represent the rate of energy loss per unit depth, calculated with stopping powers only, on the assumption that the electrons travel in a straight line (no multiple scattering) and lose energy at a rate equal to the stopping power (no straggling). The other curves were obtained with the Monte Carlo transport program ETRAN [86,88]. The long-dashed curves take into account the effects of multiple scattering angular deflections. The solid curves include in addition the effect of energy loss straggling, and the transport of energy by secondary electrons and bremsstrahlung photons. The solid curves thus

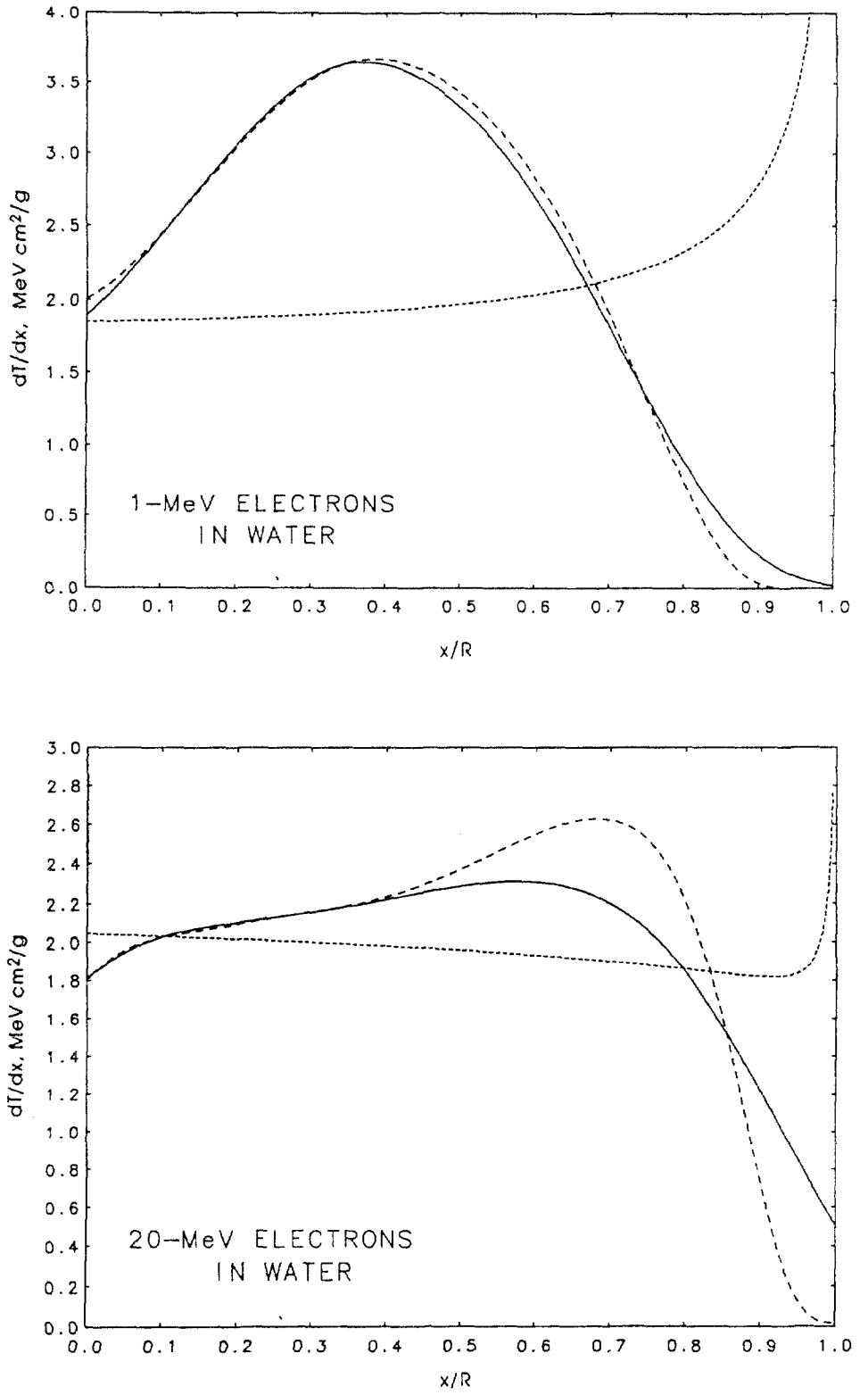

Fig.7.9. Energy loss per unit depth, dT/dx, as function of the depth in a water medium. Depths are expressed in units of the CSDA range, R. The short-dashed curves are calculated with neglect of multiple-scattering deflections and energy-loss straggling. The long-dashed curves include the effects of multiple scattering. The solid curves represent the energy imparted to the medium, and take into account energy-loss straggling and the transport of secondary electrons and photons.

a. 1 MeV electrons, CSDA range 0.4378 g/cm^2

b. 20 MeV electrons, CSDA range 9.295 g/cm^2

actually represent the energy imparted to the medium (depth-dose distribution) rather than the loss of energy by the primary electron beam.

At 1 MeV, the influence of multiple scattering is large, but that of energy-loss straggling is small. The converse is the case at 20 MeV. At this energy the depth dose is modified at shallow depths by the transport of energetic secondary electrons. Moreover, at 20 MeV the combined effect of energy-loss straggling and the transport of energy by secondary photons extends the depth dose curves beyond the CSDA range.

At energies below 10 keV the utility of stopping powers is decreased because the continuous-slowing-down-approximation becomes increasingly inaccurate. In each inelastic collision, the primary electron must lose enough energy to supply at least the energy needed for the ejection of a bound electron from the target atom, or for raising the atom to an excited

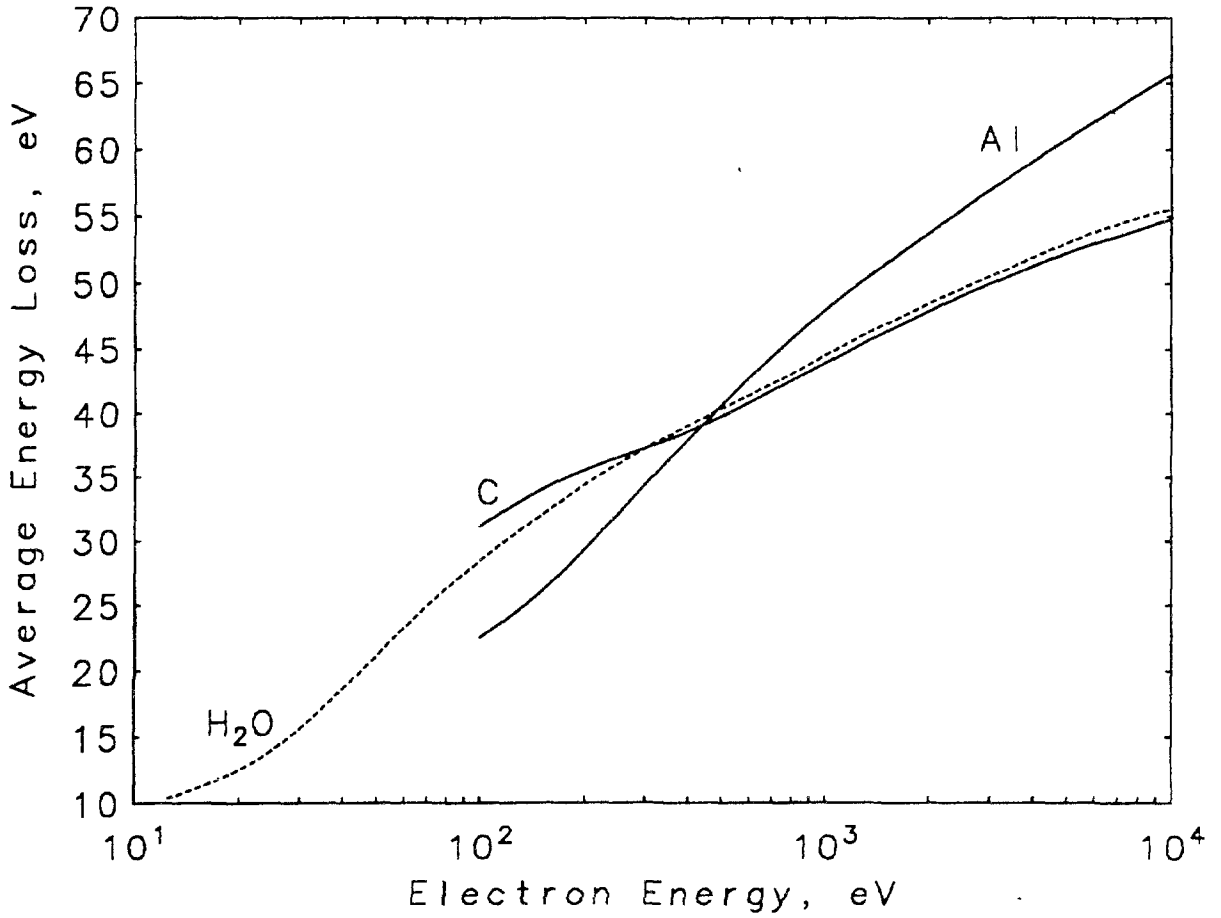

Fig.7.10. Average energy loss per inelastic collision, obtained as the product of tabulated mean free path and stopping power. Obtained from Khlupin and Akkerman [69] for C and Al, and from Ashley [66] for water.

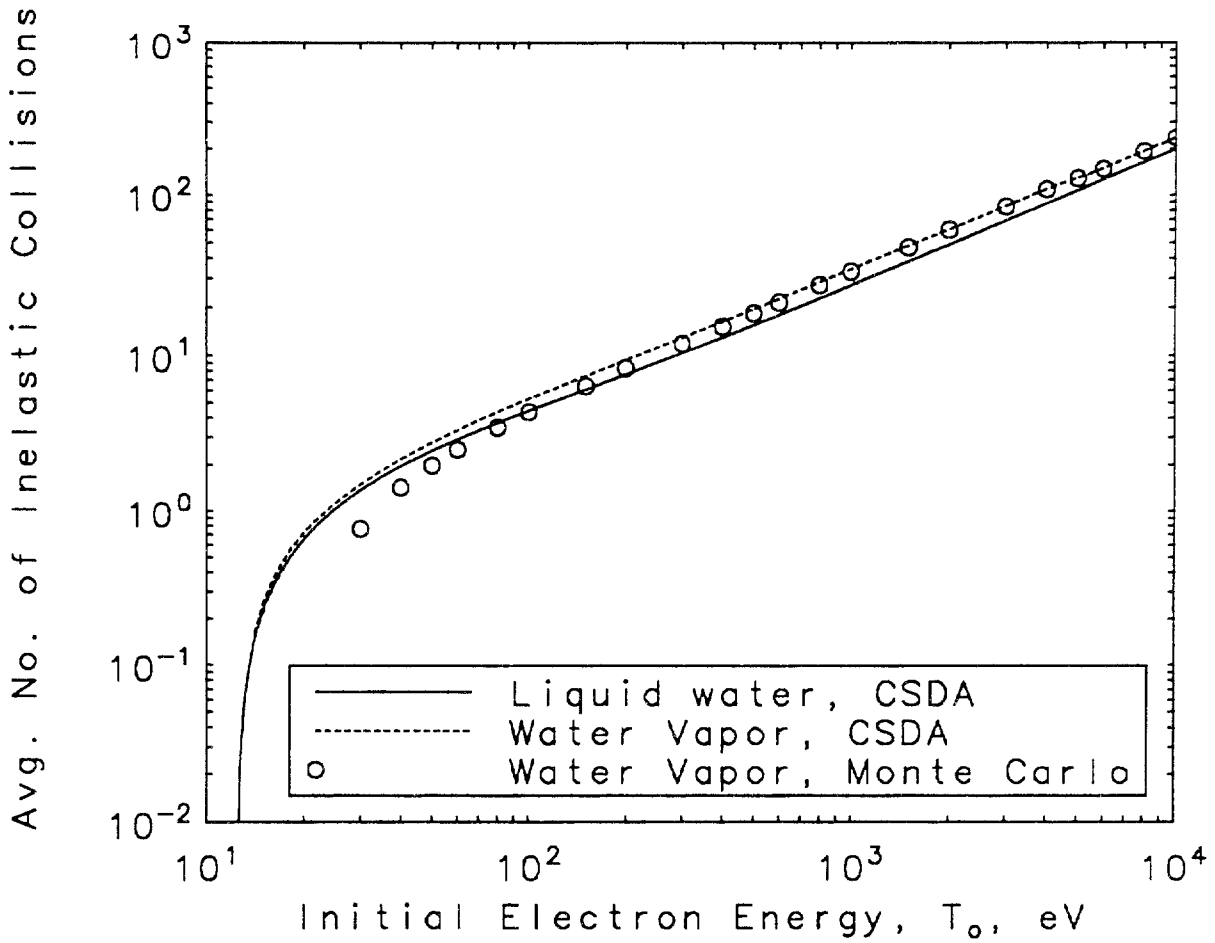

Fig.7.11. Average number of inelastic collisions made by an electron with initial energy T_0 as it slows down to an energy of 12.6 eV. Results were obtained either in the CSDA, or by the Monte Carlo method taking into account fluctuations. The results for liquid water were obtained with the stopping powers and mean free paths given by Ashley [66].

state. The average energy loss per collision can be calculated as the product p(T)S(T), where p(T) is the mean free path for inelastic collisions and S(T) the stopping power at energy T. These quantities can be obtained from the various tabulations described in Sec. 7.2.1.7. The resulting average energy loss per inelastic collision in water, carbon and aluminum is shown in Fig. 7.10. At 1000 eV, the average fractional energy loss per collision is 4 to 5 percent of the primary electron energy, but at 100 eV it is as large as 20 percent, so that the assumption of a smooth gradual decrease of the electron energy is no longer realistic.

The average number of inelastic collisions, <n>, made by an electron in the course of slowing down from an initial energy T_0 to a final energy T_f can be calculated, in the continuous-slowing-down approximation, as

$$\langle n \rangle = \int_{T_f}^{T_0} \frac{dT}{p(T)S(T)} . \qquad (7.10)$$

Plots of <n> vs. T_0 from Eq.(7.10) are shown in Fig. 7.11 for electrons slowing down in water vapor or in liquid water to an energy T_f = 12.6 eV.

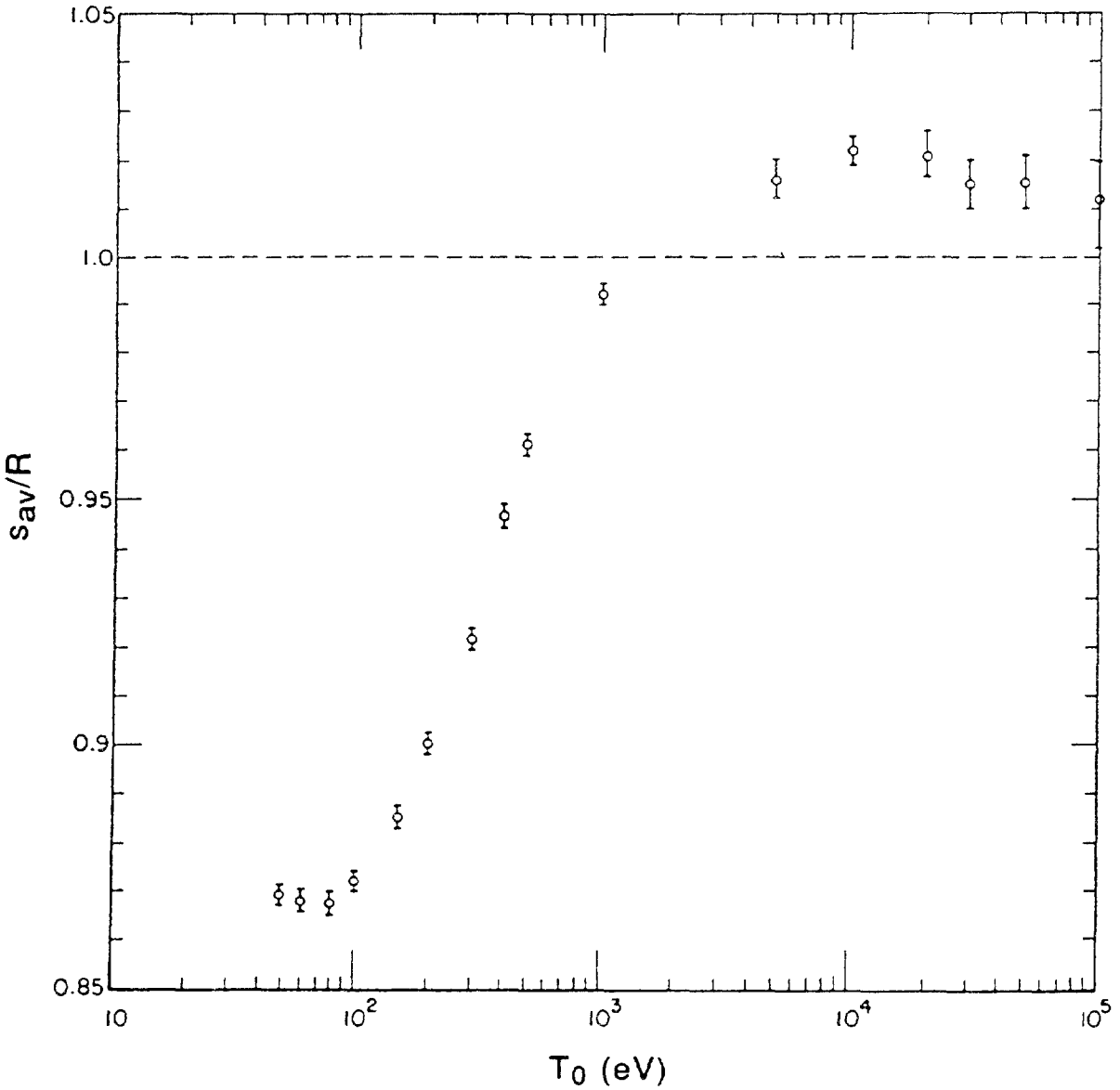

Fig.7.12. Ratio s_{av}/R of the average path length to the CSDA range, for electrons of initial energy T_0 slowing down in water vapor to an energy of 12.6 eV. From Berger [75].

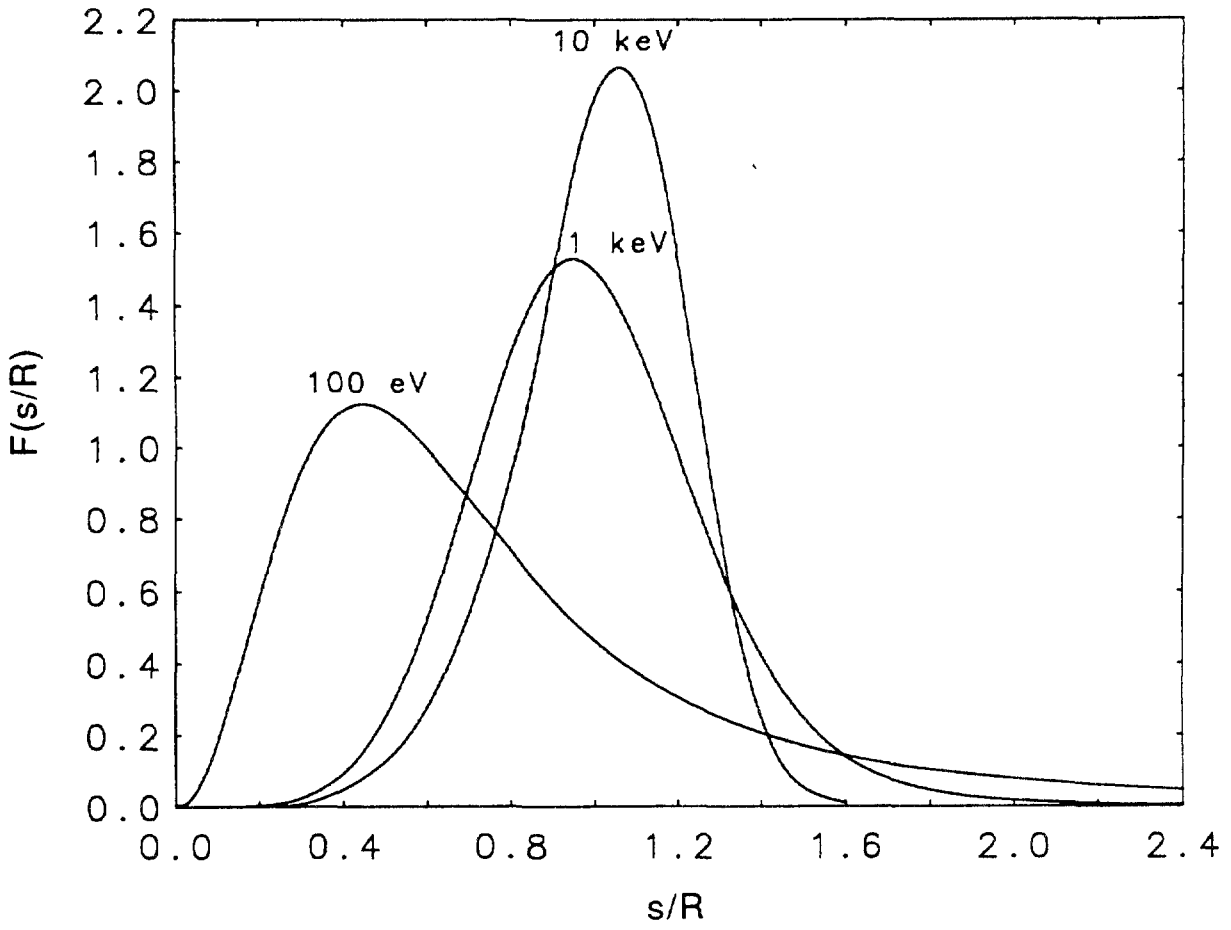

Fig.7.13. Distribution of the path lengths traveled in water vapor by electrons of various initial energies, when they have slowed down to an energy of 12.6 eV, normalized to unity. Path lengths are expressed in units of the CSDA range R.

The values of <n> are ≃ 30 at 1000 eV and ≃ 5 at 100 eV. Also shown in Fig. 7.11 are values of <n> from a Monte Carlo calculation (taking into account straggling) which - below 100 eV - become significantly smaller than the values from Eq.(7.10).

The deterioration of the continuous-slowing-down-approximation with decreasing energy can be illustrated by the relation between the average path length s_{av} and the CSDA range R. Fig.7.12 shows the ratio s_{av}/R, from a Monte Carlo calculation, for electrons that have slowed down in water vapor to an energy of 12.6 eV. For initial electron energies T_0 above 1 keV, s_{av}/R is only slightly larger than unity, so that R is a good estimate of the rectified path length (as is usually assumed). Below 1 keV, however, s_{av}/R becomes smaller than unity, reaching the value 0.87 at 100 eV. Furthermore, as shown in Fig.7.13, the shape of the distribution of the path-length/range ratio s/R changes significantly below 1 keV. For T_0 = 10

keV and 1 keV, the distribution is approximately Gaussian. At 100 eV it becomes much broader and highly skewed, and the most probable value of s/R is 0.5.

7.3. HYDROGEN IONS

7.3.1. Electronic Stopping Power

7.3.1.1. Introduction.

The mean electronic energy loss of protons in elementary substances at energies >1 MeV is well described by the Bethe-Bloch theory (see, e.g., [5]) with subsequent improvements:

$$\frac{S_{col}}{\rho} = \frac{4\pi r_e^2 m_e c^2}{u} \frac{1}{\beta^2} \frac{Z_2}{A_2} Z_1^2 \, (L_0 + Z_1 L_1 + Z_1^2 L_2). \qquad (7.11)$$

Here, S_{col}/ρ is the mass electronic (or collision) stopping power (in MeV/(gcm^{-2}), e.g.), r_e the classical electron radius, $m_e c^2$ the rest energy of the electron, u the atomic mass unit, β the projectile speed divided by the speed of light, Z_2 and A_2 are the atomic number and the relative atomic mass of the target element, and $Z_1(=1)$ is the atomic number of the projectile. The numerical constant is given in 7.2.1.1, and L_0 is given by

$$L_0(\beta) = \ln\left(\frac{2m_e c^2 \beta^2}{1-\beta^2}\right) - \beta^2 - \ln I - \frac{C}{Z_2} - \frac{\delta}{2} \qquad (7.12)$$

where I is the mean excitation energy of the target medium, C/Z_2 is the shell correction of the first order term, and $\delta/2$ the density effect correction. The terms L_1 and L_2 in eq.(7.11) extend the treatment beyond the first Born approximation (see, e.g., P.Bauer's recent review [91]). For a discussion of I-values, see Sec. 7.2.1.4 and 7.2.1.5.

Evidently, the stopping power depends on the projectile speed but not on the projectile mass, M_1. Eq.(7.11) therefore applies equally well to deuterons and to tritons. Instead of describing the stopping power as a function of speed, one conveniently uses $T_r = T/M_1$, the energy per mass unit, as an independent variable (which is proportional to β^2, for a non-relativistic projectile). If T is in MeV and if M_1 is the relative

atomic mass of the projectile, then T_r is in units of MeV u^{-1}. Another, slightly different, choice [92] is the equivalent proton energy, i.e., the energy of a proton of equal speed,

$$T_{eq} = \frac{M_p}{M_1} T \qquad (7.13)$$

where M_p is the proton mass, and M_1 may refer to p, d or t.

If differences of 1% or so do not matter, one can also use the specific energy instead, i.e., the energy per nucleon, T/A_1 (in MeV), where A_1 is the atomic *mass number* of the projectile. This is common for heavy projectiles (see Sec.7.5).

Table 7.10 contains a short resumé of the various stopping power tables and computer programs presently available. Janni (J82) gives a list of some additional tables. Conversion factors for converting S to S/ρ or to S/n or vice versa are given, e.g., by AZ77. For a list of reference codes like AZ77, see table 7.11.

The stopping power according to eq. (7.11) can be conveniently calculated using program BEST (see Table 7.11). This program is valid above about T_r = 1 MeV (see ICRU49); it contains the necessary data for all elements and for many additional substances of interest to radiology. One can also calculate additional substances it one enters the mean excitation energy (using, e.g., ICRU37). For a comparison of these I-values with recent experimental results, see Tables 7.2 and 7.4.

In the region of the maximum (near T_r = 100 keV), no reliable theory has existed until recently [93,91], but now one may hope that the charge state approach [94,95] will provide one. Indeed, Penalba et al [95] were able to reproduce the experimental stopping power of Al for protons (below 100 keV) within about 20%, taking the contributions due to H^-, H^0, and H^+ separately into account. For special cases (light targets), coupled-channel calculations [96,97] are very promising: see the recent result by Schiwietz and Grande in Fig. 7.17 below. Recently, Kaneko (K93) has produced a table of theoretical stopping powers for protons from 1 to 10000 keV, for all atomic targets ($2 \le Z_2 \le 92$), and for many elements also in the solid state. Examples of his results are shown in Figs. 7.15 and 7.16 below; they indicate agreement with experiment within 20 to 30%. It is surprising that

TABLE 7.10. FITTED CURVES AND TABLES OF ELECTRONIC STOPPING POWER FOR HYDROGEN IONS.

C ... Coefficients of fitted curve given, Tb ... Table of fitted stopping power data,
P ... Program, T ... Kinetic energy in keV, $T_r = T/M_1$, $\varepsilon = S/n$ ... Stopping cross section

Andersen-Ziegler (AZ77)	C Tb	92 elements	1 - 10 keV $\varepsilon = A_1 T_r^{0.5}$	10 - 999 keV $\varepsilon^{-1} = \varepsilon_L^{-1} + \varepsilon_H^{-1}$ where $\varepsilon_L = A_2 T_r^{0.45}$ $\varepsilon_H = \frac{A_3}{T_r} \ln\left[1 + \frac{A_4}{T_r} + A_5 T_r\right]$	0.6 - 100 MeV $\varepsilon = \frac{A_6}{\beta^2}\left[\ln\left(\frac{A_7\beta^2}{1-\beta^2}\right) - \beta^2 - \sum_{i=0}^{4} A_{i+8} (\ln T_r)^i\right]$ where $\beta = \frac{v}{c}$	
Janni (J82)	Tb	92 elements, 63 compounds or mixtures	1 - 5 keV $\varepsilon \propto T^{0.5}$	5 - 20 keV $\varepsilon \propto T^{s}$ (s variable)	20 - 1000 keV Fifth order polynomial fit to experimental data	1 - 1000 Mev Bethe equation with all necessary corrections
Bichsel-Porter (BP82)	Tb	H_2, He, N_2, O_2, CH_4, Air	0.4 - 20 MeV Bethe equation with one free parameter (in Barkas correction term)			
Ziegler-Biersack Littmark (ZBL85)	C	92 elements (for all ions)	0 - 25 keV $\varepsilon \propto T_r^{0.45}$ [but $\varepsilon \propto T_r^{0.25}$ for $Z_2 < 7$]	0.025 - 100 MeV (but should not be used above 10 MeV) $\varepsilon^{-1} = \varepsilon_L^{-1} + \varepsilon_H^{-1}$ [Coefficients A_i in file SCOEF.DATA] where $\varepsilon_L = A_1 T_r^{A2} + A_3 T_r^{A4}$, $\varepsilon_H = \frac{A_5}{T_r^{A6}} \ln\left(\frac{A_7}{T_r} + A_8 T_r\right)$		
Z89 Z90	P	92 elements, many mixtures and compounds	Program contained in TRIM89, TRIM90. Uses the same functions as ZBL85, and an updated file, SCOEF.88, of coefficients A_i. Above T_r = 10 MeV, it uses $\varepsilon = H_1 + H_2 x + H_3 x^2 + H_4/x$ (where $x = \ln T_r$, and the coefficients H_i are contained in file HICOEF.DAT)			
Berger (ICRU49)	Tb	25 elements, 48 compounds or mixtures	T = 1 keV - 10000 MeV Bethe equation, with corrections, at high energy (≥ 1 MeV), merged to experimental values at low energies. I-values from ICRU37. See appendix for program PSTAR.			
Berger-Bichsel (BEST)	P	92 elements, any compound or mixtures	Program BEST, available from the authors, calculates Bethe equation, with corrections, from about T = 1 to T = 1000 MeV.			
Bichsel (BI91)	Tb	7 elements (La - U)	Bethe equation, with corrections, fitted to experimental values from 0.3 to 100 MeV.			

TABLE 7.11. DATA REFERENCE CODES

Ab91 ABDESSELAM, M., STOQUERT, J.P., GUILLAUME, G., HAGE-ALI, M., GROB, J.J., SIFFERT, P., Nucl. Instrum. Methods B61,385, and personal communication to H. Paul

Ab92a ABDESSELAM, M., STOQUERT, J.P., GUILLAUME, G., HAGE-ALI, M., GROB, J.J., SIFFERT, P., Nucl. Instrum. Methods B72,293.

Ab93 ABDESSELAM, M., STOQUERT, J.P., HAGE-ALI, M., GROB, J.J., SIFFERT, P., Nucl. Instr. Methods B73, 115.

An68 ANDERSEN, H.H., HANKE, C.C., SIMONSEN, H., SÖRENSEN, H., VAJDA, P., Phys.Rev. 175, 389

And69 ANDREEV, V.N., NEDOPEKIN, V.G., ROGOV, V.I., Soviet Phys. JETP 29, No. 5, 807.

Ar69 ARKHIPOV, E.P.,GOTT, Yu.V., Sov. Phys. JETP 29, 615.

Ay82 ANTHONY, J.M., LANFORD, W.A., Phys. Rev. A25, 1868.

AZ77 ANDERSEN, H.H., ZIEGLER, J.F., Hydrogen Stopping Powers and Ranges in all Elements, Pergamon Press, Elmsford, New York.

Ba83a BAUMGART, H., ARNOLD, W., BERG, H., HUTTEL, E., CLAUSNITZER, G., Nucl. Instr. Meth. 204, 597.

Bd56 BADER, M., PIXLEY, R.E., MOZER, F.S., WHALING, W., Phys.Rev. 103, 32

Be81 BEDNYAKOV, A.A., BULGAKOV, Yu.V., NIKOLAEV, V.S., CHERNOV, V.L., Phys. Status Solidi A68, 187.

BEST Computer program by BERGER, M.J., BICHSEL, H., available from the authors for use on personal computer (1990).

BG65 BOOTH, W., GRANT, I.S., Nucl.Phys. 63, 481.

Bi78 BIMBOT, R., DELLA NEGRA, S., GARDES, D., GAUVIN, H., Nucl. Instr. Methods 153, 161.

Bi89 BIMBOT, R., CABOT, C., GARDES, D., GAUVIN, H., HINGMANN, R., ORLIANGE, I., DE REILHAC, L., HUBERT, F., Nucl. Instr. Methods B44, 1

BI91 BICHSEL, H., Nat. Inst. of Standards and Technology, report NIST IR-4550, and Phys. Rev. A46 (1992) 5761.

Bp71 BONDERUP, E., HVELPLUND, P., Phys. Rev. A4, 562.

BP82 BICHSEL, H., PORTER, L.E., Phys. Rev. A25, 2499.

Br90 BAUER, P., Nucl. Instr. Methods B45, 673.

Bs79 BESENBACHER, F., ANDERSEN, H.H., HVELPLUND, P., KNUDSEN, H., Kgl. Danske Vid. Selskab Mat.-fys. Medd. 40, No.3.

By55 BROLLEY, J.E., RIBE, F.L., Phys. Rev. 98, 1112.

Cr42 CRENSHAW, C.M., Phys. Rev. 62, 54.

Ct54 CHILTON, A.B., COOPER, J.N., HARRIS, J.C., Phys. Rev. 93, 413.

Do75 DOSE, V., SELE, G., Z. Phys. A272, 237.

Ef75 EFKEN, B., HAHN, D., HILSCHER, D., WUSTEFELD, G., Nucl. Instr. Methods 129, 219.

Ep93 EPPACHER, Ch., SEMRAD, D., unpublished data

Fu80 FUKUDA, A., Phys. Med. Biol. 25, 877.

Ga87 GAUVIN, H., BIMBOT, R., HERAULT, J., Nucl. Instrum. Methods B28, 191.

Gl92a GOLSER, R., EPPACHER, Ch., SEMRAD, D., Nucl. Instrum. Methods B67, 69.

Gl92b GOLSER, R., SEMRAD, D., Nucl. Instrum. Methods B69, 18.

Go67 GORODETZKY, S., CHEVALIER, A., PAPE, A., SENS, J.Cl., BERGDOLT, A.M., BRES, M., ARMBRUSTER, R., Nucl. Phys. A91, 133.

He91 HERAULT, J., BIMBOT, R., GAUVIN, H., KUBICA, B., ANNE, R., BASTIN, G., HUBERT, F., Nucl. Instrum. Methods B61, 156.

Hm62 HUBERMAN, M.N., Phys. Rev. 127, 799.

Hof76 HOFFMANN, I., JÄGER, E., MÜLLER-JAHREIS, U., Rad. Effects 31, 57.

HU90 HUBERT, F., BIMBOT, R., GAUVIN, H., At. Data Nucl. Data Tables 46, 1.

Hv71 HVELPLUND, P., Kgl. Danske Videnskab. Selskab Mat.-fys. Medd. 38, 4.

ICRU37 ICRU Report 37: Stopping Power for Electrons and Positrons, Intern. Commission on Radiation Units and Measurements, Bethesda, MD 20814, USA (1984).

ICRU49 ICRU Report 49: Stopping Powers and Ranges for Protons and Alpha Particles, Intern. Commission on Radiation Units and Measurements, Bethesda, MD 20814, USA (1993); the tables can also be produced using the programs described in the appendix

J82 JANNI, J.F., At. Data Nucl. Data Tabl. 27, 150, 341.

Jo71 JOHANSEN, A., STEENSTRUP, S., WOHLENBERG, T., Radiat. Eff. 8, 31.

K93 KANEKO, T., Atomic Data Nucl. Data Tabl. 53, 271.

Kr82 KREUSSLER, S., VARELAS, C., SIZMANN, R., Phys. Rev. B26, 6099.

La75 LANGLEY, R., Phys. Rev. B12, 3575.

Ld85 LAND, D.J., SIMONS, D.G., BRENNAN, J.G., GLASS, G.A., Nucl. Instrum. Methods B10/11, 234, and pers. communication to H. Paul (1992).

Ld92 LAND, D.J., pers. communication to H. Paul, see also: PRICE, J.L., STERN, S.H., SIMONS, D.G., LAND, D.J., BRENNAN, J.G., Nucl. Instr. Methods B56/57 (1991) 348.

Len86a LENNARD, W., GEISSEL, H., JACKSON, D., PHILLIPS, D., Nucl. Instrum. Methods B13, 127.

Len86b LENNARD, W.N., GEISSEL, H., Nucl. Instrum. Methods B27, 338.

Mar62 MARTIN, E.W., NORTHCLIFFE, L.C., Phys. Rev. 128, 1166.

Me78 MERTENS, P., Nucl. Instrum. Methods 149, 149.

Me80 MERTENS, P., KRIST, Th., Nucl. Instrum. Methods 168, 33.

Me82a MERTENS, P., KRIST, Th., Nucl. Instrum. Methods 194, 57.

Me82b MERTENS, P., KRIST, Th., J. Appl. Phys. 53, 7343.

Mh65 MOORHEAD, R.D., J. Appl. Phys. 36, 391.

Mi90 MITTERSCHIFFTHALER, C., BAUER, P., Nucl. Instrum. Methods B48, 58.

Ms66 MASON, D.L., PRIOR, R.M., QUINTON, A.R., Nucl. Instrum. Methods 45, 41.

Na68 NAKATA, H., Can. J. Phys. 46, 2765, and Erratum: Can. J. Phys.48 (1970) 1744.

Ny78 NYAIESH, A.R., STECKELMACHER, W., LUCAS, M.W., J. Phys.C ,Solid State Phys. 11, 2917.

Op75 OPHEL, T.R., KERR, G.W., Nucl. Instrum. Methods 128, 149.

Or63 ORMROD, J.H., DUCKWORTH, H.E., Can. J. Phys. 41, 1424.

Or65 ORMROD, J.H., MAC DONALD, J.R., DUCKWORTH, H.E., Can. J. Phys. 43, 275.

Or68 ORMROD, J.H., Can. J. Phys. 46, 497.

Ov79 OVERBURY, S.H., DITTNER, P.F., DATZ, S., Rad. Eff. 41, 219.

Ph53 PHILLIPS, J.A., Phys. Rev. 90, 532.

Pi68 PIERCE, T.E., BLANN, M., Phys. Rev. 173, 390.

Po59 PORAT, D.I., RAMAVATARAM, K., Proc. R. Soc. Lond. A252, 394.

Po60 PORAT, D.I., RAMAVATARAM, K., Proc. Phys. Soc. 77, 97.

Po61 PORAT, D.I., RAMAVATARAM, K., Proc. Phys. Soc. 78, 1135.

Pr91 PRICE, J.L., STERN, S.H., SIMONS, D.G., LAND, D.J., BRENNAN, J.G., Nucl. Instrum. Methods B56/57, 348.

PSS PAUL, H., SEMRAD, D., SEILINGER, A., Nucl. Instrum. Methods B61 (1991) 261

Rä91 RÄISÄNEN, J., RAUHALA, E., BJÖRNBERG, M., KISS, A.Z., DOMINGUEZ, J., Rad. Eff. and Defects in Solids, 118, 2, 97.

RBS Program due to STEINBAUER, E..

Re87 REITER, G., BAUMGART, H., KNIEST, N., PFAFF, E., CLAUSNITZER, G., Nucl. Instrum. Methods B27, 287.

Re90 REITER, G., KNIEST, N., PFAFF, E., CLAUSNITZER, G.,Nucl. Instrum. Methods B44, 399.

R160 ROLL, P.G., STEIGERT, F.E., Nucl. Phys. 17, 54.

Rn53 REYNOLDS, H.K., DUNBAR, D.N.F., WENZEL, W.A., WHALING, W., Phys. Rev. 92, 742

Sa81a SANTRY, D.C., WERNER, R.D., Nucl. Instrum. Methods 188, 211.

Sa91 SANTRY, D.C., WERNER, R.D., Nucl. Instrum. Methods B53, 7.

Sa92 SANTRY, D.C., WERNER, R.D., Nucl. Instrum. Methods B69, 167.

Sc82 SCHULZ, F., BRANDT, W., Phys. Rev. B26, 4864.

Sc85 SCHULZ, F., SHCHUCHINSKY, J., Nucl. Instrum. Methods B12, 90.

Sf78 SOFIELD, C.J., COWERN, N.E.B., PETTY, R.J., FREEMAN, J.M., MASON, J.P., Phys. Rev. A17, 859.

SG93 SCHIWIETZ, G., GRANDE, P.L., Radiation Eff. Def. in Solids 27 (1993)

Sh84 SHCHUCHINSKY, J., PETERSON, C., Radiat. Eff. 81, 221-229.

Sim75 SIMONS, D., LAND, D., BRENNAN, J., BROWN, M., Phys. Rev. A12, 2383.

Sr65 SAUTTER, C.A., ZIMMERMANN, E.J., Phys. Rev. 140, 490.

SUG89 SUGIYAMA, H., ELT Technical Report TR-89-13, Electro-technical Lab., Ibaraki, Japan

Sw70 SWINT, J.B., PRIOR, R.M., RAMIREZ, J.J., Nucl. Instrum. Methods 80, 134.

Tp62 TEPLOVA, Y.A., NIKOLAEV, V.S., DMITRIEV, I.S., FATEEVA, L.N., Sov. Phys.-JETP 15, 31.

TRIM89 Monte Carlo program describing TRansport of Ions through Matter by BIERSACK, J.P., ZIEGLER, J.F., based on ZBL85
available on diskette from ZIEGLER, J.F..

TRIM90 like TRIM89, but 3-dimensional, and with graphical output.

TRIM91 like TRIM90, but with different definition of lateral straggling and of skewness and kurtosis of range. Also, energy straggling is linearly reduced below the Bohr value for energies below the stopping power maximum. Energy straggling not calculated for $Z_1 > 3$.

TRIM92 like TRIM91, but flight path within a layer now decreases toward layer edge (see Sect. 7.3.3) *and* nuclear stopping for compounds now calculated using Bragg additivity.

T2D Two-dimensional TRIM program by BIERSACK, J.P.,
can be purchased from the author.

We53 P.K., WEYL, Phys. Rev. 91, 289.

Wi62 VAN WIJNGAARDEN, A., DUCKWORTH, H.E., Can. J. Phys. 40, 1749.

Wo63 WOLKE, R.L., BISHOP, W.N., EICHLER, E., JOHNSON, N.R., O'KELLEY, G.D., Phys. Rev. 129, 2591.

Wr79 WARD, D., ANDREWS, H.R., MITCHELL, I.R., LENNARD, W.N., WALKER, R.B., RUD, N., Can. J. Phys. 57, 645.

Ya83 YALYSHKO, S.V., WEDELL, R., Phys. stat. sol. B116, K47.

Yon80 KIM, Yong-Ki, CHENG, Kwok-tsang, Phys. Rev. A22, 61.

Z77 ZIEGLER, J.F., Helium: Stopping Powers and Ranges in all elemental Matter, Pergamon Press, Elmsford, New York.

Z80 ZIEGLER, J.F., Handbook of Stopping Cross Sections for Energetic Ions in all Elements, Pergamon Press, Elmsford, New York.
(Vol.5 of: The Stopping and Ranges of Ions in Matter)

ZBL85 ZIEGLER, J.F., BIERSACK, J.P., LITTMARK, U.,
The Stopping and Ranges of Ions in Matter, Vol. 1, Plenum, New York

Z89 Stopping power programs contained in TRIM89. The changes with respect to ZBL85 are discussed in chapters 7.3.1.1 and 7.5.1.1

Z90 Stopping power programs contained in TRIM90 (identical to Z89)

Z91 Stopping power programs contained in TRIM91 (identical to Z89)

Kaneko reaches this agreement assuming a point charge projectile at all velocities, whereas Penalba et al [95] need contributions also from H^0 and H^-.

For practical purposes, one uses empirical functions fitted to the data (see table 7.10). To predict the stopping of substances where no measurements exist, one interpolates the fitting coefficients, taking into account the empirical fact that "Z_2-oscillations" exist, i.e., that due to shell structure, S/ρ is not a smooth function of Z_2. AZ77 performed this interpolation guided by the Z_2-oscillations already known for He projectiles. ZBL85 first used the dielectric response of an electron plasma in random phase approximation together with the local density approximation (for atoms whose electron distribution corresponds to the solid state) to calculate the stopping power, and then interpolated the 10-20% difference between theory and experiments, both in velocity and in Z_2.

As an example, Fig. 7.14 shows S/n as a function of Z_2 according to AZ77, J82, Z90 and to ICRU49. At 60 keV, Z_2-oscillations are quite noticeable; in particular, the stopping cross section for the noble metals Cu, Ag, and Au is seen to be smaller than that for the neighbor elements. At higher energy, the oscillations are strongly reduced.

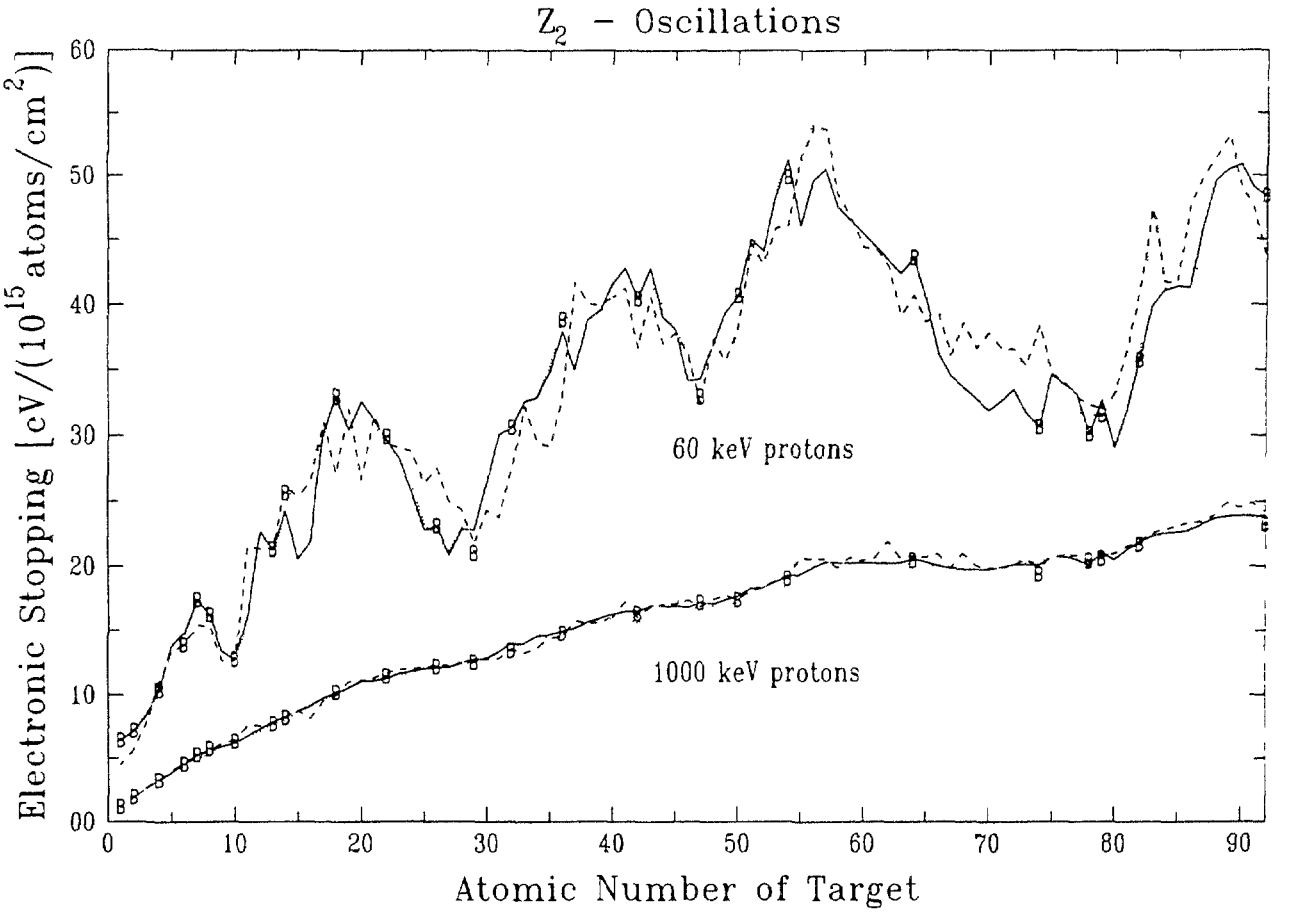

Fig.7.14. Electronic stopping cross section of all elemental targets for 60 and 1000 keV protons, according to AZ77 (---), J82 (——), Z90 (---), and ICRU49 (B); (cf. table 7.11).

Below about 20 keV, the stopping power is generally assumed to be roughly proportional to velocity [98]. Echenique, Nieminen and Ritchie [99,100], e.g., have calculated velocity proportional stopping in this energy region using a non-linear density-functional approach and describing the solid target by its one-electron radius [101] (see Fig. 7.15). In accordance with this assumption of velocity proportionality, the fitting functions (cf. table 7.10) usually assume $S \propto T^{0.5}$ or $S \propto T^{0.45}$ at low energy. For light targets (Li, Be, C), ZBL85 claim that the stopping power should be proportional to $T^{0.25}$. Our Fig.7.15 for H on C shows that this claim is rather questionable (see also Sec. 7.3.5). On the other hand, in a special case like H on He the stopping cross section depends on a power of T much *higher* than 0.5, as found recently by Golser and Semrad [102].

The book AZ77 contains the most comprehensive compilation of experimental data (S/n versus T/M_1), including graphs and tables, available to date. This includes all the elements, also those that are normally gaseous (or liquid). The densities given on the graphs for N_2 and Ne, e.g., seem to imply the solid state, but the measurements (and hence, the fitted curves) really refer to the gaseous state. It should be noted [103] that medium- and high-energy fits by AZ77 are not continuous at 1 MeV; there is, e.g., a jump by 3.6% for H ⇒ Ag.

The same data (including some new ones, see Z80) were later refitted by Ziegler (ZBL85). This has been an improvement in some cases, e.g., for

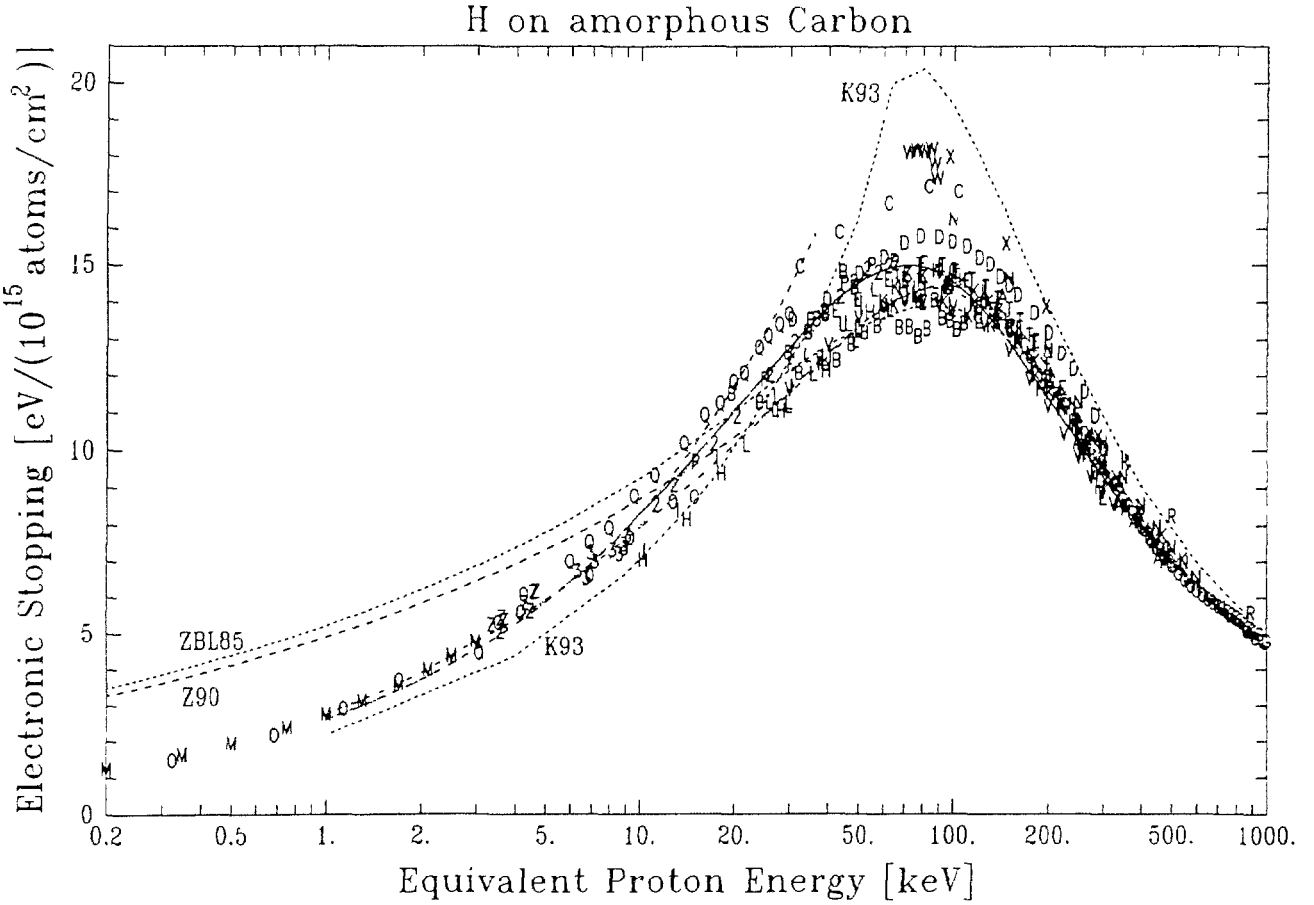

Fig.7.15. Electronic stopping cross section of amorphous carbon for hydrogen ions. The curves correspond to the following references:
—— AZ77; short dashed: ZBL85 and K93 (solid), as marked; long dashed: Z90 (without bonding corr.); —·— J82; ···· ICRU49; -·- Echenique et al [100]. The symbols indicate measured points from the following references (see table 7.11):
A Be81; B Kr82; C Me80; D Me82a; E Me82b; G Sa81a; H Sc85; I Sh84; J,K,L Br90; M Ov79; N Rn53; O Ar69; P Or65; Q Wi62; R Op75; T Mh65; U Go67; V Sr65; W Jo71; X Ny78; Z,3 Gl92a; 2 Or63.

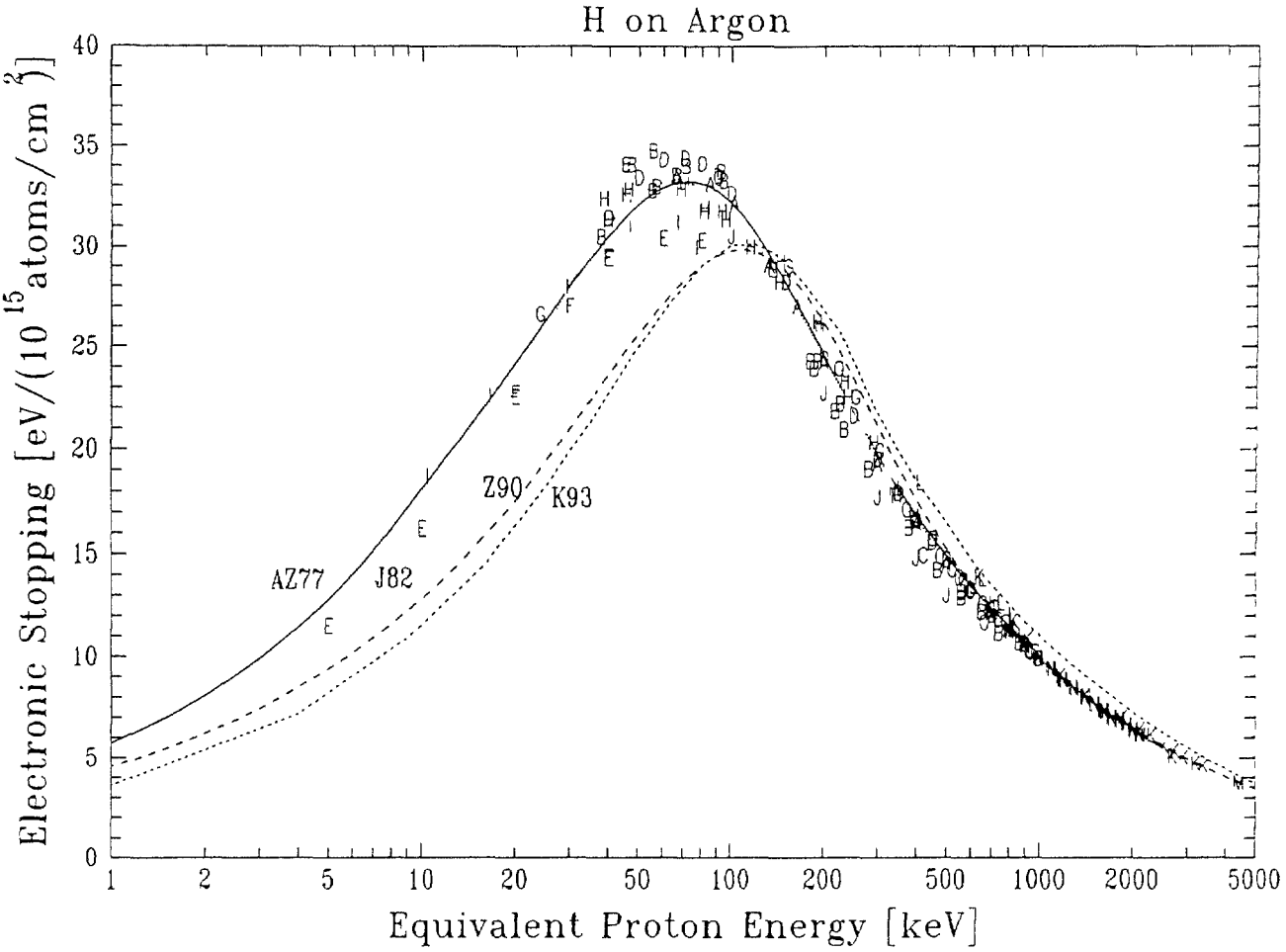

Fig.7.16. Electronic stopping cross section of argon for hydrogen ions. The curves correspond to the following references:
—— AZ77; short dashed: K93; long dashed: Z90 (identical to ZBL85);
..... J82. ICRU49 is identical to AZ77.
The symbols indicate measured points from the following references:
A Ba83a; B Bs79; C Ct54; D Rn53; E Or68; F Or68; G Wo63; H We53; I Ph53; J Bp71; K Sw70; L Ms66; M By55; N Re90

gold [103], but made agreement worse in others, e.g. for carbon (see Fig. 7.15). ZBL85, according to the title of the book, is for solids only. Elements which normally occur as gases are assumed to be at the melting point. For elements in the gaseous state one should therefore use AZ77 (or ICRU49), not ZBL85 (see Fig. 7.16 for hydrogen on Ar).

More recent versions of Ziegler's stopping power programs (referred to as Z89, Z90, Z91 or Z92 in the following), written in Quickbasic to be used on a personal computer, are contained in TRIM89, TRIM90, TRIM91 and TRIM92. Z89, Z90, Z91 and Z92 are identical. These programs contain a correction for relativistic projectiles (in the ZBL85 version, the stopping power keeps decreasing toward high energy rather than going through a

minimum). For some light elements, the coefficients A_1 to A_8 (see table 7.10) have now values different from those in ZBL85. Table 7.12 shows, for these elements, the largest differences between ZBL85 and Z90 due to this change (see also Fig. 7.15). Otherwise, the stopping power routines contained in TRIM89 to TRIM92 are identical to the one in ZBL85.

A new table for selected elements, compounds and mixtures has been produced recently [ICRU49]. It is partially based on AZ77, but takes new measurements into account. Its values can also be produced using program PSTAR (see appendix). ICRU49 also contains useful tabular and graphical comparisons between experimental data and fitted curves.

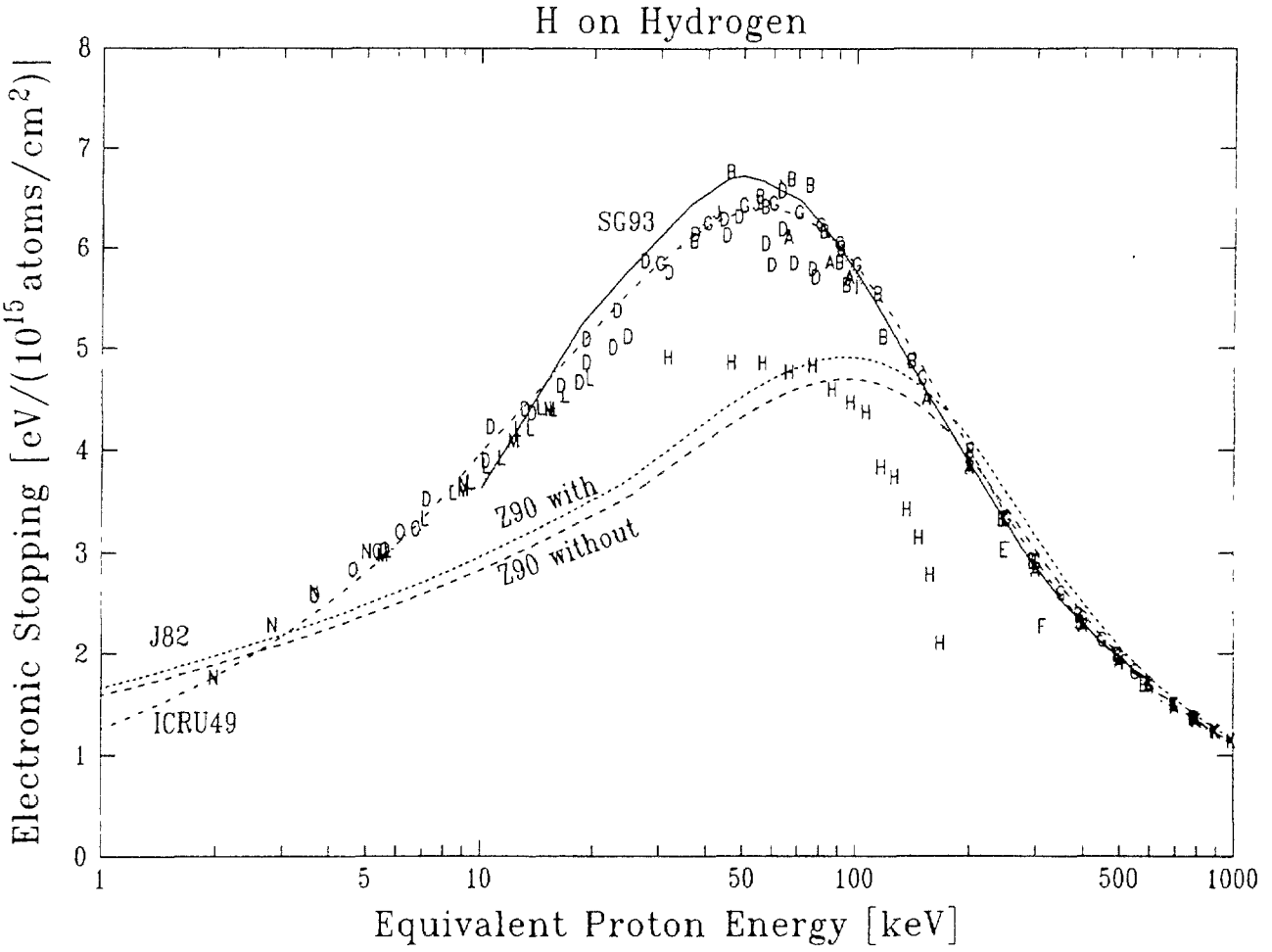

Fig.7.17. Electronic stopping cross section of hydrogen for hydrogen ions. The curves correspond to the following references:
-·-· ICRU49 (identical to AZ77); —— J82; short dashed: Z90 with bonding correction; long dashed: Z90 without bonding correction;
-·- BP82 (T > 400 keV); —— SG93.
The symbols indicate measured points from the following references:
A Ba83a; B Bs79; C By55; D Ph53; E We53; F La75; G Rn53; H Cr42; I Bp71; J Hm62; K Re90; L,M,N,O G192b.

TABLE 7.12. STOPPING POWER ACCORDING TO Z89, DIVIDED BY THE VALUE FROM ZBL85, AT THE ENERGY WHERE THE CHANGE IS LARGEST:
a) below 10 MeV; b) between 10 and 100 MeV. The unusually low value for S at 10 MeV is due to a discontinuity in the Z89 stopping for S at this energy.

	(a)		(b)	
Target	Energy	Ratio	Energy	Ratio
H_2	≤25 keV	1.12	100 MeV	1.11
He	70	1.12	100	1.21
C	≤25	0.94	100	1.15
N_2	79	1.11	100	1.14
O_2	70	1.13	100	1.13
F	≤25	1.03	100	1.13
Ne	≤25	0.81	100	1.12
Al	≤25	1.03	100	1.10
Si	5.6	0.93	44	0.98
S	40	1.13	10	0.93
Kr	≤25	1.13	100	1.05
Xe	≤25	1.08	100	1.03

The table by J82 is useful in that it also gives uncertainties for all stopping power values. These uncertainties, based on statistical methods alone, may however be too small in some cases. In the region of the stopping power maximum for Ni, e.g., J82 gives ± 2.1%, but this fit appears [103] too high by 10%.

A recent reanalysis [103] of all the published data for Au, Ag, Cu, Ni and Al targets for T_r between 10 and 2500 keV shows that the stopping maximum is lower than given by AZ77, and (for Cu and Ni) lower also than Z90 and J82. Only for Al targets, all fits agree (J82 being slightly low). Uncertainties are also given in this paper, hopefully more realistic than those by J82.

7.3.1.2. Mixtures and Compounds.

To calculate the stopping power for mixtures, one uses Bragg's additivity rule [5]:

$$S/\rho = \sum_j w_j \, (S/\rho)_j , \qquad (7.14)$$

where w_j is the fraction by weight and $(S/\rho)_j$ is the mass stopping power of the j^{th} atomic constituent. This is valid provided the condition discussed by Golser and Semrad [8] does not occur (if some gases have very different charge-changing cross sections for a particular low-energy projectile, then the addition of only a small amount of one gas will have a large effect on the population of different projectile charge states and hence on the stopping power).

Eq. (7.14) is approximately valid also for compounds above about 1 MeV, but at lower energies and for light targets, where the valence electrons contribute significantly to stopping, it becomes more and more inaccurate due to "chemical binding effects". In the extreme cases of SiO_2 and Al_2O_3, Bauer et al [104] have found the stopping in the compound reduced by as much as 14 and 27 %, resp., at about 20 keV, with respect to the Bragg value (eq. 7.14). But it is well known from the high energy measurements of Tschalär et al [105] that this reduction extends far into the Bethe region: it amounts to 4% at 1 MeV and to 2% at 10 MeV for Al_2O_3, and it corresponds to an increased I-value for the compound (see also table 7.3).

Z90 offers the possibility to calculate the stopping power of many compounds using eq. (7.14) and a bonding correction according to Ziegler and Manoyan [106], based on a joint analysis of the large amount of stopping data measured at Baylor University [107] and at Köln University [108]. Here, the molecule is not decomposed into single atoms as in eq. (7.14) but into atomic cores and different bonds (essentially between light target atoms from H to F); phase effects are assumed to be negligible. The correction is a constant factor at low energy, and it converges to unity at about 1 MeV. (Actually, the correction should differ slightly from unity even above that energy, as one can see from the results on Al_2O_3 just mentioned, and also from fig. 7.19 below). The core-and-bond approach used by Ziegler and Manoyan describes the input data well, but becomes less accurate [109] if used to describe data outside the original input set.

For heavier atoms, no bond corrections are supplied even though these are necessary at least [104,91] in the case of Al_2O_3. The constants describing the various mixtures and compounds (including bond structure!) are contained in a file COMPOUND.DAT. The file also contains information for many (especially organic) liquids and gases, but this should be used

with caution: Fig. 7.17 for H on H_2 shows that the stopping power from Z90 (with or without bonding correction) is about 30% low at the maximum. It is remarkable that the Z90 stopping power for He on H_2 seems to agree much better with the data. This may indicate that in Z90, a (bad) H stopping power has been combined with a (bad) effective charge for He to give a good He stopping power.

The bond correction contained in Z90 assumes a constant *relative* difference at low energy (see, e.g., fig.7.19 below). The results by Bauer et al [104] for Al_2O_3 and SiO_2, however, indicate that a constant *absolute* difference at low energy describes the data better.

Thwaites [109] has recently proposed an empirical scheme to calculate corrections to Bragg additivity for dosimetric materials. This scheme requires knowledge of stopping powers and I values of the constituents, and of a realistic value for the mean excitation energy I of the compound (which can be estimated using eq. 7.3 and Table 7.3); the scheme is said to provide values accurate to 5% at 100 keV and to 10% at 1 keV.

In Sec. 7.2.1.5, the small changes in electron stopping power of liquid water and various solids were discussed that result when the I-values from ICRU37 are replaced by recently measured I-values (Table 7.5). Similar changes occur of course in the proton stopping power at a similar projectile velocity. For example, for protons in liquid water, changes of -2.4%, -1.9% or -1.1% could be expected at 0.5, 1 or 10 MeV, respectively, provided the Barkas and shell corrections are left unaltered.

7.3.1.3. Difference between condensed phase and gas.

The interaction of a proton with an electron gas is weaker than that with an isolated atom, due to the dynamic screening by the electron gas [100,110]; therefore the stopping cross section for protons in the condensed phase is generally smaller than in the gas ("phase effect" or "physical state effect"). Indeed, one finds differences up to 10% at the stopping power peak [109]. Recently, P. Bauer et al [111] have found a phase difference for Zn which becomes as large as 60% at 20 keV. Calculated phase differences can be found in Kaneko's new table (K93) for many elements. For water, see the discussion in the following section, and also Ch. 9.

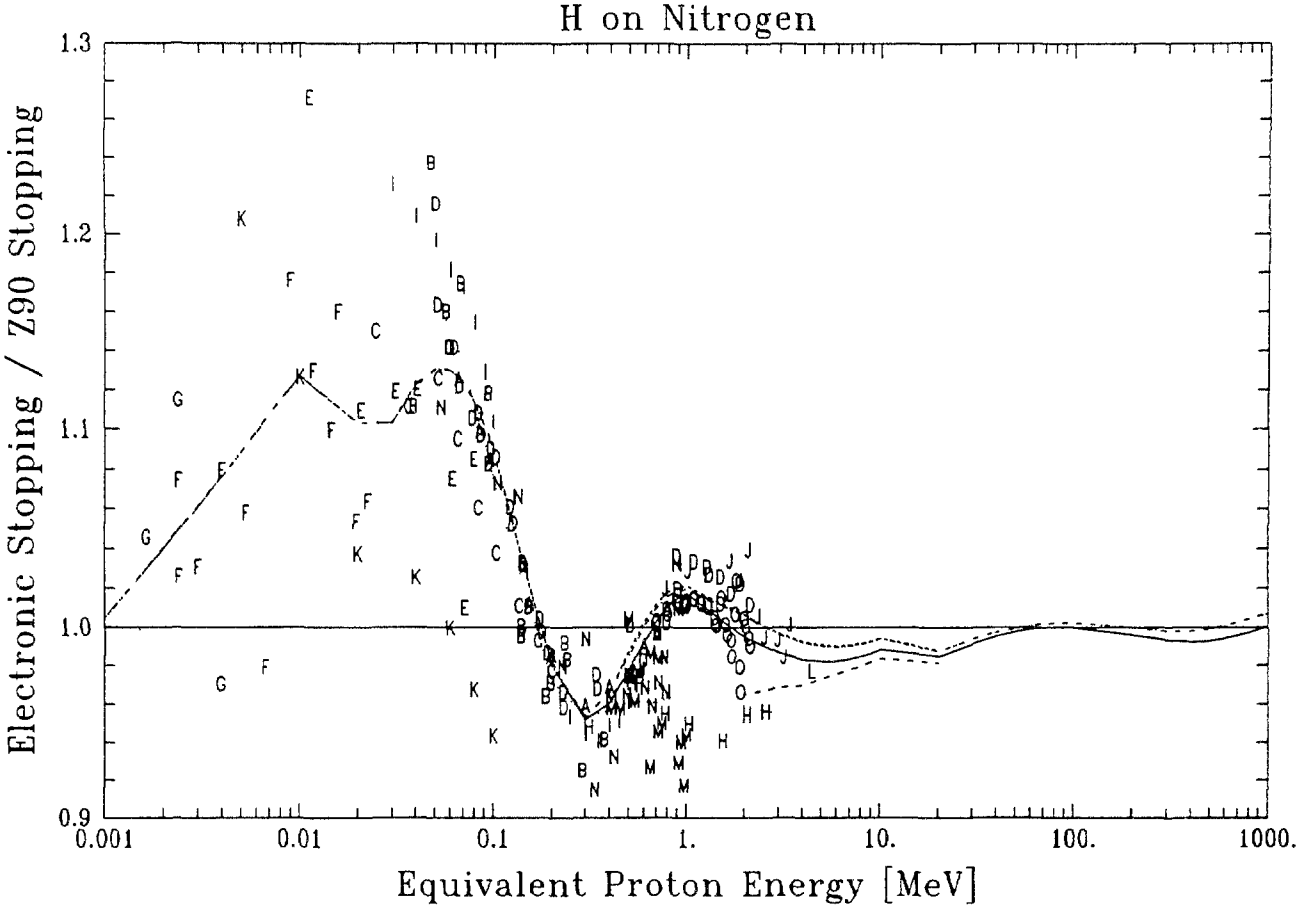

Fig.7.18. Electronic stopping cross section of nitrogen for hydrogen ions from various publications, divided by values from Z90 (without bonding correction). The curves correspond to the following references:
—— AZ77; - - J82; —·— ICRU49; -·- SUG89. ICRU49 is identical to AZ77 below 0.3 MeV and identical to BP82 (---) from 0.4 to 20 MeV.
The symbols indicate measured points from the following references:
A Ba83a; B Bs79; C Fu80; D Re87; E Ph53; F Do75; G Do75; H La75; I Rn53; J Sw70; K Or68; L By55; M Ct54; N Wo63; O Re90.

7.3.1.4. Comparison of stopping power compilations.

We have compared all the recent stopping power fits for key substances with each other, from 0.001 to 1000 MeV. For convenience, we normalize all the curves (where possible) by the Z90 function, since this is easily calculable. If this is not possible, we use a different normalization. Fig. 7.18 shows an example, for H on nitrogen. Like in the case of H on H_2, Z90 is low with respect to the measurements, below 0.1 MeV (with or without bonding correction, which is negligible here). Since AZ77, ICRU49 and J82 follow the data better, they appear high in this plot around 40 keV. The ICRU49 curve follows AZ77 at low energy but merges into BP82 above 0.3 MeV.

TABLE 7.13. RATIOS OF FITTED CURVES FOR THE STOPPING OF PROTONS IN KEY SUBSTANCES, NEAR THE MAXIMUM.
NB ... no bonding correction used; B ... bonding correction used.

		Z90		AZ77	J82	ICRU49	PSS
		NB	*B*				
Gases:							
H_2	40 keV	0.956	1	1.452	1.471	1.452	
N_2	40 keV	1.001	1	1.124	1.171	1.124	
O_2	40 keV	0.997	1	1.031	1.070	1.031	
Ar	40 keV			1	1.020	1.000	
H_2O	40 keV	1				1.110	
CO_2	40 keV				1	0.983	
Air	40 keV	1			1.160	1.115	
CH_4	40 keV	0.923	1		1.236	1.219	
C_3H_8	40 keV	0.937	1		1.211	1.121	
Solids:							
C (am.)	40 keV	1		1.098	1.080	0.994	
C (graph.)	40 keV	0.941	1	1.033	1.017	1.012	
Mg	100 keV	1		1.120	0.84		
Al	60 keV	1		0.997	0.948	0.997	1.023
Si	20 keV	1		0.996	1.097	1.156	
P	30 keV	1		0.747	1.149		
Ca	60 keV	1		1.223	1.391		
Fe	60 keV	1		0.839	0.811	0.836	
LiF	60 keV	1			1.357	1.063	
CaF_2	60 keV				1	0.791	
Al_2O_3	30 keV	1			0.987	0.785	
Lucite*)	40 keV	0.983	1		1.180	1.123	
Polyethylene	40 keV	0.947	1		1.193	1.051	
Nylon	40 keV	0.968	1		1.179	1.131	
Liquids:							
H_2O	40 keV	1.098	1		1.367	1.077	
Toluene	40 keV	0.926	1			1.052	

*) Lucite = Plexiglas = Perspex = Polymethyl methacrylate (see ICRU37)

Table 7.13 summarizes the differences between the various fits in the low energy region. The curves are compared at a single energy value (near the maximum) where the discrepancies are fairly big. This table may be used to estimate the accuracy of the fits (see also Sect. 7.3.1.5); it also shows which fits are available for the key substances.

Concerning gases, one can see that the various fits agree within a few percent (except for Z90). Evidently, measurements on gases using protons are less prone to erroneous results than measurements on solids (compare, e.g., Figs. 7.15 and 7.16). Clearly, the low Z90 values for H_2 and N_2 carry over into low values for air, water and organic gases; the bonding correction is too small to compensate for this effect. For methane, e.g., ICRU49 shows that its curve agrees with experimental data down to T_r = 20 keV within 5%; this is in contrast to the 20% deviation of Z90 (table 7.13).

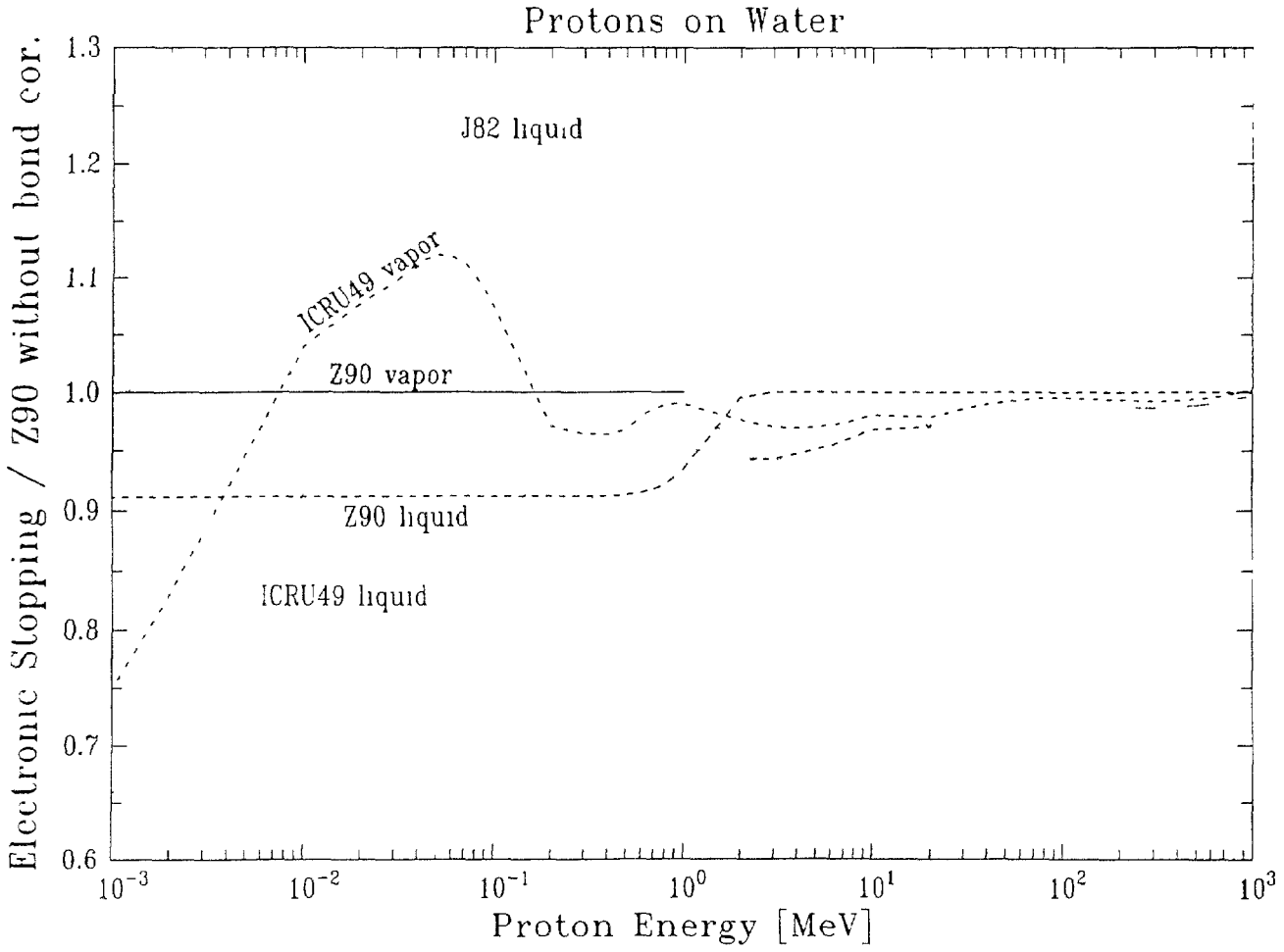

Fig.7.19. Electronic stopping power of water (liquid or vapor) for protons from various publications, divided by values from Z90 (without bonding correction). The -·- curve is from SUG89 (for liquid).

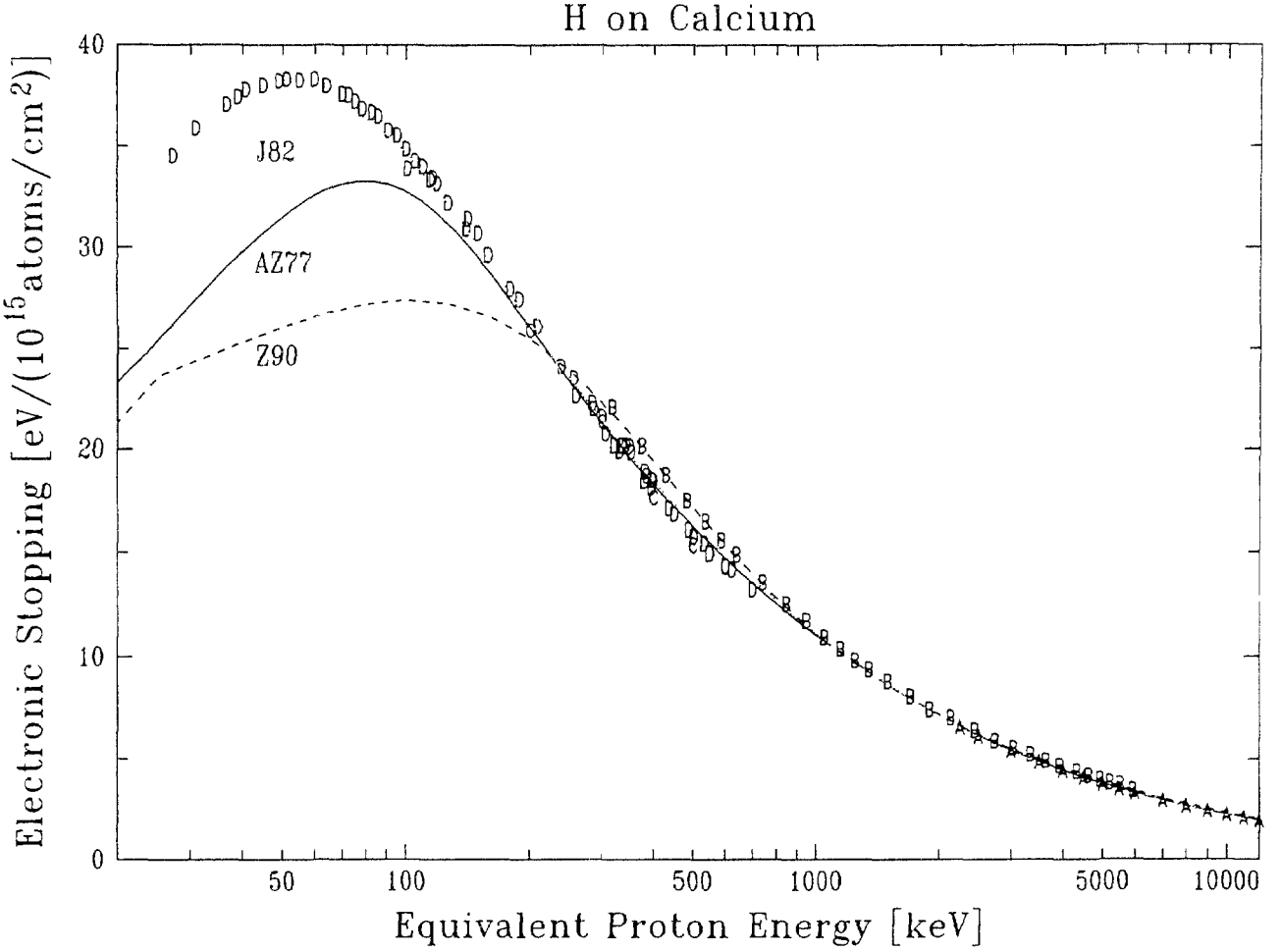

Fig.7.20. Electronic stopping cross section of calcium for H ions. The curves correspond to the following references:—— AZ77; --- Z90; ..... J82. The symbols indicate measured points from the following references: A An68; B Go67; C Bd56; D Ep93.

Fig. 7.19 shows the various stopping power curves for water normalized by the Z90 curve for water vapor. Comparison with experimental data (Ph53, Rn53, Mi90) shows that the ICRU49 curve for vapor follows the data for vapor rather well, whereas the Z90 curve is too low, as expected.

Concerning solids, table 7.13 shows that the differences between the various fits are generally as large as 20 - 40% at these low energies. Al is an exception: here all the fits (except for J82) agree quite well [103]. The discrepancies for Mg and P are not surprising, since here no experimental data are available at all, but the discrepancies are even larger in the case of Ca, where some data do exist (see fig. 7.20). The recent measurements by Eppacher and Semrad (Ep93) show that the stopping maximum of Ca is higher even than the highest fit curve (J82). The rather large difference between ICRU49 and AZ77 for Si is due to the fact that ICRU49 has taken new measurements into account.

Carbon is a special case since there are indications that the stopping powers of graphite and evaporated amorphous carbon are different (see ICRU49). Fig. 7.21 shows that indeed, both ICRU49 and Z90 give higher stopping powers for graphite than for amorphous carbon. Actually, one might expect the reverse effect since the experimental plasma energy [112] is slightly higher for graphite than for evaporated carbon. Indeed, Necas et al [113] have recently found the stopping power of graphite a few percent smaller than that of amorphous carbon for hydrogen ions below 50 keV/u (see Fig. 7.21). The computer program PSTAR, described in the Appendix, produces stopping powers for graphite that take into account the amorphous-carbon/graphite stopping power ratios measured by Necas et al. It should be noted that there are many more measurements for amorphous C than for graphite, hence the fits by AZ77 and by J82 may be assumed to refer to amorphous C, even though J82 calls it "graphite". The steep descent in Fig. 7.21 at low energy is due to the unrealistic energy dependence of Z90 (see Fig. 7.15 above).

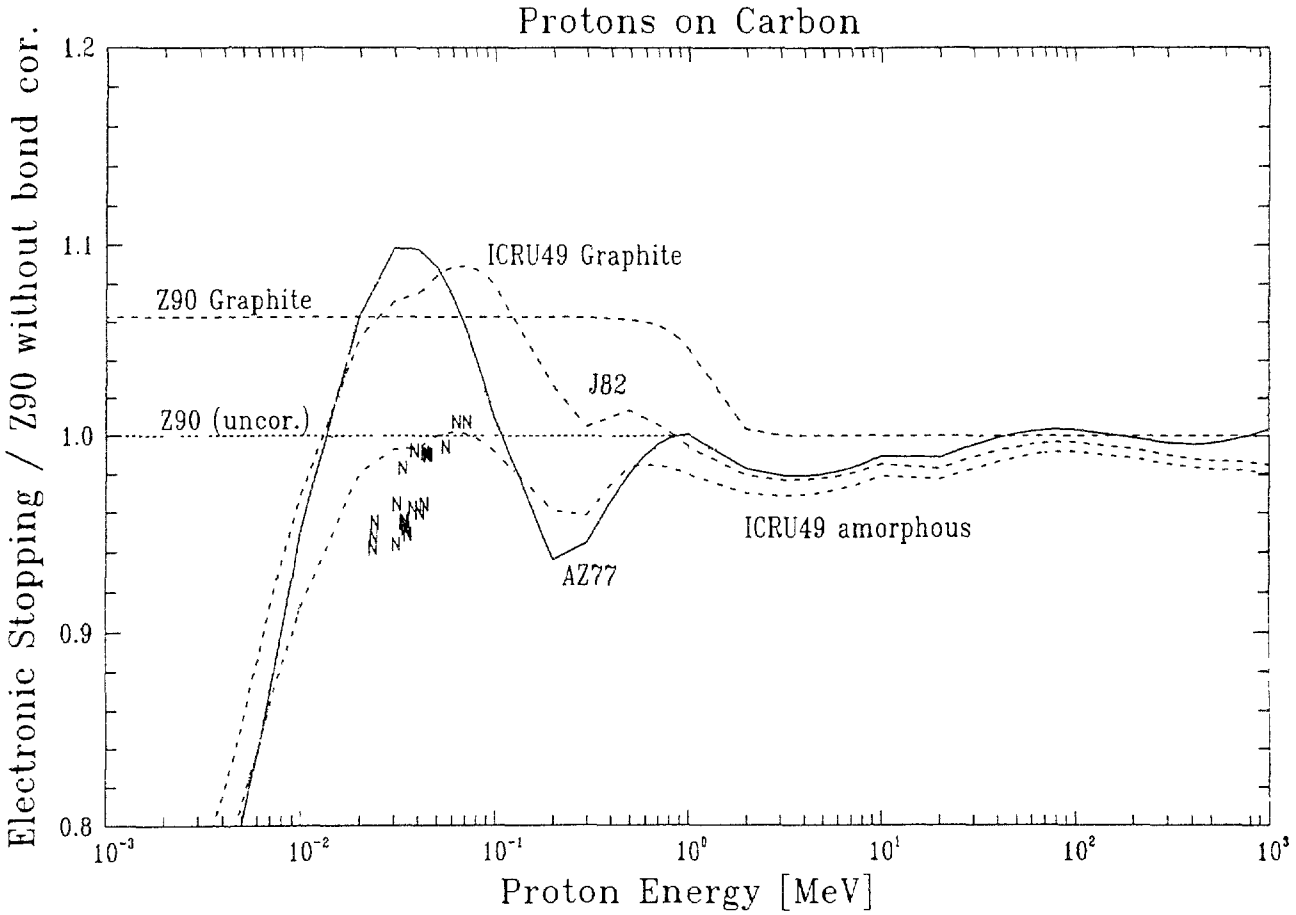

Fig.7.21. Electronic stopping power of carbon (amorphous or graphite) for protons from various publications, divided by values from Z90 (without bonding correction). N: experimental values for the ratio $S_{graphite}/S_{amorphous}$ *due to Necas et al [113].*

TABLE 7.14. RATIOS OF FITTED CURVES FOR THE STOPPING OF PROTONS IN KEY SUBSTANCES, AT 1 MEV.
NB ... no bonding correction used; B ... bonding correction used.

		T90		AZ77	J82	ICRU49/BEST	PSS
		NB	*B*				
Gases:	H_2	0.967	1	0.984	0.954	0.974	
	N_2	1.001	1	1.019	0.965	1.020	
	O_2	0.996	1	0.992	0.936	0.998	
	Ar			1	0.992	1.005	
	H_2O	1				0.989	
	CO_2				1	1.065	
	Air	1			0.963	1.022	
	CH_4	0.942	1		0.933	0.956	
	C_3H_8	0.953	1		0.944	0.968	
Solids:	C (am.)	1		1.001	0.994	0.980	
	C (graph.)	0.956	1			0.951	
	Mg	1		0.968	0.940	0.958	
	Al	1		1.012	0.987	0.988	0.989
	Si	1		1.003	0.967	0.988	
	P	1		0.992	0.996	1.002	
	Ca	1		0.993	1.001	1.036	
	Fe	1		0.981	0.980	0.983	
	LiF	1			0.964	0.981	
	CaF_2				1	0.988	
	Al_2O_3	1			0.962	0.945	
	Lucite	0.988	1		0.966	0.955	
	Polyethylene	0.960	1		0.952	0.944	
	Nylon	0.976	1		0.953	0.968	
Liquids:	H_2O	1.070	1		1.019	1.045	
	Benzene	0.941	1			0.937	
	Cyclohexane	0.960	1			0.948	
	n-Pentane	0.955	1			0.944	
	Toluene	0.945	1			0.938	
	Xylene	0.947	1			0.939	

Concerning solid compounds, it should be noted that J82 uses Bragg's rule, whereas ICRU49 takes deviations from this rule into account. Hence the ICRU49 values are always smaller than J82 (indicating that electrons in the compound are more tightly bound). In the case of Al_2O_3, e.g., ICRU49 has taken the measured values due to Bauer et al [114,104] into account. Here again, the low Z90 values for hydrogen lead to low Z90 values for lucite, polyethylene and nylon.

Concerning liquids, very little information is available at low energies, because of experimental difficulties. Fig. 7.19 shows that Z90 and ICRU49 agree in predicting a stopping power for liquid water about 10% lower than that for vapor, at low energy (as expected from Sec. 7.3.1.3). Using the common assumption that the stopping powers of liquid and solid water are the same, this difference agrees with that found experimentally by Bauer et al (Mi90). Sugiyama [115] has suggested a slightly smaller difference (4%). Above 0.5 MeV, the difference between the two curves by ICRU49 is due to the difference in I-values (as given, e.g., in ICRU37; see also table 7.3). For more water stopping powers, see also fig. 7.44.

Table 7.14 shows the differences between the various fits for 1 MeV. Here, the agreement (and hence the expected accuracy) is much better: the discrepancies amount only to a few percent.

The tissue substitute A-150 TE plastic is not shown in tables 7.13 and 7.14 since it is only given in ICRU49 and hence cannot be compared to other tables. A precise measurement of the stopping power of this substance for protons of 2.5 to 7.5 MeV was carried out recently by Ishiwari et al [36]. The result agrees within 0.2% (on the average) with that obtained using Bragg's rule and the element data from AZ77; this is surprisingly good indeed. Also, if we calculate the stopping using BEST or PSTAR, the result is, on the average, only 0.5% above Ishiwari's measurements [36], and in agreement with the calculation by Thwaites [116].

Summarizing, it seems advisable to use the ICRU49 table (or program PSTAR) for best accuracy, if possible. This table contains data for most of the key substances, and for many additional substances of interest to dosimetry. In this table, compounds are treated using either directly experimental data, if available, or else Bragg's rule (eq. 7.14); mixtures are treated by applying Bragg's rule to molecular and/or atomic constituents. Above 1 MeV, program BEST can also be used instead. Program

Z90 is convenient in that its stopping subroutine RSTOP can be included in other main programs, but it appears less reliable at least for compounds containing hydrogen. J82 is inconvenient in that it exists only in the form of printed tables; below 1 MeV, it can be replaced by the fit function due to Eppacher and Semrad [117]. J82 has the advantage of containing all elements; for compounds it has the disadvantage of neglecting chemical effects.

TABLE 7.15. FRACTION OF THE (NORMALIZED) DOSE D AT DEPTH X THAT IS CONTRIBUTED BY PROTONS WHOSE ENERGY IS SMALLER THAN T_c.

Results pertain to a 160-MeV proton beam penetrating through a water medium. R = 17.65 cm is the CSDA range at 160 MeV. The maximum of the Bragg curve is at a depth equal to 0.99 R.

			T_c(keV)	10	20	50	100	200	500	1000
x(cm)	x/R	D					Fraction (percent)			
16.94	0.960	0.606		0.0	0.0	0.0	0.0	0.0	0.0	0.0
17.03	0.965	0.650		0.0	0.0	0.0	0.0	0.0	0.0	0.1
17.12	0.970	0.707		0.0	0.0	0.0	0.0	0.0	0.1	0.2
17.21	0.975	0.782		0.0	0.0	0.0	0.1	0.1	0.3	0.6
17.30	0.980	0.872		0.0	0.0	0.1	0.1	0.3	0.6	1.3
17.39	0.985	0.958		0.0	0.0	0.1	0.2	0.5	1.2	2.4
17.47	0.990	1.000		0.0	0.1	0.2	0.4	0.8	1.9	3.9
17.56	0.995	0.953		0.1	0.1	0.3	0.6	1.1	2.8	5.5
17.65	1.000	0.802		0.1	0.1	0.4	0.7	1.5	3.6	7.3
17.74	1.005	0.572		0.1	0.2	0.4	0.9	1.8	4.5	9.0
17.83	1.010	0.341		0.1	0.2	0.5	1.1	2.1	5.3	10.6
17.91	1.015	0.165		0.1	0.2	0.6	1.2	2.5	6.2	12.4
18.00	1.020	0.065		0.1	0.3	0.7	1.4	2.9	7.1	14.2
18.09	1.025	0.020		0.2	0.3	0.9	1.7	3.4	8.1	15.9
18.18	1.030	0.005		0.2	0.4	1.0	1.9	3.8	9.3	17.9
18.27	1.035	0.001		0.3	0.6	1.5	2.9	5.2	10.5	19.4

7.3.1.5. The influence of stopping power uncertainties upon problems in dosimetry.

The tables of proton stopping powers in ICRU49 are estimated to have the following uncertainties: at energies of a few MeV or higher, 1 to 2 percent for elements, and 1 to 4 percent for compounds; at 1000 keV, 2 to 5 percent; at 100 keV, 5 to 10 percent; at 10 keV, 10 to 15 percent; and at 1 keV, at least 20 to 30 percent (see also Tables 7.13 and 7.14).

In many applications in conventional dosimetry, the proton stopping powers at high energies (with their relatively small uncertainties) are all that matters, because low-energy protons play only small role. A case in point is the depth-dose distribution in a water phantom irradiated with a high-energy proton beam used for therapy. The proton spectra from such beams, as functions of depth, have been calculated [118], and can be used to estimate the relative contributions to the absorbed dose from protons with different energies. The results of such a calculation for a 160-MeV proton beam are shown in Table 7.15. This table shows the fraction of the absorbed dose at various depths that is contributed by protons whose energies are less than 10, 20, ... 1000 keV. It can be seen that for depths up to 96% of the cdsa range, there is no contribution at all from protons with energies below 1000 keV. With increasing depth, near and beyond the Bragg peak, contributions from protons with lower energies appear, but remain small.

Another example pertains to neutron irradiation, namely, protons set in motion in elastic collisions. The proton spectrum is approximately uniform, and extends up to the neutron energy T_n. Let ϕ_c denote the fraction of the proton energy that is imparted to the medium by protons with energy smaller than T_c. It can be shown that this fraction is

$$\phi_c = \frac{\frac{1}{T_n}\cdot\int_0^{T_c} T\,dT + \frac{T_c}{T_n}\cdot\int_{T_c}^{T_n} dT}{\frac{1}{T_n}\cdot\int_0^{T_n} T\,dT} = \frac{T_c}{T_n}\left(2 - \frac{T_c}{T_n}\right). \qquad (7.15)$$

For example, for a neutron energy T_n = 14 MeV, ϕ_c is 13.4%, 1.4%, 0.14% or 0.014% for T_c = 1000 keV, 100 keV, 10 keV or 1 keV, respectively. For T_n = 1 MeV, ϕ_c is 19.0%, 2.0% or 0.2% at 100 keV, 10 keV or 1 keV, respectively.

The need for proton stopping powers at low energies, where the uncertainties are large, may, however, arise in the modeling of radiation effects on small biological structures, at the cellular or sub-cellular level. Even for such applications the energy degradation process takes place largely via secondary electrons. However, if one is concerned with the penetration of protons through very small targets, one must know the stopping powers down to energies where the residual range is smaller, perhaps by an order of magnitude, than the dimension of the target. In this connection, it should be noted that the residual proton range in water is 10 μm at 553 keV, 1 μm at 62 keV, 100 nm at 3.4 keV, and 10 nm at 380 eV.

7.3.2. Nuclear Stopping Power

Many of the tables and programs mentioned in table 7.10 also give results on nuclear stopping. This is in general quite small compared to electronic stopping. In the worst case (hydrogen projectiles on hydrogen target) it amounts to 30% at T_r = 1 keV, to 1.7% at 10 keV (see ICRU49). Actually these values are upper limits, since they include elastic scattering through *all* angles. If the energy loss of a *beam* of protons is considered, then a large angle scattering would usually remove the proton from the beam, so this proton would not contribute to the energy loss measured. This effect can be calculated using the TRIM program; a few examples have been calculated by ICRU49; see also Sec. 7.4.2.

7.3.3. Energy Loss Straggling. TRIM Programs.

Since charged particles lose their energy statistically in many small amounts, their energy after penetrating a certain amount of material is a stochastic quantity, described by its average, by its variance Ω^2 (see Sec. 7.1) and possibly by higher moments. Straggling of energetic H and He ions has been reviewed by Besenbacher et al [118a], and a general review of the statistics of charged particle penetration has been presented recently by P. Sigmund [119].

If the target is thick enough so that individual contributions W to the energy loss are small compared to the straggling, i.e., if [126]

$$3\, W_m < \Omega, \qquad (7.16)$$

but if it is thin enough so that the energy loss in the target is negligible, the energy distribution of transmitted projectiles is expected to be Gaussian [118a]. If, in addition, one assumes the target electrons to be free and initially at rest, then the variance Ω^2 of the energy distribution is given by Bohr's simple energy-independent expression [2]

$$\Omega_B^2 = 4\pi\, r_e^2\, (m_e c^2)^2\, Z_1^2\, Z_2\, n\, s = (2.6056\times10^{-13} eV^2 cm^2/atom)\, Z_1^2\, Z_2\, n\, s. \tag{7.17}$$

Here,

$$W_m = \frac{4\, m_e}{M_1 u}\, T = 2 m_e v_1^2 \tag{7.18}$$

is the maximum possible energy transfer to a free electron (for a non-relativistic projectile), and r_e is the classical electron radius.

Various refinements of the Bohr expression (7.17) are discussed in [118a]; they take into account that the target electrons are not initially at rest and that they are spatially correlated. The effect of electron binding has been discussed by Bichsel [120a]. The Bohr expression presupposes that the projectile energy remains constant throughout the target; in practice, it is valid up to a 20% loss of the initial energy [121].

It is difficult to obtain agreement between theoretical and experimental results for straggling in solids, since effects like crystal structure and non-uniform film thickness can influence the measurements in a way that is hard to control. For gaseous targets, however, these problems do not arise, and very careful measurements in 13 different gases and comparisons with theories have therefore been carried out by Besenbacher et al [120]. At first these authors checked if their measurements yield an energy variance Ω^2 proportional to target density. Fig. 7.22 shows that this is indeed true for 600 keV He ions penetrating nitrogen. According to the conditions mentioned above, Bohr straggling should be valid from 0.04 to 0.7 μm, i.e., over most of the thickness shown. Actually, the experimental results exceed the Bohr straggling (because of the intra-molecular correlation of the target electrons).

It is instructive to compare these results to calculations performed using the program for "TRansport of Ions through Matter" (TRIM) mentioned

already above. This Monte Carlo program, originally written by J.P.Biersack [122] and described in ZBL85, has since been updated many times by Ziegler. It calculates every single nuclear collision (leading to deflection and energy loss), but treats the much more numerous collisions with target electrons only in a global way: between any two nuclear collisions, it adds to the csda energy loss a stochastic contribution that corresponds to straggling.[5] TRIM90 (and its successors TRIM91, TRIM92) computes particle penetration in 3 dimensions and draws instructive pictures of all relevant processes on the screen. Another version of TRIM ("T2D"), available from J.P.Biersack, calculates penetration in 2 dimensions; it is faster but does not draw pictures. Both versions use the same stopping powers (Z90) below 10 MeV/nucleon. Above this specific energy, the T2D stopping is the original one from ZBL85 and hence inaccurate.

TRIM results are also shown in Fig.7.22. Except at small thickness,[5] T2D agrees with the Bohr straggling as it should. The TRIM90 result is consistently lower, possibly due to a different choice of the free flight path[5]. (Note that for comparing with Bohr straggling, we exclude those rare large-angle scattering events from the statistical analysis whose

---

[5] Note that the TRIM programs contain a statement forbidding an energy *increase* between two nuclear collisions. This makes the straggling too small for small flight paths (where Ω may exceed the energy loss), and it makes the straggling too small also for the entire target, if the free flight path is chosen too small (the flight path can be chosen by the user in T2D). This difficulty can be remedied in T2D by removing the statement that forbids an energy increase. In TRIM92, the difficulty is enhanced by the fact that the flight path within a layer is decreased toward the layer edge until it reaches a monolayer thickness (in order to avoid unphysical peaks or dips near an edge), *and* by the fact that straggling is artificially kept below 20% of the csda energy loss (J. Ziegler, pers. comm.). Hence, the TRIM92 straggling is even lower than that of TRIM90 (see Fig. 7.23).

In TRIM91 and TRIM92, the straggling is linearly reduced below the Bohr straggling for energies below the stopping power peak. This is a reasonable approximation (see, e.g., Fig. 7.25 below).

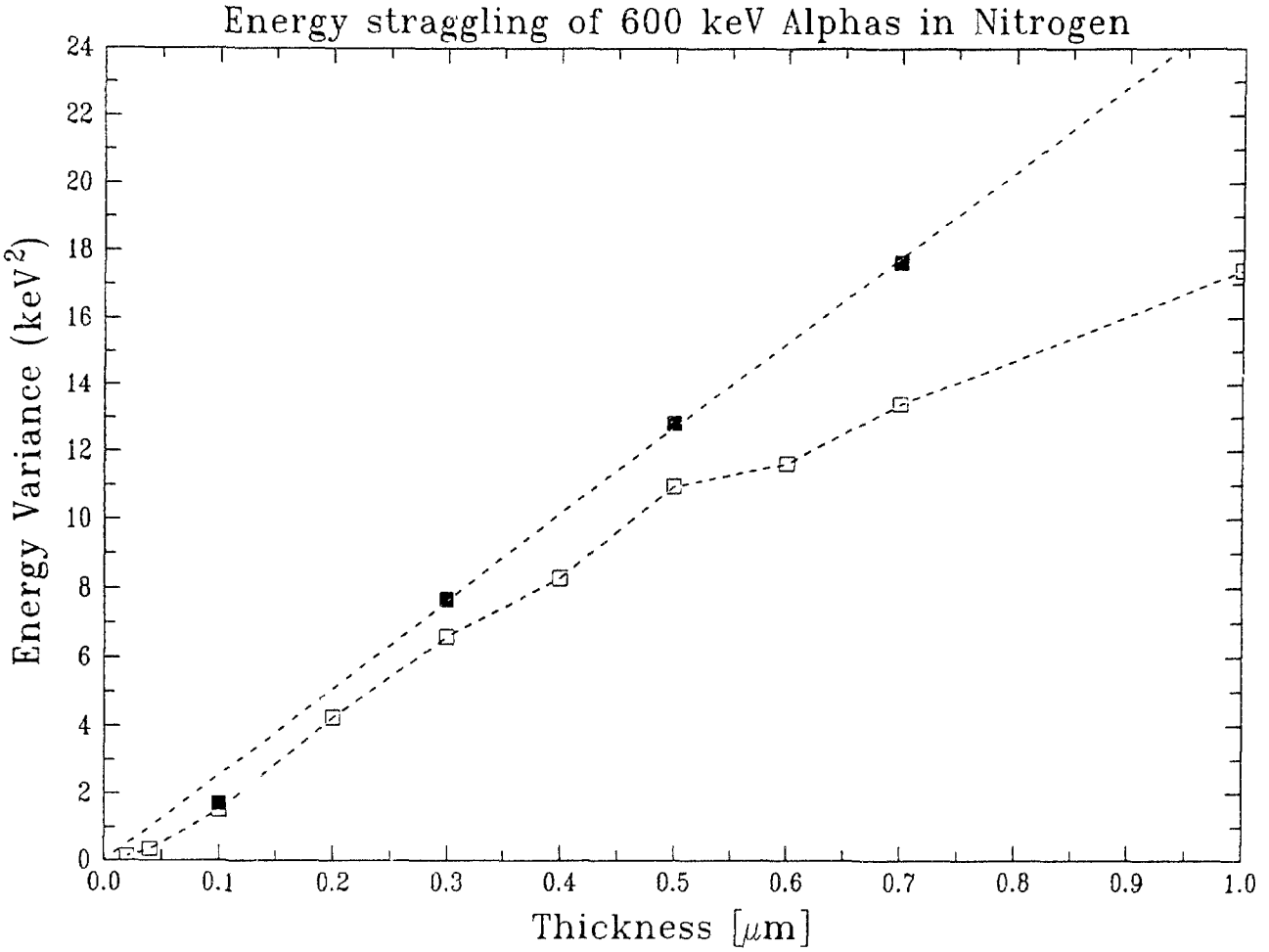

Fig.7.22. Energy straggling of 600 keV alphas penetrating nitrogen. The energy variance is plotted versus the target thickness, assuming a hypothetical density of 0.8096 g/cm^3, so that 1µm ⇔ 3.482x10^{18} atoms/cm^2. Experimental results due to Besenbacher (···) and the Bohr prediction (-·-) according to eq. (7.17) are indicated by lines. TRIM results are indicated by open squares (TRIM90, TRIM91) and full squares (T2D), resp.

energy is clearly outside the Gaussian distribution of transmitted energies)[6].

Figures 7.24 to 7.26 show the energy straggling of protons in Ar, N_2 and H_2, as examples taken from [120]. In Ar (Fig. 7.24), the straggling is

---

[6] The program TRIM90 produces an output file TRANSMIT.TXT that contains the final energy and angle of every transmitted projectile. This file can be analyzed using program TRANSMIT.BAS (also on the TRIM90 disc) that calculates energy and angular straggling and produces a histogram of final angles. We have added a section that produces a histogram of final energies also.

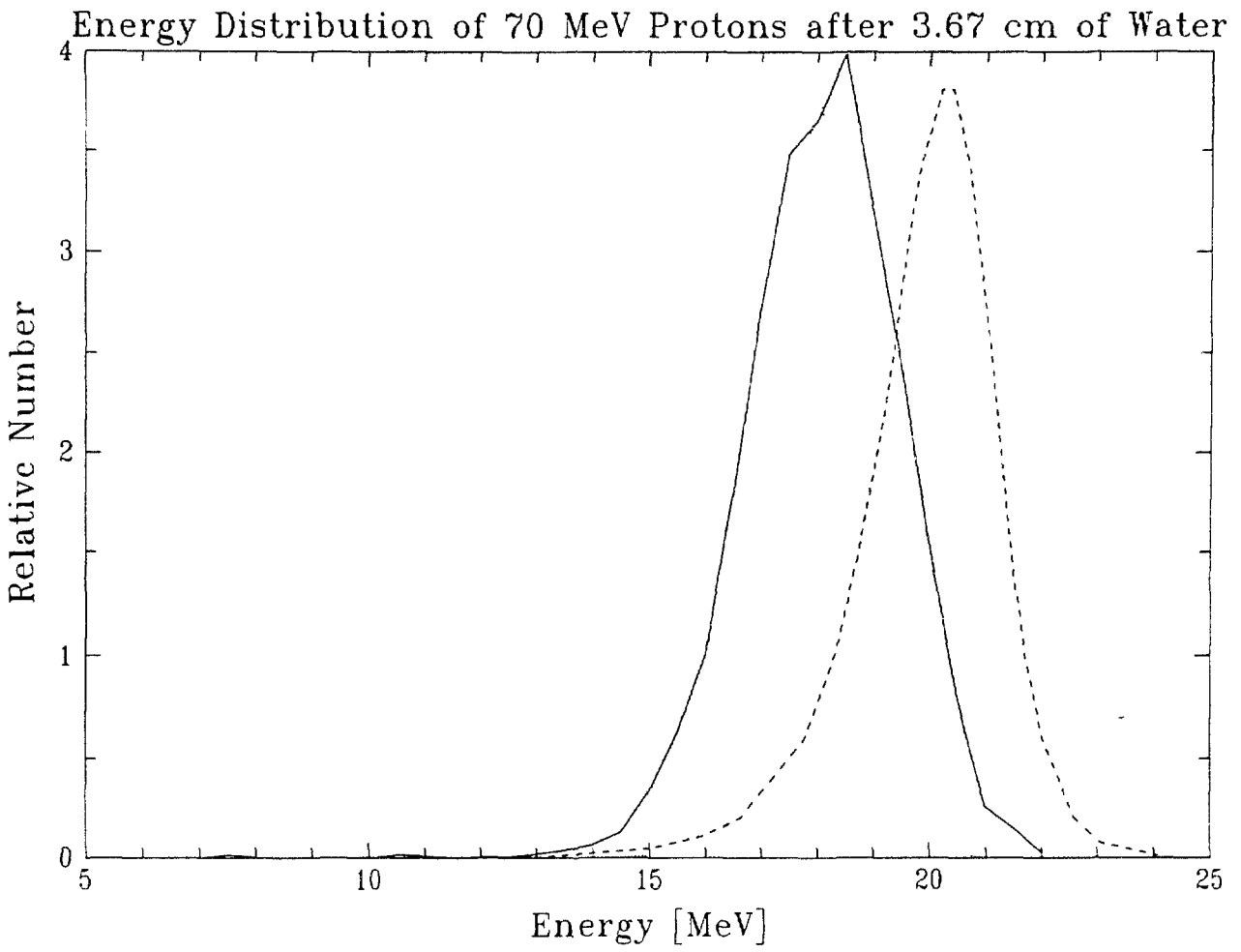

Fig.7.23. Energy distribution of 70 MeV protons after passing 3.67 cm of water (ρ = 0.997 gcm^{-3}), as calculated by Bichsel and Hiraoka [130] (dashed), and by use of TRIM90 (full curve) or TRIM92 (dotted curve). The csda range of these protons is 4.08 gcm^{-2} (ICRU49, Bichsel); the mean projected range 4.075 gcm^{-2} (ICRU49), but only 4.00 gcm^{-2} according to TRIM90. The TRIM92 curve is too narrow (see text).

slightly below the Bohr value. This can be understood by treating the atomic electron density realistically [123] and by adding a straggling term due to intra-atomic electron correlation [120]. The result for N_2 (Fig. 7.2,) can be understood by including, in addition, intra-molecular correlations. The straggling in H_2 (Fig. 7.26) is explained down to 80 keV using Fano's [11] asymptotic perturbation formula which treats the target electron speeds as not negligible compared to the projectile speed.

To see how well these measurements can be reproduced by TRIM, we consider 500 keV protons on nitrogen, at a thickness corresponding to

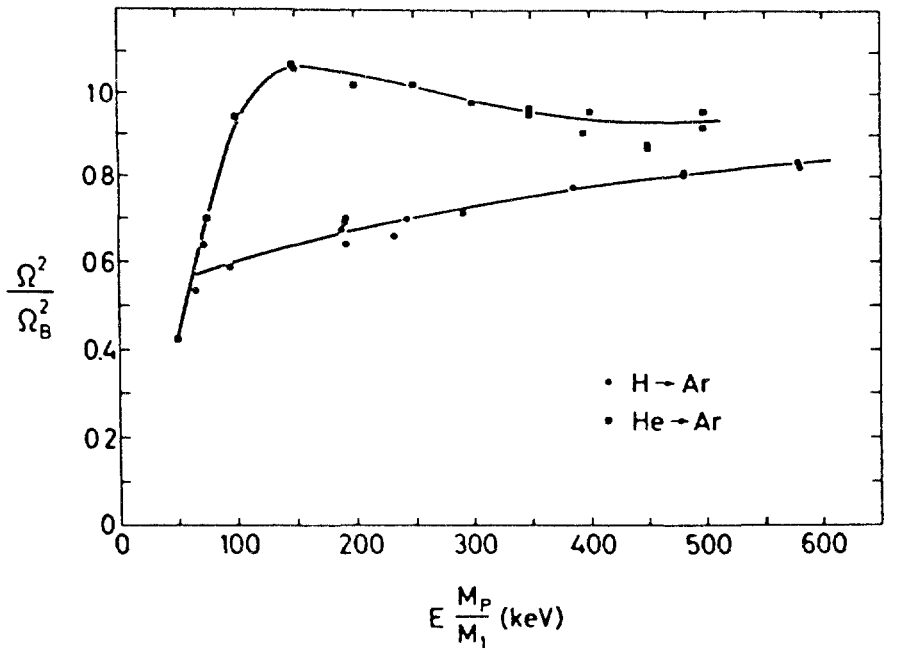

Fig.7.24 Energy straggling variance [120] of H and He ions in Argon, divided by Bohr variance, eq. (7.17), versus equivalent proton energy.

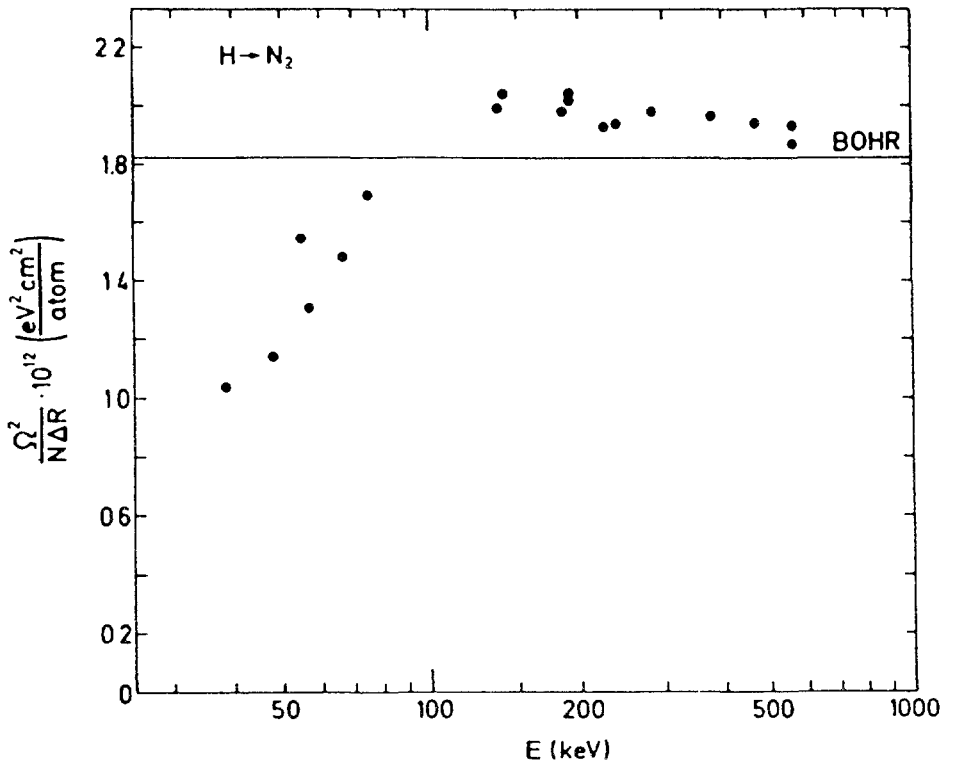

Fig.7.25 Energy straggling variance [120] of protons in nitrogen, divided by Bohr variance, eq. (7.17), versus energy.

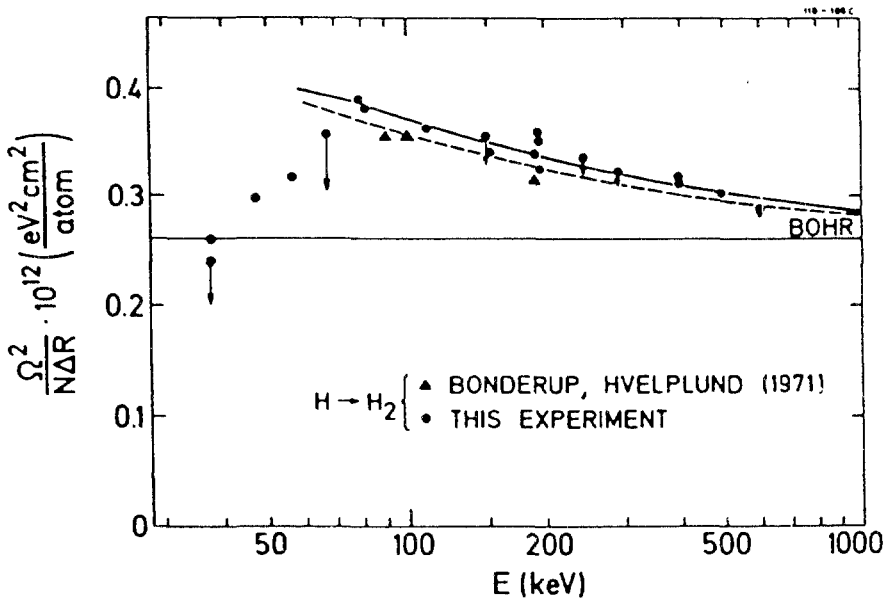

Fig.7.26 Energy straggling variance [120] of protons in hydrogen, divided by areal density, versus energy, compared to the formulas by Bohr (eq.7.17) and by Fano [11] for molecular (——) and atomic (---) targets.

6.96×10^{18} atoms per cm^2. In this case, the Bohr straggling amounts to $1.82 \times 10^{-12} eV^2 cm^2$/atom, or 12.7 keV^2 for the given thickness, and the measured value is 13.6 keV^2 (cf. Fig.7.25). Using TRIM, we obtain Ω^2 = 12.5 keV^2 (TRIM90) and 14.0 keV^2 (T2D), resp., in fair agreement. Since W_m = 1.1 keV (eq. 7), the thickness is just enough (eq. 7.16) for Bohr straggling to apply.

Using a local-electron-density model, Kaneko and Yamamura [124] have calculated the straggling for protons (and He ions) in many solid targets. They use Hartree-Fock wave functions modified to include plasma electrons, and they include collisional as well as charge-changing contributions. They find that the straggling variance is proportional to T for small T, and that it approaches the Bohr value above 1 MeV/u. Measurements by Matsunami and Kitoh [125] using 100 keV protons and He ions on C films of about 10 nm thickness and high (30 eV) resolution agree with their prediction.

For solid targets, variations of the target thickness due to surface roughness produce an important contribution to straggling. Besenbacher et al [118a] have attempted to determine this contribution by comparing the results from measurements with H, He, and Li ions. See also Sec. 7.5.3.

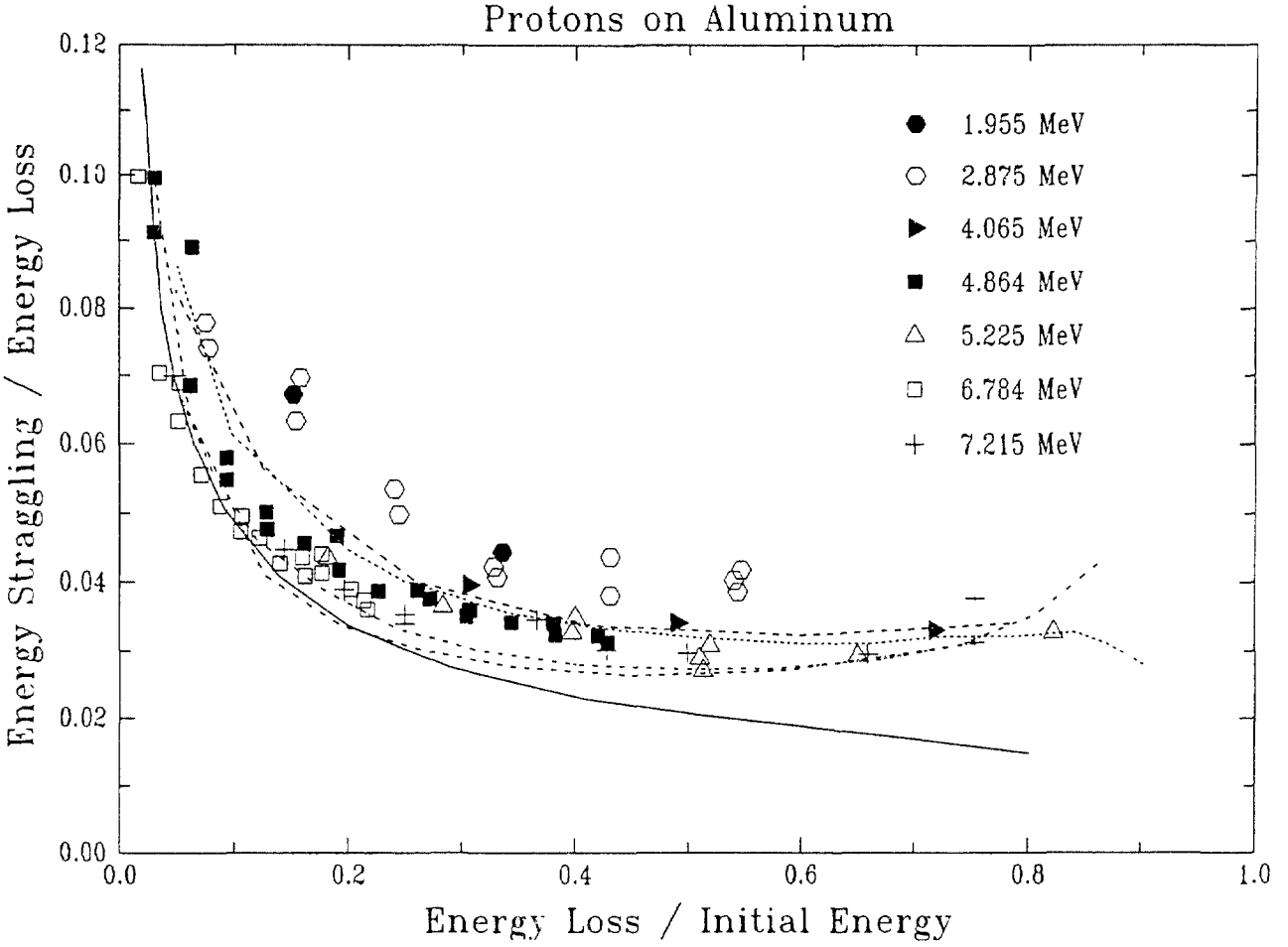

Fig.7.27 Energy straggling Ω (divided by energy loss in the foil) versus energy loss (divided by initial energy), for protons from 1.9 to 7.2 MeV in aluminium. Measurements by Bauer et al [128], indicated by symbols, are compared to the Bohr result (——), eq. (7.17), to Tschalär's [121,137] calculations (short dashed: 1.5 MeV; -·-·-: 7.6MeV), and to TRIM90 (long dashed: 2 MeV; -··-: 7.6 MeV).

For thin targets, the energy distribution of transmitted projectiles is asymetrical (see, e.g., the reviews in [119] and in ICRU49); it can be described by the Vavilov theory [126] (see Sec. 7.2.4). For very thin targets, this theory does not apply and must be replaced by other approaches (see ICRU49).

For thick targets, the Bohr theory cannot be used either. The straggling theory developed by Tschalär [121,127] can, however, be used for relative energy losses up to 80%. In fig.7.27, we compare TRIM90 calculations for 1.5 and 7.6 MeV protons on aluminum to Tschalär's calculations and to measurements by G.H.Bauer et al [128]. Although the straggling is, of course, no more energy independent, one can see in this type of representation that the *normalized* energy straggling becomes

approximately energy-independent if plotted versus the normalized energy loss. Evidently, the TRIM calculations (after excluding rare low-energy events, as above) agree well with the Tschalär results. Both calculations appear to be in fair agreement with Bauer's measurements at energies between 4 and 5.3 MeV. The results measured at energies below 3 MeV appear somewhat high; this could be partly due to non-uniformities in the target foils [cf. ICRU49]. Similar results were obtained by Armitage and Trehan [129].

As another example for a thick target, we show the energy spectrum calculated by Bichsel and Hiraoka [130] for 70 MeV protons in water. Here, the importance of the third moment (skewness) can be seen from the asymetry of the spectrum. Fig. 7.23 shows Bichsel's curve for a thickness of 3.67 cm of H_2O, calculated using the moment method by Tschalär [127] and including multiple scattering. The figure also shows the result of a Monte Carlo calculation carried out using TRIM90. The latter curve has a lower mean energy, since the Z90 stopping is slightly higher in this energy region (see Fig. 7.18), but the two curves have the same variance. A curve obtained using TRIM92 is also shown; it is much too narrow .

For a discussion of TRIM calculations of ranges and range straggling, see Sec. 7.3.5 below.

Bichsel [4] has also carefully compared measurements of Ω for high energy (>38 MeV) protons on Si with his calculations carried out by means of the convolution method; he found agreement within 1%.

7.3.4. Multiple Scattering

Multiple scattering is treated in Sec. 7.5.4, since most of the recent data refer to heavy ions. But it should be noted that Fig. 7.48 contains also data measured with H and He ions.

7.3.5. Ranges and Range Straggling

Curves for the csda range R (cf. Sec. 7.1) in all elemental targets heavier than $_3$Li are given in AZ77 (called "path length"). In addition, AZ77 show the mean projected range $\overline{R_x}$, calculated according to Schiøtt's approximation [131], and the range straggling, σ_R. They say that the results for $\overline{R_x}$ and σ_R are of limited accuracy.

Kistemaker and Sanders [132] have given a simple expression for the ratio $R/\overline{R}_x$ (based on a constant nuclear stopping power) which is a function of M_1 and M_2 only. Al-Affan [133] has used this function to convert the true stopping power to a so-called "effective stopping power" the integration of which yields the projected range, and he has produced a table of stopping powers and projected ranges in some materials of dosimetric interest (see [134] for a critical review of this work by H.H.Andersen).

The tables in ICRU49 list the "csda range" R and the "detour factor" ($= \overline{R}_x/R$). Alternatively, these values and also $\overline{R}_x$ can be calculated using program PSTAR. The Janni table (J82) separately lists the "proton range" $\overline{R}_x$, the "path length" R, the path length straggling, and, in addition, it gives the probability for the projectile to be lost from the beam due to nuclear interactions.

The computer programs TRIM89 and TRIM90 permit calculation of projected ion ranges either by the PRAL algorithm based on an analytical solution of the transport equation or by the Monte Carlo code. Both programs use the electronic stopping power and a universal scattering potential as inputs. They both give results on longitudinal and lateral straggling; in addition, TRIM90 can produce graphical range and straggling distributions (and even a distribution of deposited energy vs. depth). A newer version, TRIM91, produces generally the same results as TRIM90 (within statistics), except for the lateral straggling which has been redefined. It also calculates dimensionless measures of the higher moments of projected range, skewness and kurtosis (which appear on the screen together with the ion range distribution). Fig.7.28 (taken from ZBL85) shows graphical comparisons of experimental and calculated results for R, R_x and σ_R for Si and Ni targets. For Si at least, the agreement between experimental and calculated range is impressive. The disagreement in the straggling results is said to be due to the different straggling definition used by the experimenters.

Fig.7.29 compares the csda range R for protons on nitrogen from different tables. At 1 keV, the three curves differ by up to a factor 2; this is in part due to the different low-energy values of S (see Fig.7.18), in part due to different assumptions about the low energy integration limit. Toward higher energies, the relative differences become quite small.

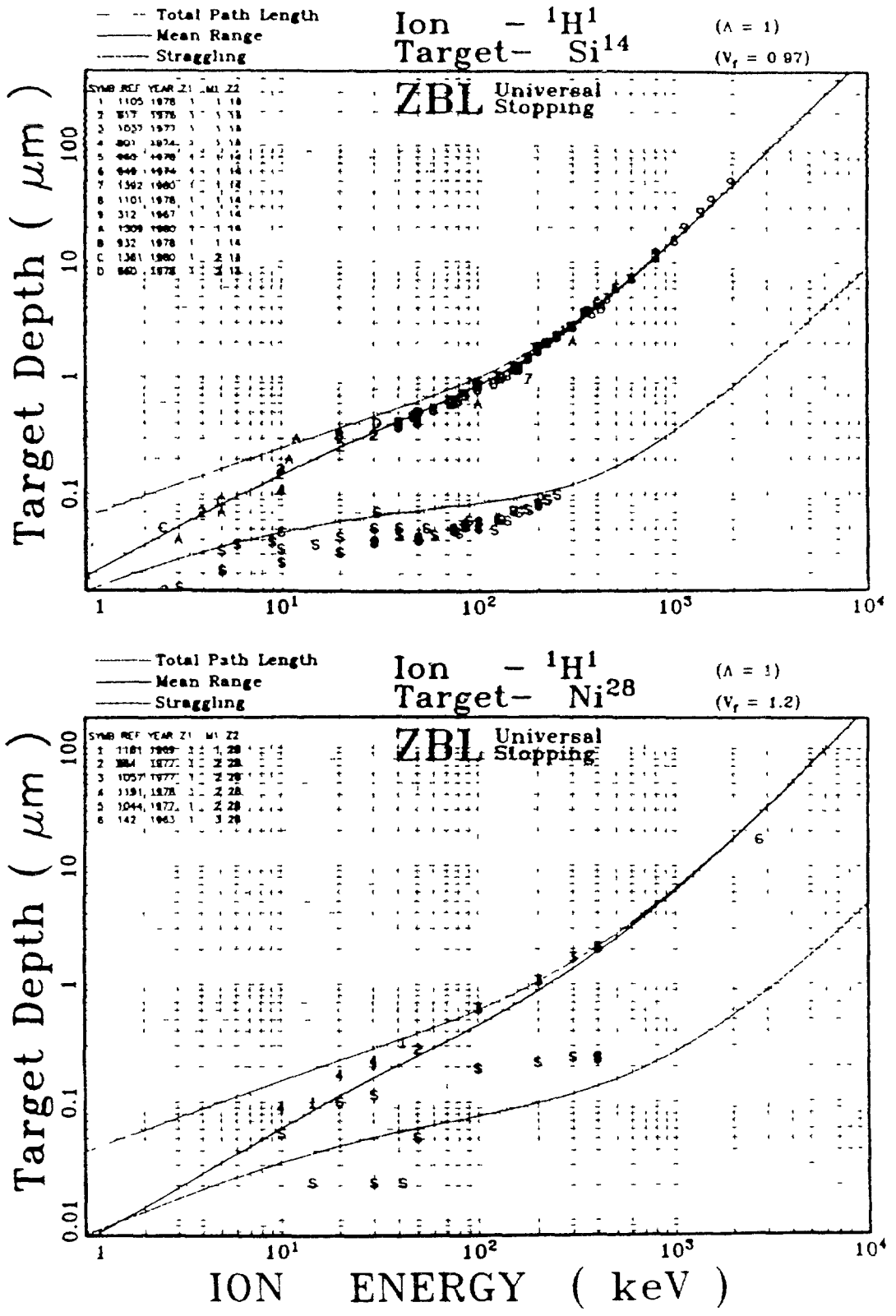

Fig.7.28 Average path length R (···), mean projected range R_x (——), and range straggling σ_R (---) for protons in Si and Ni targets, taken from ZBL85. The letter S indicates experimental straggling data, the other symbols indicate experimental data for the projected range.

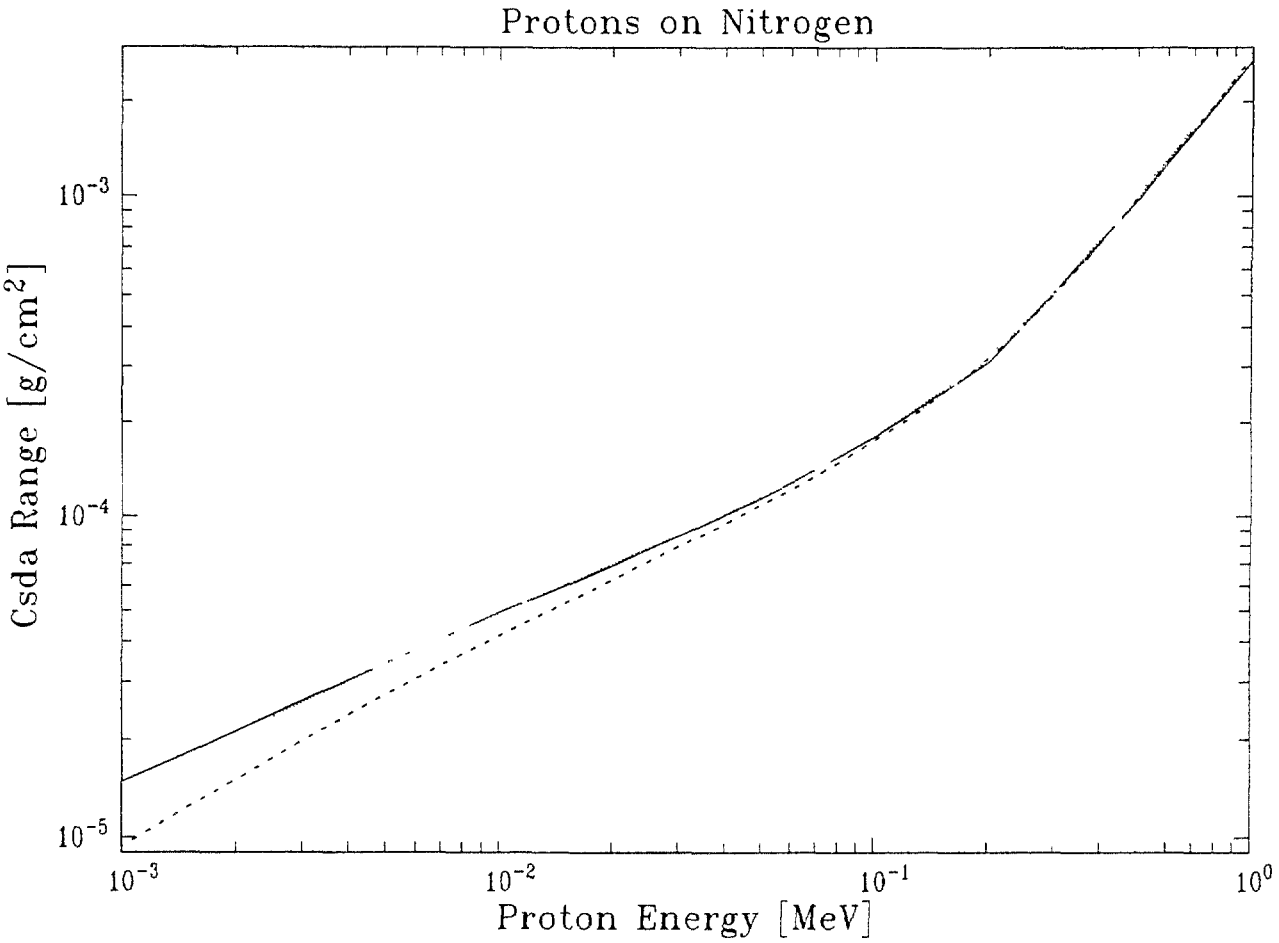

Fig.7.29 Csda range for protons on nitrogen, according to AZ77 (——), J82 (···), and ICRU49 (—··—).

Fig.7.30 shows the detour factor (= $\overline{R_x}/R$) for protons on nitrogen, taken from five different compilations. To obtain the TRIM curve, $\overline{R_x}$ was calculated using TRIM90, but the corresponding R was obtained using [135] program RBS with Z90 stopping powers. Evidently, all the calculations (except AZ77) are in pretty fair agreement with each other.

Børgesen et al [136] have measured the projected range and the range straggling of 10-30 keV deuterons implanted into various solids. Fig.7.31 shows their result for aluminum, compared to various calculations including their own (which uses the AZ77 stopping power). One can see that the range measurements agree with the TRIM90 curves within about 10%, and that the PRAL curve is slightly below the Monte Carlo result, at low energy. For the straggling width, the two Monte Carlo results agree fairly well, but the experimental result is somewhat higher. The PRAL result appears too

high. Note that Ashworth et al [137] have recently published a revised version of PRAL; they find that the first-order PRAL algorithm contained in TRIM90 is poor in predicting longitudinal and lateral straggling, due to a mathematical error.

The Børgesen results for carbon [136] (not shown here) indicate that the TRIM90 range is about 15% low due to the high stopping power (see Fig.7.15). These range measurements may be qualitatively compared to more recent measurements by Ross and Terreault [138,139] using H and D ions of energies up to 2 keV. Here, the discrepancy with the TRIM90 stopping power for carbon is even more striking. If the stopping power of carbon were proportional to $T^{0.25}$ (as assumed in TRIM90, see 7.3.1.1), the csda range would be proportional to $T^{0.75}$. Such an energy dependence is indeed found approximately by Ross and Terreault, but of course for the projected range, not for the csda range.

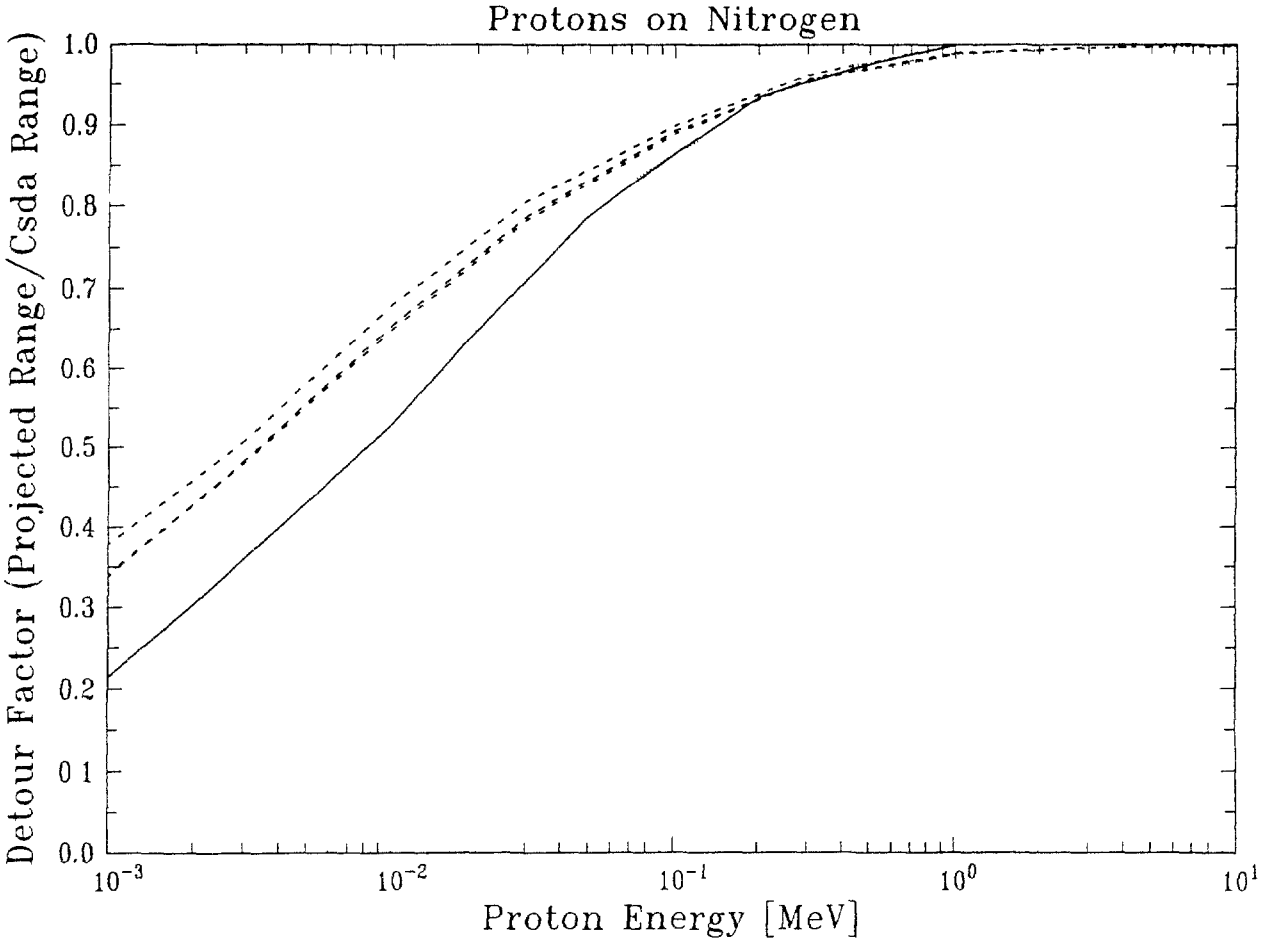

Fig.7.30 Detour factor for protons on nitrogen, according to AZ77 (——), PRAL/RBS (---), J82 (···), ICRU49 (—··—), and Al-Affan [133] (—·—)

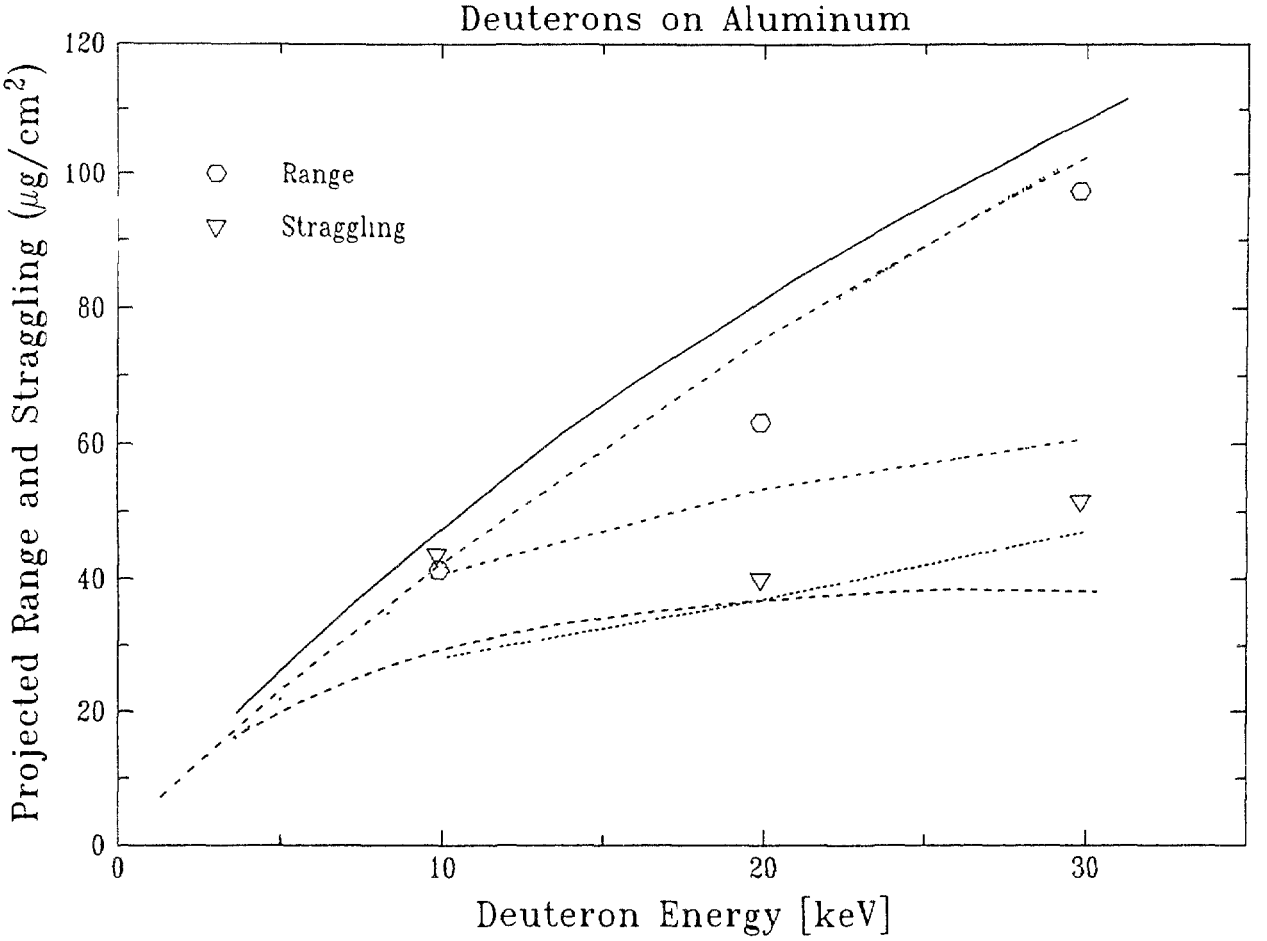

Fig.7.31 Projected range and range straggling (fwhm) of deuterons in aluminium. Measured points and two theoretical curves (full: range; long dashed: straggling) are from Bøgesen et al [136]. The remaining curves were calculated using TRIM90:

Range: Monte Carlo (- · -); PRAL (· · ·)

Straggling: Monte Carlo (short dashed); PRAL (- · · -)

For comparison with the experimental results which are given in terms of the full width at half maximum, the theoretical values σ have been multiplied by 2.35.

7.3.6. Vector Ranges

To our knowledge, no tables of the vector range $\overline{R_v}$ are available [134]. To estimate this quantity, we can calculate the longitudinal range and the "radial range" (i.e., the final perpendicular distance of the projectile from the axis of its original velocity) using TRIM90, and add them in quadrature. Taking protons on Al as an example, we find that $\overline{R_v}$ hardly differs from $\overline{R_x}$ down to about 50 keV. For 2 keV we get, e.g., a longitudinal range of 0.034 μm and a radial range of 0.023 μm, which add up to $\overline{R_v}$ = 0.041 μm. This is an upper limit, since particles that happen to have a large longitudinal range must have small radial range, and vice versa.

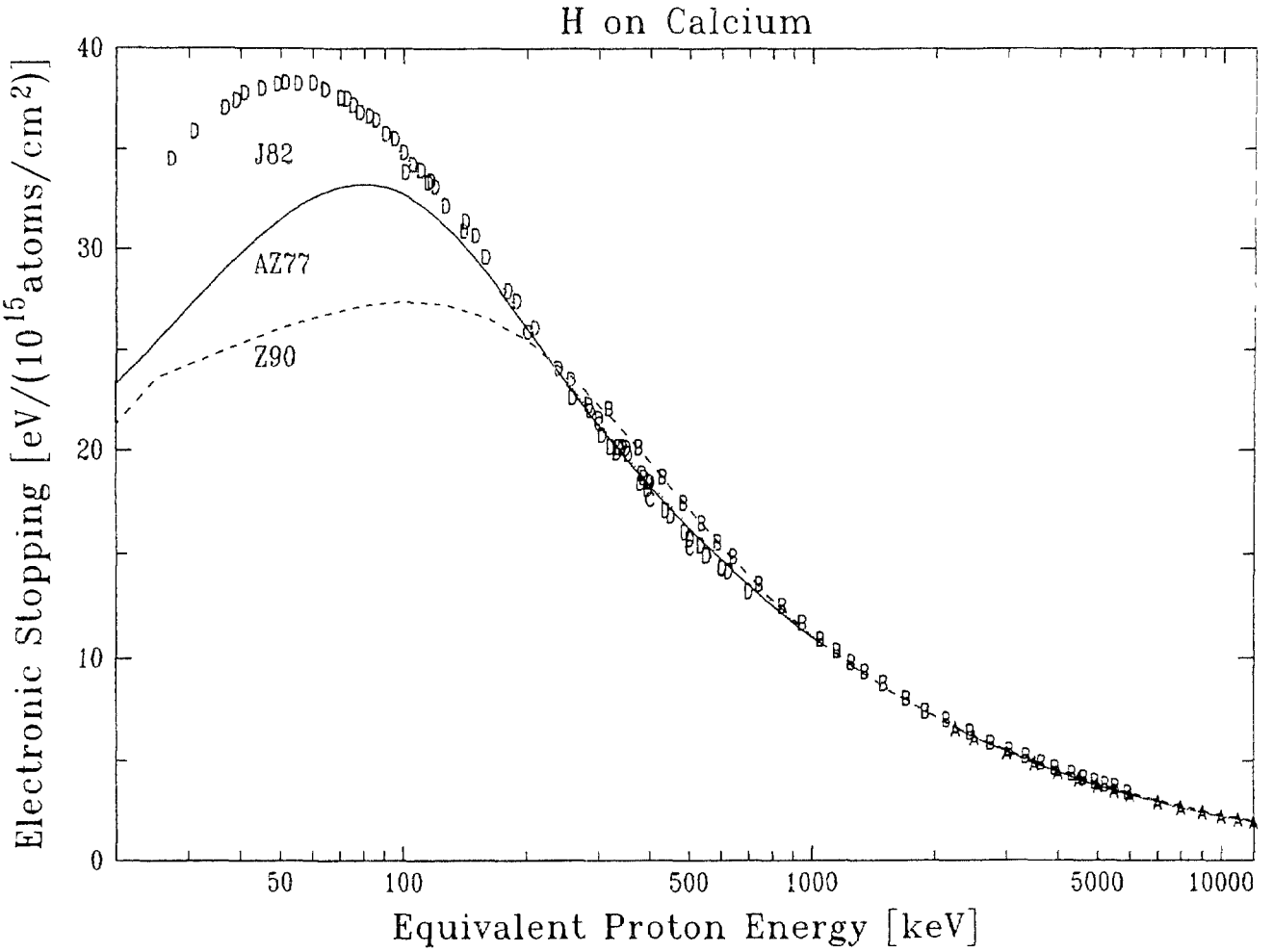

Fig.7.20. Electronic stopping cross section of calcium for H ions. The curves correspond to the following references:—— AZ77; --- Z90; ..... J82. The symbols indicate measured points from the following references: A An68; B Go67; C Bd56; D Ep93.

Fig. 7.19 shows the various stopping power curves for water normalized by the Z90 curve for water vapor. Comparison with experimental data (Ph53, Rn53, Mi90) shows that the ICRU49 curve for vapor follows the data for vapor rather well, whereas the Z90 curve is too low, as expected.

Concerning solids, table 7.13 shows that the differences between the various fits are generally as large as 20 - 40% at these low energies. Al is an exception: here all the fits (except for J82) agree quite well [103]. The discrepancies for Mg and P are not surprising, since here no experimental data are available at all, but the discrepancies are even larger in the case of Ca, where some data do exist (see fig. 7.20). The recent measurements by Eppacher and Semrad (Ep93) show that the stopping maximum of Ca is higher even than the highest fit curve (J82). The rather large difference between ICRU49 and AZ77 for Si is due to the fact that ICRU49 has taken new measurements into account.

Carbon is a special case since there are indications that the stopping powers of graphite and evaporated amorphous carbon are different (see ICRU49). Fig. 7.21 shows that indeed, both ICRU49 and Z90 give higher stopping powers for graphite than for amorphous carbon. Actually, one might expect the reverse effect since the experimental plasma energy [112] is slightly higher for graphite than for evaporated carbon. Indeed, Necas et al [113] have recently found the stopping power of graphite a few percent smaller than that of amorphous carbon for hydrogen ions below 50 keV/u (see Fig. 7.21). The computer program PSTAR, described in the Appendix, produces stopping powers for graphite that take into account the amorphous-carbon/graphite stopping power ratios measured by Necas et al. It should be noted that there are many more measurements for amorphous C than for graphite, hence the fits by AZ77 and by J82 may be assumed to refer to amorphous C, even though J82 calls it "graphite". The steep descent in Fig. 7.21 at low energy is due to the unrealistic energy dependence of Z90 (see Fig. 7.15 above).

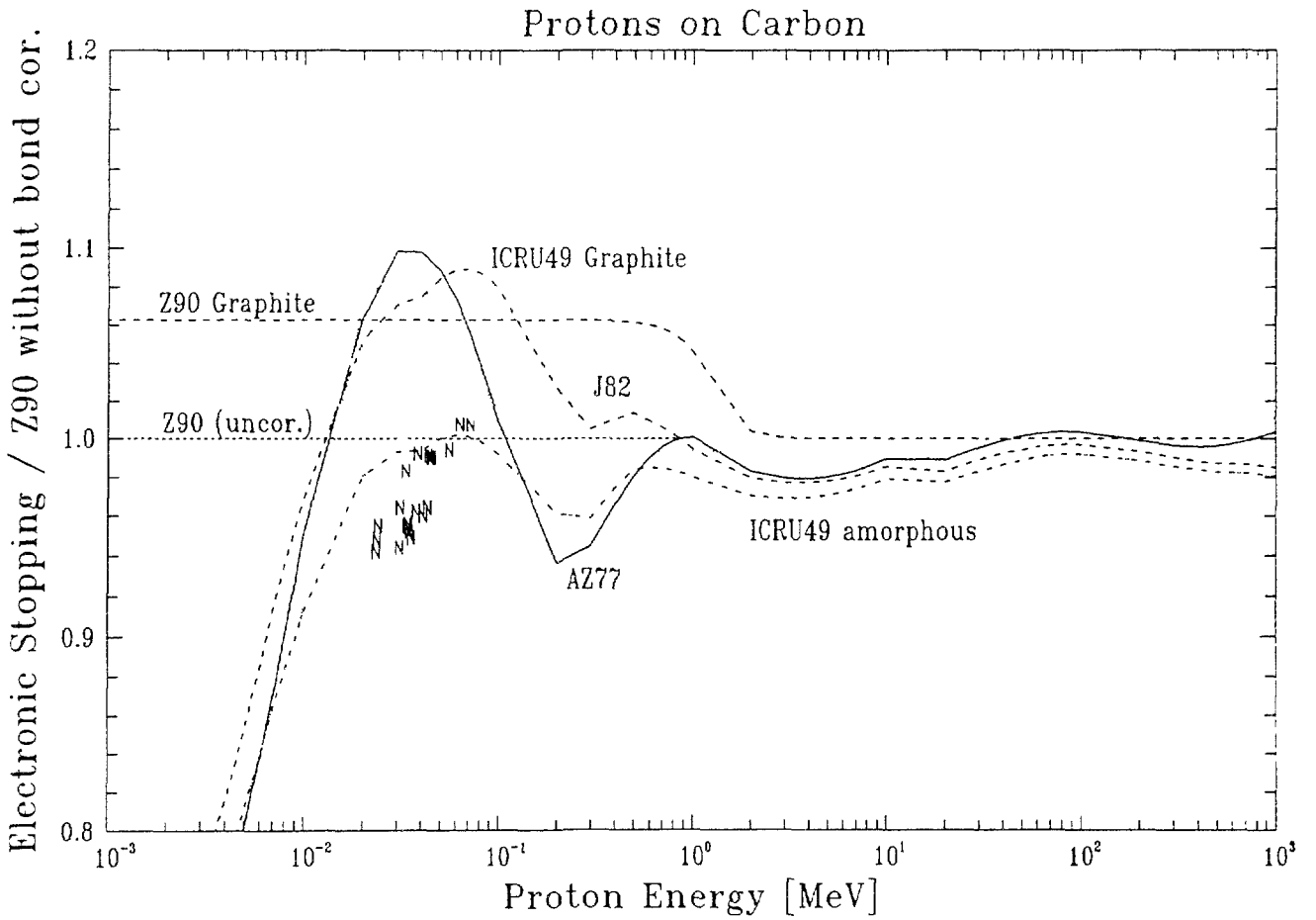

Fig.7.21. Electronic stopping power of carbon (amorphous or graphite) for protons from various publications, divided by values from Z90 (without bonding correction). N: experimental values for the ratio $S_{graphite}/S_{amorphous}$ *due to Necas et al [113].*

TABLE 7.14. RATIOS OF FITTED CURVES FOR THE STOPPING OF PROTONS IN KEY SUBSTANCES, AT 1 MEV.
NB ... no bonding correction used; B ... bonding correction used.

		T90		AZ77	J82	ICRU49/BEST	PSS
		NB	*B*				
Gases:	H_2	0.967	1	0.984	0.954	0.974	
	N_2	1.001	1	1.019	0.965	1.020	
	O_2	0.996	1	0.992	0.936	0.998	
	Ar			1	0.992	1.005	
	H_2O	1				0.989	
	CO_2				1	1.065	
	Air	1			0.963	1.022	
	CH_4	0.942	1		0.933	0.956	
	C_3H_8	0.953	1		0.944	0.968	
Solids:	C (am.)	1		1.001	0.994	0.980	
	C (graph.)	0.956	1			0.951	
	Mg	1		0.968	0.940	0.958	
	Al	1		1.012	0.987	0.988	0.989
	Si	1		1.003	0.967	0.988	
	P	1		0.992	0.996	1.002	
	Ca	1		0.993	1.001	1.036	
	Fe	1		0.981	0.980	0.983	
	LiF	1			0.964	0.981	
	CaF_2				1	0.988	
	Al_2O_3	1			0.962	0.945	
	Lucite	0.988	1		0.966	0.955	
	Polyethylene	0.960	1		0.952	0.944	
	Nylon	0.976	1		0.953	0.968	
Liquids:	H_2O	1.070	1		1.019	1.045	
	Benzene	0.941	1			0.937	
	Cyclohexane	0.960	1			0.948	
	n-Pentane	0.955	1			0.944	
	Toluene	0.945	1			0.938	
	Xylene	0.947	1			0.939	

Concerning solid compounds, it should be noted that J82 uses Bragg's rule, whereas ICRU49 takes deviations from this rule into account. Hence the ICRU49 values are always smaller than J82 (indicating that electrons in the compound are more tightly bound). In the case of Al_2O_3, e.g., ICRU49 has taken the measured values due to Bauer et al [114,104] into account. Here again, the low Z90 values for hydrogen lead to low Z90 values for lucite, polyethylene and nylon.

Concerning liquids, very little information is available at low energies, because of experimental difficulties. Fig. 7.19 shows that Z90 and ICRU49 agree in predicting a stopping power for liquid water about 10% lower than that for vapor, at low energy (as expected from Sec. 7.3.1.3). Using the common assumption that the stopping powers of liquid and solid water are the same, this difference agrees with that found experimentally by Bauer et al (Mi90). Sugiyama [115] has suggested a slightly smaller difference (4%). Above 0.5 MeV, the difference between the two curves by ICRU49 is due to the difference in I-values (as given, e.g., in ICRU37; see also table 7.3). For more water stopping powers, see also fig. 7.44.

Table 7.14 shows the differences between the various fits for 1 MeV. Here, the agreement (and hence the expected accuracy) is much better: the discrepancies amount only to a few percent.

The tissue substitute A-150 TE plastic is not shown in tables 7.13 and 7.14 since it is only given in ICRU49 and hence cannot be compared to other tables. A precise measurement of the stopping power of this substance for protons of 2.5 to 7.5 MeV was carried out recently by Ishiwari et al [36]. The result agrees within 0.2% (on the average) with that obtained using Bragg's rule and the element data from AZ77; this is surprisingly good indeed. Also, if we calculate the stopping using BEST or PSTAR, the result is, on the average, only 0.5% above Ishiwari's measurements [36], and in agreement with the calculation by Thwaites [116].

Summarizing, it seems advisable to use the ICRU49 table (or program PSTAR) for best accuracy, if possible. This table contains data for most of the key substances, and for many additional substances of interest to dosimetry. In this table, compounds are treated using either directly experimental data, if available, or else Bragg's rule (eq. 7.14); mixtures are treated by applying Bragg's rule to molecular and/or atomic constituents. Above 1 MeV, program BEST can also be used instead. Program

Z90 is convenient in that its stopping subroutine RSTOP can be included in other main programs, but it appears less reliable at least for compounds containing hydrogen. J82 is inconvenient in that it exists only in the form of printed tables; below 1 MeV, it can be replaced by the fit function due to Eppacher and Semrad [117]. J82 has the advantage of containing all elements; for compounds it has the disadvantage of neglecting chemical effects.

TABLE 7.15. FRACTION OF THE (NORMALIZED) DOSE D AT DEPTH X THAT IS CONTRIBUTED BY PROTONS WHOSE ENERGY IS SMALLER THAN T_c.

Results pertain to a 160-MeV proton beam penetrating through a water medium. R = 17.65 cm is the CSDA range at 160 MeV. The maximum of the Bragg curve is at a depth equal to 0.99 R.

			T_c(keV)	10	20	50	100	200	500	1000
x(cm)	x/R	D					Fraction (percent)			
16.94	0.960	0.606		0.0	0.0	0.0	0.0	0.0	0.0	0.0
17.03	0.965	0.650		0.0	0.0	0.0	0.0	0.0	0.0	0.1
17.12	0.970	0.707		0.0	0.0	0.0	0.0	0.0	0.1	0.2
17.21	0.975	0.782		0.0	0.0	0.0	0.1	0.1	0.3	0.6
17.30	0.980	0.872		0.0	0.0	0.1	0.1	0.3	0.6	1.3
17.39	0.985	0.958		0.0	0.0	0.1	0.2	0.5	1.2	2.4
17.47	0.990	1.000		0.0	0.1	0.2	0.4	0.8	1.9	3.9
17.56	0.995	0.953		0.1	0.1	0.3	0.6	1.1	2.8	5.5
17.65	1.000	0.802		0.1	0.1	0.4	0.7	1.5	3.6	7.3
17.74	1.005	0.572		0.1	0.2	0.4	0.9	1.8	4.5	9.0
17.83	1.010	0.341		0.1	0.2	0.5	1.1	2.1	5.3	10.6
17.91	1.015	0.165		0.1	0.2	0.6	1.2	2.5	6.2	12.4
18.00	1.020	0.065		0.1	0.3	0.7	1.4	2.9	7.1	14.2
18.09	1.025	0.020		0.2	0.3	0.9	1.7	3.4	8.1	15.9
18.18	1.030	0.005		0.2	0.4	1.0	1.9	3.8	9.3	17.9
18.27	1.035	0.001		0.3	0.6	1.5	2.9	5.2	10.5	19.4

7.3.1.5. The influence of stopping power uncertainties upon problems in dosimetry.

The tables of proton stopping powers in ICRU49 are estimated to have the following uncertainties: at energies of a few MeV or higher, 1 to 2 percent for elements, and 1 to 4 percent for compounds; at 1000 keV, 2 to 5 percent; at 100 keV, 5 to 10 percent; at 10 keV, 10 to 15 percent; and at 1 keV, at least 20 to 30 percent (see also Tables 7.13 and 7.14).

In many applications in conventional dosimetry, the proton stopping powers at high energies (with their relatively small uncertainties) are all that matters, because low-energy protons play only small role. A case in point is the depth-dose distribution in a water phantom irradiated with a high-energy proton beam used for therapy. The proton spectra from such beams, as functions of depth, have been calculated [118], and can be used to estimate the relative contributions to the absorbed dose from protons with different energies. The results of such a calculation for a 160-MeV proton beam are shown in Table 7.15. This table shows the fraction of the absorbed dose at various depths that is contributed by protons whose energies are less than 10, 20, ... 1000 keV. It can be seen that for depths up to 96% of the cdsa range, there is no contribution at all from protons with energies below 1000 keV. With increasing depth, near and beyond the Bragg peak, contributions from protons with lower energies appear, but remain small.

Another example pertains to neutron irradiation, namely, protons set in motion in elastic collisions. The proton spectrum is approximately uniform, and extends up to the neutron energy T_n. Let ϕ_c denote the fraction of the proton energy that is imparted to the medium by protons with energy smaller than T_c. It can be shown that this fraction is

$$\phi_c = \frac{\frac{1}{T_n}\cdot\int_0^{T_c} T\,dT + \frac{T_c}{T_n}\cdot\int_{T_c}^{T_n} dT}{\frac{1}{T_n}\cdot\int_0^{T_n} T\,dT} = \frac{T_c}{T_n}\left(2 - \frac{T_c}{T_n}\right). \qquad (7.15)$$

For example, for a neutron energy T_n = 14 MeV, ϕ_c is 13.4%, 1.4%, 0.14% or 0.014% for T_c = 1000 keV, 100 keV, 10 keV or 1 keV, respectively. For T_n = 1 MeV, ϕ_c is 19.0%, 2.0% or 0.2% at 100 keV, 10 keV or 1 keV, respectively.

The need for proton stopping powers at low energies, where the uncertainties are large, may, however, arise in the modeling of radiation effects on small biological structures, at the cellular or sub-cellular level. Even for such applications the energy degradation process takes place largely via secondary electrons. However, if one is concerned with the penetration of protons through very small targets, one must know the stopping powers down to energies where the residual range is smaller, perhaps by an order of magnitude, than the dimension of the target. In this connection, it should be noted that the residual proton range in water is 10 μm at 553 keV, 1 μm at 62 keV, 100 nm at 3.4 keV, and 10 nm at 380 eV.

7.3.2. Nuclear Stopping Power

Many of the tables and programs mentioned in table 7.10 also give results on nuclear stopping. This is in general quite small compared to electronic stopping. In the worst case (hydrogen projectiles on hydrogen target) it amounts to 30% at T_r = 1 keV, to 1.7% at 10 keV (see ICRU49). Actually these values are upper limits, since they include elastic scattering through *all* angles. If the energy loss of a *beam* of protons is considered, then a large angle scattering would usually remove the proton from the beam, so this proton would not contribute to the energy loss measured. This effect can be calculated using the TRIM program; a few examples have been calculated by ICRU49; see also Sec. 7.4.2.

7.3.3. Energy Loss Straggling. TRIM Programs.

Since charged particles lose their energy statistically in many small amounts, their energy after penetrating a certain amount of material is a stochastic quantity, described by its average, by its variance Ω^2 (see Sec. 7.1) and possibly by higher moments. Straggling of energetic H and He ions has been reviewed by Besenbacher et al [118a], and a general review of the statistics of charged particle penetration has been presented recently by P. Sigmund [119].

If the target is thick enough so that individual contributions W to the energy loss are small compared to the straggling, i.e., if [126]

$$3\, W_m < \Omega, \qquad (7.36)$$

but if it is thin enough so that the energy loss in the target is negligible, the energy distribution of transmitted projectiles is expected to be Gaussian [118a]. If, in addition, one assumes the target electrons to be free and initially at rest, then the variance Ω^2 of the energy distribution is given by Bohr's simple energy-independent expression [2]

$$\Omega_B^2 = 4\pi\, r_e^2\, (m_e c^2)^2\, Z_1^2\, Z_2\, n\, s = (2.6056\times10^{-13}\,eV^2cm^2/atom)\, Z_1^2\, Z_2\, n\, s. \tag{7.17}$$

Here,

$$W_m = \frac{4\, m_e}{M_1 u}\, T = 2 m_e v_1^2 \tag{7.18}$$

is the maximum possible energy transfer to a free electron (for a non-relativistic projectile), and r_e is the classical electron radius.

Various refinements of the Bohr expression (7.17) are discussed in [118a]; they take into account that the target electrons are not initially at rest and that they are spatially correlated. The effect of electron binding has been discussed by Bichsel [120a]. The Bohr expression presupposes that the projectile energy remains constant throughout the target; in practice, it is valid up to a 20% loss of the initial energy [121].

It is difficult to obtain agreement between theoretical and experimental results for straggling in solids, since effects like crystal structure and non-uniform film thickness can influence the measurements in a way that is hard to control. For gaseous targets, however, these problems do not arise, and very careful measurements in 13 different gases and comparisons with theories have therefore been carried out by Besenbacher et al [120]. At first these authors checked if their measurements yield an energy variance Ω^2 proportional to target density. Fig. 7.22 shows that this is indeed true for 600 keV He ions penetrating nitrogen. According to the conditions mentioned above, Bohr straggling should be valid from 0.04 to 0.7 μm, i.e., over most of the thickness shown. Actually, the experimental results exceed the Bohr straggling (because of the intra-molecular correlation of the target electrons).

It is instructive to compare these results to calculations performed using the program for "TRansport of Ions through Matter" (TRIM) mentioned

already above. This Monte Carlo program, originally written by J.P.Biersack [122] and described in ZBL85, has since been updated many times by Ziegler. It calculates every single nuclear collision (leading to deflection and energy loss), but treats the much more numerous collisions with target electrons only in a global way: between any two nuclear collisions, it adds to the csda energy loss a stochastic contribution that corresponds to straggling.[5] TRIM90 (and its successors TRIM91, TRIM92) computes particle penetration in 3 dimensions and draws instructive pictures of all relevant processes on the screen. Another version of TRIM ("T2D"), available from J.P.Biersack, calculates penetration in 2 dimensions; it is faster but does not draw pictures. Both versions use the same stopping powers (Z90) below 10 MeV/nucleon. Above this specific energy, the T2D stopping is the original one from ZBL85 and hence inaccurate.

TRIM results are also shown in Fig.7.22. Except at small thickness,[5] T2D agrees with the Bohr straggling as it should. The TRIM90 result is consistently lower, possibly due to a different choice of the free flight path[5]. (Note that for comparing with Bohr straggling, we exclude those rare large-angle scattering events from the statistical analysis whose

---

[5] Note that the TRIM programs contain a statement forbidding an energy *increase* between two nuclear collisions. This makes the straggling too small for small flight paths (where Ω may exceed the energy loss), and it makes the straggling too small also for the entire target, if the free flight path is chosen too small (the flight path can be chosen by the user in T2D). This difficulty can be remedied in T2D by removing the statement that forbids an energy increase. In TRIM92, the difficulty is enhanced by the fact that the flight path within a layer is decreased toward the layer edge until it reaches a monolayer thickness (in order to avoid unphysical peaks or dips near an edge), *and* by the fact that straggling is artificially kept below 20% of the csda energy loss (J. Ziegler, pers. comm.). Hence, the TRIM92 straggling is even lower than that of TRIM90 (see Fig. 7.23).

In TRIM91 and TRIM92, the straggling is linearly reduced below the Bohr straggling for energies below the stopping power peak. This is a reasonable approximation (see, e.g., Fig. 7.25 below).

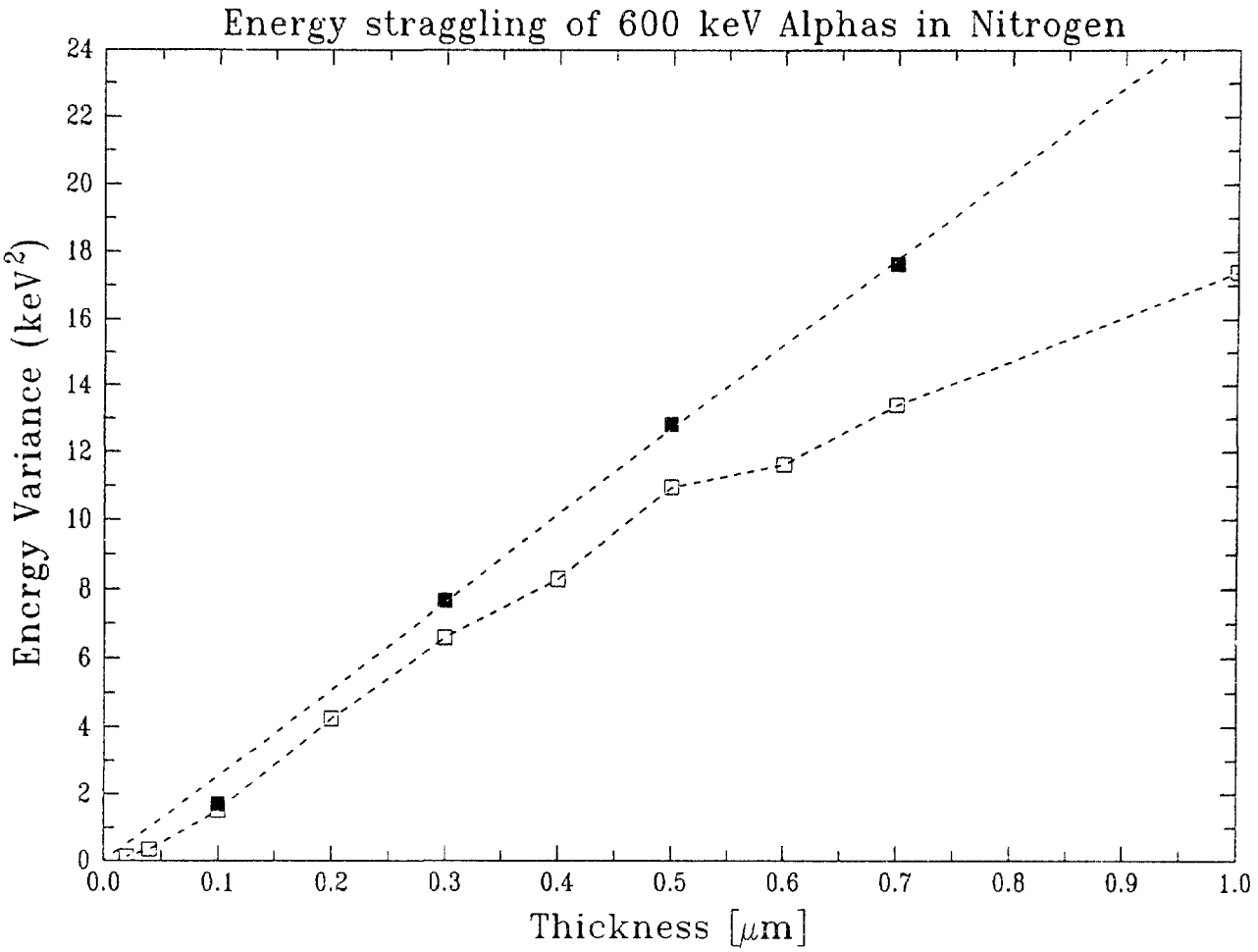

Fig.7.22. Energy straggling of 600 keV alphas penetrating nitrogen. The energy variance is plotted versus the target thickness, assuming a hypothetical density of 0.8096 g/cm^3, so that 1μm ⇔ 3.482x10^{18} atoms/cm^2. Experimental results due to Besenbacher (···) and the Bohr prediction (-·-) according to eq. (7.17) are indicated by lines. TRIM results are indicated by open squares (TRIM90, TRIM91) and full squares (T2D), resp.

energy is clearly outside the Gaussian distribution of transmitted energies)[6].

Figures 7.24 to 7.26 show the energy straggling of protons in Ar, N_2 and H_2, as examples taken from [120]. In Ar (Fig. 7.24), the straggling is

---

6) The program TRIM90 produces an output file TRANSMIT.TXT that contains the final energy and angle of every transmitted projectile. This file can be analyzed using program TRANSMIT.BAS (also on the TRIM90 disc) that calculates energy and angular straggling and produces a histogram of final angles. We have added a section that produces a histogram of final energies also.

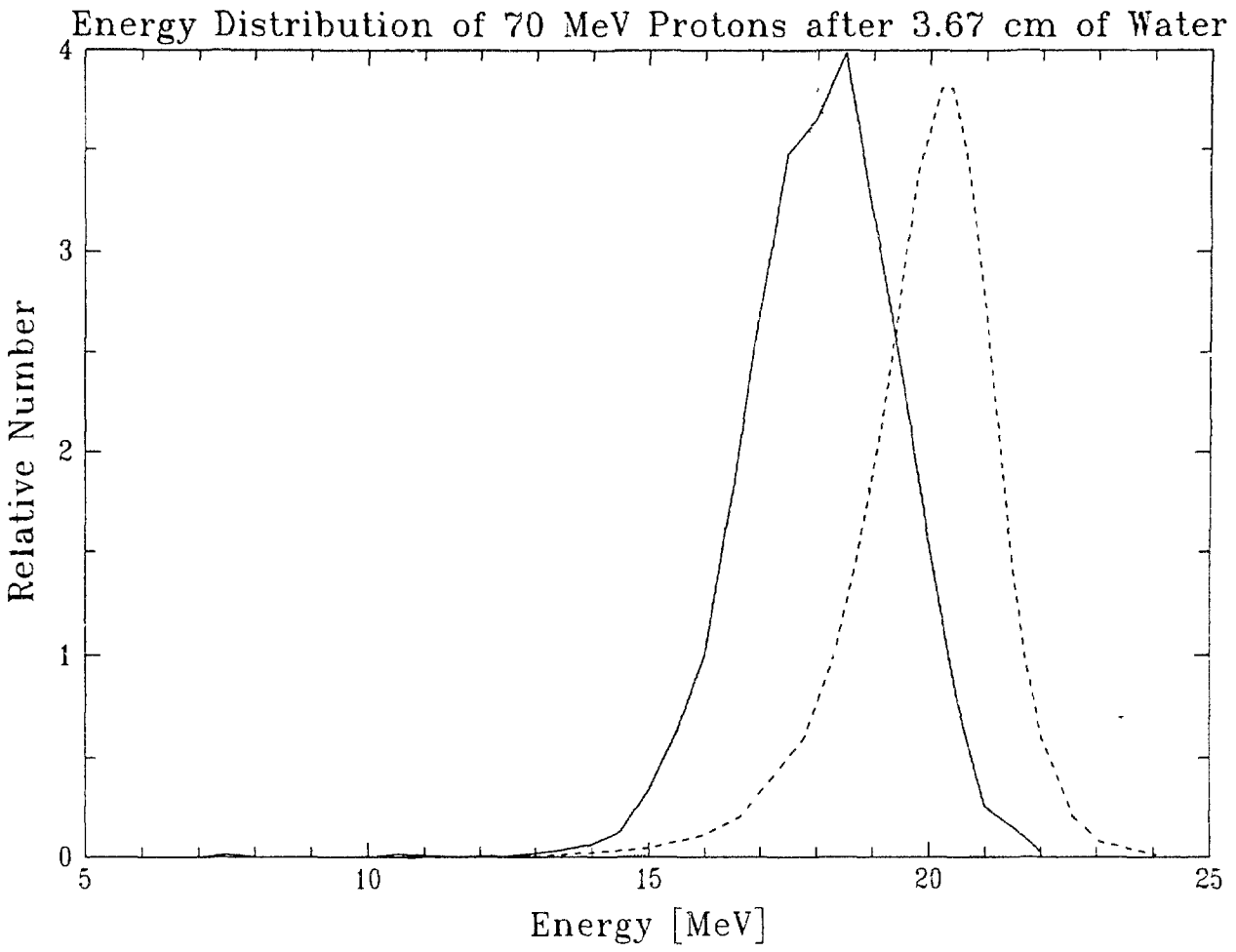

Fig.7.23. Energy distribution of 70 MeV protons after passing 3.67 cm of water (ρ = 0.997 gcm^{-3}), as calculated by Bichsel and Hiraoka [130] (dashed), and by use of TRIM90 (full curve) or TRIM92 (dotted curve). The csda range of these protons is 4.08 gcm^{-2} (ICRU49, Bichsel); the mean projected range 4.075 gcm^{-2} (ICRU49), but only 4.00 gcm^{-2} according to TRIM90. The TRIM92 curve is too narrow (see text).

slightly below the Bohr value. This can be understood by treating the atomic electron density realistically [123] and by adding a straggling term due to intra-atomic electron correlation [120]. The result for N_2 (Fig. 7.25) can be understood by including, in addition, intra-molecular correlations. The straggling in H_2 (Fig. 7.26) is explained down to 80 keV using Fano's [11] asymptotic perturbation formula which treats the target electron speeds as not negligible compared to the projectile speed.

To see how well these measurements can be reproduced by TRIM, we consider 500 keV protons on nitrogen, at a thickness corresponding to

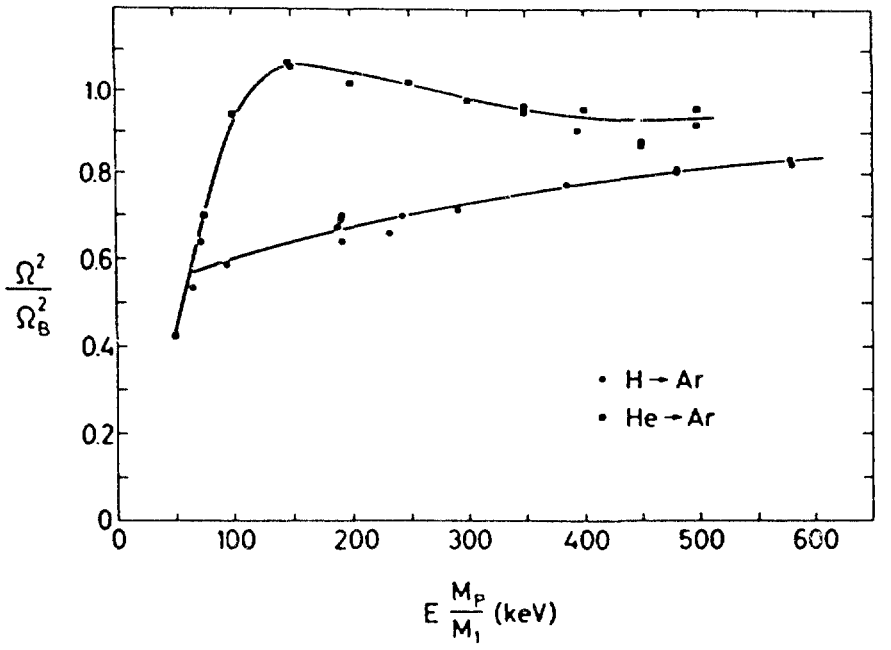

Fig.7.24 Energy straggling variance [120] of H and He ions in Argon, divided by Bohr variance, eq. (7.17), versus equivalent proton energy.

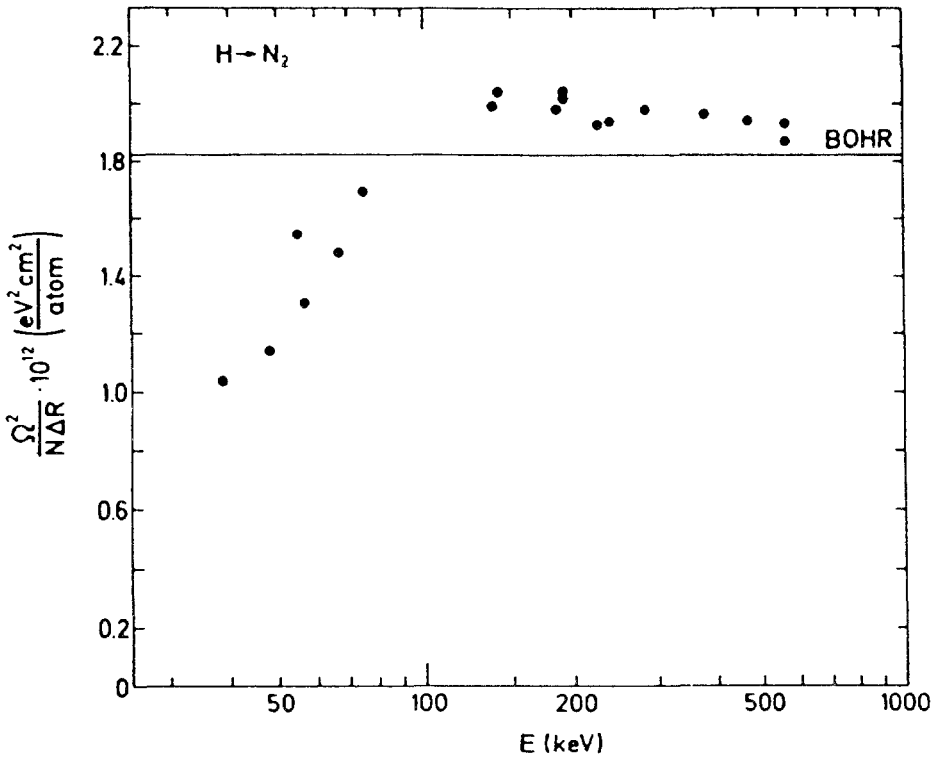

Fig.7.25 Energy straggling variance [120] of protons in nitrogen, divided by Bohr variance, eq. (7.17), versus energy.

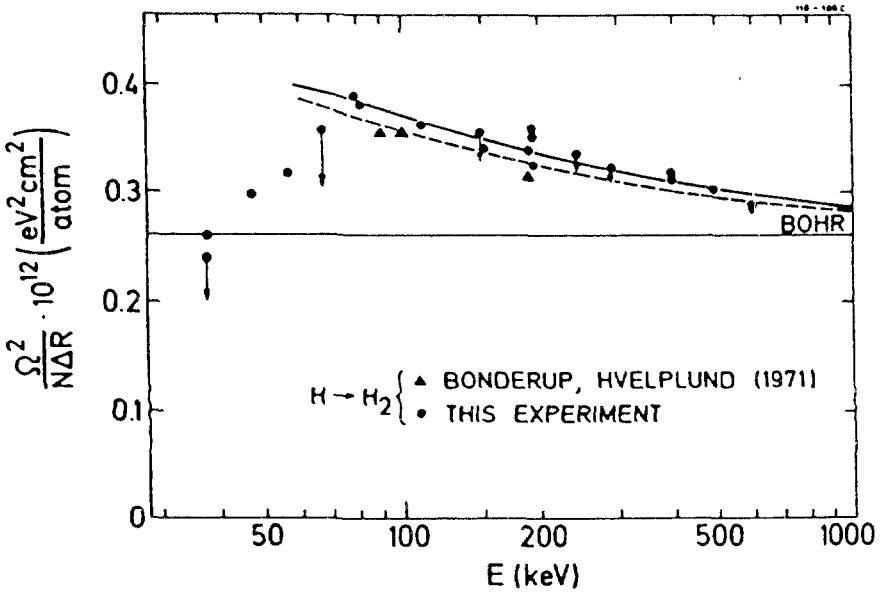

Fig.7.26 Energy straggling variance [120] of protons in hydrogen, divided by areal density, versus energy, compared to the formulas by Bohr (eq.7.17) and by Fano [11] for molecular (——) and atomic (---) targets.

6.96×10^{18} atoms per cm^2. In this case, the Bohr straggling amounts to $1.82 \times 10^{-12} eV^2 cm^2$/atom, or 12.7 keV^2 for the given thickness, and the measured value is 13.6 keV^2 (cf. Fig.7.25). Using TRIM, we obtain Ω^2 = 12.5 keV^2 (TRIM90) and 14.0 keV^2 (T2D), resp., in fair agreement. Since W_m = 1.1 keV (eq. 7), the thickness is just enough (eq. 7.16) for Bohr straggling to apply.

Using a local-electron-density model, Kaneko and Yamamura [124] have calculated the straggling for protons (and He ions) in many solid targets. They use Hartree-Fock wave functions modified to include plasma electrons, and they include collisional as well as charge-changing contributions. They find that the straggling variance is proportional to T for small T, and that it approaches the Bohr value above 1 MeV/u. Measurements by Matsunami and Kitoh [125] using 100 keV protons and He ions on C films of about 10 nm thickness and high (30 eV) resolution agree with their prediction.

For solid targets, variations of the target thickness due to surface roughness produce an important contribution to straggling. Besenbacher et al [118a] have attempted to determine this contribution by comparing the results from measurements with H, He, and Li ions. See also Sec. 7.5.3.

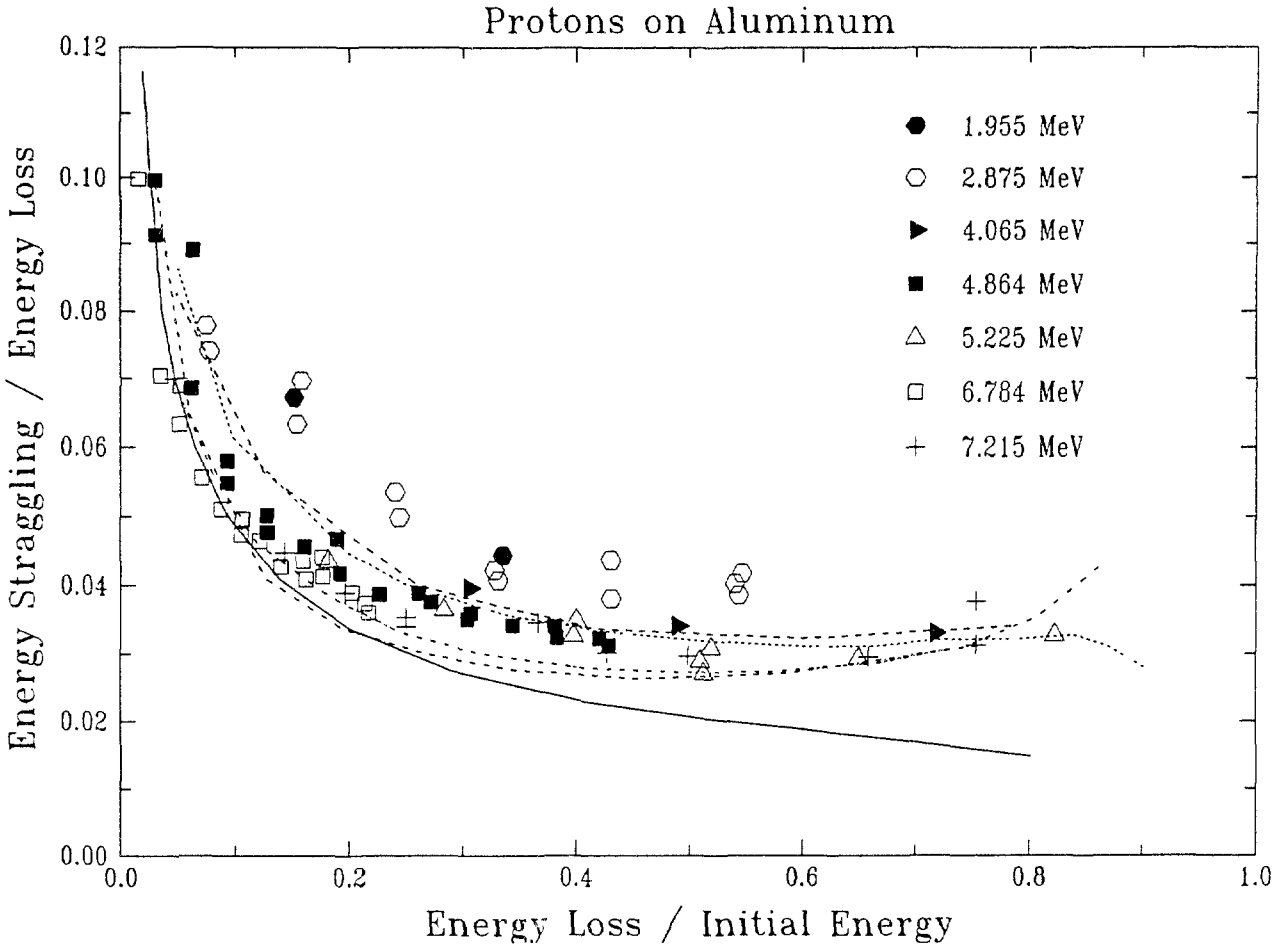

Fig.7.27 Energy straggling Ω (divided by energy loss in the foil) versus energy loss (divided by initial energy), for protons from 1.9 to 7.2 MeV in aluminium. Measurements by Bauer et al [128], indicated by symbols, are compared to the Bohr result (——), eq. (7.17), to Tschalär's [121,137] calculations (short dashed: 1.5 MeV; -·-·: 7.6MeV), and to TRIM90 (long dashed: 2 MeV; -·-: 7.6 MeV).

For thin targets, the energy distribution of transmitted projectiles is asymetrical (see, e.g., the reviews in [119] and in ICRU49); it can be described by the Vavilov theory [126] (see Sec. 7.2.4). For very thin targets, this theory does not apply and must be replaced by other approaches (see ICRU49).

For thick targets, the Bohr theory cannot be used either. The straggling theory developed by Tschalär [121,127] can, however, be used for relative energy losses up to 80%. In fig.7.27, we compare TRIM90 calculations for 1.5 and 7.6 MeV protons on aluminum to Tschalär's calculations and to measurements by G.H.Bauer et al [128]. Although the straggling is, of course, no more energy independent, one can see in this type of representation that the *normalized* energy straggling becomes

approximately energy-independent if plotted versus the normalized energy loss. Evidently, the TRIM calculations (after excluding rare low-energy events, as above) agree well with the Tschalär results. Both calculations appear to be in fair agreement with Bauer's measurements at energies between 4 and 5.3 MeV. The results measured at energies below 3 MeV appear somewhat high; this could be partly due to non-uniformities in the target foils [cf. ICRU49]. Similar results were obtained by Armitage and Trehan [129].

As another example for a thick target, we show the energy spectrum calculated by Bichsel and Hiraoka [130] for 70 MeV protons in water. Here, the importance of the third moment (skewness) can be seen from the asymetry of the spectrum. Fig. 7.23 shows Bichsel's curve for a thickness of 3.67 cm of H_2O, calculated using the moment method by Tschalär [127] and including multiple scattering. The figure also shows the result of a Monte Carlo calculation carried out using TRIM90. The latter curve has a lower mean energy, since the Z90 stopping is slightly higher in this energy region (see Fig. 7.18), but the two curves have the same variance. A curve obtained using TRIM92 is also shown; it is much too narrow .

For a discussion of TRIM calculations of ranges and range straggling, see Sec. 7.3.5 below.

Bichsel [4] has also carefully compared measurements of Ω for high energy (>38 MeV) protons on Si with his calculations carried out by means of the convolution method; he found agreement within 1%.

7.3.4. Multiple Scattering

Multiple scattering is treated in Sec. 7.5.4, since most of the recent data refer to heavy ions. But it should be noted that Fig. 7.48 contains also data measured with H and He ions.

7.3.5. Ranges and Range Straggling

Curves for the csda range R (cf. Sec. 7.1) in all elemental targets heavier than $_3$Li are given in AZ77 (called "path length"). In addition, AZ77 show the mean projected range $\overline{R}_x$, calculated according to Schiøtt's approximation [131], and the range straggling, σ_R. They say that the results for $\overline{R}_x$ and σ_R are of limited accuracy.

Kistemaker and Sanders [132] have given a simple expression for the ratio $R/\overline{R}_x$ (based on a constant nuclear stopping power) which is a function of M_1 and M_2 only. Al-Affan [133] has used this function to convert the true stopping power to a so-called "effective stopping power" the integration of which yields the projected range, and he has produced a table of stopping powers and projected ranges in some materials of dosimetric interest (see [134] for a critical review of this work by H.H.Andersen).

The tables in ICRU49 list the "csda range" R and the "detour factor" ($= \overline{R}_x/R$). Alternatively, these values and also $\overline{R}_x$ can be calculated using program PSTAR. The Janni table (J82) separately lists the "proton range" $\overline{R}_x$, the "path length" R, the path length straggling, and, in addition, it gives the probability for the projectile to be lost from the beam due to nuclear interactions.

The computer programs TRIM89 and TRIM90 permit calculation of projected ion ranges either by the PRAL algorithm based on an analytical solution of the transport equation or by the Monte Carlo code. Both programs use the electronic stopping power and a universal scattering potential as inputs. They both give results on longitudinal and lateral straggling; in addition, TRIM90 can produce graphical range and straggling distributions (and even a distribution of deposited energy vs. depth). A newer version, TRIM91, produces generally the same results as TRIM90 (within statistics), except for the lateral straggling which has been redefined. It also calculates dimensionless measures of the higher moments of projected range, skewness and kurtosis (which appear on the screen together with the ion range distribution). Fig.7.28 (taken from ZBL85) shows graphical comparisons of experimental and calculated results for R, R_x and σ_R for Si and Ni targets. For Si at least, the agreement between experimental and calculated range is impressive. The disagreement in the straggling results is said to be due to the different straggling definition used by the experimenters.

Fig.7.29 compares the csda range R for protons on nitrogen from different tables. At 1 keV, the three curves differ by up to a factor 2; this is in part due to the different low-energy values of S (see Fig.7.18), in part due to different assumptions about the low energy integration limit. Toward higher energies, the relative differences become quite small.

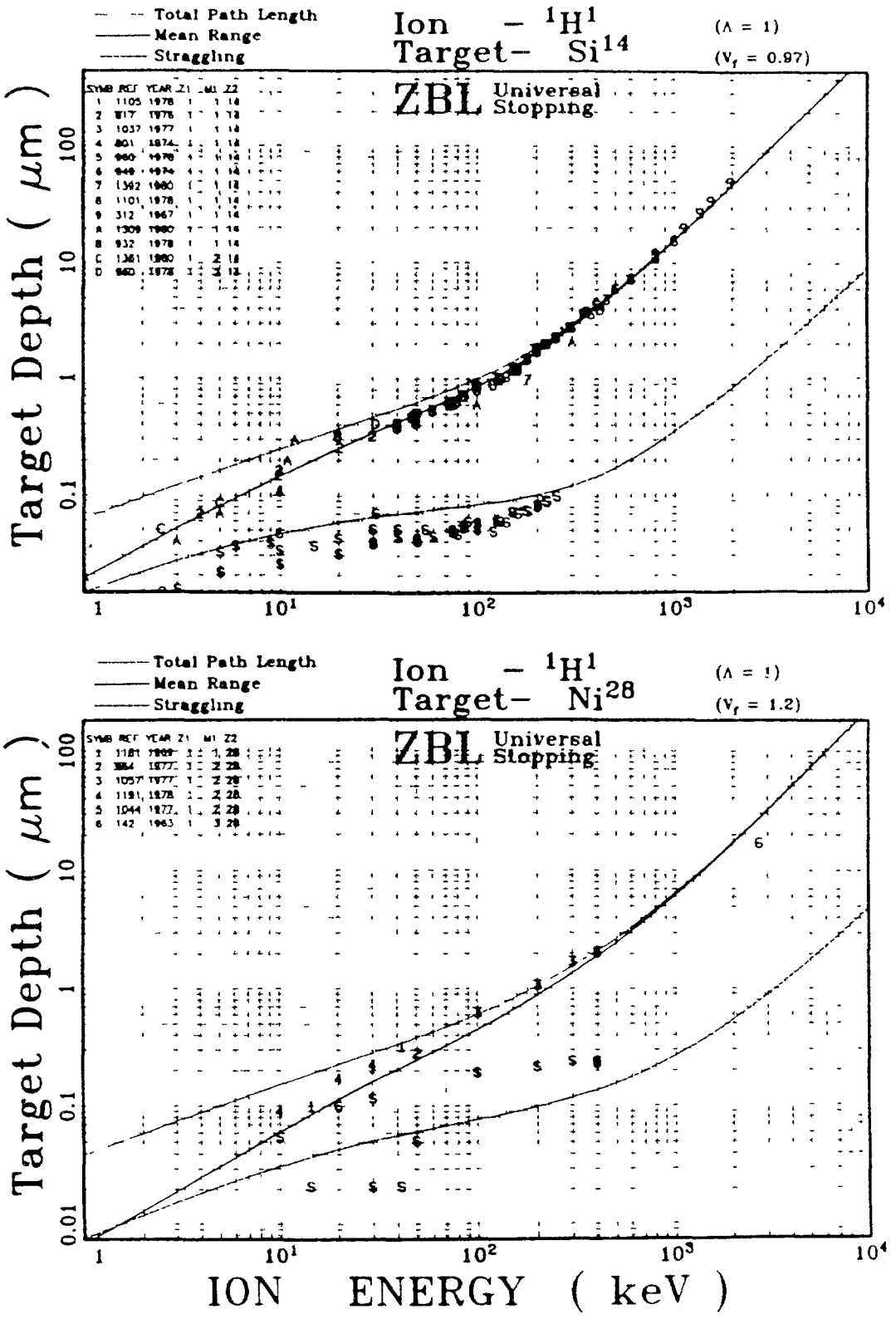

Fig.7.28 Average path length R (···), mean projected range R_x (——), and range straggling σ_R (---) for protons in Si and Ni targets, taken from ZBL85. The letter S indicates experimental straggling data, the other symbols indicate experimental data for the projected range.

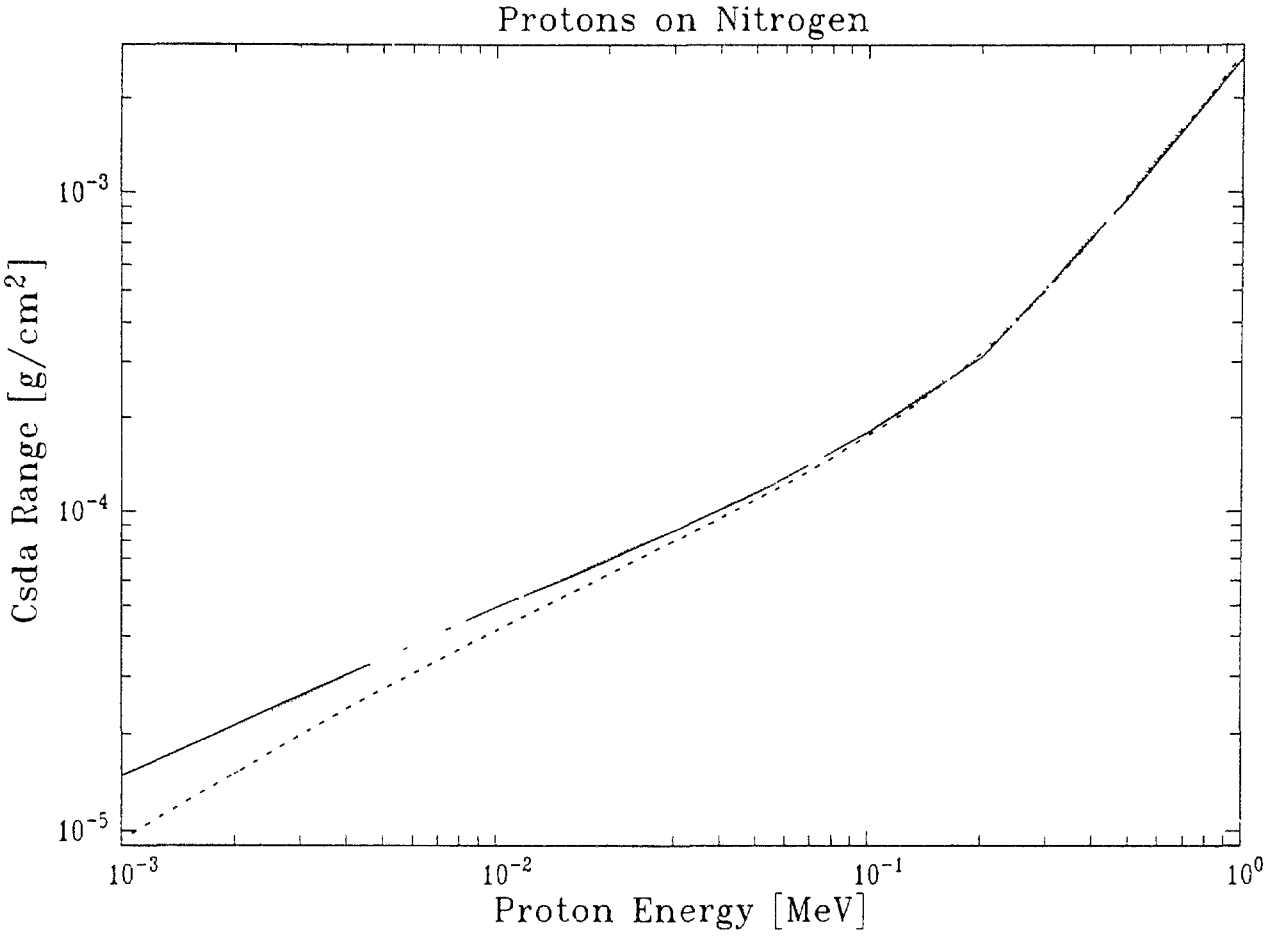

Fig.7.29 Csda range for protons on nitrogen, according to AZ77 (——), J82 (···), and ICRU49 (—··—).

Fig.7.30 shows the detour factor (= $\overline{R_x}/R$) for protons on nitrogen, taken from five different compilations. To obtain the TRIM curve, $\overline{R_x}$ was calculated using TRIM90, but the corresponding R was obtained using [135] program RBS with Z90 stopping powers. Evidently, all the calculations (except AZ77) are in pretty fair agreement with each other.

Børgesen et al [136] have measured the projected range and the range straggling of 10-30 keV deuterons implanted into various solids. Fig.7.31 shows their result for aluminum, compared to various calculations including their own (which uses the AZ77 stopping power). One can see that the range measurements agree with the TRIM90 curves within about 10%, and that the PRAL curve is slightly below the Monte Carlo result, at low energy. For the straggling width, the two Monte Carlo results agree fairly well, but the experimental result is somewhat higher. The PRAL result appears too

high. Note that Ashworth et al [137] have recently published a revised version of PRAL; they find that the first-order PRAL algorithm contained in TRIM90 is poor in predicting longitudinal and lateral straggling, due to a mathematical error.

The Børgesen results for carbon [136] (not shown here) indicate that the TRIM90 range is about 15% low due to the high stopping power (see Fig.7.15). These range measurements may be qualitatively compared to more recent measurements by Ross and Terreault [138,139] using H and D ions of energies up to 2 keV. Here, the discrepancy with the TRIM90 stopping power for carbon is even more striking. If the stopping power of carbon were proportional to $T^{0.25}$ (as assumed in TRIM90, see 7.3.1.1), the csda range would be proportional to $T^{0.75}$. Such an energy dependence is indeed found approximately by Ross and Terreault, but of course for the projected range, not for the csda range.

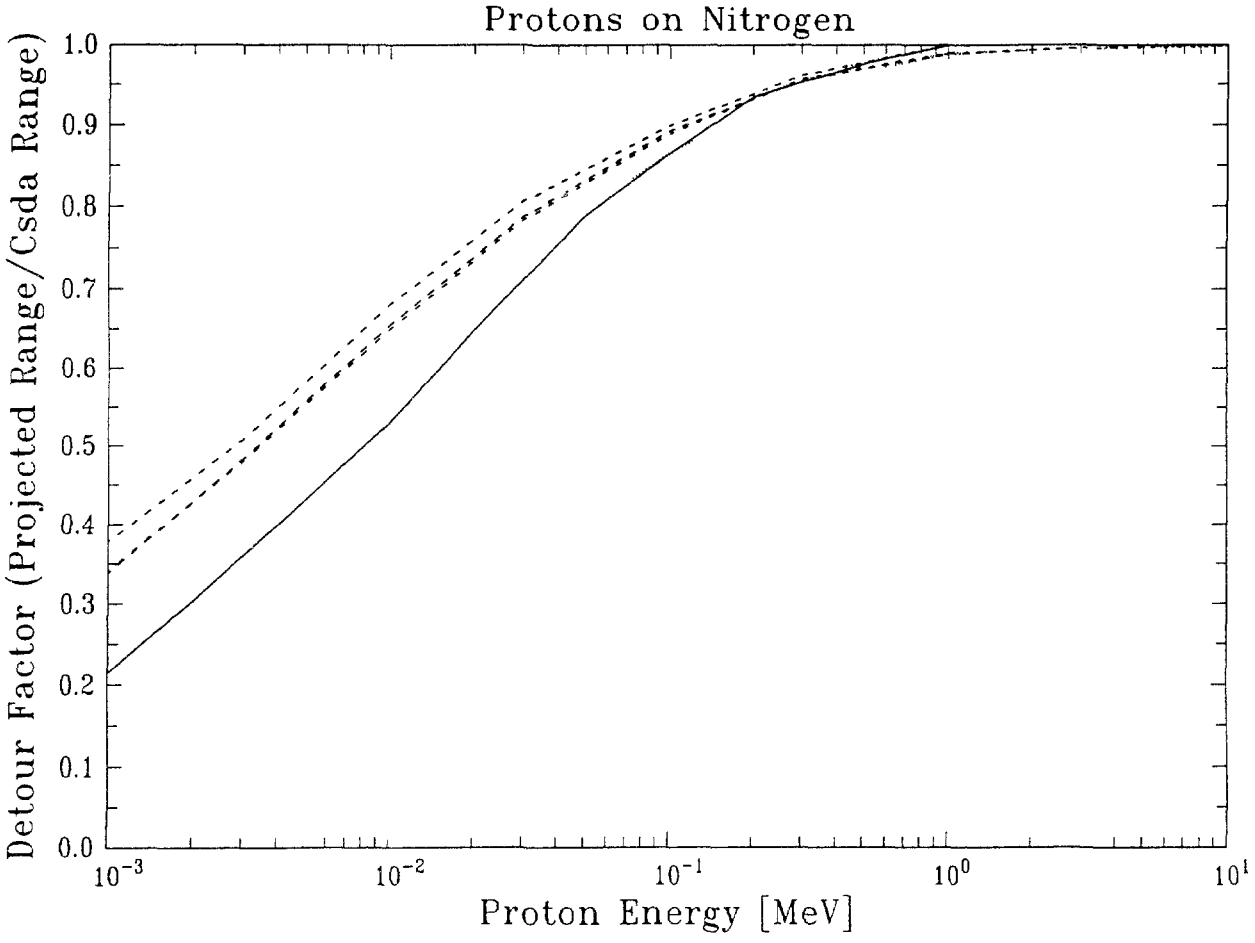

Fig.7.30 Detour factor for protons on nitrogen, according to AZ77 (——), PRAL/RBS (---), J82 (···), ICRU49 (—··—), and Al-Affan [133] (—·—)

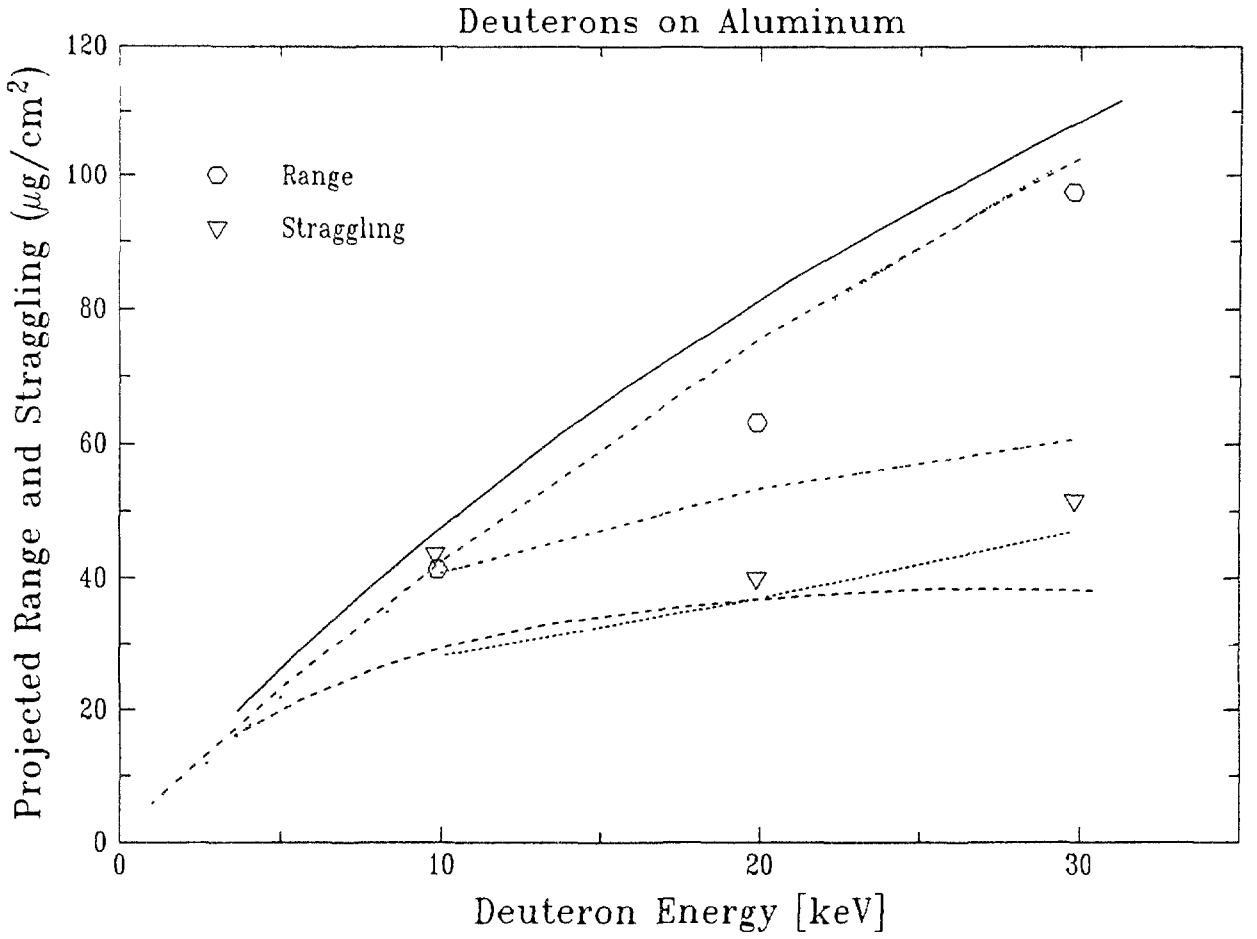

Fig.7.31 Projected range and range straggling (fwhm) of deuterons in aluminium. Measured points and two theoretical curves (full: range; long dashed: straggling) are from Børgesen et al [136]. The remaining curves were calculated using TRIM90:

Range: Monte Carlo (-·-); PRAL (···)

Straggling: Monte Carlo (short dashed); PRAL (-···)

For comparison with the experimental results which are given in terms of the full width at half maximum, the theoretical values σ have been multiplied by 2.35.

7.3.6. Vector Ranges

To our knowledge, no tables of the vector range $\overline{R_v}$ are available [134]. To estimate this quantity, we can calculate the longitudinal range and the "radial range" (i.e., the final perpendicular distance of the projectile from the axis of its original velocity) using TRIM90, and add them in quadrature. Taking protons on Al as an example, we find that $\overline{R_v}$ hardly differs from $\overline{R_x}$ down to about 50 keV. For 2 keV we get, e.g., a longitudinal range of 0.034 μm and a radial range of 0.023 μm, which add up to $\overline{R_v}$ = 0.041 μm. This is an upper limit, since particles that happen to have a large longitudinal range must have small radial range, and vice versa.

7.4.1. Electronic Stopping Power

7.4.1.1. Compilation of Ziegler

The first comprehensive compilation of stopping cross sections of all elements for helium ions was published in 1977 by Ziegler [140]. At energies from 10 MeV to 100 MeV, Ziegler used Bethe's stopping power formula with empirical shell corrections (which implicitly also included Barkas and Bloch corrections). These corrections were based on the corresponding corrections for protons of the same velocity, from Andersen and Ziegler [26]. At energies from 10 MeV to 1 keV, Ziegler used experimental data represented by the following fitting formula for the stopping cross section:

$$\frac{1}{S/n} = \frac{1}{(S/n)_{low}} + \frac{1}{(S/n)_{high}},$$

where

$$\left.\begin{aligned} (S/n)_{low} &= A_1 \, (1000\ T)^{A_2} \\ \text{and} \\ (S/n)_{high} &= (A_3/\ T)\ \log\ (1 + A_4/\ T + A_5 T), \end{aligned}\right\} \qquad (7.19)$$

and T is the kinetic energy in MeV.

The formulas for $(S/n)_{low}$ and $(S/n)_{high}$ are similar to theoretical expressions applicable at low and high energies, respectively. Used in combination, they provide a good description of the energy dependence of the stopping cross section in the vicinity of the stopping power peak. For the determination of the coefficients $A_1, \ldots . A_5$ in Eq.(7.19) Ziegler had at his disposal data for 50 elements. For the other elements he interpolated with respect to atomic number. The interpolations were also guided by knowledge of stopping cross sections for protons of the same velocity from the compilation of Andersen and Ziegler [26].

Table 7.16 lists the elements for which data were available for helium ions, and the lowest energy for each element to which the data extend. It can be seen that measurements at energies as low as 10 keV are available

TABLE 7.16. LOWEST ENERGIES AT WHICH EXPERIMENTAL STOPPING CROSS SECTIONS OF ELEMENTS FOR ALPHA PARTICLES ARE INCLUDED IN THE COMPILATION OF ZIEGLER [140].

Lowest Energy, keV	Atomic Number
2	47
4	6, 29
5	14, 79
10	7, 18, 23, 32
15	5, 13
20	1, 34, 46, 51, 83
30	28
40	24
50	25, 26, 27
75	3
100	2, 8, 10, 36, 54
150	78
200	17, 68, 74
250	63
300	9, 39, 40, 41, 42, 52, 53, 57, 66, 73
400	4, 12, 23, 49, 50
2000	64, 72, 77

for only 7 elements, and as low as 100 keV only for additional 26 elements. Clearly the use of the Eq.(7.19) down to 10 keV or 1 keV represents an extrapolation with considerable uncertainty.

7.4.1.2. Method of Ziegler, Biersack and Littmark.

Ziegler, Biersack and Littmark (ZBL)[141] introduced a different method for obtaining empirical stopping powers for helium ions below 10 MeV, which involved a scaling from protons to helium ions, in a two-step procedure. First, proton stopping cross sections for all elements are fitted by a formula similar to the one used by Andersen and Ziegler (cf. Table 7.10). Second, an effective charge parameter ζ is introduced, such

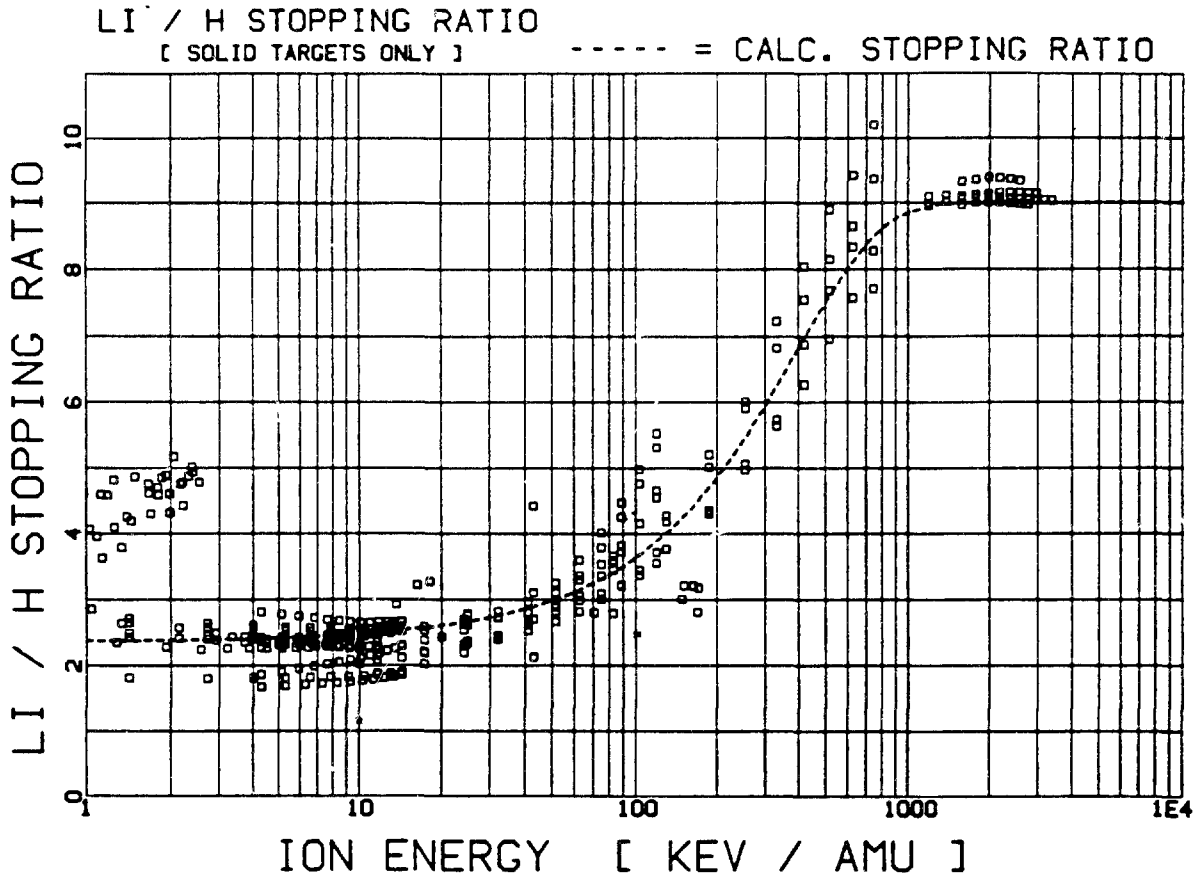

Fig.7.32 $Z_{1,eff}^2$ *as defined by eq. (7.22), for Li ions in solid elements, versus energy per mass unit [152]. Every symbol represents an experimental value; the line is a fit to the points.*

that ζZ_2 is the effective charge of an ion of charge Z_2 (see also Sec. 7.5.1). The ratio of the stopping cross section for a helium ion to that for a hydrogen ion of the same velocity is then given by

$$\frac{S_{He}}{S_H} = \left(\frac{\zeta_{He} Z_{He}}{\zeta_H Z_H} \right)^2 = 4 \left(\frac{\zeta_{He}}{\zeta_H} \right)^2 \qquad (7.20)$$

ZBL assumed that the effective charge parameter for hydrogen ions, ζ_H, is equal to unity at all energies. They determined the parameter ζ_{He} for helium ions by analyzing experimental stopping cross sections for hydrogen and helium ions with the same velocity. They found that ζ_{He} depends predominantly on the velocity. Neglecting the residual dependence of ζ_{He} on the atomic number of the target atom, they fitted ζ_{He} by an empirical formula that depends only on the energy of the helium ion. This formula predicts an effective charge that decreases monotonically with decreasing

velocity (e.g., $\zeta_{He} = 1$ at 1 keV/u). However, in a review of stopping powers of light ions near the maximum, Bauer [91] pointed out that for gas targets as well as solids such as carbon, Al_2O_3 and SiO_2, the effective charge of helium ions reaches a plateau below 50 keV/u. [Note that the effective charge shown in fig. 7.32 for Li ions does reach a plateau below 20 keV/u!] Similar results were obtained by Eppacher and Semrad [142] who also emphasize that the effective charge of helium ions is not quite independent of the target.

There is another case where the concept of effective charge is quite inappropriate: Golser and Semrad [143] have found that the squared effective charge for He ions in helium gas at 4 keV/nucleon is 5.8. This exceeds even the high-energy limit of 4 that one would naively expect somewhere above 300 keV/u; it is due to the unusually steep energy dependence of S for H ions in He.

A similar scaling procedure was applied by ZBL to all heavy ions (see Sec. 7.5.1.1), and was incorporated into a charged-particle transport code called TRIM [141] which can be applied to compounds as well as elements (cf. sections 7.3.3, 7.5.3). The TRIM programs are updated from time to time. From the 1990 version [144] on, they include bonding corrections for compounds developed by Ziegler and Manoyan [106] (cf. Sec. 7.3.1.2). Even though these bonding corrections were derived for solids, the TRIM program also offers bonding corrections for some gaseous compounds.

7.4.1.3. Compilation in ICRU Report 49.

In ICRU Report 49 [145], stopping powers for helium ions with energies above a few MeV are evaluated according to Bethe's theory, with shell, Barkas and Bloch corrections. The mean excitation energies used were the same as those adopted previously in ICRU Report 37 [5] dealing with electrons and positrons. The mean excitation energies for compounds were either taken directly from experimental data, or were obtained by a modified Bragg rule as described in section 7.2.1.5. The shell corrections and Barkas corrections were evaluated according to procedures proposed by Bichsel [5,30,145] which involve the adjustment of various parameters to obtain close agreement with measured stopping powers for alpha particles and protons. If the mean excitation energy for liquid water were changed from the value of 75 eV used by the ICRU to the value of 79.8 eV recommended by Bichsel and Hiraoka (see Table 7.4), and if the shell and

Barkas corrections were left unchanged, the stopping power for helium ions would be reduced by 2.4%, 1.8% or 1.5% at 2, 5, or 10 MeV, respectively.

At energies below a few MeV, Ziegler's fitting formula, Eq.(7.19), was used. For most elements, the numerical values of the coefficients were taken from Ziegler [140]. However, for elements with atomic numbers Z_2 = 1, 4, 6, 7, 8, and 14, the values were revised in order to take into account newer experimental data. Coefficients for amorphous carbon were adopted which differ from those for graphite. For 13 compounds for which experimental data were available, the stopping powers were evaluated with use of a different fitting-formula developed by Powers [146]. For other compounds, Bragg additivity was applied to the elemental stopping cross sections.

The tables of ICRU49 can also be calculated using program ASTAR (see appendix).

7.4.1.4. Comparisons of Electronic Stopping Powers

Table 7.17 contains comparisons of stopping powers of selected elements and compounds from three sources: the compilation of Ziegler [140], the compilation in ICRU Report 49 [145], and the TRIM program (1990 version). At 1000 keV and 100 keV the differences are moderate, on the order of a few percent, but occasionally they exceed 10 percent. At 10 keV and 1 keV the differences are large, which is not unexpected because the stopping powers at these energies often depend on rather uncertain extrapolations. The differences between Ziegler's 1977 compilation and ICRU Report 49 on the one hand, and the TRIM program on the other hand, are largely due to the reliance on experimental alpha-particle data of the former two, instead of the proton-to-alpha-particle scaling procedure of the TRIM program. See also fig. 7.44 for results on water.

Included in the stopping power tables for heavy charged particles published by Hubert et al [HU90; see table 7.11 for reference codes and Sec. 7.5.1.1 for a more complete description], are stopping powers for helium ions with energies from 10 MeV to 2000 MeV. Below 600 MeV, these stopping powers are from Ziegler [140], and differ by less than 1 percent from those from ICRU Report 49 [145]. The stopping powers in HU90 above 600 MeV were obtained from Janni's proton stopping power tables [J82], assuming Z_1^2-proportionality, and differ by less than 2 percent from those in ICRU

TABLE 7.17. RATIOS OF FITTED CURVES FOR THE STOPPING OF ALPHA PARTICLES IN SELECTED MATERIALS.

T90: TRIM-90 [144]
NB: no bonding correction used
B: bonding correction used
Z77: Ziegler [140]
ICRU49: ICRU Report 49 [145]

		1 keV				10 keV			
		T90		Z77	ICRU49	T90		Z77	ICRU49
		NB	B			NB	B		
Gases:	H_2	0.956	1	0.470	0.427	0.956	1	0.587	0.553
	N_2	1.001	1	1.367	1.317	1.001	1	1.178	1.152
	O_2	0.997	1	1.865	1.929	0.996	1	1.391	1.406
	H_2O	1			1.243	1			1.051
	Air	1			1.461	1			1.221
	CO_2	1			1.274	1			1.064
	CH_4	0.923	1		0.864	0.923	1		0.800
	C_3H_8	0.937	1		0.975	0.923	1		0.847
Solids:	Be	1		0.929	0.922	1		0.880	0.800
	C (Graphite)	1		1.730	1.567	1		1.236	1.235
	Al	1		1.130	1.130	1		1.162	1.162
	Si	1		0.922	0.969	1		1.004	1.060
	Fe	1		2.108	2.108	1		1.520	1.520
	Cu	1		1.637	1.637	1		1.333	1.333
	Ag	1		1.826	1.826	1		1.376	1.376
	Au	1		1.098	1.281	1		1.037	1.189
	Pb	1		1.557	1.557	1		1.257	1.257
	LiF	1			1.936	1			1.470
	Al_2O_3	1			1.376	1			1.157
	SiO_2	1			1.134	1			1.073
	Lucite	0.983	1		0.903	0.983	1		0.855
	Polyethylene	0.947	1		0.919	0.947	1		0.848
	Polystyrene	0.933	1		0.953	0.933	1		0.884
	Teflon	0.961	1		1.339	0.961	1		1.053
Liquids:	Water	1.098	1		1.068	1.098	1		0.973
	Toluene	0.926	1		1.162	0.926	1		0.946

---------- Table 7.17, continued.

		100 keV				1000 keV			
		T90		Z77	ICRU49	T90		Z77	ICRU49
		NB	B			NB	B		
Gases:	H_2	0.956	1	0.864	0.847	0.956	1	0.954	0.965
	N_2	1.001	1	0.914	0.908	1.001	1	1.008	1.019
	O_2	0.996	1	0.937	0.929	0.996	1	0.996	1.019
	H_2O	1			0.897	1			1.004
	Air	1			0.925	1			1.029
	CO_2	1			0.884	1			1.060
	CH_4	0.923	1		0.893	0.924	1		0.975
	C_3H_8	0.937	1		0.975	0.937	1		0.914
Solids:	Be	1		0.915	0.809	1		0.996	0.998
	C (Graphite)	1		1.049	1.143	1		0.955	0.998
	Al	1		0.986	0.986	1		1.032	1.032
	Si	1		0.974	1.002	1		0.992	0.948
	Fe	1		0.993	0.993	1		1.015	1.015
	Cu	1		0.983	0.983	1		0.990	0.990
	Ag	1		0.940	0.940	1		1.002	1.002
	Au	1		0.892	0.998	1		1.020	1.037
	Pb	1		0.919	0.919	1		0.991	0.991
	LiF	1			1.114	1			1.036
	Al_2O_3	1			0.863	1			0.935
	SiO_2	1			0.782	1			0.887
	Lucite	0.983	1		0.901	0.983	1		0.944
	Polyethylene	0.947	1		0.931	0.947	1		0.961
	Polystyrene	0.933	1		0.968	0.933	1		0.919
	Teflon	0.961	1		0.835	0.961	1		0.887
Liquids:	Water	1.098	1		0.884	1.098	1		1.028
	Toluene	0.926	1		0.940	0.927	1		0.893

Report 49 or from the computer program BEST. These small differences are due to the use of different I-values and shell corrections in the various compilations.

7.4.2. Nuclear Stopping Power

Because of the scarcity of experimental data, nuclear stopping powers are usually obtained by calculations involving three steps: (a) the determination of an appropriate projectile-target scattering potential; (b) the determination of the elastic-scattering cross section by a classical-mechanics calculation; and (c) the evaluation of the energy transferred to recoiling target atoms in elastic collisions. Confirmation of the validity of such calculations is usually obtained through comparisons between calculated and measured ranges, or with more detailed transport results.

There is no controversy in regard to steps (b) and (c), but many different prescriptions can be found in regard to step (a), the determination of the potential which must take into account the Coulomb interactions between the projectile and target, including nuclei and orbital electrons. The most detailed discussed of this problem can be found in the book by Ziegler, Biersack and Littmark [141]. It is customary to calculate such potentials for a large number of projectile-target combinations, and then to adopt a single potential that provides a good approximation to the results for all the combinations. Such potentials were developed by various authors including Kalbitzer, Oetzmann, Grahmann and Feuerstein [147], Wilson, Haggmark and Biersack [148], Bister, Hautala and Jäntti [149], and Ziegler, Biersack and Littmark [141].

For applications to alpha particles it is not necessarily best to take such a universal potential, and it might be better to rely on calculations involving alpha-particle projectiles only. However, the application of the so-called universal potential of ZBL to alpha particles appears to be justified by the transport calculations by Fink, Biersack, Städele and Cheng [150], who were able to get good agreement with measured range profiles of 50 to 1500-keV ^{3}He ions in 30 solid elemental targets.

Table 7.18 compares nuclear stopping powers of elements from four calculations. There are large differences between the results from [147]

TABLE 7.18. RATIOS OF NUCLEAR STOPPING POWER FROM VARIOUS PUBLICATIONS.

T90: TRIM-90 [144]
ICRU49: ICRU Report 49 [145]
BHJ79: Bister, Hautala and Jantti [149]
K76: Kalbitzer et al [147]

	1 keV				10 keV			
	T90	ICRU49	BHJ79	K76	T90	ICRU49	BHJ79	K76
H	1	0.996	1.259	0.730	1	1.044	1.170	0.821
Be	1	0.995	1.212	0.724	1	1.039	1.149	0.764
C	1	0.943	1.195	0.755	1	1.034	1.141	0.705
Al	1	0.997	1.137	0.844	1	1.017	1.102	0.639
Ag	1	1.003	0.962	0.928	1	0.993	1.970	0.618
Pb	1	1.002	0.863	0.859	1	0.994	0.895	0.656

and [149] on the one hand, and [144] and [145] on the other. Both [144] and [145] use the ZBL universal potential, and the small differences between them are due to the fact that the TRIM program uses an approximation formula for the calculated numerical results, whereas in [145] the numerical data are used directly.

For nuclear stopping powers of compounds, the results given in [145] are essentially identical to those obtained from the TRIM program, if one uses TRIM92 (from version 92.05 onward).

The nuclear stopping powers found in compilations are calculated without any restriction on the underlying elastic-scattering deflections. In many experimental situations such restrictions are needed. For example, when stopping powers are measured in a foil-transmission experiment, the large deflections associated with large energy transfers to atomic nuclei would tend to remove the projectiles from the cone of acceptance angles of the detector. Therefore the measured stopping power would in effect include only the electronic stopping power plus a small fraction of the nuclear

stopping power. The exact evaluation would require detailed multiple elastic scattering calculations. However, the magnitude of the effect can be estimated by calculating angle-restricted nuclear stopping powers which include contributions only from collisions with deflections smaller than a specified cut-off value. In Table 7.19, ratios of the angle-restricted to unrestricted nuclear stopping powers are given for a few elements, as functions of the cut-off angle.

TABLE 7.19. RATIO OF ANGLE-RESTRICTED TO UNRESTRICTED NUCLEAR STOPPING POWER FOR ALPHA PARTICLES.

		Cut-off angle (in the laboratory system), degrees							
		1	2	5	10	20	50	100	180
	Energy (keV)								
Be	1	0.0070	0.0188	0.0644	0.1507	0.3163	0.6694	0.9256	1.0
	10	0.0426	0.0926	0.2187	0.3680	0.5550	0.8166	0.9616	1.0
	100	0.2045	0.3115	0.4742	0.6036	0.7333	0.8933	0.9778	1.0
C	1	0.0047	0.0129	0.0463	0.1141	0.2568	0.6021	0.8946	1.0
	10	0.0282	0.0652	0.1691	0.3052	0.4909	0.7729	0.9452	1.0
	100	0.1551	0.2539	0.4182	0.5553	0.6951	0.8704	0.9692	1.0
Al	1	0.0022	0.0064	0.0250	0.0663	0.1656	0.4714	0.8226	1.0
	10	0.0117	0.0296	0.0913	0.1914	0.3536	0.6657	0.9019	1.0
	100	0.0795	0.1511	0.2985	0.4433	0.6030	0.8149	0.9480	1.0
Ag	1	0.0008	0.0025	0.0110	0.0327	0.0927	0.3315	0.7254	1.0
	10	0.0031	0.0087	0.0320	0.0810	0.1907	0.4928	0.8228	1.0
	100	0.0195	0.0467	0.1288	0.2444	0.4132	0.6962	0.9059	1.0
Pb	1	0.0006	0.0018	0.0083	0.0255	0.0760	0.2946	0.6945	1.0
	10	0.0019	0.0055	0.0215	0.0575	0.1451	0.4265	0.7866	1.0
	100	0.0104	0.0263	0.0822	0.1743	0.3291	0.6305	0.8811	1.0

TABLE 7.20. COMPARISON OF ALPHA PARTICLE RANGES: RATIOS OF PROJECTED RANGES FROM ICRU REPORT 49 [145] TO THOSE CALCULATED WITH TRIM-90 [144].

	Energy (keV)			
	1	10	100	1000
Be	0.908	1.048	1.211	1.039
Graphite	0.805	0.801	0.867	0.949
Al	0.893	0.869	0.945	0.965
Fe	0.879	0.819	0.918	1.003
Ag	0.914	0.890	0.978	0.989
Au	0.968	0.954	0.981	0.931
U	0.967	0.923	0.889	0.880
Air	0.833	0.813	0.968	0.980
Water, liquid	0.969	0.929	1.120	1.118

7.4.3. Projected Ranges

The projected range is defined as the average depth to which particles penetrate, with the depth measured along the direction in which the particles start out. In the continuous-slowing-down approximation, the projected range is given by

$$\langle R_x \rangle = \int_0^{T_0} \langle \cos \chi(T_0 \Rightarrow T) \rangle_{av} \left[S_{el}(T) + S_{nuc}(T) \right]^{-1} dT \qquad (7.21)$$

where S_{el} and S_{nuc} refer to electronic and nuclear stopping power, resp., and T_0 is the initial particle energy. The quantity $\langle \cos \chi(T_0 \Rightarrow T) \rangle_{av}$ is the average deflection cosine, due to multiple elastic scattering, that occurs as the particle is slowed down from T_0 to energy T. Projected ranges and detour factors for alpha particles are given in [145] (or can be calculated using program ASTAR, see appendix). Projected ranges are also part of the output of the TRIM program. Projected ranges from these two sources are compared in Table 7.20 for several materials and energies. Differences ranging from a few to 20 percent occur. Since the projectile-target potential in both cases is the universal potential of ZBL, the

elastic-scattering deflections and nuclear stopping powers in the two calculations can be presumed to be the same, so that the projected-range differences are probably due to differences in the assumed electronic stopping powers.

7.5. HEAVY IONS

We consider mainly ions from $_4$Be to $_{18}$Ar, in *elemental* targets. For *compounds*, we have, unfortunately, found very few measurement using these ions. Two exceptions are given in Sec. 7.5.1.2.

Instead of describing stopping power as a function of velocity, one conveniently uses T/A_1 (in MeV/nucleon) or $T_r = T/M_1$ (in MeV/u) as energy variable, as for hydrogen ions (see 7.3.1.1). The difference between these two possibilities usually amounts to about 0.1% of the energy variable in the range considered (see the list of masses of the most abundant isotope in [25], in ZBL85 or in file SCOEF.88 of TRIM90). (For the definition of reference codes like ZBL85, see table 7.11).

7.5.1. Electronic Stopping Power

7.5.1.1. The Effective Charge concept.

At sufficiently high speeds where the projectile is bare and where the first Born approximation holds, the electronic stopping power is proportional to Z_1^2 (if one compares different projectiles at equal speeds), i.e., eq.(7.11) holds with $L_1 = L_2 = 0$. At lower speeds the projectile usually carries some orbital electrons, and this reduces the stopping power. If N is the average number of electrons carried, the charge on the projectile (in units of e) is $Z_1 - N$, and the fractional projectile charge is $q = (Z_1 - N)/Z_1$. For distant collisions, all the electrons on the projectile will shield the nuclear charge of the projectile (and hence, reduce the stopping power), but for close collisions, the shielding will be reduced. One therefore introduces an *effective projectile charge* $Z_{1,eff}$ (smaller than Z_1 but larger than the true charge, $Z_1 - N$) to replace Z_1 in

the equation mentioned above.[7] If the projectile's charge state is in dynamic equilibrium with the target, one can describe the measured stopping power S for an arbitrary ion (Z_1) by comparing it to the stopping power S^{ref} for a reference ion (Z_1^{ref}) whose stopping is presumably well known, in the same target and at the same velocity (see also Sec. 7.4.1.2 and Ch. 9):

$$\frac{S}{(Z_{1,eff})^2} = \frac{S^{ref}}{(Z_1^{ref})^2} \tag{7.22}$$

Eq.(7.22) defines $Z_{1,eff}$. Clearly, $Z_{1,eff}$ not only contains information about the projectile charge, but also about deviations from Z_1^2-proportionality. In the following, we assume, unless stated otherwise, that the proton is used for reference and that $Z_1^{ref} = 1$ (note, however, that according to [95] the true equilibrium charge of a slow hydrogen ion is less than 1). As an example, Fig. 7.32, taken from Ziegler [152], shows experimental values for the squared effective charge of Li ions; they approach the value 9 at high speeds, as they should. One also introduces the relative effective charge

$$\zeta = Z_{1,eff}/Z_1. \tag{7.23}$$

The most comprehensive and most practical source of information on stopping, ranges and straggling of all ions of all energies in all solid elements (and in many mixtures and compounds) is the computer program by ZBL85 and its more recent versions Z89, Z90, Z91 or Z92 which are identical to each other and differ from ZBL85 only in some of the coefficients in file SCOEF, and above 10 MeV/u (see 7.3.1.1, and also below).

---

[7] Shima [151] and Gauvin et al [9] have compared the ionic equilibrium charges $Z_1 - N$ of fast heavy ions (as measured after exit from the target foil) to their effective charges, for many different solid targets. They find, in part, a similar behaviour as a function of Z_2, but they also find $Z_1 - N$ *equal to or even larger* than $Z_{1,eff}$, contrary to what was said above. This is presumably because the ionic charge, after exit from the foil, increases as a result of Auger electron emission.

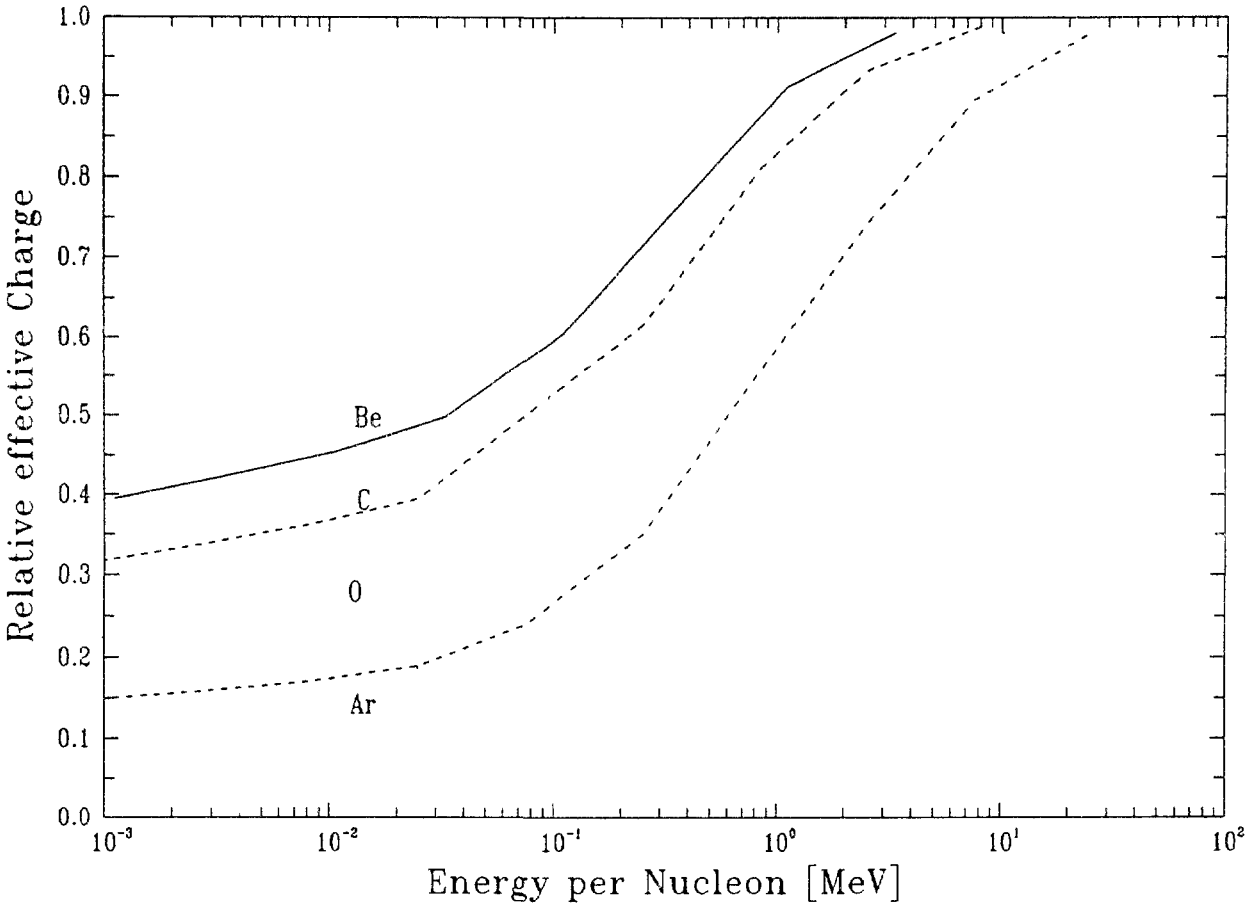

Fig.7.33. Relative effective charge ζ for $^{9}Be, ^{12}C, ^{16}O$ and ^{40}Ar ions in carbon, calculated using Ziegler's program STOP (contained in TRIM90). The curves are essentially the same for other targets, except at the low energy end (see Fig.7.34).

The semi-empirical program Z90 is based on eq. (7.22) and on the proton as a reference projectile. It uses the Brandt-Kitagawa theory [153] to calculate Z_1^{eff}, as follows: The ions penetrating the solid are assumed to be in charge state equilibrium, and their fractional ionization q is determined as a function of the relative velocity between the electrons in the solid (described by the Fermi velocity v_F) and the ion. Then the screening length Λ for the ion is calculated as a function of Z_1 and q, including an empirical correction factor LFCTR given in file SCOEF for every Z_1. Finally, the fractional effective charge ζ is found from q, v_F and Λ. In this procedure then, ζ depends on Z_2 only through v_F. Fig.7.33 shows the fractional effective charge according to Z90, for Be, C, O and Ar ions, as a function of T/A_i. As expected, the heavier the ion, the more speed is necessary to strip off all electrons.

The dependence of ζ on v_F just mentioned leads to a small Z_2-dependence of the stopping power additional to the Z_2-oscillations already present in the proton data (see Sec. 7.3.1.1). Fig.7.34 shows this additional dependence on Z_2 for carbon projectiles, according to Z90. Only for the extremely small energy of 12 keV there are sizeable variations; at 100 keV/nucleon the oscillations are practically gone, and the effective charge becomes target-independent.

In practice, this target-independence of ζ is useful as a first approximation, but it cannot be completely correct. Geissel et al [154,155] in their very useful reviews of heavy ion stopping, show that the peaks of the Z_2-oscillations found for H and He projectiles (cf. Sec.7.3.1.1) stay roughly at the same Z_2-values but become more pronounced at large Z_1 (e.g., for Pb projectiles). These enhanced oscillations can *not* be reproduced by the program Z90 (because here, ζ is essentially independent of Z_2, as noted

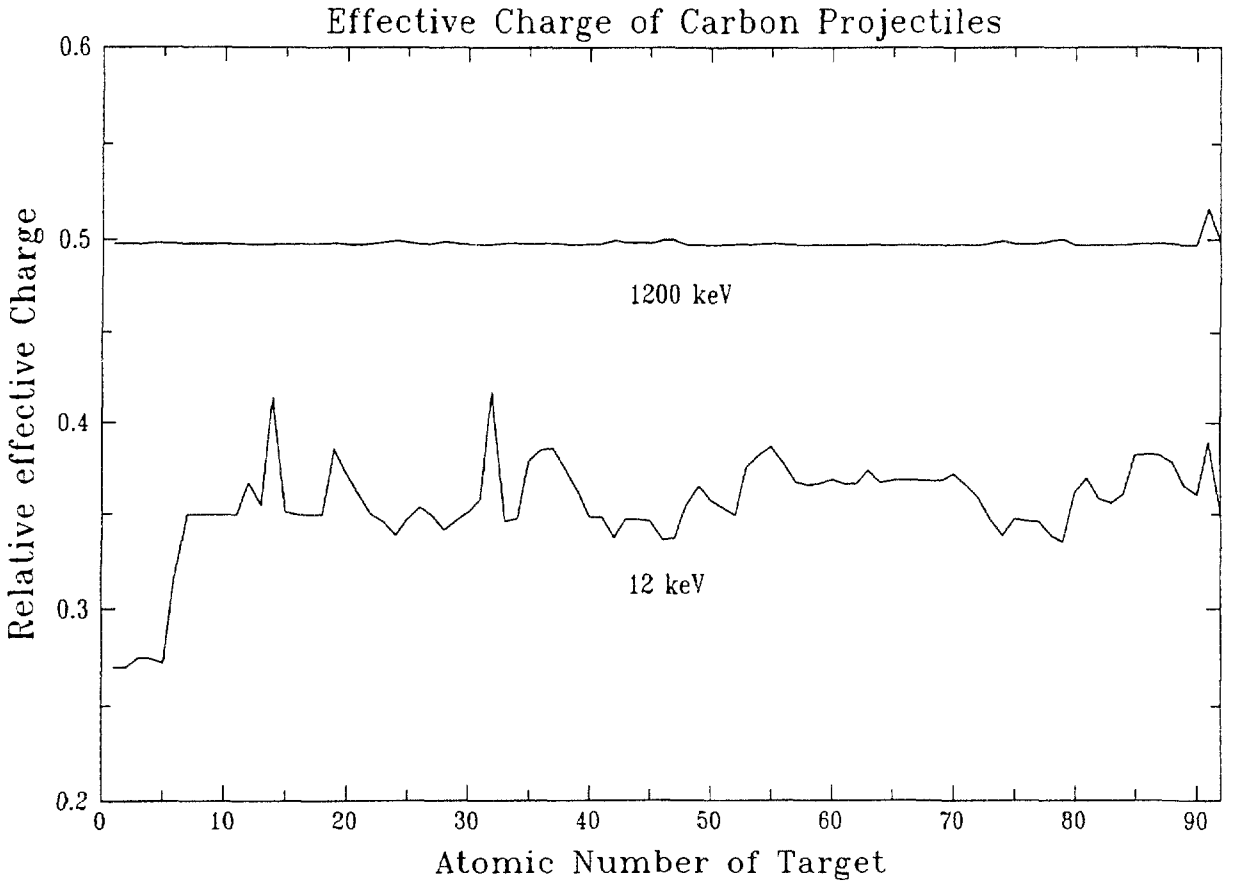

Fig.7.34. Relative effective charge ζ for carbon projectiles, versus target atomic number Z_2, according to Ziegler's stopping tables (Z90), for T = 12 keV and T = 1200 keV.

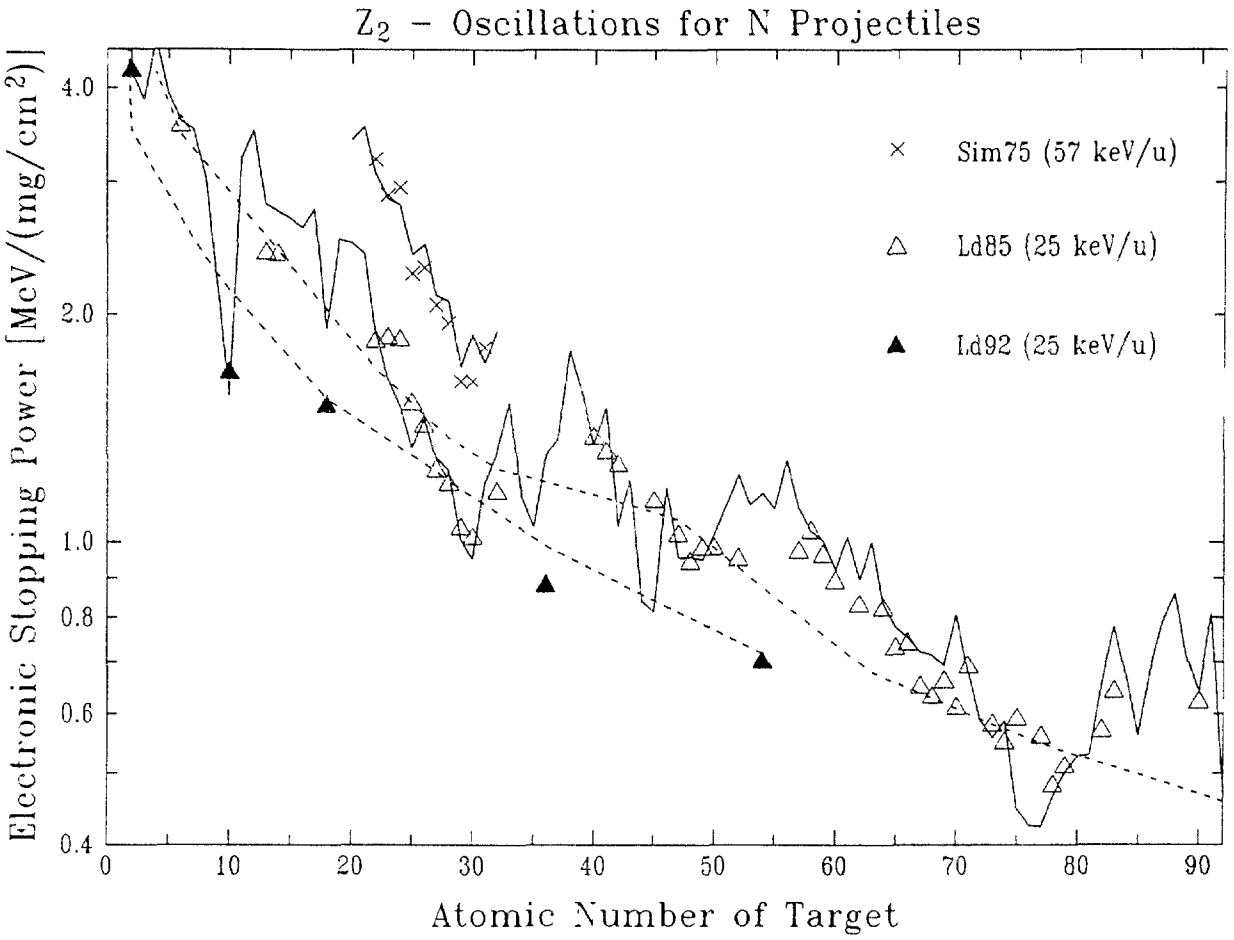

Fig.7.35. Electronic stopping power as a function of target atomic number Z_2, for nitrogen projectiles. The points shown by symbols were deduced from experimental range values, assuming a stopping power proportional to v_1 (full triangles: inert gases; other points: solid targets). Lower full curve: Z90 for 25 keV/u ($v = v_0$); upper full curve: Z90 for 57 keV/u. Remaining curves by Northcliffe and Schilling [157] for 25 keV/u: -.- solids, --- gases.

above). But for nitrogen and argon ions, the measured oscillations are still fairly well reproduced by Z90, cf. figs.7.35 and 7.36. The well-known stopping tables by Northcliffe and Schilling [157] that date from 1970 and are sometimes used even today, follow the general trend of the data (fig. 7.35) but do *not* contain Z_2-oscillations.

For specific ion energies less than about 10 - 20 keV/u, Z90 assumes $S \propto v_1^{0.75}$ for Si and Ge targets (if $Z_1 \leq 19$) and for C targets, and $S \propto v_1$ for all other targets (see, e.g., Fig. 7.45 for an Ar target).

In going from ZBL85 to Z89, some of the proton stopping coefficients in file SCOEF were changed, as mentioned in Sec. 7.3.1.1. This produced generally the same relative changes in heavy ion as in proton stopping powers. In addition, most of the values v_F were changed for $Z_2 < 19$. For ^{12}C on Na, e.g., this change reduced S by 16% (below 13 keV/u). In addition, the correction factors LFCTR (see above) were changed for Li, B, Si and P projectiles. For ^{31}P on Mg, e.g., this reduced S by 19% (below 20 keV/u). Kuronen [158] found that the difference between these two codes is less than 2% for the cases studied by him, but there are evidently larger differences in other cases.

7.5.1.2.Solid Targets.

If one plots the measured stopping cross section versus Z_1, for a given Z_2 and at a fixed projectile velocity, one also finds oscillations ("Z_1-oscillations"). Ward et al [159] and others have investigated these

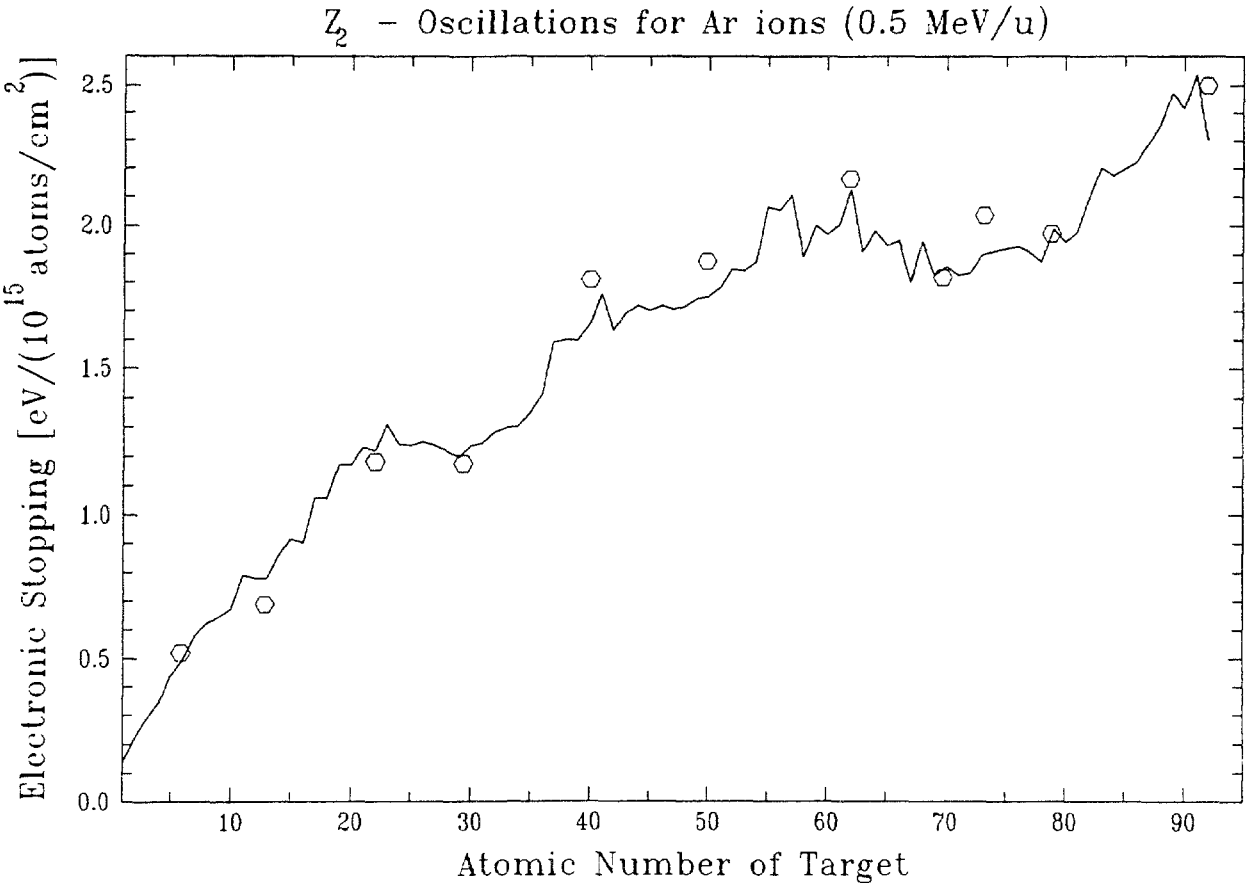

Fig.7.36. Electronic stopping power for Ar ions (0.5 MeV/u), versus Z_2. Curve: Z90; symbols: values measured on solid targets [156]

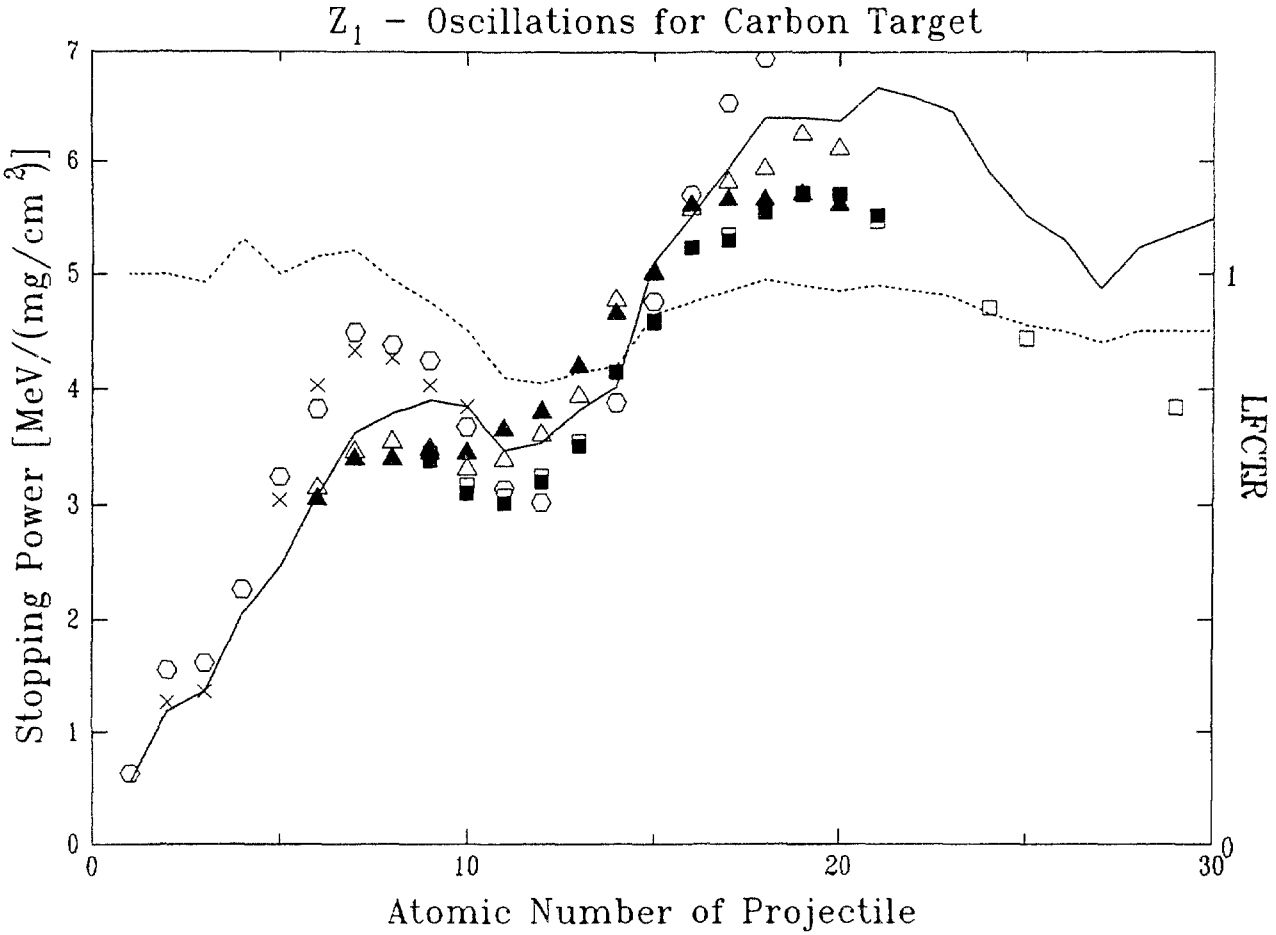

Fig.7.37. Electronic stopping power of carbon for light projectiles at $v_1 = v_0$, versus Z_1. The experimental points, measured at various ion speeds given below, were reduced to $v_1 = v_0$, assuming the stopping power to be proportional to v_1. Full curve: Z90 for $v_1 = v_0$.
Open triangles: Wr79 (0.818 v_0); full triangles: Wr79 ($v_1 = v_0$); open squares: Len86a (0.8v_0); full squares: Len86b (0.8v_0); crosses: Hof76 (0.402 v_0); hexagons: Or63, Or65 (0.41 v_0). Beyond $Z_1 = 30$, the discrepancy between Z90 and Len86a becomes very large.
Dashed curve: empirical correction factor LFCTR (Z90; right scale).

oscillations in several materials . An example for carbon is shown in fig. 7.37. Ward et al found that the amplitude and the phase of the oscillation depends on the material; the amplitude decreases with increasing projectile velocity. These oscillations have been built into Z90 by introducing the empirical correction factor LFCTR mentioned above. Fig.7.37 shows this correction factor; it also shows that Z90 represents the oscillation quite well (within about 10%), up to $Z_2 = 20$. The Z_1- oscillation for a carbon target has been calculated by Echenique et al [100] using a non-linear

density-functional approach; the result agrees rather well with experiment, except that the calculated depth of the minimum at $Z_1 \approx 12$ is too low.

For aluminum, the Z_1-oscillation is similar to that for carbon; for nickel, the amplitude is considerably smaller [159]. This change cannot be reproduced by Z90 because in this calculation, the variation of the relative effective charge with Z_1 is practically independent of Z_2 (see fig.7.38).

Evidently, it is of interest to compare the ZBL85 and the Z90 stopping powers to recent experiments. We discuss such comparisons in the following four paragraphs. Sofield [160], e.g., in a recent review of heavy-ion energy loss, finds that the ZBL85 code provides a sound practical basis for stopping power calculations, but that one may have to resort to experiment if high accuracy is required.

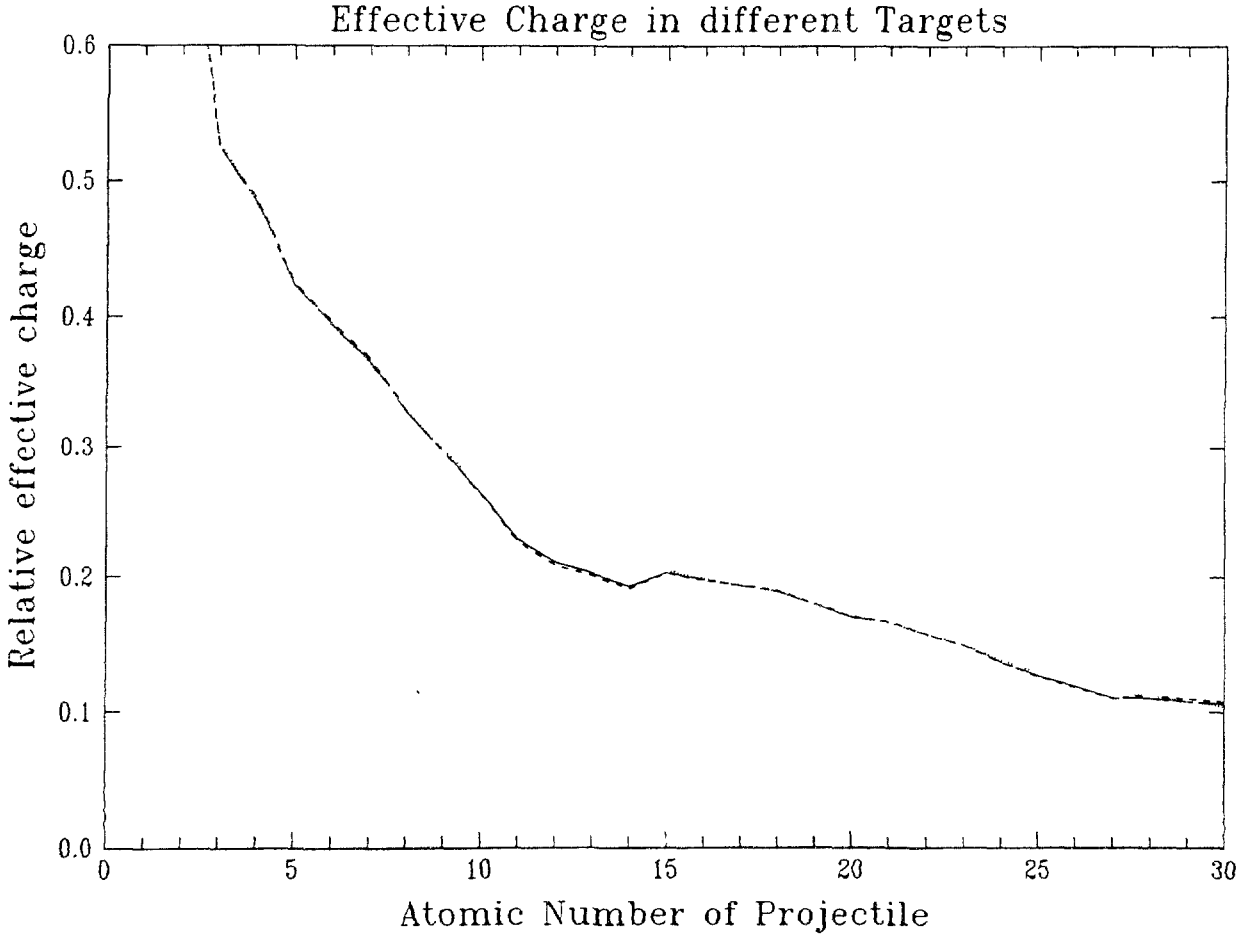

Fig.7.38. Relative effective charge ζ, according to Z90, for light projectiles in various targets: full curve: C; dashed curve: Al; dotted curve: Ni. The curves are almost identical.

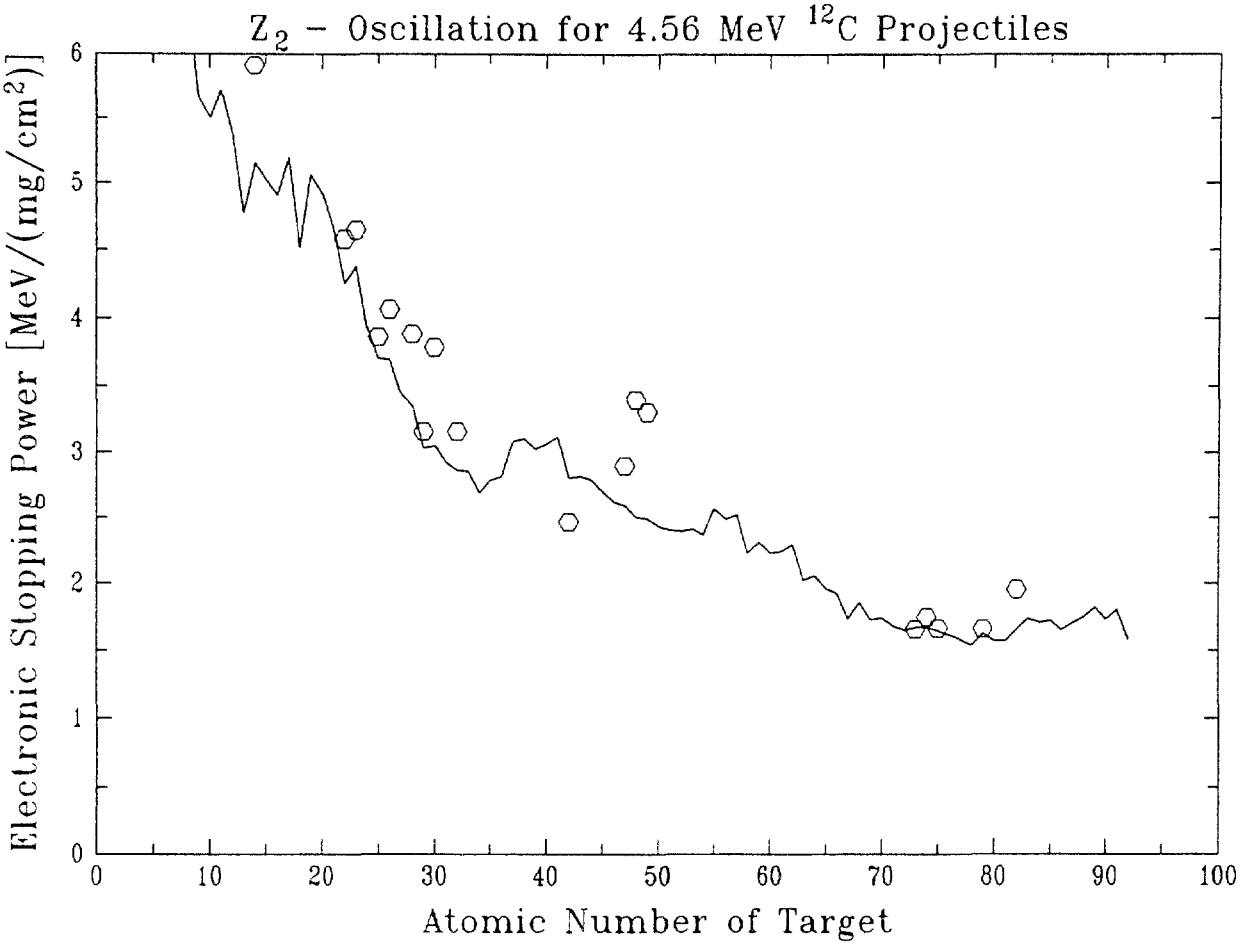

Fig.7.39. Electronic stopping power for ^{12}C ions at 4.56 MeV in various targets, versus Z_2. The experimental points are due to Kuronen et al [162], the curve is from Z90.

The Helsinki group has done many useful comparisons in recent years, for energies of about 1 MeV/nucleon or less. Räisänen and Rauhala [161] find that Z89 gives systematically better fits to experimental data than Z80 (except for ^{7}Li ions). Kuronen et al [162] measured the stopping power for ^{12}C ions (T/A_1 = 0.4 to 1.4 MeV) in 18 different elemental solids. They give correction factors f_c by which ZBL stopping should be multiplied to give their experimental results. Fig. 7.39 shows their experimental stopping power for ^{12}C ions (0.38 MeV/u), compared to the prediction of Z90. One sees agreement in most cases within the experimental error of 12%. (Note that the Z_2-oscillation appears much reduced compared to the original publication [162] since we have plotted S/ρ rather than S). For Li-, B-, C-, N-, and O- projectiles in Au, they also find mostly agreement with ZBL85, within the experimental error of 4%.

Similarly, Räisänen and Rauhala [163] measured the stopping of Li-, B-, C-, N-, and O-ions (T/A_1 = 0.2 to 2.1 MeV) in Mylar, Kapton, Havar, and nickel and compared it to Z80, ZBL85, and Z89. For Mylar and Kapton targets, Z89 (with bonding correction, see Sec. 7.3.1.2) was generally best, pointing to a positive effect of this correction; the measured values for B-ions were, however, larger than predicted; also, for Li-ions, the special values given for Li in Z80 were better. For Nickel and for Havar (a foil consisting mainly of Cr, Fe, Co, and Ni), there was agreement with ZBL85 for N- and O-ions, but for B- and C-ions, experimental values were higher than Z80 and ZBL85 by up to 15%. This result may correspond to the finding by Anthony and Lanford [164] that experimental stopping for C-ions in Cu is higher than predicted by Z_1^2-scaling; it points to a Z_1-oscillation not described by the Ziegler stopping power.

In their paper [165] on the stopping power of bisphenol A-polycarbonate $C_{16}H_{14}O_3$ for Li, B, C, N, and O ions, Rauhala and Räisänen compare their results to their previous [163] data on Mylar ($C_{10}H_8O_4$) mentioned above. Since both materials contain the same elements, comparing them will provide a good test of Bragg's rule. For all ions, the authors find that the measured stopping power of polycarbonate exceeds that of Mylar by a few percent, and that this difference is correctly predicted by Bragg's rule. (Only for Li, the predicted difference is too small to be measurable). The small bonding corrections predicted by Z89 (cf. Sec. 7.3.1.2) are, however, obscured by the noticeable Z_1- oscillation.

Bauer and Rössler [166] have recently made another test of Bragg's rule. They find that, for N ions in Al_2O_3 and SiO_2, the stopping cross section is about 20% higher at 25 keV/u than expected from Bragg's rule. This large effect is in a direction opposite to the effect found for H ions in the same materials (see 7.3.1.2); evidently the influence of projectile charge states is of importance here.

For Mg-ions in 17 elemental solids, Arstila et al [167] find fair agreement with ZBL85 stopping for $2v_0 < v_1 < 5v_0$; their correction factors f_c are given in table 7.21 (Note that v_0^2 = 24.8 keV/u). For $v_1 < 2v_0$, however, they find the electronic energy loss much higher and its velocity dependence different from that predicted by ZBL85. This is in contrast to the finding by other members of the same group [168] that for Al- and Si-ions in Ta at $0.4v_0 < v_1 < 4v_0$, the velocity dependence agrees with that predicted by ZBL85. Similarly, Land et al [169] found that the electronic

TABLE 7.21. LIST OF CORRECTION FACTORS f_c ACCORDING TO ARSTILA et al [167], *for Mg ions in the velocity range* $2v_0 < v_1 < 5v_0$. f_c *is the ratio of experimental stopping powers to* ZBL85 *values. Error of* f_c: 5%.

Target	f_c
$_{22}$Ti	1.10
$_{23}$V	0.90
$_{26}$Fe	0.93
$_{27}$Co	0.97
$_{28}$Ni	0.99
$_{29}$Cu	1.03
$_{32}$Ge	1.05
$_{41}$Nb	1.05
$_{42}$Mo	1.15
$_{46}$Pd	1.05
$_{47}$Ag	1.08
$_{72}$Hf	1.09
$_{73}$Ta	1.07
$_{74}$W	1.05
$_{75}$Re	1.05
$_{78}$Pt	1.05
$_{79}$Au	0.96

stopping power of Fe, Ni and Zr for ^{14}N ions is consistent with velocity proportionality from 14 to 140 keV/u.

To arrive at an estimate of the accuracy of stopping powers for relevant projectiles, we show here a few figures comparing experimental values to Z90. Fortunately, we find that C-, N, and O-projectiles, which are relevant for radiotherapy, have also been measured most frequently. Figs. 7.40 and 7.41 show the result for C- and O-ions in aluminum. Evidently, Z90 agrees with the experimental data within about 20% between 0.01 and 0.1 MeV/u, and within about 10% above 0.1 MeV/u. The same is true for C- and O-ions in carbon (not shown), if one disregards the slightly low data by Po60. There is similarly good agreement for C-, N, and O-ions on nickel, and for C- and O-ions on silver. The data for N-ions on aluminum form rather an exception (Fig. 7.42): here, the agreement is only within 20% in the range shown.

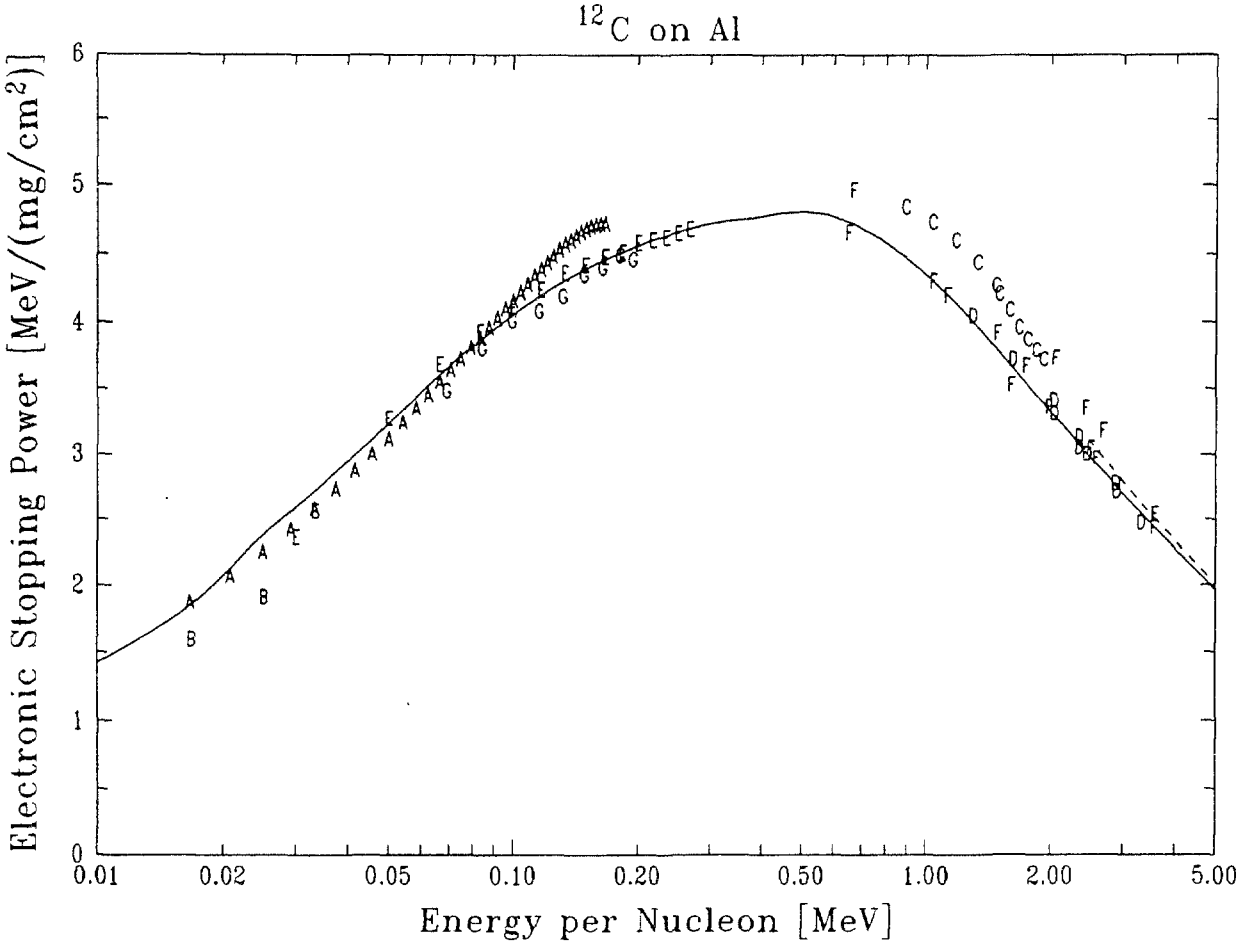

Fig.7.40. Electronic stopping power of Al for ^{12}C ions. Full curve: Z90; dashed curve: HU90. The symbols indicate measured points from the following references: A Sa91; B Wr79; C Rä91; D Ay82; E Po60; F Ab91; G Ab93.

It was mentioned above that the effective charge introduced in eq.(7.11) neglects corrections of higher order in Z_1. Anthony and Lanford [164] did extensive measurements of the stopping power of five solids for many ions near the stopping maximum; they could represent their results better by using a relative effective charge ζ that decreases with increasing Z_2 and by including L_1- and L_2-corrections, rather than by the formalism of Z80. The importance of L_1- and L_2-corrections in connection with effective charge has also been stressed by Semrad et al [170] and by Abdessalam et al [171].

For higher energies ($2.5 < T/A_1 < 500$ MeV), Hubert et al (HU90) produced a new table of stopping powers and ranges for all ions in the range $2 \leq Z_1 \leq 103$ (assuming the most probable mass for the ion), in 36 solids from Be to U, based mainly on the very accurate (1-3%) measurements

from their own group (For a recent review of this work, see Bimbot [172]). Their table is based on eq. (7.22). They find that, to represent the data adequately, one must use a ζ that decreases with increasing Z_2 [173]. They use the ^{4}He-projectile (which is fully stripped at these energies) and the He stopping power table Z77 below 150 MeV/u as a reference. Presumably, this table represents the ^{4}He data better than the all-encompassing program ZBL85 (cf. Sec. 7.4.1.4). Above 150 MeV/u, HU90 use Janni's proton table (J82) instead, converted to ^{4}He data by assuming Z_1^2-proportionality.

As an example, Fig. 7.43 compares HU90 to Z90 for 30 MeV ^{12}C ions, i.e., at the low energy end of the HU90 table. Evidently, the two agree rather well (average difference 2.6±2%). As seen in Fig. 7.41, the

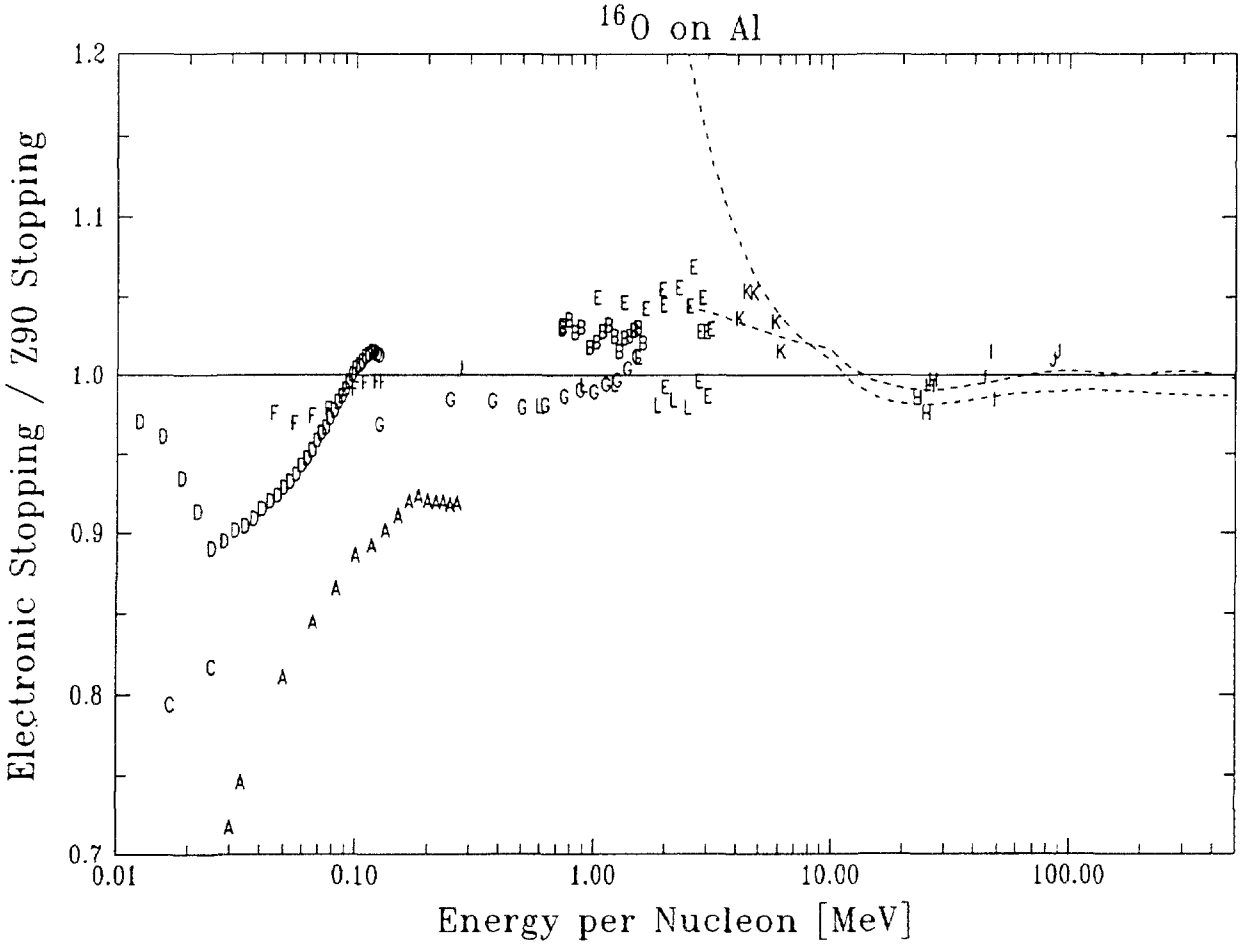

Fig.7.41. Electronic stopping power of Al for ^{16}O ions, divided by values from Z90. Dashed curve: HU90; dot-dashed curve: BEST. The symbols indicate measured points from the following references: A Po60; B Rä91; C Wr79; D Sa92; E Ab92a; F Ab93; G BG65; H,I,J: Ga87; K Bi78; L Sf78. The apparent kinks in the measurement by Sa92 at 0.025 MeV/u and in the HU90 and BEST curves at 10 MeV/u are due to the fact that the Z90 curve is continuous but not differentiable at these points.

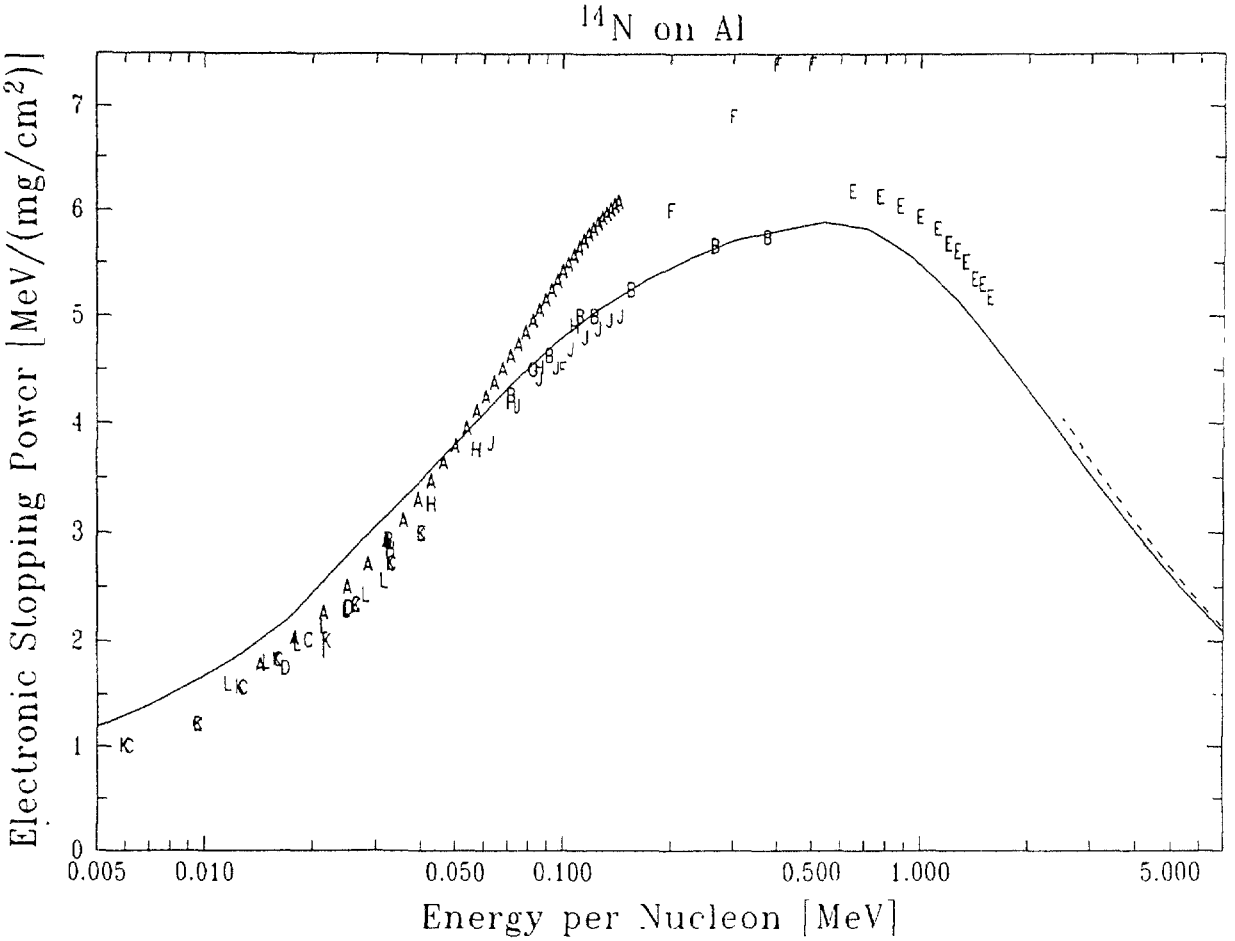

Fig.7.42. Electronic stopping power of Al for ^{14}N ions. Full curve: Z90; dashed curve: HU90. The symbols indicate measured points from the following references: A Sa91; B Po61; C Sc82; D Wr79; E Rä91; F Na68; G Tp62; H Po59; I Me78; J Ab93 (^{15}N!); K Sh84; L Ya83

agreement improves toward higher energy; the average difference becomes 0.6±2% at 120 MeV and 0.4±0.4% at 1200 MeV. For Ar ions, the difference is slightly larger at 2.5 MeV/u (-4.6±5%), but similar at the larger specific energies.

Hubert et al give ζ as an analytical function for all but the lightest targets; hence their values can be calculated for *all* solid targets, above about Z_2= 11.

At high energy, where the projectiles are fully stripped (ζ > 0.99 for C ions above 8 MeV/u, and for Ar ions above 38 MeV/u, see Fig. 7.33), one can use the BEST program in place of HU90. BEST has the advantage that it can be used for *all* target elements and for many compounds. For ^{16}O on Al,

e.g., (Fig. 7.41) the two agree within 1% above 6 MeV/u (see also fig. 7.44).

In summary, we estimate that the Z90 program describes the available empirical stopping power data of key substances for C to Ar ions from 0.01 to 0.1 MeV/u within about 20%, and above 0.1 MeV/u, within about 10%. For energies above 2.5 MeV/nucleon, HU90 state that the experimental points fall near their table values "with deviations typically less than 5%". The agreement of HU90 with Z90 and (partly) with BEST is evidently better than that over most of the energy range above 2.5 MeV/nucleon [Even for an extreme case like uranium ions at T/A_1 = 2.5 MeV in carbon, HU90 and Z90 disagree only by 16%].

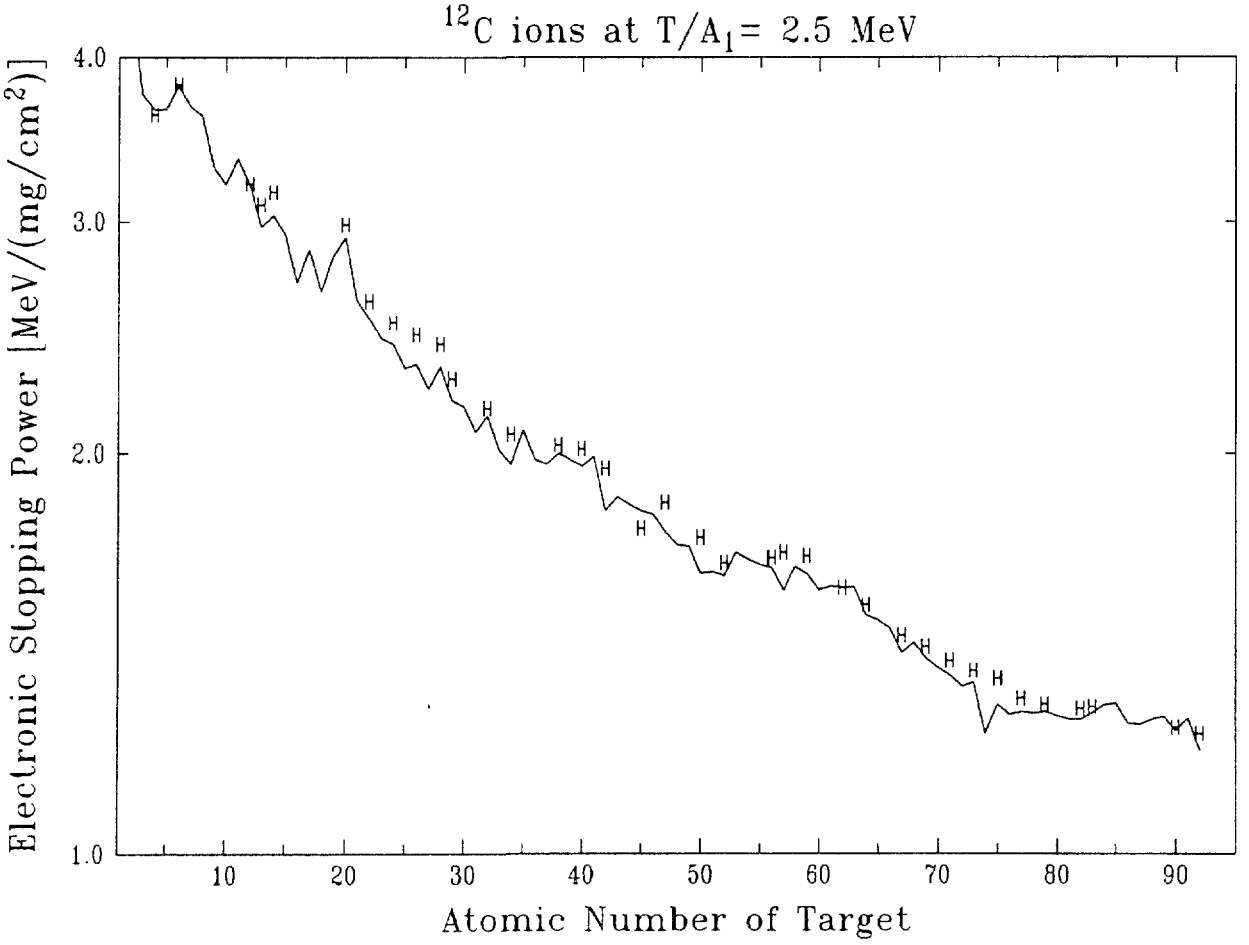

Fig.7.43. Electronic stopping power of various elemental targets for ^{12}C ions at 2.5 MeV per nucleon. The curve is due to Z90, the symbols correspond to HU90.

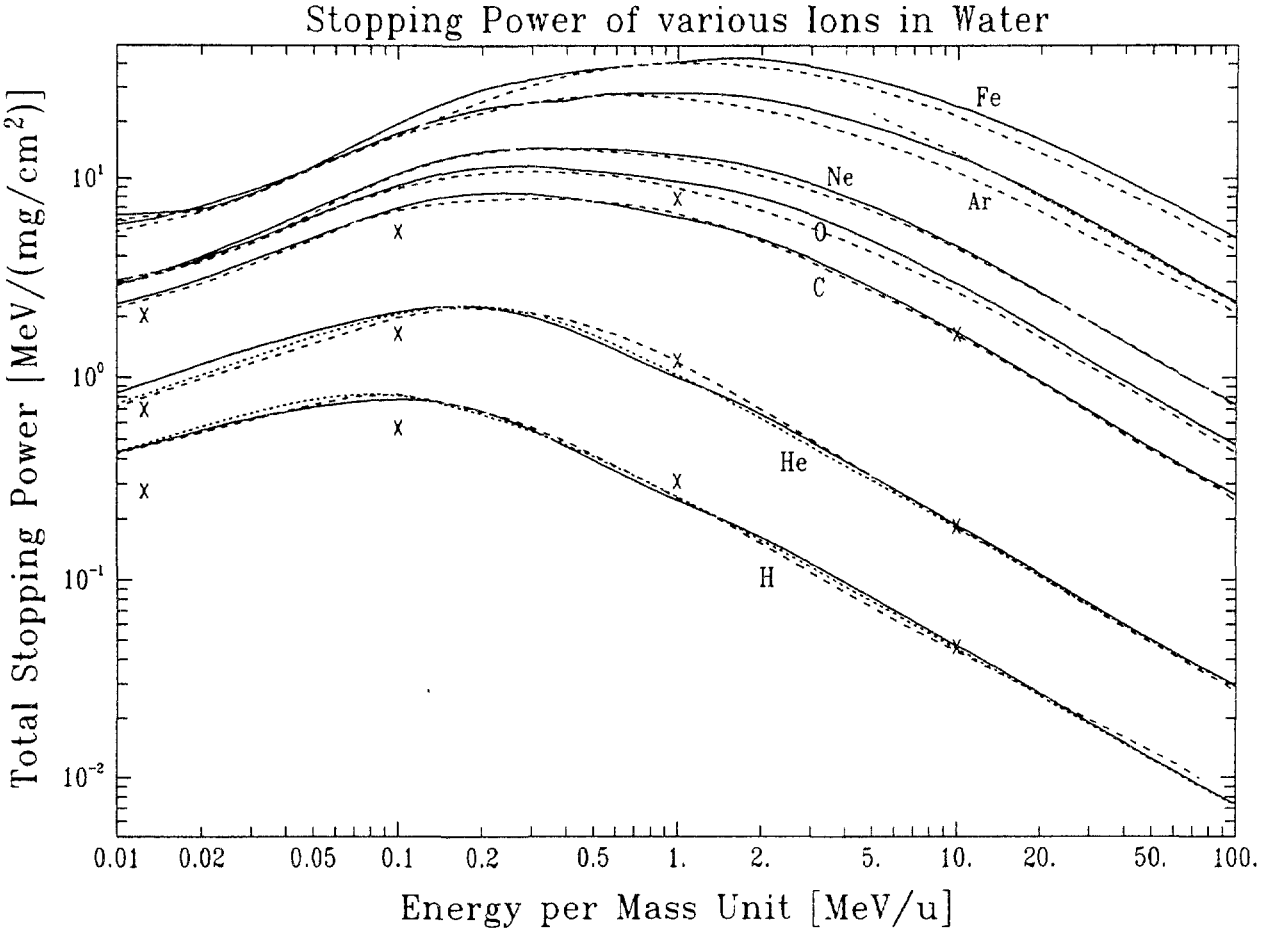

Fig.7.44. Total (electronic plus nuclear) stopping power of water for H, He, C, O, Ne, Ar, and Fe ions. Full line: Z90; dashed line: Stewart [174]; short dashed: ICRU49; dash-dotted: BEST. X...Northcliffe and Schilling [157] for H, He and C ions.

7.5.1.3. Liquid Targets: Water.

It was mentioned in Sec. 7.3.1.3 that one assumes the mass stopping power of liquid water to agree with that of ice. Figure 7.44 compares the stopping power from various tabulations for H, He, C, O, Ne, Ar and Fe ions in water. Good overall agreement between the old Stewart program [174] and Z90 can be seen for light ions up to Neon, where Stewart was able to base his calculations on experimental data. Only for He ions around 0.8 MeV/u, Stewart is about 15% high. For fast Ar and Fe ions, Stewart is about 15% low, as one can see from a comparison with BEST.

Fig. 7.44 also shows a few points from Northcliffe and Schilling [157]. Evidently, this table disagrees by as much as 30% from the other results. This is surprising since both the Stewart and the Northcliffe

calculations are based on the original work of Northcliffe [157]. Incidentally, neither calculation contains Z_1- or Z_2-oscillations (see also fig. 7.35).

Deviations from Bragg additivity cannot easily be seen in fig. 7.44, due to the scale used, but all the curves shown (except for Stewart's) are based on the existence of such deviations. See also fig. 7.19 and tables 7.13, 7.14, and 7.17.

The curves in fig. 7.44 include the contribution of nuclear stopping (see Sec. 7.5.2). This contribution is small except for Fe ions at low energy.

7.5.1.4. Gas targets.

In 1982, Geissel et al [176] observed for the first time that the mass stopping power for partially stripped very heavy ions (of several MeV/u) is considerably less in a gas than in solids of similar Z_2. This is due to a density effect as predicted by Bohr and Lindhard [177]: in a gaseous (dilute) medium, an ion excited in a collision with a target atom can de-excite before the second collision; but in a solid (dense) medium, the ion, while still excited, has a high probability of undergoing a second collision that may lead to ionization. Hence the ionic equilibrium charge, and also the effective charge, is higher in the solid than in the gas [172]. Hérault et al [178] have shown that at very high energies, where the ions are fully stripped, the gas-solid difference vanishes, as expected. They also gave a useful curve that shows the gas-solid difference as a function of the relative effective charge in the solid, ζ_s. For example, at $\zeta_s = 0.9$ (i.e., for 1.75 MeV/u ^{12}C or 7.8 MeV/u ^{40}Ar ions, see Fig. 7.33) the difference amounts to 10%.

It is worth noting that the gas-solid difference mentioned here (a projectile state effect) is opposite to the difference found for protons (a target effect), which is discussed in Sec. 7.3.1.3.

At lower energies, the gas-solid difference can be seen superimposed on Z_2-oscillations in the data by Land et al for nitrogen projectiles, Fig. 7.35, where $\zeta_s \simeq 0.37$. Here, Z90 describes the measurements for He and Ne well, but becomes progressively too high for the heavier gas targets. Although Z90 is strictly speaking for solid targets only (according to the

title of the book, ZBL85), it is still useful for gas targets, at least as a first approximation.

Hvelplund [179] found that the stopping power of air, He and Ne for light projectiles is roughly proportional to velocity between 100 and 500 keV. Price et al [180] found the stopping power of N ions in He proportional to velocity from $v_1 = v_0$ up to 2.25 v_0; for N ions in Ar, it is linear in (but not proportional to) v_1 (see Fig. 7.45). Hvelplund [179] has also investigated Z_1-oscillations in He, Ne and air at $v_1 = 0.9v_0$; he found a behaviour similar to that shown in Fig. 7.37.

A tabulation of stopping powers of gas targets for projectiles in the range 2-100 MeV/u, is being prepared by Bimbot et al [181].

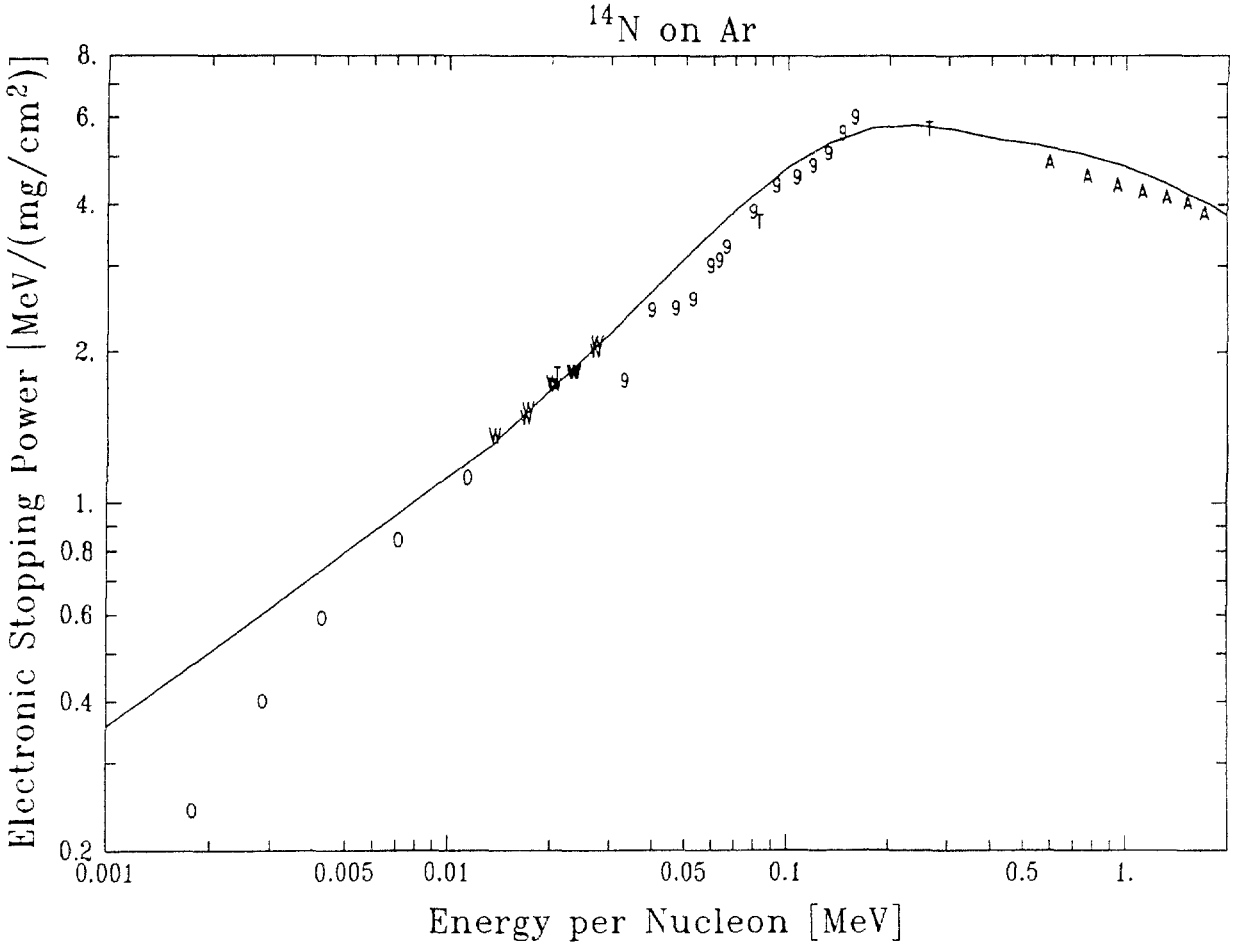

Fig.7.45. Electronic stopping power of Ar for ^{14}N ions, versus energy. Measured points are from the following references:
A And69; O Or68; T Tp62; W We53; 9 Pr91.

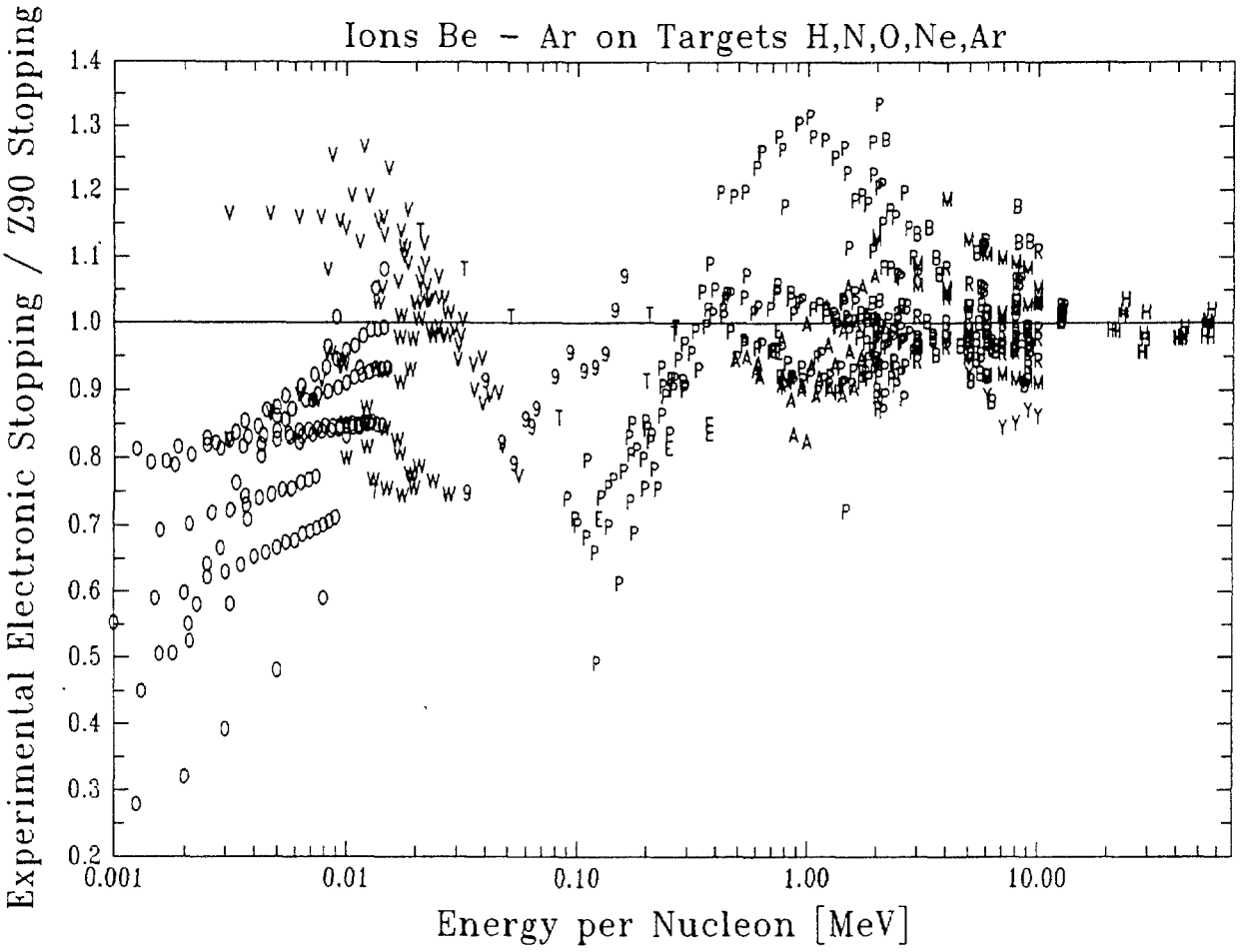

Fig.7.46. Experimental electronic stopping of light elementary gas targets for various light ions, divided by electronic stopping from Z90. The symbols have the following meaning (Here, "ion" means the most abundant isotope of the ion):

Symbol	Ref.code	Ions	Targets
A	And69	Be,B,C,N,O,Na,Al	Ar
B	Bi89	Ne,Ar	H_2,N_2,Ne,Ar
E	Ef75	N,Ne,Ar	N_2,Ar
H	He91	O,Ar	H_2,N_2,Ar
M	Mar62	C,Ar	H_2,N_2,Ar
O	Or68	B,C,N,O,F,Ne	N_2,Ar
P	Pi68	S,Cl	H_2,N_2,Ar
R	R160	B,C,N,O,F	O_2
T	Tp62	B,N,Ne	H_2,Ar
V	Hv71	Be,B,C,N,O,F,Ne,Na,Mg	H_2,O_2,Ne
W	We53	N,Ne	H_2,Ar
Y	Yon80	Ar	Ar
9	Pr91	N	Ar

Unfortunately, for gas targets, there are hardly any cases where more than four authors have measured the same projectile/target combination. An exceptional example, with data (for ^{14}N in Ar) from five authors, is shown in Fig. 7.45. To make some comparison possible in spite of the scarcity of data, we have plotted all the stopping data measured with Be,B,C,N,O,F, Ne,Na,Mg,Al,S,Cl and Ar ions in H_2,N_2,O_2,Ne and Ar, divided by the corresponding value from Z90, in Fig. 7.46. Evidently, the agreement with Z90 is worse here than for solid targets: it is within 5% from 10 to 60 MeV/u, within 15% from 1 to 10 MeV/u, and within 30% from 0.01 to 1 MeV/u. Below 0.01 MeV/u, there are even larger discrepancies, especially for the Or68 measurements in Ar (see also Fig. 7.45).

A few measurements on *compounds* (CH_4 and CO_2) have been done by Bi89 and He91, at specific energies > 2 MeV/u where Bragg's rule should be fairly accurate (indeed, Bragg additivity has been *assumed* for alpha particles in the course of the evaluation). The only measurements on a gas *mixture* have been done on air (We53, Tp62, Hv71). Even though these were at low specific energy, Bragg's rule should be valid here, provided the condition discussed by Golser and Semrad [8] does not apply (see 7.3.1.2).

7.5.2. Nuclear Stopping Power

Nuclear stopping and the universal potential due to ZBL85 have been discussed in Sec. 7.4.2. The importance of Coulomb scattering and hence, of nuclear stopping increases with increasing Z_1 and Z_2, but it is always important only at low energies. Within the range $Z_2 < 27$, i.e. for key substances, electronic stopping becomes larger than nuclear stopping for C ions above about 1 keV/u, and for Ar ions above about 10 keV/u. Like electronic stopping, nuclear stopping can be calculated using the stopping routines contained in the TRIM programs (with respect to nuclear stopping, ZBL85 and Z90 are identical; Bragg's rule for nuclear stopping in compounds is used correctly only from version 92.05 of TRIM on). As discussed for protons and for alphas, the numbers thus obtained are based on the assumption that all scattering angles are allowed, an assumption not always appropriate (see chapters 7.3.2 and 7.4.2). For ^{12}C ions of 0.017 MeV/u on Al (the lowest energy experimental points shown in Fig. 7.40), nuclear stopping according to Z90 amounts to only 6% of electronic stopping, and the actual correction in a forward scattering geometry (e.g., Sa91a) is

certainly less than that and hence negligible. For range calculations, the nuclear contribution to stopping can become quite important (e.g., in Fig. 7.49).

For light ions in polycrystalline Ta at very small velocities ($\ll v_o$), Kuronen and his coworkers [158] have found that the nuclear stopping according to ZBL85 should be multiplied by a factor between 0.7 and 0.8 (for a geometry where all scattering angles are allowed).

7.5.3. Energy Loss Straggling

Bohr's energy-independent straggling formula was given in Sec. 7.3.3, and it was stated there that crystal structure and non-uniform film thickness can influence measurements on the straggling of protons in solids to a great extent. The same holds true for heavy ions, so that here also, measurements on gas targets are preferable for a comparison with theory [154].

According to Besenbacher et al [118a], the measured straggling for gas targets consists of the contributions due to statistically independent electron excitations (corresponding to the Bohr formula), due to intra-atomic electron correlations, due to charge exchange, and (for molecular targets) due to intra-molecular correlations. For low velocity heavy ions ($v/v_0 < Z_1^{2/3}$), the intra-atomic contribution should dominate [118a]. This contribution can be approximated by the Firsov-Hvelplund formula [179,183] for the straggling variance Ω^2_{FH} (based on the Thomas-Fermi atomic model):

$$\Omega^2_{FH} = (8\times10^{-15}\ eV^2cm^2/atom)\ n\ s\ (Z_1 + Z_2)^{8/3}\ (v/v_0)^2 \qquad (7.24)$$

Fig. 7.47, taken from Geissel et al [184], compares straggling measurements carried out on gas targets by four groups [179,184-186] to eq.(7.24). The experimental results in units of Ω^2_B are plotted in reduced energy units so that eq. (7.24) appears as a straight line; the agreement is surprisingly good.

To understand straggling measurements on solid targets, one must take surface roughness into account. If this roughness is described by a

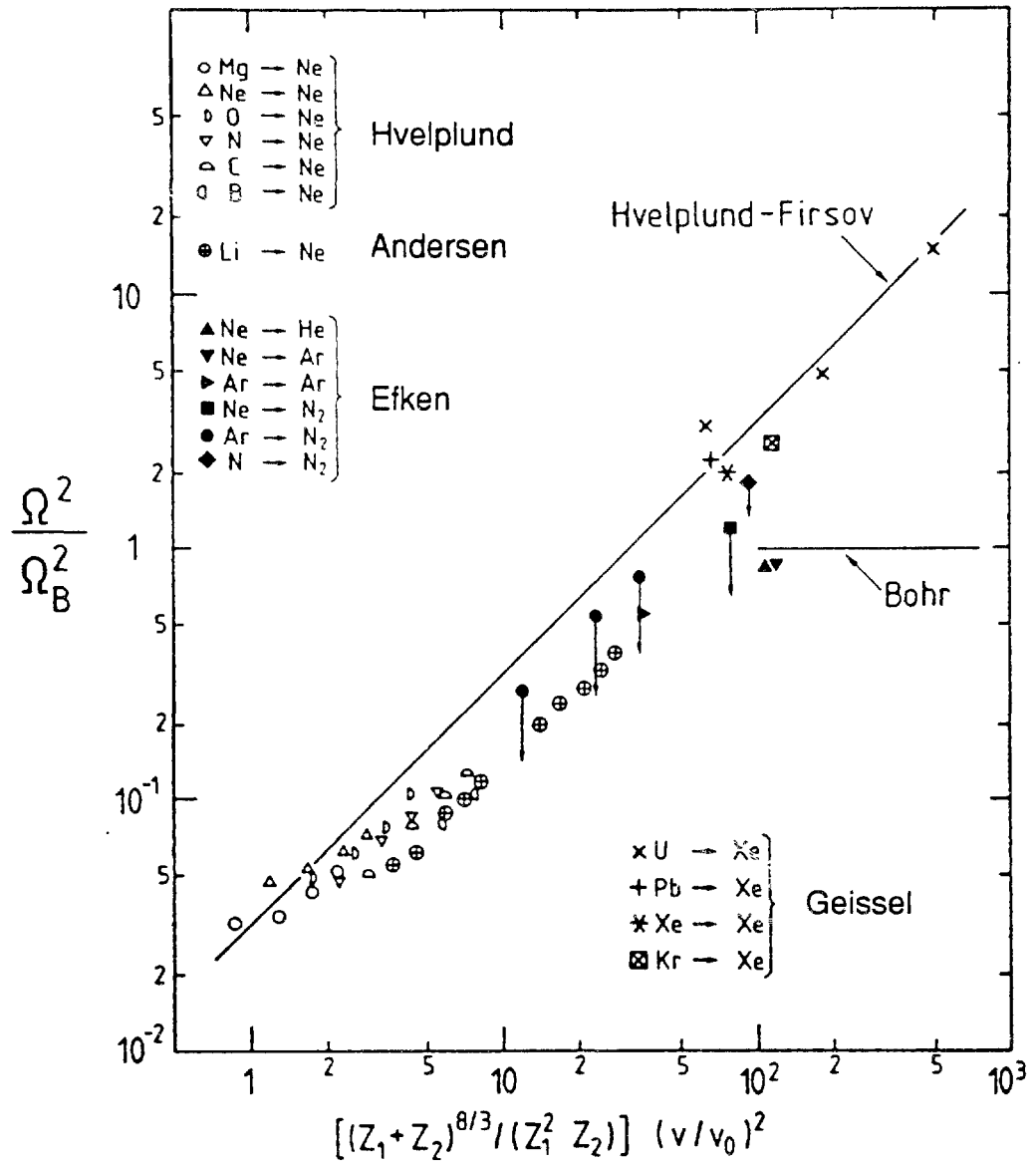

Fig.7.47. Energy loss straggling of various ions in gases, over a large energy range, divided by the Bohr value, according to Geissel et al [184]. In these units, the Firsov-Hvelplund formula (eq. 7.24) appears as a single straight line. Measured points are due to Geissel et al [184], Hvelplund [179], Andersen et al [186], and Efken et al [185]. Arrows indicate the molecular contribution.

variance Ω_s^2 (and if the effect of channeling can be neglected), then the measured energy variance Ω^2 will be given by [118a, 187]

$$\Omega^2 = \Omega_T^2(t) + (S\Omega_s)^2 \qquad (7.25)$$

where $\Omega_T^2(t)$ is the energy straggling after a foil of thickness t (assumed smooth), and S is the linear stopping power. If solid films of different thickness are measured, and if these films have equal surface roughness,

then the slope of the measured energy variance versus foil thickness will correspond to $\Omega_T^2(t)/t$, and the intercept at zero thickness will correspond to the surface roughness. Such measurements have indeed been done recently by Briere and Biersack [187] using 7 MeV ^{15}N ions in various substances. They found the surface roughness Ω_S^2 determined in this way to be in beautiful agreement with that measured using an atomic force microscope, and they found Ω_T^2 for light targets well described by the quantum mechanical formalism of Bethe and Livingston [188] that differs slightly from the Bohr result.

Lennard et al [189] have found that the energy straggling for light ions of low specific energy (16 keV/u) in carbon shows a Z_1-oscillation that peaks at $Z_1 = 14$, possibly due to L-shell ionization via electron

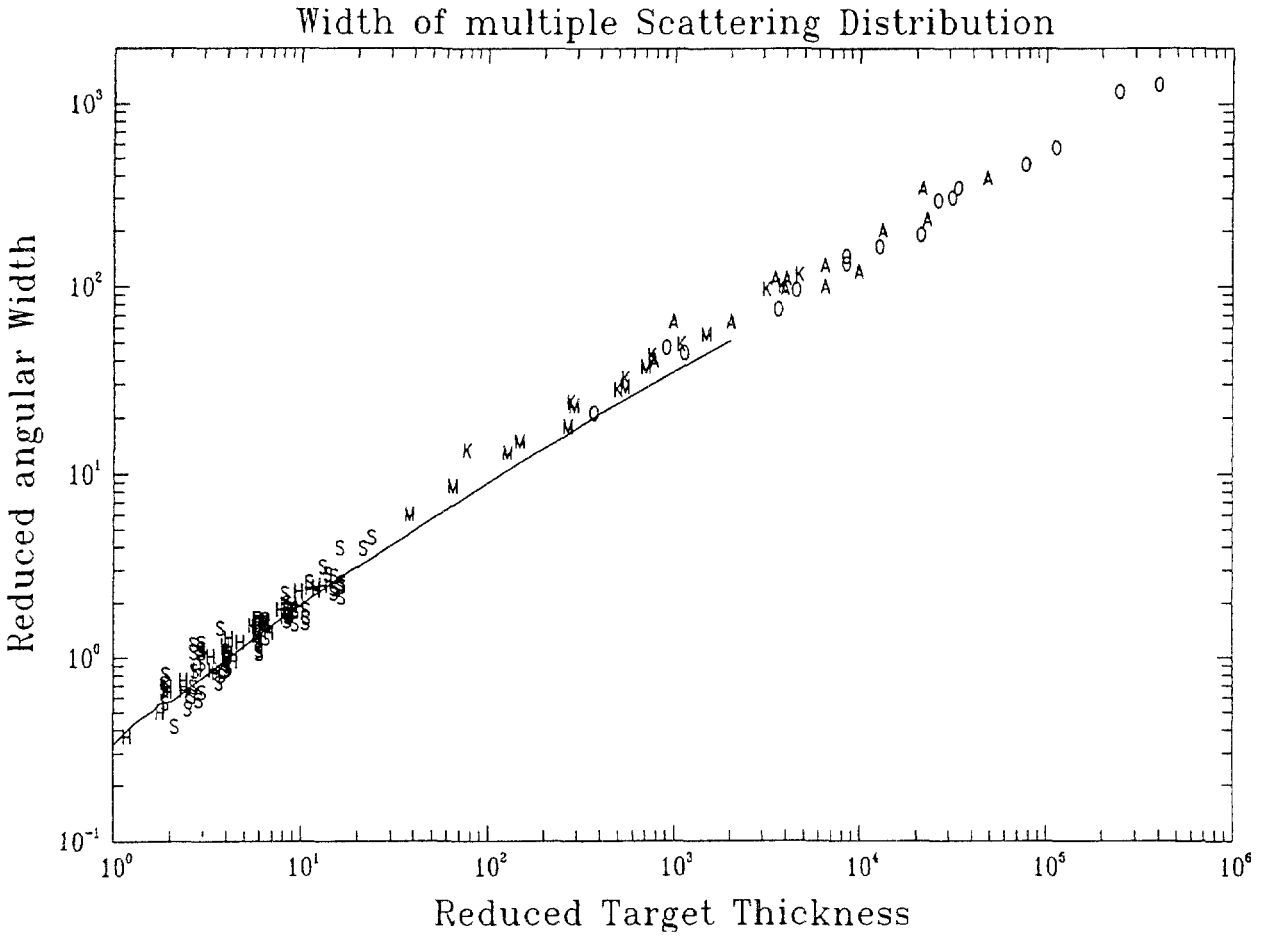

Fig.7.48. Experimental reduced half widths $\tilde{\alpha}_{1/2}$ of multiple scattering distributions versus reduced thickness τ, compared to the Sigmund-Winterbon theory [192] (full line). The symbols O, A, K, and M refer to O, Ar, Kr, and Mo ions, respectively [194], the symbol S to H, He, N, and Ne ions [195], and the symbol H to O, Cl, and Fe ions [196].

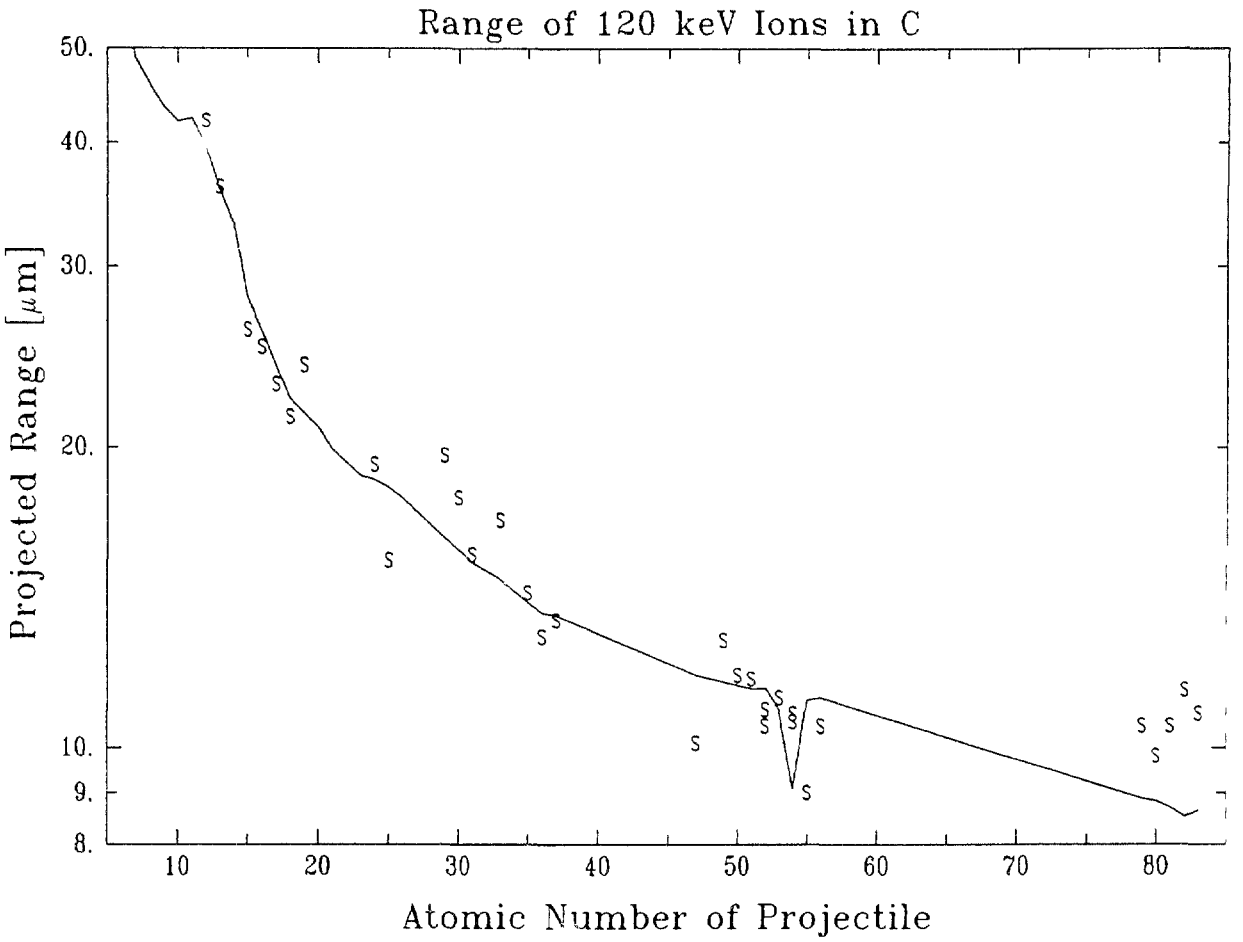

Fig.7.49. Projected range in carbon of various 120 keV ions, versus Z_1. S: experimental points due to Santry et al [201]; full curve: PRAL (TRIM90).

promotion. This peak is in a place different from where the stopping power has a peak (see Fig. 7.37), since the straggling is more sensitive to large inelastic energy transfers than the stopping power.

The TRIM programs may be used to calculate electronic straggling in an approximate way, as discussed in Sec. 7.3.3. Note that TRIM91 and TRIM92 calculate electronic straggling only for $Z_1 < 4$ [190].

7.5.4. Multiple Scattering

Sigmund [119] has recently reviewed theoretical descriptions and experimental results concerning multiple scattering.

If a particle beam enters a target foil of thickness t at a right angle, the angular distribution (per unit solid angle) of the transmitted particles consists of a central Gaussian part produced by many small-angle scatterings, and a tail at large angles that is due to a single deflection. If α is the exit angle (with respect to the direction of the incident beam), the Gaussian part can be described by the angle $\alpha_{1/2}$ where the distribution has half its maximum value. The distribution function has been calculated by Meyer [191] and by Sigmund and Winterbon [192], assuming randomly distributed scatterers and screened potentials, and neglecting energy loss. The results are given in terms of two reduced variables, τ and $\alpha_{1/2}$. The reduced target thickness is given by

$$\tau = \pi a^2 nt, \tag{7.26}$$

where

$$a = 0.8853\ a_0 (Z_1^{2/3} + Z_2^{2/3})^{-1/2} \tag{7.27}$$

is the screening length. The reduced scattering angle is defined by

$$\tilde{\alpha} = \alpha \frac{aE}{2Z_1 Z_2 e^2} \tag{7.28}$$

[Note that $e^2/a_0 = 27.2$ eV]. Sigmund and Winterbon [192] have tabulated the distribution for a very large range of thicknesses ($0.001 \leq \tau \leq 2000$). For small thickness ($\tau \leq 5$), one has [192] approximately $\tilde{\alpha}_{1/2} \cong \tau/4$, so the half-width can be conveniently approximated by

$$\alpha_{1/2} \cong \frac{\pi a^2}{2} \frac{Z_1 Z_2 e^2}{aE} nt. \tag{7.29}$$

If the transmitted particles are observed at an angle α with respect to the incident beam direction, then the path length in the foil will, on the average, be larger than t by a factor $(1 + 1/\cos\alpha)/2$, due to multiple scattering [193].

Fig. 7.48 shows the reduced half-widths of experimental multiple scattering distributions over a very large range of reduced thicknesses, compared to the Sigmund-Winterbon theory. Above $\tau = 30$, the results were measured using O, Ar, Kr and Mo ions in the range 20-90 MeV/u in solid and gaseous targets [194]. Below $\tau = 20$, the measurements were

done using H, He, N, and Ne ions (1 - 11 MeV) [195] and using O, Cl and Fe ions (12 - 40 MeV) [196]. One sees that in reduced units, all these measurements lie on a common curve, at least to a first approximation. Above $\tau = 20$, the Sigmund-Winterbon curve appears 20% low. Below this value, it appears to represent the data well, within the larger uncertainties. A closer look at the results by Hooton et al [196] shows that the Fe data tend to lie below the O data.

If the stopping power is measured in a transmission experiment with a beam at normal incidence and a detector of small solid angle, then the result appears to depend upon the angle α between the incident beam and the direction to the detector [154, Fig.16], due to multiple scattering. If the target thickness is not constant across the target but fluctuates about a mean value, then areas of different thickness contribute with different weight to the energy loss [197]. If α is close to zero, e.g., then the thin parts of the foil contribute more to the measurement than the thick parts, and the measured value S comes out too small (since it is referred to the *average* foil thickness); the opposite holds for large α. Golser et al have shown [198] that one obtains the correct value S if one measures the energy loss at an angle α such that the counting rate is about 30% of the rate at $\alpha = 0$, and by dividing this value by the average foil thickness.

The effects of multiple scattering can, of course, be calculated using the TRIM programs. If one uses TRIM91, e.g., multiple scattering can be nicely visualized by observing the computer screen during calculation.

7.5.5. Ranges and Range Straggling

Ziegler et al (ZBL85, Ch.7) discuss various methods for measuring the mean projected range. Many of these measurements have been done out of interest for ion implantation, mostly in silicon. Ziegler et al also show figures (similar to Fig. 7.28) from which one can estimate the accuracy of the results. They state an overall accuracy of 9% for the range of ions in silicon. Fichtner, Biersack et al [199] and Grande et al [200] state that the calculated projected ranges and range stragglings of ZBL85 are in overall good agreement ($\simeq$ 10%) with most of the published data, for a wide range of ion energies and for many ion-target combinations (except [200] for low energy heavy ions which are not of interest here).

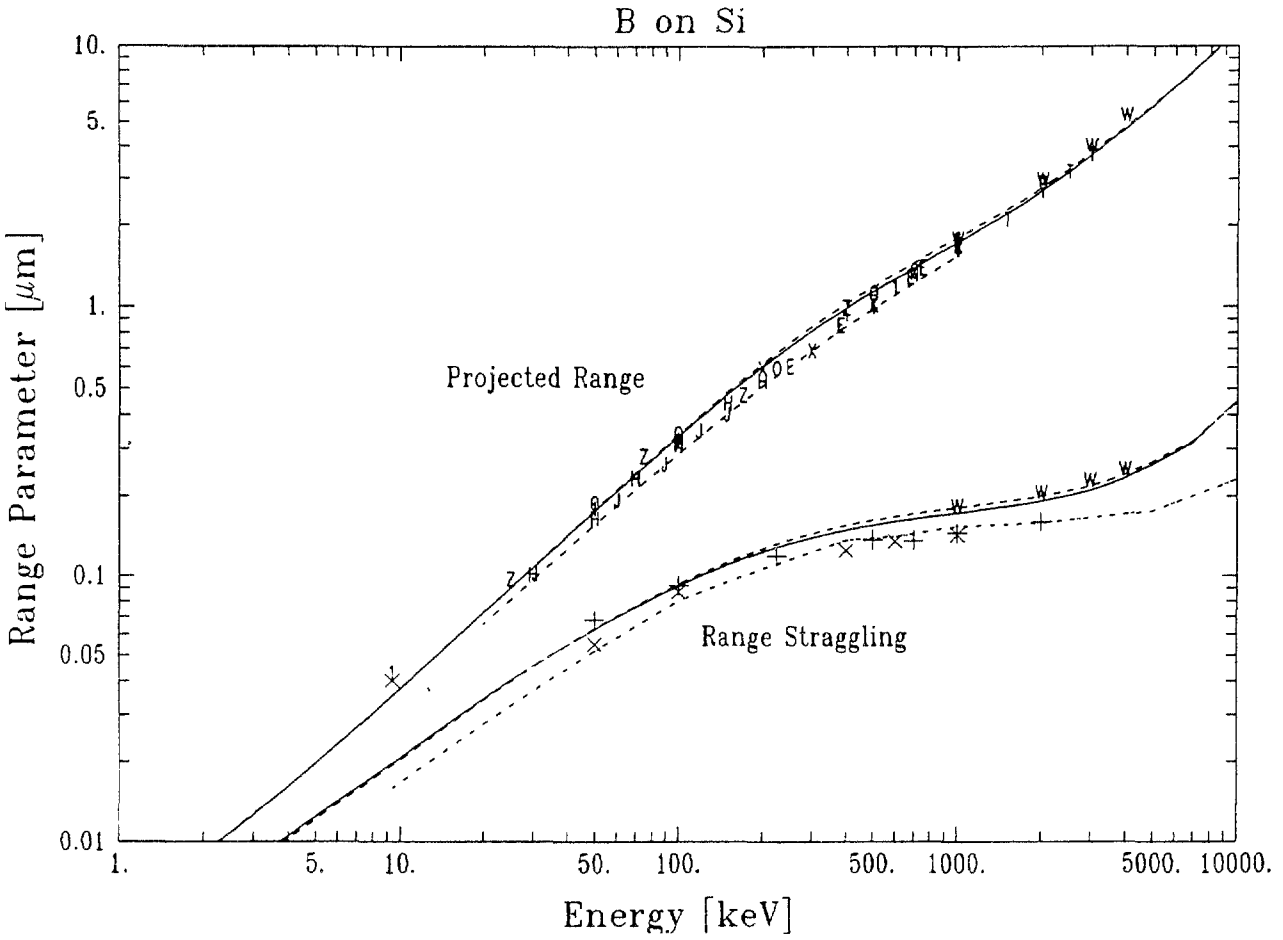

Fig.7.50. Projected range and range straggling in amorphous silicon of ^{10}B and ^{11}B ions, versus projectile energy.
———: PRAL (TRIM90) for ^{10}B; -----: PRAL (TRIM90) for ^{11}B.
-·-·-: Brice [204]; -···-: Monte Carlo (TRIM90).
Experimental points are from the following references:
E: [205]; H: [206]; J: [207]; T: [208]; W: [209]; X: [210]; Z: [211];
0 and +: [203] (^{10}B); 1 and x: [203] (^{11}B).

The TRIM calculations mentioned can be done using either the Monte Carlo code or using program PRAL (see also Sec. 7.3.5). The two approaches generally give the same result for the projected range, but not for range straggling (see Ch. 7 of ZBL85, and our Sec. 7.3.5, and Fig. 7.50). PRAL should therefore not be used to determine range straggling, except for preliminary estimates. The figures in Ch.7 of ZBL85 also permit comparisons of the projected range with the csda range.

In Fig. 7.49, we show the range of 33 different ions in carbon at 120 keV, as measured by Santry et al [201], compared to the PRAL-values from

TRIM90. Except for the heaviest ions, the agreement is within a few percent, on the average. At $Z_1 = 11$, the kink in the PRAL curve is an indication of the Z_1-oscillation also seen in Fig. 7.37.

Santry et al [201] also measured the ranges of these ions in Be, Al and Si targets, with similar results.

Recently, Schüle et al [202] have measured the range parameters of many different ions implanted at energies from 3 keV to 40 MeV into C, Si and Ge targets made amorphous to prevent channeling. For projectiles with $A_1/A_2 < 1$ in Si and Ge, they found that the projected ranges and the range straggling agree with TRIM calculations (ZBL85) within 10%. For Si, Ti and Cr ions with $A_1/A_2 > 1$, the agreement is slightly worse. Since these authors based their depth measurements on stopping powers from the same TRIM code, some of these conclusions might be circular.

Behar et al [203] have measured the mean projected range and the range straggling for B ions implanted into amorphized silicon at energies from 10 keV to 2 MeV. Their results are shown in Fig. 7.50 together with range results from other authors selected because they are new or because the range of implantation energies is large (see also the corresponding figure in ZBL85, where many other measurements are shown). One can see that most of the range measurements agree within about 10% with the PRAL calculation, and also with the Brice table [204]. For range straggling, the TRIM90 Monte Carlo calculation agrees well with experimental results, while the PRAL calculation appears too large, with respect to Behar's results (the straggling results due to Wong et al [209] are higher, but the disagreement between different results is generally larger for straggling than for ranges [203]). The apparent disagreement between Monte Carlo straggling and experimental results at low energy is due to the finite energy resolution of the measurements and can be quantitatively understood [203].

Fig. 7.50 also shows that the calculated range of ^{10}B ions is slightly smaller (by 4% at 500keV) than that of ^{11}B ions. Considering electronic stopping, this is not surprising, since at the same energy, the ^{10}B ions are faster and hence, are stopped more efficiently. But Zalm et al [211] have shown that the range of the lighter ions is always smaller, even if the additional effect of nuclear stopping is taken into consideration.

Abel et al [212] found that the projected range of ^{40}Ar ions implanted into C films at energies from 10 to 200 keV, is 20% larger than predicted by ZLB85 (PRAL or Monte Carlo). Since the stopping power of C according to TRIM90 is slightly lower than that of ZBL85 (see Table 7.12), the range according to TRIM90 is 1% larger, so there is still a 19% difference between measurements and TRIM90. This discrepancy resembles the one found by Grande et al [200] for heavier ions. We note, however, that the range of Ar ions found by Santry at 120 keV agrees with TRIM90 within 4% (see Fig. 7.49), and that the experimental range values shown in Fig. 7-13 of ZBL85 agree quite well the ZBL85 prediction.

It is obvious that range distributions should reflect the Z_1- and Z_2-oscillations found for the electronic stopping power (see figs. 7.35 to 7.39). A Z_1-oscillation was mentioned above; Geissel et al [155] have found Z_2-oscillations in the projected ranges and the range straggling observed for ^3He ions implanted at 35 keV into 14 metallic targets. But Besenbacher et al [213] have found Z_1-oscillations also where nuclear stopping dominates the range (using ions with $Z_1 \geq 18$ in Si).

ACKNOWLEDGEMENTS

The critical reading of various parts of the manuscript by Dr. P. Bauer, Dr. D. Semrad and Prof R. Ritchie is gratefully acknowledged.

REFERENCES (For data reference codes, see Table 7.11)

[1] INOKUTI, M., BERGER, M.J., Nucl. Instr. Meth. B27 (1987) 249.
[2] BOHR, N., Mat. Fys. Medd. Dan. Vid. Selsk. 18, no. 8 (1948)
[3] SIGMUND, P., in: Radiation Damage Processes in Materials, ed. by C.H.S. Dupuy, Noordhoff (Leyden) (1975)
[4] BICHSEL, H., Rev. of Modern Physics 60 (1988) 663
[5] INTERNATIONAL COMMISSION ON RADIATION UNITS AND MEASUREMENTS, ICRU Report 37, Stopping Powers for Electrons and Positrons (1984)
[6] INTERNATIONAL COMMISSION ON RADIATION UNITS AND MEASUREMENTS, ICRU Report 16 (1970)
[7] JANNI, F.J., At. Data Nucl. Data Tabl. 27 (1982) 150 and 341
[8] GOLSER, R., SEMRAD, D., Phys. Rev. A45 (1992) R4222
[9] GAUVIN, H., BIMBOT, R., HERAULT, J., KUBICA, B., ANNE, R., BASTIN, G., HUBERT, F., Nucl. Instr. Meth. Phys. Res. B47 (1990) 339

[10] NAT. ACAD. OF SCIENCES - NAT. RES. COUNCIL, Studies of Penetration of Charged Particles in Matter, Publication 1133, Washington (1964)

[11] FANO, U., Ann. Rev. Nucl. Science 13 (1963) 1

[12] KUMAKHOV, M.A., KOMAROV, F.F., Energy Loss and Ion Ranges in Solids, Gordon and Breach, New York, 1981.

[13] NELMS, A.T., Nat.Bur.Standards Circular 577 (1956).

[14] PAGES, L., BERTEL, E., JOFFRE, H., SKLAVENITIS, L., Atomic Data 4 (1972) 1.

[15] BERGER, M.J., SELTZER, S.M., NASA Publication SP-3012 (1964).

[16] BETHE, H., Ann.Phys. 5 (1930) 325.

[17] BETHE, H., Z. Phys. 76 (1932) 298.

[18] BETHE, H., ASHKIN, J., Experimental Nuclear Physics, Vol 1 (1953) 166.

[19] MØLLER, C.,Ann.Phys. 14 (1932) 568.

[20] ZEISS, G.D., MEATH, W.J., MCDONALD, J.C.F., DAWSON, C.D., Radiat. Res. 70 (1977) 284.

[21] RITCHIE, R.H., HAMM, R.N., TURNER, J.E., WRIGHT, H.A., Sixth Symp. on Microdosimetry, Vol 1 (1978) 345.

[22] ASHLEY, J., Radiat.Res. 89 (1982) 25.

[23] SHILES, E., SASAKI, T., INOKUTI, M., SMITH, D.Y., Phys.Rev. B22 (1980) 1612.

[24] TURNER, J.E., ROECKLEIN, P.D., VORA, R.B., Health Phys. 18, (1970) 159.

[25] BICHSEL, H., American Inst.of Physics Handbook, 3d Edition (1972), sect. 8d

[26] ANDERSEN, H.H., ZIEGLER, J.F., Hydrogen: Stopping Powers and Ranges in all Elements. Vol.3 of The Stopping and Ranges of Ions in Matter, Pergamon Press, Elmsford, New York (1977).

[27] AHLEN, S.P., Rev.Mod.Phys. 52 (1980) 121.

[28] SAKAMOTO, N.,SHIOMI-TSUDA, N., OGAWA, H., and ISHIWARI, R., Nucl. Instr. Meth. B33 (1988) 158.

[29] SAKAMOTO, N., OGAWA, H., MANAMI, M.,KIMURA, K.,SUSUKI, Y.,HASEGAWA, M., KATAYAMA, T., NORO, T., and IKEGAMI, H., Radiation Eff. and Def. in Solids 117 (1991) 193

[30] BICHSEL, H., Stopping Power of Fast Charged Particles in Heavy Elements, National Inst. of Standards and Technology Report NISTIR-4550 (1991).

[31] BICHSEL, H., and HIRAOKA, T., Nucl.Instr.Meth. B66 (1992) 345.

[32] THOMPSON, T.J., Report UCRL-1910 (1952).

[33] BRANDT, W., Phys.Rev. 104 (1956) 691.

[34] NORDIN, J.A., and HENKELMAN, R.M., Phys.Med.Biol. 24 (1979) 781.

[35] HIRAOKA, T.,KAWASHIMA, K.,HOSHINO, K.,FUKUMURA, A.,and BICHSEL, H., Medical Physics 20 (1993) 135

[36] ISHIWARI, R., SHIOMI-TSUDA, N., SAKAMOTO, N.,and OGAWA, H., Nucl.Instr.Meth. B47 (1990) 111.

[37] BONDERUP, E., Kgl.Danske Videnskab. Selskab., Mat-Fys. Medd 35, No.17 (1967).

[38] STERNHEIMER, R.M., Phys.Rev. 88 (1952) 851.

[39] STERNHEIMER, R.M., BERGER, M.J., SELTZER, S.M., Phys.Rev.B26 (1982) 6067.

[40] INOKUTI, M., and SMITH, D.Y., Phys.Rev. B25 (1982) 61.

[41] ASHLEY, J.,Radiat.Res. 89 (1982) 32.

[41a]WILLIAMS, E.J., Kgl.Danske Videnskab. Selskab., Mat-Fys. Medd. 13, No.4 (1935)

[42] GERHART, E., J. Chem. Phys. 62 (1975) 821.

[43] EGGARTER, J., J. Chem. Phys. 62 (1975) 833.

[44] EGGARTER, J., INOKUTI, M., Cross Sections for Electron Inelastic Collisions with Argon, Argonne National Laboratory Report ANL-50-58 (1980).

[45] PARETZKE, H.G,. Simulation von Elektronenspuren im Energiebereich 0.01 - 10 keV, GSF-Bericht 24/88 (1988).

[46] PARETZKE, H.G., TURNER, J.E., HAMM, R.N., WRIGHT, H.A., RITCHIE, R.H., J. Chem. Phys. 84 (1986) 3182.

[47] PARETZKE, H.G., Kinetics of Nonhomogeneous Processes, (FREEMAN, G.R, Ed.), Wiley, New York (1987) 89.

[48] OLIVERO, J., STAGAT, R. W., GREEN, A.E.S., J. Geophys. Res. 77 (1972) 4797.

[49] DAYASHANKAR, GREEN, A.E.S., Radiat. Phys. Chem. 40 (1992) 523.

[50] LaVERNE J.A., MOZUMDER, A., J. Phys. Chem. 90 (1986) 3242. See also MOZUMDER, A., LaVERNE, J.A., J. Phys. Chem. 89 (1985) 930.

[51] JACKMAN, C.H., GARVEY, R.H., GREEN, A.E.S., J. Geoph. Res. 82, (1977) 5081.

[52] WAIBEL, E., GROSSWENDT, B., Nucl. Instr. Meth., B5 (1991) 239.

[53] WAIBEL, E., GROSSWENDT, B., Phys. Med. Biol. 37 (1992) 1127.

[54] LINDHARD, J., K.Danske Vidensk. Selsk. Mat.-Fys. Medd. 28, No.1 (1954).

[55] RITCHIE, R.H., Phys. Rev. 114 (1959) 644.

[56] LINDHARD, J., WINTHER, A., K. Danske Vidensk. Selsk. Mat.-Fys. Medd. 34, No.4, (1964).

[57] TUNG, C.J., RITCHIE, R.H., ASHLEY, J.C., ANDERSEN, V.E., "Inelastic interactions of swift electrons in solids," Rep. ORNL/TM-5188, Oak Ridge Natl. Lab. (1976).

[58] ASHLEY, J.C., TUNG, C.J., RITCHIE, R.H., ANDERSON, V.E., IEEE Trans. on Nuclear Science, NS-23 (1976) 1833.

[59] ASHLEY, J.C., TUNG, C.J., RITCHIE, R.H., IEEE Trans. on Nuclear Science, NS-25 (1978) 1566.

[60] ASHLEY, J.C., TUNG, C.J., RITCHIE, R.H., Surface Science 81 (1979) 409

[61] TUNG, C.J., ASHLEY, J.C., RITCHIE, R.H., Surface Science 81 (1979) 427

[62] ASHLEY, J.C., COWAN, J.J., RITCHIE, R.H., ANDERSON, V.E., HOELZL, J., Thin Solid Films, 60 (1979) 361.

[63] ASHLEY, J.C., IEEE Trans. on Nuclear Science, NS-27 (1980) 1454.

[64] ASHLEY, J.C., ANDERSON, V.E., IEEE Trans. on Nuclear Science, NS-28 (1981) 4132.

[65] ASHLEY, J.C., ANDERSON, V.E., J. of Electron Spectroscopy and Related Phenomena 24 (1981) 127.

[66] ASHLEY, J.C., Radiat. Res. 89 (1982) 25, and priv. comm. to M. Berger

[67] ASHLEY, J.C., Radiat. Res. 90 (1982) 433.

[67a]ASHLEY, J.C., J. of Electron Spectroscopy and Rel. Phen. 46 (1988) 199

[67b]ASHLEY, J.C., J. of Electron Spectroscopy and Rel. Phen. 50 (1990) 323

[68] AKKERMAN, A.F., CHERNOV, G.Ya., Phys. Stat. Sol (b) 89 (1978) 320.

[69] KHLUPIN, S.I., AKKERMAN, A.F., Academy of Sciences of the Kazakh SSR, Preprint HEPI-81021 (1985).

[69a]AL-AHMAD, K.O., WATT, D.E., J. Phys. D: Appl. Phys. 16 (1983) 2257

[69b]AL-AHMAD, K.O., WATT, D.E., J. Phys. D: Appl. Phys. 17 (1984) 1899

[70] LILJEQUIST, D., J. Phys. D: Appl. Phys. 16 (1983) 1567.

[71] KIMURA, M., KRAJCAR-BRONIC, I., DILLON, M., INOKUTI, M., Phys. Rev. A 45 (1992) 7831

[72] ZEISS, G., MEATH, W.J., MacDONALD, J.C.F., DAWSON, D,J., Radiat. Res. 63 (1975) 64

[73] HELLER, J.M., HAMM, R.N., BIRKHOFF, R.D., PAINTER, L.R., J. Chem. Phys. 60 (1974) 1483.

[74] GARCIA. J.D., Phys. Rev. 177 (1969) 223.

[75] BERGER, M.J., Proc. of an Advisory Group Meeting on Nuclear and Atomic Data, IAEA Vienna (1987) 323.

[76] DAVIES, H., BETHE, H.A., MAXIMON, L.C., Phys.Rev. 93 (1954) 788.

[77] PRATT, R.H., TSENG, H.K., LEE, C.M.,KISSEL, L., MACCALLUM L., RILEY, M., Atom.Data and Nucl.Data Tables 20, 175 (1977); errat. 26 (1981) 477.

[78] SELTZER, S.M., BERGER, M.J., Nucl.Instr.Meth. B12 (1985) 95.

[79] SELTZER, S.M., BERGER, M.J., Atom.Data and Nucl.Data Tables 35 (1986) 345.

[80] HAUG, E., Z.f.Naturf. 30a, (1975) 1099.

[81] BERGER, M.J., Nat.Inst.of Standards and Technology, Report NISTIR 4999 (1992).

[82] LANDAU, L., J.Phys.USSR 8 (1944) 201.

[83] BÖRSCH-SUPAN, W., J.Res.Nat.Bur.Standards 65B (1961) 245.

[84] BLUNCK, O., LEISEGANG, S.,Z.Phys.128 (1950) 500.

[85] BLUNCK, O., WESTPHAL, K., Z.Phys.130 (1951) 641.

[86] SELTZER, S.M., Int.J.Appl.Radiat.Isot. 42 (1991) 917.

[87] CHECHIN, V.A., ERMILOVA, V.C., Nucl.Instr.Meth.136 (1976) 551.

[88] BERGER, M.J., Methods in Computational Physics, 1 (1963) 135.

[89] BICHSEL, H., SAXON, R.P., Phys.Rev. A11 (1975) 1286.

[90] BERGER, M.J., WANG, R., Monte Carlo Transport of Electrons and Photons, p. 21, Plenum , New York (1988).

[91] BAUER, P., Nucl. Instr. Methods B45 (1990) 673.

[92] ANDERSEN, H.H., HANKE, C.C., SOERENSEN, H., VAJDA, P.,Phys. Rev. 153 (1967) 338.

[93] SEMRAD, D., BAUER, P., Nucl. Instr. Methods B12 (1985) 24.

[94] ARNAU, A., PENALBA, M., ECHENIQUE, P.M., FLORES, F., RITCHIE, R.H., Phys. Rev. Lett. 65 (1990) 1024.

[95] PENALBA, M., ARNAU, A., ECHENIQUE, P.M., FLORES, F., RITCHIE, R.H., Europhys. Lett. 19 (1992) 45.

[96] SCHIWIETZ, G., Phys. Rev. A42 (1990) 296.

[97] SCHIWIETZ, G., GRANDE, P.L., Nucl. Instr. Methods B69 (1992) 1.

[98] FERMI, E., TELLER, E., Phys. Rev. 72 (1947) 399.

[99] ECHENIQUE, P.M., NIEMINEN, R.M., R.H. RITCHIE, R.H., Solid State Commun. 37 (1981) 779.

[100] ECHENIQUE, P.M., NIEMINEN, R.M., ASHLEY, J.C., RITCHIE, R.H., Phys. Rev. A33 (1986) 897.

[101] see also MANN, A., BRANDT, W., Phys. Rev. B24 (1981) 4999.

[102] GOLSER, R., SEMRAD, D., Phys. Rev. Lett. 66 (1991) 1831.

[103] PAUL, H., SEMRAD, D., SEILINGER, A., Nucl. Instr. Methods B61 (1991) 261.

[104] BAUER, P., RÖSSLER, W., and MERTENS, P., Nucl. Instr. Methods B69 (1992) 46.

[105] TSCHALÄR, C., BICHSEL, H., Phys. Rev. 175 (1968) 476

[106] ZIEGLER, J.F., MANOYAN, J.M., Nucl. Instr. Methods B35 (1988) 215.

[107] POWERS, D., Nucl. Instr. Methods B40/41 (1989) 324

[108] NEUWIRTH, W., Nucl. Instr. Methods B27 (1987) 337

[109] THWAITES, D.I., Nucl. Instr. Methods B69 (1992) 53.

[110] BAUER, P., KASTNER, F., ARNAU, A., SALIN, A., PONCE, V.H., ECHENIQUE, P.M., J. Physics: Condensed Matter 5 (1993) A273

[111] BAUER, P., KASTNER, F., ARNAU, A., SALIN, A., FAINSTEIN, P.D., PONCE, V.H., ECHENIQUE, P.M., Phys. Rev. Lett. 69 (1992) 1137.

[112] RAETHER, H., Excitations of Plasmons and Interband Transitions by Electrons, Springer, Berlin (1980).

[113] NECAS, V., KÄFERBÖCK, W., RÖSSLER, W., BAUER P., Nucl. Instr. Methods B 80/81 (1993) 41

[114] BAUER, P., MERTENS, P., MITTERSCHIFFTHALER, Ch., PAUL, H., IAEA-TECDOC-506 (1989) 151.

[115] SUGIYAMA, H., Bull. El. Techn. Lab. 51 (1987) 520.

[116] THWAITES, D.I., Radiat. Prot. Dos. 13 (1985) 65.

[117] EPPACHER, C., SEMRAD, D., Nucl. Instr. Methods B35 (1988) 109.

[118] BERGER, M.J., Penetration of Proton Beams through Water: I. Depth-dose Distributions, Spectra and LET Distributions, National Institute of Standards and Technology Report NISTIR 5226 (1993).

[118a] BESENBACHER, F.,ANDERSEN, J.U., BONDERUP, E., Nucl. Instr. Methods 168 (1980) 1.

[119] SIGMUND, P., in: Interaction of Charged Particles with Solids and Surfaces (Proc. of a NATO Advanced Study Institute in Alicante, Spain, May, 1990), (GRAS-MARTI, A., URBASSEK, H.M., ARISTA, N.R., FLORES, F., Eds.), Plenum Press, New York (1991) 73.

[120] BESENBACHER, F., ANDERSEN, H.H., HVELPLUND, P., KNUDSEN, H., Kgl. Danske Videnskab. Selskab Mat. Fys. Medd. 40, No.9 (1981).

[120a] BICHSEL, H., Phys. Rev. B1 (1970) 2854

[121] TSCHALÄR, C., Nucl. Instr. Methods 64 (1968) 237.

[122] BIERSACK, J.P., HAGGMARK, L.G., Nucl. Instr. Methods 174 (1980) 257.

[123] BONDERUP, E., HVELPLUND, P., Phys. Rev. A4 (1971) 562.

[124] KANEKO, T., YAMAMURA, Y., Phys. Rev. A33 (1986) 1653.

[125] MATSUNAMI, N., KITOH, K., Nucl. Instr. Methods B59/60 (1991) 5.

[126] VAVILOV, P.V., Zh. Exp. Teor. Fiz. 32 (1957) 920 (Soviet Physics JETP 5 (1957) 749).

[127] TSCHALÄR, C., Nucl. Instr. Methods 61 (1968) 141.

[128] BAUER, G.H., ANTOLAK, A.J., PONTAU, A.E., MORSE, D.H., HEIKKINEN, D.W., PROCTOR, I.D., Nucl. Instr. Methods B43 (1989) 497.

[129] ARMITAGE, B.H., TREHAN, P.N., Nucl. Instr. Methods 134 (1976) 359.

[130] BICHSEL, H., HIRAOKA, T., Int. J. Quantum Chem.: Quantum Chemistry Symposium 23 (1989) 565.

[131] SCHIØTT, H.E., Kgl. Danske Videnskab. Selskab Mat. Fys. Medd. 35, No.9 (1966).

[132] KISTEMAKER, J., SANDERS, J.B., Proc. 2nd L.H. Gray Conf., Inst. Physics, London (1970) 197.

[133] AL-AFFAN, I.A.M., Calculated effective stopping powers and projected ranges for H, He, C, N and O Projectiles (0.05 - 500 keV) in some Elements and Materials of dosimetric interest, South Bank Polytechnic, London (1989).

[134] ANDERSEN, H.H., Nucl. Instr. Methods B44 (1989) 121.

[135] STEINBAUER, E., priv. comm. to H.Paul

[136] BØRGESEN, P., BØTTIGER, J., MÖLLER, J., J.Appl.Phys. 49 (1978) 4401.

[137] ASHWORTH, D.G., BOWYER, M.D.J., OVEN, R., J.Phys.D: Appl.Phys. 24 (1991) 1376.

[138] ROSS, G.G., TERREAULT, B., Nucl. Instr. Methods B15 (1986) 61.

[139] ROSS, G.G., TERREAULT, B., Nucl. Instr. Methods B45 (1990) 190.

[140] ZIEGLER, J.F., Helium: Stopping Powers and Ranges in All Elemental Matter. Vol.4 of The Stopping and Ranges of Ions in Matter, Pergamon Press, Elmsford, New York (1977).

[141] ZIEGLER, J.F., BIERSACK, J.P., LITTMARK, U., The Stopping and Range of Ions in Solids. Vol.1 of The Stopping and Ranges of Ions in Matter, Pergamon Press, Elmsford, New York (1985).

[142] EPPACHER, Ch., SEMRAD, D., Nucl. Instr. Methods B69 (1992) 33.

[143] GOLSER, R., SEMRAD, D., Nucl. Instr. Methods B69 (1992) 18.

[144] ZIEGLER, J.F., TRIM-90, The Transport of Ions in Matter, (1990).

[145] INTERNATIONAL COMMISSION ON RADIATION UNITS AND MEASUREMENTS, Report 49, Stopping Powers and Ranges for Protons and Alpha Particles, (1993).

[146] POWERS, D., Stopping Cross Sections and Ranges of Alpha Particles in Matter, Report prepared for the ICRU Stopping Power Committee, Dept. of Physics, Baylor University, Waco, Texas (1978).

[147] KALBITZER, S., OETZMANN, H., GRAHMAN, H., FEURSTEIN, A., Z.Phys. A278, 223 (1976).

[148] WILSON, W.D., HAGGMARK, L.G., BIERSACK, J.P., Phys. Rev. B 15, 2458 (1977).

[149] BISTER, M., HAUTALA, M., JÄNTTI, M., Radiat.Eff. 42, 201 (1979).

[150] FINK, D., BIERSACK, J.P., STÄDELE, M., CHENG, V.K., Radiat.Eff. 104, 1 (1987).

[151] SHIMA, K., Nucl. Instr. Methods B10/11 (1985) 45.

[152] ZIEGLER, J.F., Handbook of Stopping Cross Sections for energetic Ions in all Elements Vol.5 of The Stopping and Ranges of Ions in Matter, Pergamon Press, New York (1980).

[153] BRANDT, W., KITAGAWA, M., Phys.Rev. B25 (1982) 5631.

[154] GEISSEL, H., in: Semiclassical Descriptions of Atomic and Nuclear Collisions, (BANG, J, DeBOER, J., Ed.) North-Holland (1985) p.431.

[155] GEISSEL, H., LENNARD, W.N., ARMBRUSTER, P., Rad. Effects and Def. in Solids 110 (1989) 7.

[156] GEISSEL, H., ARMBRUSTER, P., KITAHARA, T., KRAFT, G., SPIELER, H., GÜTTNER, K., Nucl. Instr. Methods 170 (1980) 217.

[157] NORTHCLIFFE, L.C., SCHILLING, R.F., Nucl. Data Tables A7 (1970) 233.

[158] KURONEN, A., Comm. physico-mathematicae, Finland, 122 (1991).

[159] WARD, D.H., ANDREWS, H.R., MITCHELL, I.V., LENNARD, W.N., WALKER, R.B., RUD, N., Can. J. Phys. 57 (1979) 645.

[160] SOFIELD, C.J., Nucl. Instr. Methods B45 (1990) 684.

[161] RÄISÄNEN, J., RAUHALA, E., Radiation Eff. and Def. in Solids 108 (1989) 21.

[162] KURONEN, A., RÄISÄNEN, J., KEIKONEN, J., TIKKANEN, P., RAUHALA, E., Nucl. Instr. Methods B35 (1988) 1.

[163] RÄISÄNEN, J., RAUHALA, E., Phys. Rev. B41 (1990) 3951, and earlier publications cited there

[164] ANTHONY, M.,LANFORD, W.A., Phys. Rev. A25 (1982) 1868.

[165] RAUHALA, E., RÄISÄNEN, J., Phys. Rev. B42 (1990) 3877.

[166] RÖSSLER, W., Diploma Thesis, Univ. of Linz (1992).

[167] ARSTILA, K., KEIKONEN, J., TIKKANEN, P., Phys. Rev. B41 (1990) 6117.

[168] KEIKONEN, J.,KURONEN, A., HAUTALA, M., KARTTUNEN, V., LAPPALAINEN, R., UHRMACHER; M, Phys. Lett. A123 (1987) 307.

[169] LAND, D.J.,SIMONS, D.G., BRENNAN, J.G., BROWN, M.D., Phys. Rev. A22 (1980) 68.

[170] SEMRAD, D., EPPACHER, Ch., TOBER, R., Nucl. Instr. Methods B48 (1990) 79.

[171] ABDESSALAM, A., STOQUERT, J.P., GUILLAUME, G., HAGE-ALI, M., GROB, J.J., SIFFERT, P., Nucl. Instr. Methods B56/57 (1991) 355 and B72 (1992) 7 and 293.

[172] BIMBOT, R., Nucl. Instr. Methods B69 (1992) 1.

[173] HUBERT, F., BIMBOT, R., GAUVIN, H., Nucl. Instr. Methods B36 (1989) 357

[174] STEWARD, P.G., UCRL-18127, Univ. of California Radiation Lab. (1968).

[175] NORTHCLIFFE, L.C., Ann. Rev. Nucl. Science 13 (1963) 67.

[176] GEISSEL, H., LAICHTER, Y., SCHNEIDER, W.F.W., ARMBRUSTER, P., Nucl. Instr. and Meth. 194 (1982) 21; Phys. Lett. A88 (1982) 26.

[177] BOHR, N., LINDHARD, J., Kgl. Dansk Videnskab. Selsk., Mat. Phys. Medd. 26 (1954) 1.

[178] HÉRAULT, J., BIMBOT, R., GAUVIN, H., KUBICA, B., ANNE, R., BASTIN, G., HUBERT, F., Nucl. Instr. Methods B61 (1991) 156.

[179] HVELPLUND, P., Kgl. Danske Vid. Selskab Mat.-fys. Medd. 38 (1971) No.4.

[180] PRICE, J.J., STERN, S.H., SIMONS, D.G., LAND, D.J., BRENNAN, J.G., Nucl. Instr. Methods B56/57 (1991) 348.

[181] BIMBOT, R., HUBERT, F.,RIVET, M.F., in preparation (see [172])

[183] FIRSOV, O.B., Sov. Phys. JETP 9 (1959) 1076.

[184] GEISSEL, H., LAICHTER, Y., SCHNEIDER, W.F.W., ARMBRUSTER, P., Nucl. Instr. Methods 215 (1983) 329.

[185] EFKEN, B., HAHN, D., HILSCHER, L., WÜSTEFELD, G., Nucl. Instr. Methods 129 (1975) 219.

[186] ANDERSEN, H.H., BESENBACHER, F., KNUDSEN, H., Nucl. Instr. Methods 149 (1978) 121.

[187] BRIERE, M.A., BIERSACK, J.P., Nucl. Instr. Methods B64 (1992) 693.

[188] LIVINGSTON, M.S., BETHE, H.A., Rev. Mod. Phys. 9 (1937) 245.

[189] LENNARD, W.N., GEISSEL, H., PHILLIPS, D., JACKSON, D.P., Phys. Rev. Lett. 57 (1986) 318.

[190] ZIEGLER, J.F., pers. comm. to H. Paul

[191] MEYER, L., Phys. Stat. Sol. 44 (1971) 253.

[192] SIGMUND, P., WINTERBON, K.B., Nucl. Instr. Methods 119 (1974) 541.

[193] BAUER, P., STEINBAUER, E., BIERSACK, J.P., Nucl. Instr. Methods B64 (1992) 711.

[194] ANNE, R., HERAULT, J., BIMBOT, R., GAUVIN, H., BASTIN, G., HUBERT, F., Nucl. Instr. Methods B34 (1988) 295.

[195] SPAHN, G., GROENEVELD, K.O., Nucl. Instr. Methods 123 (1975) 425.

[196] HOOTON, B.W., FREEMAN, J.M., KANE, P.P., Nucl. Instr. Methods 124 (1975) 29.

[197] MERTENS, P., Nucl. Instr. Methods B27 (1987) 315, 326.

[198] GOLSER, R., EPPACHER, Ch., SEMRAD, D., Nucl. Instr. Methods B67 (1992) 69.

[199] FICHTNER, P.F.P., BEHAR, M., OLIVIERI, C.A., LIVI, R.P., DE SOUZA, J.P., ZAWISLAK, F.C., BIERSACK, J.P., FINK. D., Nucl. Instr. Methods B61 (1991) 282.

[200] GRANDE, P.L., ZAWISLAK, F.C., FINK, D., BEHAR, M., Nucl. Instr. Methods B61 (1991) 282.

[201] SANTRY, D.C., WERNER, R.D., WESTCOTT, O.M., IEEE Trans. Nucl. Sc. NS-26 (1979) 1332.

[202] SCHÜLE, V., GÜNZLER, R., OBERSCHACHTSIEK, P., WEISER, M., KALBITZER, S., Nucl.Instr. Methods B62 (1992) 338.

[203] BEHAR, M., WEISER, M., KALBITZER, S., FINK, D., GRANDE, F.L., Nucl. Instr. Methods B34 (1988) 316.

[204] BRICE, D.K., Ion-Implantation and Energy Deposition Distributions, Vol.1 IFI/Plenum, New York (1975).

[205] ELLMER, K., MERTENS, A., ROCKOFF, A., RÖHRICH, J., VYSEK, W.-M.,Nucl. Instr. Methods B62 (1992) 431.

[206] HOFKE, W.K., OOSTHOEK, D.P., KOLMAN, N.J., DE GREFTE, H.A.M., Radiat. Eff. 24 (1965) 227.

[207] JAHNEL, F., RYSSEL, H., PRINKE, G., HOFFMANN, K., MUELLER, K., BIERSACK, J.P., HENKELMANN, R., Nucl. Instr. Methods 182/183 (1981) 223.

[208] THEVENIN, P., GROB, J.J., STUCK, R., SIFFERT, P., Nucl. Instr. Methods B62 (1992) 346

[209] WONG, H., DENG, E., CHEUNG, N.W., CHU, P.K., STRATHMAN, E.M., STRATHMAN, M.D., Nucl. Instr. Methods B21 (1987) 447.

[210] XIA, Y., LAU, W.M., LENNARD, W.N., Nucl. Instr. Methods B71 (1992) 165.

[211] ZALM, P.C., FONTIJN, G.M., JANSSEN, K.T.F., VRIEZEMA, C.J., Nucl. Instr. Methods B42 (1989) 397.

[212] ABEL, F., BEHAR, M., COHEN, C., Nucl. Instr. Methods B30 (1988) 13.

[213] BESENBACHER, F., BOTTIGER, J., LAURSEN, T., LOFTAGER, P., MÖLLER, W., Nucl. Instr. Methods 170 (1980) 183.

Chapter 8

YIELDS OF IONIZATION AND EXCITATION IN IRRADIATED MATTER

D. Srdoč
Brookhaven National Laboratory,
Upton, New York,
United States of America

M. Inokuti
Argonne National Laboratory,
Argonne, Illinois,
United States of America

I. Krajcar-Bronić
Rudjer Bošković Institute,
Zagreb, Croatia

The authors acknowledge valuable contributions to this chapter by E. Waibel, Physikalisch-Technische Bundesanstalt, Braunschweig, Germany, Y. Hatano, Tokyo Institute of Technology, Tokyo, Japan and I.G. Kaplan, Karpov Institute of Physical Chemistry, Moscow, Russian Federation.

GLOSSARY

C_i	relative concentration (or concentration fraction) of component *i* in a gas mixture
CSDA	continuous-slowing-down approximation
E_{ex}	energy transferred in an inelastic collision
E	electric field strength
ε	energy carried out by a subexcitation electron
F	Fano factor
FET	field effect transistor
F_i, i=2,3,4	generalized Fano factors
f_{ij}	empirical parameter in energy partition formula
G_s	number of species of kind s produced per 100 eV of absorbed energy
g_{ex}	excitation yield per 100 eV absorbed energy
g_i	ionization yield per 100 eV absorbed energy
I	ionization potential of a gas
K_T	linear operator (cross section operator) in the Spencer-Fano equation
MCA	multichannel analyzer
N_i	mean number of created ion pairs
N_s	mean number of species *s*
n	density number of molecules
σ	total ionization cross section
$\sigma_s(T)$	cross section for the production of species *s*
$P(T_0,j)$	probability distribution that an incident particle will create exactly j ion pairs after complete dissipation of its initial energy T_0
PHA	pulse height analysis
p	pressure
S_i	stopping power
T	energy of ionizing particle in matter, $T \leq T_0$
T_0	incident energy of an ionizing particle
TE gas	tissue-equivalent gas mixture
U	constant describing energy dependence of W
u(T)	energy distribution of an electron source
V_N	variance of the number of created ion pairs
W	mean energy to create an ion pair
W_a	constant value of W at high incident energy
w	differential W value
y(T), $y(T_0,T)$	degradation spectrum, slowing-down spectrum

8.1. INTRODUCTION

Chapter 8 deals with physical quantities that characterize stochastic processes induced in matter exposed to ionizing radiation and related mean values. The term *ionizing radiation* includes photons and charged particles (e.g., electrons, pions, protons, alpha particles, or heavy ions) with energy sufficient to ionize molecules. (The term *molecules* is used to indicate atoms and molecules in gases or appropriate structural units in condensed matter.) These particles collide with molecules many times and thus dissipate their energy in the absorber. Quantities treated below describe major consequences of a multitude of collisions. A review of recent progress in theoretical and experimental research on the ionization yield and its statistical fluctuations in gases, is presented. Excitation yields in gases are discussed in Section 8.5, and W and G values in the condensed phase are discussed in Section 8.6.

The ionization and excitation of molecules are the dominant processes when particles traverse matter, although non-ionizing processes such as molecular dissociation into neutral fragments also take place. Many *secondary electrons* ejected in the primary ionizing events carry sufficient energy to cause further ionizations, and a substantial fraction of radiation energy is delivered to matter through secondary electrons. The molecular entities generated by the interactions of the initial particles and the secondary electrons are termed *initial species*. Subsequently, these initial species may form new species during thermalization and in thermal collisions with other molecules, as discussed in Chapter 6. Evaluation of the initial yield of ions and excited states is essential for dosimetry, radiation chemistry, and biology.

A full description of ionization is given by the probability distribution $P(T_0,j)$, that is, the probability that a particle of initial energy T_0 will give rise to precisely j ion pairs. Often the description is condensed into two parameters: the mean number of created ion pairs N_i and the variance V_N. Statistical fluctuations in the ionization yield are usually characterized by the Fano factor $F = V_N/N_i$.

If particles lose all their energy in the absorber the average amount of energy used to create an ion pair is termed the W value, $W = T_0/N_i$. For particles losing a fraction Δ of their energy a differential value $w = \Delta/N_i$ is defined. A comprehensive review of W values in gases, including some data on W in rare gas liquids and solids, was published by the International Commission on Radiation Units and Measurements in 1979 [1]. Recent developments in experiment and theory presented in this Chapter have significantly enlarged our knowledge on the ionization yield for various kinds of ionizing radiation. In radiation chemistry, in which both ions and excited states need to be discussed, the yield $N_s(T_0)$ of any initial species *s* in irradiated matter is expressed in terms of the G value, $G_s(T_0) = (100/T_0)N_s(T_0)$, i.e., the number of species produced per 100 eV of absorbed energy.

The knowledge of W-values is crucial to radiation dosimetry using ionization chambers and to proportional counter spectroscopy. W values are the link between the energy deposited in the gas by ionizing radiation, and the resulting electric charge measured.

More precisely, in radiation dosimetry using a gas chamber, one is determining the number of ion pairs produced by either primary particles or secondary particles released in the gas, some of which may result from cavity walls. The knowledge of the W value for the particles involved remains the most fundamental in the conversion of the ionization to the energy absorbed. Notice also that the

knowledge of the stopping power (discussed extensively in Chapter 7) is also required in the analysis. For measurements in charged particle beams which traverse a chamber, the differential w value is relevant in calculating the absorbed dose, especially for parallel plate chambers, since only a portion of each track deposits energy in the chamber. Ionization chamber measurements, like proportional counter measurements can make use of W values to correct the energy calibration obtained with a reference source to that for the radiation being measured.

For electrons the degradation spectrum or the slowing-down spectrum $y(T_0,T)$ is fundamental in theoretical calculations of all previously mentioned physical quantities. Its meaning is as follows: $y(T_0,T)dT$ is the summed pathlengths of all the electrons that are generated from a stationary source of electrons of energy T_0 at unit intensity and have kinetic energies between T and T + dT. In theoretical studies, a complete database is needed of all absolute cross-sections (for ionization, excitation, and dissociation) for the interactions of photons and charged particles, especially electrons, with molecules. Once the degradation spectrum has been determined, the yield of ionization, and other initial species, can be calculated.

Calculations may be tested by comparison with experimentally determined quantities such as w, W and F, and thus the accuracy and reliability of the basic atomic and molecular data can be inferred. At the same time, values such as w, W, F, and stopping powers, which are derived from the more fundamental atomic and molecular data, are also directly pertinent to radiation dosimetry, nuclear spectroscopy and radiation chemistry. In particular they determine the accuracy of absorbed dose determination and kerma measurements of direct relevance for radiation therapy using different kind of radiations.

8.2. ELEMENTS OF THEORY

8.2.1. Introductory Remarks

The calculation of the yield of ions, excited states, or any other initial species requires two steps. The first step is to determine the cross-sections for all collision processes of the incident radiation and of all secondary particles, in particular secondary electrons, with molecules in the material.

Cross-section data have been discussed in Chapters 2-6. It is crucial to use cross-section values that are reliable and internally consistent. In particular, cross-sections for individual collisions should be consistent with the total cross-sections for all possible processes and with the stopping cross-section (treated in Chapter 7), both of which are often better known than individual cross-sections. Calculations of initial yield using unrealistic cross-sections are of little value at best and may be misleading.

The second step is the determination of the consequences of all collision processes to both the particle and the material. This analysis belongs to statistical physics [2] or physical kinematics [3] in the language of the Landau school and may be called particle transport theory. Two kinds of approaches are used. The first kind is the Monte Carlo method, in which one simulates histories of collisions for many particles on a computer and draws conclusions from statistics of those histories [4, 5]. The advantage of this approach is the relative simplicity of the algorithms and its resulting applicability to a wide range of problems. Indeed, when questions concerning

media with complicated geometry are asked, the Monte Carlo simulation is often the only practicable method. However, a challenge lies in adopting an informative scheme for statistical analysis of a large volume of numerical data, and also in reliably assessing the precision of results against the background of numerical noise. The second kind of approach is the analytic transport theory, in which one writes an equation for a quantity of interest, such as the yield of a product itself or the energy distribution of energetic particles. The advantages of this approach are the clear meaning of the results and the possibility that general consequences may be deducible without numerical solution. However, a transport equation is solvable through numerical analysis only in simpler cases. Consequently, the two kinds of approaches are complementary. (It is unwise to regard them as competitive, as unfortunately is occasionally done.) Perhaps a good approach will be a hybrid of the two kinds, in which one treats simpler parts of a problem by means of a transport equation and the rest by means of Monte Carlo simulation.

In what follows we present a resumé of the analytic transport theory as an introduction to the discussion of data on the yields of ionization and excited states.

8.2.2. Degradation Spectra

Consider a particle of kinetic energy T moving in a material consisting of n molecules of a single species per unit volume. Let $\sigma_S(T)$ be the cross-section for the formation of product *s* by a collision of the particle. A method for calculating the yield of products is as follows. The number of products *s* produced in a small track of length dx is $n\sigma_S(T)dx$. Therefore, the total number N_S of products *s* produced in a finite track segment may be written as follows:

$$N_S = n\int \sigma_S(T)\,dx \tag{8.1}$$

However, the meaning of the integral is ambiguous unless one specifies how the track length dx is related to T and determines the limits of integration. A relation between dx and T may be readily found in a simple case of an ion at sufficiently high speed losing its kinetic energy gradually, i.e., through many collisions in each of which a small fraction of its kinetic energy is lost to a molecule. Then, the kinetic energy T may be viewed as a smooth function of the track length x, and one may set dx = dT/(dT/dx), where dT/dx is the energy loss per unit track length, viz., the *stopping power*. This idea is now known as the *continuous-slowing-down approximation* (CSDA).

Fano [6] pointed out limitations of this idea and introduced the notion of the *degradation spectrum*, y(T), sometimes called the track length distribution. According to his idea, one rewrites Eq. (8.1) as follows:

$$N_S = n\int dT\, y(T)\sigma_S(T) \tag{8.2}$$

Here the infinitesimal track length dx has been written as y(T)dT, where the function y(T) is determined through methods described in Section 8.2.3. It turns out that y(T) is the same as the product of the speed v_T of the particle at energy T and the number density of such particles, apart from a constant dependent on the volume of the material. (In introducing the idea of the degradation spectrum, one

distinguishes particles by means of their kinetic energies only, regardless of their positions. This is justified so long as the goal is to evaluate the number of products regardless of their positions. For the evaluation of the spatial distribution of the products, one needs the number density of the particles which depends on both their energies and their positions).

8.2.3. Theory of Electron Degradation Spectra

The most important of all the particles generated in any material are electrons, because they are a major component of all materials and are the most readily liberated due to their small mass. Indeed, under irradiation with high-energy photons and particles, a multitude of secondary electrons appear in any material. Therefore, in what follows we shall concentrate on electrons as incident particles.

Spencer and Fano [7] founded the theory of the degradation spectrum. The theory was applied first to high electron energies (≥10 keV), far exceeding the binding energies of atomic electrons in outer shells [8]. The reason for the limitation was the availability of cross-section data; at those high electron energies, using the cross-section for collisions between free electrons (viz., the Mott cross-section at non-relativistic speeds and the Moeller cross-section at relativistic speeds) is justified.

Since the 1970s the Spencer-Fano theory has been applied to electron energies down to the lowest ionization threshold for simpler gases [9-11], for which realistic cross-section data began to be known. More recently, the theory has been extended to treat new aspects, such as statistical fluctuations [12-14] of the yields of ions and other products, mixtures [15-19], time-dependent cases [20-24], and subexcitation electrons [25-31]. The following is a summary of current theory.

8.2.3.1. The Spencer-Fano equation

For simplicity of discussion, let us consider a pure substance consisting of n molecules per unit volume. Suppose that a source in the substance steadily introduces u(T)dT electrons having kinetic energies between T and T + dT. Then, the total track length y(T)dT of electrons with kinetic energies between T and T + dT obeys the Spencer-Fano equation:

$$n K_T y(T) + u(T) = 0 \tag{8.3}$$

Here K_T is a linear operator called the cross-section operator, defined so that $nK_T y(T)dT$ represents the net change of the number of electrons in the energy interval between T and T+dT. If we write the cross-section for all collision processes in which an electron of energy T_1 disappears and an electron of energy T_2 appears as $\sigma(T_1 \rightarrow T_2)dT_1$, then we may write the following:

$$K_T y(T) = \int y(T')\sigma(T' \rightarrow T)dT - y(T)\int dT' \sigma(T \rightarrow T') \tag{8.4}$$

If a collision leads to the production of a new electron, or more, we must include them in the collision operator.

8.2.3.2. The solution for a monoenergetic source

It is useful to consider the solution of Eq. (8.3) for a monoenergetic source of unit strength, viz., $u(T) = \delta(T - T_0)$. We write this solution as $y(T_0,T)$; in other words, $y(T_0,T)$ satisfies the equation

$$n K_T y(T_0,T) + \delta(T - T_0) = 0 \tag{8.5}$$

We call $y(T_0,T)$ the *fundamental solution*. It plays the role of the Green function for our problem, in the language of mathematical physics. The solution of Eq. (8.3) for an arbitrary u(T) is expressed as follows:

$$y(T) = \int dT_0\, u(T_0)\, y(T_0,T) \tag{8.6}$$

We may call Eq. (8.6) the *superposition theorem*.

Another theorem relates three fundamental solutions of different sets of variables:

$$y(T_0,T_2) = -n K_{T_2} \int dT_1\, y(T_0,T_1)\, y(T_1,T_2) \tag{8.7}$$

Equation (8.7) follows readily from the definition of the fundamental solution, Eq. (8.5). To verify this, note that the operator nK_{T_2} acts on $y(T_1,T_2)$ under the integral on the right-hand side of Eq. (8.7). This equation may be called the *combination theorem*. The physical meaning is as follows. The unit source at T_0 causes the electron spectrum $y(T_0,T_1)$ at lower T_1. Each electron at T_1 may be viewed as a source for creating the electron spectrum $y(T_1,T_2)$ at an even lower T_2. The integral over T_1 means that contributions from all T_1 between T_0 and T_2 must be accounted for. Finally, the operator $-nK_{T_2}$ signifies the effects of collisions at T_2 that need to be incorporated to arrive at $y(T_0,T_2)$. The basis of numerical evaluation of the degradation spectrum is indeed Eq. (8.7), applied to sufficiently small steps from T_0 to T_1 and then to T_2. Notice that the degradation spectrum is determined successively by *descending in T*.

8.2.3.3. The yield of an initial species

An alternative method exists for evaluating the yield N_s of any product *s*. Consider the mean number of products *s* resulting from complete degradation starting with an electron of energy T_0:

$$N_s(T_0) = n \int_{E_s}^{T_0} dT\, y(T_0,T)\, \sigma_s(T) \tag{8.8}$$

Here the lower limit of integration is the threshold energy E_s for product *s*.

Let us consider the following integral:

$$\int_{E_s}^{T_0} dT\, N_S(T)[n K_T\, y(T_0,T) + \delta(T - T_0)] = 0 \tag{8.9}$$

Its value is evidently zero because of Eq. (8.5). Recall the definition of K_T, Eq. (8.4), and rewrite the first term in Eq. (8.9) as follows:

$$\int dT\, N_S(T) n K_T\, y(T,T) = n \int dT\, N_S(T) \int dT'\, y(T_0,T')\sigma(T' \to T) - n \int dT\, N_S(T)\, y(T_0,T) \int dT'\, \sigma(T \to T') \tag{8.10}$$

Here every integral is taken over the interval from E_S to T_0. We may interchange the integration variables T and T′ in the first term on the right-hand side, but not in the second term. The final result is expressed compactly as follows:

$$\int dT\, N_S(T) n K_T\, y(T_0,T) = \int dT [n K_T^+ N_S(T)] y(T_0,T) \tag{8.11}$$

Here K_T^+ is a new operator defined as follows:

$$K_T^+ N_S(T) = \int dT' \sigma(T \to T') N_S(T') - N(T) \int dT' \sigma(T \to T') \tag{8.12}$$

The square bracket in Eq. (8.11) means that K_T^+ operates on $N_S(T)$ but not on $y(T_0,T)$. The operator K_T^+ is called the *adjoint* of K_T. The difference between Eqs. (8.4) and (8.12) arises in the first term of each equation. The integration over T′ is taken over the electron energy *before the collision in* K_T, but it is taken over the electron energy *after the collision in* K_T^+.

Let us return to Eq. (8.9) and focus on the second term. Obviously, from the definition of $N_S(T_0)$, Eq. (8.8), this term is equal to the following:

$$\int dT\, N_S(T) \delta(T - T_0) = \int dT\, n \sigma_S(T) y(T_0,T) \tag{8.13}$$

Consequently, we insert Eqs. (8.11) and (8.13) into Eq. (8.9) to arrive at this expression:

$$n \int dT [K_T^+ N_S(T) + \sigma_S(T)] y(T_0,T) = 0 \tag{8.14}$$

Therefore, we may conclude that

$$K_T^+ N_S(T) + \sigma_S(T) = 0 \tag{8.15}$$

at every T. (For the interest of a mathematically minded reader, exceptions may arise at those values of T at which $y(T_0,T) = 0$. An example is $T_0 - E_2 < T < T_0 - E_1$, where E_1 is the lowest excitation threshold and E_2 is the second lowest excitation threshold. From the point of view of physics these exceptions are clearly insignificant for most purposes.)

Equation (8.15) may be solved by starting with the obvious boundary condition that

$$N_S(T) = 0 \tag{8.16}$$

for $T<E_S$ and *ascending in T.* This equation is useful for determining $N_S(T)$ at lower T. However, this approach suffers from accumulation of numerical errors if it is used to determine $N_S(T)$ at $T>>E_S$. Historically, Eq. (8.15) was first discovered by Fowler [32], about three decades before the Spencer-Fano equation. The relation between the Fowler equation and the Spencer-Fano equation was clarified much later [12].

8.2.3.4. The yield fluctuations

Another notable result of recent theoretical research concerns statistical fluctuations of the number of any product *s*. The most commonly used index characterizing the fluctuations is the *Fano factor*:

$$F_S = \frac{V_S}{N_S} \tag{8.17}$$

The Fano factor is the ratio of the variance V_S of the number of products *s* to the mean number N_S. Let us consider these quantities for the *fundamental case*, in which the degradation process begins with a single electron of energy T_0. Then the mean number $N_S(T_0)$ is given by Eq. (8.8). The variance $V_S(T_0)$ is likewise given as:

$$V_S(T_0) = n \int_{E_s}^{T_0} dT\, y(T_0,T)\, \rho_S(T) \tag{8.18}$$

Here $\rho_S(T)$ is a new quantity with the dimension of a cross-section, defined below. Suppose that a collision process p, either ionization or excitation, occurs with the cross-section $\sigma_p(T)$. As a result, the mean number $N_S(T)$ differs by $\Delta N_S(T)$ before and after the collision process p. Then, we may write the following:

$$\rho_S(T) = \sum \sigma_p(T) \left[\Delta N_S(T)\right]^2 \tag{8.19}$$

Here the summation includes all possible processes p. (The sum therefore includes integrals corresponding to ionization processes.)

8.2.4. Characteristics of Electron Degradation Spectra

The knowledge of electron degradation spectra, obtained from various theoretical and experimental studies, is by no means complete. However, it is useful to point out general characteristics that are understood.

8.2.4.1. Dependence of the Spectrum on Electron Energy

The spectrum varies greatly depending on T. The magnitude of the spectrum is thus often shown on the logarithmic scale, as in Fig. 8.1. The spectrum is generally bimodal; it is peaked near the source energy and is peaked more strongly near the lowest energy, I_1, i.e., the (first) ionization threshold. The peaking near I_1 results from accumulation of secondary electrons, most of which are produced at low energies owing to the general characteristics of the secondary-electron spectra (as discussed in Chapter 2).

The fundamental solution $y(T_0,T)$ peaks near the source energy T_0, and declines with decreasing T. According to the CSDA, $y(T_0,T)$ is close to the reciprocal of the stopping power dT/dx at energy T. This rule holds in the interval $T_0/2<T<T_0$, where secondary electrons make no contribution. However, notable exceptions arise at discrete energies $T_0 - E_1$, $T_0 - E_2$, ..., where E_1, E_2, ... are thresholds for discrete excitations; at these energies, the spectrum $y(T_0,T)$ has sharp peaks and vanishes between peaks. These discrete structures, known as the *Lewis effect*, arise from a small number of specific collisions that are necessary to bring down electron energies to specific discrete values. With decreasing energies, these structures diminish and eventually disappear.

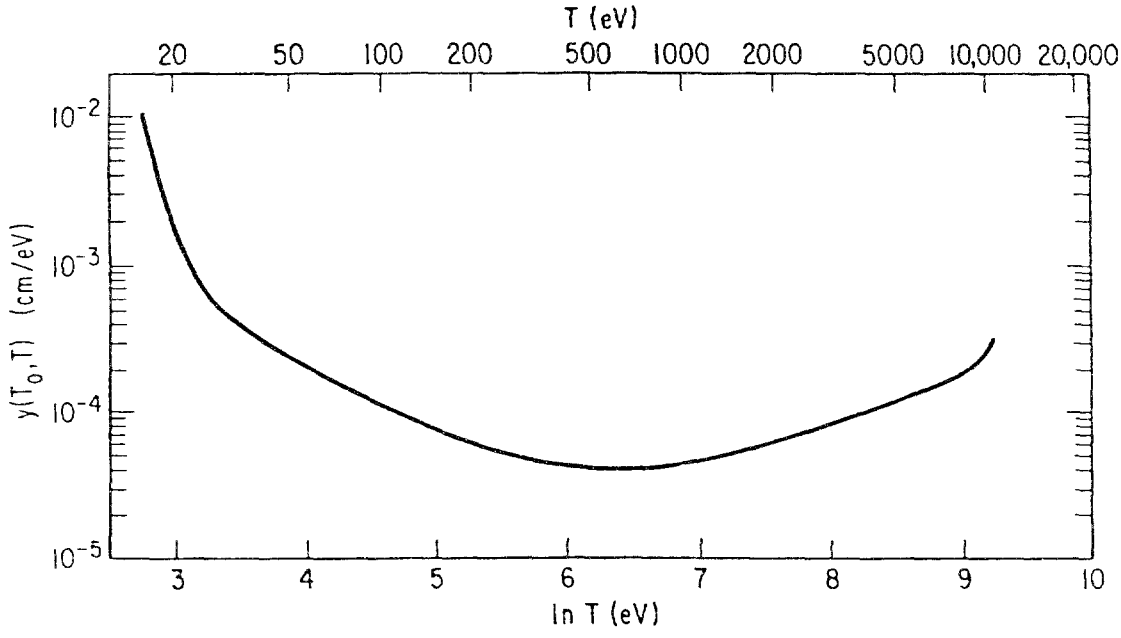

FIG. 8.1. An example of the electron degradation spectrum. The horizontal axis represents the electron energy T on a logarithmic scale. The vertical axis represents the spectrum $y(T_0,T)$ produced in H_2 gas at 0°C at one atmosphere, steadily subjected to incident electrons of initial energy T_0 = 10 keV at the rate of one electron per second per cm^3. Reproduced with permission from Douthat [11].

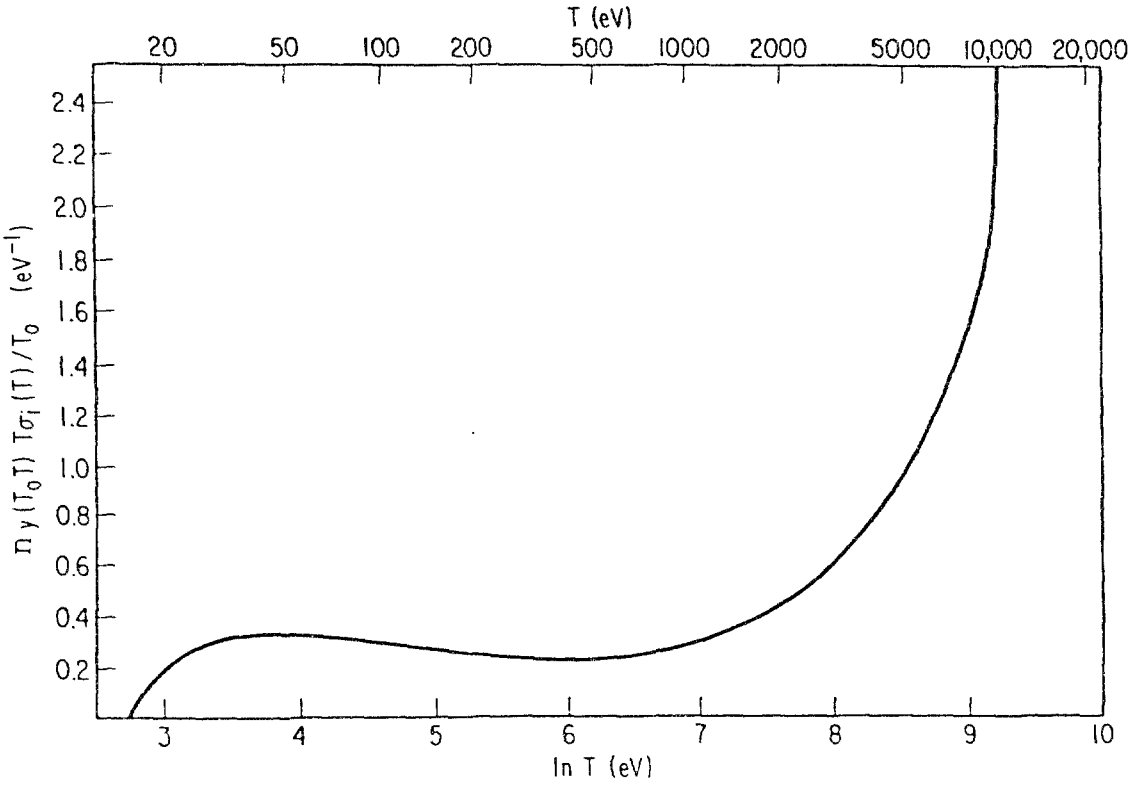

FIG. 8.2. An example of the yield spectrum. The horizontal axis is the same as in Fig. 8.1. The vertical axis represents $ny(T_0,T)T\sigma_i(T)/T_0$, where $y(T_0,T)$ is the spectrum shown in Fig. 8.1., and $\sigma_i(T)$ is the total ionization cross section of H_2 for electrons of energy T.

8.2.4.2. Dependence of Yield on Electron Energy

The relative importance of the electrons of different energies T in determining the yield of ionization or any product is represented by the integrand of Eq. (8.2). Because the T integration runs over many decades, it is best to consider it on the logarithmic scale. Thus, one may rewrite Eq. (8.2) in the following form:

$$N_s = n\int d(\ln T)\, y(T)\, T\, \sigma_s(T) \tag{8.20}$$

Then, the product $y(T)T\sigma_S(T)$ represents contributions to N_S from any unit interval in lnT. We often call the product the *yield spectrum*. Figure 8.2 shows an example. Note the flatness of the spectrum apart from the rise near the source energy. In other words, no energy region is of particular importance for determining the ionization yield; all energies between T_0 and I_1 make appreciable contributions, and the energies immediately below T_0 are somewhat more notable than others.

8.2.4.3. Scaling of the Spectrum

An example of the relations among $y(T_0,T)$ for different T_0 is shown in Fig. 8.3. The near-invariance of the rescaled spectra shown in Fig. 8.3b with respect to T_0 is an explanation of the near-constancy of the W value at high incident energies. Fano and Spencer [33] gave an analytical interpretation of the scaling.

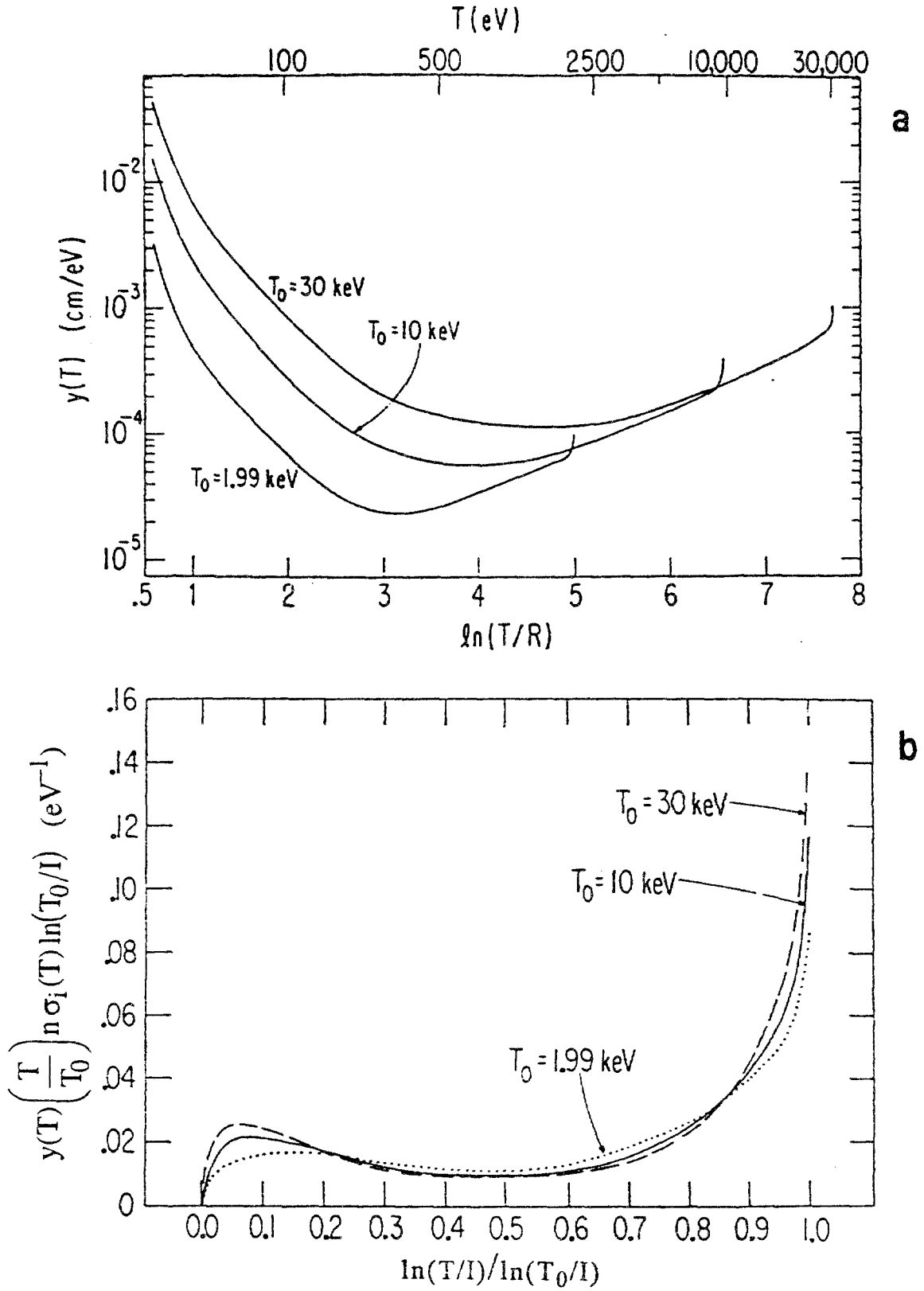

FIG. 8.3. The scaling of the degradation spectrum. The spectra $y(T_0,T)$ are for helium at 0°C at one atmosphere, subjected to incident electrons of initial energies T_0 = 1.99, 10, and 30 keV. In Fig. 8.3a, spectra themselves are shown; in the abscissa scale, R = 13.6 eV. In Fig. 8.3b, suitably scaled quantities are used for both abscissa and ordinate. The three curves are very nearly the same. The symbol $\sigma_i(T)$ represents the total ionization cross-section of He for electrons of energy T, and I represents the (first) ionization threshold, 24.58 eV, of helium. Reproduced with permission from Douthat [9].

8.2.5. Monte Carlo Calculations

Electron degradation processes have been studied by using the Monte Carlo method in various gases (He, Ne, Ar, H_2, CO_2, CH_4, N_2, H_2O vapor and liquid, mixture of Ar + 50% CH_4, and the methane-based tissue-equivalent gas mixture) [5, 34-53] The electron degradation spectra, the ionization and excitation yields, the mean energy required to form an ion pair, the probability distribution of ion pairs formed, and the statistical fluctuations of the yield were obtained from computer simulation for various incident energies Thus, it was possible to study the probability density distribution of the number of ion pairs and their moments as a function of incident electron energy The obtained values were compared to experimentally determined values and results of the Monte Carlo calculations are presented in Sections 8 3 and 8 4, together with experimental data The uncertainty of Monte Carlo calculations is primarily defined by uncertainties in cross section data needed for calculation In particular, the data for water, the principal constituent of biological cells, are important for radiation physics, chemistry, and biology However, experimental data on cross-sections and other relevant quantities for liquid water are very scarce Water in both gaseous and liquid phases was intensively studied by Paretzke and Berger [39], Hamm et al [40], Turner et al [41], Paretzke et al [5, 42], Terrissol et al [43], Malbert et al [44], and Kaplan et al [45-49] Results for liquid water are presented in more detail in Section 8 6

8 3 THE W VALUE

Let $N_i(T_0)$ be the mean number of ion pairs (the mean ionization yield) formed by incident ionizing radiation after complete dissipation of its energy T_0 The mean ionization yield is customarily expressed in terms of the mean energy per ion pair

$$W(T_0)=\frac{T_0}{N_i(T_0)} \tag{8 21}$$

At high energies (usually at $T_0 \geq 10$ keV for electrons), the W value generally approaches a constant value W_a [1] The W value increases as the incident particle energy decreases (below about 1 keV for electrons), because in the low-energy region, the ratio of the ionization cross-section to the cross-section for non-ionizing processes becomes smaller than in the high-energy region The fraction of incident energy carried by subionization electrons must also be considered Inokuti [54] proposed an analytic approximation $N_i(T_0) = (T_0 - U)/W_a$, where U is a constant close to the mean energy of the subionization electrons, and W_a is the asymptotic value of W at high energies According to this idea, we may write the following

$$W(T)=\frac{W_a}{1-U\,T_0} \tag{8 22}$$

Measurements on propane [55], methane [56], and xenon [57] give an energy dependence consistent with this relation down to quite low energy Some older measurements in air and other gases [58-60] give a much stronger energy dependence,

but several recent measurements in the same gases [50, 51, 61, 62] are in agreement with Eq. (8.22). (As a qualification we note that some of these measurements [55-57] were made with the use of photons, which act as a source of electrons having a distribution of initial energies. Therefore, comparison of those measurements with Eq. (8.22) is not altogether straightforward).

The W value is defined for complete dissipation of the initial energy T_0 to the matter. However, for high-energy particles in thin media, it is necessary to consider the differential value, w, of the mean energy necessary to produce an ion pair, defined as follows:

$$w = \frac{dT}{dN} \tag{8.23}$$

Here dT is the mean energy lost by a charged particle of energy T in traversing an absorber of thickness dx, and dN is the mean number of ion pairs produced when dT is completely dissipated in the gas. The relationship between w and W is as follows:

$$\frac{1}{w(T)} = \frac{d}{dT}\left[\frac{T}{W(T)}\right] \tag{8.24}$$

If W(T) = W = const at any particular T, then w(T) = const at that T, and its value is W. This rule holds for sufficiently high T_0, to a close approximation. (As a qualification, the above discussion presumes that dT in Eq. (8.23) is the energy *deposited* within the thickness dx. Any energy departing from dx, e.g., by means of secondary electrons must be corrected for, in a rigorous treatment).

To explain the magnitude of the W value in pure gases, Platzman [63] gave an elementary treatment based on the idea of energy balance. When the kinetic energy T of any incident particle is completely absorbed in a pure gas, the energy T may be apportioned into three parts, a part used in producing discrete excited states or neutral dissociation fragments, a part used in producing ions, and a part carried by *subexcitation electrons* (i.e., electrons that have kinetic energies lower than the first electronic-excitation threshold and are therefore incapable of producing excited states or ions). Let N_{ex} be the mean number of excited states produced and $\overline{E}_{ex}$ the mean energy transfer per excited state. Let N_i be the mean number of ions and $\overline{E}_i$ the mean energy transfer per ion pair. Note that the total number of subexcitation electrons is equal to N_i and suppose that the mean kinetic energy carried by them is ε. Then, one may write:

$$T = N_i\overline{E}_i + N_{ex}\overline{E}_{ex} + N_i\varepsilon \tag{8.25}$$

By definition the W value is the ratio T/N_i. A natural unit for the W values is the (first) ionization threshold I for the gas; therefore, we consider the ratio W/I. This ratio may be expressed as follows:

$$\frac{W}{I} = \frac{\overline{E}_i}{I} + \frac{N_{ex}}{N_i}\frac{\overline{E}_{ex}}{I} + \frac{\varepsilon}{I} \tag{8.26}$$

Each term of this equation depends on the particle energy T, but the dependence on T is weak for T>>I. For pure helium, Platzman gave the following estimates of the magnitude of each term for large T values:

$$1.71 \approx 1.06 + 0.85 \cdot 0.40 + 0.31$$

The ratio $\bar{E}_i/I$ is slightly greater than unity because excited states of He^+ ions are produced. The ratio should be greater for other atoms (for which possibilities for excited ion states are more diverse), and even greater for molecules (which lead to molecular ions that may dissociate or may carry some vibrational and rotational energy). The ratio $\bar{E}_{ex}/I$ is generally less than unity but is close to unity because excited states lie slightly below I in most cases. Molecules have superexcited states that are above I and yet produce neutral fragments; therefore, one expects a higher value of the ratio. The ratio N_{ex}/N_i is hard to evaluate without detailed analysis. It is about 0.5 for closed-shell atoms, about 1 for ordinary molecules, and about 2 for free radicals (molecules containing an odd number of electrons), according to Platzman's estimates [63], which are basically correct in the light of current knowledge. The ratio ε/I should be smaller than unity in general, and it is about 0.3 for rare gases. Consequently, the ratio W/I, for high-energy particles is 1.7 - 1.8 in rare gases and 2.1 - 2.5 in molecular gases.

A characteristic feature of rare gases is a relatively small number of excitations in comparison with the number of ionizations. This feature is reflected in relatively small values of W/I and the Fano factor compared to molecular gases. The ionization of molecular gases is more complex, because non-ionizing dissociation processes are possible after the transfer of energy T>I [64, 65], and the ionization process competes with the neutral fragmentation. Consequences of the competition to the ionization yield were pointed out by Platzman [64, 65] and were further discussed by Alkhazov [66]. This topic is closely related to the quantum yield of photoionization, as discussed in Chapter 5. A recent study by Kimura et al. [67] showed that the competition between these channels for the de-excitation of superexcited molecular states is responsible for oscillations in the W value in a series of alkanes.

Extensive knowledge of the W value for different incident particles of various incident energies in gases and liquids is needed for full elucidation of radiation effects. Measurements of absorbed dose or of *kerma* by using gas cavity chambers require precise knowledge of basic physical data. For radiotherapy it is desirable to determine doses in soft tissue with an overall absolute uncertainty of 5% [68-70]. Such an overall accuracy implies that the separate contributions of stopping power ratios, W values, and kerma ratios in ion chamber materials and tissues should be known with absolute uncertainties of ±2% or less.

The ICRU Report 31 [1] on W values provides a database of measured W values for different charged particles in various gases, published up to 1978. Most of the W values presented in ICRU Report 31 [1] were obtained at high energies, where significant energy dependence was neither expected nor observed. We will refer to the average high-energy W values as *ICRU values* in the following sections. In this Chapter we will pay more attention to new data obtained either experimentally or theoretically since 1978 and will attempt to critically assess all published data. Recent experimental W values in various gases are presented as a function of energy. Materials of interest for dosimetry and radiotherapy are argon, hydrogen, nitrogen, oxygen, methane,

propane, butane, carbon dioxide, tissue-equivalent gas mixtures, water (vapor and liquid) and air. Methane-based tissue-equivalent (TE) gas is a mixture of 64.4% CH_4, 32.4% CO_2, and 3.2% N_2 (by volume) [71], and the propane-based TE gas mixture consists of 54% propane, 40.5% CO_2, and 5.5% N_2 [72].

8.3.1. Experimental Methods and Errors in Measurement of W Values and Fano Factors

Two entirely different experimental methods have been applied in measurements of W values and Fano factors in gases. The classical method of Jesse and Sadauskis, consisting of precise measurements of electric current (DC) produced by ionizing radiation in a gas-filled chamber, was developed in the early 1950s [73-76]. The *pulse* ionization chamber method exploits the signal generated by heavy ions well above the electronic noise, to measure the charge produced by the particle to calculate the W values. The low LET radiation, such as x-ray, gamma, and beta radiation, produce pulses that are too small to be distinguished from electronic noise, therefore another technique must be applied to measure the particle counting rate, as explained in 8.3.1.2. and elaborated by Waibel [77]. A different method of measurements of W values for low energy particles (T_0<10 keV) was developed by Srdoč [55, 78] and elaborated by his co-workers [79, 80]. The new method is based on the pulse height analysis (PHA) of electrical pulses produced by multiplication of initial (primary) charges in a gas-filled proportional counter. The proportional counter is calibrated by applying a source of single electrons, enabling the measurement of spectra of ionizing radiation in terms of *number of electrons per ionizing event*, which, in turn, makes possible the calculation of the *mean value* of number of electrons per event and determination of the *shape* of the distribution of primary ionizing events. Further elaboration of the PHA method led to measurement of the W values and Fano factors for a variety of gases and gas mixtures [55, 56, 78, 81-85]; however, the total amount of data on W values in gases so far produced by applying this method is rather modest. The PHA method is convenient because it enables the determination of W *and* F values simultaneously; also, it represents an independent method for cross-checking the W values obtained by the classical ionization chamber method. It requires a source of low energy photons for W measurements (up to ≈10 keV, in its present stage of development), therefore it is of potential use for synchrotron radiation. Presently, it is widely used in microdosimetry for measurement of energy deposition in small volumes [72] and can be applied for w measurements of energetic particles. The DC and PHA methods are complementary, however, both involve inherent experimental errors, which will be briefly discussed in the following paragraphs.

8.3.1.1. Sources and energy of incident radiation

To obtain experimental W values by either the DC or PHA method, one must determine the particle energy T precisely. The most reliable particle sources with well defined energy are either radioisotopes or soft X ray machines, emitting photons that enter the measuring device (an ionization chamber or a proportional counter) through a thin window (e.g., Be or Mylar) without losing beam intensity [86]. Recently, synchrotrons with double monochromators provide photon beams with high energy resolution and high intensity. This type of particle source can be applied in the

measurement of W values for photo-electrons ejected from the K shell of gas molecules in the chamber. Depending on the chamber (or counter) size, gas density, and Z (the atomic number), the created secondary electrons are usually contained in the active gas volume up to the incident particle energy of several keV. Care must be taken at intermediate and high energies to avoid loss of energy to the chamber walls instead of the active gas volume. This may be done by increasing the gas density (pressure). However, limits often exist, beyond which the experimentalist may encounter more troubles than gain, such as an incomplete charge collection due to low E/p near the chamber walls, ruptures of fragile windows, or electric breakdowns due to the excessively high voltage required to operate the proportional counter at high gas pressures.

Sources emitting α and ß particles are usually manufactured in the form of foils or plaques having the active material electrodeposited on the base metal. Very often a thin protective layer of gold, for example, is evaporated on the active surface. In such cases one has to take into account the particle energy losses (1) due to self-absorption in the active layer; (2) in the protective layer; (3) in the gap between the source and the chamber window, if the gap is filled with a gas; and (4) in the chamber window. The energy degradation of the particle due to losses in the source and along its path to the gas-filled chamber, is often difficult to calculate precisely. In some cases, however, all the uncertainties in determining the incident particle energy can be eliminated by using internal gaseous sources, such as ^{37}Ar. Adding a small amount of radioactive gas to the working counter gas can eliminate particle energy losses due to passage through various materials outside the active gas volume in the chamber.

When electrons or ions are produced by accelerators (here we are dealing mostly with *very low energy* accelerators), care must be taken to avoid several sources of energy distortion. At low electron energies, up to a few hundred electron volts, the work function of the target material must be considered. The energy spread of the electron or ion beam must be closely controlled. The electron energy spread and the mean energy shift are caused by the space charge at the source and depend on the particular source parameters [87, 88]. The voltage ripple introduced by power supplies of ion accelerators must be measured and its effect on the spread of the electron energy must be evaluated. Loss of energy in the entrance window or in the effluent gas, if an entrance aperture is used, can lead to significant errors. Another source of energy shift can be the ion-collecting voltage in the gas chamber. At very low particle energies approaching the ionization threshold a DC method with alternate non-symmetrical pulsed primary and secondary currents is applied to avoid serious changes of the input particle energy caused by the ion collecting field [61]. In the adjacent higher energy region the current or charge integrating methods give the best results [51, 52, 62, 89]; in both cases no chamber window foils are acceptable for charged particles due to the large loss of energy in the window material. At higher particle energy the primary particle rate is measured by counting individual particles to avoid a large difference in DC current, provided that the corresponding pulse height distribution of the primary particles can be safely discriminated against noise [90]. And at very high energies where the ionization chamber dimensions should be very large and the pressure high to stop the particles it is more convenient to measure differential w values [91, 92].

8.3.1.2. Ionization chamber measurement techniques

Measurements of W values in gases by means of DC ionization chambers require a precise determination of the total number of particles entering the chamber with energy T and the number of ion pairs resulting from interaction of energetic particles with gas molecules. This setup, called the *integration mode*, is very often replaced in practice by measuring the *particle rate* and the corresponding *ionization current*, which is the electric current produced by interaction of incident particles with the investigated gas. Steady source conditions must therefore be provided, because in most cases there is no way to measure both the primary particle current and the secondary ionization current simultaneously.

The primary particle rate must be kept low to avoid space charge and recombination effects caused by high ionization density, especially at higher incident particle energies. Hence, only at lower particle energies are current or charge integration methods convenient. Particle counting methods are applied by using the ionization pulse in the gas of interest with or without gas amplification. Two main sources of error should be mentioned here: incorrect discrimination against electronic noise [93], and deadtime losses. Analysis of pulse height distribution and the theory of counting losses must be applied. For current or charge measurements, the precision and stability of the capacitors and resistors of the input preamplifier are of utmost importance [93]. Charge exchange of accelerated ions with residual gas molecules in the beam-guiding system leads to errors in particle current measurement; the corresponding cross-sections are high at low energies.

The number of ion pairs may be determined from each ionization pulse, but in most cases it is derived from the mean ionization current or an integrated charge. High collection efficiency must be ensured; this depends on the chamber geometry, the type of gas, the pressure, and the ion density. Loss of particles due to scattering in the effluent gas from the entrance aperture must be taken into account by using the pressure dependence of the ionization current. By extrapolating the pressure-dependent current from the region of complete particle stopping to $p \rightarrow 0$, the ionization and particle losses in front of the entrance aperture can be taken into account [94]. However, an optimum collection of charges can be achieved in many cases only if the collecting voltage is varied with a constant ratio E/p of electric field strength E and pressure p. From the dependence of the ionization current on the ratio E/p, the energy shift can easily be determined if a parallel-plate ionization chamber is used in the region of high collection efficiency [94]. Attention should also be given to ionization losses due to the backscattering of primary particles in the gas; this effect is especially important for electrons.

8.3.1.3. Proportional counter measurement technique

Except for alpha particles and heavy ions, most of ionizing particles produce a too small an electric charge in a chamber or counter gas to be detected directly by the coupled electronics. In spite of a significant progress in low-noise techniques [93] the signal produced by beta or gamma rays in an ionization chamber is buried in electronic noise. Therefore, gas multiplication of the order of 10^3 is required to raise the signal above the noise. A proportional counter serving that purpose delivers electric pulses proportional to the electric charge produced in the counter gas, which

is, in turn, proportional to the incident particle energy dissipated in the gas and inversely proportional to the W, i.e., the energy spent to form an ion pair.

The proportional counter technique for measurement of W values and Fano factors comprises three interconnected systems: (1) the proportional counter and the associated gas handling manifold, (2) the electronics and high-voltage power supplies, and (3) the data processing system, usually on-line for data acquisition and off-line for subsequent elaborated data processing. Each of the three steps contains specific problems and inherent measurement errors that will be discussed briefly.

To obtain by the proportional counter method a reliable and reproducible distribution of electric charges produced by incident particles in a gas, the following conditions must be met or precautions taken:

The contamination of the investigated gas in the proportional counter arising from vacuum lines and counter casing leaks should be carefully tested and eliminated. A vast selection of methods for eliminating or reducing outgassing (a slow diffusion of gases trapped in metal, especially in plastic insulators inside the gas-filled volume) have been described in high vacuum literature. Essentially, prolonged pumping and simultaneous baking at an elevated temperature of all parts of the vacuum system are recommended. A different approach consists of the so-called *flow mode*, in which a constant flow of the investigated gas maintains the required gas purity. The flow mode helps to overcome the leakage and outgassing problems, but very often the fluctuations in gas pressure due to imperfect pressure regulating devices offset all the advantages of the flow mode. Rubber or plastic gaskets used to seal various metal parts of an assembled proportional counter are prone to leaks over a prolonged period of time because of diffusion of atmospheric gases into the counter. The vacuum sealants behave similarly. A compromise leading to a good, practical solution was applied by Srdoč and Clark [86]. The procedure consisted of a combination of both techniques, that is a thorough outgassing at an elevated temperature followed by system operation in the gas flow mode. However, to avoid gas pressure fluctuations during data collection, the proportional counter was sealed off by closing the inlet and outlet valves. The gas purity was controlled by measuring a calibration spectrum before and after data collection under the closed system mode. Additional good practices are keeping the air out of the vacuum lines and the counter at all times and soaking the counter in the gas at working pressure for 24 h before measurement. The experimentalist is coping with two entirely different and very distinct phenomena in gaseous physics. A small amount of inadvertently admixed gas, very often of the order of ppm, causes no substantial change of W values or Fano factors in *regular* gas mixtures, as explained in Section 8.3.7. However, the admixture of any gas that makes the gas mixture *irregular* will drastically change the physical properties of the gas mixture by inducing the Jesse or Penning effects. The W and F values obtained in such cases are relevant to the (very often unknown) gas mixture, not to the vehicular gas. A totally different phenomenon occurs if the gas impurity contains a component having a high electron attachment coefficient, such as the ubiquitous oxygen [95]. In this case, the primary distribution of charges may not be significantly affected by, e.g., several ppm of O_2 in a gas. However, the probability that free electrons formed in the track (or in a cluster in the case of a low-energy particle) are attached to O_2 molecules is relatively high in a period of time much shorter than the average transit time for electrons to reach the gas multiplication zone in a proportional counter. Consequently, a significant fraction of created free electrons is lost for multiplication

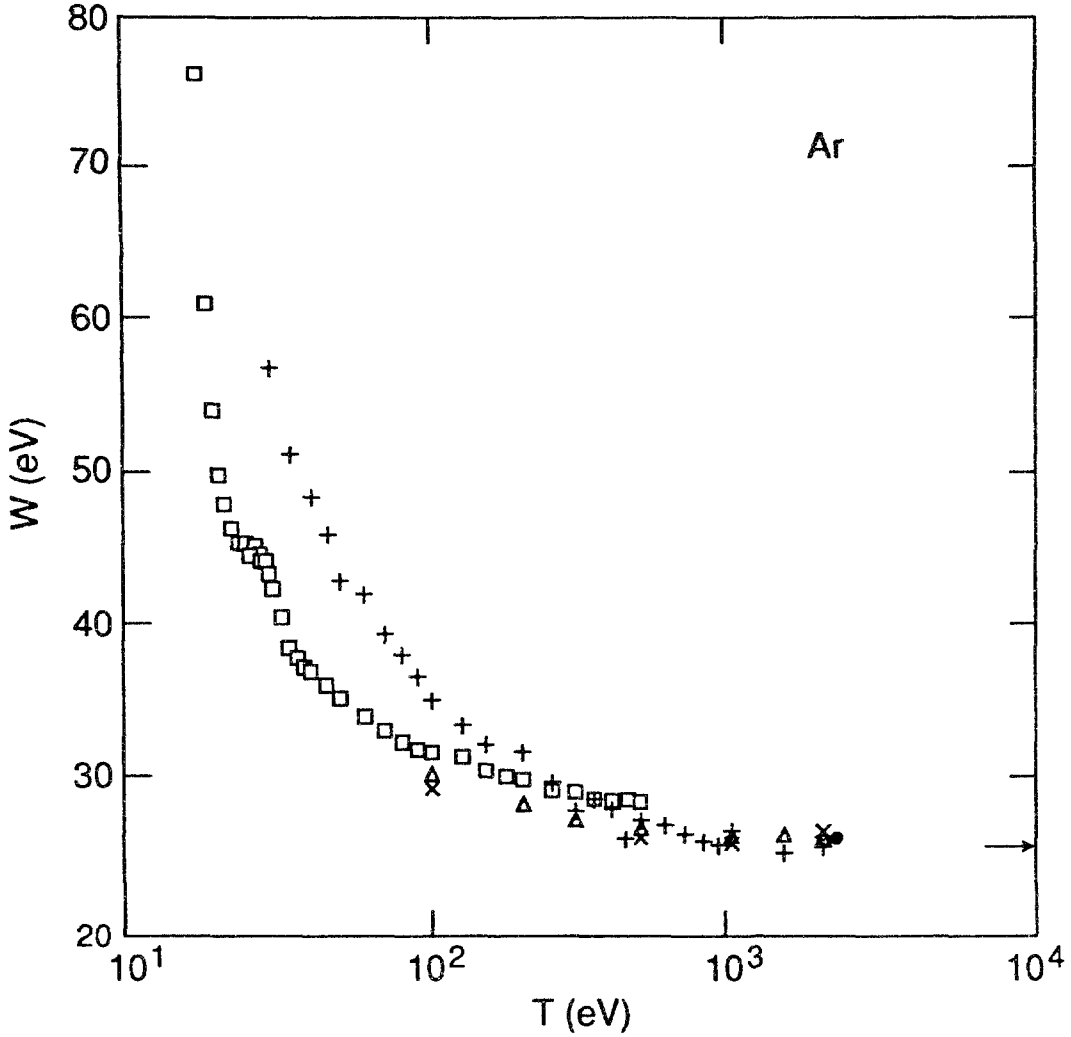

FIG. 8.4. W value for electrons in argon. The ICRU [1] reference value of 26.4 eV is denoted by the arrow. +, Smith and Booz [60]; □, Combecher [61]; Δ, Kowari et al. [14]; •, Eggarter [15]; ×, Unnikrishnan and Prasad [98]. Measured W values [60, 61] are presented together with W values calculated by applying the following methods: Monte Carlo [98], the Fowler equation [15], and the Spencer-Fano theory [14]. Monte Carlo calculation by Grosswendt [37] (not shown here) is in good agreement with measured W values [61], except at very low energies. The differential w value for ^{60}Co gamma rays, measured by Hiraoka et al. [99], is 26.0 eV.

because heavy, negatively charged O_2 molecules cannot gain enough energy in an electric field to produce additional charges on collision, and detachment coefficients are usually too low at E/p values encountered in proportional counters to free the electrons. The net result is a completely distorted spectrum, shifted toward the low-energy side, which is useless for further processing and calculation of W or F values. Low-energy electron attachment to O_2 molecules in gas mixtures has been extensively studied and summarized in a recent review [96]. The effect of the attachment process on the response-time of an air-filled ionization chamber and the consequences on W and F value measurements have been discussed in details.

Besides gas pressure and composition, gas multiplication depends strongly on the counter's high voltage. Care must be taken to provide a high-quality power supply

without ripples. Continuous monitoring of the high voltage during measurement is recommended. The input stage of a preamplifier should be coupled directly to the proportional counter anode at ground potential, to reduce excessive input capacitance, which is a major source of electronic noise. A low-noise FET preamplifier developed by Radeka [93] serves well for signal amplification.

The process of gas multiplication introduces a substantial broadening of lines in the event-frequency spectrum, which is more conspicuous with decreasing particle energy. Thus, a spectrum of monoenergetic K_α lines of Al ($T_0 \approx 1.5$ keV) or C ($T_0 \approx 0.277$ keV) consists of a broad, bell-shaped pulse height distribution, and the so-called single electron spectrum in a proportional counter is a curve stretching over two decades, which can be fitted by a gamma function. In spite of such extreme broadening of energy lines due to the very nature of electron multiplication in a gas under the influence of a strong electric field, recent developments in computer-assisted data processing have eliminated the broadening of spectral lines introduced by gas multiplication [80, 81].

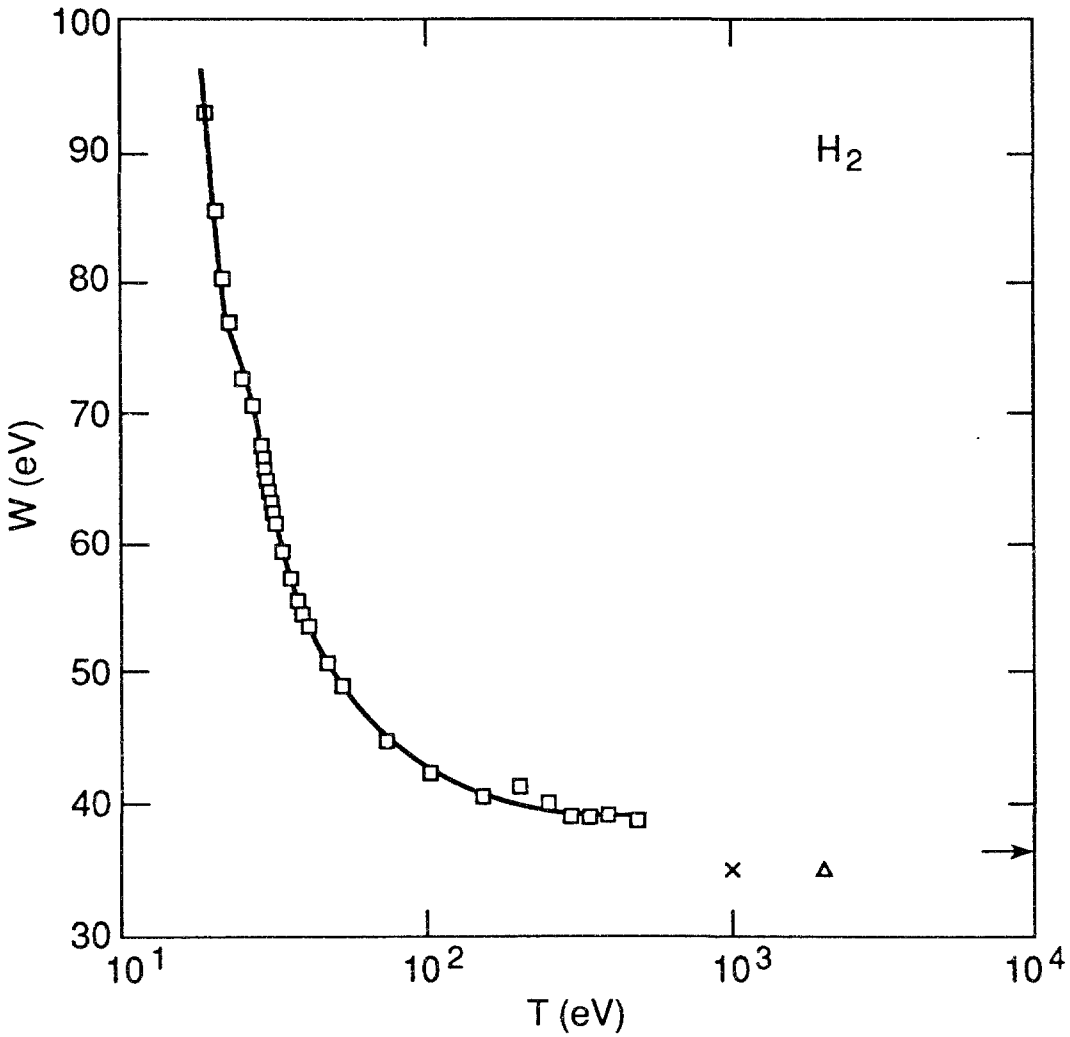

FIG. 8.5. W value for electrons in hydrogen. □, H_2, Combecher [61]; —, D_2, [61]; Δ, Eggarter [15]; ×, Kimura et al. [100]. The ICRU [1] high-energy value (36.5 ± 0.3 eV) is denoted by the arrow. W values for keV electrons in H_2 were calculated according to the Fowler equation [15] and the Spencer-Fano theory [100].

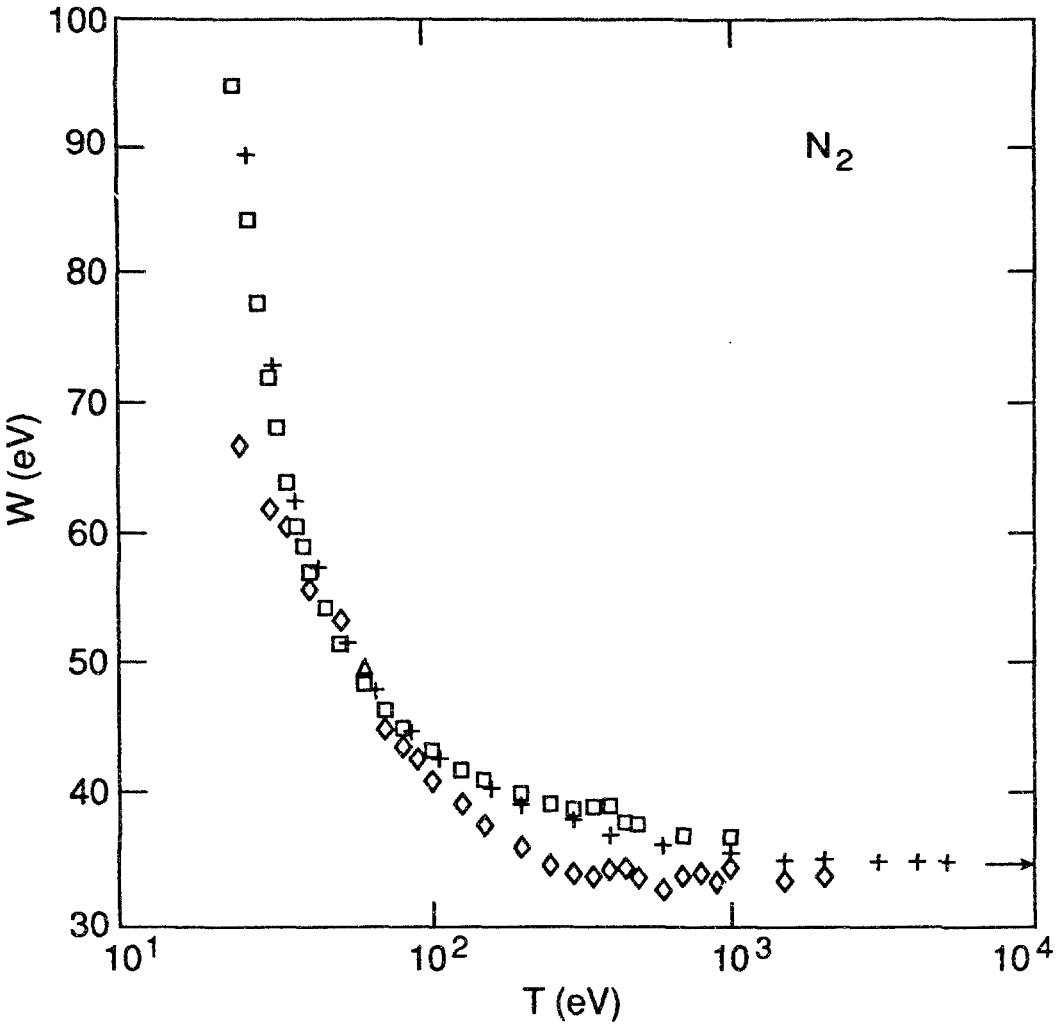

FIG. 8.6. W value for electrons in N_2. The ICRU [1] high-energy value (equal to 34.8 ± 0.2 eV) is denoted by the arrow. ◊, Smith and Booz [60]; □, Combecher [61]; +, Waibel and Grosswendt [51]. The differential w value measured by Hiraoka et al. [99] for ^{60}Co gamma rays is 35.1 eV.

The processing of spectra obtained by a proportional counter is described in some detail in [80]. Most spectra are incomplete in their original form; usually the low-energy part is buried in electronic noise and the high-energy tail is missing because of the limited range of most electronic devices (typically two decades). Careful extrapolation is required, based on the best fit to experimental data or the theoretical or empirical shape of the pulse height distribution. The deconvolution of experimentally obtained spectra, properly processed at the low- and high-energy ends, is performed by the aid of a computer [80, 81]. The final result is a frequency distribution of ion pairs in the investigated gas, irradiated by a chosen ionizing radiation of a well-defined energy. The W value and the Fano factor are easily calculated from such a frequency distribution.

The accuracy of W values and Fano factors obtained either by the ionization chamber or proportional counter method depends on so many experimental errors, as described above, that the error margins claimed by the author(s) must be taken cautiously. A *laboratory bias* is sometimes evident, meaning that a set of data published by an author or a group of authors using the same instrument in a laboratory may differ systematically from another set of data or an accepted set of average values. With typical experimental errors in ionization chamber and proportional counter techniques, an overall error of ±2% may be considered realistic for W and F values. Departures in both directions are possible. Experimental values deviating more than 3% from an accepted average value should be shelved until more data are available to confirm or definitely reject the values.

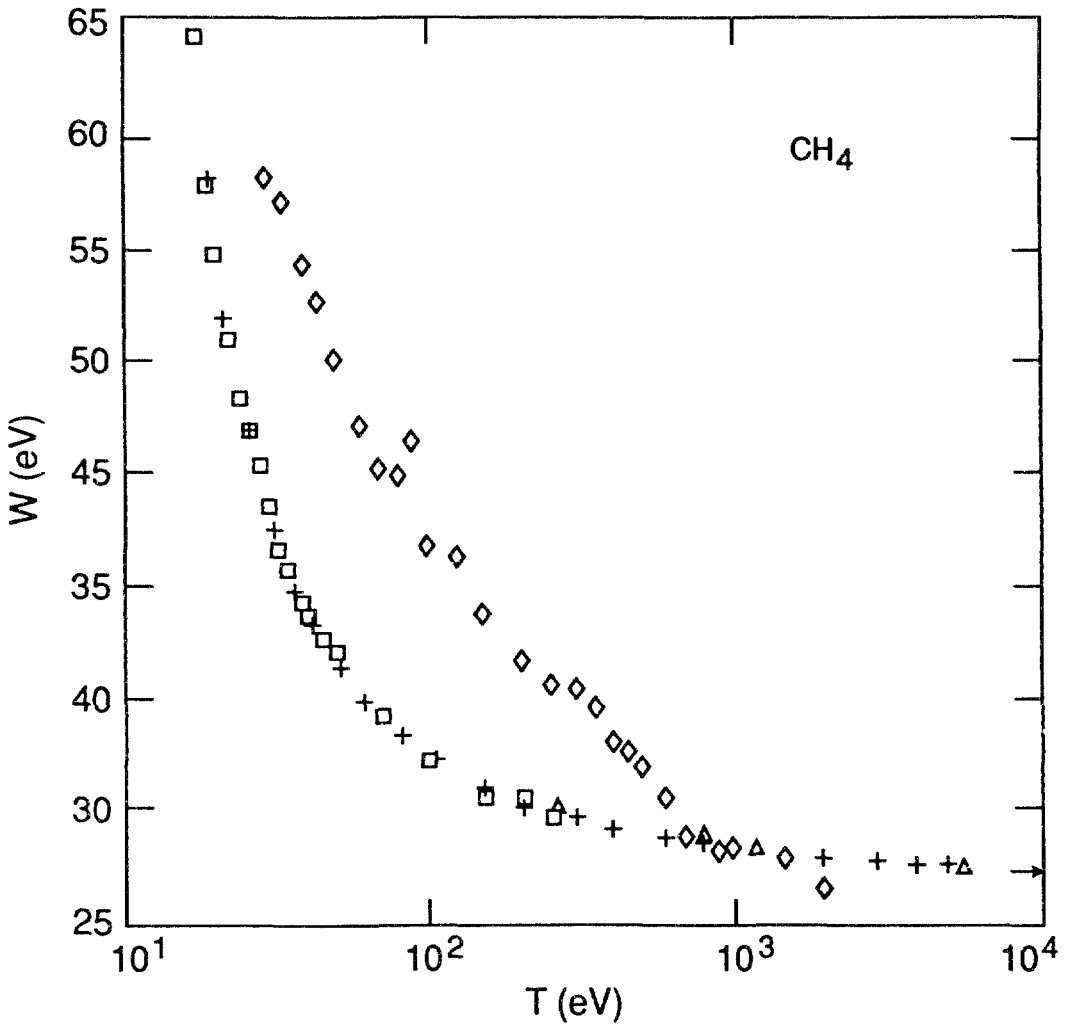

FIG. 8.7. W value for electrons in CH_4. The ICRU [1] high-energy value (equal to 27.3 ± 0.3 eV) is denoted by the arrow. ◊, Smith and Booz [60]; □, Combecher [61]; +, Waibel and Grosswendt [50]; and Δ, Krajcar-Bronić et al. [82]. Data in [60] differ significantly from other data. Monte Carlo calculations by Waibel and Grosswendt [50] (not shown here) are in good agreement with the experimental data of the same group and those of Combecher [61]. Data of Krajcar-Bronić et al. [82] are electron W values calculated from photon W values measured by Srdoč [78]. The differential w value, equal to 26.6 eV with uncertainty of 4.3% and measured by Hiraoka et al. [99] for ^{60}Co gamma rays (1.33 and 1.17 MeV), is in good agreement with the ICRU high-energy W value.

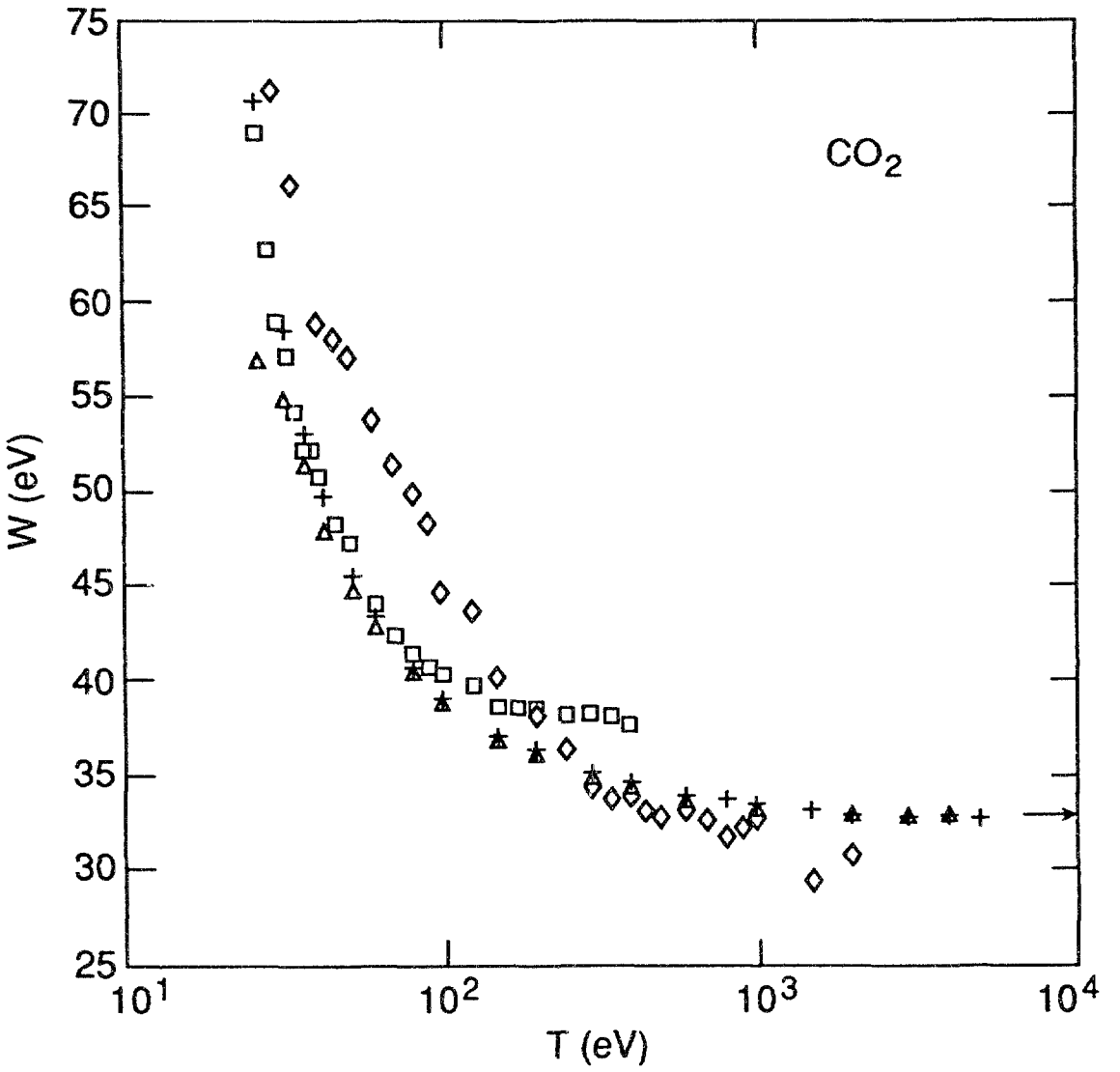

FIG. 8.8. W value for electrons in CO_2 The ICRU [1] high-energy value (equal to 33.0 ± 0.7 eV) is denoted by the arrow. ◊, Smith and Booz [60]; □, Combecher [61]; +, Waibel and Grosswendt [52]; Δ, Monte Carlo calculations by Waibel and Grosswendt [52]. Data of Combecher [61] above 100 eV and data of Smith and Booz [60] differ from data of Waibel and Grosswendt [52], which approach the high-energy W value. Monte Carlo calculations [52] closely follow the experimental W value, with a small discrepancy at the low-energy end. The differential w value for ^{60}Co gamma rays, measured by Hiraoka et al. [99], is 33.4 eV.

8.3.2. W Values for Electrons

Combecher [61] has published W values for electrons in air, N_2, O_2, CO_2, TE gases, H_2, D_2, H_2O, D_2O, Ar, Kr, Xe, methane, ethane, propane, butane, pentane, hexane, nonane, ethylene, acetylene, ethanol, acetone, C_6H_6, and C_6D_6 in the energy range from 200 eV to 1200 eV. He claimed a total experimental error in W of less than 2%. Smith and Booz [60] measured W values for electrons in methane-based TE gas, CH_4, CO_2, N_2, and Ar from 30 eV to 2 keV with quoted uncertainties larger than 5%. Waibel and Grosswendt published measured W values for air [62], CH_4 [50], N_2 [51], CO_2 [52] and methane-based TE gas [53] in the energy region from 20 eV

to 5 keV. The standard deviation of these data is less than 1% for energies between 50 eV and 5 keV and less than 2% below 50 eV in most cases. Waibel and Grosswendt gave also fitting parameters to their experimental data, carried out Monte Carlo calculations and obtained W values for CH_4 [50], N_2 [51], CO_2 [52] and methane-based TE gas [53] in good agreement with measurements. Tung and Baum [97] calculated W values for electrons of 1-10 keV in several hydrocarbons by using Inokuti's solution of the Fowler equation.

Figures 8.4-8.14 show W values for electrons in various pure gases, in tissue equivalent gas mixtures, and in air as a function of electron energy.

W values in argon are presented in Fig. 8.4. The data of Smith and Booz [60] show stronger energy dependence than data of Combecher [61] and the calculated

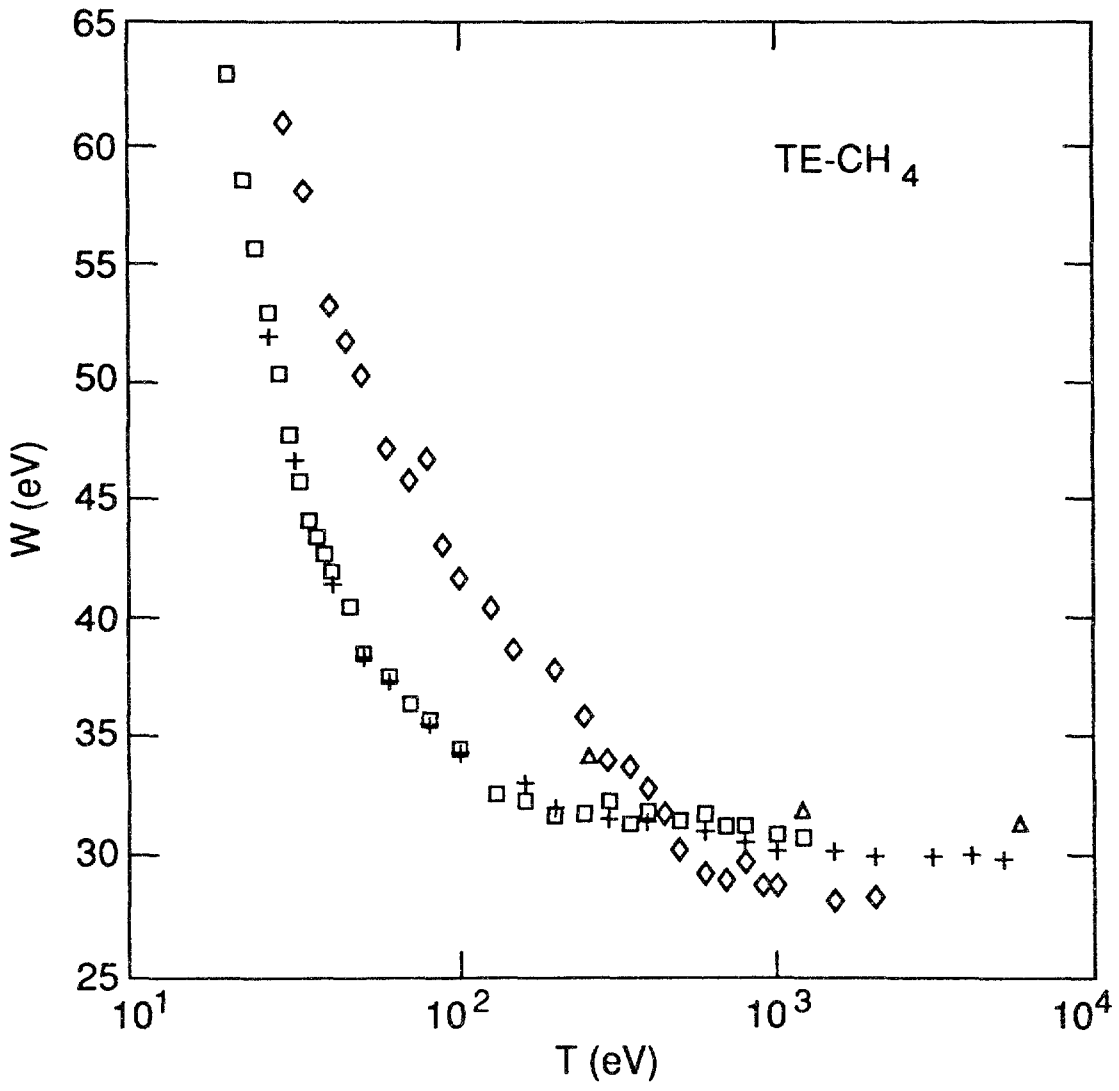

FIG. 8.9. W value for electrons in methane-based TE gas. ◊, Smith and Booz [60]; □, Combecher [61]; +, Waibel and Grosswendt [53]; Δ, Krajcar-Bronić et al. [82]. Data in [60] significantly differ from those in [61] and [53]. Data of Krajcar-Bronić et al. [82] are electron W values calculated from photon W values measured by Srdoč [78]. The differential w value for ^{60}Co gamma rays, measured by Hiraoka et al. [99], is 29.4 eV. This value may be taken as the high-energy W value.

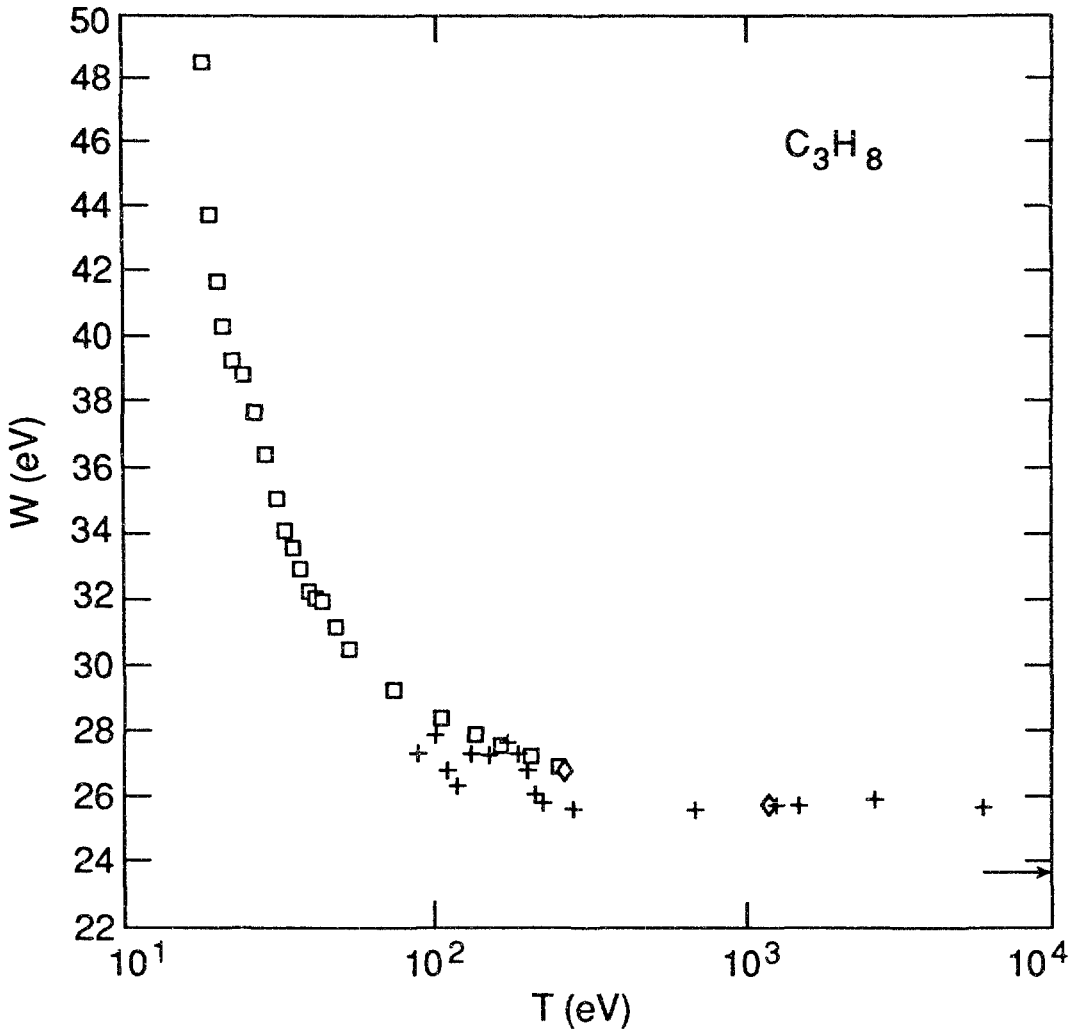

FIG. 8.10. W value for electrons and photons in C_3H_8. Electrons: □, Combecher [61]; ◊, Krajcar-Bronić et al. [82]. Photons: +, Srdoč [55]. W values for photons in the keV energy region in propane, measured by Srdoč [55], are higher than the average high-energy value of (24.0 ± 0.5) eV recommended by the ICRU [1] and denoted by the arrow. Data of Krajcar-Bronić et al. [82] are electron W values calculated from photon W values measured by Srdoč [78].

W values [14, 15, 37, 98]. The ionization is not zero at the atomic ionization threshold because of production of the diatomic rare gas ion Ar_2^+ by energy transfer from the excited atoms, $Ar^* + Ar \rightarrow Ar_2^+ + e^-$.

W values in hydrogen are presented in Fig. 8.5. No significant difference in W values for H_2 and D_2 was observed [61].

W values in N_2, CH_4 and CO_2, i.e., the constituents of the methane-based TE gas, are presented in Figs 8.6, 8.7, and 8.8, respectively, while the W values in the methane-based TE gas are presented in Fig. 8.9. The W values obtained by Combecher [61] agree very well with those of Waibel and Grosswendt (Figs 8.6, 8.7, and 8.9), except for electron energies above 100 eV in CO_2 (Fig. 8.8). The data of Smith and Booz [60] deviate from other measurements and have stronger energy dependence (Figs 8.6-8.9).

W values for low-energy electrons in propane and propane-based TE gas are presented in Figs 8.10 and 8.11.

The W values for TE gas mixtures are well represented in the energy range from about 20 eV to several keV, as evident from Figs 8.9 and 8.11, but data for medium- and high-energy electrons are very scarce [1]. The importance of these gas mixtures in radiation dosimetry and microdosimetry suggests that more attention should be given to measuring W values for electrons above 10 keV in TE gases.

W values in butane are presented in Fig. 8.12. Differences in W for electrons in chemical isomers n- and i-butane were found by Combecher [61] at energies between 13 eV and 80 eV.

W values in water vapor are given in Fig. 8.13. Paretzke et al. [42] presented a Monte Carlo calculation for the degradation of 10 keV electrons in water vapor. The W values thus obtained are in good agreement with the experimental values of Combecher [61]. Olko et al. [101] reported W values equal to 30.4 eV for

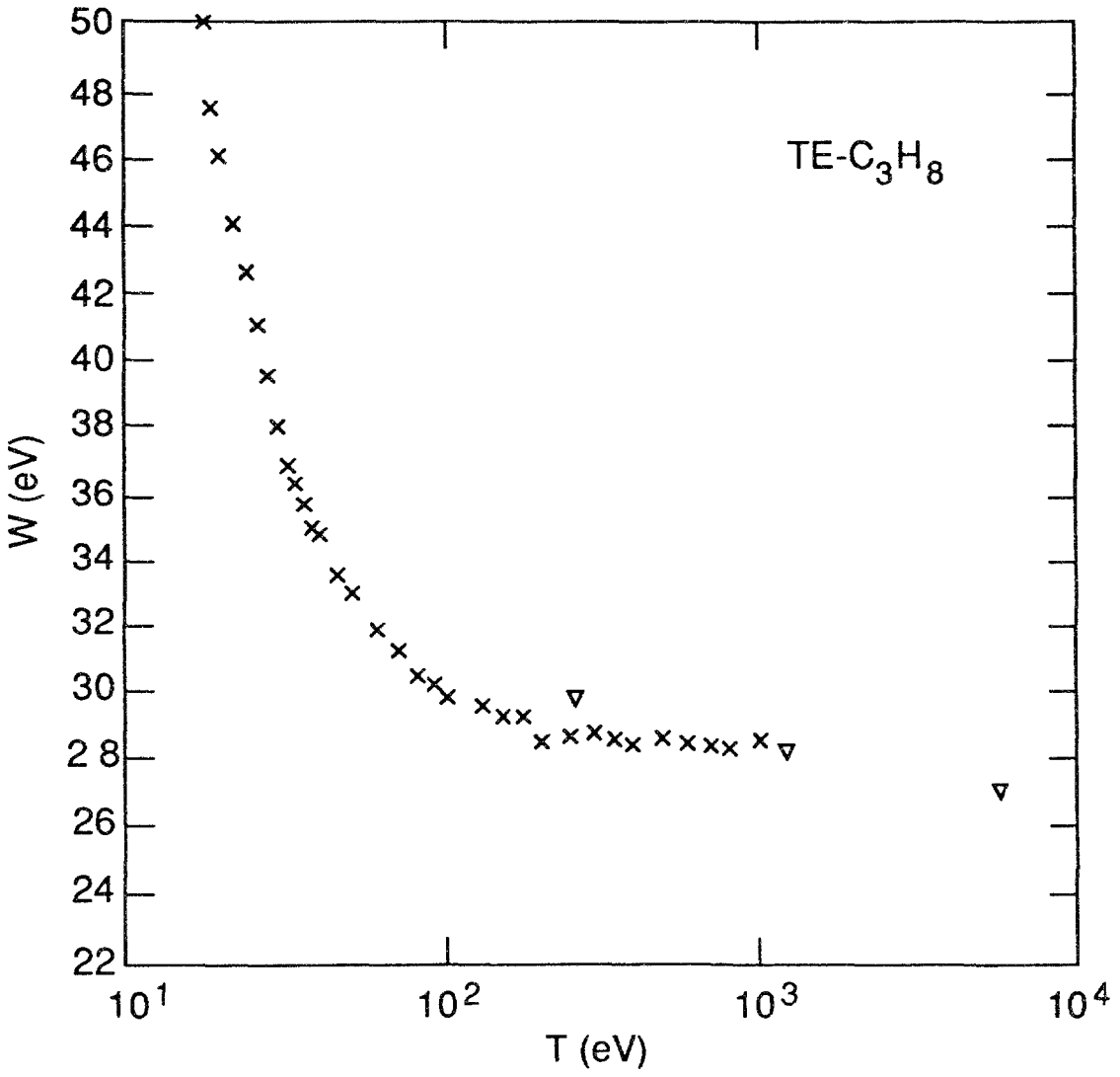

FIG. 8.11. W value for electrons in propane-based TE gas mixture. ×, Combecher [61]; ▽, Krajcar-Bronić et al. [82]. Data in [82] are electron W values calculated from photon W values measured by Srdoč [78].

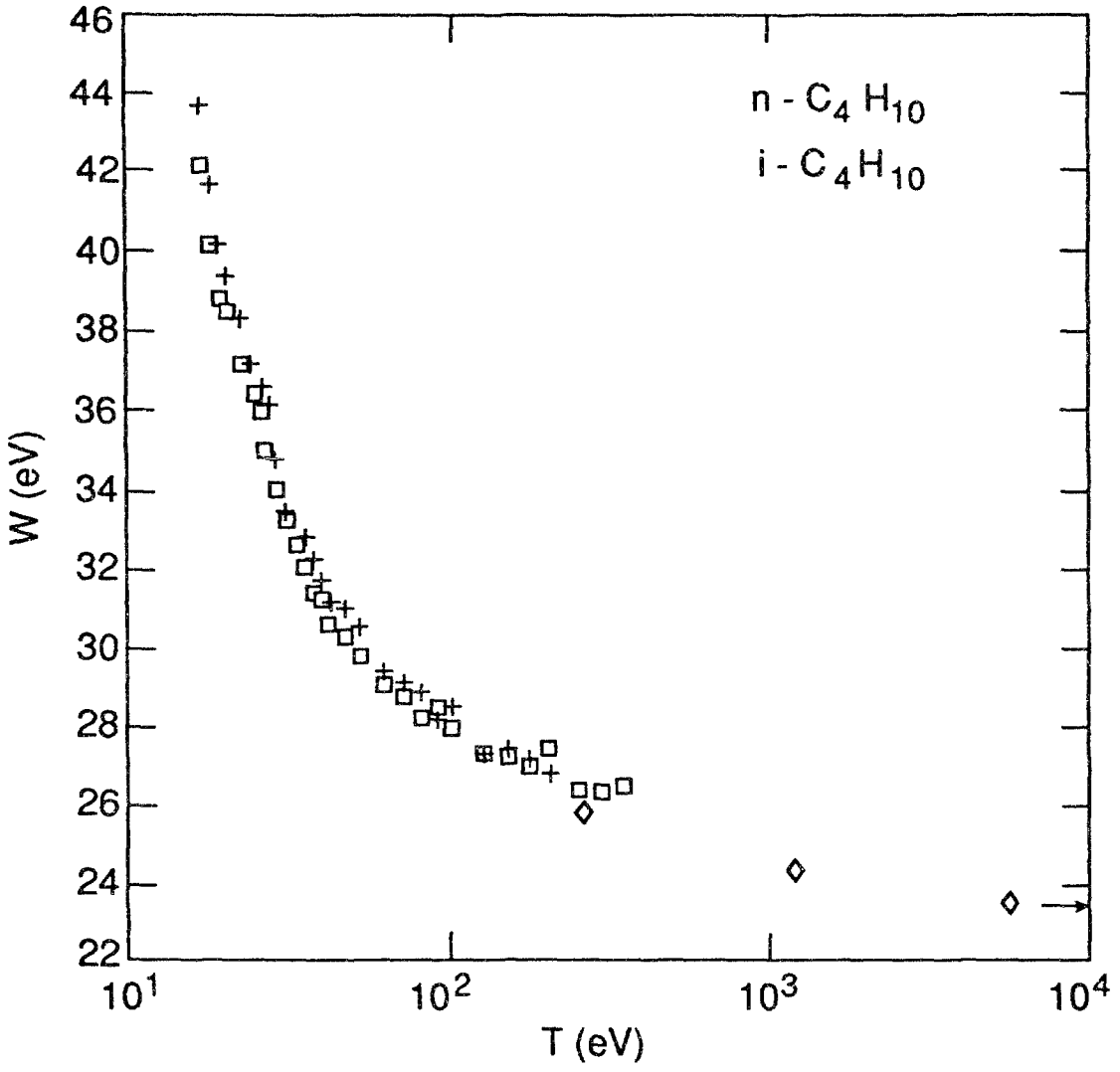

FIG. 8.12. W value for electrons in n-butane (□) and i-butane (+) as measured by Combecher [61]. The ICRU [1] high-energy value (23.4 ± 0.4 eV) is denoted by the arrow. Data of Krajcar-Bronić et al. [82] (◊) are electron W values calculated from photon W values measured by Srdoč [78].

12 keV X rays, and Marshall et al. [102] obtained 32.6 eV and 36.4 eV for electrons having energies 0.76 keV and 0.27 keV, respectively, in water vapor. Combecher [61] reported isotope effects in water vapor and benzene. Significantly lower W values were found in deuterated water and benzene at low electron energies.

W values in air are presented in Fig. 8.14. Cole [59] quoted uncertainties of 15% below 100 eV and 5% above 2 keV, and his data deviate from other experimental W values [58, 61, 62]. Data of Gerbes [58] show stronger energy dependence below 1 keV than data in [61, 62]. The dependence of W on the partial pressure of water vapor in air was published in ICRU Report 31 [1]. Measurements of W for electrons produced by ^{60}Co radiation in dry air were presented by Niatel et al. [103]. Taking into account new values for stopping powers, Boutillon and Perroche-Roux [104] re-evaluated all data for dry air (data from ICRU 31 and recent

values of Niatel et al. [103] and Kunze and Hecker [105]) and obtained the mean value W = 33.97 eV, compared to the former value of W = 33.85 eV given in ICRU 31 (Fig. 8.14).

Above 5 keV, and in some cases even above 500 eV, a discrepancy exists in measured W values for electrons in all gases. This problem may be remedied for practical purposes by smoothly extending the W values from the region between 1 keV and 5 keV, if available, to the high-energy values recommended by the ICRU Report 31 [1].

8.3.3. W Values for Photons

Very few data exist on the W value for low-energy photons. The only measurement of the W value for low-energy photons in methane was made by Srdoč

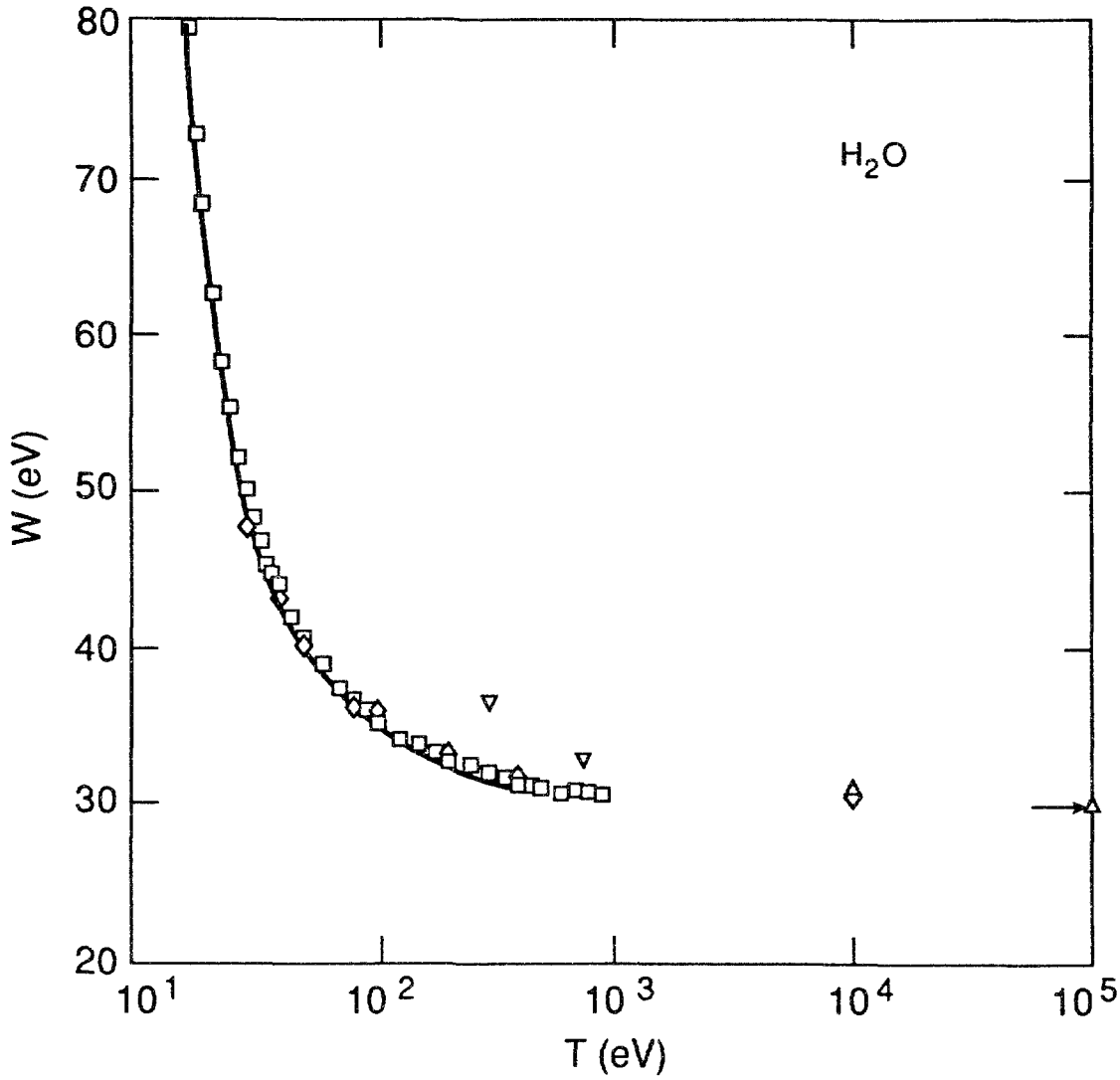

FIG. 8.13. W value for electrons in water vapor. The ICRU [1] high-energy W value (29.6 ± 0.3 eV) is denoted by the arrow. □, H_2O Combecher [61]; —, D_2O [61]; ▽, Marshall et al. [102]; ◊, Paretzke et al. [42]; △, Turner et al. [41]. Monte Carlo calculations by Paretzke et al. [42] and Turner et al. [41] agree well with the measured data.

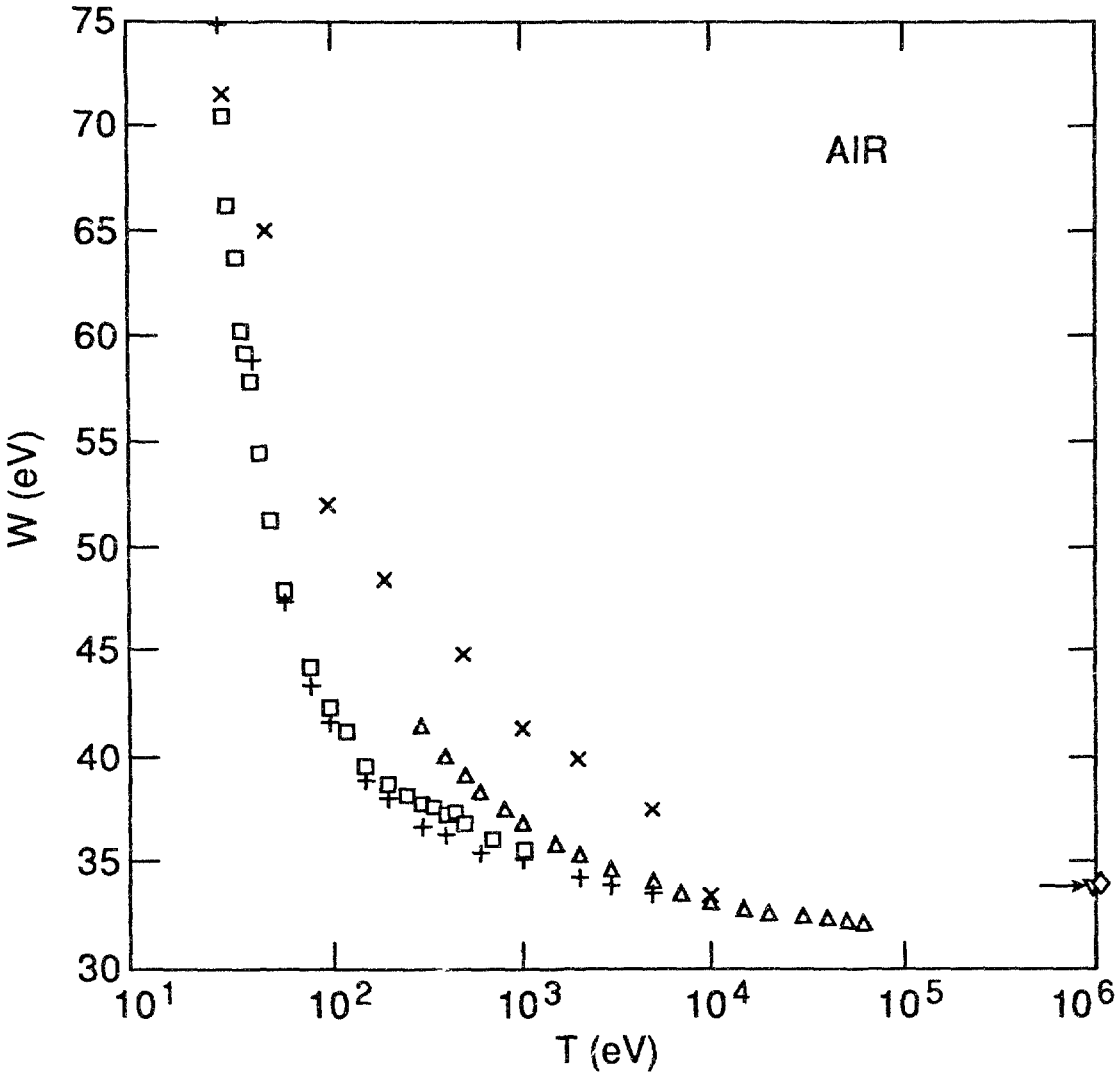

FIG. 8.14. W value for electrons in air. The ICRU [1] high-energy value (33.85 ± 0.05 eV) is denoted by the arrow. Δ, Gerbes [58]; ×, Cole [59]; □, Combecher [61]; +, Waibel and Grosswendt [62]; ◊, Niatel et al. [103]; ∇, Boutillon and Perroche-Roux [104]. Older data of Gerbes [58] and especially of Cole [59] differ from recent data of Combecher [61] and Waibel and Grosswendt [62]. Boutillon and Perroche-Roux [104] re-evaluated the ICRU [1] average W value on the basis of recently published stopping power data and obtained W = 33.97 ± 0.05 eV.

and Obelić [56]. Their results show an increasing W value with decreasing energy. Srdoč [55] measured W values for low-energy photons in propane down to 85 eV and obtained a slow increase of W up to 7% (Fig. 8.8). Srdoč [78] measured the W value for low-energy photons in both TE mixtures and compared the results to other experimental data. Suzuki and Saito [106, 107] measured W values for photons in methane and propane by using monochromatic, ultrasoft X rays generated from synchrotron radiation through a plane grating monochromator. They were primarily interested in the effects of inner-shell excitation on the fine structure of the W value near the C-K edge of methane and propane (260-360 eV). Their results were published as relative values, and therefore they will not be included in this report.

The W values for photons of 0.277, 1.49, and 5.9 keV in a series of alkanes, TE mixtures, and some other polyatomic gases were published by Srdoč et al. [81]. Generally, the conversion of photon W values to electron W values is not trivial. However, the procedure reported in [82], based on certain simplifications, offers a possibility to convert the photon W values into the electron W values by assuming that (1) each 277 eV photon ejects electron from an outer shell and (2) all 1.5 keV and 5.9 keV photons eject electrons from an inner shell, thus creating two electrons having energies 1.2 (or 5.6) keV and 250 eV [82].

An interesting feature that appears in the data of Srdoč et al. [81] and Krajcar-Bronić et al. [82] is the oscillatory structure of the W values as a function of the number of carbon atoms in an alkane molecule (Fig. 8.15). This behavior was explained by Kimura et al. [67] as follows: the oscillations are due to the strong

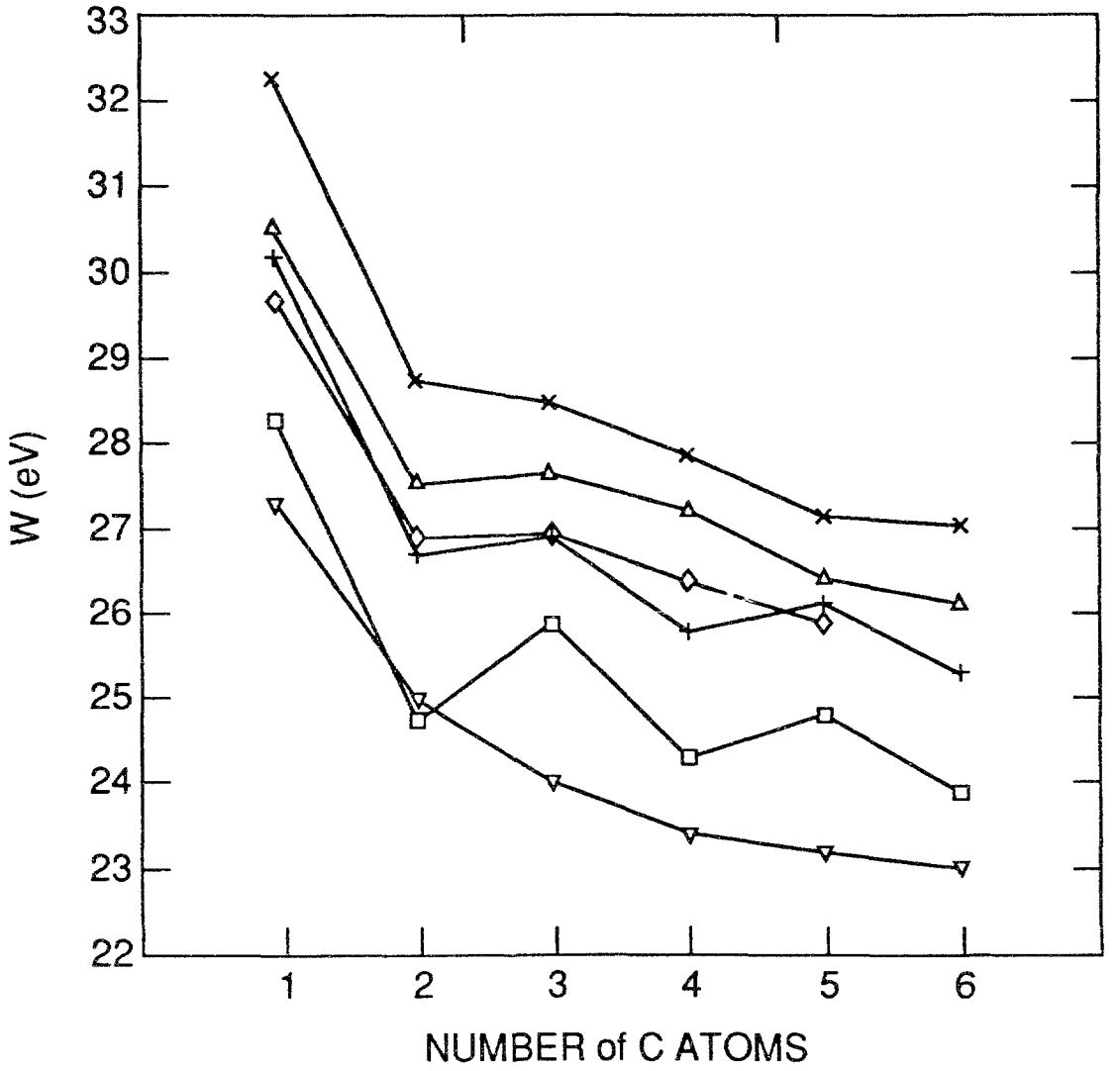

FIG. 8.15. W for electrons in alkanes (saturated hydrocarbons, C_nH_{2n+2}, n = 1 methane, n = 2 ethane, etc.) as a function of number of carbon atoms in an alkane molecule. ▽, ICRU-recommended high-energy values for electrons; ×, 100 eV, Combecher [61]; △, 150 eV [61]; ◇, 250 eV [61]; +, 0.26 keV, Krajcar-Bronić et al. [82]; □, 1.2 keV [82]. Data in [82] are electron W values calculated from photon W values measured by Srdoč [78].

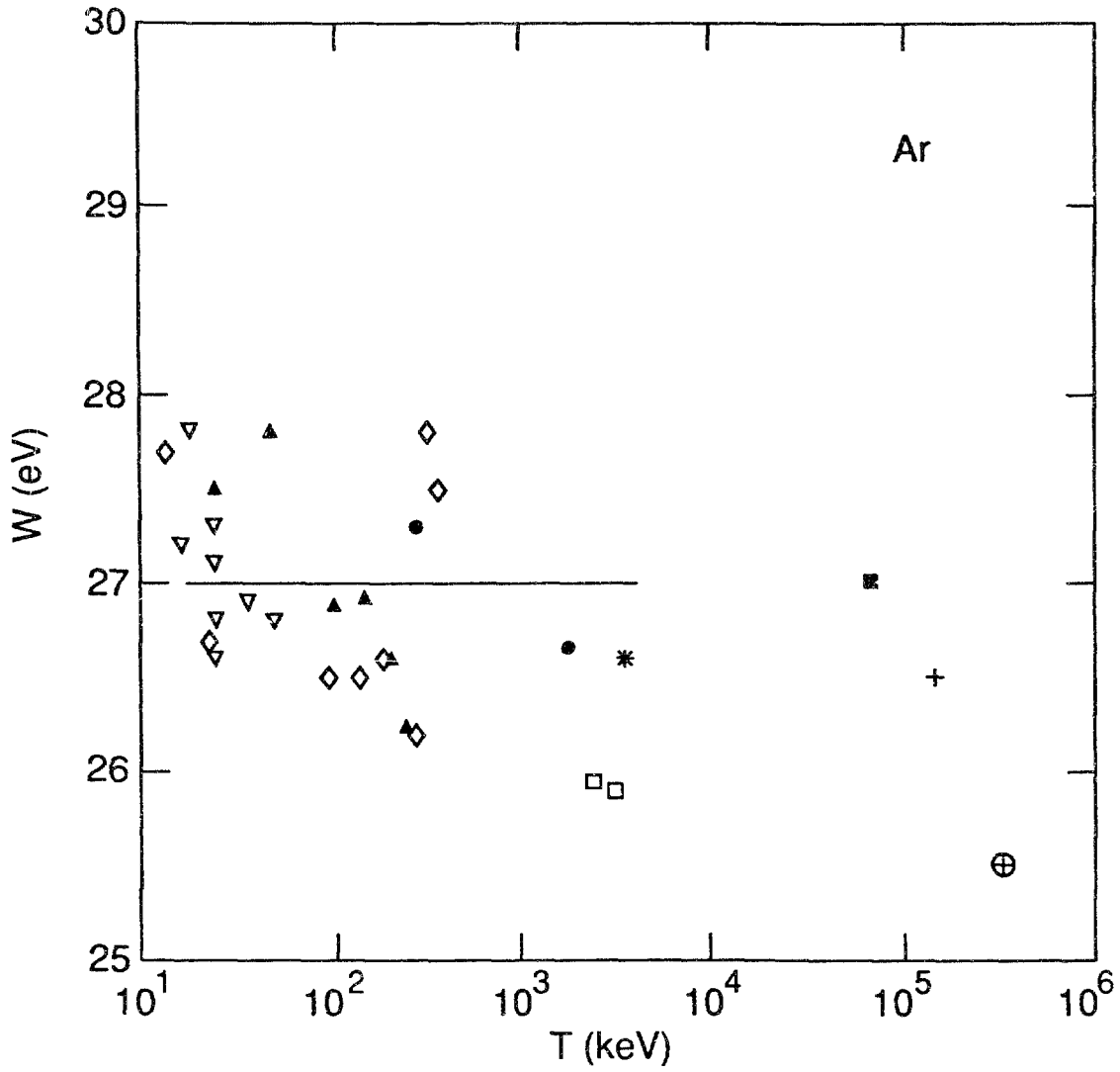

FIG. 8.16. W value for protons in argon. □, Thomas and Burke [108]; ◊, Chemtob et al. [109]; Δ, Lowry and Miller [110]; •, Larson [111]; ▽, Phipps et al. [112]. Data by Petti et al. [92] (+), Parks et al. [113] (*), Bakker and Segre [91] (⊕), and Hiraoka et al. [99] (■) are differential w values. (—), the ICRU [1] suggested value of 27.0 ± 1.0 eV for the energy range 10 keV < T_0 < $4 \cdot 10^3$ keV. Note the scattered data points and the poorly defined energy dependence.

oscillations of the branching ratio of ionization and neutral decomposition of molecular superexcited states. Similar oscillations can be seen in data of Combecher [61] at electron energies above 100 eV when plotted as the mean values given by the author (Fig. 8.15). Whereas the 2% error bar renders these oscillations less certain, the reproducibility of results presented in [81] and [82] indicated a much smaller *relative* error in W values in a series of alkanes, as opposed to the absolute W value error of ±2%.

8.3.4. W Values for Protons

Recommended W values for protons in the energy range from 20 keV to 4 MeV were given in the ICRU Report 31 [1] for the following gases: N_2, CO_2, Ar,

and methane-based TE gas, and for protons having energy between 2.5 keV and 500 keV in methane. In the following Sections 8.3.4-8.3.6 we will always indicate the kind of an incident particle.

Only three W values for protons in argon have been published since the ICRU Report [1]. Petti et al. [92] measured the differential w value for protons at 150 MeV, and Thomas and Burke [108] measured W at 2.52 MeV and 3.18 MeV (Fig. 8.16).

The W values for protons in nitrogen, displayed in Fig. 8.17, show a wide scattering between 20 keV and 1 MeV. However, the data of Waibel and Willems [89], Huber et al. [114], Boring et al. [115], and Nguyen et al. [116] confirm a

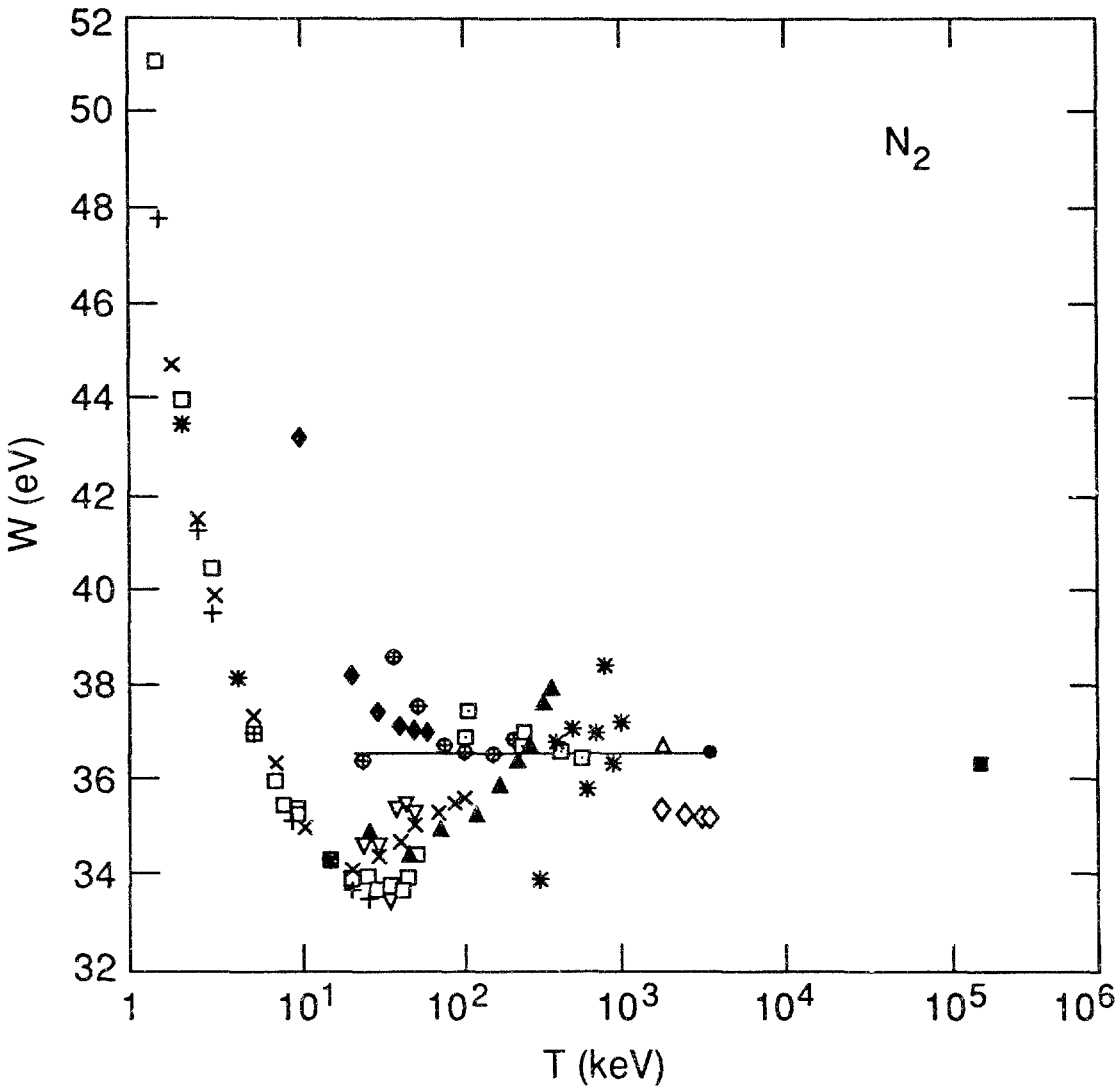

FIG. 8.17. W value for protons in N_2. □, protons, Huber et al. [114]; +, H_2^+ ions [114]; ◊, Thomas and Burke [90]; ▲, Nguyen et al. [116]; ▽, Boring et al. [115]; ⁎, Schaller et al. [118]; ♦, Sidenius [117]; ⊕, Lowry and Miller [110]; Δ, Larson [111]; ×, Waibel and Willems [89]; ⊡, Kuehn and Werba [119]. Values of Parks et al. (•) [113] and Petti et al. (■) [92] are differential w values. (—), the ICRU [1] suggested values of 36.5 ± 1.5 eV for the energy range 20 keV < T_0 < $4 \cdot 10^3$ keV. A minimum in the W(T) plot can be observed around 20-30 keV.

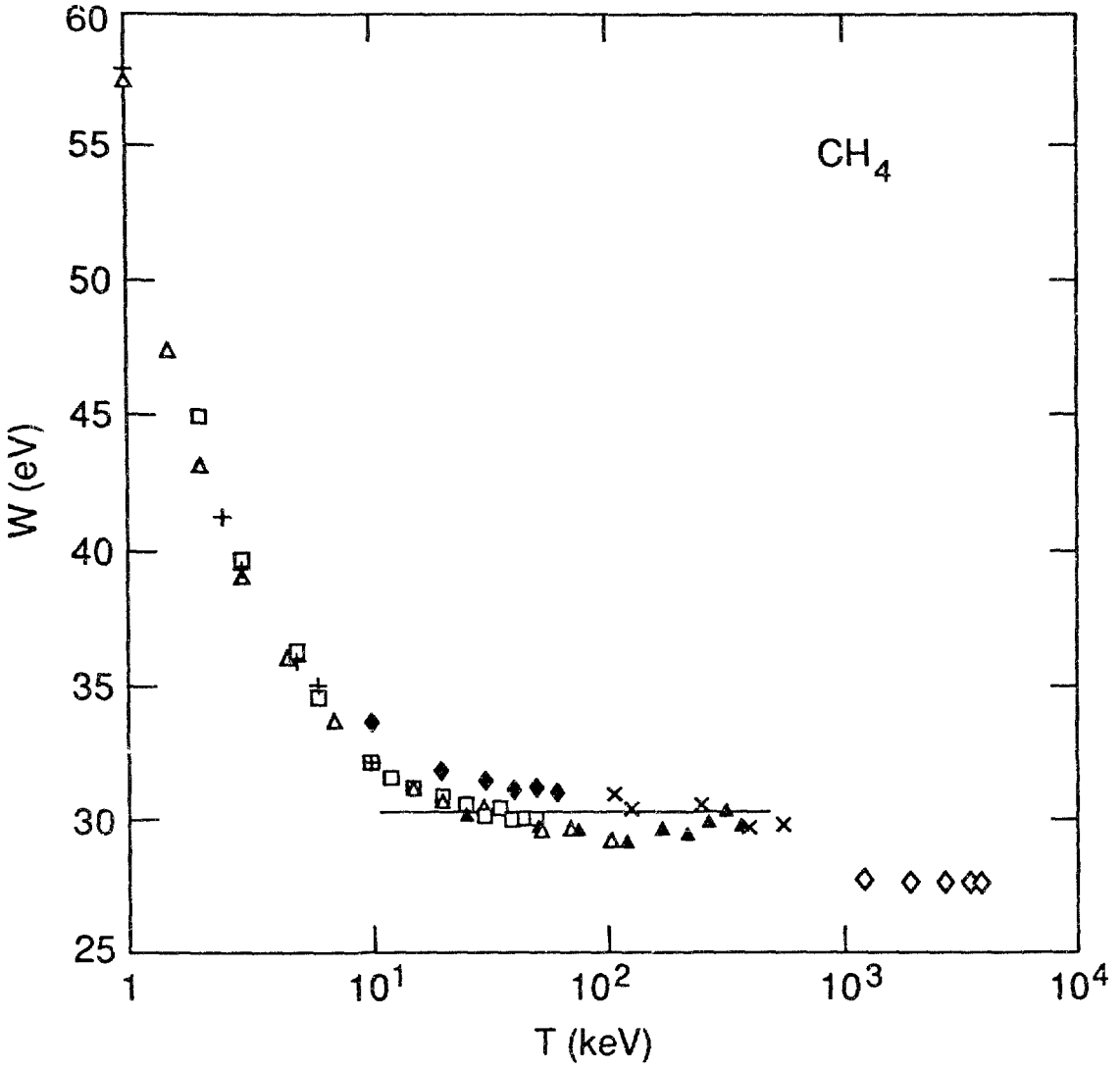

FIG. 8.18. W value for protons in CH_4. □, protons, Huber et al. [114]; +, H_2^+ ions [114]; ◊, Thomas and Burke [90]; ▲, Nguyen et al. [116]; ×, Kuehn and Werba [119]; ♦, Sidenius [117]; Δ, Waibel and Willems [89]. (—) The ICRU [1] suggested values of 30.5 ± 1.0 eV for the energy range 10 keV < T_0 < 500 keV on the basis of measurements by McDonald and Sidenius [122]. Recent measurements by Sidenius [117], Huber et al. [114]. and Waibel and Willems [89] showed that W is not constant below T_0 = 100 keV. A differential w value measured for 70 MeV protons by Hiraoka et al. [99], 27.9 eV, is comparable to W values for MeV protons measured by Thomas and Burke [90].

minimum around 20-30 keV with a depth of at least 1.5 eV. The minimum was not observed by Sidenius [117] and Lowry and Miller [110]. At much higher energies, the differential w value of Petti et al. [92] at 150 MeV agrees satisfactorily with the W data around 3 MeV, while the w value of Bakker and Segre [91] (33.6 eV) at 340 MeV is much lower. Improved data are needed between 0.1 MeV and 2 MeV and at higher energies, while a satisfactory set of W values for practical work may be derived from 1 keV to 100 keV with an overall uncertainty of about 3%, disregarding some strongly deviating data.

The experimental W values for protons in the main constituents of the methane-based TE gas, CH_4 and CO_2, as well as in the methane-based TE gas, have

been updated considerably since 1978 [1]. The data on W values have been extended to energies above 1 MeV by Thomas and Burke [90] and below 100 keV by Sidenius [117], Huber et al. [114], and Waibel and Willems [89, 120], while Chemtob et al. [109] and Nguyen et al. [116] measured W values for protons having energy between 25 and 375 keV.

The W for protons in methane (Fig. 8.18) is a smooth function of energy up to ≈1 MeV. A step of about 2 eV is then observed between the data at lower energies [89, 114, 116, 117, 119] and those of Thomas and Burke [90] and Hiraoka et al. [99] (w value). Bichsel and Inokuti [121] calculated the differential w value

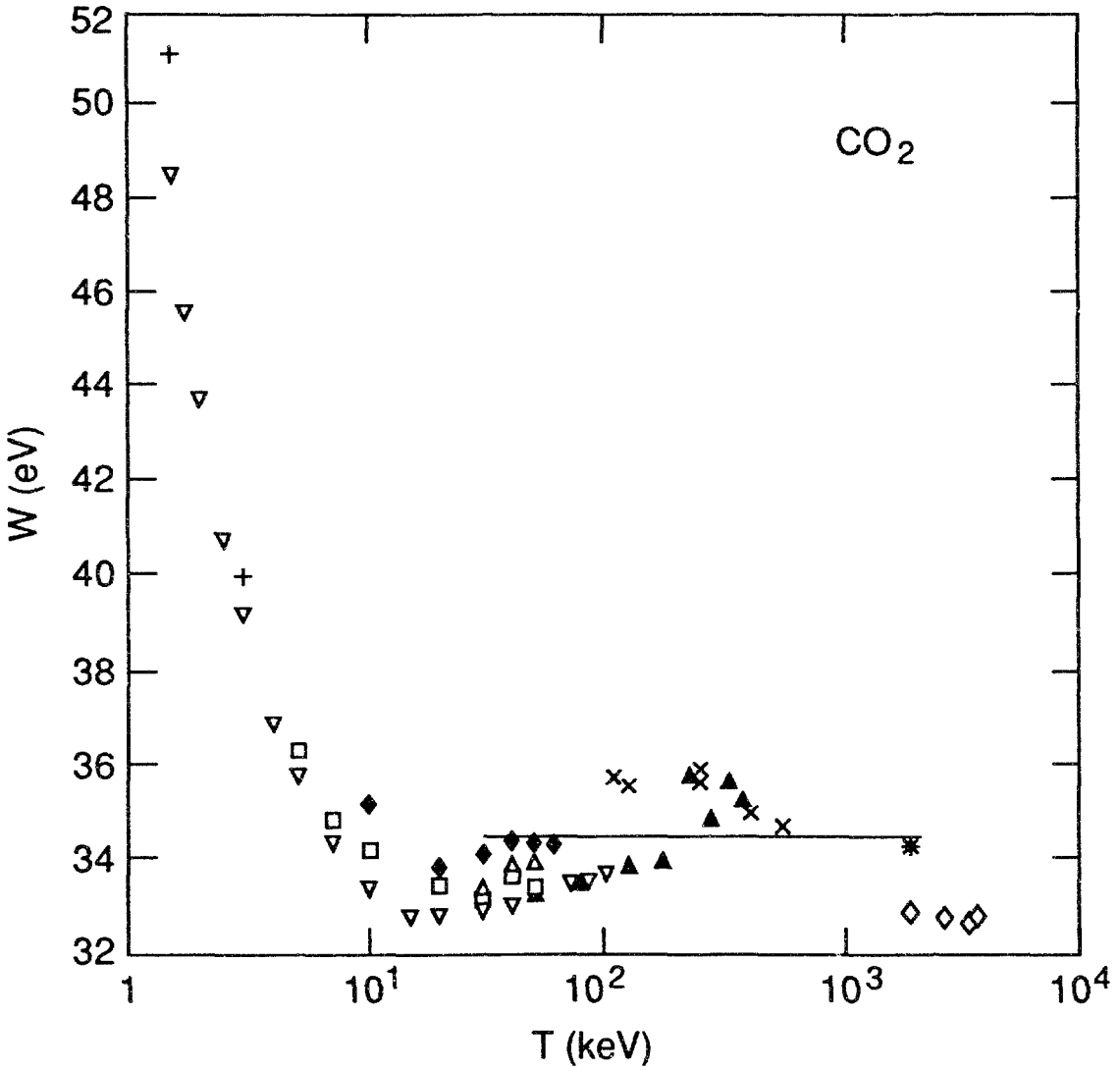

FIG. 8.19. W value for protons in CO_2. □, protons, Huber et al. [114]; +, H_2^+ ions [114]; ◊, Thomas and Burke [90], ▲, Nguyen et al. [116]; ×, Kuehn and Werba [119]; ♦, Sidenius [117]; Δ, Boring et al. [123]; *, Larson [111]; ▽, Waibel and Willems [89]; (—), value suggested by ICRU [1] (34.5 ± 1.5 eV) for the energy range 30 keV < T_0 < $2 \cdot 10^3$ keV. Recent measurements showed a broad minimum around T_0 = 20 keV. The W values measured by Thomas and Burke [90] are considerably lower than the ICRU value. A differential w value for 70 MeV protons measured by Hiraoka et al. [99] is 34.3 eV, the same as the W value measured by Larson [111] and given by ICRU [1].

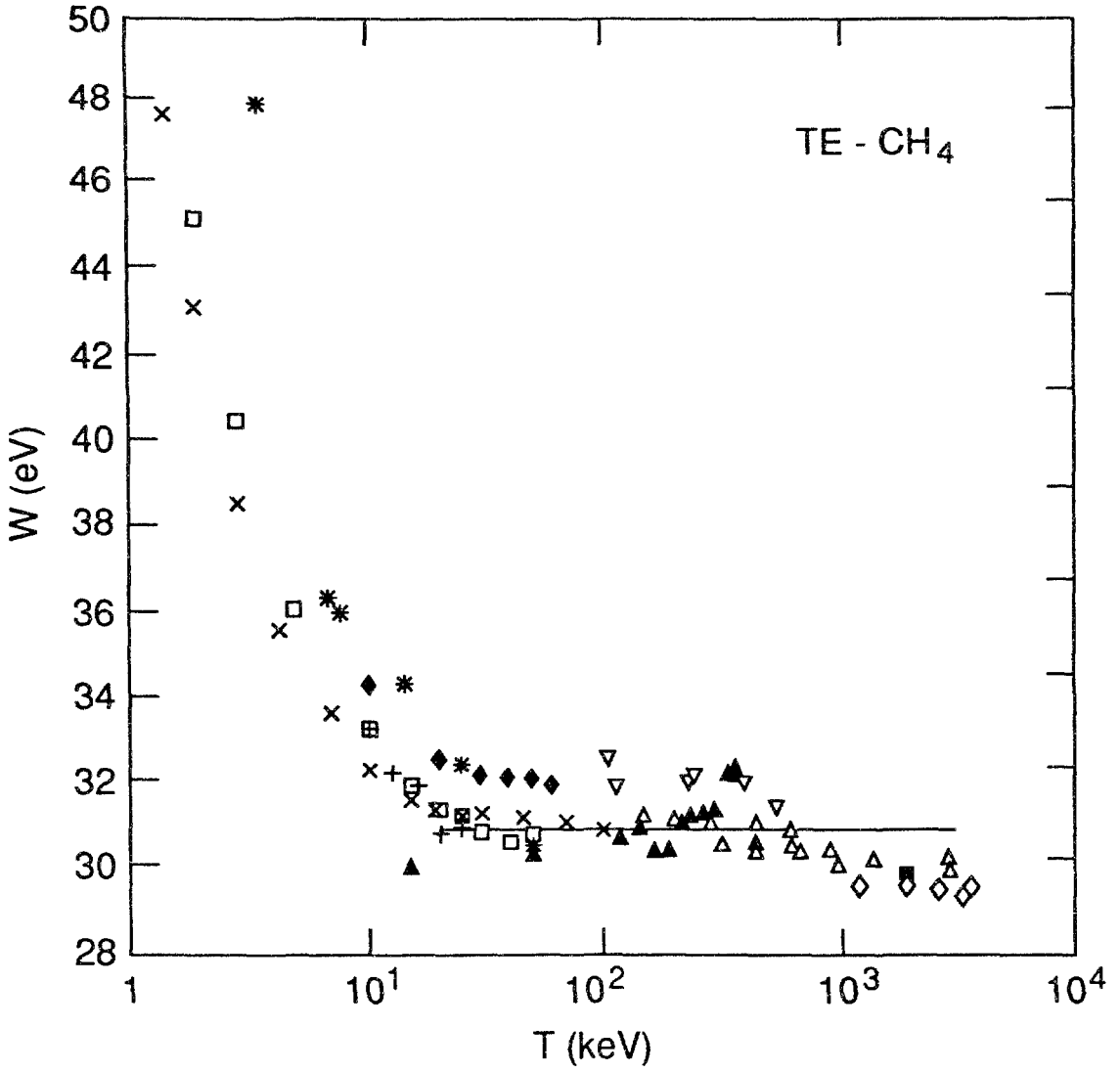

FIG. 8.20. W value for protons in methane-based TE gas. (—), the ICRU [1] suggested values of (31.0 ± 1.5 eV) for the energy range 20 keV < T_0 < $3 \cdot 10^3$ keV. □, protons, Huber et al. [114]; +, H_2^+ ions [114]; ■, Larson [111]; ◊, Thomas and Burke [90]; ▽, Kuehn and Werba [119]; ▲, Nguyen et al. [116]; *, Leonard and Boring [124]; ♦, Sidenius [117]; Δ, Rohrig and Colvett [125]; ×, Waibel and Willems [120]. The differential w value (30.4 eV) for 70 MeV protons measured by Hiraoka et al. [99] is comparable to values of Rohrig and Colvett [125] but higher than values of Thomas and Burke [90].

w=29.4 eV for 1 MeV protons in CH_4 from experimental secondary electron spectra, total ionization cross sections and W values for electrons. This value is in good agreement with the measured W values.

In contrast to the smooth energy dependence in CH_4, a flat minimum around 20 keV in CO_2 (Fig. 8.19) can be confirmed from the data of Sidenius [117], Nguyen et al. [116] and Waibel and Willems [89]. The W values measured by Thomas and Burke [90] are lower than the ICRU value and the W measured by Larson [111]. Further investigations are needed at proton energies above 100 keV.

Figure 8.20 gives W values for protons in methane-based TE gas as a function of proton energy. The energy dependence of W is very similar to that in

methane. However, the scatter of the data between ≈10 keV and 1 MeV is quite large. An apparent maximum around 350 keV suggested by Chemtob et al. [109] and Nguyen et al. [116] is questionable because of the large uncertainties quoted. A monotonic energy dependence seems to be more realistic. Further precise measurements are therefore required for this energy region and for energies above 3.5 MeV.

Propane-based TE gas is increasingly being applied in neutron dosimetry, but only Posny et al. [126] measured W values for protons in this TE gas and in propane at proton energies from 25 keV to 375 keV, (Fig. 8.21). The overall uncertainty of W for protons in propane was quoted at about 3% and for the propane-based TE gas at about 4%. As for the energy dependence, the measured W values show a shallow minimum around 175 keV. More measurements are required for the whole energy range.

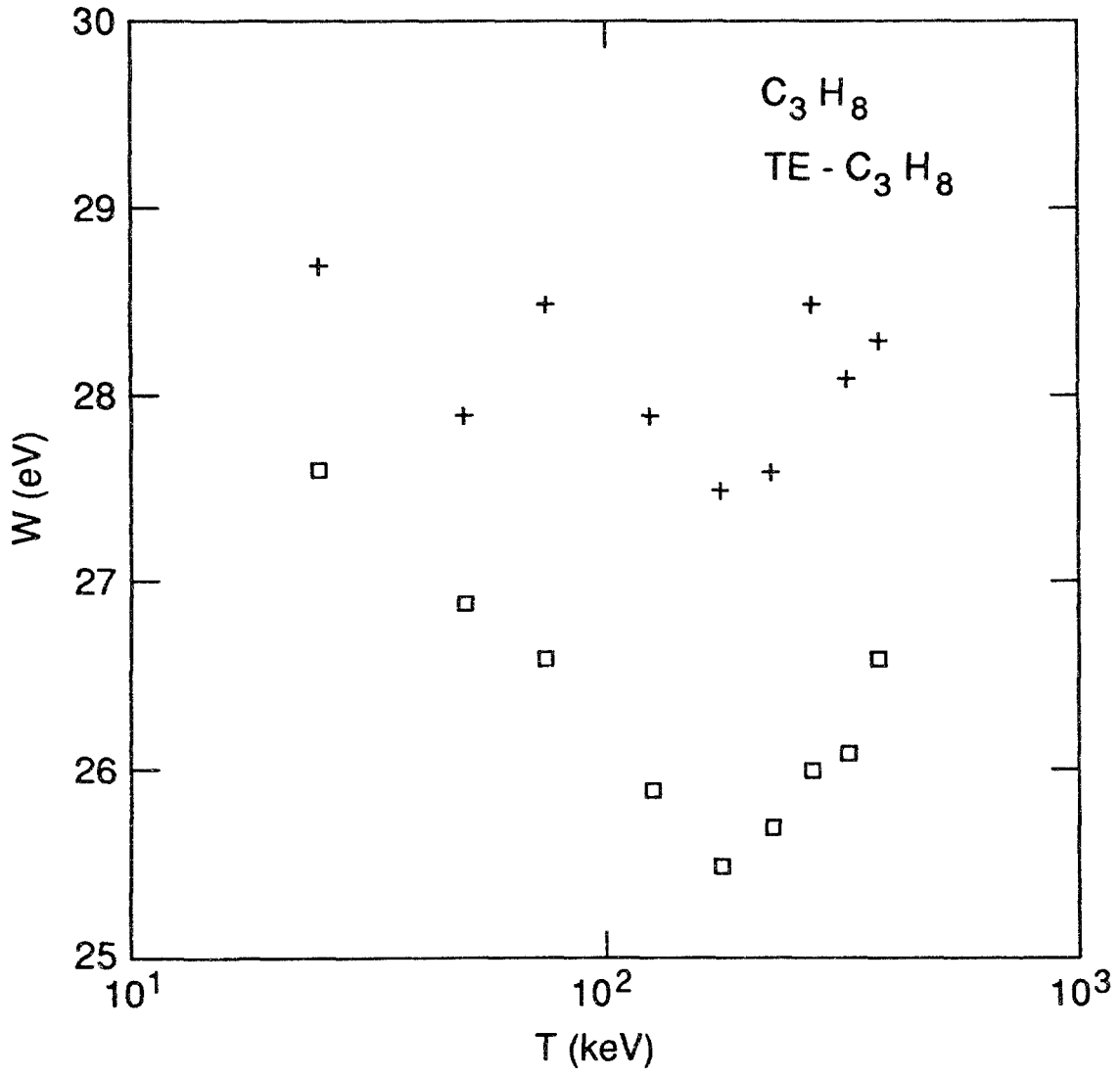

FIG. 8.21. W value for protons in C_3H_8 (□) and propane-based TE gas (+) as measured by Posny et al. [126].

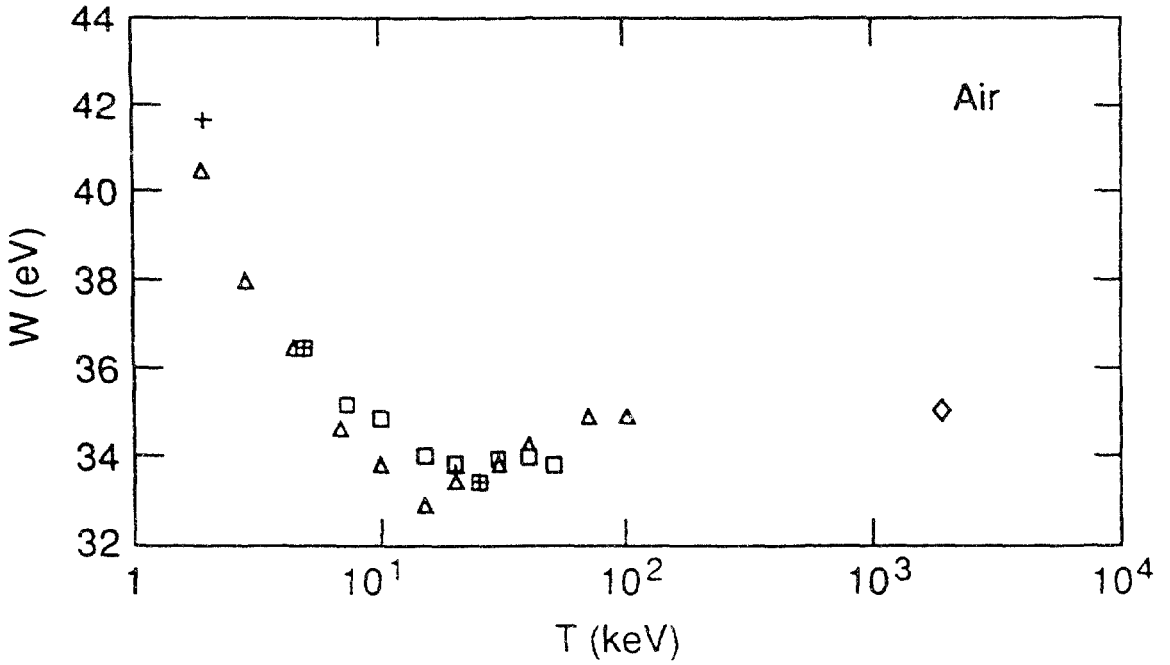

FIG. 8.22. W value for protons in air. □, protons, Huber et al. [114]; +, H_2^+ ions [114]; ◊, Larson [111]; Δ, Willems et al. [127]. A broad minimum is observed at proton energies around T_0 = 20 keV. A differential w value for 70 MeV protons measured by Hiraoka et al. [99], 35.3 eV, is comparable to the W value measured by Larson [111].

Marshall et al. [102] reported differential w values in water vapor equal to 33.6 ± 2.4, 31.9 ± 2.0, and 30.6 ± 1.9 eV for protons having energies 85 keV, 230 keV, and 390 keV, respectively. Olko et al. [101] reported differential w values for protons in water vapor, calculated by the Monte Carlo method, equal to 34.1, 33.5, and 33.1 eV for protons having energies 0.3, 1.0, and 3.5 MeV, respectively. These results are much higher than those of Marshall et al. [102].

W values for protons in air (Fig. 8.22) have been measured by Willems et al. [127] at energies from 1 keV to 100 keV and by Huber et al. [114] from 5 keV to 50 keV. The uncertainties quoted were about 2%. Waibel and Willems [128] confirmed a flat minimum around 20 keV. A single W value has been published by Larson [111] at 1.826 MeV, while the differential w values were measured by Bakker and Segre [91] at 340 MeV (w = 33.3 eV) and by Hiraoka et al. [99] at 70 MeV (w = 35.3 eV).

8.3.5. W Values for Alpha Particles

ICRU Report 31 [1] gave average W values for ≈5.3 MeV alpha particles in the following gases of radiological interest: Ar, H_2, N_2, CH_4, C_3H_8, CO_2, methane-based TE gas, H_2O, and air. The W values for alpha particles in Ar, N_2, methane, and methane-based TE gas were also given as a function of energy in the ICRU Report 31.

New measurements of W values for alpha particles in various gases were reported by Krieger et al. [129], Whillock and Edwards [130], Thomas and Burke [131], and Tawara et al. [132]; values for He^+ ions were given by Nguyen et al. [116],

Huber et al. [114], and Posny et al. [126]. They measured W in Ar, methane-based TE gas and its constituents, except that Posny et al. [126] measured W for He^+ in propane and propane-based TE gas. Figures 8.23-8.27 show the W values for alpha particles and He^+ ions in Ar, N_2, CH_4, CO_2, and methane-based TE gas, respectively.

Although the ICRU Report 31 [1] suggested the same value of W = 26.5 ± 0.5 eV for both 1 MeV and 10 MeV alpha particles in Ar, recent measurements by Tawara et al. [132] showed a slight decrease of the W value with increasing energy between 1 and 5 MeV (Fig. 8.23).

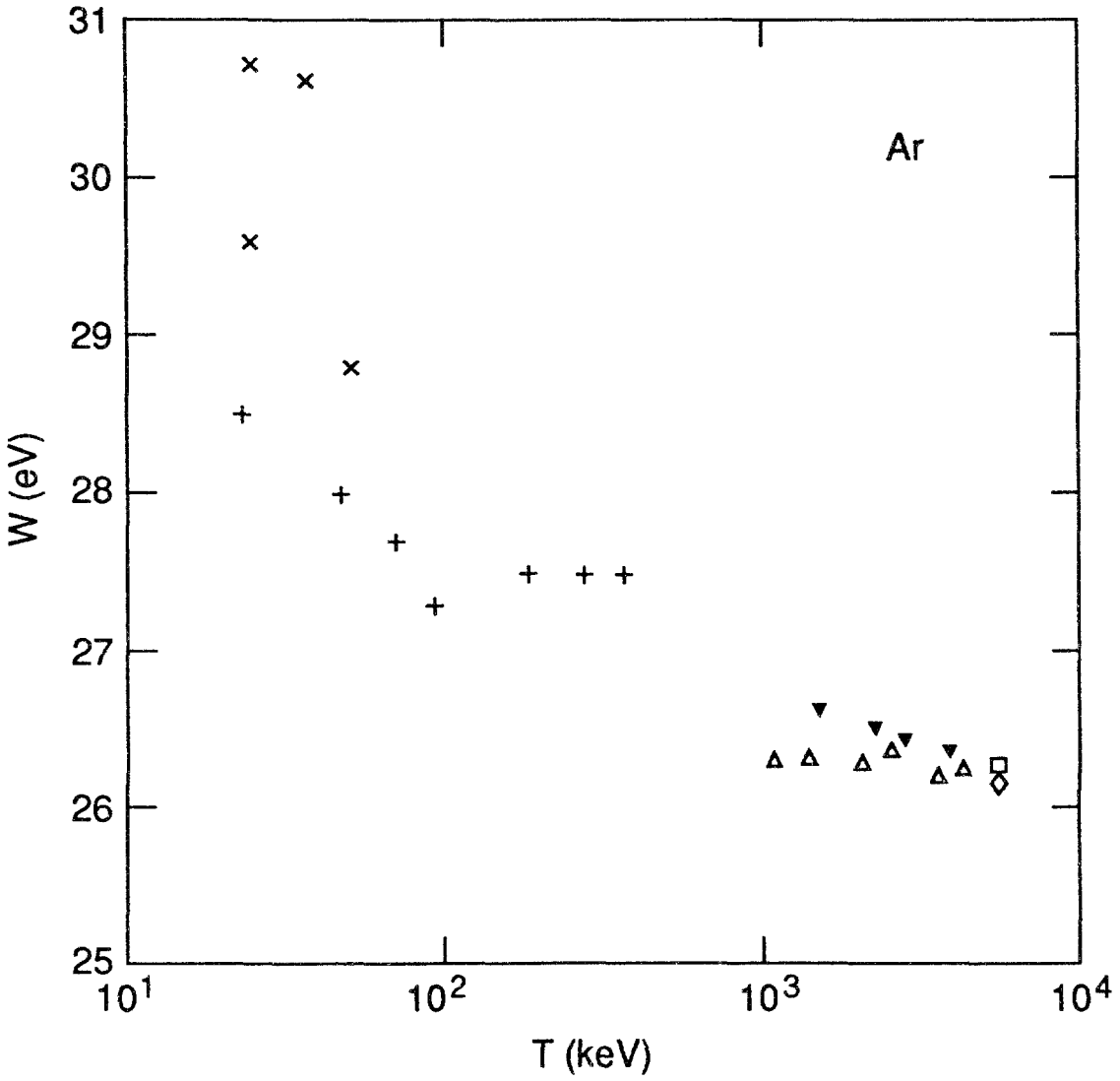

FIG. 8.23. W value for alpha particles and He^+ ions in argon. □, Krieger et al. [129]; +, Chemtob et al. [109]; ◊, Thomas and Burke [131]; Δ, Chappell and Sparrow [133]; ×, Phipps et al. [112]; ▼, Tawara et al. [132]. The ICRU [1] recommended 26.31 eV for ≈5 MeV alpha particles, with an uncertainty of at least 0.7%, and suggested 27.5 ± 1.0, 26.5 ± 0.5, and 26.5 ± 0.5 eV for alpha particles at about 0.1, 1, and 10 MeV, respectively. Recent measurements by Tawara et al. [132] showed a slight decrease of the W value with increasing energy between 1 MeV and 5 MeV. Hiraoka et al. [99] obtained 27.4 eV for the differential w value for 99 MeV ^3He ions.

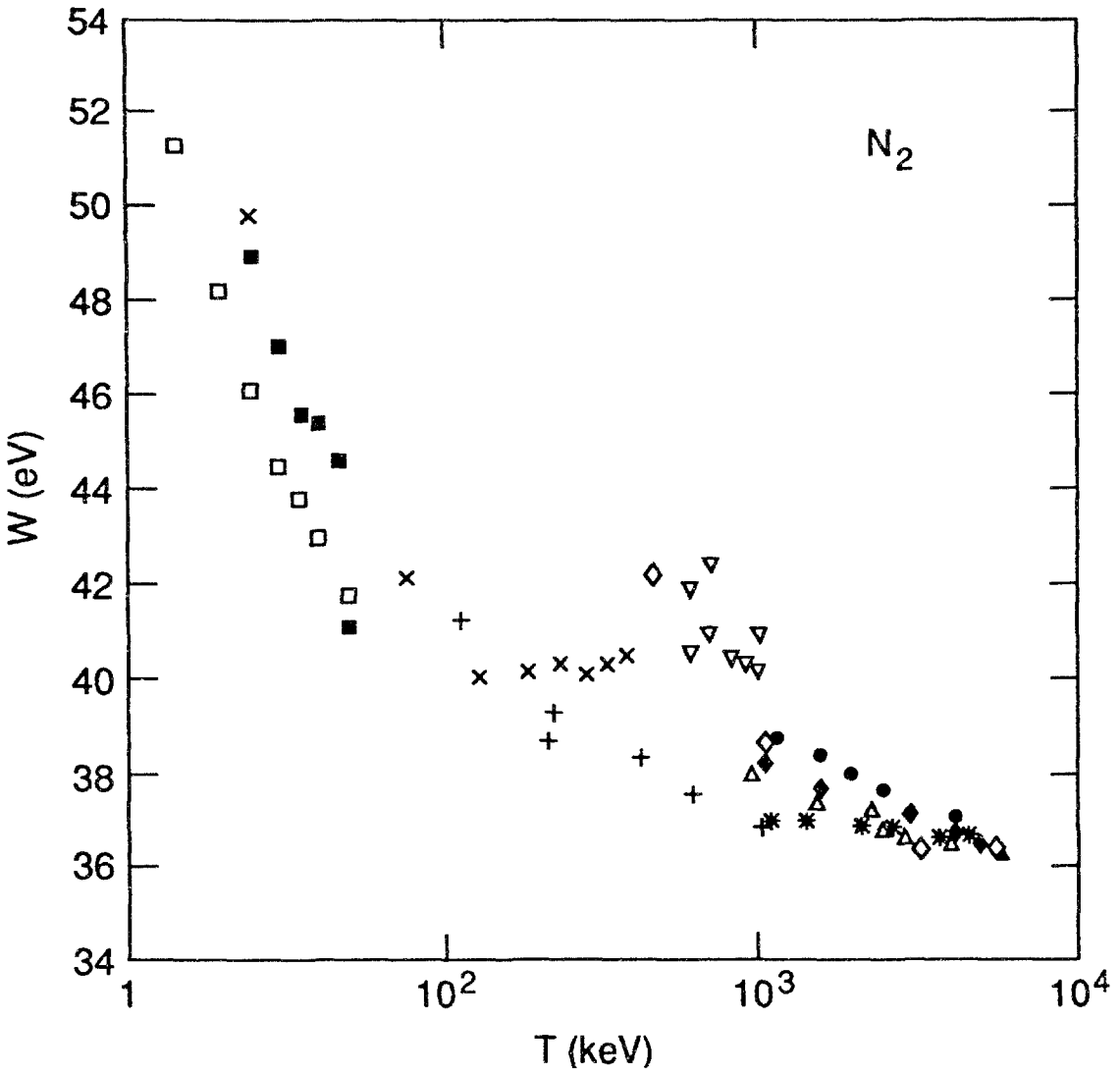

FIG. 8.24. W value for alpha particles and He^+ in N_2. □, Huber et al. [114]; •, Whillock and Edwards [130]; ◊, Varma and Baum [134]; ▲, Thomas and Burke [131]; ×, Nguyen et al. [116]; ▽, Schaller et al. [118]; ■, Boring et al. [115]; +, Kuehn and Werba [119]; ♦, Jesse [135]; Δ, Tawara et al. [132]; *, Chappell and Sparrow [133]. The ICRU [1] recommended 36.39 ± 0.23 eV for ≈5 MeV alpha particles and suggested 42 ± 1, 37.5 ± 1.0, and 36 ± 1 eV for alpha particles at approximately 0.1, 1, and 10 MeV, respectively.

More precise data are needed for alpha particle energies from 100 keV to 5 MeV in N_2 (Fig. 8.24) to confirm the maximum at about 400 keV obtained by Schaller et al. [118], Nguyen et al. [116] and Varma and Baum [134]. Kuehn and Werba [119] reported a monotonic decrease of the W value in the energy range 100 keV – 1 MeV.

W for CH_4 decreases smoothly with increasing alpha particle energy (Fig. 8.25), but the data of Kuehn and Werba [119] are approximately 2 eV lower than other data [116, 132, 134] at the same particle energy. The data points for W values in CO_2 (Fig. 8.26) are prohibitively scattered, and more measurements are needed for all energies. A weak maximum at 300 keV in methane-based TE gas (Fig. 8.27) was reported by Nguyen et al. [116], Varma and Baum [134], and by Rohrig

and Colvett [125]. It was not observed by Kuehn and Werba [119], whose data show a monotonic decrease of the W value with increasing energy, and are lower 1-2 eV than other data [116, 125, 130, 134]. Simmons [137] pointed at discrepancies between the measured W values in TE gas mixture reported by various workers and pointed out that these differences are larger than the uncertainties quoted by authors. Further comments by Waker on W value for alpha particles in TE gas can be found in [138].

The data for propane and propane-based TE gas are presented in Fig. 8.28. New measurements are needed in both gases to cover a wider energy range than that given by Posny et al. [126].

W values for alpha particles in air are presented in Fig 8.29. A gap between ≈60 keV and 1 MeV should be filled by new measurements.

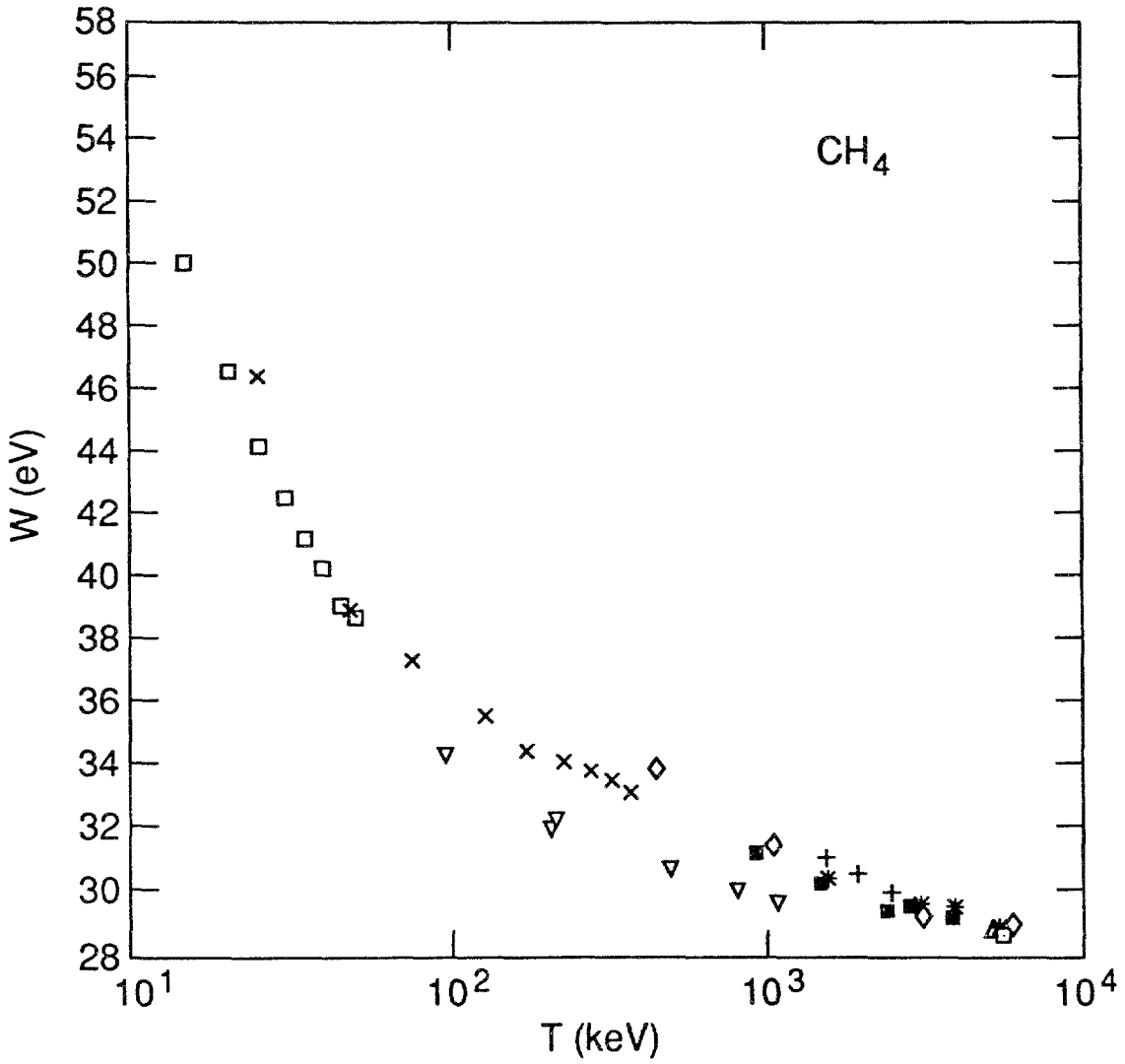

FIG. 8.25. W value for alpha particles and He^+ ions in CH_4. □, Huber et al. [1141]; ⊡, Krieger et al. [129]; ▽, Kuehn and Werba [119]; +, Whillock and Edwards [130]; ◊, Varma and Baum [134]; Δ, Thomas and Burke [131]; ×, Nguyen et al. [116]; ■, Tawara et al. [132]; *, Jesse [136]. The ICRU [1] recommended 29.11 eV for ≈5 MeV alpha particles, with uncertainty of at least 0.7%, and suggested 36.0 ± 1.5, 30.5 ± 1.0, and 29.0 ± 1.0 eV for alpha particles at approximately 0.1, 1, and 10 MeV, respectively. Hiraoka et al. [99] obtained 28.3 eV for the differential w value for 99 MeV ^3He ions.

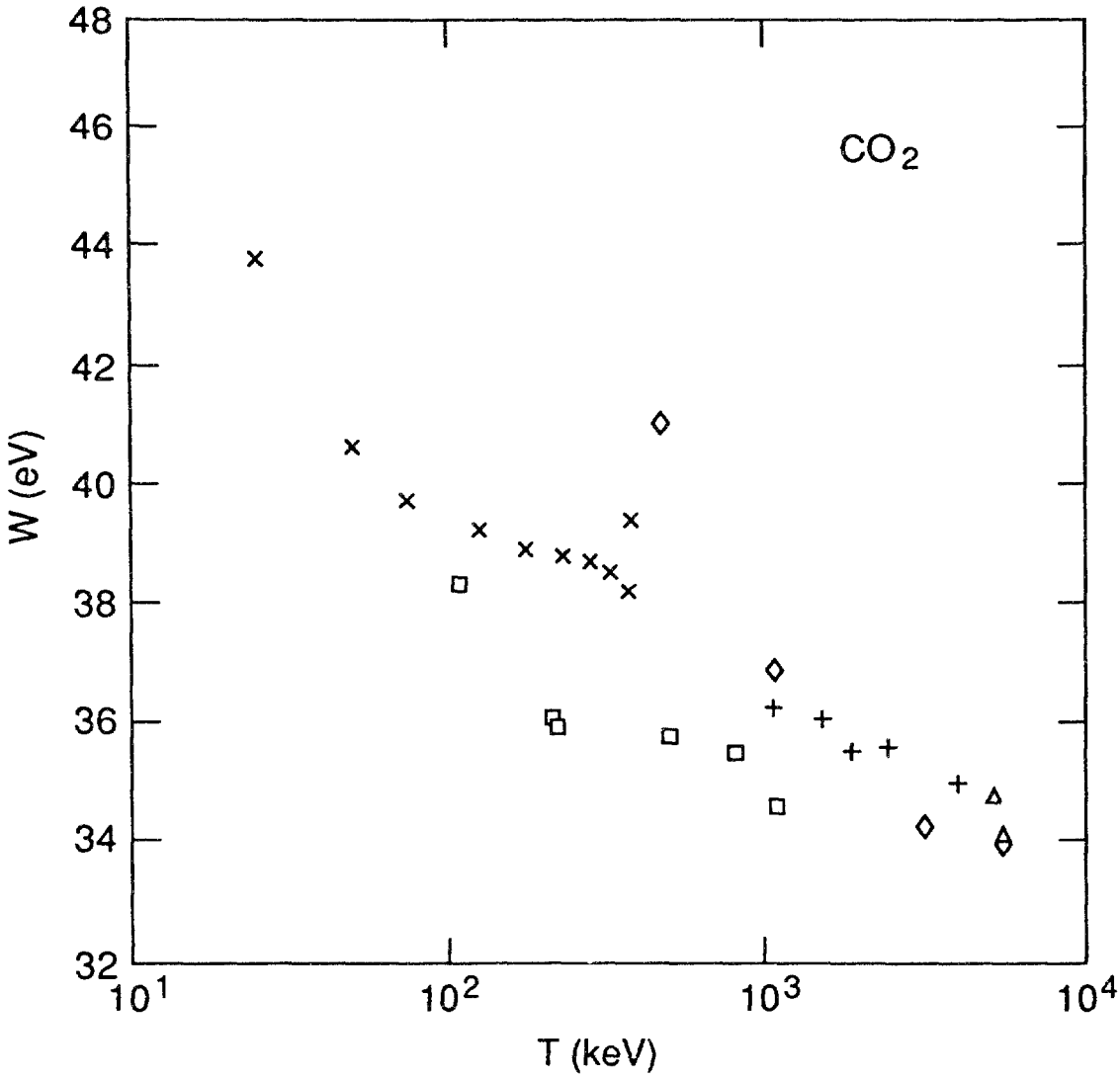

FIG. 8.26. W value for alpha particles and He^+ ions in CO_2. □, Kuehn and Werba [119]; +, Whillock and Edwards [130]; ◊, Varma and Baum [134]; Δ, Thomas and Burke [131]; ×, Nguyen et al. [116]. The ICRU [1] recommended 34.21 eV with an uncertainty of at least 0.7% for ≈5 MeV alpha particles. Hiraoka et al. [99] obtained 34.9 eV for the differential w value for 99 Mev ^3He ions.

8.3.6. W Values for Heavy Ions

Heavy ions combine the advantages, for the treatment of certain tumors, of radiation with high linear energy transfer and excellent physical selectivity. Heavy charged particles are especially needed in clinical cases where physical sensitivity is essential [70]. High-energy heavy ions used in radiotherapy have a much different range of charge, mass, and velocity than do electrons and alpha particles. Heavy ions are also important recoil particles generated after interaction of neutrons with matter.

ICRU Report 31 [1] summarized data for C^+, N^+, and O^+ ions in methane-based TE gas; heavy ions in N_2; and various ions in other gases. All data show an energy-dependent W. Two causes of energy dependence of W values for heavy ions are discussed in [1].

New data were published by Nguyen et al. [116] and Posny et al. [126] for C^+, N^+, and O^+ ions having energies of 25-375 keV in both TE gases and their components, and by Huber et al. [114] for various ions in air, CH_4, N_2, and methane-based TE gas at ion energies ranging of 0.5-50 keV/atom. Data for heavy ions are presented in the following figures: Ar, Fig. 8.30; N_2, Fig. 8.31; CH_4, Fig. 8.32; CO_2, Fig. 8.33; methane-based TE gas, Fig. 8.34; propane and propane-based TE gas, Fig. 8.35; and air, Fig. 8.36. The W value at a particular ion energy is generally higher for the heavier ion. Stronger energy dependence was observed in propane than in the propane-based TE mixture for all heavy ions (Fig. 8.35).

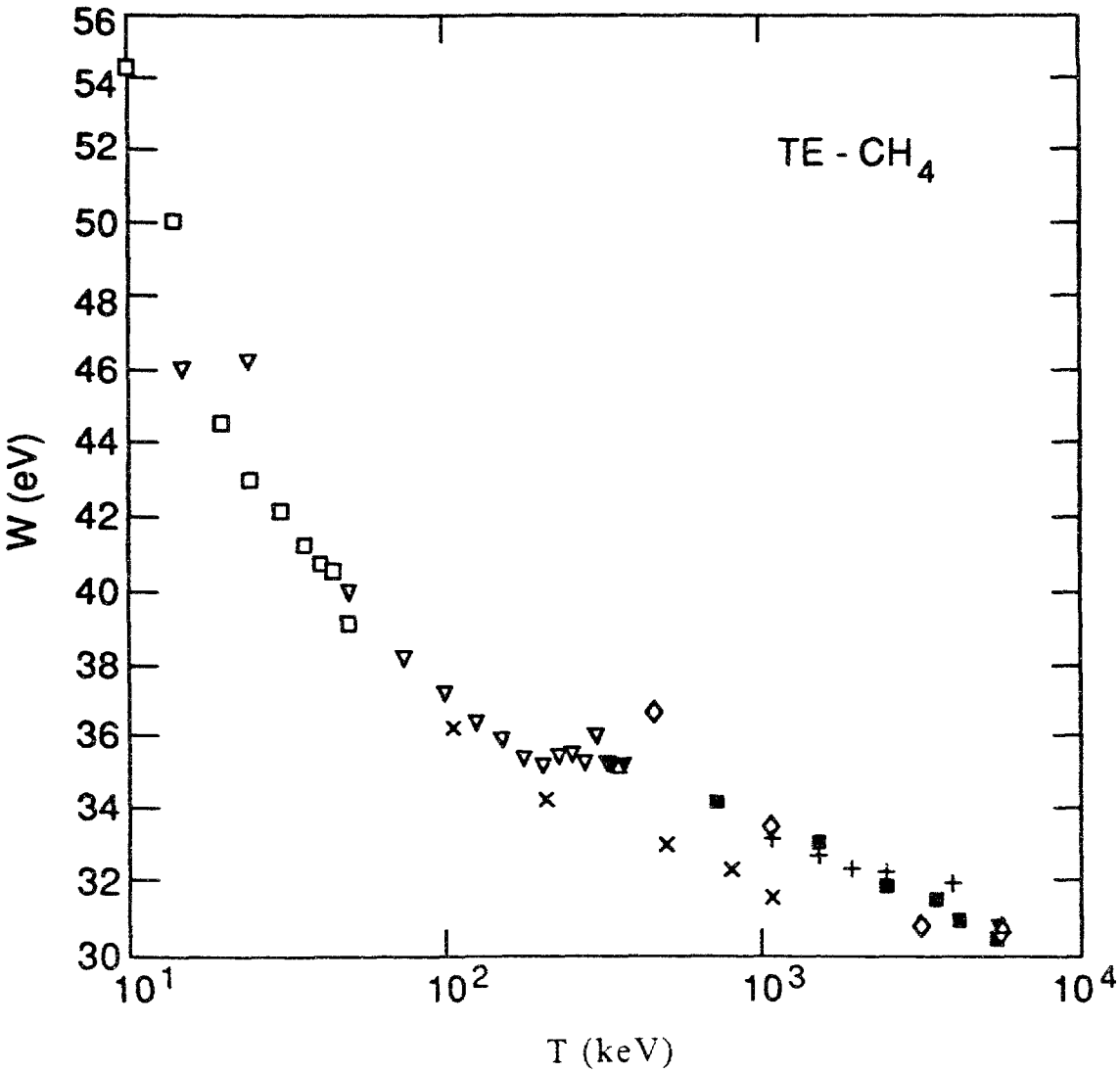

FIG. 8.27. W value for alpha particles and He^+ ions in methane-based TE gas. □, Huber et al. [114]; +, Whillock and Edwards [130]; ■, Rohrig and Colvett [125]; ◊, Varma and Baum [1340], Δ, Thomas and Burke [131]; ×, Kuehn and Werba [119]; ▽, Nguyen et al. [116]; ▼, Kemmochi [139]. The ICRU [1] recommended 31.1 ± 0.3 eV for ≈5 MeV alpha particles and suggested 37 ± 1, 33 ± 1, and 31 ± 1 eV for alpha particles at about 0.1, 1, and 10 MeV, respectively. More data are needed between 100 keV and 1 MeV, to confirm the maximum suggested by Nguyen et al. [116] and Rohrig and Colvett [125]. Hiraoka et al. [99] obtained 31.0 eV for the differential w value for 99 MeV ^3He ions.

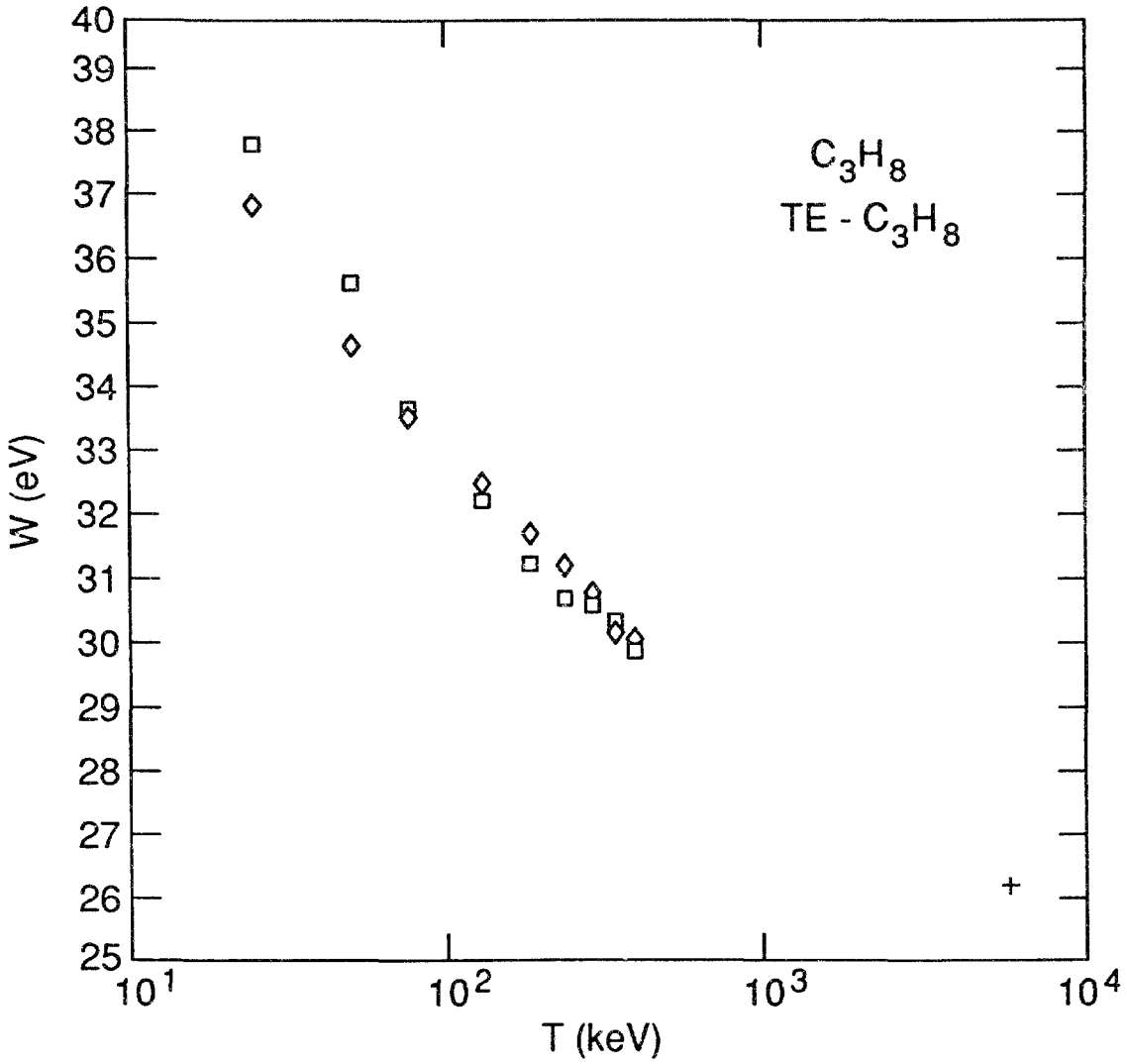

FIG. 8.28. W value for alpha particles and He^+ ions in C_3H_8 and in propane-based TE gas. C_3H_8: □, Posny et al. [126]; +, Kemmochi [139]. Propane-based TE gas: ◊, Posny et al. [126]. The ICRU [1] recommended 26.2 eV for ≈5 MeV alpha particles in propane with an uncertainty of at least 0.7%.

Schimmerling et al. [140] measured differential w values for heavy ions (Ne, Si, Al) of much higher energy (100-600 MeV/u). The measured average values were w = 26.3 ± 0.8 eV in P-7 gas (93% argon + 7% methane) and w = 33.0 ± 2.3 eV in N_2. These values are comparable to the W values reported for 5.3 MeV alpha particles in P-7 gas and slightly lower than those reported for N_2. Thomas et al. [141] reported the following differential w values in nitrogen: 36.4 ± 0.6 eV for 250 MeV/u C^{6+} ions, 35.4 ± 0.8 eV for 375 MeV/u Ne^{10+} ions, and 34.7 ± 0.5 eV for 479 MeV/u Ar^{18+} ions. Recently, Kanai et al. [141a] reported differential w values for some heavy ions in air: w=36.2 ± 1.0 eV for 6.7 MeV/u carbon ions, w = 33.7 ± 0.9 eV for 129.4 MeV/u carbon ions, and w = 34.5 ± 1.0 eV for 10.3 MeV/u ^3He ions. Additional data and a compilation of W values for heavy ions in Ar and N_2 were presented by Schimmerling [142]. Varma and Baum [143, 144] measured W values for heavy ions in various gases and determined the dependence of W values on the ion energy per atomic unit and charge.

Since δ rays are frequently produced in the collisions of charged particles, it is important to consider their ranges. Whenever a δ ray enters into the wall surrounding the gas volume in which the ionization is measured, it only produces ion pairs to the extent that energy is lost in the gas. The residual energy of the particle given to the wall will be lost to the ionization process ("wall effect"). If in Eq. (8.23) the energy lost by the particle is calculated from the stopping power, the w value will be too large. Conversely, if the energy loss is calculated from the observed ionization with the tabulated value of w, the energy loss will appear to be too small. The increases of w measured by Schimmerling et al. [140] may be due to a wall effect. An effect of the order of 20%, increasing with particle energy, was observed by Pfützner et al. [144a] for 150 to 900 MeV/u Ar, Kr and Xe ions in argon gas passing through the center of an ionization chamber with a diameter of 40 cm. A reduction of the width of the straggling function by as much as a factor of 2.5 was observed. A Monte Carlo calculation by Bichsel [144b] gave quantitative agreement for the effect.

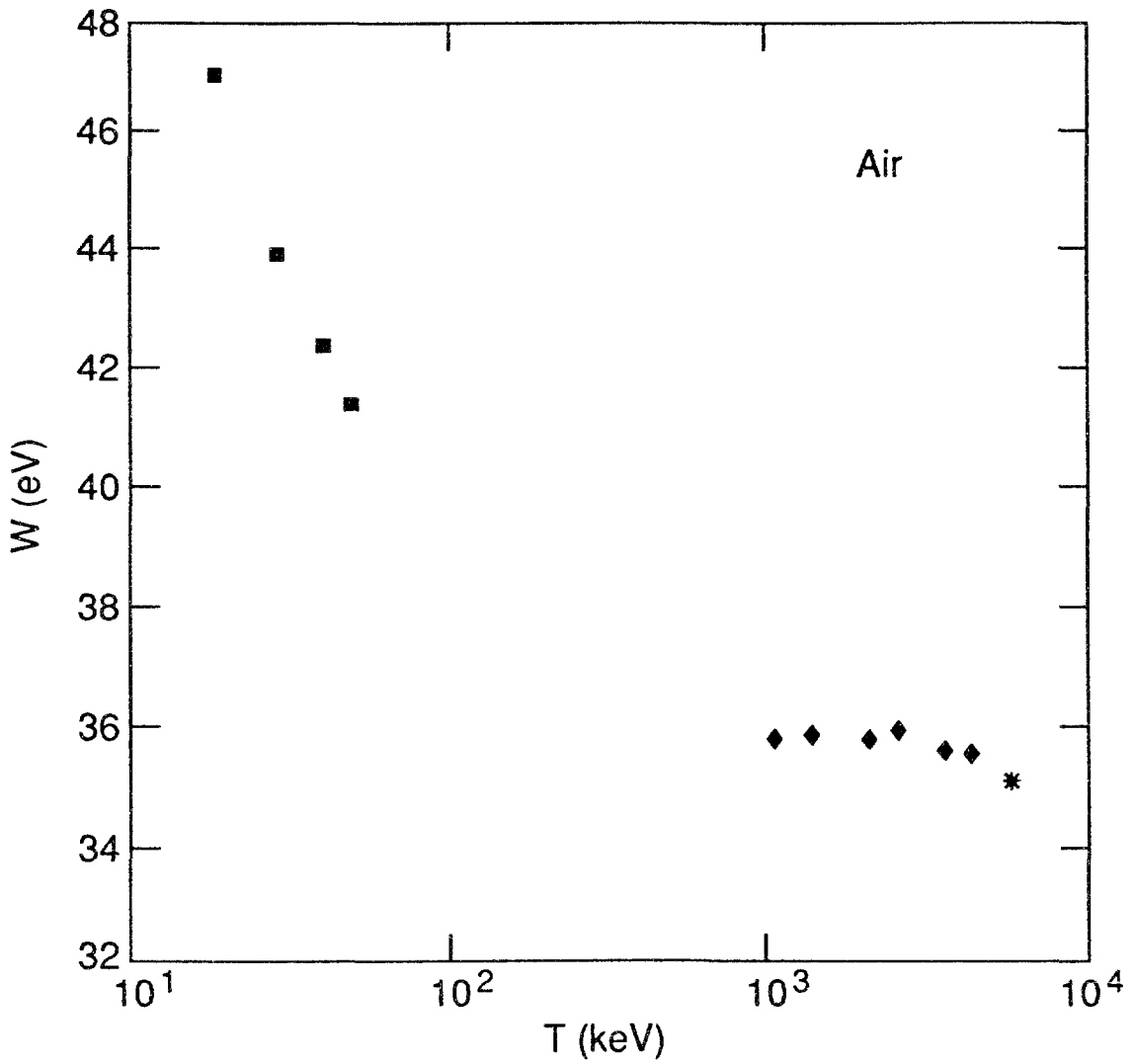

FIG. 8.29. W value for alpha particles and He^+ ions in air. ■, Huber et al. [114]; ♦, Chappell and Sparrow [133]; *, Kemmochi [139]. The ICRU [1] recommended 35.08 eV with an uncertainty of at least 0.7% for ≈5 MeV alpha particles. Hiraoka et al. [99] obtained 35.7 eV for the differential w value for 99 MeV ^3He ions.

Evidently, the wall effect is of great importance for the dosimetry of heavy ions with gaseous ionization chambers. Similarly, it must be considered for biological effects. It must be calculated for particular chamber geometry and biological models, as discussed in Chapter 9.

8.3.7. W Values in Gas Mixtures

Two groups of binary gas mixtures can be distinguished: the regular mixture and the irregular one [145]. In mixtures of molecular gases, the W value of the mixture lies between the extreme values for the pure gases and changes smoothly from one limit to the other as the composition of the mixture is changed. Such mixtures are called *regular mixtures*. In *irregular mixtures*, a small amount of admixture to a rare gas causes considerable increase in ionization. Such mixtures will be discussed separately.

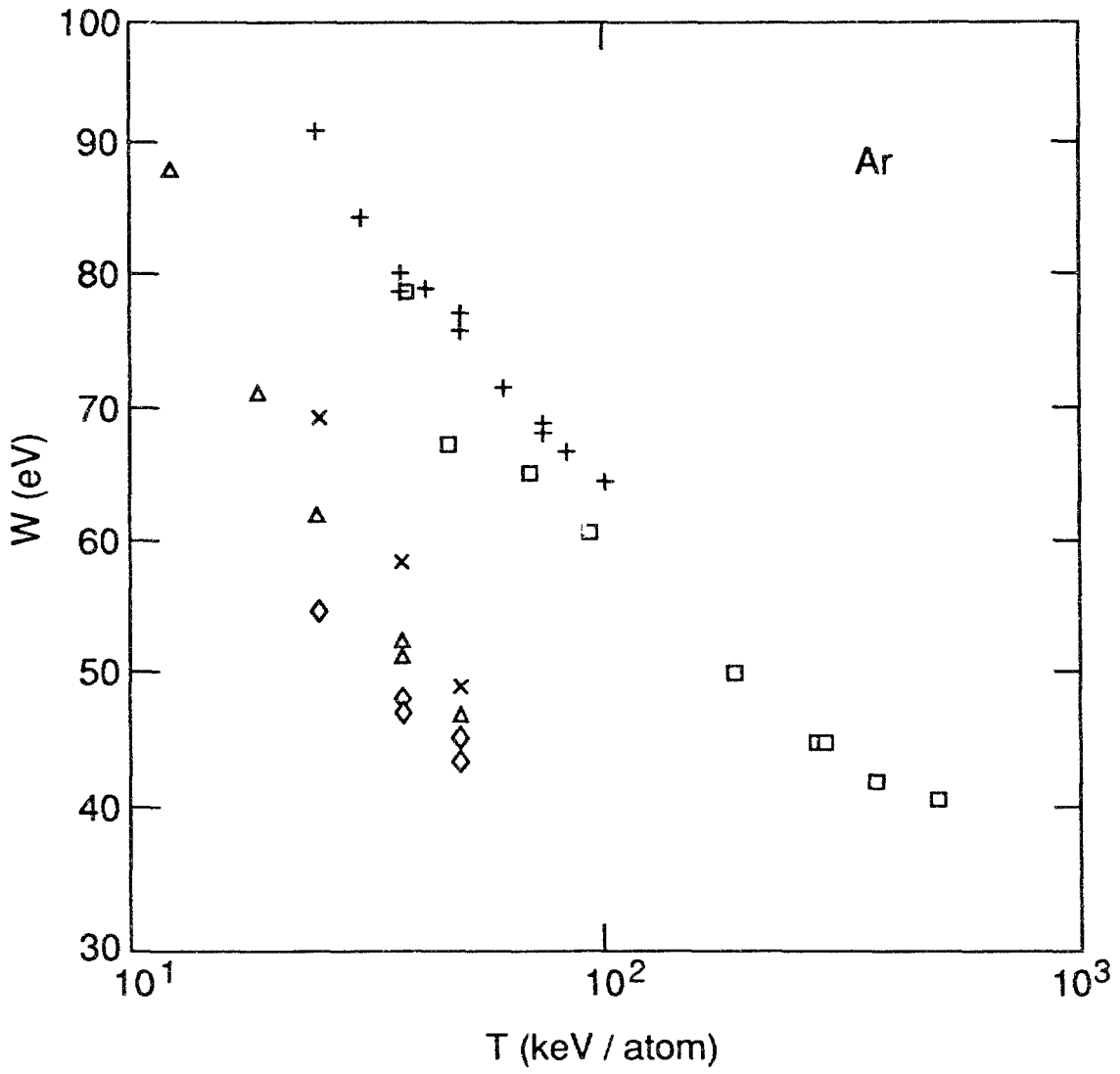

FIG. 8.30. W value for C^+, N^+, O^+, and Ar^+ ions in argon. ◊, C^+ ions; Δ, N^+ ions; ×, O^+; +, Ar^+, Phipps et al. [112]. □, Ar^+ ions, Chemtob et al. [109].

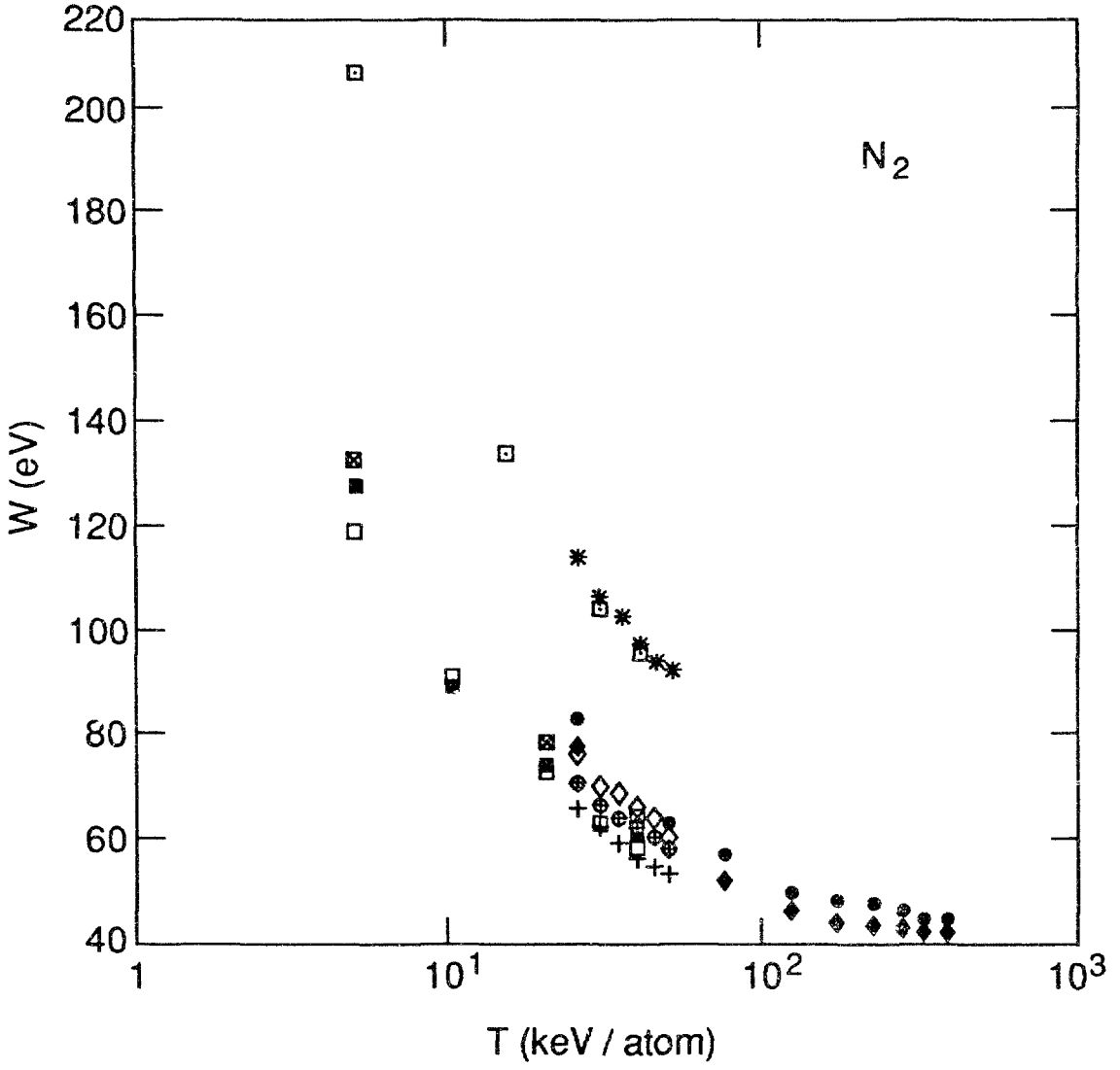

FIG. 8.31. W value for C^+, N^+, O^+, and Ar^+ ions in N_2. C^+ ions: □, Huber et al. [114]; +, Boring et al. [115]. N^+ ions: ■, [114]; ⊕, [115], ♦, Nguyen et al. [116]. O^+ ions: ⊠, [114]; •, [116], ◊, [115]. Ar^+ ions: □, [114]; ⋆, [115].

8.3.7.1. Regular Mixtures

In regular mixtures the intermolecular energy transfer is considered negligible, and the W value for the mixture can be related to the W values in pure components. Several models for calculating W values in mixtures are described in the literature. All models are based on the assumption that the presence of gas A does not affect the ionization of gas B, and vice versa. In the simplest model, the ionization yield in a mixture is obtained by simple addition of the ionizations in pure components according to their relative concentrations C_i. The corresponding W value is as follows:

$$\frac{1}{W_{mix}} = \sum_i \frac{C_i}{W_i} \tag{8.27}$$

Here C_i and W_i are the concentration fraction and the W value, respectively, for the pure component i, where i = A,B.

Other models take into account different interaction properties of the gases. The model of Haeberli et al. [146, 147] assumes that the energy T_0 of the incident particle is dissipated to the components in proportion to their respective stopping powers S_i.

$$\frac{1}{W_{mix}} = \frac{W_A^{-1} S_A C_A + W_B^{-1} S_B C_B}{S_A C_A + S_B C_B} \tag{8.28}$$

This model was modified by Bortner and Hurst [148] and Strickler [145] by replacing relative stopping powers in Eq. (8.28) with the empirical parameter f_i.

$$W_{mix} = \frac{W_A f_A C_A + W_B f_B C_B}{f_A C_A + f_B C_B} \tag{8.29}$$

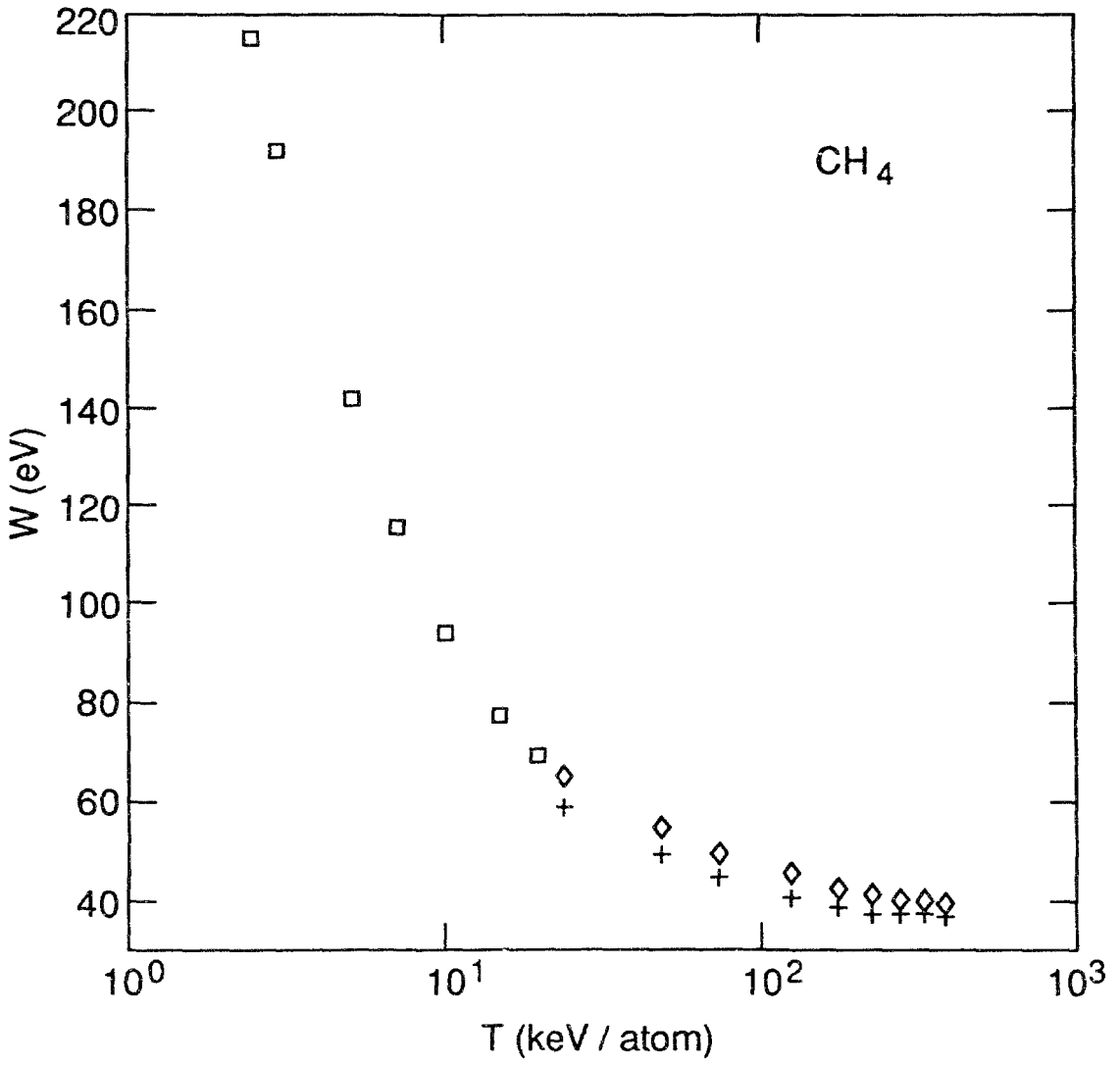

FIG. 8.32. W value for C+, N+, and O+ ions in CH_4. C+ ions: +, Nguyen et al. [116]. N+ ions: □, Huber et al. [114]. O+ ions: ◊, Nguyen et al. [116].

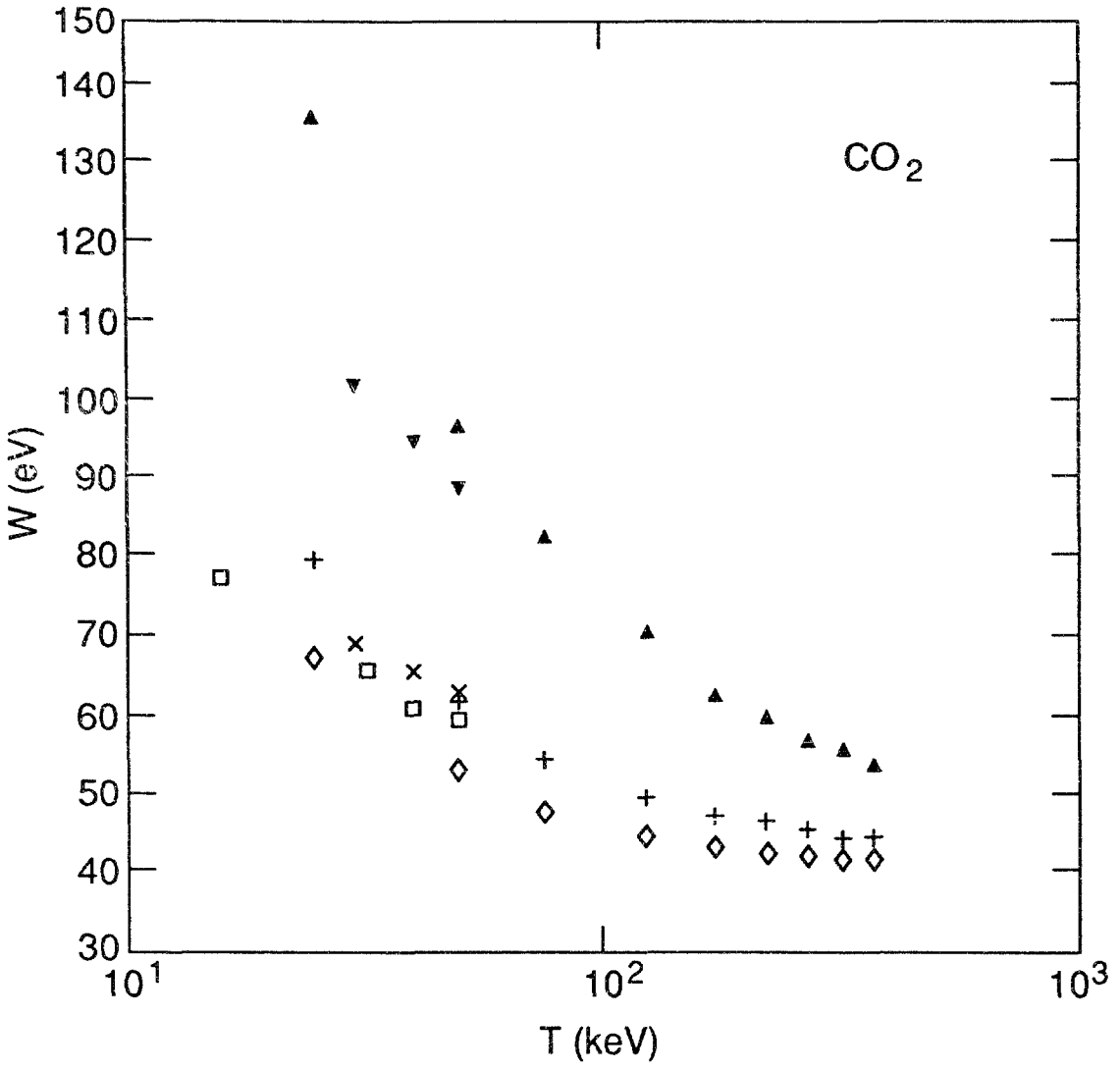

FIG. 8.33. W value for C^+, O^+, and Ar^+ ions in CO_2. C^+ ions: ◊, Nguyen et al. [116]. O^+ ions: □, Huber et al [114]; +, [116]; ×, Boring et al. [115]. Ar^+ ions: ▲, [116]; ▼, [115].

Recent considerations by Eggarter [15], Inokuti and Eggarter [16] and Swallow and Inokuti [149] showed that the energy partition is determined by the total ionization cross-sections, σ_i, evaluated at sufficiently high electron energy. The W value in a regular mixture is then given by:

$$W_{mix} = \frac{W_A \sigma_A C_A + W_B \sigma_B C_B}{\sigma_A C_A + \sigma_B C_B} \tag{8.30}$$

All these expressions can be easily extended to mixtures with more than two components, such as TE gas mixtures.

The measured W values for electrons, protons, and alpha particles in both methane-based and propane-based TE gases have been compared with the calculated W values according to Eqs (8.27-8.30) [84]. Good agreement between the experimental and the calculated values for methane-based TE gas has been obtained for all models.

This is because the values of energy partition parameters (f_i or σ_1) for CO_2 and CH_4, the main components of the mixture, are almost equal. In contrast, the values of f_i and σ_i for CO_2 and C_3H_8, the main components of the propane-based TE gas, are considerably different. The best agreement between the experimental and the calculated W values for propane-based TE gas was obtained by using Eq. 8.29 over the whole energy range and for all kinds of incident particles, and by using Eq. 8.30 for electrons having energy $T_0 \geq 100$ eV [84].

8.3.7.2. Mixtures with Irregular Effects

In sharp contrast to the properties of regular mixtures of molecular gases, a significant increase in ionization and a consequent decrease in W values are observed when small amounts (<1%) of certain gases are mixed with a rare gas, if

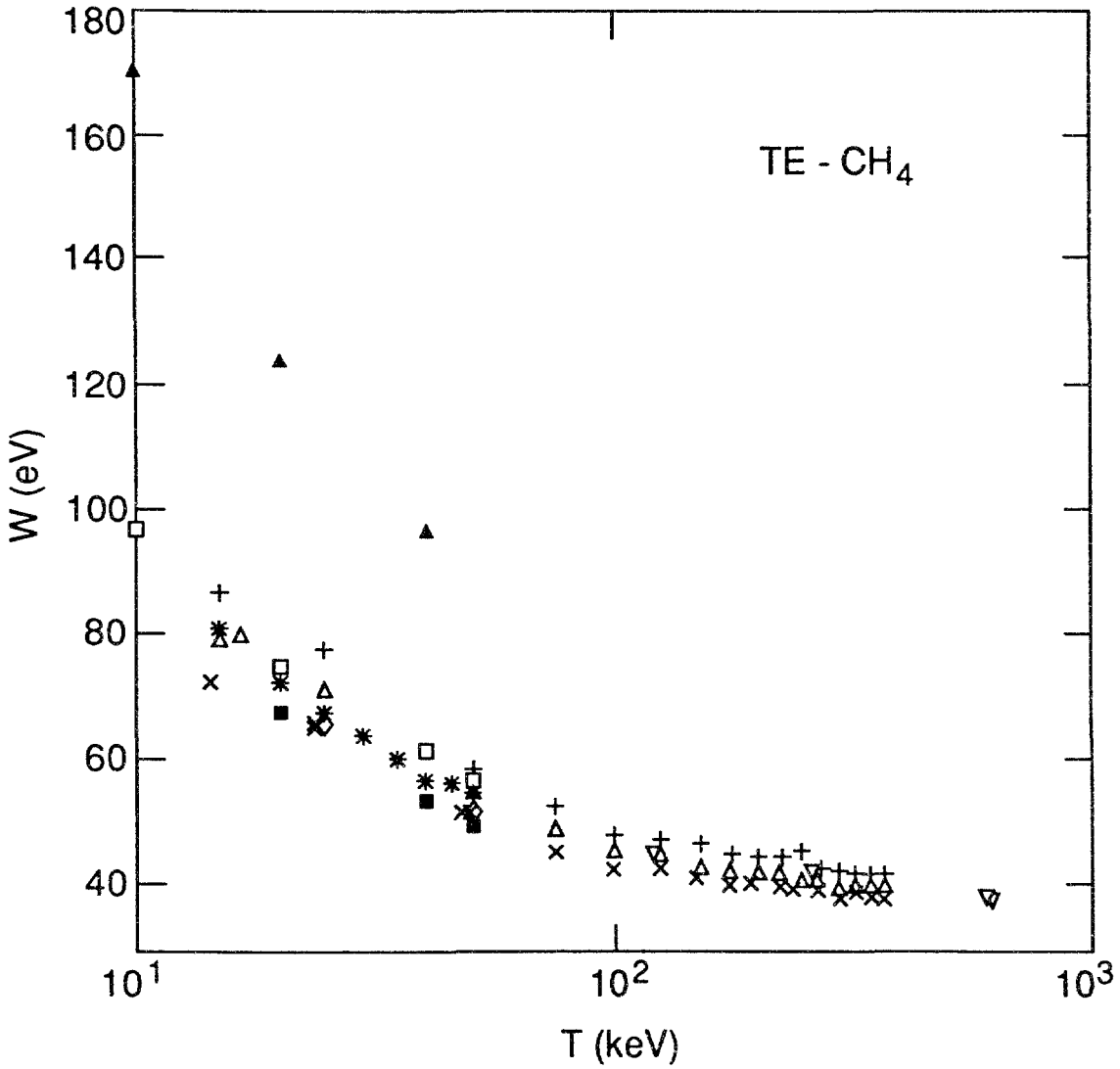

FIG. 8.34. W value for C^+, N^+, O^+, and Ar^+ ions in methane-based TE gas. C^+ ions: ■, Huber et al. [114]; ×, Chemtob et al. [109]; ▽, Rohrig and Colvett [125]. N^+ ions: *, [114]; △, [109]. O^+ ions: □, [114]; +, Nguyen et al [116]; ◊, Leonard and Boring [124]. Ar^+ ions: △, [114].

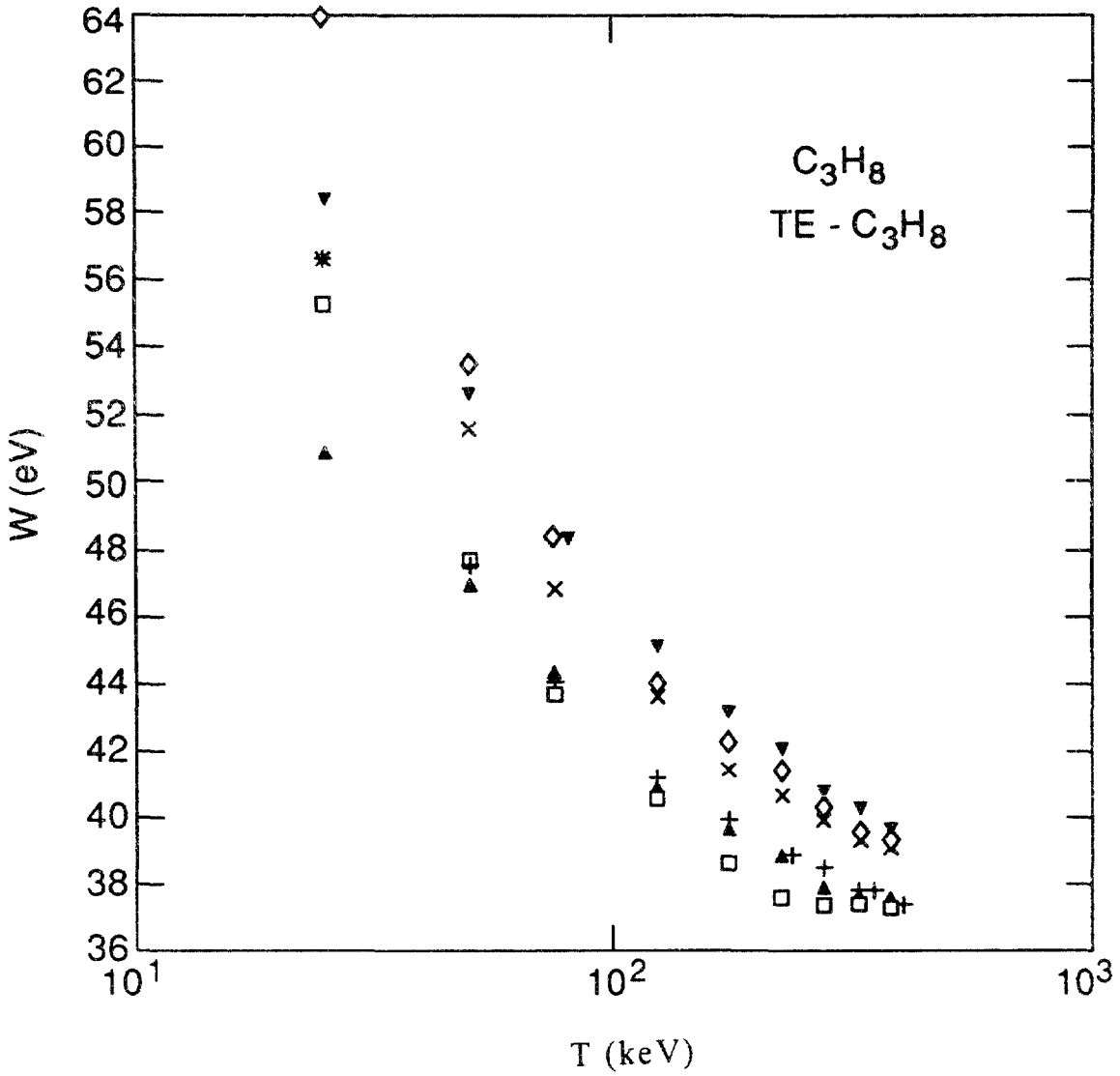

FIG. 8.35. W value for C^+, N^+, and O^+ ions in C_3H_8 and in propane-based TE gas. Propane: □, C^+ ions; +, N^+ ions; ◊, O^+ ions. Propane-based TE gas: Δ, C^+ ions; ×, N^+ ions; ▼, O^+ ions. All measurements were by Posny et al. [126].

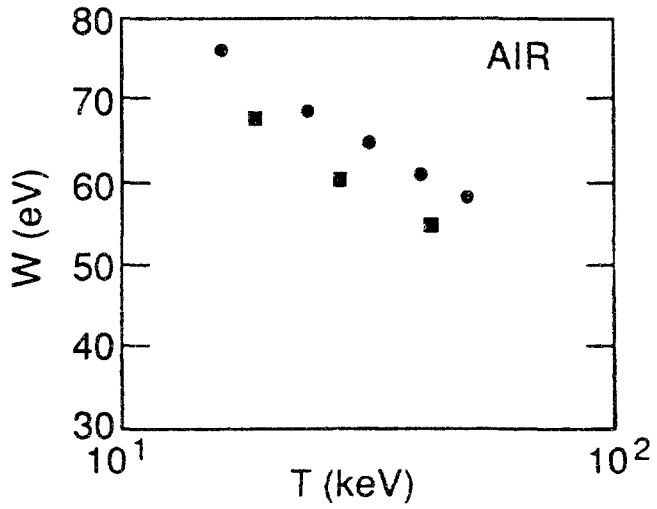

FIG. 8.36. W value for N^+ and O^+ ions in air. ■, N^+ ions; •, O^+ ions; Huber et al. [114]. More measurements are needed for heavy ions having energies above 100 keV/atom in air.

the ionization potential of the admixture is lower than that of the metastable state of the rare gas, as first reported by Jesse and Sadauskis [73-76]. This observation has been referred to as the *Jesse effect*. Melton et al. [150] also observed the increased ionization in Ar, even when the admixture had an ionization potential greater than that of the Ar metastable level, at higher admixture concentrations of 5% in argon-methane and 3% in argon-ethane. This additional yield was attributed to the non-metastable Penning processes.

The de-excitation of metastable (and other excited) rare gas atomic states by collisions with the admixture molecules leads to additional ionizations in the mixture and to a corresponding decrease in W values. The total ionization yield in such mixtures is composed of direct ionization of both gases by the incident particle and the ionization of the admixture by excited atoms of the rare gas through the Penning processes. In these mixtures, the simple additivity rule of W values (Eqs 8.27-8.30) cannot be applied.

Processes that involve excited (and metastable) states of rare gas atoms are dependent on the admixture's concentration at a constant total pressure of the mixture, as shown by Melton et al. [150] and Tawara et al. [151], and are also dependent on the total pressure of the mixture at constant admixture concentration, as shown by Parks et al. [113], Jarvinen and Sipila [152], and Krajcar-Bronić et al. [83]. The pressure dependence of the W value in argon-butane mixtures is described in some detail in [83]. These interesting features of W values in mixtures of rare gases with various atoms and molecules have been discussed in terms of the collisional de-excitation of excited rare gas atoms by atoms and molecules. Investigations of such de-excitation processes have been greatly advanced. Absolute cross section values, as well as product branching ratios have been measured extensively for a variety of electronic excited states in rare gases, both metastable and non-metastable and for various quenching atoms and molecules [153].

8.4. STATISTICAL FLUCTUATIONS

The degradation of a charged particle passing through matter occurs through many collisions of diverse kinds, which result in energy transfer of different values and in different outcomes such as excitation or ionization. Therefore, the precise history of successive collisions is different for each incident energetic particle. To express this fact compactly, one often states that the degradation process is *stochastic*.

A stochastic description of the ionization is given by the probability $P(T_0,j)$ that an incident particle of energy T_0 and all subsequent generations of secondary electrons produce a total of exactly j ions after complete dissipation of energy T_0.

The probability is normalized as follows at all T_0:

$$\sum_j P(T_0, j) = 1 \tag{8.31}$$

The mean number $N_i(T_0)$ of ions produced is given by:

$$N_i(T_0) = \sum_j j P(T_0, j) \tag{8.32}$$

It is related through Eq. (8.21) to the W value, which we have discussed extensively.

The simplest index characterizing statistical fluctuations of the number of ions is the variance defined as follows:

$$V_N(T_0) = \sum_j [j - N_i(T_0)]^2 P(T_0, j) \tag{8.33}$$

Fano [154], the first to discuss the fluctuations, showed that $V_N(T_0)$ should be proportional to $N_i(T_0)$ for sufficiently high incident energies T_0. It is customary to write the variance as follows and to call $F(T_0)$ the Fano factor:

$$V_N(T_0) = F(T_0)\, N_i(T_0) \tag{8.34}$$

Then, $F(T_0)$ tends to a constant at high energies T_0. Fano [154] also pointed out that the value of $F(T_0)$ should be less than unity. If the ionization process were described by simple Poisson statistics, the Fano factor would be unity. Actually, the ionization yield is subject to limitations due to the partitioning of energy T_0 into individual inelastic collisions resulting in ionization or excitation, and the cross-sections for these collisions are dependent on the kinetic energy of a particle. Therefore, the Poisson statistics does not apply at all.

The Fano factor represents the limit of ultimate resolution of the particle energy by ionization measurements and is therefore of interest in dosimetry and particle-detection technology.

In what follows, we shall review the values of the Fano factor for various materials and particles (in Section 8.4.1) and knowledge of $P(T_0,j)$ (in Section 8.4.2).

8.4.1. The Fano Factor

The Fano factor and the W value depend mainly on the properties of the irradiated matter and only weakly on the energy and nature of the incident particles, if they are much faster than the valence electrons in molecules of the medium. At higher particle energies the Fano factor has a constant value between ≈0.2 and 0.4 (in pure gases), increasing toward unity as the particle energy decreases toward the ionization energy of the gas.

Fano factors have characteristic values for various gases, but usually F is lower in gases in which most of the incident energy is spent on ionization. For the same reason as for W values, the Fano factor in rare gases is smaller (0.13-0.19, according to Alkhazov [155]) than in molecular gases (0.26-0.37) owing to different energy partition between ionization and other processes (excitation, dissociation) in gases. In the limiting case of ionization of a complex molecule that has a high

TABLE 8.1. FANO FACTOR IN PURE GASES AND REGULAR MIXTURES

Gas	Energy*	F	Ref.
Electrons			
H	keV	0.39	155
H_2	10 keV	0.30	13
H_2		0.40	154
H_2	keV	0.34	155
He		0.21	66
He		0.17	157
Ne		0.13	155
Ne		0.17	157
Ar		0.17	157
Ar	keV	0.16	155
Ar	>1 keV	0.15	98
Ar + 10% CH_4	2.8 keV	0.14	158
CO_2	keV	0.32	155
O_2	keV	0.37	155
N_2	keV	0.28	155
C_2H_2		0.27	163
CH_4	keV	0.22	38
CH_4	keV	0.26	157
H_2O vapor	keV	0.25	39
H_2O vapor	100 eV	0.32	39
TE (CH_4)	keV	0.25	36

* Electron energy is indicated where specified in cited reference; keV denotes incident electron energy range.

probability for pre-dissociation, so that the ionization yield is low, F should be nearly equal to unity [155, 156]. Values of the Fano factors in several gases [78, 81, 155, 157-168] are presented in Table 8.1.

In certain gas mixtures with a pronounced Penning effect (irregular mixtures), the Fano factor can be as low as 0.05. As discussed in Section 8.3.7.2, an admixture to the rare gas often converts the excitation energy of the rare gas atoms to additional ionizations, increasing the mean number of ion pairs and decreasing statistical fluctuations. Some W values and Fano factors for irregular gas mixtures are presented in Table 8.2.

A recent discovery about the systematics of the Fano factor deserves attention. A linear correlation between the Fano factor and the W value was reported by Srdoč et al. [81] for 1.49 keV photons in several polyatomic gases. Kimura et al. [100] pointed out that the Fano factor and the W value show notable correlation revealed in Fig. 8.37, where the Fano factor is plotted against the W value of argon-hydrogen mixtures of various compositions. The best fit to the calculated data points

TABLE 8.1. (cont.)

Gas	Energy	F	Ref.
Photons			
Kr	1.5 keV	<0.23	160
Kr	1.5 keV	<0.19	162
Xe	5.9 keV	0.17	161
Xe	1.5 keV	<0.15	160
Xe	5.9 keV	0.13	159
CH_4	1.5 keV	0.29	78
CH_4	1.5 keV	0.26	81
TE (CH_4)	1.5 keV	0.37	78
TE (CH_4)	1.5 keV	0.31	81
TE (CH_4)	277 eV	0.32	81
TE (see [164])	1.5 keV	0.40	164
TE (see [164])	277 eV	0.25	164
C_3H_8	1.5 keV	0.29	78
C_3H_8	1.5 keV	0.25	81
C_3H_8	277 eV	0.27	81
TE C_3H_8	1.5 keV	0.32	78
TE C_3H_8	1.5 keV	0.30	81
Ar + 10% CH_4	5.9 keV	0.21	165
Kr + 1.3% Xe	1.5 keV	0.19	160
Kr + 60% Xe	1.5 keV	0.21	160

Gas	Energy	F	Ref.
Alpha particles			
He	5.3 MeV	0.24	168
Ar	5.7 MeV	≤0.20	166
Ar + 10% CH_4	5.3 MeV	0.18	167
Ar + 0.8 % CH_4	5.7 MeV	<0.19	157

was obtained from the linear equation $F = 0.0165 \cdot W - 0.2865$, and the correlation coefficient was $r^2 = 0.99$. The correlation between the Fano factor and W values for electrons in various gases and gas mixtures was later generalized by Krajcar-Bronić et al. [170]. They found that W and F tend to increase or decrease together in series of comparable gases. In Fig. 8.38 the Fano factor is plotted against the ratio W/I for various pure gases [171]. Here the dimensionless ratio W/I is used because it is appropriate for comparison with F. The trend of simultaneous increase or decrease of W/I and F is easily understandable because a small value of W/I means a high probability of ionization, which in turn means that a small variety of inelastic collisions is involved. Hence, the value of F will be small. Conversely, a large value of W/I means a low probability of ionization, a large variety of inelastic collisions, and hence

TABLE 8.2. FANO FACTOR AND W VALUES IN MIXTURES WITH ADDITIONAL IONIZATION

Gas mixture	W (eV)	F	Ref.
Electrons			
He + 0.5% Ar	29.2	0.054	155
He + Xe (0.5-1%)	28.7	0.057	155
He + CH_4 (0.5-1%)	30.3	0.089	155
Ar + 0.5% C_2H_2	20.3	0.075	157
Ne + 0.5% Ar	25.3	0.063	155
Ne + 0.5% Ar	25.3	0.05	157
Photons			
Ar + 1% C_2H_2	20.7	-	152
Ar + 0.5% C_4H_{10}	22.3	-	152
Ne + 0.5% Ar	25.4	-	152
Protons			
Ar + 1% C_2H_4	23.8	-	113
Alpha particles			
He + 1% Ar	28.9	0.11	168
Ar + 0.5% C_2H_2	-	<0.09	157
Ar + 0.5% C_2H_2	20.3	-	166
Ar + 0.8% C_2H_2	21.2	0.09	169

a large value of F. More significantly, we see that W/I and F are related to each other virtually linearly:

$$F = a\frac{W}{I} + b \tag{8.35}$$

Here a and b are constants. The best fit given by F = 0.188 W/I − 0.15, r^2 = 0.97, approximates very well the data for electron energies higher than 50 eV. In the low-energy region, where the energy dependence of both quantities is significant, the relation is no more linear, and the Fano factor asymptotically approaches a limiting value equal to 1 for W/I>>1 (Fig. 8.38). Although this relation has not been successfully derived theoretically, the relation obtained by Kimura et al. [100] can be approximated by a linear relationship within a relatively narrow range of W/I and F values. The linear dependence of F versus W/I, which is certainly remarkable, can serve as a practical guide for gases for which no data on either F or W are available. In most cases the linear approximation may be used to estimate the Fano factor in gases and gas mixtures for which the W values are known.

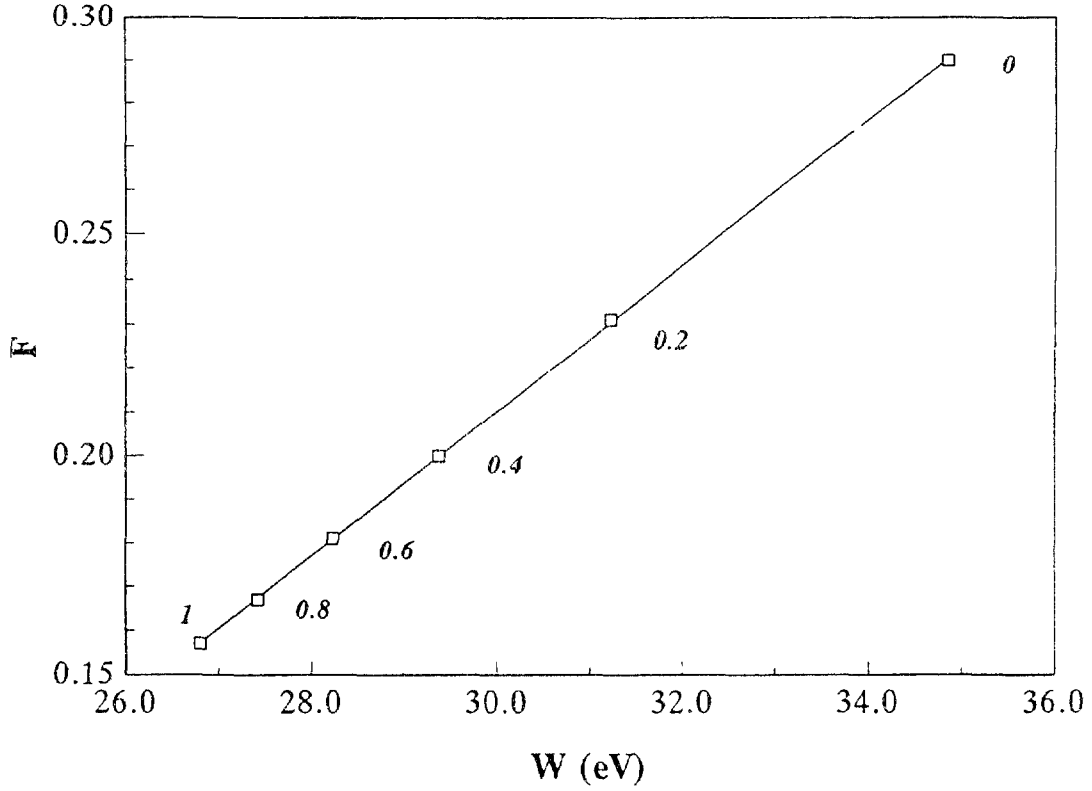

FIG. 8.37. The relation between the Fano factor (F) and the W value in Ar-H_2 mixtures. □, Calculated values from Kimura et al. [100]; — best fit. The fractional concentration of argon in the mixture is indicated along with the calculated data points.

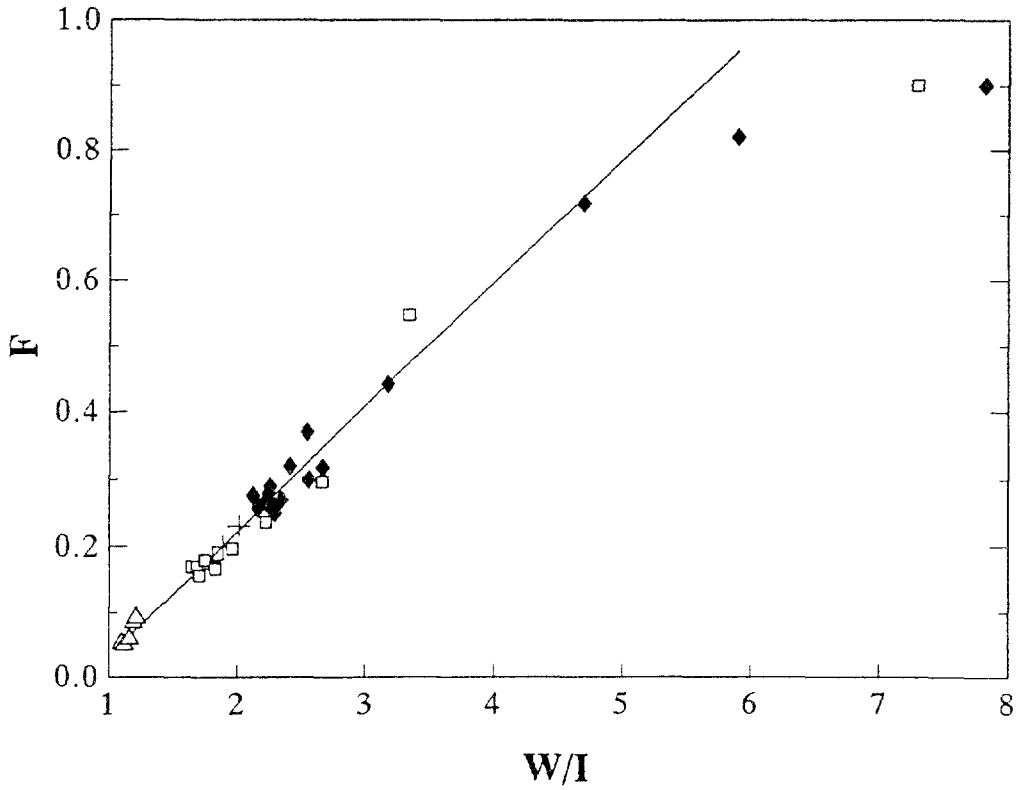

FIG. 8.38. The relationship between the Fano factor (F) and the ratio W/I in pure gases and gas mixtures. □, rare gases; ♦, molecular gases; +, regular Ar-H_2 mixture; Δ, gas mixtures exhibiting metastable Penning effect; —, best fit. Data are taken from Alkhazov [155], Combecher [61], Grosswendt [35], Kimura et al. [100], Kowari et al. [14], and Srdoč et al. [81].

The Monte Carlo method (i.e., the simulation of histories of a large number of individual particles in a computer) enables one to calculate W and F, as well as some other quantities characterizing the energy degradation process. Examples of Monte Carlo calculations of the Fano factors were given by Unnikrishnan and Prasad [98] in argon; by Grosswendt in H_2 [35], in methane-based TE gas [36, 53], and in He, Ne and Ar [37]; by Grosswendt and Waibel in N_2 and air [34] and in CH_4 and CO_2 [38]; and by Turner et al. [41] and Paretzke et al. [42] in water vapor and liquid.

As we pointed out in Section 8.2.3, the Fano factor can be evaluated from transport theory, with the use of Eqs (8.17)-(8.19). Examples of the evaluation of the Fano factor for electrons are shown in Refs [13, 14, 100], while in [172] the Fano factor is calculated for protons. If proton or alpha particle is an incident particle, than the yield and the fluctuations receive contributions from direct ionization by the incident ion and from ionization by secondary electrons. The Fano factor for protons of energies between 0.1 and 2 MeV in argon is nearly the same as that for electrons at the same speeds, but it is considerably lower than the Fano factor measured with alpha particles [172]. Doke et al. [173] summarized and compared the theoretical and experimental results on the Fano factor in pure rare gases and their mixtures. They found that the Fano factors for alpha particles are systematically larger than those for electrons.

8.4.2. Probability Distribution of the Number of Ion Pairs

The probability distribution of the number of ion pairs formed by an incident electron in various gases has been evaluated by the Monte Carlo method [34-38, 42, 53]. The generalized Fano factors, introduced by Inokuti et al. [13], have also been evaluated as functions of incident electron energy.

Monte Carlo calculations of the probability distribution at various electron energies in water [42] and in methane-based TE gas [53] have shown a rapid change in the shape of the $P(T_0,j)$ curve from a Poisson-like distribution at low energies to a Gaussian-like distribution with increasing energy. This behavior is accompanied by a very rapid decrease of the Fano factor with increasing energy and an asymptotic approach to a constant value at higher energy ($\approx$5 keV). Furthermore, Waibel and Grosswendt [53] compared the data characterizing ionization yield for electrons (W value, Fano factor, $P(T_0,j)$ distribution) in methane-based TE gas with those in water vapor [42] and showed the similarity in the ionization behavior of electrons in both media, what may be important for many purposes in radiation research and applications.

The probability distribution of the number of ion pairs can also be determined experimentally. The pulse height distribution measured with a proportional counter is the result of two independent processes: (1) ionization along the primary track in the counter gas, producing ion pairs the mean number of which is proportional to the energy spent by incident particles and depends on the gas properties, (often called the *primary ionization distribution*), and (2) multiplication of the primary electrons, which depends on the working voltage, gas properties, and pressure. If the distribution of avalanche sizes triggered by a single electron in the counter is known, the distribution $P(T_0,j)$ can be calculated from the measured pulse height

spectrum. An iterative deconvolution method was developed by Gold [174] and tested and modified by Marino and Srdoč [175] and Obelić [80]. Obelić [80] described this method in detail. By applying this method, Srdoč et al. [81] obtained the primary ionization probability density distribution for incident low-energy photons in several gases that are frequently used in radiation dosimetry. Moments, central moments, and generalized Fano factors were calculated. These values confirmed the supposition that the primary distribution approaches a Gaussian distribution at higher energies, whereas positively asymmetric shapes, more peaked than Gaussian, were obtained for incident particle energies below 1.49 keV.

Another method of measuring the probability distribution and its indices such as the Fano factor was developed by Hurst and co-workers [165]. Their method, known as *resonance-ionization spectroscopy*, is based on multiphoton ionization by laser lights combined with ingenious use of proportional counters. Unfortunately, this line of work does not seem to be pursued as vigorously as its merits warrant.

8.5. YIELDS OF EXCITED STATES

The absorption of radiation produces various electronically excited states, in addition to ions. The excited states of an isolated molecule eventually decay spontaneously in many ways, including photon emission, dissociation into fragments (which may be also excited), and internal conversion into vibrationally and rotationally excited levels of a lower electronic state (which may be the ground state). As we mentioned in Section 8.2., the yield of any excited state can be calculated as for an ion. Theory also shows that the total yields of excited states are generally appreciable. Recall the discussion (Section 8.3) of the ratio N_i/N_{ex} in the energy balance equation of Platzman, Eq. (8.26). To illustrate the yield of excited states theoretically evaluated, we cite results of Douthat [11] for molecular hydrogen (Table 8.3).

In a gas at any appreciable pressure, an excited state may survive long enough to collide with another molecule in the ground state because of thermal motion, and thus may cause important consequences. An example is seen in the Jesse effect in gas mixtures, discussed in Section 8.3.7.2. A full discussion of the rich topic is in Chapter 6. In condensed matter, an electronically excited state is in immediate contact with neighboring molecules, especially because the orbital of any excited electron is spatially more extended than that of an unexcited valence electron. Therefore, the consequences of an excited state in condensed matter are even more spectacular and diverse (as exemplified in the production of excitons and excimers, which are outside the scope of the present volume). Therefore excited states should clearly be just as important as ions in the mechanisms leading to chemical and biological effects.

Experimentally, it has been difficult to obtain absolute yields directly for the formation of excited states in radiolysis. However, qualitative evidence for their formation has been obtained with the use of the following methods [165, 176-184]:

1. Optical emission from radiative excited states
2. Optical absorption of excited states
3. Laser-induced fluorescence or ionization of excited states

4. Electron spin resonance (ESR) absorption
5. Monitoring of other spectroscopic signals attributable to excited states
6. Optical emission or absorption, and in some cases ion formation (if Penning ionization occurs), due to energy transfer from excited states to an additive quencher molecule

In general, experimental results are explained by the reaction schemes shown in Table 8.4., which are selected from all known fundamental processes of radiation chemistry for their roles in producing excited states [180, 181].

Table 8.4. shows that a molecule AB may be directly ionized, superexcited to form a superexcited state AB′ (which may autoionize or dissociate into neutral fragments), or excited to form an excited state AB^* below the ionization potential. AB^* is also formed by the recombination of AB^+ and e^-. An excited molecule AB^*

TABLE 8.3. YIELDS OF VARIOUS PRODUCTS GENERATED IN MOLECULAR HYDROGEN BY AN ELECTRON OF INITIAL ENERGY T_0 = 10 keV, ACCORDING TO DOUTHAT [11]

Transition	N_S*	$E_S N_S$ (eV)	Energy absorbed (% of total)
Lyman	96.8	1210	11.7
Werner	112.1	1457	14.0
H(2P)	5.6	84	0.8
Slow H(2S)	29.6	453	4.4
Fast H(2S)	5.3	175	1.7
H(n = 3)	3.2	47	0.5
Remaining	12.2	177	1.7
Ions	295.6	4759	45.9
Triplets	102.6	1036	10.0
Subexcitation electrons	295.6	975	9.4
	Total**	10 373	

* The symbol N_S represents the mean number of products *s*. The G value is given by $G_S = 100\, N_S/T_0$, where T_0 is the initial electron energy in eV; for T_0 = 10 keV the yield is given by $G_S = N_S/100$. The product $E_S N_S$ represents the energy used to generate product *s*. The terms *Lyman* and *Werner* indicate the excited states that emit luminescence photons associated with the names of the spectroscopists. The terms *H(2P)*, and *Remaining* indicate hydrogen atoms in various states resulting from dissociation.

**The sum of $E_S N_S$ exceeds the initial energy of 10 keV by 3.7% because of truncation and other errors in numerical work. The inconsistency is insignificant in view of uncertainties in cross-section data used as input.

TABLE 8.4 REACTION SCHEMES THAT PRODUCE EXCITED STATES [180, 181]

Reactant(s)		Product(s)	Type of reaction
AB	$\sim\!\!\rightarrow$	$AB^+ + e^-$	Direct ionization
	$\sim\!\!\rightarrow$	AB'	Excitation to superexcited states
	$\sim\!\!\rightarrow$	AB^*	Excitation to excited states below the ionization potential
AB'	$\longrightarrow$	$AB^+ + e^-$	Auto-ionization of superexcited states
	$\longrightarrow$	A + B	Dissociation of superexcited states
$AB^+ + e^-$	$\longrightarrow$	AB^*	Electron-ion recombination resulting in excited states
AB^*	$\longrightarrow$	A + B	Dissociation of excited states to ground state fragments
	$\longrightarrow$	$A + B^*$	Dissociation to an excited fragment and a ground state fragment
	$\longrightarrow$	$B + A^*$	
	$\longrightarrow$	AB + *internal vibrational and rotational energy*	Internal conversion
	$\longrightarrow$	AB + hν	Optical emission
$AB^* + S$	$\longrightarrow$	$AB + S^*$	Energy transfer
	$\longrightarrow$	$AB + S^+ + e^-$	Penning ionization
	$\longrightarrow$	ABS^*	Exciplex formation
	$\longrightarrow$	$ABS^+ + e^-$	Associative ionization
$AB^* + AB$	$\longrightarrow$	$(AB)_2^*$	Excimer formation

may dissociate into neutral fragments, cascade to lower excited states via either internal conversion or intersystem crossing, isomerize to another excited state $AB^{*\prime}$, emit a photon, or react with AB to form an excimer $(AB)_2^*$. In the presence of an additive molecule S, AB^* is collisionally quenched by S in simple energy transfer, Penning ionization, associative ionization, or exciplex formation. Some examples in the gas phase, chosen from recent advances in radiation chemistry to show the important role of excited states in radiolysis, are discussed below.

Fundamental processes of radiation chemistry of simple molecules, such as O_2, N_2, N_2O, CO, CO_2, H_2S, H_2O, and NH_3 in the gas phase, were surveyed [182] by compiling a large body of data on yields of radiolysis products; cross-sections for electron-molecule collisions; and information about ion-molecule reactions, electron-ion recombination, electron attachment, and others obtained up to the early 1970s. In this survey, G values were determined for ionization and excitation and also for individual elementary processes that are dependent on electronic states of ions and excited neutral species. Table 8.5 shows, as an example, the G values for H_2O vapor radiolysis.

TABLE 8.5. G VALUES FOR PRIMARY IONIC AND NEUTRAL DISSOCIATION AND EXCITATION PROCESSES IN THE RADIOLYSIS OF WATER VAPOR, ACCORDING TO WILLIS AND BOYD [182].

Reactant		Products		G $(100\ eV)^{-1}$
Ionic processes				
H_2O	$\sim\!\!\rightarrow$	$H_2O^+ + e^-$		1.99
H_2O	$\sim\!\!\rightarrow$	$OH^+ + H + e^-$		0.57
H_2O	$\sim\!\!\rightarrow$	$H^+ + OH + e^-$		0.67
H_2O	$\sim\!\!\rightarrow$	$H_2^+ + O + e^-$		0.01
H_2O	$\sim\!\!\rightarrow$	$H_2 + O^+ + e^-$		0.06
			Sum	3.30
Neutral dissociation and excitation processes				
H_2O	$\sim\!\!\rightarrow$	$H + OH$		3.58
H_2O	$\sim\!\!\rightarrow$	$H_2 + O$		0.45
			Sum	4.03

The understanding of these elementary processes in the gas phase has been greatly advanced both in theory and experiment, and new data on cross-sections and rate constants have been available since the early 1970s. Thus, it may be worthwhile to re-evaluate the results obtained by Willis and Boyd [182].

8.6. YIELDS OF IONIZATION AND EXCITATION IN CONDENSED MATTER

Ionization and related phenomena in condensed matter are rich in physics and chemistry, and their mechanisms are only partially delineated, as can be seen in recent books edited by Freeman [185] and by Ferradini and Jay-Gerin [186].

Therefore, the current understanding of the yield of ionization in condensed matter is limited in several respects. First, ionization phenomena manifest themselves differently, depending on the nature of the condensed matter (crystals or amorphous materials and conductors, semiconductors, or insulators). Second, to devise an experiment that produces a signal unquestionably representative of the ionization yield is often difficult. For instance, a current induced by radiation may depend on an applied electric field in a complicated manner that prevents the determination of ionization yield without a detailed analysis. Even an apparent yield of ionization that is unequivocally determined from measurements may not necessarily correspond to the *initial* yield in the sense of our discussion in Section 8.1; thus, to relate measured results with theory is not straightforward.

Generally speaking, ionization occurs at higher probability in a liquid than in a vapor consisting of the same molecular species. This difference is chiefly attributable to the lower value of the first ionization threshold in a liquid than in a vapor. For instance, the ionization threshold in liquid water is lower than that in water vapor by as much as 3.8 eV. In addition, the difference in the distributions of energy transfer, seen most clearly as the differences in the oscillator strength spectra (discussed in Chapter 6), contributes to the higher probability of ionization in liquid. In a phase change from gas to condensed matter for a single molecular species, the oscillator strength is modified often considerably, as was discussed fully by Inokuti [187]. A general modification is the shift toward higher excitation energies, which means that the spectral intensities corresponding to some of the discrete excitations in the gas will add to ionization in the liquid. Consequently, the ionization yield is expected to be higher in liquid than in vapor.

In the following sections, we shall briefly discuss several topics selected for their particular relevance to the theme of the present report.

8.6.1. Rare Gas Liquids

The ICRU Report 31 [1] briefly summarized knowledge about the W values in rare gas liquids. A review of the physical properties of liquids used in ionization chambers is presented in [188]. Various physical properties of liquid rare gases and the possibility of their application in radiation detectors have been recently studied extensively and presented at the International Conference on Liquid Radiation Detectors [189].

The W values for liquids reported in literature are 23.6 eV for Ar [190], 20.5 eV [191] and 18.4 eV [192, 192a] for Kr, and 15.6 eV for Xe [193]. Recently, Seguinot et al. [194] reported W = 9.76 ± 0.70 eV for 1 GeV electrons in liquid Xe. Their value is considerably lower than the value of Takahashi et al. [193] and only a little higher than the gap energy E_g=9.3 eV. Seguinot et al. [194] also reported W_S = 14.2 eV, i.e., the energy required to produce a scintillation photon in liquid xenon. Reported experimental W values in liquid rare gases depend on the method of extrapolation to an infinite electric field strength. Several recombination models were tested by Aprile et al. [192a] in the case of liquid krypton, and the authors found that the reported values in liquid rare gases obtained by the pulsed ionization chamber are the upper W value limits.

The W values for rare gas liquids are considerably lower than the values for gases (26.3 eV for Ar, 24.1 eV for Kr, and 21.9 eV for Xe). Doke and co-workers [190, 191, 193] interpreted the W values in rare gas liquids by extending Platzman's idea of energy balance [64], which we quoted in Section 8.3. In Eq. (8.26) they replaced the ionization threshold I with the gap E_g between the filled band and the conduction band and wrote the following:

$$\frac{W}{E_g} = \frac{\bar{E}_i}{E_g} + \frac{\bar{E}_{ex}}{E_g}\frac{N_{ex}}{N_i} + \frac{\varepsilon}{E_g} \tag{8.36}$$

Doke and co-workers and Aprile et al. [192a] estimated each term of this equation by using various pertinent data. The main conclusions of the treatment are discussed below.

The ratio W/E_g is about 1.65, only slightly smaller than the ratio $W/I = 1.7 - 1.8$ in gases. In other words, the primary reason for the low W values in liquids is the decrease in the ionization potential for the liquid relative to the gas. Second, the difference between W/E_g and W/I is chiefly attributable to very small values of N_{ex}/N_i in liquids (e.g., about 0.2 in Ar, 0.07 in Kr, and 0.05 in Xe). The small values of N_{ex}/N_i also suggest that the Fano factor in liquids should be considerably smaller than that in gases of the same element: 0.11 in liquid Ar, 0.06 in liquid krypton, and 0.04 in liquid xenon [195]. This expectation is one of the motivations for the recent development of liquid rare gas ionization counters [189, 196-203]. The present state of the art in developing liquid rare gas detectors is reviewed by Doke [204].

An increased charge per event was observed by Doke et al. [205] when liquid argon is doped with a small amount of organic molecules whose effective ionization potential is lower than the energies of photons emitted in liquid argon. In liquid argon-allene mixture the effective W value is 19.5 eV. An effect similar to the Jesse effect in gas phase was observed also in a mixture of liquid argon and 1% xenon: both the W value [195, 206, 207] and the Fano factor [195] were lower. The enhanced ionization was attributed to electronic energy transfer from exciton states of liquid argon to xenon.

8.6.2. Molecular Liquids

8.6.2.1. Summary of Experimental Knowledge

In liquids composed of polyatomic molecules, especially those with high dielectric constants, a low-energy electron ejected from a molecule may rapidly lose its energy through vibrational excitation, phonon generation, and other inelastic collisions (as discussed fully in Chapter 5) and eventually recombine with the remaining molecular ion. This process is called *geminate recombination* [183, 185, 208-212]. Electrons that are ejected at sufficiently high energies travel far from the ion, to a region where the potential energy of attraction, partly shielded by the dielectric medium, is less than the thermal energy. Then we say that a *free ion pair* is formed. The number of such ion pairs, determined by measurements at the limit of zero applied electric field, is expressed by the free ion yield, G_{fi}, which represents the number of free ion pairs produced per 100 eV of absorbed energy. Numerous measurements of G_{fi} have been made, and results have been extensively tabulated [208-212].

In contrast, the total number of ion pairs, including those that undergo geminate recombination, is difficult to measure directly in most of liquids. The total ion yield, G_{ti}, represents the total number of ion pairs produced per 100 eV of absorbed energy and is related to the W value through $G_{ti} = 100/W$. The ratio G_{fi}/G_{ti}, called the *probability of escaping geminate recombination*, has been the topic of many treatments, as seen in Chapters 2, 5, and 6 of Freeman [185]. With a theoretical estimate of the ratio G_{fi}/G_{ti}, a measured value of G_{fi} leads to an estimate

of G_{ti}. The W/I value thus derived is generally close to the value for the gas phase of the molecular species, within the sizable uncertainty of the estimate.

The measurement of G values of excited states in the condensed phase, which is much more difficult than in the gas phase, was recently summarized by Katsumura [179]. It has been generally accepted that excited states play a significant role in radiation chemistry. This role is most clearly observed in non-polar media like hydrocarbons. However, in polar media such as water and alcohols, no clearcut evidence is available about the role of excited states. The primary excited states AB′ (i.e., H_2O') should be formed in the radiolysis of water. Experimentally, however, no evidence has been obtained for AB^* or AB′. The generally accepted primary species in the radiolysis of water [177] are, therefore, e_{aq}^- (hydrated electron), H, OH, H_2, H_2O_2, and H_3O^+, which correspond to the "primary" species in the physicochemical stage. This stage should be sharply distinguished from the physical stage or the very early stage at a time between 10^{-18} and 10^{-19} sec, just after the initial interaction of ionizing radiation and water.

In the radiolysis of liquid hydrocarbons, cyclohexane, a key compound, has been investigated most extensively [213]. Measured G values of excited cyclohexane, however, still range widely, from 0.3 to 1.7, although physicochemical features of this species (e.g., its optical emission, absorption spectrum, and lifetime) have been greatly clarified [179]. The roles of excited states and their G values in the radiolysis of liquid hydrocarbons have been investigated by measuring the effect of the addition of scavengers for electrons, positive ions, and free radicals [183].

An example is shown in Table 8.6 for liquid cyclohexane [213], where H, H′, and H_2 denote thermal hydrogen atoms, hot hydrogen atoms, and hydrogen formed

TABLE 8.6. HYDROGEN FORMATION IN THE RADIOLYSIS OF LIQUID CYCLOHEXANE [213]

Reactant(s)		**Product(s)***		**Yield G (100 eV)$^{-1}$**
Direct ionization and excitation				
C_6H_{12}	$\longrightarrow$	H		0.57
	$\longrightarrow$	H′ and H_2		1.20
			Sum	1.77
Neutralization				
$C_6H_{12}^+ + e^-$	$\longrightarrow$	H		0.89
	$\longrightarrow$	H′ and H_2		3.01
			Sum	3.90
			Total G(H_2)	5.67

* H, H′, and H_2 denote thermal hydrogen atoms, hot hydrogen atoms, and hydrogen formed by molecular detachment, respectively.

by molecular detachment, respectively. The yields of excited states and ions can be inferred from the measured yields of hydrogen. Product hydrogen is formed by bimolecular processes (hydrogen abstraction from C_6H_{12} by H and H′) and by unimolecular processes (molecular detachment of H_2 from $C_6H_{12}^+$, C_6H_{12}', or $C_6H_{12}^*$). A fraction, 10-20%, of the total $G(H_2)$ is attributable to the molecular detachment as determined in experiments with C_6H_{12} and C_6D_{12}. Furthermore, the C-C bond scission is almost negligible compared with the C-H bond scission in the radiolysis of liquid cyclohexane [178]. Consequently, the total hydrogen yield of 5.67 given in Table 8.6 corresponds approximately to the sum of the yields of ions and excited states as precursors of H, H′, and H_2 [183]. The G value of 1.77 almost exclusively represents the yield of direct excitation, although it may include a minor contribution from direct ionization. More precisely, the value 1.77 corresponds to the yields of relatively highly excited states, including superexcited states. The G value of 3.90, which represents the yield of electrons that eventually undergo geminate recombination, is comparable to the ionization yield in gaseous cyclohexane. Excited states resulting from geminate recombination are believed to be generally low lying. Analyses of luminescence and related phenomena such as intermolecular energy transfer lead to G values for "excited states" of 0.3 - 1.7. These excited states are singlet states, the most important of which is the lowest singlet state.

8.6.2.2. Summary of Monte Carlo Calculations for Liquid Water

Several groups of authors have calculated yields of ions and excited states for electrons in liquid water by performing Monte Carlo calculations. Collective excitation effects have been included as the current understanding permits. Ritchie and co-workers at Oak Ridge National Laboratory in collaboration with Paretzke [39-42], Terrissol and co-workers at Centre de Physique Atomique, University of Toulouse [43, 44], and Kaplan and co-workers at the Karpov Institute of Physical Chemistry [45-49] made significant contributions to the field. Table 8.7 summarizes some salient results of the MC calculations. (The symbol g_i represents the number of all ions, and the symbol g_{ex} the number of all excited states, produced as *initial species* per 100 eV of absorbed energy). As we stated in Section 8.1, the initial species are products immediately resulting from the degradation of electrons and other energetic particles. The yield of initial species is a major result of particle transport calculations, either by Monte Carlo methods or by analytic methods. However, measurements in condensed phases seldom lead to the determination of the yields of initial species, because the initial species are often rapidly converted into other species, as we indicated in Section 8.6.2. To show the distribution between the initial species and measurable products, Platzman [214] proposed to use the symbols g_i and g_{ex} for the initial species and to reserve the symbol G for measurable products.

Returning to Table 8.7, we see general agreement in the results for water vapor. However, results for liquid water are quite different among the groups. According to Paretzke et al. [42], the ratio g_i/g_{ex} hardly changes between vapor and liquid water. However, in the calculation by Kaplan et al. [49], the ratio g_i/g_{ex} in the condensed phase is twice that in the gas phase. Similar result is obtained by Terrissol et al. [43]. The main reason for this result is a sizable decrease (3.8 eV) in the ionization potential and a shift of the excitation spectrum to higher energies for the liquid phase. Furthermore, for 10^{-16} s the collective plasmon-type state decays and

TABLE 8.7. SOME RESULTS OF MONTE CARLO CALCULATIONS ON WATER VAPOR AND LIQUID

	VAPOR		LIQUID			
Quantity*	Kaplan et al. [45]	Paretzke et al. [42]	Kaplan et al [49] *Primary yield*	Kaplan et al [49] *Account of plasmon decay*	Paretzke et al. [42]	Terrissol et al. [43]
g_i	3.39	3.3	4.52	6.04	3.88	4.02
g_{ex}	3.82	3.03	2.28	1.43	3.6	2.05
g_i/g_{ex}	0.89	1.1	2	4.22	1.08	1.96
W(eV)	29.5	30.5	22.12	16.6	25.8	

* Symbols: g_i represents the number of all ions; g_{ex} represents the number of all *excited states*, produced as initial species per 100 eV of absorbed energy.

creates an electron with energy 21.4 - 8.76 = 12.64 eV, additionally ionizing the medium and increasing the ratio g_i/g_{ex} to greater than 4, according to Kaplan et al. [49].

The yield of ionizations obtained by Paretzke et al. [42] is even lower than the experimental yield of hydrated electrons (g_{es} = 4.8 at 30 ps) reported by Sumiyoshi and Katayama [215]. According to the experiments by Jonah et al. [216], with acceptors the ionization yield equals g_i = 5.4. Nevertheless, this yield is a lower limit because we must account for the rapid geminate recombination of thermalized electrons with the parent ion, as seen in papers by Kaplan et al. [47] and Goulet et al. [217].

The different results obtained by the three groups illustrate that the topic belongs to the true frontier of current research. It is difficult to say with certainty how the discrepancies might eventually be resolved. The discrepancies may well be attributable to uncertainties in the input data used in the Monte Carlo calculations, especially for liquid water. Clearly, much work and many new ideas are needed to improve the input data both experimentally and theoretically.

Turner et al. [41] and Paretzke et al. [42] calculated statistical fluctuations (i.e., the Fano factors) in both the gaseous and liquid phases. Above 100 eV the F value for the liquid phase was only half of that for the vapor (Fig. 8.39).

Table 8.8. presents G values evaluated by Kaplan et al. [47]. All electronically excited states in liquid water except the first one have energies higher than the ionization potential I_1 = 8.76 eV and are superexcited states as discussed by Platzman [64, 65]. The decay of the superexcited states and the collective excitations results in ionization and also produces neutral excited states or *dissociation fragments.*

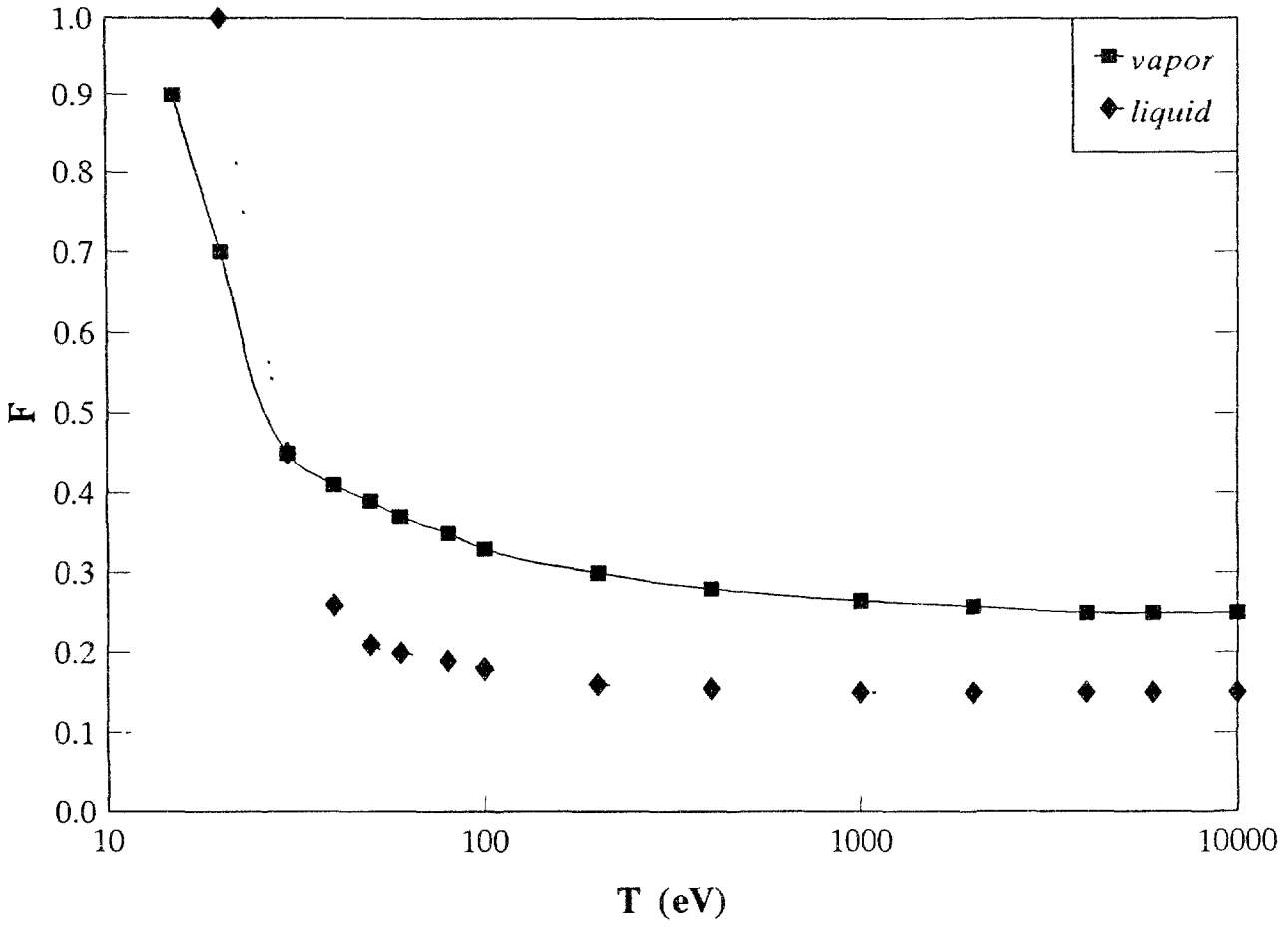

FIG. 8.39. The Fano factor F in water as a function of incident electron energy T. ■, water vapor; ♦, liquid water. Data are from Paretzke et al [42]

The competition between these decay modes is clearly an important item of study. Results so far reported on liquids are largely based on theoretical considerations rather than well established experimental data concerning the dynamics of the competition.

Excited states can be produced in another indirect way when fast electrons interact with medium. Excited water molecules result from the following geminate recombination:

$$H_2O^+ + e^- \rightarrow H_2O^{**} \qquad (8.37)$$

When we account for the energy spent on the reorganization of a medium, we obtain the value for the excited-state energy equal to 6.26 eV, which is lower than the energy of the first triplet and singlet electronically excited states of the water molecule. Thus, the water molecules produced by ion-electron recombination are in highly vibrationally excited states. The yields of these states are as large as 1.77, according to Kaplan et al. [47]. This value is compatible with the total yield of the excitations created as a result of direct interaction, $g_{ex}^{tot} = 2.3$.

In the condensed phase the vibrationally excited molecule has the following three possible decay channels:

$$H_2O_{vib}^{**} + H_2O \rightarrow \begin{cases} 2\ H_2O \\ H_2 + 2\ OH \\ H + OH + H_2O \end{cases} \qquad (8.36)$$

The last decay mode produces hot hydrogen atoms with high chemical reactivity.

TABLE 8.8. YIELD PER 100 eV OF ABSORBED ENERGY FOR ELECTRONICALLY EXCITED STATES PRODUCED BY INCIDENT ELECTRON WITH INITIAL ENERGY T_0 IN LIQUID WATER, ACCORDING TO KAPLAN et al. [47]*

State number	Excited state	Excitation energy (eV)	Oscillator strength	Yield at T_0 (keV)		
				1	5	10
1	$A^1 B^1$	8.4	0.018	0.042 0.535	0.017 0.542	0.013 0.545
2	$B^1 A^1$	10.1	0.039	0.046 0.256	0.023 0.258	0.020 0.256
3	Ry(A + B)	11.26	0.0089	0.008 0.039	0.048 0.038	0.0041 0.038
4	Ry(C + D)	11.93	0.0536	0.0442 0.187	0.022 0.191	0.0218 0.184
5	Diffusion bands	14.1	0.103	0.0627 0.209	0.035 0.202	0.033 0.200
6	Collective excitation	21.4	2.03	0.635 1.200	0 366 1.066	0.343 1.060
Total excitation yield				2.426	2.300	2.283

* The first line is related to the primary electron effect, and the second line includes the effect of the spectrum of ejected electrons.

8.6.2.3. G Values and Chemical Dosimetry

Chemical dosimetry means the determination of the radiation dose, i.e., the energy absorbed, through measurements of some chemical change induced in a material, most often in condensed matter. The G values for the chemical change monitored must be known in advance, because it enables one to convert the amount of the chemical change into the energy absorbed. The best known example is the Fricke dosimeter, which consists of an aqueous solution of ferrous sulfate and in which Fe^{2+} ions are converted to Fe^{3+} ions in a series of reactions that are well understood. The G value for the conversion is about 15.5 (per 100 eV absorbed), for a wide variety of radiations. Other examples are the ceric sulfate dosimeter, the hydrated-electron dosimeter, and the potassium dichromate dosimeter.

Full discussions of this topic can be found in ICRU Report 34 [218] and in Tabata [219].

8.6.3. Silicon, Germanium, and Other Solids

Only for semiconductors have measurements of ionization yields in solids been nearly as unequivocal in their physical meaning as for gases or rare gas liquids. When a semiconductor is subjected to ionizing radiation, one observes a current that is proportional to the electric field, and thus one attributes the current to charge carriers generated by radiation. This observation means that the recombination of the charge carriers takes a long time compared to the time necessary for the charge carriers to reach electrodes. In other words, measurements are operationally similar to the measurements of the W value in a gas.

The charge carriers are not free electrons like those found in a gas, but are the conduction electrons and holes discussed in the band theory of crystals [220].

TABLE 8.9. IONIZATION YIELDS IN SEMICONDUCTORS, EXPRESSED IN TERMS OF THE W VALUES AND RELATED QUANTITIES

Material	Temp (K)	E_g (eV)	W (eV)	W/E_g	F	Ref
Si	77	1.12	3.86	3.45	<0.1	222
	300		3.62 ± 0.02	3.23	<0.1	224
			3.68 ± 0.02	3.28		1
					0.13*	225
Ge	77	0.813	2.97 ± 0.02	3.65	<0.12	224
	90		2.95 ± 0.02	3.63	<0.12	227
	300		2.81	3.46	<0.107	226
					<0.08	222
					0.058	228

* the F value not extrapolated to infinite electric field strength

Thus, the band gap E_g, which we mentioned in connection with rare gas liquids in Section 8.6.1, plays the role of the ionization threshold I in a gas.

Table 8.9 summarizes values of the ionization yields and the Fano factor for silicon and germanium. The W values appear to be well established in the literature [1, 221]. W value in solid state is temperature dependent [1] and it also depends on the concentration of crystal imperfections [221]. Theoretical calculations [222, 224] show that the Fano factor should be less than 0.1 in Si, and close to 0.06 in Ge. Experimental F values are approaching theoretically calculated values as detectors and experimental techniques improve [222, 223]. The extrapolation to infinite electric field strength can result in large errors in experimental F values.

The mean energy required to form an electron-hole pair in mercuric iodide (HgI_2) is 4.2 eV, and the upper limit of the Fano factor determined at T = 253 K is 0.19 ± 0.03 [223].

REFERENCES

[1] INTERNATIONAL COMMISSION ON RADIATION UNITS AND MEASUREMENTS, Average Energy Required to Produce an Ion Pair, ICRU Report 31, Washington, DC (1979)

[2] LANDAU, L D, LIFSHITZ, E M, Statistical Physics, translated by SYKES, J B, KEARSLEY, M J, 2nd edn Pergamon Press, London, (1958)

[3] LIFSHITZ, E M, PITAEVSKII, L P, Physical Kinetics, translated by SYKES J B, FRANKLIN, R N, Pergamon Press, London (1981)

[4] JENKINS, T M, NELSON, W R, RINDI, A (Eds), Monte Carlo Transport of Electrons and Photons, Plenum Press, New York (1988)

[5] PARETZKE, H G, in Kinetics of Nonhomogeneous Processes, (FREEMAN, G R, Ed) John Wiley & Sons, New York (1984) 89-170

[6] FANO, U, Degradation and range straggling of high energy radiation, Phys Rev **92** (1953) 328-349

[7] SPENCER, L V, FANO, U, Energy spectrum resulting from electron slowing down, Phys Rev **93** (1954) 1172-1181

[8] McGINNES, R T, Energy spectrum resulting from electron slowing down, Nat Bur Stand Circular 597 (1959)

[9] DOUTHAT, D A, Electron degradation spectra in helium, Radiat Res **61** (1975) 1-20

[10] DOUTHAT, D A, Energy deposition by electrons and degradation spectra, Radiat Res **64** (1975) 141-152

[11] DOUTHAT, D A, Energy deposition and electron energy degradation in molecular hydrogen, J Phys B Atom Molec Phys **12** (1979) 663-678

[12] RAU, A R P, INOKUTI, M, DOUTHAT, D A, Variational treatment of electron degradation and yields of initial molecular species Phys Rev A **18** (1978) 971-988

[13] INOKUTI, M, DOUTHAT, D A RAU, A R P Statistical fluctuations in the ionization yield and their relation to the electron degradation spectrum, Phys Rev A **22** (1980) 445-453

[14] KOWARI K, KIMURA M, INOKUTI, M, Electron degradation and yields of initial products V Degradation spectra, the ionization yield, and the Fano factor for argon under electron irradiation, Phys Rev A **39** (1989) 5545-5553

[15] EGGARTER, E Theory of initial yields of ions generated by electrons in binary mixtures, J Chem Phys **84** (1986) 6123-6128

[16] INOKUTI M, EGGARTER E Theory of initial yields of ions generated by electrons in binary mixtures II J Chem Phys **86** (1987) 3870 3874

[17] KIMURA M INOKUTI M, Electron degradation and yields of initial products I Excited species generated by electrons in binary mixtures J Chem Phys **87** (1987) 3875-3879

[18] KIMURA, M, INOKUTI, M, KOWARI, K, Electron degradation and yields of initial products VI Energy spectra of subexcitation electrons in argon and molecular hydrogen, Phys Rev A **40** (1989) 2316-2320

[19] INOKUTI M KOWARI K Alternative forms of the Spencer-Fano equation, Phys Rev A **41** (1990) 5464-5467

[20] DILLON, M A, KIMURA, M, INOKUTI M, Time dependent aspects of electron degradation I Subexcitation electrons in helium or neon admixed with nitrogen, Radiat Phys Chem **32** (1988) 43 48

[21] INOKUTI, M, KIMURA M DILLON M A, Time-dependent aspects of electron degradation II General theory, Phys Rev A **38** (1988) 1217-1224

[22] INOKUTI, M, KIMURA, M, DILLON, M A, Time-dependent aspects of electron degradation III High-energy electrons incident on molecular hydrogen, Radiat Phys Chem **34** (1989) 477-480

[23] KIMURA, M, INOKUTI, M, KOWARI K, DILLON, M.A, PAGNAMENTA, A, Time-dependent aspects of electron degradation IV Subexcitation electrons in nitrogen and carbon dioxide, Radiat Phys Chem **34** (1989) 481-485

[24] KOWARI, K, INOKUTI, M, KIMURA, M, Time-dependent aspects of electron degradation V Ar-H_2 mixtures, Phys Rev A **42** (1990) 795-802

[25] KOWARI, K, KIMURA, M, INOKUTI, M, Electron degradation and yields of initial products II Subexcitation electrons in molecular nitrogen, J Chem Phys **89** (1988) 7229-7237

[26] PAGNAMENTA, A, KIMURA M, INOKUTI M, KOWARI, K, Electron degradation and yields of initial products III Dissociative attachment in carbon dioxide J Chem Phys **89** (1988) 6220-6225

[27] ISHII M A, KIMURA, M INOKUTI, M KOWARI, K, Electron degradation and yields of initial products IV Subexcitation electrons in molecular oxygen, J Chem Phys **90** (1989) 3081-3086

[28] ISHII, M A, KIMURA, M, INOKUTI M, Electron degradation and yields of initial products VII Subexcitation electrons in gaseous and solid H_2O, Phys Rev A **42** (1990) 6486-6496

[29] INOKUTI, M, "Subexcitation electrons in gases', Molecular Processes in Space, (WATANABE, T, SHIMAMURA, I, SHIMIZU, M, ITIKAWA, Y, Eds), Plenum Publishing, New York (1990) 65-86

[30] KIMURA, M, INOKUTI, M, Subexcitation electrons in molecular gases, Comments At Mol Phys **24** (1990) 269-286

[31] INOKUTI, M, Subexcitation electron An appraisal of our understanding, Appl Radiat Isotopes **42** (1991) 979-983

[32] FOWLER, R H, Contributions to the theory of the motion of α-particles through matter Part II Ionizations Proc Camb Philos Soc **21** (1923) 531-540

[33] FANO, U SPENCER L V Quasi-scaling of electron degradation spectra Int J Radiat Phys Chem 7 (1975) 63-67

[34] GROSSWENDT B WAIBEL, E, Transport of low energy electrons in nitrogen and air, Nucl Instr Meth **155** (1978) 145-156

[35] GROSSWENDT, B, Determination of statistical fluctuations in the ionization yield of low energetic electrons in hydrogen, Nucl Instr Meth **198** (1982) 403-409

[36] GROSSWENDT, B, Degradation spectra and statistical ionization yield fluctuations for low energy electrons in TE gas, (Proc Eighth Symp Microdosimetry, Luxembourg, 1982) (BOOZ, J, EBERT, H G, Eds), EUR 8385 EN Luxembourg (1983) 165-174

[37] GROSSWENDT, B Statistical fluctuations of the ionization yield of low-energy electrons in He, Ne, and Ar, J Phys B Atom Molec Phys **17** (1984) 1391-1404

[38] GROSSWENDT, B WAIBEL, E, Statistical ionization yield fluctuations and determination of spatial ionization and energy absorption for low energy electrons, Radiat Prot Dosim **13** (1985) 95-102

[39] PARETZKE, H G, BERGER, M J Stopping power and energy degradation for electrons in water vapor, (Proc Sixth Symp Microdosimetry, Brussels, Belgium, 1977) (BOOZ, J, EBERT, H G, Eds) EUR 6064, Harwood, London (1978) 749-758

[40] HAMM, R N, WRIGHT, H A, KATZ, R, TURNER, J E, RITCHIE, R H, Calculated yields and slowing-down spectra for electrons in liquid water Implications for electron and photon RBE, Phys Med Biol **23** (1978) 1149-1161

[41] TURNER, J E, PARETZKE, H G, HAMM, R N, WRIGHT, H A, RITCHIE, R H, Comparison of electron transport calculations for water in the liquid and vapor phases, (Proc Eighth Symp Microdosimetry, Luxembourg, 1983) (BOOZ, J, EBERT, H G, Eds), EUR 8395 EN, Luxembourg (1983) 175-185

[42] PARETZKE, H G, TURNER, J E, HAMM, R N, WRIGHT, H A RITCHIE, R H, Calculated yields and fluctuations for electron degradation in liquid water and water vapor, J Chem Phys **84** (1986) 3182

[43] TERRISSOL, M, BEAUDRE, A, Simulation of space and time evolution of radiolytic species induced by electrons in liquid water, Radiat Prot Dosim **31** (1990) 171-175

[44] MALBERT, M, CAREL C, PATAU J P TERRISSOL, M, Transport des protons de basse energie et de leurs electrons secondaries dans l'eau, (Proc Seventh Microdosimetry Symp, Oxford, U K, 1980) (BOOZ, J, EBERT, H G, HARTFIEL, H D, Eds), Harwood Academic Publishers, Brussels (1981) 359-374

[45] KAPLAN, I G, MITEREV, A M, SUKHONOSOV, V YA, Comparative study of yields of primary products in tracks of fast electrons in liquid water and in water vapor, Radiat Phys Chem **27** (1986) 83-90

[46] KAPLAN, I G, MITEREV, A M, Interaction of charged particles with molecular medium and track effects in radiation chemistry, Adv Chem Phys **68** (1987) 255-386

[47] KAPLAN, I G, MITEREV, A M, SUKHONOSOV, V YA, Simulation of the primary stage of liquid water radiolysis, Radiat Phys Chem **36** (1990) 493-498

[48] KAPLAN, I G, 'Computer experiment and radiation data for liquid water and water vapor irradiated by fast electrons', Atomic and Molecular Data for Radiotherapy, IAEA-TECDOC-**506**, IAEA, Vienna (1989) 80-91

[49] KAPLAN, I G, SUKHONOSOV, V YA, Simulation of the passage of fast electrons and the early stage of water radiolysis by the Monte Carlo method, Radiat Res **127** (1991) 1-10

[50] WAIBEL, E, GROSSWENDT, B, Spatial energy dissipation profiles W values, backscatter coefficients, and ranges for low-energy electrons in methane, Nuclear Instr Meth **211** (1983) 487-498

[51] WAIBEL, E, GROSSWENDT, B, Study of W values, practical ranges, and energy dissipation profiles of low-energy electrons in N_2, (Proc Eighth Symp Microdosimetry, Luxembourg, 1983) (BOOZ, J, EBERT, H G, Eds), Commission of the European Communities, Luxembourg, EUR 8395, Luxembourg (1983) 301-310

[52] WAIBEL, E, GROSSWENDT, B, Degradation of low-energy electrons in carbon dioxide Energy loss and ionization, Nucl Instr Meth B **53** (1991) 239-250

[53] WAIBEL, E, GROSSWENDT, B, W values and other transport data on low-energy electrons in tissue-equivalent gas, Phys Med Biol **37** No 5 (1992) 1127-1145

[54] INOKUTI, M, Ionization yields in gases under electron irradiation, Radiat Res **64** (1975) 6-22

[55] SRDOČ, D, Dependence of the energy per ion pair on the photon energy below 6 keV in various gases, Nucl Instr Meth **108** (1973) 327-332

[56] SRDOČ, D, OBELIĆ, B, Measurement of W at very low photon energy, (Proc Fifth Symp Microdosimetry, Verbania Pallanza, Italy, 1975), (BOOZ, J, EBERT, H G, SMITH, B G R, eds) EUR 5452 d-e-f, Luxembourg (1976) 1007-1021

[57] SAMSON, J A R, HADDAD, G N, Average energy loss per ion pair formation by photon and electron impact on xenon between threshold and 90 eV, Radiat Res **66** (1976) 1-10

[58] GERBES, W, Uber die Ionizierungswirkung von Kathodenstrahlen in Luft, Ann Phys **23** (1935) 648-656

[59] COLE, A, Absorption of 20-eV to 50,000-eV electron beams in air and plastic, Radiat Res **38** (1969) 7-33

[60] SMITH, B G R, BOOZ, J, Experimental results on W-values and transmission of low-energy electrons in gases, (Proc Sixth Symp Microdosimetry, Brussels, Belgium, 1977) (BOOZ, J, EBERT, H G Eds) EUR 6064 Harwood, London (1978) 759-775

[61] COMBECHER, D, Measurements of W values of low-energy electrons in several gases, Radiat Res **84** (1980) 189-218

[62] WAIBEL, E, GROSSWENDT, B, Determination of W values and backscatter coefficients for slow electrons in air, Radiat Res **76** (1978) 241-249

[63] PLATZMAN, R L, Total ionization in gases by high-energy particles An appraisal of our understanding, Int J Appl Radiat Isot **10** (1961) 116-127

[64] PLATZMAN, R L, Superexcited states of molecules, Radiat Res **17** (1962) 419-425

[65] PLATZMAN, R L, Probabilite d'ionisation par transfert d'energie d'atomes excites à des molecules, J Physique Radium **21** (1960) 853-858

[66] ALKHAZOV, G D, Ionization cascade in helium caused by nonrelativistic electrons, Zh Tekh Fiz **41** (1972) 2513-2523, Engl Transl Sov Phys - Techn Phys **16** (1972) 1995-2002

[67] KIMURA, M, KOWARI, K, INOKUTI, M, KRAJCAR-BRONIC, I, SRDOČ, D, OBELIĆ, B, Theoretical study of W values in hydrocarbon gases, Radiat Res **125** (1991) 237-242

[68] INTERNATIONAL COMMISSION ON RADIATION UNITS AND MEASUREMENTS, Determination of Absorbed Dose in a Patient Irradiated by Beams of X or Gamma Rays in Radiotherapy Procedures, ICRU Report 24 Washington, DC (1976)

[69] INTERNATIONAL COMMISSION ON RADIATION UNITS AND MEASUREMENTS, Basic Aspects of High Energy Particle Interactions and Radiation Dosimetry, ICRU Report 28, Washington, DC (1978)

[70] WAMBERSIE, A, VAN DAM, J, HANKS G, MIJNHEER, B J, BATTERMAN, J J, "Need for improving the accuracy in dose delivery in radio - and neutron therapy Importance of atomic and molecular data", Atomic and Molecular Data for Radiotherapy, IAEA-TECDOC-506, IAEA, Vienna (1989) 51-72

[71] ROSSI, H H, ROSENZWEIG W, A device for the measurement of dose as a function of specific ionization, Radiology **64** (1955) 404-410

[72] SRDOČ, D, Experimental technique of measurement of microscopic energy distribution in irradiated matter using Rossi counters, Radiat Res **43** (1970) 302-319

[73] JESSE, W P, SADAUSKIS, J, α-particle ionization in mixtures of noble gases, Phys Rev **88** (1952) 417-418

[74] JESSE, W P., SADAUSKIS, J, α-particle ionization in pure gases and average energy to make ion pair, Phys Rev **90** (1953) 1120-1121.

[75] JESSE, W P, SADAUSKIS, J, Ionization in pure gases and average energy to make ion pair for α and ß radiation, Phys Rev **97** (1955) 1668-1670

[76] JESSE, W P., SADAUSKIS, J, Ionization by alpha particles in mixtures of gases, Phys. Rev **100** (1955) 1755-1762

[77] WAIBEL, E, "Experimentally determined W values, stopping powers and ranges of low-energy protons and electrons in gases Methods and problems", Atomic and Molecular Data for Radiotherapy, IAEA-TECDOC-506, IAEA, Vienna (1989) 136-150

[78] SRDOČ, D, The W-value for electrons and photons in tissue-equivalent gas, Annual Report on Research Project COO-4733-2, Columbia University, New York (1979) 37-50

[79] BREYER, B, Pulse height distribution in low energy proportional counter measurements, Nucl Instr Meth **112** (1973) 91-93

[80] OBELIĆ, B, Probability density distribution of primary ionization calculated by means of an iterative deconvolution process, Nucl Instr Meth A **241** (1985) 515-518

[81] SRDOČ, D, OBELIĆ, B, KRAJCAR-BRONIĆ, I, Statistical fluctuations in the ionization yield for low-energy photons absorbed in polyatomic gases, J Phys B Atom Molec Phys **20** (1987) 4473-4484

[82] KRAJCAR-BRONIĆ, I, SRDOČ, D, OBELIĆ, B, The mean energy required to form an ion pair for low-energy photons and electrons in polyatomic gases, Radiat Res **115** (1988) 213-222

[83] KRAJCAR-BRONIĆ, I, SRDOČ, D, OBELIĆ, B, The W values for photons and electrons in mixtures of argon and alkanes, Radiat Res **125** (1991) 1-5

[84] KRAJCAR-BRONIĆ, I, SRDOČ, D, A comparison of calculated and measured W values in tissue equivalent gas mixtures, Radiat Res **137** (1994) 10-24

[85] SRDOC, D, Measurement of the Fano factor in tissue-equivalent and other gases, Annual Report on Research Project COO-4733-2, Columbia University, New York (1979) 58-63

[86] SRDOC, D CLARK, B Generation and spectroscopy of ultrasoft x-rays by non-dispersive methods Nucl Instr Meth **78** (1970) 305-313

[87] BOERSCH H, Experimentalle Bestimmung der Energieverteilung in thermisch ausgelosten Elektronenstrahlen Z Physik **139** (1954) 115-146

[88] FORST G, Uber die Energieverteilung der Ionen aus einer Hochfrequenz-Ionenquelle, Z Physik **159** (1960) 7-18

[89] WAIBEL, E, WILLEMS, G, W values for low-energy protons in methane-based tissue-equivalent gas and its constituents, Phys Med Biol **37** (1992) 249-259

[90] THOMAS, D J, BURKE, M W values measurements for protons in tissue-equivalent gas and its constituent gases, Phys Med Biol **30** (1985) 1201-1213

[91] BAKKER, C J, SEGRE, E, Stopping power and energy loss for ion pair production for 340-MeV protons, Phys Rev **81** (1951) 489 492

[92] PETTI, P L, VERHEY, L, WILSON, R, A measurement of w for 150 MeV protons in nitrogen and argon, Phys Med Biol **31** (1986) 1129-1138

[93] RADEKA, V, Low-noise techniques in detectors, Ann Rev Nucl Part Sci **38** (1988) 217-277.

[94] WAIBEL, E, GROSSWENDT, B, Zur Technik der Bestimmung von W-Werten in Gasen, PTB-Mitteilungen **87** (1977) 13-21

[95] SRDOČ, D, SLIEPČEVIĆ, A, Carbon dioxide proportional counter, effects of gaseous impurities and gas purification method, J Appl Rad **14** (1963) 481-488

[96] HATANO, Y, 'Electron attachment to van der Waals molecules', Electronic and Atomic Collisions, (LORENTS, D C, MEYERHOF, W E, PETERSON, J R, Eds) Elsevier, Amsterdam (1986), 153-173

[97] TUNG, C J, BAUM, J W, Ionization yields in hydrocarbons under electron irradiation, Radiat Res **119** (1989) 413-423

[98] UNNIKRISHNAN, K, PRASAD, M A, Energy deposition by electrons in argon, Radiat Res **80** (1979) 225-232

[99] HIRAOKA, T, KAWASHIMA, K, HOSHINO, K, FUKUMURA, A, Estimation of w-values for particle beams in several gases, Jpn Radiol Phys **9** (1989) 143-152 (in Japanese, with abstract figure captions, and tables in English, an updated English translation can be obtained from the first author)

[100] KIMURA, M, KRAJCAR-BRONIC, I, DILLON, M A, INOKUTI, M, Electron degradation and yields of initial products X The Fano factor for mixtures of argon and molecular hydrogen, Phys Rev A **45** No 11 (1992) 7831-7837

[101] OLKO, P, BOOZ, J, PARETZKE, H G, WILSON, W E, 'Energy deposition in the nanometer sites based on the track structure calculations", Atomic and Molecular Data for Radiotherapy, IAEA-TECDOC-**506**, IAEA, Vienna (1989) 105-116

[102] MARSHALL, M, STONELL, G P, HOLT, P D Ionization distributions from proton and other tracks in water vapour, Radiat Prot Dosim **13** (1985) 41-44

[103] NIATEL, M T, PERROCHE-ROUX, A M, BOUTILLON, M, Two determinations of W for electrons in dry air, Phys Med Biol **30** (1985) 67-75

[104] BOUTILLON, M, PERROCHE-ROUX A M Re-evaluation of the W value for electrons in dry air, Phys Med Biol **32** (1987) 213 219

[105] KUNZE, R, HECKER O, Determination of the mean expended energy W_L for the formation of an ion pair in air for cobalt 60 gamma radiation, Isotopenpraxis **16** (1980) 325-327

[106] SUZUKI, I H, SAITO, N, Effects of inner-shell excitation on the W-value of propane, Bull Chem Soc Jpn **58** (1985) 3210-3214

[107] SAITO, N, SUZUKI, I H, Fine structure near the C-K edge in the photon W value of methane, Chem Phys **108** (1986) 327-333

[108] THOMAS, D J, BURKE, M, Measurement of W values for protons in an A-150 plastic-equivalent gas and in argon, Phys Med Biol **32** (1987) 1119-1126

[109] CHEMTOB, M, PARMENTIER, N, NGUYEN, V D, Some experimental results on W values for heavy particles, Phys Med Biol **23** (1978) 1197-1199

[110] LOWRY, R A, MILLER, G H, Ionization yield of protons in nitrogen and argon, Phys Rev **109** (1958) 826-831

[111] LARSON, H V, Energy loss per ion pair for protons in various gases, Phys Rev **112** (1958) 1927-1928

[112] PHIPPS, J A, BORING, J W, LOWRY, R A, Total ionization in argon by heavy ions of energies 8 to 100 keV, Phys Rev **135** (1964) A36-A39

[113] PARKS, J E, HURST, G S, STEWART, T E, WEIDNER, H L, Ionization of the noble gases by protons Jesse effects as a function of pressure, J Chem Phys **57** (1972) 5467-5474

[114] HUBER, R, COMBECHER, D, BURGER, G, Measurement of average energy required to produce an ion pair (W value) for low-energy ions in several gases, Radiat Res **101** (1985) 237-251

[115] BORING, J W, STROHL, G E, WOODS, F R, Total ionization in nitrogen by heavy ions of energies 25 to 50 keV, Phys Rev 140 (1965) A1065-A1069

[116] NGUYEN, V D, CHEMTOB, M CHARY, J, POSNY F, PARMENTIER, N, Recent experimental results on W values for heavy particles, Phys Med Biol **25** (1980) 509-518

[117] SIDENIUS, G, The total ionization of low energy ions in a tissue equivalent gas and its component gases Absolute measurements, Rad Eff 39 (1978) 213-220

[118] SCHALLER, L, HUBER, P, BAUMGARTNER, E, Messung der Arbeit pro Ionenpaar in Stickstoff fur Protonen und He-Ionen im Energiegebiet unterhalb 1 MeV, Helv Phys Acta **36** (1963) 113-131

[119] KUEHN, H, WERBA, F, Measurements of the energy expenditure for the production of an ion pair in tissue equivalent gas for heavy particles, (Proc Third Symp Neutron Dosimetry in Biology and Medicine, Neuherberg/Munchen, 1977) EURATOM EUR 5848 DE/EN/FR, Luxembourg (1978) 85-95

[120] WAIBEL, E, WILLEMS G, Ionisation ranges and W values for low energy protons in tissue-equivalent gas, Radiat Prot Dosim **13** (1985) 79-81

[121] BICHSEL, H, INOKUTI, M, Calculation of the energy to form an ion pair for protons, Radiat Res **67** (1976) 613

[122] MacDONALD, J R, SIDENIUS, G, The total ionization in methane of ions with $1 < Z < 22$ at energies from 10 to 120 keV Phys Lett A **28** (1969) 543

[123] BORING J W, WOODS F R, The ionization of CO_2 C_2H_4, and C_2H_2 by low-energy heavy ions, Radiat Res **35** (1968) 472-478

[124] LEONARD B E, BORING J W, The average energy per ion pair, W, for hydrogen and oxygen ions in a tissue equivalent gas, Radiat Res **55** (1973) 1-9

[125] ROHRIG, N, COLVETT, R D, Measurements of W for protons, helium-4 ions, and carbon-12 ions in tissue-equivalent gas, Radiat Res **76** (1978) 225-240

[126] POSNY, F, CHARY, J, NGUYEN, V D, W values for heavy particles in propane and in TE gas, Phys Med Biol **32** (1987) 509-515

[127] WILLEMS, G, WAIBEL, E, HUBER, R, Energy range relation and W values for low-energy protons in air and methane, (Proc Eighth Symp Microdosimetry, Luxembourg 1982) (BOOZ, J EBERT, H G Eds) EUR 8395 EN, Commission of the European Communities Luxembourg (1983) 255-263

[128] WAIBEL, E, WILLEMS, G W values for low-energy protons in air, Phys Med Biol **37** (1992) 2319-2322

[129] KRIEGER, G L, BAUM, J W, VARMA, M N, BEACH, J L, Relative determination of W values for alpha particles in tissue-equivalent and other gases, Phys Med Biol **24** (1979) 286-298

[130] WHILLOCK, M, EDWARDS, A, Determination of W values for tissue-equivalent gas and constituents using alpha particles in the range 1 1-3 9 MeV, Phys Med Biol **28** (1983) 367-374

[131] THOMAS, D J, BURKE, M, W value measurements for ^{241}Am alpha particles in various gases, Phys Med Biol **30** (1985) 1215-1223

[132] TAWARA, H, ISHIDA, N, KIKUCHI, J, DOKE, T, Measurements of the W values in argon, nitrogen and methane for 0 93 to 5 3 MeV alpha particles, Nucl Instr Meth B **29** (1987) 447-455

[133] CHAPPELL, S E, SPARROW, J H, The average energy required to produce an ion pair in argon, nitrogen, and air for 1-to-5- MeV alpha particles, Radiat Res **32** (1967) 383-403

[134] VARMA, M N, BAUM, J W, Energy dependence on W for alpha particles in N_2, CO_2, CH_4, Ar, H_2 and Rossi-type tissue-equivalent gases, Phys Med Biol **23** (1978) 1162-1172

[135] JESSE, W P, Alpha particle ionization in polyatomic gases and the energy dependence of W, Phys Rev **122** (1961) 1195

[136] JESSE, W P, Alpha-particle ionization in argon-methane mixture and the energy dependence of the ion pair-formation energy, Phys Rev **174** (1968) 173-177

[137] SIMMONS, J A Comments on measurements of W values in tissue-equivalent gas for alpha particles, Phys Med Biol **31** (1986) 275-279

[138] WAKER, A J, W values in tissue-equivalent gas for alpha particles - 1972 revisited, Phys Med Biol **33** (1988) 984-987

[139] KEMMOCHI, M, Measurements of W values for alpha particles in tissue-equivalent gases, Health Phys **30** (1976) 439-446

[140] SCHIMMERLING, W, KAPLAN, S, SUBRAMANIAN, T S, McDONALD, W J, GABOR, G, SADOFF, A, ALPEN, E, Measurements of W for high energy heavy ions, (Proc Eighth Symp Microdosimetry Luxembourg, 1982) (BOOZ, J EBERT, H G, Eds), EUR 8395 EN, Luxembourg (1983) 311-321

[141] THOMAS, R H, LYMAN, J T, DE CASTRO, T M, A measurement of the average energy required to create an ion pair in nitrogen by high-energy ions, Radiat Res **82** (1980) 1-12

[141a] KANAI, T, KOHNO, T, MINOHARA, S, SUDOU, M, TAKADA, E, SOGA, F, KAWACHI, K, FUKUMURA, A, Dosimetry and measured differential W values of air for heavy ions, Radiat Res **135** (1993) 293-301

[142] SCHIMMERLING, W, 'Heavy ion dosimetry', Advances in Radiation Protection and Dosimetry in Medicine, (THOMAS R H, PEREZ-MENDEZ, V, Eds), Plenum Press, New York and London (1982)

[143] VARMA, N M, BAUM, J W, Dependence of the W-value on the atomic number of heavy ions", National and International Standardization of Radiation Dosimetry, IAEA-SM-222/02, IAEA, Vienna (1978) 65-71

[144] VARMA M N, BAUM J W, Stopping power and average energy to form an ion pair for 42 MeV oxygen ions, Phys Med Biol **27** (1982) 1449-1453

[144a] PFUTZNER, M, GEISSEL H, MUNZENBERG, G, NICKEL, F, SCHEIDENBERGER, Ch, SCHMIDT, K-H, SUMMERER, K, BROHM, T, VOSS, B, BICHSEL, H, Energy deposition by relativistic heavy ions in thin argon absorbers, Nucl Instr Meth B **xx** (1993) in press

[144b] BICHSEL, H, unpublished results

[145] STRICKLER, T D, Ionization by alpha particles in binary gas mixtures, J Phys Chem **67** (1963) 825-830

[146] HAEBERLI, W, HUBER, P, BALDINGER, E, Arbeit pro Ionpaar in Gasgemischen fur Alpha-Teilchen, Helv Phys Acta **23** (1950) 481-484

[147] HAEBERLI, W, HUBER, P, BALDINGER, E, Arbeit pro Ionenpaar von Gasen und Gasmischungen fur Alpha-Teilchen, Helv Phys Acta **26** (1953) 145-180

[148] BORTNER, T E, HURST, G S, Ionization of pure gases and mixtures of gases by 5-MeV alpha particle, Phys Rev **93** (1954) 1236-1241

[149] SWALLOW, A J, INOKUTI, M, Radiation-energy partition among mixture components Current ideas on an old question, Radiat Phys Chem **32** (1988) 185-189

[150] MELTON, C E, HURST, G S, BORTNER, T.E, Ionization produced by 5-MeV alpha particles in argon mixtures, Phys Rev **96** (1954) 643-645

[151] TAWARA, H, KIKUCHI, J, DOKE, T, Energy dependences of W values for MeV alpha particles in Ar-Xe, Ar-N_2, and Ar-CH_4 mixtures, Nucl Instr Meth B **29** (1987) 456-460

[152] JARVINEN, M-L SIPILA H, Average ionization energies of gas mixtures for X-rays, Nucl Instr Meth **217** (1983) 282-284

[153] UKAI, M, HATANO, Y, Collisional deexcitation of excited rare gas atoms in metastable and resonant states', Gaseous Electronics and Its Applications, (CROMPTON, R W, HAYASHI, M, BOYD, D E, MAKABE, Eds) Kluwer Academic Publ, Dordrecht (1991), 51-72

[154] FANO, U, Ionization yield of radiations II The fluctuations of the number of ions, Phys Rev **42** (1947) 26-29

[155] ALKHAZOV, G D, Ionization fluctuations in gases, Zh Tekh Fiz **41** (1971), Engl Transl Sov Phys - Tech Phys **16** (1972) 1540-1546

[156] ALKHAZOV, G D, VOROB'EV, A A, Total ionization and ionization fluctuations in helium, Phys Lett **29 A** (1969) 25-26

[157] ALKHAZOV, G D, KOMAR, A P, VOROB'EV, A A, Ionization fluctuations and resolution of ionization chambers and semiconductor detectors, Nucl Instr Meth **48** (1967) 1-12

[158] NEUMANN, W, The ultimate energy resolution of the proportional counter and the analysis of unresolved low energy spectra, (Proc Seventh Symp Microdosimetry, Oxford, UK, 1980) (BOOZ, J, EBERT, H G, HARTFIEL, H D, Eds) Harwood Academic Publishers Brussels (1981) 1067-1082

[159] ANDERSON D F HAMILTON T T, KU W H M, NOVICK, B, A large area, gas scintillation proportional counter, Nucl Instr Meth **163** (1979) 123-134

[160] RIBEIRETE, M M F POLICARPO A J P L, SALETE M, LEITE, S C P ALVES, M A F, DE LIMA E P Fano factors of krypton-xenon mixtures, Nucl Instr Meth **214** (1983) 561- 563

[161] POLICARPO, A J P L, ALVES, M A F, SALETE, M, LEITE, S C P, DOS SANTOS, M C M, Detection of soft X-rays with a xenon proportional scintillation counter, Nucl Instr Meth **118** (1974) 221-226

[162] DE LIMA, E P, SALETE M, LEITE, S C P, ALVES, M A F, POLICARPO, A J P L, Fano factors of rare gases and their mixtures, Nucl Instr Meth **192** (1982) 575-581

[163] LUKIRSKII, A P, ERSHOV, O A, BRYTOV I A, Operation of proportional counters in the ultrasoft X-ray region, Bull Acad Sci USSR, Phys Ser **27** (1963) 798-807

[164] BUDD, T, MARSHALL, M, KWOK, C S, Advances in cloud- chamber techniques and measurements of W value in a tissue-equivalent gas, Radiat Res **88** (1981) 228-239

[165] HURST, G S, PAYNE, M G, KRAMER, S D, YOUNG, J P, Resonance ionization spectroscopy and one-atom detection, Rev Mod Phys **51** (1979) 767-819

[166] KASE, M, AKIOKA, T, MAMYODA, H, KIKUCHI, J, DOKE, T, Fano factor in pure argon, Nucl Instr Meth **227** (1984) 311-317

[166a] MOE, H J, BORTNER, T E, HURST, G S, Ionization of acetylene mixtures and other mixtures by Pu-239 alpha-particles, Phys Rev **61** (1957) 422-425

[167] KASE, M, KIKUCHI, J, DOKE, T, Fano factor in gas mixture of Ar + 10% CH_4, Nucl Instr Meth **163** (1979) 289-291

[168] ISHIDA, N, KIKUCHI, J, DOKE, T, The W Values and Fano Factors in Helium and Argon-Doped Helium, Jpn J Appl Phys **31** (1992) 1465-1469

[169] VOROB'EV, A A, KOMAR, A P, KOROLEV, V A, Decrease of fluctuations of the ionization produced by alpha particles Soviet Phys-JETP **16** (1962) 306-307

[170] KRAJCAR-BRONIC I, KIMURA M INOKUTI M DILLON, M A The Fano factor for electrons in gas mixtures, Nucl Instr Meth B**71** (1992) 366-370

[171] KRAJCAR-BRONIC I, On a relation between the W value and the Fano factor, J Phys B Atom Mol Opt Phys **25** (1992) L215-L218

[172] INOKUTI, M, KOWARI, K, KIMURA, M, Statistical fluctuations in the yield of ionization due to protons or alpha particles, Phys Rev A **45** (1992) 4499-4506

[173] DOKE, T, ISHIDA, N, KASE, M, Fano factor in rare gases and their mixtures, Nucl Instr Meth Phys Res **B63** (1992) 373-376

[174] GOLD, R, An iterative unfolding method for response matrices, Argonne National Laboratory Report ANL-6984, Argonne, IL (1964)

[175] MARINO, S A, SRDOČ, D, Frequency distribution of number of electrons produced by low energy X-rays (Radiation Research Society Meeting, New Orleans, LA, 1980) Radiat Res **83** (1980) 492 (abstract).

[176] ARMSTRONG, D A, Radiation Chemistry, (FARHATAZIZ, RODGERS, M A J, Eds), VCH Publ, New York (1987) Ch 9

[177] BUXTON, ibid, Ch 10

[178] SWALLOW, ibid, Ch 11

[179] KATSUMURA, Y, Excited states in condensed media G-values of excited states", CRC-Handbook of Radiation Chemistry (TABATA Y, ITO, Y, TAGAWA, S, Eds), CRC Press, Boca Raton (1991) Ch IX B

[180] HATANO, Y, "Fundamental molecular parameters in the gas phase Fundamental processes in the gas-phase radiation chemistry', CRC-Handbook of Radiation Chemistry (TABATA, Y, ITO, Y, TAGAWA, S, Eds), CRC Press, Boca Raton (1991), Ch IV B

[181] HATANO, Y, Fundamental processes in radiolysis Collision dynamics data on some elementary processes', Atomic and Molecular Data for Radiotherapy, IAEA-TECDOC-**506**, IAEA, Vienna (1989) 200-214

[182] WILLIS, G, BOYD, A W, Excitation in the radiation chemistry of inorganic gases, Int J Radiat Phys Chem **8** (1976) 71-111

[183] HATANO, Y, "Method of studying radiation chemical processes" and 'Hydrogen atom", CRC-Handbook of Radiation Chemistry (TABATA, Y, ITO, Y, TAGAWA, S, Eds), CRC Press, Boca Raton (1991), Ch III A and X B

[184] ASMUS, K-D, WARMAN, J M, SCHULER, R H, The effect of electron, positive ion, and hydrogen atom scavengers on the yields of atomic and molecular hydrogen in the radiolysis of liquid cyclohexane, J Phys Chem **74** (1970) 246-257

[185] FREEMAN G R (Ed), Kinetics of Nonhomogeneous Processes, John Wiley & Sons, New York (1987)

[186] FERRANDINI, C, JAY-GERIN J-P (Eds), Excess Electrons in Dielectric Media, CRC Press, Boca Raton, Florida (1991)

[187] INOKUTI, M, How is the radiation energy absorption different between the gas phase and the condensed phase? Radiat Effects Defects in Solids **117** (1991) 143-162

[188] GRUHN, C R, LOVEMAN R, A review of the physical properties of liquid ionization chamber media, IEEE Trans Nucl Sci **NS-26** (1979) 110-119

[189] SIEGBAHN, K, KARLSSON, E, (Eds), Proc International Conference on Liquid Radiation Detectors Their Fundamental Properties and Applications, Tokyo, Japan, 1992, Nucl Instrum Meth A **327** (1992) 1-226

[190] MIYAJIMA, M, TAKAHASHI, T, KONNO, S, HAMADA, T, KUBOTA, S, SHIBAMURA, E, DOKE, T, Average energy expended per ion pair in liquid argon, Phys Rev A **9** (1974) 1438-1443

[191] TAKAHASHI, T, KONNO S, DOKE, T, The average energies, W, required to form an ion pair in liquified rare gases J Phys C 7 (1974) 230-240

[192] APRILE, E BOLOTNIKOV, A, CHEN, D, MUKHERJEE, R, Ionization of liquid krypton by electrons, gamma rays and alpha particles, Nucl Instr Meth in Phys Res A **327** (1993) 25-30

[192a] APRILE, E, BOLOTNIKOV, A, CHEN, D, MUKHERJEE, R, W value in liquid krypton, Phys Rev A **48** (1993) 1313-1318

[193] TAKAHASHI, T, KONNO, S, HAMADA, T, MIYAJIMA, M, KUBOTA, S, NAKAMOTO, A HITACHI A, SHIBAMURA, E, DOKE, T, Average energy expended per ion in liquid xenon, Phys Rev A **12** (1975) 1771-1775

[194] SEGUINOT, J PASSARDI, G, TISCHHAUSER J, YPSILANTIS, T, Liquid xenon ionization and scintillation Studies for a totally active-vector electromagnetic calorimeter, Nucl Instrum Meth in Phys Res A **323** (1992) 583-600

[195] DOKE, T, HITACHI, A, KUBOTA, S, NAKAMOTO, A, TAKAHASHI, T, Estimation of Fano factors in liquid argon, krypton, xenon and xenon-doped liquid argon Nucl Instr Meth **134** (1976) 353-357

[196] MIYAJIMA, M, MASUDA, K, HITACHI, A, DOKE, T, TAKAHASHI, T, KONNO, S, HAMADA, T, KUBOTA, S, NAKAMOTO, A, SHIBAMURA, E, Proportional counter filled with highly purified liquid xenon, Nucl Instr Meth **134** (1976) 403-405

[197] MIYAJIMA, M, MASUDA, K, HOSHI Y, DOKE, T, TAKAHASHI, T, HARADA, T, KUBOTA, S, NAKAMOTO, A, SHIBAMURA, E, A self-triggered liquid xenon drift chamber by use of proportional ionization or proportional scintillation, Nucl Instr Meth **160** (1979) 236-246

[198] MASUDA, K, TAKASU, A, DOKE, T, TAKAHASHI, T, NAKAMOTO, A, KUBOTA, S, SHIBAMURA, E, A liquid xenon proportional scintillation counter, Nucl Instr Meth **160** (1979) 247-253

[199] BARABASH, A S, GOLUBEV, A A, KAZACHENKO, O V, LOBASHEV, V.M, OVCHINNIKOV, B M, STERN, B E, A pulsed liquid ionization chamber filled with Xe, Ar and CH_4, Nucl Instr Meth A **236** (1985) 69-81

[200] APRILE, E, KU, W H-M, PARK, J, SCHWARTZ, H, Energy resolution studies of liquid argon ionization detectors, Nucl Instr Meth A **261** (1987) 519-526

[201] GIBONI, K L, Limited energy resolution in liquid argon due to δ-ray production Nucl Instr Meth A **269** (1988) 554-559

[202] ICHINOSE, H, DOKE, T, KIKUCHI, J HITACHI, A, MASUDA, K, SHIBAMURA, E, The response of a liquid Xe ionization chamber to 5 3 MeV α-particles, Nucl Instr Meth A **305** (1991) 111-115

[203] APRILE, E, MUKHERJEE, R, SUZUKI, M, Performance of a liquid xenon ionization chamber irradiated with electrons and gamma-rays Nucl Instr Meth in Phys Res A **302** (1991) 177-185

[204] DOKE, T A historical view on the R&D for liquid rare gas detectors, Nucl Instr Meth in Phys Res A **327** (1993) 113-118

[205] DOKE, T, CRAWFORD, H J, ENGELAGE, J M, FLORES, T, GREINER, L, KASHIWAGI, T, KIKUCHI J, MASUDA, K, NISHIJIMA, K, SHIBAMURA, E, SYMONS, T J M, Sampling calorimeter for high energy heavy particles filled with allene-doped liquid argon, Nucl Instrum Meth in Phys Res A **302** (1991) 290-300

[206] APRILE, E, KU, W H-M, PARK, J, Delta electron production and the ultimate energy resolution of liquid argon ionization detectors, IEEE Trans Nucl Sci **NS-35/1** (1988) 37-41

[207] KUBOTA, S, NAKAMOTO, A, TAKAHASHI, T, KONNO, S, HAMADA, T, MIYAJIMA, M, HITACHI, A, SHIBAMURA, E, DOKE, T, Evidence of the existence of exciton states in liquid argon and exciton-enhanced ionization from xenon doping, Phys Rev B **13** (1976) 1649-1653

[208] HUMMEL, A, SCHMIDT, W F, Ionization of dielectric liquids by high-energy radiation studied by means of electrical conductivity method, Radiat Res Rev **5** (1974) 199-297

[209] WARMAN, J M, in The Study of Fast Processes and Transient Species by Electron Pulse Radiolysis (BAXENDALE, P H BUSI F, Eds), D Reidel Publ, Dordrecht (1982) 433

[210] HOLROYD R A, in Radiation Chemistry, (FARHATAZIZ, RODGERS, M A J, Eds), VCH Publ, New York (1987) Ch 7

[211] HOLROYD, R A, SCHMIDT, W F, Transport of electrons in nonpolar fluids, Ann Rev Phys Chem **40** (1989) 439

[211a] HOLROYD, R A, SHAM, T K, YANG B-X, FENG, X-H, Free ion yields in liquids exposed to synchrotron X-rays, J Phys Chem **96** (1992) 7438-7441

[212] KLASSEN, N V, in Radiation Chemistry, (FARHATAZIZ, RODGERS, M A J, Eds), VCH Publ, New York (1987) Ch 2

[213] HATANO, Y, Hot hydrogen atoms in radiation chemistry, Hot Atom Chemistry (MATSUURA, T, Ed) Kodansha, Tokyo (1984) 98-119

[214] PLATZMAN, R L, Energy spectrum of primary activations in the action of ionizing radiation, in Radiation Research 1966, Proc Third International Congress of Radiation Research, Cortina d'Ampezzo, Italy (SILINI G, Ed) North-Holland Publishing Company, Amsterdam (1967) 20-42

[215] SUMIYOSHI, T, KATAYAMA, M, The yield of hydrated electrons at 30 picosecond, Chem Lett **12** (1982) 1887-1890

[216] JONAH, C D, MATHESON M S, MILLER, J R, HART, E J, Yield and decay of the hydrated electron from 100 ps to 3 ns, J Phys Chem **80** (1976) 1267-1270

[217] GOULET, T, PATAU, J-P, JAY-GERIN, J-P, Thermalisation and recombination of subexcitation electrons in solid water, Radiat Protect Dosim **31** (1990) 33-36

[218] INTERNATIONAL COMMISSION ON RADIATION UNITS AND MEASUREMENTS, The Dosimetry of Pulsed Radiation, ICRU Report **34** Bethesda, Maryland (1982)

[219] TABATA, Y, Radiation sources and dosimetry Radiation dosimetry', CRC Handbook of Radiation Chemistry (TABATA, Y, ITO, Y, TAGAWA, S, Eds), CRC Press, Boca Raton, Florida (1991), Ch II B

[220] KITTEL, C, Quantum Theory of Solids, John Wiley & Sons, New York (1963)

[221] BICHSEL, H, Straggling in thin silicon detectors, Rev Mod Phys **60** (1988) 663-699

[222] ZULLIGER, H R, AITKEN, D W, Fano factor fact and fallacy, IEEE Trans Nucl Sci **NS-17** (1970) 187-195

[223] RICKER, G R, VALLERGA, J V, DABROWSKI, A J, IWANCZYK, J S, ENTINE, G, New measurement of the Fano factor of mercuric iodide, Rev Sci Instrum **53** (1982) 700-701

[224] KLEIN, C A, Semiconductor particle detectors A reassessment of the Fano factor situation, IEEE Trans Nucl Sci **NS-15/3** (1968) 214-225

[225] STEINBAUER, E BAUER, P, GERETSCHLAGER, M, BORTELS, G, BIERSACK, J P, BURGER, P, Energy resolution of silicon detectors Approaching the physical limit, Nucl Instrum Meth B xx (1993) in press

[226] SHER, A H, KEERY, W J, Variation of the effective Fano factor in a Ge(Li) detector, IEEE Trans Nucl Sci **NS-17/1** (1970) 39-43

[227] DRUMMOND, W E, High purity germanium radiation detectors, IEEE Transaction on Nuclear Science, **NS-18/2** (1971) 91-100

[228] STROKAN, N, AJDAČIC, V, LALOVIĆ, B, Measurements of the Fano factor in germanium, Nucl Instr Meth **94** (1971) 147-149

Chapter 9

TRACK STRUCTURE QUANTITIES

H.G. Paretzke
GSF-Forschungszentrum für Strahlenschutz und Umweltforschung,
Neuherberg, Germany

D.T. Goodhead
Medical Research Council, Radiobiology Unit,
Chilton, United Kingdom

I.G. Kaplan
Istituti di Física, Universidad Nacional Autónoma de México,
Mexico City, Mexico

M. Terrissol
Centre de Physique Atomique, Université Paul Sabatier,
Toulouse, France

9.1. INTRODUCTION

For the analysis of radiation effects in matter, knowledge of radiation track structures is essential. The spatial distributions of species excited by the interaction of a radiation affects their reaction probabilities, which in turn govern the final changes in the micro- and macroscopic structures of the material. Examples of radiation track structures are shown in Figure 9.1. The species making up a track are ions, electrons, excited molecules, and molecular fragments (free radicals) that have lifetimes longer than, say, 10^{-10} s (1-3). These are the species that remain after the decay of plasmonlike excitations and super-excitations. The new species are the starting points of subsequent physical, chemical, and biological processes. They mark the end of the *physical stage* of radiation action and the beginning of the *chemical stage* (Figure 9.2). During the latter stage diffusion and reaction of primary species with other radiogenic species or with molecules of the irradiated object alter the pattern of the physical track structure. This occurs according to the boundary conditions set in the first stage.

Thus, it is the objective of track structure theory to:

(i) Identify the molecular changes of importance for the development of a radiation effect under consideration.

(ii) Predict and explain the spatial distribution of relevant species with a minimum of assumptions regarding preliminary processes (2); this spatial distribution should be given in terms of the joint probability to find an event of type S_1 at position x_1 and at the same time an event S_2 at position x_2 and S_3 at x_3, and so on, to account for spatial correlations for further reactions.

(iii) Identify (for example by correlation studies or modelling of subsequent processes) the parameters of physical track structure that predominantly determine the nature and magnitude of a final radiation effect and that may also be used to characterize a radiation field with regard to its radiation action when compared to other fields.

The theory that describes the generation of radiation tracks and their structure is still under development. Contributions have been made by Spencer (4), Fano (1-3), Berger (5), Boag (6,7), Platzman (8,9), Mozumder and Magee (10,11), Caswell (12,13), Voltz (14), Ritchie (15), Inokuti (16), Lea (17), Katz (18-20), Kaplan (21), Paretzke (22), Zerby (23) and others. Recent progress has been made with new simulation techniques on fast computers developed by Grosswendt *et al* (24,25), Hamm *et al* (26-29), Ito (30), Kaplan (31), Nelson *et al* (32), Paretzke (33,34), Terrissol (35), Uehara *et al* (36), Wilson and Toburen (37-40), Zaider and Brenner (41,42).

The importance of radiation track structure in biological effects was demonstrated already in 1946 (17). Applications of track structure theory include the interpretation of tracks in nuclear emulsions and other solid-state nuclear track detectors (18-20).

The first objective (i) depends on the radiation effect under consideration. Ionizations, dissociations, and the resulting ions, electrons, and radicals play a major role in further chemical or biological reactions. In this chapter emphasis is given to the second (ii) and third (iii) objectives, namely, to the prediction of track structures and their quantitative evaluation.

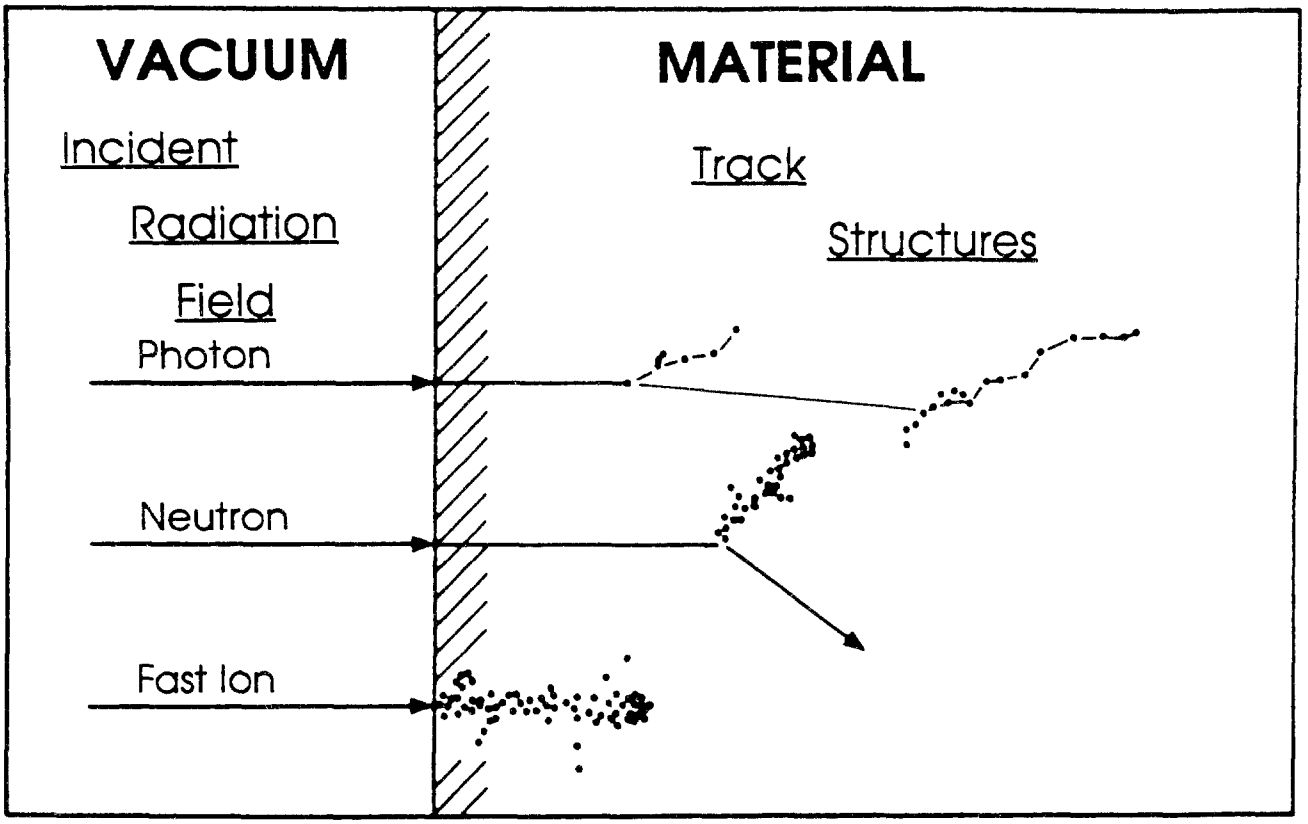

Figure 9.1 Incident radiations are characterized by particle mass, charge, and velocity; the stochastic structure of tracks resulting from interactions of these radiations with matter are described by track matrices $T(S, \mathbf{x}, t)$, where the S is the type of a new chemical species at location $\mathbf{x}$ at time t.

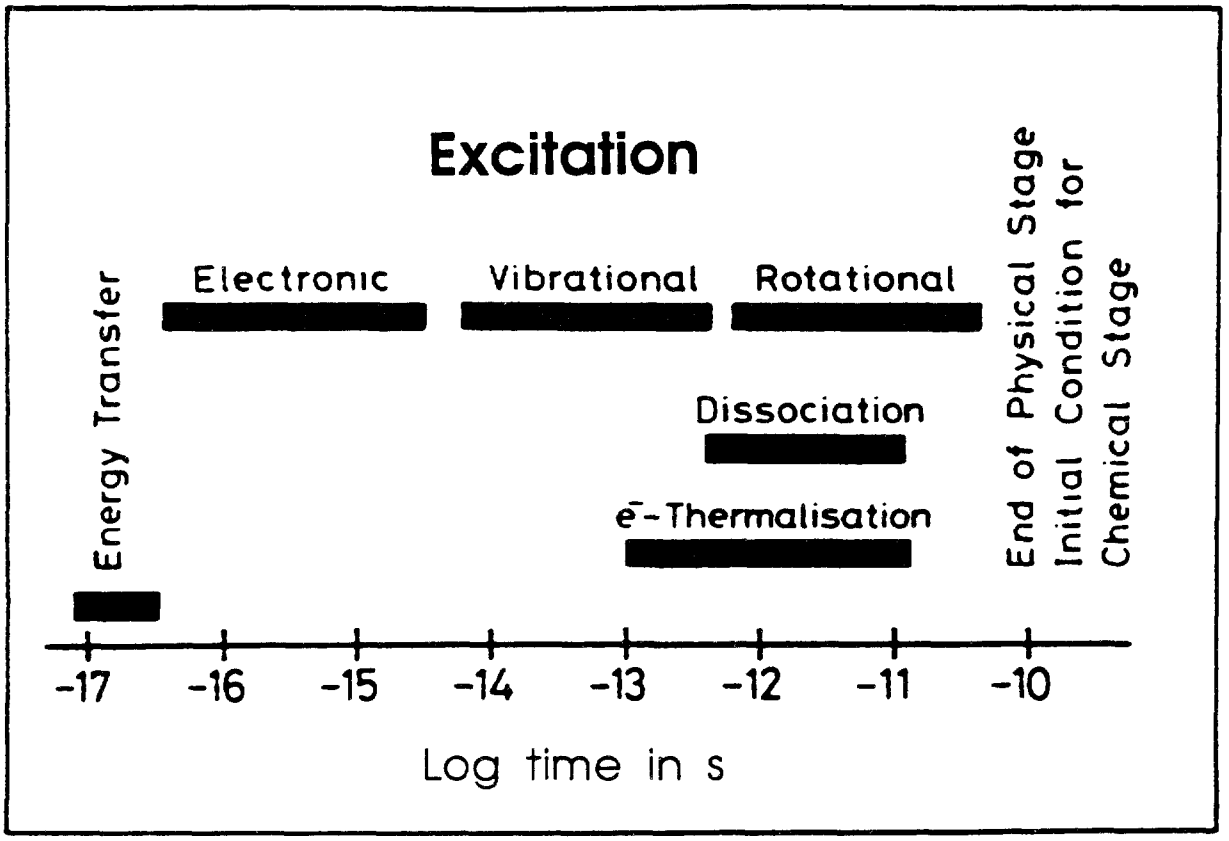

Figure 9.2 Time scale of processes occurring during the physical stage of energy transfer from ionizing radiations to molecules.

A survey of processes in which photons and neutrons transfer energy to matter is given in Sections 9.2.1 and 9.2.2. From this it is evident that electrons, in particular low-energy electrons, are the carriers that distribute most of the energy to the individual molecules in matter and thus create most of the track structures. The interactions of electrons are described in Section 9.2.3 and those of heavy charged particles in Section 9.2.4. With consistent sets of interaction cross sections, track structures can be simulated on a computer. Results of simulations for electrons, protons, α particles, and heavier ions in water vapor are described in Section 9.3. Section 9.4 outlines concepts for the quantitative evaluation of such stochastic structures for the purpose of characterization and classification.

9.2. INTERACTIONS IN TRACKS OF INDIRECTLY AND DIRECTLY IONIZING PARTICLES

9.2.1. Interactions of Photons

Photons play an important role in radiation research and in technical and medical applications of ionizing radiation. A photon normally imparts a large fraction of its energy to a single electron, which then ionizes many other molecules along its path. The track generated by a photon is therefore an electron track.

A photon of energy $h\nu$ might interact inelastically with a molecule in one of three ways (43-47):

(i) In a photoelectric process where the photon is completely absorbed and an electron is ejected with kinetic energy $E = h\nu - U$, where U is the binding energy of the electron in the molecule. This effect is dominant at low photon energies, below, say, 40 keV in materials with a small atomic number Z. It produces sharp energy spectra of photoelectrons that carry essentially all the photon energy, since the binding potential in low-Z matter is typically only about 500 eV. In addition, often Auger electrons or fluorescent photons are emitted from the target atom.

(ii) In an incoherent Compton-scattering event where only part of the photon's energy is transferred to an electron. This Compton electron is emitted from its parent atom; the scattered photon continues its flight in a new direction and with reduced energy according to the laws of energy and momentum conservation. In water and other low-Z materials this process is the most important energy loss mechanism for photons in the medium energy range from, say, 0.04 to 10 MeV. It leads to tracks of Compton electrons with a wide energy spectrum, from zero up to a substantial fraction of the primary photon energy $h\nu$.

(iii) In a pair production event, when, in the strong fields of the atomic nucleus and of the orbital electrons, the photon is transformed into an electron-positron pair. This process can only occur at photon energies above 1.02 MeV, which is the energy equivalent of the masses of an electron and positron with zero kinetic energy. The excess energy $h\nu$ - 1.02 MeV is shared as kinetic energy E^+ and E^- between the created positive and negative particles. Their energy spectrum is rather flat in the energy range from essentially zero up to E^+, $E^- = h\nu$ - 1.02 MeV. This interaction process must be taken into account only at high photon energies (above, say, 5 MeV), but it gains importance with increasing energy. For conventional X rays, ^{137}Cs γ rays (0.66 MeV) and ^{60}Co γ rays (1.17 and 1.33 MeV), pair production can be neglected.

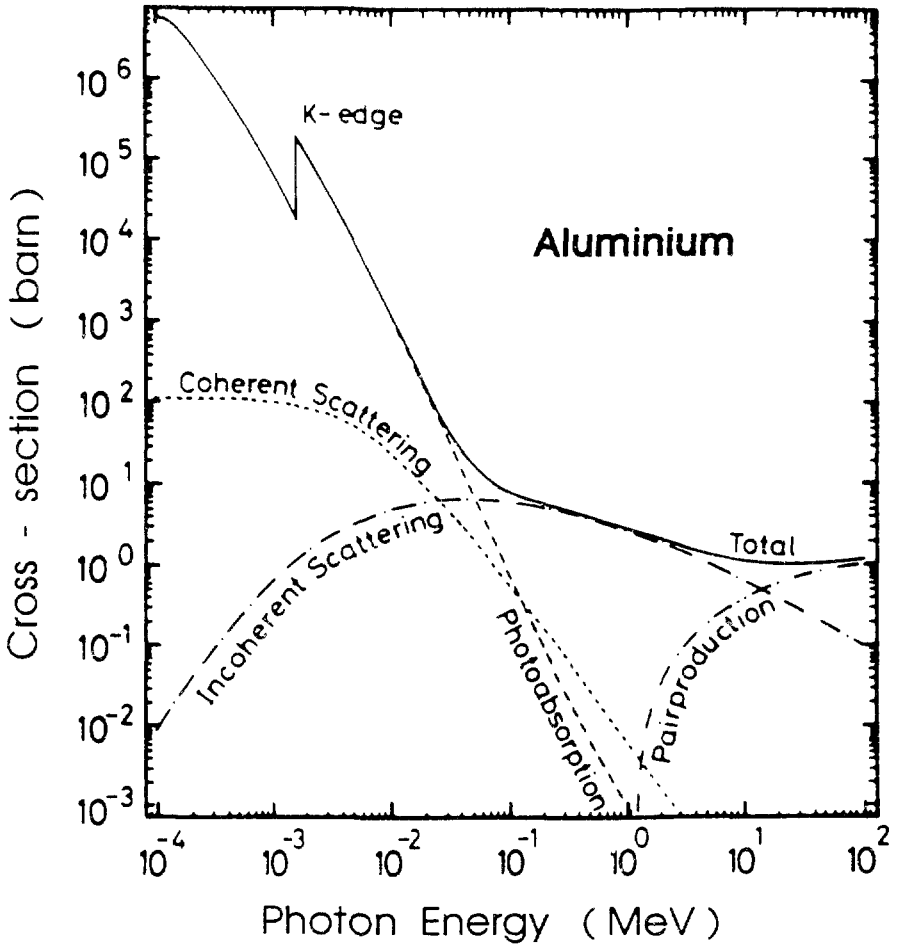

Figure 9.3 Cross sections (in barn/atom: 1 barn ≡ 10^{-28} m^2) for various types of interaction of photons with aluminium, a typical low-Z material (48).

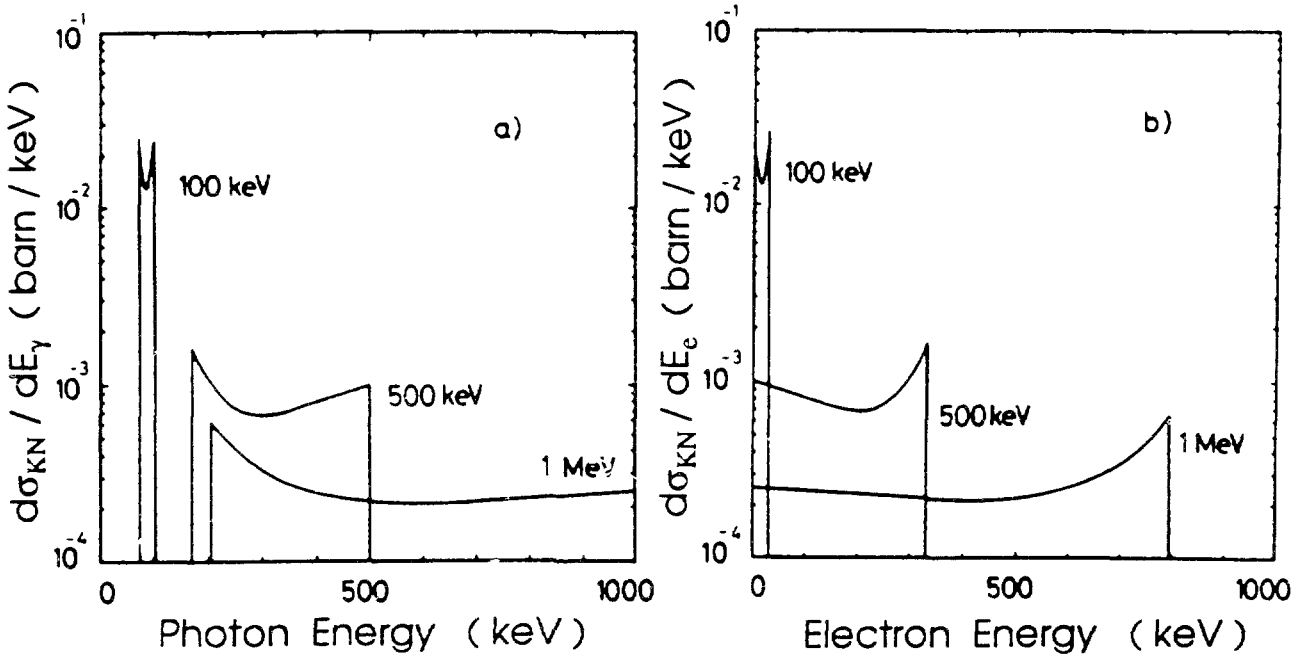

Figure 9.4 Scattered photon (*a*) and corresponding recoil electron (*b*) spectra (in barn/keV per electron) after Compton scattering of 0.1, 0.4, and 1 MeV incident photons. $d\sigma_{KN}/dE$ is evaluated by the Klein and Nishina formula (43,44).

Figure 9.3 shows cross sections for aluminium as an example of low-Z atoms. The strong absorption at low energies (say, below 40 keV) due to the photoeffect is evident, as is the importance of the Compton effect at medium to high energies and of pair production at very high energies.

The photoelectric cross section of an atom, between its resonant absorption edges, varies with the photon energy approximately as $(h\nu)^{-2.5}$ and increases approximately as the fourth to fifth power of the atomic number Z (see Chapter 5 for details). The Compton cross section of an electron, however, is almost independent of the atomic number, and it decreases only slightly with increasing photon energy. Thus, in heterogeneous objects made up by atoms of different Z, a variation in photon energy can lead to a significant change in the relative importance of interaction modes and of the locations of interactions.

The close correspondence between the photon energy after collision and Compton electron kinetic energy is visible in Figure 9.4, which shows the energy spectra of the scattered photons (a) and electrons (b) for photons with incident energy 0.1, 0.5, and 1 MeV.

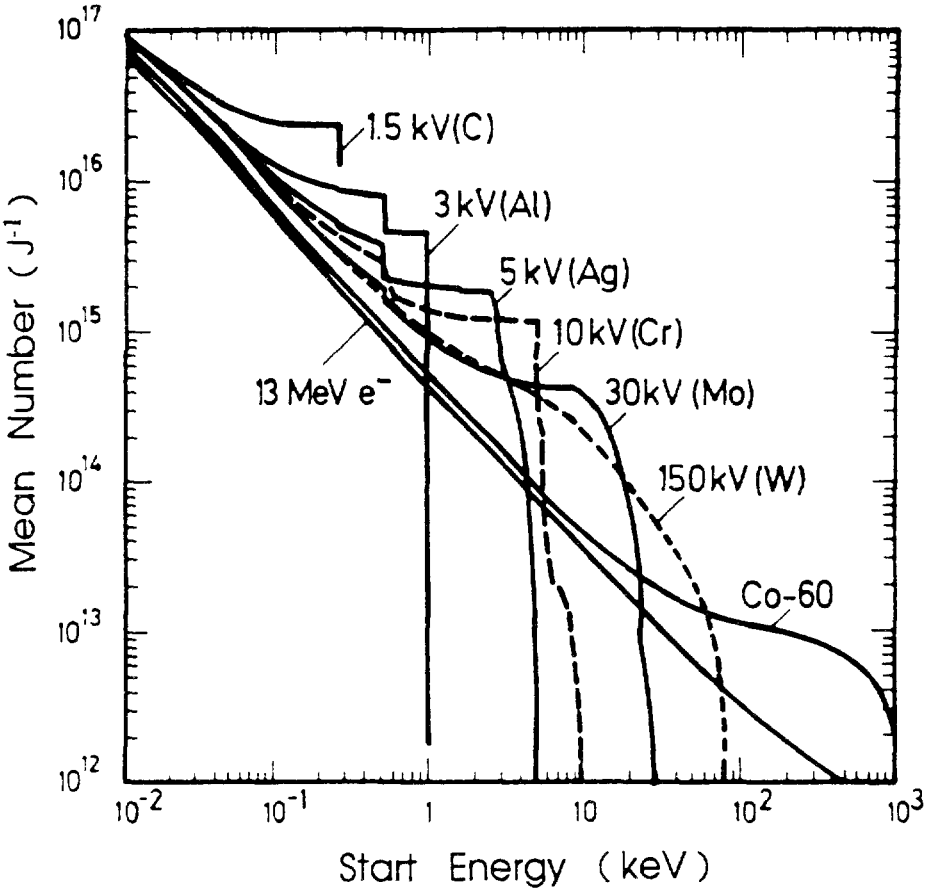

Figure 9.5 Mean number of electrons of all generations with initial energies larger than E produced by interaction of various radiation fields with water (normalized to an absorbed energy of 1 J); adapted from Ref. 49. Parameters give acceleration voltages and target materials of X-ray tubes.

Electrons set in motion by inelastic photon collisions in turn excite and ionize other molecules. Thus, the original electron can produce an avalanche of higher order generations of electrons with decreasing initial energies, which all contribute to the track formation. The number and energy spectra of the higher generation electrons depend on electron collision cross sections, which are discussed in Section 9.2.3.

Figure 9.5 shows such spectra for photon fields of widely different energies and for incident fast electrons (49). The interactions of electrons change the shapes of the initial Compton- and photo-effect start spectra.

Photon track structures, and thus their energy deposition, are mainly characterized by the start energies of the electrons ejected in inelastic photon collisions and by the distances between subsequent inelastic photon collisions.

The locations and types of energy transfers in inelastic photon events are determined by the respective cross sections of the three inelastic processes mentioned above (as well as inelastic scattering), which are governed by the photon energy and the atomic constitution of the irradiated medium. The lengths of the corresponding electron tracks are generally small (typically nanometers to millimeters in water), compared to the distance between subsequent photon collisions (typically centimeters). Thus the analysis of photon track structures can usually be reduced to the analysis of appropriate electron track structures.

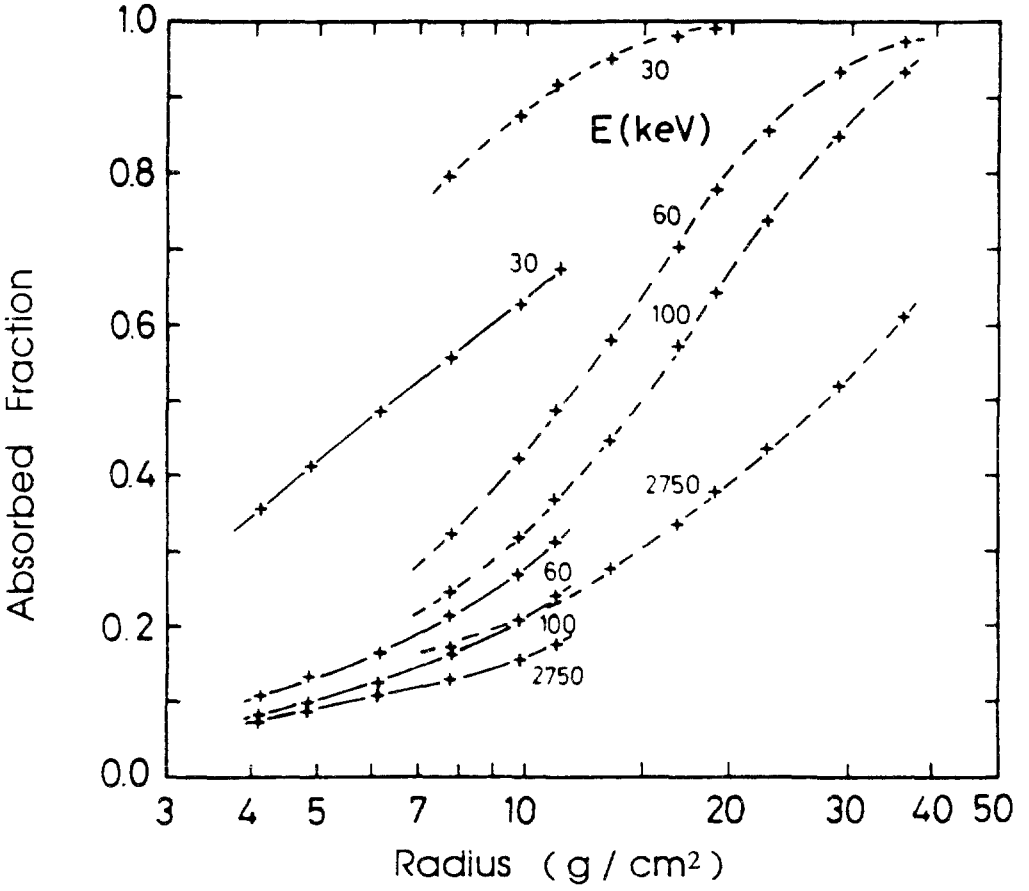

Figure 9.6 Absorbed fractions in spheres for isotropic point sources (-----) of photons of various energies and for uniformly distributed sources (——) as a function of the radius (50).

The low density of electron tracks in photon-irradiated matter and its dependence on photon energy can be estimated from Figure 9.6, which shows the fraction of photon energy absorbed within concentric spheres around photon point sources located in the center and for uniformly distributed sources (50). However, this low energy density in single-photon tracks leads to the complicating situation that, with increasing values of energy deposited in finite mass elements, many photons have interacted in that element. Thus, the spatial and temporal overlap of track structures of many secondary electrons and their physical and chemical consequences must be considered. They might lead to non-linearities in dose-effect relationships and to different effects of the same total dose if it is delivered at different dose rates or fractions.

9.2.2. Interactions of Neutrons

Whereas photons mainly interact with the electrons of molecules, ejecting electrons as charged secondary particles, neutrons collide with atomic nuclei, leading to recoil atomic ions and products of nuclear reactions as charged secondary particles. These reaction processes can be divided into elastic scattering (the most important interaction in this context) producing recoil ions, inelastic scattering (leading to an excitation of the struck nucleus and to a slower neutron), nonelastic scattering (ejecting another particle out of the hit nucleus), neutron capture processes (which are important for slow neutrons and lead to their disappearance), and spallation processes (breaking up the hit target nucleus and ejecting significant pieces of it, of importance at neutron energies above, say, 10 MeV) (44,51,52).

In hydrogen-containing media such as water and biological substances, the most important interaction is elastic scattering with hydrogen nuclei, accounting for typically more than 90% of the energy transferred. Hydrogen nuclei are protons. Neutron collisions produce a wide spectrum of recoil proton energies from zero to the neutron energy.

The contributions of the various neutron interaction processes to neutron track structures depends on the neutron energy and on the relative abundances of the elements in the irradiated object. Cross sections for elements can be found elsewhere (51,53-57). The abundance of hydrogen in an object is of great importance for neutron track structure because the cross sections for hydrogen are relatively high for neutron energies up to about 1 MeV.

As with photons, the kinetic energy of the charged secondary particles produced by the interactions of neutrons is of main importance in determining the track structure. From energy and momentum conservation in the hard-sphere approximation, it can be shown (43-46) that, to a good approximation, the energy spectrum of elastically recoiled nuclei is a rectangular distribution from zero to the maximum energy E_{max} that can be transferred from a neutron of energy E_n to a nucleus of mass A:

$$E_{max} \approx E_n \frac{4A}{(A+1)^2} \qquad (9.1)$$

This flat distribution is seen in the initial secondary particle spectra shown in Figure 9.7. The proton contribution around 1.5 MeV for 1-MeV neutrons stems from the (n, p) reaction in nitrogen. The structure in the spectra for 14-MeV neutrons is due to contributions from inelastic and nonelastic processes.

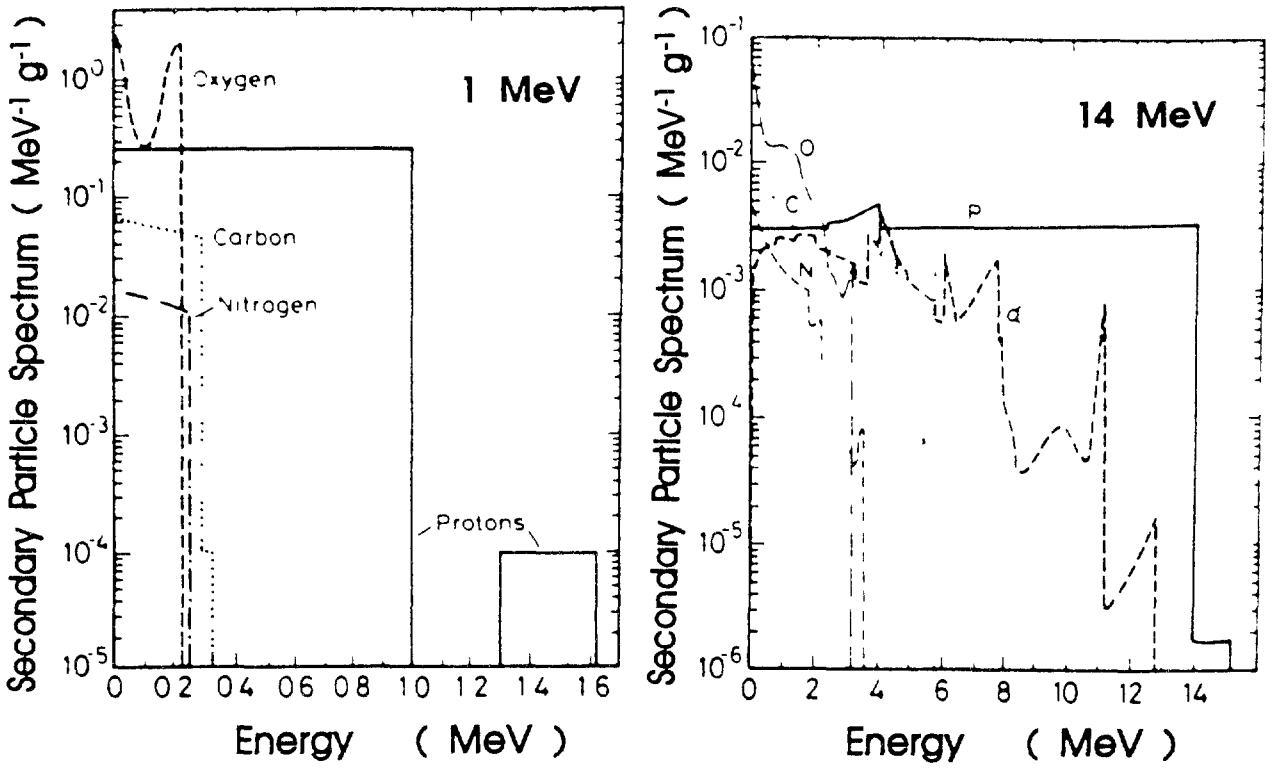

Figure 9.7 Secondary particle spectrum for 1- and 14-MeV neutrons (per 1 n/cm^2) in ICRU tissue (12,13).

The total and differential cross sections for neutron interactions generally are not as well known as those for photons; this holds particularly for neutron energies above 20 MeV that are of interest for radiation therapy. However, for low to medium-high energy neutrons, which includes many cases of practical importance in radiation research, elastic scattering dominates the energy absorption from neutrons, and these elastic cross sections are sufficiently well known for track structure calculations.

Energy deposition by neutrons is determined by the locations of energy transfer and by the type and energy of secondary particles produced. The maximum range of secondary charged particles resulting from elastic or other neutron collisions (Figure 9.8) is small compared to mean distances between subsequent neutron collisions (typically centimeters in low-Z media). Therefore, as with photons, the tracks of secondary charged particles from the same neutron are not likely to overlap. Thus, they can be analyzed separately. This simplification can be for up to doses about 10 times higher than for photons, since the ranges of recoil heavy ions are shorter than those of Compton electrons.

Although most of the energy deposition by fast neutrons in hydrogenic material is via recoil protons, neutron track structures are more complex than those for photons. Proton track structures at low energies (say, below 100 keV) are not known because relevant cross sections are lacking. In addition, there are some low-energy heavy ions, mainly carbon, nitrogen, and oxygen, for which there are essentially no cross sections available for condensed targets. Furthermore, neutrons are often accompanied by energetic photons, either from beam production or from inelastic

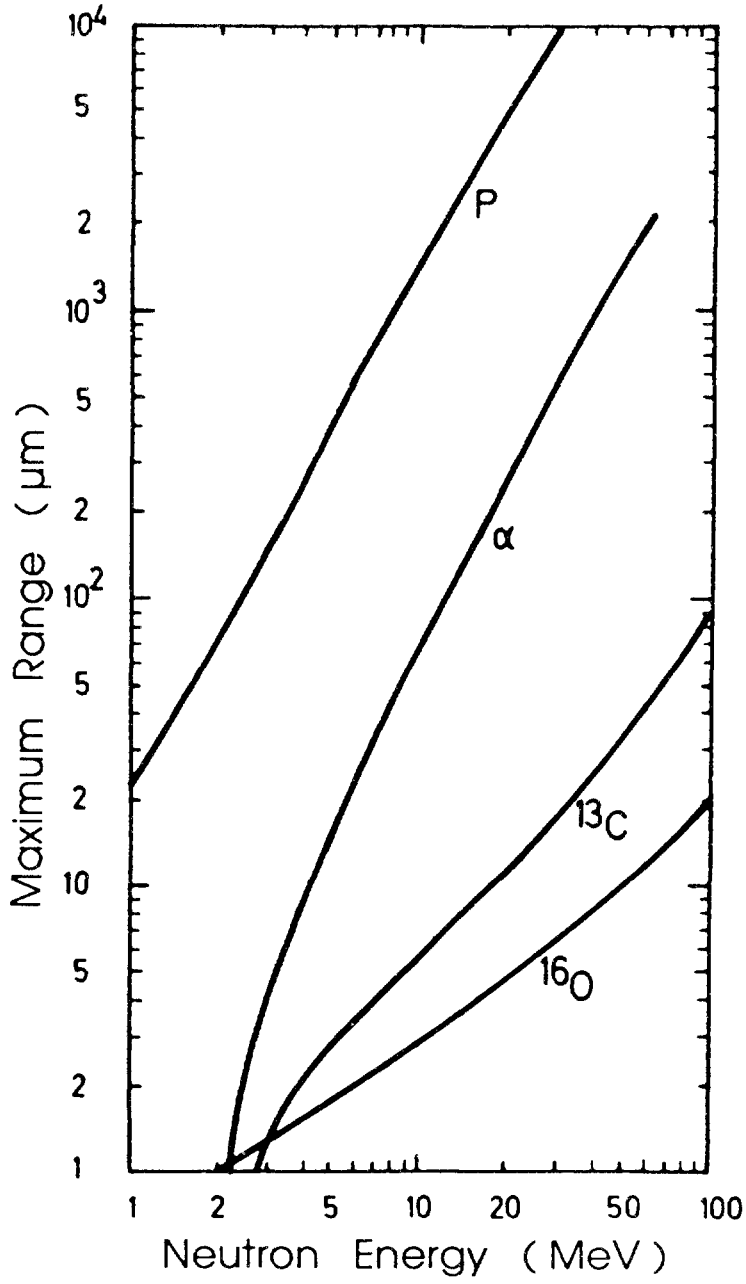

Figure 9.8 Maximum range of the most important charged particles released in tissue by neutrons [p = recoil protons, α and ^{13}C from ^{16}O (n, α)^{13}C, ^{16}O from ^{16}O (n, n')^{16}O] (52).

interactions in the irradiated object. The interaction of these photons in the volume of interest may also have to be taken into account. This mixture of various heavy charged particles, electrons, and photons and the corresponding mixture of physical events makes analysis of neutron radiation effects in terms of track structure theory more difficult than for photons or monoenergetic, fast charged particles. This may be the reason why rigorous neutron track structure calculations have not been performed yet. The deficiencies of analytical approximations (12,13,58,59) and of semi-Monte Carlo approaches (60,61) underline the need for more detailed calculations.

9.2.3. Interactions of Electrons

Electrons are of prime importance in the production of track structures. Essentially all energy from photons or primary high-energy electrons is transferred to and transported in irradiated matter by secondary and higher generation electrons. The same is true for a large fraction of the energy lost by fast ions and thus also for neutrons. Because of this importance, much has been written on various aspects of electron interactions with matter. References 3,8,62-69 can be consulted for details. For a survey of the general characteristics of interactions of low- to -medium-energy electrons, see Chapter 4.

The starting point for a study of the energy deposition of electrons is their stochastic track structure (Section 9.3.2). Input data for track structure calculations are cross sections for all relevant processes (see e.g. Chapters 2,3,4,5). Averaged quantities such as stopping power (the rate of energy loss along a particle path; see Chapter 7), range (some expectation value or extrapolated value of the length of a particle track; see Chapter 7), or yields (expectation values of the production of primary, intermediate, or long-lived new species; see Chapters 6,8) are also useful in radiation research.

The stopping power dE/dx of a medium can be considered as the sum of all single energy loss processes:

$$\frac{dE}{dx}(T) = N\left[\sum_i Q_i\,\sigma_i(T) + \sum_j \int_0^\infty Q\frac{d\sigma_j}{dQ}dQ\right] \qquad (9.2)$$

where N = number density of molecules in the medium
Q_i = energy transferred to a molecule in process i
σ_i = cross section for discrete collision process i
$d\sigma_j/dQ$ = differential cross section for jth transition into the continuum.

Stopping powers known accurately from theory or experiment can be used as constraints in the estimation of less well known cross sections (in particular of secondary electron spectra; see Chapter 7).

It is useful to mention here the so-called electron degradation spectrum $Y(E_0, E)$, which gives the sum of the path segment lengths where the degraded primary electron (start energy E_0) and all secondary electrons produced during complete slowing down have an energy between E and $E + dE$ (70-72):

$$Y(E_0,E) \approx \frac{N(E_0,E)}{dE/dx} \qquad (9.3)$$

where $N(E, E_0)$ is the absolute number of all secondary and higher order electrons created by complete slowing down of an electron of incident energy E_0, which have kinetic start energy larger than E, plus 1 for the primary electron. The electron degradation spectrum increases steeply with decreasing electron energy (Figure 9.9a), because of the increase in the number of low-energy secondary electrons and the decrease of the stopping power at energies below 100 eV. As written here, equation 9.3 is only a rough approximation that does not explicitly take into

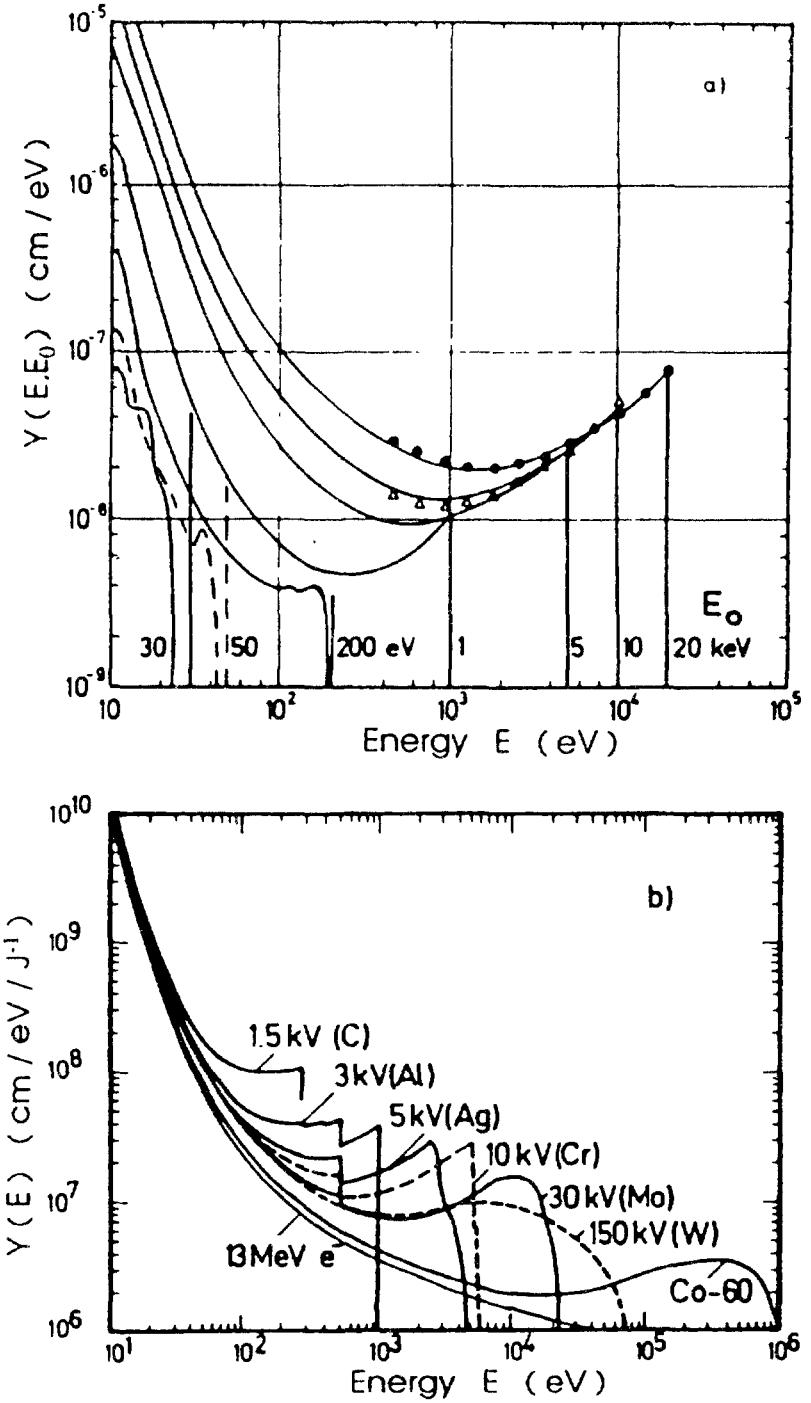

Figure 9.9 Degradation spectrum of electrons in water vapour (*a*) of various low-LET radiation fields (34) and (*b*) photon and electron fields (adapted from Ref. 49).

account departures from the continuous-slowing-down approximation or adequately describe contributions from secondary electrons. For more detailed discussion of electron degradation spectra see Chapter 8.

Figure 9.9b gives degradation spectra for several photon fields and very fast electrons. It shows the strong distortion of electron energy spectra during slowing down from their clean Compton- and photo-electron spectra produced by the initial photon interactions.

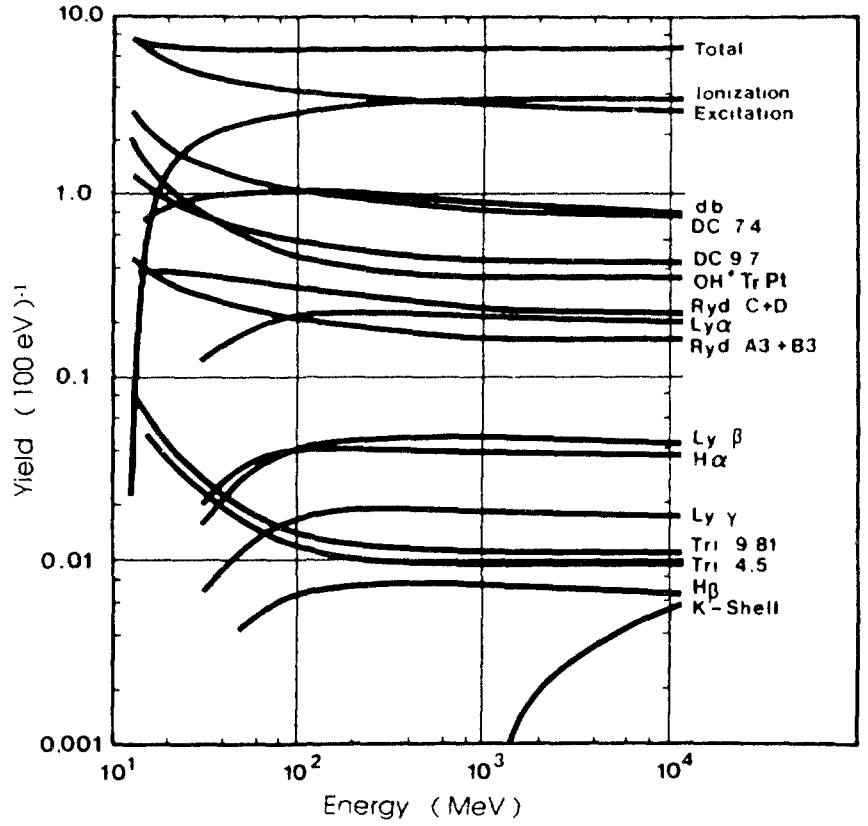

Figure 9.10 Yields of various primary excitations and of ionizations produced by complete slowing down of electrons in water vapor as a function of incident energy.

Degradation spectra are useful for the calculation of the yield G_i of any species i:

$$G_i(E_0) = \int Y(E_0, E)\sigma_i(E)\, dE \tag{9.4}$$

where $\sigma_i(E)$ is the production cross section of species i by electron of energy E. Yields (for example of ions, electrons, or light-emitting excitations) produced during the complete slowing down of a primary particle can be measured to a much higher accuracy than total or differential cross sections for single collisions. Therefore, yields represent a means to check predictions of track structure calculations against experiments and thus to improve iteratively on relevant cross sections. Figure 9.10 shows the result of such a calculation for water vapor. The predominance of ionizations at high energies and of excitations below, say, 200 eV is evident. An average of 14 eV is spent here per inelastic event ($G_i \approx 7$ events per 100 eV). For a more detailed discussion see Chapter 8.

Yields, as defined in Eq. (9.4), are expectation values averaged over many primary electron tracks. In reality, however, each track will produce a somewhat different number of new species than another track. In many cases, because of the correlation between energy loss and species production and because of the finite energy available, the frequency distributions of the number of new species is narrower than a Poisson distribution (73-76). The ratio of the variance of the observed distribution to that of a Poisson distribution is often called the *Fano factor*. Comparison of

Figure 9.11a Ionization frequency distributions for complete slowing down of electrons in water vapour (----) and in liquid water (——) (Terrissol, unpublished).

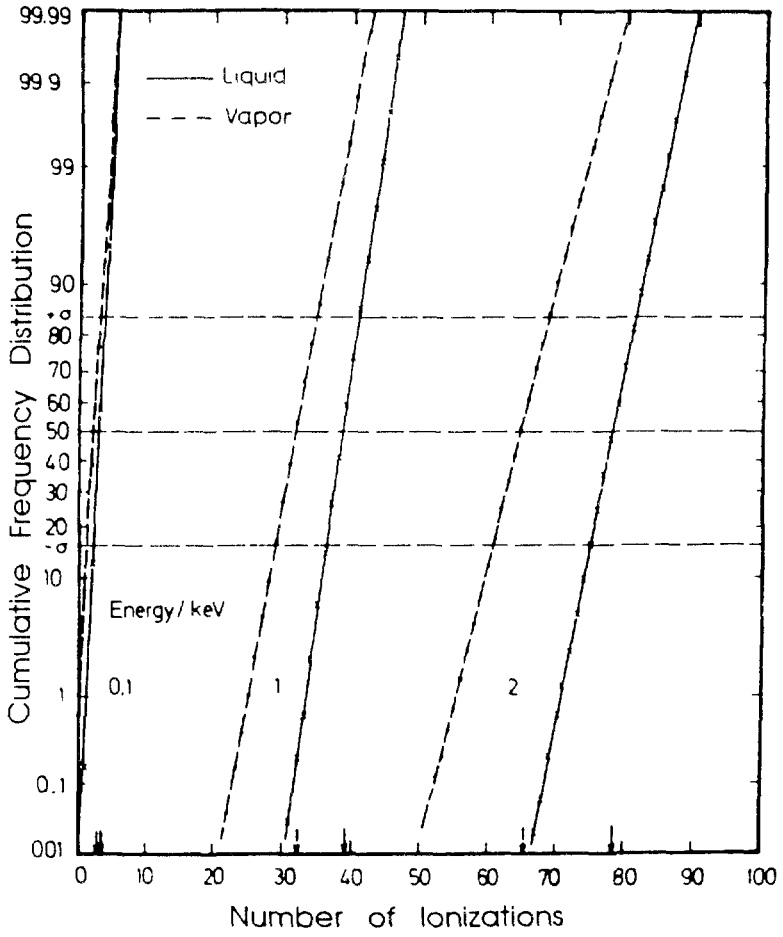

Figure 9.11b Ionization sum distributions (probability graphs) for complete slowing down of electrons in water vapor (----) and in liquid water (——); adapted from Ref. 77. Arrows indicate respective mean values.

calculated and experimental yield distributions can also be a sensitive check of consistency of single-collision cross sections (74). Figures 9.11 a and b give distributions of the number of ionizations produced in the tracks of electrons in liquid water and in water vapor. The distributions appear essentially Gaussian over a wide parameter range (Fig. 11b). The consequent G-values (Figure 9.12) show that at high electron energy more ionizations are produced in the liquid and that the outermost electron orbits contribute most to ionization (contrary to irradiation by photons). The calculated total ionization yields for the vapor are in excellent agreement with experimental data (78). The lower part of Figure 9.12 shows that (a) the frequency distributions for the total ionization yields are narrower in the liquid (i.e. their Fano factor is smaller) and (b) the respective distributions for each single shell are much broader than that for all ionizations (i.e., their Fano factor is larger).

Finally some spatial aspects of electron energy deposition shall be considered, since the spatial correlation of all initial events influences the subsequent physical and chemical reactions. The expectation values of electron energy deposition show a number of typical features, some of which are depicted in Figure 9.13 (5 keV electrons vertically incident on a slab of water). The number of transmitted electrons

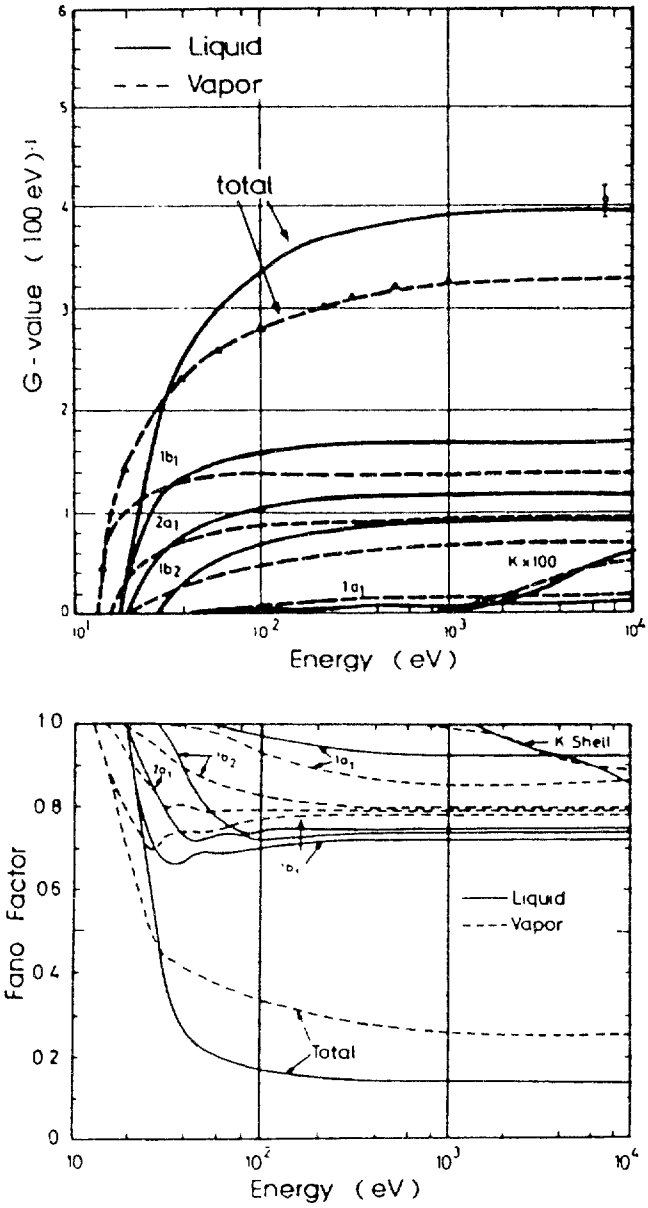

Figure 9.12 *G*-values for ionization from different molecular levels and corresponding Fano factors for electron impact on water vapor (----) and liquid water (——) (adapted from Ref. 77).

decreases strongly with increasing slab thickness (compared to corresponding plots for heavy charged particles, which show almost a step function). However, the kinetic energy per transmitted electron decreases much more slowly. At a thickness equal to their range (obtained in the continuous-slowing-down-approximation [csda, (79)] about 1% of the incident energy and around 5% of the incident number of electrons are still transmitted. With increasing slab thickness electrons are also reflected (back-scattered). Their number fraction at medium energies and for vertical incidence on low-Z matter is around 10%, and the mean energy per reflected electron is around 40-50% of the incident energy. The reflected number is independent of thickness beyond $d/R = 0.4$ because electrons are not appreciably reflected back to the surface from greater depths.

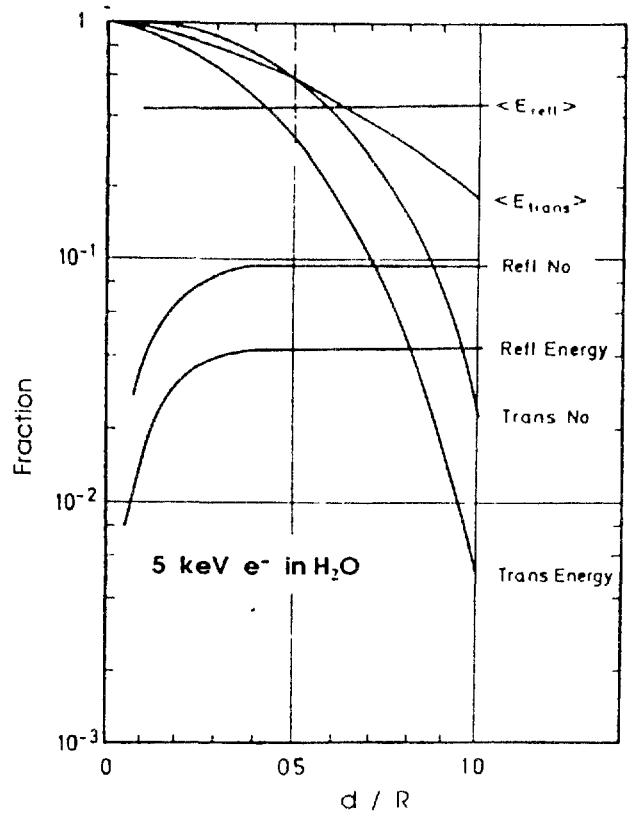

Figure 9.13 Calculated fractions of reflected and transmitted electrons and their energies as a function of slab thickness d (in units of the electron range R) (34). Vertical incidence, pencil beam, and water vapor. See Figure 9.14 for values of R.

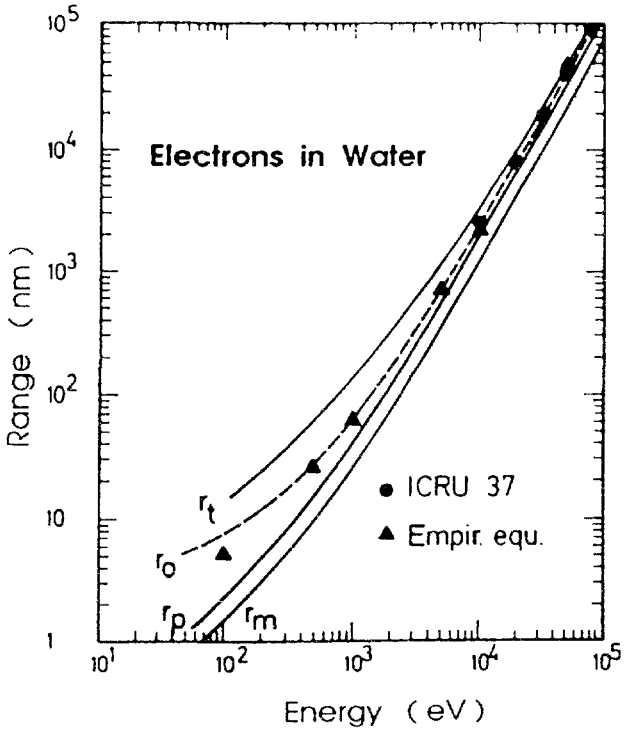

Figure 9.14 Calculated mean track length r_0, practical range r_p, mean range r_m, and total track length r_t for electrons of energy E_0 in water vapor; data from Refs. 34, 49 and 79.

The transmission curves indicate that there are many possibilities for definition of an electron "range" (csda, mean, practical, extrapolated, and so on) (49). The range becomes even less well defined at low energies (≤ 100 eV), where electrons are more or less in complete diffusion, or at subexcitation energies, where electrons can diffuse over long distances because of the reduced number of energy loss processes. Figure 9.14 shows some of these ranges calculated by a Monte Carlo electron track structure program in comparison with data from ICRU Report 37 and an empirical range-energy relationship for low-Z matter (ρ = 1 g/cm^3), which gives reasonably accurate values up to, say, 20 keV:

$$R = 40\,E(1 + 0.5\,E) \quad \text{(nm)} \tag{9.5}$$

where E = electron energy in keV.

9.2.4. Interactions of Heavy Charged Particles

Energy transfer from fast charged particles to matter occurs primarily through excitations and ionizations. For ions with specific energy E per mass in the range 0.5-100 MeV/u, around 65-75% of the energy loss is transferred to and then transported by secondary electrons, 15-25% is needed to overcome their binding energy, and the residual 5-10% produces neutral excited species. The large fraction transferred to secondary electrons emphasizes the importance of electrons also in this context. For 0.8 MeV/u particles around half of all ionizations are produced by the fast ion itself, and the rest by its secondary electrons. With increasing ion energy two out of three ionizations are ultimately due to secondary electrons and are thus not necessarily located close to the ion path (see Chapter 2).

Let us consider some characteristics of heavy charged particle (ion) tracks. The main contribution to energy losses of a fast ion comes from inelastic interactions with the electrons of a medium. The role of the elastic interactions becomes important only at the end of the ion's track. The role of charge exchange processes between a moving ion and the target molecules increases when the ion slows down, see Chapter 2 of this report. The size of regions of the energy localization depends only on speed of a charged particle. Therefore, a fast proton generates a similar track structures as does a fast electron with the same speed.

But for the whole track picture we must take into account the differences in the interactions of ions and electrons. This difference in action is based on the difference in charge and in mass.

Interaction cross-sections and stopping power depend only upon charge and speed, they are proportional ~Z^2/v^2, and do not depend upon mass of a particle. So when an ion and an electron have the same speed the ratio of inelastic cross-sections is equal to Z^2 (this is also valid for the ratio of stopping powers).

Another difference between the action of an ion and electron is the difference in the maximum energy of the knocked out electron. The ion with the speed v can transfer to a free electron in a medium the maximum energy $E^{ion}_{max} = 2\,mv^2$, where m is the electron mass, whereas a fast electron with the same speed can transfer maximum energy $E^{el}_{max} = mv^2/4$, so $E^{ion}_{max}/E^{el}_{max} = 8$. Consequently, in the case of ions the energy of the knocked out electrons will be distributed partly to regions of the medium far more remote from the point of initial ionization than in the case of electron collisions.

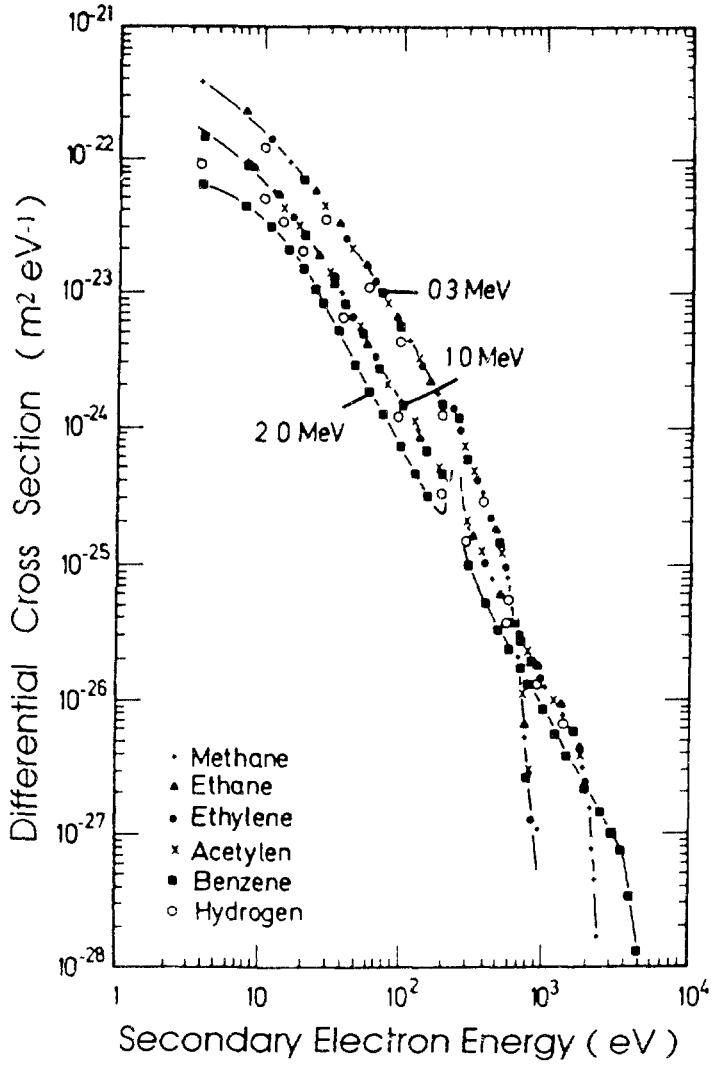

Figure 9.15 Secondary electron ejection cross section for proton impact (0.3, 1.0, and 2.0 MeV) on various target molecules, divided by the number of weakly bound target electrons (37).

There are two new interaction processes for fast ions, compared to electrons. First, heavy charged particles of medium energy (say, 0.1-5 MeV/u) can capture electrons from target molecules into their own continuum states [charge transfer to the continuum (CCT)], which leads to the ejection of additional secondary electrons. These have essentially the same speed as the ion and travel in essentially the same direction. Their production cross sections are not well known. Second, heavy charged particles are usually incompletely stripped ions that carry electrons in bound states (for example He^+ and Xe^{5+}) and can successively lose electrons and capture target electrons. This complicates the derivation of relevant cross sections for heavy charged particles.

The singly differential ionization cross sections for protons show the same general shape as those for primary electrons (Figure 9.15). This figure gives experimental data for secondary electron ejection cross sections for proton impact on various hydrocarbons and on hydrogen. The cross section (a) decreases with increasing ion

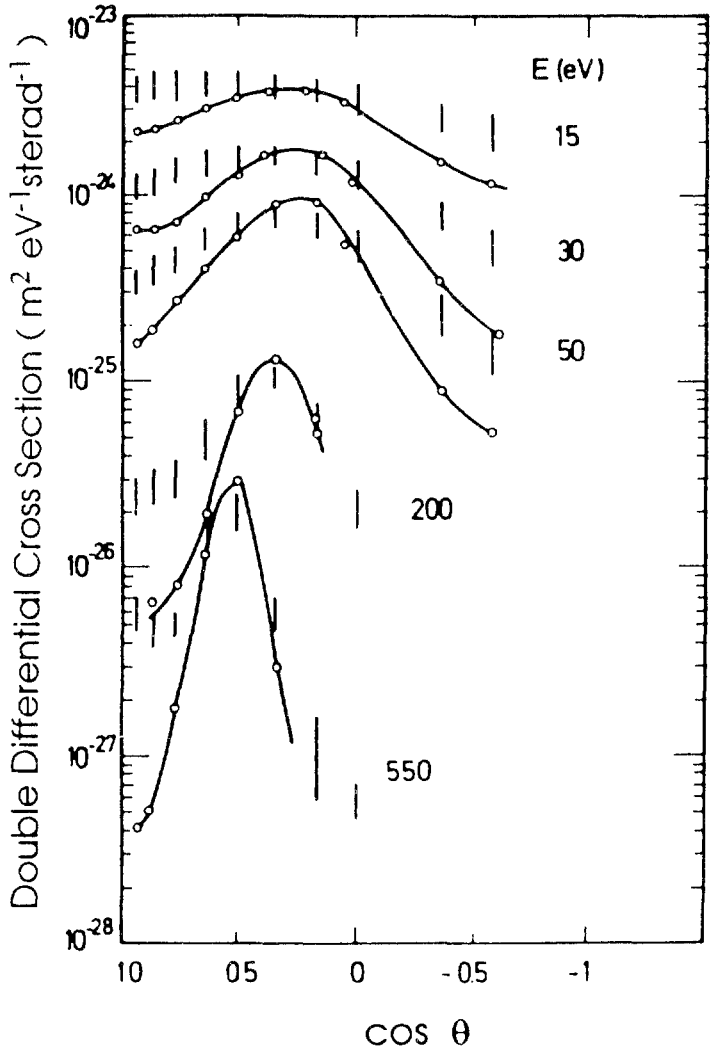

Figure 9.16 Angular distribution of secondary electrons with energies E ejected by 1-MeV proton impact on various molecules divided by the number of weakly bound target electrons. The range of data for hydrocarbons is indicated by vertical slashed (|), data for hydrogen (O) are connected to guide the eye (37).

energy ($\propto T^{-1}$) and (b) falls at medium energies of secondary electrons approximately as E^{-2}. Also, (c) the maximum electron energy increases linearly with the ion energy ($\propto T$). All this is understood from theory and is similar to cross sections for primary electrons. The features (a) and (c) are mainly responsible for the fact that there cannot exist one single parameter characterizing the "quality" of any radiation field in producing a certain radiation action (see also Section 9.4.5). The absolute value of these cross sections per weakly bound target electron (i.e., for all electrons except for the K orbital electrons) is almost independent on the chemical nature of the target molecule. The same is true for the angular distribution of the ejected secondary electrons (Figure 9.16).

The magnitude of cross sections of charged particles is proportional to the square of their electric charge Z. The classical Rutherford cross section is:

$$\frac{d\sigma}{dE} = 4\pi a_0^2 R_y^2 \frac{Z^2}{T} \frac{1}{Q^2} \tag{9.6}$$

where T = ½ mv^2
m = electron mass
v = ion speed
Q = energy transfer (= $E + U$)

This relationship is approximately correct for bare nuclei or fast ions with tightly bound electrons, but the supposition that this holds also for fast ions with loosely bound electrons is not correct. Figure 9.17 shows an example of this failure; the ions H_2^+ and H^+ are both singly charged and a constant cross section ratio might be

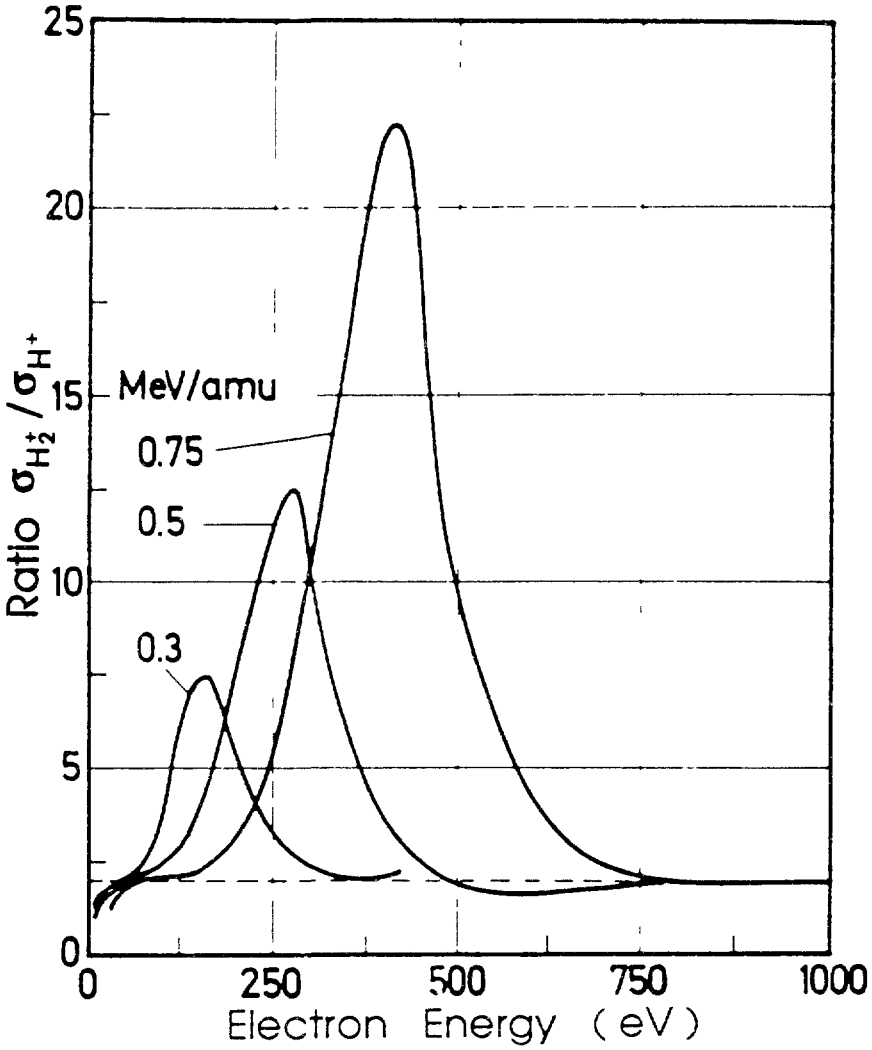

Figure 9.17 Ratio of energy differential cross sections for the production of secondary electrons by H_2^+ and H^+ projectiles of various specific energies impinging on hydrogen gas (81).

expected, but over a wide secondary electron energy range the contribution of the ejected electron of the H_2^+ molecule shows that such a simple scaling from proton cross sections to heavy-ion cross sections is not obtained. Scaling from proton data to heavier ions with a so-called effective charge Z_{eff} (83-88), however, has proven useful in stopping power analysis (see Chapter 7). The empirical formula derived by Barkas from nuclear emulsion work (89) is often adequate. His formula is also in agreement with experimental data for the charge state distribution after penetration of heavy ions through gases (Figure 9.18). The higher charge states observed after penetration through solids are most probably due to electron ejection from the highly excited fast ion after leaving the solid (82). It might be worthwhile to put more effort into understanding this apparent discrepancy between the meaningfulness of the concept of an effective charge in stopping power and the failure of this concept for those cross sections that essentially determine the stopping power.

Tracks of heavy charged particles are often characterized by their mean rate of energy loss and their range. This mean rate, the stopping power, has been the object of many theoretical and experimental studies (1,90-108), which has led to substantial knowledge about the general underlying principles (see Chapter 7). However, the accuracy of actual stopping power values for charged particles heavier than α particles and for all particles at low energies is far from satisfactory. In the context of

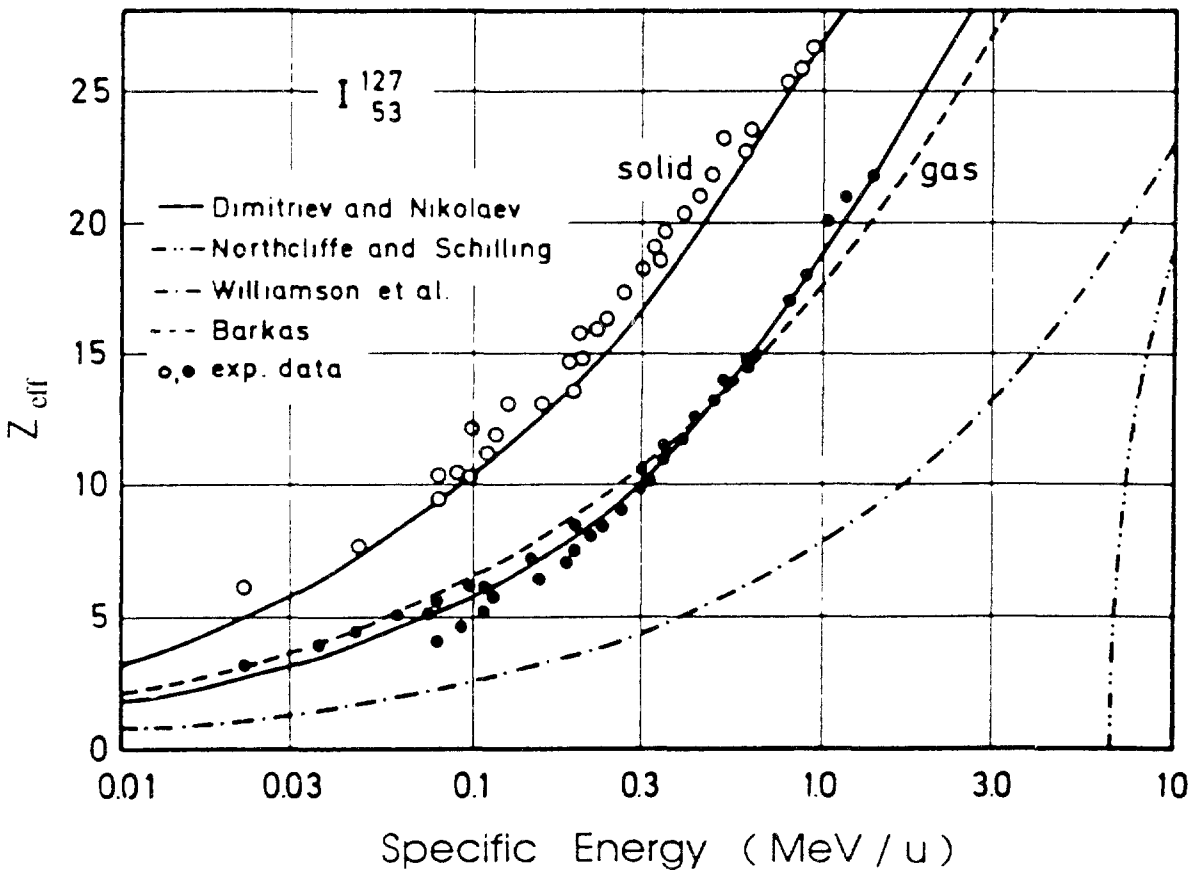

Figure 9.18 Effective charge of iodine projectiles after passing through solid, in gaseous targets, and according to various empirical formulas derived from stopping power analysis (84,85,87,89).

track structure theory it is sufficient to remember the usefulness of this integral quantity for consistency checks as outlined in the section on electrons, the insensitivity of stopping power to the physical phase of the target matter (107,108), and the principles of the dependency of material and particle parameters in the basic stopping power formula of Bethe (79,91) (see Eq. (2), Chapter 7).

$$\frac{dE}{dx} = 4\pi r_0^2\, mc^2 \frac{Z_1^2}{\beta^2}\frac{Z_2}{A_2}\left(\ln\frac{2mc^2\beta^2}{1-\beta^2} - \beta^2 - \ln I - \frac{C}{Z_2} - \frac{\delta}{2}\right) \qquad (9.7)$$

where C/Z_2 represents shell corrections (79) that are discussed in Chapter 7.

The material properties enter essentially only with Z_2/A_2 (≈ 0.5) and $\ln I$, and the dependency on the particle parameters is approximately as β^{-2} (which is similar to the case of electrons) and proportional to Z_1^2. Therefore, particles of the same velocity have different stopping powers according to their Z_1^2, whereas particles with the same stopping power and different Z_1^2 have different speeds (with the consequences for their secondary electron cross sections mentioned above). Because of the similarity in the Z_1 and β dependences of cross sections and stopping power, an apparent correlation over a restricted parameter range of the size of a radiation effect with stopping power could in reality be due to an actual correlation with one or more important basic interactions since the cross sections for these have the same dependency. Data for stopping power of heavy charged particles in water are given in Chapter 7 (Figure 7.5.13).

Beyond the considerations outlined above, the applicability of stopping power in track structure research is rather limited for several reasons. First, the molecular changes in a target material depend on energy deposited in it and not on the energy lost by the passing particle; this is an important difference which can be large when the site dimensions under consideration are small. Second, the number of collisions and the energy transferred in them are random variables with certain probability densities. Therefore, the actual energy loss in a small region of interest can vary considerably (109,110), and the physical and chemical reactions do not "know" of average values but "feel" only actual values. This variation in actual energy loss is shown in Figure 9.19 (111,112), which shows the variance σ^2 of energy loss in thin absorbers divided by the expected energy loss ΔE (stopping power times pathlength) for electrons and protons. For thin absorbers this straggling ratio is independent of absorber thickness. Third, secondary electrons can acquire rather high energy and form tracks of their own physicochemical consequence. Fourth, a site of interest might be larger than the finite range of a particle track structure; this makes considerations of mean rates of energy loss useless in some cases. The regions of influence of these various aspects are illustrated in Figure 9.19.

Chapter 7 gives data for the csda ranges of heavy charged particles in water, which can be used to estimate the longitudinal extensions of their track structures. The ranges of these particles are orders of magnitude shorter than those of electrons of the same kinetic energy.

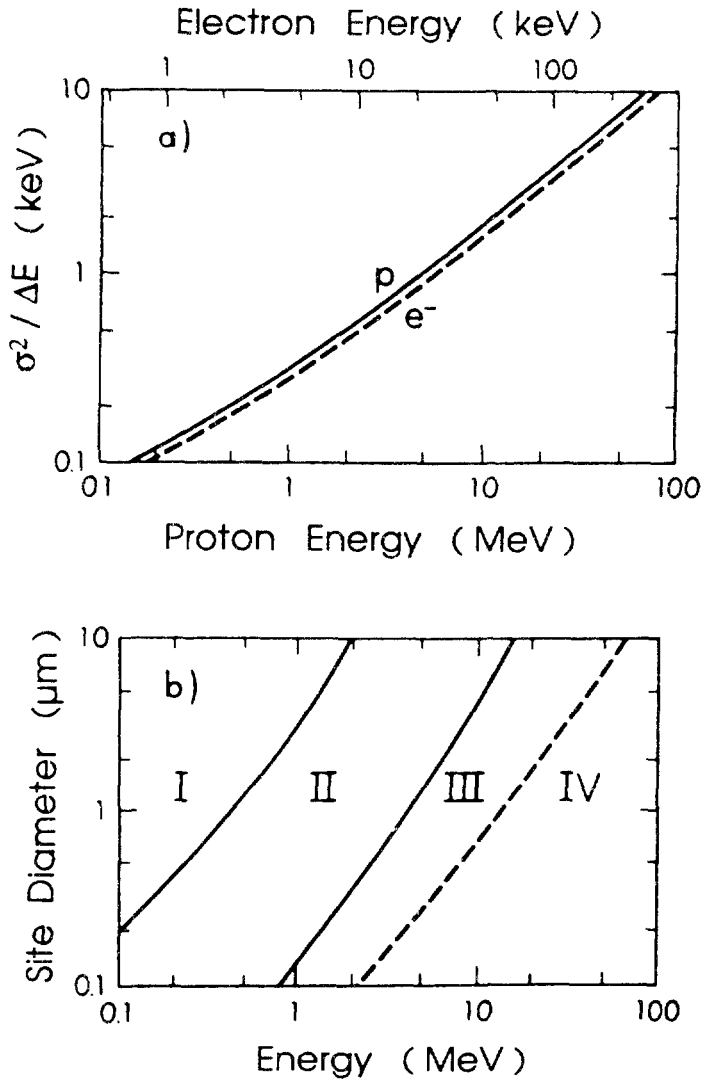

Figure 9.19 (*a*) Ratio of variance of energy loss spectrum to mean energy loss for protons and electrons in the free electron model. (*b*) Regions of site diameters and proton energies where the energy deposition is strongly influenced by their finite range (I), straggling (III + IV), and by the range of their delta rays (IV). In region II the energy deposition can be approximated by *dE/dx*. (111,112).

9.3. SPATIAL ASPECTS OF TRACK STRUCTURES

9.3.1. Characteristics of Tracks from Photons and Neutrons

Photons and neutrons in most cases produce primary events separated by distances that are large compared to the ranges of their secondary charged particles. This is illustrated in Figure 9.20 for water and air. It can also be seen by comparing the particle ranges given in Figures 9.8 and 9.14. Therefore, the track structures produced by primary electrons, protons, and heavier ions are similar to those produced by photons and neutrons. However, with the latter two radiations more than one particle sometimes leaves the same affected atom, for example, because of Auger electron emission after inner shell ionization, or an (n, 3α) reaction.

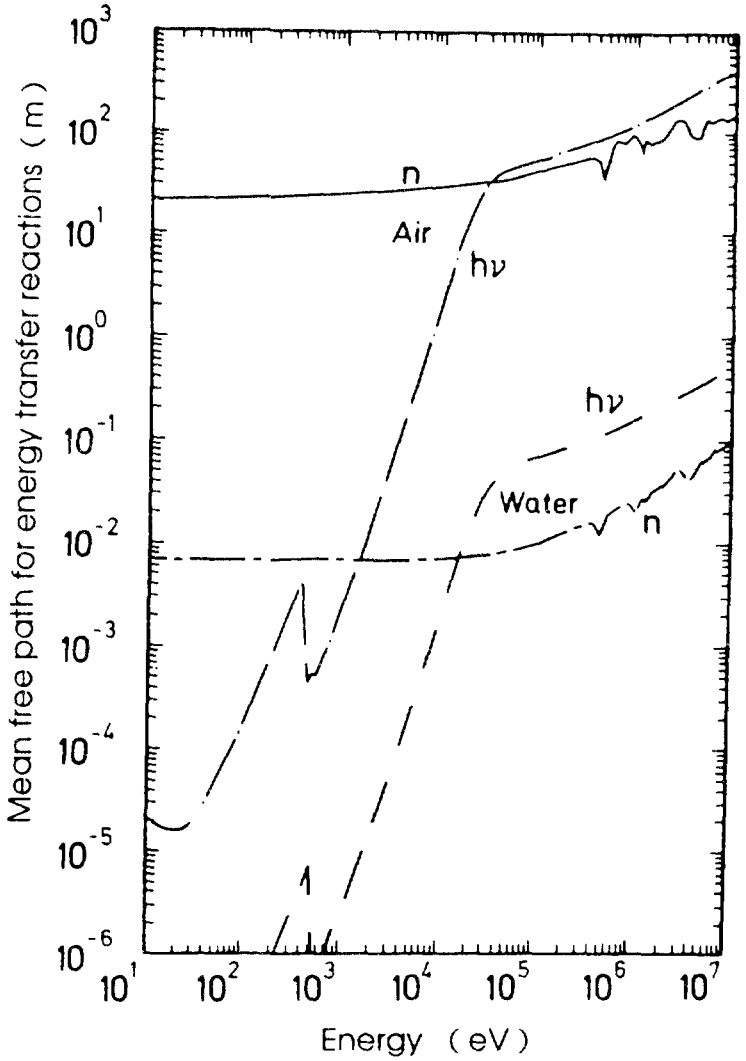

Figure 9.20 Mean free paths for energy transfer reactions of neutrons and photons in dry air and water (51-57,113).

Figure 9.21 shows another characteristic of photon and neutron track structures (114). The ranges of secondary particles from neutrons (mainly protons and heavier charged particles) are much shorter than those from photons (electrons). Therefore, for the same absorbed dose neutrons have a smaller chance to affect a certain small site of interest in the irradiated matter. But if the small site happens to be affected, the amount of energy imparted ε to that site in this interaction is much larger (because of the higher stopping power of ions compared to that of electrons). This leads to the higher expectation value of the specific (imparted) energy $\bar{z}_n$ for neutrons than for photons $\bar{z}_\gamma$ per energy deposition event, where $\bar{z}$ is the first moment of the frequency distribution f(z) of specific energy z (see Section 9.4.3). At a fixed absorbed dose, for the same reason, the standard deviation σ of the distribution of z is much broader for neutrons than for photons (Figure 9.21). The determination of such distributions is a main objective of proportional counter microdosimetry. Further discussions of the properties of these characteristic functions can be found in the literature (112).

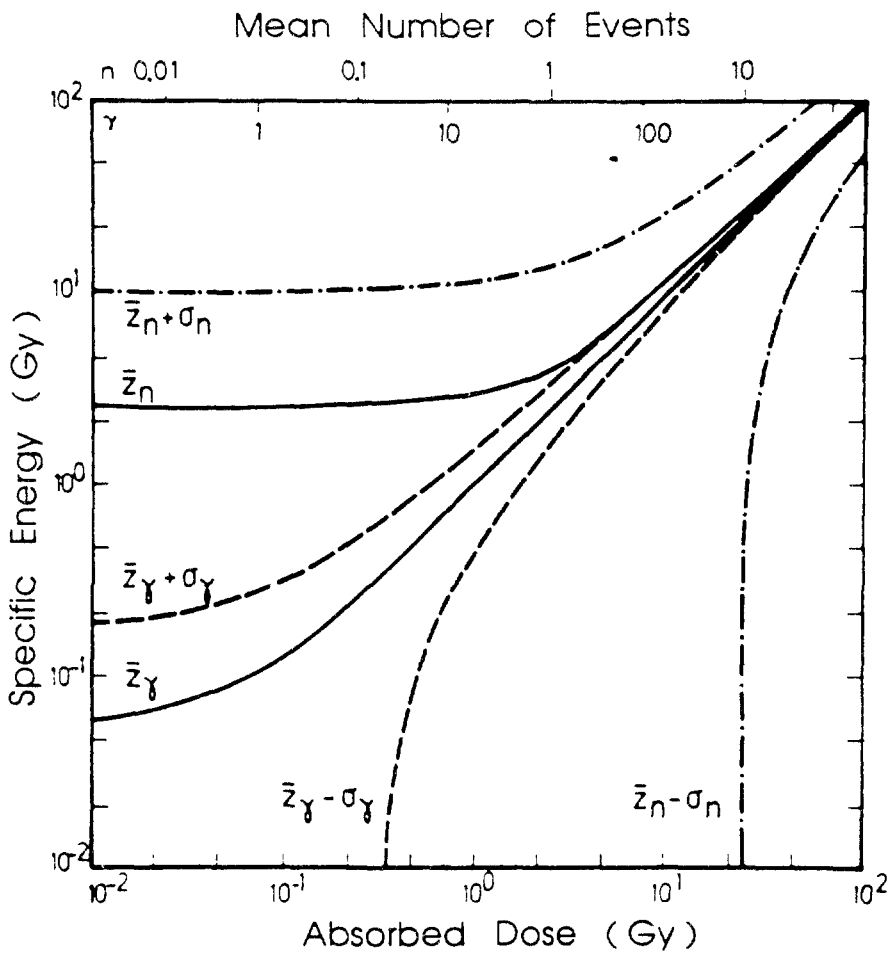

Figure 9.21 Range of specific energies (mean values $\bar{z}$ ± standard deviation σ) and mean number of events as a function of absorbed dose for 14-MeV neutrons (*n*) and ^{60}Co γ rays in tissue spheres of 1 μm diameter (112).

9.3.2. Structures of Electron Tracks

The distance an electron travels between two consecutive events of energy transfer is called the *free path length* l_{in} with respect to inelastic scattering. Its average value equals $l_{in} = (n\,\sigma_{tot})^{-1}$, where n is the density of molecules in the medium and σ_{tot} is the total cross section for inelastic scattering. For fast electrons with E > 10 keV, the value of $\bar{l}_{in}$ exceeds significantly the region of localization of the energy transferred to the medium. For relativistic electrons (E > 100 keV) in water, $\bar{l}_{in}$ is equal to 200-300 nm, while for a 10 keV-electron it is an order of magnitude smaller. At the same time the size of the energy localization region or a *spur* (following Samuel and Magee (80)) is several nm. Thus, the track of a fast electron is regarded as a set of nonoverlapping microregions (*isolated spurs*) containing excited and ionized molecules. In the approach of Samuel and Magee, with decreasing electron energy, the spurs in the track are no longer isolated from each other and at E < 1 keV the track structures are described as a continuous region of overlapping spurs.

Electron track structures have been calculated for energies from about 10 eV to several MeV, and for gases, liquids, and solids (5,22,24-29,34,35,115-125). Here a few characteristic results are shown, using tracks of keV electrons in water vapor.

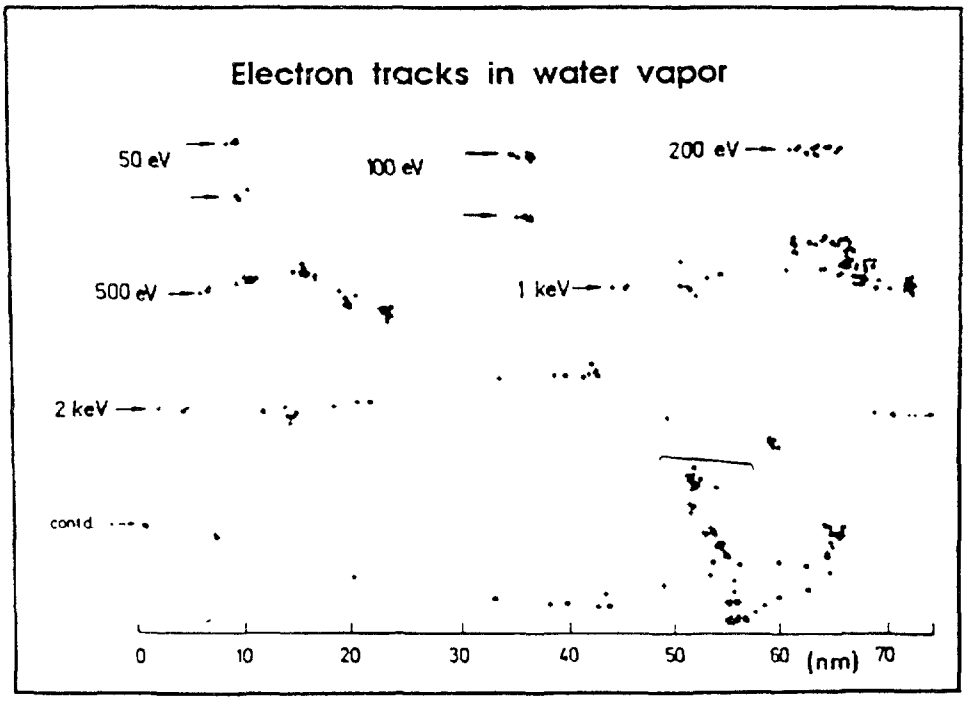

Figure 9.22 Two-dimensional projections of electron tracks in water vapor calculated with a Monte Carlo simulation program (MOCA-8). For graphical reasons the 2-keV e^- track is continued in the last line. For this plot all 20 types of activations are divided into two classes: +, excitation; •, ionization.

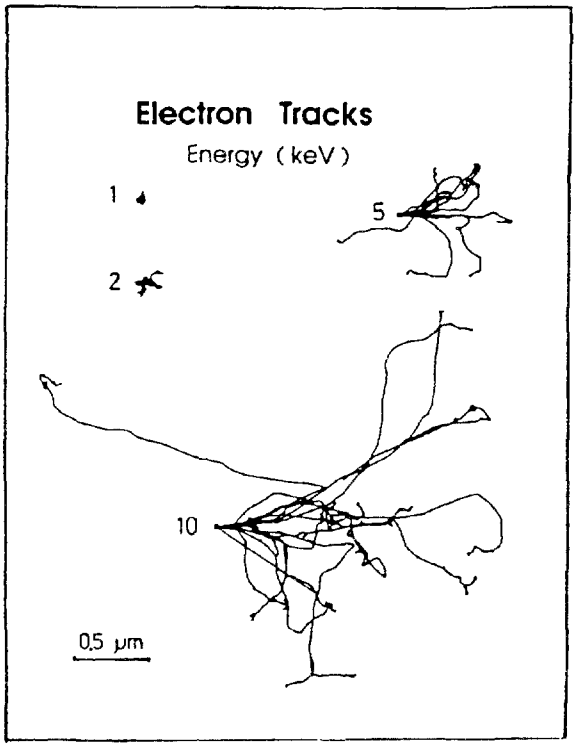

Figure 9.23 Ten tracks of 1-, 2-, 5-, and 10-keV electrons each in water, showing the stochastic nature of paths of identical projectiles and the widely different degrees of spatial concentrations of energy absorption events.

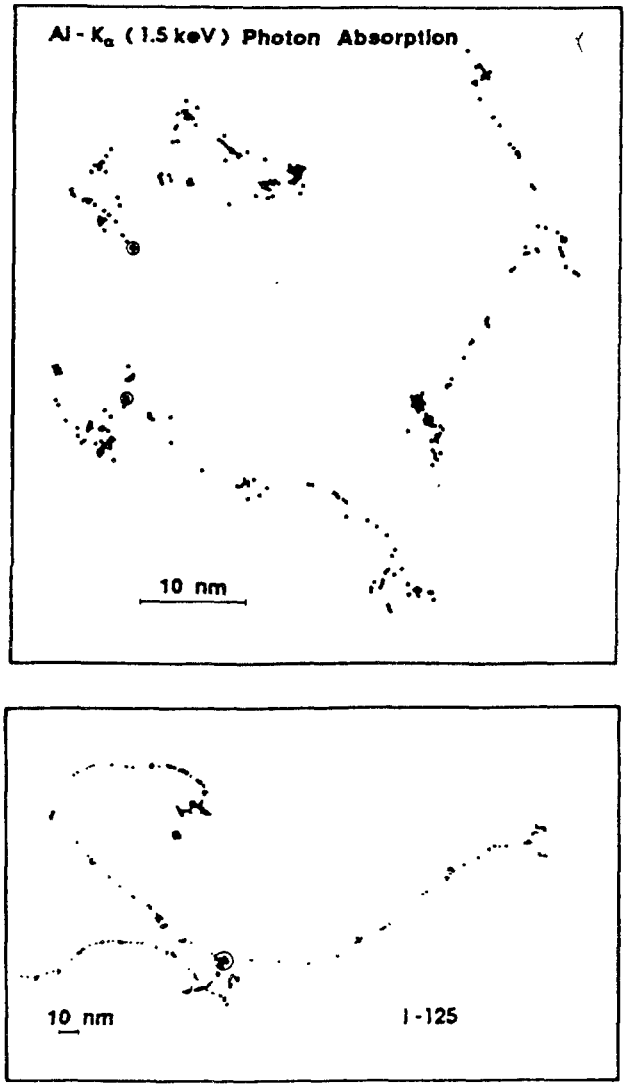

Figure 9.24 Simulated electron tracks from the absorption of Al-K_α X rays in water (leading typically to one photoelectron and one Auger electron) and from an ^{125}I decay (up to 22 electrons of widely different energies ejected per decay).

Figure 9.22-9.24 (and track structures in later sections) are two-dimensional projections of three-dimensional computed tracks, which originally contain full information about the location of each event and its physicochemical nature. For the decay mode of initially excited or ionized states, evaluated experimental data of Tan *et al* (126) were used. The figures show that (a) the number of events increases with electron energy (69), (b) with increasing electron energy the mean distance between inelastic collisions increases, (c) electrons suffer appreciable angular scattering, and (d) the event density is particularly high in the track ends of the primary and secondary electrons.

The largest number of events with small distances to their neighbors can be found in tracks of electrons of around 500 eV; electrons with less energy produce less events per energy deposited, and those with higher energies produce them further apart on the average. This can be seen from the frequency distribution to the next neighbors (Figure 9.25).

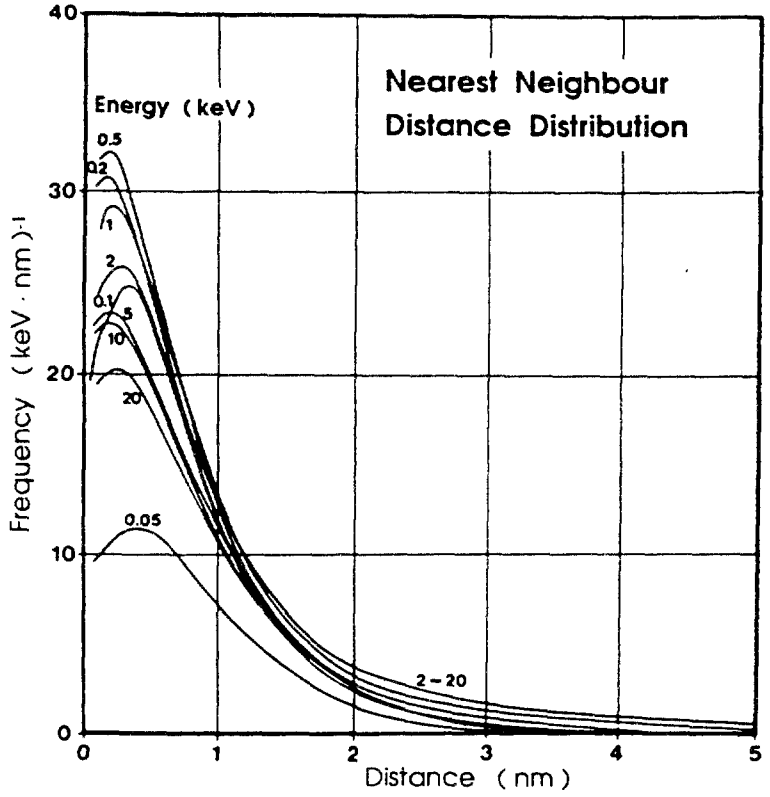

Figure 9.25 Frequency distributions of nearest neighbor distances between excitations and ionizations in tracks of electrons with starting energies from 0.05 to 20 keV.

For electrons with energies in the keV range the probability to find less than 1, 2, 3, ... additional events within a certain distance follows approximately a Gaussian function. However, this distribution describes only expected distances averaged over many events and tracks. Actual reactions of events in a track do not know of these averages and react according to their actual distances. If the reaction probabilities vary nonlinearly with reactant separation distances, for example, in a second-order reaction, the distance distributions must also be weighted nonlinearly. This is possible with Monte Carlo simulations.

9.3.3 Structures of Proton Tracks

Proton track structures have been calculated for comparison with experimental proton data, for neutron track structure studies, and to provide basic data for radiation biology (127-133). Figure 9.26 gives three tracks each for simulated short segments of 0.3-, 1-, and 3-MeV protons in water vapor to demonstrate the similarities and differences between fast ion tracks of the same energy compared to those of different energy. In general, these tracks are straight because the heavier mass of fast ions prevents them from being scattered as much as electrons in elastic and inelastic collisions. With increasing ion energy the relative fraction of all events produced directly by the fast ion decreases from more than two-thirds for energies T around 0.3 MeV/u to around one-third at 5 MeV/u. The fraction of events on or close to the ion path also decreases. This is due to the T^{-1} ln T behaviour of the secondary electron inelastic cross sections and the "hardening" of the secondary electron spectrum with increasing ion energy (the secondary electron maximum energy increases with T).

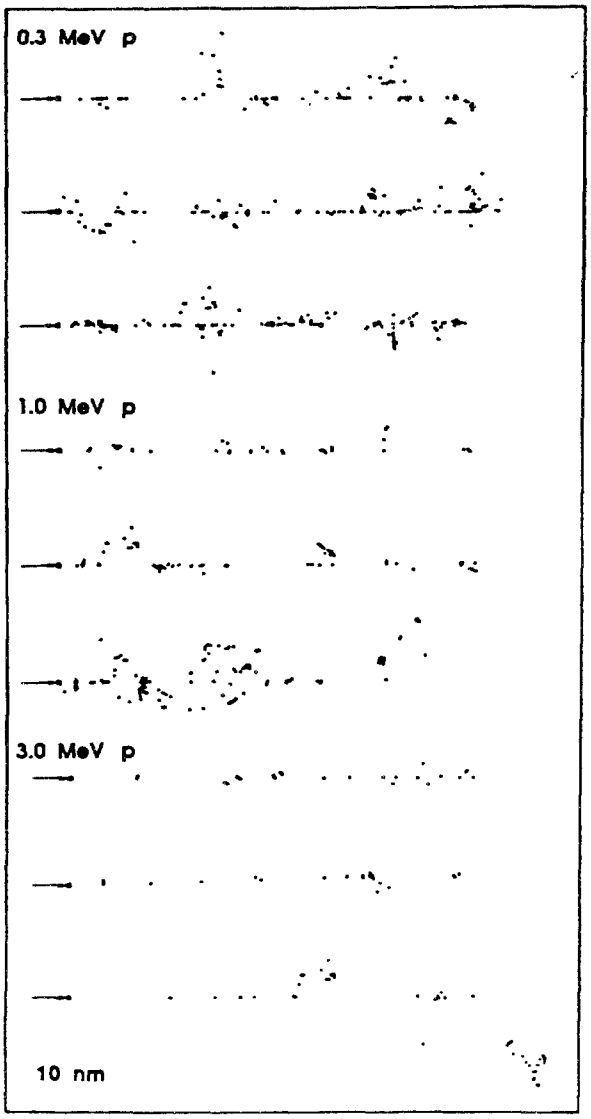

Figure 9.26 Proton track segments in water (0.3, 1.0, and 3.0 MeV, three tracks per energy) calculated with a Monte Carlo simulation program (MOCA-14).

The linear density of fast secondary electrons along the ion path, however, is rather small, and it decreases with increasing secondary electron energy ($\propto E^{-2}$). Therefore, the usefulness of a "radial dose concept" for classification of heavy-ion tracks (Section 9.4.4), which averages the energy deposited by secondary electrons at certain radial distances from the ion path along the path, is not obvious (at least for protons and α particles).

The differences in the three track structures produced by protons of the same energy are completely due to the stochastic nature of all single-collision processes. It is still a challenging problem to derive a rigorous strategy for the classification of such track structures, regarding the similarities of tracks produced by identical particles and dissimilarities between tracks from different particles.

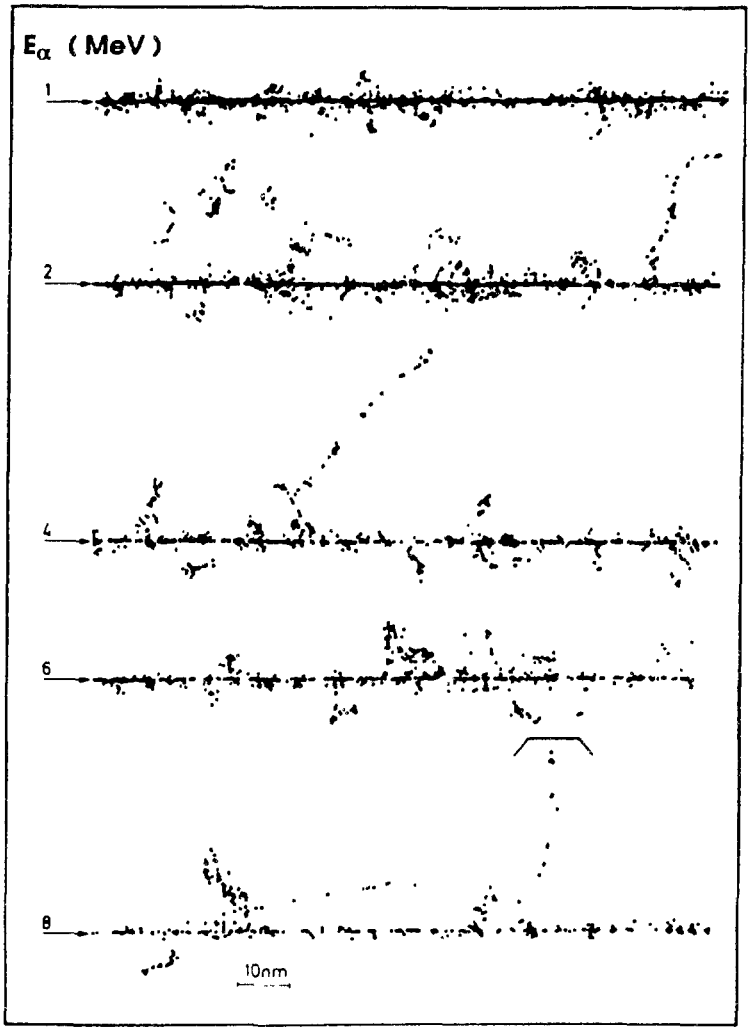

Figure 9.27 Calculated α particle track segments (1, 2, 4, 6, and 8 MeV) in water (MOCA-14).

9.3.4. Structures of Heavy Charged Particle Tracks

The great difference between the ion mass and electron mass results in the great difference in the geometry of ion and electron tracks. While an electron can lose up to half of its energy, the energy lost by an ion in colliding with an electron is less than one thousandth of its kinetic energy. This leads to the rectilinearly of an ion trajectory, since the energy that an ion loses in each event and the corresponding change in its momentum amount to only a small fraction of its total energy and momentum; it is proportional to m/M, where M is the mass of an ion. Therefore, along the whole track except its end part, where elastic collisions are dominating, the trajectory of an ion can be considered as a straight line.

For protons and α particles experimental cross section data and theory permit estimates of basic input data for track structure calculations with reasonable accuracy for a few target media (e.g., water vapor) for a restricted energy range (say, 0.3-10 MeV/u). Figure 9.27 shows two-dimensional projections of track segments from 1 to 8 MeV α particles in water vapor. The higher density of events (all primary and

secondary inelastic events are symbolized by a dot, though the full information on their chemical nature is available in the computer program) stems from the Z^2 dependence of all ion cross sections. The electron transport, however, is independent of the charge of the ejecting ion. Because of the Z^2 dependence of the primary cross section, more higher energy secondary electron tracks are also visible per unit track length for α particles than for protons (Figure 9.26).

In these computed α particle tracks one can see the transition from the "grain count" (single, separated events along the ion path) regime at high particle energies to the "track width" (overlapping events on and close to the ion path) regime at lower energies. This can lead to different types of radiation action (17) and can actually be seen microscopically in fast heavy-ion tracks registered in nuclear emulsions (18,134).

Presently it is still impossible to perform reliable track structure calculations for ions heavier than α particles and for condensed targets, because of the lack of reliable or comprehensive experimental absolute cross sections and the lack of accurate enough

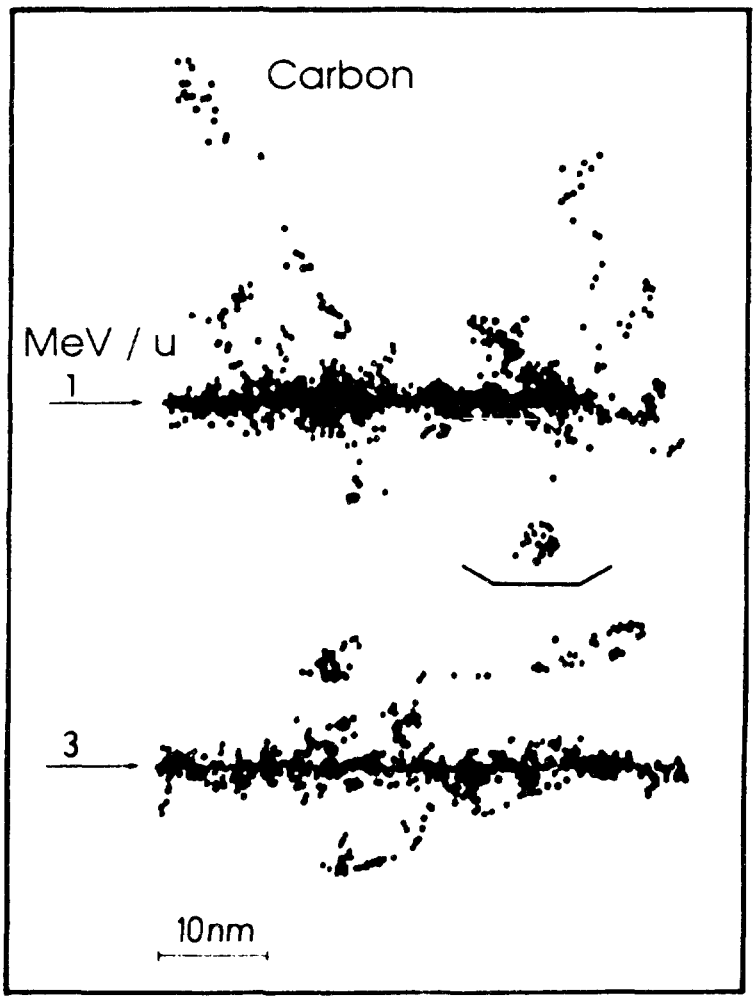

Figure 9.28 Track segments of 1- and 3-MeV/u carbon ions in water (MOCA-14) scaled from proton tracks of the same velocity by multiplication of primary electron ejection cross sections by the effective charge squared.

theories. As mentioned above, the existence of loosely bound electrons in the projectile is the main reason for this problem. However, to give a semiquantitative example, track structures of fast carbon ions were derived from proton tracks by multiplying all primary ion cross sections with the speed-dependent effective charge squared, as calculated from Barkas's formula (89). Figure 9.28 gives an impression of such a heavy-ion track. The event density is very high along, and even at some distance from, the ion path. Quite different chemical reactions and dynamics might be expected in the "core" of such tracks than in sparsely ionizing electron tracks, such as are encountered at larger distances from an ion track or due to photon interactions.

9.4. CLASSIFICATIONS OF TRACK STRUCTURES

9.4.1. Concepts of Classification

As demonstrated in the preceding section, radiation track structures, due to their stochastic nature and the usually large number of events per track, contain much detailed information. This fact introduces the problem of data reduction and classification (135-137). This is a general problem in science and various approaches to its solution can be found in different fields. It is a common objective in research to identify the essential parameters in the usually large number of descriptors that can be attached to an object, process, or phenomenon. Such an identification for data reduction is necessary for the derivation of underlying principles. The aim should first be to establish quantitative criteria for similarities and dissimilarities between objects of study (here track structures) and then to derive strategies for classification and discrimination.

Classification of incident radiation fields (even of mixed fields) is an easy task. In most cases they can conveniently be described at any point in space by their spectral distributions of particle radiances p_i (i identifies the particle type) as a function of energy, solid angle, and time (138). These radiances are related to the particle fluence ϕ_i, which is the number of particles per unit area, by

$$\phi_i = \int_E \int_\Omega \int_i p_i(E, \Omega, t)\, dt\, d\Omega\, dE \qquad (9.8)$$

The classification of track structures produced in matter, however, is a difficult task and presently there is no rigorous solution. A few limited approaches are mentioned below, and ways are shown that might lead to improvements.

9.4.2. Macroscopic Dose, Kerma and Fluence

One possibility of classification is by the energy spent to produce all events of tracks, or of that spatial subgroup, which is in a certain site element of interest. Essentially this means that tracks are ordered according to the energy needed to produce them. The chemical nature of the events and their spatial arrangement (within a site element of interest) is ignored. This could be justified if the so-called optical approximation were valid throughout (8,9), namely, the relative spectrum of physicochemical initial species produced by interaction is independent of the parameters of the radiation and depends only on material properties (for example on its dipole oscillator strength distribution). However, this approximation is valid only for fast charged particles and not for slow electrons, which are very important for track structure formation.

Examples of Concepts of Macro- and Microscopic Dosimetry

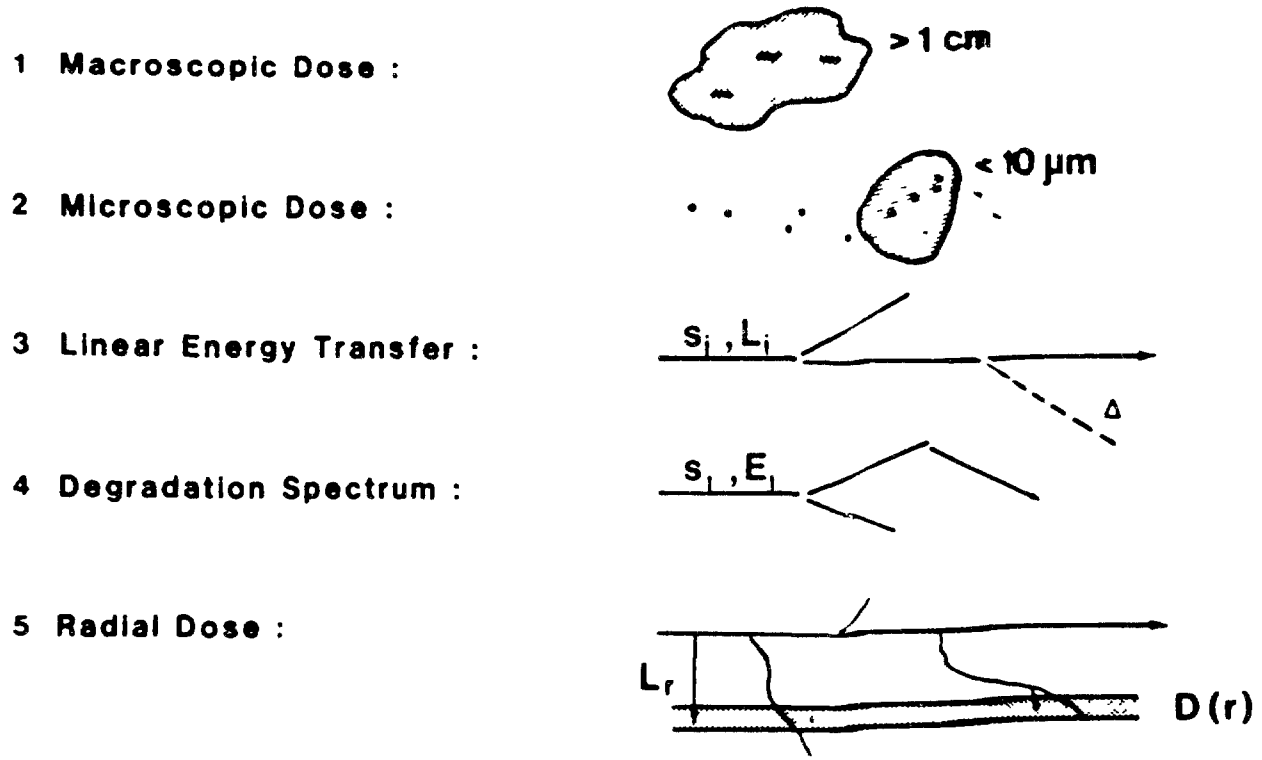

Figure 9.29 Some dosimetric classification concepts for charged particle tracks.

Examples of Concepts of Track Structure Analysis

$$\text{Track} = \{S_1, \vec{x}_1; S_2, \vec{x}_2; \ldots S_n, \vec{x}_n\}$$

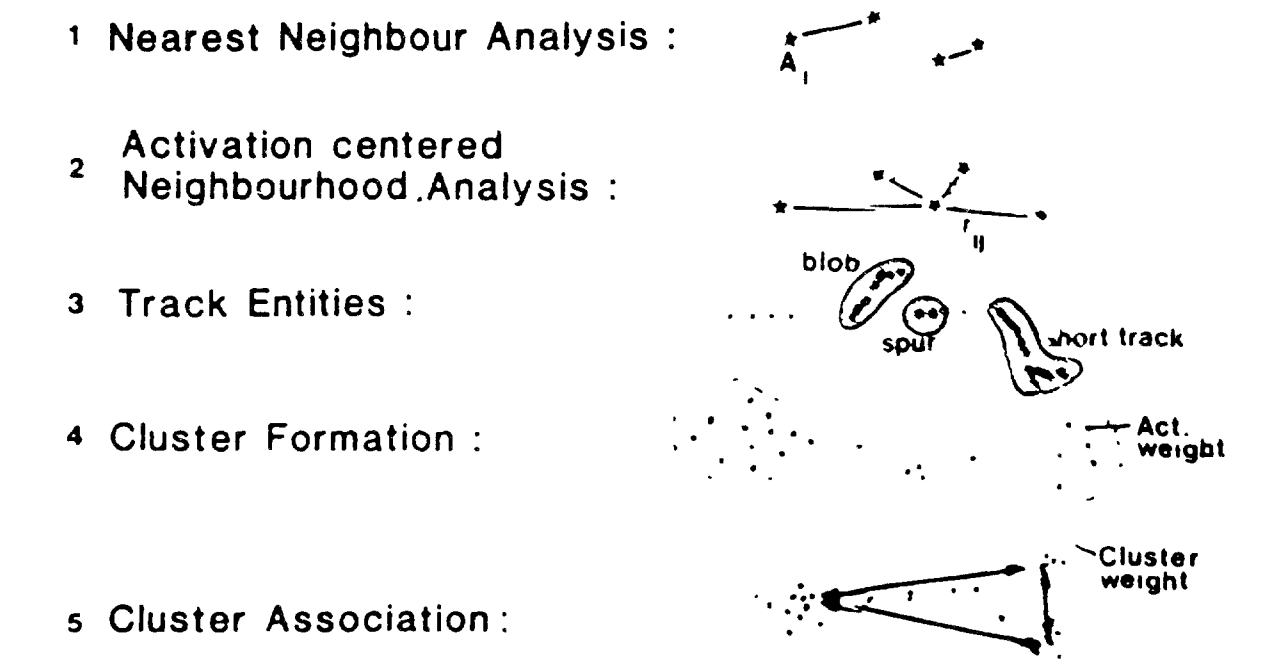

Figure 9.30 Some classification concepts based on locations and types of new chemical species in charged particle tracks.

Furthermore, the primary interactions of photons, neutrons, and charged particles are quite different and the direct consequences of these primary collisions can also be quite different. Thus, the energy absorbed to produce a track is not a very good quantity for classification in radiation research in spite of its wide usage. Its frequent use, in fact, might be a major reason that insight into radiation action mechanisms is not more advanced.

For some applications, however, absorbed energy in mass elements might be an acceptable classification quantity, for example, in calorimetry, or if exactly the same radiation field and irradiation condition is used repeatedly to investigate the dose-effect relationship for this field. Absorbed energy can then be used as an implicit integral measure of the number of charged particle tracks produced. However, if the density in space and time of tracks from different primary particle interactions becomes so high that the track structures overlap and interfere with each other, even in this restricted sense classification by absorbed energy in a mass element can initiate misleading interpretations of observed radiation actions. For mixed fields or when comparing radiation effects produced by different irradiation modalities, even use of a "radiation quality" factor (accounting for different actions of different radiations at the same absorbed dose) cannot overcome the general shortcomings of the quantity "energy absorbed in a mass element" for classification of track structures and their effects. Therefore, it is doubtful whether dosimetric quantities actually "provide a physical measure to correlate with actual or potential effects" (138).

It is mainly for historical reasons and because of its usefulness in certain applications (see above) that absorbed dose is mentioned in this context. Absorbed dose D can be defined (138) as the quotient of the expectation value of the energy ε absorbed in an infinitesimally small element (still containing many molecules) divided by its mass m:

$$D = \frac{d\bar{\varepsilon}}{dm} = \lim_{m \to 0} \bar{z} \qquad (9.9)$$

where $z = \varepsilon/m$ = specific energy

$\bar{z}$ = first moment of $f(z)$

Figure 9.29 gives a survey of classification schemes based essentially on dosimetry. By contrast, Figure 9.30 shows preliminary concepts for characterization of track structures based on the locations and types of events rather than on the total energy needed to produce them. Some of these concepts are discussed in more detail below.

Closely related to the quantity absorbed dose is the quantity *kerma*, which is the *k*inetic *e*nergy *r*eleased in *ma*tter by uncharged particles (photons, neutrons) divided by the mass of the scattering element (52,139,140).

$$K = \frac{dE_{tr}}{dm} = \phi E \frac{\mu_{tr}}{\rho} = \Psi \frac{\mu_{tr}}{\rho} \qquad (9.10)$$

where ϕ = particle fluence (particles/m^2)

Ψ = energy fluence (MeV/m^2)

E = particle energy

μ_{tr}/ρ = mass energy transfer coefficient (100)

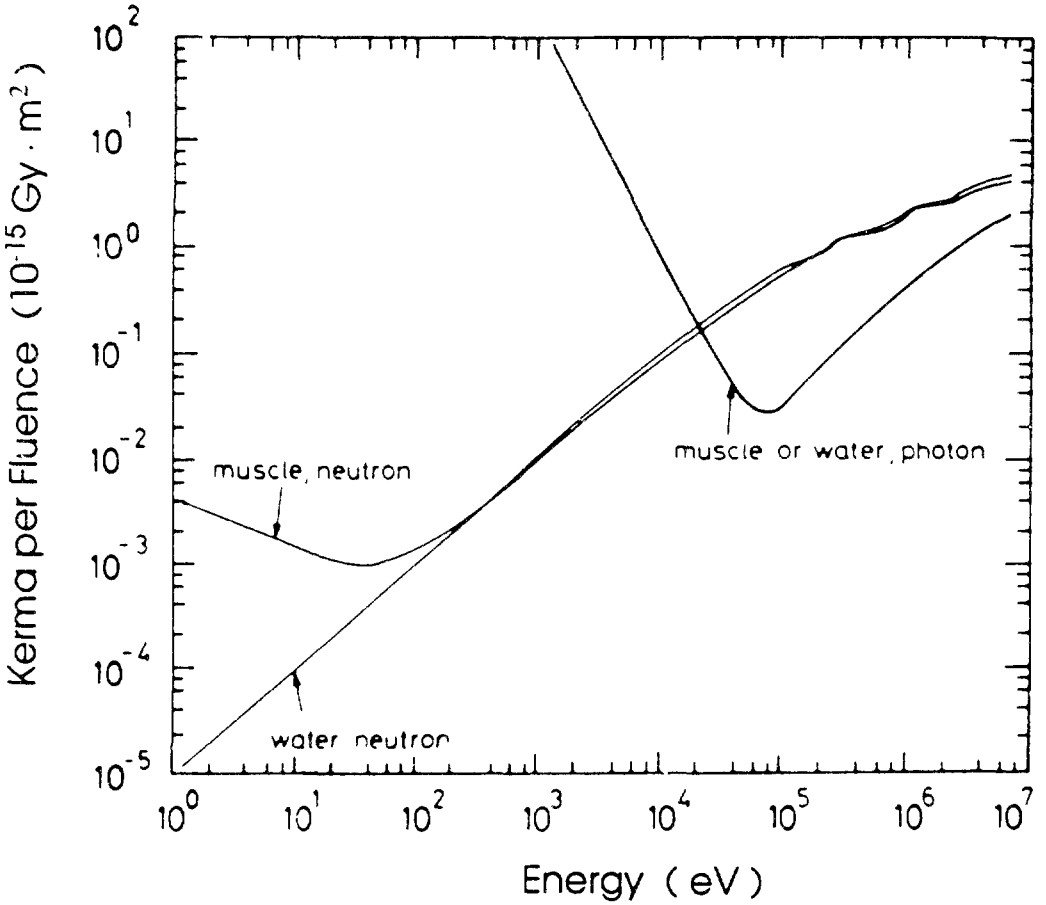

Figure 9.31 Kerma per fluence for photons and neutrons in water and tissue (muscle) (48,139).

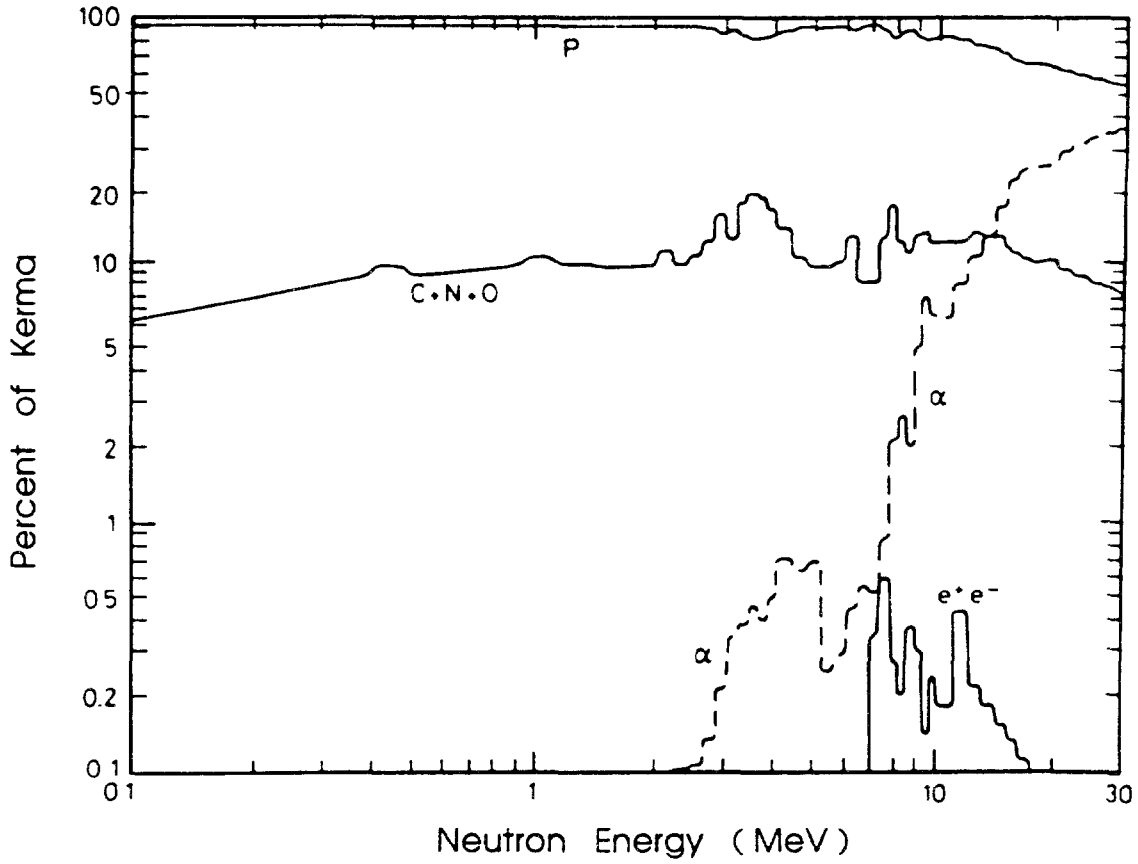

Figure 9.32 Partitioning of kerma in tissue-equivalent plastic (A 150) into the contributing charged particles (141).

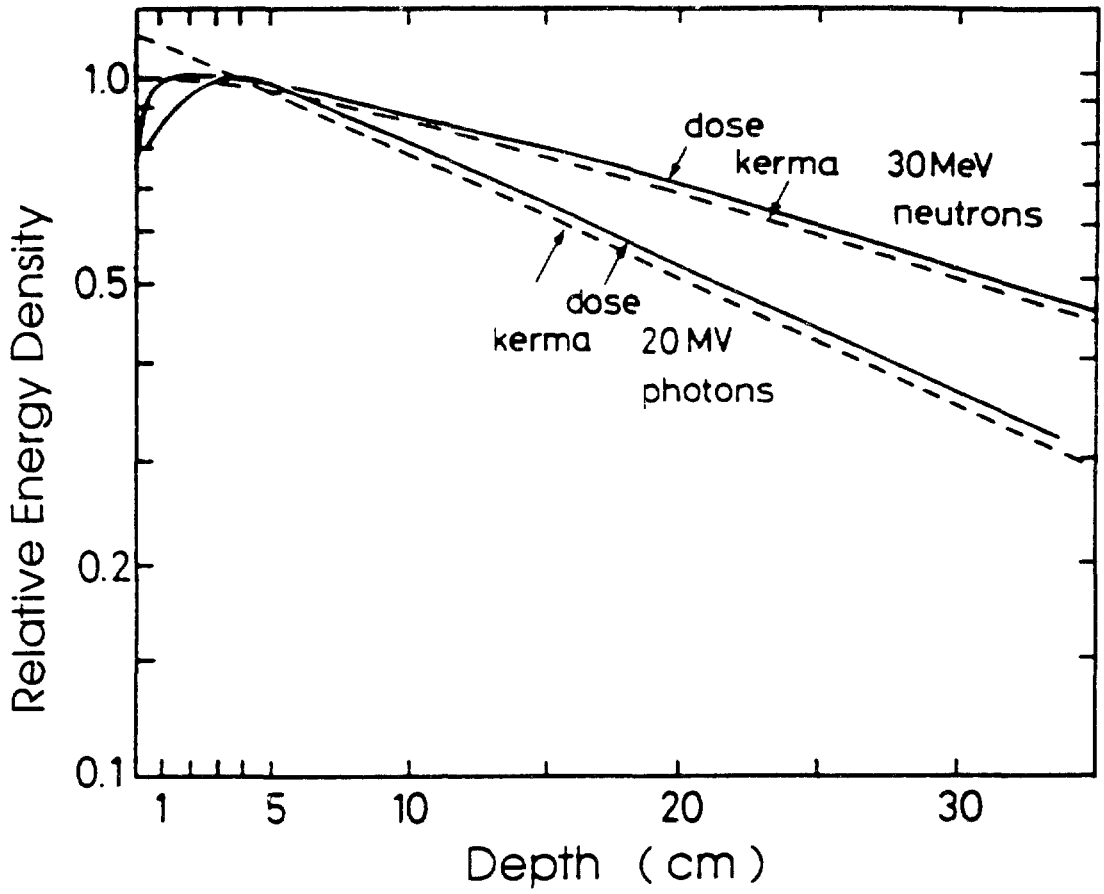

Figure 9.33 Kerma and absorbed dose on the central axis as a function of depth for high-energy photons and neutrons in tissue (derived from Refs. 52, 140 and 142 and normalized to the dose maximum).

Kerma factors (kerma/fluence) for neutrons and photons in water and tissue are given in Figure 9.31. Both materials have low Z and thus the cross sections are almost identical, except for the additional nitrogen content of muscle, which influences the low energy neutron values through its (n, p) reaction. The partitioning of the kerma of neutrons in tissue in Figure 9.32 shows the dominance of proton recoils in neutron track structure, as mentioned in Section 9.2.2. At higher neutron energies nuclear (n, α) and (n, 3α) reactions in carbon and oxygen start to play a significant role.

Whereas absorbed dose is proportional to the energy actually absorbed in a mass element, kerma is the energy lost from a radiation field (into kinetic energy of secondary charged particles). The spatial distribution of energy lost by the primary radiations differs from that of the energy imparted to the medium, because of the transport of energy (mainly in the forward direction) by secondary radiations including electrons and Bremsstrahlung. This can be seen in Figure 9.33.

For the classification of track structures and their action, the differential particle radiance (138) is recommended to specify the local radiation field by direction, particle type, energy spectrum, time, and so on. At the next higher level of data reduction the fluence or fluence rate can be used [see Eq. 9.8]. These primary quantities characterize the radiation field, and the corresponding track structures characterize its action on matter. A change in the energy spectrum of the radiation

field can be used for classification of the interactions that this field experiences but not for classification of the track structures produced in matter, where the new physico-chemical species and their spatial arrangements are of interest and not the energy needed to produce them. If absorbed dose should be used at all as a derived quantity, the radiation modality should be stated in parentheses, for example D (X, 150 kV_p, 1 mm Cu), or D (^{60}Co, 2 cm steel), or D (n, 0.2-6 MeV, 2 mm Perspex).

9.4.3 Concepts of Microscopic Energy Deposition

Track structures can be classified according to the energy of events in a particular, small volume element of interest. Due to the stochastic nature of track formation, the imparted energy ε is also a stochastic quantity, and one can consider the frequency

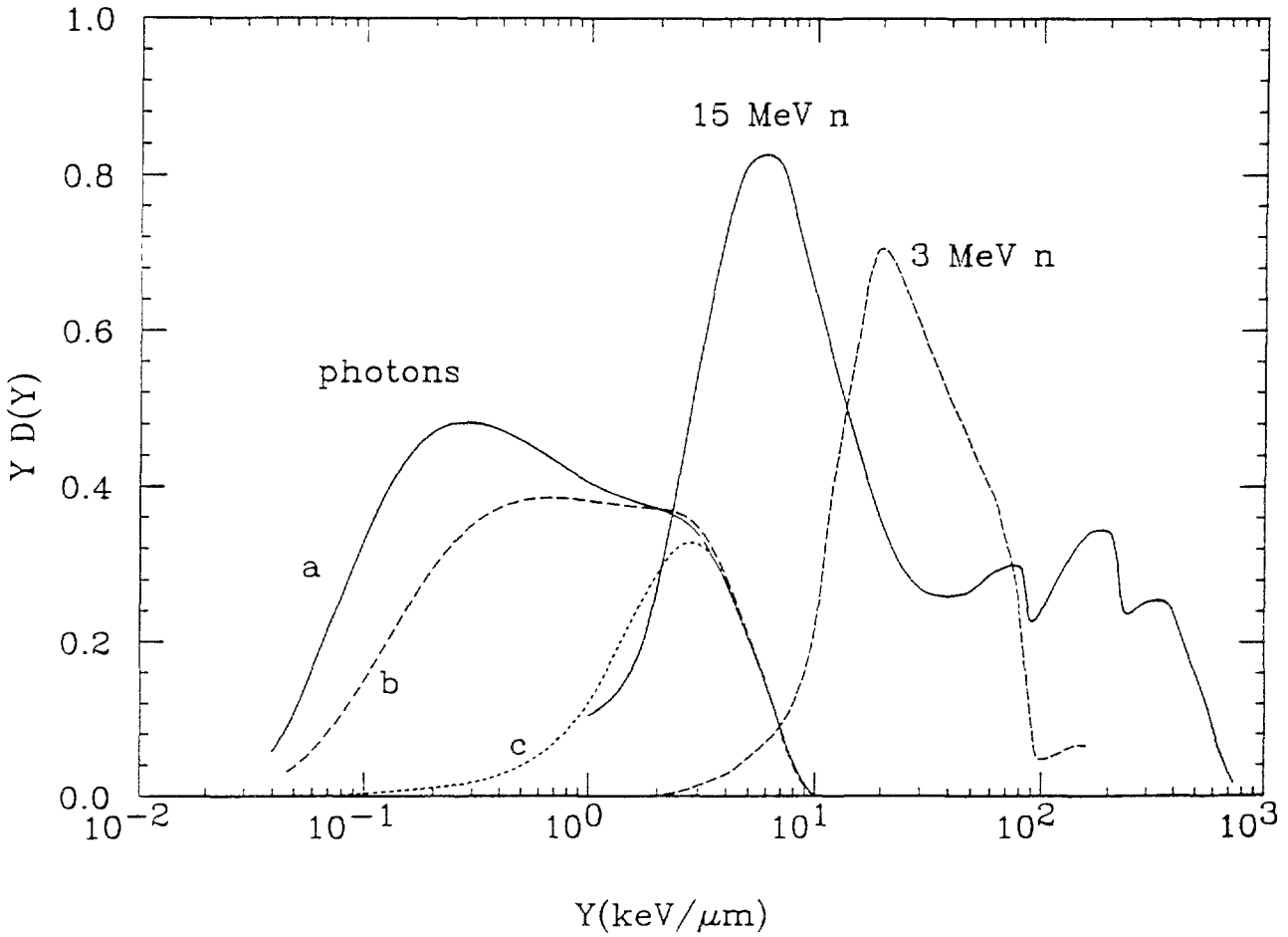

Figure 9.34 Distribution of D(Y) in lineal energy Y (= ε/d) measured with a spherical proportional counter with diameter (d) equivalent to 2 μm of tissue. (For a sphere $\bar{l}$ = (2/3)d and hence Y = (2/3)y.) Measurements were made with photons and neutrons (142a, 142b). The ordinate represents YD(Y) with arbitrary scales. Photon energies are (a) 1.37 and 2.75 MeV, (b) 0.66 MeV, (c) approximately 60 keV. Note that the shape of the function between 3 and 10 keV/μm varies little with photon energy. Neutron energies are 14.6 MeV and 2.95 MeV. Peaks can be seen for protons (that have a maximum value of Y of about 100 keV/μm), for alpha particles (maximum Y of about 250 keV/μm) and for heavier ions (up to about 700 keV/μm).

distribution $f(\varepsilon)$ and its mean value $\bar{\varepsilon}$. In a major branch of microdosimetry that developed from experimentally-measurable proportional counter quantities (112,143), the quantity ε itself plays only a minor role compared to the two derived quantities lineal energy y and specific energy z defined as:

$$y = \frac{\varepsilon}{\bar{l}} \qquad z = \frac{\varepsilon}{m_v} \tag{9.11}$$

where $\bar{l}$ = mean chord length of volume element (for convex bodies $\bar{l}$ is four times the volume divided by the surface area)

m_v = mass of volume element.

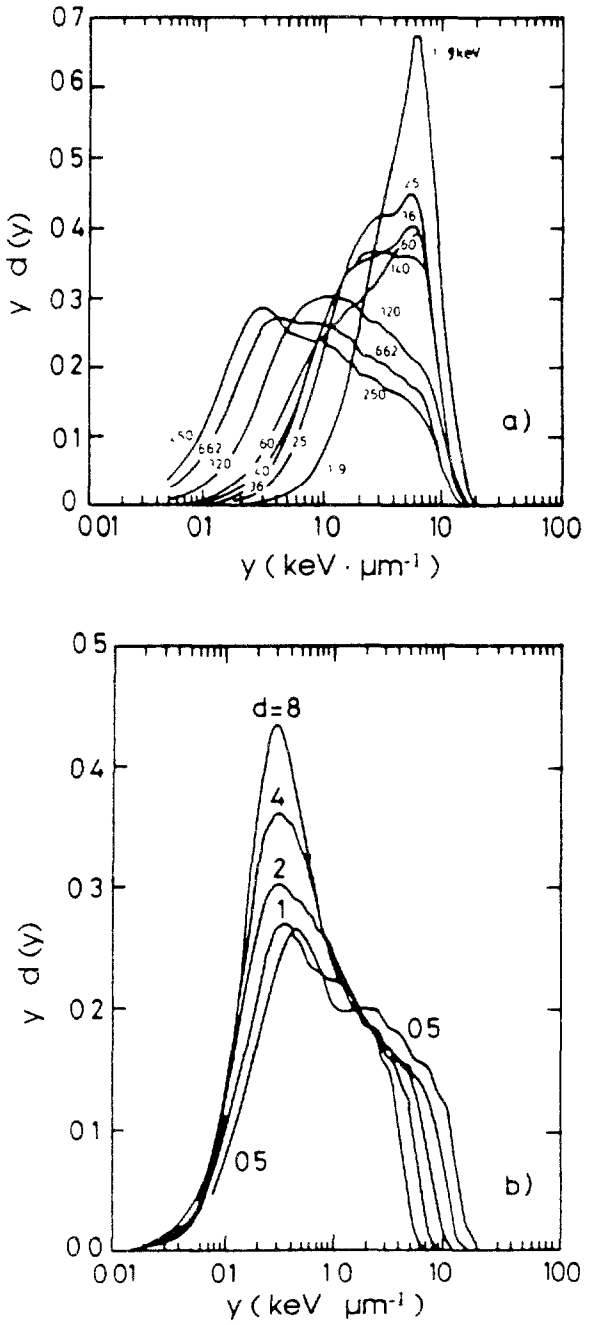

Figure 9.35 Spectra of lineal energy y for (*a*) a 1-μm-diamter site and various photon energies; (*b*) ^{60}Co γ rays and various site diameters (μm); adapted from Ref. 79, data from Ref. 144.

Distributions of y and z in a spherical volume element of tissue show large differences for sparsely ionizing radiations (photons) and densely ionizing radiations (neutrons) (Figure 9.34) and also differences among photon fields (Figure 9.35). This can be understood from the preceding discussion of the respective secondary particles and their track structure properties. Thus measured y or z spectra might be used to derive particle and energy radiances of the incident radiation and thus provide the basic information needed for a more appropriate classification. For tissue-like volume elements of dimensions greater than about 0.3 μm, y and z spectra can be measured experimentally and also computed from track-structure simulations for comparison (145, 145a-f). For much smaller dimensions the computational methods are essential because experimental measurement is usually not possible (112,146).

The first moment, $\bar{y}_F$, of the distribution and the second moment divided by the first moment, $\bar{y}_D$, are also characteristics of the energy deposition by radiation in a particular site (Figure 9.36) and have been used for classification in microdosimetry (112,114,143). However, all these distributions depend on the size and shape of the volume element of interest, and thus this information must be stated for each y or z spectrum and for their mean values. The frequency mean specific energy $\bar{z}_F$ has wide application as a normalizing factor because the event frequency per unit macroscopic dose is $1/\bar{z}_F$ (112,146). The dose means, $\bar{z}_D$ and $\bar{y}_D$, have application only for very much more restricted assumptions (112,146).

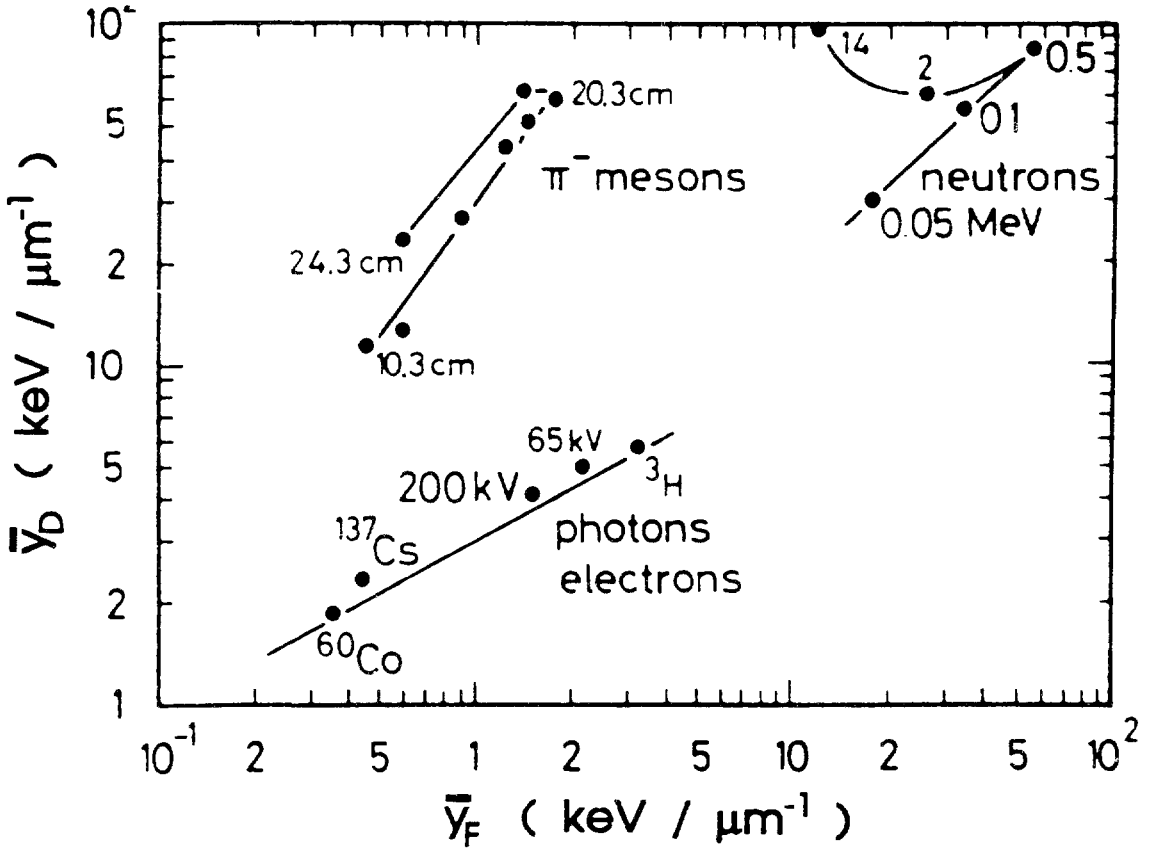

Figure 9.36 Second moment divided by first moment, $\overline{y_D}$, vs. first moment $\overline{y_F}$ of linear energy spectra in 1-μm-diameter sites for various radiation fields (112).

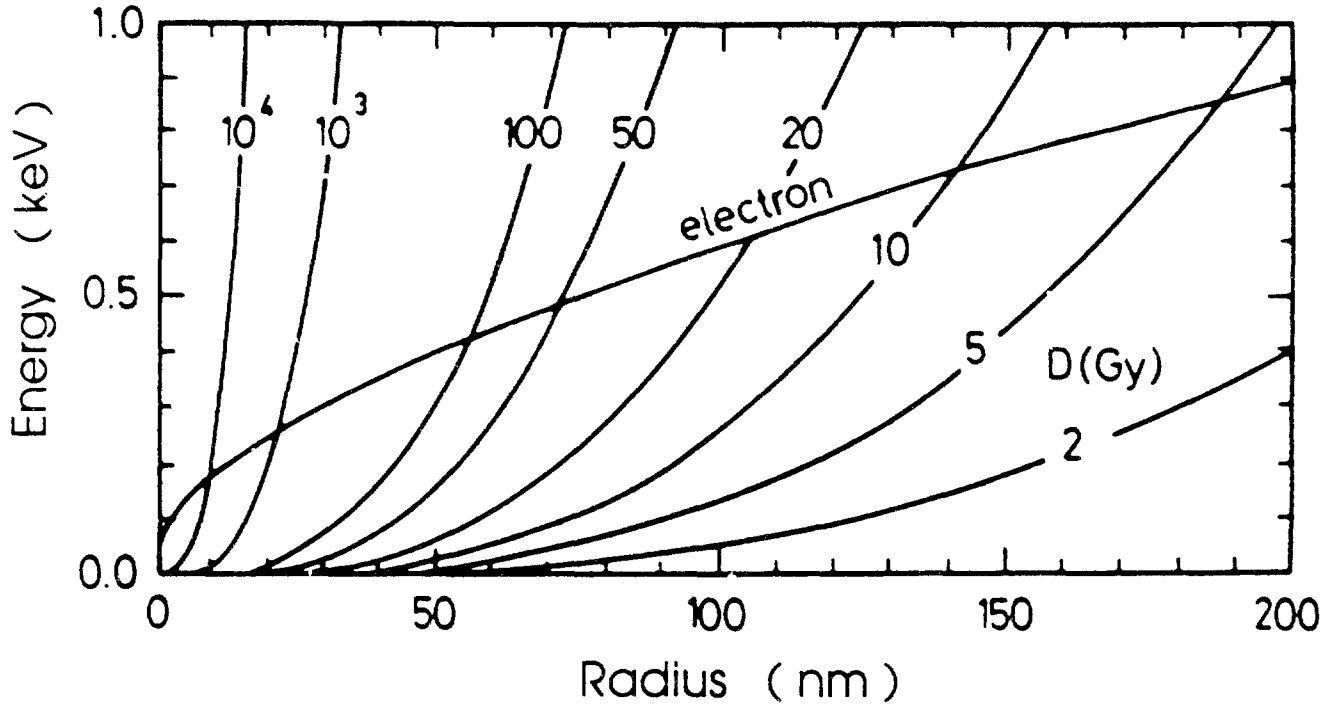

Figure 9.37 Comparison of inter- and intratrack contributions to the energy imparted within spheres around arbitrary activations in high-energy electron tracks: "electron" indicated the intratrack component, the parameterized lines show the intertrack part as a function of absorbed dose (112). The curve labelled electron correspond to the proximity function T(r) for a single high-energy electron.

Another possibility to classify track structures within the concept of microdosimetry is the integral proximity function $T(r)$. It gives the average energy deposited around initial species as a function of radial distance (112). For one track $T(r)$ increases with increasing distance. At higher doses it includes a contribution from an "average" single track (intratrack) and a component from track overlaps (intertrack) (Figure 9.37). The objections raised against dose and possibly wrong averages also apply to the above microdosimetric descriptions.

It is sometimes more useful to obtain and present the energy deposition information as spectra of ε directly rather than converting to y or z. In this way, for example, chemical and biological consequences of given events in DNA can be estimated empirically or on the basis of numbers of ionizations or excitations in the events (see Section 9.6). Large consistent databases have been generated for many different radiations, evaluating absolute frequency distributions $f(\varepsilon)$ particularly in cylindrical volume elements of dimensions varying from 0.5 to 100 nm or larger (147-152) using the MOCA track structure codes for electrons, protons and alpha-particles (34,130). If other track structure codes are used, some differences in $f(\varepsilon)$ are obtained, particularly for larger values of ε in smaller volume elements (153,154). Frequency distributions have also been evaluated directly in terms of numbers of ionizations in the volume elements (130,155,156) but these are substantially dependent on the total ionization yield of the medium including its state of condensation (26,77,157).

9.4.4. Average Track Characteristics for Different Ions

At high speeds the track of an ion can be considered as consisting of separate track structures similar to those of a fast electron. On the other hand an ion with energy E < 10 MeV/u produces a region of continuous ionizations and excitations consisting of overlapping spurs (10). The inner cylindrical part of this region is then characterized by the increased concentration of ionizations and excitations and is called a *core*. The region of track outside the core is called *penumbra* (Figure 9.38). It is characterized by a "diffuse" concentration of ionizations and excitations and is formed by electrons with enough energy to leave the core.

Inside the core the density of ionizations and excitations is produced by both the primarily ion itself and by secondary electrons it has generated. In this model the core has the shape of a cylindrical column with a radius r_{core}. The value of r_{core} is estimated on the basis of the direct action only of the primary ion. There are several formulas for r_{core}. Mozumder (10) defined r_{core} from qualitative considerations equating the effective time of collision and the average time of the quantum transition on the lowest excited level (transition energy $\hbar\omega_{01}$) as

$$r_{core} = \frac{v}{2\,\omega_{01}} \tag{9.12}$$

where v is the speed of the ion. Kaplan and Miterev (21) defined r_{core} by equating to zero the distribution function of the probability of exciting a molecule to the lowest excited level. According to Ref. (21),

$$r_{core} = \frac{\pi\, v}{\omega_{01}} \tag{9.13}$$

This expression is 2π times greater than (9.12).

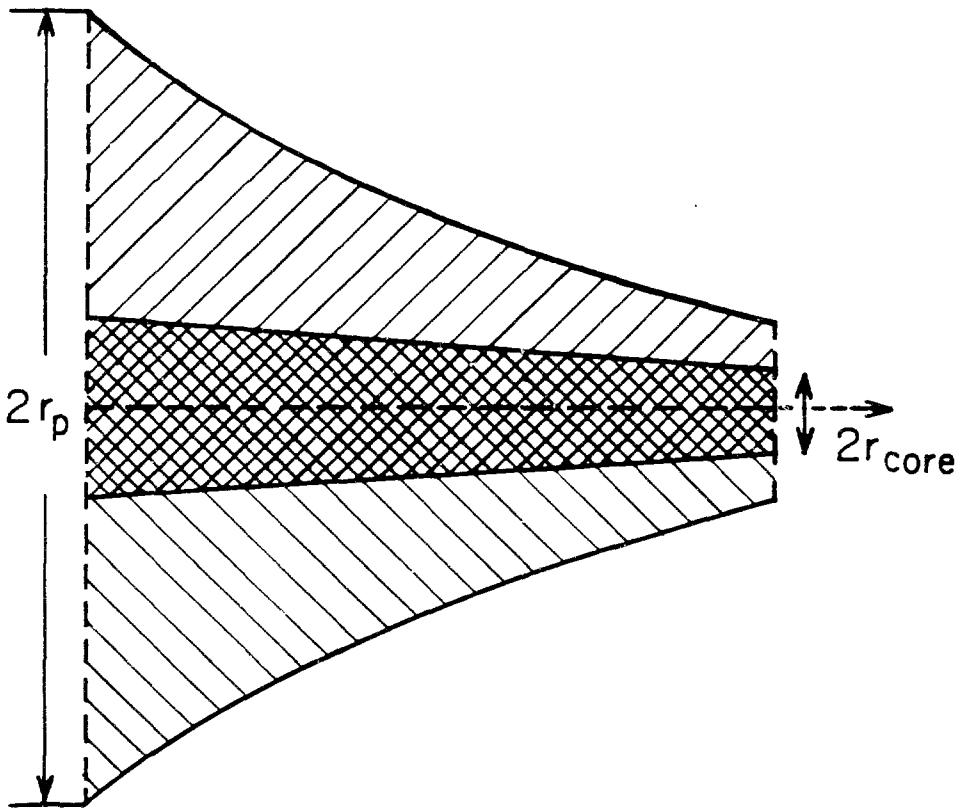

Figure 9.38 The geometrical picture of heavy ion track; r_p is the radius of penumbra which is equal to maximum range of δ-electrons, r_{core} is the radius of a core.

Formula (9.13) is valid for nonrelativistic speeds of an ion, when $\beta^2\varepsilon(\omega) \ll 1$, where $\beta = v/c$, $\varepsilon(\omega)$ is the dielectric permittivity. The formula for r_{core} for arbitrary velocities of an ion taking into account the dielectric properties of condensed medium was obtained by Miterev (158). It can be transformed to the following form:

$$r_{core} = (\sqrt{2\pi}\,\beta c / \omega_{01}) / \left\{ \left[|1-\beta^2\varepsilon_1(\omega_{01})|^2 + \beta^4\varepsilon_2^2(\omega_{01}) \right]^{1/2} + |1-\beta^2\varepsilon_1(\omega_{01})| \right\}^{1/2} \quad (9.14)$$

where $\varepsilon_1(\omega_{01})$, $\varepsilon_2(\omega_{01})$ are real and imaginary components of the dielectric permittivity. For $\beta^2\,\varepsilon \ll 1$ the formula (9.14) is similar to the formula (9.13). But in contrast to the monotone behaviour of (9.13), r_{core} according to the formula (9.14) takes a maximum value at $\beta = [\varepsilon_1(\omega_{01})]^{-1/2}$. For increases of speed above this value, the radius of r_{core} decreases (relativistic reduction). In Table 9.1 are presented the dependence r_{core} on the speed of charged particle for water ($\hbar\,\omega_{01} = 8.4$ eV).

The distribution of excited and ionized molecules produced directly by the primary ion inside the core of the track can be found from the following formula:

$$N_{oj}(r) = n\,P_{oj}(r) \quad (9.15)$$

where n is the concentration of molecules, and $P_{oj}(r)$ is the probability of creation of the electronic state j by direct action of the primary ion at radial distance r. In the nonrelativistic case, when $\beta^2\,\varepsilon \ll 1$ a sufficiently good approximation for $N_{oj}(r)$ is

$$N_{oj}(r) = \frac{2\,Z^2\,e^4 F_{oj}\,n}{m\,v^2\,\hbar\,\omega_{oj}\,r^2} \exp\left[-\frac{\omega_{oj}^2\,r^2}{2\,v^2} \right] \quad (9.16)$$

where Z is the ion charge and F_{oj} is the oscillator strength; in the condensed phase it is obtained by integrating the continuous distribution of the oscillator strengths (9.19) over the peak width. According to this formula, N_{oj} decreases very rapidly with increase of r and this decrease is steeper the smaller the ion speed.

The distribution of excitations and ionizations produced by knocked out secondary electrons can be calculated by the Monte Carlo method. In the model of continuous slowing down an analytical expression can be obtained (Butts and Katz (159), Miterev *et al* (160)), which is more convenient in a number of practical applications. When the range of an electron R (E) ~ E, this analytical expression can be presented in the following form:

$$q(r) = \frac{2\,\pi\,Z^2\,e^4\,N_v\,n}{m\,v^2\,r^2}\left(1 - \frac{r}{r_{max}}\right) \quad (9.17)$$

where N_v is the number of valence electrons in the molecule, and r_{max} is the range of electrons with maximum energy.

Now let us consider the track characteristics for ions with different charges. In Table 9.2 we compare the characteristics of tracks of protons and α-particles with the same stopping power. The difference between them is based on the difference in their charges. The stopping power is roughly proportional to the factor Z^2/v^2. So for the

Table 9.1.

The dependence of r_{core} on the velocity of charge particle for water according to formula (9.14).

Velocity $\beta = v/c$	Energy MeV/u	r_{core} nm
0.01	0.047	0.74
0.1	4.73	7.4
0.25	30	19.0
0.5	145	52.4
0.693	363	118.0
0.75	480	96.8
0.9	1214	73.3
0.935	1707	70.8
0.999	20047	68.4

Table 9.2.

Characteristics of tracks of protons and α-particles with the same LET in water*

Track Characteristics	**proton**	**α-particle**
LET, eV/nm	98	98
Energy, MeV	0.082	4.5
Speed, 10^8 cm/s	4	15
Core radius, nm	1.2	4.5
Maximum energy of δ electrons, keV	0.18	2.2
Penumbra radius, nm	3.74	65.7
Average density of energy absorption in track core,		
eV/nm^3	19.2	1.56
eV/molecule	$5.8 \cdot 10^{-1}$	$4.7 \cdot 10^{-2}$
Average density of ionizations in track core, nm^{-3}	1.16	$9.4 \cdot 10^{-3}$
Average density of ionizations in the track, nm^{-3}	$1.3 \cdot 10^{-1}$	$4.3 \cdot 10^{-4}$

* Kaplan and Miterev (unpublished).

Table 9.3.

Characteristics of tracks of α-particles and multicharged ^{127}I ions with the same speed in water*

Track Characteristics	**α-particle**	**^{127}I ion**
Speed, 10^8 cm/s	10	10
Energy, MeV	2	63.5
Effective charge	1.86	10.76
LET, eV/nm	146.8	4920.6
Number of δ electrons per 1 nm track length	3.2	117
Core radius, nm	2.4	2.4
Penumbra radius, nm	29.3	29.3
Average density of energy absorption in track core,		
eV/nm^3	4.48	150
eV/molecule	0.134	4.49
Average density of ionizations in track core, nm^{-3}	$2.7 \cdot 10^{-1}$	9.04
Average density of ionizations in the track, nm^{-3}	$4.9 \cdot 10^{-3}$	$1.6 \cdot 10^{-1}$

* Kaplan and Miterev (unpublished).

same stopping powers the speed of α-particles is almost 4 times greater than the speed of protons if we neglect a weak dependence of the logarithmic term. This is the reason for different values of E_{max} (for secondary-electrons) and radius of penumbra r_p. The r_p is greater for α-particles and as a consequence the average concentration of ionizations created in the tracks of the α-particles is lower than in the proton tracks.

In Table 9.3 we present the characteristics of tracks of α-particles and multiply-charged ^{127}I ions with the same speed. The high value of the effective charge of iodine results in a very high stopping power. We see that the number of ionizations and their concentration are extremely high for a multicharged ion. The number of ionizations near the axis of the track of a multicharged ion exceeds the number of molecules. We can conclude that each molecule undergoes multiple ionization and with great probability dissociates into fragments. This fact can be very important for radiation effects.

9.4.5. Linear energy transfer

Higher densities of events in charged particle tracks are often more effective than lower densities in producing certain radiation effects (though sometimes the opposite is true). Therefore, concepts have been put forward to classify radiation track structures according to their stopping power or their stopping power distribution (161). The average energy locally imparted to the medium is called *L*inear *E*nergy *T*ransfer (LET), which is essentially the same quantity as stopping power.

Energetic ionizing radiation can lead to the ejection of energetic secondary electrons. These electrons can travel considerable distances away from the path of the primary particle and virtually form sparse density tracks of their own. Therefore, modified classifications have been put forward (161) that neglect the energy expended in sparse tracks because it is almost "wasted". This neglect can be introduced either by an energy cutoff (L_q) in the energy transfer distribution or a radius cutoff (L_r) in the radial distance up to which energy is considered "locally imparted" (161). Figure 9.39 demonstrates the effect of extending the integral over the energy transfer distributions (essentially the secondary electron kinetic energy distributions) only up to the cutoff energy q (162-164). Around 50% of the stopping power is contained in energy transfers below 100 eV and thus remains rather close (say, within a few nanometers) to the point of interaction.

Whereas L_q can readily be calculated from basic differential cross sections by simple integration but not measured directly, L_r, which is the energy absorbed locally at a certain radial distance from the path of a primary particle, has been measured for

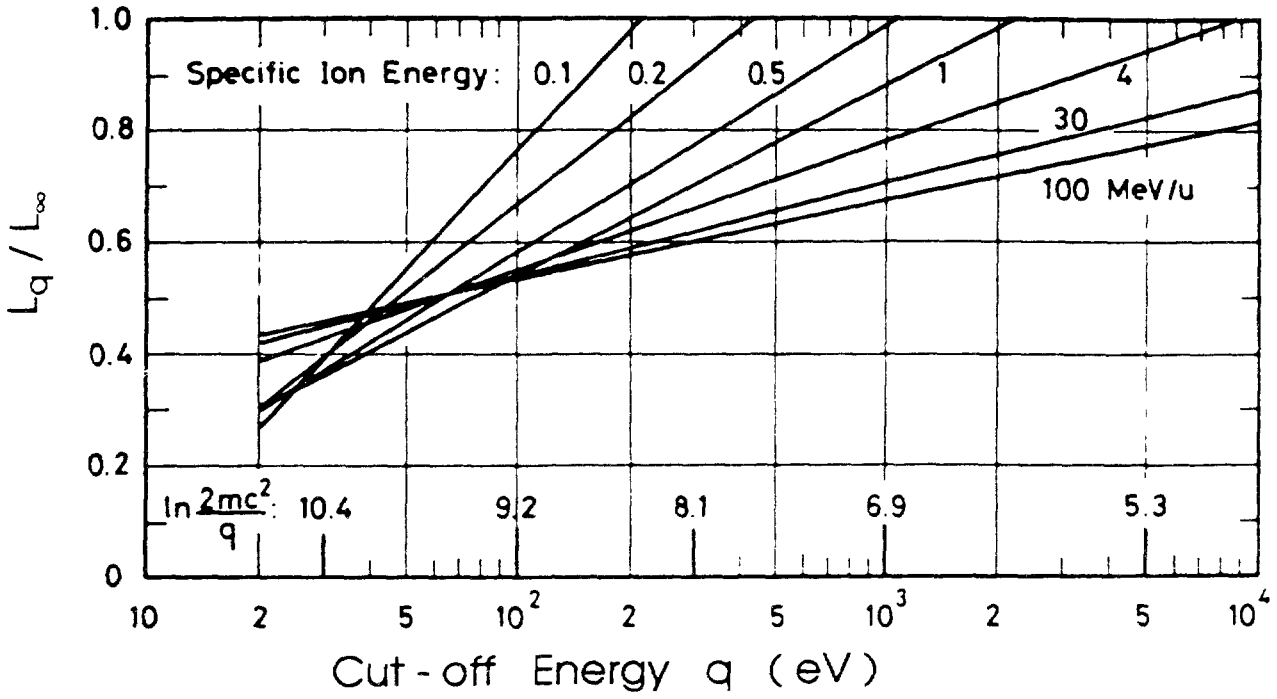

Figure 9.39 Ratio of the energy restricted stopping power L_q to the unrestricted stopping power L_∞ for various specific ion energies as a function of cutoff energy (162,163).

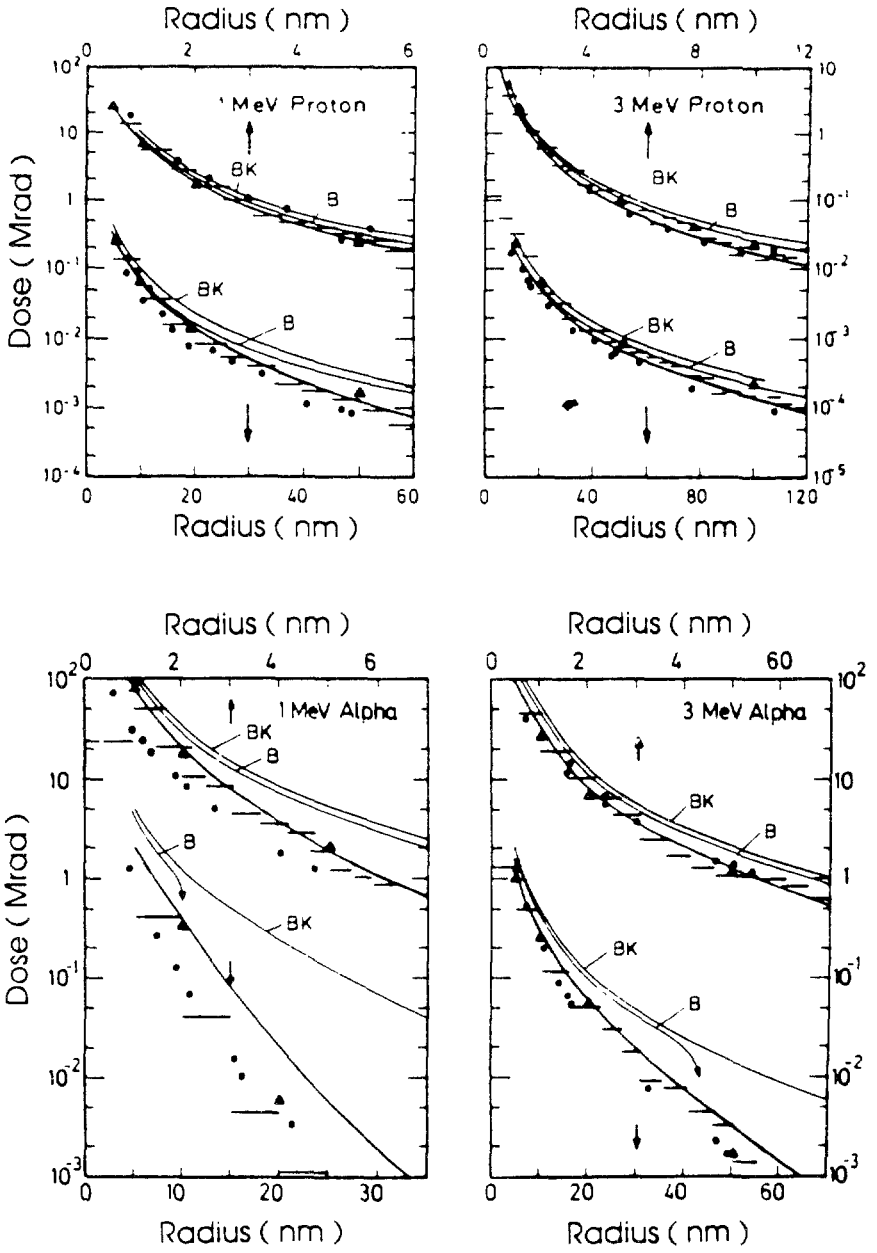

Figure 9.40 Calculated radial dose profiles around photon paths and α particle paths in tissue equivalent [csda (heavy line), mixed csda-Monte Carlo (triangles), and full Monte Carlo (histograms) models, for explanation see Ref. 88] compared to experimental data (•, Ref. 165), Baum's model (B, Ref. 166), and the model of Butts and Katz (BK, Ref. 159).

several fast ions and used to check the reliability of track structure calculations (159,165-180) (Figure 9.40). In general, these radial dose profiles decrease approximately with $1/r^2$ up to the range of the maximum energy secondary electrons, which is proportional to the ion energy. They are also proportional to the square of the (effective) charge of the incident ion.

These general properties are depicted in Figure 9.41a, which also shows the contributions of secondary electrons ejected from inner and outer shells of target molecules. Based on such radial dose distributions averaged along the ion path, Katz has put forward an empirical classification scheme (18-20,159) that agrees with many observations.

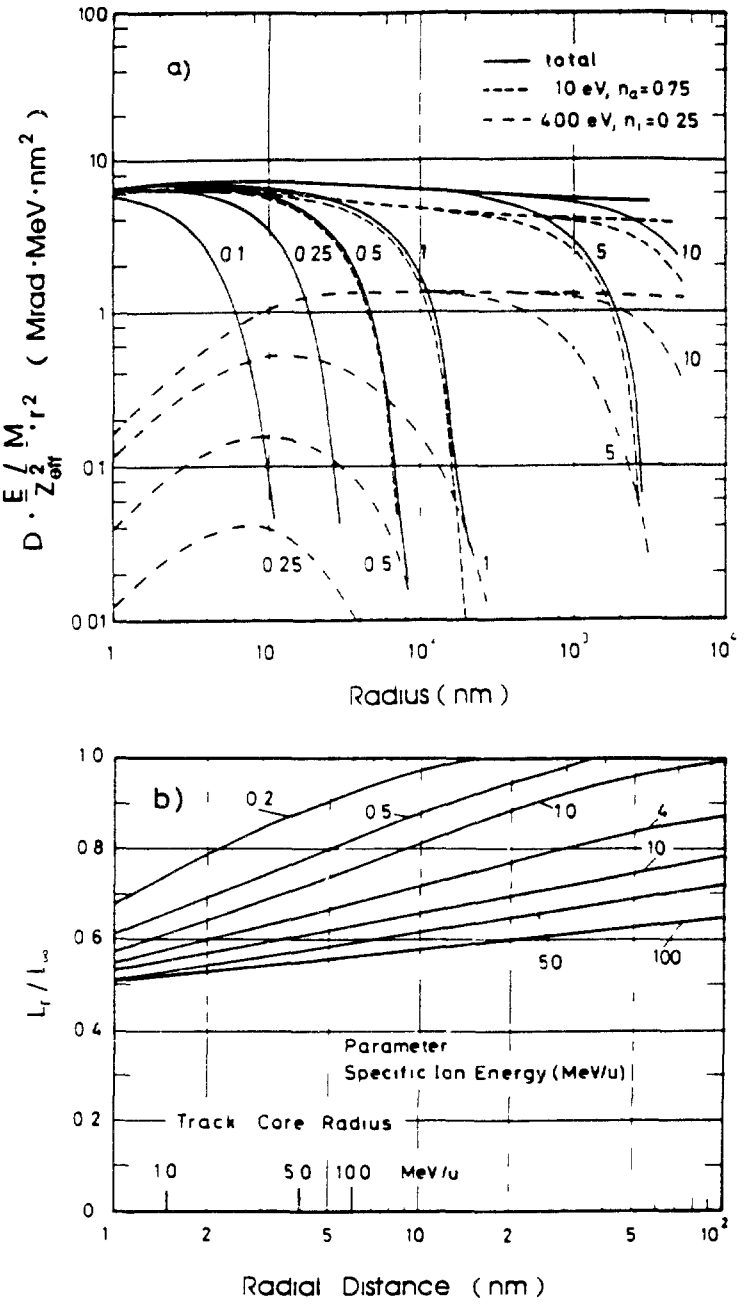

Figure 9.41 (*a*) Generalized radial dose profiles around heavy-ion tracks in a model substance (outer shell potential 10 eV, electron occupation fraction 0.75; inner shell potential 400 eV, electron occupation fraction 0.25). (*b*) Quotient of radius restricted stopping power L_r to unrestricted stopping power L_∞ as a function of radial distance from the ion path. For comparison the adiabatic limit for excitations is indicated as track core radius (175) for several specific ion energies.

Figure 9.41b shows calculated L_r/L_∞ ratios (L_∞ is the unrestricted linear energy transfer and is thus essentially equal to the stopping power). As mentioned above, a large fraction of the energy lost by fast ions stays within the first nanometer around the path, but with increasing ion energy a large fraction can be transported by energetic electrons to large distances from that path. Also shown in this figure is the radius of the so-called track core as introduced by Mozumder and Magee (175), see Section 9.4.4.

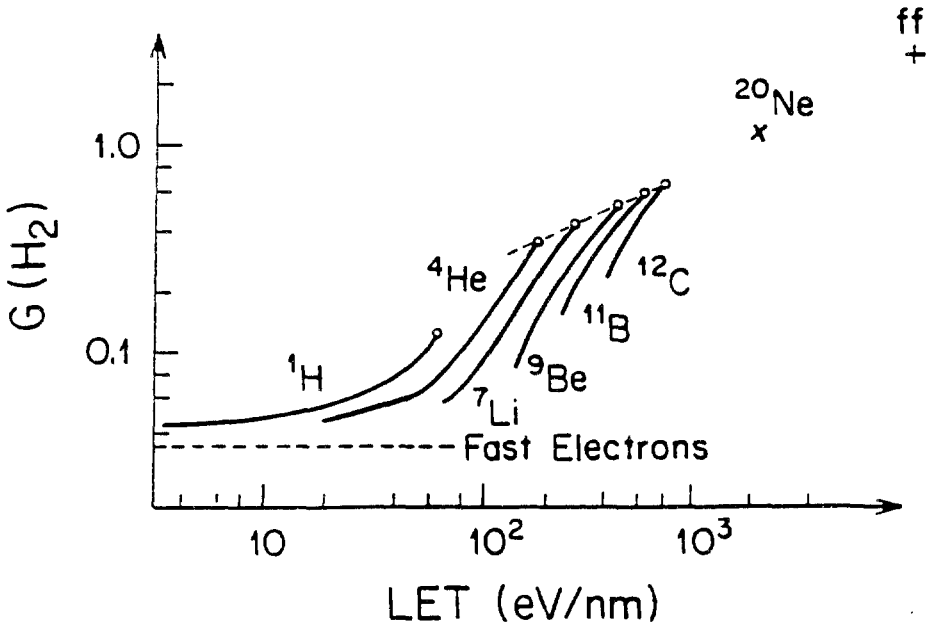

Figure 9.42 Variation of the differential molecular hydrogen yield $G(H_2)$ with ion LET in benzene for the various ions. (La Verne and Schuler (181)).

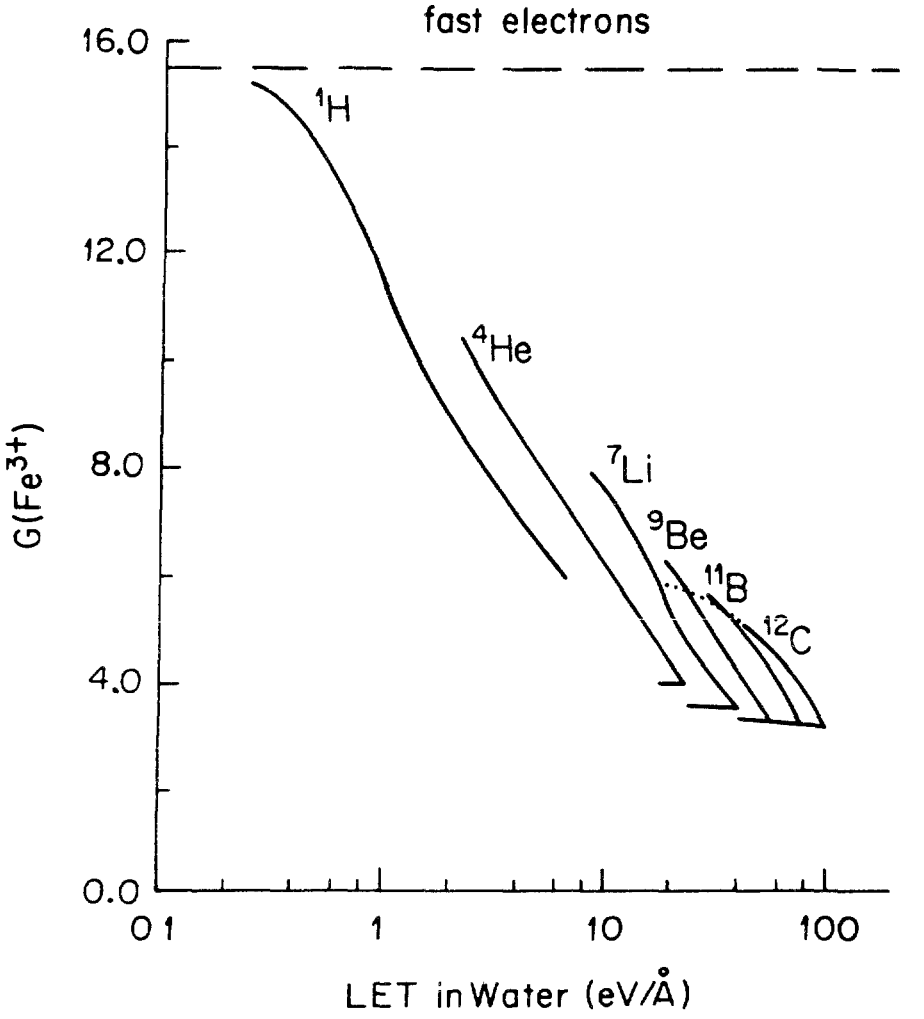

Figure 9.43 Differential Fe^{3+} yields in aerated Fricke dosimeter for the various ions as a function of ion LET (La Verne and Schuler (182)).

One of the important questions is the following: can LET be a universal characteristic of the quality of radiation? If we consider radiochemical and radiobiological actions the answer is very definite: it cannot be. Experimental evidences have been demonstrated by La Verne and Schuler (181,182) see Figure 9.42 and 9.43. The same value of LET corresponds to different values of $G(H_2)$ and $G(Fe^{3+})$, if we irradiate benzene or Fricke dosimeter by different ions. The reason for such behaviour has already been explained above when we discussed Table 9.2. For equal stopping powers an ion with greater Z has greater speed and can create faster δ-electrons which spread their energy over larger distances. As a result for an ion with greater charge the same energy spreads in a greater volume and as a consequence the value of $G(H_2)$ in benzene is lower for an ion with greater charge. For these reasons $G(Fe^{3+})$ also is lower for the ion with greater charge.

So we conclude that LET should not be used as a sufficient characteristic of radiation effect when we compare different ions. This conclusion is not surprising because LET is a one-dimensional characteristic but all reactions proceed in volume. From all this follows an important conclusion for chemical dosimetry: each type of radiation must have its own dosimetric curve. The well known curve of Bibler (183) for a Fricke dosimeter cannot be recommended for practical dosimetry.

Thus, LET cannot serve as a universal characteristic of radiation quality. Attempts have been undertaken to introduce other parameters instead of LET, but they were unsuccessful. This can be understood because the identical set of track structures can be obtained only for charged particles with all the three parameters being equal (charge, speed and mass), i.e. only in the case of a particle and its antiparticle. For particles differing in at least one parameter the track structures will be different. This is obvious for particles that differ in charge or in speed (see Tables 9.2, 9.3).

The differences in the track structures are less obvious if the particles differ only in mass. To reveal these differences it should be taken into account that a heavy particle under other equal conditions (equal Z and v) is more slowly retarded in the matter as compared with a light one. Therefore, the change of distributions (9.16) and (9.17) along the trajectory of particles of different mass will be different. The track of a particle with lower mass is more compressed. As a result averaged concentration of the primary active particles in this case will be higher.

For example let us consider protons with the energy of E_p = 100 MeV and electrons with E_e = 55 keV. They have almost the same values of ν and the initial LET values are also rather close (S^p = 0.75 eV/nm, S^e = 0.6 eV/nm). When such electrons pass through the water layer of 5.10^{-3} cm thickness their energies decrease down to E_e = 7.5 keV, and the LET value increases up to S^e = 2.5 eV/nm. By contrast the protons traverse this same layer of water without any practical change in the energy and LET values. Due to such rapid slowing down the electrons will form more dense track structures in a layer than the protons.

As was discussed above there is no universal parameter of radiation quality. However, for practical purposes (e.g. simulation or prediction of particular radiation effects) it is desirable to have at least an approximate parameter by means of which it could be possible to estimate the radiation effect when we substitute one type of radiation for another.

A useful characteristic of the ion track for some purposes can be the average specific energy absorption in the track core D_c (184):

$$D_c = \frac{S - S_\delta}{\pi r_{core}^2} \tag{9.18}$$

where S is the energy transferred by the primary ion to the electrons of a medium per unit length of the track; S_δ is energy carried by secondary electrons to outside the core. The track characteristic D_c takes into account the three-dimensional character of energy absorption in the microvolume of irradiated matter and is mainly dependent on the parameters of the primary ion. Therefore, it can be used as an approximate equivalence parameter.

The correlation of radiation effects of different ions with D_c value were applied to the radiolysis of benzene by La Verne and Schuler (181). In Figure 9.44 we presented the differential yields $G(Fe^{3+})$ in a Fricke dosimeter (182) as a function of D_c, calculated according to formula (9.18). The value of r_{core} was calculated according to (9.14). We see that beginning with ^7Li ions the $G(Fe^{3+})$ curves as a function of D_c are close to each other. So the representation of $G(Fe^{3+})$ as a function of D_c removes the ambiguity which exists in the LET dependencies of $G(Fe^{3+})$, when for one type of an ion there are several values of $G(Fe^{3+})$ corresponding to the same LET value (see Figure 9.43). Although the representation of differential yields as a function of D_c does not allow to exclude completely the dependence of the radiation effect on the ion type, nevertheless, by means of D_c one can make more realistic estimations of the change of effect under substitution of one type of an ion for another.

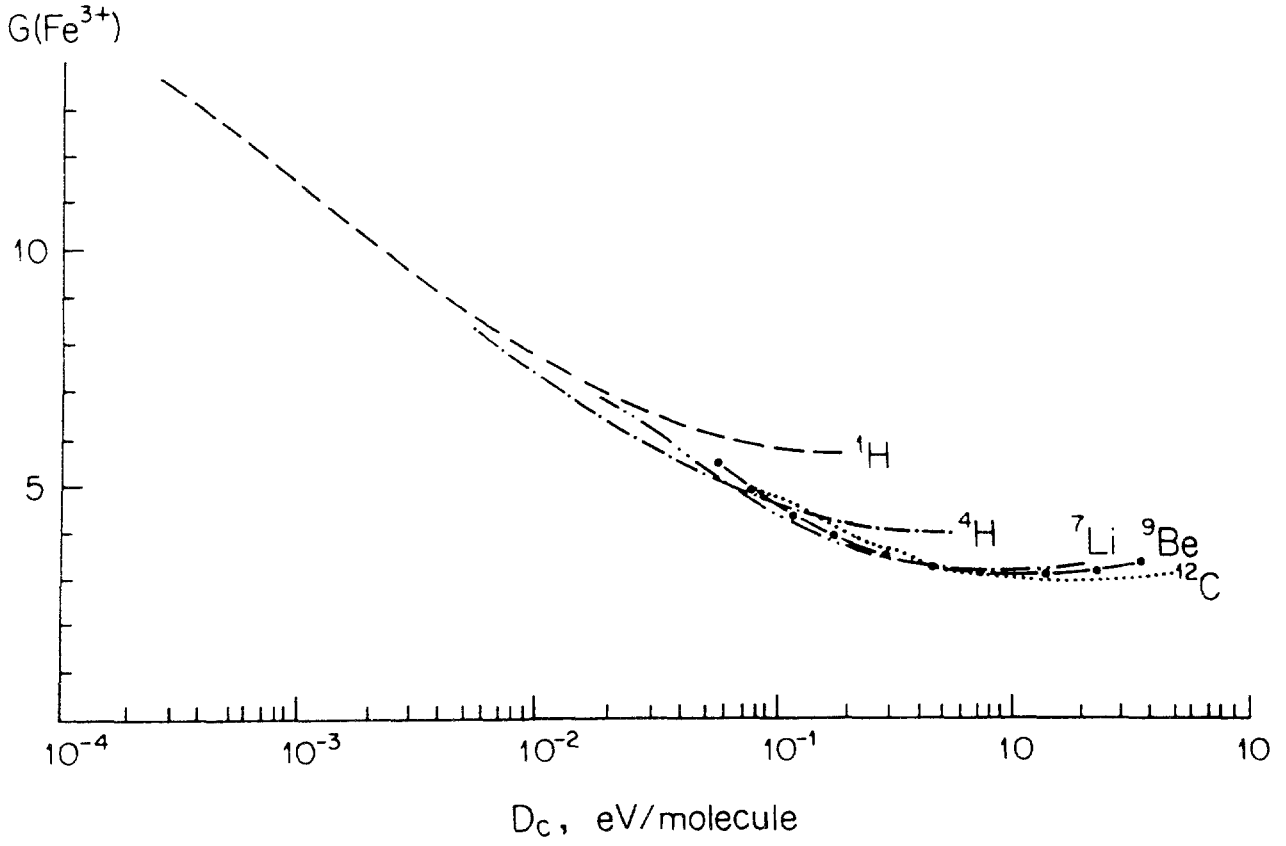

Figure 9.44 The dependence of $G(Fe^{3+})$ on D_c (eqn. 9.18) for different ions (184).

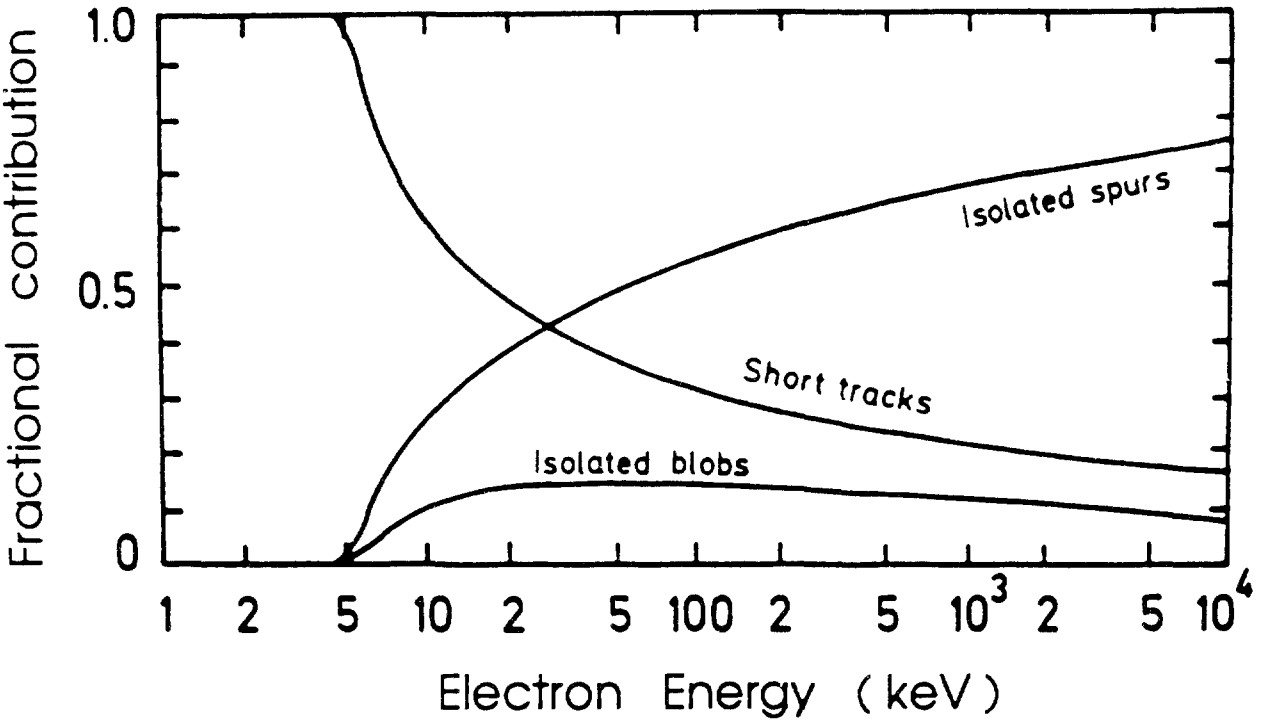

Figure 9.45 Track structure classification by so-called track entities spurs, blobs, and short tracks (10).

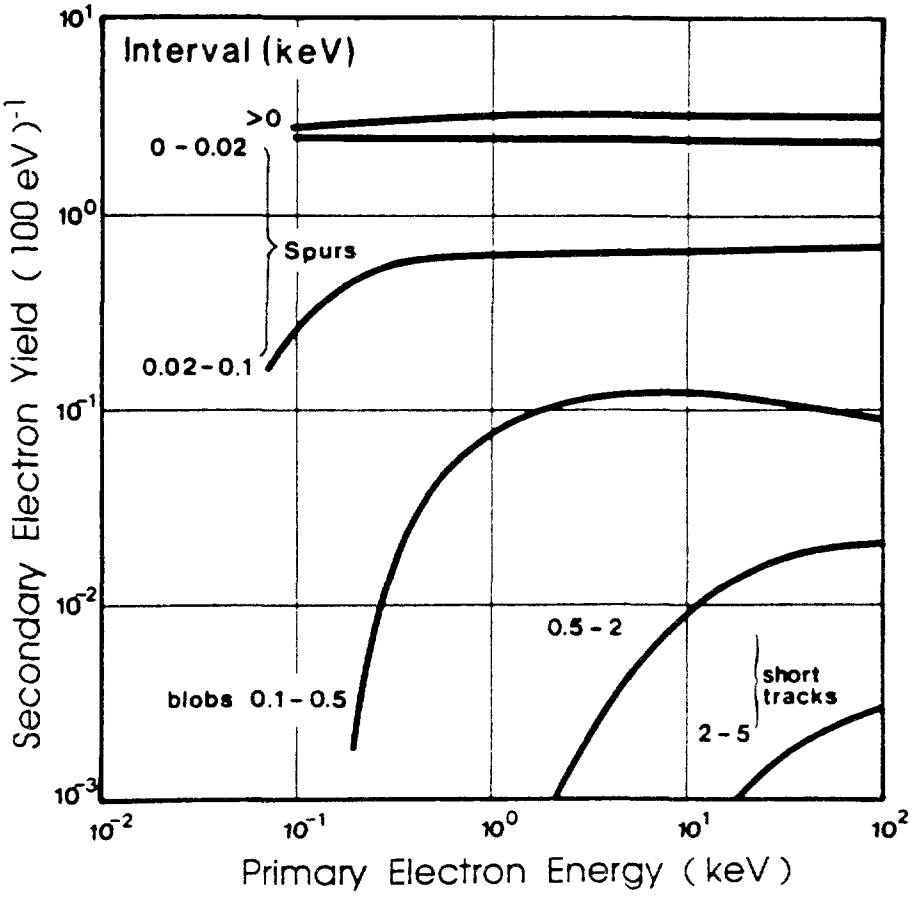

Figure 9.46 Yields in water vapor of secondary electrons in energy intervals relevant to track entity classification.

In conclusion of this section we note that LET concepts and radial dose concepts for the classification of track structures depend also on the validity of the averaging procedure. If an effect depends on the types and actual densities of events on a microscopic scale, averages of the initial energy depositions can lead to doubtful conclusions. In many radiation effects averages are meaningful only for final yields, after the reactions are complete. Energy density in itself does not contain enough information.

9.4.6. Track Entities

Ninety-five percent of the energy loss events of fast electrons transfer less than 100 eV to matter. Each of the resulting low-energy electrons produces three or less additional ionizations during their own slowing down, which can be seen in the decrease of the yield curves (per 100 eV) in Figure 9.10. About 60% of them do not produce any further ionizations. Therefore, in most cases there are only one or a few events in such isolated spatial areas, which are called "spurs" (10,11,185-187), and the subsequent chemical reactions and their dynamics are quite different from those encountered in areas of higher ionization density. Areas of higher density are classified by Mozumder and Magee (10,11) as "blobs" (energy transfers between 100 and 500 eV) or "short tracks" (energy transfers between 0.5 and 5 keV). Secondary electrons produced in energy transfers above 5 keV are considered as "branch tracks", which are not likely to overlap with the other entities. The fraction of energy spent by fast electrons to form such entities is given in Figure 9.45. Figure 9.46 shows the yields of such entities for fast and slow electrons, depicting the decrease of secondary blobs and spurs at low electron energies. Similar calculations have been performed for electrons by Berger (191) and for radiation chemical yields from heavy charged particles by Turner *et al* (192) and Miller and Wilson (193). The high event density in blobs and short tracks favors recombination of radiogenic species over reaction with molecules of the material. The low-event density in spurs may favor reaction with molecules of the material (80,185-190).

The old concept of track entities is still a useful approach for the classification of track structures, since it takes into account the spatial arrangements of initial species, which affects their subsequent reactions. Refinement of this concept is needed in particular for heavy charged particle tracks.

9.4.7. Outlook for Other Clustering Concepts for Track Structures

In 1937 Gray stated that "the most natural unit of radiation dosimetry is the absolute increase of energy of the absorbing medium" (194), and dosimetric concepts (for example, LET) have been used for classification of track structures for many decades. However, dosimetric concepts are inadequate to explain recently observed differences between results obtained with different radiation fields. Track structures are a better starting point for classification. This is illustrated in Figure 9.47, which compares energy-based evaluation concepts (left panel) with event-based evaluation (right panel). Such evaluation or similar approaches can follow the principles outlines in Figure 9.48. First, track structures are measured [for example, in a low-pressure cloud chamber (196-198)] or calculated with an appropriate Monte Carlo program. Then the important distances and their distributions are derived from the structures. Finally, from these distributions of event densities reaction probabilities are computed and evaluated.

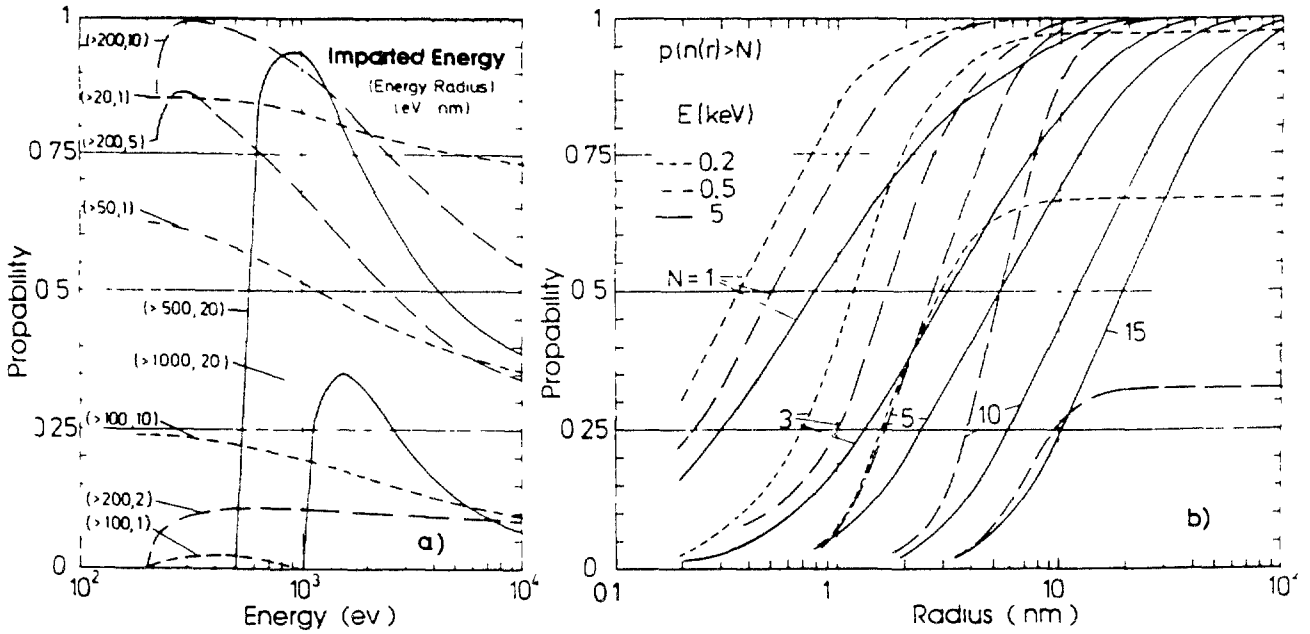

Figure 9.47 (*a*) Probability of finding more than a certain imparted energy within a certain radial distance around an excitation or ionization in electron tracks as a function of electron start energy. (*b*) Probability of finding more than N additional ionizations within a certain distance r around an arbitrary ionization in water for electrons of 0.2-, 0.5-, and 5-keV start energy (136,195).

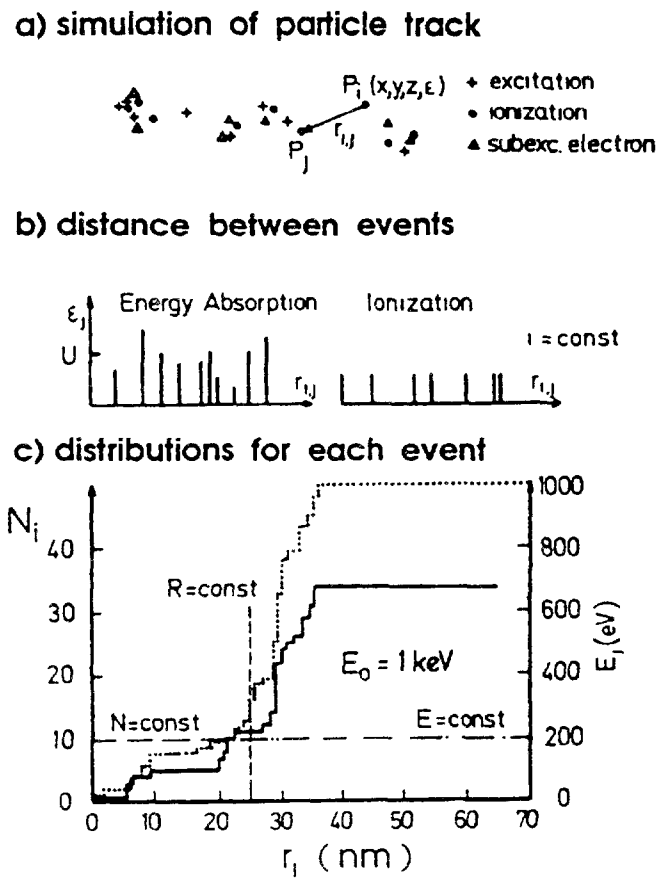

Figure 9.48 Some possibilities of track structure evaluation for the purpose of information reduction.

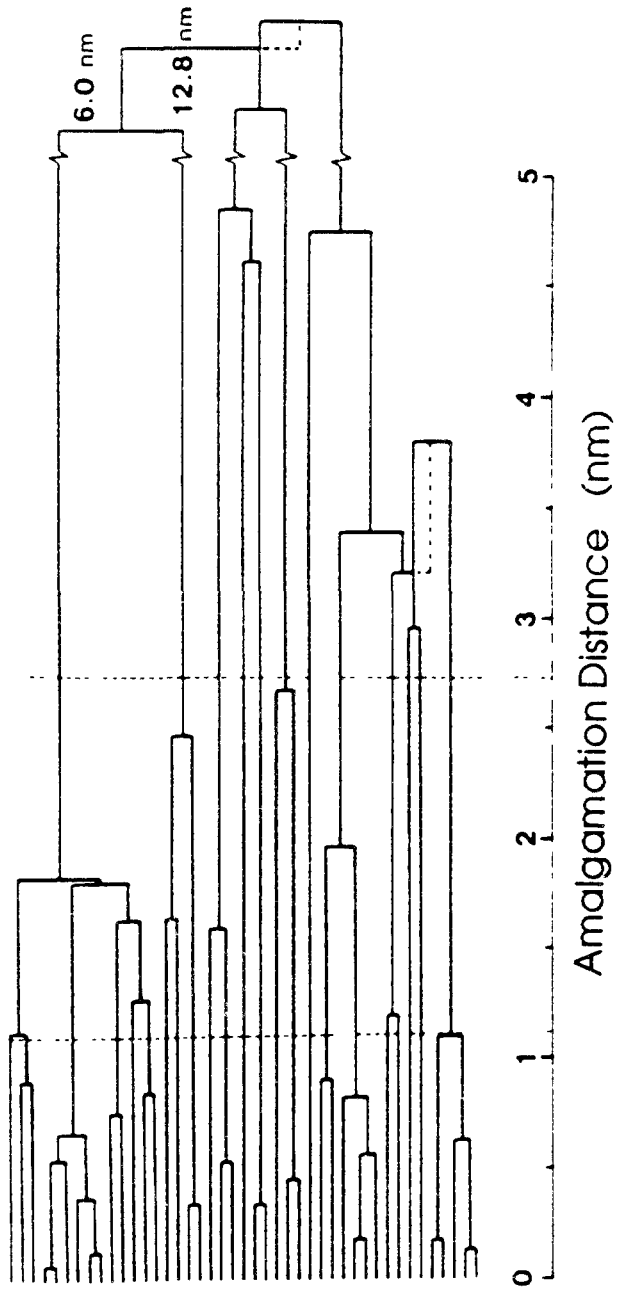

Figure 9.49 Dendrogram of 1-keV electron track using the *k*-means algorithm.

The evaluation can be made by using conventional cluster algorithms (199-203) designed for the analysis of more-dimensional data. Results from such types of classification can be displayed in the form of dendrograms (Figures 9.49 and 9.50). Here the merging to clusters of increasing sizes of closely located initial events is shown as a function of their increasing amalgamation distance (for example the square root of the sum of the distances of all members of a cluster to its virtual center) until the whole track forms one large cluster. The dendrograms of Figure 9.50 can be used to demonstrate that there are fewer events in electron tracks in water vapor than in liquid water (scaled for the density), they are further apart on a mass basis in the liquid (because of the assumed delocalization through plasmon diffusion), but the total track lengths scaled for the density are very similar (as is also expressed in the phase state insensitivity of stopping power).

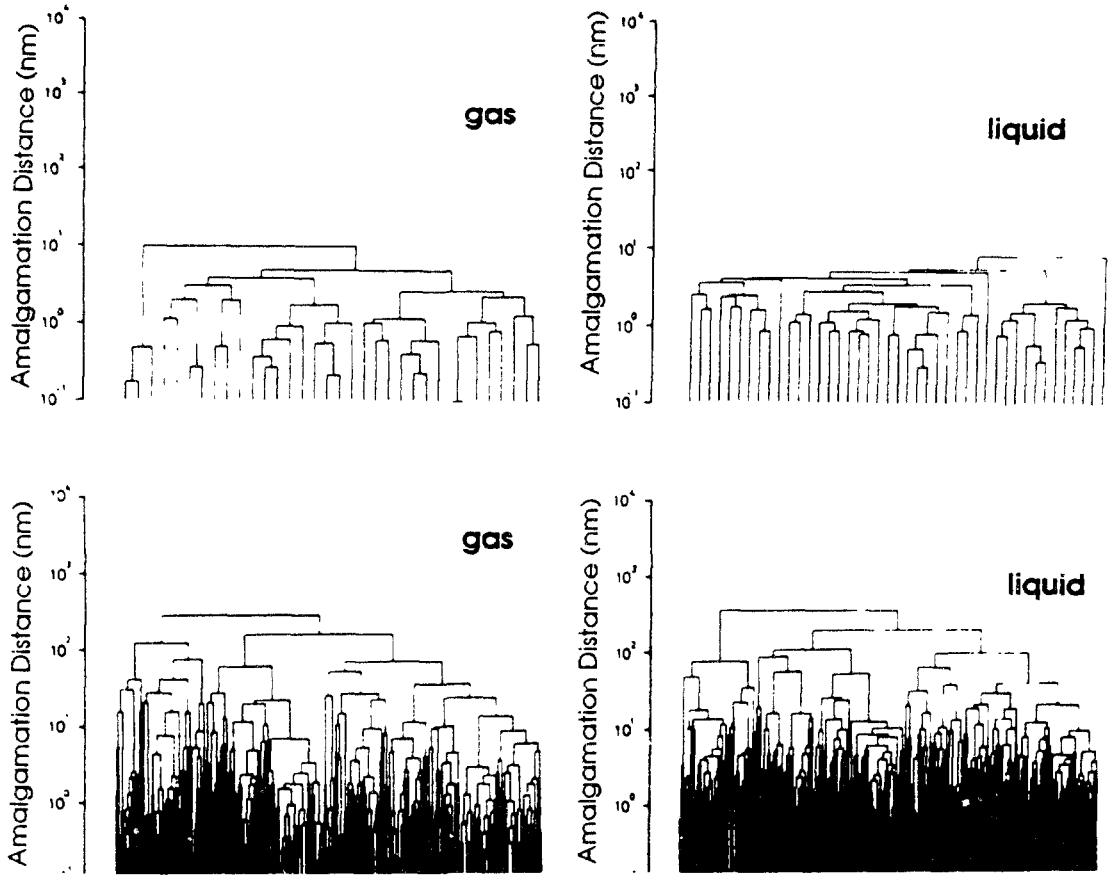

Figure 9.50 Dendrograms of single 0.5- and 5.0-keV electron tracks in water vapor and liquid water.

The classification of track structures requires further improvement. There are classification concepts used in other fields, for example, in fuzzy set theory (204-207), in pattern recognition, and in artificial intelligence (208-210), which should be explored for usefulness in this context.

9.5. PHASE EFFECTS

All substances of the living organism are in a condensed phase. So for simulation of penetration of charged particles through matter we must take into account the specific features of a condensed phase (210a).

One of them is the high density of a condensed phase as compared with gas and as a consequence the necessity of using such macroscopic characteristic as the dielectric permittivity $\varepsilon(\omega)$ (see Chapter 5, Section 5.5). The probability of energy losses by a charged particle in a condensed medium is described by the *energy loss function*, which is equal to the imaginary part of the inverse permittivity: Im $[-1/\varepsilon(\omega)]$. It is this function that determines the distribution of oscillator strengths in the liquid phase

$$F(\omega) = \frac{2\,\omega\,Z_m}{\pi\,\omega_{pl}^2}\ \mathrm{Im}\left[-\frac{1}{\varepsilon(\omega)}\right] \qquad (9.19)$$

where Z_m is number of electrons in a molecule, $\omega_{pl} = (4\pi N_e e^2 / m)^{1/2}$ is the plasmon frequency, N_e is the number of electrons in a unit volume of the medium, m and e are the mass and charge of an electron.

The distribution of the oscillator strengths of water in the condensed phase strikingly differs from that in the gaseous phase (210a). The discrete peaks at low energies that one observes in the gaseous phase transform into a continuous distribution with a wide absorption peak around 21 eV. The latter peak is often attributed to collective plasmon-type excitations (for details see review by Kaplan and Miterev (21). This peak is independent of the kind of condensed state: liquid or solid (see Figure 9.51a for ice) and is typical of various condensed materials, (see Figure 9.51b).

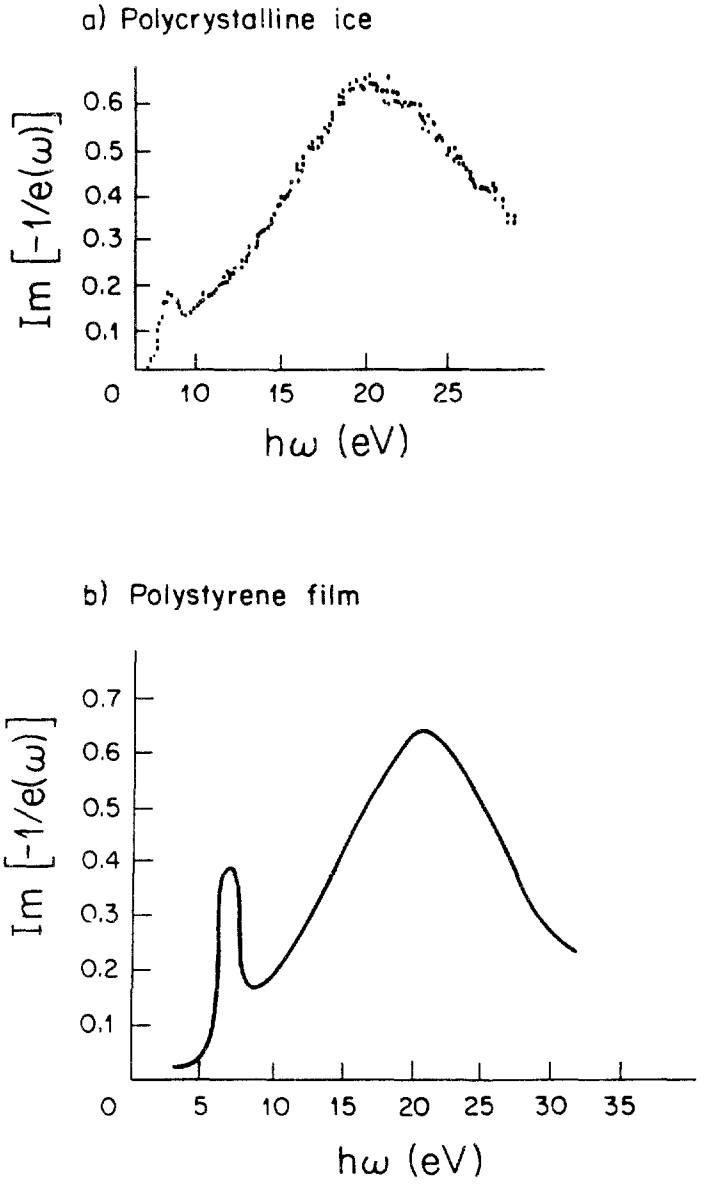

Figure 9.51 Spectra of energy losses in condensed phase for polycrystalline ice (184) and polystyrene film (211).

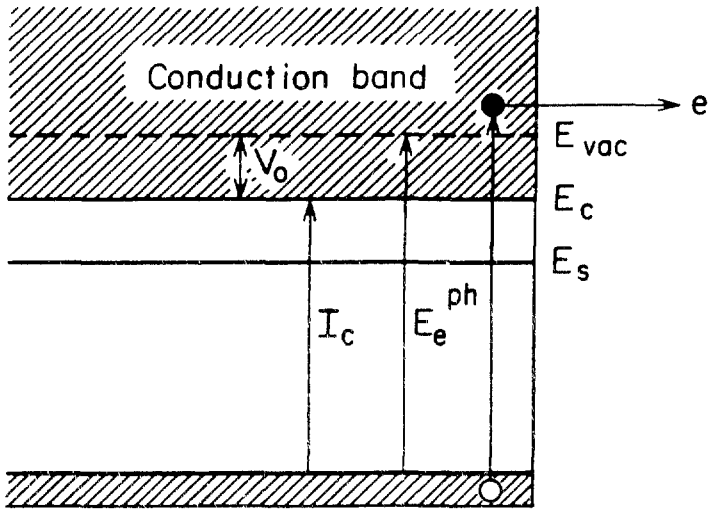

Figure 9.52 Scheme of energy levels in a dielectric. I_c is the ionization potential in the condensed state, E_e^{ph} is the photoemission threshold, V_o is the bottom energy of the conductivity band (E_c) counted off the vacuum level, E_s is the energy level of a solvated electron.

Another peculiarity of the condensed phase is the lowering of the ionization potential. In the condensed phase ionization takes place when an electron appears on the conductivity band, see Figure 9.52. The ionization potential I_c equals the energy needed to transfer an electron to the bottom of the conductivity band

$$I_c = E_c^{ph} + V_o \qquad (9.20)$$

E_c^{ph} is the photoemission threshold, V_o is the so-called work function which equals the energy the electron has at the bottom of the conductivity band. The ionization potential in a condensed phase I_c is connected with the ionization potential I_g in a gaseous phase by the following equation

$$I_c = I_g + P_t + V_o \qquad (9.21)$$

where P_t is the energy required for reorganizing the medium after one of the molecules has been replaced by a positive ion (this energy being approximately equal to the polarization energy). P_t and V_o are negative, so the ionization potential in a liquid phase is always lower than in a gaseous phase. The difference is the greatest for water, $\Delta I = I_g - I_c = 3.8$ eV.

The comparative simulation and computer experiments on interaction of fast electrons with water in liquid and gaseous phases with regard to the above mentioned specificity of the liquid phase have been performed by several groups (Turner *et al* (27); Kaplan *et al* 31,212-214); Paretzke *et al* (77); Terrissol and Beaudre (35)). If we are interested only in ranges and stopping powers, then for electrons with E > 200 eV the dependence upon phase state is small (77,31). So for calculating these quantities the model of tissue-equivalent gas is quite satisfactory. But this model fails increasingly if we are interested in the yields of excitations and ionization for lower energy electrons, see Chapter 8, Section 8.6.2.2. Further details regarding phase effects are discussed in Chapter 5.

9.6. RECENT TRACK STRUCTURE APPROACHES TO BIOLOGICAL DAMAGE

Track simulation methods now make it possible to describe the stochastic tracks of different radiations down to dimensions of the order of a nanometre, although there remain significant limitations on resolution due to phase effects and cross sections for particular media. This development has given wide scope for attempts to describe the mechanisms by which the radiations cause damage to DNA and other biological molecules and the consequent cellular effects after the majority of the damage has been repaired. Because of the complexity of the overall process, different model approaches tend to concentrate on particular stages and to use experimental information on intermediate damage, such as DNA, to constrain their assumptions. Subsequent combination of the stages should then lead to more complete descriptions. Four recent model approaches are summarized below (215) as non-exhaustive examples. These four approaches have many features in common but also notable differences in their methods, emphasis, detailed assumptions and some of their conclusions. By closer comparisons between the models, and close comparison with experimental data, it should be possible to evolve improved integrated approaches. Other examples can be seen in the proceedings of recent meetings on track structure, biophysical modelling and microdosimetry and other reviews, such as in References 216-221.

9.6.1. Energy Deposition Frequencies in Microscopic Targets

The basic philosophy of this approach is that radiation quality effects should be due predominantly to the spatial properties of the radiation tracks on a microscopic scale, and that comparison of relative biological effectiveness (RBE) with features of simulated track structures for different radiations should lead to the identification of biologically relevant track properties and hence closer to the biomolecular mechanisms. Although DNA is a likely target of interest, this is not an *a priori* assumption of the approach and the dimensions of the targets of interest are sought from the correlations themselves (222-226).

There are still uncertainties about the fine details of track structure simulations at the nanometre and subnanometer levels, even for water. For the analysis of biological effects we would be concerned also with track structures in materials such as DNA and protein (and inhomogeneous combinations), for which track simulation cross sections are not at present available. Hence the approach taken is to seek robust properties that may serve as a useful guide to evolving studies, without being mislead by possible code or medium differences.

An approach used to date (147-149,224) has been to evaluate the absolute frequencies of energy depositions in cylindrical targets of dimensions 1 to > 100 nm and hence to seek regions of energy and volume that correlate with RBE and may therefore provide focus for more detailed mechanistic studies (227) (Fig. 9.53). Energy has been used rather than numbers of ionizations because it is clear that ionization yields would be strongly dependent on the medium chosen, its state of condensation and details of assumed cross sections and because there is no *a priori* reason to exclude a possible role for excitations in the locally-clustered damage that may be more severe and of particular relevance to final biological effects after cellular repair has eliminated the minor damage (228,229).

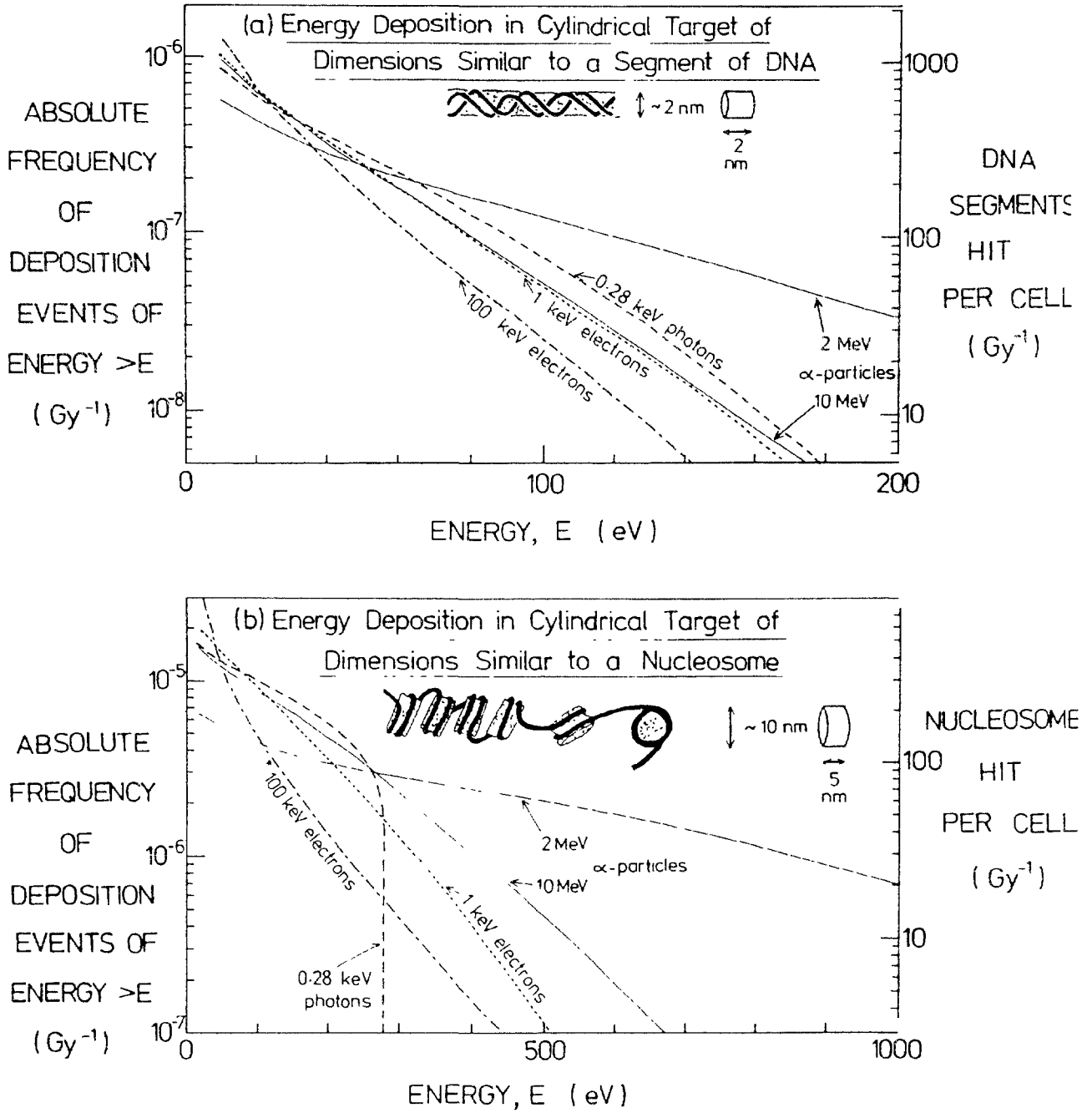

Figure 9.53 Absolute frequencies of energy deposition events, by various radiations in water, in randomly positioned cylindrical volumes corresponding to the sizes of DNA structures (146). The right-hand axis shows the corresponding frequencies of such events in DNA of a typical mammalian cell (224).

It seems likely that detailed results for the smallest dimensions and smallest energy depositions will be the least reliable because they are most dependent on code-specific assumptions regarding individual interactions or small combinations of a few adjacent interactions. For larger dimensions and numbers of interactions, averaging within the target should increase robustness of the results and interpretations. Robustness should be further enhanced by expression of the frequencies of energy deposition as ratios between radiations, for comparison with experimental RBEs.

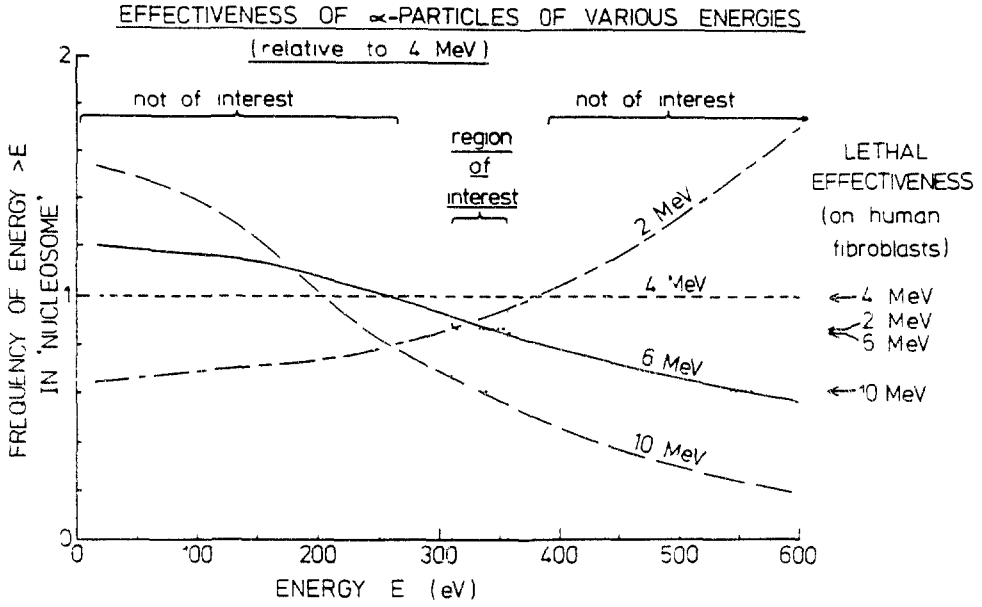

Figure 9.54 Relative effectiveness of track segments of α-particles of selected energies in depositing energy > E in cylindrical targets of diameter 10 nm and length 5 nm (similar in size to a nucleosome). Comparison with relative effectiveness for cell killing (222) suggests as a relevant property E ≈ 340 eV for these high-LET radiations (215).

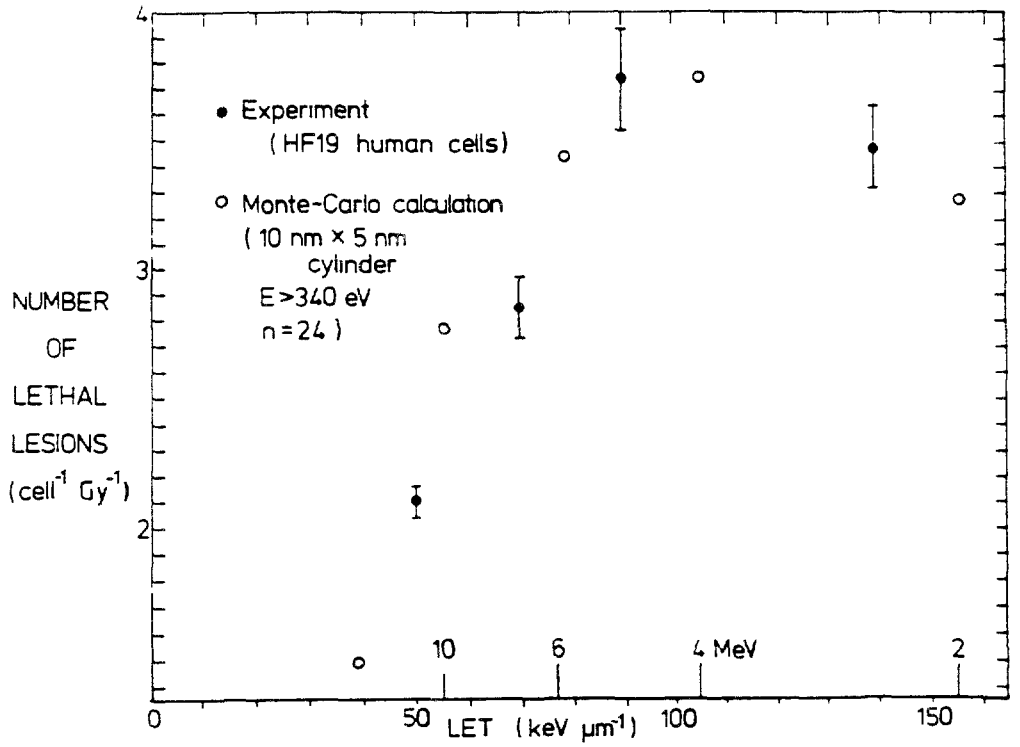

Figure 9.55 Comparison of observed numbers of lethal lesions (222) (versus α-particle LET) with absolute frequencies of E > 340 eV in nucleosomes, assuming that 1/24 of nucleosomes contain information relevant to cell survival (231).

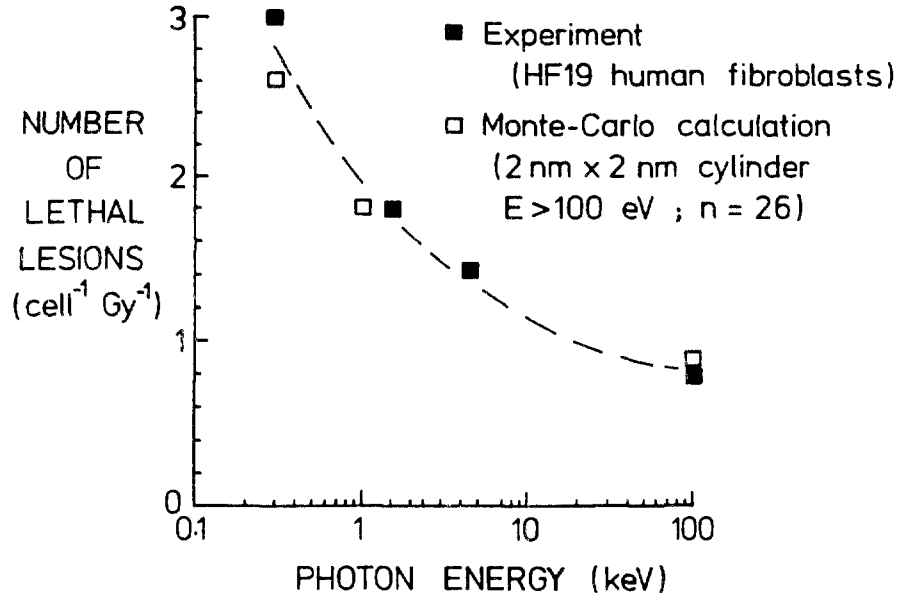

Figure 9.56 Comparison of observed numbers of lethal lesions (232) (versus X-ray energy) with absolute frequencies of E > 100 eV in DNA-segment, assuming 1/26 of DNA segments contain information relevant to cell survival (231).

With this philosophy a very large consistent database has now been generated for many radiations (147-154,230), using the Monte Carlo codes MOCA8b and MOCA14. This can serve also as a baseline for comparison with other codes (153,154).

Figure 9.54 illustrates how the scored data for α-particles of different LET, when compared to RBEs for inactivation of human fibroblasts, defines a track property of potential interest, namely f(> 340 eV) in a nucleosome-sized target, where f(>E) is the absolute frequency of deposition of energy >E in the specified target volume placed at random in the irradiated medium. This correlation is illustrated further in Fig. 9.55.

These and other analyses have suggested that there are different critical properties for the readily-modifiable and repairable dominant damage from low-LET radiations and that from slow high-LET ions. Figure 9.56 illustrates a property of potential interest for X-rays of 0.3 to 100 keV, namely f(> 100 eV) in a target of DNA dimensions.

It should be emphasised that this approach makes no *a priori* assumptions as to the molecular nature or dimensions of the biologically critical targets. However, where regions of correlation are obtained, more detailed studies and interpretations of mechanisms may be assisted by more specific assumptions, such as for example in assessing yields of DNA breaks (224,233) or in assessing the molecular nature of the larger target volumes apparently involved in the less-repairable high-LET damage (227,228). A number of related approaches have also been taken to identifying, from track structure simulation, the ionization-clustering properties that may be predominantly responsible for DNA double-strand breaks and for final cellular effectiveness (156,234-236).

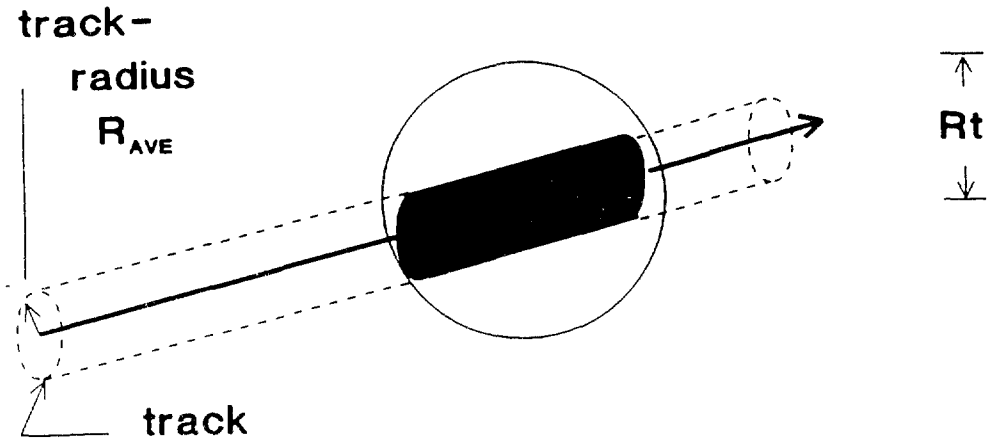

Figure 9.57a Schematic representation of the interaction of a track with a single-hit detector (231).

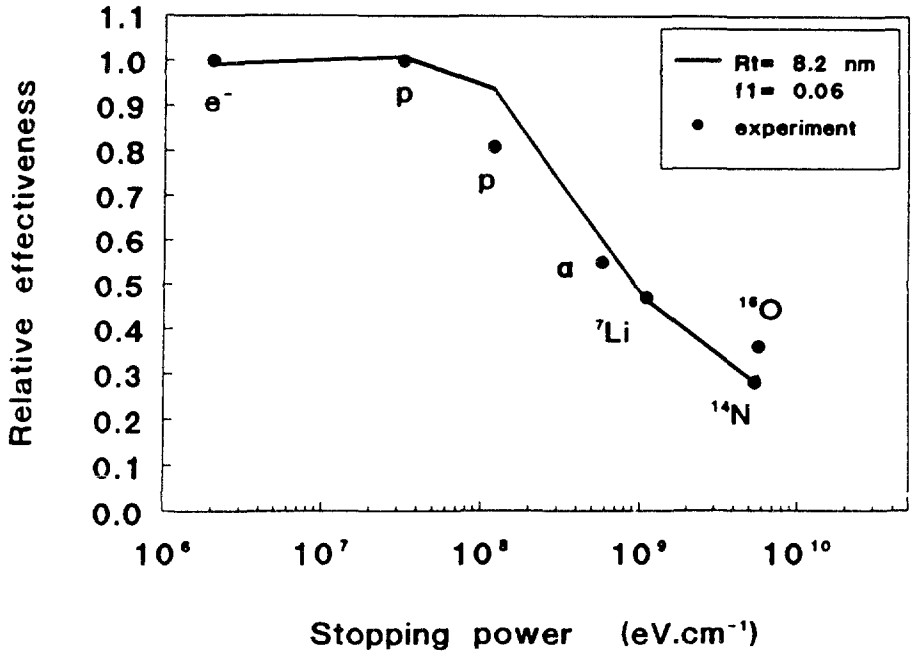

Figure 9.57b Comparison of calculated and experimental data on the relative efficiency of a radiochromic dye film exposed to different types of radiaton (231).

9.6.2. The Radiation Track Segment Model

A track structure model (237) has been developed which provides a description of the spatial distribution of events for both electron and ion tracks. For each ionizing particle, both primary and all secondary particles, the parameters of stopping power, average energy loss per event and average track radius are calculated over a limited track segment. Using these quantities the complete slowing down process, i.e. the complete inventory of all particles generated by the primary particle and their respective contribution to dose is calculated in liquid water down to subionization energies. The model thus permits calculations of radiation effectiveness to be made taking into account the three dimensional structure of the target at nanometer dimensions. Only secondary particles with an initial energy greater than 25 eV are

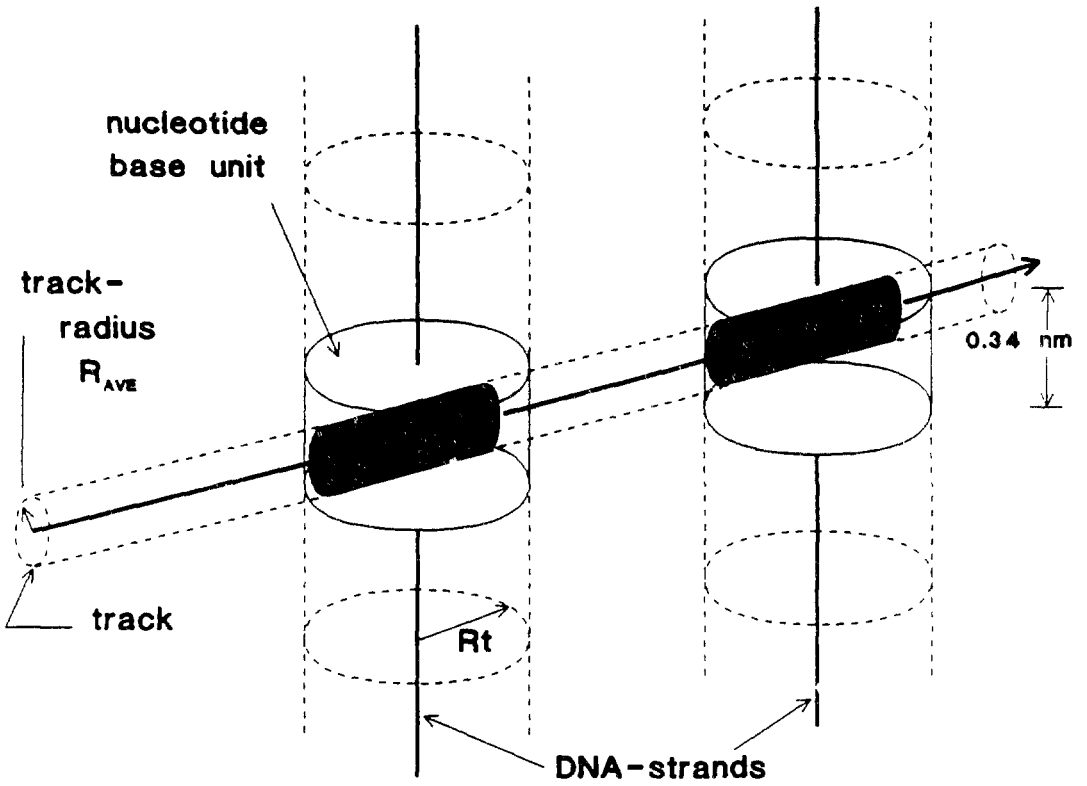

Figure 9.58a. Schematic representation of the interaction of a track with a DNA double helix (231).

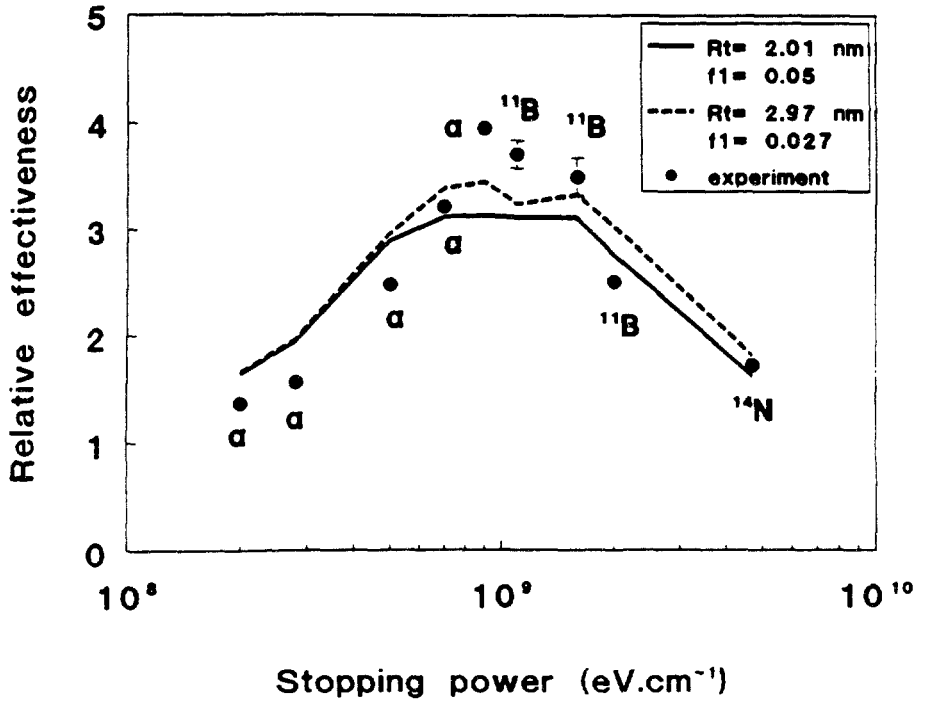

Figure 9.58b Comparison of calculated and experimental data on the relative efficiency of radiaton induced DNA double-strand breaks for different types of radiation (231).

treated as separate particles for the calculation of the three parameters, although their contribution to the radiation effect forms part of the complete slowing down inventory.

This model has been applied to calculate the efficiency of different types of radiation on single hit detectors and for DNA double-strand breaks. The target of a single-hit detector is represented by a sphere with interaction radius R_1 (see Fig. 9.57a). Each energy deposition in this sphere is assumed to have a probability f_1 to cause an effect.

The results of calculations using $f_1 = 0.06$ and $R_1 = 8.2$ nm have been compared with data for radiation effects in the radiochromic dye film (238). Fig.9.57b clearly demonstrates that a family of curves is predicted for the different radiation types, which indicates that, although different radiation types may have the same stopping power their relative effectiveness is not necessarily the same, because there are differences in delta ray spectrum and average energy loss per event and thus in track structure geometry.

The model has also been applied to calculate the efficiency for the induction of DNA double-strand breaks because this lesion has been assumed to be crucial for radiobiological effects. The double stranded DNA helix presents a structured molecular target of nanometer dimensions and has been represented by two associated cylinders having an interaction radius of R_1 and the axes of which are separated by 2 nm (see Fig. 9.58a). It is assumed that an energy deposition event in the cylinder with radius R_1 has a probability of f_1 of causing a strand break. Two adjacent strand breaks induced by the passage of the same primary particle are assumed to lead to a double-strand break. The initial slope of cell survival curve has been used as a surrogate for the induction of DNA double-strand breaks by the passage of one particle. In Fig. 9.58b the experimental data for human fibroblasts (239) are compared with two sets of calculations. The humped behaviour with stopping power revealed by the experimental data is closely approximated by the calculations and arises because the probability that the track intersects the two cylinders causing an event in each cylinder increases as the stopping power and the average track radius increase. At high stopping powers excessive energy depositions in the two cylinders cause a decrease in the relative efficiency of the radiation effect. The initial slopes of survival curves of several other cell lines show a stronger dependence on LET than the factor of about 3 shown in Fig. 9.58b. These other cell lines generally have a more pronounced shoulder on their low-LET survival curves, in contrast to the unshouldered curves of the human diploid fibroblasts.

This continuous slowing down track structure model is derived from basic physical principles but is not as advanced as the Monte Carlo based track structure models. However, it also offers the possibility of calculating energy deposition events on a nanometer scale which is important when energy deposition events in a geometrically structured target such as the DNA helix are considered. The results presented in Fig. 9.57b and 9.58b demonstrate the importance of the target structure and the usefulness of the model.

9.6.3. PARTRAC-Model

The Monte Carlo track structure simulation codes MOCA8 (for incident electrons up to 100 keV) (88) and MOCA14 (for protons and alpha particles) (240) were

developed for the model target 'homogeneous water vapour' and are used in many radiation physical calculations (for a review see Ref. 34). This particle track model has been extended into the PARTRAC code (241,242) which in its present status; (a) follows also incident photons (10 eV - 100 MeV) with their photoelectric, coherent and incoherent scattering, and pair production effects; (b) extends the electron energy range considered up to 100 MeV; (c) considers phase dependent differences in ionization cross sections for the condensed state (243,244); (d) permits the use of complex geometry algorithms to simulate structured, heterogeneous targets (e.g. 'DNA' in 'chromatin' in a 'nucleus' in a 'cell' in 'tissue'); and (e) follows also the fate of primary or secondary chemical species (e.g. H, OH, hydronium ions, solvated electrons, DNA-breaks) produced by radiation action in the target.

The PARTRAC code was used to calculate the induction of single and double strand breaks for photons of various energy spectra (C- and Al-K-lines, filtered 30 kV and 150 kV X-rays), to study the importance of indirect (via OH-radical attack) and direct (via energy deposition in the DNA above a certain threshold energy (E_t)) radiation action for these end points, and the sensitivity of the yield of single-strand breaks (SSB) and double-strand breaks (DSB) on model assumptions regarding the direct energy deposition in the sugar phosphate backbone, threshold energy needed to produce a SSB and the maximum SSB-interaction distance d to form a DSB.

If a minimum energy deposition E_t for the production of a single-strand break by direct action of 17.5 eV in the DNA (245) is assumed, SSB-yields per Dalton and Gy of $(4.0 \pm 0.5) \times 10^{-10}$ are calculated for the X-ray photon spectra and of ca. 2.6×10^{-10} for the Al- and C-K-photons. This is somewhat higher than the experimental values of 1.2 to 2.8×10^{-10} reported for high energy photons (246,247). However, this calculated yield decreases with increasing threshold E_t, e.g. to ca. 50% at E_t twice the 17.5 eV used here, which might indicate that a somewhat higher value of E_t would lead to more consistency with experimental observations.

Under the assumptions of random diffusion of OH-radicals within ca. 3 nm towards a cylindrical DNA target (248) and of 80% probability for a radical interaction with the DNA taking place on the bases (leading only to point mutations but no breaks) and 20% with the desoxyribose (249), about one third of the calculated SSBs appear to result from indirect action and two thirds from direct.

The formation of DSBs was assumed to result from the interaction of two SSBs on opposite strands if their distance was less than d base pairs. Setting d to a plausible value of 10 base pairs the calculated DSB-yield increases from ca. 2.3×10^{-11} per Dalton and Gy to ca. 3×10^{-11} with the photon energy decreasing from 150 kV X-rays to C-K-photons which is also somewhat higher than the reported experimental values (typically around 1.5×10^{-11}). This calculated yield decreases to ca. 50% its above value for d decreasing to ca. 3 base pairs. Again the contribution from indirect action was found to be smaller than that from the direct action with roughly one third of the DSBs resulting apparently from radical plus direct action and ca. one tenth from radical only action. The calculated DSB-yield in the low dose regime increases only slightly (i.e. by ca. 20%) for d larger than 10 base pairs, since the action is here essentially by intra-track effects and most of the primary chemical modifications in photon produced electron tracks are located to each other closer than these 10 base pairs.

9.6.4. Modelling of Chemical Stage

The space and time distributions of radicals and molecular products coming from the water radiolysis between 10^{-15} and 1 second have been calculated with Monte Carlo type codes (35,31). This allows the possibility to add various finite volumes containing solutes like scavengers (Tris, formate ions, ...) which are chemically reactive with water radicals, or volumes containing a set of biological molecules (DNA or other) also chemically reactive with water radicals or scavengers. All the chemical reactions between these species can be taken into account. The addition of a scavenger was necessary as a substitute for incorporation in the model of numerous biomolecules and chemistry associated with DNA in a cellular environment (250). It is a step towards the real simulation of what happens in an irradiated cell. Due to computer time and relative memory limitation, these finite volumes were limited in initial studies to about hundreds of cubic nanometers, sufficient to contain a DNA helix of 14 nm length with 2 nm radius and surrounding media of liquid water with a scavenger concentration not exceeding 2M.

As a first example, an infinite medium of liquid water was considered (see Figure 9.59) inside which is placed a small volume V_1 of interest supposedly containing a DNA molecule, taken as a cylinder of 2 nm radius and 14 nm length, and a larger second scavenger volume V_2 is drawn (shape unimportant) large enough to contain all the species involved around V_1 until 10^{-8}s. An electron with 278 eV energy is to be introduced, as indicated by the small arrow on Figure 9.59, at a distance of 2 nm from the axis of V_1.

At early times, say between 10^{-18} and 10^{-15}s, the slowing down of the electron is almost complete, elastic and inelastic (ionisations and excitations) collisions have taken place, and every ionisation localised in the volume of interest is counted as one 'direct' product, and removed from the track. Then thermalization and solvation of electrons and creation of water radicals are simulated and a data set in a four co-ordinates systems (t, x, y, z) is obtained for each species: e^-_{aq}, $OH\cdot$, $H\cdot$, H_3O^+, H_2O_2, OH^-, H_2, HO_2, starting at 10^{-15}s. In V_2, molecules of scavenger are added. As a function of time, all water species and scavengers can diffuse and react together. When $OH\cdot$ or $H\cdot$ radical enters V_1, these are counted as 'indirect' products, and removed from the species set.

For 278 eV electrons (e.g. C_K-Auger electrons), and in the case represented in Figure 9.59, the analysis gave a 'direct' product yield of 0.242 per electron and a value of 0.192 for the 'indirect' product yield at 10^{-12}s. The variations of 'indirect' yields as a function of time and concentrations of Tris and Formate ion, are represented in Figure 9.60. At about 10^{-10}s the indirect yield is twice the direct, and then increases with time. Wright *et al.* (251), found comparable results with a ratio indirect/direct of 2.1 for ^{125}I Auger electrons (mean energy close to 300 eV), without a scavenger. The Tris effect on cumulated direct yield is small, as mentioned also by Holley and Chatterjee (250). The present model has been applied also to take into account chemical reactions with DNA after the Auger-cascade decay of ^{125}I incorporated into DNA (252).

Such chemical-stage computer models are powerful tools for biophysical investigations. They are stochastic in nature and it can be improved as more information becomes available.

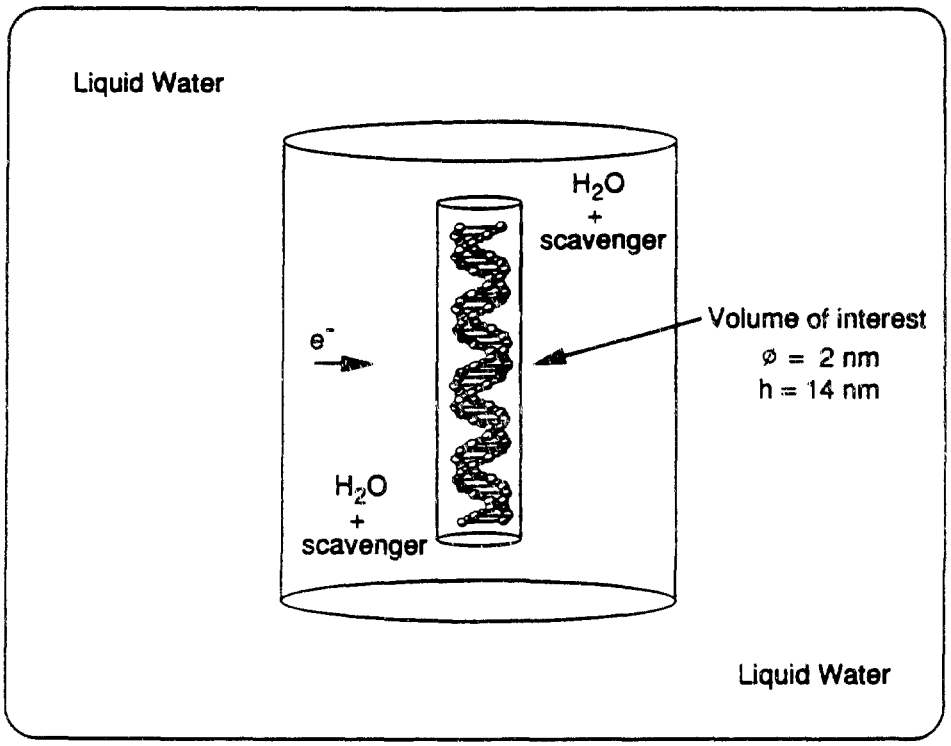

Figure 9.59 Schema of the model used. Monoenergetic 278 eV electrons are emitted in the direction of the volume of interest as indicated by e^- and the small arrow (231).

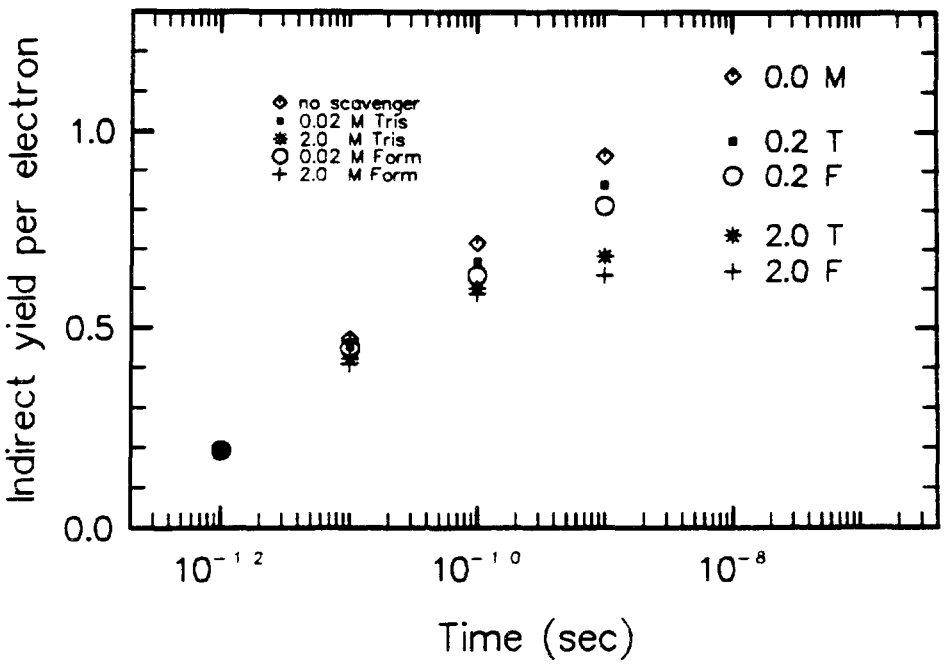

Figure 9.60 Variations of 'indirect' yield, the number of OH and H radicals entering the volume of interest per electron, as a function of time. 0.0 M represent the case without scavenger. 0.02 T and 2.0 T are concentrations in mole per litre of Tris and 0.02 F and 2.0 F for Formate ion (231).

9.7. INTERCOMPARISON OF TRACK STRUCTURE CODES

Most of our knowledge on spatial distribution of track structure is based on Monte Carlo calculations. Results of such calculations are often used in modelling the biological effects of radiation. In the absence of direct experimental checks, some assessment of the confidence one might place in our present theoretical understanding of the physics of track structures can be obtained by comparing specific results calculated by using different independently developed, particle transport codes.

9.7.1. Vapour and Liquid Water Codes

The development of Monte Carlo codes (252a) for charged particle transport track structure studies arose in 1963 with Berger (5). Since many authors have developed their own track structure codes, it is not possible to present here an intercomparison of all existing codes, but we can focus on ones dealing with water medium, most often used as tissue equivalent. Comparisons have been done for electrons in the vapor and liquid phase (27,115,153,154,157). We can see for instance on Figure 9.61 the cumulative percentage of interactions at 1 nm intervals plotted against the radial distance from the starting point of the electron. The codes used MOCA (33) and KURBUC (36) are for water vapor, while OREC (253) and CPA (35,254) are for liquid water. The distributions are very similar for all four electron track codes. Some differences are observed at distances around 20 nm.

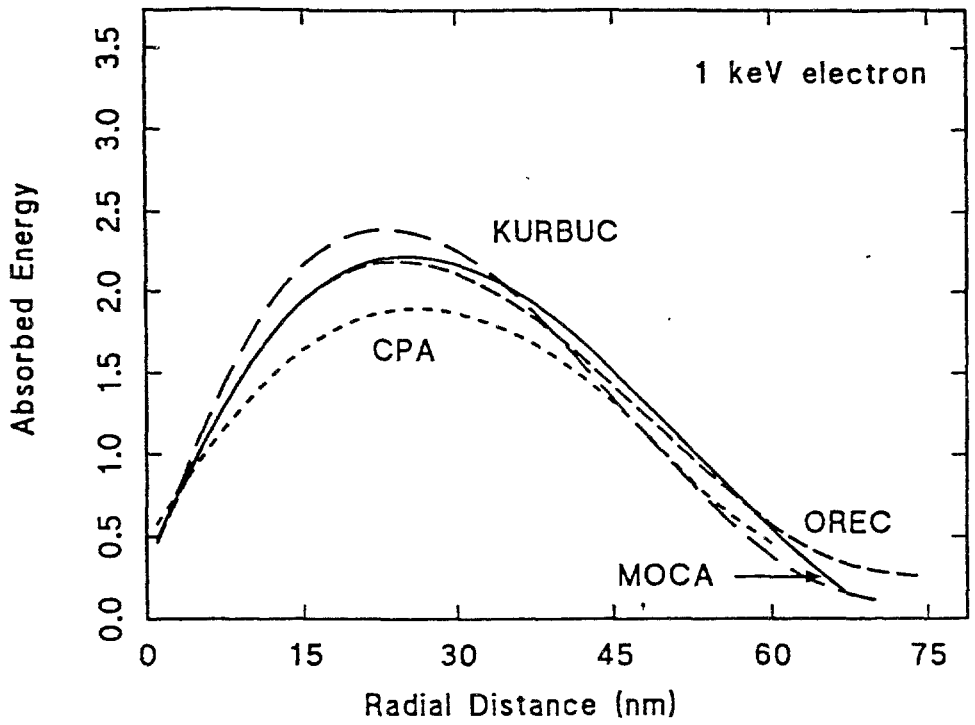

Figure 9.61 Radial distribution of interactions represented as cumulative % of interactions, normalized to total number of interactions, for 100 tracks of 1 keV electron, plotted at 1 nm intervals, for each of the four Monte Carlo track structure codes.

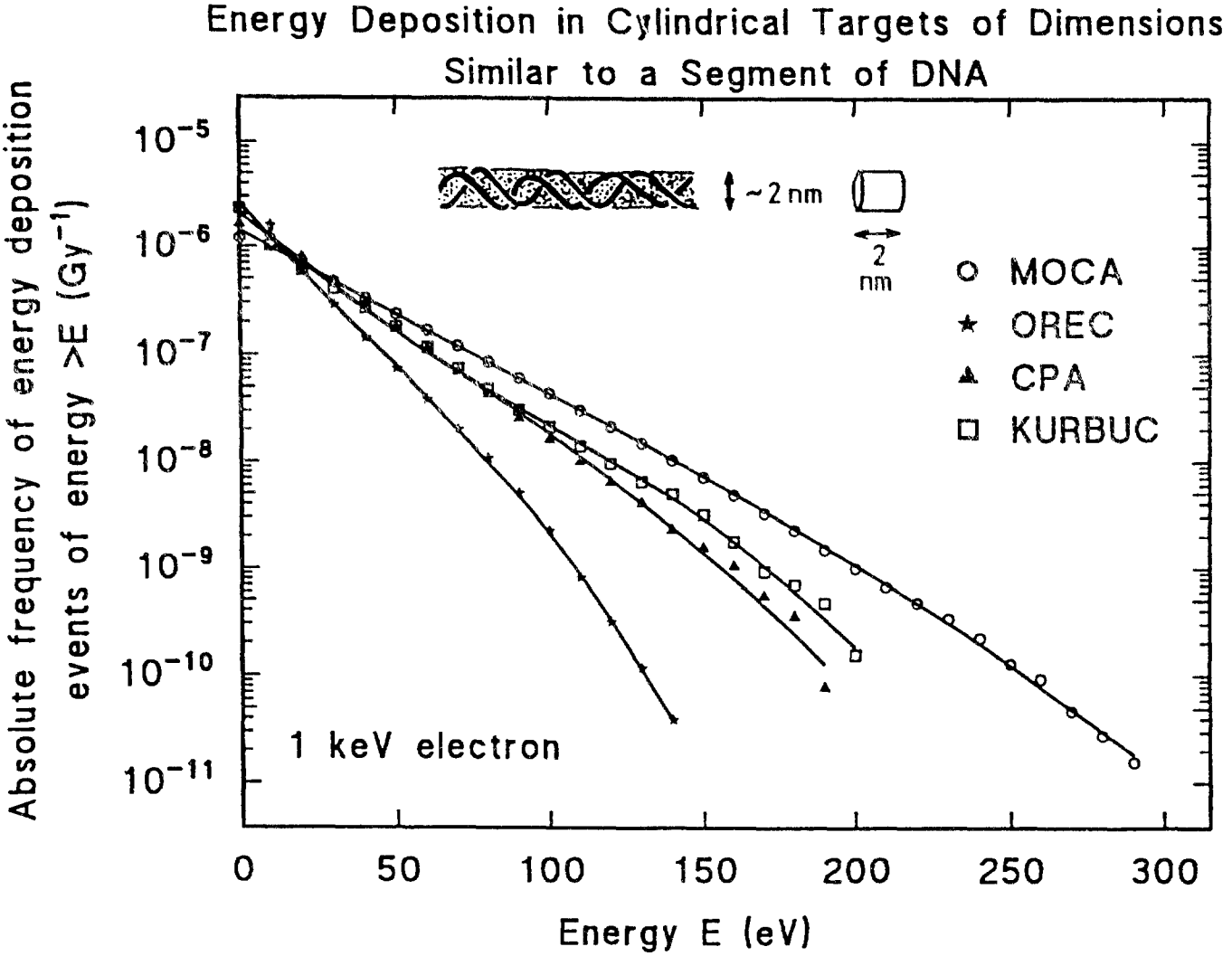

Figure 9.62 Absolute frequency distributions of energy deposition f(>E) greater than a given amount of energy E per gray in a single cylindrical target volume of diameter 2 nm and length 2 nm, placed at random in water (1 g/cm^3) homogeneously irradiated with the full slowing down tracks of 1 keV electrons.

A major application of track structure is in the field of radiobiology. Track structure calculations have been used (153,154) to investigate the properties of the energy deposition events in volumes similar to biological target sizes that may correlate with biological effects of ionizing radiations. In Figure 9.62 are shown the distributions for target size similar to a short segment of DNA (approximated by a 2 nm by 2 nm cylinder) positioned randomly in water irradiated uniformly with 1 Gy of monoenergetic electrons of 1 keV.

9.7.2. Comparison for Liquid Water Codes

This complexity is shown by a comparison of three codes written specially for liquid water, simulating water radiolysis taking into account the physical, physico-chemical and the chemical stages: the codes OREC (253), CPA (35) and KIPC (31,214). In this energy domain and for condensed media, insufficient is known and a set of

uncontested cross sections does not exist. So, depending on the age of the code, the model of computer used and the results expected, the analysts are making assumptions and nobody does this exactly the same. It is also possible that very recently a few points in the large cross section sets and different assumptions have been improved and inserted in the codes, but the results presented here have been obtained with the described set of cross sections up to 1990.

9.7.2.1. Cross Sections Used

As one can see in Tables 9.4, 9.5 and 9.6, the basic input data are similar but nevertheless different. Such large codes make assumptions and use algorithms that are similar but designed for specific objectives, so that comparisons cannot be done in a large scale. For elastic cross sections (Table 9.4) in the low energy domain (0-200 eV) agreement is not satisfactory and more data are needed (see Chapter 4). For excitation cross sections there is reasonable agreement, except for subexcitation electrons.

Table 9.4 - Elastic cross sections used in liquid water Monte Carlo codes

Code	Energy Range	Cross Sections Used
KIPC	< 200 eV	experimental data of Danjo-Nishimura (255) assuming: liquid = vapor
	> 200 eV	Thomas - Fermi
OREC	0 - 10 eV	experimental data of Trajmar, Itikawa (256,257) assuming liquid = 0.6*vapor
	< 1000 eV	phase-shift Mott-Dirac formula
	> 1000 eV	Thomas - Fermi
CPA	0 - 8.4 eV	experimental data of Sanche-Michaud (258) assuming liquid = ice
	up to 30 keV	phase-shift Mott-Dirac formula (254)

Table 9.5 - Excitation Cross Sections Used in Liquid Water Monte Carlo Codes

Code	Excitation State	Energy	Cross Section Used
KIPC	A^1B_1	8.4 eV	Integration of energy loss function
OREC	B^1A_1	10.1 eV	within the limits of each peak width,
CPA	Rydberg (A+B)	11.26 eV	using differential oscillator strengths
	Rydberg (C+D)	11.93 eV	determined with dielectric response
	Diffuse bands	14.1 eV	function derived from experiments
	Collective	21.4 eV	
OREC	Subexcitation electrons	< 8.4 eV	Stopping power calculated with optical data and Fermi age theory
CPA	Subexcitation electrons	< 8.4 eV	Exper. cross sections of Sanche-Michaud, assuming liquid = ice

Table 9.6 - Ionization Cross Sections Used in Liquid Water Monte Carlo Codes

Code	Ionization Level	Cross Section Used
KIPC	Oxygen K shell For outer shells: 8.76 - 25 eV > 25 eV	Asymptotic Bethe cross section Use of dielectric response function and Jain-Khare semi-empirical cross sections (259)
OREC	Oxygen K and $1b_1$, $1b_2$, $2a_1$ $3a_1$ shells	Partitioning of the imaginary part of the dielectric function between the five levels with sum rules
CPA	Oxygen K shell For outer shells: $1b_1$, $1b_2$, $2a_1$, $3a_1$	Gryzinski cross section (260) Partitioning of the dielectric response function between the four levels

Table 9.7 - Initial Radiation Yield, for 5 keV Electron in Liquid Water

Code	g_{ion}	g_{ex}
KIPC	4.51	2.30
OREC	4.36	3.09
CPA	4.02	2.05

Table 9.8 - Yields at 10^{-12} s for 5 keV Electrons in Liquid Water

Code	H_3O^+	OH	e^-_{aq}	H	H_2	H_2O_2	OH^-
KIPC	4.8	6.8	4.8	0.84	0.62		
OREC	6.3	8.4	6.3	2.1	0.3		
CPA	4.51	4.8	4.5	1.5	0.4	0.98	0.01

Table 9.9 - Yields at 10^{-7} s for 5 keV Electron in Liquid Water

Code	H_3O^+	OH	e^-_{aq}	H	H_2	H_2O_2	OH^-
KIPC	3.78	4.65	3.32	0.85	0.62	0.80	0.46
OREC	2.62	2.2	1.63	0.92	0.76	0.92	
CPA	2.6	1.5	2.05	0.95	0.9	1.45	0.55

Table 9.10 - Calculated Fricke G values at $0.28\ 10^{-6}$ s in Liquid Water

Code	1 keV	5 keV
KIPC		18.7
OREC	12.1	12.9
CPA	13.8	13.4

9.7.2.2. Results

Table 9.7 presents initial ionization and excitation yields (at about 10^{-15} second), resulting from the physical step. Differences may be due to including or not the deexcitation scheme and then disappear in Table 9.8, obtained after the physico-chemical step.

Table 9.9 is presented at 10^{-7} second, which is the beginning of a stationary phase. And for greater times it is then possible to calculate the so-called Fricke G value with:

$$G_{Fricke} = 2G_{H2O2} + G_{OH} + 3(G_H + G_{e\text{-}aq})$$

Table 9.10 shows Fricke G values calculated for 1 and 5 keV. The KIPC value is calculated at 10^{-7} second, with data of Table 9.9.

9.7.3. Remarks

Studies of this nature are important to allow better understanding, modelling and interpretation of biophysical mechanisms of action of ionizing radiations in biological media. Although the different codes are developed from the same initial phenomena, methods by which the subsequent processes involved have been treated produce different track parameters. These differences could lead to significant differences in physical, chemical and then in biological interpretations. Therefore more work is needed to identify the most realistic description for an electron track.

References

1. FANO, U., Ann. Rev. Nucl. Sci. 13 (1963) 1.

2. FANO, U., in Charged Particle Tracks in Solids and Liquids, (ADAMS, G.E., BEWLEY, D.K., BOAG, J.W., Eds.), Institute of Physics, Conference Series No. 8, London (1970) p.1.

3. FANO, U., in Radiation Biology, Vol. 1, (HOLLANDER, A., Ed.), McGraw-Hill, New York, (1954) p.1.

4. SPENCER, L.V., Phys. Rev. 98 (1955) 1597.

5. BERGER, M.J., in Methods in Computational Physics, Vol. 1, (ALDER, B., FERNBACH, S., ROTENBERG, M., Eds.), Academic Press, New York (1963) p.135.

6. BOAG, J.W., in Advances in Radiation Research, Vol. 1, (DUPLAN, J.F., CHAPIRO A., Eds.), Gordon and Breach, New York (1973) p.9.

7. BOAG, J.W., in Progress and Problems in Contemporary Radiation Chemistry (Proc. of the 10th Czechoslovac Ann. Meeting on Radiat. Chem., Marianske Lazne, Czechoslovakia, June 22-25, 1970) Vol. 1 (TEPLY, J. *et al.*, Eds.), Academy of Science, Prague (1971) p.19.

8. HART, E.J., PLATZMAN, R.L., in Mechanisms in Radiobiology Vol. 1 (ERRERA, M., FORSSBERG, A., Eds.), Academic Press, New York (1961) p.93.

9. PLATZMAN, R.L., in Radiation Research: Proceedings of the 3rd International Congress, Cortina d'Ampezzo, Italy (Silini, G., Ed.), Wiley, New York (1967) p.20.

10. MOZUMDER, A., in Advances in Radiation Chemistry Vol. 1 (BURTON, M. and MAGEE, J.L., Eds.), Wiley (1969) p.1.

11. MOZUMDER, A., MAGEE, J.L., Radiat. Res. 28 (1966) 203.

12. CASWELL, R.S., COYNE, J.J., Radiat. Res. 52 (1972) 448.

13. CASWELL, R.S., COYNE, J.J., RANDOLPH, M.L., Radiat. Res. 83 (1980) 217.

14. VOLTZ, R., in Progress and Problems in Contemporary Radiation Chemistry, (Proc. of the 10th Czechoslovac Ann. Meeting on Radiat. Chem., Marianske Lazne, Czechoslovakia, June 22-25, 1970) Vol. 1 (TEPLY, J. *et al.*, Eds.), Academy of Science, Prague (1971) p.45, 139.

15. BRANDT, W., RITCHIE, R.H., in Physical Mechanisms in Radiation Biology, (COOPER, R.D., WOOD, R.W., Eds.), Technical Information Center, US Atomic Energy Commission, Oak Ridge, TN (1974) p.20.

16. INOKUTI, M., Applied Atomic Collision Physics, Vol. 4, Academic Press, New York (1983) p.179.

17. LEA, D.E., Actions of Radiations on Living Cells, University Press, Cambridge (1946).

18. KATZ, R., SHARMA, S.C., HOMAYOONFAR, M., in Topics in Radiation Dosimetry, Radiation Dosimetry Supplement 1, (ATTIX, F.H., Ed.), Academic Press, New York (1972) p.317.

19. KATZ, R., KOBETICH, E.J., Phys. Rev. 186 (1969) 344.

20. KATZ, R., KOBETICH, E.J., in Charged Particle Tracks in Solids and Liquids, (ADAMS, G.E., BEWLEY, D.K., BOAG, J.W., Eds.), Institute of Physics, Conference Series No. 8, London (1970) p.109.

21. KAPLAN, I.G., MITEREV, A.M., Adv. Chem. Phys. 68 (1987) 257.

22. PARETZKE, H.G., in Advances in Radiation Protection and Dosimetry, (THOMAS, R.H., PEREZ-MENDEZ, V., Eds.), Plenum Press, New York (1980) p.51.

23. ZERBY, C.D., in Methods in Computational Physics, Vol. 1, (ALDER, B., FERNBACH, S., ROTENBERG, M., Eds.), Academic, New York (1963) p.89.

24. GROSSWENDT, B., in Eighth Symposium on Microdosimetry, (BOOZ, J., EBERT, H.G., Eds.), EUR 8395, Commission of the European Communities, Luxembourg (1982) p.79.

25. GROSSWENDT, B., WAIBEL, E., Nucl. Instr. Meth. 155, (1978) 145.

26. HAMM, R.N., WRIGHT, H.A., RITCHIE, R.H., TURNER, J.E., TURNER, T.P., in Fifth Symposium on Microdosimetry, (BOOZ, J., EBERT, H.G., SMITH, B.G.R., Eds.), Report EUR 5454, Commission of the European Communities, Luxembourg (1976) p.1037.

27. TURNER, J.E., PARETZKE, H.G., HAMM, R.N., WRIGHT, H.A., RITCHIE, R.H., *Radiat. Res.* 92 (1982) 47.

28. WRIGHT, H.A., TURNER, J.E., HAMM, R.N., RITCHIE, R.H., MAGEE, J.L., CHATTERJEE, A., in Eighth Symposium on Microdosimetry, (BOOZ, J., EBERT, H.G., Eds.), EUR 8395, Commission of the European Communities, Luxembourg (1982) p.101.

29. RITCHIE, R.H., HAMM, R.N., TURNER, J.E., WRIGHT, H.A., in Sixth Symposium on Microdosimetry, (BOOZ, J., EBERT, H.G., Eds.), Report EUR 6064, Harwood Academic Publishers, London (1978) p.345.

30. ITO, A., in Monte Carlo Transport of Electrons and Photons, (JENKINS, T., NELSON, W., RINDI, A., Eds.), Plenum Press, New York (1988) p.361.

31. KAPLAN, I.G., SUKHONOSOV, V. Ya., Radiat. Res. 127 (1991) 1.

32. NELSON, W.R., HIRAYAMA, H., ROGERS, D.W.O., The EGS4 Code System, Stanford Linear Accelerator Center report, SLAC-265 (1985).

33. PARETZKE, H.G., Simulation von Elektronenspuren im Eneergiebereich 0,01-10 keV in wasserdampf, Report GSF 24/88, GSF Neuherberg, Munich (1988).

34. PARETZKE, H.G., in Kinetics on Nonhomogeneous Processes, (FREEMAN, G.R., Ed.), Wiley, New York (1987) p. 89.

35. TERRISSOL, M., BEAUDRE, A., Radiat. Prot. Dosim., 31 (1990) 175.

36. UEHARA, S., NIKJOO, H., GOODHEAD, D.T., Phys. Med. Biol., 38 (1993) 1841.

37. WILSON, W.E., PARETZKE, H.G., in Fourth Symposium on Microdosimetry, (BOOZ, J., EBERT, H.G., EICKEL, R., WAKER, A., Eds.), Report EUR 5122, Commission of the European Communities, Luxembourg (1974) p.113.

38. TOBUREN, L.H., WILSON, W.E., in Radiation Research: Proceeding of the 6th Int. Congress, (OKADA, S., IMANURA, M., TERASHIMA, T., YAMAGUCHI, H., Eds.), Japan Association of Radiation Research, Tokyo (1979) p.80.

39. TOBUREN, L.H., Phys. Rev. A3 (1971).

40. TOBUREN, L.H., WILSON, W.E., J. Chem. Phys. 60 (1977) 5202.

41. ZAIDER, M., BRENNER, D.J., Radiat. Res. 100 (1984) 213.

42. ZAIDER, M., BRENNER, D.J., Radiat. Res. 100 (1984) 245.

43. EVANS, R.D., in Radiation Dosimetry, Vol. 1 (ATTIX, F.H., ROESCH, W.C., Eds.), Academic Press, New York (1968) p.93.

44. EVANS, R.D., The Atomic Nucleus, McGraw-Hill, New York (1955).

45. DYSON, N.A., X-Rays in Atomic and Nuclear Physics, Longmans Green, New York (1973).

46. ANDERSON, D.A., Absorption of Ionizing Radiation, University Park Press, Baltimore (1984).

47. JOHNS, H.E., CUNNINGHAM, J.R., The Physics of Radiology, Charles Thomas Publisher, Springfield IL (1984).

48. PLECHATY, E.F., CULLEN, D.E., HOWERTON, R.J., Tables and Graphs of Photon-Interaction Cross Sections form 0.1 keV to 100 MeV derived from the LLL Evaluated-Nuclear Data Library, Lawrence Livermore National Laboratory, Report UCRL-50400, Vol. 6, Rev. 3, Livermore, CA (1981).

49. BLOHM, R., Durchgang von Elektronen durch Strahlenempfindliche Bereiche des Zellkerns, Dissertation, Universität Göttingen, Federal Republic of Germany (1983).

50. BROWNELL, G.L., ELLETT, W.H., REDDY, A.R., J. Nucl. Med., MIRD 3 (1968) 27.

51. BECKURTS, K.H., WIRTZ, K., Neutron Physics, Springer-Verlag, Berlin (1964).

52. INTERNATIONAL COMMISSION ON RADIATION UNITS AND MEASUREMENTS, Neutron Dosimetry for Biology and Medicine, ICRU-Report 26, ICRU, Bethesda MD (1977).

53. HOWERTON, R.J., CULLEN, D.E., MACGREGOR, M.H., PERKINS, S.T., PLECHATY, E.F., The LLL Evaluated Nuclear Data Library (ENDL): Graphs of Cross Sections from the Library, UCRL-50400, Vol. 15, Part B, University of California, Berkeley (1976).

54. MUGHABGHAB, S.F., GARBER, D. (Eds.), Neutron Cross Sections, Vol. I, Resonance Parameters, BNL-325, Brookhaven National Laboratory, Upton, NY (1973).

55. KINSEY, R.R., GARBER, D.I. (Eds.), Neutron Cross Sections, Vol. II, Graphical Data, BNL-325, Brookhaven National Laboratory, Upton, NY (1979).

56. GOLDBERG, M.D., MUGHABGHAB, S.F., PUROHIT, S.N., MAGURNO, B.A., MAY, V.M. (Eds.), Neutron Cross Sections, Vol. IIB, Z = 41-60, Report BNL-325, Brookhaven National Laboratory, Upton, NY (1966).

57. GARBER, D.I., STROMBERG, L.E., GOLDBERG, M.D., CULLEN, D.W., MAY, V.M. (Eds.), Angular Distributions in Neutron Induced Reactions, Vol. I: Z = 1-20, Vol. II, Z = 21-94, BNL-400, Brookhaven National Laboratory, Upton, NY (1970).

58. EDWARDS, A.A., DENNIS, J.A., Phys. Med. Biol., 20 (1975) 395.

59. PARETZKE, H.G., GRÜNAUER, F., MAIER, E., BURGER, G., in First Symposium on Neutron Dosimetry in Biology and Medicine, (BURGER, G., SCHRAUBE, H., EBERT, H.G., Eds.), EUR 4896, Commission of the European Communities, Luxembourg (1972) p.73.

60. OLDENBURG, U., BOOZ, J., Radiat. Res. 51 (1972) 551.

61. BOOZ, J., COPPOLA, M., in Annual Report of the Joint Research Center, EUR 5260, Commission of the European Communities, Luxembourg (1974) p.396.

62. CHRISTOPHOROU, L.G., Atomic and Molecular Radiation Physics, Wiley, New York (1971).

63. CHRISTOPHORU, L.G. (Ed.), Electron-Molecule Interactions and their Applications, 2 vols., Academic Press, New York (1984).

64. SCHNATTERLY, S.E., in Solid State Physics, Vol. 34, (EHRENREICH, H., SEITZ, F., TURNBULL, D., Eds.), Academic Press, New York (1979) p.275.

65. RAETHER, H., Excitations of Plasmons and Interband Transitions in Solids, Springer Tracts in Modern Physics 88, Springer-Verlag, New York (1980) p.1.

66. KLOTS, C.E., in Fundamental Processes in Radiation Chemistry, (AUSLOOS, P., Ed.), Wiley, New York (1968) p.1.

67. MOTT, N.F. MASSEY, H.S.W., The Theory of Atomic Collisions, Third Edition, Oxford University Press, London (1965).

68. MASSEY, H.S.W., BURHOP, E.H.S., and GILBODY, H. B., Electronic and Ionic Impact Phenomena, Second Edition in Five Volumes, Clarendon Press, Oxford (1969-1974).

69. INOKUTI, M., KIM, Y.-K., PLATZMAN, R.L., Phys. Rev. 164 (1967) 55.

70. SPENCER, L.V., FANO, U., Phys. Rev. 93 (1954) 1172.

71. DOUTHAT, D.A., Radiat. Res. 61 (1975) 1.

72. FANO, U., SPENCER, L.V., Int. J. Radiat. Phys. Chem. 7 (1975) 63.

73. FANO, U., Phys. Rev. 72 (1947) 26.

74. INOKUTI, M., DOUTHAT, D.A., RAO, A.R.P., Phys. Rev. A22 (1980) 445.

75. ALKHAZOV, D.G., KOMAR, A.P., VOROB'V, A.A., Nucl. Instr. Meth. 48 (1967) 1.

76. NEUMANN, W., in Seventh Symposium on Microdosimetry, (BOOZ, J., EBERT, H.G., HARTFIEL, H.D., Eds.), EUR 7147, Harwood Academic, London (1981) p.1067.

77. PARETZKE, H.G., TURNER, J.E., HAMM, R.N., WRIGHT, H.A., RITCHIE, R.H., J. Chem. Phys. 84 (1986) 3182.

78. COMBECHER, D., Radiat. Res. 84 (1980) 189.

79. INTERNATIONAL COMMISSION ON RADIATION UNITS AND MEASUREMENTS, Stopping Power for Electrons and Positrons, ICRU-Report 37, ICRU, Bethesda MD (1984).

80. SAMUEL, A.H., MAGEE, J.L., J. Chem. Phys. 21 (1953) 1080.

81. WILSON, W.E., TOBUREN, L.H., Phys. Rev. A7 (1973) 1535.

82. BETZ, H-D., Rev. Mod. Phys. 44 (1972) 465.

83. BETZ, H-D., WITTKOWER, A.B., Phys. Rev. A 6 (1972) 1485.

84. NORTHCLIFFE, L.C., SCHILLING, R.F., Nucl. Data A 7 (1970) 233.

85. WILLIAMSON, C.F., BOUJOT, J.P., PICARD, J., Tables of Range and Stopping Power of Chemical Elements for Charged Particles of Energy 0.5 to 500 MeV, Rapport CEA-R 3042, Fontenay-aux-Roses (1966).

86. DIMITRIEV, I.S., NIKOLAEV, V.S., Soviet Phys. JETP 20 (1965) 409.

87. NIKOLAEV, V.S., DIMITRIEV, I.S., Phys. Lett. 28A (1968) 277.

88. PARETZKE, H.G., in Fourth Symposium on Microdosimetry, (BOOZ, J., EBERT, H.G., EICKEL, R., WAKER, A., Eds.), Report EUR 5122, Commission of the European Communities, Luxembourg (1974) p.141.

89. BARKAS, W.F., Nuclear Research Emulsions, Academic Press, New York (1963).

90. BETHE, H.A., Ann. Phys. 5 (1930) 325.

91. BETHE, H.A., in Handbuch der Physik, Vol. 24, Part I, (GEIGER, H., SCHEEL, K., Eds.), Springer-Verlag, Berlin (1933) p.273.

92. INOKUTI, M., Rev. Mod. Phys. 43 (1971) 297.

93. INOKUTI, M., ITIKAWA, Y., TURNER, J.E., Rev. Mod. Phys. 50 (1978) 23.

94. BICHSEL, H., in American Institute of Physics Handbook, 3rd ed., (GRAY, D.E., Ed.), McGraw-Hill, New York(1972) p.8.142.

95. BICHSEL, H., in Radiation Dosimetry, Vol. 1 (ATTIX, F.H., ROESCH, W.C., Ed.), Academic Press, New York (1968) p.157.

96. NORTHCLIFFE, L.C., Ann. Rev. Nucl. Sci. 13 (1963) 67.

97. SIGMUND, P., in Radiation Damage Processes in Materials, (DUPUY, C.H.S., Ed.), Noordhoff, Leyden (1975) p. 3.

98. LINDHARD, J., SCHARFF, M., DANSKE, K., Vidensk. Selsk. Mat.-Fys. Medd. 34 (1953).

99. AHLEN, S.P., Rev. Mod. Phys. 52 (1980) 121.

100. INTERNATIONAL COMMISSION ON RADIATION UNITS AND MEASUREMENTS, Basic Aspects of High Energy Particle Interactions and Radiation Dosimetry, Report 28, ICRU, Bethesda MD (1978).

101. RITCHIE, R.H., BRANDT, W., Phys. Rev. A 17 (1978) 2102.

102. STEWARD, P.G., Stopping Power and Range for any Nucleus in the Specific Energy Interval 0.01-500 MeV/amu in Any Nongaseous Material, UCRL-18127, University of California, Berkeley (1968).

103. ANDERSEN, H.H., The Stopping and Ranges of Ions in Matter, Vol. 2, Bibliography and Index of Experimental Range and Stopping Power Data, Pergamon Press, New York (1977).

104. ANDERSEN, H.H., ZIEGLER, J.F., Ref. 75a, Vol. 3, Hydrogen: Stopping Powers and Ranges in all Elements (1977).

105. ZIEGLER, J.F., Ref. 75a, Vol. 4, Helium: Stopping Powers and Ranges in all Elemental Matter (1977).

106. ZIEGLER, J.F., Ref. 75a, Vol. 5, Handbook of Stopping Cross Sections for Energetic Ions in all Elements (1980).

107. DENNIS, J.A., POWERS, D., in Sixth Symposium on Microdosimetry, (BOOZ, J., EBERT, H.G., Eds.), Report EUR 6064, Harwood Academic Publishers, London (1978) p.661.

108. PALMER, R.B.J., AKHAVAN-REZAYAT, A., in Sixth Symposium on Microdosimetry, (BOOZ, J., EBERT, H.G., Eds.), Report EUR 6064, Harwood Academic Publishers, London (1978) p.739.

109a. VAVILOV, P.V., Sov. Phys. JETP 5 (1957) 749.

109b. BICHSEL, H., Rev. Med. Phys. 60 (1988) 663.

110. TSCHALÄR, C., MACCABEE, H.D., Phys. Rev. B 1 (1970) 2863.

111. KELLERER, A.M., CHMELEVSKY, D., Radiat. Res. 63 (1975) 226.

112. INTERNATIONAL COMMISSION ON RADIATION UNITS AND MEASUREMENTS, Microdosimetry, ICRU-Report 36, ICRU, Bethesda, MD (1983).

113. STORM, E., ISRAEL, H.I., Nucl. Data Tabl. A7 (1971) 565.

114. BOOZ, J., in Third Symposium on Neutron Dosimetry in Biology and Medicine, (BURGER, G., EBERT, H.G., Eds.), EUR 5848, Commission of the European Communities, Luxembourg, p.499 (1978).

115. PARETZKE, H.G., BERGER, M., in Sixth Symposium on Microdosimetry, (BOOZ, J., EBERT, H.G., Eds.), Report EUR 6064, Harwood Academic Publishers, London (1978) p.749.

115a. COMBECHER, D., KOLLERBAUR, J., LEUTHOLD, G., PARETZKE, H.G., BURGER, G., in Sixth Symposium on Microdosimetry, (BOOZ, J., EBERT, H.G., Eds.), Report EUR 6064, Harwood Academic Publishers, London (1978) p.295.

116. BERGER, M.J., in Second Symposium on Microdosimetry, (EBERT, H.G., Ed.), Report EUR 4452, Commission of the European Communities, Brussels (1969) p.541.

116a. BERGER, M.J., in Third Symposium on Microdosimetry, (EBERT, H.G., Ed.), EUR 4810, Commission of the European Communities, Luxembourg (1972) p.157.

116b. BERGER, M.J., SELTZER, S.M., MAEDA, K., J. Atmos. Terr. Phys. 32 (1970) 1015.

117a. TERRISSOL, M., PATAU, J.P., in Seventh Symposium on Microdosimetry, (BOOZ, J., EBERT, H.G., HARTFIEL, H.D., Eds.), EUR 7147, Harwood Academic, London (1981) p.414.

117b. TERRISSOL, M., PATAU, J.P., EUDALDO, T., in Sixth Symposium on Microdosimetry, (BOOZ, J., EBERT, H.G., Eds.), Report EUR 6064, Harwood Academic Publishers, London (1978) p.169.

118. SINGHAL, R.P., JACKMAN, C.H., GREEN, A.E.S., J. Geophys. Res. 85 (1980) 1246.

119. GREEN, A.E.S., RIO, D.E., in Workshop on the Interface between Radiation Chemistry and Radiation Physics, Argonne National Laboratory, Report ANL-82-88 (1982) p.65.

120. KYSER, D.F., in Electron Beam Interactions with Solids for Microscopy, Microanalysis and Microlithography, Scanning Electron Microscopy, POB 66507, AMF O'Hare, IL (1984) p.119.

121. NEWBURY, D.E., MYKLEBUST, R.L., in Electron Beam Interactions with Solids for Microscopy, Microanalysis and Microlithography, Scanning Electron Microscopy, POB 66507, AMF O'Hare, IL (1984) p.153.

122. REIMER, L., Optik 27 (1968) 86.

123. SHIMIZU, R., KATAOKA, Y., IKUTA, T., KOSHIKAWA, T., HASHIMOTO, H., J. Phys. D 9 (1976) 101.

124. MURATA, K., KYSER, D.F., TING, C.H., J. Appl. Phys. 52 (1981) 4396.

125. LOVE, G., COX, M.G., SCOTT, V.D., J. Phys. D 10 (1977) 7.

126. TAN, K.H., BRION, C.E., VAN DER LEEUW, P.E. VAN DER WIEL, M.J., Chem. Phys. 29 (1978).

127. PARETZKE, H.G., LEUTHOLD, G., BURGER, G., JACOBI, W., in Fourth Symposium on Microdosimetry, (BOOZ, J., EBERT, H.G., EICKEL, R., WAKER, A., Eds.), Report EUR 5122, Commission of the European Communities, Luxembourg (1974) p.123.

128. BAUM, J.W., VARMA, M.N., WINGATE, C.L., PARETZKE, H.G., KUEHNER, A.V., in Fourth Symposium on Microdosimetry, (BOOZ, J., EBERT, H.G., EICKEL, R., WAKER, A., Eds.), Report EUR 5122, Commission of the European Communities, Luxembourg (1974) p.93.

129. PARETZKE, H.G., SCHINDEL, F., in Seventh Symposium on Microdosimetry, (BOOZ, J., EBERT, H.G., HARTFIEL, H.D., Eds.), EUR 7147, Harwood Academic, London (1981) p.387.

130. WILSON, W.E., PARETZKE, H.G., Radiat. Res. 87 (1981) 521.

131. MALBERT, M., CAREL, C., PATAU, J.P., TERRISSOL, M., in Seventh Symposium on Microdosimetry, (BOOZ, J., EBERT, H.G., HARTFIEL, H.D., Eds.), EUR 7147, Harwood Academic, London (1981) p.359.

132. CHARLTON, D.E., GOODHEAD, D.T., WILSON, W.E., PARETZKE, H.G., Energy Deposition in Cylindrical Volumes: a) Protons, Energy 0.3-4.0 MeV, b) Alpha Particles, Energy 1.2-20.0 MeV, Monograph 85/1, Medical Research Council, Radiobiology Unit, Chilton (1985).

133. ZAIDER, M., BRENNER, D.J., WILSON, W.E., Radiat. Res. 96 (1983) 231.

134. FOWLER, P.H., in Advances in Radiation Research, vol. 1, (DUPLAN, J.F., CHAPIRO, A., Eds.), Gordon and Breach, New York (1973) p.39.

135. PARETZKE, H.G., in Solid State Nuclear Track Detectors: Proceedings of the 11th International Conference, Bristol, Pergamon Press, Oxford (1982) p.3.

135a. PARETZKE, H.G., in Eighth Symposium on Microdosimetry, (BOOZ, J., EBERT, H.G., Eds.), EUR 8395, Commission of the European Communities, Luxembourg (1982) p.67.

136. PARETZKE, H.G., in Sixth Symposium on Microdosimetry, (BOOZ, J., EBERT, H.G., Eds.), Report EUR 6064, Harwood Academic Publishers, London (1978) p.925.

137. BURGER, G., COMBECHER, D., KOLLERBAUR, J., LEUTHOLD, G., IBACH, T., PARETZKE, H.G., in Seventh Symposium on Microdosimetry, (BOOZ, J., EBERT, H.G., HARTFIEL, H.D., Eds.), EUR 7147, Harwood Academic, London (1981) p.537.

138. INTERNATIONAL COMMISSION ON RADIATION UNITS AND MEASUREMENT, Radiation Quantities and Units, ICRU-Report 33, ICRU, Bethesda MD (1980).

139. INTERNATIONAL COMMISSION ON RADIATION UNITS AND MEASUREMENTS, Neutron Fluence, Neutron Spectra and Kerma, ICRU-Report 13, ICRU, Washington, DC (1969).

140. NATIONAL COUNCIL ON RADIATION PROTECTION AND MEASUREMENT, Protection against Neutron Radiation, NCRP-Report 38, NCRP-Publications, Washington, DC (1971).

141. COYNE, J.J., in Ion Chambers for Neutron Dosimetry, (BROERSE, J.J., Ed.), Commission of the European Communities, EUR 6782, Harwood Academic Publishers, London, p.195 (1980).

142. COHEN, M., JONES, D.E.A., GREENE, D., Br. J. Radiol. Suppl. 11 (1972) 12; 11 (1972) 81.

142a. BICHSEL, H. *et al.*, in First Symposium on Neutron Dosimetry in Biology and Medicine, Commission of the European Communities, Luxembourg, EUR 4896 (1972) p.93.

142b. BICHSEL, H. *et al.*, in Biomedical Dosimetry, IAEA publ. 401 (1975) p.3.

143. KELLERER, A.M., ROSSI, H.H., Curr. Top. Radiat. Res. Q. 8 (1972) 85.

144. KLIAUGA, P.J., DVORAK, R., Radiat. Res., 73 (1978) 1.

145. BRENNER, D., ZAIDER, M., DICELLO, J.F., BICHSEL, H., in Seventh Symposium on Microdosimetry, (BOOZ, J., EBERT, H.G., HARTFIEL, H.D., Eds.), Report EUR 7147, Harwood Academic Publishers, London (1981) p. 677.

145a. RUBACH, A., BICHSEL, H., Phys. Med. Biol. 27 (1982) 893.

145b. RUBACH, A., BICHSEL, H., Phys. Med. Biol. 27 (1982) 1003.

145c. RUBACH, A., BICHSEL, H., Phys. Med. Biol. 27 (1982) 1231.

145d. RUBACH, A., BICHSEL, H., Phys. Med. Biol. 27 (1982) 1455.

145e. RUBACH, A., BICHSEL, H., Phys. Med. Biol. 28 (1983) 913.

146. GOODHEAD, D.T., in The Dosimetry of Ionizing Radiation, Vol. II, (KASE, K.R., BJÄRNGARD, B.E., ATTIX, F.H., Eds.), Academic Press, Orlando (1987) p.1.

147. CHARLTON, D.E., GOODHEAD, D.T., WILSON, W.E., PARETZKE, H.G., Radiat. Prot. Dosim. 13 (1985) 123.

148. NIKJOO, H., GOODHEAD, D.T., CHARLTON, D.E., PARETZKE, H.G., Phys. Med. Biol. 34 (1989) 691.

149. NIKJOO, H., GOODHEAD, D.T., CHARLTON, D.E., PARETZKE, H.G., Int. J. Radiat. Biol. 60 (1991) 739.

150. CHARLTON, D.E., GOODHEAD, D.T., WILSON, W.E., PARETZKE, H.G., Energy Deposition in Cylindrical Volumes: (a) Protons, Energy 0.3 MeV to 4.0 MeV, (b) Alpha Particles 1.2 MeV to 20.0 MeV. MRC Radiobiology Unit Monograph 85/1, Medical Research Council Radiobiology Unit, Didcot, U.K. (1985).

151. NIKJOO, H., GOODHEAD, D.T., CHARLTON, D.E., PARETZKE, H.G., Energy Deposition in Cylindrical Volumes in Water Irradiated with Ultrasoft X-rays of Energy 0.28, 1.5, 4.5 and 8.1 keV. MRC Radiobiology Unit Monograph 88/1, Medical Research Council Radiobiology Unit, Didcot, U.K. (1988).

152. NIKJOO, H., GOODHEAD, D.T., CHARLTON, D.E., PARETZKE, H.G., Energy Deposition in Cylindrical Targets by Monoenergetic Electrons, 100 eV to 100 keV. MRC Radiobiology Unit Monograph, Medical Research Council Radiobiology Unit, Didcot, U.K. (in press).

153. NIKJOO, H., TERRISSOL, M., HAMM, R.N., TURNER, J., UEHARA, S., PARETZKE, H.G., GOODHEAD, D.T., Radiat. Prot. Dosim. (in press).

154. NIKJOO, H., UEHARA, S., in Proc. DOE Workshop on Monte Carlo Methods in Track Structure, 27-29 April 1993, Irvine, California (in press).

155. WILSON, W.E., METTING, N.F., Radiat. Res. 115 (1988) 389.

156. MICHALIK, V., Phys. Med. Biol. 36 (1991) 1001.

157. PARETZKE, H.G., TURNER, J.E., HAMM, R.N., WRIGHT, H.A., RITCHIE, R.H., Radiat. Res. 127 (1991) 121.

158. MITEREV, A.M., High Energy Chemistry 21 (1987) 332.

159. BUTTS, J.J., KATZ, R., Radiat. Res. 30 (1967) 855.

160. MITEREV, A.M., KAPLAN, I.G., BORISOV, E.A., High Energy Chemistry 8 (1974) 461.

161. INTERNATIONAL COMMISSION ON RADIATION UNITS AND MEASUREMENTS, Linear Energy Transfer, ICRU-Report 16, ICRU, Bethesda MD (1970).

162. PARETZKE, H.G., in Solid State Nuclear Track Detectors: Proceedings of the 9th International Conference, Neuherberg/Munich, Pergamon Press, Oxford (1978) p.87.

163. BENTON, E.V., NIX, W., Nucl. Instr. Meth. 67 (1969) 343.

164. ROHRLICH, F., CARLSON, B.C., Phys. Rev. 93 (1954) 38.

165. WINGATE, C.L., BAUM, J.W., Radiat. Res. 65 (1976) 1.

166. BAUM, J.W., in Second Symposium on Microdosimetry, (EBERT, H.G., Ed.), Report EUR 4452, Commission of the European Communities, Brussels (1969) p.653.

167. VARMA, M.N., PARETZKE, H.G., BAUM, J.W., LYMAN, J.T., HOWARD, J., in Fifth Symposium on Microdosimetry, (BOOZ, J., EBERT, H.G., SMITH, B.G.R., Eds.), Report EUR 5454, Commission of the European Communities, Luxembourg (1976) p.75.

168. VARMA, M.N., BAUM, J.W., KUEHNER, A.V., Radiat. Res. 62 (1975) 1.

169. VARMA, M.N., BAUM, J.W., Radiat. Res. 81 (1980) 363.

170. VARMA, M.N., BAUM, J.W., KUEHNER, A.V., Phys. Med. Biol. 25 (1980) 651.

171. VARMA, M.N., BAUM, J.W., KLIAUGA, P., in Sixth Symposium on Microdosimetry, (BOOZ, J., EBERT, H.G., Eds.), Report EUR 6064, Harwood Academic Publishers, London (1978) p.227.

172. KLIAUGA, P., ROSSI, H.H., in Fifth Symposium on Microdosimetry, (BOOZ, J., EBERT, H.G., SMITH, B.G.R., Eds.), Report EUR 5454, Commission of the European Communities, Luxembourg (1976) p.127.

173. MENZEL, H.G., BOOZ, J., in Fifth Symposium on Microdosimetry, (BOOZ, J., EBERT, H.G., SMITH, B.G.R., Eds.), Report EUR 5454, Commission of the European Communities, Luxembourg (1976) p.61.

174. IBACH, T., COMBECHER, D., in Seventh Symposium on Microdosimetry, (BOOZ, J., EBERT, H.G., HARTFIEL, H.D., Eds.), EUR 7147, Harwood Academic, London (1981) p.191.

175. MOZUMDER, A., J. Chem. Phys. 60 (1974) 1145.

176. CHATTERJEE, A., MACCABEE, H., TOBIAS, C., Radiat. Res. 54 (1973) 479.

177. CHATTERJEE, A., SCHÄFER, H.J., Radiat. Environ, Biophys. 13 (1976) 215.

178. FAIN, J., MONNIN, M., MONTRET, M., in Fourth Symposium on Microdosimetry, (BOOZ, J., EBERT, H.G., EICKEL, R., WAKER, A., Eds.), Report EUR 5122, Commission of the European Communities. Luxembourg (1974) p.169.

179. MONNIN, M., in International Topical Conference on Nuclear Track Registration in Insulating Solids and Applications, Vol. 1, (ISABELLE, D., MONNIN, M., Eds.), Universite de Clermont-Ferrand (1969) p. II-73.

180. HANSEN, J.W., OLSEN, K.J., Radiat. Res. 97 (1984) 1.

181. LA VERNE, J.A., SCHULER, R.H., J. Phys. Chem. 88 (1984) 1200.

182. LA VERNE, J.A., SCHULER, R.H., J. Phys. Chem. 91 (1987) 5770.

183. BIBLER, N.E., J. Phys. Chem. 79 (1975) 1991.

184. MITEREV, A.M., MAMEDJAROV, D.Y., KAPLAN, I.G., High Energy Chem. 26 (1992) 20.

185. MAGEE, J.L., J. Chim. Phys. 52 (1955) 528.

186. MOZUMDER, A., MAGEE, J.L, J. Chem. Phys. 45 (1966) 3332.

187. MAGEE, J.L, CHATTERJEE, A., in Radiation Research: Proceeding of the 6th Intern. Congress, (OKADA, S., IMANURA, M., TERASHIMA, T., YAMAGUCHI, H., Eds.), Japan Association of Radiation Research, Tokyo (1979) p.166.

188. KUPPERMANN, A., in Radiation Research: Proceedings of the 3rd International Congress, Cortina d'Ampezzo, Italy, (SILINI, G., Ed.), Wiley, New York (1967) p.212.

189. FREEMAN, G.R., in Workshop on the Interface between Radiation Chemistry and Radiation Physics, Argonne National Laboratory, Report ANL-82-88 (1982) p.9.

190. BURNS, W.G., in Seventh Symposium on Microdosimetry, (BOOZ, J., EBERT, H.G., HARTFIEL, H.D., Eds.), EUR 7147, Harwood Academic, London (1981) p.471.

191. BERGER, M.J., in Seventh Symposium on Microdosimetry, (BOOZ, J., EBERT, H.G., HARTFIEL, H.D., Eds.), EUR 7147, Harwood Academic, London (1981) p.521.

192. TURNER, J.E., MAGEE, J.L., HAMM, R.N., CHATTERJEE, A., WRIGHT, H.A., RITCHIE, R.H., in Seventh Symposium on Microdosimetry, (BOOZ, J., EBERT, H.G., HARTFIEL, H.D., Eds.), EUR 7147, Harwood Academic, London (1981) p.507.

193. MILLER, J.H., WILSON, W.E., in Workshop on the Interface between Radiation Chemistry and Radiation Physics, Argonne National Laboratory, Report ANL-82-88 (1982) p.73.

194. GRAY, L.H., Br. J. Radiol. 10 (1937) 600; (1937) 721.

195. PARETZKE, H.G., in Fifth Symposium on Microdosimetry, (BOOZ, J., EBERT, H.G., SMITH, B.G.R., Eds.), Report EUR 5454, Commission of the European Communities, Luxembourg (1976) p.41.

196. DELAFIELD, H.J., HOLT, P.D., in Charged Particle Tracks in Solids and Liquids, (ADAMS, G.E., BEWLEY, D.K., BOAG, J.W., Eds.), Institute of Physics, Conference Series No. 8, London (1970) p.35.

197. BUDD, T., MARSHALL, M., Radiat. Res. 93 (1983) 19.

198. BUDD, T., KWOK, C.S., MARSHALL, M., LYTHE, S., Radiat. Res. 95 (1983) 217.

199. SPÄTH, H., Cluster Analysis Algorithms for Data Reduction and Classification of Objects, Wiley, New York (1980).

200. SOKAL, R.R., in Classification and Clustering, (VAN RYZIN, J., Ed.), Academic Press, New York (1977) p.1.

201. SNEATH, P.H.A., SOKAL, R.R., Nature 193 (1962) 855.

202. SOKAL, R.R., ROHLF, F.J., Taxonomy 11 (1962) 33.

203. SNEATH, P.H.A., SOKAL, R.R., Numerical Taxonomy, Freeman, San Francisco (1973).

204. ZADEH, L.A., in Classification and Clustering, (VAN RYZIN, J., Ed.), Academic Press, New York (1977) p.251.

205. BEZDEK, J.C., J. Math. Biol. 1 (1974) 57.

206. KACPRZYK, J., YAGER, R.R. (Eds.), Management Decision Support Systems Using Fuzzy Sets and Possibility Theory, Verlag TÜV Rheinland, Köln (1985).

207. GOGALA, E., Probabilistic Sets in Decision Making and Control, Verlag TÜV Rheinland, Köln (1984).

208. HAKEN, H. (Ed.), Pattern Formation by Dynamic Systems and Pattern Recognition, Springer-Verlag, Berlin (1979).

209. FU, K.S., Digital Pattern Recognition, Springer-Verlag, Berlin (1976).

210. CHEN, C.H. (Ed.), Pattern Recognition and Artificial Intelligence, Academic Press, New York (1976).

210a. INOKUTI, M., Radiat. Eff. Defects Solids 117 (1991) 143.

211. SWANSON, N., POWELL, C.J., Phys. Rev. 145 (1966) 195.

212. KAPLAN, I.G., MITEREV, A.M., SUKHONOSOV, V. Ya, Radiat. Phys. Chem. 27 (1986) 83.

213. KAPLAN, I.G., IAEA -TECDOC 506 (1989) 80.

214. KAPLAN, I.G., MITEREV, A.M., SUKHONOSOV, V. Ya, Radiat. Phys. Chem. 36 (1990) 493.

215. GOODHEAD, D.T., LEENHOUTS, H.P., PARETZKE, H.G., TERRISSOL, M., NIKJOO, H., BLAAUBOER, R., Radiat. Prot. Dosim. (in press).

216. PROC. TENTH SYMP. ON MICRODOSIMETRY, Radiat. Prot. Dosim. 31 (1990) 1-4.

217. PROC. ELEVENTH SYMP. ON MICRODOSIMETRY, Gatlinburg, Sept 1992. Radiat. Prot. Dosim. (in press).

218. HOWELL, R.W., NARRA, V.R., SASTRY, K.S.R., RAO, D.V. (Eds.), Biophyiscal Aspects of Auger Processes. American Institute of Physics, Woodbury, USA (1992).

219. CHADWICK, K.H., MOSCHINI, G., VARMA, M.N. (Eds.), Biophysical Modelling of Radiation Effects, Adam Hilger, Bristol (1992).

220. PROC. DOE WORKSHOP ON MONTE CARLO METHODS IN TRACK STRUCTURE, 27-29 April 1993, Irvine, California (in press).

221. NYGAARD, O.F., SINCLAIR, W.K., LETT, J.T. (Eds.), Effects of Low Dose and Low Dose Rate Radiation, Advances in Radiat. Biol. 16, Academic Press, San Diego (1992).

222. GOODHEAD, D.T., MUNSON, R.J., THACKER, J., COX, R., Int. J. Radiat. Biol. 37 (1980) 135.

223. GOODHEAD, D.T., BRENNER, D.J., Phys. Med. Biol. 28 (1983) 485.

224. GOODHEAD, D.T., NIKJOO, H., Int. J. Radiat. Biol. 55 (1989) 513.

225. HOWARD-FLANDERS, P., Adv. Biol. Med. Phys. 6 (1958) 553.

226. BARENDSEN, G.W., Int. J. Radiat. Biol. 8 (1964) 453.

227. GOODHEAD, D.T., Int. J. Radiat. Biol. 56 (1989) 623.

228. GOODHEAD, D.T., THACKER, J., COX, R., Int. J. Radiat. Biol. 63 (1993) 543.

229. GOODHEAD, D.T., Int. J. Radiat. Biol. 65 (Jan. 1994).

230. CHARLTON, D.E., NIKJOO, H., GOODHEAD, D.T., in Radiation Research, A twentieth-Century Perspective, (DEWEY, W.C., EDINGTON, M., FRY, R.J.M., HALL, E.J., WHITMORE, G.F., Eds.) (1992) p. 421.

231. GOODHEAD, D.T., CHARLTON, D.E., WILSON, W.E., PARETZKE, H.G., in Radiation Protection: Fifth Symposium on Neutron Dosimetry, (SCHRAUBE, H., BURGER, G., BOOZ, J.J., Eds.), Report EUR 9762, Commission of the European Communities, Luxembourg (1985) p. 57.

232. GOODHEAD, D.T., THACKER, J., COX, R., Phys. Med. Biol. 26 (1981) 1115.

233. CHARLTON, D.E., NIKJOO, H., HUMM, J.L., Int. J. Radiat. Biol. 56 (1989) 1.

234. MICHALIK, V., Int. J. Radiat. Biol. 62 (1992) 9.

235. MICHALIK, V., Radiat. Environm. Biophys. 32 (1993) 251.

236. BRENNER, D.J., WARD, J.F., Int. J. Radiat. Biol. 61 (1992) 737.

237. PRUPPERS, M.J.M., LEENHOUTS, H.P., CHADWICK, K.H., Radiat. Prot. Dosim. 31 (1990) 185.

238. HANSEN, J.W., OLSEN, K.J., Radiat. Res. 97 (1984) 1.

239. COX, R., MASSON, W.K., Int. J. Radiat. Biol. 36 (1979) 149.

240. WILSON, W.E., PARETZKE, H.G., Radiat. Res. 81 (1980) 326.

241. HENSS, S., Biophysikalisches Modell zur Induktion Dizentrischer Chromosomen durch Ionisierende Strahlung, Dissertation, Technische Universitat, Munchen (1991).

242. HENSS, S., PARETZKE, H.G., in Biophysical Modelling of Radiation Effects, (CHADWICK, K.H., MOSCHINI, G., VARMA, M.N., Eds.), Adam Hilger, Bristol (1992) p. 69.

243. LONG, K.A., PARETZKE, H.G., MUILLER-PLATHE, F., DIERCKSEN, G.H.F., J. Chem. Phys. 91 (1989) 1569.

244. LONG, K.A., PARETZKE, H.G., J. Chem. Phys. 95 (1991) 1049.

245. CHARLTON, D.E., HUMM, J.L., Int. J. Radiat. Biol. 53 (1988) 353.

246. MILLAR, B.C., SAPORA, O., FIELDEN, E.M., LOVELOCK, P.S., Radiat. Res. 86 (1981) 506.

247. BOYE, E., KIRSCH, R.E., Int. J. Radiat. Biol. 37 (1980) 119.

248. MARK, F., BECKER, U., HERAK, J.N., SCHULTE-FROHLINDE, D., Radiat. Environm. Biophys. 28 (1989) 81.

249. VON SONNTAG, C., The Chemical Basis of Radiation Biology, Taylor & Francis, London (1981).

250. HOLLEY, W.R., CHATTERJEE, A., in The Early Effects of Radiation on DNA, (FIELDEN, E.M., O'NEILL, P., Eds.), NATO ASI Series (1991) p. 195.

251. WRIGHT, H.A., HAMM, R.N., TURNER, J.E., HOWELL, R.W., RAO, D.V., SASTRY, K.S.R., Radiat. Prot. Dosim., 31 (1990) 59.

252. TERRISSOL, M., POMPLUN, E., Radiat. Prot. Dosim. (in press).

252a. KALOS, M.H., WHITLOCK, P.A., Monte Carlo Methods Vol. I: Basics. Wiley and Sons, New York (1986).

253. HAMM, R.N., TURNER, J.E., RITCHIE, R.H., WRIGHT, H.A., Radiat. Res. 104 (1985) S20.

254. TERRISSOL, M., Méthode de simulation du transport des électrons d'énergies comprises entre 10 eV et 30 keV. Thesis no 839 UPS Toulouse (1978).

255. DANJO, A., NISHIMURA, H., J. Phys. Soc., Japan, 54 (1985) 1224.

256. ITIKAWA, Y., J. Phys. Soc. Japan, 36 (1974) 1127.

257. TRAJMAR, S., WILLIAMS, W., KUPPERMANN, A., J. Chem. Phys. 58 (1973) 2521.

258. MICHAUD, M., SANCHE, L., Phys. Rev. A36 10 (1987) 4672.

259. JAIN, A., KHARE, S.P., J. Phys. B: Atom. Mol. Phys. 15 (1982) L867.

260. GRYZINSKI, M., Phys. Rev. A138 (1965) 305.

APPENDIX

ESTAR, PSTAR and ASTAR: Computer Programs for Calculating Stopping Powers and Ranges for Electrons, Protons and Helium Ions

M.J. Berger
National Institute of Standards and Technology,
Gaithersburg, Maryland,
United States of America

This Appendix describes three computer programs, ESTAR, PSTAR and ASTAR, which calculate stopping-powers and ranges for electrons, protons and alpha particles (helium ions). ESTAR is applicable to any element, compound or mixture. PSTAR and ASTAR are applicable to 74 materials, including many of interest in biomedical dosimetry. A detailed description of the methods used in these programs can be found in ICRU Reports 37 and 49 [1,2].

The original versions of PSTAR and ASTAR [3] are based on calculations with a fixed set of mean excitation energies from [1,2]. In Version 2 presented here, stopping powers and ranges can be adjusted so that they correspond to mean excitation energies that differ by up to 10 percent from the values used in Version 1. Furthermore, the stopping powers of graphite in version 2 of PSTAR are modified to take into account recent measurements of the amorphous-carbon/graphite stopping power ratio by Necas *et al.* [4].

The files for ESTAR, PSTAR and ASTAR are stored in compressed form in three archive files EST.EXE, PST.EXE and AST.EXE. These archives contain executable code (for use with IBM-compatible personal computers), data files, and Fortran source code. The latter can be used to compile the programs on other types of computers. The archive files are self-extracting. When used with an IBM-compatible personal computer, the commands EST, PST or AST will extract and decompress all the files from the archives.

The archive files are stored on two 3.5-inch 1.44-Mb floppy disks. Disk 1 contains EST.EXE and AST.EXE, and Disk 2 contains PST.EXE. The two disks can be obtained from the Nuclear Data Section, Division of Physical and Chemical Sciences, International Atomic Energy Agency, Wagramerstrasse 5, P.O. Box 100, A-1400 Vienna, Austria.

A.1. ESTAR: Stopping Powers and Ranges for Electrons.

A.1.1. Output from ESTAR

ESTAR calculates the following quantities:

a) *Electronic mass stopping power* – average rate of energy loss per unit path length, due to Coulomb collisions that result in the ionization and excitation of atoms, MeV cm^2/g.

b) *Radiative mass stopping power* – average rate of energy loss per unit path length due to collisions with atoms and atomic electrons in which bremsstrahlung quanta are emitted, MeV cm^2/g.

c) *Total mass stopping power* – sum of a) and b), MeV cm^2/g.

d) *Density effect correction* – correction term in the stopping power formula that takes into account the reduction of the electronic mass stopping power due to the polarization of the medium by the incident electron.

e) *CSDA range* – a close approximation to the average path length traveled by a charged particle as it slows down to rest, calculated in the continuous-slowing-down approximation, g/cm^2. Obtained by integrating the reciprocal of the total stopping power with respect to energy.

f) *Radiation yield* – fraction of the energy of primary electron converted into bremsstrahlung, calculated in the continuous-slowing-down approximation.

There are two output options:

Option 1 A table is produced that includes all of the quantities a) through f) at a standard set energies between 10 keV and 1000 MeV. The spacing of the energy grid is approximately logarithmic. The output is a two-page table with a format similar to that of the tables in [1].

Option 2 Output quantities a) through d) are tabulated at a user-selected set of energies between 1 keV and 10 GeV.

A.1.2. Method used for Electrons

Electronic mass stopping powers are calculated from the theory of Bethe [5,6], using Eq. (7.1) of Chapter 7.2, with a density-effect correction evaluated according to Sternheimer [7,8]. By default, I-values are used which are identical with those recommended in [1,2]. However, the user is given the opportunity of choosing different I-values.

The uncertainties of the calculated electronic mass stopping powers for electrons are estimated in [1] to be 1 to 2 percent above 100 keV, and 2 to 3 percent (in low-Z materials) and 5 to 10 percent (in high-Z materials) between 100 keV and 10 keV. The increasing uncertainties at low energies are mainly due to the lack of shell corrections.

Radiative stopping powers are evaluated in ESTAR with a combination of theoretical bremsstrahlung cross sections described by Seltzer and Berger [9]. Analytical formulas (using high-energy approximations) are used above 50 MeV, and numerical results of Pratt *et al.* [10] below 2 MeV. Cross sections in the intermediate energy region from 2 MeV to 50 MeV are obtained by interpolation. The uncertainties of the radiative stopping powers are estimated to be 2 percent above 50 MeV, 2 to 5 percent between 50 and 2 MeV, and 5 percent below 2 MeV.

A.1.3. Required Program Files and Data Files

ESTAR can be run on an IBM-compatible personal computer, using the DOS operating system (Version 2.1 or higher). A mathematical coprocessor is required. The following files are used:

ESTAR.EXE executable code

UEDAT atomic data, in an unformatted direct-access file

UCOMP — data pertaining to the composition of materials, in a binary direct-access file

IDLIST.COM — executable code that displays a list of material names included in the database UCOMP

COMPOS.EXE — executable code for examining the contents of the database UCOMP

ENG.ELE — default energy list (81 values between 0.01 and 1000 MeV).

For the installation of the program on a different type of computer, the following Fortran-77 source-code and data files (in ASCII format) are available:

ESTAR.FOR, COMPOS.FOR, EDCONV.FOR, CONVERT.FOR, FEDAT, and FCOMP.

These files are to be used as follows:

a) ESTAR.FOR, COMPOS.FOR, EDCONV.FOR and CONVERT.FOR must be compiled individually to produce executable codes.

b) EDCONV must be run, using FEDAT as input. The output is the unformatted direct-access file UEDAT.

c) CONVERT must be run, using FCOMP as input. The output is the unformatted direct-access file UCOMP.

A.1.4. Specification of the Properties of the Stopping Medium

ESTAR must be supplied with information about the atomic composition, density, and mean excitation energy (I-value) of the material. There are two ways in which this information can be provided:

Option 1 — For 279 materials, the required information can be read from the data file UCOMP.

Option 2 — The information for any material can be supplied from the keyboard, in response to prompts from ESTAR.

With both options, ESTAR provides a default I-value, which the user can accept, or replace by another value. Because of the scarcity of experimental data for electrons, such a choice has to be based on a data analysis for protons or alpha particles, or on the determination of I-values from the analysis of oscillator strengths or dielectric response functions.

The UCOMP file includes data for 279 materials, which are referenced by identification (ID) numbers 1,2,...,278, and 906. Carbon appears twice, as amorphous carbon (ID = 6) and as graphite (ID = 906). ID numbers smaller than 99 pertain to elements, and are identical with atomic numbers. The other ID numbers pertain to compounds or mixtures. Table 1 gives a listing of ID numbers and names of materials. Elements appear in this list in order of increasing atomic number, and are followed by compounds and mixtures arranged alphabetically by name. The command IDLIST can be used to start a program which lists, on the monitor screen, all ID numbers and material names in UCOMP. This display can be scrolled.

Included in UCOMP are default I-values for 279 materials. The values for 25 elements and 48 compounds are identical those used in [1,2]. Those for the other compounds in UCOMP are obtained with approximate procedures adopted in [1] for materials for which direct experimental information is lacking. This involved use of a modified Bragg rule using I-values for atomic constituents that in a crude way take into account chemical-binding and phase effects (see Section 7.2.1.5).

The contents of UCOMP for a specified ID number can be examined by running the program COMPOS. The program prompts the user to specify the ID number of the material of interest, and lists the atomic numbers and weights of the atomic constituents, the density of the material, and the I-value.

If the composition data are entered from the keyboard, the user is prompted to supply the following information:

a) Name of the material, to be used in table headings;

b) The density of the material, g/cm^3;

c) The classification of the material: element, compound or mixture;

d) The chemical symbol for the element, or the chemical formula for the compound, which must be entered in standard chemical notation, with upper and lower case letters; subscripts must be written on-line. For example, silicon is to be entered as Si, silicon dioxide as SiO2, and water as H2O.

e) For mixtures, the user must provide the number of constituents (which can be elements or compounds), the fractions by weight of these constituents, and their chemical symbols or formulas. If data for a constituent are included in the UCOMP file, it is possible (but not required) to enter the information from the UCOMP file by using the appropriate ID number. For example, for Pyrex glass (80.7% SiO_2, 12.9% B_2O_3, 3.8% Na_2O, 2.2% Al_2O_3 and 0.4% K_2O by weight) the input for Al_2O_3 and SiO_2 can be taken from UCOMP.

ESTAR calculates, and displays on the monitor screen, the fractions by weight of the atomic constituents in a mixture. The user is prompted to inspect these fractions, and can either accept them or enter different composition data. With entry from the keyboard, the composition data are used by ESTAR to determine the I-value of the material. For compounds this is done by the modified Bragg-additivity rule described above. The use of this procedure results in I-values that for elements are the same, and for compounds are either identical with, or very close to, those stored in UCOMP.

ESTAR provides the option of storing the composition data entered from the keyboard in a designated file, which can be merged into the FCOMP file. When an enlarged FCOMP file is used, the data statements KMAX/279/ in CONVERT.FOR and KLST/278/ in COMPOS.FOR must be appropriately changed.

A.1.5. Specification of Electron Energies

With Output Option 2 (see Section A.1.1) a list of energies must be supplied at which stopping powers are to be calculated. This can be done in three ways:

a) A list of energies can be read a from default file ENG.ELE, containing 81 energies between 1 keV and 1000 MeV.

b) A list of energies can be read from a previously prepared file. The first line of this file must contain the number of energies in the list; subsequent lines must contain the energies (in MeV), separated by blanks.

c) The desired list of energies can be entered from the keyboard, in response to prompts from ESTAR.

In cases b) and c), ESTAR issues a warning if at least one of the requested energies is smaller than 10 keV. ESTAR halts if it encounters an energy below 1 keV.

A.2. PSTAR and ASTAR: Stopping Powers and Ranges for Protons and Helium Ions

A.2.1. Output from PSTAR and ASTAR

The following quantities are calculated:

a) *Electronic mass stopping power* – average rate of energy loss per unit path length, due to Coulomb collisions that result in the ionization and excitation of atoms, MeV cm^2/g.

b) *Nuclear mass stopping power* – average rate of energy loss per unit path length, due to elastic Coulomb collisions with atomic nuclei, MeV cm^2/g.

c) *Total mass stopping power* – sum of a) and b), MeV cm^2/g.

d) *CSDA range* – an extremely close approximation to the average path length traveled by a charged particle as it slows down to rest, in g/cm^2, calculated in the continuous-slowing-down approximation. Obtained by integrating the reciprocal of the total stopping power with respect to energy.

e) *Projected range* – average value of the depth to which a charged particle penetrates in the course of slowing down to rest, in MeV cm^2/g. This depth is measured along the initial direction of the particle.

f) *Detour factor* – ratio of the projected range to the CSDA range (always smaller than unity, due to multiple-scattering detours)

A.2.2. Method of Calculation for Protons and Helium Ions

PSTAR and ASTAR rely on interpolation in a database of stopping powers and ranges. A brief description will now be given of the methods used for producing this database.

A.2.2.1. Merger of High-Energy Theory and Low-Energy Data. Electronic mass stopping powers are evaluated from Bethe's theory at high energies, and from experimentally-based fitting formulas at low energies. The experimental stopping powers at energies below a cut-off energy T_1, together with the theoretical values from the Bethe theory at energies above a cut-off energy T_2, are fitted by a cubic spline. Actually the cubic-spline fit is made for the

quantity $\beta^2(S/\rho)$, where β is the particle speed in units of the speed of light, and S/ρ is the mass stopping power. The cubic-spline function is used to obtain, by interpolation, stopping powers at energies between T_1 and T_2. The values of T_1 and T_2 are adjusted individually for each material to obtain a visually pleasing plot of stopping power *vs.* energy. The adopted values of T_1 and T_2 are given in Table 2 for protons, and in Table 3 for helium ions.

The uncertainties of the electronic mass stopping powers in the high-energy region are estimated to be 1 to 2 percent for elements, and 1 to 4 percent for compounds. The uncertainties in the low-energy region are estimated to be 2 to 5 percent at 1000 keV, 5 to 10 percent at 100 keV, 10 to 15 percent at 10 keV, and at least 20 to 30 percent at 1 keV.

A.2.2.2 Stopping Power Theory at High Energies. Stopping powers are calculated according to the formulas given in Chapter 7.3.1.1.* The shell corrections for most elements are based on semi-empirical formulas developed by Bichsel (described in [1]). For most materials the shell corrections, together with the default I-values, are those denoted as "Model 1" in [2].

For elements with atomic numbers Z = 47, 64, 74, 78, 79, 82 and 92 two sets of calculations are made, one with shell corrections from Model 1, and another with shell corrections and I-values from a Model 2 due to Bichsel [11]. The calculations with Model 2 are used up to an energy T_3, and those with Model 1 above energy T_4, and stopping-power values between T_3 and T_4 are obtained by cubic-spline interpolation. The values of T_3 and T_4 are taken to be 25 MeV and 100 MeV for protons, and 100 MeV and 400 MeV for helium ions.

The Barkas correction is calculated according to the method of Ashley *et al.* [12,13], with parameter values used in [1]. For elements with atomic numbers Z = 47, 64, 74, 78, 79, 82 and 92, empirical Barkas correction from [14] are used. The density-effect correction is evaluated according to Sternheimer [7,8], and is significant only for protons with energies of several hundred MeV or higher.

A.2.2.3. Adjustment of Mean Excitation Energy. For each material ESTAR calculates the stopping powers in the high-energy region three times, with different I-values: with the default value (from [1,2]) and with values that are 10 percent lower, and 10 percent higher, than the default value. The results from these three calculations are merged with the same set of fitted low-energy stopping powers. Stopping powers with intermediate I-values can be accurately calculated by interpolation with respect to logI.

For elements with atomic numbers Z = 47, 64,74, 78, 79, 82 and 92, the Bethe formula with Model-2 shell corrections quite accurately represents a large body of experimental data in the energy region from 0.3 MeV to 20 MeV [11]. For these elements the changes of the stopping power due to differences of the I-value from the default value are therefore only evaluated for protons above 25 MeV and helium ions above 100 MeV.

In view of the differences between the I-values recommended by various authors (see, e.g., the discussion in Chapter 7.2.1), the opportunity of varying the I-values in ESTAR is

*This was done with a program BEST, which combines codes from ESTAR for the calculation of the density effect correction with subroutines for the calculation of the Bloch, Barkas and shell corrections from an unpublished program of H. Bichsel. With BEST one can obtain stopping powers for stripped particles of any mass or charge.

useful, but should be used with care. One should keep in mind that many of the default I-values adopted in [1,2] are obtained in an analysis of measured stopping powers or ranges that involved the simultaneous determination of I-values and of various parameters pertaining to the shell corrections and Barkas corrections. A change of an I-value may therefore require a corresponding adjustment of these corrections, to ensure that the calculated and experimental stopping powers remain in adequate agreement. References to the available experimental literature for such an analysis can be found in the bibliographies of Andersen [15] and Powers [16].

A.2.2.4 Empirical Stopping Powers at Low Energies. In the low-energy region, stopping powers are calculated from fitting formulas that represent experimental data for many elements and a limited number of compounds. Extensive use is made of a fitting formula of Varelas and Biersack [17] with numerical coefficients adopted in [2], which - except for a few materials - are from Andersen and Ziegler [18] for protons, and from Ziegler [19] or Watt [20] for alpha particles. For a few materials use is made of a different fitting formula for alpha-particle stopping powers developed by Powers [21].

For compounds for which no experimental stopping power data are available, the Bragg additivity rule is used, and mass stopping powers are calculated as linear combinations of the mass stopping powers of the constituents atoms. When applying the additivity rule to mixtures, these are treated, to the extent possible, as a mixtures of compounds and elements. For example, the stopping power of "muscle" is obtained by as a weighted sum of the stopping power of water (assumed to be 78.6% by weight) and the stopping powers of the other elemental constituents.

A.2.2.5. Nuclear Stopping Powers. Cross sections for the elastic scattering of charged particles by atoms are obtained by a classical-mechanics orbit calculation, using the method of Everhart *et al.* [22]. For protons the screened potential is assumed to be the Thomas-Fermi potential as parameterized by Molière [23]. For alpha particles, the "universal" ion-atom potential of Ziegler *et al.* [24] is used. Nuclear stopping powers are calculated using the relation between the deflection angles and the energy transfers to the recoiling atom in elastic collisions. In [2] the uncertainties of nuclear stopping powers for alpha particles are estimated to be 5 to 10 percent at 100 keV, 10 percent at 10 keV, and 10 to 20 percent at 1 keV.

A.2.2.6 CSDA and Projected Ranges. CSDA ranges are calculated by integrating the reciprocal of the total stopping power (electronic plus nuclear) with respect to energy. Projected ranges are obtained in a transport calculation according to the method of Lewis [25], which uses the elastic scattering cross sections mentioned above.

A.2.3. Required Program and Data Files*

PSTAR and ASTAR can be run on an IBM-compatible personal computer using the DOS operating system (Version 2.1 or higher). A mathematical coprocessor is required. The following files are required to run PSTAR:

---

*The files FCOMP, UCOMP, COMPOS.EXE, COMPOS.FOR and CONVERT.FOR are used in ESTAR as well as PSTAR and ASTAR. However, PSTAR and ASTAR use only part of the information stored in FCOMP and UCOM.

PSTAR.EXE	executable code for generating a stopping-power and range table
UPROT0	database that contains stopping power and range data calculated with default I-values
UPROTL	similar to UPROT, but calculated with I-values 10 percent smaller than the default I-values
UPROTH	similar to UPROT, but calculated with I-values 10 percent larger than the default I-values
NAMES	set of names of the 74 materials in the database
ENG.PRO	default energy list (133 energies between 1 keV and 10,000 MeV)
UCOMP	file that contains material composition data
COMPOS.EXE	executable code for examining the contents of UCOMP
IDL.COM	executable code that displays a list of material names and corresponding ID numbers;

The following files are required to run ASTAR:

ASTAR.EXE	executable code for generating a stopping-power and range table
UALPH0	database that contains stopping power and range data
UALPHL	similar to UPROT, but calculated with I-values 10 percent smaller than the default I-values
UALPHH	similar to UPROT, but calculated with I-values 10 percent larger than the default I-values
NAMES	set of names of the 74 materials in the database
ENG.ALF	default energy list (122 energies between 1 keV and 1000 MeV)
UCOMP	file that contains information about the composition of the materials included in the database;
COMPOS.EXE	executable code for examining the contents of UCOMP for a specified material;
IDL.COM	executable code that displays a list of material names and corresponding ID numbers.

For the installation of the program on a different type of computer, the following Fortran-77 source-code and data files (in ASCII format) are available:

For Protons:	For Helium Ions:	For Both:
PSTAR.FOR	ASTAR.FOR	COMPOS.FOR
PCONVERT.FOR	ACONVERT.FOR	CONVERT.FOR
FPROT	FALPH	FCOMP
FPROTL	FALPHL	
FPROTH	FALPHH	

These files are to be used as follows:

a) PSTAR.FOR, ASTAR.FOR, PCONVERT.FOR , ACONVERT.FOR and CONVERT.FOR must be compiled individually to generate executable code

b) PCONVERT must be run, using formatted files FPROT0, FPROTL or FPROT1 as input, to generate unformatted direct-access files UPRPOT0, UPROTL or UPROTH

c) ACONVERT must be run, using formatted files FALPH0, FALPHL or FALPHH as input, to generate unformatted direct-access files UALPH0, UALPHL or UALPHH

d) CONVERT must be run, using formatted file FCOMP as input, to generate unformatted direct-access file UCOMP.

A.2.4. List of Materials

For easy reference in the computer programs, each material is given an identification (ID) number. For elements the ID numbers are identical with atomic numbers (except for graphite which has ID number 906, to distinguish it from amorphous carbon with ID number 6).

Table 4 list the names and ID numbers of the 74 materials in the data files. The list includes 26 elements and 48 compounds and mixtures. A listing of ID numbers and names can also be displayed, and scrolled, on the monitor screen by running the program IDL. The information in the composition file UCOMP for each material consists of:

a) The atomic numbers and fractions by weight of the constituent atoms
b) The density of the material
c) The mean excitation energy of the material

A.2.5. Specification of Energies

A list of energies must be supplied at which stopping powers are to be calculated. This can be done in three ways:

a) A list of energies can be read from a default file ENG.PRO for protons (133 energies between 1 keV and 10,000 MeV) or from a default file ENG.ALF for helium ions (122 energies between 1 keV and 1000 MeV).

b) A list of energies can be read from a previously prepared file. The first line of this file must contain the number of energies in the list; subsequent lines must contain the energies (in MeV), separated by blanks.

c) The desired list of energies can be entered from the keyboard, in response to prompts from PSTAR or ASTAR.

A.2.6. Choice of Mean Excitation Energy

PSTAR and ASTAR display on the monitor screen the default I-value of the material, and prompt the user to indicate whether this value is acceptable. If the reply is negative, the program displays the three I-values for which stopping powers are available for interpolation: the default value I_{def}, $I_1 = I_{def}/1.1$ and $I_2 = 1.1\ I_{def}$. The user is then asked to specify the desired I-value, I_s. When making this choice, the user should keep in mind the cautionary remarks in Section A.2.2.4.

If I_s lies between I_1 and I_2, the program uses quadratic polynomial interpolation with respect to logI to determine the stopping power. If I_s is smaller than I_1 or larger than I_2, the program uses linear extrapolation with respect to logI. Extrapolation should of course be used with caution.

Table A.1. List of ID numbers and names of materials for which data are included in file UCOMP.

1	HYDROGEN
2	HELIUM
3	LITHIUM
4	BERYLLIUM
5	BORON
6	AMORPHOUS CARBON (density 2.0 g/cm^3)
7	NITROGEN
8	OXYGEN
9	FLUORINE
10	NEON
11	SODIUM
12	MAGNESIUM
13	ALUMINUM
14	SILICON
15	PHOSPHORUS
16	SULFUR
17	CHLORINE
18	ARGON
19	POTASSIUM
20	CALCIUM
21	SCANDIUM
22	TITANIUM
23	VANADIUM
24	CHROMIUM
25	MANGANESE
26	IRON
27	COBALT
28	NICKEL
29	COPPER
30	ZINC
31	GALLIUM
32	GERMANIUM
33	ARSENIC
34	SELENIUM
35	BROMINE
36	KRYPTON
37	RUBIDIUM
38	STRONTIUM
39	YTTRIUM
40	ZIRCONIUM
41	NIOBIUM
42	MOLYBDENUM
43	TECHNETIUM
44	RUTHENIUM
45	RHODIUM
46	PALLADIUM
47	SILVER
48	CADMIUM
49	INDIUM
50	TIN
51	ANTIMONY
52	TELLURIUM
53	IODINE
54	XENON
55	CESIUM
56	BARIUM
57	LANTHANUM
58	CERIUM
59	PRASEODYMIUM
60	NEODYMIUM
61	PROMETHIUM
62	SAMARIUM
63	EUROPIUM
64	GADOLINIUM
65	TERBIUM
66	DYSPROSIUM
67	HOLMIUM
68	ERBIUM
69	THULIUM
70	YTTERBIUM
71	LUTETIUM
72	HAFNIUM
73	TANTALUM
74	TUNGSTEN
75	RHENIUM
76	OSMIUM
77	IRIDIUM
78	PLATINUM
79	GOLD
80	MERCURY
81	THALLIUM
82	LEAD
83	BISMUTH
84	POLONIUM
85	ASTATINE
86	RADON
87	FRANCIUM
88	RADIUM
89	ACTINIUM
90	THORIUM
91	PROTACTINIUM
92	URANIUM
93	NEPTUNIUM
94	PLUTONIUM
95	AMERICIUM
96	CURIUM
97	BERKELIUM
98	CALIFORNIUM
99	A-150 TISSUE-EQUIVALENT PLASTIC
100	ACETONE
101	ACETYLENE
102	ADENINE
103	ADIPOSE TISSUE (ICRP)
104	AIR, DRY (NEAR SEA LEVEL)
105	ALANINE
106	ALUMINUM OXIDE
107	AMBER
108	AMMONIA
109	ANILINE
110	ANTHRACENE
111	B-100 BONE-EQUIVALENT PLASTIC
112	BAKELITE
113	BARIUM FLUORIDE
114	BARIUM SULFATE
115	BENZENE
116	BERYLLIUM OXIDE
117	BISMUTH GERMANIUM OXIDE
118	BLOOD (ICRP)
119	BONE, COMPACT (ICRU)
120	BONE, CORTICAL (ICRP)
121	BORON CARBIDE
122	BORON OXIDE
123	BRAIN (ICRP)
124	BUTANE
125	N-BUTYL ALCOHOL
126	C-552 AIR-EQUIVALENT PLASTIC
127	CADMIUM TELLURIDE
128	CADMIUM TUNGSTATE
129	CALCIUM CARBONATE
130	CALCIUM FLUORIDE
131	CALCIUM OXIDE
132	CALCIUM SULFATE
133	CALCIUM TUNGSTATE
134	CARBON DIOXIDE
135	CARBON TETRACHLORIDE
136	CELLULOSE ACETATE, CELLOPHANE
137	CELLULOSE ACETATE BUTYRATE
138	CELLULOSE NITRATE
139	CERIC SULFATE DOSIMETER SOLUTION
140	CESIUM FLUORIDE

Table A.1. (Continued)

141 CESIUM IODIDE
142 CHLOROBENZENE
143 CHLOROFORM
144 CONCRETE, PORTLAND
145 CYCLOHEXANE
146 1,2-DICHLOROBENZENE
147 DICHLORODIETHYL ETHER
148 1,2-DICHLOROETHANE
149 DIETHYL ETHER
150 N,N-DIMETHYL FORMAMIDE
151 DIMETHYL SULFOXIDE
152 ETHANE
153 ETHYL ALCOHOL
154 ETHYL CELLULOSE
155 ETHYLENE
156 EYE LENS (ICRP)
157 FERRIC OXIDE
158 FERROBORIDE
159 FERROUS OXIDE
160 FERROUS SULFATE DOSIMETER SOLUTION
161 FREON-12
162 FREON-12B2
163 FREON-13
164 FREON-13B1
165 FREON-1311
166 GADOLINIUM OXYSULFIDE
167 GALLIUM ARSENIDE
168 GEL IN PHOTOGRAPHIC EMULSION
169 Pyrex Glass
170 GLASS, LEAD
171 GLASS, PLATE
172 GLUCOSE
173 GLUTAMINE
174 GLYCEROL
175 GUANINE
176 GYPSUM, PLASTER OF PARIS
177 N-HEPTANE
178 N-HEXANE
179 KAPTON POLYIMIDE FILM
180 LANTHANUM OXYBROMIDE
181 LANTHANUM OXYSULFIDE
182 LEAD OXIDE
183 LITHIUM AMIDE
184 LITHIUM CARBONATE
185 LITHIUM FLUORIDE
186 LITHIUM HYDRIDE
187 LITHIUM IODIDE
188 LITHIUM OXIDE
189 LITHIUM TETRABORATE
190 LUNG (ICRP)
191 M3 WAX
192 MAGNESIUM CARBONATE
193 MAGNESIUM FLUORIDE
194 MAGNESIUM OXIDE
195 MAGNESIUM TETRABORATE
196 MERCURIC IODIDE
197 METHANE
198 METHANOL
199 MIX D WAX
200 MS20 TISSUE SUBSTITUTE
201 MUSCLE, SKELETAL (ICRP)
202 MUSCLE, STRIATED (ICRU)
203 MUSCLE-EQUIVALENT LIQUID, WITH SUCROSE
204 MUSCLE-EQUIVALENT LIQUID, WITHOUT SUCROSE
205 NAPTHALENE
206 NITROBENZENE
207 NITROUS OXIDE
208 NYLON, DU PONT ELVAMIDE 8062
209 NYLON, TYPE 6 AND TYPE 6/6
210 NYLON, TYPE 6/10
211 NYLON, TYPE 11 (RILSAN)
212 OCTANE, LIQUID
213 PARAFFIN WAX
214 N-PENTANE
215 PHOTOGRAPHIC EMULSION
216 PLASTIC SCINTILLATOR (VINYLTOLUENE BASED)
217 PLUTONIUM DIOXIDE
218 POLYACRYLONITRILE
219 POLYCARBONATE (MAKROLON, LEXAN)
220 POLYCHLOROSTYRENE
221 POLYETHYLENE
222 POLYETHYLENE TEREPHTHALATE (MYLAR)
223 POLYMETHYL METHACRALATE (LUCITE, PERSPEX)
224 POLYOXYMETHYLENE
225 POLYPROPYLENE
226 POLYSTYRENE
227 POLYTETRAFLUOROETHYLENE(TEFLON)
228 POLYTRIFLUOROCHLOROETHYLENE
229 POLYVINYL ACETATE
230 POLYVINYL ALCOHOL
231 BUTYRAL
232 POLYVINYL CHLORIDE
233 POLYVINYLIDENE CHLORIDE, SARAN
234 POLYVINYLIDENE FLUORIDE
235 POLYVINYL PYRROLIDONE
236 POTASSIUM IODIDE
237 POTASSIUM OXIDE
238 PROPANE
239 PROPANE, LIQUID
240 N-PROPYL ALCOHOL
241 PYRIDINE
242 RUBBER, BUTYL
243 RUBBER, NATURAL
244 RUBBER, NEOPRENE
245 SILICON DIOXIDE
246 SILVER BROMIDE
247 SILVER CHLORIDE
248 SILVER HALIDES IN PHOTOGRAPHIC EMULSION
249 SILVER IODIDE
250 SKIN (ICRP)
251 SODIUM CARBONATE
252 SODIUM IODIDE
253 SODIUM MONOXIDE
254 SODIUM NITRATE
255 STILBENE
256 SUCROSE
257 TERPHENYL
258 TESTES (ICRP)
259 TETRACHLOROETHYLENE
260 THALLIUM CHLORIDE
261 TISSUE, SOFT (ICRP)
262 TISSUE, SOFT (ICRU FOUR-COMPONENT)
263 TISSUE-EQUIVALENT GAS (METHANE BASED)
264 TISSUE-EQUIVALENT GAS (PROPANE BASED)
265 TITANIUM DIOXIDE
266 TOLUENE
267 TRICHLOROETHYLENE
268 TRIETHYL PHOSPHATE
269 TUNGSTEN HEXAFLUORIDE
270 URANIUM DICARBIDE
271 URANIUM MONOCARBIDE
272 URANIUM OXIDE
273 UREA
274 VALINE
275 VITON FLUOROELASTOMER
276 WATER, LIQUID
277 WATER VAPOR
278 XYLENE
906 GRAPHITE (density 1.7 g/cm^3)

Table A.2. Cutoff energies T_1 and T_2 used in combination of low-energy experimental and high-energy theoretical stopping powers for protons.

ID No.	T_1 (MeV)	T_2 (MeV)	ID No.	T_1 (MeV)	T_2 (MeV)
1	0.2	0.5	134	0.2	0.5
2	0.25	0.5	138	0.3	0.5
4	0.3	0.5	139	0.2	0.5
6	0.2	0.5	141	0.8	2.0
7,8	0.25	0.5	155,160,169	0.2	0.5
10,13	0.3	1.0	179	0.3	0.5
14	0.5	0.8	185,189	0.2	0.5
18	0.5	1.0	191	0.2	0.5
22	0.5	1.5	197	0.2	0.5
26,29	0.5	1.0	200	0.3	0.5
32,36	0.5	1.5	201,202,203,204	0.2	0.5
42,47	0.75	2.0	209,213	0.3	0.5
50	0.5	1.5	215	0.8	3.0
54,64	0.5	1.0	216,219,221,222	0.3	0.5
74,78 79	0.3	0.5	223	0.2	0.5
82	0.5	1.0	225,226	0.3	0.5
92	0.25	1.0	227,232,238	0.2	0.5
99	0.5	1.0	245	0.3	0.5
101	0.2	0.5	252	0.8	3.0
103	0.3	0.5	255	0.2	0.5
104,106	0.2	0.5	263,264,266	0.3	0.5
111,119,120	0.3	0.5	276	0.15	0.5
126	0.2	0.5	277	0.3	0.5
130	0.3	0.5			

Table A.3. Cutoff energies T_1 and T_2 used in combination of low-energy experimental and high-energy theoretical stopping powers for helium ions.

ID No.	T_1 (MeV)	T_2 (MeV)
1	1.0	2.0
2	1.5	3.0
4	1.0	4.0
6	1.0	3.0
7,8,10	1.0	2.0
13,14	2.0	4.0
18	0.8	3.0
22,26,29,32	2.0	6.0
36	3.0	7.0
42,47,50,54	2.0	5.0
64,74,78	1.0	3.0
79,82	1.0	2.0
92	1.0	4.0
99	1.0	2.0
101	1.0	3.0
103	0.8	2.0
104,106,111,119,120	1.0	2.0
126,130,134,138,139	1.0	3.0
141	1.0	5.0
155,160,159,179	1.0	2.0
185	1.0	3.0
189	0.8	2.0
191	1.0	2.0
197	0.6	2.0
200,201,202,203,204,209,213	1.0	2.0
215	0.6	5.0
216,219,221,222,223,225,226,227	1.0	2.0
232	1.0	4.0
238,245,252	1.0	2.0
255	1.0	3.0
263.264,266,276,277	1.0	2.0

Table A.4. List of ID numbers and names of materials for which codes PSTAR and ASTAR provide stopping powers and ranges.

1	HYDROGEN
2	HELIUM
4	BERYLLIUM
6	AMORPHOUS CARBON (density 2.0 g/cm^3)
7	NITROGEN
8	OXYGEN
10	NEON
13	ALUMINUM
14	SILICON
18	ARGON
22	TITANIUM
26	IRON
29	COPPER
32	GERMANIUM
36	KRYPTON
42	MOLYBDENUM
47	SILVER
50	TIN
54	XENON
64	GADOLINIUM
74	TUNGSTEN
78	PLATINUM
79	GOLD
82	LEAD
92	URANIUM
99	A-150 TISSUE-EQUIVALENT PLASTIC
101	ACETYLENE
103	ADIPOSE TISSUE (ICRP)
104	AIR, DRY (NEAR SEA LEVEL)
106	ALUMINUM OXIDE
111	B-100 BONE-EQUIVALENT PLASTIC
119	BONE, COMPACT (ICRU)
120	BONE, CORTICAL (ICRP)
126	C-552 AIR-EQUIVALENT PLASTIC
130	CALCIUM FLUORIDE
134	CARBON DIOXIDE
138	CELLULOSE NITRATE
139	CERIC SULFATE DOSIMETER SOLUTION
141	CESIUM IODIDE
155	ETHYLENE
160	FERROUS SULFATE DOSIMETER SOLUTION
169	Pyrex Glass
179	KAPTON POLYIMIDE FILM
185	LITHIUM FLUORIDE
189	LITHIUM TETRABORATE
191	M3 WAX
197	METHANE
200	MS20 TISSUE SUBSTITUTE
201	MUSCLE, SKELETAL (ICRP)
202	MUSCLE, STRIATED (ICRU)
203	MUSCLE-EQUIVALENT LIQUID, WITH SUCROSE
204	MUSCLE-EQUIVALENT LIQUID, WITHOUT SUCROSE
209	NYLON, TYPE 6 AND TYPE 6/6
213	PARAFFIN WAX
215	PHOTOGRAPHIC EMULSION
216	PLASTIC SCINTILLATOR (VINYLTOLUENE BASED)
219	POLYCARBONATE (MAKROLON, LEXAN)
221	POLYETHYLENE
222	POLYETHYLENE TEREPHTHALATE (MYLAR)
223	POLYMETHYL METHACRALATE (LUCITE, PERSPEX, PLEXIGLAS)
225	POLYPROPYLENE
226	POLYSTYRENE
227	POLYTETRAFLUOROETHYLENE(TEFLON)
232	POLYVINYL CHLORIDE
238	PROPANE
245	SILICON DIOXIDE
252	SODIUM IODIDE
255	STILBENE
263	TISSUE-EQUIVALENT GAS (METHANE BASED)
264	TISSUE-EQUIVALENT GAS (PROPANE BASED)
266	TOLUENE
276	WATER, LIQUID
277	WATER VAPOR
906	GRAPHITE (density 1.7 g/cm^3)

REFERENCES

[1] International Commission on Radiation Units and Measurements, ICRU Report 37, *Stopping Powers for Electrons and Positrons*, 1984.

[2] International Commission on Radiation Units and Measurements, ICRU Report 49, *Stopping Powers and Ranges for Protons and Alpha Particles*, 1993.

[3] M. J. Berger, *ESTAR, PSTAR and ASTAR: Computer Codes for Calculating Stopping Power and Range Tables for Electrons, Protons and Helium Ions*, National Institute of Standards and Technology Report NISTIR 4999, 1992.

[4] V. Necas, W. Käferbock, W. Rossler and P. Bauer, Nucl. Inst. Meth. B, in press.

[5] H. Bethe, Ann. d. Physik **5**, 325, 1930.

[6] H. Bethe, Z. Phys. 76, **293**, 1932.

[7] R. M. Sternheimer, Phys.Rev. **88**, 851, 1952.

[8] R. M. Sternheimer, S. M. Seltzer, and M. J. Berger, Phys. Rev. B. **26**, 6067, 1982.

[9] S. M. Seltzer and M. J. Berger, Nucl. Instr. Meth. **B12**, 95, 1985.

[10] R. H. Pratt, H. K. Tseng, C. M. Lee, L. Kissel, C. MacCallum, and M. Riley, Atomic Data Nucl. Data Tables **20**, 175, 1977. Errata in **26**, 477, 1981.

[11] H. Bichsel, Phys. Rev. A, **46**, 5761, 1992.

[12] J. C. Ashley, R. H. Ritchie and W. Brandt, Phys. Rev. B, **5**, 2393, 1972.

[13] J. C. Ashley, R. H. Ritchie and W. Brandt, Phys. Rev. A, **8**, 2402, 1973.

[14] H. Bichsel, Phys. Rev. A, **41**, 3642, 1990.

[15] H. H. Andersen, *Bibliography and Index of Experimental Stopping Power and Range Data*, Pergamon Press (Elmsford, N.Y.), 1977.

[16] D. Powers, *Topical Survey of the Literature on Experimental and Theoretical Stopping Power Phenomena for Energetic Protons, Helium Ions, and Heavy Ions in Matter for the Period 1977-1987*, Internal Report, Department of Physics, Baylor University, Waco, Texas, 1988.

[17] C. Varelas and J. Biersack, Nucl. Instr. Meth. **79**, 213, 1970.

[18] H. H. Andersen and J. F. Ziegler, *Hydrogen: Stopping Powers and Ranges in All Elements*, Pergamon Press (Elmsford, N.Y.), 1977.

[19] J. F. Ziegler, *Helium: Stopping Powers and Ranges in All Elemental Matter*, Pergamon Press (Elmsford, N.Y.), 1977.

[20] D. E. Watt, *Stopping Cross Sections, Mass Stopping Powers and Ranges in 30 Elements for Alpha Particles (1 keV to 100 MeV)*, Internal Report, Department of Physics and Astronomy, University of St. Andrews, Scotland, 1988.

[21] D. Powers, *Stopping Cross Sections and Ranges of Alpha Particles in Matter*, Internal Report, Department of Physics, Baylor University, Waco, Texas, 1977.

[22] E. Everhart, G. Stone, and R. J. Carbone, Phys. Rev. **99**, 1287, 1955.

[23] G. Molière, Z. f. Naturf. **2a**, 133, 1947.

[24] J. F. Ziegler, J. P. Biersack and U. Littmark, *The Stopping and Range of Ions in Solids*, Pergamon Press (Elmsford, N.Y.), 1985.

[25] H. W. Lewis, Phys. Rev. **78**, 526, 1950.

SUBJECT INDEX

LIST OF CRP MEMBERS AND CONSULTANTS

Dr. M.J. Berger
Center for Radiation Research
Div. 846
National Institute of Standards
and Technology (NIST)
Gaithersburg, MD 20899, U.S.A.
Tel.: 301-975-5551
Fax: 301-656-8331

Dr. H. Bichsel *(Consultant)*
1211 22nd Avenue East
Seattle, Washington 98112-3534
U.S.A.
Tel.: 206-329-2792
Fax: 206-685-4634
E-mail: BICHSEL@
NPL.NPL.WASHINGTON.EDU

Dr. D.T. Goodhead
Medical Research Council
Radiobiology Unit
Chilton, Didcot OX11ORD
United Kingdom
Tel.: 44-235-834393
Fax: 44-235-834776

Professor Y. Hatano
Department of Chemistry
Faculty of Science
Tokyo Institute of Technology
Ohkayama 2-21-1, Meguro-ku
Tokyo 152, Japan
Tel.: 81-3-3726-1111
Fax: 81-3-3729-0099
E-mail: YHATANO@CHEM.TITECH.AC.JP

Dr. Z. Herman
J. Heyrovsky Institute of Physical
Chemistry and Electrochemistry
Dolejskova 3, 182 23 Prague
The Czech Republic
Tel.: 42-2-858-3751 or 42-2-815-3514
Fax: 42-2-858-2307
E-mail: HERMAN@CSPGAS11

Dr. M. Inokuti
Argonne National Laboratory
9700 S. Cass Avenue, Bldg. 203
Argonne, IL 60439, U.S.A.
Tel.: 708-252-4186
Fax: 708-252-7415
E-mail: B10757@ANLVM

Dr. I.G. Kaplan
Instituto de Física
Universidad Nacional Autónoma
de México
Apdo. Postal 20-364
01000 México, D.F.
Tel.: 525-622-5014 to 17

Dr. N.P. Kocherov
Nuclear Data Section
International Atomic Energy Agency
Wagramerstrasse 5, P.O. Box 100
A-1400 Vienna, Austria
Tel.: 43-1-2360-1718
Fax: 43-1-234564
E-mail: RNC@IAEA1 or
KOCHEROV@IAEAND.IAEA.OR.AT

Dr. I. Krajcar-Bronić *(Consultant)*
Rudjer Bosković Institute
Bijenicka 54
41001 Zagreb, Croatia
Tel.: 38-41-424-239
Fax: 38-41-434-467 or 425-497
E-mail: INES.KRAJCAR@IRB.AC.MAIL.YU
or KRAJCAR@OLIMP.IRB.HR

Professor T.D. Märk
Institut für Ionenphysik
der Universität Innsbruck
Technikerstrasse 25
A-6020 Innsbruck, Austria
Tel.: 43-512-218-5124
Fax: 43-512-218-5032
E-mail: TILMANN.MAERK@UIBK.AC.AT

Dr. H.G. Paretzke
GSF-Forschungszentrum für
Strahlenschutz und Umweltforschung
Ingolstädter Landstrasse 1
D-85758 Oberschleissheim
Germany
Tel.: 49-89-31870-4006
Home: 49-89-916984
Fax: 49-89-3187-3323
E-mail: PARETZKE@GSF.DE

Professor H. Paul
Institut für Experimentalphysik
der Universität Linz
Abteilung Atom- und Kernphysik
Altenbergerstrasse 69
A-4040 Linz, Austria
Tel.: 43-732-2468-508
Fax: 43-732-2468-10
E-mail: K340570@ALIJKU11

Dr. P. Pihet *(Consultant)*
Institut de Protection et Sûreté Nucléaires
B.P. 6
F-92265 Fontenay aux Roses Cedex
France
Tel.: 33-1-46-54-9121
Fax: 33-1-47-46-9777

Professor L. Sanche
Faculty of Medicine
University of Sherbrooke
Stoke Road
Sherbrooke, Quebec JIH 5N4
Canada
Tel.: 819-563-5555 ext. 4678
Home: 819-562-4236
Fax: 819-564-5442
E-mail: QAAB@UDESVM

Dr. D. Srdoč
Safety & Environmental Protection
Bldg. 535A
Brookhaven National Laboratory
Upton, N.Y. 11973, U.S.A.
Tel.: 516-282-5641
Home: 516-345-6947
Fax: 516-282-5773
E-mail: SRDOC@SEP2.SEP.BNL.GOV

Dr. M. Terrissol
Centre de Physique Atomique
Université Paul Sabatier
118 Route de Narbonne
F-31062 Toulouse, France
Tel.: 33-6155-6851
Fax: 33-6155-6332
E-mail: MICHEL@CPA20.UPS-TLSE.FR

Dr. L.H. Toburen
Board on Radiation Effects, NAS-342
National Academy of Sciences
2101 Constitution Avenue, NW
Washington, DC 20418, U.S.A.
Tel.: 202-334-3163
Fax: 202-334-1639
E-mail: LTOBUREN@NAS

Professor E. Waibel *(Consultant)*
Physikalisch-Technische Bundesanstalt
Gruppe 6.1, Bundesallee 100
D-38116 Braunschweig, Germany
Tel.: 49-0531-592-6100
Home: 49-05341-26876
Fax: 49-0531-592-4006

Professor A. Wambersie *(Consultant)*
Unité de Radiothérapie
Neutron- et Curiethérapie
Cliniques Universitaires St. Luc
UCL 10/4752
1200 Brussels, Belgium
Tel.: 32-2-764-1111/4726
Fax: 32-2-764-3703

95-00805

QUESTIONNAIRE ON IAEA-TECDOCs

It would greatly assist the International Atomic Energy Agency in its analysis of the effectiveness of its Technical Document programme if you could kindly answer the following questions and return the form to the address shown below. Your co-operation is greatly appreciated.

Title: **Atomic and molecular data for radiotherapy and radiation research**
Number: **IAEA-TECDOC-799**

1. How did you obtain this TECDOC?

[ ] From the IAEA:
  [ ] At own request
  [ ] Without request
  [ ] As participant at an IAEA meeting
[ ] From a professional colleague
[ ] From library

2. How do you rate the content of the TECDOC?

[ ] Useful, includes information not found elsewhere
[ ] Useful as a survey of the subject area
[ ] Useful for reference
[ ] Useful because of its international character
[ ] Useful for training or study purposes
[ ] Not very useful. If not, why not?

3. How do you become aware of the TECDOCs available from the IAEA?

[ ] From references in:
  [ ] IAEA publications
  [ ] Other publications
[ ] From IAEA meetings
[ ] From IAEA newsletters
[ ] By other means (please specify)
[ ] If you find it difficult to obtain information on TECDOCs please tick this box

4. Do you make use of IAEA-TECDOCs?

[ ] Frequently
[ ] Occasionally
[ ] Rarely

5. Please state the institute (or country) in which you are working:

Please return to:
R.F. Kelleher
Head, Publishing Section
International Atomic Energy Agency
P.O. Box 100
Wagramerstrasse 5
A-1400 Vienna, Austria